



ExHFT-10

10th World Conference on Experimental Heat
Transfer, Fluid Mechanics and Thermodynamics

BOOK OF ABSTRACTS



August, 26-30 2024

RHODES ISLAND, GREECE





Committees

ASSEMBLY

J. Barbosa (BRA)

G. Celata (ITA, vice-president)

C. van der Geld (NLD, president)

Jungho Kim (USA)

S. Maruyama (JPN)

P. Stephan (DEU)

LOCAL ORGANIZING COMMITTEE

Chairman

Prof. Theodoros Karapantsios Aristotle University of Thessaloniki, Greece

Committee

Prof. Margaritis Kostoglou, Aristotle University of Thessaloniki, Greece

Dr. Ourania Oikonomidou, Aristotle University of Thessaloniki, Greece

Ms. Nikoleta Chatzipapa, Aristotle University of Thessaloniki, Greece

SCIENTIFIC ORGANIZING COMMITTEE

Adrian R., U.S.A.

Barbosa J., Brazil

Bontozoglou V., Greece

Borges E.T., Portugal

Celata G.P., Italy

Cheng L., U.K.

Clausse A., Argentina

Coelho P., Portugal

Colin C., France

De Paepe M., Belgium

Di Marco P., Italy

Franklin E., Brazil

Garimella Srinivas, U.S.A.

Garimella Suresh, U.S.A.

Glezer A., U.S.A.

Guo L., China

Hewakandamby B., U.K.

Hwang Y., U.S.A.

Iwai H., Japan

Jacobi A.M., U.S.A.

Kandlikar S.G., U.S.A.

Karapantsios T., Greece

Kim J., U.S.A.

Kostoglou M., Greece

Liang X.G., China

Luke A., Germany

Markides C., U.K.

Maruyama S., Japan

Mewes D., Germany

Meyer J.P., South Africa

Morini G.L., Italy

Murata A., Japan

Nowak A.J., Poland

Palm B., Sweden

Patterson J., Australia

Pinho F.T., Portugal

Pollard A., Canada

Poulikakos D., Switzerland

Revellin R., France

Ribatski G., Brazil

Saha S.K., India

Sefiane K., U.K.

Simon T.W., U.S.

Skiepko T., Poland

Stephan P., Germany

Suga K., Japan

Sundén B., Sweden

Szmyd J., Poland

Tao W.Q., China

Thome J.R., Switzerland

Tomiyama A., Japan

van der Geld C.W.M., Netherlands

Vasiliev L., Belarus

Westerweel J., Netherlands

Yanagihara J.I., Brazil

Zubair S.M., Saudi Arabia

ABSTRACTS

HEAT TRANSFER AND FLUID FLOW IN PDMS NANOCOMPOSITE MICRO-PIN FIN HEAT SINKS

Elaine Maria Cardoso^{a,b,*}, Reinaldo Rodrigues de Souza^c, Raíssa Guimarães Mendonça Correa^b, Utsab Banerjee^d, Sushanta K. Mitra^d

^aUNESP - São Paulo State University, School of Engineering, Av. Brasil, 56, Ilha Solteira, SP 15385-000, Brazil.

^bUNESP - São Paulo State University, School of Engineering, São João da Boa Vista, Brazil.

^cIN+, Center for Innovation, Technology and Policy Research, Instituto Superior Técnico, Universidade de Lisboa, Av. Rovisco Pais, 1049-001 Lisboa, Portugal

^dMicro & Nano-Scale Transport Laboratory, Waterloo Institute for Nanotechnology, Department of Mechanical and Mechatronics Engineering, University of Waterloo, Waterloo, Ontario, Canada N2L 3G1.

*corresponding author: elaine.cardoso@unesp.br

Keywords: micro-pin fin array, nanoPDMS, heat transfer, pressure drop

1. INTRODUCTION

Industries such as energy, automotive, chemical engineering, and other critical sectors rely on more efficient heat exchangers. One viable option that could potentially enhance heat transfer is the utilization of micro-pin fin arrays with dimensions ranging from tens to hundreds of micrometers. The distinct flow disruptions created by these separated pin fins contribute to enhanced flow mixing, modified pressure drop, and increased heat exchange area (Mohammadi and Koşar, 2018; Alihosseini et al., 2020).

Polydimethylsiloxane (PDMS), an elastomer characterized by its lightweight and corrosion resistance, is an alternative for thermal management materials due to its flexibility and compressibility (Wei et al., 2020). Despite PDMS's relatively low thermal conductivity, incorporating materials with enhanced thermal properties, such as graphene and metal oxide nanoparticles (Long and Wang, 2021), could mitigate this drawback.

Incorporating thermally conductive materials into the PDMS matrix has been suggested to enhance the thermal properties of the resulting composites even at very low concentrations. Han et al. (2020) explored a polymer assembly approach to construct a 3D graphene architecture integrated into a PDMS composite. The introduction of graphene foam resulted in a composite with a thermal conductivity 22% higher than pure PDMS at a concentration of 0.7 wt%. Timbs et al. (2021) conducted experiments to assess the heat dissipation performance of 3D printed heat sinks using carbon-filled polymer and two commercially available metal-based filaments (copper and bronze). The carbon-filled polymer heat sink exhibited significantly superior heat dissipation capabilities.

Recently, Fakiridis et al. (2023) investigated the impact of incorporating graphene nanoplatelets (GNPs) and hexagonal boron nitride (hBN) into a PDMS matrix to enhance its thermal and mechanical properties for application as thermal interface materials (TIMs). Combining 10 wt% GNPs and 40 wt% hBN with PDMS resulted in TIMs exhibiting a thermal conductivity of 1.24 W/m·K, *i.e.*, a substantial 519% increase compared to the pure PDMS matrix.

Achieving favorable thermophysical and mechanical properties in PDMS composites remains a challenge. While carbon fillers exhibit superior thermal conductivity compared to other fillers, their costly manufacturing processes limit their suitability for industrial applications. On the other hand, metal fillers offer appreciable thermal properties but may result in high-density composites. This way, hexagonal boron nitride (hBN) has low density, high thermal conductivity, and resistance to high temperatures, making it ideal for application in cooling systems.

In this context, the current work introduces a method to improve the thermal conductivity of a PDMS micro-pin fin heat sink matrix for an enhanced heat exchange by incorporating thermally conductive nanoparticles, namely hexagonal boron nitride (hBN) at a concentration of 20 wt%. The present study tested two heat sink arrays — one in-line diamond micro-pin fin and another staggered diamond micro-pin fin. Experimental measurements were conducted to understand the thermal and hydraulic performance of microfluidic systems, investigating the heat transfer coefficient and pressure drop behavior for the single-phase flow of DI water.

2. MATERIALS AND METHOD

Figure 1 shows the schematic drawing containing its main components. Two absolute pressure transducers (with an accuracy of $\pm 2\%$ FS) were used to measure the inlet and outlet pressures. Power was supplied to a microheater using a DC power supply. The microheater (IST AG, 10 W/12 V) was integrated into the PDMS or PDMS nanocomposite 1 mm away from the side wall of the micro-pin fins. The working fluid (DI water) was circulated using a syringe pump (Chemix, Fusion 100-X). A data acquisition system (DATAQ DI-245) was used to acquire all signals.

The polydimethylsiloxane (pure PDMS or PDMS/hBN nanocomposite) test section with dimensions of 27.5 mm x 57.5 mm x 7.5 mm, was integrated onto a microscopic glass slide of 1 mm thickness. An IR camera (FLIR A400 IR) was used to measure the wall temperature. The glass surface was coated with black paint (Acktar black coating), and the surface emissivity was adjusted before conducting temperature measurements.

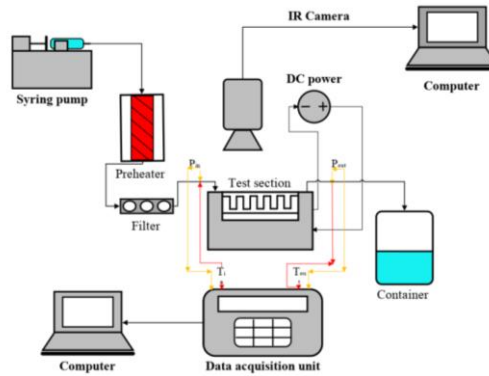


Figure 1. Schematic drawing of the experimental setup.

The micro-pin fin heat sink comprises a 20 x 15 mm footprint with 285 square cross-section micro-pin fins (0.5 mm length, 0.5 mm height, and 0.5 mm inter-fin space). These dimensions were determined by the geometry of the deposited filament and the characteristics of the 3D printer (Formlabs) used to fabricate the transparent resin mold.

The PDMS base and curing agent (SYLGARD™ 184, Dow Corning) were mixed at a weight ratio 10:1 and degassed inside the desiccator to eliminate trapped air bubbles. The PDMS mixture was then poured onto the mold and cured in an oven at 80 °C for 120 min. The substrate was allowed to cool down for 30 min before being removed from the mold. Adhesion between the PDMS and the glass was achieved through oxygen plasma pre-treatment.

For the fabrication of the PDMS/hBN nanocomposite heat sink, hexagonal boron nitride nanoparticles (~700 W/m·K, 99.5%, average diameter < 100 nm) were purchased from SkySpring Nanomaterials, Inc. The desired mass percentage of hBN nanoparticles was added into the PDMS matrix (20 wt%) and manually stirred for 10 min, followed by a shaker at a speed of 2000 rpm for 20 min. Then, the curing agent was added to the mixture to form a 10:1 ratio. The centrifuge stirred the sample at a speed of 2000 rpm for 10 minutes and then degassed for 30 minutes using a desiccator. The PDMS/hBN nanocomposite was poured onto the mold and cured in an oven for 120 min.

In order to obtain the thermal properties, the thermal conductivity, thermal diffusivity, and specific heat were measured by Hot Disk Thermal Constant Analyzer, TPS 2500S (Souza et al., 2023). Pure PDMS presents a thermal conductivity of 0.20 W/m·K. In contrast, the thermal conductivity of the PDMS/hBN nanocomposite sample increased to 0.48 W/m·K, representing a 140% enhancement compared to pure PDMS.

For single-phase flow tests, volumetric flow rates of 5, 10, 15, and 20 ml/min were analyzed with a power input of 6 W to heat the sample. The temperature in the inlet plenum was maintained at ~22 °C during all the tests. Experimental data were acquired after the system reached the steady-state regime, characterized by temperature measurement variations lower than the experimental uncertainties for 5 min. As thermal images were obtained using the infrared camera, temperatures were recorded at 30 fps, and the last 200 points recorded at steady-state were considered.

The heat loss was, on average, 15% over varied parameters; and, the experimental uncertainty was calculated using the Python free package Uncertainties (© 2010–2019, EOL), based on the Taylor series method. The effective heat flux and heat transfer coefficient uncertainty were 4.5% and 5%, respectively.

3. RESULTS AND DISCUSSION

An increase in the volumetric flow rate consistently reduces the average surface temperature, indicating enhanced heat dissipation from the heat sink. A lower T_s confirms that it has dissipated more heat, thereby revealing superior heat transfer capabilities. Therefore, the staggered configuration may be more effective in promoting heat transfer, although it comes with a higher pressure drop (an average of 13%) due to the complexity of the flow. The more complex flow pattern formed by the staggered micro-pin fins can result in vortices that enhance fluid mixing, potentially leading to improved heat transfer compared to an array of aligned micro-pin fins.

Given that the staggered diamond micro-pin fins array showed superior results in terms of thermal performance, this configuration was selected to analyze the influence of incorporating hexagonal boron nitride (hBN) nanoparticles at 20 wt% in the PDMS matrix. Figure 2 depict the heat transfer behavior and the pressure drop for the PDMS/hBN nanocomposite compared to pure PDMS (in-line and staggered arrays).

One may observe that the augmentation in the thermal conductivity of the PDMS/hBN nanocomposites leads to an HTC enhancement (an average of 25.2% compared to the pure PDMS staggered micro-pin fin and 41.5% higher than the pure PDMS in-line micro-pin fin heat sink). Regarding pressure drop, no significant difference is observed between the pure PDMS and PDMS/hBN nanocomposite for the staggered micro-pin fins array. Therefore, the array configuration appears to be the primary factor influencing the difference in pressure drop among the micro-pin fins heat sinks analyzed in this study.

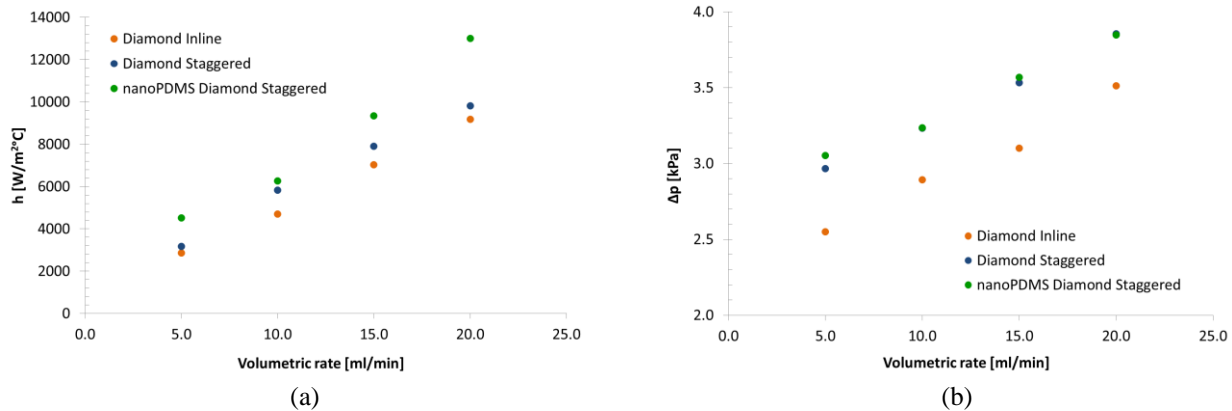


Figure 2. Heat transfer coefficient (a) and pressure drop (b) behavior for PDMS/hBN staggered micro-pin fin array compared to the pure PDMS configurations.

To assess how thermal and hydraulic performances vary for different micro-pin fin materials and configurations and Reynolds number ranges, the Thermal Performance Index (TPI), based on pure PDMS in-line diamond micro-pin fins was analyzed. The PDMS/hBN staggered micro-pin fin configuration demonstrates the highest TPI (~ 4) across the Reynolds number range. This indicates that incorporating hexagonal boron nitride nanoparticles can result in a well-dispersed and optimized microstructure within the nanocomposite material.

4. CONCLUSIONS

In this study, an experimental analysis of single-phase flow behavior in different polymer micro-pin fin arrays was conducted within a low Reynolds number range ($10 < Re < 100$). Additionally, to improve the thermal conductivity of the PDMS micro-pin fin heat sink matrix, hexagonal boron nitride (hBN) at 20 wt% was incorporated. Based on the obtained results, the following conclusions are drawn:

- ✓ The pure PDMS heat sink with in-line diamond micro-pin fins exhibits a higher surface temperature (up to 5.5%) than the configuration with staggered micro-pin fins.
- ✓ Staggered micro-pin fins create a more complex flow pattern, with vortices enhancing fluid mixing and potentially leading to improved heat transfer compared to an array of aligned micro-pin fins.
- ✓ The heat sink featuring staggered micro-pin fins exhibits the highest pressure drop, 13% higher than the aligned micro-pin fin array, due to the introduction of more disturbances and obstructions in the flow path.
- ✓ In the PDMS/hBN nanocomposite, the augmentation in thermal conductivity leads to an enhancement in the HTC (~ 34%) compared to the pure PDMS staggered and in-line micro-pin fin heat sinks.
- ✓ No significant difference in pressure drop is observed between pure PDMS and PDMS/hBN nanocomposite for the staggered micro-pin fins array, suggesting that array configuration is the primary factor influencing the difference in pressure drop among the micro-pin fins heat sinks.
- ✓ The PDMS/hBN staggered micro-pin fin configuration demonstrates the highest TPI across the Reynolds number range, suggesting that the incorporation of hexagonal boron nitride nanoparticles results in a well-dispersed and optimized microstructure within the nanocomposite material, providing an effective solution for thermal cooling.

5. REFERENCES

- Alihosseini Y, Targhi MZ, Heyhat MM, Ghorbani N.. Effect of a micro heat sink geometric design on thermo-hydraulic performance: A review. *Applied Thermal Engineering*, 170, 114974, 2020.
- Fakiridis S, Hodge AS, Karagiannidis PG. Thermal interface materials with hexagonal boron nitride and graphene fillers in PDMS matrix: thermal and mechanical properties. *Energies* 16, 2522, 2023.
- Han B, Chen H, Hu T, Ye H, Xu L. High electrical conductivity in polydimethylsiloxane composite with tailored graphene foam architecture. *Journal of Molecular Structure*, 1203, 127416, 2020.
- Long L, Wang L. Structured Polydimethylsiloxane (PDMS) Composite with enhanced thermal and radiative properties for heat dissipation. *Journal of Enhanced Heat Transfer*, v. 28, n. 4, 2021.
- Mohammadi A, Koşar A. Review on heat and fluid flow in micro pin fin heat sinks under single-phase and two-phase flow conditions. *Nanoscale and Microscale Thermophysical Engineering*, v. 22, n. 3, p. 153-197, 2018.
- Souza RR, Barbosa FS, Nobrega G, Cardoso EM, Teixeira JCF, Moita AS, Lima R. An innovative PDMS cell to improve the thermal conductivity measurements of nanofluids. *Thermal Science and Engineering Progress*, 42, 101926, 2023.
- Timbs K, Khatamifar M, Antunes E, Lin W. Experimental study on the heat dissipation performance of straight and oblique fin heat sinks made of thermal conductive composite polymers. *Thermal Science and Engineering Progress*, 22, 100848, 2021.
- Wei J, Liao M, Ma A, Chen Y, Duan Z, Hou X, et al. Enhanced thermal conductivity of polydimethylsiloxane composites with carbon fiber. *Compos Commun* 2020;17:141–6.

©Copyright 2010–2019 *Uncertainties: a Python package for calculations with uncertainties*, Eric O. LEBIGOT.

Initial Investigation of the Performance of a Transcritical CO_2 Vortex Tube

Ahmed Mansour^{a,*}, Raphaël Oberti^a, Hakim Nesreddine^b, Dominique Monney^c, Sébastien Poncet^a

^aDepartment of Mechanical Engineering, Université de Sherbrooke, 2500 boulevard de l'Université, Sherbrooke (QC), J1K 2R1, Canada

^bLaboratoire des Technologies de l'Énergie, Hydro-Québec, 600 rue de la montagne, Shawinigan (QC), G9N 7N5, Canada

^c Copeland, 145 Sherwood Dr, Brantford (ON), N3T 5S7, Canada

* ahmed.mansour@USherbrooke.ca

Keywords: vortex tube, carbon dioxide, transcritical condition, experimental measurement

1. INTRODUCTION

This abstract outlines the development of an experimental test bench designed to assess the efficiency of a vortex tube operating in transcritical carbon dioxide (CO_2) conditions. The counter-flow vortex tube (Fig. 1) is a device characterized by its simplicity. Typically, it includes inlet tangential nozzles, a vortex generator, a cold exit, a hot tube, and a flow regulator. The inlet flow expands through the inlet nozzles, dividing into two streams. One stream, typically with higher enthalpy, exits along the hot tube periphery, while the other, with lower enthalpy, exits through the vortex tube's core and emerges from the cold exit. In this work, the vortex tube is subjected to testing within a closed-cycle configuration to emulate the conditions of a heat pump. To the best of the authors' knowledge, no prior investigations into vortex tubes under such conditions have been conducted. However, a few studies are briefly discussed here that can have a relevance to the topic of this abstract.

Collins and Lovelace (1979) investigated the impact of two-phase propane on the degradation of vortex tube performance. Their findings revealed that when the inlet flow mass quality exceeds 0.8, a distinct temperature separation can still be sustained. Conversely, when the quality drops below 0.8, the performance experiences significant deterioration, primarily attributed to a substantial decrease in the hot exit temperature. Mansour *et al.* (2022) formulated a thermodynamic model to mainly assess the exit characteristics of a vortex tube functioning with CO_2 under non-ideal conditions. Through validation using experimental data involving air, R134a, and CO_2 , Mansour demonstrated that the model exhibited a maximum error of only 3.9% in predicting the exit temperatures. Liu *et al.* (2019) conducted a theoretical analysis of a basic heat pump incorporating a vortex tube using the Maurer cycle (Maurer and Zinn, 1999)]. Specifically, at a defined operating condition with a discharge pressure of 90 bar and an inlet temperature of 45 °C, they achieved a noteworthy 33% improvement in Coefficient of Performance (COP) compared to a conventional heat pump cycle. Additionally, their findings indicated that raising the cold mass fraction in the vortex tube led to an improvement in COP by up to 10%.

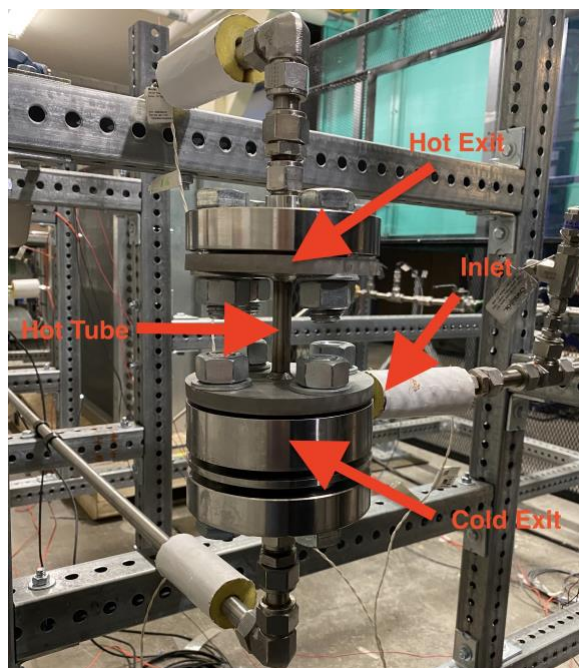


Figure 1. The vortex tube used in the testing.

2. METHODOLOGY

In this section, a short explanation of the cycle used to test the vortex tube is introduced. As depicted in Fig. 2, the cycle closely resembles a typical heat pump cycle with a few modifications. The CO₂ undergoes compression by compressor and subsequently undergoes cooling through a gas cooler, facilitating control over the inlet temperature to the vortex tube. Subsequently, the flow passes through either an expansion valve to control the inlet pressure or a bypass tubing to maintain a similar compressor discharge pressure. Afterwards, the CO₂ enters the vortex tube to undergo separation into two distinct flows. Each flow is subjected to a back-pressure valve after the vortex tube, enabling control over exit pressures and the mass flowrates of both streams getting out of the vortex tube. The two flows are then blended in a mixing connector before passing through a coil of tubes enveloped by electric heaters. These heaters serve the purpose of evaporating any liquid CO₂ before the compressor.

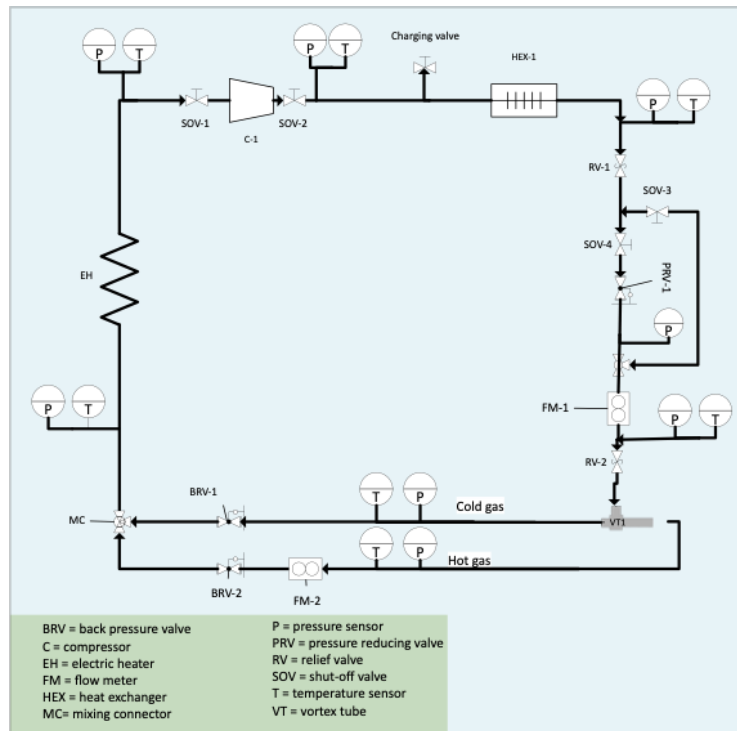


Figure 2. Developed closed cycle for testing the vortex tube.

3. RESULTS

In this section, a selection of the results produced by the setup is presented. Table 1 displays the inlet conditions (T_{in} = inlet temperature, P_{in} = inlet pressure, \dot{m}_{in} = inlet mass flowrate, P_{in}/P_c = ratio of inlet to cold exit pressures, μ_c = cold mass fraction) utilized for investigating the impact of the inlet mass flowrate on both hot and cold exit temperatures for two cases: transcritical and subcritical pressures. The variation in mass flowrate is also accompanied by adjustments in inlet pressure to examine the combined effects of these parameters.

First of all, the influence of the inlet mass flowrate at transcritical conditions is examined. The mass flowrate is manipulated by adjusting the charge of the closed system, with tested rates of 0.084 kg/s and 0.117 kg/s, comparable to charges of 2.1 kg and 2.6 kg, respectively. Table 2 illustrates the hot (T_h) and cold (T_c) exit temperatures and temperature separation (ΔT_{h-c}) of the vortex tube for the tested inlet mass flowrates under inlet pressures of 78, 80, and 82 bar. Notably, with an increase in flowrate, both exit temperatures exhibit a significant decrease, with the cold exit temperature dropping by at least 11% and the hot exit temperature by 9.5%. The elevation in mass flowrate corresponds to a subsequent increase in the flow density. This rise in density may offer an explanation for the observed reduction in temperatures as the mass flow rate increases. The second notable observation derived from the table is the relatively substantial increase in temperature separation with the inlet mass flowrate. For inlet pressure of 78 bar, the augmentation in temperature separation from 0.084 kg/s to 0.117 kg/s is nearly threefold, while for inlet pressure of 80 bar, it rises to almost 3.1 times, and for inlet pressure of 82 bar, it reaches approximately 2.9 times. Importantly, it is evident that the inlet pressure does not exert a significant impact on temperature separation.

In this concluding paragraph, attention is directed towards examining the utilization of subcritical inlet pressures and discerning any notable distinctions compared to the transcritical pressures discussed earlier. Furthermore, the impact of

the inlet mass flowrate is showcased. Table 1 outlines the system's input parameters for investigating mass flowrate variations at subcritical inlet pressures. Concurrently, Table 2 illustrates the consequential effects on hot and cold exit temperatures, as well as temperature separation. Similar to the observations in the transcritical case, analogous phenomena occur at subcritical inlet pressures compared to transcritical pressures. The increase in mass flowrate from 0.08 kg/s to 0.11 kg/s induces a reduction in both exit temperatures. Additionally, this elevation in mass flowrate contributes to an augmentation in temperature separation. Specifically, for inlet pressure of 67 bar, the increase in the temperature separation from 0.08 kg/s to 0.11 kg/s is nearly 2.3 times; for inlet pressure of 69 bar, it rises to almost 3 times; for inlet pressure of 71 bar, it reaches approximately 3.3 times, and finally, for inlet pressure of 73 bar, it is 2.4 times.

Regardless of the regime in which the operating conditions are within, the temperature separation in general is very poor alternating around only 1 °C, registering a maximum of only 1.18 °C at an inlet pressure of 80 bar.

Table 1. Input operating conditions of the system for transcritical and subcritical cases.

Case	T_{in} (°C)	P_{in} (bar)	\dot{m}_{in} (kg/s)	P_{in}/P_c (-)	μ_c (-)
Transcritical	47.2	78, 80, 82	0.084, 0.117	1.08-1.18	0.5
Subcritical	36.5	67, 69, 71, 73	0.08, 0.11	1.08-1.19	0.5

Table 2. Results comparison in terms of inlet mass flowrate on temperature separation of the vortex tube at transcritical and subcritical inlet pressures.

P_{in} (bar)	T_h (°C)	T_c (°C)	ΔT_{h-c} (°C)	T_h (°C)	T_c (°C)	ΔT_{h-c} (°C)
Transcritical	0.084 (kg/s)			0.117 (kg/s)		
78	44.41	44.04	0.37	39.89	38.79	1.1
80	44.42	44.04	0.38	39.55	38.37	1.18
82	44.49	44.15	0.34	40.28	39.28	1
Subcritical	0.08 (kg/s)			0.11 (kg/s)		
67	32.54	32.14	0.40	27.82	26.91	0.91
69	32.46	32.10	0.36	27.26	26.19	1.07
71	32.58	32.29	0.29	27.77	26.81	0.96
73	32.95	32.66	0.29	28.44	27.75	0.69

4. CONCLUSION

In this extended abstract, a setup that was developed to test the vortex tube was briefly discussed to mainly investigate its performance under transcritical carbon dioxide operating conditions. The results have mainly showed that the temperature separation degrades significantly under the studied conditions. The maximum temperature separation reached was only 1.18 °C. Different modifications to the system might be needed to understand why this degradation happens and how to improve the temperature separation.

5. REFERENCES

- R. L. Collins, R. B. Lovelace, Experimental study of two-phase propane expanded through the Ranque-Hilsch tube, *Journal of Heat Transfer* 101 (1979) 300–305.
- Y. Liu, Y. Sun, D. Tang, Analysis of a CO₂ transcritical refrigeration cycle with a vortex tube expansion, *Sustainability* 11 (2019).
- A. Mansour, J. Lagrandeur, S. Poncet, Analysis of transcritical CO₂ vortex tube performance using a real gas thermodynamic model, *International Journal of Thermal Sciences* 177 (2022) 107555.
- T. Maurer, T. Zinn, Untersuchung von {Entspannungsmaschinen} mit mechanischer {Leistungsauskopplung} für die transkritische CO₂-Kältemaschine, *DKV-Tagungsbericht* 26 (1999) 264 – 277.

INFLUENCE OF INCLINATION ON A MULTI-PARALLEL-CONNECTED NATURAL CIRCULATION LOOPS: PRELIMINARY RESULTS

M. Misale(*), **A. Marchitto**, **J. A. Bocanegra**

DIME – Department of Mechanics, Energetics, Managements and Transportation Thermal Engineering and Environmental Conditioning Division

University of Genoa, Via All'Opera Pia 15°, (I), 16145 Genova, Italy

*Corresponding author: mario.misale@unige.it

Keywords: Single-phase natural circulation, multi-parallel-connected loops, loops inclination, power steps

Abstract

To convey heat using a working fluid, it is possible to employ forced or natural circulation. The former guarantees high thermal performance, whereas the latter guarantees less thermal performance; this lower performance is compensated by the maximum reliability because the motion of the fluid is ensured by the buoyancy force caused by a local gradient in fluid density without the use of any active system such as a pump. In literature are available papers focused on both large natural circulation loop (NCLs) and new complex NCLs realized by two or more circuits interacting with each other. Other aspects were studied, in the case of only one NCL, such as inner loop diameter, presence of localized pressure drops, input power step, loop inclination, and so on. In this paper, the influence of the inclination of multi-parallel-connected NCLs was experimentally investigated.

1. INTRODUCTION

Natural circulation loops (NCLs) have been widely used in various engineering applications due to their advantages, such as lower complexity, higher reliability, and lower maintenance requirements. NCLs employ buoyancy forces caused by a local gradient in fluid density to transport heat without requiring an active system, such as a pump. Although NCLs offer less thermal performance than forced circulation systems, they are preferred in many applications due to their simplicity and reliability.

From the early studies, the transient and stability behavior of the natural circulation loop emerges as a relevant research topic (Grief et al., 1979). The behavior and stability of a single natural circulation loop have been extensively studied in the literature. Some factors affecting the NCL flow stability have been analyzed, e.g., the wall thermal conductivity (Jiang and Shoji, 2003), the aspect ratio of the loop (Nakul et al., 2023), pipe diameter, loop length, and local losses (du Toit, 2021). Moreover, the dynamics of single-phase natural circulation loops under harmonic excitation (Mazumder et al., 2022) or power steps (Misale, 2016) have been studied. In the former paper a 1-D transient model was developed showing how different nonlinear effects of harmonic forcing, such as an exhibition of quasiperiodic dynamic of forced synchronization, whereas in the latter paper an experimental study on a single-phase rectangular loop showed that the power steps at the heater cause flow oscillations and their frequency could be expressed by an exponential law as a function of power. Moreover, as the power increases, the frequency of flow oscillations, as well as their amplitude, increases.

Analytical and numerical models for a single NCL have been developed based on experimental data (Luzzi et al., 2017). In particular, the Lattice Boltzmann Method is employed to simulate the thermohydraulic behavior of NCL (Bocanegra et al., 2023, Bocanegra and Misale, 2023). Recently, the effect of some modeling assumptions (Boussinesq hypothesis or temperature dependence of other properties) on the steady-state and transient behavior of single-phase natural circulation loops has been investigated (Sahu, 2021) as well as the employing of a new category of fluid called nanofluid (Choi and Eastman, 1995). The nanofluids consist of a base fluid (water) and nanoparticles (Al_2O_3 , TiO, CuO, and so on) suspended in it. The nanofluid guarantees the better thermal performance of the base fluid even if the nanoparticles tend to sediment after a long period (Misale et al., 2023). To reduce the nanoparticle sedimentation, a surfactant can be added to the nanofluids (Khairul et al., 2016; Xuan et al., 2013). The study by Nayak et al. (2009) is more interesting because they demonstrated that a small amount of Al_2O_3 nanoparticles can suppress the instability (flow reversal) in a single-phase natural circulation loop.

There has been a growing interest in investigating the performance of more complex NCL configurations than the most common single vertical loop. Coupled loops in two configurations: series-coupled (Elton et al., 2022; Adinarayana et al., 2022) and parallel coupled (Misale et al., 2020; Misale et al., 2021) are currently under study to understand the mutual influence between the connected loops and the stability and thermophysical behavior. The first research items

regarding parallel connected NCLs have been focused on studying (experimentally) the thermo-hydraulic performance of NCLs with small inner diameters in vertical orientation; only a small influence between the parallel circuits was noted.

Previous studies have focused on large NCLs and complex NCLs realized by two or more circuits interacting. Other aspects of NCLs, such as inner loop diameter, presence of localized pressure drops, input power step, and loop inclination, have been studied in single loops. However, the influence of the inclination in parallel-connected NCLs has not been experimentally investigated before. This work will fill part of this research gap by examining the thermal and hydraulic behavior of parallel coupled NCLs varying the inclination under different operational conditions (heating powers) for the first time. The preliminary results of an experimental investigation on the influence of inclination are presented using three rectangular parallel-connected NCLs characterized by small inner diameters. The results of this study will provide valuable insights into the behavior of multi-parallel-connected NCLs under different inclination angles and contribute to the optimization of NCLs for various engineering applications.

2 EXPERIMENTAL SETUP

The experimental setup consists of three connected rectangular loops with an inner diameter $ID=7$ mm. Figure 1 shows a schematic representation of the experimental setup. Each rectangular loop has an independent power supplier at the bottom side and a heat sink at a controlled temperature on the upper side. The horizontal and vertical pipes are made of copper tubes and are connected by silicone tubes at the corners. The NCLs are connected in parallel at the bottom side via a silicone tube; the inner diameter is the same as the copper tube. The parallel loops are fixed to a tilting bench which gives the possibility to select the inclination angle α measured with respect to the vertical position.

The tests were carried out with different orientations: 15 deg, 30 deg, and 60 deg.

The working fluid is distilled water. All the geometric characteristics of the NCLs are reported in Table 1.

Each heater is made with nichrome wire wrapped around the bottom side of each loop, whereas each cooler consists of a coaxial heat exchanger controlled by a cryostat (LAUDA VC2000). The fluid in the cooling system (secondary fluid) is a mixture of 50 % water and 50 % ethylene glycol, with a mass flow rate high enough (around 10 l/min) to guarantee an almost isothermal fluid condition (maximum outlet-inlet temperature difference of 1 K).

To reduce the heat loss to the ambient, the NCLs were thermally insulated to reduce both the conductive and radiative heat losses to the ambient. Based on the empiric natural convection correlations for cylindrical geometries (Nejan and Kraus (2003)), the maximum heat loss was calculated to be lower than 5%.

The fluid temperature is measured in the two vertical tubes of each loop, with a total of six thermocouples on each rectangular loop, three for each vertical tube. Two more thermocouples measure the outlet-inlet temperature difference in the secondary flow. T-type shielded calibrated thermocouples are used (outside diameter of 0.5 mm; precision ± 0.1 K). The hot junction of the thermocouples is in the center of the cross-section area of the tube.

No decrease in the cross-section or induced pressure drops are attached to the thermocouple's presence (Misale and Frogheri (1999)).

The temperature measurements were stored by a National Instruments data acquisition (Lab PC+, SCXI-1000, SCXI-1102, SCXI-1303) and an electronic ice point. The fluid temperature map was acquired every second (1.0 s), and each of these temperature measurements was obtained as an average of 100 readings. All the tests were conducted at a constant room temperature of 20 °C. The measurements are made with a characteristic time high enough to allow reaching the steady state in the temperature trends.

3 EXPERIMENTAL PROCEDURE

The experimental procedure adopted (for each fixed NCLs inclination α) consists of varying the heat power at the heaters. Starting from 20 W for each circuit, after 600 s, all the heaters were fixed at 40 W, then one of the circuits varied the power up to 100 W with a step of 20 W, whereas the other two circuits remained at the same power (40 W). The increment of power was applied every 1200 s. Only for the runs at $\alpha=60$ deg the maximum power was limited to 80 W, to avoid bubbles in the flow. All the experiments were conducted by fixing the temperature of the secondary flow at 20 °C (fixed heat sink temperature).

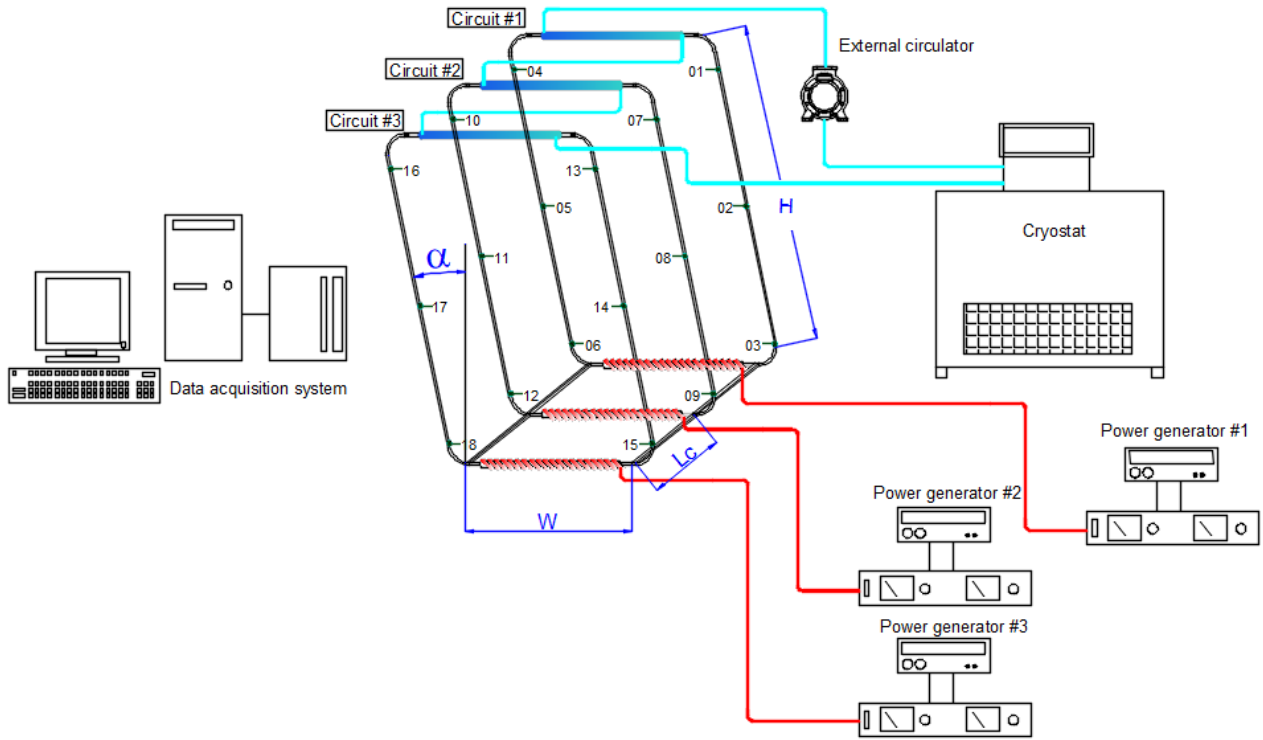


Figure 1. Experimental setup, three parallel NCL are shown. Each loop has three thermocouples per vertical leg.

Table 1. Geometric parameters of the vertical Natural Circulation Loops experimental setup.

Parameters	
Internal tube diameter (ID), m	0.007
Number of connected loops	3
Width (W), m	0.590
Height (H), m	0.975
Heated length (L_H), m	0.380
Cooled length (L_L), m	0.400
Total length (L_t), m	3.130
Connecting tube length (L_c), m	0.035
Connecting int. diam. tube (D_c), m	0.007
Aspect ratio (L_t/W)	5.30
Aspect ratio (H/W)	1.65
Aspect ratio (L_c/D_c)	5
Aspect ratio (L_t/ID)	447.1
Internal heat exchanger volume (V_H), m^3	$1.46 \cdot 10^{-5}$

4 RESULTS AND DISCUSSION

The fluid flow in a natural circulation loop (NCL) is based on the interaction of two forces, i.e., the buoyancy force caused by a heat source at the bottom of a thermal system and the friction force induced by the fluid velocity that induces a shear stress with the pipe wall. The interaction between these two forces can induce different thermo-hydraulic behaviors. In particular, if the friction force is greater than buoyancy one, the flow in the NCL is stable (steady temperature difference across the heat sinks); on the other hand, it could be neutral stable (oscillations of the temperature difference across the heat sinks without amplification), or unstable (amplification of the temperature oscillations across the heat sinks that causes flow reversal). The latter thermo-hydraulic behavior (unstable) can appear in the large-scale NCL, whereas for NCL characterized by small internal tube diameter, it is always stable (friction is greater than buoyancy). The results presented in this paper always show stable behavior because the internal diameter of the tube is small, and the aspect ratio between the total length of the tube and the internal diameter is more than four hundred.

The results can be shown, for each circuit, in terms of the average temperature difference between the mean temperature in the hot leg and the cold one:

$$\Delta T_{avg} = \overline{T}_h - \overline{T}_c \quad (1)$$

All the tests can be summarized in Figs. 2-4. The figures represent the average temperature differences vs. time for all the NCLs inclinations when the power step was applied to circuit #1 (Fig. 2), circuit #2 (Fig. 3), and circuit #3 (Fig. 4); moreover, the pink lines indicate the moment when each power step applied.

The trends depicted in Figs. 2-3 show how there is a combined effect of the NCL inclination and the circuit where the power is varied. When the NCL inclination moves from vertical to 60°, the circuit #1 is characterized by a worst thermal performance for all the runs performed. The figures also show, at every power step, a significant initial temperature overshoot that is immediately followed by a rapid damping until stationarity conditions. This behavior is more evident when the power for this circuit is varied as well as when it remains at the power of 40 W and the power change in circuit #2 (less evident than the case described above) or circuit #3 (significant temperature overshoot at 1800 s and less evident, but present, at 3000 s, and 4200 s).

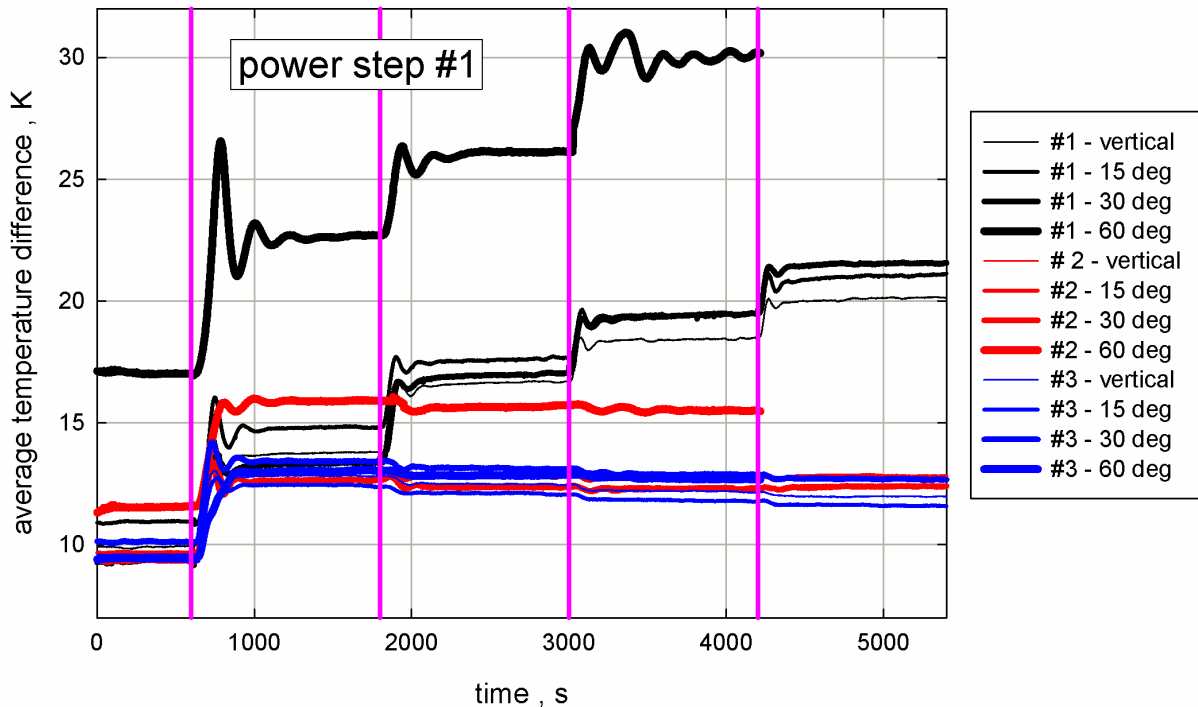


Figure 2. Average temperature difference versus time: only circuit #1 increments the power.

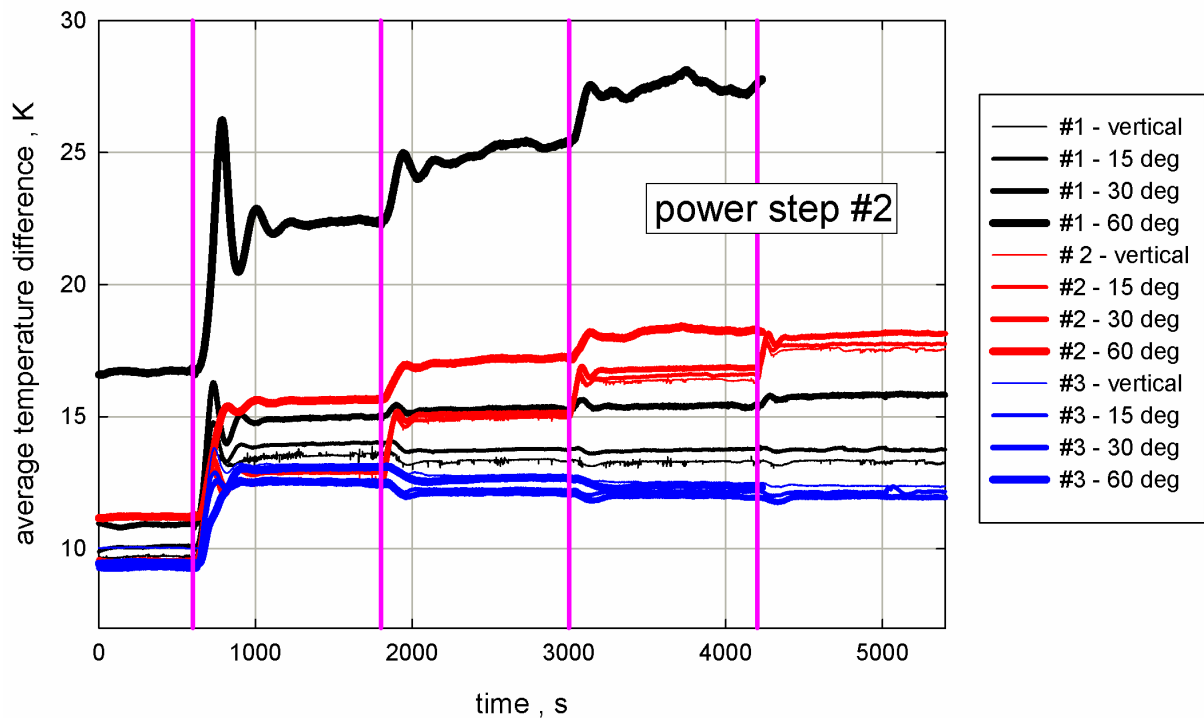


Figure 3. Average temperature difference versus time: only circuit #2 increments the power.

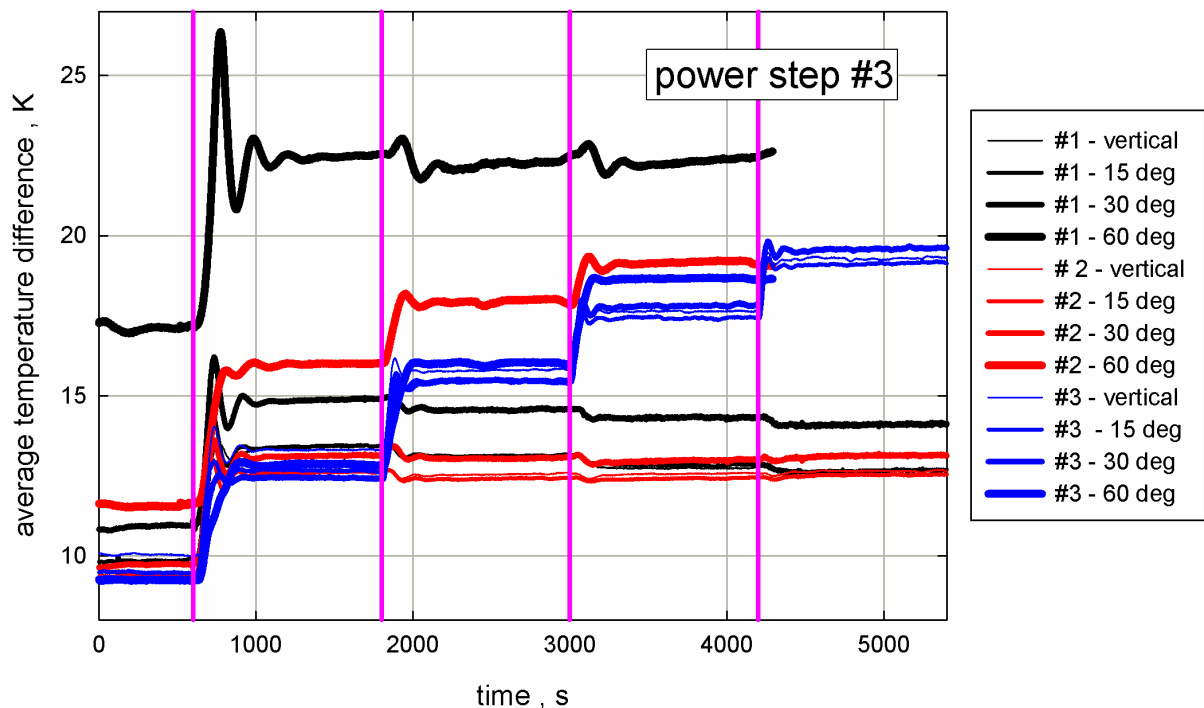


Figure 4. Average temperature difference versus time: only circuit #3 increments the power.

For circuit #2, moving from vertical displacement to 60 deg, the trend of average temperature difference shows that the influence of the NCLs inclination is reduced with respect to the same parameter of the behavior of circuit #1. Probably, there is an interaction through the connecting tubes between circuit #2 and #1 (when the NCLs are inclined, the heater of circuit #1 is at an elevation higher than circuit #2). Completely different is the thermos-hydraulic behavior of circuit #3 (Fig. 4). When this circuit moves from vertical to 60 deg, the influence of loop inclination is less evident if referred to the

behavior of circuits #1 and #2. A reduced temperature overshoot appears at 0 deg (vertical) and 15 deg, whereas even in the case of the power step applied, the average temperature increases, but the steady-state is reached without any temperature overshoot. However, the connecting tubes among the circuits (heated section) probably induce a flow circulation among the three heaters.

To better investigate the interaction of the connected NCLs, in Figs. 5, 6, and 7 are depicted the trends of the fluid temperatures along the three hot legs. This analysis is reported for the NCLs inclination of 60 deg, which seems more significant than the other NCLs inclinations. The fluid temperatures shown in the figures are:

- TC. 6, TC. 5, TC. 4 – circuit #1
- TC. 12, TC. 11, TC. 10 – circuit #2
- TC. 18, TC. 17, TC. 16 – circuit #3

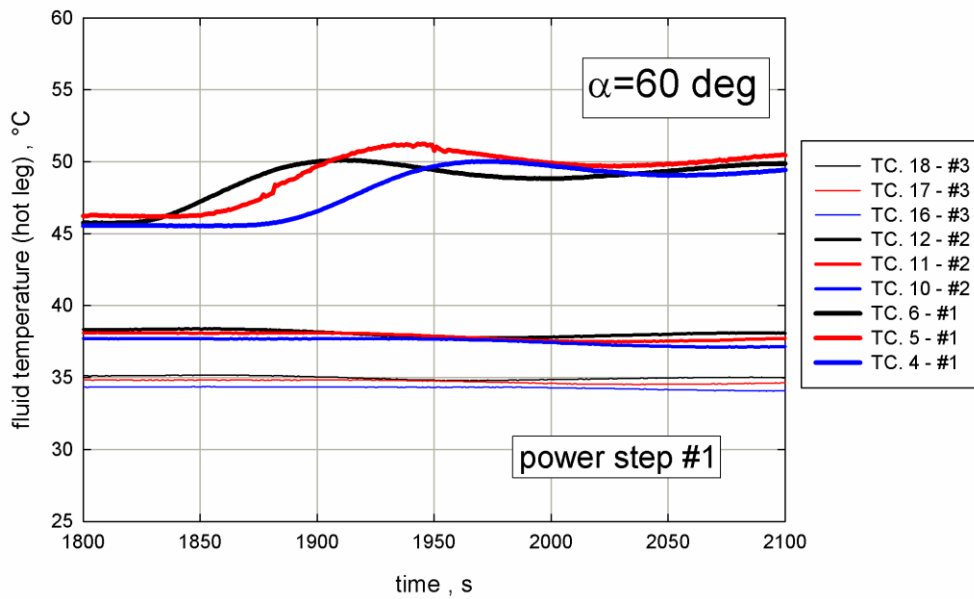


Figure 5. Fluid temperatures (hot leg) vs. time. Power step after 1800 s for the three inclined circuits (only circuit #1 is characterized by power step)

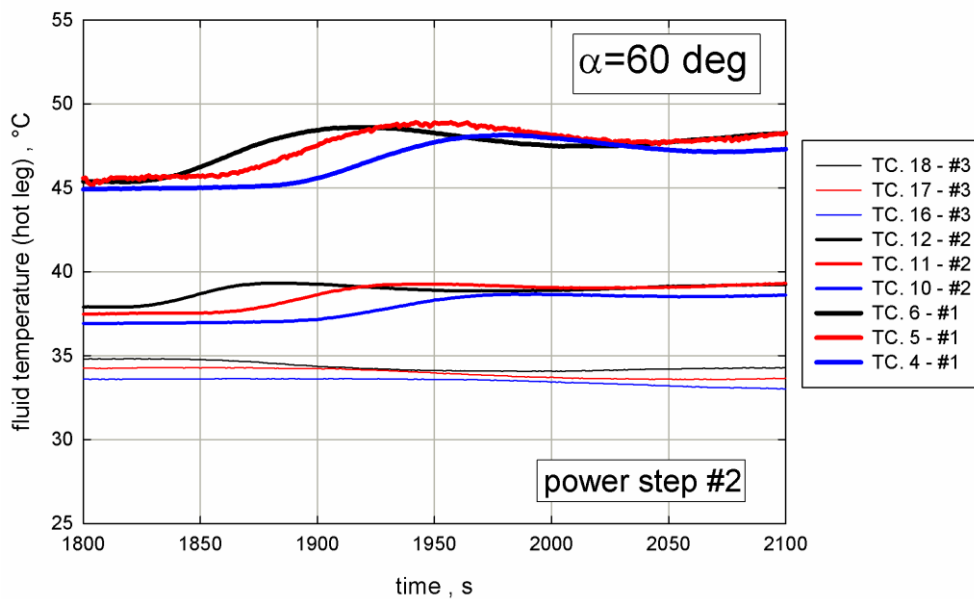


Figure 6. Fluid temperatures (hot leg) vs. time. Power step after 1800 s for the three inclined circuits (only circuit #2 is characterized by power step)

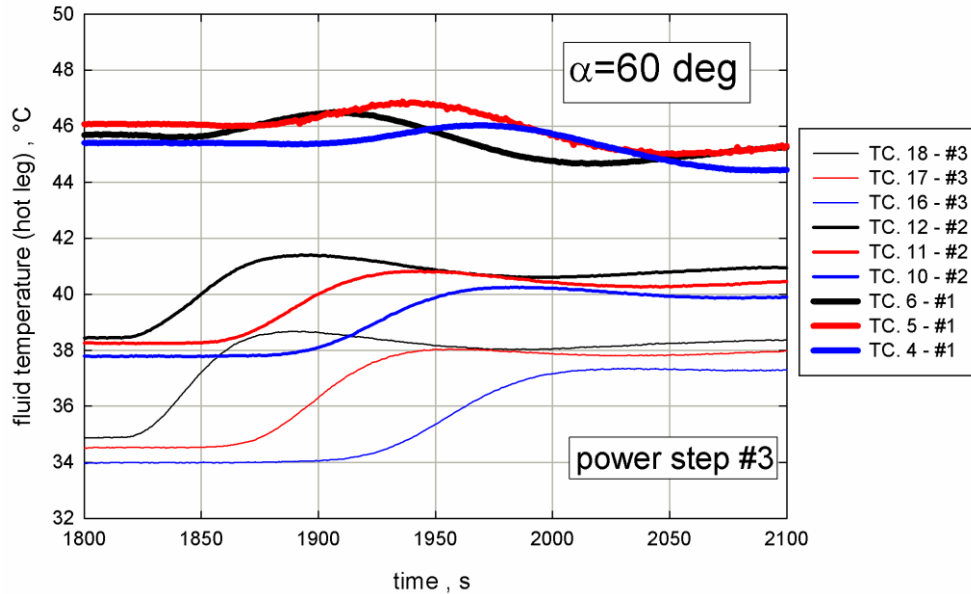


Figure 7. Fluid temperatures (hot leg) vs time. Power step after 1800 s for the three inclined circuits (only circuit #3 is characterized by power step)

After 1800 s from the start of the experiments, one of the three circuits powered with 40 W, moves to another power step (60 W). The comparison of the fluid temperature trends depicted in Figs. 5, 6, and 7 show an interesting behavior. When the power step is imposed at circuit #1 (the highest location of the NCLs) the other two circuits seem to be not influenced by the power variation in circuit #1. Their trends remain quite constant, whereas the fluid temperatures (TC. 5 and TC. 4) in circuit #1 show a delay starting from TC. 6 (closest to the heated section) that is due to the small fluid velocity (less than 0.1 m/s). Different behavior appears when the power step is applied to circuit #2 or #3. In the case of the former situation (Fig. 6), the power step induces a fluid temperature fluctuation in the above circuit #1, whereas circuit #3 seems not influenced by this power step, whereas in the latter situation, the power step I applied at the circuit #3 (Fig. 7) and this fact induce temperature fluctuations in both adobe NCLs (circuit #2 and #1).

4. CONCLUSIONS

In this paper, an experimental work on the influence of inclination on the interaction between three parallel-connected natural circulation loops is reported.

The conclusions can be summarized as follows:

- The thermo-hydraulic behavior is always stable, even though a few flow temperature overshoots were measured during a power step.
- The circuit #1 (see Fig. 1, the highest even in the case of NCLs inclination) shows the worst thermal performance because it shows the largest average temperature differences between the hot and cold leg even when its power dissipation remains constant (40 W) and instead power steps are imposed on circuit #3.
- The increase in the inclination of the NCLs both reduces the buoyancy force, and this causes the increase in the average temperature difference and at the same time there is a greater influence of the interconnection of the circuits.
- The connected tubes and the bottom-heated section always influence the NCL loop located above the circuit where the power was varied and the experimental apparatus is inclined. Obviously, this is not applicable to circuit #1 when the power step is imposed on it.

5. REFERENCES

- Adinarayana, K.N.V, Mangarjuna Rao, P., Seik Mansoor Ali, 2022. "Numerical investigations on dynamic characteristics of series coupled single-phase natural circulation loops", *International Journal of Thermal Sciences*, Vol. 181.
- Bejan, A. Kraus, A.D., 2003, *Heat Transfer Handbook*, New York, USA.
- Bocanegra, J.A., Marchitto, A., Misale, M., 2023. "Study of a Square Single-Phase Natural Circulation Loop Using the Lattice Boltzmann Method", *Applied Mechanics* 2023, 4, 927–947.
- Bocanegra, J.A., Misale, M., 2023. "Lattice Boltzmann model of a square natural circulation loop with small inner diameter: working fluid effects", *Journal of Physics: Conference Series*, Vol. 2509(1), 012007.
- Choi, S. U. S., Eastman, J. A., 1995. "Enhancing thermal conductivity of fluids with nanoparticles". In *Proceedings, ASME International Mechanical Engineering, Congress & Exposition, San Francisco*.
- Elton, D.N., Arunachala, U.C., Vijayan, P.K., 2022. "Stability performance of series coupled natural circulation system with different operating procedures", *International Journal of Thermal Sciences*, Vol. 179, 107693.
- Greif, R., Zvirin, Y., Mertol, A., 1979. "The transient and stability behavior of a natural circulation loop", *Trans. of ASME*, Vol. 101, pp. 684-688.
- Jiang, Y.Y., Shoji, M., 2003. "Flow stability in a natural circulation loop: influence of wall thermal conductivity", *Nuclear Engineering and Design*, Vol. 222, pp. 16-28.
- Khairul, M.A., Shah, K., Doroodchi, E., Azizian, R., Moghtaderi, B., 2016. "Effects of surfactant on stability and thermo-physical properties of metal oxide nanofluids", *International Journal of Heat and Mass Transfer*, Vol. 98, pp. 778–787.
- Luzzi, L., Misale, M., Pini, A., Cauzzi, M.T., Fanale, F., Cammi, A., 2017. "Assessment of analytical and numerical models on experimental data for the study of single-phase natural circulation dynamics in a vertical loop", *Chemical Engineering Science*, Vol. 162, pp. 262-283.
- Mazumder, A. G., Saha, R., Mondal, S., Ghosh, K., Mukhopadhyay, A., Sen, S., 2022. "Dynamics of a single-phase natural circulation system under harmonic excitation", *Chaos*, Vol. 32, 123125.
- Misale, M. Frogheri, M., 1999. "Influence of pressure drops on the behavior of a single-phase natural circulation loop: Preliminary results", *International Communications in Heat and Mass Transfer*, Vol. 26, pp. 597–606.
- Misale, M., Garibaldi, P., Passos, J.C., and Ghisi de Bitencourt, G., 2007. "Experiments in a single-phase natural circulation mini-loop", *Experimental Thermal and Fluid Science*, Vol. 31 (8), pp. 1111-1120.
- Misale, M., 2016. "Experimental study on the influence of power steps on the thermohydraulic behavior of a natural circulation loop", *Int. J. Heat and Mass Transfer*, Vol. 99, pp. 782-791.
- Misale, M., Bocanegra, J.A., Borelli, D., Marchitto, A., 2020. "Experimental analysis of four parallel single-phase natural circulation loops with small inner diameter", *Applied Thermal Engineering*, Vol. 180 (5), 115739.
- Misale, M., Bocanegra, J.A., Marchitto, A., 2021. "Thermo-hydraulic performance of connected single-phase natural circulation loops characterized by two different inner diameters", *International Communications in Heat and Mass Transfer*, Vol. 125, 105309.
- Misale, M., Bocanegra, J.A., Marchitto, A., 2023. "Long-term experimental study on gravitational sedimentation of water aluminum oxide nanofluid at different volumetric concentrations", *International Journal of Sediment Research*, Vol. 38 (3,) pp. 303-315.
- Nakul, S., Arunachala, U.C., Vijayan, P.K., 2023. "Experimental and analytical study on the stability of a low aspect ratio single-phase natural circulation loop coupled to a parabolic trough collector", *International Communications in Heat and Mass Transfer*, Vol. 144, 106751.
- Nayak, A.K, Gartia, M.R., Vijayan, P.K., 2009. "Thermal–hydraulic characteristics of a single-phase natural circulation loop with water and Al₂O₃ nanofluids", *Nuclear Engineering and Design*, Vol. 239 (3), pp. 526-540.
- Sahu, M., Sarkar, J., Chandra, L., 2021. "Effects of various modeling assumptions on steady-state and transient performances of single-phase natural circulation loop", *International Communications in Heat and Mass Transfer*, Vol. 124, 105247.
- du Toit, C. G., 2021. "Fundamental evaluation of the effect of pipe diameter, loop length and local losses on steady-state single-phase natural circulation in square loops using the 1D network code Flownex", *Thermal Science and Engineering Progress*, Vol. 22, 100840.
- Xuan, Y., Li, Q., Tie, P., 2013. "The effect of surfactants on heat transfer feature of nanofluids", *Experimental Thermal and Fluid Science*, Vol. 46, pp. 259-262.

Gaining mechanistic insight into crystallization fouling through integrated *in-situ* thermofluidic-optical methods

Tobias Armstrong^{a,+}, Julian Schmid^{a,+}, Moritz Bischof^a, Niklas Denz^a, Lukas Hegner^a, Lars Heller^a, Andreas Hugentobler^a, Jovo Vidic^b, Constantin Scheuer^a, Gabriel Schnoering^b, Thomas M. Schutzius^{a,*}

^aLaboratory for Multiphase Thermofluidics and Surface Nanoengineering, Department of Mechanical and Process Engineering, ETH Zurich, Sonneggstrasse 3, CH-8092 Zurich, Switzerland

^bLaboratory of Thermodynamics in Emerging Technologies, Department of Mechanical and Process Engineering, ETH Zurich, Sonneggstrasse 3, CH-8092 Zurich, Switzerland

*To whom correspondence should be addressed: thomschu@ethz.ch

+These authors contributed equally to this work.

Keywords: heat transfer resistance, crystallization fouling, calcium salt, continuous flow, optical measurement

1. INTRODUCTION

Various industries, such as the water or energy industry, face problematic fouling on surfaces. Crystallization fouling is an important type and it occurs whenever water that contains retrograde soluble minerals, such as calcium carbonate or calcium sulfate, is used to cool a heated surface, and the growing deposit is termed “scale” and the process “scaling”. Scale leads to decreased performance in cooling and separation processes by clogging membranes and pipes and by forming thermally insulating layers on heat transfer surfaces. Counteracting scaling benefits the performance of a host of systems and devices and thus improves their environmental impact by increasing their efficiencies and performance. Müller-Steinhagen (1999) explains the fundamentals of cooling-water fouling phenomena, while Berce *et al.* (2021) additionally summarize recent studies of crystallization fouling in heat exchanger.

Experimental setups to study crystallization fouling combine a variety of measurement techniques and flow designs. Kim *et al.* (2002) reported a system that included real-time microscopic visualization on a heat exchanger surface with fluids on cooling and heating side of a heat transfer material. Their system experienced bulk supersaturation on the cooling side through mixing prior to the test section. Pääkkönen *et al.* (2012) studied fouling in a semi-batch continuous flow system with a fluid only at the cooling side of the heat exchanger. Using an ohmic heater, they heated the test section without optical access. Recently, Al-Gailani *et al.* (2021) demonstrated a batch setup with an optical access of the test section, and a temperature control system using a heating cartridge within the sample geometry.

In this study, we present a novel continuous flow experimental setup that mimics a cooling section of a heat exchanger and allows us to holistically investigate the complex process of crystallization fouling and the parameters affecting it. Such a system will allow us to gain mechanistic insight into what determine the onset of nucleation, growth, and adhesion of scale. Through visual microscopic observations of the entire fouling process, i.e. onset of crystallization, growth, removal, and simultaneous tracking of its influence on heat transfer, we gain a better understanding of the formation of deposit layers and their effects on heat transfer. We perform experiments on one type of heat transfer surface and show the resulting phenomena under variable flow conditions demonstrating the promise of this approach. The resulting small crystals grow over time and form layers, which increase the reference sample temperature. We believe that our new setup provides profound information on the fundamental aspects of crystallization fouling and will contribute to the development of heat transfer surfaces that inherently prevent crystallization or behave scale-repellent.

2. OUR EXPERIMENTAL METHODS

Figure 1 shows the experimental setup of this work. The fluid flow section of the setup consisted of a reservoir on a cold plate cooler (TE Technology/ CP-200HT-TT), a membrane pump (SHURflo/8000-543-290), a Coriolis flowmeter (Endress+Hauser/Cubemass DCI), and a self-build experimental unit. The reservoir temperature ($\pm 5\%$) was maintained by cooling or heating the cold plate cooler to ensure a constant bulk fluid temperature in the heat transfer zone. The membrane pump was powered by a controlled external power supply to reach the control volume flow variable, which was measured by the Coriolis flowmeter. The system operated in a range of $Re = 0-10000$ ($\pm 6\%$). The continuous flow setup allowed long experimental runs with saturated calcium carbonate or calcium sulfate solutions, which reach supersaturation only at the heated sample surface. The ramp up of the system used purified water, preventing fouling deposition before quasi-steady state conditions are reached.

The optical access to the sample during experiments enabled the simultaneous acquisition of the visual fouling on the sample. The optical section consisted of a Köhler illumination reflected light microscopy with two attachable cameras (FLIR/Grasshopper 3 and Thorlabs/ DCC1645C). The light source was variable and used in brightfield imaging mode. This variability allows applying other optical methods as micro particle imaging velocimetry.

The tested sample has a geometrical surface area of 18x18 mm. Due to the localized removal of heat on the sample surface, there is no fouling on other surfaces of the system. The exchangeable samples allowed studying different sample surface chemistries, and morphologies, both micro- and nanostructured textures.

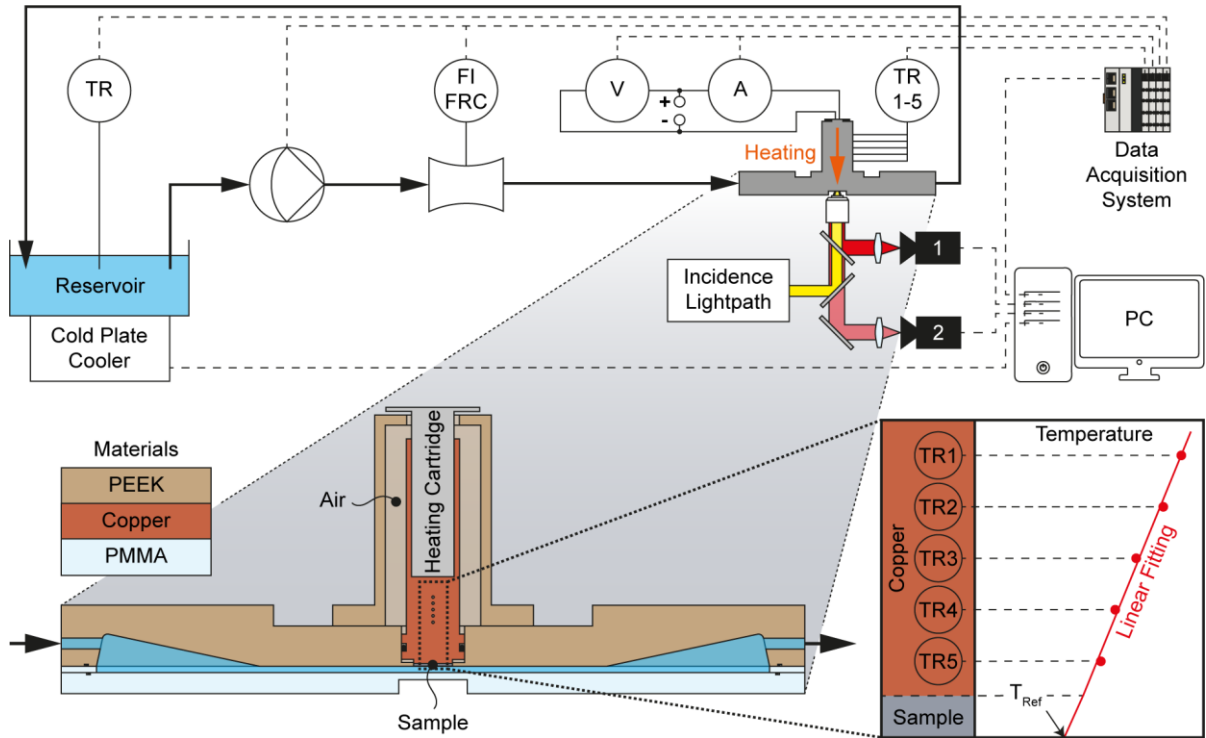


Figure 1: Schematic piping and instrumentation diagram of the experimental setup including its optical access (top). The enlarged experimental unit depicts its design and materials to scale (bottom left). The inset shows a schematic of thermocouple measurements and their linear fitting, which allows the extrapolation of the reference temperature.

The heating zone consisted of an external powered heating cartridge (PROBAG HS 208, max. Power 400 W) which was connected to an external power source, an intermediate copper block and the variable sample. The controllable heater cartridge provided a constant defined power ($\pm 2\%$) over the experiment, which was monitored by reading current and voltage. The sample to study was connected to the heating cartridge with the use of thermal paste and through an intermediate copper cylinder that allowed uniform temperature distribution across the sample. Five previously calibrated thermocouples (T-Type, ± 0.1 K, $d=1$ mm) were embedded in the copper block with axially uniform spacing to determine the heat flux q'' ($\pm 5\%$) using Fourier's law of conduction (inset, Figure 1), which in turn facilitated the determination of the reference sample temperature T_{Ref} by a linear extrapolation. Optionally, upstream and downstream inserted thermocouples allowed to measure the temperature difference of the solution across the sample, as well as the sample temperature with attached thermocouples.

Despite the accelerated conditions in the fouling experiments, long experimental times are necessary to detect a rise in the reference temperature. To allow long term experiments, the automatic shutdown feature was implemented and executed when the reference temperature T_{Ref} rose above 105 °C (temperature limit, Figure 2d) or the experiment time exceeded 8 hours (time limit, Figure 2d).

All data acquisition and control of the experiments were handled by a custom-built data acquisition system (Beckhoff) connected to a PC using TwinCat 3 and LabView as the control software.

3. RESULTS – PROOF OF CONCEPT

To demonstrate the capabilities of our setup, we performed experiments on previously polished copper surfaces (Roughness $Ra = 0.13$ μm , Figure 2a) under two flow conditions, $Re = 350$ and $Re = 950$. The fixed source heat flux values equal to 108 kW/m^2 and 123 kW/m^2 for the two flow conditions respectively, were found in advance with deionized water runs, such that a steady state reference temperature of $T_{Ref} = 80$ °C was present. Degassing bubbles initially form on the surface due to the heating of the sample, and once these bubbles are removed from the surface, individual crystals in the form of gypsum remain on the surface. The time sequence (Figure 2b), show the following *in-situ* fouling growth of the crystal structures. The crystals start to intergrow with the surrounding crystals (Figure 2b, 60-420 min), forming a closed porous layer (Figure 2c) which subsequent grow in vertical direction. The vertical growth (Figure 2c, Side view) affects the reference temperature, which increases steadily due to the raised thermal resistance and

insulating effect of the fouling layer. We define $T_{Ref,0}$ and t_0 as when the reference temperature first starts to rise steadily. Figure 2d shows the evolution of the normalized reference temperature θ starting at t_0 for the two Re numbers. It is evident that the flow condition has an influence on the growth, since the reference temperature rises more steeply with a lower Re number. As a result, the experiments for $Re = 350$ reach the temperature limit while for $Re = 950$ the time limit is reached. Error bars in Figure 2d indicate the mean and the standard deviation of three independent experiments. Limits $T_{Ref} = 105\text{ }^\circ\text{C}$ and $t = 8\text{ h}$.

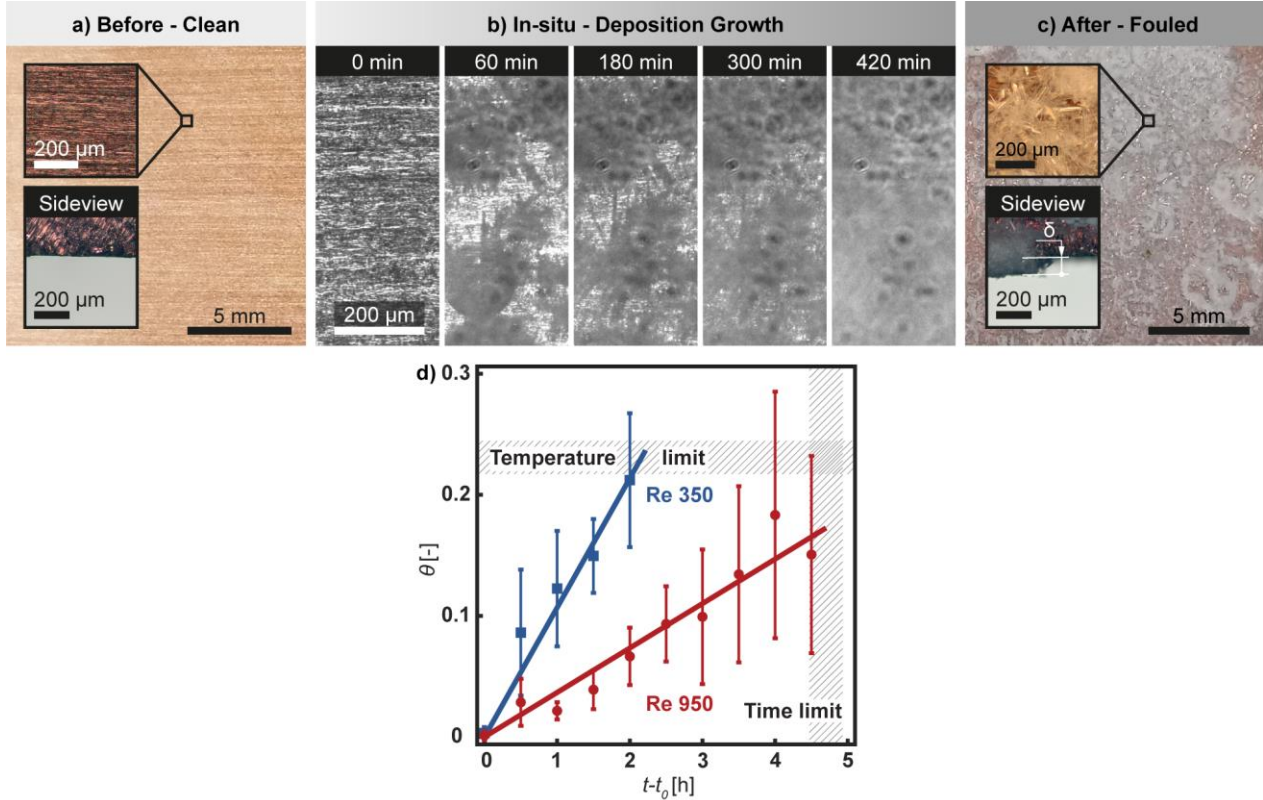


Figure 2: Fouling experiment with copper substrate and calcium sulfate inorganic salt: a) Images of the clean copper surface. b) in-situ time sequence of a growing crystal layer $Re = 950$. c) Images of the fouled surface. d) Normalized reference temperature evolution $\theta = (T_{Ref} - T_{Ref,0}) / T_{Ref,0}$ over $t - t_0$.

4. CONCLUSIONS

In this work, we show and prove a novel experimental setup to continuously study fouling phenomena with localized increased supersaturation on a sample surface. The combination of the optical and heat transfer methods enabled the correlation between visual fouling onset, its growth, and its influence of the heat transfer properties. The experimental setup allows studying crystallization fouling for variable substrates and alternating fluid flow properties. Study of both aspects simultaneously is essential for inhibiting fouling of heat transfer interfaces. We believe our new setup will provide new insights on the fundamentals of crystallization fouling by utilizing the experimental variability on fluid flow and surface properties. Thereby, we aim to improve the design of future heat transfers surfaces with anti-fouling behaviour in known flow regimes.

5. REFERENCES

- Al-Gailani, A., Sanni, O., Charpentier, T., Crisp, R., Bruins, J., Neville, A., 2021. "Inorganic fouling of heat transfer surface from potable water during convective heat transfer". *Applied Thermal Engineering*, Vol. 184, 116271.
- Berce, J., Zupančič, M., Može, M., Golobič, I., 2021. "A Review of Crystallization Fouling in Heat Exchangers.". *Processes*, Vol. 9(8), 1356.
- Kim, W., Bai, C., Cho, Y., 2002. "A study of CaCO_3 fouling with a microscopic imaging technique". *International Journal of Heat and Mass Transfer*, Vol. 45, pp. 597-607.
- Müller-Steinhagen, H., 1999. "Cooling-Water Fouling in Heat Exchangers". Vol. 33, pp. 415-496.
- Pääkkönen, T., Riihimäki, M., Simonson, C., Muurinen, E., Keiski, R., 2012. "Crystallization fouling of CaCO_3 – Analysis of experimental thermal resistance and its uncertainty". *International Journal of Heat and Mass Transfer*, Vol. 55, 6927–6937.

ASSIMILATION OF TOMOGRAPHIC PARTICLE IMAGE VELOCIMETRY DATA OF TURBULENT MIXED CONVECTION IN A CUBOIDAL CELL

Christian Bauer^{a,*}, Michael Mommert^a and Claus Wagner^{a,b}

^aInstitute of Aerodynamics and Flow Technology
German Aerospace Center, Göttingen, Germany

^bInstitute of Thermodynamics and Fluid Mechanics
Technische Universität Ilmenau, Germany

*christian.bauer@dlr.de

Keywords: tomographic particle image velocimetry, turbulent mixed convection, data assimilation, direct numerical simulation

1. INTRODUCTION

Data assimilation, i.e. applying numerical algorithms on experimental data to extract additional information, has become an increasingly important topic in the field of fluid dynamics and turbulence research in the past decades (di Leoni et al. 2020). Although tomographic particle image velocimetry (tomo PIV) allows to capture largely temporally and spatially resolved, three-dimensional velocity fields of turbulent flow, usually not all essential parts of the flow problem can be measured. Due to the reflection of the laser light sheet and low tracer particle densities near solid walls, boundary layers are often difficult to capture using PIV. In addition, turbulent small-scale structures are often filtered out, since velocity vectors represent surface- or volume-averaged quantities obtained from a correlation step.

Moreover, for fluid problems involving thermal convection, the temperature field—next to the velocity field—is essential for the flow problem. However, to capture the temperature field simultaneously with the velocity field requires additional elaborate measurement techniques which are often not feasible.

Thus, Bauer et al. (2022) present an algorithm for the problem of turbulent Rayleigh–Bénard convection that allows to assimilate tomo PIV measured velocity fields and extract corresponding temperature fields without additional measurements, but solely by exploiting the governing flow equations. In our present work, we extend our data assimilation scheme to the problem of turbulent mixed convection in a cuboidal cell, where pressure-driven forces act on the flow besides buoyancy. Moreover, we use the assimilation scheme to expand the measurement data from one fourth of the complete sample of Mommert et al. (2020) to the entire sample, i.e. to regions that were not initially captured by the tomo PIV measurements (see Figure 1).

The extended abstract is organized as follows: In Section 2, the experimental set up of the mixed convection cell measurement is introduced. Subsequently, the data assimilation algorithm applied to the measured velocity field as well as the first results are depicted in section 3. Finally, the abstract is concluded in section 4.

2. EXPERIMENTAL SET UP

The experimental data set is obtained from the tomographic PIV (tomo PIV, Elsinga, 2006) measurement of a mixed convection cell reported by Mommert et al. (2020). The experiment consists of a rectangular sample with dimensions $L_x=2500\text{mm}$, $L_y=L_z=\hat{H}=500\text{mm}$, as shown in Figure 1.

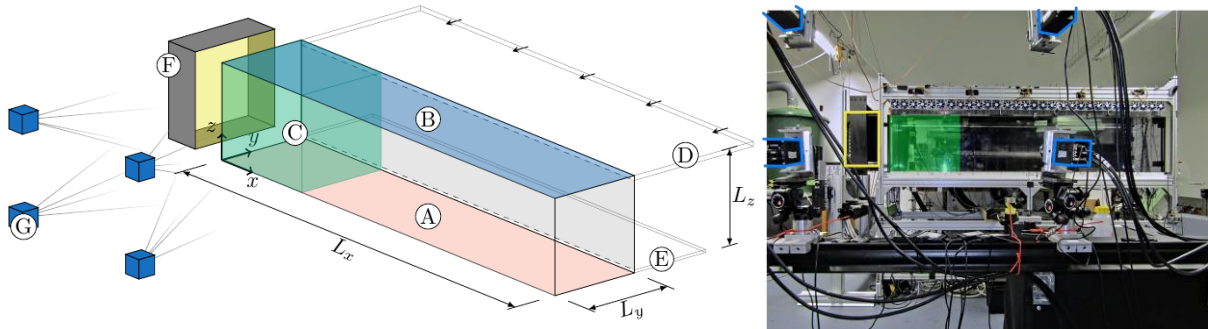


Figure 1. Left: Sketch of the mixed convection sample with heated bottom (A) and cooled top plate (B); Measurement volume (C); Velocity inlet (D) and outlet (E); LED light system (F) and PIV camera system (G). Right: Photograph of the mixed convection sample. Figure adapted from Mommert et al. (2020).

The aluminum bottom plate (A) is heated by tempered water whereas the aluminum top plate (B) is passively cooled to room temperature. In order to minimise heat exchange with the surroundings while allowing optical access, the side walls of the sample were made of double-walled, 10mm-thick polycarbonate. Moreover, a 25mm high velocity inlet (D) and a 15mm high velocity outlet (E) were attached to the top and the bottom edge, respectively. The flow in a subvolume of the mixed convection cell (C) is captured by tracking helium-filled soap bubbles illuminated by an LED light system (F) with a PIV camera system (G). For more details the reader is referred to Mommert et al. (2020).

3. DATA ASSIMILATION SCHEME

The flow of turbulent mixed convection can be characterised by the Prandtl number $\text{Pr} = \hat{\nu}/\hat{\kappa}$, representing the ratio of momentum diffusivity and thermal diffusivity, the Rayleigh number $\text{Ra} = \hat{\alpha}\hat{g}\hat{H}\Delta\hat{T}/(\hat{\nu}\hat{\kappa})$, reflecting the ratio of buoyancy and diffusive forces, and the Reynolds number $\text{Re} = \hat{u}_{in}\hat{H}/\hat{\nu}$, representing the ratio of inertial and viscous forces, with $\hat{\nu}$ the kinematic viscosity, $\hat{\kappa}$ the thermal diffusivity, $\hat{\alpha}$ the thermal expansion coefficient, \hat{g} the gravitational acceleration, \hat{H} the mixed convection cell height, $\Delta\hat{T}$ the vertical temperature difference, and \hat{u}_{in} the inlet velocity. In the following, dimensional quantities are denoted with circumflex and the dimensionless without. The equations governing the problem are the transport equations for mass, momentum, and energy, which for an incompressible fluid and the Boussinesq approximation read in dimensionless form

$$\nabla \cdot \mathbf{u} = 0, \quad (1)$$

$$\frac{\partial \mathbf{u}}{\partial t} + \mathbf{u} \cdot \nabla \mathbf{u} = -\nabla p + \sqrt{\frac{\text{Pr}}{\text{Ra}}} \nabla^2 \mathbf{u} + T \mathbf{e}_z, \quad (2)$$

$$\frac{\partial T}{\partial t} + \mathbf{u} \cdot \nabla T = \sqrt{\frac{1}{\text{PrRa}}} \nabla^2 T, \quad (3)$$

with \mathbf{u} the velocity vector (u_x, u_y, u_z) , p the pressure, T the temperature and \mathbf{e}_z the unit vector in vertical direction. In experimentally-measured data, the conservation of mass, equation (1), is often not fulfilled. Hence, we apply the following algorithm to the measured velocity field to ensure the divergence-free condition: First, we compute the divergence of the measured velocity field. Then, a pseudo-pressure is obtained by solving the Poisson equation for the measured velocity field. Finally, the velocity field is corrected via the pseudo-pressure. Figure 2 portrays the vertical velocity component v in an xz -plane at $y/h=0.5$ before (a) and after (b) the divergence has been removed as well as the divergence of the measured velocity field (c).

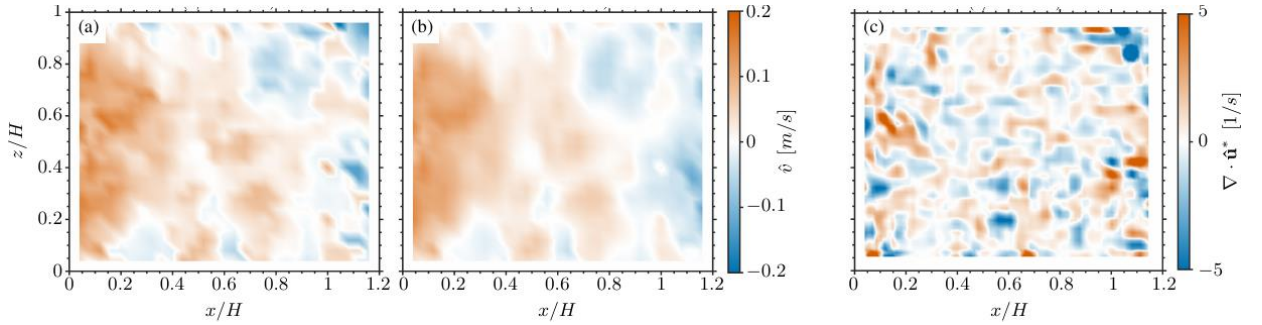


Figure 2. The v velocity component before (a) and after (b) divergence has been removed in an xz -plane at $y/h=0.5$. (c) The divergence of the initial tomo PIV measured velocity field.

As Figure 2 indicates, our algorithm successfully removes discontinuities from the measured velocity data by imposing the divergence-free condition. The obtained divergence-free velocity fields are then fed into a nudging algorithm, which is a further development of the algorithm we used for Rayleigh–Bénard convection (Bauer et al., 2022) and similar to the one introduced by Suzuki and Yamamoto (2015). Starting from an initial velocity and temperature field provided by a direct numerical simulation conducted for the characteristic dimensionless numbers of the experiment $\text{Ra}=1.4 \times 10^8$, $\text{Re}=7350$, and $\text{Pr}=0.7$ for air, the governing equations (1-3) are integrated in time with the momentum equation being expanded by a feedback term that penalizes the deviation of the computed velocity from the experimentally-obtained, divergence-free velocity field, i.e.

$$\frac{\partial \mathbf{u}}{\partial t} + \mathbf{u} \cdot \nabla \mathbf{u} = -\nabla p + \sqrt{\frac{\text{Pr}}{\text{Ra}}} \nabla^2 \mathbf{u} + T \mathbf{e}_z + \alpha(\mathbf{u}_{ref} - \mathbf{u}), \quad (4)$$

where α is the feedback gain and \mathbf{u}_{ref} represents the experimentally-obtained, divergence-free velocity field linearly interpolated from two consecutive snapshots. A schematic sketch of the algorithm is depicted in Figure 3 (left). In the subvolume of the mixed convection sample where tomo PIV velocity data has been captured (green volume in Figure 1),

the time-integrated velocity field is every time step subjected to a force, which is proportional to the deviation of the velocity field from the corresponding tomo PIV velocity field. Thus, after an initial transient phase, the simulated flow field evolves towards the measured one in the measurement volume, while its extension in the rest of the sample evolves accordingly due to the conservation of mass, momentum and energy (equations 1-3). As a consequence, the flow field becomes accessible not only in the measurement volume, but also in the rest of the sample as well as in the boundary layers in the vicinity of solid walls, which have not been captured, initially. Furthermore, the temperature field that corresponds to the simulated velocity field, and therefore, to the measured velocity field, becomes accessible as well. As a preliminary result, Figure 3 (right) displays the measured velocity field together with the corresponding simulated velocity and temperature fields during the initial transient phase.

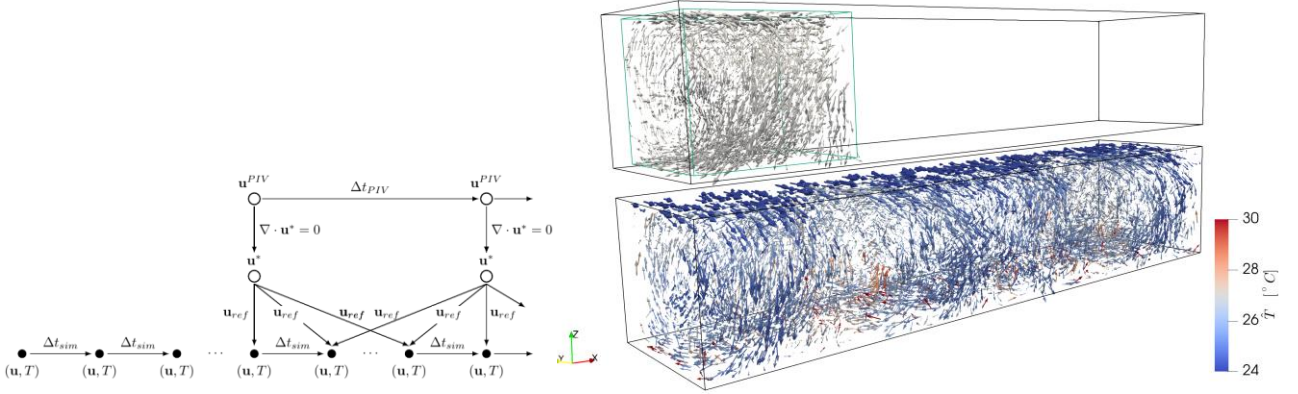


Figure 3. Left: Schematic sketch of the nudging algorithm. \mathbf{u} , time-integrated velocity; T , time-integrated temperature; \mathbf{u}^{PIV} , tomo PIV-measured velocity; \mathbf{u}^* , divergence-free velocity for each tomo PIV snapshot; \mathbf{u}_{ref} , linearly interpolated velocity at every time step from consecutive PIV snapshots; Δt_{sim} , simulation time step; Δt_{PIV} , tomo PIV time step. Right: Measured tomo PIV velocity field \mathbf{u}^{PIV} (top) and preliminary simulated velocity and temperature fields \mathbf{u} , T (bottom).

4. CONCLUSIONS

In order to extract additional information from tomo PIV measured velocity fields of turbulent mixed convection as well as to extend the measurement domain, we adapt our recently published data assimilation scheme (Bauer et al., 2022), considering the governing equations of the problem. The divergence-free condition is fulfilled by solving the Poisson equation for the experimentally-measured velocity field and by correcting the fields according to a fractional step method (see Figure 2). Moreover, since the measurement contains only data of approximately one-fourth of the flow domain, we are expanding the measured velocity field to the flow region where no data has been measured by applying the nudging algorithm sketched in Bauer et al (2022). In this way, we do not only increase the quality of the velocity measurement by making it divergence-free, but we also assess parameters that are not directly measured—such as the pressure and the temperature—and expand them into regions that have not been accessible by the measurement, as well. At the conference, we are going to present and evaluate velocity and temperature fields of turbulent mixed convection extracted from tomo PIV measurements with the methods mentioned above. We strongly believe that such methods are a valuable contribution to the field of PIV measurements, as they help to extract information initially hidden in the measurement data without additional measurements.

5. REFERENCES

- Bauer, C., Schiepel, D. and Wagner, C., 2022. “Assimilation and extension of particle image velocimetry data of turbulent Rayleigh–Bénard convection using direct numerical simulations”. *Experiments in Fluids*, Vol. 63(22), pp. 1-17.
- Di Leoni, P.C., Mazzino, A. and Biferale, L., 2020. “Synchronization to big data: Nudging the Navier-Stokes equations for data assimilation of turbulent flows”. *Physical Review X*, Vol. 10(1), 011023.
- Elsinga, G.E., Scarano, F., Wieneke, B. and van Oudheusden, B.W., 2006 “Tomographic particle image velocimetry”. *Experiments in Fluids*, Vol. 41(6), pp. 933-947.
- Mommert, M., Schiepel, D., Schmeling, D. and Wagner, C., 2020. “Reversals of coherent structures in turbulent mixed convection”. *Journal of Fluid Mechanics*, Vol. 904, A33.
- Schiepel, D., Schmeling, D. and Wagner, C., 2021. “Simultaneous tomographic particle image velocimetry and thermometry of turbulent Rayleigh–Bénard convection”. *Measurement Sciences and Technology*, Vol. 32(9), 095201.
- Suzuki, T. and Yamamoto, F., 2015. “Hierarchy of hybrid unsteady flow simulations integrating time-resolved PTV with DNS and their data-assimilation capabilities”. *Fluid Dynamics Research*, Vol 47(5), 051407.

HYDRODYNAMIC INNOVATION: USING TWO-PHASE FLOW AND COMPLIANT SURFACES FOR DRAG REDUCTION

Raminta Skvorčinskienė^{a,*}, Lina Vorotinskienė^b, Marius Urbonavičius^c, Nerijus Striūgas^d

^a Combustion processes laboratory, Lithuanian Energy Institute, Breslaujos st. 3, Kaunas, Lithuania

^b Combustion processes laboratory, Lithuanian Energy Institute, Breslaujos st. 3, Kaunas, Lithuania

^c Center for hydrogen energy technologies, Lithuanian Energy Institute, Breslaujos st. 3, Kaunas, Lithuania

^d Combustion processes laboratory, Lithuanian Energy Institute, Breslaujos st. 3, Kaunas, Lithuania

[*Raminta.skvorcinskiene@lei.lt](mailto:Raminta.skvorcinskiene@lei.lt)

Keywords: two-phase flow, boiling crisis, heat flux, hydrodynamic, friction drag.

1. INTRODUCTION

The Leidenfrost effect, discovered in 1751, remains a subject of intense research due to its potential applications in reducing friction drag for marine vessels. While much effort has been devoted to understanding and controlling this phenomenon, there's a growing interest in leveraging it for drag reduction. It is important to highlight that the majority of research efforts are directed towards mitigating the Leidenfrost effect. This is because the phenomenon obstructs efficient heat transfer and poses a safety risk to systems where effective cooling is critical. Reducing or nearly eliminating friction resistance is crucial for creating an efficient process to reduce emissions when transporting cargo by sea vessels. This incentive has opened a separate branch of scientific inquiry focused on understanding the conditions and requirements for achieving the Leidenfrost effect (Prasad et al., 2022) and droplet levitation (McElligott et al., 2022). Various types of materials, surfaces, liquids were studied to investigate unpredictable phenomenon. Researchers (Kim et al., 2014) conducted interesting experiments exploring the behavior of water droplets near the Leidenfrost temperature on surfaces made of zirconium alloy. Their findings revealed that the structural surface exhibited a delay in the Leidenfrost temperature, attributable to the heightened wetting condition caused by robust capillary absorbing forces. Several scholarly works delve into experiments examining electric field effects on droplets, while others propose a correlation between the intensity of such effects and the hydrophobicity (Shi et al., 2021) and wetting parameters (Zhong & Guo, 2017) of the heated surface. Studies suggest that surface coatings can alter the hydrophobicity-hydrophilicity balance, affecting vapor bubble formation (Dietzel & Poulikakos, 2007) and heat transfer efficiency (Mohamed et al., 2023). The dynamics of bubble formation have a significant impact on the heat transfer coefficient (HTC) during the boiling process and the critical heat flux (CHF), both of which influence the efficiency of heat transfer from the body surface to the liquid through the vapor film that forms. Despite these challenges, advancements in material science offer promising opportunities for manipulating two-phase flow dynamics and improving heat transfer coefficients. Overall, understanding the intricate interplay between surface properties and boiling dynamics is crucial for optimizing drag reduction strategies in maritime applications. Moreover, experiments have shown that modifying surface characteristics using specific alloys can influence the Leidenfrost temperature. However, challenges persist, particularly in managing the boiling crisis and integrating innovative materials.

Given the focus on inhibiting rather than promoting the Leidenfrost effect in current research, there is an opportunity for new analysis and potential further studies. Activated surfaces (Urbonavičius et al., 2020) such as activated aluminium coatings are known to be hydrophobic; however, these materials react well with water vapor. Consequently, these characteristics may facilitate the formation of vapor under more favorable conditions. To achieve a groundbreaking advancement, innovative coatings are being developed that combine a thermal process to reduce frictional drag force by a factor of two. Thus, the interdisciplinary nature and novelty of this research lie in the application of innovative coatings that influence the conditions of thermal processes to achieve friction reduction.


2. MATERIALS AND METHODS

The hemisphere aluminum specimens (Table 1) were prepared for the experiments. These samples were evaluated to study boiling crisis patterns and determine the Leidenfrost temperature. Surface microstructure can affect boiling; thus, different surfaces were prepared with some polished and others activated via plasma flow.

The designed experimental setup (Figure 1) was employed to investigate thermochemical processes within the context of two-phase flow generation. The setup comprises a heating furnace (1), a water tank (2), a data collection unit (3), and an image capture device (4), specimen (5). Hemispherical aluminum samples were heated in an air environment up to 580°C to prevent metal melting. The water temperature in the tank was regulated by an automatic heater. The water circulator was only turned off during the immersion of the sample into the water reservoir to avoid forced convection

effects. Additionally, the water was supplemented with a 0.2M NaOH solution. The sample was mounted onto a steel rod with K-type thermocouple inserted at the tip. This thermocouple was linked to a data logger positioned above the setup, allowing for continuous data logging at predefined intervals. This thermocouple was employed to measure the temperature 1.5 mm away from the surface. The cooling dynamics experiments were conducted under boiling crisis conditions. The samples were tested once they reached a surface temperature of 580°C. First, experiments were conducted at 17°C temperature of water. Then, others experiments were repeated at elevated water temperatures, specifically 40°C and 60°C.

Table 1. Basic parameters of the specimens.

Specimens	Height, mm	Diameter, mm	Thread length, mm	Example
Hemisphere	19.5	19.5	18.5	

A simple way to detect the Leidenfrost effect is to analyze the temperature graph. If the temperature immediately or rapidly declines upon immersion, it suggests the absence of any vapour films. Conversely, if the sample's temperature remains elevated for a period, it indicates the formation of a vapour film, which effectively insulates the sample from its surroundings. Put differently, comparing changes in temperature velocity enables the identification of the precise Leidenfrost temperature, representing the transition point between a stable vapor film and a disrupted film.

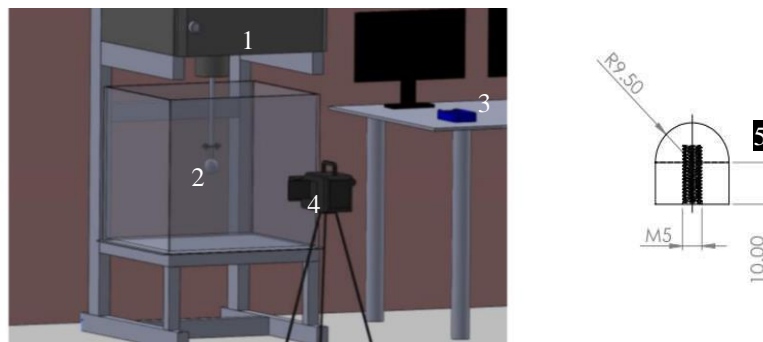


Figure 1. An experimental stand for identification of boiling crisis.

3. RESULTS AND DISCUSSION

Hemisphere specimens with varying surface properties were used for the experiments. The primary objective of the initial testing phase was to determine the temperature at which the most effective interaction between the specimen's surface and water vapor could be achieved for the second stage of experimentation. The specimens underwent categorization based on their surface properties and were exposed to varying water temperatures, including activated and non-activated aluminum surfaces. This facilitated an examination of how distinct surface properties and temperatures influenced the interactions of the specimens within the testing environment. The cooling curves of the samples are presented in Figure 2.

Based on the experimental data, the presence of abundant steam bubbles surrounding the specimen's body (Figure 2, A, B) suggests the absence of the Leidenfrost effect. This indicates that the sample immediately comes into contact with water and induces boiling upon immersion. Additionally, the steep decline in temperature curves at 17°C and 40°C (Figure 2, A, B) implies a lack of apparent isolation between the sample and its environment. Despite repeating the testing of the same sample multiple times, no formation of a steam film was observed. Further testing was conducted by raising the temperature of the water to 60°C.

During the test conducted at a water temperature of 60°C (Figure 2, C), a stable vapour film was observed, albeit disintegrating in under 2 seconds. This is likely attributed to the inadequate hydrodynamic properties of the sample's shape, particularly where the steam film can readily break along the sharp edge of the cylindrical part. Video analysis of the experiment strongly supports this scenario. As previously assessed and now confirmed, the slower temperature decrease (Figure 2, C) can be attributed to the formation of a steam film, consequently indicating the presence of the Leidenfrost effect.

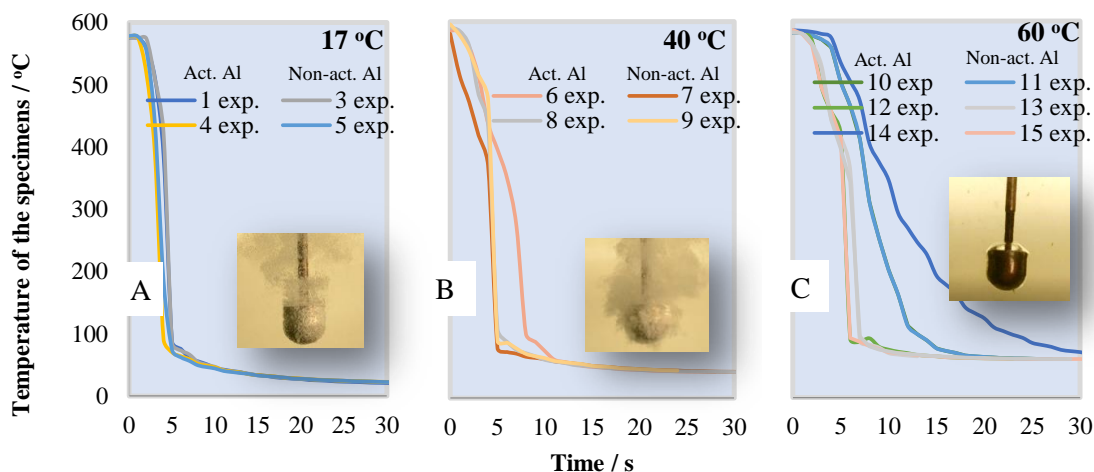


Figure 2. Temperature exchange graph of the specimens at 580 °C temperature after immersion in 17 °C, 40 °C and 60 °C water.

4. CONCLUSIONS

While the long-term Leidenfrost effect was not attained, the groundwork for future experiments was established, and significant observations were made. Despite the slight difference in vapor film generation propensity between hydrogen plasma-treated and untreated samples, elevating the environmental temperature constrained the temperature exchange rate to a specific threshold. The release of vapour resulting from the sample's interaction with the test conditions has a negligible effect on sustaining the Leidenfrost effect. However, a layer of vapour has a more pronounced impact on reducing friction against moving objects.

5. ACKNOWLEDGMENT

This project has received funding from the Research Council of Lithuania (LMTLT), agreement No. S-MIP-22-77.

6. REFERENCES

- Dietzel, M., & Poulikakos, D. (2007). On vapor bubble formation around heated nanoparticles in liquids. *International Journal of Heat and Mass Transfer*, 50(11–12), 2246–2259. <https://doi.org/10.1016/j.ijheatmasstransfer.2006.10.035>
- Kim, S. H., Ahn, H. S., Kim, J., Kim, M. H., & Park, H. S. (2014). Experimental study of water droplets on over-heated nano/microstructured zirconium surfaces. *Nuclear Engineering and Design*, 278, 367–376. <https://doi.org/10.1016/j.nucengdes.2014.06.042>
- McElligott, A., Guerra, A., Wood, M. J., Rey, A. D., Kietzig, A.-M., & Servio, P. (2022). TinyLev acoustically levitated water: Direct observation of collective, inter-droplet effects through morphological and thermal analysis of multiple droplets. *Journal of Colloid and Interface Science*, 619, 84–95. <https://doi.org/10.1016/j.jcis.2022.03.082>
- Mohamed, M. A., Ahmed, S. A., Emeara, M. S., Mesalhy, O., & Saleh, M. A. (2023). Experimental study for enhancing condensation on large-scale surface using hybrid hydrophilic-hydrophobic patterns. *Case Studies in Thermal Engineering*, 45, 102984. <https://doi.org/10.1016/j.csite.2023.102984>
- Prasad, G. V. V., Dhar, P., & Samanta, D. (2022). Postponement of dynamic Leidenfrost phenomenon during droplet impact of surfactant solutions. *International Journal of Heat and Mass Transfer*, 189, 122675. <https://doi.org/10.1016/j.ijheatmasstransfer.2022.122675>
- Shi, M., Das, R., Arunachalam, S., & Mishra, H. (2021). Suppression of Leidenfrost effect on superhydrophobic surfaces. *Physics of Fluids*, 33(12). <https://doi.org/10.1063/5.0064040>
- Urbonavicius, M., Varnagiris, S., Pranevicius, L., & Milcius, D. (2020). Production of Gamma Alumina Using Plasma-Treated Aluminum and Water Reaction Byproducts. *Materials*, 13(6), 1300. <https://doi.org/10.3390/ma13061300>
- Zhong, L., & Guo, Z. (2017). Effect of surface topography and wettability on the Leidenfrost effect. *Nanoscale*, 9(19), 6219–6236. <https://doi.org/10.1039/C7NR01845B>

EXPERIMENTAL INVESTIGATION OF TWO-PHASE CROSS-FLOW INTERACTION USING WIRE MESH SENSOR

Antonio Chahine*, Guillaume Brillant and Daniele Vivaldi

Institut de Radioprotection et de Sûreté Nucléaire (IRSN), 13115 Saint-Paul-lez-Durance, France

*antonio.chahine@irsn.fr

Keywords: Two-phase cross-flow, Tube bundle, Wire Mesh Sensor

1. INTRODUCTION

Two-phase cross-flow is encountered in several industrial applications, such as heat exchangers and steam generators. In such configuration, the tube bundle can be concerned by flow-induced vibrations. The experimental investigation of the related fluid-structure mechanisms is not straightforward, considering the complex geometry and the several two-phase flow patterns that can develop inside it. The numerous experimental campaigns that have been published (see, for example, Pettigrew *et al.*, 1989; Axisa *et al.*, 1990) focused mainly on the tube vibration response, providing poor details about the two-phase flow behavior. However, the comprehensive understanding of the two-phase flow dynamics is mandatory to achieve a consistent interpretation of the flow-induced forces on the tubes and of the associated vibration response. To achieve this goal, the present paper presents an experimental study of an air-water cross-flow in a square tube bundle, where both the flow and structure details are accessed. This is done by employing different measurements techniques (bi-optical probe, high-speed camera and wire mesh sensor) to study the local two-phase flow features, together with accelerometers to measure the tube vibrations. Besides providing new insights of the two-phase flow, the present experimental analysis is aimed at generating CFD-scale data, required for the assessment of CFD numerical simulation results. CFD simulations can represent a powerful approach to evaluate fluid-structure interactions phenomena for such configurations, considering the unfeasibility of designing experimental facilities operating at prototypical thermodynamic conditions (high temperatures and pressures).

2. EXPERIMENTAL CONFIGURATIONS

The experimental campaigns were carried out within the TREFLE facility (Spina, 2023), featuring a square array of 5×5 cylinders exposed to air/water cross-flow, as illustrated in Fig. 1(a). The array, which features a pitch (P)-to-diameter (D) ratio of 1.44, is composed of relatively large-diameter cylinders ($D=30$ mm). This design leads to relatively wide gaps ($P-D = 13.2$ mm) between the cylinders, enabling an easier access for measurements of the two-phase flow dynamics when optical probes are employed within the tube bundle.

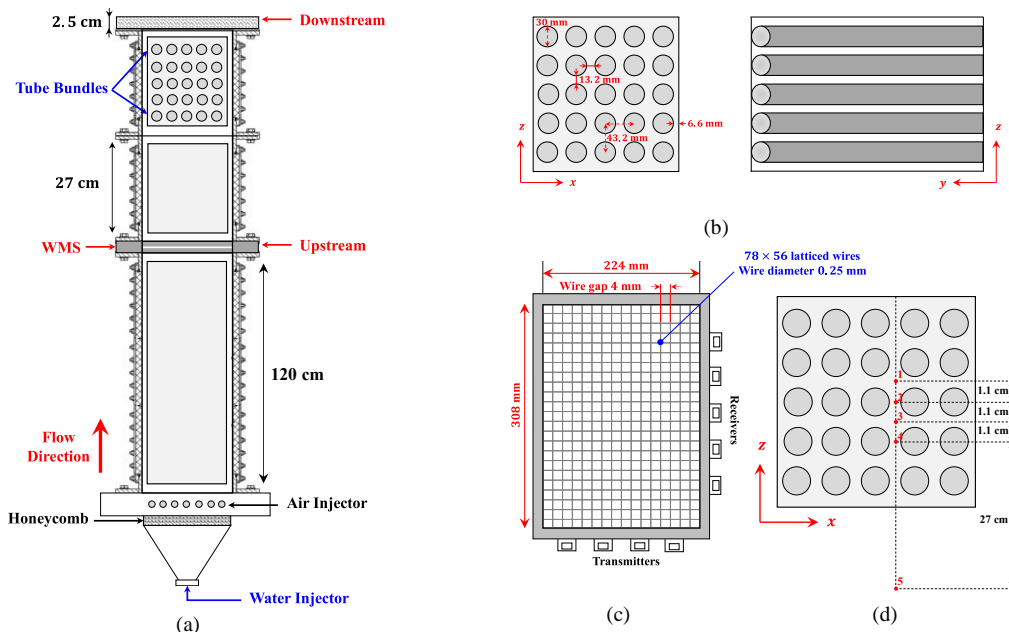


Figure 1. Experimental Configuration: (a) Configuration of TREFLE facility layout and positions of the WMS, (b) Two

side views of the tube bundle section, (c) Schematics of the rectangular WMS and (d) Position of the bi-optical probe measurements.

Horizontal void fraction contour measurements were achieved by employing a WMS with the same dimensions of the section ($308 \text{ mm} \times 224 \text{ mm}$), as presented in Fig. 1(c). The wire mesh has cells of $3.94 \text{ mm} \times 4 \text{ mm}$. The sensor has a high time resolution that can reach 2500 Hz. Within the TREFLE facility, the WMS was strategically positioned at two distinct locations: first, approximately 27 cm upstream of the tube bundle, and second, directly downstream of 2.5 cm the tube bundle. The upstream position allows us to study the two phase flow in the free duct region before entering the tube bundle, whereas the downstream position is able to capture the impact of the tube bundle on the two phase-flow. It has to be noted that the distance between the WMS and the last row of tubes (for the downstream position) corresponds to about $2P$: we can reasonably assume that this position is representative of what occurs inside the tube bundle. A different measurement system was utilized, employing a bi-optical probe positioned at various locations inside the tube bundles, including the upstream position as illustrated in Figure 1(d).

Figure 2 illustrates the cartography depicting various flow regimes observed in the two-phase flow (air-water) within a vertical free duct from the work of Abbs and Hibiki (2019). The dashed line represents the cartography in tube bundle reported in the literature by Mao and Hibiki (2019). Our investigation involved manipulating the gas superficial velocity (j_g) within the range of 0.02 to 1.35 m/s while maintaining a constant water superficial velocity (j_l) at 1.2 m/s. The experimental points that we set as the initial conditions are depicted on the graph, with three points representing a bubbly regime and three corresponding points for the intermittent flow regime.

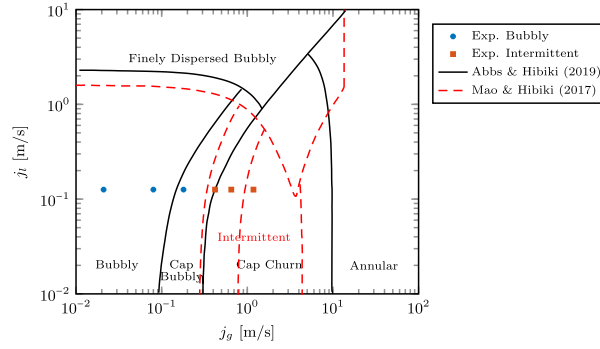


Figure 2. Cartography of Two-Phase Flow Regimes (air-water) in a Vertical Free Duct. Experimental points are based on our research and are integrated findings reported in the literature by Abbs and Hibiki (2019), The dashed line represent the cartography in tube bundle reported in the literature.

3. RESULTS AND DISCUSSIONS

The void fraction measurements were performed at a frequency of 1000 Hz for an extended duration of 800 s. Each set of conditions was subjected to two repetitions. The WMS measures the void fraction (α_s), representing the ratio of gas occupied cross-surface to the total cross-surface.

The void fraction evolution over time for a water velocity $j_l = 1.2 \text{ m/s}$ and air velocity $j_g = 0.65 \text{ m/s}$ at the upstream position were measured using the wire mesh sensor. The signal displayed in Fig. 3(a) exhibits oscillations of 20 % between two distinct values, which correspond to the lower and upper limits of the void fraction. At its lowest value, the void fraction corresponds to instants where mainly relatively small bubbles cross the WMS, as clearly demonstrated in Fig. 3(b). On the contrary, as presented in Fig. 3(c), the highest values of void fraction correspond to large gas structures crossing the WMS. These structures are the main contributors to the high void fraction values measured.

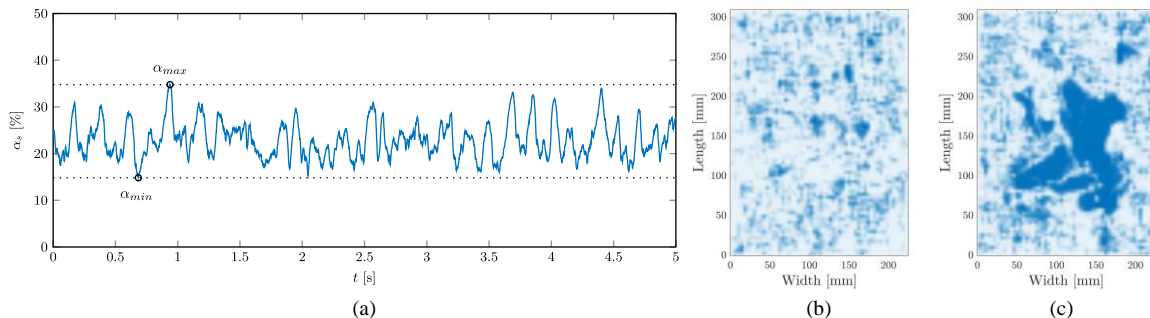


Figure 3. (a) Void fraction evolution over time for a water velocity $j_l = 1.2 \text{ m/s}$ and air velocity $j_g = 0.65 \text{ m/s}$, (b) Void fraction distribution at $\alpha_{min} = 14.82 \%$, and (c) Void fraction distribution at $\alpha_{max} = 34.77 \%$.

The variation in void fraction (α_s) over time is shown by the graph in Fig. 3(a), where the interplay between gas and water velocities influences the presence and size of bubbles, thereby influencing the observed changes in void fraction magnitude. It is clearly observed in the case of maximum void fraction that the small bubbles consistently reside around the borders, while the substantial gas structure traverses through the center.

Figure 4 represents the Probability Density Functions (PDFs) corresponding to the void fraction (α_s) and Bubble diameter at the Upstream, and Downstream positions. These configurations are evaluated at specific fluid velocities, with a liquid velocity (j_l) of 1.2 m/s and an air velocity (j_g) of 0.65 m/s. The presence of the tube bundle significantly influences the flow, leading to reduced void fraction, increased coalescence, and higher bubble velocity within the tubes, compared to the upstream position.

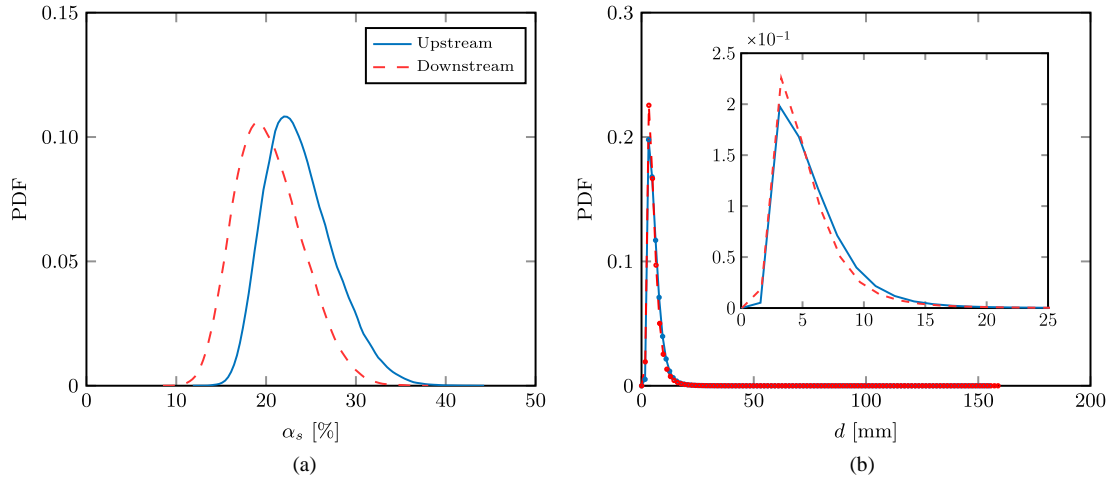


Figure 4. Probability density functions (PDF) at configurations: Upstream, Downstream for $j_l = 1.2$ m/s and air velocity $j_g = 0.65$ m/s representing the (a) void fraction, and (b) Bubble diameter.

4. CONCLUSIONS

This research offers valuable insights on the two-phase cross-flow phenomena occurring within a square tube bundle. A wire mesh sensor was strategically positioned both upstream and downstream of the bundle to enhance data collection, and can provide more information about the bubble characteristics. The bi-optical probe provides valuable insights into bubble velocity, diameter, and void fraction profile along the tube bundle. An instrumentation utilizing a force gauge is currently in production to further understand the flow forces acting on the center tube.

5. REFERENCES

- Abbs, T. and Hibiki, T., 2019. "One-dimensional drift-flux correlation for vertical upward two-phase flow in a large size rectangular channel". *Progress in Nuclear Energy*, Vol. 110, pp. 311–324.
- Axisa, F., Antunes, J. and Villard, B., 1990. "Random excitation of heat exchanger tubes by cross-flows". *Journal of Fluids and Structures*, Vol. 4, pp. 321–341.
- Mao, K. and Hibiki, T., 2017. "Flow regime transition criteria for upward two-phase cross-flow in horizontal tube bundles". *Applied Thermal Engineering*, Vol. 112, pp. 1533–1546.
- Pettigrew, M.J., Taylor, C.E. and Kim, B.S., 1989. "Vibration of tube bundles in two-phase cross-flow: Part 1-hydrodynamic mass and damping". *Journal of Pressure Vessel Technology*, Vol. 111, pp. 466–477.
- Price, S.J., 1995. "A review of theoretical models for fluidelastic instability of cylinder arrays in cross-flow". *Journal of Fluids and Structures*, Vol. 9, pp. 463–518.
- Selima, Y., Hassan, M., Mohany, A. and Ahmed, W., 2021. "Modelling of fluidelastic instability in tube bundles under two-phase bubbly flow conditions". *Journal of Fluids and Structures*, Vol. 103, pp. 103256.
- Spina, G., 2023. "Experimental and numerical study of two-phase flows and of fluid-structure interactions inside a cross-flow tube bundle". Ph.D. thesis, INP Toulouse, Toulouse, France.
- Weaver, D.S. and Fitzpatrick, J.A., 1988. "A review of cross-flow induced vibrations in heat exchanger tube arrays". *Journal of fluids and structures*, Vol. 2, pp. 73–93.

EXTENSION OF THE HOT BOX METHOD TO THE DETERMINATION OF DYNAMIC PROPERTIES OF BUILDINGS COMPONENTS

Giorgio Baldinelli^{a,*}, Francesco Bianchi^b, Cristiano Turrioni^b,

^aDepartment of Engineering - University of Perugia, Via Duranti 67 - 06125 Perugia - Italy

^bINFN Sezione di Perugia, Via Pascoli - 06123 Perugia - Italy

*giorgio.baldinelli@unipg.it

Keywords: hot box, dynamic properties, periodic thermal transmittance

1. INTRODUCTION

The growing attention to energy saving issues has involved the entire building chain, which is in fact responsible, according to statistics, for 39% of the world global energy consumption and 38% of the total global CO₂ emissions [1].

The deep knowledge of the building envelope, in particular the study of the thermal characteristics of its parts, appears therefore fundamental. Furthermore, while the study of the static behaviour is advanced and mature, as regards the dynamic performance, gaps are still present, as the approach is limited to ideal situations with little practical feedback (uniform and homogeneous materials, one-dimensional and wall-perpendicular flow, etc...).

This study sets itself the goal of dynamically characterizing experimentally the thermal properties of any part of the building envelope, using the hot box measurement system.

2. METHODOLOGY

The idea behind this research consists of moving from the calibration and static measurement methodology for the hot box system, already known from the Standard EN ISO 12567 [2], and tailoring it to a dynamic characterization of the samples to assess their periodic thermal transmittance.

The first step is the dynamic calibration of the hot box, which is done using a panel with known thermal properties. A sinusoidal temperature variation is imposed in the cold side and the periodic thermal flow that crosses the panel is calculated and subtracted, together with the thermal flow dispersed in the laboratory, from the total power introduced into the hot chamber. The harmonic flow passing through the support panel (including the insulation edges) is so found. Once these data have been obtained, it is possible to calculate the periodic thermal transmittance of the support apparatus, the same in each measurement, which will allow to carry out evaluations on the different measurement samples.

In fact, in the second step, the calibration panel is replaced with the sample under analysis, recreating the same thermal conditions of the calibration test in the two climatic chambers. By acquiring data in these conditions, it is possible to derive the heat flow passing through the sample as the difference between the total power introduced into the hot chamber, the heat flow towards the environment and that which passes through the support panel. At this point, also knowing the room temperatures, the periodic thermal transmittance of the component under examination is obtained.

It is important to remark that in all these calculations, as heat flows and temperatures are sinusoidal quantities, it is necessary to use complex numbers.

3. EXPERIMENTAL TESTS

The tests have been executed in the calibrated hot box setup of the University of Perugia (figure 1). The dynamic calibration procedure was carried out using a calibration panel made up of a 2 cm polystyrene plate enclosed by two 4 mm thick glass plates (the same used for the hot box static calibration). The hot chamber has a fixed temperature of 20°C and the cold one has a temperature sinusoidal trend ranging between -5°C and +5°C, with a period of 24 hours.

The acquisition of the signals coming from the measuring instruments had a total duration of 3 days, to obtain a stabilised periodic regime, the last complete oscillation of 24 hours was then used for the calculations. The data processing has been implemented with the Field PointTM System of National InstrumentTM and the FieldPoint Explorer software of the same house.

Figure 2 shows the graph that represents the temperature fluctuation on the cold side calibration panel and the trend of the power fed into the hot chamber.



Figure 1. The hot box setup used for the experimental tests.

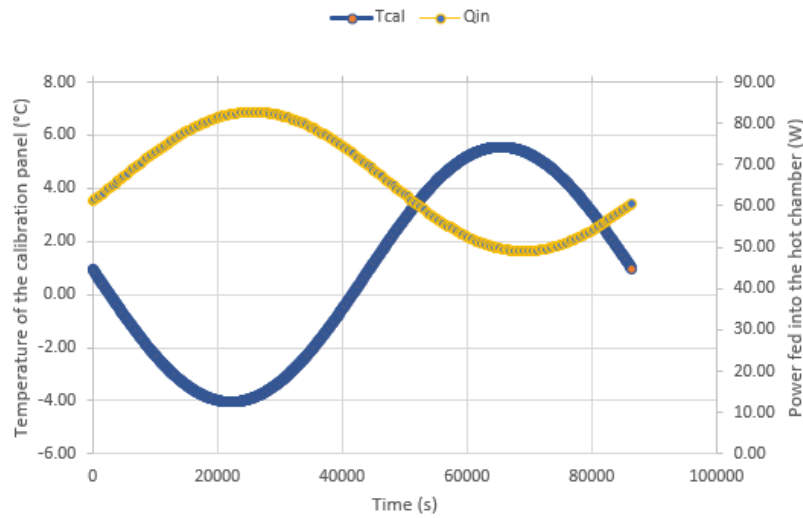


Figure 2. Surface temperature of the calibration panel and power fed into the hot chamber.

Referring to Standard EN ISO 13786 [3] and using the acquired temperatures and power input data, the periodic thermal transmittance of the calibration panel (Y_{12}) is retrieved according to Equation (1):

$$Y_{12} = -\frac{1}{Z_{12}} \quad (1)$$

Maintaining the same thermal conditions in the two climatic chambers, the calibration panel was replaced with a 2 cm thick wood chipboard. The procedure seen in the calibration was then repeated, inverting the input data and the unknown ones: starting from the periodic thermal transmittance of the support panel and from the data acquired with the hot box system, the thermal transmittance of the test sample is calculated.

Since the thermophysical properties of the chipboard are known from the Literature and the sample itself was equipped with heat flow meters, a comparison between the periodic thermal transmittance obtained with the three methods can be implemented (table 1).

Table 1. Comparison among the three different methods for the evaluation of the periodic thermal transmittance.

METHOD	Module [W/m²]	Phase [hours]	Difference (module) [W/m²]	Difference (module) [%]	Difference (phase) [hours]	Difference (phase) [%]
Dynamic hot box	3.67	+ 0.30	-	-	-	-
ISO 13786	3.52	- 0.27	+ 0.15	+ 4.1	+ 0.57	+ 2.4
Heat flow meter	3.33	+ 0.33	+ 0.34	+ 9.3	- 0.03	- 0.1

The proposed method appears quite aligned with the results retrieved from the Standard and from the measurements done with the instruments and the calculation of the Standard, with a difference not higher than 10% in terms of heat flow module and lower than 3% in terms of the heat flow phase.

4. CONCLUSIONS

The proposed methodology for the use of hot box systems to determine the dynamic properties of building components showed satisfactory results. The good match of the experimental data gathered with the hot box system with those obtained by other techniques demonstrated that the approach described in this study is valid for the calculation of the transmittance periodic temperature of any building element. In particular, the advantage of this approach consists on the possibility of obtaining the dynamic thermal properties of inhomogeneous materials such as windows and non-parallel layers walls, or particular envelope discontinuities as, for instance, thermal bridges.

5. REFERENCES

- [1] Hai Zhong, Jiajun Wang, Hongjie Jia, Yunfei Mu, Shilei Lv, *Vector field-based support vector regression for building energy consumption prediction*, Appl. Energy 242 (2019) 403-414.
- [2] EN ISO 12567-1, *Thermal performance of windows and doors — Determination of thermal transmittance by the hot-box method — Part 1: Complete windows and doors*, 2010.
- [3] ISO 13786, *Thermal performance of building components — Dynamic thermal characteristics — Calculation methods*, 2017.

SENSITIVITY STUDY ON POD ANALYSIS OF NEAR WAKE BEHIND CIRCULAR CYLINDER

Keh-Chin Chang*, Tzu-Hsun Lin, Chia-Chun Chu

Department of Aeronautics and Astronautics, National Cheng Kung University

1 University Road, Tainan, 70101, Taiwan

*kcchang@ncku.edu.tw

Keywords: proper orthogonal decomposition, particle image velocimetry, near wake, coherent structure

1. INTRODUCTION

Progress on both high spatial resolution and temporal resolution of the particle image velocimetry (PIV) promotes the measured information for the spatially phase-correlated vorticity to be used for studying the dynamic of a coherent structure (Zhang, et al., 2014; Gao, et al., 2020; Chu and Chang, 2023). The proper orthogonal decomposition (PDO) is a widely applied method to extract the essential feature from a snapshot sequence of flow fields from experimental measurements or numerical simulations (Berkooz, et al., 1993; Aranyi, et al., 2013; Zhang, et al., 2014). POD is a procedure for extracting a basis for a model decomposition from an ensemble of data; in other words, POD decomposes a large quantity of data set into spatial eigenfunctions (or eigenmodes) and temporal coefficients that correspond to each eigenmode (Sirovich, 1987; Berkooz, et al., 1993). Eigenmodes are sorted in an order based on their energy contribution.

Although POD has been widely used in analyzing experimental data, there still remain some parametric problems to be clarified further. For instance, almost all of the experimental studies using POD for the analysis of turbulent flow were performed with the total number of image pairs which they collected in the measurements. Table 1 shows the total numbers of image pairs for previous studies using POD. Nevertheless, there were no evidences showing the achievement of the stationary POD results using the collected image pairs in these studies. The next issue is regarded to the choice for the window size for PIV measurement, that is, the field of view (FOV). It is agreed that FOV should not be less than the maximum spacing (λ) of vortices in the Karman vortex street, which can be estimated using the following relationship:

$$\lambda = \frac{U_{ref}}{f} = \frac{d}{St} \quad (1)$$

where U_{ref} is the freestream velocity, f is the Karman vortex shedding frequency, d is the diameter of cylinder and St is Strouhal number. What effect for use the FOV which is different from λ will be for the POD analysis? A sensitivity study of the two aforementioned parameters on the POD analysis is conducted in the study.

Table 1 Summary of experimental conditions for previous studies using POD

Flow type	Reynolds number	Image resolution (pixel by pixel)	Sampling rate (H_z)	Number of Image pairs
Wake (Perrin, et al., 2007)	1.4×10^5	2752×2200	1000	3000
Wake (Zhang, et al., 2014)	8×10^3	--	100	2000
Wake with an upstream plate (Gao, et al., 2020)	2.66×10^4	1600×1200	8	> 400
Wake of finned cylinder (Islam and Mohany; 2020)	2×10^4	2752×2200	15	1000
Wake (Chu and Chang; 2022)	3.86×10^3	1024×1024	10000	10915

2. EXPERIMENTAL METHOD

Experiments are conducted in a vertically downward, rectangular wind tunnel with the freestream velocities of 5.97 m/s, which is equivalent to Reynolds numbers (based on d) of 3860. The test section has a cross sectional area of 150 mm \times 150 mm and a length of 600 mm. A circular cylinder with diameter of 10 mm is mounted in the middle of the cross section, 75 mm down from the top of the text section, and acts as a wake generator. The transverse coordinate (y) is positive toward the right and the stream-wise coordinate (x) is positive downward. The origin is at the center of the

cylinder. The domain of interest (measured area) is $150 \text{ mm} \times 100 \text{ mm}$ (x by y direction) in the central plane behind the cylinder.

A two-component PIV system is used for velocity measurement. The frame rate is 10^4 frame/s with a spatial resolution of 1024 by 1024 pixels. The tracers are silicon oxide with a nominal mean size of $1.9 \mu\text{m}$. The uncertainty in the PIV measurement under the employed experimental conditions is estimated about 3.1%. More information for the PIV system and its operational condition is referred to the study of Chu and Chang (2023) except the memory capacity is magnified from 16 GB to 64 GB, so a total of 43683 PIV image pairs are analyzed for the study.

3. POD ANALYSIS AND IDENTIFICATION OF COHERENT STRUCTURE

POD is used for turbulent wake analysis to identify coherent structures by extracting an orthogonal set of spatial eigenfunctions from the second-order statistics for an instantaneous flow field. Snapshot POD method (Sirovich, 1987) decomposes the two-dimensional temporal velocity field at instant time t_ℓ as a sum of the mean $\bar{u}_i(x, y)$ and fluctuating $u'_i(x, y, t_\ell)$ velocity components using the Reynolds decomposition:

$$u_i(x, y, t_\ell) = \bar{u}_i(x, y) + u'_i(x, y, t_\ell) = \bar{u}_i(x, y) + \sum_{n=1}^N a_{i,n}(t_\ell) \phi_{i,n}(x, y) \quad (2)$$

where $\phi_{i,n}(x, y)$'s and $a_{i,n}(t_\ell)$'s are respectively the spatial eigenmodes and the temporal mode coefficients that correspond to each eigenmode. Theoretically, N must be infinite for an exact representation of u_i . Nevertheless, the N is a finite number in engineering practice and will be determined in the study.

The turbulent wake has a dual character, with organized (coherent, which are large scales) and chaotic (fluctuating, which are microscales) motions interacting nonlinearly. The triple decomposition can further distinguish the two time-dependent velocity components as

$$u_i(x, y, t_\ell) = \bar{u}_i(x, y) + \tilde{u}_i(x, y, t_\ell) + u''_i(x, y, t_\ell) \quad (3)$$

where $\tilde{u}_i(x, y, t_\ell)$ and $u''_i(x, y, t_\ell)$ are respectively a component of organized and randomly fluctuating motion. A Fourier transform is used to identify the coherent motions in the study. Large-scaled organized frequencies of the coherent structure in each mode coefficient are identified in terms of a condition of their peak magnitudes greater than the smallest magnitude of the identified harmonic-frequency family (Chu and Chang, 2023).

4. PRELIMINARY RESULTS AND DISCUSSION

Figure 1 shows the energy contribution for each mode and the cumulative distribution for the first 1000 modes in the subregion of $0.5 d$ to $5.5 d$. The curve of the kinetic-energy percentage contributed by each mode reduces sharply after the first two modes and then monotonously collapses to a negligible level. The Fourier power spectrum for the 10^{th} mode coefficient is shown in Fig. 2 and is used to demonstrate how to identify the large-scaled organized motions. The harmonic frequencies can be found from a Fourier spectrum analysis of the PIV data in the flow field. Figure 3 shows the power spectrum of the PIV data for the stream-wise velocity component at location $(x/d = 4, y/d = 0.3)$, which is within the near-wake core of the domain of interest. A moving average method with a window of size 25 is used to help identify the frequency subrange in which the gradient of the log-log curve is equal to $-5/3$, which is referred to the inertia subrange. An eddy with a frequency within the inertia subrange has a Taylor microscale size and is classified as the randomly fluctuating component in Eq. (3). Figure 3 shows that the 1st, 2nd and 3rd harmonic frequencies are in the integral-scale (i.e., large-scale) subrange, which are beyond the inertia subrange. The 4th harmonic frequency (504 Hz) is within the inertial subrange, thus, the other harmonic frequencies behind the 3rd one are treated as the randomly fluctuation component. The 1st harmonic frequency, which is equivalent to the Karman vortex shedding frequency (f), is 126 Hz in Fig. 3. The FOV ($= \lambda$) can be determined using Eq. (1) and to be approximately equal to $4.8 d$. Thus, the FOV is set to be $5 d$ long for the PIV measurement. The Karman vortex street has large-scale organized motions so the peak frequencies for which the magnitudes are greater than that of the 3rd harmonic frequency (the smallest magnitude of the harmonic family in Fig. 2) in the power spectrum for the 10^{th} mode are large-scaled, organized motions (Zhang, et al., 2014; Chu and Chang, 2023). The kinetic energy that is contributed by the 10^{th} mode is 0.835% (see Fig. 1) in which the coherent structure contributes 24.69% in it. It is reported by Chu and Chang (2023) that the weighting for the kinetic energy contributed by the organized motions to the total kinetic energy in a mode (if these exist) decreases generally as the mode number increases. For instance, the contribution to the total kinetic energy for the 12^{th} mode drops to 0.724% (see Fig. 1) in which the coherent structure contributes 13.0% in it.

To investigate the issue of how many image pairs (i.e., N value in Eq. (2)) in the POD analysis, seven trials with $N = 8000$ to 18000 are performed in the POD analysis in the subregion of $0.5 d$ to $5.5 d$. Since all the eigenmodes are calculated from the second-order statistics of an instantaneous velocity component, the uncertainty is two times of the first-order statistics which is 3.1% in the PIV measurement, that is 6.2%. The baseline for comparison is set with the results using the maximum total number of image pairs (43863) and the first 45 modes of which the cumulative kinetic energy on entire eigenmodes reaches 80% (see Fig. 1). The maximum relative deviation for either each mode or the cumulative sum of the first 45 modes which is respectively performed for seven trials is recorded in Fig. 4. A regression

curve is fitted using the seven values of the maximum relative error and is plotted in Fig. 4. The intersecting point of the regressive curve and the line of $y = 6.2\%$ is around 14300, which means that it needs no less $N = 14300$ to attain a confident result for the coherent structure within the measurement accuracy in Eq. (2). Similar analyses for the downstream subregions of 5.5 d-11 d and 11 d-16.5 d will be presented in the final manuscript. A parametric study using various FOVs on the PIV measurement and the resultant POD analysis will be presented too.

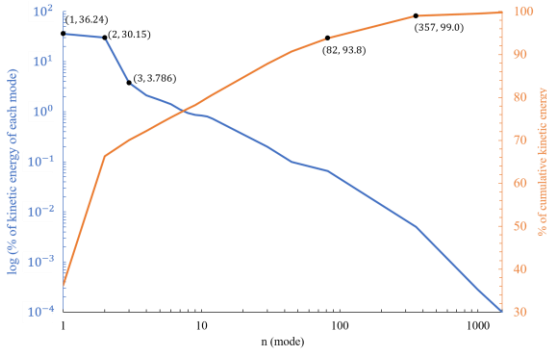


Figure 1 Distributions of the kinetic-energy contribution for each mode and the accumulation for the first 1000 modes

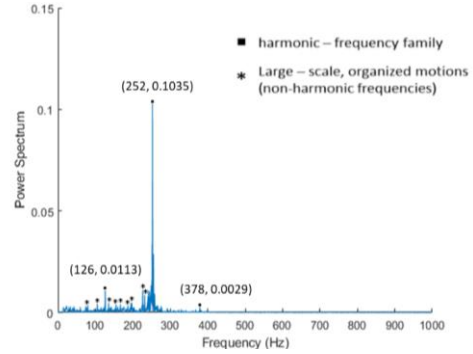


Figure 2 Fourier power spectrum for the tenth POD mode

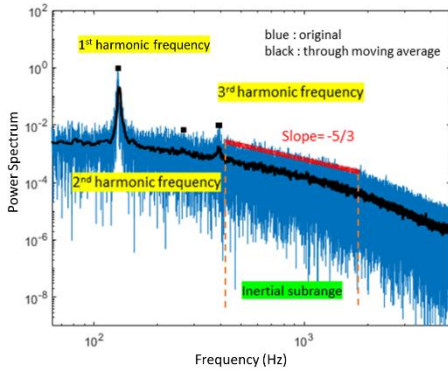


Figure 3 Power spectrum of the stream-wise velocity at the location ($x/d = 4, y/d = 0.3$)

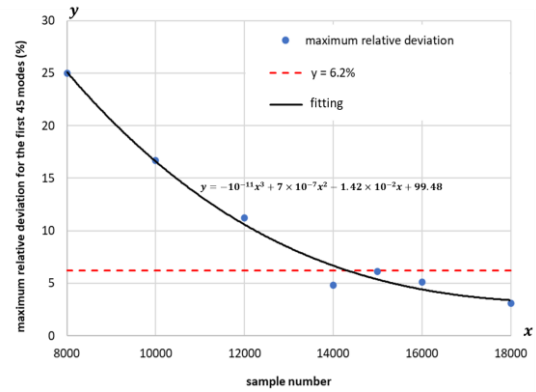


Figure 4 Evolutions of kinetic energy percentage contributed by coherent structure versus stream-wise

5. REFERENCES

- Aranyi, P., Janiga, G., Zahringer, K. and Thevenin, D., 2013. "Analysis of different POD methods for PIV measurements in complex unsteady flow". *International Journal of Heat and Fluid Flow*, Vol. 43, pp. 204-211.
- Berkooz, G., Holmes, S. and Lumley J.L., 1993. "The proper orthogonal decomposition in the analysis of turbulent flows". *Annual Review of Fluid Mechanics*, Vol. 25, pp. 539-575.
- Chu, C.C. and Chang, K.C., 2023. "Estimating the energy contribution of coherent structure in a cylindrical near-wake flow using proper orthogonal decomposition". *Journal of Fluid Science and Technology*, Vol. 18(1) (DOI: 10.1299/jfst.2023jfst0004).
- Gao, D.L., Chen, G.B., Huang, Y.W., Chen, W.L. and Li, H., 2020. "Flow characteristics of a fixed circular cylinder with a upstream splitter plate: on the plate-length sensitivity". *Experimental Thermal and Fluid Science*, Vol. 117, pp. 110-135.
- Islam, M.R. and Mohany, A., 2020. "Vortex shedding characteristics in the wake of circular finned cylinder". *Physics of Fluid*, Vol. 22, 045113.
- Perrin, R., Braza, M., Cid, E., Cazin, S., Barthet, A., Sevrain, A., Mochett, C. and Thiele, F., 2007. "Obtaining phase averaged turbulence properties in the near wake cylinder at high Reynolds number using POD". *Experiments in Fluids*, Vol. 43, pp. 341-355.
- Sirovich, L., 1987. "Turbulence and the dynamics of coherent structure". *Quarterly of Applied Mathematics*, Vol. 45, pp. 561-590.
- Zhang, Q., Liu, Y. and Wang, S., 2014. "The identification of coherent structures using proper orthogonal decomposition and dynamic mode decomposition". *Journal of Fluids and Structure*, Vol. 49, pp. 53-72.

EXPERIMENTAL ANALYSIS OF METAL FOAM GEOMETRY ON THE BIO-BASED PCM MELTING PERFORMANCE

Fábio Becker^a, Jacqueline Biancon Copetti^{a*}, Elaine Maria Cardoso^{b, c}, Mirella Callage da Silva^a

^aUNISINOS - University of Valley of the Rio dos Sinos; Avenida Unisinos, 950, São Leopoldo – RS, 93022-750, Brazil.

^bUNESP - São Paulo State University, School of Engineering, Av. Brasil, 56, Ilha Solteira, SP 15385-000, Brazil.

^cUNESP - São Paulo State University, School of Engineering, São João da Boa Vista, Brazil.

*corresponding author: jcopetti@unisinos.br

Keywords: Phase Change Material (PCM), bio-based PCM, Melting process, Metal Foam, Energy Storage

1. INTRODUCTION

The increasing implementation of renewable energy sources, combined with their seasonality, which generates intermittency in the energy supply, makes storing excess energy generated for later use important (Mitali et al., 2022). Moreover, as the need for enhanced heat transfer capability surges within high-tech sectors, there is a growing focus on enhancing thermal management technologies.

Phase Change Materials (PCMs) have the characteristic of storing and releasing energy through sensible and latent heat at a practically constant temperature (Lawag and Ali, 2022). These can be used in the production of energy storage systems, in buildings, batteries thermal control, temperature control of microelectronics, as well as in the human body and transport (Mehari et al., 2020; Irfan Lone and Jilte, 2021; Mehling et al., 2022). Therefore, due to the wide range of applications, it is important to use PCM that is environmentally friendly in order to avoid environmental negative impacts. In this context, bio-based PCMs have become a promising alternative (Nazari et al., 2020). Bio-based PCMs are materials derived from renewable and ecological resources with a lower impact on carbon generation, making reducing greenhouse gas emissions possible (Sharma et al., 2024).

However, these materials have low thermal conductivity, which increases the charging (melting) and discharging (solidification) period and limits their use in the countless possibilities of thermal systems. Therefore, it is necessary to implement methodologies to intensify heat transfer rates (Ismail et al., 2022), such as the insertion of fins (Yu et al., 2020), microencapsulation, use of nanoparticles (Li et al., 2020) and metal foams (Shi et al., 2023).

The insertion of metal foams is one of the most efficient alternatives due to improved thermal conductivity and surface area (Aramesh and Shabani, 2022), increasing the contact area between fluid and surface (Shi et al., 2023). The current work investigates the influence of metal foam geometry on the melting performance of bio-based phase change materials (PCM), focusing on two distinct types of metal foams: uniform foam and pin-fin foam. The objective is to elucidate the thermal enhancement capabilities of these foam structures when applied in conjunction with a bio-based PCM (palm wax). This study aims to analyze the advantages and limitations of a system with pin-fin metal foam, providing valuable insights into its applicability in enhancing the melting behavior of bio-based PCMs.

2. METHODOLOGY

The experimental setup consists of a test reservoir, a power source, a power quality analyzer, a video camera and a portable computer, as represented in Fig. 1.

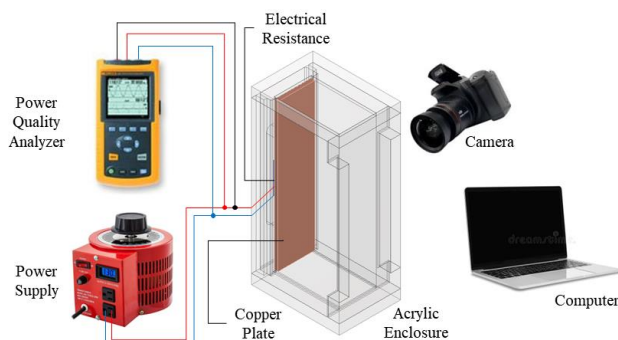


Figure 1 - Experimental setup.

The test reservoir comprises an acrylic box, a copper plate and an electrical resistance. A 120 mm long, 30 mm wide and 3 mm thick copper plate was inserted into the box's left wall to transfer the heat generated by the electrical

resistance to the interior of the reservoir. The electrical resistance is a PTC type 4 k Ω , and it is fixed to the backside wall of the copper plate using thermo-conductive adhesive to reduce the thermal contact resistance. The walls of the acrylic box are 10 mm thick, bonded with high-temperature silicone; the internal dimensions are equal to 50 mm long, 120 mm high and 30 mm wide. All external surfaces were thermally insulated with 27 mm thick Styrofoam, and the insulation from the front view was removed for approximately 15 seconds every 5 minutes to record images as well as videos by the video camera (DSLR D5300 NIKON). The power supply control occurs through an AC power source, where voltage and electrical current are measured using a Fluke[®] power quality analyzer (model 43B, with uncertainty of $\pm 1\%$). The heat flux (q'') was estimated as a function of time (t), such as $q'' = 21.956 t^{-0.021}$ [W m⁻²].

Different cases were designed to analyze the melting process of bio-based PCM (palm wax) under the influence of metal foam with distinct geometries. In case A, the reservoir was filled only with bio-based PCM; in case B, a uniform Nickel foam (Fig. 2a) was incorporated into bio-based PCM; and, in case C, a square pin-fin Nickel foam (Fig. 2b) was incorporated into bio-based PCM. The same amount of bio-based PCM mass was used for all cases (120 g).

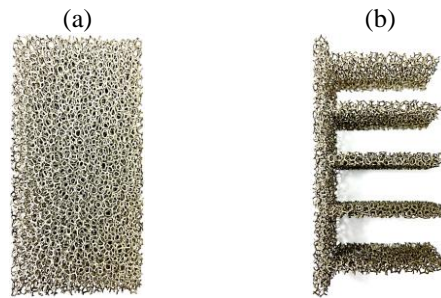


Figure 2 – Different metal foam geometry analyzed: (a) Uniform Nickel foam; (b) Pin-fin Nickel foam.

As mentioned, palm wax was selected as a bio-based PCM. In the solid state, it is white; in the liquid state, it is colorless. The phase change temperatures and latent heat were obtained using a differential scanning calorimeter (DSC), Perkin Elmer model STA 8000, corresponding to 56.64 – 63.54 °C ($\pm 5\%$) and 110.014 kJ/kg ($\pm 5\%$), respectively. According to the manufacturer (BeiHai Composite[®]), the Nickel foam has a porosity of 98% and a pore density of 20 PPI (porous per inch).

3. RESULTS

In Fig. 3(a-g), the melt fraction (β) is presented at different instants of time (t) for pure bio-based PCM (Case A). Melt fraction values vary from 0 to 1, where 0 corresponds to bio-based PCM completely in solid state and 1 completely in liquid state. From Fig. 3(a and b), it can be noted that the initiation of melting happens closely to the copper plate. This pattern implies that heat conduction plays a significant role in the early instants. Additionally, the melting front takes a convex form, tilting towards the upper-right direction, Fig. 3(c-g). This indicates that heat transfer is more prominent at the top, attributed to the prevailing buoyant force and the significant impact of natural convection in facilitating heat transfer, compared to the lower part.

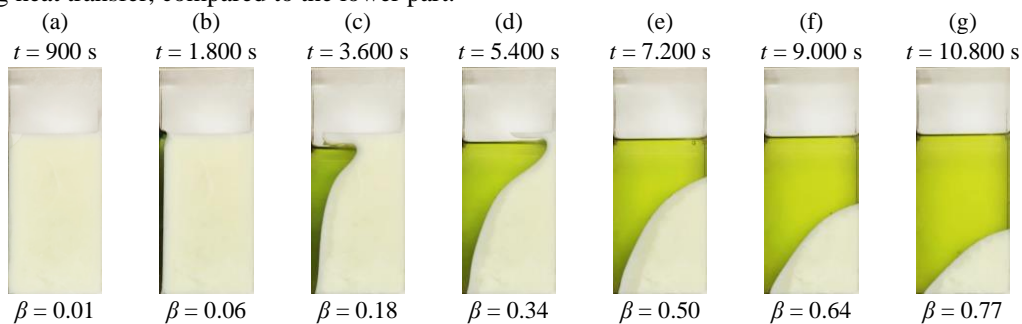


Figure 3 - Melting front behavior for Case A (pure palm wax PCM) at different instant times (t).

Figure 4 presents the melt fraction (β) and energy storage capacity (E) as a function of time (t), considering the pure bio-based PCM (Case A) and uniform Nickel foam inserted (Case B). A notable enhancement in thermal processes becomes apparent upon incorporating Nickel foam, resulting in a reduced melting process compared to using only bio-based PCM. In Case B, the melting process took 12600 seconds, whereas in Case A, it occurred in 16680 seconds, corresponding to a difference of 4080 seconds (24%). Therefore, the bio-based PCM/Nickel foam demonstrated superior heat transfer performance compared to pure bio-based PCM, as shown by the energy storage capacity (an improvement in the energy storage rate of 26% is observed for Case B, due to the addition of Nickel foam).

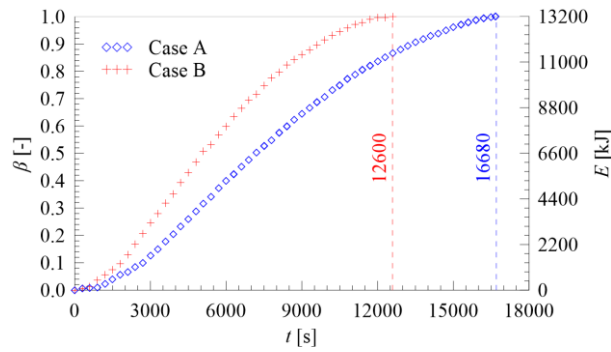


Figure 4 - Melt fraction (β) and energy storage capacity (E) as a function of time for Case A (pure PCM) and Case B (PCM + uniform Nickel foam)

4. CONCLUSIONS

In this study, the bio-based PCM melting process is experimentally analyzed through tests for different conditions: Case A corresponds to the pure bio-based PCM; Case B corresponds to the presence of uniform Nickel foam incorporated in the PCM matrix; and Case C (ongoing), to the square pin-fin Nickel foam incorporated into PCM matrix. The thermal properties have been improved by incorporating Nickel foam in palm wax (the bio-based PCM chosen for this study). The following conclusions were possible until this moment:

- Incorporating Nickel foam into bio-based PCM accelerates its melting process, leading to an increase in heat transfer performance. The foam porous structure increases the surface area for heat exchange, facilitating enhanced convective heat transfer. Besides, the high thermal conductivity of metal foam promotes heat transfer.
- The energy storage rate was higher for the case with the metal foam inserted in the PCM matrix (case B). Nickel foam can shorten the total melting time by 24% and increase the thermal energy storage rate by 26% compared with the case without its presence.

A comprehensive comparative analysis between Case A (pure bio-based PCM), Case B, and Case C will provide insights into the impact of different Nickel foam configurations on the melting process. This analysis will highlight the relative effectiveness of the square pin-fin design in contrast to the uniform Nickel foam. This could lead to recommendations for specific design parameters or configurations to achieve the best thermal enhancement.

5. REFERENCES

- Aramesh, M., Shabani, B. (2022). Metal foam-phase change material composites for thermal energy storage: A review of performance parameters. *Renewable and Sustainable Energy Reviews*, 155, 111919.
- Irfan Lone, M., Jilte, R. (2021). A review on phase change materials for different applications. *Materials Today: Proceedings*, 46, 10980–10986.
- Ismail, K.A.R., Lino, F.A.M., Machado, P.L.O., Teggari, M., Arıcı, M., Alves, T.A., Teles, M.P.R. (2022). New potential applications of phase change materials: A review. *Journal of Energy Storage*, 53, 105202.
- Lawag, R. ., Ali, H.M. (2022). Phase change materials for thermal management and energy storage: A review. *Journal of Energy Storage*, 55, 105602.
- Li, Z., Shahsavari, A., Al-Rashed, A., Talebizadehsardari, P. (2020). Effect of porous medium and nanoparticles presences in a counter-current triple-tube composite porous/nano-PCM system. *Applied Thermal Engineering*, 167, 114777.
- Mehari, A., Xu, Z.Y., Wang, R.Z. (2020). Thermal energy storage using absorption cycle and system: A comprehensive review. *Energy Conversion and Management*, 206, 112482.
- Mehling, H., Brütting, M., Haussmann, T. (2022). PCM products and their fields of application - An overview of the state in 2020/2021. *Journal of Energy Storage*, 51, 104354.
- Mitali, J., Dhinakaran, S., Mohamad, A. A. (2022). Energy storage systems: a review. *Energy Storage and Saving*, 1(3), 166–216.
- Nazari, M., Jebrane, M., Terziev, N. (2020). Bio-Based Phase Change Materials Incorporated in Lignocellulose Matrix for Energy Storage in Buildings-A Review. *Energies*, 13(12), 3065.
- Sharma, A., Singh, P.K., Makki, E., Giri, J., Sathish, T. (2024). A comprehensive review of critical analysis of biodegradable waste PCM for thermal energy storage systems using machine learning and deep learning to predict dynamic behavior. *Heliyon*, 10(3), e25800.
- Shi, J., Du, H., Chen, Z., Lei, S. (2023). Review of phase change heat transfer enhancement by metal foam. *Applied Thermal Engineering*, 219, 119427.
- Yu, C., Zhang, X., Chen, X., Zhang, C., Chen, Y. (2020). Melting performance enhancement of a latent heat storage unit using gradient fins. *International Journal of Heat and Mass Transfer*, 150, 119330.

A HYBRID TRIPLE-LAYER LIQUID-LIQUID ENCAPSULATION TECHNIQUE

Utsab Banerjee^a, Sirshendu Misra^a, Sushanta K. Mitra^{a,*}

^a Micro & Nano-Scale Transport Laboratory, Waterloo Institute for Nanotechnology, Department of Mechanical and Mechatronics Engineering, University of Waterloo, Waterloo, Ontario, Canada N2L 3G1.

*corresponding author: skmitra@uwaterloo.ca

Keywords: Interfacial energy, Liquid-liquid encapsulation, Core-shell structures

1. INTRODUCTION

Encapsulation protects the vulnerable cores in an aggressive environment by wrapping the core in a shell layer. Owing to its unique core-shell morphology and the high flexibility of the material selection, encapsulated cargos could be imparted with diverse properties and functionalities. Therefore, they have been extensively utilized in various applications, including food processing (Gibbs *et al.*, 1999), aromatherapy (Saifullah *et al.*, 2019), and pharma/nutraceuticals (Reque and Brandelli, 2021). In single-layer encapsulation, the core material is wrapped by a shell layer. Multilayered encapsulation is achieved by adding one or more wrapping layers between the core and the outermost shell. Multilayered cargos provide better protection to the core and enable additional functionalities. Encapsulation techniques can be classified into physical and chemical methods (Niu *et al.*, 2022), including coacervation, ionic gelation, solvent evaporation, spray drying, in situ polymerization, and interfacial polymerization. However, these techniques suffer from various restrictions, including challenges in controlling the shell thickness, low yield, and stability, and using large numbers of equipment, limiting the utility of these conventional techniques. On the other hand, microfluidic-based techniques possess several challenges, including multiple syringe pumps for fluid infusion, desirable wettability at each channel wall, complex devices, and synchronization of droplet generators.

We previously achieved stable, ultrafast, and robust liquid-liquid encapsulation, where a liquid droplet impacts another liquid layer floating on a water bath, giving rise to single-layer encapsulation (Misra *et al.*, 2019), (Mitra *et al.*, 2020). However, the sole dependence of encapsulation on the impact-driven technique possesses several restrictions to produce multilayer encapsulated cargos. First, for triple-layered encapsulation, it is a prerequisite that the liquid triplet (the host bath and two shells) should always satisfy the criterion for density stratification and interfacial tension, which ensures the floating of two interfacial layers on the host bath and thus restricting the choice of liquids. Second, the impact-driven approach solely depends on the kinetic energy of the core drop. Therefore, for a successful encapsulation, the method demands a larger core drop or higher impact height for sufficient kinetic energy of the core drop to penetrate completely through the interfacial layers. This criterion further restricts the minimum size and impact height for successful encapsulation. Third, wrapping water-soluble cores inside a water host bath using the purely impact-driven liquid-liquid encapsulation technique is challenging, resulting in a lower success rate of encapsulation.

The present work presents a holistic approach to liquid-liquid encapsulation by combining a Y-junction and our impact-driven liquid-liquid encapsulation technique to demonstrate triple-layered encapsulations. This hybrid technique resolves all the above issues while retaining the simplicity and robustness of our previous approach. In this technique, the Y-junction generates compound droplets consisting of a core and a shell. These compound droplets from the Y-junction impact the interfacial layer floating on the host bath, generating triple-layered encapsulated cargos. This technique is further exploited to encapsulate water-soluble analytes inside liquid shells, which is challenging by the impact-driven liquid-liquid encapsulation technique.

2. MATERIALS AND METHOD

The framework involves triple-layered encapsulation; thus, the liquids are named in a particular manner, as shown in Figure 1. In the case of triple-layered encapsulation (Figure 1a), the liquids in the Y-junction involve the core and the shell liquid, which are termed L_c and $L_{s,1}$, respectively. The host liquid, L_h is chosen to be deionized (DI) water purified by Milli-Q, MilliPoreSigma, Ontario, Canada) with density $\rho_h = 1000 \text{ kg/m}^3$, dynamic viscosity $\mu_h = 1 \text{ mPa s}$, liquid-air surface tension $\gamma_h = 72 \text{ mN/m}$. The liquid that floats on the host bath is termed the interfacial layer $L_{s,2}$ forming the outermost shell as indicated in Figure 1a. Throughout the study, the shell liquid ($L_{s,1}$ in the Y-junction) is kept fixed, which is a class of laser liquid – a mixture of silicanes and polyphenol ethers with a water solubility of $< 0.1 \%$ (Cargille Laboratories Inc., NJ, USA) is used to form the core drop. Hence, the triple-layer encapsulated cargo will have the inner core L_c , the intermediate shell layer $L_{s,1}$ and the outermost shell layer $L_{s,2}$. The relevant material properties are as follows: density $\rho_{s,1} = 1900 \text{ kg/m}^3$, dynamic viscosity $\mu_{s,1} = 1024 \text{ mPa s}$, liquid-air surface tension $\gamma_{s,1} = 50 \text{ mN/m}$, and liquid-water interfacial tension $\gamma_{s,1-h} = 39.4 \text{ mN/m}$. The experiments were conducted in a distortion-free glass cuvette (Krüss GmbH, Germany) of inner dimension $36 \text{ mm} \times 36 \text{ mm} \times 30 \text{ mm}$ with a 2.5 mm wall thickness. Before each experiment, the glass cuvette is thoroughly cleaned by soaking and subsequent ultrasonication (Emerson Electric Co., USA) in hexane for 30 min. After that, the cuvette is thoroughly rinsed with DI water and acetone, followed by drying

with compressed nitrogen. Next, the cleaned cuvette was treated in air plasma (Plasma Etch, USA) for 10 min. At first, the cuvette was partially filled with 20 ml of the host liquid (DI water). Subsequently, a predetermined volume of the interfacial liquid is dispensed on top of the water bath from proximity using a pipette (DiaPETTE, Canada) and allowed to spread uniformly for ~ 2 min, forming a thin interfacial layer of respective thickness. Using the linear translating stage, the dispenser is taken to the predetermined height, H . A Y-junction flow arrangement was employed to generate a compound droplet, as shown in Figure 1a. Laser oil was pushed through the vertically oriented microtip attached to a syringe. At the same time, the core drop was introduced from the side using a flat-tipped stainless-steel needle (Nordson EFD, USA) of internal diameter 0.25mm mounted on a 1 ml NORM-JECT syringe, using a programmable syringe pump (Chemyx Fusion 4000). Then, the compound droplet was dispensed by pumping laser oil using the programmable syringe pump at a controlled rate as desired.

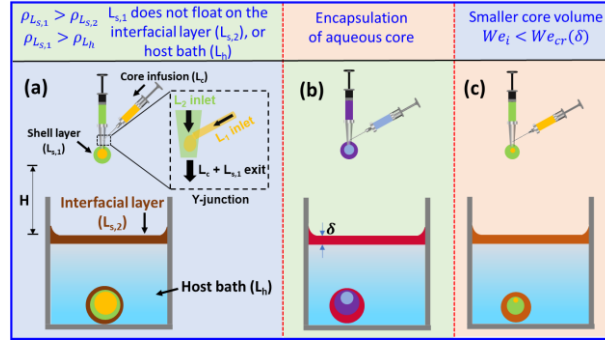


Figure 1. Hybrid triple-layered liquid-liquid encapsulation leading to the formation of wrapped droplets at the bottom of the cuvette - (a) shows the experimental setup and inset schematically demonstrates the Y-junction arrangement for generating the compound droplet. (b) Wrapping of an aqueous core liquid by two oil layers. (c) Encapsulation of a small core drop inside two shell layers. The shell liquid ($L_{s,1}$) is heavier among all four participating liquids for all three cases.

3. RESULTS AND DISCUSSION

A stepwise process of the high-speed encapsulation process for triple-layered encapsulation is depicted in Figure 2a. The encapsulation process involves a complex interplay between interfacial (surface) tension forces, viscous forces, and momentum at the five fluids (air, interfacial layer, host liquid, shell layer, and the core drop) interface. Due to the vertical separation H between the interfacial layer ($L_{s,2}$) and the dispensing needle, the core drop gains kinetic energy before encountering the interfacial layer. The compound drop (consisting of core L_c and shell layer $L_{s,1}$), possessing sufficient kinetic energy, encounters the interfacial layer. Upon contact with the interfacial layer ($L_{s,2}$), the compound drop attempts to penetrate through the interfacial layer ($L_{s,2}$), as indicated by “interfacial penetration by the compound drop” in Figure 2a. Due to its momentum, the compound drop drags the $L_{s,2}$ layer downward through the host liquid (L_h) due to its momentum, which deforms the interfacial layer-water interface and increases its surface area. However, interfacial forces acting on the deformed interface between $L_{s,2}$ - L_h attempt to restore the interface to its original position to minimize the interfacial energy. Further, the viscous resistance offered by the interfacial layer also opposes the downward motion of the drop by dissipating its momentum. Owing to the sufficient momentum, the compound drop overcomes the barrier imposed by both the interfacial forces and the viscous resistance, leading to the initiation of the necking process. During the necking of the interfacial layer, the thinning of the liquid threads of canola oil can be seen, as indicated in Figure 2a. Finally, the neck thins beyond a critical thickness, separating the wrapped compound droplet from the interfacial layer, and the cargo settles at the bottom of the cuvette. Figure 2b shows the non-dimensional regime map depicting the successful encapsulation of the compound droplet with the variation in the viscosity of the interfacial layer. In Figure 2b, a non-dimensional experimental regime for encapsulation is identified in terms of the impact Weber number We_i , and the viscosity ratio α . The impact Weber number is defined as $We_i = [\beta\rho_c + (1 - \beta)\rho_{s,1}] \frac{D_{s,1}V^2}{\sigma_{s,1}}$, where β is the volume fraction of the core liquid in the compound droplet, ρ_c and $\rho_{s,1}$ are the density of the core (L_c) and shell liquid ($L_{s,1}$), $D_{s,1}$, $\sigma_{s,1}$ are the diameter of the compound droplet and the surface tension of the shell liquid ($L_{s,1}$), respectively, and V is the impact velocity of the compound droplet, estimated as $V = \sqrt{2gH}$, where g is the acceleration due to gravity, H is the impact height. The viscosity ratio is defined as $\alpha = \frac{\mu_{L_{s,2}}}{\mu_{L_{s,1}}}$. The result indicates whether the compound droplet will be able

to penetrate through the interfacial layer or will be trapped at the interfacial layer depending on the viscosity ratio α and the impact We_i . In both cases, the compound droplet will be wrapped by the interfacial layer, as found in one of our recent studies (Misra *et al.*, 2023). In Figure 2b, the volume of each of the interfacial layer is kept fixed at $V_{L_{s,2}} = 120 \mu\text{l}$. The variation in We_i for each of the interfacial layers is achieved by changing the impact height H between the interfacial layer and the dispensing needle. In Figure 3a, for canola oil ($\alpha = 0.062$), the transition from complete penetration of the compound droplet to the trapped state of encapsulation occurs at $We_i = 165$. On the contrary, for PDMS ($\alpha = 3.41$), the

transition occurs at $We_i = 611$. This fact can be attributed to the higher viscosity of the PDMS, which is 55 times that of the canola oil's viscosity.

The practical utility of efficient encapsulation lies in providing efficient protection to target analytes by safeguarding them in aggressive surroundings and preventing unwanted release. Figure 2c-f demonstrates the applicability of the developed hybrid technique framework in generating triple-layered encapsulated cargos inside the water bath where the inner core is water-soluble. We have used a compound droplet consisting of ethylene glycol (EG) as the core liquid (L_c), laser oil as the shell ($L_{s,1}$) impinging on the interfacial layer floating on the host water bath as shown in the schematic of Figure 2c. Further, to establish the versatility of our method, we have demonstrated successful triple-layered encapsulation (Figure 2d-f) using dyed canola oil, silicone oil, and oil-based ferrofluid, as the interfacial layers ($L_{s,2}$). The selection of EG as one of the core liquids shows that despite being water-soluble, our hybrid encapsulation technique can efficiently protect the encapsulated cargo inside the host water bath.

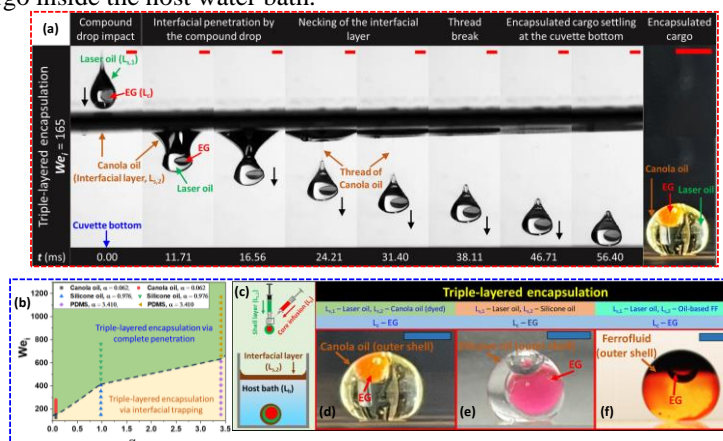


Figure 2. (a) Stepwise process depicting the high-speed interface evolution of the triple-layered encapsulation. (b) Regime map showing the region of applicability for the successful triple-layered encapsulation. (c) Schematic representation of the hybrid triple-layered liquid–liquid encapsulation framework leading to the formation of wrapped droplets at the bottom of the cuvette with interfacial layers as – (d) canola oil (dyed), (e) silicone oil, (f) oil-based ferrofluid. The scale bar in each image represents 2 mm.

4. CONCLUSIONS

In summary, this work presents a holistic framework of liquid-liquid encapsulation to fabricate triple-layered encapsulated cargo using the combination of Y-junction and impact-driven liquid-liquid encapsulation, which we refer to here as a hybrid encapsulation technique. Compound droplets consisting of a liquid core and liquid shell are generated using the Y-junction geometry. Impingement of the compound droplet on the liquid interfacial layer (shell) floating on the host liquid bath results in wrapping the compound droplet by the liquid shell, forming the triple-layered encapsulated cargo. Using this hybrid liquid-liquid encapsulation technique, we have demonstrated wrapping a smaller and aqueous core that poses challenges in impact-driven liquid-liquid encapsulation. We have performed a large set of experiments with three different interfacial layer liquids to identify a non-dimensional experimental regime depicting the effect of the impact Weber number We_i , and the viscosity ratio α on the outcome of the encapsulation. Finally, to demonstrate the universality of the technique, we used dyed canola oil, silicone oil, and an oil-based ferrofluid as interfacial layer liquids to generate the triple-layered encapsulated cargo.

5. REFERENCES

Gibbs, B. F.; Kermasha, S.; Alli, I.; Mulligan, C. N., 1999. "Encapsulation in the Food Industry: A Review". *Int J Food Sci Nutr*, 50, 213-224.

Misra, S.; Trinavee, K.; Gunda, N. S. K.; Mitra, S. K., 2019. "Encapsulation with an Interfacial Liquid Layer: Robust and Efficient Liquid-Liquid Wrapping". *J Colloid Interface Sci*, 558, 334-344.

Misra, S.; Banerjee, U.; Mitra, S. K., 2023. "Liquid – Liquid Encapsulation: Penetration vs. Trapping at a Liquid Interfacial Layer". *ACS Appl Mater Interfaces*, 15, 23938–23950.

Mitra, S.; Gunda, N. S. K.; Misra, S.; Trinavee, K., 2020. "Liquid Encapsulation Method and Compositions and Uses Related Thereto". <https://patentscope.wipo.int/search/en/detail.jsf?docId=WO2020168432> (accessed Nov 30, 2022).

Niu, Y.; Wu, J.; Kang, Y.; Zhao, Q.; Xiao, Z.; Zhao, D., 2023. "Encapsulation Technique and Application Progress of Mechanical Stimuli-Responsive Microcapsules". *Progress in Organic Coatings*, 176, 107390.

Reque, P. M.; Brandelli, A., 2021. "Encapsulation of Probiotics and Nutraceuticals: Applications in Functional Food Industry". *Trends Food Sci Technol*, 114, 1-10.

Saifullah, M.; Shishir, M. R. I.; Ferdowsi, R.; Tanver Rahman, M. R.; Van Vuong, Q., 2019. "Micro and Nano Encapsulation, Retention and Controlled Release of Flavor and Aroma Compounds: A Critical Review". *Trends Food Sci Technol* 86, 230-251.

Experimental Investigation of Dual Swirl Partially Premixed Flame Structure with Escalating Flow Rate Ratio

Sibo Huang^{a,*}, Kazuki Tanimoto^a, Sayaka Suzuki^a, Masayasu Shimura^{a,b}, Mamoru Tanahashi^a

^aDepartment of Mechanical Engineering, Tokyo Institute of Technology, 1-2-1, Meguro, Tokyo, 152-8550, Japan

^bRenewable Energy Research Center, National Institute of Advanced Industrial Science and Technology, 1-2-1 Namiki, Tsukuba, Ibaraki, 305-8564, Japan

*huang.s.ah@m.titech.ac.jp

Keywords: Dual swirl burner, Flame fluctuation, OH-PLIF, OH chemiluminescence, OH thermal-assisted laser-induced fluorescence thermometry

1. INTRODUCTION

Partially premixed combustion for the gas turbine combustors is utilized widely as propulsion engines and power generation systems, because of no risk of flashback and flexibility of combustion control. Hence it is often utilized as a pilot flame for a main premixed flame. To enhance the mixing of fuel and air in the partially premixed burner, combinations of swirl flows such as coaxial dual swirl air flows with fuel jet, so-called dual swirl, twin annular premixing swirler, and coaxial swirl flows for fuel and air have been introduced for gas turbine combustors. Laboratory-scale modeled gas turbine combustors have been investigated to deepen the understanding of interactions between coherent vortical motions, turbulence, thermoacoustic, and intrinsic instabilities.

For the DLR dual swirl burner, Weigand *et al.* (2006) conducted laser Doppler velocimetry (LDV) and OH/CH-planar laser-induced fluorescence (PLIF) and revealed that intense velocity fluctuations occur in the shear layer between the inner recirculation zone (IRZ) and influent gas, and that reaction zone are strongly corrugated. Meier *et al.* (2006) conducted laser Raman scattering and reported that the unreacted or partially reacted gas exists in the same region because of local flame extinction and ignition delay. Stöhr *et al.* (2012) have conducted particle image velocimetry (PIV) and OH PLIF at 5 kHz and found that the recessing vortex core (PVC) induces an unsteady lower stagnation point. Oscillation characteristics of the dual swirl burner were investigated, and it is revealed that variations of air mass split rate between dual swirl flows are significant on fuel-air mixing characteristics in thermoacoustic oscillation cycles. Recently, Litvinov *et al.* (2021) have investigated mixing and reaction characteristics in the dual swirl burner with separately supplied air flows by using time-resolved stereo-PIV, OH-PLIF, and acetone-PLIF and revealed that PVC and double helical vortex are generated in inner and outer shear layer and cause flame roll-up, mixing of burnt and unburnt gases and subsequent ignition both in the inner and outer shear layers. For partially premixed flames in dual swirl configurations, Degenveve *et al.* (2021) investigated the effect of the swirl number on the lift-off height of partially premixed combustors with outer air swirl and inner fuel swirl flows. Weigand *et al.* (2006) and Meier *et al.* (2006) fully investigated the flow field, temperature, flame structure, species contribution, and turbulence-chemistry interactions with flow ratio close to unity. However, there is a lack of discussion on the flame structure and stability of dual-swirling flames at high air-flow ratios.

In this work, in order to investigate the effects of air-flow ratio on the exothermic region, the temperature field, and the flame structure, a laboratory-scale modeled dual swirl burner, in which the ratio of two swirl air flow rates can be supplied separately, is developed, and used in conditions without thermoacoustic instability. High-speed OH chemiluminescence (OH*) at 5 kHz, OH planar laser-induced fluorescence (PLIF), and OH thermal-assisted laser-induced fluorescence (TALF) temperature measurement at 10 Hz were applied on the burner. The results show the area of high OH* intensity separates under a high air-flow ratio and it is more likely to occur at equivalence ratios close to 1, and the peak frequency of fluctuations of the sum of OH* changes as separation occurs. From the measured OH PLIF and temperature distribution, it is found as the flow ratio increases, intensity in the inner circulation region is suppressed, and the thickness of the high-temperature region at the flame edge is thinned, while the OH concentration in the inner air flow decreases. However, as the flow ratio rises further, the flame edge stability decreases, and the outer air flow enters the inside, reacts with the remaining methane, and forms a new flame in the downflow, at which point a circulation region appears at the downflow, where the OH concentration rises again.

2. EXPERIMENTAL SETUP

Figure 1 shows a schematic of the dual swirl burner used in this study. The streamwise direction on the axis of the burner is defined as the y -axis, and the center of the bottom plane is the origin. The nozzles are co-axial triple cylinders for air, methane, and air in order from the inside. Both of the two air nozzles are equipped with swirlers whose blade angle is 45 degrees to the center axis, and inner swirl flow is clockwise, and the outer swirl flow is counterclockwise viewed from the negative region of the y -axis. The diameters of the nozzles are 24 mm (D_i), 26 mm, and 39 mm (D_o),

respectively and the outlet of the inner air and fuel nozzle are located 5 mm upstream from the bottom of the chamber. To remove the effect of the wall-flame interaction, the flame is kept in an open space.

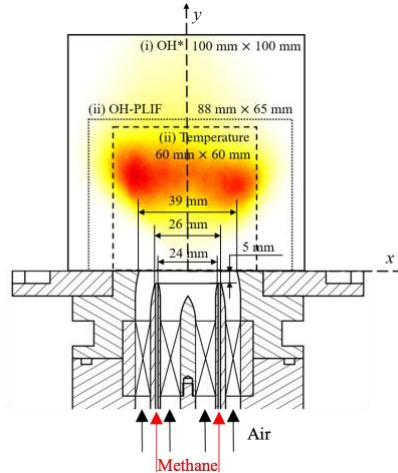


Figure 1. Schematic of a dual swirl burner used in this study and observation areas for measurement (i), OH* (hard line), measurement (ii) OH-PLIF (dot line), temperature (dash line). The area was illustrated by an example of mean distribution for 300 L/min and $Q_o/Q_i = 2.4$, $\phi = 0.7$.

In the experiment, the total flow rate, Q_t , was fixed at 300 L/min. Equivalence ratio, ϕ , was set at 0.7, 0.8, and 0.9. The ratio of the outer air flow rate, Q_o , to the inner air flow rate, Q_i , was set at 2.4, 5.0, 7.0, 10.0 and 15.0. To investigate characteristics of lift-off height, two measurements were performed: (i) OH* measurements with one high-speed camera at 5 kHz; and (ii) simultaneous measurement of OH-PLIF and temperature distribution based on OH TALF thermometry at 10 Hz.

For the measurement (i), OH* was collected by a UV microlens (Nikon, Micro Nikkor, 105mm, f/4.5) equipped with a bandpass filter (Semrock, FF01-320/40-50-D) and amplified by an image intensifier (I.I.) (Hamamatsu Photonics, C10880-03F), and recorded by a CMOS camera (Photron, SA-X2). The gate width was set at 50 μ s. Measurement area and frequency were set at 100 mm \times 100 mm (see Fig. 1) and 5 kHz.

For the measurement (ii), Nd:YAG pumped frequency-doubled dye lasers (LOTIS TII, LS-2137/2; LIOPTEC, Liopstar) are used to excite OH radicals. In this study, Q2(8) absorption line in the (1,0) vibrational band of A $2\Sigma^-$ -X 2Π electronic transition was used to excite OH radicals. The excitation laser wavelength was 283.9 nm and the radiation energy was 12 μ J/pulse. Fluorescence in the (0,0) and (1,1) vibrational bands of A-X transition in the range of 306-320 nm was collected by a UV microlens (Nikon, Micro Nikkor, 105mm, f/4.5) equipped with a bandpass filter (Semrock, FF01-320/40-50-D), and fluorescence in A-X (2,0) transition band was collected by a UV microlens (Sodern, 100mm F/2.8 type CERCO 2178) equipped with another bandpass filter (Semrock, FF01-260/15-25). The two fluorescence signals were amplified by two I.I. (Hamamatsu Photonics, C10880-03F) and collected by two CCD cameras (Princeton Instruments, Mega Plus II ES4020) separately. To reduce the noise caused by OH*, the gate width of two I.I. was both set as 40 ns.

3. RESULTS AND DISCUSSION

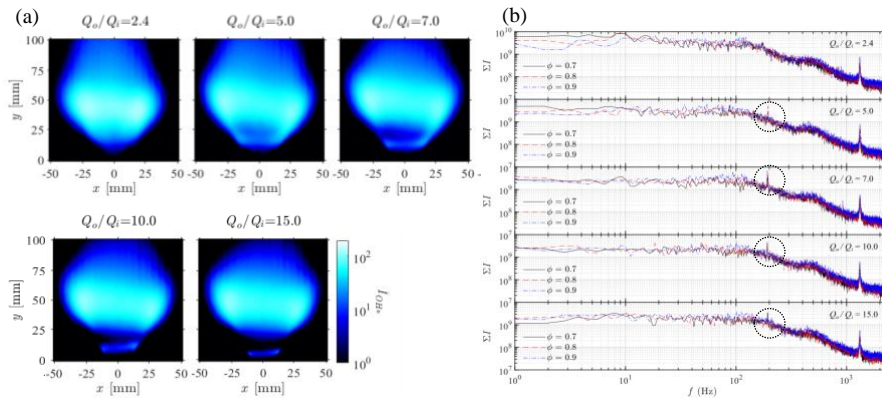


Figure 2. (a) Examples of mean distribution of OH* for $\phi = 0.7, 0.8, 0.9$ and $Q_o/Q_i = 15.0$ at 300 L/min. (b) Intensity spectrum of total OH* intensity in the observation field, ΣI , for $\phi = 0.7, 0.8, 0.9$ and $Q_o/Q_i = 2.4, 5.0, 7.0, 10.0, 15.0$.

Figure 2(a) shows the examples of mean distributions of OH^* for $Q_o/Q_i = 15.0$ at $\phi = 0.9$. It was seen that the flow rate ratio, Q_o/Q_i , increases, the region with high OH^* intensity intends to separate. After Q_o/Q_i reaches 10, the ring structure is completely separated from the upper flame. When the flow ratio reaches 15, the lift-off height of the annular flame further decreases, while the OH^* intensity of the annular flame decreases at the same time. Intensity spectrums of total OH^* intensity within the observation field were calculated and shown in Fig. 2(b). With the gradual separation of the annular flame, a new peak frequency appears at 197 Hz. At the same time, the peak height at 1321 Hz decreases gradually.

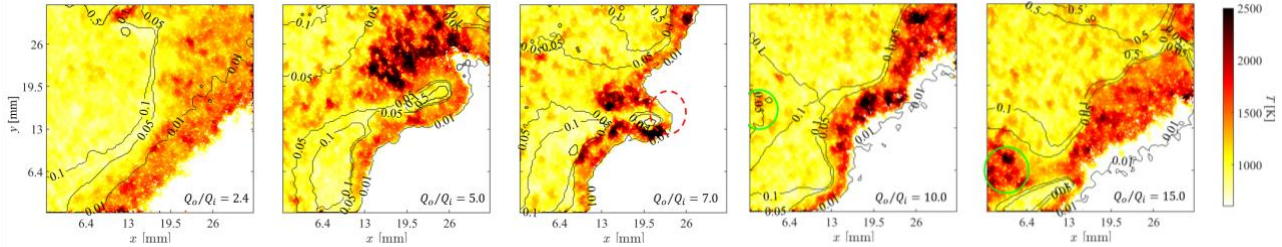


Figure 3. Examples of instantaneous distributions of temperature and boundaries of the regions where local I_{OH} is above 0.01, 0.05, 0.1, 0.5 times $\max(I_{\text{OH}})$ for $\phi = 0.9$ and $Q_o/Q_i = 2.4, 5.0, 7.0, 10.0, 15.0$ (from left to right).

Figure 3 shows the examples of instantaneous distributions of temperature and boundaries of the regions where local I_{OH} is above 0.01, 0.05, 0.1, 0.5 times $\max(I_{\text{OH}})$. It was found that the thickness and relative position of the high-temperature layer to the OH distribution in the IRZ are affected by changes in the flow rate ratio. When the flow rate ratio is 2.4, the high-temperature layer is mainly distributed in the shear layer and is relatively thick, while the local OH concentration is generally less than $0.01\max(I_{\text{OH}})$. With the increase in flow rate ratio, the formation of the v-shape flame results in the thickness of the high-temperature layer gradually becoming thinner, and the fluctuation of the flame edge results in curling occurs. When the flow rate ratio reaches 7.0, curling leads to a break in the high-temperature layer (red dot line area in Fig. 3), while the local OH concentration increases to $0.01\max(I_{\text{OH}})$ to $0.05\max(I_{\text{OH}})$. As the flow rate ratio increases further, the high-temperature layer curls further, and a high-temperature region appears in the central of the center when the annular flame separates from the main flame (green solid line area in Fig. 3).

4. CONCLUSIONS

In this work, we observed a separation of high OH^* intensity areas in partially premixed dual swirl flames at high air-flow rate ratios and investigated the flame stability, flame structure, and temperature distribution, by measuring OH^* , OH -PLIF, and temperature fields.

We found that as the flow rate ratio increases, the flame gradually changes to a V-shaped flame. As the flow ratio is further increased, the length of the V-shaped flame is gradually shortened, and the remaining fuel reacts with the air in downstream to form a new flame. At this point, the OH concentration at downstream increases, while the high OH^* intensity region is divided into two parts.

By analyzing the intensity spectrum of the high-frequency OH^* image, we find that a new peak at 197 Hz appears with the formation of a V-shaped flame, and the peak intensity at this position decreases with the emergence of flame downstream. At the same time, the lift-off height of the new flame does not have a distinct spectral signature, whereas the lift-off height of the upstream V-flame maintains the same spectral characteristics as at the low flow rate ratio. This suggests that high flow ratios can reduce the vibration of the flame downstream to some extent, which is meaningful for the development of future gas turbines.

5. REFERENCES

- Degeneve, A., Vicquelim, R., Mirat, C., Caudal, J., Schuller, T., 2021. "Impact of co- and counter-swirl on flow recirculation and liftoff of non-premixed oxy-flames above coaxial injectors", *Proceeding of Combustion Institute*, Vol. 38, pp. 5501-5508.
- Litvinov, I., Yoon, J., Noren, C., Stöhr, M., Boxx, I., Geigle, K.P., 2021. "Time-resolved study of mixing and reaction in an aero-engine model combustor at increased pressure", *Combustion and Flame*, Vol. 231, pp. 111474.
- Meier, W., Duan, X.R., Weigand, P., 2006. "Investigations of swirl flames in a gas turbine model combustor II. Turbulence-chemistry interactions", *Combustion and Flame*, Vol. 144, pp. 225-236.
- Stöhr, M., Boxx, I., Carter, C. D., Meier, W., 2012. "Experimental study of vortex-flame interaction in a gas turbine model combustor", *Combustion and Flame*, Vol. 159, pp. 2636-2649.
- Weigand, P., Meier, W., Duan, X.R., Stricker, W., Aigner, M., 2006. "Investigations of swirl flames in a gas turbine model combustor I. Flow field, structures, temperature, and species distributions", *Combustion and Flame*, Vol. 144, pp. 205-224.

Experimental Investigation of Impingement Jet Characteristics using Particle Image Velocimetry on Convective Heat Transfer in Thermal Processing Plants

Eileen Trampe^{a,*}, Dominik Büschgens^a, Herbert Pfeifer^a

^a Department for Industrial Furnaces and Heat Engineering, RWTH Aachen University, Germany

*trampe@iob.rwth-aachen.de

Keywords: Heat transfer, Convective heat transfer, Impingement jet characteristic, Particle Image Velocity, Numerical Modelling

1. INTRODUCTION

In continuous strip processing lines and chamber furnaces for the heat treatment of steel, aluminium and copper strip, nozzle systems are used to heat and cool the strip. The nozzles are aimed at the strip in such a way that the resulting impingement jet ensures the highest possible and most homogeneous heat transfer. The heat transfer between the strip and the fluid of the jet is mainly convective. A heat transfer coefficient h is defined to assess the heat transfer.

The heat transfer coefficient is a measure of the cooling or heating rate of the strip. A higher heat transfer coefficient ensures better heat transfer between the fluid and the strip. A number of factors such as the nozzle exit velocity, the fluid properties and the nozzle geometry affect the heat transfer coefficient of impingement jets. Typically, nozzle fields consisting of round or slotted nozzles are used in thermal processing plants. The design of these systems is often based on empirically derived knowledge from the manufacturers and similarity theories. A detailed design of these systems is also supported by numerical modelling. However, it is necessary to describe the known limits of the numerical models and to develop a turbulence model that is optimised for the application of impingement jets in thermal processing plants.

2. EXPERIMENTAL WORK

The experimental investigations for a complete examination of the impingement jet characteristics are divided into two parts. In the first part, the mean and local heat transfer coefficients of an individual nozzle are determined. Subsequently, the flow characteristics are analysed using the non-contact optical measuring method Particle Image Velocimetry (PIV) to determine the velocity distributions in the impingement jets.

The experimental setup for analysing the convective heat transfer of the impingement jets consists of a fan, an inlet section with a volume flow measurement, a distribution chamber, a variable nozzle array and a conductively heated strip with a total size of $8 \times 5 \times 4 \text{ m}^3$ (length \times width \times height). Ambient air is drawn in by the fan, which allows for a maximum pressure increase of $\Delta p = 22,800 \text{ Pa}$ at a maximum fan speed of $r = 3000 \text{ min}^{-1}$. The fan is connected to the distribution chamber with a tube. A Wilson measurement grid for volumetric flow measurement is incorporated into the tube. Various nozzle systems can be easily mounted on the distribution chamber to analyse different nozzle geometries and nozzle pitches s . The distribution chamber has a maximum mounting area for nozzle fields of $1480 \times 1560 \text{ mm}^2$. Above the nozzle field is a conductively heated strip with an area of $630 \times 1160 \text{ mm}^2$ representing the impingement surface. The strip is heated by resistance heating using three transformers with an electrical power of $P = 12.5 \text{ kVA}$ each. The distance H between the strip and the nozzle field can be adjusted in the range of $H = 0 - 250 \text{ mm}$. During the measurement of the heat transfer coefficient, an impingement jet causes a convective heat transfer that locally cools the strip. This, together with the electrical resistance heating of the strip, creates a specific temperature field. This temperature field is measured using an infrared thermal camera and is used to calculate an energy balance from which the heat transfer coefficient is derived. Table 1 summarises the test parameters used to determine the heat transfer coefficients and the nozzle geometries investigated.

Table 1. Test parameters for determining heat transfer coefficients

Nozzle Geometry	Slot Nozzle	Round Nozzle
Hydraulic Diameter D_h in mm	10	25
Nozzle Length L in mm	100	80
Strip Distance H in mm	50	50
Nozzle Box Pressure p in Pa	1520	1550
Nozzle Exit Velocity u in m/s	51,2	52.6
Reynold Number Re	34,490	88,780

For the PIV measurements, a second setup was built consisting of similar components as the heat transfer setup, but on a smaller scale. This setup is shown in Fig. 1.

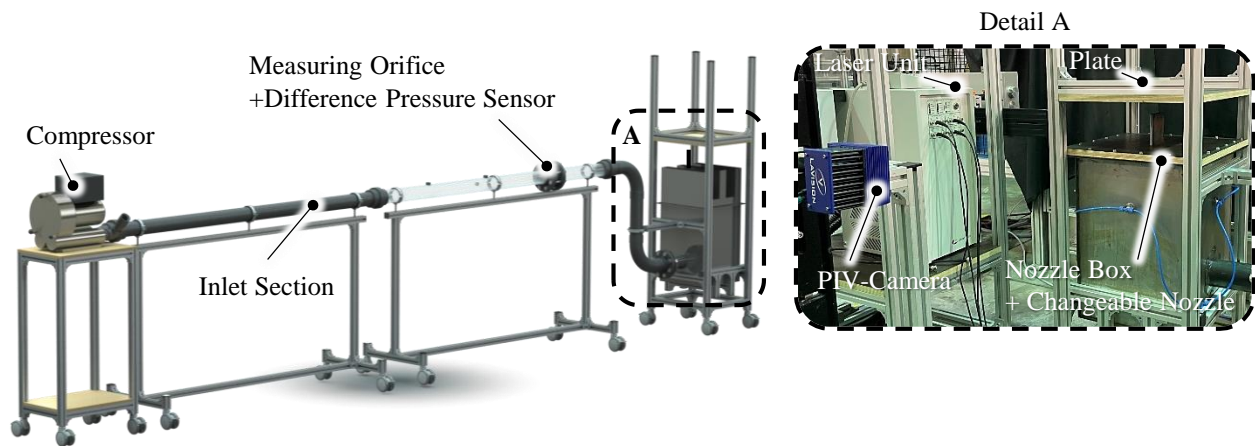


Figure 1. Experimental setup to determine the velocity distribution in impingement jets using PIV

At the beginning of the inlet section a compressor draws in ambient air and accelerates it into the inlet section, which is essential for an even flow to the nozzle box. A measuring orifice and various pressure sensors are located in the inlet section to measure the volume flow. Here, the tracer particles are also introduced into the fluid flow. A nozzle box with a volume of $550 \times 400 \times 400 \text{ mm}^3$ is connected to the inlet section. Various nozzles can be assembled here. A plate above the nozzle outlet serves as the impingement surface. The PIV setup consists of a double frame camera (Imager CX2-16, resolution 5312×3024 pixels) and a double pulsed Nd:YAG laser (Litron LPU 550, $\lambda=532 \text{ nm}$).

3. EXPERIMENTAL RESULTS

Figure 2 a) shows the locally determined heat transfer coefficients of forced convection per pixel, while Fig. 2 b) shows these heat transfer coefficients in the longitudinal direction through the centre of a single round nozzle in section A-A. The results of the heat transfer measurements are based on the test parameters shown in Table 1. The characteristic cooling pattern of a single round nozzle can be seen. A first maximum can be seen in the centre of the nozzle, which is subject to local fluctuations. This is followed by a local minimum towards the nozzle wall, which is then again followed by a second local maximum. The formation of two local maxima with increased heat transfer is typical for round nozzles. The distribution of the maxima and minima can be regarded as rotationally symmetrical.

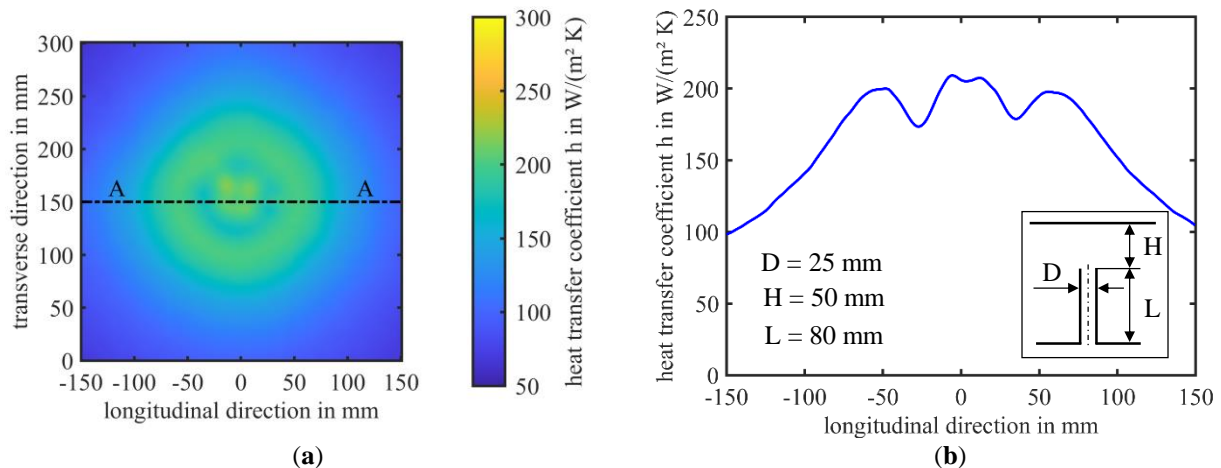


Figure 2. a) Distribution of forced local heat transfer coefficient and b) heat transfer coefficient at section A-A through the centre of a single round nozzle

Figure 3 a) illustrates the locally determined heat transfer coefficients per pixel, where Figure 3 b) shows the heat transfer coefficient in the longitudinal direction through a single slot nozzle in cross section A-A. The cross-section for the local heat transfer coefficients is shown as an example, although it can be assumed to be the same for a slot nozzle over its entire length. The outlet flow of a slot nozzle is not rotationally symmetrical in contrast to that of a round nozzle. The distribution of local heat transfer coefficients of a slot nozzle is characterised by a maximum at the centre of the slot. Thereafter, the local heat transfer coefficient decreases continuously with increasing distance from the centre of the slot nozzle.

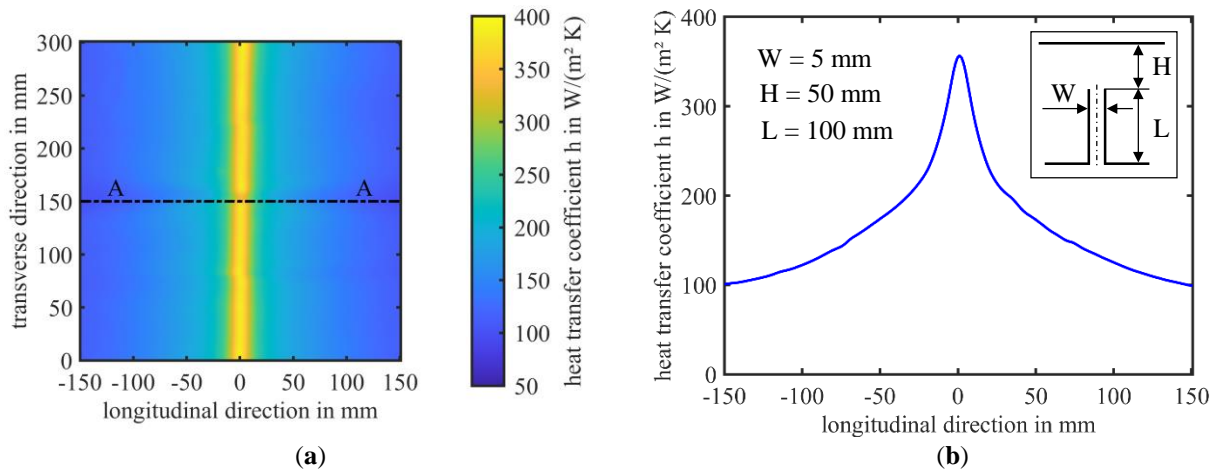


Figure 3. a) Distribution of forced local heat transfer coefficient and b) heat transfer coefficient at section A-A through the centre of a single slot nozzle

The velocity profiles of the impingement jets determined by using the PIV measurement method show their different flow zones. The velocity decreases after the nozzle exit until it is zero when it reaches the impact surfaces. The subsequent wall flow is recognisable.

4. CONCLUSION

The experimental data leads to a better understanding of the convective heat transfer of impingement jets. This serves as a basis for optimising the numerical modelling of impingement jets and for critically reviewing numerical results. In a first step, the experimentally determined local heat transfer coefficients of the longitudinal cross section A-A are compared with the calculated heat transfer coefficients of the numerical model. Figure 4 shows the local distribution of the heat transfer coefficients in the cross-section, determined experimentally and numerically for a) a single slot nozzle and b) a single round nozzle. Three turbulence models shear stress transport (SST) $k-\omega$ turbulence model, generalized $k-\omega$ (GEKO) turbulence model and Reynolds Stress Model (RSM) were chosen in the numerical modelling.

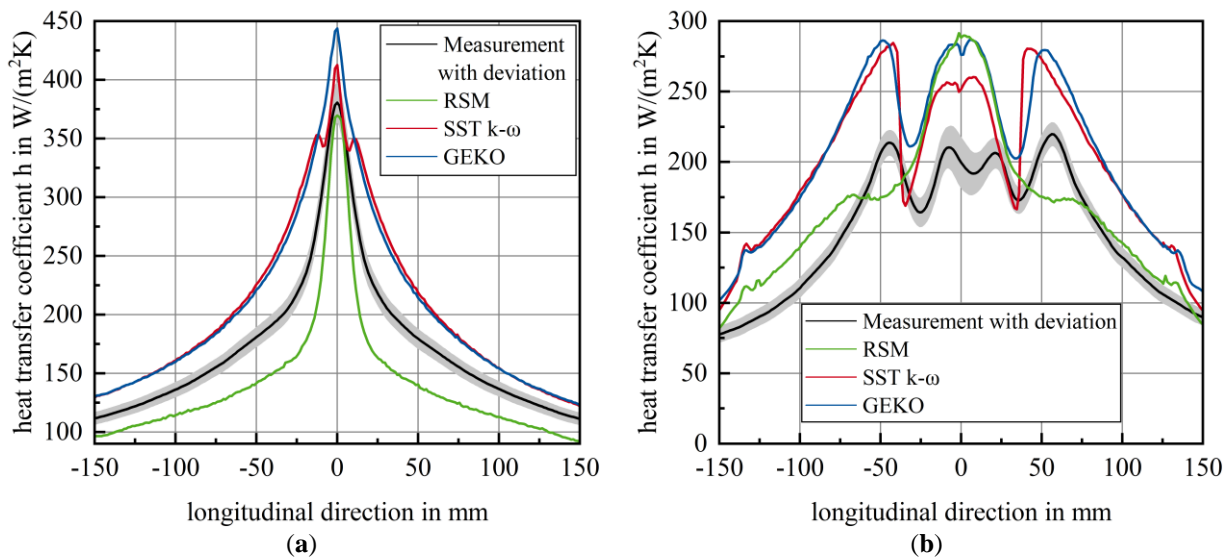


Figure 4. Local distribution of heat transfer coefficients in the cross-section determined experimentally and numerically for a) single slot nozzle and b) single round nozzle

The comparison of the experimentally determined heat transfer coefficients with the numerically calculated heat transfer coefficients shows that no numerical model completely reproduces the measured data. The average deviation of all numerical calculations is about 19 % for the slotted nozzle and 34 % for the round nozzle, whereby the RSM model achieves an average of 11 % but incorrectly depicts the typical pattern. In particular, the characteristic flow patterns are not reproduced by any model, so that the SST $k-\omega$ turbulence model specifies a second secondary maximum for the slot nozzle that does not even exist. The flow patterns of the numerical calculations are compared with the recorded velocity fields of the PIV measurements in order to understand why the turbulence models do not correctly reproduce the impingement jet characteristic.

Experimental study of the vaporisation of consecutives and simultaneous water drops impacting a heated wall under conditions of low pressure

Antoine Courouble^{a,*}, Romuald Rullière^a, Jocelyn Bonjour^a

^a Univ Lyon, CNRS, INSA-Lyon, Université Claude Bernard Lyon 1, CETHIL UMR5008 Villeurbanne, 69100, France

*Corresponding author: Antoine.Courouble@insa-lyon.fr

Keywords: Water, Vaporisation, Low Pressure, Drops, Evaporators

1. INTRODUCTION

Nowadays modern chillers are compelled to adapt to environmentally friendly fluids. The emergence of new-generation fluids with low global warming potential is noteworthy, albeit they may come with drawbacks such as fire hazards. Alternative refrigerants, including water, which has been historically used in sorption systems, are being revisited due to their environmentally friendly characteristics. However, the efficiency of systems employing water as a refrigerant is constrained by various unfavourable thermohydraulic phenomena during vaporisation. At lower pressures, the vapour bubble size generated is far larger than at atmospheric pressure, with bubbles reaching diameters of up to 10 cm (Michaïe et al., 2017). This larger bubble size creates dry areas between the surface and the fluid, resulting in reduced system efficiency. To improve the efficiency of the evaporators, spray cooling is a possible option to limit the formation of dry areas. Indeed, the dispersion of the liquid showed that spray cooling has an interesting potential in the heat exchanger technology (Sienski et al., 1996). Dispersing the liquid into small daughter drops onto the solid wall through sprays enhances the effective heat transfer area, providing a larger surface for heat exchange. Some studies conducted at atmospheric pressure (Yu et al., 2019) demonstrated that explosive nucleation can project drops around the mother drops. At low pressure, a benefit taken from the size of the large bubbles can be utilised to improve the dispersion of the liquid and increase the exchange area.

Preliminary studies on drop vaporisation at low pressure have been conducted to observe the initial manifestation of spray generated by the burst of a bubble within a water droplet (Lada et al., 2023; Courouble et al., 2023). However, these studies focused on the vaporisation of a single drop under low-pressure conditions. The investigations revealed various vaporisation behaviours, indicating the potential to enhance the efficiency of heat exchangers using water at low pressure levels. Explosive boiling, as demonstrated by Courouble et al. (2023), involved the atomisation of a mother drop into multiple daughter drops, spread across the heated wall. This phenomenon resulted in an increase of the heat transfer area, leading to a shorter vaporisation time for the same volume. The present study aims at reaching an advanced understanding of vaporisation under low-pressure conditions, particularly in a configuration more representative of real heat conditions than in the previously mentioned works, involving the vaporization and dispersion of successive and/or simultaneous drops.

2. TEST FACILITY

The test facility primarily consists of a gas- and liquid-tight cylindrical tank made of stainless steel. This tank houses a drop generation system and a heated wall, where the phenomena of vaporisation of interest occur. The tank is equipped with three circular viewports allowing observation inside the tank using a high-speed camera with ombroscopy technique. The tank contains a volume of vapour and a volume of liquid, establishing thermodynamic equilibrium. The saturation temperature, and therefore the saturation pressure, is controlled using two heat exchangers.

The heated wall is square shaped with a surface area of 64 cm² and composed of three elements. The topmost element is a copper foil with a thickness of 50 μm. Below the copper foil is an arrangement of 25 individual heat flux sensors organised in a matrix of five rows and five columns. These sensors enable precise and localised measurement of heat flux on the heated wall. In conjunction with the heat flux sensors, a T-type thermocouple is situated on the connection ribbon of the heat flux sensors set. This thermocouple functions as a reference point (T_{co}) for temperature measurements. Additionally, three thermocouples (T1, T2, and T3) are differentially positioned to measure temperature differences relative to T_{co} ($\Delta T_i = T_i - T_{co}$). These thermocouples offer insights into the temperature gradient across the wall surface. The undermost element is an electrical resistance utilized to generate heat through the Joule effect. With this bench a lower pressure of 1kPa, the surface can reach a maximum of 70°C without degradation of the resin for the sensor.

A system is used to consistently and reproducibly generate drops and deposit them onto the heated wall. This system includes a plastic vessel connected to a peristaltic pump. Water is propelled through an 18-gauge injection needle (i.e.

diameter = 1.22 mm) or a 24-gauge injection needle for simultaneous drop generation (*i.e.* diameter = 0.5 mm), centrally positioned above the heated wall in the case of successive droplet injection. For simultaneous drop injection, two needles of the same size are used to generate drops of the same volume. Each needle is connected to a peristaltic pump. Once the drops are deposited the pumps are turned off. Both the injection needle and the water tank are affixed to a stainless support structure, connected to a linear translator with a stroke length of 10 cm. This translator allows adjustment of the injection height, providing indirectly a certain control of the impact velocity of the drops.

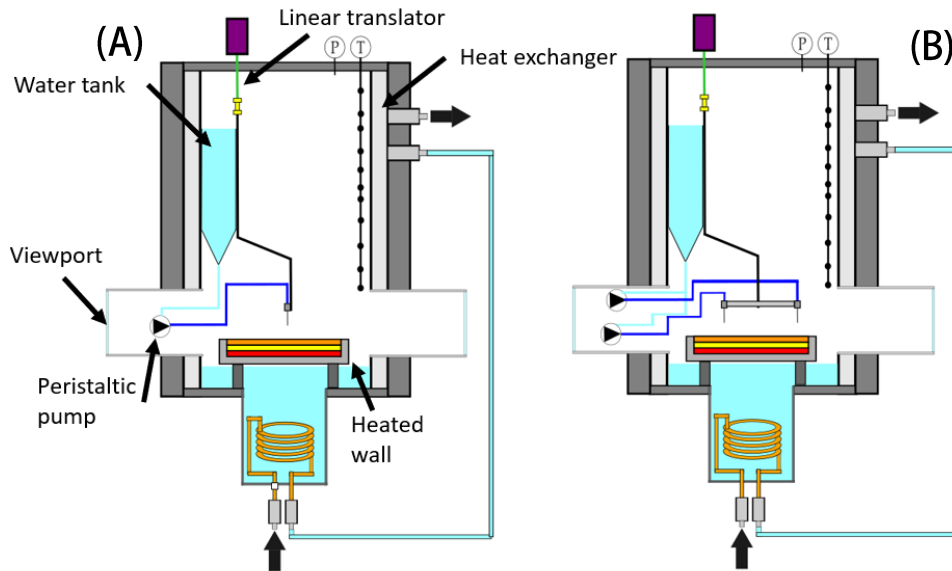


Figure 1. Experimental setup for the study of vaporisation of consecutive drops (A) and simultaneous drops (B)

For the present test campaign, all experiments were performed for a controlled saturation pressure equal to 1.2 kPa that corresponds to a saturation temperature of 10 °C. The consecutive drops were injected 50 seconds after the previous drop was totally vaporised. For the simultaneous drops, the two peristaltic pumps were launched in the same moment. The drops reached the surface with a gap time lower than one second.

3. RESULTS OF THE CAMPAIGNS

A previous work performed with this test bench revealed the existence of four different regimes of vaporisation of drops at low pressure: the regimes of evaporation, rebound, soft boiling and explosive boiling. The objective of this study is to observe as much as possible the regime of explosive boiling, as it results to a rapid vaporization of the drop by spreading daughter droplets all over the heated wall.

The heat flux signals and the visual observations unveiled some interesting features for the case of the vaporisation of successive drops. In a first stage of the test, each time a drop was deposited on the heated wall, a large bubble of vapour was generated inside it. As shown on figure 2 (A), the first six drops were thus submitted to explosive boiling, with particularly high heat fluxes and with a very short life time due to the quasi-immediate vaporisation. But after these six drops, the next five drops would vaporise under the regime of evaporation. The main difference between these two regimes was the speed of vaporisation: for the same volume, the average time of vaporisation in the explosive boiling regime was about 5 seconds, while the time of vaporisation for the evaporation regime was close to 40 seconds. A spray was observed in the explosive boiling regime, resulting from the atomization of the mother drop to a multitude of daughter drop spread on the surface. To generate this spray, in the current configuration after a vaporisation of a previous drop, the surface temperature needed to reach again a sufficiently high value to trigger the nucleation of a new vapor bubble inside the new deposited drop. A heater with a greater mass may be less affected (*i.e.* be submitted to a lower temperature decrease) by the vaporization of a single drop and could potentially sustain a chain of vaporization with shorter intervals between each drop.

For the case of the vaporisation of simultaneous drops, two needles were tested with three heights of injection. When the difference between the wall temperature and the saturation temperature was high enough (above 40 K), bubbles could nucleate within the drops. Explosive boiling was thus recorded but nucleation never occurred inside both drops: when

explosive boiling took place from one drop, the other would vaporize in the regime of evaporation or occasionally of light soft boiling, with a very limited dispersion. However, when two drops were recorded in the evaporation regime, the total vaporization time was similar to the time of vaporization in a single-drop evaporation case. Multiple sites of evaporation do not lead to longer vaporization times in the observed cases.

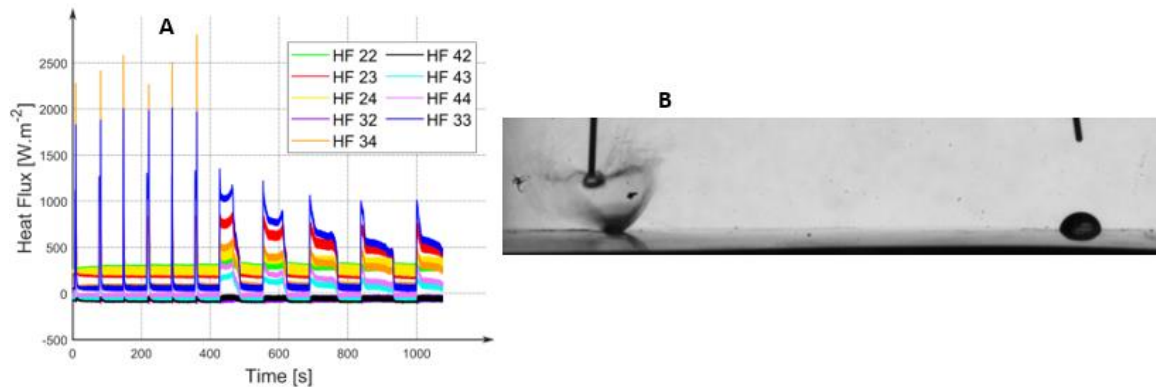


Figure 2. Heat flux measurements performed with selected heat flux sensors during the vaporisation of consecutive drops over 1000 seconds (A) and photo of simultaneous drops with one submitted to explosive boiling (B)

4. CONCLUSIONS

This paper presents the results of an experimental investigation of the phenomenon of the vaporisation process of water drops at low pressure on a heated horizontal surface in a configuration meaningful with respect to the application to future evaporator technologies as alternative to falling film evaporators or spray evaporators. In current spray heat exchangers, the drops are generated continually and in multiple spots. In this way this study describes the phenomenology of the various modes of vaporisation of water drops at low pressure, the main feature of the phase change phenomena as well as the associated thermal performance.

The regime of explosive boiling is favourable to an efficient vaporisation of consecutive drops as it is characterized by small times of vaporisation. The atomisation of the drop that is typical of this regime enhances the total heat transfer area. Such atomisation is made possible by the bursting of large bubbles generated inside the drop. The measurements of local heat fluxes showed that even the periphery of the wall contributes to the overall heat transfer owing the presence of the daughters drops. The vaporization of two drops deposited simultaneously onto the wall was also investigated. It was noted that the regime of explosive boiling could not take place in both drops in the same time. In the regime of evaporation, the duration for two drops was similar to that for a single drop. This observation is related to the test conditions performed for a 24G needle with a surface temperature of 40°C and for height of injection of 0.5cm and 3.5cm.

This study demonstrates that spray evaporator could be based on the bursting of mother drops to form a thermally-induced spray. Such spray could lead to an efficient vaporisation of water under conditions of low pressure. Such thermally-induced spray evaporator could be an alternative to falling film evaporators or nozzle-generated spray evaporators. However, the inertia of the system used in this study limited the ability of the system to release heat into the deposited drops. The surface temperature is an important parameter for triggering the nucleation of a bubble inside the drops. In this study, consecutive or simultaneous drops greatly impact the surface temperature. In a future study, maintaining a constant surface temperature could lead to better control of the phenomenon of bubble nucleation.

5. REFERENCES

- Michaie, S., Rullière, R., & Bonjour, J., 2017. "Experimental study of bubble dynamics of isolated bubbles in water pool boiling at subatmospheric pressures". *Experimental Thermal and Fluid Science*, 87, 117-128.
- Sienski, K., Eden, R., & Schaefer, D. (1996, February). "3-D electronic interconnect packaging". In *1996 IEEE Aerospace Applications Conference*. Proceedings (Vol. 1, pp. 363-373). IEEE.
- Yu, X., Hu, R., Zhang, X., Xie, B., & Luo, X. (2019). "Explosive bouncing on heated silicon surfaces under low ambient pressure." *Soft Matter*, 15(21), 4320-4325.
- Lada, W., Wojtasik, K., Halon, T., Rullière, R., Zajackowski, B., & Bonjour, J. (2023, August). "Experimental investigation on water vaporisation at subatmospheric pressure in different liquid geometrical configuration." In *26th IIR International Congress of Refrigeration*. Paris, France.
- Courouble, A., Rullière, R., & Bonjour, J. (2023, August). "Experimental study of the vaporisation of water drops impacting a heated wall under conditions of low pressure." In *26th IIR International Congress of Refrigeration*. Paris, France

Scaling of a hot test stand including a tangential fan

Justin Christian Hauch^{a,*}, Jan Erik Menzler^a, Dominik Büschgens^a, Herbert Pfeifer^a

^aDepartment for Industrial Furnaces and Heat Engineering, RWTH Aachen University, Germany

*hauch@iob.rwth-aachen.de

Keywords: industrial furnaces, heat treatment, tangential fan, affinity law, fan characteristics

1. INTRODUCTION

In industrial furnaces, especially for the heat treatment of metallic products, fans are used for convective heating up to approximately 750 °C. One example of this are discontinuous furnaces used in the aluminum and copper industry. There, the fans are used to circulate the process gas inside these thermal processing plants. The process gas is heated by flowing through or past a heat source (e.g. heating elements, radiant tube, burner, ...) by forced convection. Afterwards, the transferred energy is again transferred to the product inside the furnace by convection. Uniform and high-volume flows are required for homogeneous heating with high heating rates.

The Department for Industrial Furnaces and Heat Engineering has been researching the possible use of tangential fans for heat treatment processes in the aluminum industry at temperatures up to 550 °C. Tangential fans offer the advantage of a homogeneous outflow of the process gas and do not require flow straighteners which introduce an additional pressure loss. For this reason, the department has a hot test stand with a tangential fan that can be used to investigate the flow behavior at high process temperatures.

The construction of test stands and experimental trials at industrial size are generally associated with high costs for research institutes, but also for the industry. For this reason, the use of scaled test models is to be investigated. The department owns a 3D-printer that is capable of printing pressure-tight 3D-Models. In the presented work, this is used to print a cold model of the hot test stand scaled to 1: 5. The model will be used to analyze the scalability of tangential fans as well as the scalability of a whole test stand. The aim of these investigations is to demonstrate the potential use of rapid prototyping for the construction of cost-effective scaled test rigs.

2. EXPERIMENTAL SETUP

The scaled model is based on the hot test stand at the department, which is shown in Figure 1. The enclosed flow channel is built around a tangential fan with guide housing. The fan is driven by a motor with a frequency converter. The outlet of the fan has a size of 800 x 191 mm and expands to 1000 x 300 mm in the flow channel through a diffuser. Behind the diffuser, there is a first flow measuring point with five equidistantly distributed S-Pitot tubes. These are used to measure the dynamic pressure and additionally contain thermocouples. After the first 90 ° deflection, a throttle with actuator can be used to continuously adjust the throttle state and thus record fan characteristics. An alternative flow measuring point is positioned on the upper half of the flow channel. Behind the third 90 ° deflection, there is another diffuser, which is used to change the flow channel cross-section to 800 x 490 mm. A heating register is located directly behind. The heating register is used to heat the gas with achievable flow temperature of up to 550 °C. Holes in the flow channel wall are used for static pressure measurement to determine the pressure loss within the heating section and the pressure increase of the fan. These are located upstream of the heating register and on the inlet and outlet section of the fan.

The scaled model is printed in Formlabs Form 3L. The printer is able to print wall thicknesses down to 0.2 mm. This is necessary in order to be able to scale the thin blades of a tangential fan appropriately.

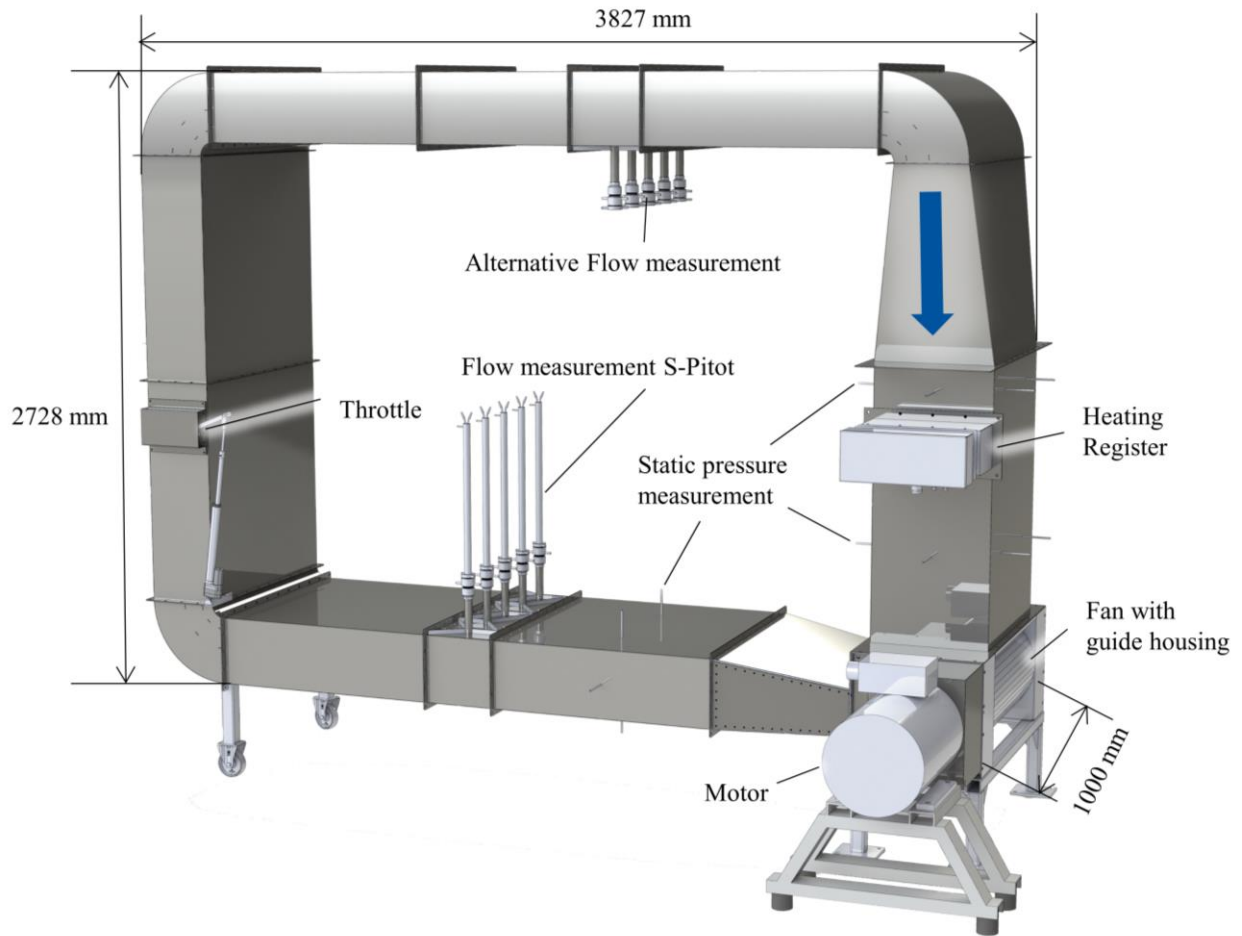


Figure 1. Hot test stand at the Department for Industrial Furnaces and Heat Engineering

3. EXPERIMENTAL RESULTS

The scaled size of the entire test model is based on the geometry of the fan. The geometric similarity of the fan is designed in such a way that it follows the dimensionless characteristic curves of the real model, see Figure 2. The non-dimensional curve shows a pressure coefficient Ψ around $\Psi = 2.5$ at the lowest flow rate φ and rises up to $\Psi = 3.25$ at a flow rate of $\varphi = 1$. At the highest flow rate of $\varphi = 1.5$ the pressure coefficient drops to $\Psi = 1.5$.

To perform the scaling of the fan, the affinity laws, equations 1-3 are used. Therefore, the volume flow \dot{V} , the total pressure increase Δp_t , the density ρ and the rotational velocity n are used to define the outer diameter D_A of the scaled fan. The affinity laws can also be used to determine the required shaft power P_W via the speed ratio λ . The scaled dimensions of the whole model are derived from the geometry of the fan. The flow pattern, volume flow, pressure increase and efficiency are analyzed. The results of the investigations of the hot test stand are used for comparison.

$$\varphi_1 = \varphi_2 \Leftrightarrow \frac{\dot{V}_1}{\dot{V}_2} = \left(\frac{D_{A1}}{D_{A2}}\right)^3 \cdot \frac{n_1}{n_2} \quad (1)$$

$$\Psi_1 = \Psi_2 \Leftrightarrow \frac{\Delta p_{t1}}{\Delta p_{t2}} = \frac{\rho_1}{\rho_2} \cdot \left(\frac{D_{A1}}{D_{A2}}\right)^2 \cdot \left(\frac{n_1}{n_2}\right)^2 \quad (2)$$

$$\lambda_1 = \lambda_2 \Leftrightarrow \frac{P_{W1}}{P_{W2}} = \frac{\rho_1}{\rho_2} \cdot \left(\frac{D_{A1}}{D_{A2}}\right)^5 \cdot \left(\frac{n_1}{n_2}\right)^3 \quad (3)$$

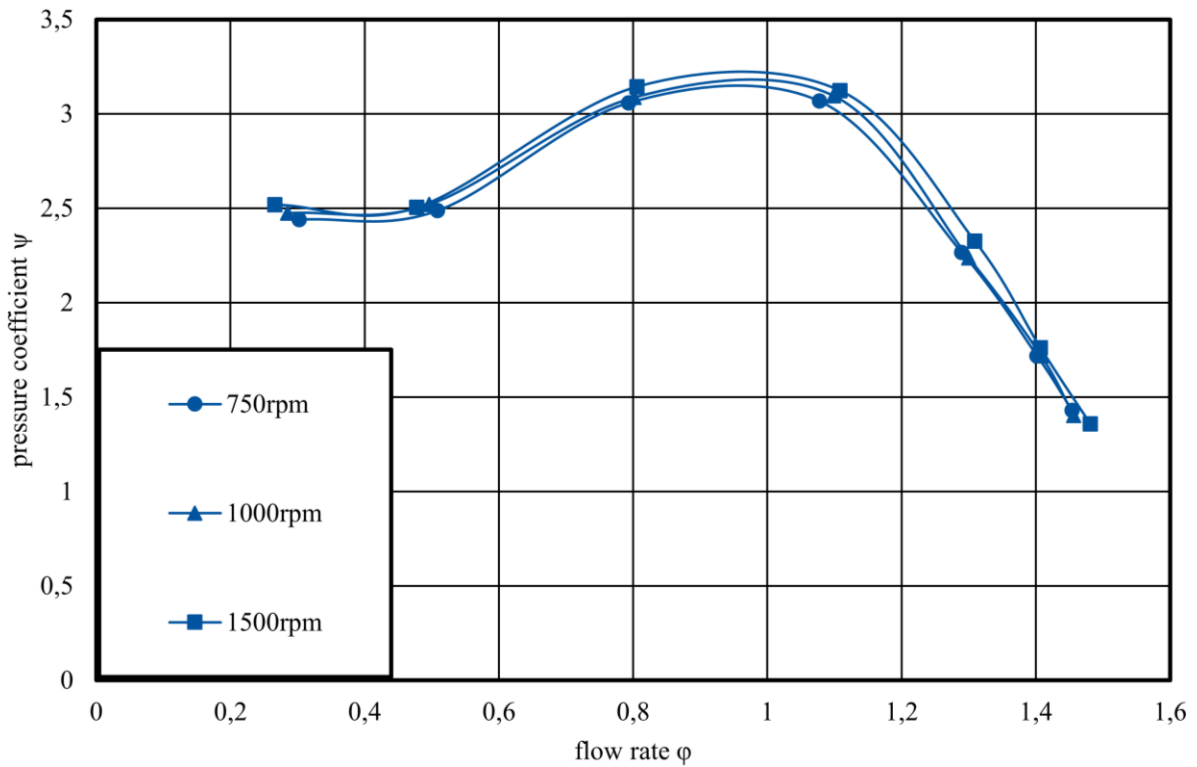


Figure 2. Non-dimensional fan characteristic curve of the tangential fan in the hot test stand

4. CONCLUSIONS

The investigations show that rapid prototyping can be used to reduce costs when investigating flows in industrial furnaces. The hot test stand at the Department of Industrial Furnaces and Heat Engineering provides an excellent baseline with an availability of sufficient experimental data. It serves as an example of a thermal processing plant dominated by convection for the heat treatment of aluminum. The installed tangential fan is an example of the application of the affinity laws and their limits. The investigations show the possibilities that arise from the rapid developments in 3D printing. In particular, the continuous improvement of metallic 3D printing could make it possible to scale down thermal process models in the future.

TWISTED WIRE FLAT HEAT PIPE

Larissa Krambeck*, Kelvin Guessi Domiciano, Marcia Barbosa Henriques Mantelli

Heat Pipe Laboratory, Department of Mechanical Engineering, Federal University of Santa Catarina, Florianópolis, Brazil

* larissa.krambeck@labtucal.ufsc.br

Keywords: flat heat pipes, diffusion bonding, porous media, twisted wires, thermal performance

1. INTRODUCTION

The complexity of thermal management of electronics, which usually works in narrow temperature ranges, grows with the advancement of technology, as electronic devices dissipate progressively more heat and, moreover, their components are allocated in increasingly small volumes, usually inside compact casings. Therefore, removing the excess heat from electronic components is imperative to ensure proper electronic operation. Heat pipes are considered highly efficient thermal solutions, which use the phase change of a working fluid to transfer heat passively. Flat heat pipes have been widely considered in actual high heat fluxes applications, especially when only narrow volumes are available to install the device, as for several electronics boards in boxes (Li et al., 2016).

The main components of the heat pipes are the container, the wick structure, and the working fluid. The porous media is responsible for pumping back the condensed liquid from the condenser to the evaporator region and guaranteeing that the working fluid is distributed over the heat pipe (Mantelli, 2021). The most commonly used capillary structures are metal screens, sintered metal powders, and grooves. Screen mesh porous media are simple, low cost, and easy to manufacture, but show low permeability, many times resulting in high thermal resistance devices. Instead, sintered metal powder wicks have low thermal resistance and high pumping capacity. As negative points, the sintered capillary structures present low permeability and require an additional thermal cycle for the sintering, which increases the costs and difficulty of manufacturing heat pipes with these structures. The grooved wicks have high permeability and average capillarity, and many different manufacturing processes can be used in their fabrication (Peterson, 1994).

In this context, in an attempt to develop a porous media that is simple to manufacture, has high permeability, and results in low thermal resistance when used in heat pipes, the present research experimentally investigates a new capillary structure for flat heat pipes designed for electronics cooling. This novel wick is made of twisted copper wires using commercial electrical cable threads. In the present paper, a flat heat pipe with twisted wires is tested under several thermal loads to evaluate the efficiency of the proposed wick.

2. FLAT HEAT PIPE AND POROUS MEDIA

The heat pipe container was made of two closing copper sheets of $55 \times 100 \text{ mm}^2$ in area and 0.55 mm in thickness, filled by a 3 mm width hollow frame, with the same external dimensions as the closing sheets, but with 1.5 mm thick and by the novel capillary structure, consisting of 5 rolls of twisted wires using commercial electrical stranded cables. Each roll is fabricated by twisting 35 copper wires with 0.1 mm in diameter and 92 mm in length. Due to the final height of the twisted wire rolls, in addition to the work as porous media, they prevent deformations during the diffusion bonding cycle. Figure 1 shows a schematic design of the proposed heat pipe and the wick structure.

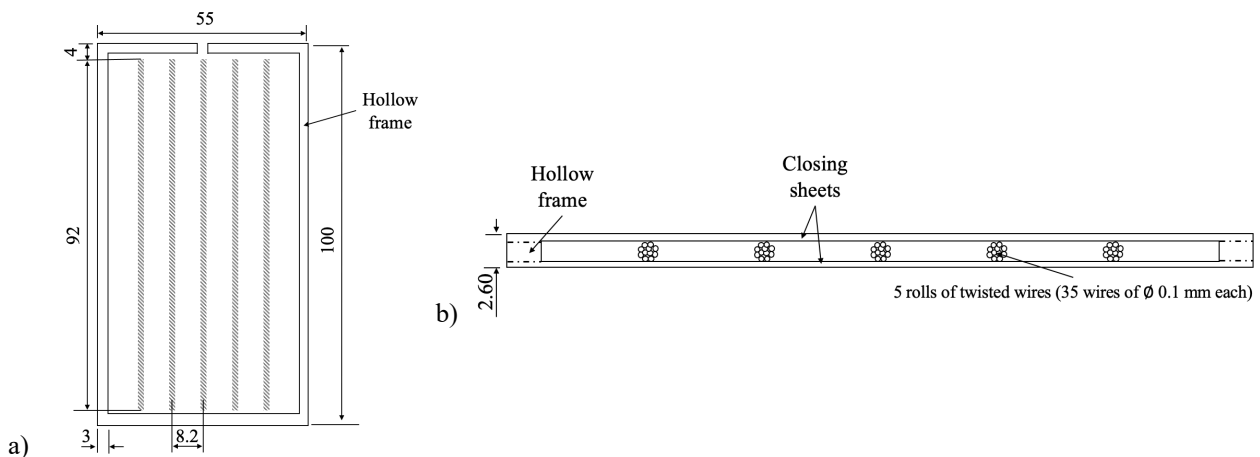


Figure 1. Schematic design of the flat heat pipe with twisted wires: a) internal view and b) cross-section.

As mentioned, the main advantages of this wick structure are the low cost, simplicity, and fabrication facility. The closing sheets and the hollow frame are cut by a water-cutting machine, followed by cleaning with acetone and sulfuric acid. The copper wires are dimensioned, separated, and twisted forming rolls. The rolls and the frame are fixed in their positions by spot welding on one of the closing sheets, as shown in Figure 2a. Then, the closing plate is stacked, finalizing the stack that will be diffusion bonded.

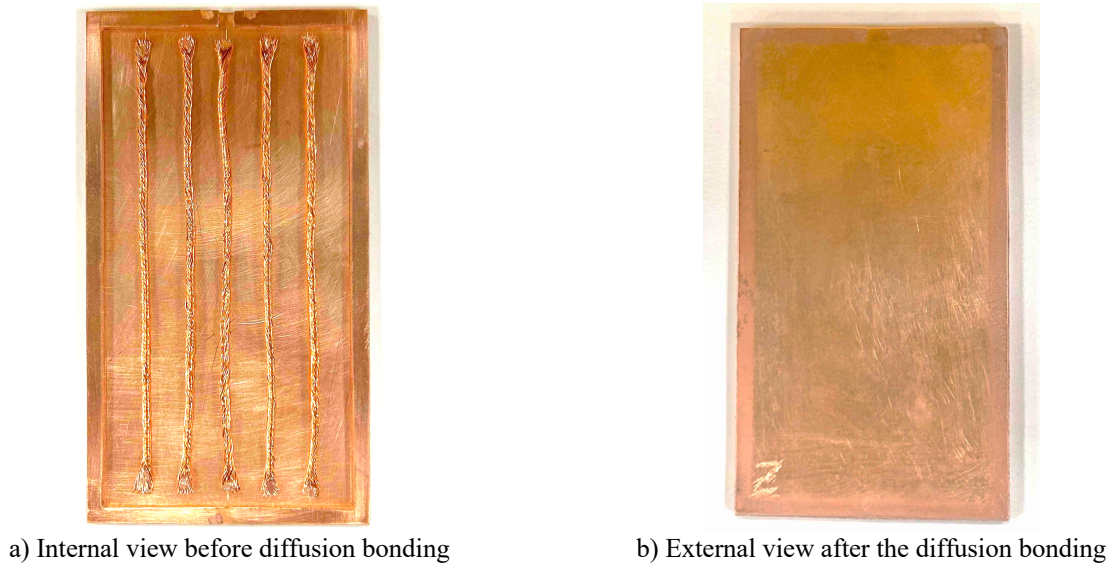


Figure 2. Resulting heat pipe with twisted wires.

The diffusion bonding cycle consisted of subjecting the stack to pressure and a thermal cycle at 875 °C for 3600 seconds in an inert atmosphere. After the bonding, the resulting device has the same characteristics of a monolithic piece, as shown in Figure 2b. Table 1 shows the principal features of the resulting twisted wire heat pipe. More details about the procedure of diffusion bonding can be found in Krambeck et al. (2023).

Table 1. Principal characteristics of novel heat pipe

Characteristics	Heat Pipe
Total size [mm ³]	100 x 55 x 2.60
Container material	Copper
Weight [g]	77.07 ± 0.1
Void volume [ml]	5.60 ± 0.02
Working fluid	Deionized distilled water
Working fluid volume [ml]	1.12 ± 0.02

3. EXPERIMENTAL SETUP

Figure 3 presents the experimental apparatus used for the thermal tests, which is composed of a programmable power supply unit (TDK-Lambda™ GEN300-17), a data acquisition system (DAQ-NI™ SCXI-1000), a Dell™ laptop, a thermal bath (Lauda Ecoline™ RE212), and T-type thermocouples (Omega Engineering™).

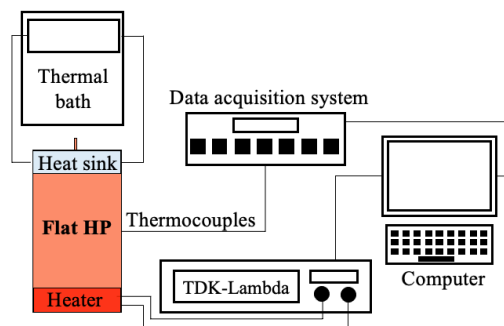


Figure 3. Experimental apparatus.

The two-phase device was divided into an evaporator of 14 mm, an adiabatic section of 71 mm, and a condenser of 15 mm, totaling 100 mm in length. In the evaporator, a copper block (14 x 55 x 15 mm³) with a cartridge-type thermal resistor is fed by a programmable power unit, which works as the heater, mimicking the heat dissipation from electronic gadgets. In the condenser, cooling water from a thermal bath flowing into a metallic block (15 x 55 x 22 mm³) operates as the heat sink. The heater and the heat sink are stuck on the same side, while the other side is attached to nine T-type thermocouples (*Omega Engineering*TM) by a thermosensitive adhesive strip (*Kapton*TM).

3. RESULTS AND DISCUSSION

The temperature transient for the flat heat pipe with the novel porous media, under thermal loads from 10 to 80 W, at the horizontal orientation, is shown in Figure 4. The left vertical axis shows the thermocouple temperatures and the right axis (and the black line) presents the applied heat level. As soon as the heat load was applied, all temperatures increased, getting steady-state conditions (maximum temperature variation of 0.1 °C in 1 minute), which means that, since the first power input level, the heat pipe worked satisfactory, with the evaporator and condenser temperatures reaching close values, showing that the vapor was able to reach the condenser and the liquid could return to the evaporator through the wick structure. This behavior shows the great capacity of the twisted wires to work as capillary structures. At 70 W, the onset of dry-out in the evaporator could be observed, i.e., the porous medium was not able to provide enough liquid to replenish the liquid evaporated, as noticed by the sudden evaporator temperature increases at approximately 4000s, which continued rising with the power increase until the evaporator hit 100 °C.

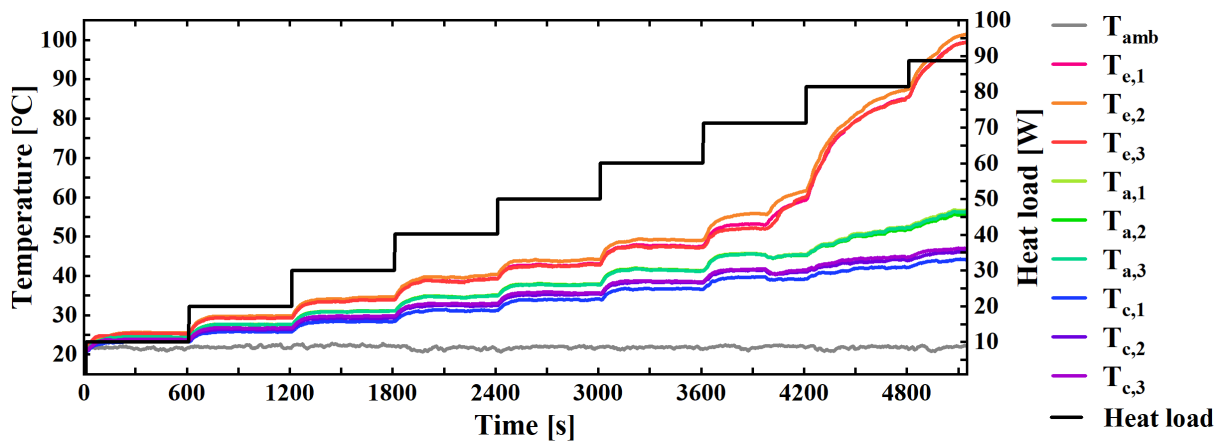


Figure 4. Transient temperature operating in the horizontal orientation.

4. CONCLUSIONS

The thermal performance of a flat heat pipe using a novel twisted wire capillary structure was experimentally studied in this paper. The new wick structure is made of 5 rolls of twisted wires using commercial electrical stranded cables. The proposed flat heat pipe operates successfully in the horizontal orientation. The novel twisted wire structure demonstrated high thermal efficiency as a capillary structure for flat heat pipes. Its ease of manufacturing and low cost make this porous media interesting for industrial-scale production especially for electronics cooling applications.

5. REFERENCES

- Krambeck, L., Domiciano, K.G., Mantelli, M.B.H., 2023. "Thermal Performance of Mini Flat Heat Pipes for High-power Chips," in: Proceeding of 27th International Congress of Mechanical Engineering (27th COBEM). Florianopolis, Brazil.
- Li, Y., Zhou, W., He, J., Yan, Y., Li, B., Zeng, Z., 2016. "Thermal performance of ultra-thin flattened heat pipes with composite wick structure." *Applied Thermal Engineering*, Vol. 102, pp. 487–499.
- Mantelli, M.B.H., 2021. *Thermosyphons and Heat Pipes: Theory and Applications*, Thermosyphons and Heat Pipes: Theory and Applications. Springer International Publishing.
- Peterson, G.P., 1994. *An Introduction to Heat Pipes: Modeling, Testing and Applications*. Wiley-Interscience, New York, USA.

NEW DEVELOPMENTS OF A MINIATURE LOOP HEAT PIPE FOR COMPACT ELECTRONICS

Kelvin Guessi Domiciano*, Larissa Krambeck, Marcia Barbosa Henriques Mantelli

Heat Pipe Laboratory, Department of Mechanical Engineering, Federal University of Santa Catarina, Florianópolis, Brazil.

*kelvin.guessi@labtucal.ufsc.br

Keywords: loop heat pipes, electronics, diffusion bonding, thermal performance

1. INTRODUCTION

In the last decades, electronic gadgets have become more compact and sophisticated, with their components working at higher processing velocities. Consequently, the demand for more efficient thermal control processes increased as high temperatures jeopardize their performances and the user experience. However, the application of conventional methods for removing the increasing heat generation, such as heat spreader plates and TIM (thermal interface materials) has shown not to be enough (Domiciano et al., 2022). To overcome this issue, many research groups concentrate efforts in improving thermal control devices for electronics, including heat pipes.

Loop Heat Pipes (LHPs) can be considered a variation of the classic heat pipes. One of the most important features of LHP is that the evaporator and condenser are physically separated but connected by liquid and vapor tubes, being able to fit easily in actual applications. The LHP operation principle is simple: heat supplied to the evaporator causes the working fluid to change of phase from liquid to vapor. The formed vapor flows to the condenser through the vapor line. In the condenser, the heat is rejected, condensing the vapor. The liquid returns to the evaporator by the liquid line, closing the loop. In the evaporator, a wick structure is responsible for pumping the liquid through the loop. Some LHP configurations contain a compensation chamber between the liquid line and the evaporator to keep the porous wick saturated.

The present paper shows new progresses in the development of a diffusion bonded miniature loop heat pipe, designed for smartphones, as described in (Domiciano et al., 2022) and (Domiciano et al., 2023), with external geometry of 76 x 60 mm. The major improvement described is in the reduction of the thickness, from 1.6 and 1.1 mm to 0.8 mm, keeping good heat transfer characteristics.

2. LOOP HEAT PIPE

The two-phase device of the present study consists of a miniature flat loop heat pipe. It is fabricated by diffusion bonding a stack of three copper plates, a sandwich formed by two external full sheets and one internal channelled sheet, all with 0.3 mm of thicknesses and with the same external geometry (see Figure 1a). The channels drilled in the internal plates allows for the working fluid to flow. After the diffusion bonding, the total thickness of the flat LHP is 0.8 mm, as shown in Figure 1b. Two wick structures, one in the evaporator and the other in the liquid line guarantee that the working fluid flows inside the flat LHP.

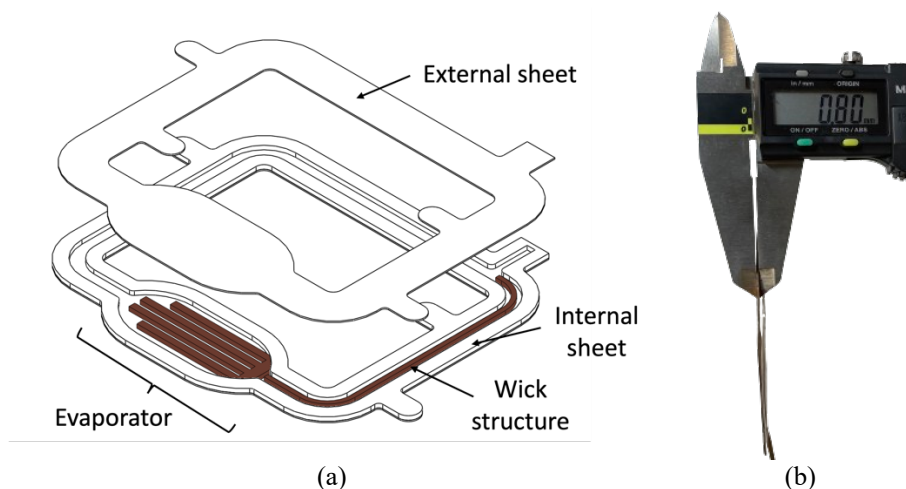


Figure 1. (a) Schematic design of the proposed LHP (b) LHP thickness after diffusion bonding.

Both wick structures, located in the evaporator and liquid line, have the same properties. They are fabricated from sintering copper powder, resulting in a porosity of 53%, an effective porous radius of 21 μm , and a permeability of 2×10^{-10} m².

¹² m². Distilled and deionized water is used as the working fluid with a filling ratio of 58% (0.14 ml). For more details regarding the manufacturing procedures, see (Domiciano et al., 2022).

3. EXPERIMENTAL PROCEDURE

The experimental study mainly consists of evaluating the thermal performance of the proposed LHP at steady-state conditions. Heat is applied on the outer surface of the evaporator section (see Figure 1a) by an electrical resistor embedded in a copper block, with 1 cm² of contacting area. The thermal investigation starts with the application of 0.5 W, with steps of 1 W, until the evaporator temperature of the LHP reaches 100 °C. This limit was selected based on the temperature limitations of real electronic components (Maydanik et al., 2011). Seven temperature measurements are taken along the LHP. Thermocouple T₁ measures the evaporator temperature, T₂ evaluates the evaporator outlet temperature, T₃, T₄, and T₅ read the inlet, middle, and outlet sections of the condenser, and T₆ computes the inlet evaporator temperature. T_{amb} assesses the ambient temperature. The device was tested in the horizontal, gravity assisted (evaporator beneath condenser) and antigravity vertical positions. The steady-state condition is considered achieved when the evaporator temperature variation is less than 0.1 °C in 1 minute.

4. PRELIMINARY RESULTS

Figure 2 shows the transient temperature of LHP with 58% water filling ratio, as a function of time, horizontal position. It is clear that the device started to operate as a two-phase system when a power of 3 W was applied, once the condenser temperature (T₄) suppressed the inlet evaporator temperature (T₆). The LHP did not show dry-out of the working fluid under the tested conditions, supporting a heat dissipation of 7 W/cm² before reaching the limit temperature of 100°. The LHP operated more efficiently with the increasing heat input, reaching a thermal resistance (ratio of the temperature difference between T₁ and T₄ and the heat load applied) of 2.51 ± 0.30 °C/W at 7 W/cm².

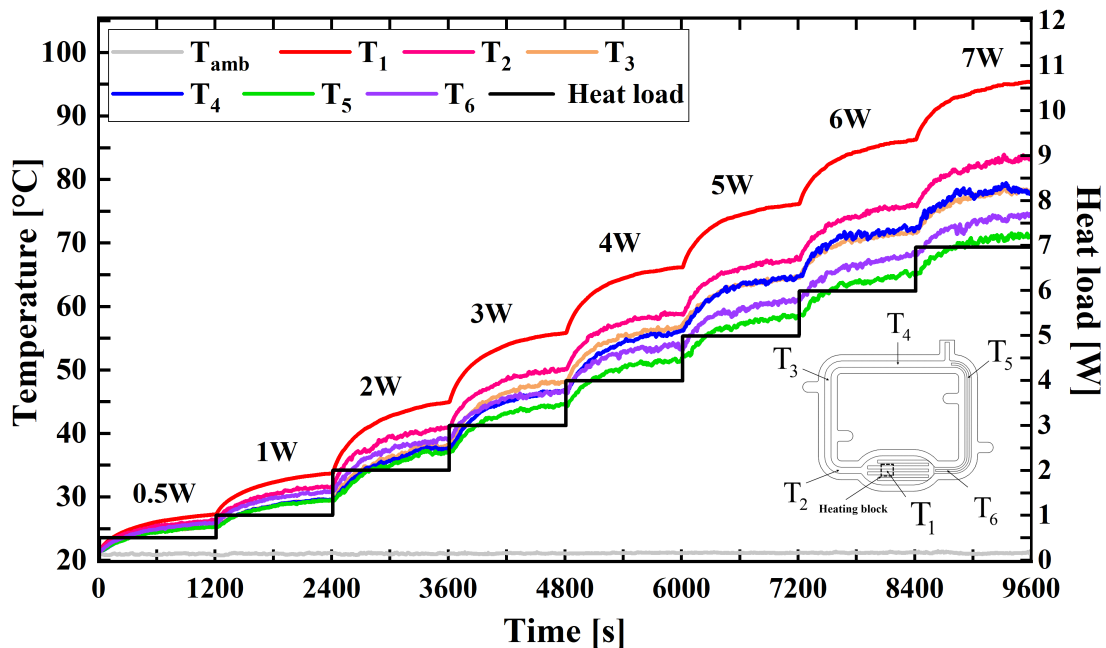


Figure 2. Transient temperature of LHP with FR 58% of water as function of time in the horizontal position.

Figure 3 provides the average temperature of the LHP (except T_{amb}), under steady-state conditions, for a 58% of water filling ratio, in the horizontal (square dots), gravity-assisted (round dots), and against-gravity orientations (triangle dots). The applied thermal power varied from 0.5 to 7 W for the horizontal and against gravity position and up to 8 W for the gravity-assisted orientation. The curves relating to the 1 and 6 W powers are not shown on the graph, to improve visualization quality.

From Figure 3 it can be seen that the only heat transfer mechanism for heat loads below 3 W was conduction, since, up to this power, in all positions tested, the thermocouples along the LHP condenser presented temperatures lower than the evaporator inlet temperature (T₆). For the LHP operating in the gravity-assisted and against-gravity orientations, the startup occurred at 4 W. However, starting with 2 W, temperature differences were already observed between the thermocouples from T₁ to T₄, due to the condensation phenomenon that already occurred, and between T₅ and T₆. In the horizontal position, the LHP started operating when it reached an evaporator temperature of around 55 °C (steady state). In the vertical positions (against and gravity assisted), this temperature was close to 64 °C. The temperature differences

between T₁ and T₆ for the startup in the orientations: horizontal, gravity-assisted, and against gravity were 9.17 °C, 11.50 °C and 10.31 °C, respectively.

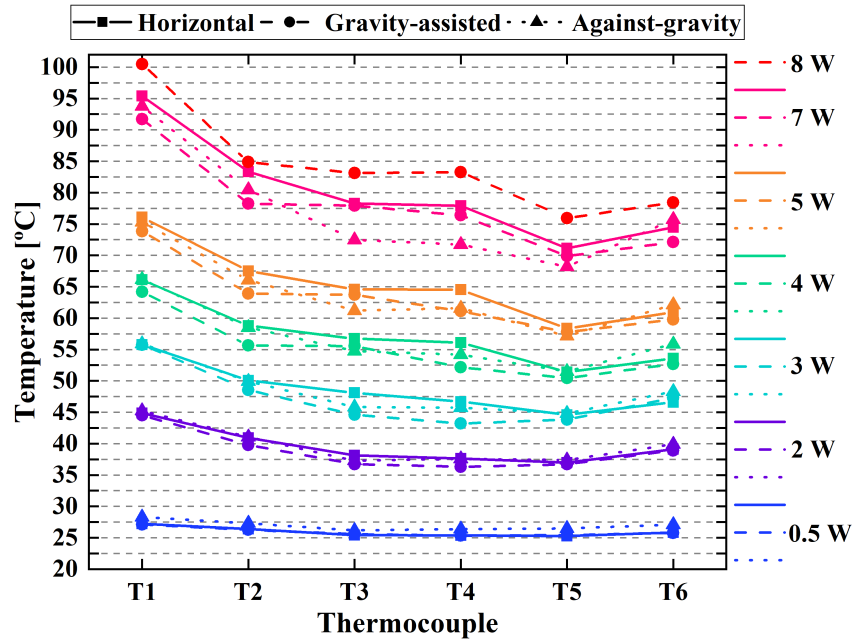


Figure 3. Average steady-state temperature of the LHP operating in all orientations.

Up to now, the general major conclusion is that the LHP is capable of operating regardless of gravity and removing heat up to 8 W, with an evaporator temperature of less than 100 °C. In this way, the preliminary results show that the LHP is a good solution for compact electronic gadgets.

5. REFERENCES

- Domiciano, K.G., Krambeck, L., Floréz, J.P.M., Mantelli, M.B.H., 2022. Thin diffusion bonded flat loop heat pipes for electronics: Fabrication, modelling and testing. *Energy Convers Manag* 255. <https://doi.org/10.1016/j.enconman.2022.115329>
- Domiciano, K.G., Krambeck, L., Mera, J.P.F., Mantelli, M.B.H., 2023. Study of a new thin flat loop heat pipe for electronics. *Heat and Mass Transfer/Waerme- und Stoffuebertragung*. <https://doi.org/10.1007/s00231-023-03381-9>
- Maydanik, Y., Vershinin, S., Chernysheva, M., Yushakova, S., 2011. Investigation of a compact copper-water loop heat pipe with a flat evaporator. *Appl Therm Eng* 31, 3533–3541. <https://doi.org/10.1016/j.applthermaleng.2011.07.008>

EFFECT OF FIN HEIGHT AND GEOMETRY ON EVAPORATION HEAT TRANSFER ON HORIZONTAL OUTER-FINDED TUBE

Sho Fukuda^{a,*}, Tomonobu Matsuno^b, Hiroyuki Takahashi^b

^a Department of Mechanical Engineering, Faculty of Science and Engineering, Kyushu Sangyo University, Fukuoka 813-8503, Japan

^bHatano Plant, Research & Development Section, Technical Department, KMCT Corporation

*s.fukuda@ip.kyusan-u.ac.jp

Keywords: heat transfer, evaporation, fin height, outer-finned tube, centrifugal chiller

1. INTRODUCTION

The global warming potential of refrigerants has become an issue. Thus, there is an urgent need to switch to lower-GWP refrigerants used in heat pump systems. The same situation in centrifugal chiller has led to the conversion from R134a to low-GWP HFO and HCFO refrigerants. However, most HFO and HCFO refrigerants have lower operating pressures in turbo refrigerators compared to R134a. Therefore, the appropriate tube geometry for the heat transfer of the refrigerant in the heat exchanger is different.

In this study, pool boiling (evaporating) heat transfer is measured at different operating pressures using outer-finned tubes with different fin heights, and the appropriate fin height and geometry for each operating pressure is investigated.

2. EXPERIMENT METHOD

Fig. 1 shows an experimental apparatus to measure the pool boiling HTC on a horizontal tube. This is a natural circulation system, in which the liquid refrigerant condensed on a test tube (4) and sub-condensers (6) flows down to a boiling chamber, while the vapor evaporated on the test tube and electric heaters (8) returns to a condensation chamber. The heat transfer on the test tube is obtained from the temperature change measured in the mixing chambers and the flow rate of the water flows in the test tubes. To determine the refrigerant saturation temperature, the pressure is measured very close to the test tube. The saturation temperature is checked with the temperature measured by K-type thermocouples installed in those chambers. An electric current of 40 A is conducted to the test tube, so that the mean wall temperature is calculated as a function of the electric resistance measured by a voltage meter. The wall temperature is calibrated in the preliminary test; meanwhile, the heat loss from the chambers to ambient air is also measured. The heat flux on the tube wall q_{wall} was defined as follows:

$$q_{\text{wall}} = \frac{V_{\text{H}_2\text{O}} \rho_{\text{H}_2\text{O}} (h_{\text{H}_2\text{O},\text{o}} - h_{\text{H}_2\text{O},\text{i}}) - Q_{\text{loss}}}{\pi D_o L} \quad (1)$$

where $V_{\text{H}_2\text{O}}$, $\rho_{\text{H}_2\text{O}}$, and $h_{\text{H}_2\text{O}}$ are the volumetric flow rate, density, and specific enthalpy of water, respectively, evaluated at the average mixing temperature of inlet and outlet water in the test tube; Q_{loss} is the heat loss correlated with the temperature difference between water and ambient air; and D_o and L are the outer diameter and effective heat transfer length, respectively, of the test tube. Therefore, the heat transfer coefficient (HTC) was expressed as follows:

$$\alpha = \frac{q_{\text{wall}}}{T_{\text{sat}} - T_{\text{wall}}} \quad (2)$$

where T_{sat} is the saturation temperature evaluated at the measured pressure and T_{wall} is the tube wall temperature correlated with the electric resistance. The thermodynamic and transport properties of R1233zd(E) were calculated by REFPROP Version 10 (Lemmon, E. W., et al., 2018), with the incorporated coefficients optimized by Akasaka (Akasaka, R., and Lemmon, E. W., 2018). When measuring the HTC, the Evaporation formation on the test tube through the glass window was captured by a high-speed camera.

The test tubes, which were made of copper, had a 19.04-mm outer diameter and 400-mm heat transfer length, and were set in a perfectly horizontal configuration. Figure 2 shows the fin geometries of test tubes of axial cross section. Table 1 shows test tube parameters. The fin height of Type A is the lowest, that of Type C is the highest. Fin pitch and fin width are almost the same for all types. The higher the fin height, the larger the capacity of the tunnel section between fins. The shapes of the tunnel sections also differ.

The test refrigerant is R1233zd(E). The HTC was quantified at a saturation temperature of 10 and 60°C. Table 2 shows Thermal and transfer properties of R1233zd(E) and R134a. The measurement range of the heat flux was 5–40 kW·m⁻² for the evaporation. A comparison of the thermodynamic and transport properties of R134a at 10°C and R1233zd(E) at 60°C shows relatively close values. Their surface tensions are very close. Surface tension is very important for heat transfer with a phase change in a very small volume, such as in the tunnel section of the test tube used in this study.

Therefore, we compare the heat transfer coefficients of refrigerants with different operating pressures by comparing experiments with R1233zd(E) at saturation temperatures of 60°C and 10°C. The measurement range of the heat flux was 5-50 kW·m⁻² for the evaporation.

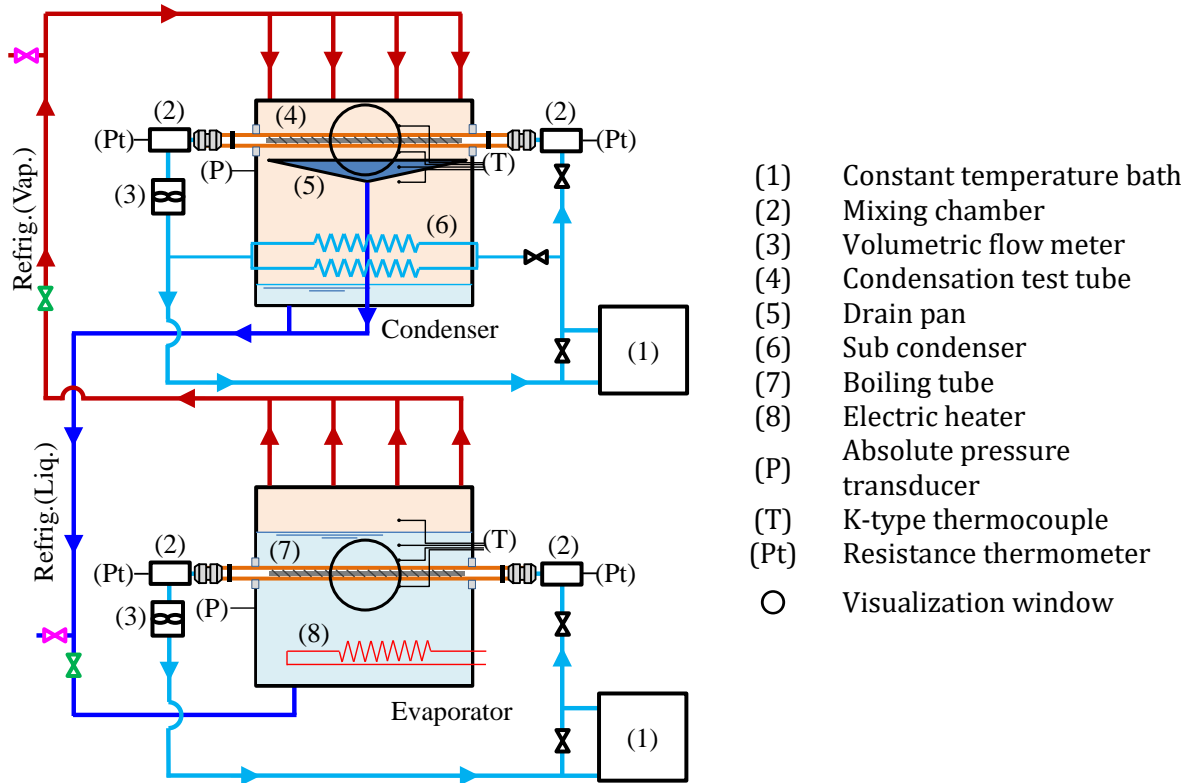
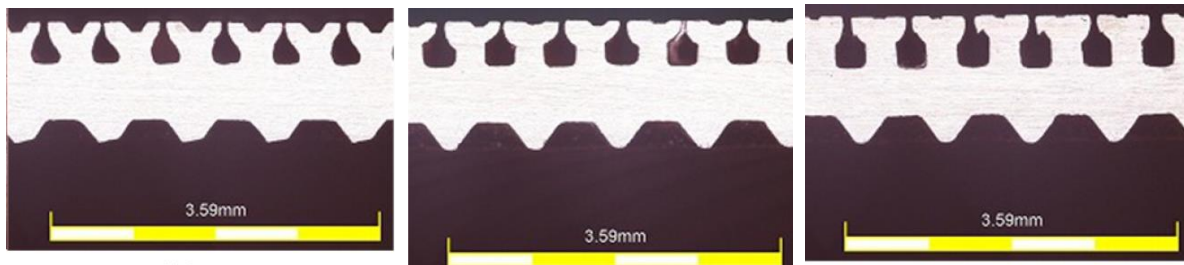


Figure 1. Schematic diagram of the experimental apparatus.



(a) Type A (Fin height = low) (b) Type B (Fin height = middle) (c) Type C (Fin height = high)

Figure 2. Fin geometry of axial cross section.

Table 1. Test tube parameters.

Parameter	Unit	Type A	Type B	Type C
Out diameter of tube end	D_o mm	19.04	19.04	19.04
Out diameter of fin area	D_f mm	18.4	18.49	18.46
Fin height	H_f mm	0.47	0.51	0.57
Fin pitch	P_f mm	0.66	0.67	0.66
Heat transfer surface area of tube outer	S_{out} m ² /m	0.135	0.138	0.152

Table 2 Thermal and transfer properties of R1234zd(E) and R134a.

Refrigerant	Saturation temp. °C	Saturation pressure MPa	Density		viscosity		TCX		surface tension mN·m ⁻¹
			liq. kg·m ⁻³	vap. kg·m ⁻³	liq. μPa·s	vap. μPa·s	liq. mW·m ⁻¹ ·K ⁻¹	vap. mW·m ⁻¹ ·K ⁻¹	
R1233zd(E)	10	0.07337	1298	4.212	333.3	9.782	87.3	9.418	16.56
R1233zd(E)	60	0.3909	1173	20.73	204.2	11.56	72.55	13.67	10.13
R134a	10	0.4146	1261	20.23	234.9	11.1	87.62	12.4	10.04

3. EXPERIMENT RESULT

Figure 3 shows the variation in the evaporation HTC with the heat flux in the test tubes. The red and blue symbols represent the experimental values of HTC at saturation temperature 60 °C and 10 °C. Figure 3 (a), (b) and (c) show results on tube type A, type B and type C, respectively.

In figure 3(a), at the same heat flux, the HTC at saturation temperature of 60 °C is lower than the HTC at saturation temperature of 10 °C. In general, the nucleate boiling heat transfer coefficient increases with increasing saturation temperature. Thus, nucleate boiling is not the main phenomenon, but thin liquid film evaporation is. After the start of boiling, the void fraction in the tunnel increased, and the liquid phase of the refrigerant was attracted to the tunnel corners by surface tension, forming a thin liquid film around the tunnel corners. In this case, the lower the saturation temperature, the higher the surface tension, and the thinner the liquid film around the tunnel corner, the higher the heat transfer coefficient at lower saturation temperatures.

In figure 3(b), the results for Type B are similar to those for Type A. The fin height of Type B is higher than that of Type A and the volume of the tunnel is larger, but the effect on heat transfer is expected to be small.

In figure 3(C), Type C results differ significantly from those of other tubes. The HTC at the saturation temperature of 60°C is higher than the results for the other tubes, and the heat transfer coefficient at the saturation temperature of 10°C is high at low heat flux but decreases significantly after reaching its peak. The fin corner of Type C has a smaller radius of curvature than that of the other tubes and is closer to a right angle. This is not due to the effect of fin height, but rather to the shape of the tunnel corner, which has a smaller radius of curvature and is closer to a right angle than the other tubes. The shape of the tunnel corner causes a strong force generated by surface tension, and the liquid phase is more attracted to the tunnel corner, resulting in a thinner liquid film near the tunnel corner. This is thought to be the reason for the higher heat transfer coefficient. However, at the saturation temperature of 10°C, the liquid film became too thin, and part of the film dried out, resulting in a lower heat transfer coefficient.

The results suggest that in a tube shape with a tunnel section, such as the test tube used in this study, the shape of the tunnel corner has a greater effect on heat transfer than the height of the fins.

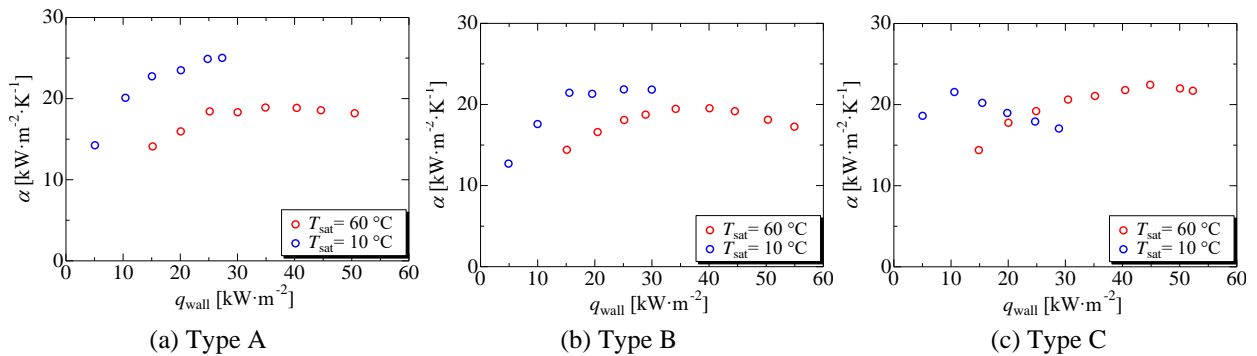


Figure 3. Variation in the falling film evaporation HTC with the heat flux.

4. CONCLUSIONS

Heat transfer measurements were conducted on three horizontally installed test tubes with varying fin heights, using different refrigerants at different operating pressures. The main conclusions are as follows:

- The heat transfer coefficient in finned tubes with tunnel sections is primarily affected by liquid film evaporation rather than nucleate boiling.
- The impact of fin height on the heat transfer coefficient in finned tubes with tunnel sections is smaller.
- The shape of the corner of the tunnel significantly affects the heat transfer coefficient. A smaller radius of curvature results in a thinner liquid film around the corner, which in turn leads to a higher heat transfer coefficient. However, if the liquid film becomes too thin, a portion of it will rupture, causing a decrease in the heat transfer coefficient.

5. REFERENCES

Akasaka, R., and Lemmon, E. W., 2018, Helmholtz equation of state for R-1233zd(E), Refprop Ver. 10.
 Lemmon, E. W., Huber, M. L., and McLinden, M. O., 2018, Reference Fluid Thermodynamic and Transport Properties - REFPROP Ver. 10, National Institute of Standards and Technology, Boulder, CO, USA.

PIV experimental analysis of the gasper jet in an aircraft cabin

João Henrique Antoniazzi de Gouveia^{a,*}, Jurandir Itizo Yanagihara^a

^aUniversity of São Paulo, Polytechnic School, Department of Mechanical Engineering – Av. Prof. Mello Moraes, 2231, São Paulo/SP, Brazil.

*jhagouveia@usp.br

Keywords: Aircraft, Comfort, Gasper, PIV, Entrainment

1. INTRODUCTION

In commercial aircraft, passengers and flight crew share the same space for the entire flight duration at a cruising altitude of approximately 12 km; therefore, an environmental control system (ECS) that provides cabin pressurization and thermal control is essential for their survival under such hostile external environmental conditions (Giaconia *et al.*, 2013). In most commercial aircraft, the air conditioned in the ECS is distributed to the cabin by a mixing ventilation method (Zhang *et al.*, 2017). Such a ventilation mode cannot meet all passengers' thermal comfort requirements and results from previous studies showed a high concentration of particles within their breathing zone in the cabin (Giaconia *et al.*, 2013; LI *et al.*, 2021). Although aircraft are equipped with a high efficiency filter to remove virus and bacteria from recirculated air, Hertzberg *et al.* (2018) demonstrated that an infected passenger represents a high risk of infection for those who are immediately close to them. In addition to that, the aviation sector faced a substantial disruption over the outbreak of SARS-CoV-2 (COVID-19) due to the risk of in-flight transmission or even due to the concern of carrying infected passengers to different locations (LI *et al.*, 2021).

Therefore, there are two main approaches discussed in the literature to improve aircraft cabin ventilation. The first one is the replacement of the mixing ventilation method to a displacement ventilation concept. Although the displacement ventilation promotes a better air quality, primarily by directing contaminants towards passengers' thermal plume direction, they become vulnerable to discomfort due to temperature stratification (Zhang *et al.*, 2017). The second approach is the implementation of personalized ventilation systems in combination with main ventilation systems. Despite efforts related to the development of innovative systems, the gasper remains the standard equipment used in commercial aircraft due to its ease of installation, use, and control (Dai *et al.*, 2015; Li *et al.*, 2018).

The gasper can create an individual microenvironment at passengers' breathing zone through a high-speed jet, and field research conducted by Fang *et al.* (2015) pointed that more than 50% of them have chosen to use gasper during flight to improve their thermal comfort. This way, a deeper understanding of the gasper jet airflow characteristics is crucial to the process of creating a thermally comfortable and healthy cabin environment. Studies focused on gasper can be carried out via experimental or numerical methods. The former usually are more time consuming and expensive than the latter, however, numerical methods rely on data from experiments that need to be validated. Point-wise techniques as hot-wire anemometers are used by several authors such as Dai *et al.* (2015) to evaluate gasper characteristics. Despite its usefulness, these techniques are intrusive due to the need of inserting a probe inside the airflow, and it is necessary to repeat the measurement along the area of interest to observe the jet domain. Thus, there is an important gap that must be filled by global-wise techniques, such as particle image velocimetry (PIV). Our literature review has led us to two main works focused on the measurement of gasper airflow with PIV. The first was performed by You *et al.* (2016) to identify which turbulence model is suitable to represent a small region above a heated simulator where its thermal plume interacts with gasper jet and mixing ventilation. The second one was conducted by Li *et al.* (2018) and the authors evaluated the influence of mixing ventilation on the gasper airflow measuring a plane in front of a heated dummy.

Hence, in this work PIV measurements were conducted inside a realistic cabin mockup to evaluate gasper jet characteristics and its performance at different operational conditions as well as the influence of mixing ventilation in its airflow. In addition, the acquisition of multiple planes allows us to reconstruct the jet domain to discuss its performance from the perspective of air quality.

2. MATERIALS AND METHODS

The experiments were performed inside a fully functional cabin mockup of an Embraer E-170 planned for 30 passengers, as well as one flight attendant. Furthermore, the mockup has the capacity to simulate mixing ventilation and its airflow rate was set to 1050 m³/h at 21°C, which corresponds to ASHRAE (2018) recommendation for 31 occupants. Besides that, a gasper is positioned above each seat, and they were set vertically downward. Passengers also can adjust the gasper's flow rate through a knob that moves an internal cone and can change its opening size (Fig. 1.a); thus, the PIV experiments were repeated for a gasper fully opened and for an opening size of 50%. ASHRAE (2018) has established a minimum airflow rate capacity of 3.384 m³/h per personal outlet, therefore two airflow rates ($Q_{0,1}=4.212$ m³/h and $Q_{0,2}=7.463$ m³/h) were selected for a total of four experimental conditions.

A 2D-PIV system was used to measure the gasper jet velocity fields. This system consists of a double cavity Nd:YAG laser at a sampling frequency of 6 Hz and a camera with a resolution of 2048 x 2048 pixels equipped with a 50 mm planar

f/1.4 lens. Three traverses were used to move the system inside the cabin to capture the entire region under gasper influence. All the mentioned equipment was mounted inside the cabin (Fig. 1.b) due to the absence of an optical access since the mockup is set inside a low-pressure chamber. The only equipment outside the chamber was an atomizer which was connected to the main ventilation ducts to seed diethylhexyl sebacate (DEHS) particles in the airflow.

After image recording, a mean image was subtracted from each frame to allow for an adequate identification of particle movement and distribution (Wereley *et al.*, 2022), along with a 3 x 3 gaussian filter and a 3 x 3 laplacian filter applied to increase the cross-correlation peak and avoid the peak-locking effect (Adrian and Westerweel, 2011). At the end of image processing, the instantaneous spurious vectors were replaced via the use of a universal outlier detection (UOD) applied in a neighborhood of 5 x 5 (Westerweel and Scarano, 2005).

The velocity inside jet domains undergoes a rapid decrease, and within the same measurement windows it can vary from 30 m/s to less than 1 m/s. Thus, to increase the velocity dynamic range of mean velocity maps, each experimental condition was measured with four different time delays between double frames, as follows: 10 μ s, 25 μ s, 50 μ s, and 100 μ s. Thus, the best mean velocity vector was selected according to the method described by Persoons and O'Donovan (2011), which considers the highest primary peak ratio (PPR) weighted by the relative uncertainty, previously calculated using the method developed by Xue *et al.* (2014). Finally, this process of mean velocity vector selection is exemplified on Fig. 1.c where it is possible to observe that the jet core is better represented by a short time delay between double frame than its surroundings.



Figure 1. Summary of material and methods

3. RESULTS

Velocity vector maps (with an average based on 1000 images), which have been obtained for all four experimental conditions, are shown on Fig. 2. Due to the presence of a cone to control the airflow rate, the gasper jet is treated in the literature as an annular jet; however, just a small portion of jet transition zone was observed at mean velocity maps because the jet was measured from 15 mm of overhead bins due to laser reflections. Thus, it was found that the velocity centerline increases to an apex at the reattachment point, and after that, the jet velocity centerline decay as a round jet in the fully developed zone. At this point, an important finding was that the velocity apex was achieved at the same axial coordinate for the same gasper opening size regardless of airflow rate.

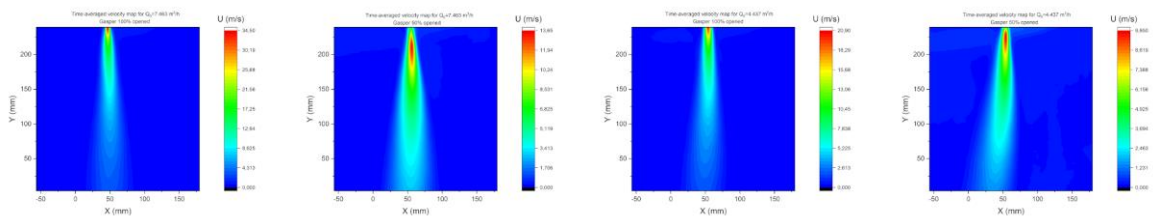


Figure 2. Mean velocity field for all four experimental conditions

The main functions of personal ventilation are to supply fresh air near users' breathing zones and to improve air quality in such a manner that the gasper fresh air transport capability and effectiveness can be evaluated by measuring the local airflow rate. With the acquisition of 15 equidistant planes in each experimental condition it was possible to reconstruct the measurement volume (Fig. 3.a); thus, it was verified that the jet has a round cross section (Fig. 3.b) in its entire extension length. Therefore, the local airflow was calculated by integrating the velocity profile inside the jet domain, which was defined by Khayurulina *et al.* (2017) as $2 \cdot x_{1/2}$ (Fig. 3.c) ($x_{1/2}$ represents the radial coordinate where the velocity is half of the centerline local velocity). Fig. 3.d shows that the rapid increase of local airflow rate for one of the four experimental conditions and the average airflow rate increase for all scenarios was 70%. Furthermore, Kabanshi (2020) demonstrated that for a local airflow rate equal to $2.718 \cdot Q_0$, the contaminant concentration inside the jet is the same as the concentration in the environment, thus its airflow rate was highlighted in Fig. 3.d and it was found that this condition was reached very fast and at an axial position near passengers' breathing zone.

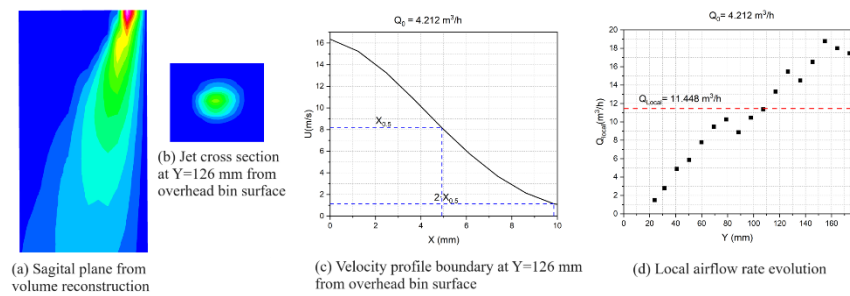


Figure 3. Summary of steps taken to calculate the local airflow rate

4. CONCLUSIONS

PIV measurements were carried out inside a realistic cabin mockup to evaluate the main characteristics of gasper jets, such as centerline velocity decay and entrainment ratio under four experimental conditions. The gasper utilized in this study belongs to an Embraer aircraft, so the results obtained may not be extrapolated to other models. However, some jet features agree well with those found in previous studies. For example, the maximum velocity occurs at the same point for the same opening size and changing the nozzle opening has shifted the velocity apex downward.

One of the gasper drawbacks is the maximum velocity because passengers are closer to it than in buses or trains due to limited cabin space. Thus, users are subjected to the risk of draft sensation even though the centerline velocity decays very fast. Furthermore, the entrainment ratio is high for all cases and this result indicated that most of the air in the passengers' breathing zone is air that has been recirculated from the environment.

5. REFERENCES

- Adrian, R.J. and Westerweel, J., 2011. *Particle image velocimetry*. Cambridge University Press, Cambridge.
- ASHRAE – AMERICAN SOCIETY OF HEATING, REFRIGERATING AND AIR CONDITIONING, 2018. *ANSI/ASHRAE standard 161-2018: Air quality within commercial aircraft*. Ashrae, Atlanta.
- Dai, S., Sun, H., Liu, W., Guo, Y., Jiang, N. and Liu, J., 2015. “Experimental study on characteristics of the jet flow from an aircraft gasper”. *Building and Environment*, Vol. 93, pp. 278-284.
- Fang, Z., Liu, H., Baldwin, A., Wang, J. and Xia, K., 2015. “Experimental investigation of personal air supply nozzle use in aircraft cabin”. *Applied Ergonomics*, Vol. 47, pp. 193-202.
- Giaconia, C., Orioli, A. and Di Gangi, A., 2013. “Air quality and relative humidity in commercial aircrafts: An experimental investigation on short-haul domestic flight”. *Building and Environment*, Vol. 67, pp 69-81.
- Hertzberg, V.S, Weiss, H., Elon, L., Si, W. and Norris, S.L., 2018. “Behaviors, movements, and transmission of droplet-mediated respiratory diseases during transcontinental airline flight”. *Proceedings of the National Academy of Science*, Vol. 115, pp. 3623-3627.
- Kabanshi, A., 2020. “Near-field flow structure and entrainment of a round jet at low exit velocities: Implications on microclimate ventilation”. *Computation*, Vol. 8.
- Khayrullina, A., Van Hoff, T., Blocken, B. and Van Heijst, G. J. F., 2017. “PIV measurements of isothermal plane turbulent impinging jets at moderate Reynolds number”. *Experiment in Fluids*, Vol. 58, pp. 1-16.
- Li, J., Liu, J., Dai, S., Guo, Y., Jiang, N. and Yang, W., 2018. “PIV experimental research on gasper interacting with the main ventilation in an aircraft cabin”. *Building and Environment*, Vol. 138, pp. 149-159.
- Li, X., Zhang, T., Fan, M., Liu, M., Chang, D., Wei, Z., Lin, C., Ji, S., Liu, J., Shen, S. and Long, Z., 2021. “Experimental evaluation of particle exposure at different seats in a single-aisle aircraft cabin”. *Building and Environment*, Vol. 202.
- Persoons, T. and O’Donovan, T. S., 2011. “High dynamic velocity range particle image velocimetry using multiple pulse separation”. *Sensor*, Vol. 11.
- Wereley, S.T., Gui, L. and Meinhart, C.D., 2002. “Advanced algorithm for microscale particle image velocimetry”. *AIAA Journal*, Vol. 40, pp. 1047-1055.
- Westerweel, J. and Scarano, F., 2005. “Universal outlier detection for PIV data”. *Experiments in Fluids*, Vol. 39, pp. 1096-1100.
- Xue, Z., Charonko, J. J., Vlachos, P. P., 2014. “Particle image velocimetry correlation signal-to-noise ratio metrics and measurement uncertainty quantification”. *Measurement Science and Technology*, Vol. 25.
- You, R., Chen, J., Shi, Z., Liu, W., Lin, C., Wei, D. and Chen, Q., 2016. “Experimental and numerical study of airflow distribution in an aircraft cabin mock-up with gasper on”. *Journal of Building Performance Simulation*, Vol. 9, pp. 1675-1684.
- Zhang, Y., Liu, J., Pei, J., Li, J. and Wang, C., 2017. “Performance evaluation of different air distribution system in an aircraft cabin mockup”. *Aerospace Science and Technology*, Vol. 70, pp. 359-366.

EFFECT OF ZnO NANOWIRES COATING HYDROPHOBICITY ON VAPOR FILM FORMATION AND FRICTION REDUCTION

Lina Vorotinskienė^{a,*}, Raminta Skvorčinskienė^a, Vladas Šatas^a, Ainė Povilaikaitė^a, Simas Račkauskas^b, Rita Kriūkienė^c

^aLaboratory of Combustion Processes, Lithuanian energy institute, Breslaujos Street 3, Kaunas, Lithuania

^bDepartment of Physics, Kaunas University of Technology, Studentu Street 50, LT-51368 Kaunas, Lithuania

^cLaboratory of Materials Research and Testing, Lithuanian energy institute, Breslaujos Street 3, Kaunas, Lithuania

[*Lina.Vorotinskiene@lei.lt](mailto:Lina.Vorotinskiene@lei.lt)

Keywords: ZnO nanowires coating, vapor film, Leidenfrost effect, hydrophobicity, friction reduction

1. INTRODUCTION

Increased global awareness of greenhouse gas emissions, as well as stricter government regulations, have led to the need for new technologies to reduce energy losses due to friction, drag and aerodynamics, thus increasing the efficiency of the next generation vehicles (Ali Erdemir & Holmberg, 2015; Holmberg et al., 2012, 2014). The application of advanced friction control technologies could significantly reduce energy losses due to friction and lead to significant reductions in greenhouse gas emissions.

Reducing friction between solids or between solids and water can be achieved through passive and active means. One passive measure is the use of hydrophobic coatings on solid bodies. A significant high-level study was carried out by Bowden and Tabor determined that acid molecules are chemically adsorbed on the surface of a substrate and then chemically react with the substrate through a frictional process to form a layer of fatty soap (F.P. Bowden & D. Tabor, 1967). Long chain fatty acids have long been used as a friction reducing agent (D. Dowson, 1979), but in our study this is difficult to apply due to the low evaporation temperatures of fatty acids.

Another passive means of reducing friction, surface texturing, has also been extensively studied recently. Surface texturing reduces surface adhesion and increases sliding at the point of contact (Menezes et al., 2011; Shafiei & Alpas, 2009). The creation of texture on relatively flat surfaces is very effective in reducing adhesion and friction of micro/nano-scale materials due to the reduction of the actual contact area, which directly reduces friction due to the reduced contact between solids. In work investigated a two-step process. In the first stage, textured aluminium samples were treated with sodium hydroxide to give them hydrophobic properties. In the second step, a stearic acid film was deposited on the samples. The textured surface and the stearic acid film were found not only to reduce friction but also to significantly extend the lifetime of the metallic substrate, in this case aluminium (Zhang et al., 2013).

ZnO nanowires obtained by synthesis can also be an excellent coating for friction reduction, not only because of their superhydrophobicity but also because they are stable at high temperatures. ZnO is environmentally friendly and can be produced from abundant crustal materials. The advantage of ZnO nanowires obtained by synthesis, which distinguishes them from other coatings, is that they exhibit reversible switching of surface wettability. This property allows ZnO nanowire-coated surfaces to vary from superhydrophobic to hydrophilic under changing environmental conditions (Mardosaitė et al., 2021).

The primary objective of this research is to find the optimum conditions and the most appropriate means to achieve the formation of a boiling crisis process with the lowest possible energy consumption. To this end, two measures, passive and active, have been applied in this work to reduce friction. The passive one is ZnO nanowires with hydrophobic properties, which were coated on aluminium samples. The active friction reduction measure is the formation of a vapour film around the sample due to the heat exchange process. The formation of a vapour film on a heated surface at the moment of contact with water has been studied for a long time and is also known as the Leidenfrost effect. The aim of this study is to obtain the Leidenfrost effect at the lowest possible temperatures between the body and the cooling water, or in other words to induce the formation of a vapour film due to the heat exchange between the heated surface and water. Contact angle measurements were carried out to verify the hydrophobic properties of the ZnO nanowires coated samples. The morphological and microstructural properties of the samples were investigated using scanning electron microscopy (SEM) with nanometre resolution.

2. MATERIALS AND METHODS OF EXPERIMENTAL PROCEDURES

2.1 Sample materials preparation and identification

Two types of spherical ($d=19.05$ mm) samples were used in the experimental studies for the identification of the boiling crisis: polished aluminium (Al) and aluminium coated with ZnO nanowires (Al-ZnO) Fig. 2. The ZnO powder

was mixed with ethanol (1 mg/ml) and sprayed at a pressure of 1.5 bar at a distance of 10 cm using an Adler AD-776B MAR EW-6000B air spray with a nozzle of 0.2 mm. Coating thickness 100 μm .

In order to give the synthesised tetrapods hydrophobicity, the samples were exposed to certain environmental conditions after coating. Fig. 1 a, b show surface photographs of Al-ZnO samples stored under different conditions, taken with a scanning electron microscope SEM EVO MA 10 and magnified by a factor of 40 000. In Fig. 1 a the Al-ZnO samples were stored in the light and at room temperature, in Fig. 1 b the Al-ZnO samples were stored for 4 weeks in the dark at 80 $^{\circ}\text{C}$.

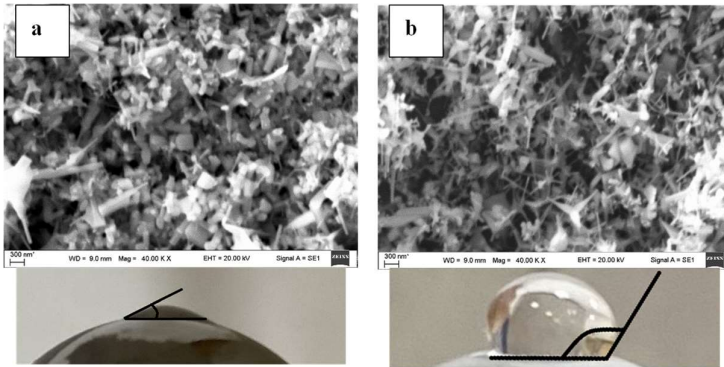


Fig. 1. Photographs of an aluminium sample coated with ZnO nanowires and held (a) in the light at room temperature; (b) in the dark at 80 $^{\circ}\text{C}$, SEM images of the surface and contact angle.

can break Zn-O bonds on the zinc surface, resulting in a large number of free oxygen bonds that can form hydrogen bonds with the water molecule (Mardosaitė et al., 2021). This can be seen in Fig. 1 b, where a drop of water with a contact angle of 27 $^{\circ}$ is dropped onto a ZnO film stored at room temperature and in the light, indicating hydrophilicity.

Fig. 1 a shows the uncompact granules. Fig. 1 b highlights the oblique tetrapods, which are almost invisible compared with Fig. 1 a. The structure of the oblique tetrapods reduces the surface energy and creates air pockets, which improves hydrophobicity. This can be seen in Fig. 1 a for a water droplet deposited on a ZnO film with a contact angle of 121 $^{\circ}$, which was obtained using Young's equation. Lower temperatures and darkness accelerate the rate of removal of the -OH groups and thus render the nanostructure hydrophobic by eliminating the loose bonds to which the water molecule can bind. Also, external energy sources such as light and high temperature

2.2 Experimental investigation methodology for vapor film formation

The experimental investigations on the determination of the boiling crisis process and the temperature changes on the surface of the sample were carried out in several steps Fig. 2.

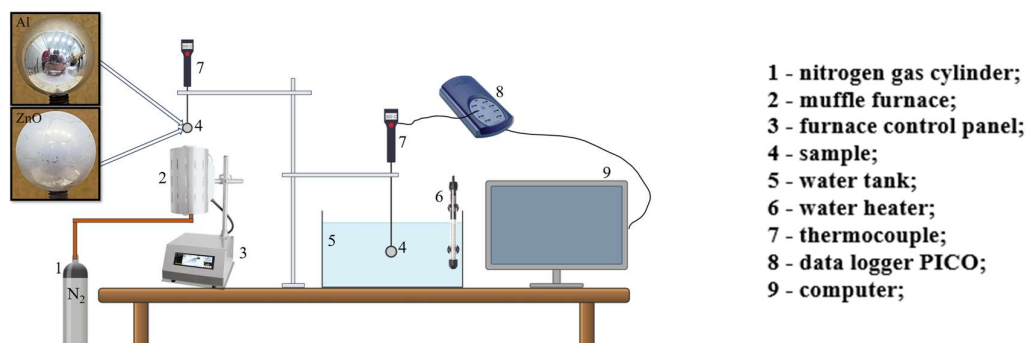


Fig. 2. Experimental equipment for identifying vapor film formation.

First, nitrogen gas is fed into the heated muffle furnace from below. The Al and Al-ZnO samples were then loaded into the muffle furnace using a holder to heat the samples to 300 $^{\circ}\text{C}$. At the same time, a water heater is used to heat the water tank to a selected temperature (25, 30, 35, 40 $^{\circ}\text{C}$). The surface temperature of the sample is recorded by an E-type thermocouple every 200 ms. During the experimental tests, the temperature data are collected using the Pico TC-08 data acquisition system and transmitted to a computer.

When the surface temperature of the sample reaches 300 $^{\circ}\text{C}$, the sample is immersed in heated water and the boiling crisis effect on the surface of the sample is observed. To determine the accuracy of the results, the experiment is repeated 3 times at different water temperatures. The formation of a film on the surface of the sample captured by camera.

3. RESULTS

The ZnO nanowires coating can be hydrophobic due to the tetrapods formed during the synthesis process (Mardosaitė et al., 2021), and it was therefore expected that the ZnO coating would have an influence not only on the vapour film

formation but also on its lifetime. However, experimental investigations for vapour film formation and comparison of the temperature change curves for Al and Al-ZnO samples showed that water temperature does not significantly affect the cooling dynamics of ZnO nanotube coated samples Fig. 3 a, b, c. The surface of the Al-ZnO samples cooled uniformly throughout the experiment, i.e. for 10 s, and reached 100°C after 10 s, while the Al samples started out with a similar cooling behaviour as the Al-ZnO samples, but after some time the temperature dropped sharply downwards. This is due to the different thermal conductivities of Al and ZnO, and Al cools more rapidly after the unstable boiling process because the ZnO coating acts as a protective layer which prevents the sample from suddenly giving up its heat to the water. Increasing the initial temperature of the water slows down the heat transfer and prolongs the lifetime of the vapour film formed on the Al samples. A vapour film around the ZnO nanowires coating the surface of the Al samples, which would have a visible effect on the unstable boiling process, did not form even when the water temperature was increased to 40°C Fig. 3 c. This is confirmed by the sharp decrease in the temperatures of the Al-ZnO samples from the first second of the experiment. In the experimental studies, immersion of Al samples heated to 300°C in water at 30°C and 35°C resulted in the formation of a vapour film on only a small part of the sample and in the disintegration of the sample before the whole sample was immersed, which could be said to be only a hint of the Leidenfrost effect Fig. 3 a, b. However, when the water temperature was raised to 40°C, a vapour film formed and enveloped the entire sample and remained stable for 0.5 s Fig. 3c.

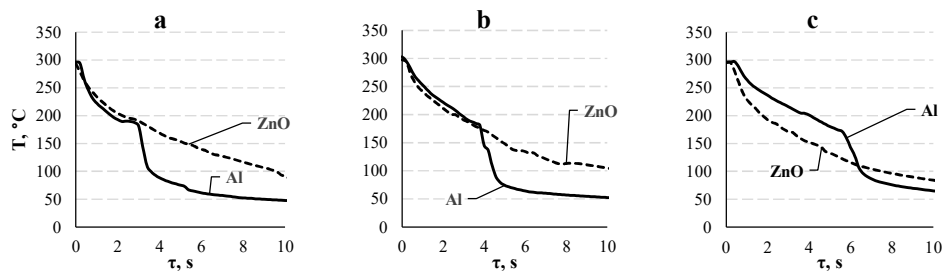


Fig. 3. Al and Al-ZnO specimens cooling dynamic when water temperature (a) 30 °C (b) 35 °C and (c) 40 °C.

4. CONCLUSIONS

1. The microstructure of Al samples coated with ZnO nanowires was compared and analysed. Differences in tetrapod arrangement and structure, which affect hydrophobicity, were observed, and the measured contact angle differed by as much as a factor of 4.7.
2. The hydrophobic coating of ZnO nanowires has a negative effect on the formation of a vapour film on the surfaces and no Leidenfrost effect was observed even after heating the Al-ZnO samples up to 300°C and immersion in water at 40°C.
3. It was found that increasing the water temperature slows down the heat transfer and increases the lifetime of the boiling crisis on the Al samples.

5. REFERENCES

- Ali Erdemir, & Holmberg, K. (2015). Energy Consumption Due to Friction in Motored Vehicles and Low-Friction Coatings to Reduce It. In *Coating Technology for Vehicle Applications* (pp. 1–23). Springer International Publishing.
- D. Dowson. (1979). History of tribology. *Longman*.
- F.P. Bowden, & D. Tabor. (1967). *Friction and Lubrication*. Methuen & Co Press.
- Holmberg, K., Andersson, P., & Erdemir, A. (2012). Global energy consumption due to friction in passenger cars. *Tribology International*, 47, 221–234.
- Holmberg, K., Andersson, P., Nylund, N.-O., Mäkelä, K., & Erdemir, A. (2014). Global energy consumption due to friction in trucks and buses. *Tribology International*, 78, 94–114.
- Mardosaitė, R., Jurkevičiūtė, A., & Račkauskas, S. (2021). Superhydrophobic ZnO Nanowires: Wettability Mechanisms and Functional Applications. *Crystal Growth & Design*, 21(8), 4765–4779.
- Menezes, P. L., Kishore, Kailas, S. V., & Lovell, M. R. (2011). Role of Surface Texture, Roughness, and Hardness on Friction During Unidirectional Sliding. *Tribology Letters*, 41(1), 1–15.
- Shafiei, M., & Alpas, A. T. (2009). Nanocrystalline nickel films with lotus leaf texture for superhydrophobic and low friction surfaces. *Applied Surface Science*, 256(3), 710–719.
- Zhang, Q., Wan, Y., Li, Y., Yang, S., & Yao, W. (2013). Friction reducing behavior of stearic acid film on a textured aluminum substrate. *Applied Surface Science*, 280, 545–549.

SIO₂ NANOPARTICLES IN MOLTEN LiCl-KCl EUTECTIC FOR ENHANCED HEAT STORAGE CAPACITY: A MOLECULAR DYNAMICS STUDY WITH MACHINE LEARNING POTENTIALS

Fei Liang^a, Jing Ding^b, Jianfeng Lu^b, Duu-Jong Lee^{a,*}, Shule Liu^{b,c,*}

^aDepartment of Mechanical Engineering, City University of Hong Kong, Kowloon Tong 999077, Hong Kong SAR

^bSchool of Materials Science and Engineering, Sun Yat-sen University, Guangzhou 510275, China

^cKey Laboratory for Polymeric Composite & Functional Materials of Ministry of Education, Sun Yat-sen University, Guangzhou 510275, China

*tuclee@cityu.edu.hk (D.J. Lee); *liushle@mail.sysu.edu.cn (S. Liu).

Keywords: molten salt, nanofluid, molecular dynamics, machine learning, agglomeration

1. INTRODUCTION

The Gen 3 concentrating solar power (CSP) equipped with a high-temperature molten chloride salt reheating device can continuously generate electricity, providing a high-efficiency retrofitting configuration. Nanoparticles could be applied to the molten salts to increase the suspension's thermal conductivity and heat capacity. As a powerful aid to experiments, simulations have succeeded to reveal various mechanisms on enhancement. However, these still discuss only the heat transfer and storage performance under ideal conditions. Wen and Zhao (2022) coated hydroxyl groups at the surface of 1 % w/w SiO₂ nanoparticle for experimental samples and simulated solid-liquid interface. The increased specific heat capacity is up to 19 % for NaNO₃/KNO₃ (60:40 w/w) and Li₂CO₃/K₂CO₃ (47:53 w/w). These interface effects need to be considered and analyzed as important influencing factors of agglomeration to support the futural large-scale applications in engineering. This study investigated the enhanced mechanism of the most common multiple SiO₂ nanoparticles on the heat transfer and storage properties in the most potential molten LiCl-KCl eutectic by molecular dynamics (MD) simulations with machine learning (ML) potentials to fill the lack of current researches.

2. METHODS

In this study, the model system of the nanocomposite-based molten salts consists of binary molten chlorides LiCl-KCl eutectics (59.5:40.5 % w/w) and α -cristobalite (SiO₂) nanoparticles (snapshots of Fig. 1(a) and (c)). The molten salts fluids included 4600 Li⁺, 3130 K⁺, and 7730 Cl⁻. In order to study the effect of nanoparticles' size, the 6 to1 SiO₂ nanoparticles with a side length of 13 to 28 Å keep the maximum relative distance in molten salts under periodic boundary conditions with the same loadings 6 % w/w. Similarly, the increased loadings (1 to 6 % w/w) refer to the 1 to 6 nanoparticles of 13 Å diameter. ML potentials can make a high accuracy for MD simulations. The previous work (Liang et al., 2023) trained the deep potentials (DPs) of the solid-liquid interface SiO₂/LiCl-KCl simulated system using the DeePMD-kit package. Applying a new "pair style" in LAMMPS to realize the atomic interaction described by DPs, the simulation was implemented in the isothermal-isobaric ensemble (NPT) with the fixed pressure 1.0 atm and the researched temperatures (900 K, 1000K, 1100K, 1200K).

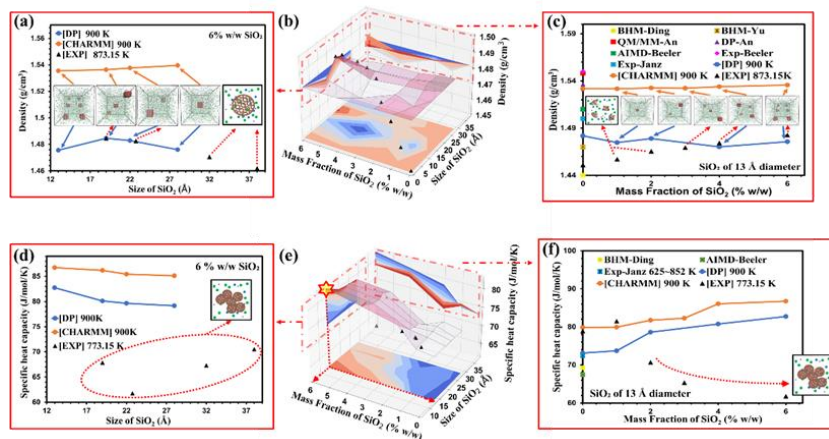


Figure 1. (a) and (c) are the profiles of (b) the three-dimensional contour map, representing the simulated density of nanocomposites with different loadings and sizes of nanoparticle at 900 K. The black triangles refer to the experimental values. The above settings apply to (d)-(f) for the specific heat capacity.

All KCl, LiCl, and SiO₂ nanoparticles were dried at 120 °C over 48 h before suspension preparation. The two-step method from Wei et al. (2020) was performed for suspension preparation. First, the eutectic mixture was melted in an alumina crucible at 400 °C for three hours to yield the molten salt. Then, SiO₂ nanoparticles were added at 1-6% w/w into the molten salt and stirred at constant temperatures. The 6% w/w nanocomposites were stirred at 300-500 rpm and 400 °C for 60-100 min to yield four samples of different dispersity.

2. EFFECT ON THERMAL PROPERTIES

The MD simulations with ML potentials have more accurate results of density by comparing with experimental values. The contrast between the experiments and simulations found that the specific heat capacity of experimental samples was significantly reduced due to the agglomeration of nanoparticles. This is most likely to occur in the case of large loadings by monitoring the density and specific heat capacity of molten salt nanocomposites with nanoparticle sizes and loadings in Fig. 1.

As the Fig. 2(a) shows, the enhancement on thermal conductivity decreases as the increase in the mass fraction of SiO₂ with 13 Å diameter, which is opposite to the specific heat capacity. This suggests that there is an optimal loading of SiO₂ nanoparticles for LiCl-KCl eutectics. Along with the threat of significantly increased viscosity, the 2 % w/w SiO₂ becomes the best choice. In Fig. 2(b), the larger size of nanoparticles cannot reduce viscosity, but the significant improvement in thermal conductivity enhancement is very valuable.

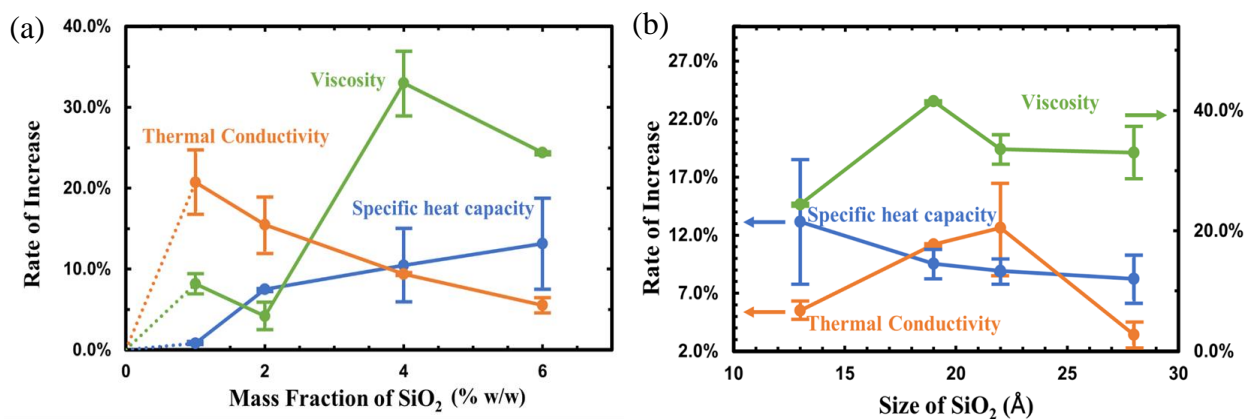


Figure 2. The rate of increase on specific heat capacity, thermal conductivity and viscosity as a function of (a) mass fraction and (b) diameter of the SiO₂ nanoparticle in the nanocomposites at 900 K by DPs.

3. MECHANISM ON ENHANCEMENT

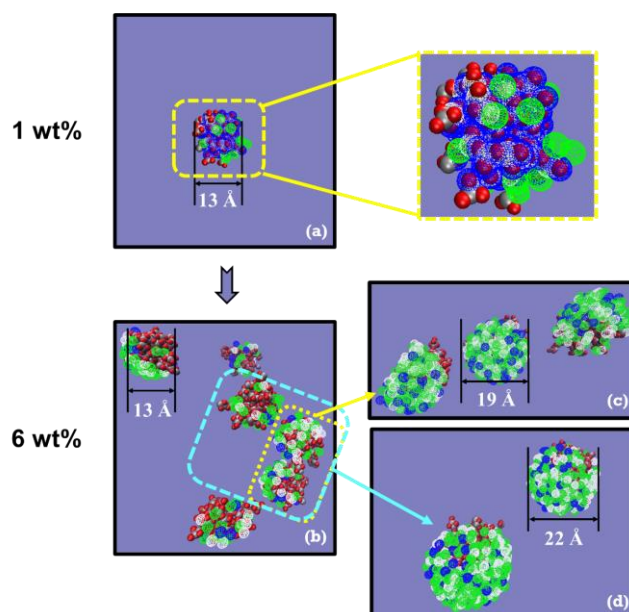


Figure 3. Snapshots of ionic distribution configurations around the surface of nanoparticles. For SiO₂ nanoparticles, the red refers to O and the gray refers to Si; for LiCl-KCl eutectic molten salts, the white cages refer to Li⁺, blue cages refer to K⁺, and green cages refer to Cl⁻.

The more small-size SiO₂ nanoparticles utilize larger specific surface area to increase the specific heat capacity of LiCl-KCl eutectics. The MD simulations reveal the more ionic permeation in nanoparticles (Fig. 3(a)) as enhanced heat storage, which indicates the increase of interaction between particles, especially for SiO₂-Cl⁻, is the microscopic mechanism on enhanced heat capacity of molten chlorides with SiO₂ nanoparticles even other nanofluids. Meanwhile, the clustering of these nanoparticles (Fig. 3(b)) is also discovered in analysis on simulated configurations, which limits the enhancement on heat and mass transfer (Fig. 2(a)). The reduction of additives is the effective measure, such as 2 % w/w SiO₂ of 13 Å diameter. However, the larger size of nanoparticles (19-22 Å diameter) can form the interfacial adsorption of molten salt ions especially for Li⁺ (Fig. 3(c)-(d)) to increase the thermal conductivity and prevent the following agglomeration. The remaining problems about high viscosity and dilemma between high heat transfer and heat storage can be solved by the comprehensive evaluation, which uses the accurate thermal properties over the wide temperature and component range in these simulations.

In the microscopic level, the diffusion of Li⁺ around or into the SiO₂ nanoparticles regulates the enhancement on Coulomb force field of solid surface, reflected by the change of charge density distribution on SiO₂ slab in contact with LiCl-KCl eutectics. In Fig. 4(a, c), increased number and strength of positive centers are marked by black dotted circles, while strengthening of negative centers and weakening of positive centers are pointed by blue arrows in the final configuration of simulations. And then the excess interaction of solid surface leads to the ordered interfacial microstructures of molten salt ions (Fig. 4(b, d)) near the solid-liquid interface. The former helps heat to be stored in the form of special bonds, and the latter can obtain a high-speed heat transfer path between nanoparticles and molten salts.

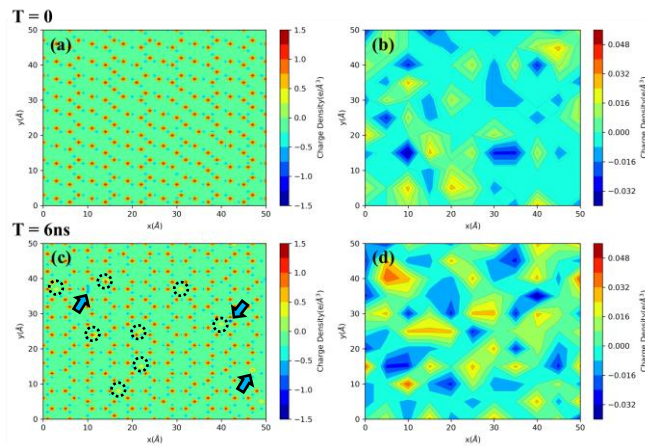


Figure 4. The charge density distribution of (a, c) SiO₂ slab/(b, d) LiCl-KCl eutectics solid-liquid interface.

4. CONCLUSIONS

As parameters, the specific heat capacity and the suspension density were monitored with molten salt temperature, particle sizes, and loadings. Adding 13-28 Å SiO₂ at 1-6% w/w increases the specific heat capacity of the molten eutectic. Nanoparticle agglomeration, if it occurs, would deteriorate the heat transfer and storage performance or even fail the molten salt device. Interfacial adsorption of molten salt ions onto the nanoparticles leads to a unique microstructure, effectively preventing particles' agglomeration and enhancing inter-particle heat transport rates. The specific surface area of nanoparticles is still the primary factor in determining the thermal performance; however, the surface area impact diminishes with nanoparticles of reducing sizes because of agglomeration. Detailed comparisons of the ion distributions around the nanoparticles reveal that the considerable interfacial adsorption of Li⁺ ions principally regulates the force field near the interface, leading to excess surface bonds, thereby increasing the heat capacity of the medium. The molecular configurations for the LiCl-KCl nanofluids are detailed and adopted for the first time to present practical ways to enhance their heat storage performance. The strategy to minimize particle agglomeration in the molten LiCl-KCl eutectic is discussed based on the conclusions obtained.

5. REFERENCES

- Wen, H. R., Lin, S. C., Zhao, C. Y. and Wang, E. L., 2022. "Nanoparticle surface charge-enhanced heat capacity in molten salt phase change materials for thermal energy storage". *Solar Energy Materials and Solar Cells*, Vol. 243, pp. 111795.
- Liang, F., Ding, J., Wei, X., Pan, G. and Liu, S., 2023. "Interfacial heat and mass transfer at silica/binary molten salt interface from deep potential molecular dynamics". *International Journal of Heat and Mass Transfer*, Vol. 217, pp. 124705.
- Wei, X., Yin, Y., Qin, B., Wang, W., Ding, J. and Lu, J., 2020. "Preparation and enhanced thermal conductivity of molten salt nanofluids with nearly unaltered viscosity". *Renewable Energy*, Vol. 145, pp. 2435-2444.

EXPERIMENTAL AND NUMERICAL INVESTIGATION OF THE MULTIPHASE FLOW CHARACTERISTICS OF THE IN-LINE TYPE SEPARATOR

**Sang Mok Han^a, Hae Jin Jo^a, Nam Sub Woo^a, Wang Do Lee^a,
Young Ju Kim^{a,*}**

^aKorea Institute of Geoscience and Mineral Resources

*kyjp7272@kigam.re.kr

Keywords: In-line Type Separator, Multiphase Flow, Internal Swirl Element(ISE)

1. INTRODUCTION

With abundant offshore oil and gas resources, and offshore oil production accounting for about 30% of the total as of 2019, the ocean is an important alternative region for future oil and gas resources. According to Mao *et al.* (2023), the current global daily production of crude oil is about 80 million barrels, and the daily production of produced water is about 250 million barrels. The ratio of crude oil to water is about 1:3, which means that the water content of produced water is more than 70%, and the water content of produced water in some oil fields is more than 90%. In addition, the degree of emulsification of oil droplets in the produced water is considerable, and many emulsified oil droplets smaller than 10 μm appear, which is difficult to process. The pretreatment of fluids produced on the seabed is a separator-based separation process to separate oil, water, and gas.

Various studies have been conducted on efficient multiphase flow separators and techniques for water-oil-gas separation on the seabed. Gravity separators have been used for a long time, but their long residence times of 30 minutes or more make them time-consuming to process and their large equipment size makes them unsuitable for offshore platforms. Production separators have been increasingly studied, from the classic gravity separators (Martinez and Ortiz (2014)) to more recent inline multiphase flow separators of various types (Zeng *et al.* (2020), Al-Kayiem *et al.* (2020)). Slot *et al.* (2011) numerically analyzed the separation of water and oil through an Internal Swirl Element (ISE). Ji *et al.* (2015) demonstrated the principle of vortex separator through numerical analysis and proved the low-pressure zone caused by the increase of tangential velocity at the tail of ISE through velocity distribution graph. Yang *et al.* (2019) conducted an experimental study based on a gas-liquid separator by installing two blade-type swirlers. In the case of Putra *et al.* (2019), the gas-liquid flow characteristics depending on the ISE shape were analyzed through numerical analysis-based studies, and CFD studies were performed based on three different ISE shapes: blade, single helix, and double helix.

In this study, the multiphase flow characteristics of an in-line type separator utilizing a ISE were studied through experiments and numerical analysis. The fluids used were gas and liquid (water) in different proportions, focusing on the separation of the two-phase flow after the mixture passes through the ISE. Numerical analysis and experiments were performed to verify the separation efficiency results when the flow rate and different volume fractions were varied.

2. EXPERIMENTAL CONDITIONS

In the case of the liquid-gas separator illustrated in Figure 1, a single separation section is constructed, including a 4-inch ISE (Inlet Separator Element) to prevent rotation, with an inner diameter equivalent to the diameter of the piping, including a 4-inch pipe. For the 3-inch pipe, a two-stage separation section is formed, including a 3-inch ISE, and the last section is a 2-inch pipe with bottom (liquid discharge) and top (gas discharge) exits.

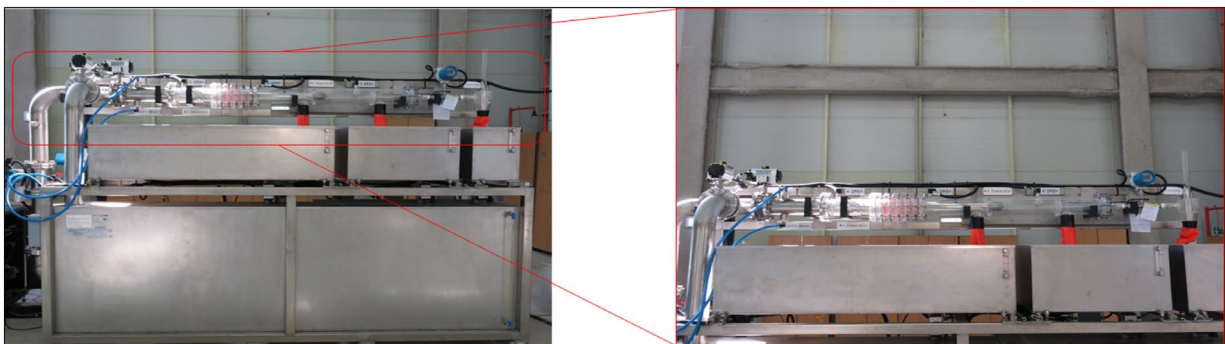


Figure 1. Liquid-Gas Separator in KIGAM.

The overall length of the fluid line is approximately 2.5m, designed with small diameter pipes connecting to facilitate the discharge of high-density fluid as it exits before entering the next section. The importance of density in separators with ISE is due to the relatively high-density fluid flowing along the inner wall of the pipe, and the low-density fluid forming a core and flowing centrally. In the case of a three-dimensional structure, a circular annulus structure is formed where the high-density fluid adheres to the wall and encases the low-density fluid. In the case of liquid-gas multiphase flow, the liquid forms along the inner wall of the pipe, and the gas forms the core as the flow progresses.

The piping of the separator and the exits where separation occurs are made of high-strength acrylic to allow direct observation by the experimenter. The ISE used in the experiment is made of stainless steel 304 to prevent wear and corrosion of vein wings, tails, etc. The separator is designed to handle a maximum flow rate of 16 L/s based on 20°C water in a 4-inch pipe, and the experimental equipment consists of a piston-type compressor, gas flow meter [resolution: 0.01 L/s], gas control valve, liquid flow meter [resolution: 0.01 L/s], pressure gauge, etc. A control panel [processing 15 data per second] is installed for control and measurement. The separated fluids accumulate under the acrylic pipe and are connected to a steel fluid storage tank, and the quantity of separated fluid is measured using a load cell [resolution: 0.01kg]. By comparing the actual input fluid (liquid basis) with the fluid quantity in the 1st, 2nd, and 3rd storage tanks, direct and quantitative verification of separation efficiency is possible.

3. NUMERICAL CONDITIONS

In this study, analysis was conducted using the commercial computational analysis program ANSYS CFX 19.2, known for its excellent performance in fluid mechanics analysis. Generally, in turbulence modeling based on Reynolds Averaged Navier-Stokes (RANS), the k-ε model and k-ω model are commonly used. The k-ω model is often applied in the vicinity of wall boundaries, while the k-ε model exhibits turbulence prediction strengths in free-flow regions. For numerical analysis in this study, the SST model, incorporating the advantages of both the k-ω and k-ε models, was employed for fluid analysis.

The analysis was conducted considering only the first separation section to account for computational time constraints. The fluid domain of the piping, including the 4-inch Inlet Separator Element (ISE) model, was established by modeling an ISE with the same diameter as the 4-inch inner diameter. The structural area was then excluded through Boolean operations to ensure the fluid domain. The grid for fluid analysis consisted of 1,433,322 nodes and 5,075,521 elements based on entrance, exit, and node criteria. Through orthogonal quality assessment, the grid quality was found to have an average value of approximately 0.799, roughly equivalent to 0.8, indicating that it falls within the Very Good category.

The analysis was performed using water and air as the working fluid at an ambient temperature of 25 °C. Boundary conditions were set with inlet conditions as flow rate and outlet conditions as average static pressure.

4. RESULTS AND DISCUSSIONS

In the experiment, a constant flow rate was applied by flowing a mixture of liquid (water) and gas (air) through a pipeline containing an ISE simultaneously. Liquid flow was measured by a liquid flow meter, and gas flow was measured by a gas flow meter. The total flow rate, determined by combining the flow rates of liquid and gas, was recorded. The quantity of liquid in each storage tank at the exit, where separated fluids were collected using load cells, was measured. The separation efficiency for each exit was quantitatively compared by processing the measured data. The separation efficiency was calculated by dividing the measured quantity of liquid at each exit by the total amount. Experiments were conducted by varying the mixed flow rate and the liquid-gas ratio. The liquid-gas ratio was altered to 7:3 and 8:2, while the mixed flow rate ranged from 4 to 16 L/s with a 1 L/s increment. To minimize experimental errors, five experiments were conducted for each case, and the average of the experimental results was obtained.

In numerical analysis, for comparison with the experiment, the water and air ratio at the inlet was numerically simulated with a ratio of 8:2 and 7:3. The inlet boundary conditions were set to match the range of a gas-liquid separator available at KIGAM, ranging from 4 to 16 L/s with an increment of 1 L/s. Figure 2 shows the volume fraction for water and gas. It can be observed that when the mixed fluid enters the ISE front, separation occurs in the ISE rear, forming a boundary layer. Gas is represented in red, while water is represented in blue, and numerical values close to 1 indicate gas, while values close to 0 indicate water. The volume fraction contour through numerical analysis visually demonstrates the separation of water and gas.

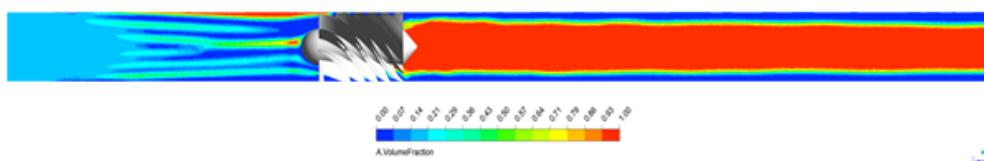


Figure 2. Results of numerical analysis of a separator with 4inch ISE: Volume fraction plot.

To compare the separation efficiency between the experimental and numerical analysis results, a comparison graph of separation efficiency based on flow rate and liquid-gas ratio is presented in Figure 3. In numerical analysis, only the first stage of the separator was simulated rather than the entire device, so the separation efficiency was compared only for the first stage separation. In the experiments, there is a general trend of increasing separation efficiency with flow rate up to a certain point, reaching a maximum level of around 85%, and then stabilizing. In contrast, numerical analysis yielded results with a maximum separation efficiency of 95%, and it was observed that the separation efficiency increases with higher liquid ratios and flow rates.

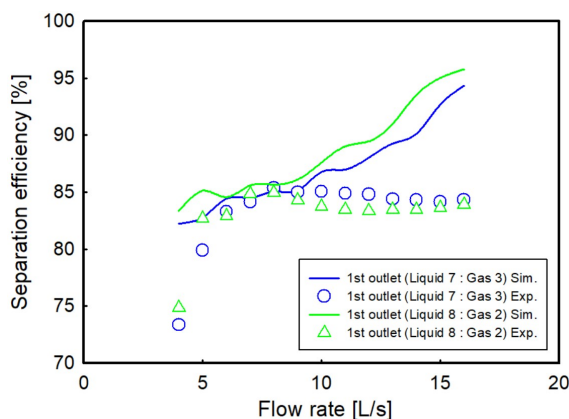


Figure 3. Comparison of separation efficiency by flow rate and liquid-gas volume ratio.

5. CONCLUSIONS

In this study, we conducted research on the multiphase flow characteristics and separation efficiency of an inline separator utilizing the Inlet Separator Element (ISE) through experimentation and numerical analysis. Taking into account the analysis time, we compared only the results of the first separation section instead of comparing the overall outcomes. When the flow rate increases at the same water-air ratio, an increase in separation efficiency can be observed, reaching a maximum at approximately 6~9 L/s. However, it should be noted that an increase in flow rate does not necessarily lead to a proportional increase in separation efficiency, and beyond a certain flow rate, a consistent separation efficiency is maintained. From a practical perspective, defining that increasing the flow rate is advantageous in real-scale applications is not solely based on a simplistic comparison of separation efficiency. This is because, at higher flow rates, processing larger volumes within the same time frame or significantly reducing the time required for separation is possible, especially when dealing with the same quantity of mixed fluids.

5. REFERENCES

- Mao, R., Li, Y., Liu, Y., Zhu, H., Wang, N., Yang, Q. and Lu, H., 2023. "Separation characters of an axial-flow hydrocyclone with oil collecting pipe". *Separation and Purification Technology*, Vol. 305, pp. 122139.
- Martinez, J.L.H. and Ortiz, V.M., 2014. "A method to size gas-liquid horizontal separators handling nonstable multiphase streams". *SPE Latin America and Caribbean Petroleum Engineering Conference*, Maracaibo, Venezuela
- Zeng, X., Zhao, L., Zhao, W., Hou, M., Zhu, F., Fan, G. and Yan, C., 2020. "Experimental study on a novel axial separator for oil-water separation". *Industrial & Engineering Chemistry Research*, Vol. 59, pp. 21177-21186.
- Al-Kayiem, H.H., Hamza, J.E. and Lemmu, T.A., 2020. "Performance enhancement of axial concurrent liquid-liquid hydrocyclone separator through optimization of the swirler vane angle". *Journal of Petroleum Exploration and Production Technology*, Vol. 10, pp. 2957-2967.
- Slot, J.J., Van Campen, L.J.A.M., Hoeijmakers, H.W.M. and Mudde, R.F., 2011. "Numerical analysis of a novel gas-liquid pre-separation cyclone". *8th International Conference on CFD in Oil & Gas, Metallurgical and Process Industries*, Trondheim, Norway.
- Ji, Y., Chen, J., Jiao, X., Cai, X. and Li, P., 2015. "Theoretical modeling and numerical simulation of axial-vortex separation technology used for oily water treatment". *Sep. Sci. Technol.*, Vol. 50, pp. 1870-1881.
- Yang, Y., Wang, D., Niu, P., Liu, M. and Zhang C., 2019. "Measurement of vertical gas-liquid two-phase flow by electromagnetic flowmeter and image processing based on the phase-isolation". *Experimental Thermal and Fluid Science*, Vol. 101, pp. 87-100.
- Putra, R.A., Neumann-Kipping, M., Schafer, T. and Lucas, D., 2019. "Comparison of gas-liquid flow characteristics in geometrically different swirl generating devices". *Energies*, Vol. 12, pp. 4653.

Contact behavior between soft wall and bubble formed near rigid wall sandwiched by soft walls

Jun Matsui^a, Yasuhiro Sugimoto^{b,*}

^aGraduate school of Kanazawa Institute of Technology, Ohgigaoka, Nonoichi, Ishikawa, Japan

^bKanazawa Institute of Technology, Ohgigaoka, Nonoichi, Ishikawa, Japan

*y-sugi@neptune.kanazawa-it.ac.jp

Keywords: Laser induced bubble, URS, Lithotripsy, Ho:YAG laser, Adjacent rigid and soft wall

1. INTRODUCTION

Urolithiasis is a disease in which stones form in the urinary tract from the kidneys to the urethra. Ureteroscopy (URS) is one of lithotripsy method and performed by inserting an endoscope through the urinary tract and irradiating a pulsed laser directly onto the stone. The laser used for URS is a Ho:YAG laser, which has a high absorption rate in water. The lithotripsy factor in URS is the heat generated by the laser and the impact of the collapse of the bubbles generated by the heat of the laser. These factors can act on the surrounding biological tissues and lead to complications such as ureteral perforation or ureteral rupture.

Various approaches have been used to present safe treatment conditions for URS. One of the authors (Sugimoto and Hamamoto, 2019) showed bubble behavior near a rigid wall in a narrow space with a cylinder made of soft material. Sugimoto *et al.* (2018) show bubble behavior in a confined space between walls of two different materials. From these, several approaches have been made using both soft and rigid walls. On the other hand, no work has been done on bubble behavior in situations where a rigid wall and a soft wall are adjacent to each other and treated as a wall with two different properties. One of the factors that can cause complications is the heat of the laser and the impact action of the collapse of the bubble on the surrounding biological tissue. Therefore, it is important that bubbles do not touch the surrounding biological tissue, and it is necessary to study bubble behavior and bubble contact in the vicinity of the surrounding biological tissue. In a previous study, Sugimoto *et al.* (2020) showed the contact time that causes thermal damages in the contact of bubbles at a wall surface. They showed that thermal damage might occur at a contact time of 0.65 ms or longer between the bubble and the wall surface in one event when the pulsed laser irradiated continuously at 40 Hz for 10 seconds. Therefore, it is important to understand the contact time between the bubble and the surrounding tissue for safe stone treatment.

In this study, we used a plane wall that simulates the surrounding biological tissue as a soft wall and a stone as a rigid wall, and observed the behavior of laser-induced bubbles by changing the laser irradiation conditions and the width of the rigid wall. In addition, the contact time between the bubbles and the soft wall is measured.

2. EXPERIMENTAL APPARATUS AND PROCEDURE

In this experiment, a pulsed laser therapy device (Lumenis, VersaPulse Select 80:100) used in medical practice was used (Sugimoto *et al.*, 2018). The laser is a Ho:YAG laser with a wavelength of 2100 nm, irradiated through a 200 μm diameter optical fiber to the test section. Tap water is used as the sample water, and water temperature T_w and dissolved oxygen content β are measured before and after the experiment. A high-speed video camera (Photron, FASTCAM SA5, 100,000 fps) is used to capture images. A hydrophone is connected to the high-speed video camera to capture bubbles triggered by the sound pressure at the time of bubble collapse. The fiber is installed parallel to the flat wall. Figure 1 shows the details of the test section. The test section was simulated with a rigid wall made of acrylic resin for the stone and a soft wall made of gelatin (modulus of elasticity 55 ± 5 kPa) for the surrounding biological tissue. In this experiment, the laser irradiation position (x and y), rigid wall width W (2, 3, and 5 mm), and laser energy E (0.2, 0.5, and 1.0 J) were changed. The laser irradiation position was set at the origin at the boundary between the rigid wall and the soft wall, with the x -axis parallel to the wall surface and the y -axis perpendicular to the wall surface. The laser irradiation positions in the x and y axes are set to $x = -2.5, -1.5, -1.0, 0, 2.0$ mm, and $y = 1, 2, 3, 4, 5$ mm.

3. BUBBLE BEHAVIOR

Figure 2 shows the bubble behavior under different laser irradiation positions along the y -axis for $W = 3$ mm, $E = 1.0$ J, and $x = 0$ mm. $t = 0$ ms is the time just before the bubble formation is confirmed. After the bubble formation is confirmed, the bubble behaves as follows: expansion, maximum expansion, contraction, first collapse, rebound, and second collapse.

At $y = 5$ mm, the bubble collapses away from the wall, so no contact with the soft wall is observed. At $y = 3$ mm, the bubbles behave in such a way that they approach the rigid wall during contraction, and no contact between the bubbles and the soft wall is observed until the first collapse, while contact with the soft wall is observed during rebound. At $y = 1$ mm, contact with the soft wall is observed from the time of expansion and continues until the second collapse.

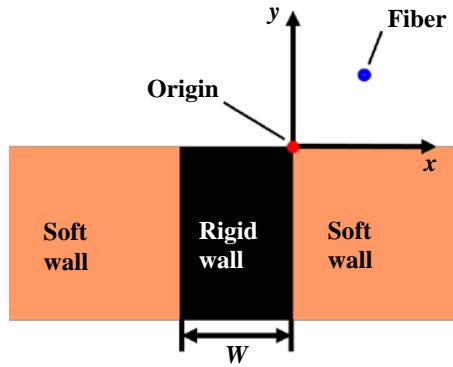
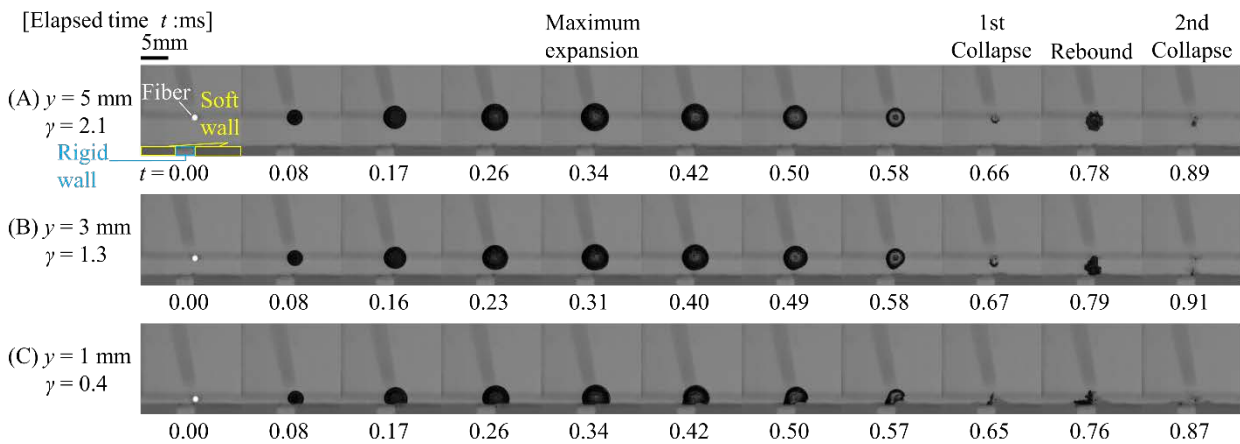


Figure 1. Schematics of test section.



$$T_w = 291-292 \text{ K}, \quad \beta = 6.7-6.9 \text{ mg/L}$$

Figure 2. Bubble behavior ($x = 0$ mm, $W = 3$ mm, $E = 1.0$ J).

4. CONTACT TIME BETWEEN BUBBLE AND SOFT WALL

Figure 3 shows the contact time CT between the bubble and the soft wall during bubble formation on the boundary between the rigid and soft walls. γ in the figure is the dimensionless value of the distance L from the bubble formation point to the soft-wall surface with the maximum bubble radius R_{\max} (see schematic in the figure). A, B, and C in the figure show the contact time measured at $y = 5, 3,$ and 1 mm in Figure 2, respectively, and the dashed line α in the figure shows the contact time at which burns occur, 0.65 ms (Sugimoto et al. 2020). In Figure 3, the contact time increases with decreasing γ . In the range where γ is very small, the contact time is greater than the contact time at which damages occur.

5. CONCLUSIONS

To ensure safe treatment in URS, we observed the contact behavior between pulsed laser-induced bubbles and nearby soft walls and measured the contact time between bubbles and soft walls.

(1) Contact between a bubble and a flat wall was observed when the distance γ from the laser irradiation position to the wall surface was less than about 1.3.

(2) The contact time between the bubble and the soft wall increased with decreasing γ , indicating that the bubble reached a condition where it caused thermal damages to the tissue if it was formed very close to the soft wall.

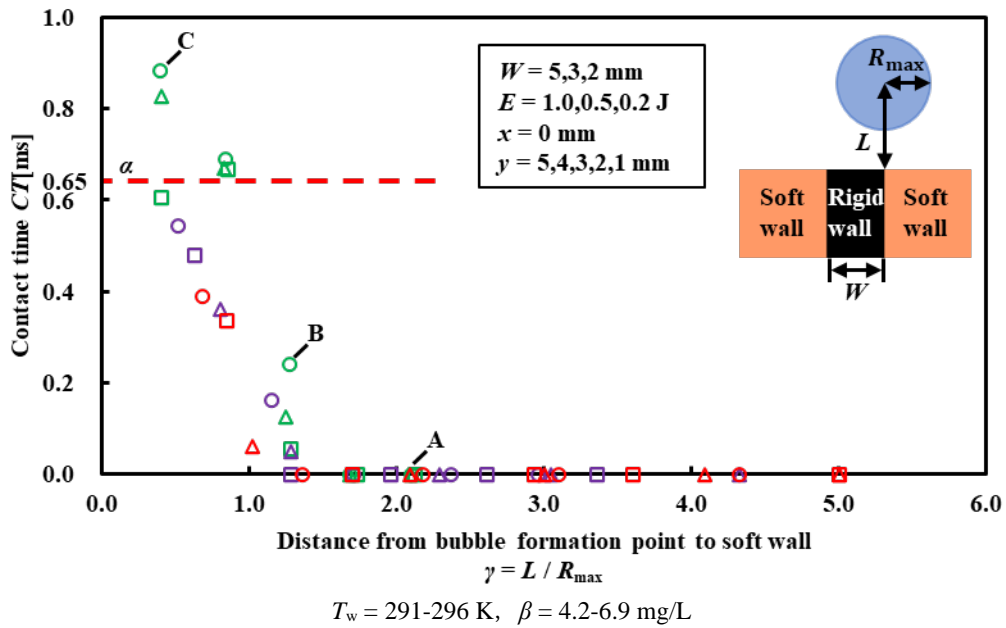


Figure 3. Contact time between bubble and soft wall.

6. REFERENCES

- Sugimoto, Y., Nagata, D. and Sato, K., 2018. "Behavior of bubble induced by fiber-type laser for TUL near soft wall with deformability", In *Proceedings of 10th International Symposium on Cavitation*, pp. 135-139.
- Sugimoto, Y. and Hamamoto, M., 2020. "Measurements of laser induced bubble behavior in elastic tube and temperature around bubble in TUL treatment", *Journal of Flow Control, Measurement & Visualization*, Vol. 8(3), (2020), pp. 134-145.
- Sugimoto, Y., Araga, I. and Fukue, T., 2023. "Evaluation of thermal damage area of tissue around pulsed laser-induced bubbles in URS treatment based on CEM43°C", *Journal of Biomechanical Science and Engineering*, In press.

EXPERIMENTAL INVESTIGATION ON THE EVAPORATION CHARACTERISTICS OF A SINGLE AND A BINARY COMPONENT DROPLET IN HOT AIR STREAM

Rajab Omar^{a,*}, **Conrado Zanutto**, **Stephen Ambrose**, **David Hann**, **Carol Eastwick**

^aMechanical and Aerospace Systems Research Group, Faculty of Engineering, University of Nottingham, UK

*Rajab.Omar@nottingham.ac.uk

Keywords: Droplet evaporation, Forced convection, Heat transfer

1. INTRODUCTION

Studying the evaporation of droplets within a forced convection environment is important for various engineering applications. Despite the existing research on droplet evaporation, there are still numerous aspects of droplet evaporation processes that lack a comprehensive understanding. Understanding droplet evaporation characteristics is crucial for predicting and optimising the performance of internal combustion engines, including gas turbines. Therefore, investigating liquid droplet evaporation in a forced convection environment can provide valuable insights into various engine-related processes. This ranges from understating the evaporation process of fuel droplets inside combustors to gaining a better understanding of oil droplet behaviour within bearing chambers.

Many droplet evaporation experiments have been conducted over the years with the main intent to understand the mechanism of spray combustion. Wang et al. (2022) reviewed the progress in experimental studies on the evaporation of a fuel droplet. Multiple methods were considered to investigate drop evaporation with the suspension method being the most common approach. Several aspects of droplet evaporation were investigated including the effect of turbulence intensity (Xu et al., 2004), the impact of forced convection (Strizhak et al., 2018), and nanoparticle concentration (Li et al., 2022) on the evaporation characteristics of single and multicomponent droplets.

Droplet motion in bearing chambers has been always modelled as a rigid sphere without the consideration of the evaporation and deformation of large droplets due to windage (Zhu et al., 2023). However, this assumption is indefensible for the actual conditions of aeroengine bearing chambers where the surface tension of the droplets is low and a strong windage effect is inevitable mainly on large droplets ($>700 \mu\text{m}$). Numerical and mathematical modelling of single droplet evaporation can provide the effect of multiple parameters such as temperature, concentration, and relative velocity on the evaporation rate of single and multicomponent droplets. Thus, experimental investigations are required to validate and improve the accuracy of those models under real conditions.

The modelling of droplet heating and evaporation has been efficiently performed by using both analytical solutions and numerical modelling. The isothermal evaporation of mono-component droplets has been widely predicted by the well-known D2 law, introduced by Spalding, which suggests that the change in the normalised square diameter of a droplet is linearly proportional to the evaporation time. For multi-component droplets, the evaporation process is not only governed by the difference in volatility of the components but also by the liquid and gas phase mass diffusion and other factors. Sazhin et al. (2010) developed a simplified model for the heating and evaporation of binary component droplets which considers multiple factors including temperature distribution, diffusion in the liquid phase, and the effect of recirculation.

Although several simplified models have been developed to predict the evaporation of single and binary component droplets, there is a lack of experimental data to compare and test those models. Therefore, the objective of this work is to investigate the effect of air velocity on the evaporation of single and multicomponent droplets to generate high-accuracy data that can be utilised to validate numerical evaporation models.

2. Methodology and instrumentation

The experimental setup used in this work consists of a flow conditioning section, a heating element, a droplet holder, and a high-speed imaging arrangement. The air temperature was controlled using piccoloTM P116 controller. A schematic of the experimental apparatus is shown in Fig.1. The air mass flow and temperature were measured using a mass flow meter and a $50 \mu\text{m}$ diameter K-type thermocouple located in the vicinity of the droplet. The air velocity at the center of the air jet was measured using an L-type pitot tube with an integrated K-type thermocouple and a differential pressure sensor. During the experiment, the regulated air flow passes through an inline heater which is controlled to achieve the required air temperature. Then the air travels through the settling chamber that includes a honeycomb flow straightener, and two flow conditioning meshes before it leaves through a 20 mm ID nozzle. The airflow path is fully insulated using thermal insulation sheets. The droplet holder is located 10mm downstream of the air jet nozzle. It is made of a $75 \mu\text{m}$ diameter Chromega-Alomega K-type thermocouple wire that is fitted over a swivel metal arm to form forms U-shape holder. A second metal wire was horizontally positioned beneath the main droplet holder to provide additional support at high air velocities. The motion of the droplet holder is controlled so that it always attains the same testing position where

the droplet is in the center of the air jet. The Droplet was generated using a 2 μl pipette with small tips. The experiments were conducted using Acetone and Ethanol in pure form and binary mixtures of 25, 50, and 75 wt.%. Acetone and Ethanol were selected due to the tangible difference in their volatility. The experiments were conducted at 40 $^{\circ}\text{C}$ temperature and different air jet velocities.

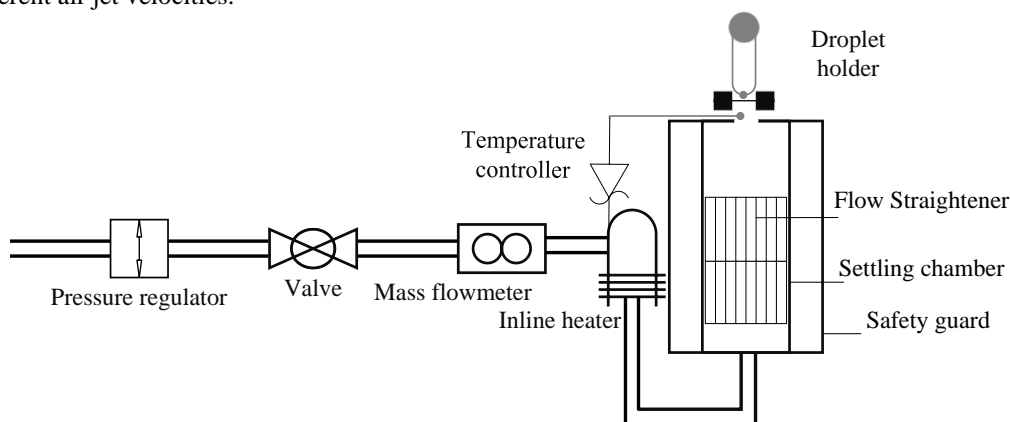


Figure 1: A schematic of the experimental setup

DATA PROCESSING

For air velocity measurement the Temperature and pressure drop data were recorded for 120 seconds at an acquisition rate of 10Hz and 100 Hz respectively. The steady-state data was then averaged over the testing period and used to estimate the air velocity using equation (1).

$$V = C_F \sqrt{\frac{2\Delta P}{\rho}} \quad (1)$$

Where $C_F = 1.0015$ is the Coefficient of the pitot tube, ΔP is the dynamic pressure, and ρ is the air density at a given temperature. The evaporation process was captured using an IDT high-speed camera at an acquisition rate of 20 frames per second. The images were analysed using an in-house MATLAB code to estimate the change in the frontal area of the droplet over time.

ANALYTICAL SOLUTION

The Effective Conductivity and Effective Diffusivity models (ECM and EDM) are analytical solutions to the transient heat conduction and transient species diffusion equations based on the assumptions that the heat and mass diffusion processes within the droplet are spherically symmetric and the convective heat and mass transfer coefficients are constant over the same time step. The ECM and EDM solutions that will be used in this work also consider: the effect of the Stefan flow on the interfacial heat and mass transfer, non-unitary Lewis number and thermophysical properties as functions of temperature and chemical composition.

3. RESULTS AND DISCUSSION

The experimental results have been processed for three air velocities while the experimental campaign is still in progress. A wider range of testing conditions will be presented in the full draft of the paper.

The droplet diameter slightly varied for different tests where the average droplet diameter was 1.6 mm. It was found that the evaporation curves for similar test conditions collapse on the same line when normalised by the initial droplet diameter. It should be noted that the contrast part of the frontal area or normalised droplet diameter curves at the end of the evaporation process corresponds to the area of thermocouple wires.

The evaporation tests of Ethanol droplets at 40 $^{\circ}\text{C}$ and different air velocities indicated that the evaporation process goes through three stages as shown in Figure 2. Non-isothermal evaporation where the droplet temperature increases in the first two seconds and then quasi-steady evaporation during which the droplets evaporate almost at a constant temperature (~ 10 C) for up to 20 seconds. The final stage is more transient heating of the droplet as the frontal area approaches zero (i.e., complete evaporation). In contrast for the mixture that contains 75 wt.% of Acetone, there was a continuous increase of the temperature during the entire lifetime of the droplet. The sharp increase in temperature at the late stage of evaporation indicates complete evaporation.

The effect of air velocity is obvious on the evaporation of Ethanol droplets as illustrated in Figure 2. The droplet lifetime decreases from 48 seconds to 35 seconds with the increase of air velocity from 3.2 to 6 m/s. The effect of air velocity is less significant for the mixture of 75 wt.% Acetone as shown in Figure 3. The droplet lifetime is constant at air velocities of 4.8 and 6 m/s. It seems that the effect of force convection diminishes beyond a certain threshold of air velocity. The normalised droplet diameter curves in Figure 2 can be represented with a straight line for the most part of the evaporation except the transient stage of evaporation. Whereas for the binary mixture of 75 wt.% Acetone, the D2 curve (In Figure 3) does not represent a straight line. Although the evaporation process does not follow the trend expected

from a fraction distillation of binary mixture, the evaporation curve indicates two stages with different evaporation rates. Each stage has a reasonably constant evaporation rate where the D^2 law can be perhaps applied.

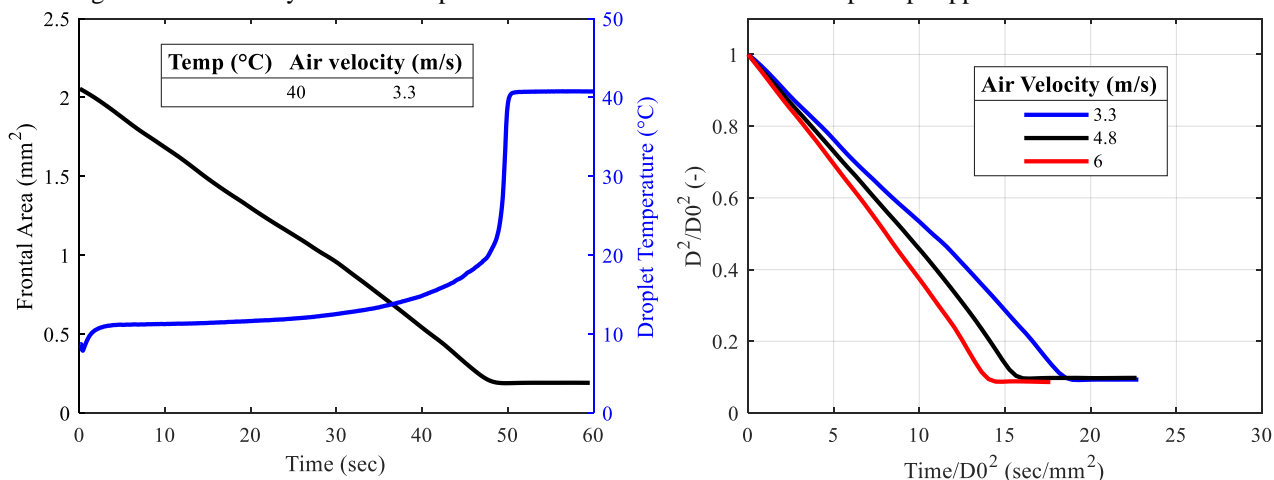


Figure 2: The frontal area curve and droplet temperature of Ethanol at 40 °C and different air velocities.

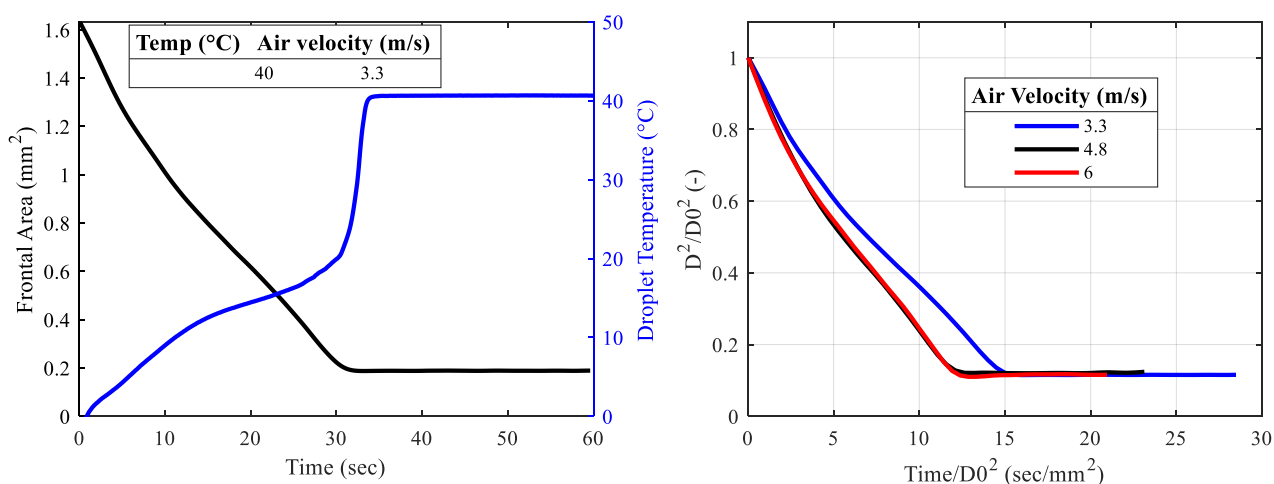


Figure 3: The frontal area curves and droplet temperature of 75 wt.% Acetone mixture at 40 °C and different velocities.

4. CONCLUSIONS

An experimental campaign is being conducted to investigate the effect of air velocity on the evaporation of single and multicomponent droplets. The initial results indicate that the evaporation rate increases with the increase of air velocity for pure Ethanol droplets. Whereas the effect of air velocity seems intangible for a mixture of 75 wt.% Acetone beyond a certain threshold (>4.8 m/s). Further data will be analysed to reach a conclusion.

5. REFERENCES

- LI, S., Yang, Q., YE, L., DU, H., Zhang, Z., Huang, X. & XU, J. 2022. Effect of Nanoparticle Concentration on Physical and Heat-Transfer Properties and Evaporation Characteristics of Graphite/n-Decane Nanofluid Fuels. *ACS Omega*, 7, 3284-3292.
- Sazhin, S. S., Elwardany, A., Krutitskii, P. A., Castanet, G., Lemoine, F., Sazhin, E. M. & Heikal, M. R. 2010. A simplified model for bi-component droplet heating and evaporation. *International Journal of Heat and Mass Transfer*, 53, 4495-4505.
- Strizhak, P. A., Volkov, R. S., Castanet, G., Lemoine, F., Rybdylova, O. & Sazhin, S. S. 2018. Heating and evaporation of suspended water droplets: Experimental studies and modelling. *International Journal of Heat and Mass Transfer*, 127, 92-106.
- Wang, Z., Yuan, B., Huang, Y., CAO, J., Wang, Y. & Cheng, X. 2022. Progress in experimental investigations on evaporation characteristics of a fuel droplet. *Fuel Processing Technology*, 231, 107243.
- XU, G., Ikegami, M., Honma, S., Ikeda, K., Dietrich, D. L. & Struk, P. M. 2004. Interactive influences of convective flow and initial droplet diameter on isolated droplet burning rate. *International Journal of Heat and Mass Transfer*, 47, 2029-2035.
- Zhu, D., Chen, G., Wang, L. & Zhang, R. 2023. Effects of droplet deformation, evaporation, and mutual interaction with air on droplet motion and droplet-film impingement in aeroengine bearing chambers. *Applied Thermal Engineering*, 224, 120008.

DETERMINATION OF THE SUPERCRITICAL HEAT TRANSFER OF THE LOW GWP REFRIGERANT R1234ZE(E)

Jera Van Nieuwenhuys^{a,*}, Steven Lecompte^{a,b}, Michel De Paep^{a,b}

^aGhent University, Department of Electromechanical, Systems and Metal Engineering, Ghent, Belgium

^bFlanders Make – Core lab MIRO, Leuven, Belgium, FlandersMake@ugent.be

*jera.vannieuwenhuys@ugent.be

Keywords: supercritical, heat transfer, convection, experimental, refrigerant

1. INTRODUCTION

In order to design the heat exchangers of supercritical cycles such as the transcritical organic Rankine cycles or supercritical heat pumps, reliable supercritical heat transfer correlations are required. Under these conditions, constant property correlations like the Dittus-Boelter correlation (Dittus and Boelter, 1985) cannot be applied with confidence. This is because in the near-supercritical region, a fluid exhibits large property variations transitioning from a liquid-like to a vapor-like fluid when heated (or vice versa when cooled) (Yoo, 2013). These property variations can induce complicated secondary flow phenomena, including buoyancy, of which the influence on the heat transfer is dependent on the applied operating conditions (including mass flux, heat flux and pressure) (Pioro *et al.* (2004), Zahlan (2015)). For horizontal flows, the heat transfer is further complicated as buoyancy acts perpendicular to the flow direction, resulting in non-uniformity in heat transfer in the radial direction of the flow.

In literature, correlations exist which have been developed for supercritical horizontal flow of certain refrigerants. However, when applied to another refrigerant, they lack accuracy. In addition, most of the investigated refrigerants have a relatively high Global Warming Potential (GWP), making them less interesting for future applications. Therefore, a larger refrigerant heat transfer database is required. This database should contain supercritical heat transfer data on multiple refrigerants (with a low GWP) and for a wide range of operating conditions (Van Nieuwenhuys *et al.*, 2022).

In this work, an experimental investigation has been carried out, where supercritical heat transfer measurements are performed on the low GWP refrigerant R1234ze(E) flowing in a horizontal cylindrical tube with an inner diameter of 22.9 mm. First, the experimental test rig is discussed in more detail. Second, the data reduction and validation of the test rig is highlighted. Finally, the influence of several operating conditions is discussed based on the results of local heat transfer coefficient measurements performed for varying mass fluxes, heat fluxes and pressures.

2. SUPERCRITICAL HEAT TRANSFER TEST RIG

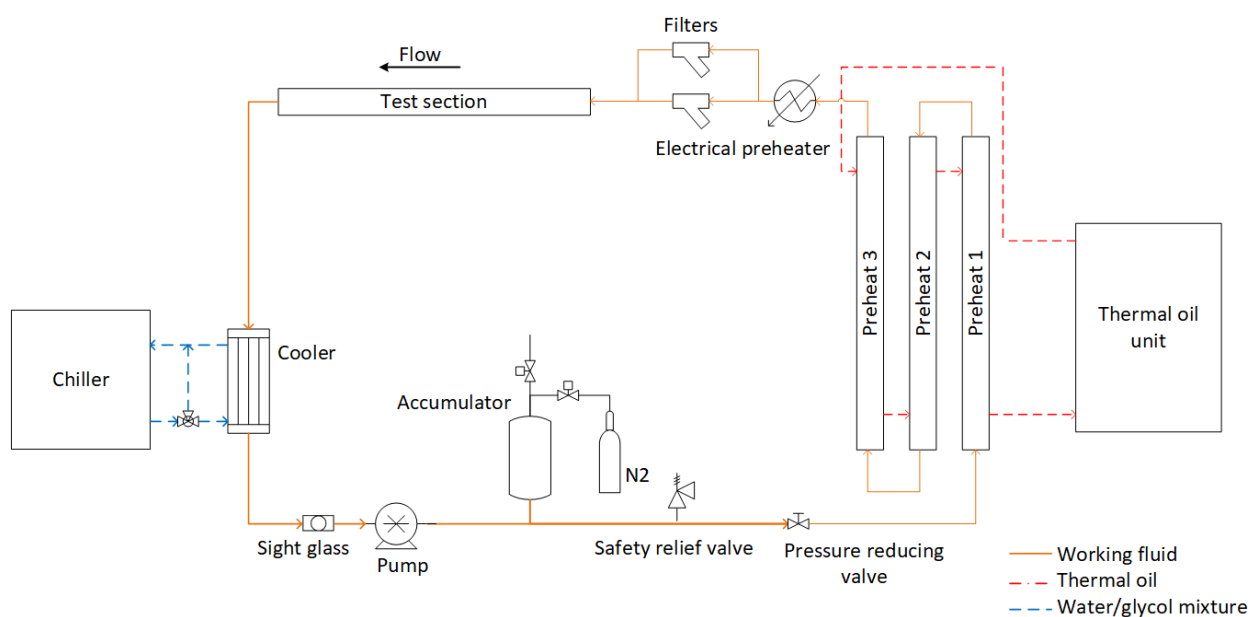


Figure 1: Hydraulic schematic of supercritical experimental test rig.

In Fig. 1, a simplified hydraulic schematic of the test rig is given. In the test section, the heat transfer measurements are performed. All the other components and sections are used to condition the refrigerant to the required test conditions. A 3/4" tube is selected for the test section, which has an inner diameter d_i of 22.9 mm. The length of the test section is 4 m and is heated by Joule heating of the stainless steel tube. This means a voltage is put over the test section, and due to the resistance of the stainless steel tube itself a current (and correspondingly power) is generated inside the tube wall. The voltage delivered by a DC source (with a capacity of 30 kW) is put over the test section through copper clamps. The remainder of the test rig is protected (both thermally and electrically) by a high temperature resistant cathodic protection between the connecting flanges. To achieve both thermally and hydraulically developed turbulent flow at the inlet of the test section, an unheated adiabatic calming section of 1 meter ($> 40 d_i$) precedes the test section.

K-type thermocouples are installed both in the bulk of the test section tube and on the outer wall every 20 cm to measure refrigerant bulk and wall temperatures (at the top, side and bottom of the tube). An absolute pressure sensor is installed up- and downstream of the test section to monitor the pressure (drop) during measurements. The mass flow rate of refrigerant is measured by a Coriolis type mass flow meter. Based on a voltage and current measurement, the power delivered to the test section can be calculated.

All thermocouples of the test section and the voltage over the test section are read out by a Keithley 2700. The current in the test section is monitored by the DC source itself (EA-PSI 10080-1000 4U). The other sensors are read out by a NI cRIO 9074 with several modules for the different type of signals. This instrument is also used to steer certain components such as the refrigerant pump, electrical preheater and three-way valve in the cooling circuit. A control program is written in the LabVIEW software to monitor all variables, steer the test rig, and perform the data collection.

Pressure, temperature, mass flow rate and heating power are measured in order to determine the local convection coefficients (htc) and Nusselt numbers (Nu) of the refrigerant. These are calculated as follows:

$$htc = \frac{\dot{q}}{T_{w,i} - T_b} \quad (1)$$

$$Nu = \frac{htc \cdot d_i}{k} \quad (2)$$

In the equations above, k is the thermal conductivity of the refrigerant evaluated at the bulk temperature (T_b) (calculated with REFPROP v10.0 (Lemmon *et al.*, 2018)), \dot{q} is the heat flux to the refrigerant and $T_{w,i}$ is the temperature at the inside of the test tube. Because the latter cannot be measured directly, it is calculated based on the temperature measurement at the outside of the wall ($T_{w,o}$). The correlation between these two temperatures can be derived based on a one dimensional heat conduction problem:

$$\frac{1}{r} \frac{d}{dr} \left(k_{ss}(T) \cdot r \frac{dT}{dr} \right) + \dot{q}_v = 0 \quad (3)$$

Here, \dot{q}_v is the volumetric heating rate (equal to the supplied power divided by the volume of the heated stainless steel tube), r is the tube's radius and k_{ss} is the thermal conductivity of the stainless steel tube, which is a function of the tube wall temperature.

The absolute uncertainty on the local heat transfer coefficient is a function of the uncertainty on the heat flux measurement and on the thermocouple measurements. In Table 1, an overview of the measurement equipment and their corresponding uncertainties is given. The error on the voltage measurement consists of two parts. The first part (expressed in percentage) is dependent on the reading, the second part (expressed in V) is dependent on the total measurement range and thus fixed for every reading. As measurements are performed in the supercritical region, the uncertainties reported by REFPROP v10.0 (Lemmon *et al.*, 2018) are higher compared to the uncertainties in the liquid or gas phase. However, no exact uncertainty value in the critical region is reported. Therefore, the uncertainty on the thermal conductivity k used in Eq. 2 is taken as 10%. In the subcritical liquid region, the uncertainty on k is equal to 1%.

Table 1. Measurement equipment and their corresponding uncertainties.

Sensor type	Uncertainty
K-type thermocouple	± 0.1 K
Coriolis flow meter	± 0.1 %
Pressure sensor	± 6 kPa
Current sensor (built-in)	± 1 A
Voltage sensor (Keithley)	$\pm (0.0045\% + 0.0007 \text{ V})$

3. RESULTS AND DISCUSSION

The refrigerant under consideration in the current work is the low GWP refrigerant R1234ze(E), which has a critical temperature of 109.4°C and a critical pressure of 36.3 bar. The experimental test rig is validated by performing measurements under subcritical liquid phase conditions. The heat transfer coefficients are measured for several conditions (varying heat flux and mass flux) and compared to the commonly used Dittus-Boelter correlation (Nu_{DB} , see Eq. 5), with a correction added to take into account the property variation (i.e. in dynamic viscosity μ) of the refrigerant between the wall (w) and the bulk (b) of the flow. Re expresses the Reynolds number of the flow, Pr is the Prandtl number of the fluid. The properties of R1234ze(E) are evaluated at an average bulk temperature and wall temperature. The former is determined as the average of the refrigerant temperature at the in- and outlet of the test section. Similarly, an average wall temperature at the top, side and bottom of the tube wall is calculated based on the measurements at the first and last wall thermocouple position. An uncertainty of 10% on the calculation of the Nusselt number via the correlation is assumed. When the measurements fall within the uncertainty limits of the prediction using the Dittus-Boelter correlation, the test rig performs as desired.

$$Nu_{DB} = 0.023Re^{0.8}Pr^{0.4}\left(\frac{\mu_b}{\mu_w}\right)^{0.11} \quad (5)$$

The energy balance over the test section is calculated as well in order to validate the test rig and estimate the losses.

The supercritical heat transfer of R1234ze(E) was measured for varying operating conditions. The mass flux ranged from 100 to 1000 kg/m²s, heat flux from 10 to 70 kW/m² and average test section pressures from 5 to 20% above the critical pressure.

Note to reviewers: the experimental campaign will be finished in the coming weeks. By the time the final manuscript is due, this section of the paper will be completed. The validation experiments will be included, and results will be presented, discussing the influence of mass flux, heat flux and pressure on the supercritical heat transfer of R1234ze(E).

4. CONCLUSIONS

An experimental test rig was built to measure the supercritical heat transfer to low GWP refrigerants flowing in a large diameter horizontal tube. This data is key in the development of a generally applicable supercritical heat transfer correlation used to design the heat exchangers in supercritical systems such as the transcritical organic Rankine cycle and supercritical heat pumps. In this work, the supercritical test rig itself is discussed, as well as the data and uncertainty analysis. The validation of the test rig consists of calculating the energy balance over the test section and performing heat transfer measurements under subcritical liquid conditions and comparing these results to the predictions from the Dittus-Boelter correlation. The supercritical heat transfer measurements were performed for varying mass fluxes, heat fluxes and pressures, and the influence of these parameters on the heat transfer is discussed. Future work entails performing similar experiments on other low GWP refrigerants in order to create a large refrigerant heat transfer database for correlation development purposes.

5. REFERENCES

- Dittus, F.W. and Boelter, L.K.M., 1985, "Heat transfer in automobile radiators of the tubular type". *International communications in heat and mass transfer*, Vol. 12 (1), pp. 3-22.
- Lemmon, E.W., Bell, I.H., Huber, M.L. and McLinden, M.O., 2018, *NIST Standard Reference Database 23: Reference Fluid Thermodynamic and Transport Properties-REFPROP, Version 10.0*, National Institute of Standards and Technology, Standard Reference Data Program, Gaithersburg.
- Pirola, I.L., Khartabil, H.F. and Duffey, R.B., 2004, "Heat transfer to supercritical fluids flowing in channels – empirical correlations (survey)". *Nuclear Engineering and Design*, Vol. 230 (1-3), pp. 69-91.
- Van Nieuwenhuyse, J., Lecompte S. and De Paepe, M., 2022, "Current status of the thermohydraulic behavior of supercritical refrigerants: A review". *Applied Thermal Engineering*, Vol. 218, 119201.
- Yoo, J.Y., 2013. "The turbulent flows of supercritical fluids with heat transfer". *Annual Review of Fluid Mechanics*, Vol. 45, pp. 495-525.
- Zahlan, H.A.M., 2015. *Derivation of a look-up table for trans-critical heat transfer in water-cooled tubes*. Ph.D. thesis, Université d'Ottawa/University of Ottawa, Canada.

Cooling Design Improvement of Trailing Edge by Adding the Impingement Plate

Shanjie Liu^a, Tao Guo^{a,*}, Cunliang Liu^a, Hui ren Zhu^a, Guodong Li^a, Xinyu Wang^a, Jiayu Li^a, Changwei Li^a

^aSchool of Power and Energy, Northwestern Polytechnical University, Xi'an 710072, China

*guotao@nwpu.edu.cn

Keywords: Turbine blade, Trailing edge, Impingement, Transient liquid crystal

ABSTRACT

Reducing the coolant consumption at the blade trailing edge and improving cooling performance are the keys to extending the blade service life and improving the aero-engine efficiency. The traditional cooling design of the trailing edge is placed with the pin-fin, which can strengthen the airflow disturbance and ensure the strength of the turbine blade. This investigation proposes an improved cooling design by adding an impingement plate before the pin-fin structure. The transient liquid crystal experiment measures the Nusselt number (Nu) of the two types of cooling design. Then, The flow state is obtained through numerical simulations using the 3-D steady-state Reynolds Averaged Navier-Stokes (RANS) model. The cooling characteristics of the traditional and improved cooling structures are compared. The main conclusions are as follows: compared with the traditional cooling design, arranging the impingement plate gives the airflow at the inner of the channel a higher and more uniform velocity. Hence, the coolant can cover the entire channel surface. The impingement jet scours the pin-fin surface and creates a high heat transfer area around the pin fins, significantly improving the cooling performance of the heat transfer area and making the Nu distribution more uniform. Under the engine working condition, the surface-averaged Nu of the improved cooling design increased by 86.5% compared with the pin-fin structure. The impingement structure brings better heat transfer but shows more flow resistance. The pressure coefficient (C_p) in the region near the pin-fin increases significantly and decreases gradually along the radial direction of the blade.

MATHEMATICAL DESCRIPTION OF THE TEMPERATURE-EFFECTIVE HEAT CAPACITY RELATIONSHIP OBTAINED BY DIFFERENTIAL SCANNING CALORIMETRY FOR PHASE CHANGE MODELLING

Martin Zálešák^{a,*}, Pavel Charvát^a, Lubomír Klimeš^a, Jakub Kúdela^b

^aBrno University of Technology, Energy Institute, Technická 2869/2, Brno, 616 69, Czech Republic

^bBrno University of Technology, Institute of Automation and Computer Science, Technická 2869/2, Brno, 616 69, Czech Republic

*Martin.Zalesak1@vut.cz

Keywords: phase change material, effective heat capacity, inverse heat transfer problem

1. INTRODUCTION

An accurate representation of the temperature-enthalpy or the temperature-effective heat capacity relationships is essential for the modelling of phase changes. This is even more the case when the phase transition is non-isothermal and happens in a temperature range, which is typical for organic phase change materials (PCMs). Over recent years, diverse parametrization approaches have surfaced, ranging from basic rectangular or triangular step functions to more sophisticated models incorporating elements such as Gaussian functions with varying degrees of symmetry (Jin *et al.*, 2014). Experimental results, obtained with differential scanning calorimetry (DSC) or the temperature-history method, point towards the phase change behaviour, which is very difficult to capture with Gaussian curves alone (see Figure 1), as the results exhibit various spikes or multiple peaks (Zálešák *et al.*, 2021).

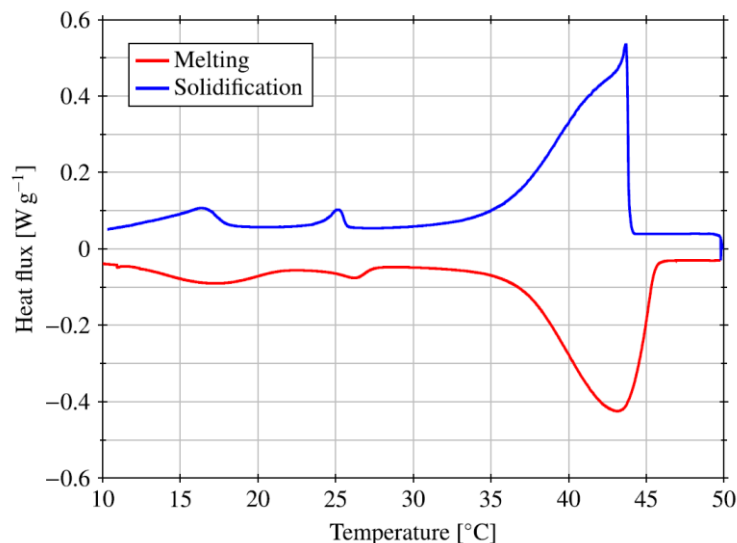


Figure 1. Processed DSC results for RT42 (the heat flow–temperature dependency), adopted from (Zálešák *et al.*, 2021).

2. METHODS

One of the approaches to the modelling of phase transitions is the effective heat capacity method (Zalba *et al.*, 2003). This approach incorporates latent heat into the specific heat capacity of the material. The effective heat capacity is denoted as c_{eff} . The most straightforward way to prescribe the effective heat capacity is to linearly distribute latent heat over the temperature interval between the start and end of the phase change process as

$$c_{\text{eff}}(T) = \begin{cases} c_s, & T < T_1 \\ \frac{L_f}{T_2 - T_1}, & T_1 \leq T \leq T_2 \\ c_l, & T > T_2 \end{cases} \quad (1)$$

where T_1 is the temperature at the beginning of melting or end of solidification, T_2 is the temperature at which the PCM completes the melting process or starts the solidification, L_f is the enthalpy of fusion, c_s and c_l is the specific heat capacity

of the solid and liquid state, respectively. It was previously shown by Kúdela *et al.* (2024), that separating c_s and c_ℓ could lead to a significant improvement in modelling accuracy.

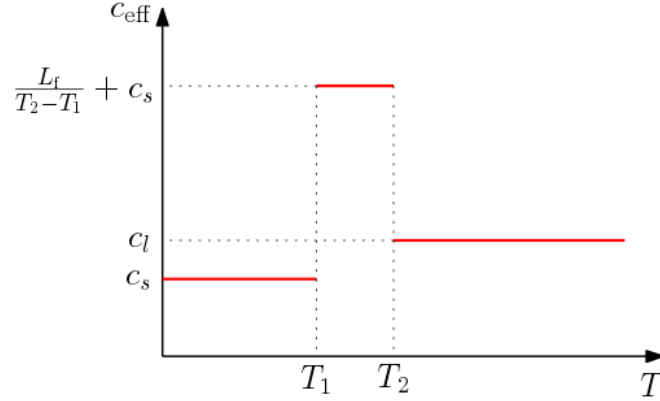


Figure 2. Parametrisation of the effective heat capacity curve with a rectangular step function.

This approach is usually unsuitable for paraffin-based PCMs, which exhibit significantly non-isothermal phase transitions (Mauder *et al.*, 2017). In such cases, phase change takes place over a specific temperature interval, therefore, the parameterisation based on Gaussian function is much more suitable approach. In this respect, an analogy with a two-piece normal distribution could be utilised with the formulation adapted from (Villani and Larsson, 2005) and (Wallis, 2014) as

$$c_{\text{eff}}(T) = \begin{cases} c_s + (c_\ell - c_s)\xi(T) + A \exp\left\{\frac{-(T-T_{\text{peak}})^2}{2\sigma_s^2}\right\}, & \text{for } T < T_{\text{peak}} \\ c_s + (c_\ell - c_s)\xi(T) + A \exp\left\{\frac{-(T-T_{\text{peak}})^2}{2\sigma_\ell^2}\right\}, & \text{for } T > T_{\text{peak}} \end{cases} \quad (2)$$

where $A = L_f \sqrt{\frac{2}{\pi}} (\sigma_s + \sigma_\ell)^{-1}$ is a scaling factor, L_f is the enthalpy of fusion, $\xi(T)$ represents the liquid fraction of PCM (defines the distribution of the enthalpy of fusion), T is the temperature, T_{peak} denoted a peak phase change temperature, and σ_s and σ_ℓ is a skewness parameter for the solid and liquid state, respectively.

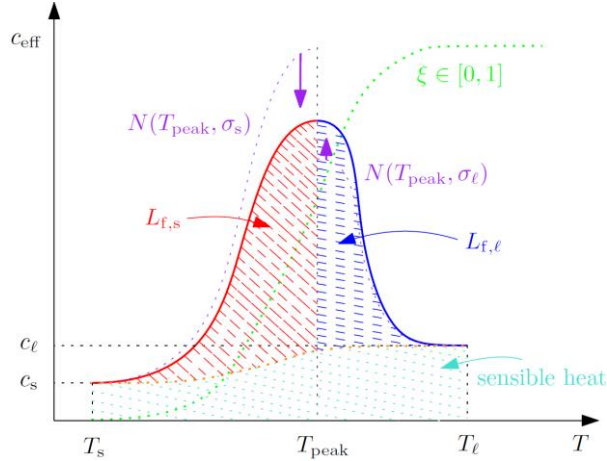


Figure 3. Parametrisation of the effective heat capacity curve with an asymmetrical Gaussian function.

The effective heat capacity function is therefore formed as the left half of the probability distribution function (PDF) of the normal distribution with parameters $\mu = T_{\text{peak}}$, $\sigma = \sigma_s$, and the right half of the PDF of the normal distribution with parameters $\mu = T_{\text{peak}}$, $\sigma = \sigma_\ell$, scaling both of them down to their common value $c_{\text{eff}}(\mu) = A$ in the modus μ . The complete curve for the effective heat capacity as a function of the temperature can be seen in Figure 3. The left and right PDF are scaled by factors $\frac{2\sigma_s}{\sigma_s + \sigma_\ell}$ and $\frac{2\sigma_\ell}{\sigma_s + \sigma_\ell}$, respectively, separating the amount of latent heat as

$$\begin{aligned} L_f &= L_{f,s} + L_{f,\ell} = \int_{T_s}^{T_{\text{peak}}} (c_{\text{eff}}(T) - (c_s + (c_\ell - c_s)\xi(T)))dT + \int_{T_{\text{peak}}}^{T_\ell} (c_{\text{eff}}(T) - (c_s + (c_\ell - c_s)\xi(T)))dT = \\ &= \frac{2\sigma_s}{\sigma_s + \sigma_\ell} L_{f,s} + \frac{2\sigma_\ell}{\sigma_s + \sigma_\ell} L_{f,\ell}, \end{aligned} \quad (3)$$

where $L_{f,s}$ and $L_{f,\ell}$ is the latent heat of the “solid” and “liquid” part of Gaussian function, respectively. Temperatures T_s and T_ℓ are reference temperatures in the solid and liquid phases, which are outside of the phase change temperature range.

Table 1. Effective heat capacity function descriptions

Parametrisation	Parameters
Rectangular step function	c, T_1, T_2, L_f
Symmetrical Gaussian function	$c, T_{\text{peak}}, L_f, \sigma$
Asymmetrical Gaussian function	$c_s, c_\ell, T_{\text{peak}}, L_f, \sigma_s, \sigma_\ell$

3. RESULTS AND DISCUSSION

The experimental techniques, such as DSC or the temperature-history method, indicate a rather intricate thermal behaviour of organic PCMs. While the rectangular step function is quite simple in its definition and easy to implement, it falls short in accurately representing the thermal behaviour of organic PCMs. To precisely describe the distribution of enthalpy of fusion, a minimum of four parameters is necessary for this parametrization, equivalent to a symmetrical Gaussian function as shown in Table 1. Consequently, the rectangular step function fails to achieve parameter reduction and is surpassed by the symmetrical Gaussian function.

To enhance the accuracy of the parametrization model, introducing asymmetry into the effective heat capacity curve is proposed. The asymmetry can arise from either different specific heat capacities in the solid and liquid states (c_s and c_ℓ) or variations in the shapes of the Gaussian function "bell" using the TPND-based approach. In this scenario, the modeling complexity increases, requiring a total of six parameters to describe the thermal behavior. Nevertheless, this modification leads to a significant improvement in fit accuracy.

In the situations involving phase change hysteresis (PCH), a separate temperature-effective heat capacity relationships needs two be used for the melting and solidification processes (two-curve approach). The number of required parameters doubles since both melting and solidification curves are modelled separately. Frequently, when seeking the ideal material or as part of the inverse heat transfer problem (IHTP), resolving an optimization problem becomes necessary. In such cases, selecting a more straightforward symmetrical model could lead to a reduction in parameters, although this comes at the cost of accuracy, aiming to minimize computational expenses.

4. CONCLUSIONS

Modelling of phase change processes is quite often a daunting task, requiring the selection of an appropriate parameterization model for the temperature-enthalpy relationship. While the asymmetrical Gaussian functions provide a rather precise representation of the temperature-effective heat capacity relationships derived from the DSC results, none of the currently used parametrization approaches effectively address sharp peaks and multiple peaks found in the effective heat capacity curves derived from the DSC results, as illustrated in Figure 1. As a further step to achieving better fit between the mathematical description and the DSC results, the parameterisation based on the spline interpolation will be investigated.

5. REFERENCES

- Jin, Xi., Xu, X., Zhang, X., Yin, Y., 2014. “Determination of the PCM melting temperature range using DSC”. *Thermochimica Acta*, Vol. 595, pp. 17–21.
- Kúdela, J., Zálešák, M., Charvát, P., Klimeš, L., Mauder, T., 2024. “Assessment of the performance of metaheuristic methods used for the inverse identification of effective heat capacity of phase change materials”. *Expert Systems With Applications*, Vol. 238, 122373.
- Mauder, T., Charvat, P., Stetina, J., Klimes, L., 2017. “Assessment of Basic Approaches to Numerical Modeling of Phase Change Problems—Accuracy, Efficiency, and Parallel Decomposition”. *Journal of Heat Transfer*, Vol. 139, 084502.
- Villani, M., Larsson, R., 2005. “The Multivariate Split Normal Distribution and Asymmetric Principal Components Analysis”. *Communication in Statistics- Theory and Methods*, Vol. 35, pp. 1123–1140.
- Wallis, K.F., 2014. “The Two-Piece Normal, Binormal, or Double Gaussian Distribution: Its Origin and Rediscoveries”. *Statistical Science*, Vol. 29, pp. 106–112.
- Zalba, B., Marín, J.M., Cabeza L.F., Mehling, H., 2003. “Review on thermal energy storage with phase change: materials, heat transfer analysis and applications”. *Applied Thermal Engineering*, Vol. 23, pp. 251–283.
- Zálešák, M., Charvát, P. and Klimeš, L., 2021. “Identification of the effective heat capacity–temperature relationship and the phase change hysteresis in PCMs by means of an inverse heat transfer problem solved with metaheuristic methods”. *Applied Thermal Engineering*, Vol. 197, 117392.

EXPERIMENTAL STUDY OF GAS ENTITIES IN UPWARD “LAMINAR” TWO-PHASE FLOW IN A MINICHANNEL

Salim Zeguai^{a,*}, Salah Chikh^b, Lounès Tadrist^c

^a Yahia Farès University, Faculty of Technology, LMP2M Laboratory, Ain d'heb, Médéa 26000, Algeria

^b USTHB, Faculty of Mechanical and Process Engineering, LTPMP, Alger 16111, Algeria

^c Aix-Marseille Université, CNRS, Laboratoire IUSTI, UMR 7343, Marseille 13453, France

Zeguai_salim@hotmail.com ; salahchikh@yahoo.fr ; lounes.tadrist@univ-amu.fr

Keywords: Two-phase mini-fluidics, visualization and imaging, flow pattern, gas-liquid entities.

1. INTRODUCTION

The state of the art revealed that the first experimental investigation carried out on gas-liquid two-phase flows in a small diameter channel in a vertical position was developed by Sugawara et al., 1967. Since then, a number of studies have been carried out on two-phase flows in capillary tubes in vertical upward orientation. The authors consider adiabatic gas-liquid two-phase flow in small-diameter circular tubes for different phase mixing configurations and operating conditions. Among these works, we can cite those of Kariyasaki et al., 1992, Fukano et al., 1993, Mishima and Hibiki, 1996, Wölk et al., 2000, Zeguai et al., 2020. In all these references the authors have studied the effects of the superficial gas and liquid velocities on the flow patterns. The authors identified bubbly, slug and annular patterns. However, the flow maps and the fineness of the description of the patterns differ from one author to another. The state of the art has also revealed that the flow structures have been extensively studied and that until now no experimental study has been established on the size of the gas and liquid entities and their evolution as a function of velocities of phases.

The aim of this work is to determine the sizes of two-phase entities from the bubbly to the annular regime. The two-phase flow regime considered is “laminar”. The so called regime corresponds to superficial Reynolds number ($Re_{LS} = \rho_L U_{LS} D / \mu_L$, $Re_{GS} = \rho_G U_{GS} D / \mu_G$) ranging from 2.3 to 230 for the liquid phase and from 0.2 to 710 for the gas phase yielding smooth interfaces. The evolution of the size of the gas entity with the variation of the gas velocity along the tube is discussed and a conclusion can be drawn from the phenomena of rupture or coalescence along the tube. Two-phase flow patterns sizes are constructed using two measurement methods: the image processing method (IPM) and the frequency method associated with imaging (FMM). Transitions from one flow pattern to another are determined for the downstream region away from the inlet zone at $L/D=420$. A comparison of the results obtained by the two methods makes it possible to consolidate and validate the measurements carried out and used later in the rest of this work.

2. EXPERIMENTAL DEVICE AND MEASUREMENT TECHNIQUES

The experimental device is composed, mainly, of a duct where the two-phase flow is carried out and of a tranquilization chamber and creation of the two-phase mixture. We recall that the main characteristics of the experimental device which has been the subject of a detailed description might be found in the reference Zeguai et al., (2013). The sizes of the entities formed from the gas phase at the level of the injection nozzle are measured at downstream of the entry zone of the two-phase flow at two positions of the pipe from the nozzle $L/D=10$ and 420. In this communication we focus on the results obtained at a distance $L/D=420$, because in this zone the two-phase flow patterns are supposed to be fully developed.

To ensure the validity and accuracy of the measurements, two measurement methods were implemented: the image processing method (IPM) and the frequency measurement method associated with imaging (FMM). The IPM method makes it possible to measure the geometric characteristics of gas entity moving in the liquid, equivalent diameter is deduced from the measurement of the volume of the gaseous entity. However, the principle of the FMM method consists in the inspection of video image sequences recorded frame by frame where the passage frequency of gas entities is determined by counting the number of bubbly or slug produced at $L/D=420$ during a fixed time window.

3. EXPERIMENTAL RESULTS

3.1. GAZ ENTITY FREQUENCY

The bubble frequency is measured on a sample of 830 images. At $L/D=420$, at low superficial gas velocity the frequency is 142 Hz. With a gradual increase in the superficial gas velocity up to $U_{GS} = 0.066 \text{ ms}^{-1}$ the frequency decreases rapidly in a linear manner down to a value of 18 Hz. The gas entities (bubbly, slug) increase in size which results in a decrease in frequency. Starting from this situation, the frequency continues to decrease towards low values with the increase in the gas velocity and the bubbly/slug two-phase pattern transits towards the slug pattern and slug/annular, successively.

An increase and a decrease in the law of variation of the frequency of the slug entity with the increase in the superficial gas velocity is observed up to a superficial gas velocity $U_{GS} = 0.37 \text{ ms}^{-1}$ (see figure 1). This increase and decrease in the frequency is probably due to the phenomena of rupture and coalescence of the slug entities which occur in the pipe in the explored zone or in the concealed area that precedes the explored area. These two phenomena are translated into the curve (see figure 1) by decreasing and increasing in the comportment of the equivalent diameter parameter of the gas slug.-Beyond this superficial gas velocity, the frequency of the slug/annular entity decreases and tends towards zero with the increase in gas velocity. In this regime, the gas entity evolves towards the annular pattern. This pattern is characterized by the presence of two continuous phases. The gaseous phase in the core zone of the tube and the liquid phase located in the annular zone between the wall and the gas.

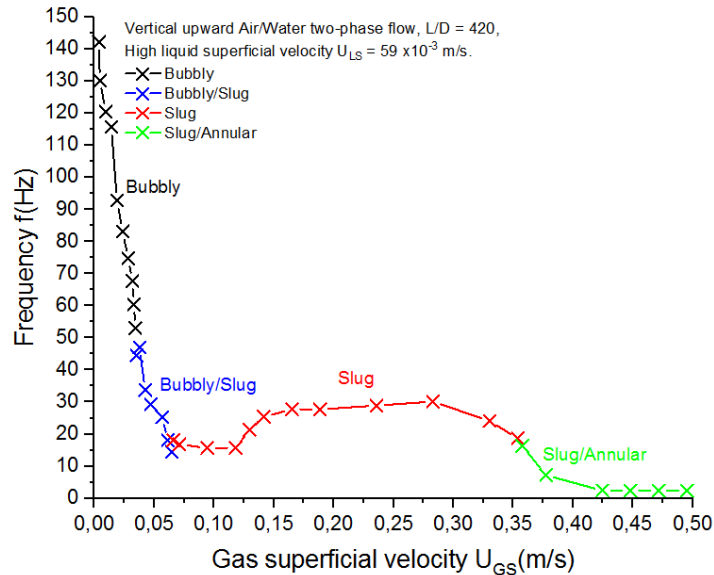


Figure 1: Gas entity frequency as a function of the superficial gas velocity for Air/Water vertical upward flow at $L/D=420$, at room temperature $T= 23^\circ\text{C}$ and atmospheric pressure $P = 1 \text{ Atm}$.

3.2 SIZE OF GAS ENTITIES

At a given apparent liquid velocity $U_{LS} = 59 \times 10^{-3} \text{ ms}^{-1}$, the equivalent diameters of the gas entities, at $L/D=420$, vary as a function of the superficial gas velocity (Figure 2). The results obtained by the two methods IPM and FMM exhibit similar behaviors with very small deviations. The gas entities vary in an increasing way with different laws depending on whether it is in the bubbly regime, slug, bubbly/slug and slug/annular transition zones (figure 2). For the case of the two-phase flow studied, from a low value of the superficial gas velocity $U_{GS} = 0.0038 \text{ ms}^{-1}$, the laws of the bubbly and bubbly/slug patterns increase linearly with increasing superficial gas velocity up to a value of $U_{GS} = 0.057 \text{ ms}^{-1}$. In the bubbly flow pattern, small bubbles of approximately similar size of $D_{Eq-B} = 1 \text{ mm}$ in diameter tend to concentrate along the axis of the test tube (Figure 2.a). By increasing the superficial gas velocity to $U_{GS} = 0.032 \text{ ms}^{-1}$, the large bubbles of $D_{Eq-B} = 1.68 \text{ mm}$ in diameter form a train of bubbles in helical motion are observed (Figure 2.b), whereas for larger superficial gas velocities $U_{GS} = 0.033 \text{ ms}^{-1}$, small bubbles of distinct sizes disperse over the entire section of the tube stuck behind a slug of gas of equivalent diameter less than the diameter of the pipe of $D_{Eq-B/S} = 1.64 \text{ mm}$ of equivalent diameter thus forming a dispersed bubbly/slug flow transition pattern (Figure 2.c), in this situation the presence of bubbles is greater than that of the slug, which will generate a predominance of bubbles over the slug. By further increasing the superficial gas velocity to $U_{GS} = 0.057 \text{ ms}^{-1}$, the spacing becomes narrower between the bubbles which leads to an increase in the coalescence rate. Then, the number of gas slug begins to take over the number of bubbles and we obtain the bubble/slug transition pattern with bubbles and larger gas slug of equivalent diameter $D_{Eq-B/S} = 2.81 \text{ mm}$. At the end of the bubbly/slug transition zone at $U_{GS} = 0.061 \text{ ms}^{-1}$, the number of slug becoming dominant with respect to the bubbly with an equivalent diameter greater than the diameter of the pipe $D_{Eq-B/S} = 3.26 \text{ mm}$ (Figure 2.d and e). By further gradually increasing the superficial gas velocity by small increments, the secondary bubbly/slug transition pattern transits towards the main slug pattern with an equivalent diameter of the gas slug equal to $D_{Eq-S} = 4 \text{ mm}$ (Figure 2.f).

Beyond this gas velocity $U_{GS} = 0.075 \text{ ms}^{-1}$, the laws of variations in the size of the slug and slug/annular increases “exponentially”. For this pattern, the equivalent diameter of the entity is greater than the diameter of the cross section of the pipe. The bubble confined in the radial direction, then elongates in the axial direction. The slug pattern is in the form of a cylinder surmounted by two ellipsoidal caps. The liquid plugs separate the gas slug, satellite bubbles in agitated oscillations in the liquid plugs may be also observed. A liquid film is inserted between the wall and the gas slug, while the slug/annular transition pattern is characterized by the successive appearance of an elongated slug and an annular

pattern. There is either a formation of slugs which can associate by coalescence or a successive formation of slug followed by an annular pattern. The frequency of formation of these entities is calculated according to the number of gas entities crossing a fixed time window. In order to evaluate the equivalent diameter of the gaseous entity, the formula $D_{G/IPM} = (6V_{G/IPM}/\pi)^{1/3}$ is used.

From a gas velocity $U_{GS} = 0.35 \text{ ms}^{-1}$ (see Fig. 2), the equivalent diameter of the slug/annular pattern estimated by the FMM method is greater than that calculated by the IPM method. This difference is perhaps due to the uncertainties committed during the geometric imaging processing and/or following the coalescence effects produced in the $L/D=420$ zone or in the vicinity of this zone, which will generate an increase in the equivalent diameter of the slug pattern.

In the slug/annular transition zone, the FMM method is not applicable due to the absence of the alternating principle between gas entities and liquid plugs. It is approximate because it underestimates the size of the entity. Under these condition, by increasing the superficial gas velocity the diameter of the gas entity tends at infinity (see Fig.2).

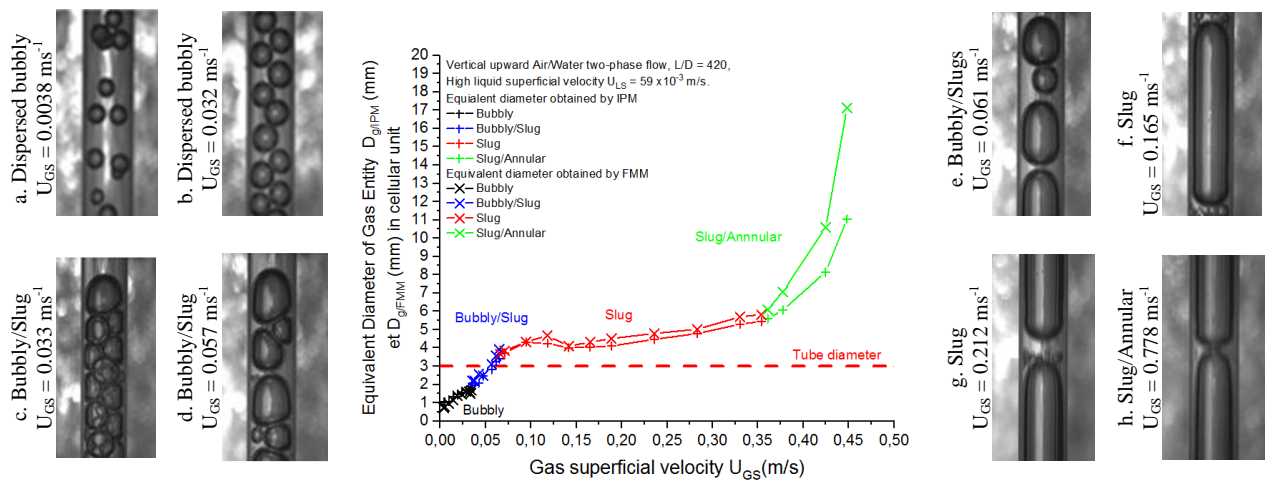


Figure 2: Equivalent diameter of the gas entity vs apparent gas velocity obtained by IPM and FMM in the case of an ascending vertical Air/Water flow at $L/D=420$.

4. CONCLUSION

An experimental investigation is carried out to analyze the size of the gas-liquid pattern in a “laminar” two-phase flow in an upward vertical orientation in a pipe with a diameter close to the capillary length of liquid water in air. The experiments were carried out in a zone very far from the entrance zone ($L/D=420$) where the two-phase flow is supposed to be “established”. The laws of variation of the equivalent diameter of the gas entities were determined by the two methods IPM and FMM which present a very good agreement. The variation laws obtained differ depending on whether the regime is bubbly or slug. The transition zones present particular variation laws, no doubt linked to confinement effects. These first investigations and results obtained open new perspectives in the characterization and understanding of two-phase flows where current simulation tools can contribute to this understanding and provide information that is difficult to access through experience.

5. REFERENCES

- Fukano, T., Kariyasaki, A., 1993. Characteristics of gas-liquid two-phase flow in a capillary tube. Nucl. Eng. Des. 141, 59–68.
- Kariyasaki, A., Fukano, T., Ousaka, A., Kagawa, M., 1992. Isothermal air-water two-phase up and downward flows in a vertical capillary tube (1st report, Flow pattern and void fraction). Trans. JSME (Ser. B) 58, 2684–2690, in Japanese.
- Mishima, K., Hibiki, T., 1996. Some characteristics of air-water two-phase flow in small diameter vertical tubes. Int. J. of Multiphase Flow, Vol 22, No. 4, 703–712.
- Sugawara, S., Katsuta, K., Ishihara, I., Muto, T., 1967. Consideration on the pressure loss of two-phase flow in small-diameter tubes. In Proc. 4th National Heat Transfer Symp. of Japan, 169–172, in Japanese.
- Wölk, G., Dreyer, M., Rath, H.J., 2000. Flow patterns in small diameter vertical non-circular Channels. Int. J. of Multiphase Flow, 26, 1037–1061.
- Zeguai, S., Chikh S., Tadrist L., 2013. Experimental study of two-phase flow pattern evolution in a horizontal circular tube of small diameter in laminar flow conditions. Int. J. of Multiphase Flow, 55, 99–110.
- Zeguai, S., Chikh S., Tadrist L., 2020. Experimental Study of Air-Water Two-Phase Flow Pattern Evolution in a Mini tube: Influence of Tube Orientation with Respect to Gravity. Int. J. of Multiphase Flow, 132, 103413.

EXPERIMENTAL INVESTIGATIONS OF THE MICROSTRUCTURE OF A 316L POROUS MATERIAL FOR A FLAT LHP EVAPORATOR WICK

Paweł Szymański ^a, Piotr Radomski ^a, Tadeusz Miruszewski ^b, Krystian Gehrke ^a, Grzegorz Gajowiec ^a,
Jae-Ho Jeon ^a, Dariusz Mikielewicz ^{a*}

^aFaculty of Mechanical Engineering and Ship Technology, Gdansk University of Technology, Narutowicza 11/12, 80-233 Gdańsk, Poland

^bFaculty of Applied Physics and Mathematics, Gdansk University of Technology, Narutowicza 11/12, 80-233 Gdańsk, Poland

*dariusz.mikielewicz@pg.edu.pl

Keywords: loop heat pipe; capillary pressure; porosity; permeability;

1. INTRODUCTION

Passive two-phase thermal management device based on loop heat pipe (LHP) can offer a very promising cooling solution for remote thermal management of highly loaded devices such as electronic devices or others due to its high reliability and long-distance heat transfer ability. This paper discusses the effect of porous wick microstructure properties on heat transfer performance of a flat-type LHP (F-LHP). The porous wick is made of stainless steel 316L, developed as a disc with a diameter of 60 mm and thickness of 11,2 mm to fit the F- LHP evaporator. In the experimental investigation, wick structure with multiple physical properties including pore radius distribute, total and effective porosity, and permeability with different structural topology including chemical composition were measured and tested in order to precisely determine the capillary performance necessary for heat and mass transport. The current work analyses the importance of the wick properties in the enhancement of the thermal characteristics for F-LHP.

LHPs are high-performance and high-reliable passive capillary two-phase heat transport devices that allow the transport of heat over long distances by the evaporation and condensation of a working fluid that flows around the loop. Its advantages of flexibility and robustness in design and assembly have made the LHP an excellent thermal management device. LHPs utilize latent heat of vaporization of working fluid inside a loop to transport heat from a source to a sink, and to achieve this they take advantage of surface tension generated in a porous structure (a.k.a. ‘wick’) to create the capillary forces needed for the circulation of the fluid [1]. Traditional LHP consists of five main components: evaporator, vapour and liquid line, condenser, and compensation chamber. Only the evaporator incorporates a complex porous wick structure, while the rest of the device is made of smooth wall elements. A schematic of the LHP is presented in Fig. 1. The wick is to provide necessary capillary force to the working fluid for continuous circulation in the loop and enabling LHP to provide a permeable media that enables the flow direction of the liquid to the evaporation area at the same time while preventing a backflow of vapour. The pressure drop across the wick is characterised by the wick's structural parameters such as open porosity, permeability, mean pore radius and working fluid properties. An important benefit of LHP evaporator is that the meniscus inside the wick adjusts automatically due to heat load by reducing its radius of curvature to match the effective pore radius of the wick, creating the highest possible capillary pressure to counter possible to overcome the total pressure drop in the system. This maximum pressure is determined by the Young-Laplace equation:

$$\Delta P_{cap,max} = \frac{2\sigma\cos\theta}{r_p} \quad (1)$$

where r_p is the wick meniscus curvature radius, σ is the liquid surface tension and θ is the liquid-solid contact angle.

The other important parameter that determines a wick's performance is the pressure drop it can create. Such pressure drop is characterized by the liquid viscosity and wick permeability and can be approximated by Darcy's equation:

$$\Delta P_{wick} = \frac{l\mu_l}{\rho_l A_l \kappa_l} \dot{m}_l \quad (1)$$

where $\frac{A_l}{l}$ is the average area for the flow divided by the length of the flow path, μ_l is the liquid dynamic viscosity, κ_l is the liquid permeability and \dot{m}_l is the liquid mass flow rate across the porous wick. The Carman-Kozeny equation provides a simple model that relates permeability to the average pore diameter such that:

$$\kappa_l = \frac{r_p^2 \varepsilon^3}{37.5(1-\varepsilon)^2} \quad (2)$$

where ε is the porosity of the wick.

Another key feature for evaluating the wick structure is to analyse the chemical composition of the wick material to assess its purity and chemical content. This analysis is very important as some materials and working fluids might be not chemically compatible with others and this analysis should be performed at the early stage of the design process of LHP.

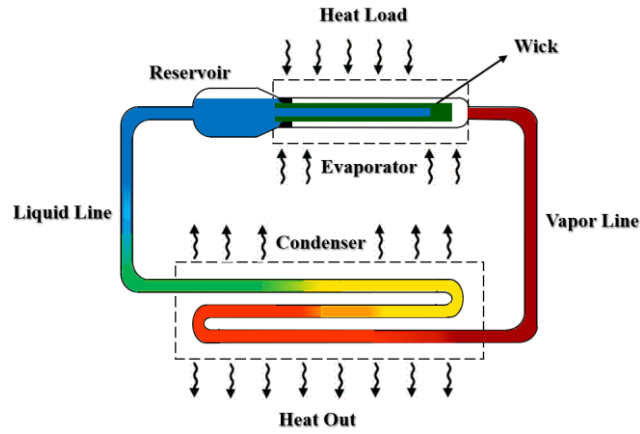


Figure 1. A general schematic of the LHP [1].

2. WICK ANALYSIS

As stated before, a disk shape porous wick manufactured by the Tridelta SiperM GmbH company [2] has been selected for testing. The photo of the wick is presented in Fig. 2 and the evaporator body is presented in Fig. 3.



Figure 2. Photograph of the wick

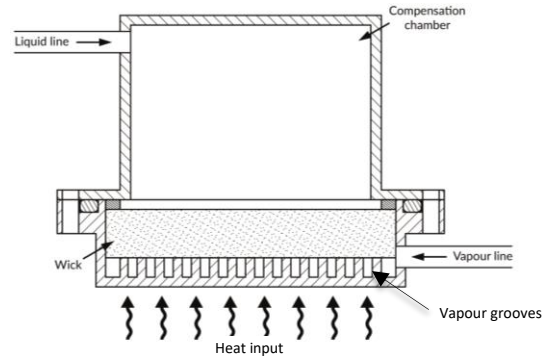


Figure 3. Schematic of the LHP experimental prototype

A. Porosity measurement The wick has been measured and weighted in order to determine data necessary for evaluation of its porosity. Porosity has been calculated using two methods, i.e. percolation theory to determine total porosity:

$$\varepsilon = \left(1 - \frac{\rho_{measured}}{\rho_{theoretical}}\right) \cdot 100\% \quad (3)$$

where $\rho_{theoretical}$ is the theoretical density of 316L stainless steel taken from the standard (PN - EN 10027 -2) $\rho_{theoretical} = 0,008\text{g/mm}^3$, and $\rho_{measured}$ is the density measured experimentally:

$$\rho_{measured} = \frac{m_{dry\ sample}}{v} \quad (4)$$

The second method to calculate the porosity is the Archimedes method, which allows to calculate of the open porosity (a.k.a. 'effective') which is responsible for pumping the working fluid around the loop. The procedure was first to measure the dry weight m_1 of the wick using the electronic scale, and then, saturate the wicks with acetone (CH_3COH_3 , CAS:67-64-1 – density 0.00079 g/mm^3) for 6 h, and measure the weight of saturated wicks in the air m_2 and in the acetone m_3 :

$$\varepsilon_o = \frac{m_2 - m_1}{m_2 - m_3} \cdot 100\% \quad (5)$$

B. Pore size measurement and permeability calculation. Pore size of the wick has been determined using three methods i.e. scanning electron microscope (SEM), bubble point measurement and porosimetry evaluation. The first method, namely using SEM allows for the measurement of the pore sizes only at the external-cut surface of the wick and hence represent only the largest pores (SEM images are presented in Fig. 3). Moreover, the pore channels inside the material changes change its dimensions due to irregular microstructure, which could enhance the capillary pressure. Therefore, it is necessary to measure pore sizes inside the sample using bubble point method and the pore size distribution using porosimetry evaluation. These results are presented in Tab. 2 and Tab. 3 respectively.

Table 1. Wick properties

Diameter [mm]	59.949 (1)
Thickness [mm]	11.1736 (1)
Volume [mm ³]	31538.9251
Mass of dry sample m ₁ [g]	161.874
Mass of saturated sample saturated in acetone and weighed in air m ₂	169.342
Apparent mass of the sample saturated and weighed in acetone m ₃	145.102
Total porosity calculated using the perlocation theory [%]	35.843
Effective porosity calculated by the Archimedes method [%]	30.809

Table 2. Bubble point measurement [2]

Bubble point test (26.07mbar)	17.6 μm
Mean Flow Pore Size (89.48 mbar)	5.1 μm
Mean Pore Size	8.9 μm
Median Pore Size	4.5 μm
Modal Pore Size	3.6 μm
Standard deviation	4.9 μm

Table 3. Porosimetry analysis of the sample [2]

Pore size lower (Xuk)[μm]	Pore size medium [μm]	Pore size upper (Xok) [μm]	Portion [%]
0.4	1.4	2.5	21.793
2.5	3.6	4.7	31.005
4.7	5.7	6.8	22.419
6.8	7.9	8.9	8.902
8.9	10.0	11.1	8.408
11.1	12.2	13.2	7.460
13.2	14.3	15.4	0.007
15.4	16.5	17.5	0.007

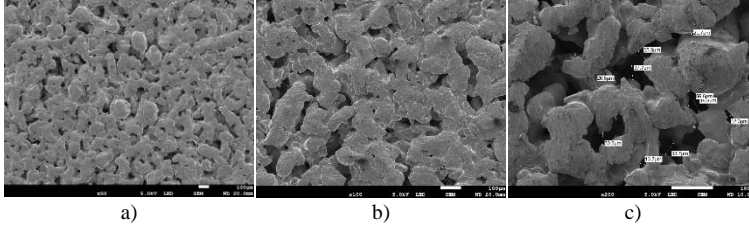


Figure 3. Microscopic view of the wick sample (a) at x50 (b) x100 (c) x 200 magnification

As it can be seen from Tab. 2 and Tab. 3 the mean diameter of the single pore is around 8 μm, therefore using Eq. (2) the permeability can be calculated to be $14.04 \times 10^{13} \text{ m}^2$.

C. Chemical composition. Energy Dispersive X-ray Spectroscopy (EDS/EDX) measurements allow to establish the chemical composition of each atom in the structure, which is indicated for alloys. Tab. 4 specifies the weighted composition of metals of which the sample is made. The portions confirm the quality of the sample and its corrosion resistance properties, although the standards are established for continuous alloys.

Table 4. Chemical composition of the investigated sample compared to the standard (PN - EN 10027 -2)

Element	Weights %	Certified standards for steel 316L (sheet) %
Al	0.17	0.0
Si	0.97	<1.0
Mo	1.99	2.5 – 3.0
Cr	19.11	17.0 – 19.0
Mn	0.11	<2.0
Fe	65.99	60.0 – 68.0
Ni	11.65	12.5 – 15.0
Total	100.00	100.00

D. Thermal conductivity of the wick. Due the fact that, that exact geometric internal configuration of the wick is random, Johuara et al. [3] suggested, that sintered wick is best represented by continuous solid phase containing a random dispersion of randomly sizes spheres of liquid and presented an equation that gives the thermal conductivity of such a heterogenous material

$$k_w = k_s \left[\frac{2+k_l/k_s-2\varepsilon\left(\frac{1-k_l}{k_s}\right)}{2+k_l/k_s+\varepsilon\left(\frac{1-k_l}{k_s}\right)} \right] \quad (6)$$

Where k_w is the thermal conductivity of sintered wick, k_s is a thermal conductivity of a solid phase (for material made by SS316L $k_s=15\text{W/m}\cdot\text{K}$), k_l - thermal conductivity of the liquid working fluid.

4. CONCLUSIONS

The porous structure has been studied to evaluate its chemical composition and improve the efficiency of the heat exchange process of F-LHP. The flow properties of the wick are very important for the proper operation of LHP and good heat transfer performance of the evaporator. A high porosity of the wick is necessary to minimize the parasitic heating (heat leak) from the evaporator zone towards compensation chamber. High permeability of the wick helps to reduce the pressure losses through the porous wick. Moreover, the wick should be able to generate sufficient capillary pressure and keep the fluid in continuous circulation and be chemically compatible with working fluid.

5. REFERENCES

- [1] Szymanski, P., Mikielwicz, D., Fooladpanjeh, S., 2022. "Current Trends in Wick Structure Construction in Loop Heat Pipes Applications: A Review". *Materials*. Vol. 15:5765.
- [2] Tridelta Siperem GmbH, <https://www.siperem.com>
- [3] Jouhara, H., Reay, D., McGlen, R., Kew, P., McDonough, J. 2023 *Heat Pipes Theory, Design and Applications* 7th Edition - October 1, Butterworth-Heinemann, Elsevier Science.

NEAR-WALL HEAT TRANSFER PHENOMENA DURING BUBBLE GROWTH IN NUCLEATE BOILING

Cassiano Tecchio^{a,*}, Corentin Le Houedec^a, Benjamin Cariteau^a, Guillaume Bois^a, Elie Saikali^a, Gilbert Zalczer^b, Pere Roca i Cabarrocas^c, Pavel Bulkin^c, Jérôme Charliac^c, Simon Vassant^b, Vadim S. Nikolayev^b

^aUniversité Paris-Saclay, CEA, STMF, 91191 Gif-sur-Yvette Cedex, France

^bUniversité Paris-Saclay, CEA, SPEC, CNRS, 91191 Gif-sur-Yvette Cedex, France

^cInstitut Polytechnique de Paris, Ecole polytechnique, LPICM, CNRS, 91120 Palaiseau, France

*cassiano.tecchio@cea.fr

Keywords: microlayer, contact line, boiling, heat transfer

1. INTRODUCTION

During the growth of bubbles on a heated wall, a thin layer of liquid having a thickness of a few μm (known as microlayer) (Jung and Kim 2014, Guion, et al. 2018, Urbano, et al. 2018) can be formed between the wall and the liquid-vapor interface of the bubble, as illustrated in Fig. 1. A dry spot is also formed on the wall, establishing a triple liquid-vapor-solid contact line. The wall heat flux is very low in the dry spot, resulting in a local rapid temperature increase. Unlike the dry spot, the microlayer acts as a heat transfer bridge between the wall and the liquid-vapor interface of the bubble, creating heat fluxes of the order of MW/m^2 that cool down the heater and promote the microlayer evaporation. Two thermal resistances act to decreasing the microlayer evaporation rate. The first is the conductive through the film thickness, which is well determined by measuring the microlayer thickness. The second is the interfacial thermal resistance at the liquid-vapor interface. The issue of the interfacial thermal resistance in water is important but highly controversial, being under active discussion in the literature (Eames, Marr and Sabir 1997, Giustini, et al. 2016). In this work, we perform experiments on single bubble growth at nucleate boiling to investigate the near-wall heat transfer phenomena, in particular, to study the interfacial thermal resistance in the microlayer.

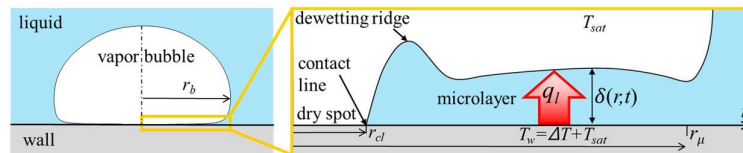


Figure 1. Schematics of the microlayer profile underneath a bubble.

2. EXPERIMENTS

The experimental setup is schematized in Fig. 2. The boiling cell consists of a water pool at atmospheric pressure surrounded by a temperature-regulated jacket. The heater consists of a $\sim 1 \mu\text{m}$ thick indium-tin-oxide (ITO) film deposited on a magnesium fluoride (MgF_2) optical porthole. MgF_2 is transparent to both visible and infrared (IR) light whereas ITO is transparent to visible but opaque to IR. The growth of a single bubble at a time is produced by heating up the ITO film locally with a $1.2 \mu\text{m}$ wavelength IR continuous laser beam of $\sim 1.5 \text{ mm}$ diameter. High-speed (4000 fps) and high-resolution optical techniques are employed. The bubble macroscopic shape (Fig. 2a) is observed by sidewise shadowgraphy. The microlayer thickness δ is measured by white light interferometry (WLI). A LED light source produces a collimated beam of white light that is sent towards the bubble from below with perpendicular incidence to the heater. The light reflected at the interfaces MgF_2/ITO , $\text{ITO}/\text{microlayer}$ and $\text{microlayer}/\text{vapor}$ produces a colored fringe pattern directed towards a spectrometer with a visible light beam splitter. At the entrance of the spectrometer, a slit defines a scanning line on the heater. The fringe pattern is then dispersed into wavelength λ by a diffraction grating inside the spectrometer, producing a spectral fringe map. In Fig. 2b, the ordinate corresponds to λ and abscissa, to the physical position r on the heater along the scanning line. The microlayer thickness distribution $\delta(r)$ is determined by comparing the experimental spectral intensity with a two beam interference model (Tecchio 2022). From Fig. 2b one can also obtain the dry spot (contact line) radius r_{cl} and the microlayer radius r_{μ} . The diffraction grating can be replaced by a mirror to observe the dry spot and microlayer extents over the heater as shown in Fig. 2c.

The IR thermography is used to measure the temporal evolution of the wall temperature distribution $T_w(x, y, t)$ (Fig. 2d). We use a custom-made multilayer visible-IR light beam splitter. It is transparent to visible light but reflective to IR waves and is produced with the radio-frequency magnetron sputtering. It is positioned between the boiling cell and the visible light beam splitter to reflect the IR radiation emitted by the ITO to the fast IR camera sensitive in the range 3-

5 μm . The temperature is deduced from the recorded intensity thanks to the preliminary pixel-wise calibration (Tecchio 2022).

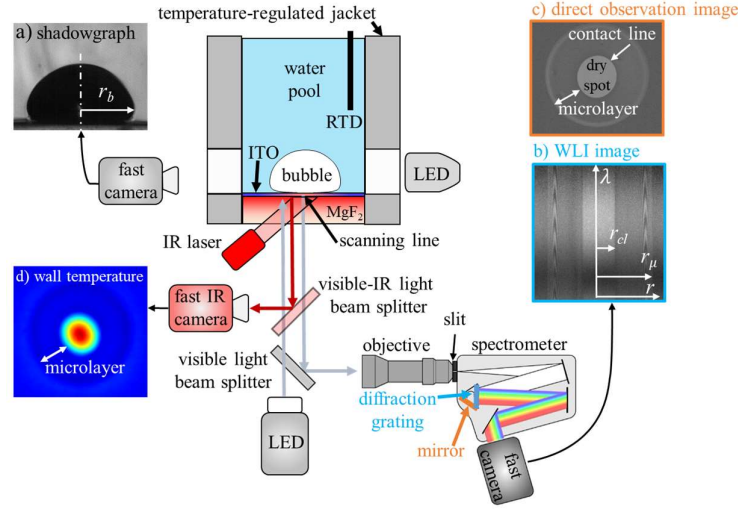


Figure 2. Schematics of the experimental setup.

3. RECONSTRUCTED HEAT FLUX AND INTERFACIAL THERMAL RESISTANCE

One can reconstruct the wall heat flux q_l (Fig. 1) by solving the energy balance in the ITO film. It yields the expression (Tecchio 2022)

$$q_l = j_0 + q_p + hk_w \left(\frac{\partial^2 T_w}{\partial x^2} + \frac{\partial^2 T_w}{\partial y^2} \right) - h\rho_w c_w \frac{\partial T_w}{\partial t} \quad (1)$$

where j_0 is the equivalent surface heat flux induced externally by the IR laser and q_p is the heat flux towards the porthole (MgF₂). q_p is obtained by solving numerically the transient heat diffusion in the MgF₂. The third and fourth terms in the RHS of Eq. (1) represent the heat diffusion and accumulation in the ITO, respectively. h is the ITO thickness measured *in-situ* by WLI. ρ_w , c_w and k_w stand for the density, specific heat and thermal conductivity of the ITO film. The wall temperature T_w is given by the IR thermography. Equation (1) is valid everywhere on the wall, including the dry spot and the microlayer.

The wall heat flux expression involving the microlayer thickness and the interfacial thermal resistance R^i reads

$$q_l = \frac{\Delta T}{\delta / k_l + R^i} \quad (2)$$

where $\Delta T = T_w - T_{sat}$ is the wall superheating. k_l is the microlayer thermal conductivity. Therefore, one can determine R^i using Eq. (2), with ΔT and δ measured by IR thermography and WLI, respectively, and q_l from Eq. (1). A theoretical value of the interfacial thermal resistance is obtained from the kinetic theory of gases with the accommodation coefficient equal to 1. It represents a resistance to the evaporation flux at the liquid-vapor interface due to a finite velocity of the vapor molecules leaving the interface during the phase change. $R_{theo}^i = 0.064 \mu\text{K}\cdot\text{m}^2/\text{W}$ is its theoretical value for water at 1 bar and 100°C.

4. RESULTS

Figure 3a shows the ΔT distribution obtained 6.25 ms after the bubble nucleation (the entire bubble growth period, from bubble nucleation up to departure from the wall, takes only 20 ms). The dry spot and the microlayer are formed within the very first moments of the inertia-controlled bubble growth regime. The microlayer signature on ΔT is the cooling of the wall seen in Fig.3a as a cold ring. On the other hand, the accumulation of heat promotes a higher ΔT in

the dry spot at the center of the image. The non-uniformity of the ΔT distribution in the dry spot is a result of the IR laser heating.

The reconstructed heat flux of Fig.3b was obtained from Eq. (1). The heat flux in the dry spot is nearly zero whereas in the microlayer it reaches up to 0.6 MW/m^2 . The maximum heat flux occurs near the contact line, where the mass evaporation fluxes are higher. The time evolution of the ratio R^i / R_{theo}^i is shown in Fig. 3c for a fixed point in the microlayer. While in the beginning of microlayer growth $R^i = R_{theo}^i$, R^i increases in time, becoming up to 60 times higher than R_{theo}^i . The temporal increase of R^i seems to indicate an effect of electrochemical properties of water that cause accumulation of impurities present in the liquid at the liquid-vapor interface at evaporation, in spite of ultra-high purity of water used in the experiments (it is difficult to avoid completely the water contamination by the boiling cell itself in spite of its careful cleaning). In comparison with these similar experiments (Giustini, et al. 2016, Bucci 2020), the main outcome of our results is the clear indication of the time dependence of R^i .

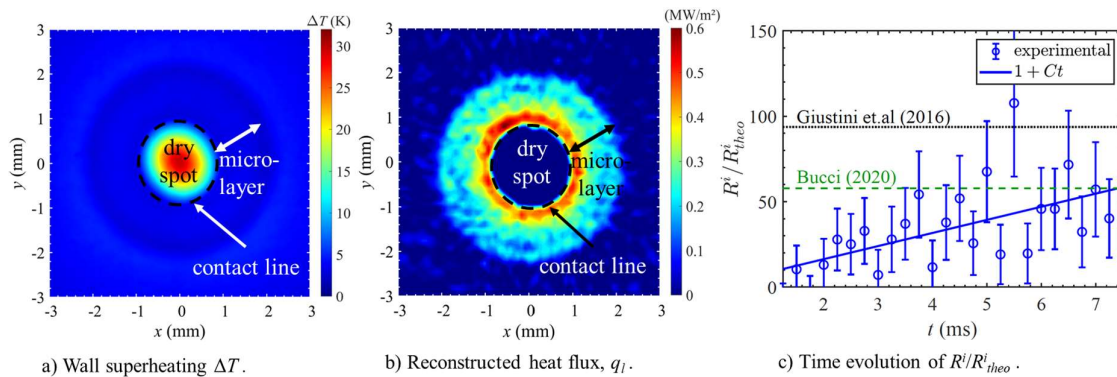


Figure 3. Wall superheating and reconstructed heat flux distributions after 6.25ms of bubble nucleation. The time evolution of R^i / R_{theo}^i is obtained for a point in the microlayer at $(x = 1.6 \text{ mm}, y = 0)$.

5. CONCLUSION

We report experimental results of single bubble nucleate boiling at atmospheric pressure and saturation temperature. The near-wall heat transfer phenomena during the microlayer evaporation is analyzed using high-speed and high resolution optical techniques. White light interferometry, infrared thermography and side wise shadowgraphy measure the microlayer thickness, wall temperature and bubble macroscopic shape, respectively. The wall heat flux is determined numerically by solving the transient heat diffusion inside the porthole. We reveal that the interfacial thermal resistance increases over time while the microlayer evaporates, becoming finally up to 60 times higher than the theoretical value. This increase can be explained by progressive accumulation of water impurities at the liquid-vapor interface during microlayer evaporation.

REFERENCES

- Bucci, M., 2020. "A theoretical and experimental study of vapor bubble dynamics in separate effect pool boiling conditions." Master thesis, University of Pisa, Italy.
- Eames, I. W., Marr, N. J., and Sabir, H., 1997. "The evaporation coefficient of water: a review". *Int. J. Heat Mass Transfer* 40: 2963-2973.
- Giustini, G., Jung, S., Kim, H., and Walker, S. P., 2016 "Evaporative thermal resistance and its influence on microscopic bubble growth." *Int. J. Heat Mass Transfer* 101: 733-741.
- Giustini, G., 2024. "Hydrodynamic analysis of liquid microlayer formation in nucleate boiling of water." *Int. J. Multiphase Flow* 172: 104718.
- Guion, A., Afkhami, S., Zaleski, S., and Buongiorno, J., 2018. "Simulations of microlayer formation in nucleate boiling." *Int. J. Heat Mass Transfer* 127: 1271-1284.
- Jung, S., and Kim, H., 2014 "An experimental method to simultaneously measure the dynamics and heat transfer associated with a single bubble during nucleate boiling on a horizontal surface." *Int. J. Heat Mass Transfer* 73: 365-375.
- Tecchio, C. 2022. "Experimental study of boiling: Characterization of near-wall phenomena and bubble dynamics." Ph.D. thesis, Université Paris-Saclay.
- Urbano, A., Tanguy, S., Huber, G., and Colin, C., 2018. "Direct numerical simulation of nucleate boiling in micro-layer regime." *Int. J. Heat Mass Transfer* 123: 1128-1137.

EXPERIMENTAL INVESTIGATION ON THERMAL PERFORMANCES OF THE COLD PLATES IN A PUMP DRIVEN TWO-PHASE COOLING SYSTEM

Hongbo Xu^{a,b,*}, Ming Liu^b, Kongrong Li^{a,b}

^aKey Laboratory of Cryogenic Science and Technology, Beijing, China

^bTechnical Institute of Physics and Chemistry, CAS, Beijing, China

*hbxu@mail.ipc.ac.cn

Keywords: Pump driven two-phase cooling; Cold plate; Temperature uniformity; Ice cool storage

Abstract: As electronic devices are more and more complex and small-sized, higher requirements are proposed for the thermal management of electronic equipment which includes not only high heat dissipation efficiency but also well temperature uniformity. The pump driven two-phase cooling system has the advantages of high heat flux dissipation, excellent temperature uniformity, and low power consumption compared with the traditional cooling technologies, such as air cooling, single-phase liquid cooling, and heat pipe cooling. It is extremely crucial to conduct experimental investigation on the pump driven two-phase cooling system.

This study presents an experimental investigation on a mechanical pump driven two-phase cooling system to improve the heat transfer capacity and temperature uniformity of the cold plate evaporators. The working fluid of the system is the refrigerant R236fa. Dual cold plates were connected in parallel with 12 uniform heating blocks attached to their surface to simulate the actual heat sources. The condenser used a spiral coil heat exchanger which exchanged heat with ice water. The start-up and operating performances of the system were tested. The surface temperature uniformity of the cold plates was analyzed under various flow rates and heat loads, respectively. The experimental results showed that the system presented a rapid start-up characteristic and the surface temperature fluctuation of cold plates was relatively small. Reducing the mass flow rate of the refrigerant, increased the refrigerant gasification rate and the ratio of phase change heat. The lower average surface temperature, maximum temperature difference, and less pump power consumption were realized at a low flow rate when the system was steady. In the variable heat load tests, the average surface temperature and maximum temperature difference increased as the heating power added from 417.2 W to 784.2 W. The cold plates performed well temperature uniformity during the experiments and the maximum temperature difference of cold plates were all below 2 °C.

CRITICAL CONDITIONS FOR SECONDARY FRAGMENTATION OF COMPOSITE LIQUID DROPLETS

Antonov D.V.^a, Vysokomornaya O.V.^a, Yanovskiy L.S.^a, Strizhak P.A.^{a,*}

^aNational Research Tomsk Polytechnic University, Heat and Mass Transfer Laboratory
30 Lenin Avenue, Tomsk 634050, Russia

*pavelspa@tpu.ru

Keywords: composite liquid droplet; puffing; micro-explosion; droplet breakup; dimensionless criteria

1. INTRODUCTION

The critical conditions of puffing and micro-explosion modes in composite liquid droplets can be described using three approaches: (i) by superheating degree of the water/fuel interface above the water boiling temperature; (ii) by thinning of the flammable liquid film around the vapor bubble; (iii) by the critical radius reached by the parent composite liquid droplet swelling due to bubble growth. The experimental and theoretical findings (Sazhin and Bar-Kohany, 2020) were obtained for several types of flammable liquids as part of heterogeneous droplets. Critical conditions and delay times of droplet breakup were found to heavily depend on the liquid properties, heating rate, geometry of the parent composite liquid droplet, etc. As the next step to develop the findings (Sazhin and Bar-Kohany, 2020), it seems sensible to summarize the known data on different droplet heating arrangements and a wide variety of potential liquids for those composite liquid droplets. It is also important to experimentally determine the combined and separate contribution of several boosting and inhibiting factors and describe this contribution by modeling. That was our motivation for this research. The aim of this research was to generalize the critical conditions leading to puffing and micro-explosion modes during heterogeneous fuel-water droplets in the form of dimensionless criteria (Ohnesorge (or Laplace), Kutateladze (or Stefan), Gretz, Nusselt (or Stanton), Sherwood, Prandtl, Reynolds, Fourier, Lewis, Jacob, and Weber numbers) following different approaches to puffing and micro-explosion identification. This is the first attempt at conducting such generalization. Given the sheer volume of data obtained, this generalization will require a long time. In this research, we propose a novel approach to such generalization and present its first outcomes. We are planning to further develop this approach by incorporating emerging theoretical and experimental data on puffing and micro-explosion modes. Basic principles have been formulated and tested in this research, which is presented in the form of a brief communication.

2. DIMENSIONLESS CRITERIA OF CRITICAL CONDITIONS LEADING TO PUFFING AND MICRO-EXPLOSION

The fragmentation of composite liquid droplets in the puffing and micro-explosion regimes is a rather complex phenomenon depending on thermophysical and hydrodynamic factors. Dimensionless criteria should be selected to estimate whether the initial parameters of the environment and composite liquid droplets meet the critical conditions necessary for their puffing and micro-explosion. Today, there are a lot of experimental methods to determine the velocity of small objects (for instance, child droplets) as well as detect variations in their temperature and volume. Most thermodynamic and rheological characteristics of substances and materials are taken from reference data and rely on their temperature relationships. The degree of water/fuel superheating degree with respect to the water nucleation temperature can be estimated using the dimensionless Kutateladze number (Ku) (or Stefan number). This criterion estimates the balance of heat fluxes at a certain surface as an interface between two media (Almaraz and López, 2014; Sarafraz and Pourmehran, 2019). When studying the heating of a composite liquid droplet in terms of the water/fuel superheating degree, it is necessary to estimate how much the energy actually supplied to the interface differs from the energy required for the complete phase transition (heat of water evaporation). It can be assumed that rapid vaporization starts at the moment of puffing or micro-explosion. Before that, water in the center of a droplet is in the liquid aggregate state. Then the Kutateladze criterion, which reflects the necessary conditions of interfacial superheating in a droplet in terms of the first criterion from section 4, is given by the following equation before the puffing/micro-explosion:

$$Ku = \frac{L_w}{c_{pw} \Delta T_{SH}},$$

where L – latent heat, J/kg; c_p – isobaric heat capacity, J/(kg·K); ΔT_{SH} – superheating degree, K; the subscript w refers to the dispersed phase (water).

The critical (minimum) energy of superheating that the water core must accumulate can be calculated using the equation for enthalpy (Moussa and Tarlet, 2020):

$$\Delta H = c_{pw} m_w \Delta T_{SH}, \text{ J, where } m - \text{mass, kg.}$$

Fig. 1 illustrates the calculated values of ΔH for composite liquid droplets, depending on heating rates. The mass of the water core is derived from the water to fuel ratio in a droplet. In Fig. 1 (right), the region (1) characterizes the conditions leading to the occurrence of puffing, while the region (2) characterizes the conditions leading to the occurrence of micro-explosion.

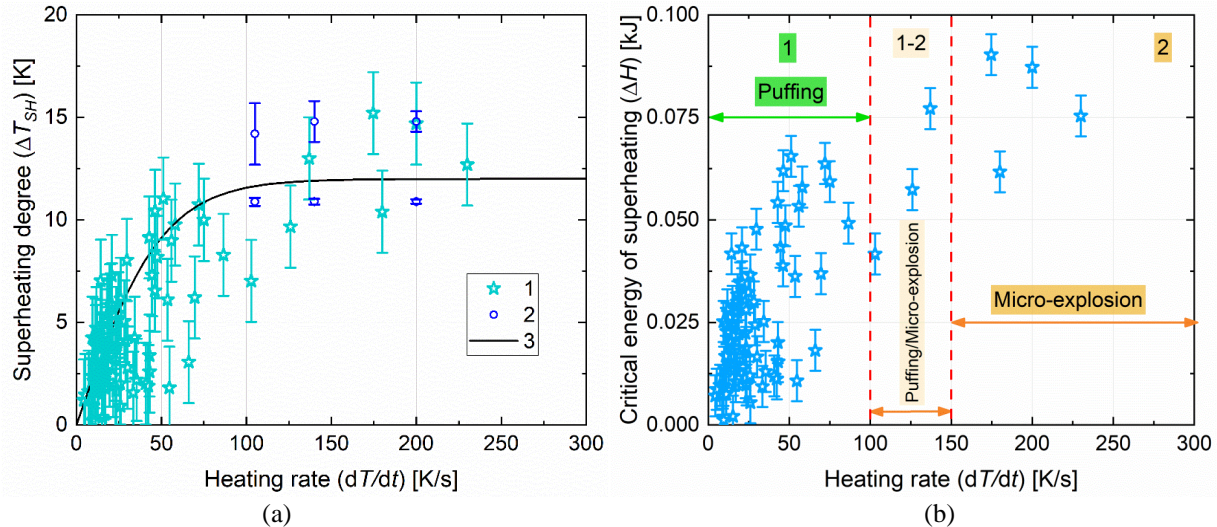


Figure 1 Interfacial superheating temperature degree against heating rate (1 – experimental findings by Antonov et al. [6,69], 2 – experimental findings (Su and Bucci. 2016), 3 – approximation $\Delta T_{SH} = 12 \cdot \tanh((dT/dt)/50)$ (Sazhin and Bar-Kohany, 2020) (a) and Critical energy of superheating at the moment of puffing and micro-explosion versus heating rate (b). Regions 1 and 2 are for the puffing and micro-explosion, respectively.

2. DERIVING THE DIMENSIONLESS CRITERION OF PUFFING AND MICRO-EXPLOSION “ME”

Using the Buckingham-Fiderman π theorem, the dimensions were analyzed to find the following variable complexes defining the critical conditions of explosive breakup: $(\Delta H_f/\Delta H_w)$, $(\rho_w \cdot \Delta H_w \cdot R_w)/\sigma_{fw}$, $(\mu_f/(\Delta H_w)^{1/2} \cdot \sigma_{fw})$. Thus, it is proposed to use criterion $Me = f(\Delta H_f/\Delta H_w; (\rho_w \cdot \Delta H_w \cdot R_w)/\sigma_{fw}; \mu_f/(\Delta H_w)^{1/2} \cdot \sigma_{fw})$ as a combined criterion of micro-explosive breakup of two-liquid droplets based on the Ku, Ja, Oh numbers determining puffing and micro-explosion.

To obtain a new overall dimensionless criterion of the occurrence of puffing and micro-explosion Me , it is necessary to bring together some physical quantities characterizing the explosive breakup of droplets, included in the criteria Ku, Ja and Oh, namely, $\Delta H_w = c_{pw} \cdot \Delta T_{sh}$ – a change in the enthalpy of water as a result of superheating (J/kg); ρ_w ; μ_f ; σ_{fw} ; R_w . These characteristics and parameters are functionally related to the enthalpy supplied to a composite liquid droplet, $\Delta H_f = C_{pf} \cdot (T_g - T_{av,f})$ (J/kg):

$$\Delta H_f = f(\Delta H_w, \rho_w, \mu_f, \sigma_{fw}, R_w), \text{ where } \rho - \text{density, kg/m}^3; \mu - \text{viscosity, Pa}\cdot\text{s}; \sigma - \text{surface tension, N/m}; R - \text{radius, m.}$$

The main quantities were Δh , σ_{fw} and R_w . The dimensions of the main quantities were: $[\Delta H_w] = L^2 \cdot T^{-2}$; $[\sigma_{fw}] = M \cdot T^{-2}$; $[R_w] = L$, where L is the characteristic of length, M is the characteristic of mass, T is the characteristic of time.

The new overall dimensionless criterion Me :

$$Me = \left(\Delta H_f \cdot \rho_w \cdot R_w \cdot \mu_f \cdot \Delta H_w^{1/2} \right) / \sigma_{fw}^2$$

At $Me = 0$, droplets start to evaporate monotonically (there is no superheating of the low-boiling liquid ($\Delta h=0$)); puffing occurs at $0 < Me \leq 3 \cdot 10^{10}$, micro-explosion occurs at $Me > 3 \cdot 10^{10}$. Thus, it is possible to provide the conditions of occurrence of a regime for a practical application and satisfying the corresponding requirements by selecting individual and combined physicochemical properties of liquids for the carrier and dispersed phase, as well as parameters of the heating medium. Fig. 11 graphically represents the critical (minimum) Fourier criterion characterizing the time of initiation of puffing/micro-explosion as a function of the proposed criterion Me .

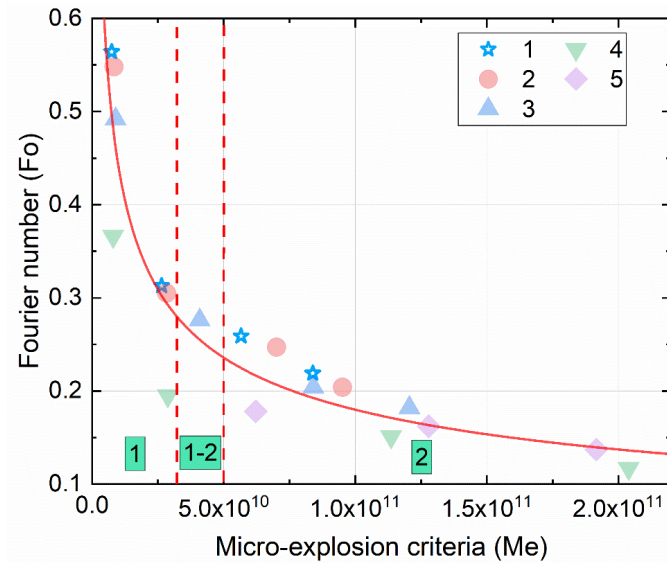


Figure 2. Fo versus Me at the moment of puffing/micro-explosive breakup of heterogeneous droplets: 1 – current study, water/n-decane; 2 – current study, water/n-undecane; 3 – current study, water/n-dodecane; 4 – current study, water/kerosene; 5 – (Fedorenko and Antonov, 2022; Antonov and Volkov, 2021), water/rapeseed oil. Regions 1 and 2 are for the puffing and micro-explosion, respectively.

3. CONCLUSIONS

The ranges of five dimensionless criteria reflecting the conditions leading to the puffing and micro-explosive breakup of composite liquid droplets were estimated on the basis of new and earlier findings, as well as published experimental data of other authors. The dimensionless criteria are comparable for different compositions in similar physical conditions ($Oh=0.002-0.04$, $Ku=10-300$, $Ja=5-150$, $We=50-4000$, $Fo=0.1-0.6$). Thus, the proposed approach can be used for predicting the conditions necessary for the consistent occurrence of puffing and micro-explosion in heterogeneous liquid droplets in various applications: fuel technologies, evaporation of impurities from water, creation of multiphase flows, of heat transfer intensification, etc. The newly obtained dimensionless criterion of micro-explosive breakup (Me) is based on the degree of interfacial superheating in a binary droplet and includes the minimum number of variables derived from the dimensional analysis.

4. REFERENCES

- Antonov, D.V., Volkov, R.S., Fedorenko, R.M., Strizhak, P.A., Castanet, G., Sazhin, S.S., 2021. “Temperature measurements in a string of three closely spaced droplets before the start of puffing/micro-explosion: Experimental results and modelling”. *International Journal of Heat Mass Transfer*, Vol. 181, 121837.
- Almaraz, A., López, C., Arellano, I., Barrón, M.A., Jaramillo, D., Reyes, F., Plascencia, G., 2014. “CFD modelling of fluid flow in a Peirce–Smith converter with more than one injection point”. *Minerals Engineering*, Vol. 56, pp. 102–108.
- Fedorenko, R.M., Antonov, D.V., Strizhak, P.A., Sazhin, S.S., 2022. “Time evolution of composite fuel/water droplet radii before the start of puffing/micro-explosion”. *International Journal of Heat Mass Transfer*, Vol. 191, 122838.
- Moussa, O., Tarlet, D., Massoli, P., Bellettre, J., 2020. “Investigation on the conditions leading to the micro-explosion of emulsified fuel droplet using two colors LIF method”. *Experimental Thermal and Fluid Science*, Vol. 116, 110106.
- Sarafraz, M.M., Pourmehran, O., Yang, B., Arjomandi, M., 2019. “Assessment of the thermal performance of a thermosyphon heat pipe using zirconia-acetone nanofluids”. *Renewable Energy*, Vol. 136, pp. 884–895.
- Sazhin, S.S., Bar-Kohany, T., Nissar, Z., Antonov, D., Strizhak, P.A., Rybdylova, O.D., 2020. “A new approach to modelling micro-explosions in composite droplets”. *International Journal of Heat Mass Transfer*, Vol. 161, 120238.
- Su, G.Y., Bucci, M., McKrell, T., Buongiorno, J., 2016. “Transient boiling of water under exponentially escalating heat inputs. Part I: Pool boiling”. *International Journal of Heat Mass Transfer*, Vol. 96, pp. 667-684.

Suppression of boiling in a two-phase closed thermosyphon under horizontal vibration

Sohyeun Kang^a, Daegyoun Kim^{a,*}

^aDepartment of Mechanical Engineering, KAIST

*daegyoun@kaist.ac.kr

Keywords: Two-phase closed thermosyphon, Vibration, Phase change, Boiling suppression

1. INTRODUCTION

Two-phase closed thermosyphons, also called wickless heat pipes, are passive heat transfer devices with high efficiency that exploit phase change as their primary operating principle. Thermosyphons have been used in various industrial applications such as solar collectors, cooling of electronic devices, gas turbine blades, and batteries. These applications frequently include dynamic situations such as translation, rotation, and vibration. Previous research has demonstrated that such dynamic motions have significant impacts on phase change and heat transfer phenomena in general two-phase flow systems, including bubble ebullition dynamics (Navruzov *et al.*, 1992 & Mondal and Bhattacharya, 2021), convective heat transfer (Antonenko *et al.*, 1992) and gas-liquid flow regimes (Chen *et al.*, 2017). Meanwhile, most of previous studies on thermosyphons have focused on stationary environments, the mechanisms of boiling phenomena inside the thermosyphon when subjected to motions still remain unclear. In this study, we experimentally investigated the phase change characteristics of a vertical two-phase closed thermosyphon, which is subjected to horizontal vibrations. Furthermore, the effects of horizontal vibration on thermosyphon are explored by varying heat input, vibration frequency and amplitude.

2. EXPERIMENTAL SETUP

The experimental setup of a vertical thermosyphon system is depicted in Figure 1. The main component of the thermosyphon is a Pyrex tube with a length of 200 mm and an inner diameter of 10 mm. The working fluid is distilled water and it was degassed to minimize the impacts of non-condensable gases. The thermosyphon consists of an evaporator and condenser section. An electrical heater enveloping the outer surface of the evaporator and the evaporator section was ohmically heated by a DC power supply (N5767A, Keysight). For the condenser section, the water jacket was encompassed by a copper block. The copper block was linked to a chiller (RW3-3035, Jeiotech) that maintained the coolant temperature at 20°C.

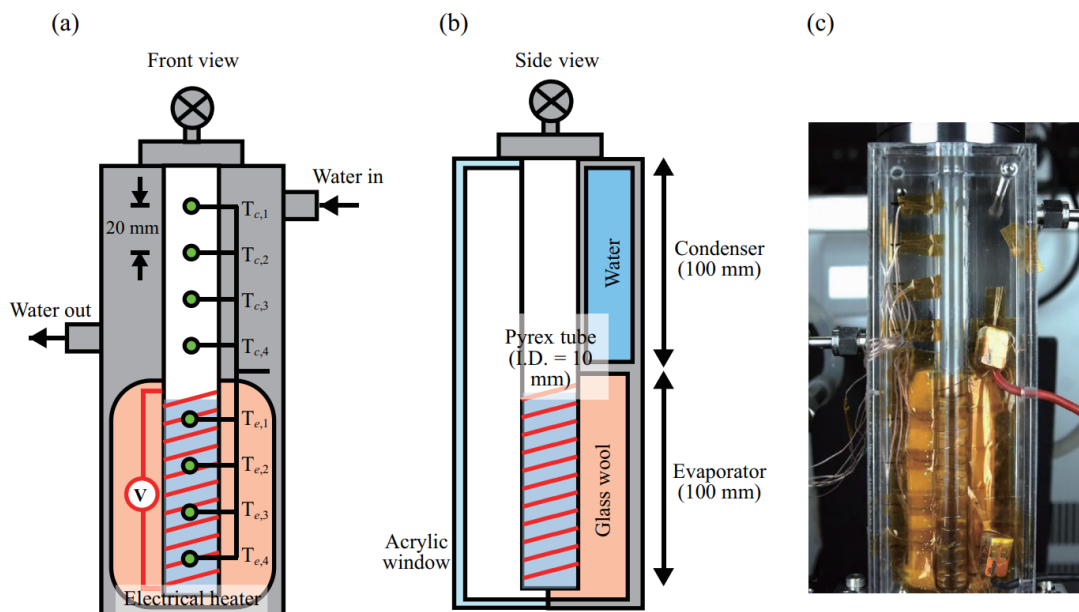


Figure 1. Schematics of two-phase closed thermosyphon: (a) frontal view and (b) side view. (c) Photograph of the thermosyphon.

The thermosyphon system was mounted on a linear stage for horizontal vibrations. The horizontal vibration of the linear stage was prescribed to be sinusoidal, with the amplitude and frequency controlled by a PC connected to the linear stage. The operating conditions of input parameters are presented in Table 1. In addition to the vibration cases, cases with no vibration were also investigated. Surface temperatures were measured and recorded with K-type thermocouples at a sampling rate of 5 Hz. Along with the temperature measurement, images inside the thermosyphon were also captured by the high-speed camera (FASTCAM Mini UX50, Photron Inc.) at a frame rate of 500 Hz.

Degassed distilled water was injected into the thermosyphon which was evacuated using a vacuum pump (GHP-150K, KODIVAC). The filling ratio, which is defined as the volume of the working fluid relative to the volume of the evaporator section, was set to 95%.

Table 1. Ranges of input parameters.

Parameter	Operating condition
Heat input Q_{in}	20–40 W
Vibration amplitude A	5–30 mm
Vibration frequency f	2–8 Hz

3. RESULTS

To determine the effects of horizontal vibration on thermosyphon, temperature fluctuations on the evaporator surface are presented between thermosyphons in stationary and horizontal vibration situations (Figure 2). Figure 2 presents the time series temperature varying frequency f (Figure 2(a)) and amplitude A (Figure 2(b)) at the heat input $Q_{in} = 20$ W. Temperature fluctuations are significant in both the stationary and the vibration conditions with lower amplitudes and frequencies, indicating the presence of geyser boiling.

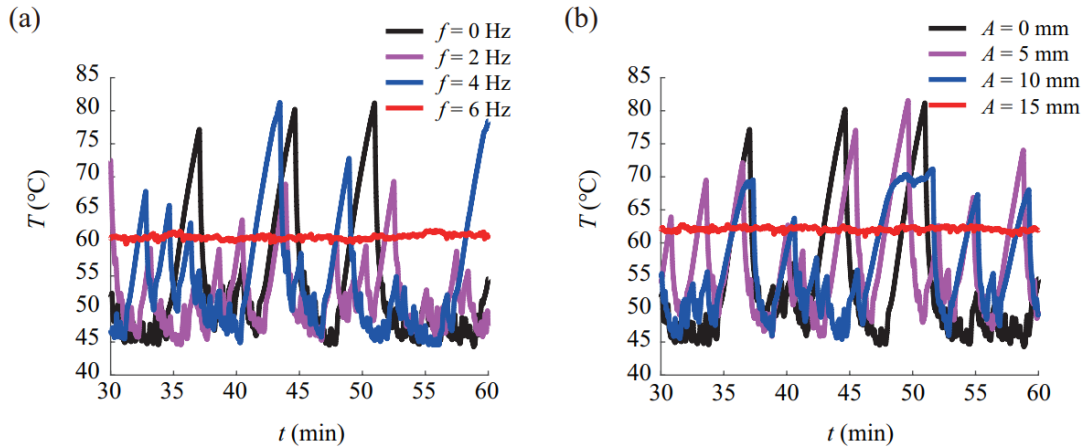


Figure 2. Time histories of temperature at $T_{e,4}$ over 30 minutes, (a) for several frequencies f at a fixed amplitude $A = 10$ mm and (b) for several amplitudes A at a fixed frequency $f = 5$ Hz. The heat input is $Q_{in} = 20$ W.

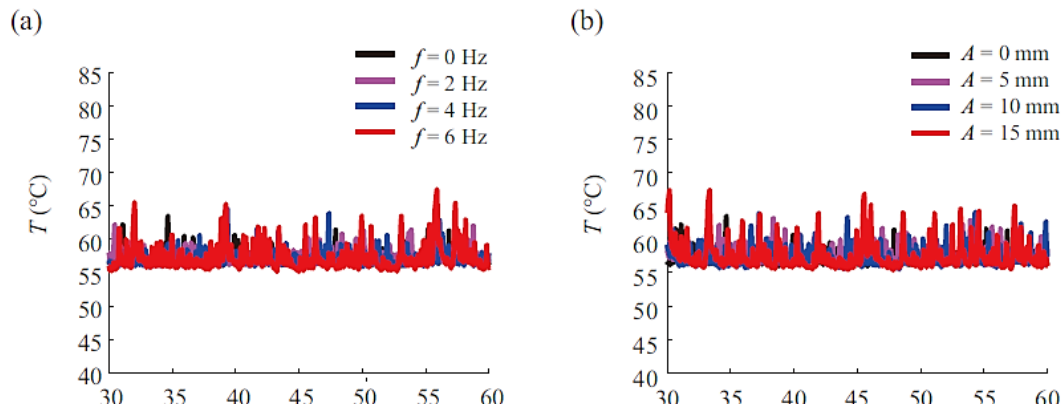


Figure 3. Time histories of temperature at $T_{e,4}$ over 30 minutes, (a) for several frequencies f at a fixed amplitude $A = 10$ mm and (b) for several amplitudes A at a fixed frequency $f = 5$ Hz. The heat input is $Q_{in} = 40$ W.

Meanwhile, increasing the frequency to $f = 6$ Hz causes insignificant temperature fluctuations less than 3°C which indicates the absence of geyser boiling (Figure 2(a)). Under these vibration conditions, nucleate boiling does not occur and a similar pattern emerges as the amplitude increases at a fixed frequency. That is, geyser boiling is effectively suppressed under the conditions of intense vibrations.

With increasing heat input to 40 W, there is a clear shift in the boiling pattern, resulting in negligible temperature fluctuations (Figure 3), indicating that boiling continues continuously. For this heat input condition, the effects of severe vibration conditions have been reduced, and continuous churn flow boiling occurs even under high frequency and amplitude vibrations.

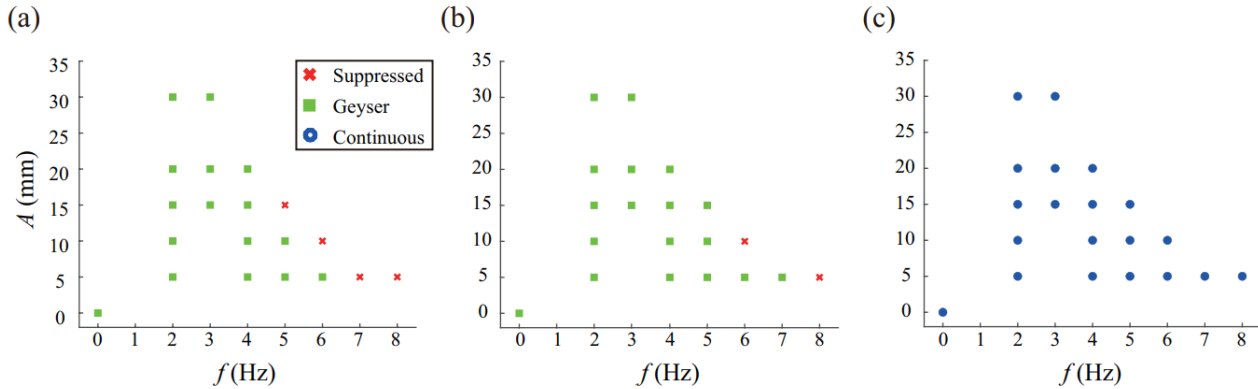


Figure 4. Boiling pattern maps with respect to amplitude A and frequency f for $Q_{in} =$ (a) 20 W, (b) 30 W, and (c) 40 W.

Boiling pattern maps based on temperature data and flow visualization images are presented in Figure 4 for three distinct boiling patterns. Those three boiling patterns are classified as suppressed boiling, geyser boiling and continuous boiling based on the temperature fluctuations. For $Q_{in} = 20$ W, as the frequency becomes larger, transition occurs from geyser boiling to suppressed boiling even with low amplitudes, whereas this transition does not occur for high amplitude and low frequency conditions.

The boundary between geyser boiling and suppressed boiling shifts to the right as the heat input increases from 20 W to 30 W (Figure 4 (a) and (b)), indicating that the impacts of vibration on boiling in a thermosyphon becomes negligible. According to Figure 4(c), continuous boiling occurs for all the vibration conditions.

4. CONCLUSIONS

In this study, we have investigated how horizontal vibration affects boiling behaviors in a two-phase closed thermosyphon by varying vibration amplitude and frequency. Based on temperature measurements and flow visualization, the boiling characteristics are classified as three distinct patterns: geyser, suppressed, and continuous boiling. This fundamental study provides insightful ideas on how to design and operate the two-phased closed thermosyphon when a vibration condition involves.

5. REFERENCES

- Navruzov, Y. V., Mamontov, P., Stoychev, A., 1992. "Subcooled liquid pool boiling heat transfer on a vibrating heating surface". *Heat Transfer Research*, Vol. 24, pp. 771–776.
- Mondal, K., and Bhattacharya, A., 2021, "Pool boiling enhancement through induced vibrations in the liquid pool due to moving solid bodies—a numerical study using Lattice Boltzmann Method (LBM)". *Physical Fluids*, Vol. 33
- Antonenko, V., Chistyakov, Y. G., Kudritskiy, G., 1992. "Vibration-aided boiling heat transfer". *Heat Transfer Research*, Vol. 24, pp. 1147–1151.
- Chen, S.W., Hibiki, T., Ishii, M., Mori, M., Watanabe, F., 2017, "Experimental investigation of horizontal forced-vibration effect on air-water two-phase flow". *International Journal of Heat and Fluid Flow*, Vol. 65, 33–46.

ICE BLOCK TEMPERATURE MEASUREMENT USING PLANAR LASER-INDUCED FLUORESCENCE

Strizhak P. A.^{a,*}, Shlegel N. E.^a, Podgornaya E.R.^a

^aNational Research Tomsk Polytechnic University, Heat and Mass Transfer Laboratory
30, Lenin Avenue, Tomsk, 634050, Russia

*pavelspa@tpu.ru

Keywords: planar laser-induced fluorescence, rhodamine B, temperature field, ice block, freezing temperature and rate

The measurement and accurate prediction of the temperature of ice blocks through non-contact optical methods have gained significance, especially considering the heightened interest of various countries in the development of the Extreme North and the Arctic Region. Given the extreme low temperatures in these regions, optimizing resource utilization for energy, fuel, chemicals, and other applications is imperative (Erdiwansyah et al., 2021). Industrial processes involving gas hydrates—intricate crystalline formations comprising gas (associated gas, methane, ethane, propane, carbon dioxide, etc.), water, and ice—are particularly intriguing (Lin, Y. et al., 2023). The characteristics of these structures are highly contingent on temperature and pressure variations (Gambelli, A. M. and Rossi, F., 2022). Accurately measuring temperature in different segments of these structures during gas production, transportation, and storage is crucial. Placing sensors within hydrate layers can lead to the formation of additional crystallization centers, diminishing the precision of temperature, pressure, and other process parameter measurements (Manjhi, S. K. and Kumar, R., 2020). In gas hydrate structures, heat and mass transfer occur rapidly (Antonov, D. V. et al., 2023). In such scenarios, non-contact measurement systems become essential for obtaining dependable information on the fundamental processes taking place in the three phases: gas, water, and ice.

During the investigation, temperature measurements were conducted in various sections of ice agglomerates utilizing the Planar Laser Induced Fluorescence (PLIF) method. Simultaneously with capturing images of the ice agglomerate, its temperature was measured by thermocouples (Manjhi, S. K. and Kumar, R., 2020). The outcomes of these experiments were used to construct temperature trends. Subsequently, the obtained temperature values were juxtaposed with the luminosity values of the ice agglomerate, obtained through image processing in the DaVis software. A calibration curve was then established, illustrating the relationship between the temperature and luminosity of the ice agglomerate. In the final phase, the temperature field of the ice agglomerate was reconstructed using the calibration curve, converting the luminosity values of each pixel in the ice agglomerate image into temperature values.

Figure 1a shows the temperature trends of ice blocks with three distinct volumes obtained through thermocouple measurements. Notably, larger ice blocks exhibited a more gradual increase in their average temperature. Figure 1b illustrates the trends of average fluorescence from ice blocks with varying volumes, obtained through image processing in the DaVis software. An analysis of the data in Figure 1b has brought to light interesting aspects in the variation of signal intensity during the melting of ice blocks. The fluorescence intensity of the ice blocks exhibited non-uniform patterns, escalating from the periphery to the depth of the samples.

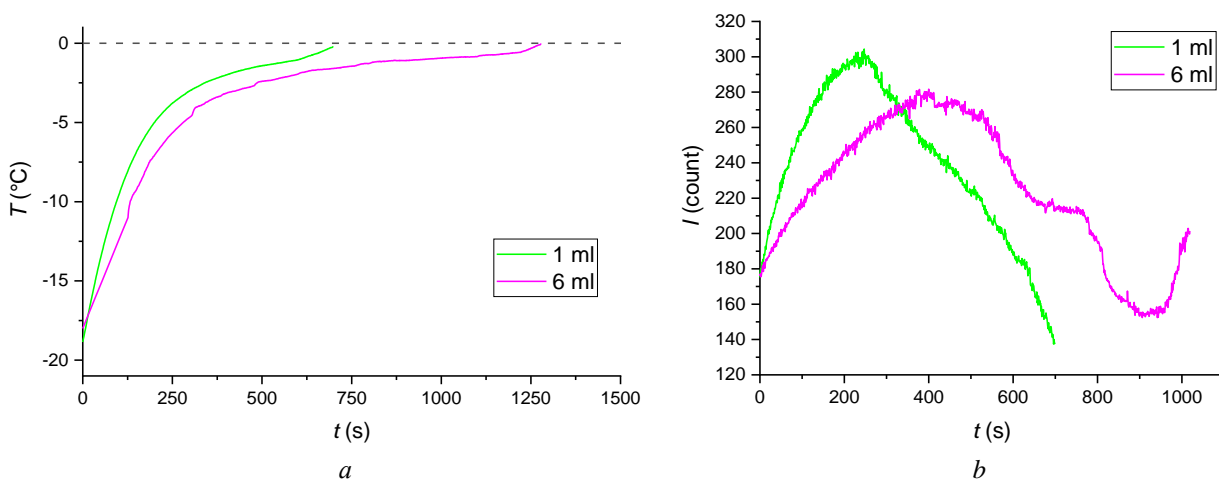


Figure 1. Average ice block temperature (a) and fluorescence (b) trends obtained by thermocouple measurement for samples of two different volumes (1 ml and 6 ml) 30 s after they were taken out of the freezing chamber.

Moving to Figure 2, the calibration curves are presented, generated by comparing the temperature (T) and intensity (I) trends for ice blocks with volumes of 1 ml and 6 ml. Although discrepancies arise in the calibration curves due to variations in shape and size between the two ice blocks, they exhibit acceptable agreement within the temperature range of $-4 \dots 0$ °C.

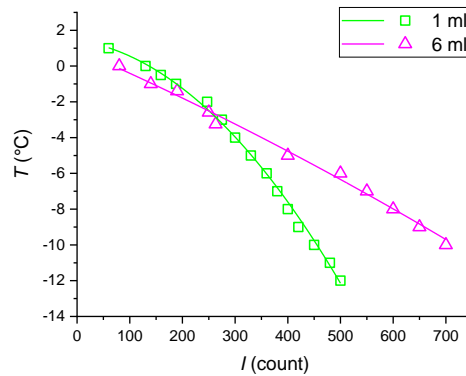


Figure 2. Calibration curves for ice blocks of two volumes (1 ml and 6 ml) obtained experimentally.

The images in Figure 3 depict ice blocks (1 ml and 6 ml) along with their temperature fields, obtained by PLIF. The temperature fields were established using the calibration curves (Fig. 2). Notably, these temperature fields exhibit significant unevenness, revealing that the internal layers of the ice block have considerably lower temperatures compared to those near the surface. Simultaneously, the temperature at the ice surface approaches the phase transition point (approximately 0 °C). Consequently, unlike thermocouple measurements, this proposed approach can monitor temperature dynamics at various points inside the ice block.

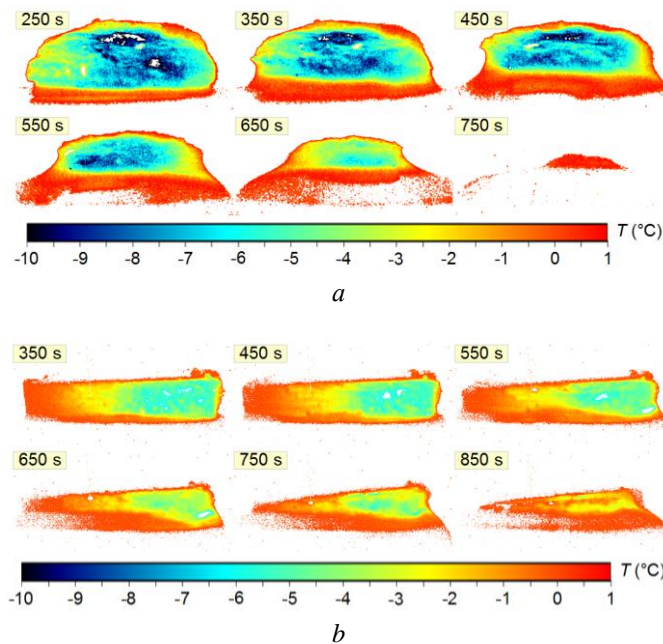


Figure 3. Temperature fields of a 1-ml (a) and 6-ml (b) ice blocks obtained using PLIF.

The research outcomes validate the hypothesis that the fluorescence intensity of the ice block is closely linked to its size, influencing temperature measurement accuracy. For example, Fig. 3a illustrates comparable fluorescence along the vertical symmetry axis of a 12-mm-thick ice block, indicating effective penetration of the laser sheet without substantial power loss. Experiments with a larger ice block (approximately 28 mm thick) demonstrate a different outcome. As the laser sheet delves beyond 15 mm into the ice block, both power and emission intensity begin to decrease by 5–10% (Fig. 3b). Thus, the proposed data processing approach (Fig. 3b) enables the construction of a temperature field, providing accurate temperature determination at a depth of no more than 15 mm.

However, a strategy is proposed to broaden the applicability of PLIF, specifically by increasing the thickness of the layer where accurate ice block temperature measurements can be conducted. This involves correcting the fluorescence intensity of the source image using a technique known as White Image Correction in the DaVis software. Figure 4 showcases temperature fields for a 6-ml ice block obtained through PLIF and White Image Correction. In contrast to

Fig. 3b, these temperature fields (Fig. 4) demonstrate relative smoothness, allowing temperature determination at any point throughout the ice block thickness with the aid of adjustments.

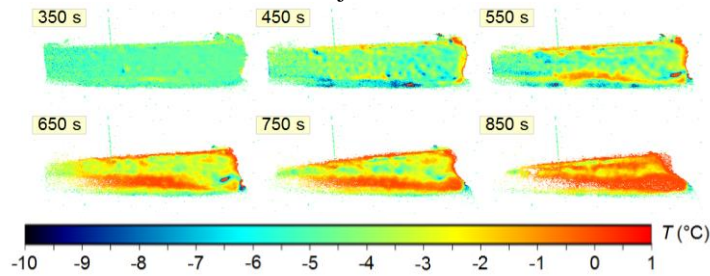


Figure 4. Temperature fields of a 6-ml ice block obtained using PLIF with White Image Correction.

Figure 5 illustrates the variation ranges of Rhodamine B concentration in an ice block where PLIF is applicable and, on the contrary, where optical measurements have a large systematic error.

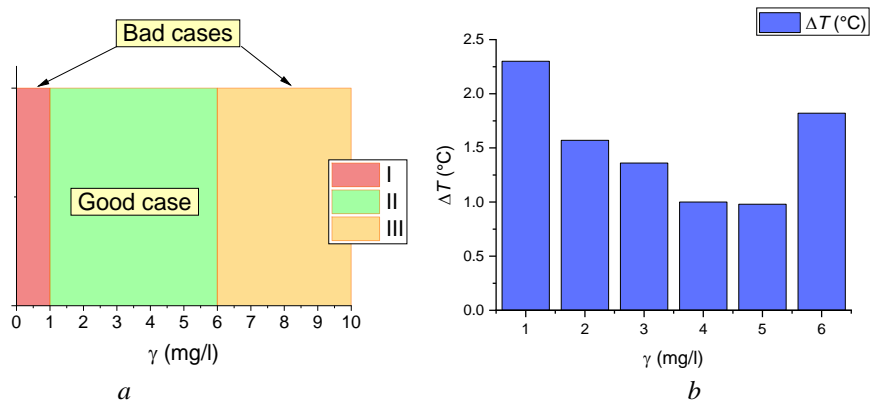


Figure 5. Rhodamine B concentration ranges in an ice block in which PLIF provides accurate temperature measurement and those in which such optical measurements are inapplicable (a), PLIF data deviation from thermocouple measurements for zone II (b).

CONCLUSIONS

This research has brought to light certain limitations of PLIF in measuring ice block temperature:

- PLIF demonstrates acceptable measurement accuracy when the fluorophore concentration in the water solution is around 5 mg/l. Lower concentrations result in insufficient light intensity emitted by Rhodamine B, barely surpassing the image's background intensity. Conversely, at higher concentrations, excessive laser light absorption by the ice block causes the emitted light intensity to significantly exceed the sample's fluorescence intensity;
- PLIF proves effective for determining ice block temperature when the temperature is above $-5\text{ }^{\circ}\text{C}$;
- PLIF is suitable for determining ice block temperature at a depth of no more than 20 mm.

REFERENCES

- Antonov, D. V., Gaidukova, O. S., Dorokhov, V. V., Misyura, S. Y., Morozov, V. S., Shlegel, N. E. and Strizhak, P. A., 2023. "Heat and mass transfer at the ignition of single and double gas hydrate powder flow in a reactor". *International Journal of Heat and Mass Transfer*, Vol. 209, N. 124121.
- Erdiwansyah, Mahidin, Husin, H., Nasaruddin, Zaki, M. and Muhibbuddin, 2021. "A critical review of the integration of renewable energy sources with various technologies". *Protection and control of modern power systems*, Vol. 6, pp. 1–18.
- Gambelli, A. M. and Rossi, F., 2022. "Formation rate as parameter to distinguish nucleation from hydrate massive growth phase: Experimental investigation in presence of two different porous media". *Experimental Thermal and Fluid Science*, Vol. 131, N. 110525.
- Lin, Y., Li, T., Liu, S., Shi, Q., Xu, K., Zhang, Z. and Wu, J., 2023. "Interfacial mechanical properties of tetrahydrofuran hydrate-solid surfaces: Implications for hydrate management". *Journal of Colloid and Interface Science*, Vol. 629, pp. 326–335.
- Manjhi, S. K. and Kumar, R., 2020. "Performance analysis of coaxial thermocouples for heat flux measurement of an aerodynamic model on shock tube facility". *Measurement*, Vol. 166, N. 108221.

MODELING OF EFFECTIVE HEAT INSULATION METHODS FOR VERTICAL FARMING IN A GREENHOUSE

Vitaly Haslavsky^{a,*}, Helena Vitoshkin^b

^aAzrieli Academic College of Engineering 26 Yaakov Shreibom Street, Jerusalem, Israel

^bAgricultural Research Organization, The Volcani Center P.O.Box 6, 5025001, 68 Dereh Hamacabim, Rishon Iesion, Israel

*vitaliha@jce.ac.il

Keywords: thermal screens, U -value; heat loss; greenhouse insulation

1. INTRODUCTION

Vertical farming is becoming a possible solution to mitigate food security risks resulting from soil degradation, a reduced amount of available arable lands and climate instabilities. It is gaining popularity due to its ability to utilize space and raw materials more effectively, and to manage more growth seasons during a year. However, significant challenges remain, including high initial investment and operation costs, energy consumption, and limited experience with plant cultivation in controlled environments (Kozai *et al.*, 2019, Van Delden *et al.*, 2021). The proposed approach involves utilizing existing buildings and incorporate growth system inside them. This method allows gradual experimentation and making more informed decisions with an investment of time and money acceptable to any farm owner. The objective of the current study is to integrate different models investigated in previous studies into a computational fluid dynamics (CFD) simulation platform. The modeling aims to evaluate different heat insulation methods for multilevel greenhouses under various external weather conditions.

2. METHODS

A three dimensional greenhouse CFD model was developed using ANSYS Fluent software based on the dimensions of a real commercial hydroponic greenhouse located in Bnei Atarot in the central region of Israel. The CFD model was utilized to simulate airflow dynamics using k - ϵ turbulent model, solar radiation using Monte-Carlo method, and temperature distribution in the greenhouse using conservation equations for free convection. Plant transpiration rates, assumed to be uniform, were included to the energy equations as constant mass rates. Further details on the model setup and validations can be found in our previous publications (Vitoshkin *et al.*, 2021a, Haslavsky *et al.*, 2022a, Vitoshkin *et al.*, 2023). We investigate a three-level growth system employing nutrient film technique (NFT) channels, which were distributed at two different densities (30% and 20%) above standard growth tables located at the lower level with 80% planting density. Three levels of growing crops were examined, each positioned 1 meter above the lower level and 1 meter above the middle level, as illustrated in Figure 1a. The domains of the crop growth channels were modeled as rectangular parallelepipeds of $2 \times 0.2 \times 0.06$ m (L \times H \times W) using porous medium approach (Fang *et al.*, 2020). Different aerodynamic porosity coefficients were applied referencing various planting densities and plant development stages. The porosity coefficients were determined through experiments in a wind tunnel using different types and dimensions of leafy plant. The experimental setup is shown in Figure 1b. The insulation characteristics of the thermal screens, quantified in terms of U -values, were determined using an analytical model that was validated through experiments (Vitoshkin *et al.*, 2021b). These values were then integrated into the numerical model using User Defined Function (UDF). The overall heat transfer coefficient, U , was defined as inverse value of the total system thermal resistance including outdoor, R_{out} , thermal screens $R_{screen,i}$, gaps between screens, $R_{gap,i}$, and indoor, R_{in} , resistances:

$$U = 1 / \left(R_{out} + \sum_{i=1}^n R_{screen,i} + \sum_{i=1}^n R_{gap,i} + R_{in} \right) \quad (1)$$

where R_{out} is the thermal resistance on the outdoor side of the glazing system involving radiative heat transfer between the system and environment and convective heat transfer modelled using correlations for heat transfer coefficient representing natural or forced convection over a flat plate.

After integration of all components of the model, the internal climate within the three-level greenhouse was simulated using ambient climatic data as the boundary conditions. Several extreme hot days during the summer and cold night periods in the winter within the Israeli climatic zone were investigated. For reference and validation of the model, indoor microclimate monitoring, global and photosynthetic active radiation (PAR) irradiation measurements, and measurements of the light spectrum were conducted in the hydroponic greenhouse. These measurements were then compared with

calculated results from the model. This analysis aimed to define effective heat insulation strategies for cultivation within a multi-level greenhouse.

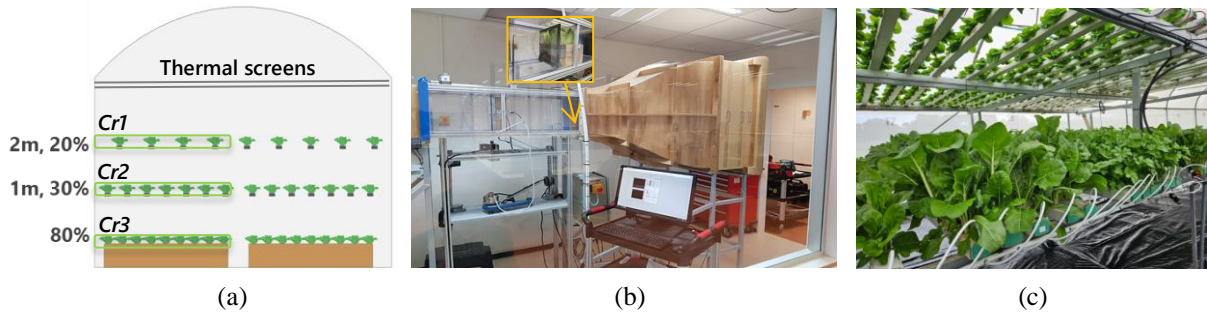


Figure 1. a) The geometry of the numerical model of the three-level hydroponic greenhouse (utilizing NFT growth method) was created using ANSYS Fluent software. The crop domains (porous media) were defined using different resistance factors, $C_{r,i}$. Thermal resistance of the thermal screens was implemented using UDF function. b) Wind tunnel tests were introduced to find the aerodynamic porosity of different planting densities and type of plants. c) A snapshot of the hydroponic growing method implemented in the reference greenhouse in Bnei Atarot, Israel.

3. RESULTS

The air temperatures and humidifies measured within the reference greenhouse during a hot summer day and in cold winter night are presented in Figure 2a. It is shown that air temperature may reach larger than 40°C in summer and may drop to less than 10°C during cold winter night, while optimal air temperature ranges between of $20\text{--}23^{\circ}\text{C}$. Relative air humidity is recommended to be in the range between 70% and 80% during the light periods. Figure 2b illustrates the comparison between measured and calculated daily light integral. During the summer period, shading nets were used in the greenhouse to avoid heat overload due to high ambient temperatures. The recommended daily light integral for lettuce ranges between 12 and $30\text{ mol m}^{-2}\text{ day}^{-1}$, depending on the plant variety.

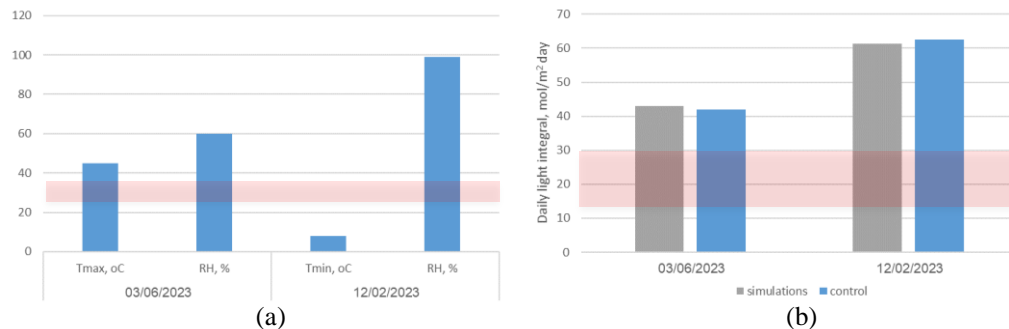


Figure 2. a) Indoor air temperatures and humidifies measured in the reference hydroponic greenhouse. b) Comparison between measured and calculated daily light integral. The recommended conditions for lettuce cultivation are depicted by the red rectangles.

The plants aerodynamic porosity was measured in a wind tunnel based on relationship between wind velocity, static pressure and density of the planting. The average porosity at varied plant densities was found to be 0.018, 0.145 and 0.42 for 20%, 30% and 80%, respectively. Additionally, the overall heat transfer coefficients (U -values) for horizontal single and doubled thermal screens were obtained as $8.4\text{ W/m}^2\text{C}$ and $3.8\text{ W/m}^2\text{C}$, respectively, based on properties of a commercial aluminized thermal screen of type NT16D (Hemming *et al.*, 2017). These aerodynamic porosity coefficients and U -values were used as input data in the simulation studies.

Figure 3 illustrates the results of the CFD simulations in the three-level greenhouse for the summer case. It is shown that implementing two horizontal ventilating fans above each level will provide uniform air velocity (Figure 3a). In addition, Figure 3b shows that for the configuration with a single thermal screen and given input parameters, the temperature is uniformly distributed between growth levels and is obtained as about 20°C , as required according to recommendations, while the greenhouse roof temperature is about 40°C . For the winter case, results indicate that two doubled thermal screens are required in order to maintain the microclimate conditions in the recommended range. Utilizing double-screen insulation during winter is a common practice among local farmers. Considering all these results, we assume that the proposed model is capable of replicating outcomes that closely resemble real-world scenarios.

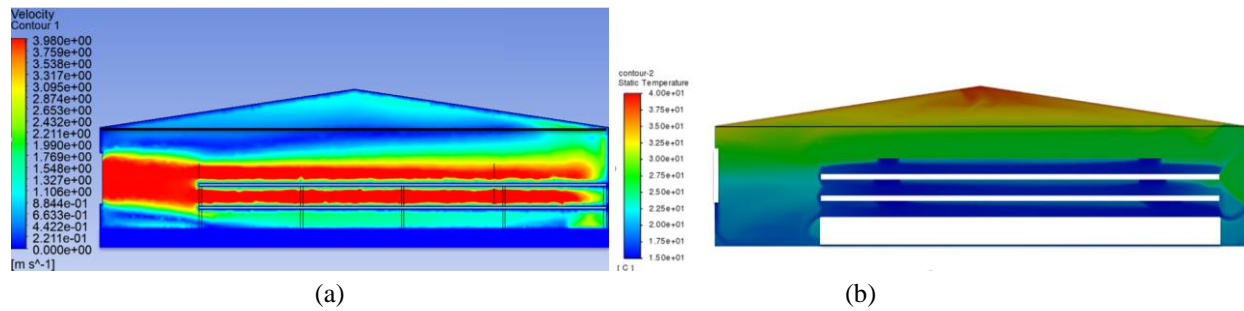


Figure 3. Results of CFD simulations in terms of a) velocity contours and b) static temperature distribution for a hot day in summer.

4. CONCLUSIONS

In the current study, numerical simulations were conducted to analyze air velocity and temperature distribution within a tree-level greenhouse. Our approach integrated solar radiation distribution, thermal insulation, and plant aerodynamic porosity models into the CFD model using ANSYS Fluent software. The model demonstrated capability to address radiative heat transfer problems and provide insights into the thermal, dynamic, and radiation fields across different growth levels. The analysis of data revealed that (i) adequate ventilation promotes more uniform growth conditions among levels, and (ii) comparison with measured greenhouse microclimate data showed good agreement, validating our model's accuracy. Therefore, the proposed model can be implemented as a valuable tool for further simulation thermal performance in vertical farming under different climatic conditions.

5. REFERENCES

- Kozai, T., Niu, G., & Takagaki, M. (Eds.), 2019 *Plant factory: an indoor vertical farming system for efficient quality food production*. Academic press.
- Van Delden, S. H., SharathKumar, M., Butturini, M., Graamans, L. J. A., Heuvelink, E., Kacira, M., & Marcelis, L. F. M. 2021 "Current status and future challenges in implementing and upscaling vertical farming systems." *Nature Food*, 2(12), 944-956.
- Vitoshkin H., Sacks M., Haslavsky V., 2021a "Microclimate analysis to test the performance of an experimental two-level unit in the hydroponic greenhouse", *Acta Hort. 1321. ISHS 2021. Proceedings of the III International Symposium on Soilless Culture and Hydroponics*.
- Haslavsky V., Ziffer E., Vitoshkin H., 2022a " Optical Modelling of supplemental LED Lighting in a Hydroponic Grenhouse ", *Proceedings of the 9th International Conference on Fluid Flow, Heat and Mass Transfer*.
- Vitoshkin H., Ziffer E., Sacks M., Haslavsky V., 2023 " Light Distribution in a Two-level Unit with Supplemental LED Lighting in a Hydroponic Greenhouse ", *Acta Hort. ISHS 2023. GreenSys International Symposium on on New Technologies for Sustainable Greenhouse Systems*.
- Fang, H., Li, K., Wu, G., Cheng, R., Zhang, Y., & Yang, Q., 2020 "A CFD analysis on improving lettuce canopy airflow distribution in a plant factory considering the crop resistance and LEDs heat dissipation" *Biosystems Engineering*, 200, 1-12.
- Haslavsky, V., Vitoshkin, H., Barak, Arbel, A., 2022b. Heat transfer coefficients of layers of greenhouse thermal screens. *Proceedings of the 8th World Congress on Mechanical, Chemical, and Material Engineering*.
- Vitoshkin, H., Haslavsky, V., Barak, M., Ziffer, E., & Arbel, A., 2021b "Numerical and experimental investigation of heat transfer across semi-transparent horizontal screen layers." *Journal of Building Engineering*, 42, 103082.
- S. Hemming, E.B. Romero, V. Mohammadkhani, B. van Breugel, 2017 "Energy Saving Screen Materials: Measurement Method of Radiation Exchange, Air Permeability and Humidity Transport and a Calculation Method for Energy Saving" (No. 1431) Wageningen University & Research, BU Greenhouse Horticulture

Effect of surface temperature on splashing of droplets impacting a cold superhydrophobic surface

Yuheng Shang^{a*}, Matic Može^b, Sylvie Castagne^c, David Seveno^d and Maria Rosaria Vetrano^a

^aKU Leuven, Department of Mechanical Engineering, Division of Applied Mechanics and Energy Conversion (TME), B-3001 Leuven, Belgium

^bUniversity of Ljubljana, Faculty of Mechanical Engineering, SI-1000 Ljubljana, Slovenia

^cKU Leuven, Department of Mechanical Engineering, Division of Manufacturing Processes and Systems (MaPS) and Flanders Make@KU Leuven M&A, B-3001 Leuven, Belgium

^dKU Leuven, Department of Materials Engineering, Division of Structural Composites and Alloys, Integrity and Nondestructive Testing (SCALINT), B-3001 Leuven, Belgium

*Yuheng.shang@kuleuven.be

Keywords: Droplet impact, splashing phenomenon, surface temperature, superhydrophobic surface

1. INTRODUCTION

The impact of droplets on solid surfaces is a common phenomenon in natural and technological processes, as exemplified by spray cooling (Almohammadi and Amirfazli, 2019), ink-jet printing (Zhao *et al.*, 2019), pesticide spraying (Zhang *et al.*, 2021). A droplet can either spread or splash when it impacts a solid surface and identifying the conditions under which splashing occurs plays a crucial role in the applications mentioned above. Therefore, significant efforts have been made to study the splashing behavior influenced by impact factors (droplet size D_0 , impact velocity V_0), liquid properties, and surface conditions. Almohammadi *et al.* found that when the viscosity of the liquid droplet is below 5 cSt, an increase in viscosity promotes splashing. However, when the viscosity of the liquid is above 5 cSt, an increase in viscosity suppresses splashing. Additionally, the impact of different liquid droplets, such as silicone oil (Almohammadi and Amirfazli, 2019), glycerol (Qin *et al.*, 2019), ethanol (Goede *et al.*, 2018), and surfactant solution droplets (Aytouna *et al.*, 2010), were investigated to understand the effect of surface tension. The results from Goede (Goede *et al.*, 2018) showed that the splashing velocity is independent of the wetting properties of the surface but increases roughly linearly with an increasing surface tension of the liquid. The above studies suggest that liquid viscosity and surface tension significantly affect splashing. However, most relevant studies concentrate on the influence of either viscosity or surface tension by using different liquids or a mixture of liquids. The combined effects of viscosity and surface tension on the splashing lowering temperature remain elusive. As the temperature decreases, viscosity and surface tension of water increase at the same time. This study is therefore focused on the effect of surface temperature on the splashing phenomenon of impacting water droplets on a cold surface at different initial Weber numbers.

2. METHODS

The experimental setup used for this study is schematized in Fig. 1. The experimental substrate and droplet delivery system are enclosed in a plexiglass chamber. To prevent frosting on the superhydrophobic surface, the relative humidity in the chamber is controlled by injecting dry nitrogen to replace the air in the chamber until the relative humidity is below 10%. The droplet diameter is fixed to 2.5 mm ($V = 8.2 \mu\text{L}$), while the impact velocity varies from 1.44 m/s to 2.41 m/s, corresponding to Weber numbers ($We = \rho V_0^2 D_0 / \sigma$) varying between 71 and 200. The superhydrophobic surface is made of aluminum coated with fluorinated alkyl phosphonic acid. To fabricate the surface, the aluminum substrate (1100 aluminum alloy from McMaster-Carr) was first finely ground and etched in 3M HCl solution to remove the native oxide layer. After rinsing in a wash bottle with DI water, the substrate was immersed in boiling water for 90 min, followed by drying in a convection oven. This ensured growth of pseudoboehmite and bayerite in the form of nanoneedles on the exposed aluminum. Prior to hydrophobization, the sample was treated in a UV/ozone cleaner to remove adsorbed volatile organic compounds (VOC), after which the hydrophobization agent (fluorinated alkyl phosphonic acid) was applied via drop casting of its 3 mM solution in isopropyl alcohol to create a low-surface-energy self-assembled monolayer. The static contact angle of a 5 μL MilliQ water droplet on this surface is $159.5 \pm 2.4^\circ$, which is obtained by tangent method. The substrate temperature is controlled by a Peltier element cooled by a chiller. The surface temperature varies from -9.8°C to -35.3°C , measured by a T-type thermocouple placed on the top of the surface. Two synchronized high-speed cameras are used to record the droplet impact processes. One camera provides the side view of the droplet impact, while the other ensures visualization of the process at an oblique view.

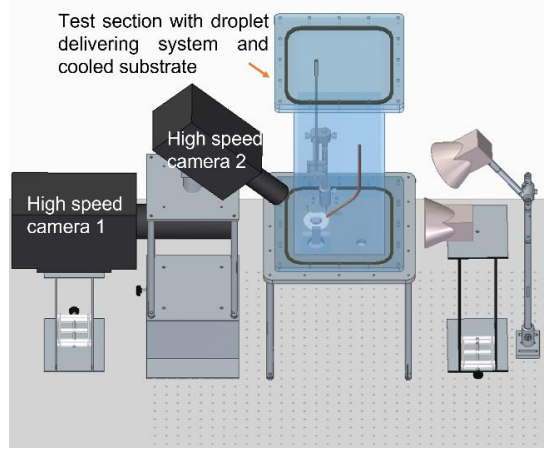


Figure 1. Schematic of the experimental setup.

3. RESULTS AND DISSCUSION

The dynamic behavior of impacting droplets is illustrated in Fig. 2. The time $t=0$ ms is defined as the moment immediately before the droplet makes contact with the surface. At the initial stage of spreading, the upper part of the droplet maintains a spherical shape, while the bottom part, in contact with the surface, spreads out to create a thin layer of liquid called a lamella (Almohammadi and Amirfazli, 2019). Next, the droplet continues to spread until it reaches its maximum diameter at around 2-3 ms, as denoted by the red rectangle in Fig. 2. Subsequently, the droplets retract to different extents. The interplay between the retraction velocity and freezing rate influences the retraction process. Then, the droplet keeps oscillating until reaching an equilibrium state. Based on the images taken at the maximum spread in Fig. 2, we find that the droplet profile varies greatly with surface temperature and Weber number. At $We=139$, an increase in surface temperature leads to the formation of splashing, producing many secondary droplets from the head of the fingering pattern around the main droplet, as demonstrated by the white circles in Fig. 2(b). With increasing surface temperature, the splashing phenomenon is enhanced and more secondary droplets are formed (Fig.2 (c)). Fixing the surface temperature to $T_s=-15.2$ °C, the following trends can be observed as the Weber number decreases. The splashing is reduced (Fig.2 (c) and (d)), and when We is reduced to 71, the droplet only forms a regular lamella rim. These results suggest that a sufficiently large Weber number is necessary for the formation of the splashing, and a relatively high surface temperature can further reinforce this phenomenon, which agrees with the formation mechanism of the splashing. The literature (Bird *et al.*, 2009) indeed states that splashing happens when the lamella's kinetic energy significantly surpasses the lamella's surface energy. A higher We leads to a more significant kinetic energy of the lamella, which is the prerequisite for splashing to appear. Moreover, the surface energy of the lamella decreases by increasing the surface temperature, which is beneficial to the occurrence of splashing.

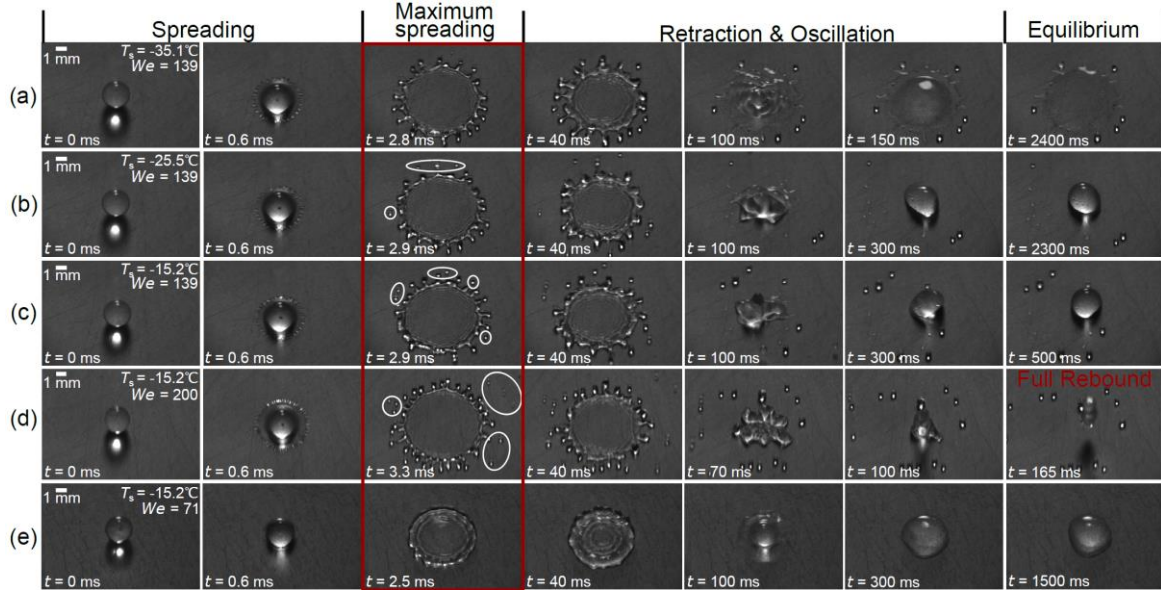


Figure 2. Dynamic behavior of droplets impacting a surface at different surface temperatures and Weber numbers: (a) $T_s=-35.1^\circ\text{C}$, $We=139$; (b) $T_s=-25.5^\circ\text{C}$, $We=139$; (c) $T_s=-15.2^\circ\text{C}$, $We=139$; (d) $T_s=-15.2^\circ\text{C}$, $We=200$; (e) $T_s=-15.2^\circ\text{C}$, $We=71$;

To characterize the dynamics of the process, the spreading factor can be defined as $\beta(t)=D(t)/D_0$, where $D(t)$ is the contact diameter of the droplet at the time t . Figure 3(a) shows the evolution of the spreading factor with the time for various surface temperatures and We numbers. Initially, β increases quickly for all cases until reaching a maximum value β_{max} . We see that β_{max} is larger at a higher We due to the increased inertial force, while the surface temperature only has a minor effect on β_{max} . The time when the droplet reaches β_{max} is denoted as t_{max} and changes insignificantly with We and surface temperature. In the retraction stage phase, we can observe two behaviors. First, for $We=139$, we see that the droplet retracts more (evidenced by β becoming constant) as the surface temperature increases since the freezing process is triggered later. Also, with a fixed surface temperature ($T_s=-15.2^\circ\text{C}$) the droplet retracts more as We increases. The possible outcomes in this study, *i.e.* spreading and splashing of the droplet impacting onto a superhydrophobic surface for various Weber numbers and surface temperatures are shown in Fig. 3 (b). The increase in We causes the transition from spreading to splashing. Furthermore, raising the surface temperature within a certain We range also intensifies the appearance of splashing.

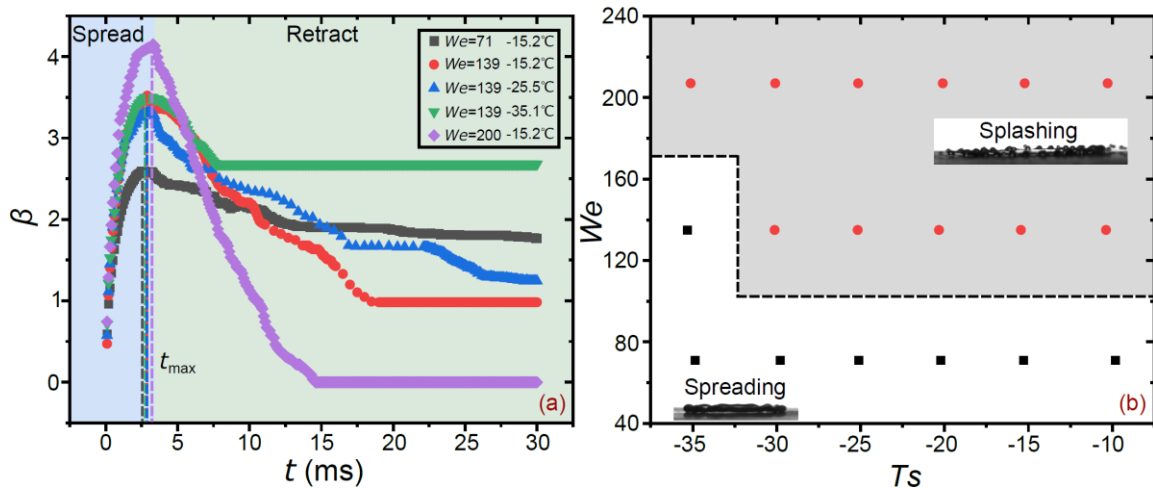


Figure 3. (a) Evolution of spreading factor at different experimental conditions. (b) Outcomes of droplets impacting on a superhydrophobic surface with different surface temperatures as a function of the Weber number.

4. CONCLUSIONS

The role of surface temperature in affecting splashing under different Weber numbers is studied. The results show that a relatively high Weber number is crucial for the formation of splashing and can enlarge the spreading area because a high Weber number leads to a significant kinetic energy of the lamella. Furthermore, the surface temperature affects splashing only in a specific Weber number range. A decrease in surface temperature leads to a larger surface energy of the lamella, which weakens the splashing phenomenon. The maximum spreading time is barely affected by the Weber number and surface temperature, while the retraction process highly depends on these two parameters.

5. REFERENCES

- Almohammadi H. and Amirfazli A., 2019. "Droplet impact: Viscosity and wettability effects on splashing". *Journal of Colloid and Interface Science*, Vol. 553, pp. 22-30.
- Aytouna M., Bartolo D., Wegdam G., Bonn D. and Rafai S., 2010. "Impact dynamics of surfactant laden drops: dynamic surface tension effects". *Experiments in Fluids*, Vol. 48, pp. 49-57.
- Bird J. C., Tsai S. S. H. and Stone H. A., 2009. "Inclined to splash: triggering and inhibiting a splash with tangential velocity". *New Journal of Physics*, Vol. 11, pp. 1-10.
- Goede T. C., Laan N., Bruin K. G. and Bonn D., 2018. "Effect of wetting on drop splashing of newtonian fluids and blood". *Langmuir*, Vol. 34, pp. 5163-5168.
- Qin M., Tang C., Tong S., Zhang P. and Huang Z., 2019. "On the role of liquid viscosity in affecting droplet spreading on a smooth solid surface". *International Journal of Multiphase Flow*, Vol. 117, pp. 53-63.
- Zhang H., Zhang X., Yi X., He F., Niu F. and Hao P., 2021. "Effect of wettability on droplet impact: spreading and splashing". *Experimental Thermal and Fluid Science*, Vol. 124, pp. 1-11.
- Zhao Y., Zhu F., Zhang H., New T. H., Jin L. and Yang C., 2019. "Triple condensate halo from a single water droplet impacting upon a cold surface". *Applied Physical Letters*, Vol. 114, pp. 1-5.

EXPERIMENTAL SETUP FOR MEASURING THE THERMAL NON-EQUILIBRIUM EFFECTS WITHIN TWO-PHASE EXPANSION

Xander van Heule^{a,*}, Michel De Paepe^{a,b}, Steven Lecompte^{a,b}

^aGhent University, Department of Electromechanical, systems and Metal Engineering,
Sint-Pietersnieuwstraat 41 Ghent Belgium

^bFlanders Make, Leuven, Belgium, FlandersMake@Ugent.be

*xander.vanheule@ugent.be

Keywords: Setup, thermal non-equilibrium, expander

1. INTRODUCTION

Currently, more than half of the primary energy that is burned is lost in the form of waste heat. Additionally, around 60% of this waste heat is within the low-temperature region of below 100°C (Forman *et al.*, 2016). This is in line with more recent findings of potential sources for waste heat recovery within the European Union (Bianchi *et al.*, 2019). Therefore, a necessity arises for heat-to-power cycles. Specifically for low-temperature heat sources. There exist multiple technologies to convert heat to power as summarized by Garofalo *et al.* (2020). In this work, the focus is on the Organic Rankine Cycle (ORC) and alternatives as this cycle can be used within the temperature ranges of waste heat. The alternatives of the ORC that are of importance in the context of this work are the trilateral flash cycle (TFC) and the partially evaporating organic Rankine cycle (PEORC). Both these alternatives differ from the basic ORC within the evaporator. In the basic ORC, the working fluid at the outlet of the evaporator is in a superheated state while in the TFC it is a saturated liquid. The PEORC is in between with an evaporator outlet in the two-phase region. It has been shown that these alternative cycles have higher energy recovery efficiencies for low-temperature heat sources (Saghafifar *et al.*, 2019)(Paanu *et al.*, 2012). The improved energy recovery is due to the better temperature profile matching within the evaporator (Lecompte *et al.*, 2015).

When the TLC, PEORC, or other cycles which incorporate two-phase expansion are studied in literature, the expansion is modeled under certain assumptions. Often, this occurs via an isentropic efficiency similar to vapour expansion machines. The other assumption frequently taken is that of thermodynamic stability during the expansion process. This assumption has been shown to not fully agree with experimental data for all expander types. For Lysholm expanders operating under two-phase expansion conditions, it was found to correlate relatively well with experiments (Öhman and Lundqvist, 2013) but not for reciprocating expanders (Kanno and Shikazono, 2015), where there were thermal non-equilibrium conditions measured during the expansion. The temperature of the liquid was determined to be greater than the saturation temperature corresponding to the instantaneous pressure. These observations were paired with non-equilibrium losses (Kanno and Shikazono, 2017). These losses could have an impact on the predictions of cycle performance which incorporate this type of expansion within its cycle. Therefore, it is necessary to predict these thermal non-equilibrium phenomena occurring. The goal of the constructed setup is to measure the thermal non-equilibrium expansion process and to quantify the losses with an empirical model.

2. EXPERIMENTAL SETUP

The P&ID of the experimental setup is presented in Fig. 1. The setup consists of two loops. The blue loop in the Figure is the chiller loop. The chiller vessel is a Thermoflex TF7500 which includes the pumping unit. The mass flow rate of the coolant to the heat exchangers can be finer controlled by an adjustable three-way valve (TV-0204). The cooling capacity ratio between the condenser (HX-0152) and the subcooler (HX-0104) is controlled with an extra valve (FV-0207). This valve can be operated with a constant signal or via a feedback signal with a subcooling setpoint at the outlet of the subcooler. The black loop is the refrigerant loop. Before an expansion experiment can occur, the refrigerant needs to be conditioned to the desired thermodynamic state. This thermodynamic state is achieved by increasing the pressure with the pump (PE-0106) and afterward heating the subcooled liquid to the desired state which is achieved with an electrical heater (HT-0113). The required amount of heat can be calculated with the energy balance over this heater as the subcooled liquid state can be determined by the pressure (PT-0111) and temperature (TT-0112) measurements. While the refrigerant is being conditioned, the setup runs in by-pass to minimize any leakages within the piston expander. Once the desired setpoint is reached, the piston can be loaded by toggling the pneumatic valves. After toggling the valves again, the test chamber is isolated and an expansion experiment can be performed by controlling the linear actuator (LA-0147). All volumes are connected to the by-pass with safety valves in the event of overpressure in any part of the setup.

The goal of the setup is to measure the expansion process of a known two-phase thermodynamic state within a piston with a predefined movement profile. The predefined movement is achieved with a linear motor (LA-0146) which can be

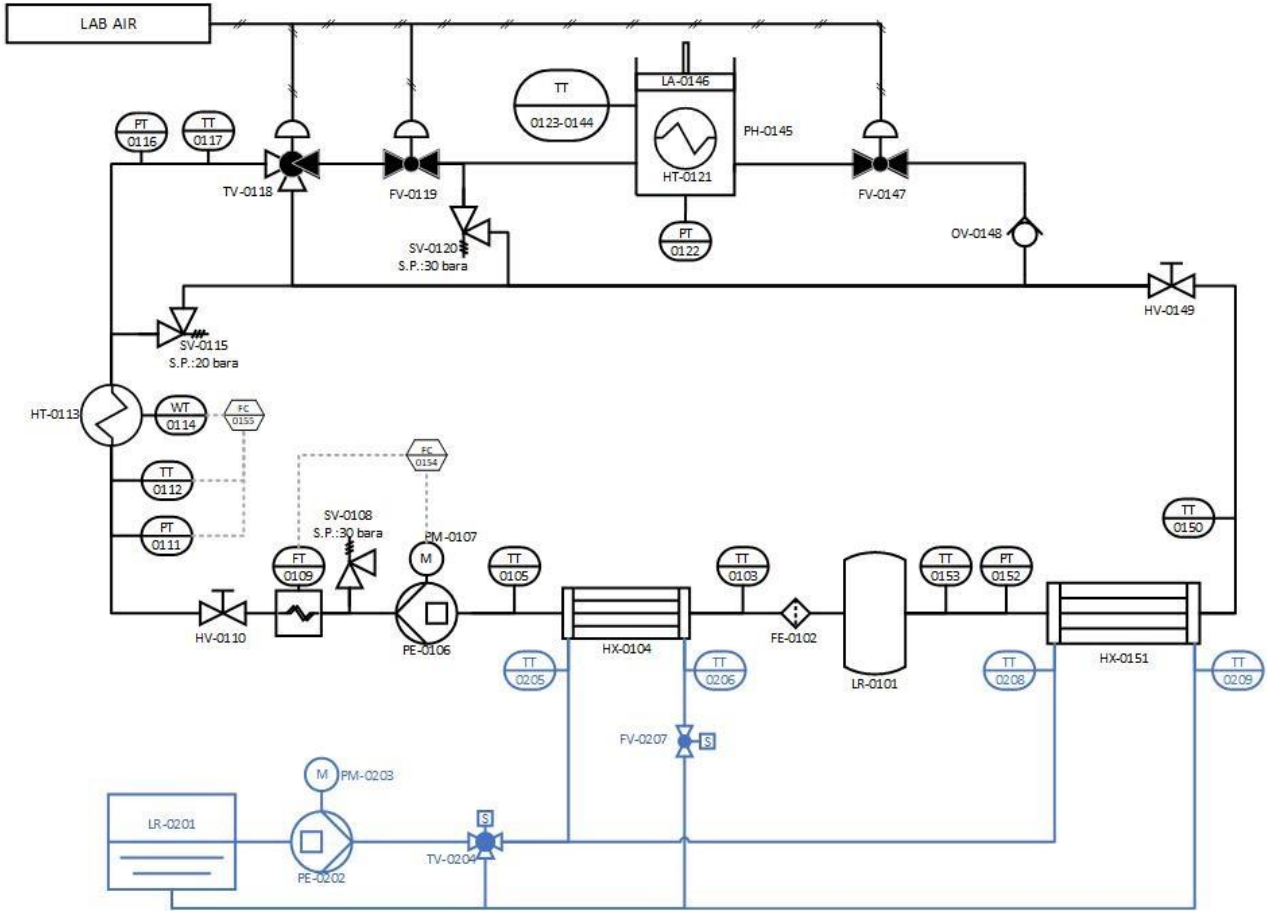


Figure 1: P&ID of the experimental setup.

position controlled. In this manner, the volume of the expansion chamber can be controlled and determined at each moment in time. The thermodynamic state of the fluid which expands needs to be conditioned to the desired state. The rest of the setup is used for this purpose as will be explained hereafter. First, the refrigerant is a two-phase mixture within the liquid receiver (LR-0101). The desired pressure (PT-0122) is set with a combination of the pump (PE-0106) and the position of the manual valve (HV-0149). A subcooler (HX-0104) is installed between the pump and the liquid receiver to protect the pump against cavitation. The degree of subcooling can be controlled with the valve (FV-0207) in the chiller circuit. The thermodynamic state at the outlet of the pump, in the liquid region, is determined with a temperature (TT-0112) and pressure (PT-0111) measurement. The flow rate needs to be known for later calculations, therefore a Coriolis mass flow meter (FT-0109) is installed in this liquid region. The manual valve (HV-0110) is used to zero the mass flow meter whenever necessary. In this region, an overpressure safety valve (SV-0108) is also installed to protect the entire setup from overpressures. After setting the desired pressure, the desired vapour quality (or superheat) can be set. This is achieved with an electrical heater (HT-0113). The energy balance across this heater is used to determine the vapour quality at the outlet of the heater as presented in Eq. (1) and Eq. (2).

$$x_{out} = \frac{h_{out} - h_{liq}}{h_{vap} - h_{liq}} \quad (1)$$

$$h_{out} = \frac{Q_{heater}}{\dot{m}} + h_{in} \quad (2)$$

where x_{out} is the vapour quality at the outlet of the heater, h_{out} and h_{in} the enthalpy at the outlet and inlet of the heater respectively, Q_{heater} the heat input within the heater, and \dot{m} the mass flow rate of the working fluid through the heater.

While conditioning the working fluid, the setup runs in bypass. The three-way valve (TV-0118) is unpowered and shuts off the intake of the expansion chamber. The quick-acting valves (FV-0119, FV-0147) are also closed, which isolates the expansion chamber. Once the working fluid is conditioned to the desired thermodynamic state, all three valves are toggled. The working fluid now flows through the expansion chamber. The linear motor keeps the piston at its top position. Once the flow is steady, all three valves are toggled again. This isolates the expansion chamber once again and returns the flow through the bypass in the three-way valve. During this toggling, there is a risk of dead-end tubes where

the pressure would drastically increase. Therefore, multiple overpressure safety valves (SV-0115, SV-0120) are installed. If the pressure in any volume is too high, this overpressure gets vented to the bypass.

The preconditioned working fluid is isolated in the expansion chamber with a known dead volume. With the density at this state, it is possible to determine the mass content of the working fluid in the isolated volume. The linear motor is freely controlled to expand the working fluid with a predefined movement profile. The pressure (PT-0122) in the expansion chamber is logged together with multiple temperature (TT-0123-TT-0144) measurements all around the expansion chamber. After the expansion stroke, time is given for the fluid to achieve thermodynamic equilibrium. Afterwards, if this equilibrium is within the two-phase region, the expansion chamber is heated with a trace heater (HT-0121) to evaporate the working fluid. At a superheated vapour state, the density can be determined based on temperature and pressure measurements. This density and end volume result in a second method to calculate the mass content of the isolated volume. The two calculated masses will be compared to one another for a measure of the leakage losses. These losses will have to be minimized for reliable experiments.

Finally, after the experiment. The outlet valve (FV-0147) is opened and the linear motor moves back to the start position while venting the previous measurement working fluid to the bypass through the check valve (OV-0148). The condenser (HX-0151) condenses the working fluid to close the refrigerant loop.

3. MEASUREMENTS

Currently, the setup is finished and the measurement equipment is calibrated. However, the refrigerant is not yet loaded. This will happen in the near future and measurements should be available before the paper submission deadline.

The refrigerant that will be used is R1233ZD(E) as it is a low GWP refrigerant with fitting thermo-physical properties and is well-suited for low-temperature heat recovery applications (Iqbal et al., 2019).

4. CONCLUSIONS

Methods to recover low-temperature waste heat streams are a necessity to recover a large amount of the energy that is currently lost. There are some promising technologies for this, such as the trilateral flash cycle and the partially evaporating organic Rankine cycle. However, these technologies still require more knowledge. Mostly in the area of the expansion device. It has been shown that under certain circumstances, the working fluid can exist in thermal non-equilibrium thermodynamic states due to the required speed of evaporation. This results in non-equilibrium losses. In this work, a setup was constructed to measure the thermal non-equilibrium phenomena occurring within a reciprocating expander. With this data, an empirical model can be constructed to predict the behavior and performance of the expander and cycle.

5. REFERENCES

- Bianchi, G., Panayiotou, G.P., Aresti, L., Kalogirou, S.A., Florides, G.A., Tsamos, K., Tassou, S.A. and Christodoulides, P., 2019. "Estimating the waste heat recovery in the European Union Industry". *Energy, Ecology and Environment*, Vol. 4, pp. 211–221.
- Forman, C., Muritala, I.K., Pardemann, R. and Meyer, B., 2016. "Estimating the global waste heat potential". *Renewable and sustainable Energy Reviews*, Vol. 57, pp. 1568–1579.
- Garofalo, E., Bevione, M., Mattiussi, F. and Chiolerio, A., 2020. "Waste heat to power: Technologies, current applications, and future potential". *Energy Technology*, Vol. 8, pp. 1-22.
- Iqbal, M.A., Rana, S., Ahmadi, M., Date, A. and Akbarzadeh, A., 2019. "Trilateral Flash Cycle (TFC): a promising thermodynamic cycle for low grade heat to power generation". *Energy Procedia*, Vol 160, pp. 208-214.
- Kanno, H. and Shikazono, N., 2015. "Experimental and modeling study on adiabatic two-phase expansion in a cylinder". *International Journal of Heat and Mass Transfer*, Vol 86, pp. 755-763.
- Kanno, H. and Shikazono, N., 2017. "Modeling study on two-phase adiabatic expansion in a reciprocating expander". *International Journal of Heat and Mass Transfer*, Vol 104, pp. 142-148.
- Lecompte, S., Huisseune, H., van den Broek, M. and De Paepe, M., 2015. "Review of organic Rankine cycle (ORC) architectures for waste heat recovery". *Renewable and sustainable energy reviews*, Vol. 47, pp. 448-461.
- Öhman, H. and Lundqvist, P., 2013. "Experimental investigation of a lysholm turbine operating with superheated, saturated and 2-phase inlet conditions". *Applied Thermal Engineering*, Vol. 50, pp. 1211-1218.
- Paanu, T., Niemi, S. and Rantanen, P., 2012, "Waste heat recovery – bottoming cycle alternatives". In *Proceedings of the University of Vaasa*, Vol. 175: p. 1-26.
- Saghafifar, M., Omar, A., Mohammadi, K., Alashkar, A. and Gadalla, M., 2019, "A review of unconventional bottoming cycles for waste heat recovery: Part I – Analysis, design, and optimization", *Energy conversion and Management*, Vol. 198, pp. 110905.

EXPERIMENTAL COMPARISON OF THERMAL STORAGES WITH PCM AND WATER

Raniero Trinchieri^a, Maurizio Pieve^{a*}, Francesco D'Annibale^a

^aENEA, Via Anguillarese 301, 00123 Roma

*maurizio.pieve@enea.it

Keywords: heat storage, PCM, heat exchangers

1. INTRODUCTION

PCM-based systems can be used to store quantities of heat greater than those of conventional water tanks of the same volume by exploiting the latent heat of the phase change. Recently, the building sector has also benefited from their use. For instance, PCMs can be adopted for space heating and cooling applications by integrating them into the heat pump equipment in many configurations, in order to shift buildings' peak energy demand and improve stability to the electric grid. Another application deals with the defrosting of finned coils of air sourced heat pumps, where the stored heat may be used for preheating the external ambient air entering the evaporator, so that the frosting point conditions are prevented or delayed. In the latter case, the advantage of using a PCM storage compared to water increases, as it is possible to operate with reduced temperature differences, appropriately choosing the features of the PCM based on the temperatures of the media with which the tank exchanges heat.

In this study, we analyse a tank consisting of a container filled with PCM, where a finned heat exchanger is immersed in which a heat transfer fluid circulates, in our case water. Such a configuration would allow the improvement of the heat transfer, especially in terms of increase of the thermal conductivity.

An experimental comparison is made between a traditional storage system and a PCM (Phase Change Material) one. More than 150 tests were performed, as well as the analysis of the system response to a fluid temperature step variation at the inlet of the main heat exchanger. The outlet temperature of the heat exchanger fluid and the heat transferred were monitored during the charging and discharging phases. Two different finned heat exchangers immersed in the storage medium (water or PCM, type paraffin PlusICE A46 by PCM Products Ltd) were used for testing many different temperature steps, mass flow rates and boundary conditions.

2. EXPERIMENTAL APPARATUS

In order to evaluate the efficiency of the PCM based thermal storage, an experimental loop was created using a system capable of measuring the thermal energy stored over time, after a change of the primary fluid temperature, for different types of storage. The system is made by two closed circuits, both connectable to the test section (Fig. 1). The first circuit (upper part of the diagram) brings the test section to the initial conditions, providing a water mass flow at the initial temperature of the step to be tested. For this purpose, a thermostated tank is used with part of the flow rate of the circulation pump diverted onto the external circuit. The second circuit is designed to provide the water mass flow at the final temperature of the step, keeping this temperature at the test section inlet as constant as possible. The flow rate supplied by a volumetric pump is preheated to the desired temperature and introduced into an insulated tank, which stabilizes the temperature by absorbing any oscillations, especially at the beginning of the transient. It then goes through the test section and finally into a heat exchanger to dissipate the energy provided by the storage.

Table 1. Main features of tested heat exchangers

Heat Exchanger 1 (HX1)		Heat Exchanger 2 (HX2)	
Weight [kg]	0.461	Weight [kg]	0.304
Internal volume [cm ³]	117	Internal volume [cm ³]	56.3
Tube length [mm]	1720	Tube length [mm]	1706
Tube inner diameter [mm]	8.98	Plate width [mm]	32.2
Tube outer diameter [mm]	10.0	Plate thickness [mm]	2.0
Tube thickness [mm]	0.508	n. of channels	25
Flow section area [mm ²]	63.40	Flow section area [mm ²]	25
Overall HX thermal capacity [J/K]	280.1	Overall HX thermal capacity [J/K]	264.96

The measurement of temperatures at the inlet and outlet of the test section provides the heat transfer rate between the primary water and the thermal storage. The test section consists of a container with a finned heat exchanger immersed in the storage material with thermocouples for measuring the temperature of the primary liquid (inlet, outlet) and the storage. The preheater power supply and the pump speed are regulated by the automatic control system to maintain the inlet temperature and flow rate at the set values, respectively. The loop is appropriately instrumented to allow possible technical evaluations. The heat exchangers features are summarized in Table 1.

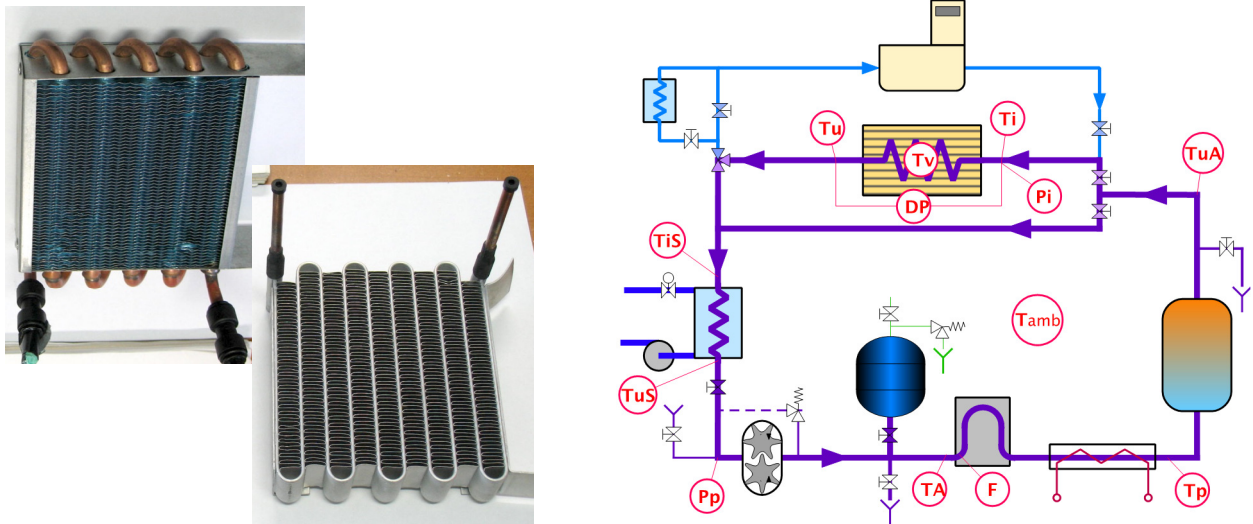


Figure 1. Tested heat exchangers (HX1 and HX2) and schematic of experimental loop

3. PROCEDURES FOR TESTING AND EXPERIMENTAL TESTS

Operationally, the preparation and testing procedures are as follows: an upward step (Heaviside-like), starting with cold (solid) PCM where we introduce water at a higher temperature, to store heat by “charging” the PCM and a downward step, where starting with hot (liquid) PCM we introduce water at a lower temperature, to “discharge” the PCM. More than 150 experimental tests were carried out, with two different heat exchangers, whose details are summarized in Table 2. The temperature steps are generally symmetrical with respect to the phase change temperature of the PCM used ($T_{pc}=46^{\circ}\text{C}$). In order to compare the performances, the same steps were also used in tests with water, where obviously there is no phase change.

4. EXPERIMENTAL RESULTS

Main results concern the comparison between the storage capacity of the two systems (water and PCM) and the efficiency of the two different geometries of the exchangers. As regards the storage capacity, the PCM storage guarantees greater specific heat transfer rate during the transient, especially when the thermal difference of the primary fluid is lower (ΔT 20°C vs ΔT 40°C), because of the better exploitation of the latent heat phase and the reduction of heat transfer due to convection and conduction in water (Fig. 2).

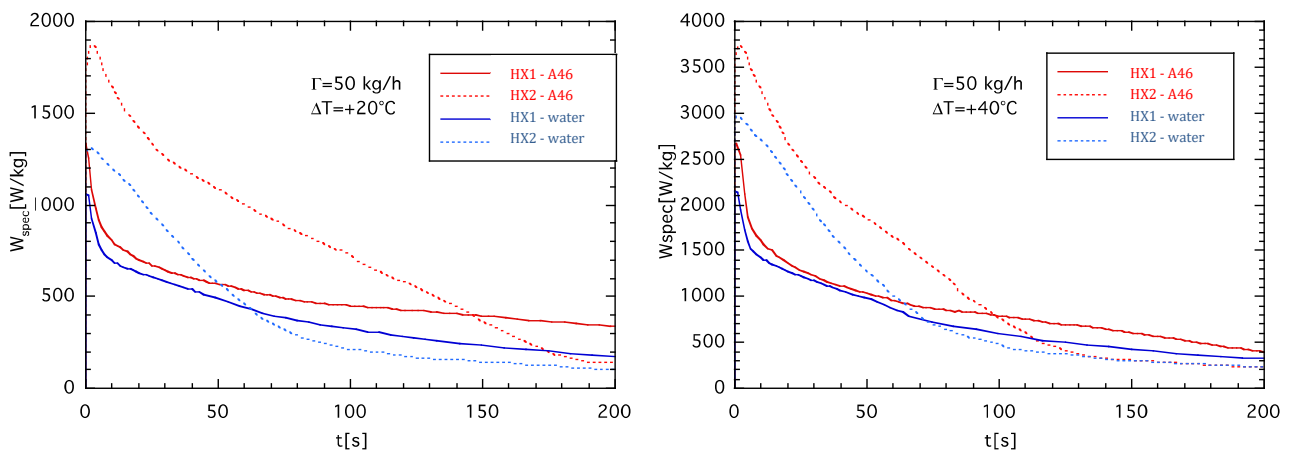


Figure 2. Comparison between specific heat transfer rate with water and PCM A46, different ΔT , HX1 and HX2.

Table 2. Experimental test matrix

Storage fluids: water and PCM A46		
Primary mass flow rate: Γ [kg/h]= 15, 30, 50, 70		
Temperature steps		
ΔT [°C]	T_{in} [°C]	Description
10, 20, 30, 40	41, 36, 31, 26	Symmetrical step referred to T_{pc}
-10, -20, -30, -40	51, 56, 61, 66	

The heat storage capacity is strongly affected by the geometry of the exchangers inside the tank, as already seen in Fig. 2. In addition, Fig. 3 shows, for the case with $\Delta T = 20$ °C, that the geometry of HX2 offers advantages compared to HX1 in terms of specific energy transferred and an energy storage index r_E , defined as the ratio between the energy actually exchanged over time and the theoretical maximum that can be stored.

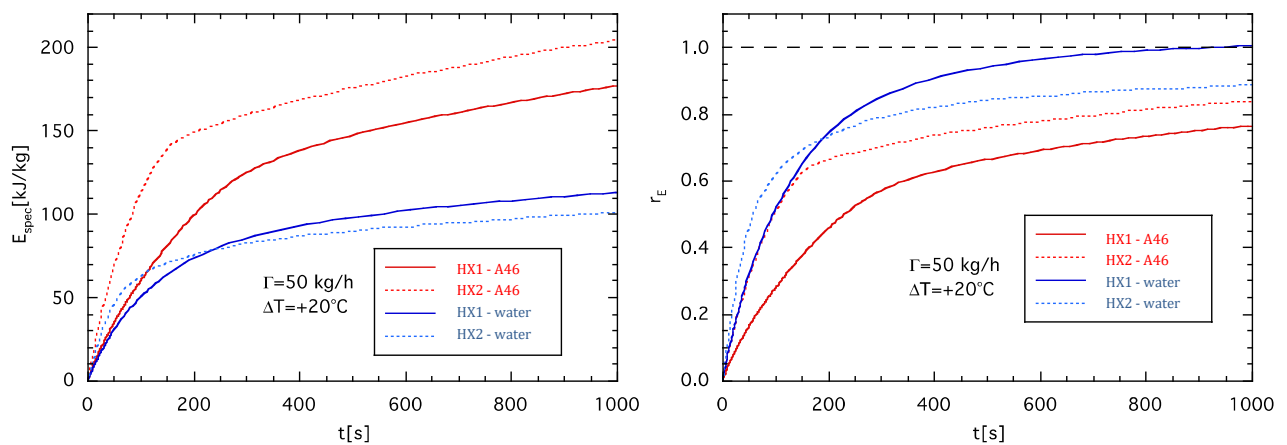


Figure 3. Specific stored energy and energy storage index with water and PCM A46, $\Delta T = 20$ °C, HX1 and HX2.

In the case of water storage, it can be noted that the energy storage index has higher values, especially in the beginning stages due to the shorter duration of the transient, that is consistent with the lack of a phase change in the range of operating temperatures. Therefore, a water storage would reach its theoretical limit of storable energy (e.g. charging phase) more quickly, which in any case would be significantly lower than that achievable with the PCM. The superiority of the latter in terms of storable energy overcompensates for its lower r_E in the first stages, so that the useful energy actually stored by the PCM is higher. The comparisons were carried out on the two heat exchangers by evaluating different temperature steps of the primary fluid, symmetrical with respect to T_{pc} and different flow rates.

5. CONCLUSIONS

The most important indication from the experimental tests is that the PCM storage is potentially suitable for many technical applications. First of all, it guarantees a greater specific thermal energy storability, if its latent heat phase is exploited by the heat transfer mechanisms of primary fluid.

The heat transfer rate capability during the analyzed transients of PCM storage is always better than a water conventional storage. The energy actually transferred depends on how the storage tank is operated. With the PCM such energy is conditioned by the operating temperature range of the primary fluid. In particular, as the temperature variation of the primary fluid (being around T_{pc}) decreases, the advantage of the PCM storage increases.

The tests also demonstrate that the heat exchanger geometry is crucial for exploiting the storage potential of the PCM tank. In particular, the HX2 exchanger with microchannels proved to be much more effective than the other, probably because of a better arrangement of the finned surface, and a more widely distributed layout of the primary water in the microchannels, which increases the heat transfer with the PCM even with lower ΔT . Such an effect may be exploited for instance for the frosting prevention of air-sourced finned coils of heat exchangers by means of a suited choice of the PCM temperature range.

MODELING AND INVESTIGATION OF THE TURBULENT WAKE RECOVERY IN THE WIND FARM AREA

Vladislav N. Kovalnogov*, Andrei V. Chukalin, Maria I. Kornilova, Ruslan V. Fedorov
Ulyanovsk State Technical University, Laboratory of Interdisciplinary Problems in Energy Production,
432027 Ulyanovsk, Russia
*kvn@ulstu.ru

Keywords: wind farm, RANS, mathematical modeling, aerodynamics, velocity deficit, turbulence intensity

1. INTRODUCTION

Renewables overtake coal in early 2025 to become the largest energy source for electricity generation globally. By 2028, potential renewable electricity generation is expected to reach 14 430 TWh, an increase of almost 70% from 2022. Over the next five years, several renewable energy milestones could be achieved: in 2024, variable renewable generation surpasses hydropower; in 2025, renewables surpass coal-fired electricity generation; in 2025, wind surpasses nuclear electricity generation; in 2026, solar PV surpasses nuclear electricity generation; in 2028, solar PV surpasses wind electricity generation.

The development of wind energy in the world is progressing due to reasonable efficiency in combating the carbon footprint and energy independence. According to the International Energy Agency, in 2024 the share of energy generated using wind is 8.6%, by 2028 the share is planned to grow to 12.1% (Renewables 2023 Analysis and forecast to 2028). 35 wind farms with a total capacity of 2,310 MW are operating in Russia by 2023, with another 3,569 MW to be commissioned by 2024 (Global Wind Report 2023).

When determining the wind farm location, the key parameter is the gross potential of the wind energy of the site, reflecting the feasibility of wind generation [Bezrukikh \(2010\)](#). Considering the Ulyanovsk wind farm area, the estimated specific gross potential of wind energy is $132 \text{ kW} \cdot \text{h}/(\text{m}^2 \cdot \text{year})$, taking into account the presence of the "air platinum" factor, according to which the complete restoration of flow parameters during flow obstacles with a height of H occur at a distance of $20H$ from it. According to research [Naumov et al. \(2016\)](#) for wind farms, a complete restoration of flow parameters is observed at a distance of $15D$ - $20D$ after wind turbines (where D is the diameter of the wind rotor). However, for reasons of some limitations (allocated area, length of cable lines, terrain and geology of the area), in practice, the distance between individual wind turbines can be only $5D$ - $7D$, which leads to a pronounced influence of the turbulent wake. Due to the aerodynamic effect of the turbulent wake, wind turbines generate less power in certain wind directions, and under certain turbulence conditions ($Re > 10^5$) can lead to increased fatigue loads of wind blades and their premature failure.

Modern work in the field of wind farm aerodynamics is mainly aimed at studying the structure of turbulent wakes of wind turbines and their interaction in order to find optimal wind farm layout. Wind farms interact with the lower part of the atmospheric boundary layer (ABL), which is characterized by significant turbulence. The issues of the influence of atmospheric stability and surface roughness on the ABL, their influence on the dynamics of wind turbines have not been sufficiently studied. In this connection, in order to maintain effective aerodynamic modes of wind farms operation, a comprehensive study of turbulent flows in the wind farm area is necessary, taking into account the complex nature of the interaction of the wind turbine array and the relief surface of the local territory with the ABL. In order to understand the interaction patterns and wind farms influence on the state of ABL, it is necessary to develop a methodology for mathematical modeling of exchange processes, which will allow taking into account the influence of a wind turbines array and terrain, as well as evaluate the effectiveness of wind turbine management in the actual conditions of ABL.

2. EXPERIMENTAL METHODS

2.1 The object of research

The wind farm is located on the territory of the Ulyanovsk region in the Cherdakli district. The capacity of the wind farm is 85 MW (Forward Energy). The wind farm includes 14 Dongfang DF 2500-110 wind turbines and 14 Vestas V126-3.45 wind turbines. The location of the wind farm is characterized by flat terrain, the height difference from south to north is no more than 22 m. The average height of the wind farm above sea level is no more than 90.5 m. The object of research in this work is a part of the Ulyanovsk wind Farm in the form of seven wind turbines located in the northern region of the wind farm. During the research work at the wind farm, the results of which were presented at the ICTIMESH 2023 conference and the analysis of the wind energy potential of the region [Kovalnogov et al. \(2022\)](#), the initial conditions for the development of digital wind turbine twins and modeling of the ABL were obtained.

2.2 Mathematical modeling

The mathematical formulation includes the equations of motion for the components of the air flow velocity, the equation of state and boundary conditions. To analyze turbulent flows in the wind farm area, it was decided to use the RANS approach and the $k - \varepsilon$ Garbaruk et al. (2012) turbulence model. The choice of this model is due to its advantages: accurate prediction of the properties of free shear flows, correct description of wall turbulence, test and description the method to solve the system of equations for this type of problems are described in Kornilova et al. (2023).

2.3 Computational domain and experimental conditions

The commercial software Star-CCM+ Academic Pack was used to perform the computational tasks. Fig. 1 shows a digital model of the wind turbine and the northern part of the Ulyanovsk wind Farm, which includes seven Vestas 126-3.45 MW wind turbines Kovalnogov et al. (2022).

The rotating part of wind turbines are highlighted. A study of grid convergence for calculating the turbulent wake in the near and far wake of wind turbines is presented in the work Kornilova et al. (2023). In this study, all wind turbines are oriented perpendicular to the flow direction (west wind direction), the number of revolutions is 8 rpm, the air flow velocity at the hub level is 7.5 m/s, the temperature is 295 K. The type of mesh used is Polyhedral mesh. The total number of calculated cells of the polyhedral grid was 14.9 million. pieces.

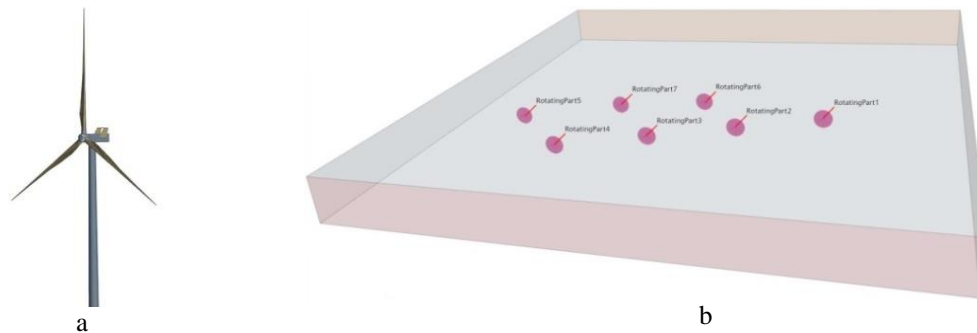
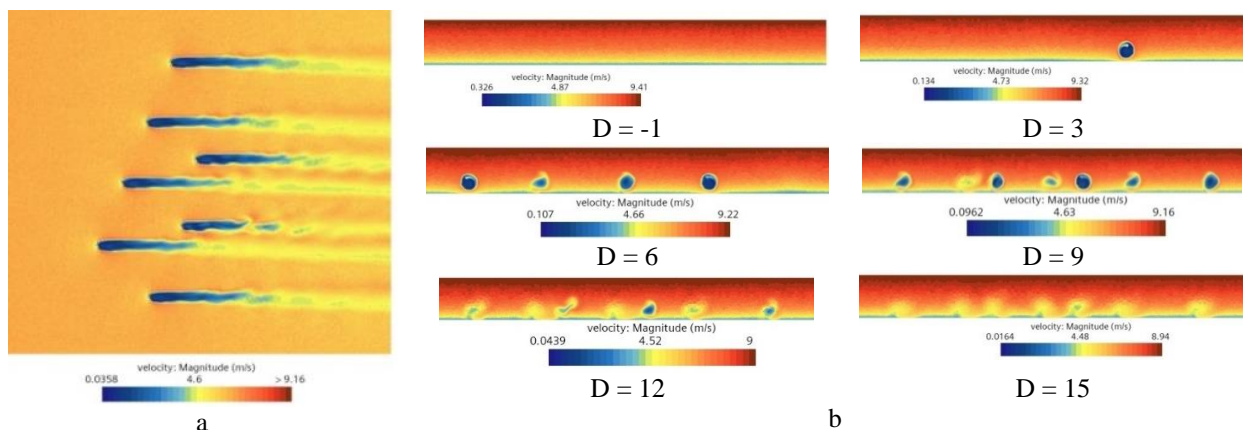


Figure 1. Digital model of the northern part of the wind farm: a) V126-3.45 MW wind turbine model; b) wind farm model

3. EXPERIMENTAL METHODS

In order to understand the interaction patterns and influence of wind farms on the state of the ABL, it is necessary to study the effect of air flow turbulence on the damping effect of the turbulent wake and its extent. Due to interaction with the terrain, changes in density, humidity and direction, the surface layer has a high level of initial turbulence. A series of calculations was performed at different initial values of the turbulence level: 0.01%; 0.05%; 0.08%; 0.13%. The simulation of the wind farm operation was carried out for sufficient time to ensure quasi-stationary flow conditions and statistical convergence of the results and amounted to more than 2 minutes of physical calculation time. The adequacy of the numerical solution obtained is confirmed by the convergence of calculations, the residuals of the quantities (Continuity, Energy, Sdr, Tke, X-momentum, Y-momentum, Z-momentum) are stable, without fluctuations, limited in magnitude. Fig. 2 shows the contours of the time-averaged flow velocity in the horizontal and vertical planes. The value D is the diameter of the wind turbine, equal to 126 meters.



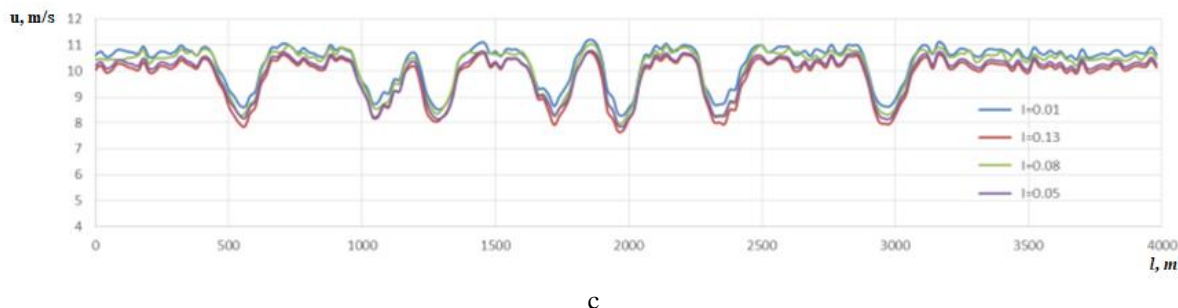


Figure 2. Distribution of the air flow velocity at the hub level of wind turbines: a) in the horizontal plane; b) in vertical planes; c) in the vertical plane at a distance of $D = 12$ at different values of the turbulence level: 0.01%; 0.05%; 0.08%; 0.13%

In the presented version, with a westerly wind direction, the location of wind turbines is optimal, since there is practically no wind turbine hits in the area of high turbulence of air masses. The velocity deficit is greatest near the wind turbine and becomes smaller as the wake expands and carries away the surrounding air. Nevertheless, the wake effect is still noticeable even at distances reaching $D = 15$. Figures 6 shows the wind turbines wakes. The calculation results demonstrate a non-axisymmetric distribution of the average velocity profile and, consequently, the average shear in the turbine wake. This is explained by the inhomogeneous (power-law) velocity profile of the incoming flow. As the next wind turbine flows around, a local drop in speed is observed. As can be seen from Fig. 3c, the velocity profile did not have time to recover at the simulated distance. The results showed that the recovery of the profile occurs somewhat faster with a higher value of atmospheric turbulence. Thus, with external atmospheric turbulence 0.08%, the velocity profile is restored 9.2% faster for the conditions under consideration than with the lowest considered turbulence value $I = 0.01$. The nature of the movement of air flows in the wind farm is unsteady and turbulent. The initial turbulence affects the velocity field both in the near ($2D-4D$) wake and in the far ($\geq 5D$) wake.

4. CONCLUSIONS

The paper presents the results of modeling and research of ABL in the Ulyanovsk wind farm area, consisting of seven wind turbines. The RANS approach was used to calculate with the $k - \varepsilon$ turbulence model, which is most suitable for studying small groups of wind turbines. The obtained values allow us to form a conclusion about several factors. Firstly, the turbulent wake of wind turbines is maintained at a distance of more than 15 diameters of the rotor of the wind turbine, which is successfully consistent with the conclusions of other authors, and secondly, high turbulence of the flow leads to the restoration of the flow by 9.2% faster compared to a flow with low turbulence. The nature of the movement of air flows in the territory of the wind farm is non-stationary and has a high level of turbulence. The initial turbulence affects the velocity field both in the near ($2D-4D$) wake and in the far ($\geq 5D$) wake.

5. ACKNOWLEDGEMENTS

The research was supported by the grant of the Russian Science Foundation No. 22-19-00030, <https://rscf.ru/project/22-19-00030/>.

6. REFERENCES

- Bezrukikh, P.P., 2010. "Wind Energy. Reference and methodological manual". Publishing house "Energiya", 320 p.
- Garbaruk, A.V., Strelets, M.H., Shur, M.L., 2012. "Turbulence modeling in calculations of complex flows: textbook" Publishing House of Polytechnic University, 88 p.
- Kornilova, M.I., Khakhalev, Yu.A., Kovalnogov, V.N., Chukalin, A.V., Tsvetova, E.V., 2023. "Mathematical Modeling and Numerical Research of the Aerodynamic Wake Behind the Wind Turbine of the Ulyanovsk Wind Farm". Thermal Power Engineering, No. 12. pp. 114-125.
- Kovalnogov, V.N., Fedorov, R.V., Chukalin, A.V., Tsvetova, E.V., Kornilova, M. I., 2022. "Modeling and Investigation of the Effect of a Wind Turbine on the Atmospheric Boundary Layer". Energies, Vol. 15, No. 21. – P. 8196.
- Naumov, I. V., Mikkelsen, R. F., Okulov, V. L., 2016. "Estimation of the range of propagation of the trace and the level of its pulsations behind the rotors of wind turbines". Thermal Power Engineering, No. 3, pp. 54-60.

DEVELOPMENT OF STATOR SECTOR MOCK-UP OF A HAIRPIN ELECTRIC MOTOR FOR DETAILED THERMAL TESTING OF DIRECT COOLED END-WINDINGS

Steven Vanhee^{a,b,*}, Jasper Nonneman^{b,c}, Frederik Desmet^b, Michel De Paepe^{b,c}

^aDana Incorporated, Light Vehicle Advanced Engineering, Bruges, Belgium

^bGhent university, Department of Electromechanical Systems and Metal Engineering, Ghent Belgium

^cFlandersMake@UGent, Core lab MIRO, Ghent, Belgium

*steven.vanhee@dana.com / steven.vanhee@ugent.be

Keywords: Electric Motor, Thermal Testing, Hairpin Winding, Direct Oil Cooling

ABSTRACT

This paper proposes a new testbench that is specifically developed to validate conjugate heat transfer CFD models for direct oil cooled electric motors. Firstly, the overall specification of the testbench will be introduced. Secondly, the setup instrumentation is discussed. Subsequently, initial test results are provided and, finally, a measurement accuracy analysis is made.

1. INTRODUCTION

Electrification in many industrial sectors, especially in automotive and aerospace, has created a new demand for highly power dense electric motors that can operate under very dynamic duty cycles (USDRIIVE, 2017). This demand has initialized the introduction of integrated cooling and lubrication systems (Carriero, Locatelli, Ramakrishnan, Mastinu, & Gobbi, 2018) (Gai, et al., 2019). These integrated systems demand for oil cooled electric motor solutions. Apart from lubrication and cooling of the bearings and gears, oil has attractive dielectric properties which enables to directly impinge the electric motor end-windings. Oil jet impingement cooling has been successfully implemented in several commercial electric drive units. Due to its high local heat transfer coefficients, oil jet cooling has a large cooling potential (Nonneman, Schlimpert, T'Jollyn, & De Paepe, 2020). In literature, the modelling of oil jet cooling is restricted to empirical heat transfer correlation of free oil jets. Ma et al. (Ma & Zheng, 1997) , Bennion et al. (Bennion & Moreno, 2015) and follow-up work by Feng et al. (Feng, et al., 2021) propose several empirical heat transfer correlations of oil jet impingement cooling. These authors provide valuable insights into the flow and heat transfer of oil jets impingement on horizontal circular target surfaces. However, the end-winding geometry is much more complex, limiting the accuracy of the existing models for electric motor applications (Nonneman, T'Jollyn, Sergeant, & Michel, 2020). The study of oil jet and spray cooling on hairpin end-windings has recently been focused on the development empirical heat transfer correlations for the complete end-winding (Liu, et al., 2021) (Liu, et al., 2022). Due to the geometric complexity of the hairpin end-winding and the difficulty to measure end-winding temperatures, makes these measurements difficult to interpret. As a consequence, This data is hard to use to validate thermal lumped parameter models or CFD models.

This paper proposes a new testbench that is specifically developed to validate conjugate heat transfer CFD models for direct oil cooled electric motors. Firstly, the overall specification of the testbench will be introduced. Secondly, the setup instrumentation is discussed. Subsequently, initial test results are provided and, finally, a measurement accuracy analysis is made.

2. TEST BENCH SETUP

Figure 1 shows the electric motor stator assembly that is being studied. The stator assembly includes a state-of-the-art 48-slot lamination stack with an outer diameter of 215mm and an active length of 145mm. The stator assembly further incorporates an 8-layer hairpin winding. The hairpin winding is formed from 4.115x1.83mm rectangular coated hairpin wires. Once inserted into the stator stack, the hairpin wires are bended and welded to form the required winding scheme.

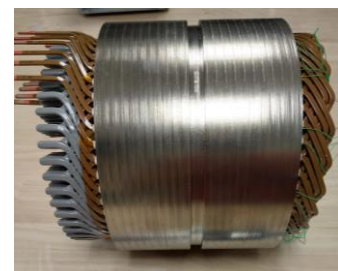


Figure 1 Stator assembly

In order to make a sector mock-up setup, the hairpin scheme is adapted to form a closed coil within 45° sector of the stator. In order to do so the hairpin design was mirrored on the weld side of the winding. As such a closed coil can be formed. A schematical overview of the winding configuration can be found in the Figure 2. Since this study is limited

to the cooling of the end-winding, the active section is not included in the proposed mock-up. Further, the electrical wires are made from stainless steel. The use of stainless steel not only allows to reduce the current density is the wires but also increases the temperature variation within the wires making it more suitable to measure temperature variation. The wires in between the stainless steel wires are 3D-printed from PFTE. An exploded view and the produced parts of both the PFTE 3D-printed winding layers and stainless steel wires are shown in Figure 3.

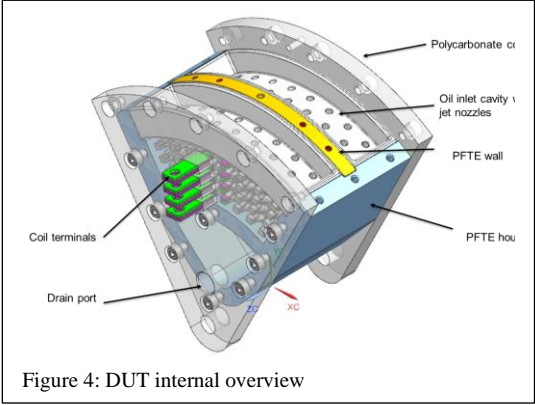
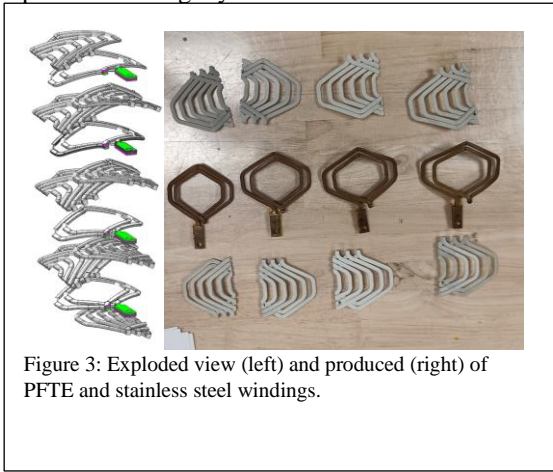
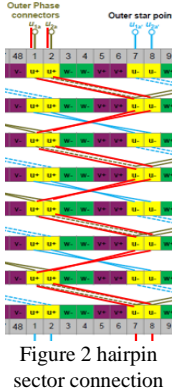
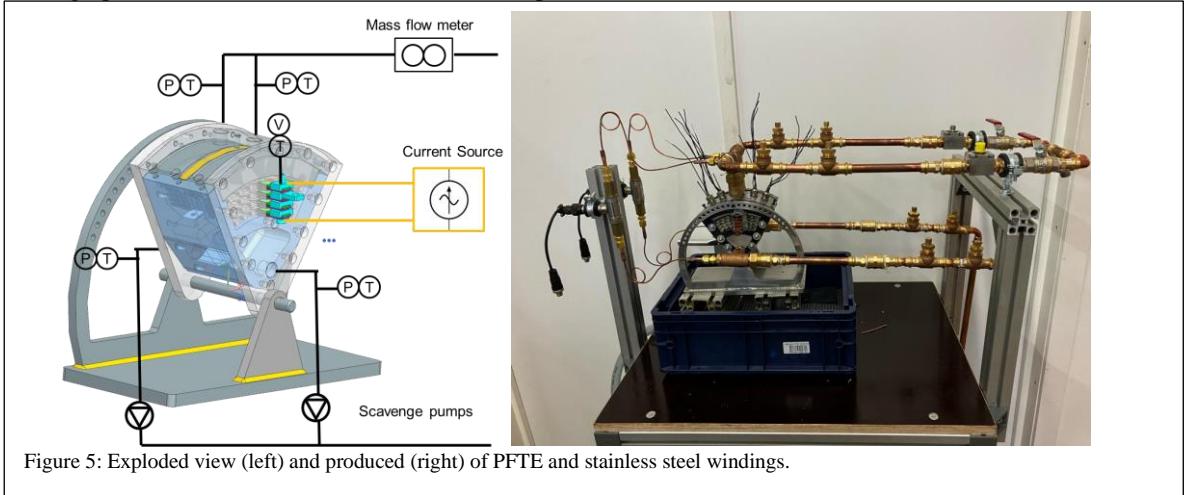


Figure 4 displays an overview of some key internal and external design features. The DUT housing is made from PFTE to limited parasitic heat transfer from the winding. The DUT further includes an oil inlet cavity for both for both the crown-and weld side of the winding. This cavity is equipped with 3 arrays of openings that can be equipped with jet nozzles. As such 3 axial jet positions can be tested with a single oil inlet cavity design. Between the crown and the weld side a PFTE wall is present to separate the crown and weld end-space.

3. INSTRUMENTATION

Figure 5a presents a schematically overview of the entire test setup and Figure 5b presents the physical setup in the lab. The DUT is connected an an existing hydraulic circuit. At each of the 2 oil inlets, the oil pressure and oil temperature is measured. At the bottom of the DUT, a drain port is present on both sides of the DUT. The drain ports are hydraulically connected to 2 scavenge pumps which drain the sumps in the DUT. Two breather holes are made on the side of the sump in order to ensure proper functioning of the scavenge pumps (no shown). The four layers of stainless steel wires are connected in series through external terminals to form a complete coil. The coil is energized by a DC current source, heating up the stainless steel wires within the setup.



Further, the stainless steel wires are instrumented with multiple temperature and voltage sensors. These sensors are present in the center of the winding, the weld location and the wire terminals. The temperature measurement are done with calibrated K-type thermocouples. These thermocouples are soldered directly to the stainless steel wires in order to ensure a proper thermal connection. The local temperature of the wire is determined by the voltage difference caused by the Seebeck effect in the TC wires. The soldering also provide an electrical connection between the stainless steel wires and the sensor wires. Therefore, by comparing the absolute voltage of two TC sensor, the voltage drop within a specific wire section can be calculated. In case a constant current is fed to the wires, the voltage drop varies with the average temperature in the wire section. Therefore, the measured voltage drop in the winding can be used to indirectly measure the average

wire temperature over a specific winding section. The advantage of the latter method is that the method is not impacted by the thermal bonding of the TC sensors to the stainless steel wires and, therefore, the sensor reading is not impacted by the oil flow on the wires.

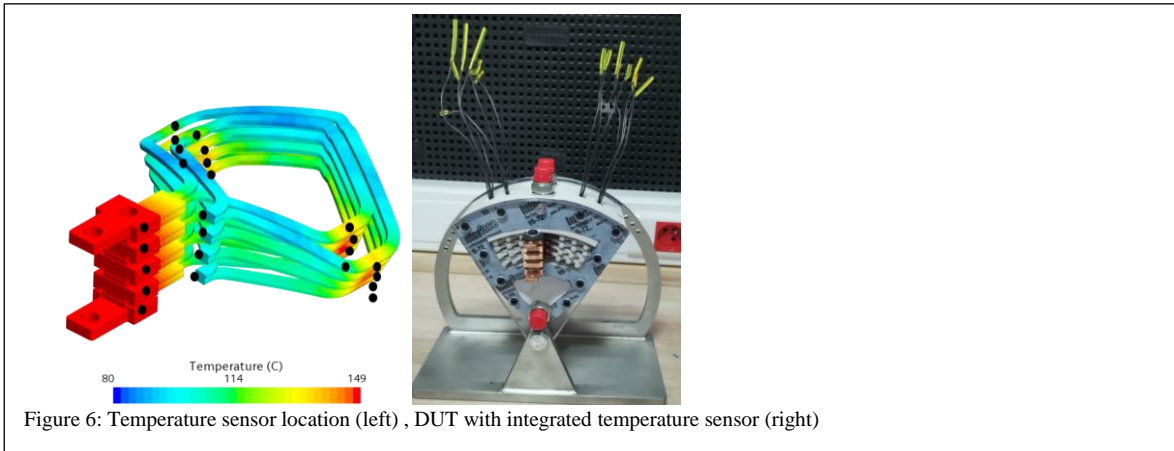


Figure 6: Temperature sensor location (left) , DUT with integrated temperature sensor (right)

4. TEST RESULTS

Will be available in the full paper

5. MEASUREMENT ACCURACY ANALYSIS

Will be available in the full paper

5. REFERENCES

- Bennion, K., & Moreno, G. (2015). Convective Heat Transfer Coefficients of Automatic Transmission Fluid Jets With Implications for Electric Machine Thermal Management. *International Technical Conference and Exhibition on Packaging and Integration of Electronic and Photonic Microsystems* (p. V003T04A010). 10.1115/IPACK2015-48382.
- Carriero, A., Locatelli, M., Ramakrishnan, K., Mastinu, G., & Gobbi, M. (2018). A Review of the State of the Art of Electric Traction Motors Cooling Techniques. doi:10.4271/2018-01-0057
- Feng, X., Cousineau, E., Bennion, K., Moreno, G., Kekelia, B., & Narumanchi, S. (2021). Experimental and numerical study of heat transfer characteristics of single-phase free-surface fan jet impingement with automatic transmission fluid. *International Journal of Heat and Mass Transfer*, 166, 120731. Opgehaald van <https://www.sciencedirect.com/science/article/pii/S001793102033667X>
- Gai, Y., Kimiabeigi, M., Chuan Chong, Y., Widmer, J. D., Deng, X., Popescu, M., . . . Steven, A. (2019). Cooling of Automotive Traction Motors: Schemes, Examples, and Computation Methods. *IEEE Transactions on Industrial Electronics*, 66, 1681-1692. doi:10.1109/TIE.2018.2835397
- Liu, C., Gerada, D., Xu, Z., Chong, Y. C., Michon, M., Goss, J. a., . . . Zhang, H. (2021). Estimation of Oil Spray Cooling Heat Transfer Coefficients on Hairpin Windings With Reduced-Parameter Models. *IEEE Transactions on Transportation Electrification*, 7, 793-803. doi:10.1109/TTE.2020.3031373
- Liu, C., Xu, Z., Gerada, D., Zhang, F., Chong, Y. C., Michon, M., . . . Zhang, h. (2022, 01). Experimental Investigation of Oil Jet Cooling in Electrical Machines With Hairpin Windings. *IEEE Transactions on Transportation Electrification*, PP, 1-1. doi:10.1109/TTE.2022.3186947
- Ma, C., & Zheng, Q. (1997). Local heat transfer and recovery factor with impinging free-surface circular jets of transformer oil. *International Journal of Heat and Mass Transfer*, 40, 4295-4308.
- Nonneman, J., Schlimpert, S., T'Jollyn, I., & De Paepe, M. (2020). Modelling and Validation of a Switched Reluctance Motor Stator Tooth with Direct Coil Cooling. *2020 19th IEEE Intersociety Conference on Thermal and Thermomechanical Phenomena in Electronic Systems (ITherm)*, (pp. 306-314). Orlando, FL, USA. doi:10.1109/ITherm45881.2020.9190255
- Nonneman, J., T'Jollyn, I., Sergeant, P., & Michel, D. P. (2020). Quality Assessment of a 2D FE Based Lumped Parameter Electric Motor Thermal Model Using 3D FE Models. *2020 International Conference on Electrical Machines (ICEM)*. Gothenburg, Sweden. doi:10.1109/ICEM49940.2020.9270820
- USDRIVE. (2017). *Electrical and Electronics Technical Team Roadmap*. U.S. Department of Energy, Vehicle Technology Office. USA: <https://www.energy.gov/sites/prod/files/2017/11/f39/EETT%20Roadmap%2010-27-17.pdf>. Opgehaald van <https://www.energy.gov/sites/prod/files/2017/11/f39/EETT%20Roadmap%2010-27-17.pdf>

FIRST RESULTS OF A SINGLE-TUBE PCM-STORAGE FOR OPTIMISED STEAM PRODUCTION

Larissa Dietz*, Tobias Garbe, Michael Fiss, Inga Bürger, Andrea Gutierrez
German Aerospace Center (DLR), Pfaffenwaldring 38-40, 70569 Stuttgart, Germany
*larissa.dietz@dlr.de

Keywords: PCM, latent heat thermal energy storage, two-phase fluid, operation strategies, steam production

1. INTRODUCTION

The shell and tube heat exchanger is one of the most commonly used designs for thermal energy storage units in industrial applications (Li, Li et al. 2019). It can be used for latent heat thermal energy storage (LH-TES) systems where the storage medium in the shell of the device is a phase change material (PCM). A recent example of a large-scale LH-TES integrated into a steam supply system to reduce the amount of fossil fuels required is reported by Johnson et al. (Johnson and Fiss 2023). The optimal design of such passive LH-TES and a controlled dynamic operation is only possible if the transient phenomena occurring in the PCM and the heat transfer fluid (HTF) in the storage unit are known in detail, as they determine the thermal power profile of the system. A single-tube test rig in a 1 kW scale was designed and built to investigate the influence of an indirect transient operation parameter in LH-TES systems with a two-phase HTF on the thermal charging and discharging power: The so-called dominant heat transfer surface (DHS). It can be adjusted by the HTF mass flow rate as well as by the temperature difference between the HTF inlet temperature and the PCM phase change temperature. Advanced operation strategies for passive LH-TES have been proposed and reported before (Garcia, Largiller et al. 2022) for a complete tube bundle. This work presents the first experimental results on the coupled phase change in PCM and HTF in a single-tube test rig during charging for detailed data acquisition as well as on the feasibility of the optimised operation strategies exploiting the concept of DHS.

2. SETUP AND MATERIALS

The storage element under investigation consists of a steel tube with clamped aluminum fins, which is embedded in a steel container filled with the storage material. As it can be seen in Figure 3, the container is 2 m long and a series of temperatures are measured at 0.3 m intervals on each of the five levels L1 to L5. To enable temperature measurements in all relevant positions a customised container design was developed. The container has mounting options for thermocouples with maximum measurement uncertainties of 1.6 K in the pressure tube and the PCM at each level. Based on the measured temperatures and the pressure in the HTF tubes, the State of Charge (SoC) of the PCM and the state of the HTF can be derived. The storage material in the test section is approximately 4.5 kg of PLUSICE A133, an organic pure and single chain length compound, supplied by Phase Change Material Products Ltd, with a melting temperature of 133 °C and a phase change enthalpy of 200 kJ/kg. The HTF is demineralised water.

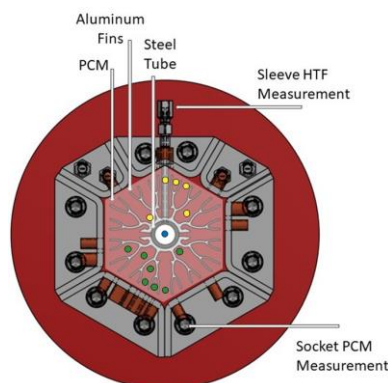


Figure 1: Cross section of the HTF tube with clamped-on aluminum fins, PCM and customised container.

Thermocouple positions in the PCM on levels L1 to L5 (green), additional positions in the PCM on level L3 (yellow) and position in the HTF (blue).

For charging, saturated steam is generated in the evaporator. The steam is superheated when it is throttled by a control valve and electrical heating wires are used to prevent condensation before the steam reaches the upper part of the test section. In the storage part of the test rig, it condenses and the energy released is transferred to the solid PCM which then melts. Depending on the SoC of the PCM, the water leaves the bottom of the tube as a gas, liquid or as a two-phase fluid.

In the subsequent condenser, the fluid is condensed and/or cooled down to 60 °C and fed back into the circuit. During discharging, the HTF inlet temperature is set in the electrical preheater and the saturated liquid water flows through the tube in the opposite direction, entering at the bottom of the tube. Figure 2 shows the infrastructure for operating the test section.

The special feature of the steam cycle is the ability to control the mass flow rate of the HTF and the pressure in the system simultaneously with the help of a back-pressure regulator (a) and mass flow rate control valves during charging (b)/during discharging (c). The HTF mass flow rate, the inlet and outlet pressures and temperatures as well as the mass flow rate and inlet and outlet temperatures of the cooling water flowing through the condenser are recorded with the Siemens PLC system SIMATIC S7-1500. Temperatures of the HTF outside of the test section are measured with resistance thermometers resulting in a maximum measurement uncertainty of 1.1 K.

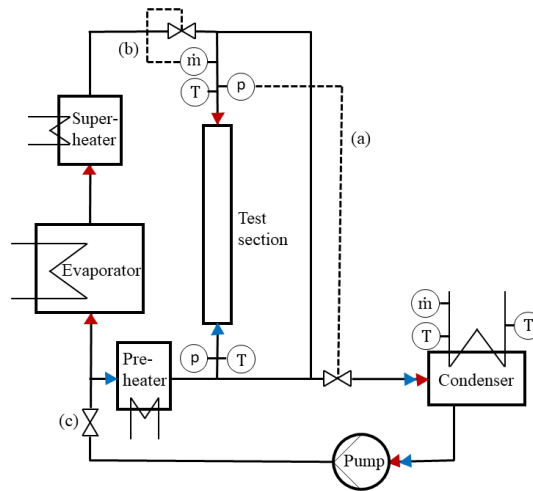


Figure 2: Charging and discharging infrastructure with main components, control valves and positions of mass flow rate, temperature and pressure measurements in the HTF.

3. RESULTS

The temperature results of a charging experiment can be seen in Figure 3. At the beginning of the process, the temperatures of the storage are between 80 °C and 103 °C and the superheated HTF at approximately 176 °C with a pressure of 6.7 bar and a mass flow rate of 2.44 kg/h enters the test section from above. The diagram shows the temperatures of the HTF on the five measurement levels in the pressure tube (solid lines) and the mean PCM temperatures of the corresponding cross sections in the storage (dashed lines). On the right hand, a schematic of the test section with the correspondingly coloured measurement levels L1 to L5 is shown. The PCM in the storage heats up and melts from top to bottom while the HTF simultaneously cools down and condenses. At the beginning of the charging process, the HTF is already subcooled at measurement level L5 - after one minute, it reaches the saturation temperature of 163 °C. This indicates that the fluid is two-phase here, while it is still subcooled at all other measurement levels. The two-phase region in the tube moves from one level to the next during the process until, after approximately 20 minutes, the phase change occurs in the HTF leaving the storage at level L1. This point in time is marked with a vertical dashed line in Figure 3 as well as in Figure 4, in which the constant heat flow rate of the storage ends simultaneously. Axial charging behaviour can be clearly derived from these results. The melting range of the PCM is indicated by the reduced gradient of the temperature rise of the PCM between 123°C and 133°C.

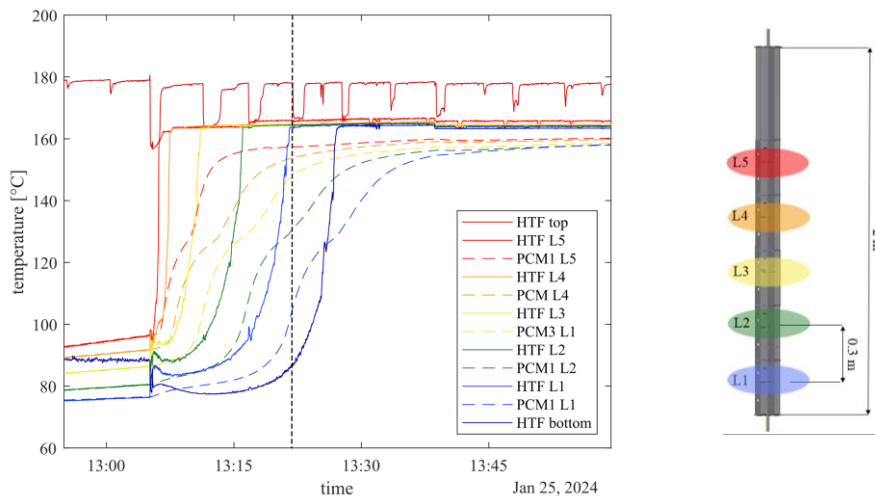


Figure 3: Temperatures of HTF and mean temperatures of PCM on five measurement levels. The colours in the schematic indicate the corresponding measurement positions. The vertical dashed line marks the HTF at level L1 reaching saturation temperature and the end of the constant power plateau in Figure 4.

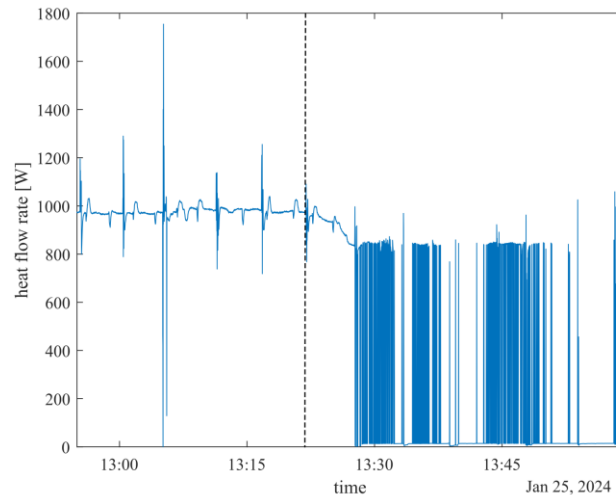


Figure 4: Storage heat flow rate during charging. The vertical dashed line marks the end of the constant power plateau and the HTF at level L1 reaching saturation temperature in Figure 3.

4: CONCLUSIONS

The initial results reported in this work indicate that axial charging of the storage is possible by simultaneously controlling the pressure and the mass flow rate of the HTF and thus adjusting the size of the two-phase region in the tube –the DHS. In further measurements, the setting of the HTF inlet conditions and the uniformity of the initial storage temperature for charging and discharging will be optimised to derive more quantitative data on the instantaneous heat flow rate.

REFERENCES

- Garcia, P., G. Largiller, G. Matringe, L. Champelovier and S. Rougé (2022). "Experimental results from a pilot scale latent heat thermal energy storage for DSG power plants – Advanced operating strategies". SOLARPACES 2020: 26th International Conference on Concentrating Solar Power and Chemical Energy Systems.
- Johnson, M. and M. Fiss (2023). "Superheated steam production from a large-scale latent heat storage system within a cogeneration plant." *Communications Engineering* 2(1).
- Li, Q., C. Li, Z. Du, F. Jiang and Y. Ding (2019). "A review of performance investigation and enhancement of shell and tube thermal energy storage device containing molten salt based phase change materials for medium and high temperature applications." *Applied Energy* 255.

High heat transfer chip cooling: capillary based flow boiling model and a novel experimental analysis method

C.M. Rops^{a*}, R. Betsema^a, G.D. Mensink^a, R.B.J. Koldeweij^a, P.B.T.H Boerboom^a

^aTNO High Tech Industry

*cor.rops@tno.nl

Keywords: Microfluidic cooling, Two-phase heat transfer, Flow boiling, Power electronics.

1. INTRODUCTION

Over the last six decades the number of transistors per square centimeter approximately doubled every two years. This observed trend is known as Moore's law as introduced in his IEEE speech in 1975 (Moore, 1975). Currently, one of the main challenges for the future miniaturization of electronics is its thermal management. The generated heat fluxes of the electronic devices continue to increase over the years. Over the last 20 years a linear increase from approximately 50W/cm² to almost 200w/cm² is observed (Zhang *et al.*, 2021). Conventional air cooling has reached its limits, and depending on the application more efficient cooling methods are being explored, such as liquid cooling, thermo-electric cooling and fluid boiling cooling.

An example of the increase in power densities is given in (Rajan *et al.*, 2022). Here the Thermal Design Power (TDP) in the datacenter community is identified to exceed 400W in 2030, which would not be far from 300W/cm². Rajan identified as main challenges: the opportunity to continue unlocking the full device performance and to contain the thermal management overhead (energy and water consumption). An essential goal is to operate the devices at a lower junction temperature (Guler *et al.*, 2020) to reduce the leakage power, and thus the energy consumption. Furthermore, lower junction temperature increases the lifetime of the devices. Determining the junction temperature is crucial, since Silicon based inverters typically allow a maximum junction temperature of about 120 °C (Kempiak *et al.*, 2018).

Another example of increasing power densities is found in the electrification of vehicles. During the fast charging of the battery and the operation of the electro-engine large portions of energy are converted in a small amount of time. Wide Band Gap (WBG) technologies such as SiC and GaN, increase the device's switching performance. Although the efficiency of these inverters is above 99.5% (Zhu *et al.*, 2018), the heat losses remain significant. Abramushkina *et al.* (2021) and co-workers showed that these technologies can deal with the heat fluxes above 120W/cm² and elevated junction temperatures above 175 °C.

These examples from practice show that innovative cooling methods are essential to attain the high heat fluxes (>100W/cm²) and transport high amounts of energy (~1kW per device). Two-phase cooling in microchannels is a promising solution if the commonly observed drawbacks such as unstable flow and intermittent reduced heat transfer can be overcome (Kandlikar, 2001). TNO has developed a microfluidic flow boiling method which ensures stable flow boiling in a microchannel structure (Rops *et al.*, 2009). Over the years TNO has refined their modelling to more accurately predict the heat transfer in these structures. Earlier it was observed that an analytical description of the lateral conduction in the heat conducting wall in their thermal models was essential for a better estimation of the chip interface temperature (Betsema *et al.*, 2022). The current work discusses the inclusion of surface tension effects on the flow pattern to more accurately predict the microfluidic flow boiling heat transfer. In order to validate this proposed model, a novel experimental analysis method is developed to estimate the microfluidic flow boiling heat transfer coefficient in the microfluidic test setup more accurately.

2. MODEL DEVELOPMENT AND EXPERIMENTAL ANALYSIS METHOD

Capillary based flow boiling model

Similar as reported in literature (e.g. Kandlikar, 2001, Sun *et al.*, 2018), in our microfluidic flow boiling experiments the annular flow regime is observed over a wide range of vapour qualities. Therefore, for simplicity reasons, to model the heat transfer, it is assumed that the microfluidic flow boiling takes place in an annular flow pattern. The vapour quality in a section is dependent on the amount of energy inserted in the fluid. The void fraction, however, strongly depends on the shape of the liquid film. The TNO model calculates the flow boiling heat transfer coefficient as the liquid thermal conductivity over the liquid film thickness, as proposed by Thome *et al.* (2004) in their so-called 3-zone model. A thin film induces a high flow boiling heat transfer. Therefore, an accurate prediction of the film thickness is essential. In microchannels the shape of the liquid film is significantly affected by the surface tension. Accurate calculation of the film thickness is profoundly complicated in rectangular microchannels. Typically more liquid is accumulated in the corners, therefore thinning the liquid film over the side walls.

Wang and Rose (2005) developed a numerical method to calculate the equilibrium state of a liquid interface in a rectangular channel. Using a dual coordinate system for the top and bottom corner a combined mass and momentum balance can be solved including viscosity, gravity and surface tension. The TNO model is extended with an empirical evaporation resistance and including this numerical method for the film thickness calculation. The effect of this inclusion on the liquid film shape can be seen in Figure 1.

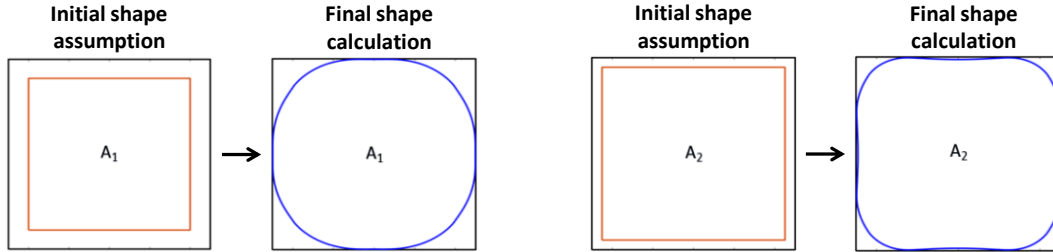


Figure 1. Surface tension effect on film shape for different void fractions, TNO microfluidic flow boiling model results. Left: void fraction 0.8. Right: void fraction 0.9.

Novel experimental analysis method

Due to the typical size of a microchannel, local estimation of the temperatures and the heat fluxes is complex. The unsteady flow behaviour, and the size and positioning of the temperature sensors affect the measurement (Sun *et al.*, 2018). The wall of a microchannel is relatively thick compared to its length, therefore lateral conduction has a significant effect (Betsema *et al.*, 2022). Realization of a constant heat flux along the channel length is very difficult to achieve in an experiment. A (near) constant wall temperature can be achieved by deliberately thickening of the heated wall of the microchannel. This principle is used in an Aluminum mockup setup to obtain a better defined thermal boundary layer, mimicking a half bridge chip cooler, see Figure 2.

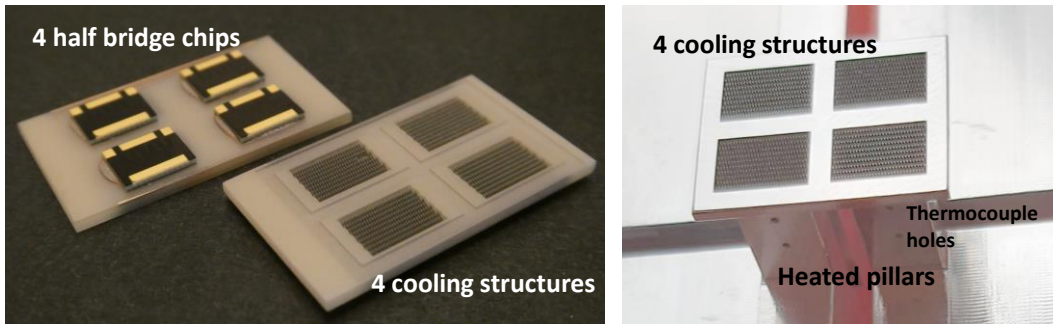


Figure 2. Left: top side with chips, and bottom side with cooler structure. Right: Aluminum mock up setup with the pillars to mimic the chip heat load and the thermocouple holes to estimate the heat flux and wall temperature.

The Aluminum pillar allows lateral heat conduction with a relatively small temperature gradient, thus approaching the uniform wall temperature at the bottom of the microfluidic flow boiling structure. By means of the two thermocouple holes above each other, the vertical temperature gradient is measured in each pillar. This vertical gradient is used to estimate the wall temperature by linear extrapolation and the heat flux by assuming one dimensional conduction in the pillar.

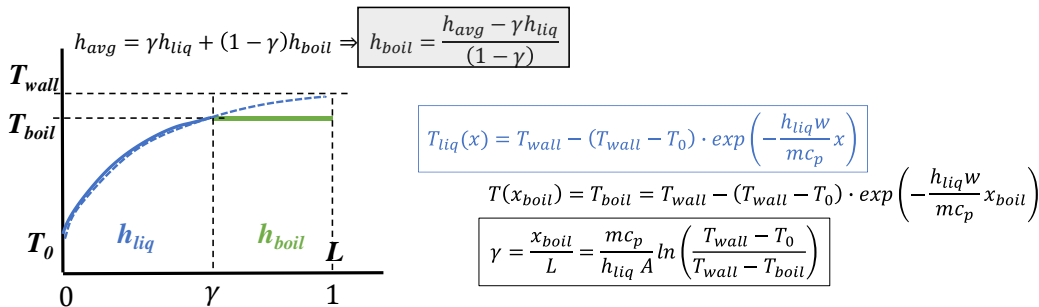


Figure 3. Schematic derivation to determine the boiling heat transfer coefficient from the measured average heat transfer coefficient and the single phase liquid heat transfer coefficient.

With the novel analysis method, presented in Figure 3, the microfluidic flow boiling heat transfer, h_{boil} , can be estimated. The liquid heat transfer coefficient, h_{liq} , the relative boiling location, γ , and the average heat transfer coefficient,

h_{avg} , need to be determined. It is possible to extract h_{liq} from single-phase-only experiments. The average liquid temperature is calculated by means of the exponential temperature profile obtained for a constant wall temperature. Using γ , as given in Figure 3, the average fluid temperature can be calculated in the flow boiling experiments. Finally, h_{avg} can be determined using the applied heat flux and the wall temperature during the flow boiling experiment.

3. EXPERIMENTAL RESULTS AND CONCLUSIONS

The temperature at the virtual chip interface and the microfluidic flow boiling heat transfer coefficient are determined for various chip powers. Figure 4 (left), shows the chip interface temperature. Even for the highest power it remains slightly below 90 °C. Using a typical internal chip resistance of about 0.8 K/W the junction temperature remains below 120 °C at a chip dissipation of 40W. Furthermore the temperature is little dependent on the flow rate for one chip.

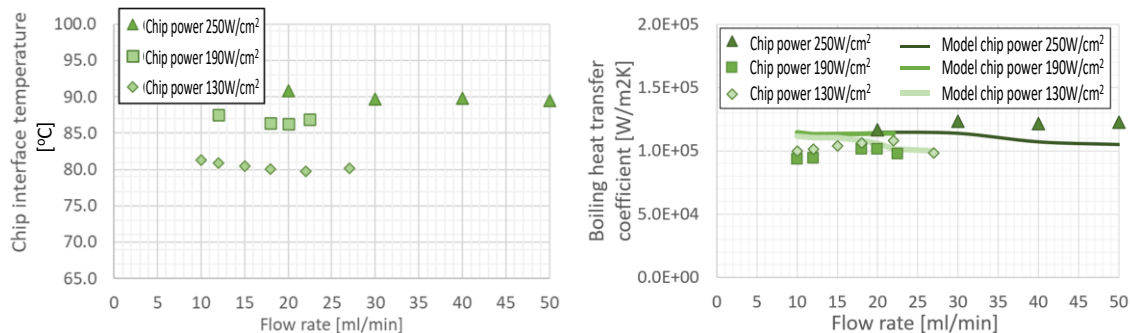


Figure 4. Microfluidic flow boiling results: experiments (markers) and model (lines). Left: (virtual) chip interface temperature for three individual chip powers. Right: Estimated microfluidic flow boiling heat transfer coefficient.

The right graph of Figure 4 shows that the boiling heat transfer coefficient is little dependent on the flow rate. However, going to low flow rates, resulting in vapour qualities above 0.5 (not shown in the graph), the risk of dry-out increases. This destabilises the flow boiling process. The 250 W/cm² case (which corresponds to 40W per chip) shows the highest boiling heat transfer coefficients. This can be understood since the highest heat flux will result in the thinnest liquid film.

The heat transfer coefficient graph (right graph of Figure 4) shows the model results with inclusion of the surface tension. A nice correspondence with the experiments is found. Both the near independence on the flow rate as well as the slight increase on increasing heat flux is captured by the model.

The maximum mimicked chip heat flux of 250W/cm² is roughly a factor 2 improvement in relation to current state-of-the-art coolers reported in literature (e.g. Zhang *et al.*, 2021). Further geometry optimisation allows to achieve cooling heat fluxes above 300W/cm² as foreseen for power electronics beyond 2030 (Rajan *et al.*, 2022).

4. REFERENCES

- Abramushkina, E., Zhaksylyk, A., Geury, T., El Baghdadi, M., Hegazy, O., 2021, "A Thorough Review of Cooling Concepts and Thermal Management Techniques for Automotive WBG Inverters: Topology, Technology and Integration Level.", *Energies*, vol. 14.
- Betsema, R., and Rops, C.M., 2022, "A coupled model of heat spreading and flow boiling in microchannels", *ASDAM 2022*, Smolice castle, Slovakia.
- Guler, A. and Jha, N. K., 2020, "McPAT-monolithic: An area/power/timing architecture modeling framework for 3-D hybrid monolithic multicore systems.", *IEEE Trans. Very Large Scale Integr. (VLSI) Syst.*, vol. 28(10), pp. 2146-2156.
- Kandlikar, S.G., 2001, "Fundamental issues related to flow boiling in minichannels and microchannels", *Exp. Thermal and fluid science*, vol. 26., pp. 389-407.
- Kempiak, C., Lindemann, A., Thal, E. and Idaka, S., 2018, "Investigation of the usage of a chip integrated sensor to determine junction temperature during power cycling tests," *10th Int. Conference on Integrated Power Electronics Systems*, Stuttgart, Germany.
- Moore, G., 1975, *IEEE International Electron Devices Meeting*, Washington, D.C., USA.
- Rajan, S.K., Ramakrishnan, B., Allisa, H., Kim, W., Belady, C. and Bakir, M., 2022, "Integrated silicon microfluidic cooling of a high-power overclocked CPU for efficient thermal management", *IEEE Access Electronics packaging*, vol.10.
- Rops, C.M., Velthuis, J.F.M., Graaf, F. and Geers, L.F.G, 2009, "Multiple connected channel micro evaporator", WO2009/082230.
- Sun, Y., Guo, C., Jiang, Y., Wang, T. and Zhang, L., 2018, "Transient film thickness and microscale heat transfer during flow boiling in microchannels", *International Journal of Heat and Mass Transfer*, vol.116, pp.458–470.
- Thome, J.R., V. Dupont, V. and Jacobi, V., 2004, "Heat transfer model for evaporation in microchannels. Part I: presentation of the model", *International Journal of Heat and Mass Transfer*, vol.47, pp.3375–3385.
- Wang, H.S. and Rose, J.W., 2005, "Theory of film condensation in horizontal noncircular section microchannels", *Journal of Heat Transfer*, vol. 127(10), pp.1096–1105.
- Zhang, Z., Wang, X., and Yan, Y., 2021, "A review of the state-of-the-art in electronic cooling", *Advances in Electrical Engineering, Electronics and Energy*, Vol. 1, pp. 1-26.
- Zhu, J., Kim, H., Chen, H., Erickson, R. and Maksimović, D., 2018, "High efficiency SiC traction inverter for electric vehicle applications," *IEEE Applied Power Electronics Conference and Exposition (APEC)*, San Antonio, USA.

VELOCITY MEASUREMENTS OF THIN FALLING FILMS USING NUCLEAR MAGNETIC RESONANCE

Georges C. Saliba^{*}, Jan G. Korvink, Jürgen J. Brandner

^aInstitute of Microstructure Technology (IMT), Karlsruhe Institute of Technology (KIT)

*georges.saliba@kit.edu

Keywords: thin-falling-films, velocity, experimental, nuclear magnetic resonance

1. INTRODUCTION

Micro-reactor technology has benefited over the years from developments in microfabrication techniques. Reduction in size affords safer processes since smaller quantities are required to perform and study chemical reactions. It also increases efficiency for several devices of which falling-film micro-reactors are one example. Falling-film reactors (FFR) are used to absorb a reagent from a gas phase into a liquid phase before the desired reaction can take place. For this reason, optimizing the ratio of the surface area of the gas-liquid interface to the volume of the film is crucial, as it will allow for a more intense mass transport between the two phases and for a quicker diffusion of the dissolved gas across the entire thickness of the film. It is evident that if the dimensions of the device were reduced, the surface-to-volume ratio, $R=S/V$, would increase, since it is inversely proportional to the characteristic length scale L . More interestingly, at smaller scales, surface tension plays a much more prominent role comparable to that of viscous forces, flow inertia or gravitational acceleration. For narrow channels, surface tension becomes strong enough to pull the interface at the edges, and thus increase its surface area with respect to the volume of the film. The effect of surface tension is inconsequential at much larger scales.

Complementary to optimizing the surface-to-volume ratio is the question of how to perform flow measurements at this scale. Optical techniques have been widely used to map the depth of the film across its width. The most common techniques are stereo digital microscopy (Yang et al. (2019)), confocal laser scanning microscopy and laser profilometry (Yeong et al. (2006)). Micro-Particle Image Velocimetry (Anastasiou et al. (2013), Koupa et al. (2019)) is also a common technique to obtain both thickness profiles and velocity maps. However, velocity can only be measured in planes parallel to the bottom of the channel. The present work takes a different approach by using a non-optical, non-intrusive method based on nuclear magnetic resonance. This method yields three-component, three-dimensional (3C-3D) velocity maps. Although it is common in the medical and chemical fields, it is still widely unused to the fluid mechanics and engineering communities. In the available literature on falling films, and more generally on thin open channel flows, the only work that has used this measurement method was Heine et al. (2001). In their study, a film 40mm wide and 1mm deep was investigated and the velocity profiles across the depth of the film were presented. Here, we perform experiments in channels 1mm deep and 2mm wide, in which water films can flow with a thickness of less than 60 μ m. In comparison to Heine et al. (2001), the channel is 20 times narrower, resulting in a prominently curved gas-liquid interface. The aim is to measure the velocity field along the cross-section of the film and to study the effect of channel geometry on the surface-to-volume ratio.

2. EXPERIMENTAL SETUP

An 11.7T cryomagnet system from Bruker (Ettlingen, Germany) was used to conduct the experiments. The probes constructed for this system can hold 5mm or 10mm test tubes containing chemical samples. For this reason, the microfluidic system designed for the present experiments had the same dimensions as a 10mm NMR tube. Aside from the inlet channel to pump the liquid, and the outlet channel to extract it, the system includes two ventilation channels to maintain the air at atmospheric pressure. Since the flow is not pressure driven, two separate pumps introduce and extract the fluid, respectively. The microfluidic cell consisted of either a rectangular, chamfered, wedge or round channel, with an inlet reservoir upstream and a sump downstream to collect the water before it is extracted. Figure 1 shows a simplified diagram of the experimental setup.

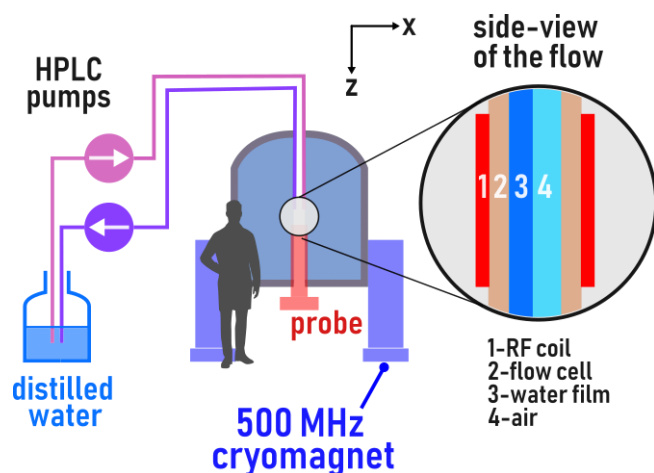


Figure 1. Diagram of the experimental setup used to measure the velocity field inside of a microfluidic falling film in a 500MHz cryomagnet.

3. RESULTS

Although magnetic resonance velocimetry can resolve the three spatial components of flow in 3D, the current setup only results in a 1C-2D flow. Figure 2 shows an example of the information that can be obtained from the MRV measurements. In Figure 2 (a), the time-averaged velocity along the vertical z -axis, $\bar{u}_z(x, y)$, is shown in a cross section of the film. Besides providing information about the distribution of the velocity in the film, it is possible to detect the gas-liquid interface and the volume occupied by the liquid and then deduce both the thickness distribution of the film (Figure 2 (b)) as well as the surface-to-volume ratio $R=S/V$ (Figure 2 (c)).

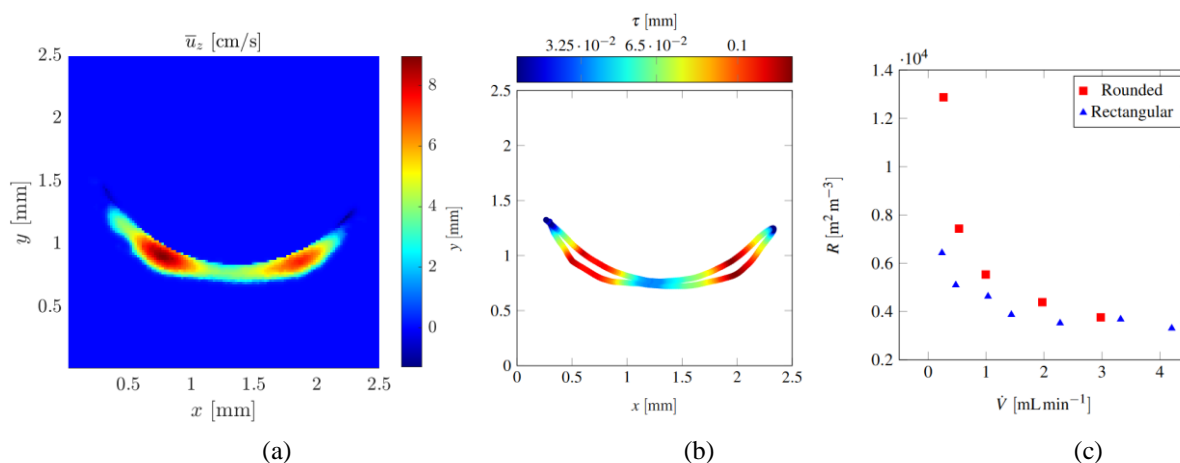


Figure 2. Results from the MRV measurements showing (a) the velocity field for the round channel, (b) the corresponding contour colored according to the thickness of the film and (c) the surface-to-volume ratio $R=S/V$ for different mass flow rates for the rectangular and round channels.

Values of R for the rectangular channel were added in Figure 2 (c) for comparison. Although the surface-to-volume ratio is comparable for large mass flow rates, the values diverge significantly with decreasing mass flow rates. In the round channel, it is possible to reach a surface-to-volume ratio of around $13,000 \text{ m}^2/\text{m}^3$ whereas its value is barely above $6,000 \text{ m}^2/\text{m}^3$ for the rectangular channel. This is due to two factors: First, the sharp corners in rectangular channel mean that the volume of liquid is larger and so the ratio R is relatively smaller. Second, the film in the round channel remains complete down to about $0.2 \text{ mL}/\text{min}$ whereas the film in the rectangular channel is broken and the onset of rivulet flow occurs at a flow rate of more than $2 \text{ mL}/\text{min}$.

4. CONCLUSIONS

Magnetic resonance velocimetry has the potential of becoming the method of choice for measuring 3C-3D velocity fields in microfluidic systems with complex geometries. In the current study, the velocity distribution in falling films having a thickness of down to 60 μ m were measured. With the gathered data, it was possible to resolve the shape of the meniscus as well as the thickness distribution across the film. The surface-to-volume ratio of the films could then be deduced. The flow configuration here was relatively simple. Nevertheless, complex flows with 3C-3D velocity fields can be measured equally well by magnetic resonance velocimetry. This would afford a deeper understand into more complex flow patterns that could arise in falling films due to temperature gradients or to structured micro-channels that induce chaotic mixing. In these situations, optical techniques are no longer capable of providing relevant information about the flow.

5. REFERENCES

- Anastasiou, A. D., Gavriilidis, A., & Mouza, A. A. (2013). "Study of the hydrodynamic characteristics of a free flowing liquid film in open inclined microchannels". *Chemical Engineering Science*, 101, 744–754. <https://doi.org/10.1016/j.ces.2013.07.031>
- Heine, C., Kupferschläger, K., Stapf, S., & Blümich, B. (2002). "NMR velocimetry of falling liquid films". In *Journal of Magnetic Resonance* (Vol. 154, Issue 2, pp. 311–316). Academic Press Inc. <https://doi.org/10.1006/jmre.2001.2495>
- Koupa, A. T., Stergiou, Y. G., & Mouza, A. A. (2019). "Free-flowing shear-thinning liquid film in inclined μ -channels". *Fluids*, 4(1). <https://doi.org/10.3390/fluids4010008>
- Yang, Y., Zhang, T., Wang, D., & Tang, S. (2019). Investigation of the liquid film thickness in an open-channel falling film micro-reactor by a stereo digital microscopy. *Journal of the Taiwan Institute of Chemical Engineers*, 98, 27–36. <https://doi.org/10.1016/j.jtice.2018.07.033>
- Yeong, K. K., Gavriilidis, A., Zapf, R., Kost, H. J., Hessel, V., & Boyde, A. (2006). "Characterisation of liquid film in a microstructured falling film reactor using laser scanning confocal microscopy". *Experimental Thermal and Fluid Science*, 30(5), 463–472. <https://doi.org/10.1016/j.expthermflusci.2005.09.006>

AN OVERVIEW ON ATOMIC LAYER THERMOPILE HEAT-FLUX SENSOR AND ITS APPLICATIONS

Kai Yang^{a,b,*}, Bowan Tao^c, Xi Chen

^aHypervelocity Aerodynamics Institute (HAI), China Aerodynamics Research and Development Center (CARD), Mianyang 621000, People's Republic of China

^bNational Key Laboratory of Aerospace Physics in Fluids, China Aerodynamics Research and Development Center (CARD), Mianyang 621000, People's Republic of China

^cState Key Laboratory of Electronic Thin films and Integrated Devices, University of Electronic Science and Technology of Electronic, Chengdu 610054, People's Republic of China

*yg.hit@hotmail.com

Keywords: atomic layer thermopile, heat-flux sensor, sensitivity, calibration, flexible

1. INTRODUCTION

Measuring the heat flux density is one of the main tasks in the research field of hypervelocity experimental aerodynamics[Liu, 2013]. Especially, High-frequency fluctuation heat-flux is focused on in experimental investigations on the hypervelocity boundary layer transition[Camillo, 2020; KEGERISE, 2016; ROEDIGER, 2009], one of the basic aerodynamic problems. And the measurement of high-frequency fluctuation heat flux is achieved with atomic layer thermopile (ALTP) heat-flux sensors[ROEDIGER, 2008; KNAUSS,2009]. However, it is hard to detect the stable heat flux when the experiment is conducted in a hypervelocity quiet wind tunnel, while the stable heat flux can be used to determine the flow state, because ALTP sensors have a medium sensitivity of about $10\mu V/(kW.m^{-2})$ and the stable heat flux is low in the quiet wind tunnel[ROEDIGER, 2009]; $YBa_2Cu_3O_{7-\delta}$ (YBCO) film, the sensitive element of common ALTP sensor, has a low temperature tolerance, because YBCO film begins to lose the oxygen element when the temperature is higher than $200^\circ C$ and phase transition will happen when the temperature is above $450^\circ C$ [Xiong, 2008; Wu, 2016]. If a water-cooled structure is designed to cool the YBCO film[Bhatnagar, 2019], the so-called "cold-spot effect" may generate a negative effect on the local flow. Namely, common ALTP sensors can not be used in a high-temperature condition for a long time, but there is a strong demand for the heat-flux measurement in a high-temperature environment; Flexible sensors are required, when the experimental models have a curved surface. But inclined $SrTiO_3$ slice, the substrate of general ALTP sensors, cannot be buckled. Hence, ALTP sensors also have the development motivation of high sensitivity, small size and high-temperature tolerance and flexibility.

2. HIGH SENSITIVITY AND SMALL SIZE

Generally, the sensitivity of ALTP sensor can be defined as [Yang, 2020]

$$\alpha_A = \frac{V_A}{q} = \frac{l(s_{ab} - s_c) \sin 2\beta}{2\lambda_z} \quad (1)$$

In which, l is the effective length of YBCO film, d is the film thickness, β is the inclined angle between the c axis of YBCO film and the normal of $SrTiO_3$ surface, ΔT_z is the temperature difference between the top and bottom surface of YBCO film, s_{ab} and s_c are the Seebeck coefficients in the directions of ab-plane and the c-axis, respectively. λ_z is the thermal conductivity of YBCO film in the z axis. Eq. (1) indicates that the sensitivity of ALTP sensor is positively dependent on the effective length of YBCO film, while there are scientific papers on the optimal inclined angle β [Zhang, 2008]. However, the limited size of ALTP sensor places constraint on the effective length of YBCO film. Fortunately, (1) reveals no evidence on the width of YBCO film. To achieve a higher sensitivity, as shown in Fig.1, multi YBCO films, are connected in series by conductive films.

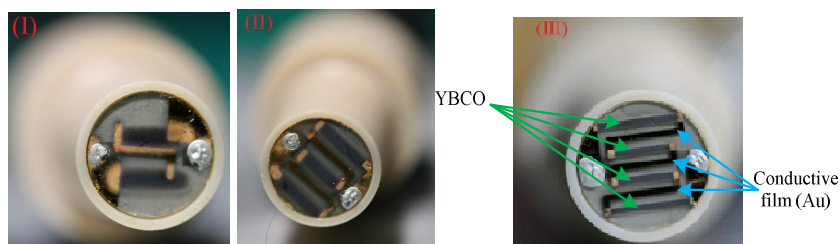


Fig. 1 High-sensitivity ALTP heat-flux sensors; (I) two YBCO films; (II) three YBCO films; (III) four YBCO films [Yang, 2024]

The static calibration results shown in Fig.2(I) reveal that the sensitivity of the ALTP sensor with four YBCO films is about 8.2 times larger than that of the normal one, while it is about 4.1 and 1.5 times for ALTP sensors with three and two YBCO films, respectively. Fast dynamic response is the main characteristic of ALTP sensors. Hence, the amplitude-frequency curves are determined by the sine-wave calibration method. As shown in Fig.2(II), thicker and longer YBCO film results in a faster decline in the amplitude-frequency curve [Yang, 2024]. Discussion on the tradeoff between high sensitivity and fast dynamic response helps develop small-sized ALTP sensors with optimized performance in the near future.

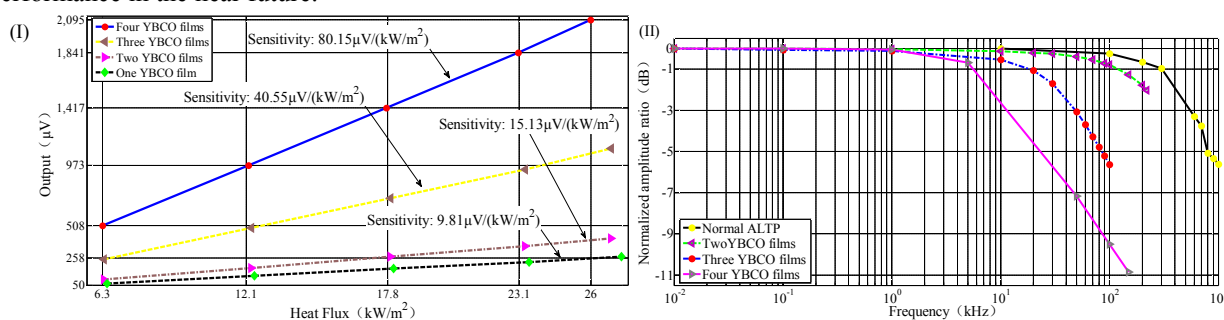


Fig.2 The static and dynamic calibration results of the revised ALTP heat-flux sensor with multiply YBCO films; (I) the static calibration results; (II) the dynamic calibration results [Yang, 2024]

3. HIGH-TEMPERATURE TOLERANCE

As a matter of fact, LCMO ($\text{La}_{1-x}\text{Ca}_x\text{MnO}_3$) [Chen, 2022], CaMnO_3 [Ferreira, 2019] and Ca_3CoO_9 [Brinks, 2015] have the the same light-induced transverse voltage effect as YBCO. And LCMO and other materials have a higher tolerance temperature. Hence, LCMO can be used to develop new-generation ALTP sensors, which may have a effective function in a high temperature environment. Static calibration results shown in Fig.3(II) reveals the LCMO-based ALTP sensor have a obvious ascending trend in a short calibration time of about 0.3s, even when the calibration heat flux is low to 42.9kW/m^2 . So further research is required on LCMO or other material based ALTP sensors. In addition, multi LCMO lines are alternately connected in series by conductive lines, because LCMO can be treated as the semiconductor to alter its electrode polar.

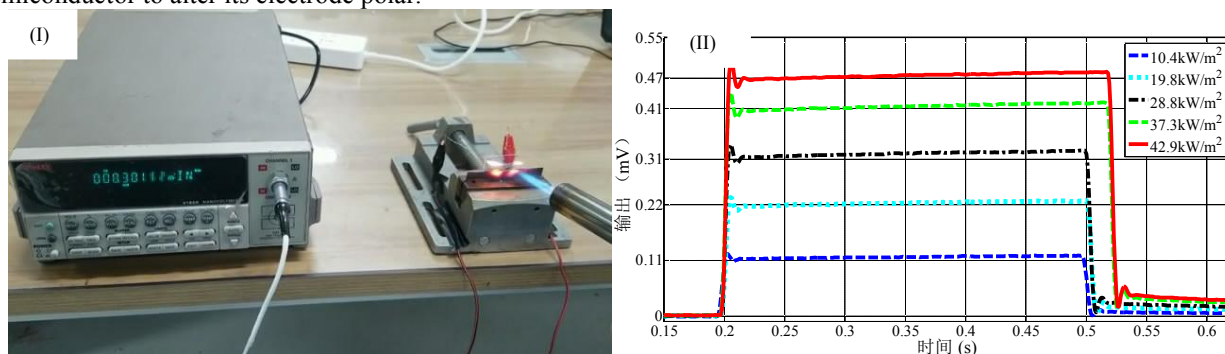


Fig.3 LCMO-based ALTP sensor and its static calibration results; (I) the test on ALTP sensor based on LCMO thin film in an oxyacetylene flame; (II) the static calibration results of ALTP sensor based on LCMO [Chen, 2022]

4. FLEXIBILITY

As stated above, inclined SrTiO_3 slice, the substrate of general ALTP sensors, cannot be buckled. Hence, flexible ALTP sensors are developed, in which flexible Hastelloy C-276 film with MgO interlayer is used as the substrate. The static calibration result of about $2.81\ \mu\text{V}/(\text{KW}\cdot\text{m}^2)$ shows the potential.

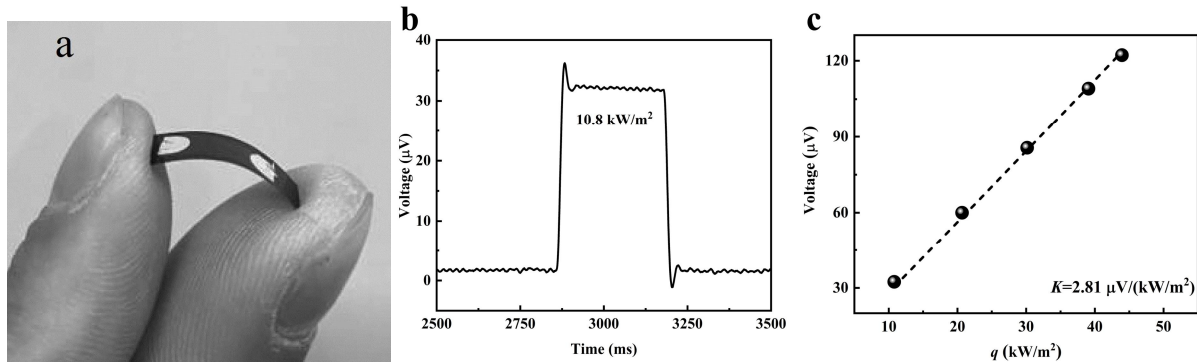


Fig.4 Flexible ALTP sensor and its static calibration results; (a) Flexible ALTP sensor[Xia, 2022]; (b) Original data of static calibration test; (c) Static calibration results

5. CONCLUSIONS

ALTP heat-flux sensors are essential in the experimental investigation on the hypervelocity boundary layer transition, one of the basic aerodynamic problems because on its good characteristics of fast dynamic response and linearity. The research results on high sensitivity, high-temperature tolerance and flexibility show the potential of new-generation ALTP sensors.

6. REFERENCES

- P Brinks, N Van Nong, N Pryds, et al, 2015 . “High-temperature stability of thermoelectric $\text{Ca}_3\text{Co}_4\text{O}_9$ thin films”. *Applied Physics Letters*, Vol.106, No.14, 143903
- X. Chen, Bowan Tao, Ruipeng Zhao, et al, 2022. “High-frequency response heat flux sensor based on the transverse thermoelectric effect of inclined $\text{La}_{1-x}\text{Ca}_x\text{MnO}_3$ films” . *Applied Physics Letters*, Vol. 121, No. 204102
- N M Ferreira, N R Neves, M C Ferro, et al, 2019. “Growth rate effect on the thermoelectric performance of CaMnO_3 -based ceramics” . *J. Eur. Ceram. Soc.*, Vol. 39, pp. 4184-4188
- Giannino Ponchio Camillo, Alexander Wagner, Christian Dittert, et al, 2020 . “Experimental investigation of the effect of transpiration cooling on second mode instabilities in a hypersonic boundary layer” . *Experiments in Fluids*, Vol. 61, 162
- KEGERISE M A, RUFER S J, 2016. “Unsteady heat-flux measurements of second-mode instability waves in a hypersonic boundary layer”. *Experiments in Fluids*, Vol. 57, 130
- KNAUSS H, ROEDIGER T, BOUNTIN D A, et al, 2009 . “Novel Sensor for fast heat-flux measurements”. *Journal of Spacecraft and Rockets*, Vol. 46, No.2, pp.255-265
- Lakshya Bhatnagar, Guillermo Paniagua, 2019 . “Development of high speed and high temperature atomic layer thermopiles”. In *Proceedings of ASME Turbo Expo 2019: Turbomachinery Technical Conference and Exposition*, June 17-21, Phoenix, Arizona, USA
- Liu Chuping, 2013. *Heat flux measurement in aerothermodynamic test*. Beijing: National Defend Industry Press
- ROEDIGER T, KNAUSS H, GAISBAIER U, et al, 2008 . “Time-resolved heat transfer measurements on the tip wall of a ribbed channel using a novel heat flux sensor-Part I: Sensor and Benchmarks”. *Journal of Turbomachinery*, Vol. 130, pp. 011018
- ROEDIGER T, KNAUSS H, KRAEMER E, et al, 2009. “Hypersonic instability waves measured using fast-response heat-flux gauges”. *Journal of Spacecraft and Rockets*, Vol. 46, No. 2, pp. 266-273
- X. Tao, Zhao Ruipeng, Chen Xi, et al, 2022. “Fabrication of tilted-texture thin films for flexible atomic layer thermopile heat flux sensor” . *Journal of Functional Materials*, Vol. 53, No. 9, pp. 09018-09023
- C. B. Wu, Zhao Gaoyang, Fang Po, et al, 2016. “Effect of oxygen content in atmospheres of heat treatment on the properties of YBCO thin films” . *Rare Metal Materials and Engineering*, Vol. 45, No. 10, pp. 2534-2538
- F. Xiong, Zhang Hui, Li Hong-Shan, et al, 2008. “Influence of annealing oxygen pressure on the laser-induced thermoelectric voltage effect in $\text{YBa}_2\text{Cu}_3\text{O}_{7-x}$ thin films”. *Acta Physica Sinica*, Vol. 57, No. 8, pp. 5237-5243
- K. Yang, Tao Zhu, Xiong Wang, et al, 2020 . “ Self-innovated ALTP heat flux sensor and its performance tests”. *Journal of Experiments in Fluid Mechanics*, Vol.34, No.6, pp.86-91 (in Chinese)
- K. Yang, et al., 2024, "High-Sensitivity Atomic Layer Thermopile Heat- Flux Sensor and Its Application in Hypersonic Low-Density Wind Tunnel Tests". *IEEE Transactions on Instrumentation and Measurement*, vol. 73, No.1001307, pp. 1-7
- P X Zhang and H –U Habermeier, 2008 . “Atomic Layer Thermopile Materials: Physics and Application”. *Journal Of Nanomaterials*, No.329601

THERMAL AND HYDRAULIC ANALYSIS OF AN INVERTED TWO-PHASE THERMOSYPHON

Ricardo Schneider Calomeno^{a,*}, Fernando Henrique Milanez^b, Marcia Barbosa Henriques Mantelli^a

^aFederal University of Santa Catarina, Department of Mechanical Engineering, Florianópolis, SC, 88040-900, Brazil

^bFederal University of Santa Catarina, Department of Energy Engineering, Araranguá, SC, 88905-120, Brazil

*ricardoschneider@labtucal.ufsc.br

Keywords: Inverted two-phase thermosyphon, downward heat transfer, shell-and-tube condenser, periodic operation

1. INTRODUCTION

Heat pipes and thermosyphons are efficient, reliable and simple passive heat transfer technologies for operation in the industry. When the heat source is beneath the heat sink, gravity guarantees operation. However, the downward heat transfer (heat source above heat sink) capability is limited for heat pipes, since limited capillary forces dictate the height of liquid lifting. For this condition, inverted two-phase thermosyphons have been proposed, which uses the pressure difference between hot and cold components of a closed loop in order to pump a working fluid against gravity (De Beni and Friesen, 1985; Dobriansky and Wojcik, 2019).

Inverted two-phase thermosyphon prototypes have been studied in the last years (e.g., Fantozzi and Filippeschi, 2002, Kadoguchi and Yamazaki, 2004, Koito *et al.*, 2009; Duda *et al.*, 2018). In most devices, the heat transferred between the heat source and sink range from 0,3 to 1,2 kW, separated from 1 to 3 m and total liquid lifting heights from 2,0 to 3,3 m.

The objective of the present work is to experimentally evaluate the thermal and hydraulic performances, as well as the overall behaviour of an inverted two-phase thermosyphon, with heat transfer capacity up to 13 kW. The geometry is based on the previous work of Calomeno *et al.* (2023), who used a shell-and-tube heat exchanger as the condenser. It should be noted that heat transfer rates higher than 2 kW have barely been explored in inverted two-phase thermosyphons.

2. EXPERIMENTAL APPARATUS

The inverted two-phase thermosyphon under study in this work has the geometry presented on Fig. 1 and uses water as working fluid. The device is composed by an evaporator, a condenser and an accumulator, which are connected to each other by four lines: equalization (L_1), drainage (L_2), vapor transport (L_3) and liquid lifting (L_4). All components and lines are made of stainless steel, all the lines have an internal diameter of 1,905 cm, and lines L_1 and L_2 have each a manual valve. The evaporator and the accumulator are both cylinders with 21,2 L of capacity (30 cm internal diameter, 30 cm height). The evaporator has three 5kW electrical resistances (15 kW total thermal load capacity). The condenser is a shell-and-tube heat exchanger (15 cm shell diameter, 25 tubes with 1,06 cm internal diameter and length 60 cm each, 5 baffles with a baffle cut of 18 %), the condenser is cooled down by water from a cooling tower. The evaporator, the condenser and line L_3 have thermal insulation on the outside, while all other components are not thermal insulated. The liquid lifting height is 2 m.

The operation cycle of this inverted two-phase thermosyphon is divided into two processes: i) vapor transport and ii) drainage. For the beginning of the first process, both valves in lines L_1 and L_2 are closed and then the electrical resistances inside the evaporator are turned on. So, the thermal load is applied to the working fluid and the formed vapor starts to flow downwards to the condenser through line L_3 due to vapor pressure differences. A liquid pool starts to form at the bottom of the condenser and inside line L_4 . The pressure difference between evaporator (hot) and accumulator (cold) elevates the liquid inside line L_4 until it reaches the accumulator. After a certain amount of liquid is delivered to the accumulator, the drainage process starts. The electrical resistances are switched off and both valves are opened, equalizing the pressure between the accumulator and the evaporator mainly through line L_1 . Under these conditions, the liquid can finally return by gravity to the evaporator by line L_2 . The valves are then closed again for a new cycle to start.

3. RESULTS AND DISCUSSION

In order to evaluate the thermal performance of the present inverted two-phase thermosyphon, a test was carried out. The device is filled with: 16 L of water in the evaporator. Also, there are 1,6 L in the bottom and the internal tubes of the condenser and part of line L_4 remaining from the previous cycle. The thermal load was continuously increased from 1 kW to 13 kW by 2 kW steps, divided into four operation cycles. The thermal load (Q_E) increase happened when a certain volume of liquid (ΔV_E) was evaporated from the evaporator. In the first cycle, thermal loads of 1, 3 and 5 kW were applied for $\Delta V_E = 2$ L. In the second cycle, thermal loads of 7 and 9 kW were applied for a $\Delta V_E = 3$ L each. In the third and fourth cycles the thermal loads were of 11 and 13 kW, for $\Delta V_E = 6$ L each. The device was tested in a room where the environment temperature (T_0) is controlled, the cooling fluid flow rate at the condenser during the test was approximately of 10,8 L/min. The temperature, pressure, thermal load and heat transferred profiles of this test can be seen on Fig.2.

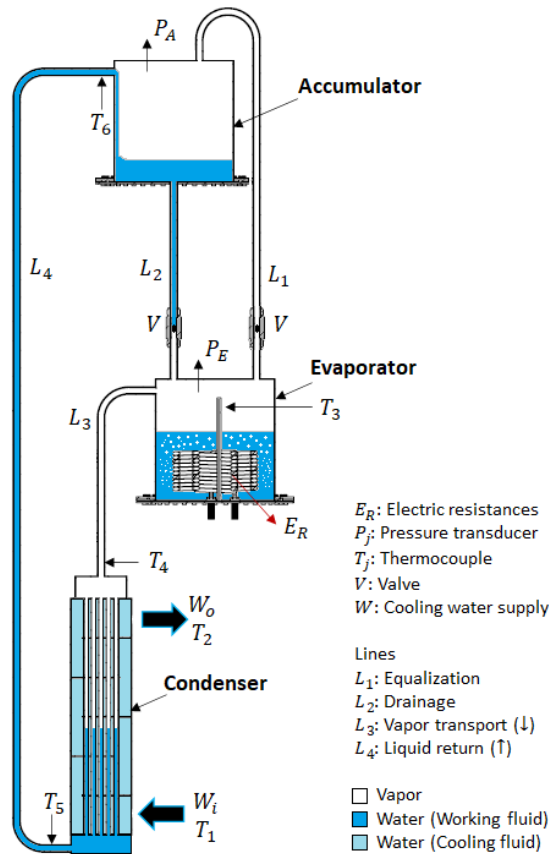


Figure 1. Sketch of the experimental apparatus.

The inverted two-phase thermosyphon is initially at the atmospheric pressure, as can be seen at Fig. 2. In order to allow the operation of the device, the pressure inside the system is reduced by a vacuum pump between the instants $t=320$ s and $t=700$ s, the valves are closed and at $t=1350$ s the first cycle begins with $Q_E=1$ kW. The working fluid is heated and the vapor temperature inside the evaporator (T_3) and at the inlet of the condenser (T_4) increase until the minimum temperature is achieved to start the operation of the device at $t=4330$ s when the heat rejected by the condenser (Q_C) increases and the liquid in line L_4 can be lifted to the accumulator. After that, the temperature increase becomes smooth. Due to the use of transparent hoses liquid level measurements at the evaporator, the condenser and the accumulator, a small infiltration of air into the device is observed through a smooth increase of the accumulator pressure (P_A) with time. Despite the air infiltration, the device continues to operate but with a continuous increase of T_3 , inside the evaporator, thus increasing its pressure (P_E). For the next two thermal load levels, the device shows a fast thermal response until achieving a new stable operation condition. The cycle is finished with the drainage process, with the electrical resistances turned off and the opening of the valves. The pressure equalization starts and the accumulator is heated with the income of hot vapor while the liquid level on line L_4 drops (indicated by the sudden increase of T_6 and P_A), while the evaporator is cooled by the liquid returning from the accumulator (indicated by T_3). The same behaviour is observed for $Q_E=7$ kW, in the second cycle, while the accumulator temperature and pressure are reduced by natural convection with the external environment and by the incoming water. However, when $Q_E=9$ kW the condenser starts receiving water from the cooling tower at slightly higher temperature (T_1) of $28,2$ °C. Under these conditions, the condensed liquid cannot be completely cooled down, thus the accumulator starts receiving water at higher temperatures. In the third cycle this behaviour is intensified with $Q_E=11$ kW and $T_1 \cong 31$ °C, and the condenser is no longer capable to cool the condensed liquid down. This can be clearly observed with the condenser heat transfer rate Q_C from 8 to 9 kW. During this cycle, the fluid reaches the accumulator with T_6 achieving a maximum value of 55 °C. During this cycle, a noise similar to a bubble implosion is heard at the bottom of the condenser. The liquid level at the condenser tubes, measured with a transparent hose, varies abruptly between 10 to 18 cm from the bottom of the condenser. On the beginning of the last cycle, with $Q_E=13$ kW, the liquid level varies between 6 to 17 cm from the bottom of the condenser, provoking an even stronger and louder noise, followed by two-phase flow in line L_4 , detected by sudden increase on temperatures T_5 and T_6 and by the characteristic noise of vapor flow. An increase in P_A is observed with the income of hot vapor and liquid (two-phase flow) and the decrease on T_3 , T_4 and P_E . After the finish of the two-phase flow, a new operation condition is achieved. The noise persists, but not so louder as before. The maximum heat rejection rate at the condenser during this cycle was $Q_C \cong 11$ kW.

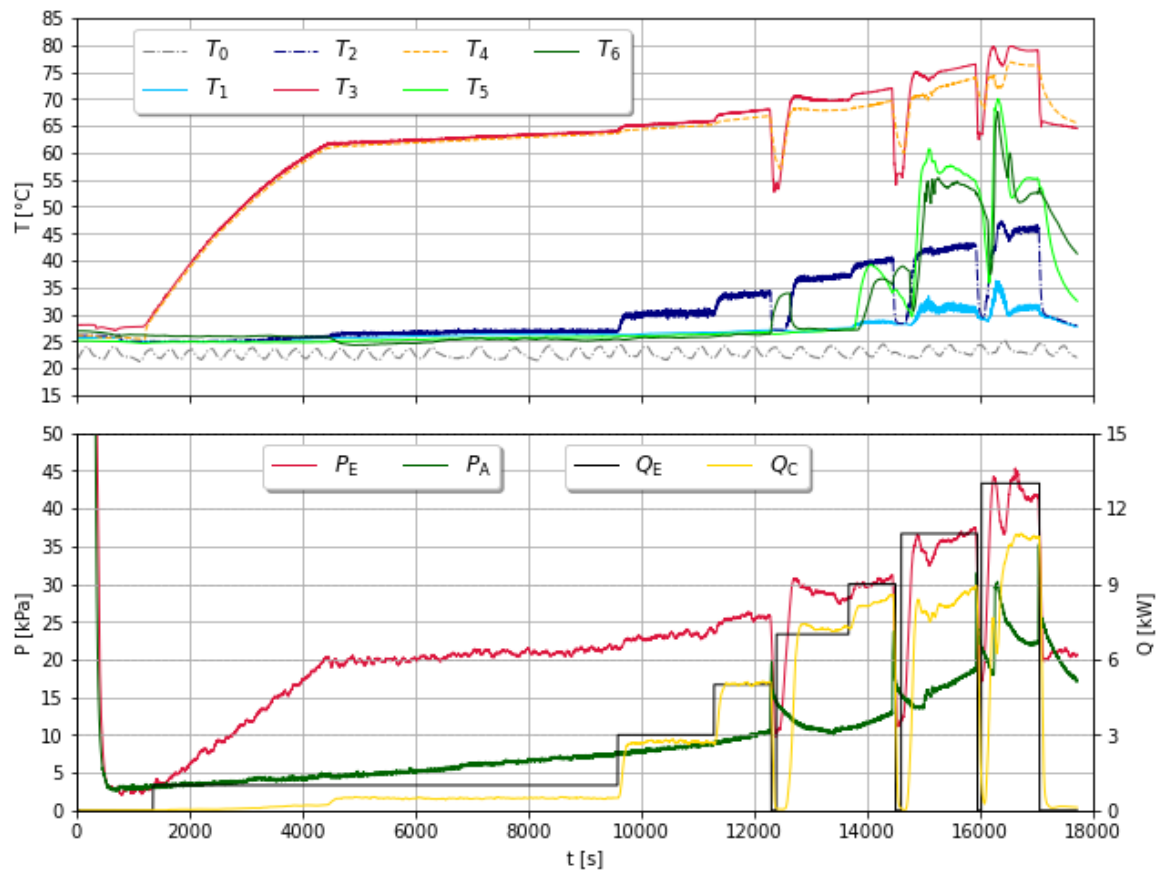


Figure 2. Measured temperature, pressure, evaporator thermal load and condenser heat transfer as a function of time.

4. CONCLUSIONS

In the present work, the experimental thermal and hydraulic behaviours of an inverted two-phase thermosyphon prototype using a shell-and-tube heat exchanger as a condenser is presented for different thermal loads. This device is capable of self-regulating its operation condition in order to transfer heat downwards and to lift liquid from the condenser to the accumulator. The prototype worked very well until 9 kW, when the condenser reached the heat transfer limit due to ambient conditions, which affected the cooling tower performance.

More tests are being carried out in order to study the heat transfer limits and the thermal and hydraulic phenomena of the device at thermal loads for 9 to 13 kW and to ensure a stable and safe operation. The results will be presented in the final manuscript.

5. REFERENCES

- Calomeno, R. S., Milanez, F. H., Mantelli, M. B. H., 2023. "Simplified hydraulic and thermal models for inverted two-phase thermosyphons". *21th International Heat Pipe Conference (21th IHPC)*, Melbourne, Australia.
- De Beni, G. and Friesen, R., 1985. "Passive downward heat transport: experimental results of technical unit". *Solar Energy*, Vol. 34, n. 2, pp 127-134.
- Dobriansky, Y. and Wojcik, R., 2019. "State of the art review of conventional and anti-gravity thermosyphons: focus on two working fluids". *International Journal of Thermal Sciences*, Vol. 136, pp. 491-508.
- Duda, M., Dobriansky, J., Chludzinski, D., 2018. "Analysis of the possibility of applications for a two-phase reverse thermosyphon in passive heat transport systems". *E3S Web conference, SOLINA 2018 – VII Conference SOLINA Sustainable Development: Architecture – Building Construction – Environmental Engineering and Protection Innovative Energy – Efficient Technologies – Utilization of Renewable Energy Sources*. Vol. 49.
- Fantozzi, F., Filippeschi, S., 2002. "Pulsated two-phase thermosyphons for electronic equipment thermal control". *International Conference on Environmental Systems*, San Antonio, United States of America.
- Kadoguchi, K. and Yamazaki, M., 2004. "Intermittent heat transportation by discharge of accumulated vapor". *Applied Thermal Engineering*, Vol. 29, pp. 259-264.
- Koito, Y., Ahamed, M. S., Harada, S., Imura, H., 2009. "Operation characteristics of a top-heat-type long heat transport loop through a heat exchanger". *Applied Thermal Engineering*, Vol. 29, pp.25-264.

Thermal conductance of insulation foams at sub-ambient temperature

Z Zhang*, RMA Spijkers, S Vanapalli*

Applied Thermal Sciences Lab, University of Twente, Enschede, Post Bus 217, 7500 AE, Overijssel, the Netherlands

*z.zhang-3@utwente.nl; s.vanapalli@utwente.nl

Keywords: Thermal conductivity, Cryogenics, Insulation foam, Sub-ambient temperature, Heat transfer

1. INTRODUCTION

The development in the transportation of temperature-sensitive goods have catalyzed the emergence of a cold chain ecosystem that significantly contributes to the global economy (Ashok, 2017). Specifically, pharmaceuticals (Lloyd and Cheyne, 2017), bio-pharmaceuticals (Bishara, 2006), and perishable food items (Mercier *et al.*, 2017) necessitate precise temperature control to preserve their quality during transit (Ramanujan, 2019). The temperature requirements for these products span across various ranges, including ambient (15°C to 25°C), refrigerated (2°C to 8°C), frozen (-80°C to -20°C), and cryogenic temperatures (below -150°C). Temperature-sensitive air cargo shipments frequently utilize dry ice as a cooling agent owing to its high sublimation enthalpy (571000 J/kg), thereby facilitating the sustained maintenance of desired temperatures over extended durations. Typically, these shipments entail the utilization of insulated containers comprising an expanded polystyrene (EPS) foam box.

During the temperature-sensitive transportation, such as vaccines, the heat transfer rate to the system needs to be estimated to determine the sublimation rate of the dry ice. The thermal conductivity of insulation foams utilized in such applications becomes paramount, especially under cryogenic conditions where temperature differences between the internal environment of the transportation vessel and the external ambient surroundings are substantial. The thermal conductivity of the foam is intricately linked to the efficiency of thermal insulation, as it determines the heat transfer rate across the insulating material. Consequently, precise measurement and understanding of the thermal conductance of insulation foams under cryogenic temperatures are imperative to ensure the preservation and stability of temperature-sensitive cargo during transit. Recent work (Purandare *et al.*, 2020), examines dry ice sublimation in insulation packages for shipping temperature-sensitive goods experimentally and numerically, indicating heat transfer rate occur through the inner wall area of the insulation package in contact with dry ice. Two cases of foam thermal conductivity namely $k_f=0.025$ W/(m·K) and $k_f=0.023$ W/(m·K) are inserted into the modelling in comparison with the experimental results due to the lack of the temperature-dependent foam thermal conductivity under sub-ambient conditions. It is shown that foam thermal conductivity chosen affects the accuracy of predicting sublimation rate and end-of-sublimation time of dry ice (Purandare *et al.*, 2020).

In the present study, an apparatus is designed to measure the thermal conductance of insulation foam within the sub-ambient temperature range of 160 to 280 K. Employing a guarded heater on the hot side enhances precision in heat flux measurement. The hot side of the sample remains at room temperature 295 K (also denoted as the reference temperature). By assessing heat flux across the sample under varying cold side temperatures, thermal conductivity integral of the sample is determined with respect to the reference temperature.

2. METHODOLOGY

The heat flux through a material depends on the temperature difference, the cross-sectional area and the thickness. For a rectangular sample (with thickness d and cross-sectional area A) that at the top is in contact with a material at a temperature T_h and at the bottom with a material at temperature T_c (where $T_h > T_c$), the conduction heat flow \dot{q} is described by the Fourier's law $\dot{q} = k(T)AdT/dx$, where $k(T)$ is the temperature-dependent thermal conductivity of the material. If the cryostat part has a uniform cross-sectional area as in the present case, the Fourier's law can be further integrated as:

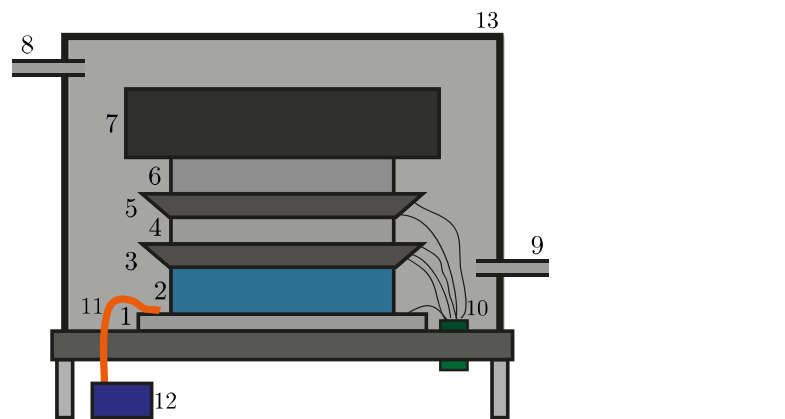
$$\dot{q} = A/d \int_{T_1}^{T_2} k(T) dT = A/d \left[\int_{T_f}^{T_2} k(T) dT - \int_{T_f}^{T_1} k(T) dT \right] \quad (1)$$

Because of the strong temperature dependence of $k(T)$, thermal conductivity integral $\int_{T_1}^{T_2} k(T) dT$ is normally utilized (Ekin, 2006). Knowing the thermal conductivity integral at different temperatures (T_2) with respect to the reference temperature (T_f), the heat flow through a solid material of uniform cross-sectional area A and length d between two arbitrary temperatures T_1 and T_2 can be determined Eq. (1).

The experimental setup used in the present study is schematically shown in Fig. 1. In order to measure the heat flux through a material, a temperature difference needs to be applied between both sides of the sample (2). On the bottom of the sample, an aluminum cold plate (1) was cooled using a copper litze strip whose far end was immersed in a liquid

nitrogen bath. The temperature of the cold side can be controlled be at a temperature T_c ($160 \text{ K} \leq T_c \leq 280 \text{ K}$). Since the cold plate was cooled through indirect contact with liquid nitrogen, a heating element was also incorporated into the temperature control mechanism to ensure that the temperature levels could be maintained at the desired set point without overcooling. Such a temperature control system comprising dual cooling/heating makes it possible to achieve precise temperature control of the cold plate. On the top of the sample a heater (3) is placed that can be controlled to be at a temperature T_h (around room temperature). Above the first heater a second guard heater (5) is placed that is always kept at the same temperature as the first heater, such that there is no heat flow in the upwards direction, improving the measurement accuracy. Therefore, it can be assumed that all the heat from the heater goes through the sample to the cold end.

The experimental procedure mainly involves adjusting the cold side temperature (T_c) and monitoring the power input required by the first heater (3) to maintain constant temperature, serving as an indicator of the heat flowing through the material. Regulation of the heater output is achieved through a CryoCon 24C temperature controller. The entire test-rig is encased within an airtight enclosure, flushed with moderate nitrogen gas flow to avoid the formation of ice during the cooling process of the cold plate. Additionally, a heavy copper block (7) is positioned at the top of the assembly to ensure optimal thermal conductivity and uniform thermal contact across all layers.



- | | |
|-------------------------------------------------------------------------------------------------------|------------------------------------------|
| 1. Cold aluminum plate at a controlled temperature T_c with a DT-670 diode, a PT1000 and 2 heaters. | 6. Insulation |
| 2. Material sample | 7. Weight (copper block) |
| 3. Heater 1 at a controlled temperature T_h with a DT-470 diode | 8. Gas outlet |
| 4. MLI insulation | 9. Gas inlet |
| 5. Heater 2 (guard heater) at a controlled temperature T_h with a DT-470 diode | 10. 2 connectors for sensors and heaters |
| | 11. 2 copper litze wires |
| | 12. LN ₂ bath |
| | 13. Airtight box |

Figure 1. Schematic of the experimental set-up.

3. PRELIMINARY RESULTS

Initial assessments were conducted utilizing Polymethyl Methacrylate (PMMA) sheets, each measuring 4 mm and 10 mm in thickness and 10 cm in width. The power input required for maintaining the hot side at room temperature under varying cold side temperature is illustrated in Figure 2. It is observed that the heat flux decreases linearly with the increasing of the cold side temperature. However, as the cold side temperature converges toward the hot side temperature, non-zero power input is noticed, indicating the effect of the parasitic heat leak. The data points denoted by red symbols in Fig. 2 represent the respective heat leak values for the two samples under consideration. Once the heat leak is determined, the corrected heat flux can be determined by

$$\dot{q}_r = \dot{q}_t - \dot{q}_p \quad (2)$$

where \dot{q}_r is the corrected heat flux through the material, \dot{q}_t is the total measured heat flux, \dot{q}_p is the parasitic heat leak. The corrected heat flux is used to calculate the thermal conductivity integral using Eq. (1). Figure 3 illustrates the calculated thermal conductivity integral as a function of the cold side temperatures. This demonstrates the efficacy of the proposed methodology in accurately measuring the thermal conductance of samples within sub-ambient conditions, while also exhibiting high repeatability.

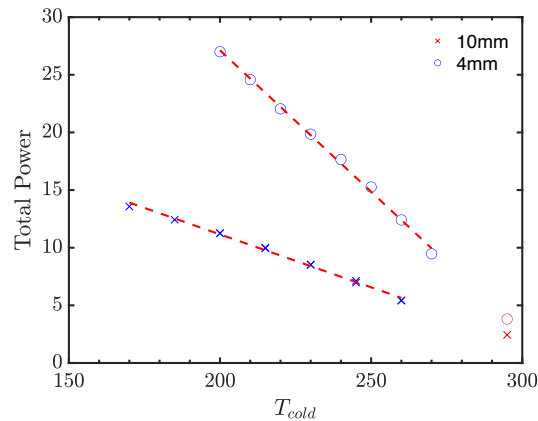


Figure 2. The measured power input as a function of cold side temperature. The blue symbols are the measured data points, while the red symbol represent extrapolated values.

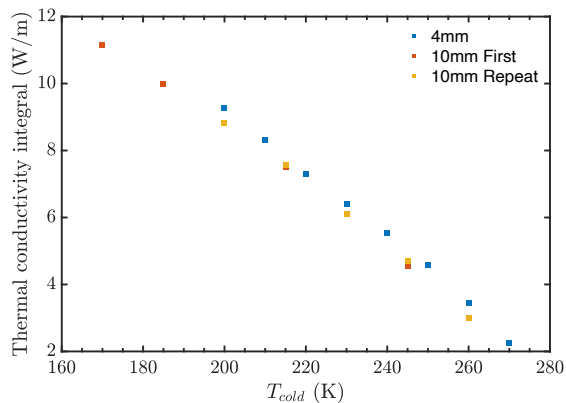


Figure 3. Thermal conductivity integral at varying cold side temperatures.

4. CONCLUSIONS

In the present work, a guarded-plate apparatus for the thermal conductance measurement is proposed. For the preliminary test, the feasibility and repeatability of measuring the thermal conductance under various cold side temperatures is confirmed using test sample PMMA. The insulation foam will be used in the next step.

5. REFERENCES

- Ashok, A., Brison, M., & LeTallec, Y. (2017). *Improving cold chain systems: Challenges and solutions*. *Vaccine*, 35(17), 2217-2223.
- Bishara, R. H. (2006). *Cold chain management—an essential component of the global pharmaceutical supply chain*. *American Pharmaceutical Review*, 9(1), 105-109.
- Ekin, J. (2006). *Experimental techniques for low-temperature measurements: cryostat design, material properties and superconductor critical-current testing*. Oxford university press.
- Lloyd, J., & Cheyne, J. (2017). *The origins of the vaccine cold chain and a glimpse of the future*. *Vaccine*, 35(17), 2115-2120.
- Mercier, S., Villeneuve, S., Mondor, M., & Uysal, I. (2017). Time–temperature management along the food cold chain: A review of recent developments. *Comprehensive reviews in food science and food safety*, 16(4), 647-667.
- Purandare, A. S., van Lohuizen, S. W., Spijkers, R. M. A., & Vanapalli, S. (2021). *Experimental and numerical study of insulation packages containing dry ice pellets*. *Applied thermal engineering*, 186, 116486.
- Ramanujan S. (2019), Emirates skycargo works with dubai start-up for efficient and transparent sourcing of seafood, 2019, <https://www.emirates.com/media-centre/emirates-skycargo-sees-a-successful-summer-season-for-transporing-perishables-and-pharma-through-dubai/>.

INVESTIGATION ON DIFFUSER FILM HOLES STRUCTURAL DESIGN OF TURBINE TWIST BLADE

Ren Ming^a, Ye Lin^{a,b*}, Wu Si-Qi^c, Ni Yu-Hao^d, Li Bing-Ran^a, Liu Song^c, Liu Cun-Liang^{a,b}

^a School of Power and Energy, Northwestern Polytechnical University, Xi'an, Shaanxi 710072, China

^b Shaanxi Key Laboratory of Thermal Sciences in Aero-engine System, Xi'an, Shaanxi 710129, China

^c AECC Sichuan Gas Turbine Establishment, Chengdu, Sichuan 610500, China

^d Expace Technology Co., Ltd., Wuhan, Hubei 430000, China

*linye@nwpu.edu.cn

Keywords: Film cooling, Diffuser shaped holes, Pressure sensitive paint, Twisted blade

1. INTRODUCTION

The film cooling technique [1] has been widely used in thermal protection of aero-engine turbine blades. The coolant inside the blade flows out through holes in the blade surface and forms a thin film over the wall surface. The thin film prevents hot gases from impinging on the blades directly. Over the years, this technique has significantly increased the service temperature limit of the blades. With the deepening of the research, it is found that the traditional cylindrical film hole has the disadvantages of small coverage, poor film adherence to the wall, and poor adaptability at high blowing ratios. In recent years, a variety of shaped hole structures have been proposed to obtain higher film cooling effectiveness. Among these shaped holes, the diffuser hole [2] have been widely studied due to its good cooling performance.

Zhang et al [3] and Liu et al [4] experimentally investigated the film cooling characteristics of laid-back-fan-shaped holes on blade. Film cooling effectiveness of blade was measured by utilizing pressure sensitive paint (PSP) measurement techniques. They found that the shaped holes tend to allow coolant to attach near the wall compared to cylinder holes. This is because the shaped holes with expanded exit reduces the momentum of the coolant jet, and low momentum of coolant jet reduces the degree of mixing with the mainstream gas. Zhao et al [5] numerically investigated the vortex system structure at the exit of shaped holes by means of a large vortex simulation method. It was found that the intensity of the kidney vortex pair at the exit of diffuser film hole was significantly weakened. Fox [6] investigated the effect of compressible flow on the film cooling effectiveness of shaped hole in a high-speed wind tunnel. It was found that the adjoint optimised hole [7] showed jet bias phenomenon, and its air film cooling efficiency was still better than that of the 7-7-7 laid-back-fan-shaped holes. This is due to the fact that the adjoint optimised hole has a larger exit width, which could be obtained wider film coverage. There are two main objectives in the design of shaped holes, i.e., to improve the air film cooling effectiveness and to expand the lateral coverage. However, the geometrical parameters of the shaped holes include hole diameter, hole length-to-diameter ratio, hole expansion section length, hole expansion angle, hole inlet/outlet area ratio, etc., and there is complex relationship of constraints between these parameters. This makes it very difficult for engineers to design shaped hole structures.

Based on previous research, we can easily find out that diffuser shaped holes provide wider film coverage downstream of the hole exit. This characteristic is one of the reasons why the shaped hole was designed. Therefore, we believe that the key structural parameter affecting the film cooling effectiveness of the diffuser shaped holes is the exit width. In this paper, a twisted blade is selected as the research object, and the film cooling characteristics of diffuser shaped holes were experimentally studied. We intend to find the suitable range of hole exit widths for excellent film cooling performance of blade.

2. EXPERIMENTAL SETUP

The blade with diffuser shaped holes was placed in a low-speed wind tunnel as shown in Fig.1. PSP [8-9] measurement technique was using to obtained the film cooling effectiveness distributions. In this experiment, N₂ and CO₂ were used to achieve different density ratios of the coolant to the mainstream. The test conditions are shown in Table 1.

Figure 2 presents the model of test blade and the structure parameters of the diffuser shaped holes.

Table 1. Test Conditions.

Variables	Ranges
Mainstream Reynolds number Re	1.5×10^5
Mainstream turbulence Tu	6%
Mainstream temperature T (K)	295 ± 0.2
Blowing ratio M	0.6, 1.0
Density ratio	1.0, 1.5

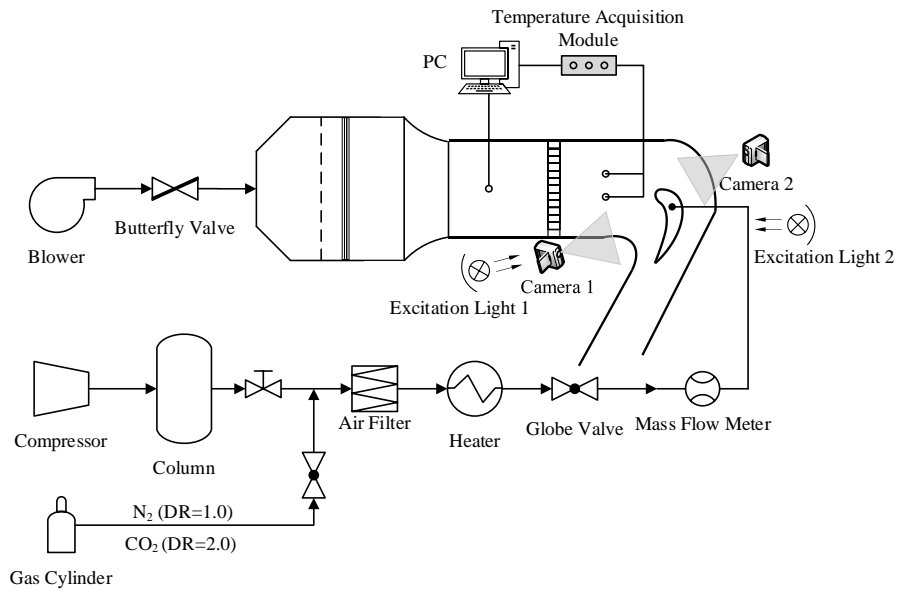


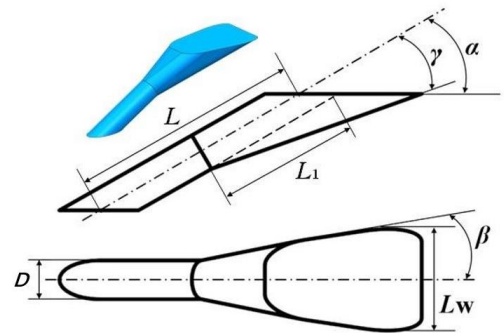
Figure 1. Experimental system.



a) Suction side



b) Pressure side



c) Hole structure parameters

Figure 2. Test blade model and diffuser shaped holes.

3. RESULTS AND DISCUSSION

Figure 3 shows the distribution of film cooling effectiveness for different holes exit widths (L_w) on suction side. Figure 4 shows the distribution of film cooling effectiveness for different holes exit widths (L_w) on pressure side. Figure 5 shows the distribution of spanwise average film cooling effectiveness for different holes exit widths (L_w).

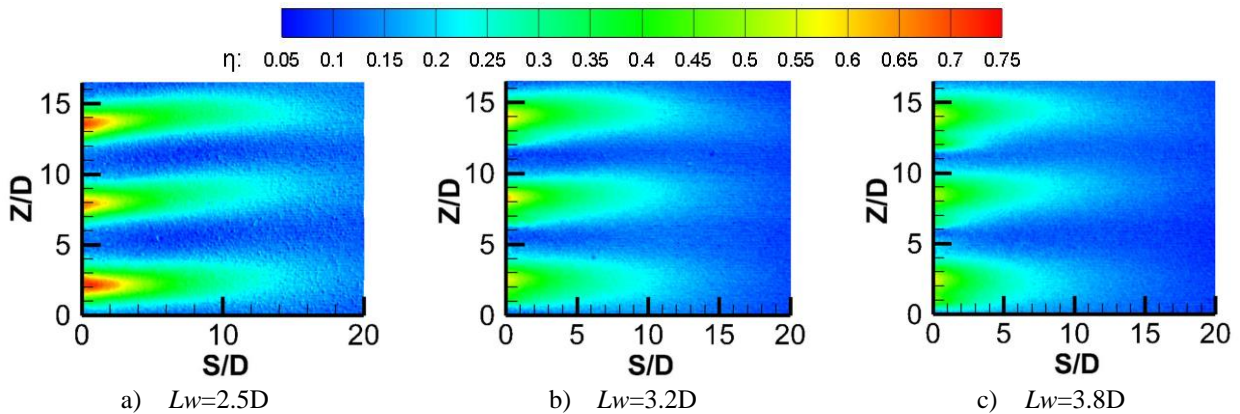


Figure 3. Distribution of film cooling effectiveness for different holes exit widths (L_w) on suction side

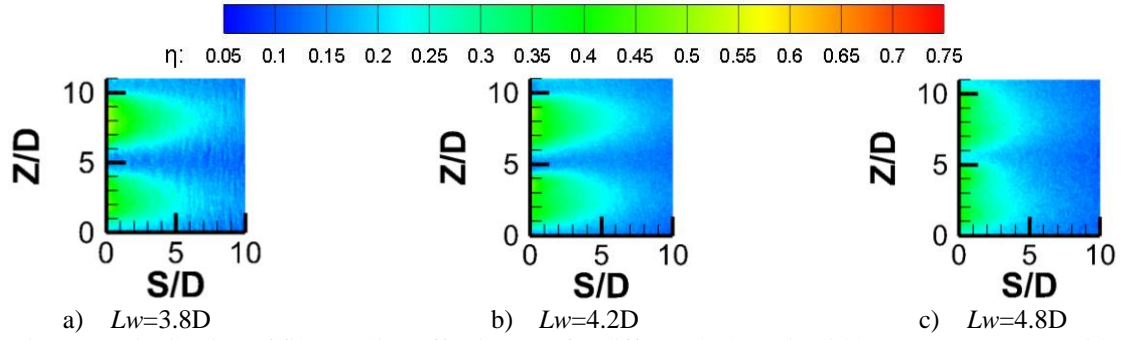


Figure 4. Distribution of film cooling effectiveness for different holes exit widths (L_w) on pressure side

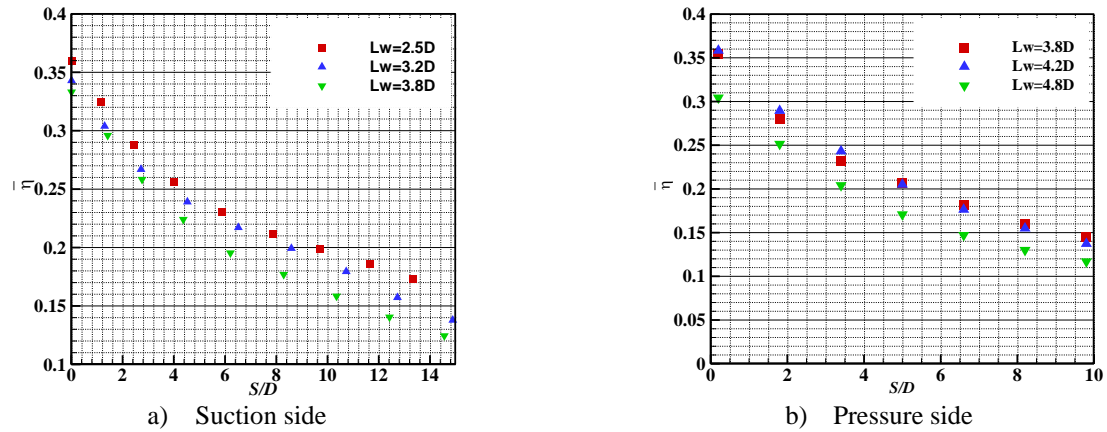


Figure 5 shows the distribution of spanwise average film cooling effectiveness for different holes exit widths (L_w).

4. CONCLUSIONS

This study showed that the optimal hole exit width of the laid-back fan-shaped hole on suction side of blade ranges from 3.0D to 3.2D. The diffusion hole with a compound angle has the better film cooling performance between outlet widths of 3.8D and 4.2D on the pressure side.

5. REFERENCES

- [1] Bunker R S., 2017. "Evolution of turbine cooling", *In Proceedings of ASME Turbo Expo 2017: Turbomachinery Technical Conference and Exposition*. Charlotte, North Carolina, USA: ASME, 2017: GT 2017-63205.
- [2] Bunker R S., 2010. "Film cooling: breaking the limits of diffusion shaped holes". *Heat Transfer Research*, Vol. 41, pp. 627-650.
- [3] Zhang B L, Zhu H R, Yao C Y, et al., 2021. "Experimental study on film cooling and heat transfer characteristics of a twisted vane with staggered counter-inclined film-hole and laid-back-shaped-hole", *International Journal of Heat and Mass Transfer*, Vol. 176, pp. 121377.
- [4] LIU C L, ZHANG F, ZHANG S Q, et al., 2022. "Experimental investigation of the full coverage film cooling effectiveness of a turbine blade with shaped holes", *Chinese Journal of Aeronautics*, Vol. 35, pp. 297-308.
- [5] Zhao Z Y, Wen F B, Tang X L, et al., 2021 "Large eddy simulation of an inclined jet in crossflow with vortex generators", *International Journal of Heat and Mass Transfer*, Vol. 170, pp. 121032.
- [6] Fox D W, Furgeson M, Flachs E M, et al., 2023. "Experimental Study of Compressible Film Cooling Scaling and Hole Geometry" *In Proceedings of ASME Turbo Expo 2023: Turbomachinery Technical Conference and Exposition*. Boston, Massachusetts, USA: ASME, 2023: GT2023-104038.
- [7] Jones F B, Oliver T, Bogard D G. 2021. "Adjoint Optimization of Film Cooling Hole Geometry", *In Proceedings of ASME Turbo Expo 2023: Turbomachinery Technical Conference and Exposition*. Virtual, Online, 2021: GT2021-59332.
- [8] Ye L, Liu C L, Li B R, et al., 2022. "Detailed showerhead cooling effectiveness measurements on the notched leading-edge surface: Effect of freestream turbulence and density ratio", *International Communications in Heat and Mass Transfer*, Vol. 135, pp. 106142.
- [9] Ye L, Liu C L, Du K, et al., 2022. "Influences of groove configuration and density ratio on grooved leading-edge showerhead film cooling using the pressure sensitive paint measurement technique", *International Journal of Heat and Mass Transfer*, Vol. 190, pp. 122641.

EXPERIMENTAL STUDY ON SEVERE SLUGGING FLOW IN PIPELINE-RISER UNDER DIFFERENT START-UP CONDITIONS

Tianyu Liu^a, Suifeng Zou^{a,*}, Hanxuan Wang^a, Liangsheng Zhou^b, Liejin Guo^{a,*}

^aState Key Laboratory of Multiphase Flow in Power Engineering, Xi'an, 710049, China

^bChina National Offshore Oil Corporation Research Institute Co., Ltd., Beijing, 102200, China

* zou_suifeng@xjtu.edu.cn (Zou S.), lj-guo@mail.xjtu.edu.cn (Guo L.)

Keywords: Two-phase flow, Severe slugging, Start-up transportation, Initial Condition, Flow characteristic

1. INTRODUCTION

Gas-liquid two-phase flow is common in the offshore oil and gas pipelines. Due to the complicated gas-liquid two-phase flow characteristics, the flow behavior of multi-phase flow in pipelines has become a great concern. Severe slugging is a hazardous flow pattern in offshore pipeline-riser system. A typical severe slugging cycle consists of four stages: liquid slug growth, liquid slug outflow, gas-liquid eruption, and liquid fallback. It will cause cutoff or overflow of gas-liquid separator, and also pipe vibration because of large amplitude of pressure fluctuation. In past studies, researchers have studied slugging under steady conditions in different pipe structures (Taitel, 1990; Montgomery, 2002; Malekzadeh *et al*, 2012). Elimination of severe slugging were also studied under steady conditions where inlet flow rates and separator pressure were kept nearly constant (McGuinness and Cooke, 1993; Jansen *et al*, 1996). Besides under steady conditions, severe slugging may also form under transient conditions, like start-up, flow rate adjustment, pigging, lost control of pressure, etc (Sivertsen *et al*, 2010). The severe slugging behaviors under transient conditions are not exactly the same with those under steady conditions. Hence, the control strategies and models developed for steady conditions are not always applicable. In this study, the start-up period is studied, during which the transient severe slugging commonly occurs. The start-up condition can be divided into three cases – new production, restart after a shutdown, and the repurpose of a gas pipeline for a new neighborhood oil well. The initial condition of pipeline for the three cases can be described by the full occupation of liquid, part occupation of liquid, and almost empty pipeline, respectively. In this study, the formation of severe slugging during the three start-up conditions are experimentally investigated and compared, so as find the most proper operation and control strategy in the future.

2. EXPERIMENTS

The experimental system is shown in Fig.1. Air and water are pressurized by a compressor and a centrifugal pump, respectively. After being measured by the corresponding flowmeters, they flow into the loop through a mixer. For the initial state of full liquid, the water flow rate is first adjusted; then, the air flow rate is adjusted from zero to the set value of this test. For the initial state of empty pipe, on the contrary, the gas phase flow is first adjusted, then turn up the liquid flow rate from zero to the set value of this test. For the initial condition of part occupation of liquid, first fill the loop with water, then, stop the pump and let the liquid level in the riser fall back to 1/2 of its height, and then jointly turn up the liquid flow and gas flow from zero to the set values. The set values of superficial velocities in the experiments are shown in Table 1. The difference between SS1 and SS2 patterns is that liquid outflow stage is absent in an SS2 cycle.

Table 1. Experimental operation conditions

Initial State	Final pattern: severe slugging 1 (SS1)		Final pattern: severe slugging 2 (SS2)	
	Superficial Gas Velocity (m/s)	Superficial Liquid Velocity (m/s)	Superficial Gas Velocity (m/s)	Superficial Liquid Velocity (m/s)
Full Water	0.1	0.1	0.6	0.1
Full Gas	0.1	0.1	0.6	0.1
Gas-Water Two-Phase Flow	0.1	0.1	0.6	0.1

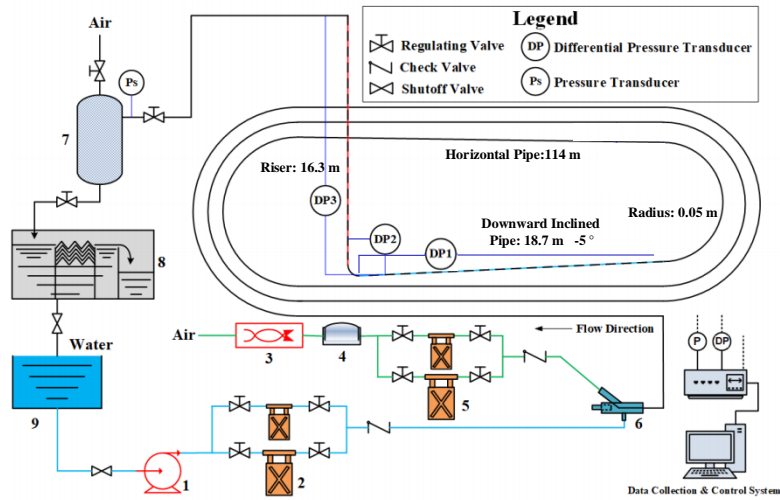


Figure 1. Experimental system of Oil-Gas-Water multiphase flow (1. plunger pump, 2. mass flowmeter for liquid, 3. air compressor, 4. air buffer vessel, 5. mass flowmeter for gas, 6. mixer, 7. gas-liquid separator, 8. liquid-liquid separator, 9. water tank).

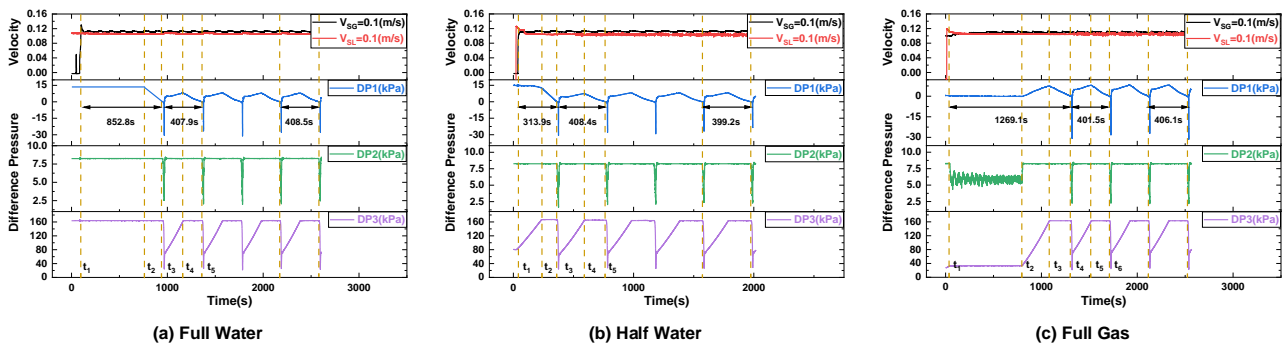


Figure 2. Pressure fluctuations under different start-up conditions ($V_{SG} = 0.1 \text{ m/s}$, $V_{SL} = 0.1 \text{ m/s}$)

3. RESULTS

For the initial state of full water, as shown in Fig.2 (a), the superficial liquid velocity was adjusted to 0.1m/s first. At t_1 , the superficial gas velocity was adjusted from 0 to 0.1m/s. At this time, the downward inclined pipe, the elbow and the riser were fully occupied by water. DP1, DP2 and DP3 were at the maximum values, and the outlet of the riser is pure liquid phase. During the $t_2 - t_3$ period, the gas chamber reached the downward inclined pipe and extended to the bottom of the riser, and DP1 gradually decreased. At t_3 , the gas chamber reached the elbow at the bottom of the riser. Due to the effect of pressure, the concentrated gas chamber and the liquid phase erupted at a high speed. The outlet of the riser was two-phase flow, and DP1, DP2 and DP3 declined rapidly. The first severe slugging cycle began at t_3 .

For the initial state of part occupation of water, as shown in Fig.2 (b), both superficial gas velocity and superficial liquid velocity were adjusted to 0.1 m/s at t_1 . Because the initial liquid level in the riser was lower, the initial pressure was also lower than that in the previous case. Hence, the time for the gas chamber to extend to the downward inclined pipe was much less. During the period of $t_1 - t_2$, the liquid phase in the riser rose slowly. At t_3 , the gas chamber reached the elbow at the bottom of the riser, and then the gas-liquid two-phase flow erupted at a high speed. Although the first complete severe slugging cycle began at t_3 , the period of $t_1 - t_2$ is also like the stages of severe slugging.

For the initial state of almost empty pipeline, as shown in Fig.2 (c), the superficial gas velocity was adjusted to 0.1m/s at first. Then, the superficial liquid velocity was adjusted to 0.1 m/s at t_1 . During the $t_1 - t_2$ period, the liquid phase entering the loop after start-up had not yet reached the bottom of the riser. It can be seen from DP2 that at this stage, although there was small amount of water at the bottom of the riser (which was unable to be exhausted before start-up), the gas phase was still able to pass of the elbow, preventing the formation of severe slugging. When the newly-entered water finally reached the bottom of the riser, the slug formed and blocked the elbow, and the liquid phase in the riser gradually rises. The first complete severe slugging cycle began at t_2 ; however, it was not until t_4 that the waveforms became repeatable.

By comparing the three cases displayed in Fig. 2, it is concluded that the duration of start-up process was longest for the initial state of full water. Liquid blockage existed for the cases of full and part occupation of water. The first eruption occurred earliest for the initial state of part occupation of water. These three results are same at higher start-up superficial gas velocity, as illustrated by Fig. 3. It is clear that the duration time was shorter at higher superficial velocity under the same start-up condition.

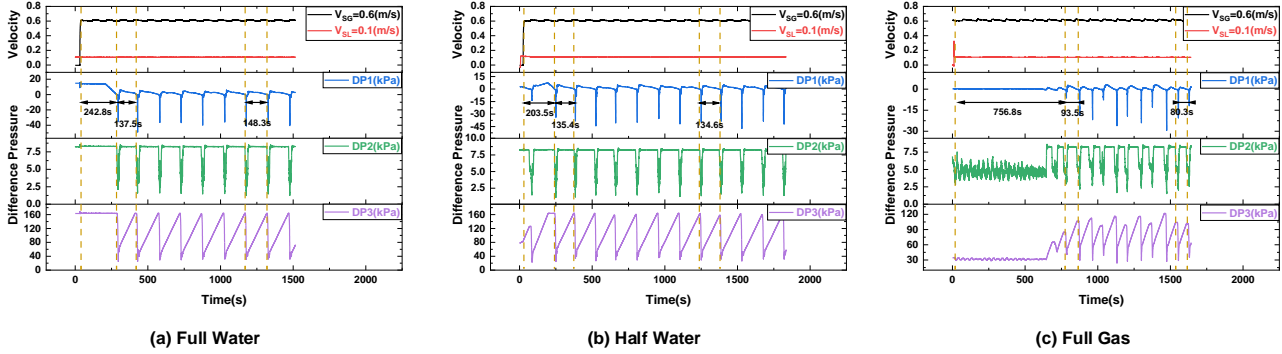


Figure 3. Pressure fluctuations under different start-up conditions ($V_{SG} = 0.6$ m/s, $V_{SL} = 0.1$ m/s)

There are three differences between the results displayed by Fig. 2 and Fig. 3. For the final pattern of SS1, the period of the first slugging cycle time was close to the following cycles, and it could be considered that the steady flow condition was established at the end of the first complete slugging cycle for all three initial conditions. While for the final pattern of SS2, the steady flow condition was established after two complete cycles for the initial condition of almost empty pipeline. The second difference is that the first complete slugging cycle may not be the same with the final pattern for the initial condition of part occupation of liquid, as illustrated by Fig. 3 (b), where the first complete cycle showed SS1 behavior. The third difference was that the final condition was dependent on the initial condition for the case of gas velocity = 0.6 m/s. The period and the pressure amplitude under the initial state of full gas were smaller than the other two conditions. A repeated test showed the same qualitative result.

4. CONCLUSIONS

In this study, the formation of slugging flow in pipeline-riser under different start-up conditions were experimentally investigated. Among three initial conditions, the first eruption occurred earliest under the initial condition of partly occupation of liquid; while transient full occupation was also likely to occur even if the final flow pattern was SS2. Therefore, more caution should be put on the surveillance of eruption. Under the initial condition of full liquid, with gas chamber accumulating in the pipeline, attention should be paid on large slug velocity during the start-up process owing to the incompressibility of water. Another noticeable finding is that at certain superficial velocities, the final state of pressure fluctuation amplitude and period was dependent on initial condition, which is worthy of further investigation.

5. REFERENCES

- Jansen FE, Shoham O, Taitel Y, 1996. "The elimination of severe slugging - experiments and modeling". *International Journal of Multiphase Flow*, Vol. 22 (6), pp. 1055-1072.
- McGuinness, M., Cooke, D., 1993. "Partial stabilization at st. joseph". In: *Proceeding of the 3rd International Offshore and Polar Engineering Conference*, pp. 235-241.
- Malekzadeh R, Henkes RAWM, Mudde RF, 2012. "Severe slugging in a long pipeline-riser system: experiments and predictions". *International Journal of Multiphase Flow*, Vol. 46 (0), pp. 9-21.
- Montgomery JA, Yeung HC, 2002. "The stability of fluid production from a flexible riser". *Journal of Energy Resources Technology-Transactions of the Asme*, Vol. 124 (2), pp. 83-89.
- Sivertsen, H., Storkaas, E., Skogestad, S., 2010. "Small-scale Experiments on Stabilizing Riser Slug Flow". *Chemical Engineering Research and Design*, pp. 213-228.
- Taitel Y, Vierkandt S, Shoham O, et al, 1990. "Severe slugging in a riser system: Experiments and modeling". *International Journal of Multiphase Flow*, Vol. 16 (1), pp. 57-68.

ACKNOWLEDGMENT

This work is financially supported by National Key Research and Development Program of China (Grant Number 2022YFC2806200).

EFFECTS OF TURBULENCE INTENSITY AND DENSITY ON FILM COOLING EFFECTIVENESS OF TURBINE BLADE

Zhou Tian-liang^a, Ye Lin^{a,b,*}, Xu Wei-Jiang^{a,b}, Yan Hao-nan^a, Liu Cun-liang^{a,b}

^a School of Power and Energy, Northwestern Polytechnical University, Xi'an, Shaanxi 710072, China

^b Shaanxi Key Laboratory of Thermal Sciences in Aero-engine System, Xi'an, Shaanxi 710129, China

*linye@nwpu.edu.cn

Keywords: Film cooling, Pressure sensitive paint, Turbulence intensity

1. INTRODUCTION

Film cooling is an essential technique for turbine blades, as it can enhance the upper performance limit and reduce NO_x emissions of the engine[1]. By creating film holes on the surface of high temperature blades, coolant can be ejected, and an insulating layer of relatively cold air can be formed on the surface of the blade, reducing convective heat transfer in that region[2].

Film cooling is a process wherein the coolant and mainstream fluid are combined and diffused downstream with the mainstream. According to fluid dynamics theory, the exchange of velocity between the coolant and mainstream primarily occurs in the vicinity of the hole outlet. Matching the velocity ratio experimentally seems to characterize the velocity field at the hole outlet under engine conditions, a conclusion demonstrated by Pietrzyk[3]. Nevertheless, when attention is diverted to the region beyond the hole exit, the velocity ratio becomes inapplicable and does not precisely quantify the thermal effect of the coolant flow[4]. It was discovered that the role of density cannot be overlooked, prompting the introduction of two novel scaling parameters, the blowing ratio M (the ratio of coolant to the mass flux of the main flow) and the momentum ratio I (the ratio of coolant to the momentum flux of the main flow). When the coolant adheres to the surface, M is a suitable scaling factor for η [5]. However, when the coolant is detached from the wall, M becomes inapplicable, and I becomes a more appropriate scaling parameter[6]. Researchers have performed a significant amount of work to investigate the impact of the density ratio (DR) on η . Sinha[7] measured the η of a row of inclined film holes on a flat plate using thermocouples and discovered that an increase in DR significantly increased lateral diffusion (diffusion perpendicular to the flow direction) of the jet flow, thus boosting the lateral average η . By large eddy simulation, Sakai[8] uncovered the mechanism behind this phenomenon, where an increase in DR resulted in the enhancement of the jet shear-layer vortex, allowing for more coolant to be delivered to the wall. The crucial role of the DR has made it an important scaling parameter for many researchers conducting modeling experiments[9-12].

Scholars have also applied the above theory in the measurement of η . Especially in recent years, pressure sensitive paint (PSP) measurement techniques based on heat and mass transfer theory have been widely utilized [13]. Li [14] employed CO₂ and N₂ as coolants to investigate the impact of film hole diameter on the leading edge region of rotating twisted blades. Similarly, Wang [15] utilized CO₂ as a coolant to explore the cooling performance of crescent-shaped crater holes, whereas Zhang [16] employed a coolant mixture of 15% SF₆ and 85% Ar to simulate the conditions of a real engine with a DR close to 2.0.

2. EXPERIMENTAL METHODS AND PARTIAL RESULTS

In this paper, the cooling effectiveness of a turbine blade with 7 rows of film was measured in the low-speed wind tunnel by pressure sensitive paint (PSP) measurement technique. The inlet Reynolds number is 100000, and the mass flow ratio of mainstream and secondary flow ranges from 1.29% to 5.29%. Three coolants were meticulously selected for experimentation in order to evaluate the effect of density on η . The position of the grid in the mainstream has been adjusted to change the turbulence intensity level from 8% to 16%. The test conditions are shown in Table 1.

The linear cascade and measuring system utilized in the experiment are shown in Fig.1. The mainstream was supplied by a blower and then directed into an air storage tank to stabilize pressure. It subsequently underwent a series of filtration processes, including passing through a strainer to filter out dust and impurities and a honeycomb rectifier to break down eddies into smaller sizes. Finally, the mainstream was introduced into the linear cascade channel through a turbulence grid, which generated high turbulence intensity at the inlet of the first-stage guide vane.

Figure 2 shows the contours of η with different MFR.

Figure 3 and shows streamwise distribution of η with different Tu and DR .

3. FIGURES AND TABLES

Table 1. Test Conditions.

Variables	Ranges
Inlet Reynolds number Re_m	100000
Inlet turbulence intensity Tu	8%, 12%, 16%
Inlet temperature $T(K)$	297 ± 0.2
Mass flow ratio MFR	1.29%, 3.29%, 5.29%
Density ratio DR	1.0, 1.5, 2.8

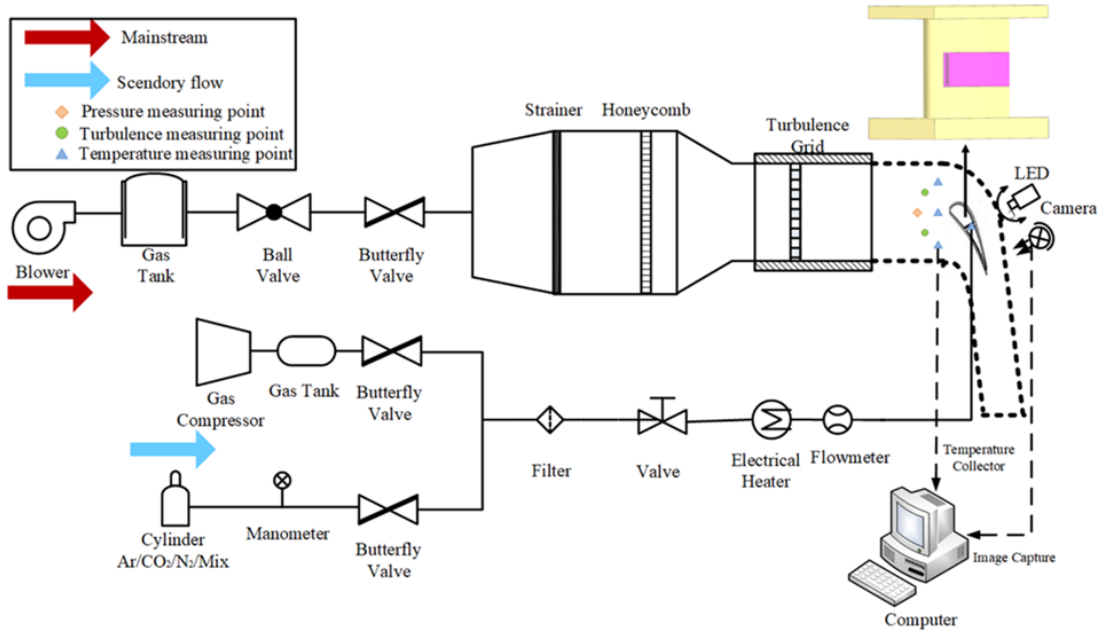


Figure 1. Experimental system.

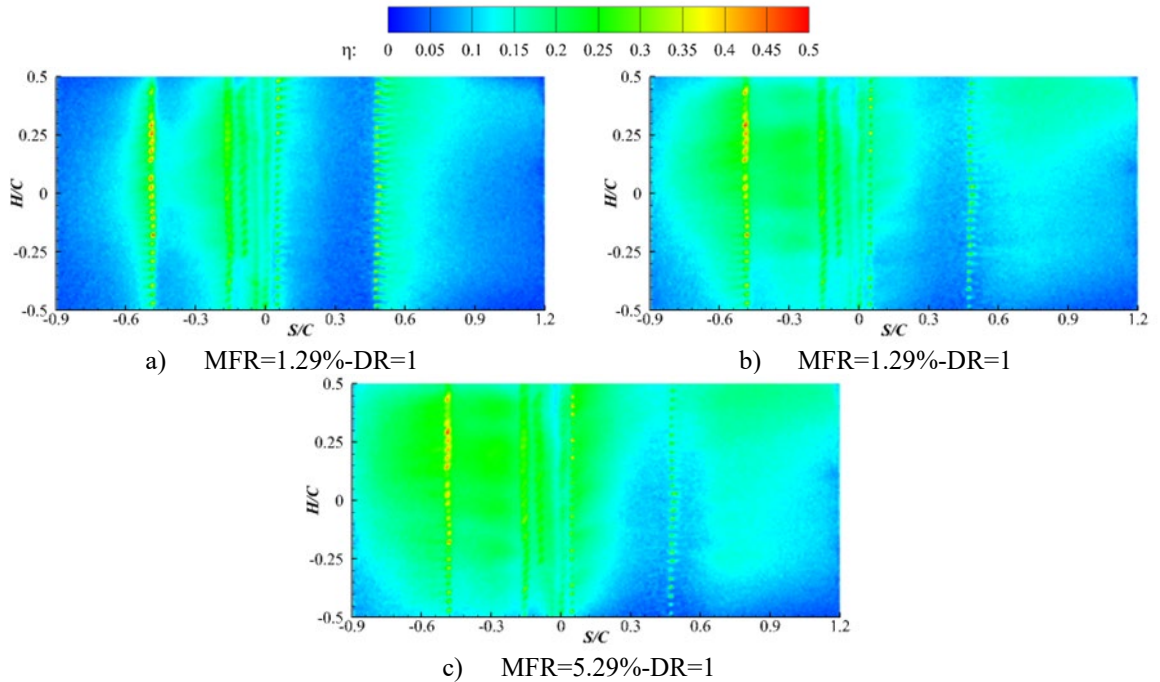


Figure 2. Contours of η with different MFR .

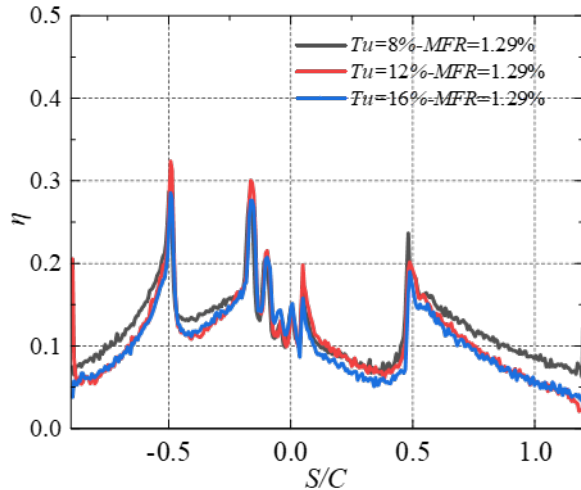


Figure 3. Streamwise distribution of η with different Tu

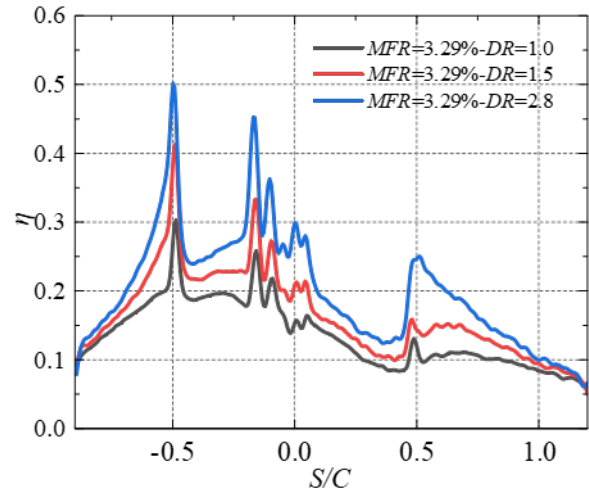


Figure 4. Streamwise distribution of η with different DR

4. CONCLUSIONS

The results demonstrate that low turbulence intensity is beneficial for the attachment of coolants and the increase of η . The effect of density is significant, the η under high density ratio increases obviously for all mass flow ratios.

5. REFERENCES

- [1] Wu Z, Zhu H-R, Liu C-L, et al. 2022, "Investigation of the roughened target plate to enhance the impingement heat transfer with reduced pressure loss". *Applied Thermal Engineering*, 208 (118264).
- [2] Bogard D G, Thole K A. 2006, "Gas Turbine Film Cooling". 22 (2), pp: 249-270.
- [3] Pietrzyk J R, Bogard D G, Crawford M E. 1990, "Effects of Density Ratio on the Hydrodynamics of Film Cooling". *Journal of Turbomachinery*, 112 (3), pp: 437-443.
- [4] Thole K A, Sinha A K, Bogard D G, et al. 1992, "Mean temperature measurements of jets with a crossflow for gas turbine film cooling application". *Rotating Machinery Transport Phenomena*, A93-54626 24-34, pp: 69-85.
- [5] Johnson B, Tian W, Zhang K, et al. 2014, "An experimental study of density ratio effects on the film cooling injection from discrete holes by using PIV and PSP techniques". *International Journal of Heat and Mass Transfer*, 76, pp: 337-349.
- [6] Ito S, Goldstein R J, Eckert E R G. 1978, "Film Cooling of a Gas Turbine Blade". *Journal of Engineering for Gas Turbines and Power* 100 (3), pp: 476-481.
- [7] Sinha A K, Bogard D G, Crawford M E. 1991, "Film-Cooling Effectiveness Downstream of a Single Row of Holes With Variable Density Ratio". *Journal of Turbomachinery*. 113 (3), pp: 442-449.
- [8] Sakai E, Takahashi T. 2017, "Numerical Study on Effects of Density Ratio on Film Cooling Flow Structure and Film Cooling Effectiveness". *ASME Turbo Expo 2017: Turbomachinery Technical Conference and Exposition, Volume 5A: Heat Transfer*, GT2017-63168.
- [9] Liu R, Li H, Lin J, et al. An experimental and numerical investigation of film cooling effectiveness on a gas turbine blade tip region[J]. *International Journal of Thermal Sciences*, 2022, 177: 107544.
- [10] He J, Yao J, Yang X, et al. Effects of mainstream attack angles on film-cooling effectiveness of double-jet film-cooling[J]. *International Journal of Thermal Sciences*, 2020, 149: 106183.
- [11] Gritsch M, Schulz A, Wittig S. Film-cooling holes with expanded exits: near-hole heat transfer coefficients[J]. *International Journal of Heat and Fluid Flow*, 2000, 21(2): 146-155.
- [12] Zhang F, Song H, Liu C, et al. 2023, "Study on the film cooling effectiveness of shaped holes in the suction surface gill region of the turbine blade". *International Journal of Thermal Sciences*, 184: 107977.
- [13] Li F, Jia Z, Zhang W, et al. 2022, "Investigation into the film cooling performance of multi-cavity tips with different cavity depths". *International Journal of Thermal Sciences*, 181: 107766.
- [14] Li H W, Zhang D W, Han F, et al. 2021, "Experimental investigation on the effect of hole diameter on the leading edge region film cooling of a twist turbine blade under rotation conditions". *Applied Thermal Engineering*, 184: 116386.
- [15] Wang K, Shao H, Peng D, et al. 2022, "Transonic vane film cooling with crescent-shaped craters using an endoscopic pressure-sensitive paint technique". *Applied Thermal Engineering*, 205: 118081.
- [16] Zhang B L, Zhu H R, Yao C Y, et al. 2021, "Experimental study on film cooling and heat transfer characteristics of a twisted vane with staggered counter-inclined film-hole and laid-back-shaped-hole". *International Journal of Heat and Mass Transfer*, 176: 121377.

Experimental Investigation of Tween-40 Surfactant Effects on Boiling Phenomena

Rodrigo Cavalcanti Alvarez^a, Mario R. Mata^b, H. Jeremy Cho^b, Matteo Bucci^{a,*}

^aMassachusetts Institute of Technology, 77 Massachusetts Avenue, Cambridge, MA 02139, US

^bUniversity of Nevada, Las Vegas, 4505 S Maryland Pkwy, Las Vegas, NV, 89052, US

*mbucci@mit.edu

Keywords: boiling, surfactant, heat transfer coefficient, critical micelle concentration

1. INTRODUCTION

Boiling is an effective heat removal process widely used in the power generation industry, e.g., nuclear reactors (Todreas, 2021). Its effectiveness as a heat removal process arises from the high amount of energy required to transform liquid into vapor (i.e., the latent heat of evaporation) (Carey, 1992), besides other effects, e.g., the fluid agitation created by the bubbles (Aguiar, 2023). The heat removed during this *nucleate boiling* regime is directly related to nucleation site density (i.e., the area density of points on the surfaces from where bubbles nucleate), bubbles size and release frequency. Numerous studies have investigated the meanings of enhancing the boiling heat transfer performance by surface modification (Li et al., 2020) and/or fluid modification (Liang & Mudawar, 2018). Among these, the addition of surface-active agents - namely surfactants - in water attracted great attention. Surfactants present a chemical structure with opposing functional groups with different affinity, i.e., a hydrophobic and a hydrophilic group within the same molecule (Nakama, 2017). Previous studies suggested that the HTC is optimized for solutions near the critical micelle concentration (CMC) regardless of the surfactant, occurring when, at a specific concentration, additives start forming aggregates within the bulk fluid (Cheng et al., 2007). The decrease in the surface tension is one of the key factors leading to the boiling enhancement. It reduces the energy required to nucleate a bubble which in turn results into smaller and more frequent bubbles, and higher nucleation site density (Hetsroni et al., 2001; Wasekar & Manglik, 2000; Wen et al., 2022). On the other hand, some researchers have reported that the HTC stayed unchanged despite the lowering in the surface tension caused by the addition of surfactants (e.g., see Yang et al., 2002 and T.A.T. Wang, 1994) as reported by (Cheng et al., 2007). Recently, a work testing multiple surfactants on a wide range of concentrations has shown that an optimum concentration for the heat transfer enhancement exists irrespectively to the CMC, pointing to the dynamic adsorption of surfactants to the interface as the critical physical mechanism for the HTC enhancement (Mata et al., 2022).

The present work aims to shed light on the existing controversy regarding the effects of surfactants in the boiling phenomena. Specifically, the results of Tween-40, a nonionic surfactant, on a wide range of concentration, from $0.001 \text{ mol} \cdot \text{m}^{-3}$ to $1 \text{ mol} \cdot \text{m}^{-3}$, are evaluated when boiled on a nanosmooth transparent heater. Tween-40 was chosen given it was one of the surfactants evaluated in Mata et al. (2022). The current experimental setup enables the recording of the phases in contact with the surface (vapor and liquid, including liquid microlayers) through a high-speed video camera imaging the boiling surface from the bottom, allowing for insightful observations of the bubbles' dynamic.

2. METHODOLOGY

The experimental setup used in the investigation is schematically shown in Figure 1. It consists of a hollow 3D-printed square boiling chamber with four lateral windows, manufactured with a high temperature resin. The water surfactant solution is heated up to saturation by two immersion cartridge heaters, and two T-type thermocouples at different elevations guarantee that the temperature is uniform throughout the liquid. The boiling phenomenon per se is studied through a flat-surface infrared heater positioned at the central-bottom part of the boiling chamber (see Figure 1). The heater consists of a sapphire substrate (20 mm x 20 mm wide and 1 mm thick), coated through physical vapor deposition (PVD) with an electrically conductive indium tin oxide (ITO) layer, 700 nm thick. The ITO film is transparent to visible light and opaque to infrared light, whereas the sapphire is transparent to both. Chromium pads are coated on opposite sides and atop the ITO film to serve as electrical connections. They limit the ITO heating area to a 10 mm x 10 mm square. By applying a current along this assembly, the ITO, which is in contact with the surfactant solution, dissipates heat by the Joule effect.

A hot mirror is positioned under the heater, aligned with a high-speed infrared (IR) camera (IRC806) recording the radiation emitted by the heater with a spatial resolution of 83 microns per pixel and a temporal resolution of 1,600 frames per second (fps). The radiation measured by the IR camera comprises the radiation emitted by the ITO heater, the sapphire substrate and the reflection of the background and structures radiation. The time-dependent temperature and heat flux distributions on the boiling surface are measured from the infrared recordings using the calibration technique developed by Bucci et al. (2016). The average heat flux is evaluated as the product of the voltage drop across the active ITO area and the current circulating through it, divided by the active ITO area. Given the negligible thermal resistance of the ITO film combined with the use of IR cameras, the temperature measurement of the current tests corresponds to the actual

temperature of the boiling surface. Besides using IR thermometry, the boiling behavior is laterally recorded by a high-speed video (HSV) camera, Phantom® v12.1, positioned in front of an LED light source. The bubbles' dynamic is registered at a pixel resolution of 27 microns and a temporal resolution of 1,600 fps. Additionally, the phase detection technique proposed by Kossolapov et al. (2021) is used to track the time-dependent distributions of the vapor and liquid phase on the boiling surface using a second HSV camera, Phantom® v2512, at a pixel resolution of 29 microns at 6,400 fps, i.e., a temporal resolution four times larger than the other cameras. The synchronized IR thermometry with the HSV lateral and bottom recordings enables us to characterize the behavior of the bubbles at the different combinations of heat fluxes and surfactant solution concentrations tested.

Boiling curves of pure DI water and four different concentrations of Tween-40 surfactant solutions, from 0.001 mol.m^{-3} to 1 mol.m^{-3} with one order of magnitude increase intervals, were tested. These concentrations were chosen because they coincide with expected increases in dynamically adsorbed surfactant to interfaces and associated changes to boiling behavior, e.g., nucleation site density, frequency of departure and coalescence. In each boiling curve, the heater power progressively increases up to the maximum heat flux condition tested through discrete steps of two-seconds steady state condition. Three boiling curves are performed for each concentration tested, including pure DI water, to guarantee the mixing of the fluid and the repeatability of the tests, totalizing 15 boiling curves.

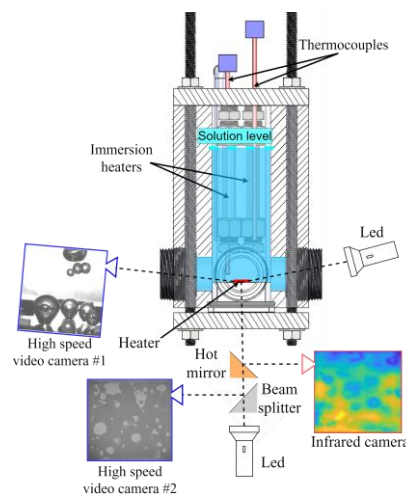


Figure 1– Schematic representation of the pool boiling test section. The boiling occurs atop an infrared sapphire-ITO heater (in red). An assembly of led lights, mirrors and high-speed cameras allows recording the bubbles lateral dynamics, footprint and the infrared radiation emitted by the boiling surface. Sample high-speed video and infrared recordings are shown.

3. RESULTS AND DISCUSSION

Figure 2a shows the boiling curves for the DI water and the different concentrations of Tween-40 solutions for the complete data set. Figure 2b shows the corresponding plots of the heat transfer coefficient (HTC) versus the heat flux. As previously mentioned, each boiling curve was repeated three times at each concentration, and the tests are numbered from 01 to 15 in Figure 2. As seen in Figure 2, the Tween-40 surfactant solutions at concentrations of 0.001 mol.m^{-3} and 0.01 mol.m^{-3} showed similar superheat temperature for the same heat flux, and consequently similar values of HTC, with respect to the reference case of DI water. However, changes occur at a concentration of 0.1 mol.m^{-3} . Firstly, a substantial increase in the maximum superheat values reached before the onset of nucleate boiling (ONB) is noticed, in which a maximum of 144°C is reached for case 11. Secondly, a decrease in the HTC is noticed for increasing values of heat flux. These changes are even more pronounced for the 1 mol.m^{-3} cases tested, numbered 13 to 15 in Figure 2. Once again, an increase in the maximum superheat temperature values is reached, with values scattering from around 128°C to 145°C . The HTC deterioration is more pronounced than in the previous case, reaching a decrease of approximately 30% with respect to the DI water at 45 W/cm^2 . Such behavior was also noticed in preliminary tests, which led us to reduce the maximum heat flux value to be tested for cases of higher concentration in order to prevent the potential failure of the heater by reaching the critical heat flux. We emphasize that the observed decrease in the HTC seen in Figure 2 and described above is in contradiction with the results previously reported in (Mata et al., 2022). The differences in the heater surface properties, e.g., roughness, can be at the origin of this discrepancy. As previously described, the heater tested in the current experiment is a nanosmooth sapphire slab coated with a heating ITO layer, while the heater used in (Mata et al., 2022) consists of a vertically oriented copper tube with an embedded cartridge heater. The cleaning procedure of the heater surface prior to the tests might also influence the results observed. Further analysis of the surface properties of the heaters is to be done.

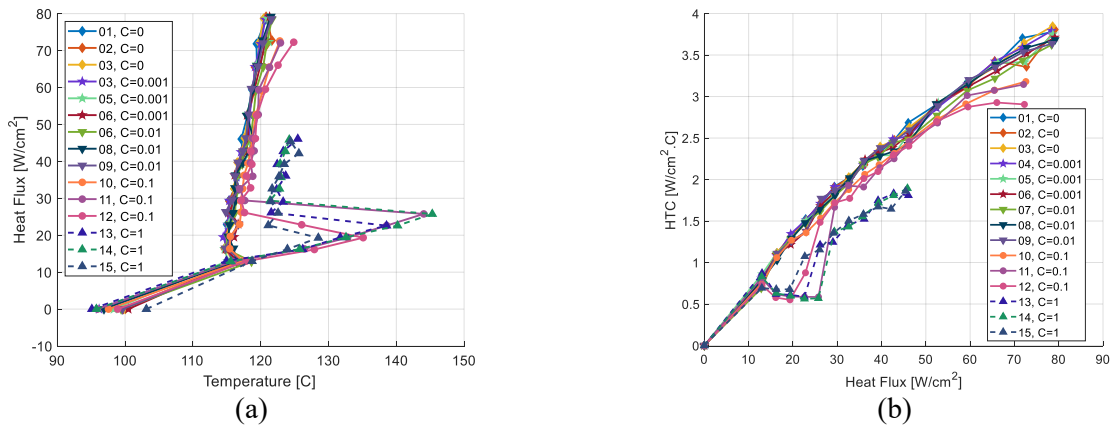


Figure 2 – (a) Heat flux vs. temperature superheat and (b) heat transfer coefficient vs. heat flux for the different concentrations of Tween-40 solutions tested. Each boiling curve was successively repeated three times to guarantee mixing and homogeneity of the boiling fluid, in tests numbered from 01 to 15.

Figure 3 compares snapshots of the phase detection (*a* and *c*) and the side view visualization (*b* and *d*) at 33 W/cm^2 for the tests number 03 (left side figures, *a* and *b*) for pure DI water, and 14 (right side figures, *c* and *d*), for the maximum concentration tested, of 1 mol.m^{-3} . Surfactants decreased the coalescence of bubbles in the bulk, decreasing the size of the vapor structures in the bulk fluid above the heater, as can be seen by the side view snapshots comparison. In addition, and seemingly in contrast with the observations reported in the literature, the side-view footages show a lower number of bubbles nucleating on the surface for the case with the maximum concentration of surfactants. The phase detection snapshot of the DI water test, case *a*, shows comparable results to the ones previously described in Kossolapov et al. (2021). In particular, the micro-layer is identified through light-interference fringes (e.g., see inside the orange-framed area). Conversely, numerous spherical dry spots are seen within a growing micro-layer for the test with the maximum surfactants concentration, as seen in case *c* of Figure 3. At this stage of the analysis, the origin of these newly appearing spherical dry spots is still unclear. It is speculated that they may be the result of the fragmentation of the microlayer, given the decrease in the force required to rupture a liquid in tension with the reduction of the surface tension. To the best of the authors' knowledge, the described behavior has not yet been reported in the literature through bottom view photographs.

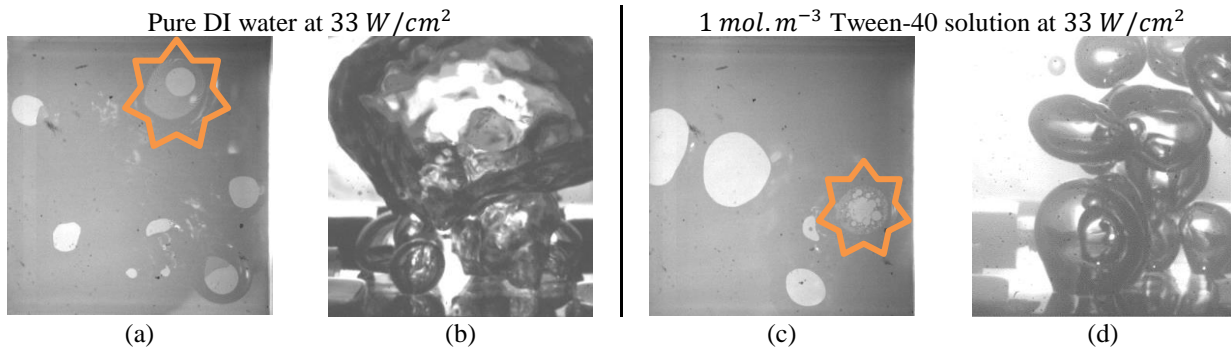


Figure 3 – Snapshots of the phase detection (*a* and *c*) and the side view visualization (*b* and *d*) at 33 W/cm^2 for test number 03 (left side figures, *a* and *b*), of pure DI water, and test 14 (right side figures, *c* and *d*), of 1 mol.m^{-3} Tween-40 solution. The detail in orange attempts to the appearance of multiple spherical dry spots within the microlayer of a growing bubble for the highest concentration tested with respect to the DI water reference case.

4. CONCLUSIONS

This study investigated the effects of Tween-40 surfactant solutions on boiling phenomena across a range of concentrations using advanced experimental techniques. The results revealed nuanced impacts on heat transfer and bubble dynamics. While lower concentrations of Tween-40 exhibited marginal changes in heat transfer coefficients compared to pure DI water, higher concentrations led to notable increases in superheat temperatures and significant reductions in heat transfer coefficients. Surfactant addition also influenced bubble dynamics, limiting coalescence and altering nucleation

patterns. Different from the results commonly reported in the literature, the increase in the surfactant concentration did not cause a clear decrease in the size of the nucleating bubbles and an increase in the number of nucleating bubbles and their frequency of departure. Further analysis of the HSV data is necessary to quantitatively scrutinize the results obtained, and to understand the reasons driving the difference in behavior of the current tests with the results reported in the literature. On the other hand, the coalescence behavior did reduce with surfactant concentration increase, resulting in smaller bubbles in the bulk fluid after detachment. Furthermore, multiple spherical dry spots were seen within the microlayer of a growing bubble in the case of the highest concentration tested, in a pattern not yet visually described in the literature. Surface properties (e.g., roughness and, broadly speaking, the number and size distribution of nucleation sites) might be at the origin of the observed behaviors. Such a hypothesis is to be verified by a comprehensive statistical distribution analysis of the fundamental boiling parameters from the high-speed video and infrared thermometry, as well as the further characterization of the heater surface, and by conducting tests on surfaces with different morphology and wettability.

5. REFERENCES

- Aguiar, Gustavo Matana. (2023). Infrared Thermometry Analysis of Surface Effects in Subcooled and Saturated Boiling of Water. In (*Doctoral dissertation*). Massachusetts Institute of Technology.
- Bucci, M., Richenderfer, A., Su, G. Y., McKrell, T., & Buongiorno, J. (2016). A mechanistic IR calibration technique for boiling heat transfer investigations. *International Journal of Multiphase Flow*, 83, 115–127. <https://doi.org/10.1016/j.ijmultiphaseflow.2016.03.007>
- Carey, V. P. (1992). *Liquid-vapor phase-change phenomena : an introduction to the thermophysics of vaporization and condensation processes in heat transfer equipment* [Book]. Taylor & Francis.
- Cheng, L., Mewes, D., & Luke, A. (2007). Boiling phenomena with surfactants and polymeric additives: A state-of-the-art review. *International Journal of Heat and Mass Transfer*, 50(13–14), 2744–2771. <https://doi.org/10.1016/j.ijheatmasstransfer.2006.11.016>
- Hetsroni, G., Zakin, J. L., Lin, Z., Mosyak, A., Pancallo, E. A., & Rozenblit, R. (2001). The effect of surfactants on bubble growth, wall thermal patterns and heat transfer in pool boiling. *International Journal of Heat and Mass Transfer*, 44(2), 485–497. [https://doi.org/https://doi.org/10.1016/S0017-9310\(00\)00099-5](https://doi.org/https://doi.org/10.1016/S0017-9310(00)00099-5)
- Kossolapov, A., Phillips, B., & Bucci, M. (2021). Can LED lights replace lasers for detailed investigations of boiling phenomena? *International Journal of Multiphase Flow*, 135, 103522. <https://doi.org/10.1016/j.ijmultiphaseflow.2020.103522>
- Kossolapov, Artyom. (2021). Experimental Investigation of Subcooled Flow Boiling and CHF at Prototypical Pressures of Light Water Reactors. In (*Doctoral dissertation*). Massachusetts Institute of Technology.
- Li, W., Dai, R., Zeng, M., & Wang, Q. (2020). Review of two types of surface modification on pool boiling enhancement: Passive and active. *Renewable and Sustainable Energy Reviews*, 130, 109926. <https://doi.org/10.1016/j.rser.2020.109926>
- Liang, G., & Mudawar, I. (2018). Review of pool boiling enhancement with additives and nanofluids. *International Journal of Heat and Mass Transfer*, 124, 423–453. <https://doi.org/10.1016/j.ijheatmasstransfer.2018.03.046>
- Mata, M.R., Ortiz, B., Luhar, D. et al. How dynamic adsorption controls surfactant-enhanced boiling. *Sci Rep* 12, 18170 (2022). <https://doi.org/10.1038/s41598-022-21313-1>
- Nakama, Y. (2017). Surfactants. In *Cosmetic Science and Technology: Theoretical Principles and Applications* (pp. 231–244). Elsevier Inc. <https://doi.org/10.1016/B978-0-12-802005-0.00015-X>
- T.A.T. Wang, J. P. H. (1994). Pool boiling of heat transfer from a horizontal wire to aqueous surfactant solutions. *Proceedings of 10th International Heat Transfer Conference*, 177–182.
- Todreas, N. E. (2021). Nuclear systems. Volume 1, Thermal hydraulic fundamentals . In *Nuclear systems. Volume 1, Thermal hydraulic fundamentals* (Third edition.). CRC Press, Taylor & Francis Group.
- Wasekar, V. M., & Manglik, R. M. (2000). Pool Boiling Heat Transfer in Aqueous Solutions of an Anionic Surfactant. *Journal of Heat Transfer*, 122(4), 708–715. <https://doi.org/10.1115/1.1316785>
- Wen, T., Luo, J., Jia, K., & Lu, L. (2022). Pool boiling heat transfer enhancement of aqueous solution with quaternary ammonium cationic surfactants on copper surface. *International Journal of Heat and Mass Transfer*, 190. <https://doi.org/10.1016/j.ijheatmasstransfer.2022.122761>
- Yang, Y.-M., Lin, C.-Y., Liu, M.-H., & Maa, J.-R. (2002). Lower Limit of the Possible Nucleate Pool-Boiling Enhancement by Surfactant Addition to Water. *Journal of Enhanced Heat Transfer*, 9(3–4), 153–160. <https://doi.org/10.1080/10655130215734>

Pressure drop and heat transfer of the refrigerant mixture of R32/R1234yf inside horizontal microfin tubes

I Wayan Sugita^{a,b,*}, Hakimatul Ubudiyah^a, Afdhal Kurniawan Mainil^c, Keishi Kariya^d, Akio Miyara^{d,e}

^aGraduate School of Science and Engineering, Saga University, Saga-shi 840-8502, Japan

^bDepartment of Mechanical Engineering, Universitas Negeri Jakarta, Jakarta 13220, Indonesia

^cDepartment of Mechanical Engineering, Universitas Bengkulu, Bengkulu 38371A, Indonesia

^dDepartment of Mechanical Engineering, Saga University, Saga-shi 840-8502, Japan

^eInternational Institute for Carbon-Neutral Energy Research, Kyushu University, Fukuoka-shi 819-0395, Japan

*wayan-sugita@unj.ac.id

Keywords: Pressure drop, Heat transfer, Microfin, R32, R1234yf

1. INTRODUCTION

Refrigerants are used by many contemporary appliances, including water heaters, air conditioners, heat pumps, and refrigerators, to transport heat from sources to sinks. In recent years, R410A has become one of the most used refrigerants worldwide (Zhao et al., 2015). Recently, R32 has been used as a replacement for R410A in domestic air conditioners, and nearly 40% of domestic air conditioners in Japan use it as a refrigerant (Vuppaladadiyam et al., 2022). However, since the Kigali amendment required that HFCs be drastically reduced over the next decades to avoid an increase in the global average temperature of 0.5 °C by 2100, the global warming potential (GWP) of R32 was not sufficiently low to comply with the amendment. On the other hand, due to its thermophysical properties close to R134a and low GWP, researchers have focused on R1234yf (Del Col et al., 2010; Diani et al., 2017). However, R1234yf is not suitable for replacing R32 due to its limited thermophysical properties. Combining R32 and R1234yf as refrigerant mixtures to achieve better performance is one way to solve the problem. The R32 / R1234yf refrigerant mixtures are gaining attention due to their potential as replacements for refrigerants of high global warming potential (GWP) in air conditioning and refrigeration systems. Not only to improve heat transfer efficiency, but also to reduce system pressure drop. Therefore, although the R32 / R1234yf mixture refrigerants offer advantages in terms of lower GWP and improved environmental impact, more studies are required to evaluate their performance. The use of small diameter tubes ($d_o = 5\text{--}2.5$ mm) is another element that influences the improvement in heat transfer, the reduction in refrigerant charge and the reduction in weight and cost of the heat exchanger. Therefore, this article will study the pressure drop and heat transfer characteristics of the R32 / R1234yf mixtures (R454C) within a small diameter horizontal microfin tube. The effects of vapor quality and mass velocity on adiabatic pressure drop and condensation heat transfer are evaluated.

2. EXPERIMENTAL SETUP

The schematic of the experimental apparatus is shown in Fig. 1. There are two main loops: the refrigerant loop and the water loop. The liquid refrigerant is driven using a pump through the control valve, Coriolis flow meter, mixing chamber, preheater, and test section. The refrigerant coming out from the test section is then cooled by the cooler and sub-cooler. The experiments will be carried out in a small diameter microfin tube with 3.5 outer diameter, at saturation temperatures of 20 °C, a vapor quality of 0 to 1, and a mass velocity of 50 kg m⁻² s⁻¹ to 200 kg m⁻² s⁻¹.

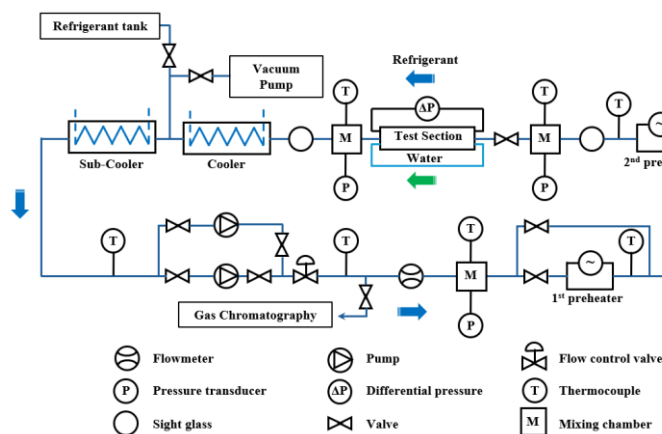


Figure 1. Experimental Apparatus

Figure 2 shows the details of the test section. The test tube is a copper microfin tube with a 3.5 mm outer diameter. The total length that the pressure drop measured was 852 mm and an effective heat transfer length of 744 mm. The test section wall temperature is measured using multiple T-type thermocouples connected to the data logger. The test tube has a 0.15 mm thick wall (δ), a 0.10 mm fin height, a 10° helix angle (θ), a 35° apex angle (γ), and 25 fins. The experiments are conducted at mass velocities ranging from 50 to $200 \text{ kg m}^{-2} \text{ s}^{-1}$, with saturation temperature of 20°C and vapor quality ranging from 0.1 to 0.9.

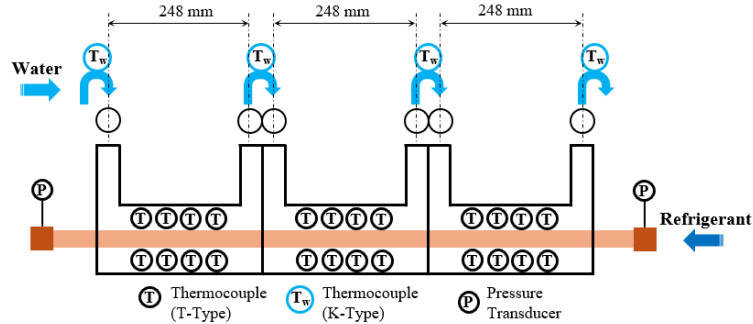


Figure 2. Experimental Apparatus

The pressure drop experiment was carried out in the adiabatic setting by maintaining the refrigerant and water temperature at the same temperature, and the heat transfer experiment was conducted in the condensation setting.

3. DATA REDUCTION

The frictional pressure drop of the mixtures R32 / R1234yf (R454C) within a small diameter horizontal microfin tube will be calculated using the Eq. (1).

$$\Delta P = \Delta P_f + \Delta P_c + \Delta P_e \quad (1)$$

where ΔP is the total two-phase pressure drop, ΔP_f is the friction pressure drop and ΔP_c and ΔP_e are the pressure drop due to sudden contraction and expansion in the inlet and outlet headers of the test section.

The local condensation heat transfer coefficient is determined by the Eq. (2).

$$HTC = \frac{Q_{wat,i}}{\pi d_{eq} Z_i (T_{r,i} - T_{wi,i})} \quad (2)$$

where Q_{wat} , d_{eq} , and Z are the heat transfer rate of the water side of each sub-section, the equivalent diameter of the test tube (microfin) and the length of local point, respectively. T_r is refrigerant temperature that is estimated from the measure refrigerant pressure, and T_{wi} is temperature of the inner wall of the test tube.

4. RESULTS AND ANALYSIS

Figure 3 shows the effect of mass velocity and vapor quality on the frictional pressure drop at a saturation temperature of 20°C . Frictional pressure drops increase along with an increase in mass velocity, as expected. This is because the shear stress and interfacial friction between the two-phase vapor-liquid flow in the tube increase, which is attributable to the increased pressure with the mass velocities. The highest-pressure drop is found at the highest mass velocity, $200 \text{ kg m}^{-2} \text{ s}^{-1}$.

Figure 4 shows the local condensation heat transfer for R454C in the relation between HTC and vapor quality ($1-x$) at a saturation temperature of 20°C and mass velocities ranged from 50 to $200 \text{ kg m}^{-2} \text{ s}^{-1}$. The heat transfer coefficient increases with an increase in the vapor quality and mass velocity. The increase in heat transfer is due to an increase in the vapor shear stress and a reduction in the heat transfer resistance of the condensate film. As the quality of the vapor gradually increases, the condensation decreases and the resistance to heat transfer decreases. Consequently, the heat transfer coefficient increases with the decrease in resistance. Furthermore, with an increase in the mass velocity, the velocity of the vapor and liquid also increases. Consequently, the ratio of velocity between the vapor and liquid phases is higher, which increases the intensity of turbulence and thus improves heat transfer performance. The highest HTC is $8.5 \text{ kW m}^{-2} \text{ K}^{-1}$ with a vapor quality of 0.87 and a mass velocity of $200 \text{ kg m}^{-2} \text{ s}^{-1}$.

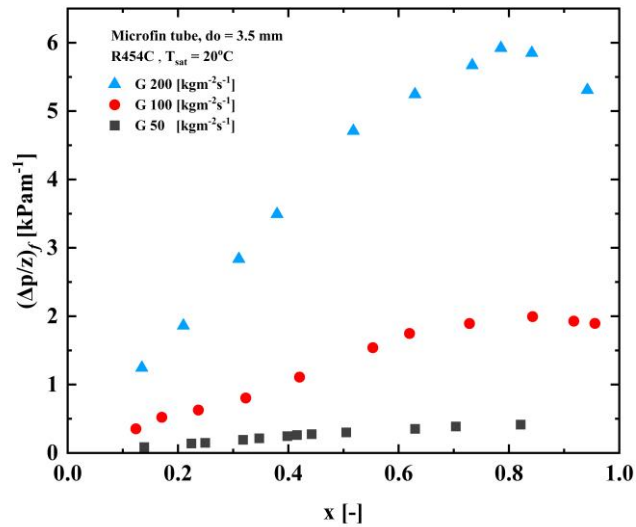


Figure 3. Effect of mass velocity and vapor quality on frictional pressure drop

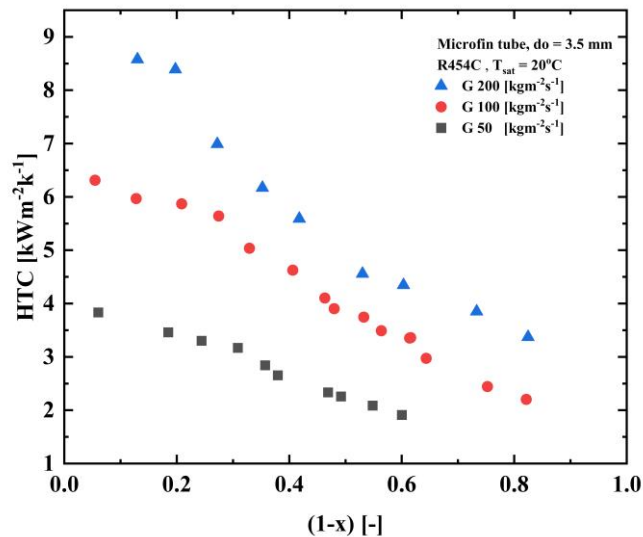


Figure 4. Relation between heat transfer coefficient and vapor quality at different mass velocity

5. CONCLUSIONS

The effects of mass velocity and vapor quality on the frictional pressure drop and heat transfer coefficient of a low GWP refrigerant mixture of R32 and R1234yf (R454C) inside a small-diameter horizontal microfin tube were investigated. The results show that the increase in vapor quality and mass velocity increases the frictional pressure drop and heat transfer coefficient.

6. REFERENCES

- Del Col, D., Torresin, D., & Cavallini, A. (2010). Heat transfer and pressure drop during condensation of the low GWP refrigerant R1234yf. *International Journal of Refrigeration*, 33(7), 1307–1318. <https://doi.org/https://doi.org/10.1016/j.ijrefrig.2010.07.020>
- Diani, A., Cavallini, A., & Rossetto, L. (2017). R1234yf condensation inside a 3.4 mm ID horizontal microfin tube. *International Journal of Refrigeration*, 75, 178–189. <https://doi.org/10.1016/J.IJREFRIG.2016.12.014>
- Vuppaladadiyam, A. K., Antunes, E., Vuppaladadiyam, S. S. V., Baig, Z. T., Subiantoro, A., Lei, G., Leu, S. Y., Sarmah, A. K., & Duan, H. (2022). Progress in the development and use of refrigerants and unintended environmental consequences. *Science of the Total Environment*, 823, 153670. <https://doi.org/10.1016/j.scitotenv.2022.153670>
- Zhao, L., Zeng, W., & Yuan, Z. (2015). Reduction of potential greenhouse gas emissions of room air-conditioner refrigerants: A life cycle carbon footprint analysis. *Journal of Cleaner Production*, 100, 262–268. <https://doi.org/10.1016/J.JCLEPRO.2015.03.063>

Possibility Research on Heat Transfer Enhancement by Combination of Pulsating Flow and Fin Array

Jumpei Hatakeyama^{a,*}, Kota Fujisawa^b, Takashi Fukue^b, Hidemi Shirakawa^a

^aNational Institute of Technology, Toyama College, 13 Hongo, Toyama, Toyama, Japan

^bKanazawa Institute of Technology, 3-1 Yatsukaho, Hakusan, Ishikawa, Japan

*jhatake@nc-toyama.ac.jp

Keywords: Pulsating flow, Heat sink, Heat transfer enhancement, Thermal design, Thermal management

1. INTRODUCTION

The development of electronic packaging technology has made it possible to manufacture high-current power converters for electric vehicles and increase the performance of integrated circuits. However, it has also led to issues such as an increase in heat generation and complications of thermal design. As the performance of integrated circuits increases, the functional requirements of electronic devices also become more complicated, and the power consumption and heat generation of the integrated circuits in which they are mounted increase. On the other hand, consumer demand is driving the trend toward more miniature equipment housings, and the substrate is designed to be as small as possible. Therefore, the heat generation density is increasing due to the increment of heat generation and the miniaturization of devices. In addition, the miniaturization of enclosures leads to more complex internal structures and increases the power required to transport refrigerant. Against this background, optimizing the thermal design of electronic equipment is the key to stable operation and energy conservation of electronic equipment.

The authors have focused on pulsating flow, a highly efficient fluid transport method, and have studied the possibility of heat transfer enhancement in a pulsating flow field. In a previous study, steady and pulsating flows were applied to heat transfer accelerators such as cylinders and ribs, and we investigated whether the pulsating flow improves cooling performance. The results showed that the pulsating flow tended to enhance the heat transfer by generating a counter flow from the main flow toward the rear of the heat transfer accelerator during the deceleration period of the pulsation. Furthermore, since the pulsating flow promotes heat transfer, equivalent cooling performance was obtained even with a lower time-averaged flow rate than the steady flow. Therefore, pulsating flow can enhance heat transfer and reduce the energy required for refrigerant transport.

This study aims to develop a cooling performance evaluation model of the combination of heat transfer accelerator and pulsating flow and a design method for the cooling system of electronic devices with the pulsating flow that uses the cooling performance evaluation model. In this report, we report the results of CFD analysis that investigates the cooling performance of three pillars in a pulsating flow field and a plan of experiment based on the analysis.

2. Analysis model and the results

OpenFOAM, an open-source CFD toolbox, was used for the analysis code, and a two-dimensional thermal-fluid analysis was performed. Figure 1 shows a schematic of the analytical model. Three pillar-shaped heating elements simulating heat sink pins were placed in a row and subjected to steady and pulsating flow to compare their cooling performance. Three heating elements were placed in a row to simulate the pillars of a heat sink, and the cooling performance of steady and pulsating flow was compared. The physical properties of the refrigerant are based on the air.

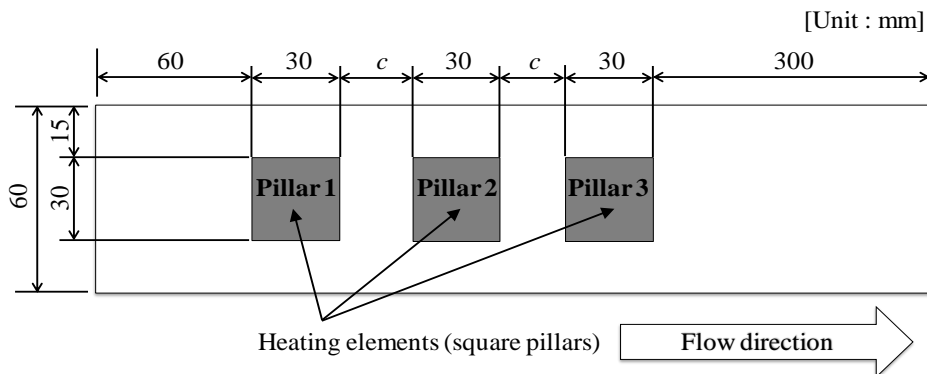


Figure 1. Schematic of analytical model.

Three conditions were given for the pillar spacing c : 10 mm, 20 mm, and 30 mm. Hereafter, the square pillars are referred to as Pillar 1, Pillar 2, and Pillar 3 from the upstream side. Figure 2 shows the pattern of the pulsating flow, which is a 1 Hz trapezoidal wave, and the time-averaged velocity of the steady flow and the pulsating flow is 0.32 m/s. Time-averaged Reynolds number = 1,000, based on time-averaged velocity as representative velocity and channel height as representative dimension.

The Nusselt number, defined by the following equation, was used to evaluate the time-averaged heat transfer performance of the pillar.

$$Nu = \frac{hb}{\lambda} [-] \quad (1)$$

Here, h [W/(m²·K)] is the time-averaged heat transfer coefficient obtained from the temperature difference between the average temperature of each wall surface of the pillar and the initial temperature of the incoming air, b is the width of the pillar, and λ is the thermal conductivity of air.

Figure 3 shows the time-averaged Nusselt number for all pillars for spacing c when the columns are subjected to steady or pulsating flow. Overall, heat transfer performance improves when the flow is pulsating. In particular, the rate of heat transfer enhancement of the pulsating flow is more pronounced when the clearance is wider.

Figure 4 shows the difference in Nusselt number between each pillar with clearance c . The heat transfer performance of Pillar 1, located upstream of the flow, has not significantly improved. On the other hand, the heat transfer enhancement of square Pillar 2 and 3, located downstream, is remarkable. At Pillar 1, which is the most upstream, the heat transfer performance is high even in steady flow because the flow hits the front of the pillar. Therefore, at pillar 1, depending on the clearance between the pillars, the steady flow has higher heat transfer performance than the pulsating flow. At the same time, at Pillar 2 and 3, the pulsating flow has higher heat transfer performance than the steady flow. At Pillar 2 and 3, the front face of the pillar faces a flow separation zone of steady flow. Therefore, in a pulsating flow, the heat transfer performance at the front face of Pillars 2 and 3 is improved.

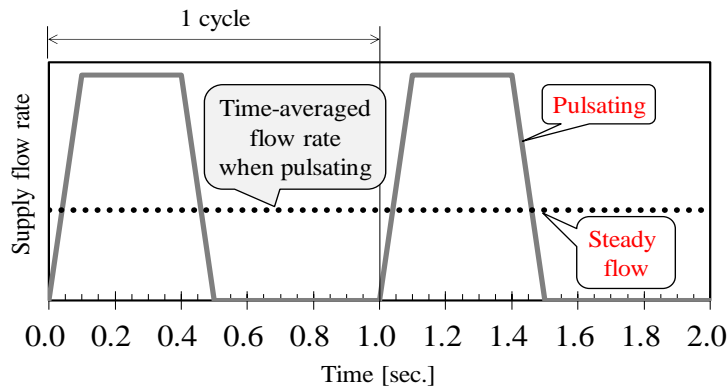


Figure 2. Condition of pulsating waveform.

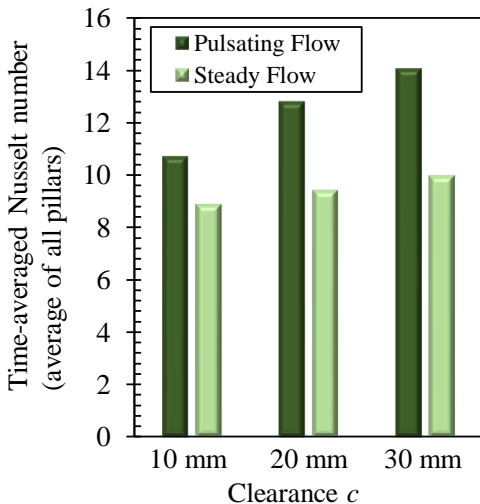


Figure 3. Relationship between Nu and clearance.

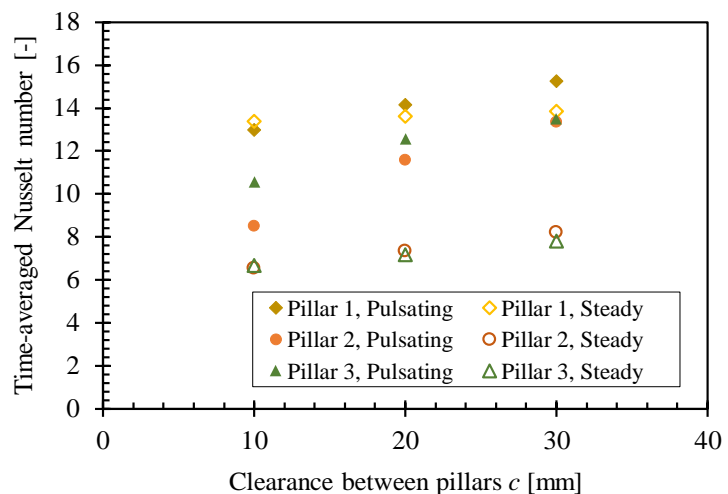


Figure 4. Difference of Nu between each pillar with clearance c .

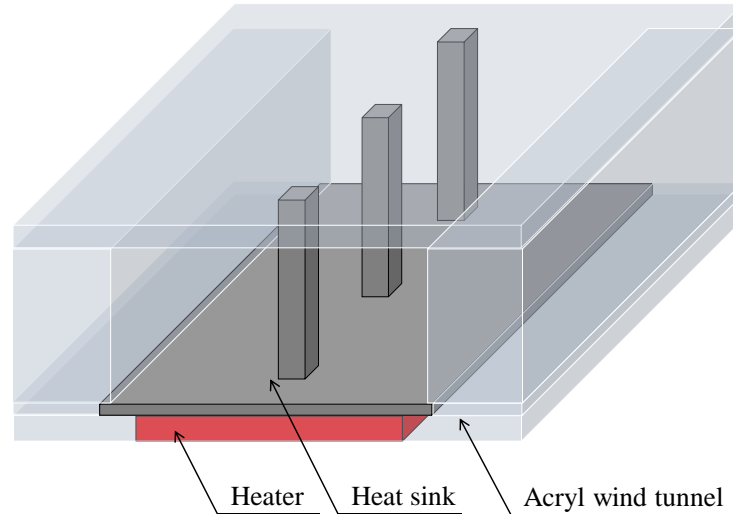


Figure 5. Sufficiently descriptive caption of the figure.

3. SUMMARIES

This paper investigated the advantages of pulsating flow in heat transfer obtained by the analysis. The analysis obtained two trends for heat transfer phenomena due to pulsating flow. Firstly, when pulsating flow is used for cooling heat sinks, higher heat transfer performance can be obtained than with steady flow. Secondly, the clearance between pin fins gets wider; heat transfer performance increases.

The full paper will explain the additional experimental results of the heat transfer around the proposed fin array by the pulsating flow.

4. REFERENCES

- Hatakeyama, J., Hirose, K., Uchidate, M., Fukue, T. and Wang, Q. S., 2016. "Basic Study on Reduction of Measurement Time for Evaluating Thermophysical Properties of Thermal Interface Materials by Steady Temperature Prediction Method". *Transactions of The Japan Institute of Electronics Packaging* 9, Paper No. E16-014.
- Muhammad, J. H., Alperen, G., Andrew, S., Yashraj, G., Robert C. N. P., and Nenad M., 2021. "Modular Heat Sinks for Enhanced Thermal Management of Electronics". *Journal of Electronic Packaging*, Vol. 143, pp. 020903-1 -12.
- Hao, Z., Robert, B., and Markus, D., 2021. "Electromigration in Power Devices: A Combined Effect of Electromigration and Thermal Migration". *Journal of Microelectronics and Electronic Packaging*, 18, pp.1-6
- Hayakawa, S., Fukue, T., Sugimoto, Y., Hiratsuka, W., Shirakawa, H. and Koito, Y., 2022. "EFFECT OF RIB HEIGHT ON HEAT TRANSFER ENHANCEMENT BY COMBINATION OF A RIB AND PULSATING FLOW". *Frontiers in Heat and Mass Transfer*, pp. 18-29.

NUMERICAL MODELING AND EXPERIMENTAL VALIDATION OF AN ACTIVE MAGNETIC REGENERATOR

Hideto Nikawa^a, Tsuyoshi Kawanami^b, Daisuke Baba^c, Masayuki Tanino^c, Yoshiaki Kawakami^c

^aGraduate School of Science and Technology, Meiji University
1-1-1 Higashimita, Tama-ku, Kawasaki 214-8571, Japan

^bDepartment of Mechanical Engineering Informatics, Meiji University
1-1-1 Higashimita, Tama-ku, Kawasaki 214-8571, Japan

^cTakasago Thermal Engineering Co., Ltd.,
2-19 Fujimigaoka, Tsukubanirai-shi, Ibaraki, 300-2417, Japan
kawanami@meiji.ac.jp

Keywords: Magnetocaloric material, Magnetic heat pump, Active magnetic regenerator, Honeycomb structure

1. INTRODUCTION

Heat pumps using F-gases have a negative impact on ozone depletion and global warming. However, magnetic heat pumps using solid refrigerants can mitigate these adverse effects by reducing both the use and discharge of greenhouse gases. The Active Magnetic Regenerator (AMR), an important component of the magnetic heat pump system, has a packed structure filled with magnetocaloric material for generating larger temperature span. The heat exchange fluid passes through the void within the magnetocaloric materials in the AMR. Therefore, the packed structure such as shape of materials and its void fraction significantly influences the pressure loss due to friction between the heat exchange fluid and the magnetocaloric materials, and the heat transfer behavior in the AMR bed (Kawanami, et al. 2015). Though, the low-pressure loss and high heat transfer coefficient structure is requested for the AMR bed to obtain an appropriate performance (e.g. COP), the technique for fabricate the AMR bed from magnetocaloric materials that has various shape has not yet been tested. In this study, the honeycomb-shaped AMR with magnetocaloric materials was fabricated by 3D printing technique. Then, the studies were carried out to evaluate the characteristics of the generation of temperature span as the heat pump and its cooling performance as compared with the spherical particle packed bed experimentally as well as numerically. As a result, it was found that the generated temperature span was larger in the sphere-particle-filled structure. The experimental value of generated temperature span of the honeycomb-filled structure is 0.69K smaller than the analytical value.

2. PRINCIPLES OF MAGNETOCALORIC EFFECT AND AMR CYCLE

The temperature change of the magnetocaloric material is very small. For instance, the temperature change of gadolinium, that is a benchmark refrigerant of magnetic heat pump at one Tesla magnetic field is around 2.6K. Therefore, an active magnetic regenerator (AMR) was used to expand the temperature span. The AMR is a heat exchanger that made from the magnetocaloric materials, and it works as the thermal regeneration/storage device. The AMR heat pump cycle can amplify temperature changes by repeating the magnetization and demagnetization of the magnetocaloric material. The AMR comprises a layer filled with magnetocaloric material and displacers positioned at the high and low temperature ends. A heat exchange fluid exchanges heat with the magnetocaloric material, oscillating between the gaps within the filled layer and its high and low temperature ends, thereby generating a temperature difference. The four process of AMR cycle is shown below. (1): The magnetocaloric material filled layer is adiabatically magnetized. The temperature of AMR bed elevates due to the magnetocaloric effect. (2): While in the magnetized state, the heat exchange fluid is moved to the high-temperature side while exchanging the heat with the magnetocaloric material.(3): Adiabatic demagnetization of the magnetocaloric material filled layer drops the temperature due to the magnetocaloric effect. (4): While in the demagnetized state, the heat exchange fluid is moved to the low-temperature side while exchanging the heat with the magnetocaloric material, which has experienced a temperature drop. By repeating these four processes, the temperature difference between the high and low temperature ends is expanded.

3. INFLUENCE OF MAGNETOCALORIC MATERIALS ON MAGNETIC HEAT PUMP VIA 3D PRINTING

3-1. Numeric Analysis

Figure 1 shows the analytical model of the AMR used in this analysis. The analytical domain spans from $x = 0\text{mm}$ to 110mm , with the packing layer of magnetocaloric material designated as $x = 25\text{mm}$ to 85mm . Two types of AMR bed layer were modeled as a honeycomb structure and a spherical particle packed structure. The pressure loss, the temperature span generated, and refrigeration capacity were examined through numerical analysis using the energy conservation

Equation (1) to (3) for the heat exchange fluid outside the filled layer, inside the filled layer, and within the magnetocaloric material in the analysis domain.

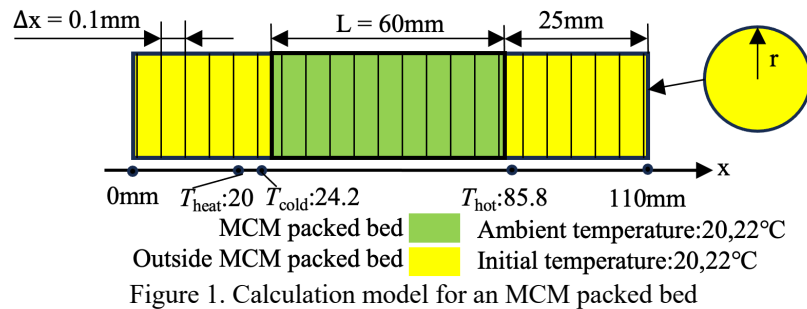


Figure 1. Calculation model for an MCM packed bed

$$\rho_f c_f \left(\frac{\partial T_f}{\partial t} + u \frac{\partial T_f}{\partial x} \right) = \lambda_f \frac{\partial^2 T_f}{\partial x^2} \quad (1)$$

$$\rho_f c_f \left(\frac{\partial T_f}{\partial t} + u' \frac{\partial T_f}{\partial x} \right) = \lambda_{\text{eff},f} \frac{\partial^2 T_f}{\partial x^2} + \frac{A}{V_s} h (T_s - T_f) + \frac{u}{L} \Delta P \quad (2)$$

$$\rho_s c_s \frac{\partial T_s}{\partial t} = \lambda_{\text{eff},s} \frac{\partial^2 T_s}{\partial x^2} + \frac{A}{V_f} h (T_f - T_s) + \frac{Q_{\text{mag}}}{\Delta t V_s} \quad (3)$$

where, ρ , c , T , t , u , u' , x , λ , λ_{eff} , A , V , h , L , ΔP , and Q_{mag} in the equations represent density, specific heat, temperature, time step, velocity, gap velocity, space step, thermal conductivity, effective thermal conductivity, area, volume, heat transfer coefficient, length of packed bed, pressure drop in packed bed, and heat due to magnetocaloric effect (Lu, 1999), respectively. The subscripts f and s represent the liquid and solid phases. The radius r of the pipe channel was set to $r = 8$ mm and $r = 7.35$ mm for the particle packed structure and the honeycomb structure, respectively. The space grid for x direction Δx was set at 0.1 mm through the calculation area. And $x = 24.2$ mm and $x = 85.8$ mm were designated as the temperature evaluation points as the cold end temperature T_{cold} and the hot end temperature T_{hot} . The initial temperature conditions were set to 20°C for the particle packed structure and 22°C for the honeycomb structure for the heat exchange fluid, magnetocaloric material, and ambient temperature. Gadolinium was used as the testing magnetocaloric material for the particle packed structure, and a lanthanum-based magnetocaloric material $\text{La}(\text{Fe}_{1-x}\text{Si}_x)_{13}\text{-H}$ with a Curie temperature of 22°C was employed for the honeycomb structure. Distilled water was used as the heat exchange fluid for analysis. Figure 2 illustrates the analytical result of pressure drop through the AMR bed and the temperature span between the hot and cold end ΔT . From the result, the honeycomb-filled structure has a lower the pressure drop, however can generate a higher temperature span. This is because the filling ratio of the magnetocaloric material is higher in the particle packed structure and the heat transfer area with the heat exchange fluid is larger.

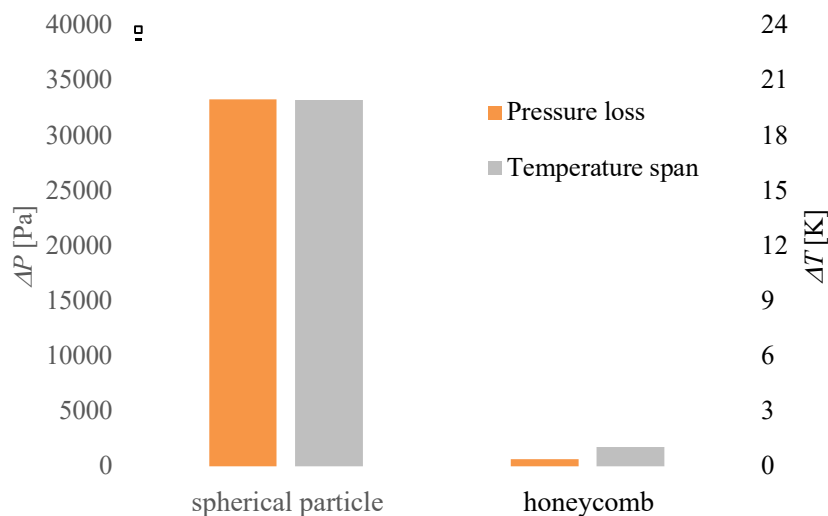
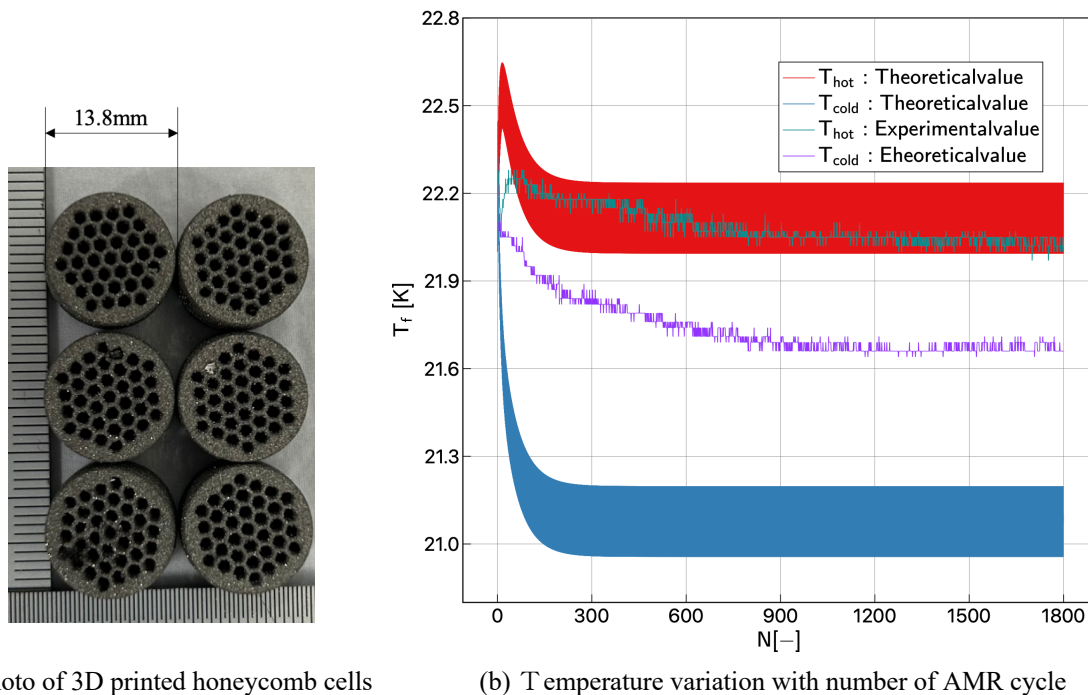


Figure 2. Analysis results for each filling structure

3-2. EXPERIMENTAL INVESTIGATION

In the previous section, numerical analysis was conducted on the generated temperature span. In this section, a honeycomb-shaped magnetocaloric material is created by 3D printing technique. Figure 3 (a) shows the printed honeycomb cells. The created honeycomb cell has a radius of 13.8 mm and a height of 10 mm. Five honeycomb components are installed in the AMR test section with O-rings of 1.5 mm wire diameter. This configuration constitutes the honeycomb structure. Platinum resistance temperature detectors were designated as 1 mm apart on each side, and the temperatures at the high-temperature end (T_{hot}) and low-temperature end (T_{cold}) are measured as temperature evaluation points. The temperature span between T_{hot} and T_{cold} is denoted as ΔT . An experimental investigation is then conducted to clarify the generation of temperature span in a magnetic heat pump, which is compared with and discussed in the previous section. Figure 3 (b) illustrates the number of AMR cycles $N[-]$ on the horizontal axis and T_{hot} and T_{cold} at the temperature evaluation point of the heat exchange fluid on the vertical axis. From the result, the experimental value of generated temperature span of the honeycomb-filled structure is 0.69K smaller than the analytical value. This may have been caused by mixing UV resin and dispersant in addition to magnetocaloric material when creating the honeycomb cell.



(a) Photo of 3D printed honeycomb cells

(b) Temperature variation with number of AMR cycle

Figure 3. Experimental results for honeycomb structure

4. CONCLUSIONS

In the honeycomb-filled structure, the pressure drop was lower than that in the particle packed structure, but the generated temperature span was higher in the particle packed structure. During the experimental investigation of the honeycomb-filled structure, it was confirmed that mixing another substance with the magnetocaloric material resulted in a decrease in the generated temperature span between the hot end and the cold end.

5. REFERENCES

- Kawanami, T., Hirano, S., Toba, A. and Vuarnoz D., 2015. "Comprehensive Consideration on AMR Configuration for Magnetocaloric Heat Pump". *TEION KOGAKU (J. Cryo. Super. Soc. Jpn)*, Vol. 50, No. 2, pp. 72–79.
- T.J. Lu, 1999. "Heat transfer efficiency of metal honeycombs". *International Journal of Heat and Mass Transfer*, Vol. 42, pp. 2031–2040.
- W. F. Giaque., 1927. "A thermodynamic treatment of certain magnetic effects. A proposed method of producing temperatures considerably below 1° absolute, *Journal of American Chemical society*". *Journal of the American Chemical Society*, Vol.49, No.8, pp. 1864–1870.

An Approach of Hot-to-Cold(H2C) Process for Axial Compressor

Subin Kim^a, Seong-Han Bae^a, Hyun-Su Kang^b, Youn-Jea Kim^{c,*}

^aGraduate School of Mechanical Engineering, Sungkyunkwan University, Suwon 16419, South Korea

^bEnergy Research Center, Research Institute of Industrial Science & Technology, Pohang 37673, South Korea

^cSchool of Mechanical Engineering, Sungkyunkwan University, Suwon 16419, South Korea

*yjkim@skku.edu

Keywords: Axial Compressor, Hot-to-Cold (H2C) Process, Inverse Solving, CFD, Rotor 37

1. INTRODUCTION

The shape of a compressor blade is delineated into a hot blade shape, representing its form under operational conditions, and a cold blade shape, post-manufacturing. The hot blade configuration, when assumed by the manufactured blade, tends to undergo excessive deformation under external loads. To mitigate this, it is crucial to transform the hot blade shape into a cold blade shape through a process known as the Hot-to-Cold (H2C) during manufacturing. The basic concept of the H2C process is to derive the pre-deformation shape, the cold blade shape, with external loads removed, by performing inverse solving on the compressor blade shape deformed by external loads.

2. METHODOLOGY

The analysis model was selected as NASA rotor 37, which is used in many studies due to the disclosure of shape information and performance test data. According to Ameri (2009) and Dunham (1998), the reliability of the data was secured through many verification processes. Therefore, the NASA rotor 37 interpretation model was designed with shape specifications extracted from previous papers and reports and implemented in 3D shapes using ANSYS Bladegen and Design Modeler. The grid of the generated model was constructed using Turbogrid, and for the reliability of numerical analysis, the grid dependency test was conducted as shown in Fig 1. The grid dependency test was performed based on the adiabatic efficiency, and 1.2 million grids were adopted. Analysis was performed using ANSYS CFX for the generated NASA rotor 37 verification.

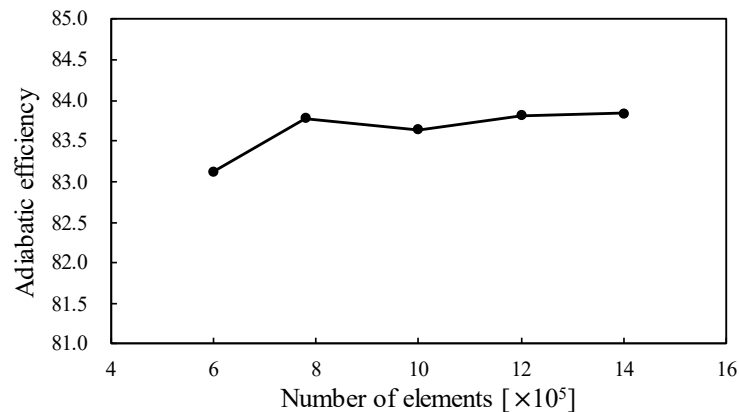


Figure 1. Grid dependency test

The boundary conditions used in the analysis are shown in Table 1. The analysis results were compared with the NASA test results for 100% speed of Reid and Moore (1978), as shown in Fig 2, and the analysis model was verified from the test.

Table 1. CFD boundary conditions applied in this study

Working fluid		Ideal gas
Rotational velocity		17,188.7 [rev/min]
Turbulence model		SST $k - \omega$
Inlet	Total pressure	101.325 [kPa]
	Total temperature	288.15 [K]
Outlet	Static pressure	90~133 [kPa]

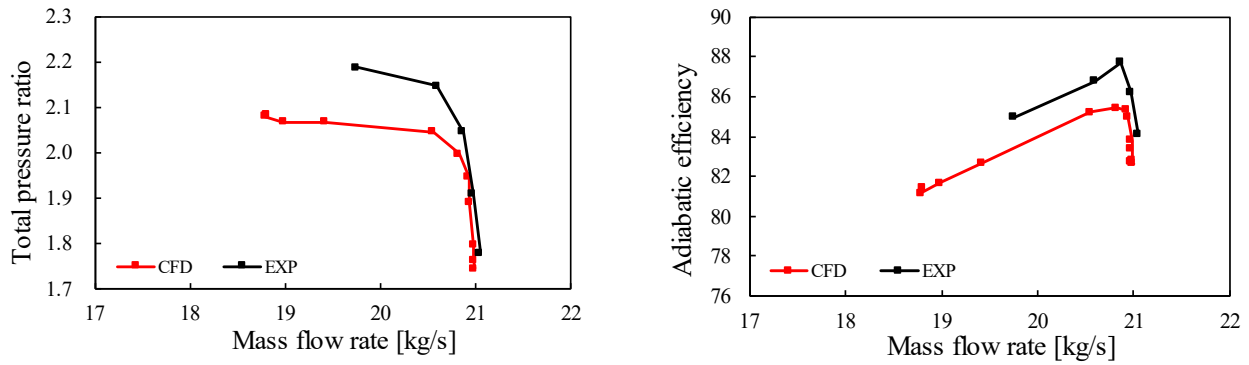


Figure 2. Comparison of 100% design speed analysis and experimental results of the NASA rotor 37 model

The H2C process by inverse solving was applied to the verified model, and the inverse solving process is shown in Fig. 3. The external load applied to the verified hot blade shape is applied once more to cause the deformation of the hot blade shape deformation(dU). Assume that the cold blade shape is the same as the hot blade shape with the dU applied in the reverse direction. Analyze the assumed cold blade shape to derive the hot blade shape. Compare the derived hot blade with the validation model, the hot blade, to determine the error and finally obtain the cold blade.

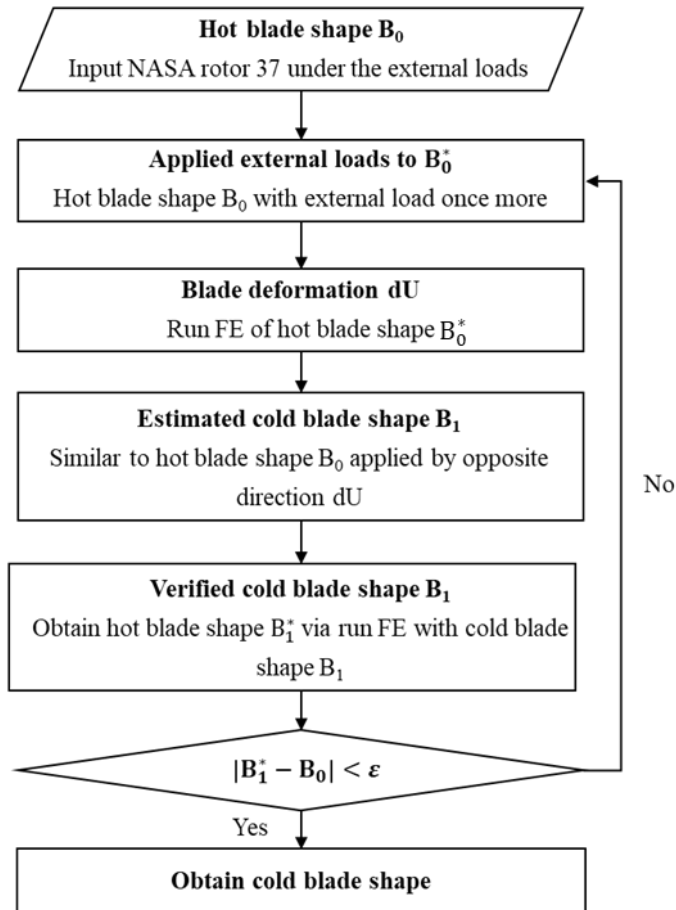


Figure 3. Flow chart of Hot-to-Cold process by inverse solving

3. CONCLUSIONS

The process of converting it into a cold blade shape is necessary for manufacturing after designing the compressor. In this study, the hot blade was first designed to derive the cold blade, and it was compared and verified with the NASA test results. The cold blade was derived by applying the H2C process from the verified model.

ACKNOWLEDGEMENT

This research was supported by the Korea Agency for Infrastructure Technology Advancement (KAIA) grant funded by the Ministry of Land, Infrastructure, and Transport, grant number (RS-2022-00142936).

REFERENCES

- Ameri, A., 2009, "NASA rotor 37 CFD code validation glenn-ht code," Proc. 47th AIAA Aerospace Sciences Meeting including The New Horizons Forum and Aerospace Exposition, p. 1060.
- Dunham, J., 1998, "CFD validation for propulsion system components (la validation CFD des organes des propulseurs)," Advisory Group for Aerospace Research and Development Neuilly-sur-Seine (FRANCE), AGARD Advisory report 355.
- Reid, L. and Moore, R. D., 1978, "Design and overall performance of four highly loaded, high speed inlet stages for an advanced high-pressure-ratio core compressor," NASA/TP-2013-19780025165.

LIQUID FRACTION EVOLUTION DURING THE DIFFERENT MELTING REGIMES IN A VERTICAL TUBE IN TUBE HEAT EXCHANGER

Maité Goderis^{a,b,*}, Julie Van Zele^{a,b}, Kenny Couvreur^{a,b}, Wim Beyne^{a,b}, Michel De Paepe^{a,b}

^aDepartment of Electromechanical, Systems and Metal Engineering – UGent, Ghent, Belgium

^bFlandersMake@UGent – Core lab EEDT-MP, Leuven, Belgium, www.flandersmake.be

*maite.goderis@ugent.be

Keywords: latent thermal energy storage, heat exchanger, liquid fraction, experimental, tube in tube

1. INTRODUCTION

Latent thermal energy storage (LTES) systems have proven to be an efficient way to store energy. In these systems Phase Change Materials (PCMs) are used as storage materials and undergo a phase change while storing or releasing energy. LTES systems can reach a 5-14 times higher volumetric storage density compared to sensible thermal energy storage units, where no phase change takes place (Garg et al., 1985). However, in LTES systems, the phase change taking place during the charging and discharging, introduces a moving-boundary problem that needs to be solved. Because of this transient behavior, design methods used for regular heat exchangers are not applicable for LTES systems. As a result, general characterization and design methods for LTES systems are still under development.

The past few decades have seen significant research efforts dedicated to obtaining more insight into the complexity of phase change problems. Pioneering work of Jany and Bejan (Jany & Bejan, 1988) identified different regimes during the melting process within a rectangular enclosure. Initially, heat transfer between the heated wall and the PCM is dominated by conduction, as the solid PCM conducts heat efficiently. As the phase change progresses and more PCM changes from solid to liquid phase, natural convection within the liquid region starts playing a significant role, enhancing heat transfer. As more PCM becomes liquid, heat transfer by natural convection will gain importance until convection is the dominant heat transfer mode. The last regime is the solid shrinking regime. This final stage starts when the liquid PCM reaches the wall opposite to the heated wall for the first time. As the remaining solid region shrinks, heat transfer primarily occurs through the liquid layer.

One of the most important parameters in an LTES system is the liquid fraction, which directly reflects the state of charge of the storage system. The liquid fraction of a system refers to the percentage of PCM that has undergone the phase change from solid to liquid, compared to the total PCM mass. Numerous studies have explored the evolution of the liquid fraction during the melting process of PCMs. For instance, Ho and Viskanta (Ho & Viskanta, 1984) developed a correlation for the liquid fraction, based on experiments on a rectangular PCM enclosure with an isothermally heated side wall. The liquid fraction was given as a function of the Stefan number, Fourier number and Rayleigh number. The liquid fraction was determined based on the shape of the phase change front, which was assumed to be two-dimensional. The variable heat transfer dynamics over the different melting regimes were not taken into account.

In a recent study by Wang et al. (Wang et al., 2023), correlations for the liquid fraction evolution in each melting regime are given based on an extensive set of numerical simulations of a rectangular PCM geometry with variable dimensions, variable wall temperature and variable initial temperature. In these correlations, the effects of either dominant conduction or convection can be recognised.

Rectangular enclosures have been studied a lot in past research and are relevant to obtain important insights in PCM behavior. However, in practice, shell-and-tube heat exchangers are seen as the most efficient geometry thanks to their high efficiency for minimum size (Zayed et al., 2020). Therefore, PCM behavior in cylindrical enclosures needs to be studied thoroughly. Kalapala and Devanuri (Kalapala & Devanuri, 2019) performed numerical simulations on a cylindrical enclosure, where PCM was placed in the annulus and the HTF flows from top to bottom in the inner tube. A correlation for the melting fraction was constructed based on various dimensionless numbers and material properties (Eq. 1). Based on an extensive set of simulations, it was seen that the influence of the Rayleigh number varies throughout the melting process (Eq. 2).

$$MF = \left[\frac{0.1FoRe^{0.064} Ra^a St^{*1.206} \varphi^{0.0106} \left(21.178\sigma + \frac{0.1}{\sigma} \right)}{\left(\frac{L}{D} \right)^{0.3795}} \right]^{0.7} \quad 1$$

$$a = \begin{cases} \frac{e^{Fo.Ste^{0.6}\left(\frac{L}{D}\right)^{0.04}} - 1}{4.2} & \text{if } Fo.Ste^{0.6} \leq 0.35 \\ 0.1 \left(\frac{L}{D}\right)^{0.4} & \text{if } 0.35 < Fo.Ste^{0.6} \leq 0.74 \\ \frac{0.08 \left(\frac{L}{D}\right)^{0.025}}{Fo.Ste^{0.6}} & \text{if } Fo.Ste^{0.6} > 0.74 \end{cases} \quad 2$$

In Eq. 1 and Eq. 2, the Reynolds number is purely linked to the HTF and the Rayleigh number is based on the width of the PCM channel. φ represents the ratio of the thermal diffusivity of the tube to that of the PCM. σ is the ratio of the heat transfer fluid (HTF) tube thickness to the inner diameter of the PCM shell. $\frac{L}{D}$ is the ratio of the length of the heat exchanger to width of the PCM channel, representing the aspect ratio of the geometry. The numerical data set included tube in tube geometries with aspect ratios up to 10.

However, in practice, shell-and-tube systems with much higher aspect ratios will be used, as typically large heat transfer areas are required for thermal storage applications and specific complete melting and solidification times are desired (Rathod & Banerjee, 2015). PCM geometries with high aspect ratio will have different melting behavior, as now the solid shrinking phase will be much longer.

In this study, a tube in tube LTES system with high aspect ratio will be experimentally tested. The liquid fraction evolution will be measured during the melting process by the means of a camera installed next to the PCM heat exchanger. A correlation to predict the liquid fraction evolution is constructed, taken into account the different regimes throughout the melting process.

2. EXPERIMENTAL SETUP

Figure 1 shows a schematic of the experimental setup used for this study. A tube in tube heat exchanger with a length of one meter is tested. The PCM RT35HC (Table 1) is placed in the annulus of the heat exchanger, while water flows in the inner tube from top to bottom as HTF. The HTF-tube is a copper tube with an outer diameter 15 mm and a thickness of 2 mm. The PCM is contained in a transparent polycarbonate tube with an outer diameter 60 mm and thickness of 3 mm. Next to the heat exchanger, a camera is installed to measure the height of the PCM volume. This height will change throughout the experiment, due to the volume expansion taking place during melting. Based on the measured volume expansion, the liquid fraction can be determined. The camera is placed on a linear slider, to ensure the complete range of variable PCM height can be captured. *A photograph of a liquid fraction measurement will be added in the full paper.*

The heat exchanger and camera are placed in a large box made by Recticel insulation panels. This box is filled with insulation granules to limit heat losses to the environment. In the box, LED-lights are attached to the polycarbonate tube to enable visual observations with the camera in the closed, dark box.

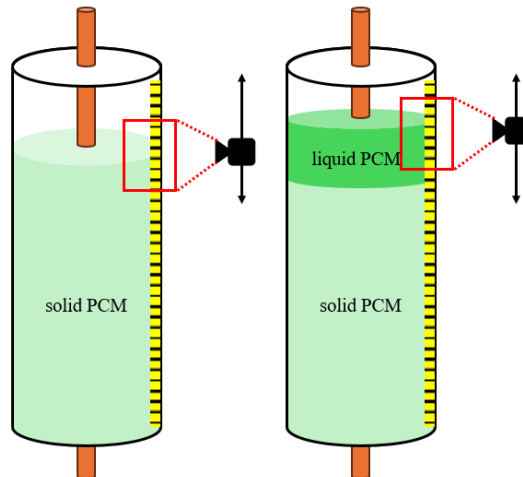


Figure 1. Schematic of the tube in tube setup equipped with a camera to measure the liquid fraction evolution.

Table 1. RT35HC properties (*Rubitherm GmbH*, n.d.).

Melting area	34-36	°C
Congealing area	36-34	°C
Specific heat capacity	2	kJ/kgK
Density solid (at 25°C)	0.88	kg/l
Density liquid (at 60°C)	0.77	kg/l

Heat conductivity	0.2	W/mK
Max. operating temperature	70	°C
Melting area	34-36	°C

Melting experiments with variable HTF inlet temperature (55, 60, 65°C) and HTF mass flow rate (20, 30, 50 kg/h) are performed to investigate the influence of these inlet parameters on the liquid fraction evolution. Table 2 gives an overview of the different inlet conditions and accompanying dimensionless numbers. All tests are performed with an initial PCM temperature of 25°C. The characteristic length used for the Rayleigh number is the width of the PCM channel.

Table 2. Experimental matrix.

Table will be added in full paper: HTF inlet temperature, HTF mass flow rate, Rayleigh number ($\sim 10^6$), Reynolds number (1000-5000) for each melting experiment.

3. LIQUID FRACTION MEASUREMENTS AND CORRELATION

Currently, some adaptations are still being made to the experimental setup. The experimental study will start soon and no practical problems are expected. Experiments with variable HTF inlet temperature and HTF mass flow rate will be executed, while tracking the liquid fraction evolution over time as explained in the previous section. It is expected that a higher HTF inlet temperature will lead to a faster rising of the liquid fraction, and earlier complete melting of the PCM. Plots with the liquid fraction as a function of time will be presented for the various operational conditions and the different melting regimes will be identified based on the shape of the liquid fraction curves.

The experimental obtained liquid fraction data will be compared to the results obtained with the correlation given by Kalapala et al. (Kalapala & Devanuri, 2019). Also the transitions between the different melting regimes are compared to the transition values given by Kalapala et al. It is expected that the prediction of Kalapala et al. will deviate from the experimental results, as the experimentally tested tube in tube setup has a significant larger aspect ratio compared to the considered geometries in the study of Kalapala et al.

Furthermore, a new liquid fraction correlation will be fitted. In each regime, a separate correlation for the liquid fraction will be fitted of the following shape:

$$LF = aRa^b Re^c Ste^d Fo^e$$

4. CONCLUSION

A one meter long tube in tube PCM heat exchanger was experimentally tested. The HTF inlet temperature and HTF mass flow rate were varied to study the effect on the evolution of the liquid fraction throughout the melting process. The different melting regimes are identified: dominant conduction, mixed conduction-convection, dominant convection, and solid shrinking. For each regime, a correlation for the liquid fraction was retrieved with a maximum error of ...%.

5. REFERENCES

- Garg, H. P., Mullick, S. C., & Bhargava, A. K. (1985). *Solar Thermal Energy Storage* (1st ed.). Springer Netherlands. <https://doi.org/10.1007/978-94-009-5301-7>
- Ho, C. J., & Viskanta, R. (1984). Heat transfer during melting from an isothermal vertical wall. *Journal of Heat Transfer*, 106(1), 12–19. <https://doi.org/10.1115/1.3246624>
- Jany, P., & Bejan, A. (1988). Scaling theory of melting with natural convection in an enclosure. In *hr. J. ifeat Mass Transfer* (Vol. 31, Issue 6).
- Kalapala, L., & Devanuri, J. K. (2019). Parametric investigation to assess the melt fraction and melting time for a latent heat storage material based vertical shell and tube heat exchanger. *Solar Energy*, 193, 360–371. <https://doi.org/10.1016/j.solener.2019.09.076>
- Rathod, M. K., & Banerjee, J. (2015). Thermal performance enhancement of shell and tube Latent Heat Storage Unit using longitudinal fins. *Applied Thermal Engineering*, 75, 1084–1092. <https://doi.org/10.1016/j.applthermaleng.2014.10.074>
- Rubitherm GmbH. (n.d.). Retrieved September 16, 2022, from <https://www.rubitherm.eu/en/productcategory/organische-pcm-rt>
- Wang, Z., Li, Y., Wang, Y., & Li, A. (2023). Stagewise melting heat transfer characteristics of phase change material in a vertically placed rectangular enclosure. *Journal of Energy Storage*, 62. <https://doi.org/10.1016/j.est.2023.106917>
- Zayed, M. E., Zhao, J., Li, W., Elsheikh, A. H., Elbanna, A. M., Jing, L., & Geweda, A. E. (2020). Recent progress in phase change materials storage containers: Geometries, design considerations and heat transfer improvement methods. In *Journal of Energy Storage* (Vol. 30). Elsevier Ltd. <https://doi.org/10.1016/j.est.2020.101341>

NUMERICAL AND EXPERIMENTAL STUDY OF PARALLELIZED TWO-PHASE HEAT EXCHANGERS FOR HIGH PERFORMANCE COMPUTING PROCESSORS

Matthieu Amate-Vignon^{a,b,*}, Marc Raeth^b, Alexandre Labergue^a, Michel Gradeck^{a,*}

^aUniversité de Lorraine, CNRS, LEMTA, F-54000 Nancy – France

^bEviden, Avenue Jean Jaurès, 78340 Les Clayes-sous-Bois

*matthieu.amatevignon@eviden.com

Keywords: HPC, cooling, evaporation, flow distribution

1. BACKGROUND

Because of the power to dissipate to maintain optimal working conditions, cooling is compulsory for High Performance Computing (HPC). The choice of the cooling system greatly depends on the power consumption of the chips, the server density, and the data center infrastructure. Engineers must design the most effective cooling method balancing between available cold source and lowering the costs of an installation. Among the available cooling technology, the simpler is air cooling associated with fins and fans, which cannot however provide very high heat flux dissipation. The more recent direct liquid cooling (DLC) technology can provide much higher cooling heat-flux but is limited by pumping dissipations. Immersion cooling can also provide high heat-flux but needs a dielectric fluid which can be difficult to manage in some data centers. With the current and future generations of HPC chips, all these cooling technologies are now far from being adapted for processors dissipating up to 1000 W or whose temperature must remain below 55°C for some cases. Meanwhile, one of the main criteria for HPC centers in the selection of a provider is the temperature of the cold source to cool down the infrastructure. Following ASHRAE's Thermal Guidelines for Data Processing Environments, most Eviden customers look for a cold source temperature of 40°C, enabling free cooling all year long in most parts of the Earth.

As the quick evolution of the processors is currently rendering the gains of performances of DLC unfit to meet the clients' requirements, two-phase - or evaporative - cooling has gained momentum in being a successor of DLC in power-dense, compact, and highly parallel HPC products to be commercialized by Eviden in the future.

The performance of the various types of evaporators has been extensively studied, although mainly for only one heat spreader. Behavior of the hydraulic assembly of a highly parallelized rack of blade servers remains overall undocumented. Mainly, the power dissipated varies independently over time between each processor, leading to uneven variations of the pressure drop inside the corresponding evaporator, which modifies the repartition of the flow inside the system.

2. OBJECTIVES

The main objective of this paper is to study the distribution of the flowrate inside a parallelized installation like a blade server. A typical blade server designed by Eviden can dissipate up to 5 kW of thermal power, which is cooled down by a hydraulic circuit made of tubes, elbows and T-junctions connecting the inlet and outlet of the blade server to the heat-sinks. Because of the size constraint, the inner diameter of this circuit can take values between 3 and 6 mm, and up to 50 cm for the lengths. Heat-fluxes can reach up to 100 W/cm². To dissipate 5 kW, the coolant flowrate is set between 1 and 7 l/min.

A python code and an experimental apparatus are designed to simulate a typical blade server. Results will then be used to develop a strategy to implement this mode of cooling inside future products.

3. METHODS

The first axis consists in the development of a python code to simulate the two-phase flow and determine its repartition inside any installation. This installation is decomposed into branches of parts connected to each other (Fig.1). The modelling of the pressure drop of the parts is based on various correlations. Amongst others, the correlations developed in Idel'cik (1960) (various parts in single phase flow), Lockhart-Martinelli (1949) and Friedel (1979) (adiabatic two-phase flow), Kim & Mudawar (2016) (evaporation in micro-channel heat sink, MCHS), Longo et al (2014) (condensation in brazed-plate heat-exchanger, BPHE) are used.

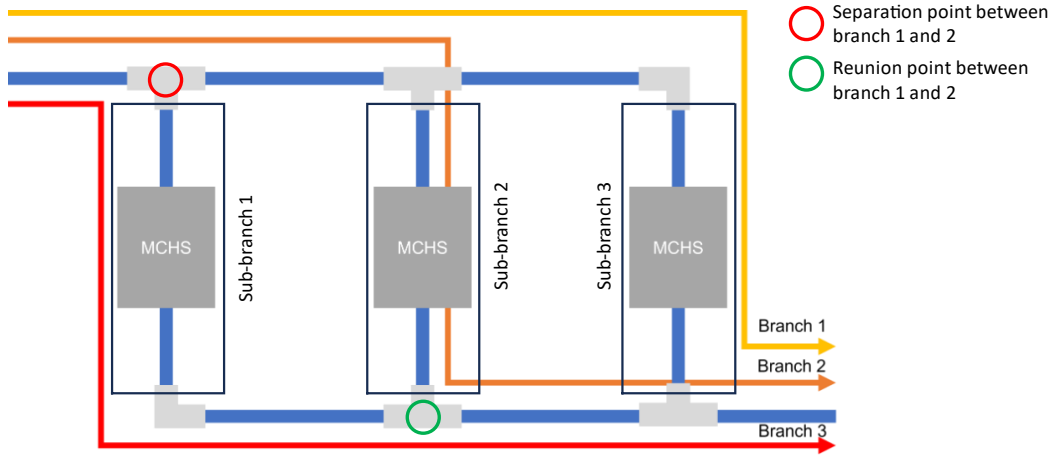


Figure 1: Three MCHS installed in parallel forming the same number of branches from the inlet of the installation to its outlet. In DLC, this system is naturally evenly equilibrated, provided that each independent sub-branch produces the same pressure drop at a given flowrate.

The code relies on determining the repartition of the mass flowrates by equalizing the pressure drop between all the pairs of branches which have a separation and a reunion point in common (Fig1.). With the `scipy.optimize` library in `python`, the mass flowrate in each branch i is computed by solving the following equations:

$$(\dot{m}_1, \dots, \dot{m}_n, P_1, \dots, P_n) \rightarrow (|\Delta p_1 - \Delta p_2|, \dots, |\Delta p_{n-1} - \Delta p_n|) \quad (1)$$

where \dot{m}_i , P_i and Δp_i correspond respectively to the mass flowrate, dissipated power and the pressure drop of the branch i .

The numerical values are compared to the results obtained experimentally with the set-up shown in Fig. 2.

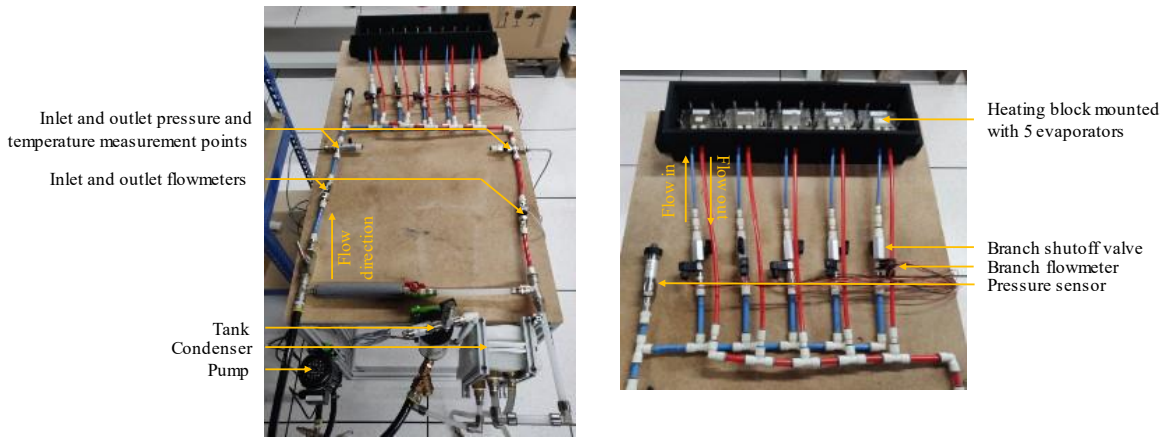


Figure 2 : Overview (left) and details (right) of the testbench used to study the flow repartition inside parallel branches of a two-phase cooling installation. The blue pipes correspond to the distribution of the coolant, the red ones to its collection.

This testbench is designed to enable quick reconfiguration of the hydraulic assembly. The heating block (equipped with heating cartridges) can dissipate up to 2.5 kW over five micro-channel evaporators. The width, spacing, length and height of the fins are respectively 0.2mm, 0.2mm, 70mm and 3mm.

4. RESULTS

A simulation based on the geometry depicted in Fig. 2 with a total flowrate of $1.6E-5 \text{ m}^3/\text{s}$ (1 l/min) has been carried out. Numerical results obtained by the home-made code are summarized in Table 1 which presents four cases: equal, random, increasing and decreasing power distribution across the five evaporators.

Case 1 shows an ideal case where the flowrate is equally distributed. This situation rarely happens as the processors tend to have a much more random power to dissipate which varies over time with their computing load. This phenomenon

corresponds to case 2 where random values of power are distributed across the evaporators. Although evaporators 1 and 5 dissipate close power, they are supplied individually with very different flowrates. Cases 3 and 4 show that the way the hydraulic assembly is made influences the flow distribution, as evaporators 4 and 5 in case 4 are fed respectively 2.2 and 1.7 times the flowrate of evaporators 1 and 2 in case 3 for the same dissipated power.

		Evap1	Evap2	Evap3	Evap4	Evap5
Case 1	Power (W)	500	500	500	500	500
	Flow distribution	18,7%	18,8%	19,3%	22,7%	20,5%
Case 2	Power (W)	439	385	469	261	411
	Flow distribution	7,2%	9,4%	6,2%	9,3%	67,9%
Case 3	Power(W)	500	400	300	200	100
	Flow distribution	1,8%	2,6%	5,4%	45,1%	45,0%
Case 4	Power (W)	100	200	300	400	500
	Flow distribution	43,3%	43,0%	5,2%	4,5%	4,0%

Table 1: Parameters and results of the simulation of the experimental apparatus in Fig. 2. Flow distributions correspond to percentages of the flowrate fed to the entire assembly of five evaporators.

5. CONCLUSIONS

The first results of the simulation show interesting theoretical behavior of the hydraulic installation under conditions which can be seen in real applications (unevenly distributed power to dissipate across the blade server). A future iteration of the code will consider the thermal performances of the evaporators with respect to the flow distribution to predict the capacity of two-phase cooling to be efficiently integrated in future products.

Moreover, several quantities can be accessed at the inlet(s) and outlet(s) of each part of the simulated hydraulic circuit, such as pressure, mass flowrate, enthalpy, and vapor quality/void fraction. To validate the code, overall quantities (branch mass flowrate and pressure drop) and values at specific points (pressure, temperature) will be compared with the experiment to confirm the models of the behavior of each part in single- and two-phase flow.

6. REFERENCES

- Friedel, L. "Improved Friction Pressure Drop Correlation for Horizontal and Vertical Two-Phase Pipe Flow." (1979).
- Idel'cik, I. E. "Memento des pertes de charge : coefficients de pertes de charge singulières et de pertes de charge par frottement", in *Collection de la Direction des Etudes et Recherches d'Electricité de France*. Editions Eyrolles, Paris, 1986.
- Kim, S.-M., and Mudawar, I. "Thermal design and operational limits of two-phase micro-channel heat sinks". *International Journal of Heat and Mass Transfer* 106 (Mar. 2017), 861–876.
- Lockhart, R. W., and Martinelli, R. C. "Proposed correlation of data for isothermal two-phase, two-component flow in pipes". *Chemical Engineering Progress* (1949).
- Longo, G. A., Righetti, G., and Zilio, C. "A new computational procedure for refrigerant condensation inside herringbone-type Brazed Plate Heat Exchangers". *International Journal of Heat and Mass Transfer* 82 (Mar. 2015), 530–536.

Experimental study on novel anti-slug control scheme based on choke valve pressure drop

Hanxuan Wang^a, Suifeng Zou^{a,*}, Xiaojun Ma^a, Bo Yang^b, Liejin Guo^{a,*}

^aState Key Laboratory of Multiphase Flow in Power Engineering, Xi'an, 710049, China

^bChina National Offshore Oil Corporation Research Institute Co., Ltd., Beijing, 102200, China

* zou_suifeng@xjtu.edu.cn (Zou S.), lj-guo@mail.xjtu.edu.cn (Guo L.)

Keywords: Off shore, Oil and gas, Multi-phase flow, Anti-slug, Flow control

1. INTRODUCTION

Slugging flow is a hazardous multiphase flow regime induced by the particular topology of an offshore pipeline, exhibiting periodic flow behaviors. A classic slugging flow period in a pipeline-riser system can be divided into four sequential phases: (1) slug formation, (2) liquid outflow, (3) gas-liquid blow out, (4) liquid fallback. In such a severe slugging regime, the pipeline pressure and outlet flow rate fluctuate vigorously periodically. Because of the unexpected pressure and flow variations, severe slugging can initiate and activate flow system instability, reducing production, jeopardizing downstream equipment, and potentially even shutting down the system. Elimination and avoidance of severe slugging is of huge economic interest.

It is a common use method to avoid slug flow by real-time slug regime detection and regulating the valve openings with PIDs (Pedersen et al. 2016; Oliveira et al. 2015). The theoretical best approach is using riser bottom pressure or riser pressure drop signal, or their statistical parameter, as the controlled variable (Park et al. 2021), but such a deep-water signal is costly to acquire. Besides, direct control of the valve opening is a big problem because of the nonlinearity relation between the valve opening and the controlled variable (Jahanshahi and Skogestad, 2013).

For these reasons, a new control scheme is studied and proposed. The scheme can be divided in two parts: (1) a new criterion using choke pressure drop as signal source to detect slug flow online, (2) a PID control valve friction coefficients instead of valve openings. The performance is validated by experiments.

2. EXPERIMENTAL SETUPS

Experiments were performed on the following experimental setup as shown in Figure 1. The facility consists of horizontal, downward and vertical pipes to simulate a real pipeline-riser system. The working fluid supply system includes gas phase and water phase, and the working fluid is compressed air and water. The gas phase is supplied by the compressor and enters the system via a buffer tank (to stabilize the pressure) and three orifice meters with different ranges (for precise measurement). The water phase is driven by a centrifugal pump and enters the system via a water tank and two electromagnetic flow meters of different ranges. Before entering the system, the inlet pressure is raised by adjusting the opening of the return valve, which in turn stabilizes the liquid phase inlet flow rate. An electric ball valve which acts as the choking valve is installed on the connection pipe between the riser top and the separator. The flow characteristic of the valve is equal percentage. The parameters of the experimental system are shown in Table 1.

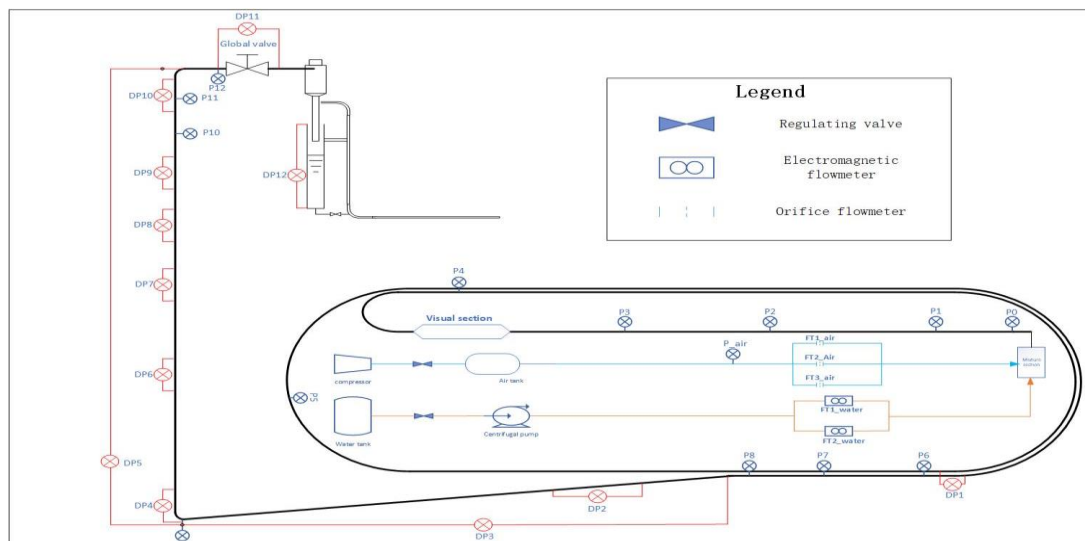


Figure 1. Experimental system figure.

Table 1. Experimental system parameters

Horizontal pipe length (m)	114	inclination angle (°)	-2
Downward pipe length (m)	18.7	Pipe inner diameter(mm)	50
Riser length (m)	16.3	Operating temperature(°C)	25

3. CONTROL SCHEME

First, digitize the choke pressure drop using Eq. (1). Then, calculate the cut-off ratio, D , using Eq. (2) and D to detect slug flow. $D > 0$ means slug flow happens; and $D = 0$ means not.

$$F(x) = \begin{cases} 0, & x \leq \text{threshold} \\ 1, & x > \text{threshold} \end{cases} \quad (1)$$

$$D = 100 \frac{\text{sum}(F(x))}{\text{len}(F(x))} \quad (2)$$

$$kv_z = f(kv_{\max}, Z) \quad (3)$$

$$f_z = \sqrt{2 \left(\frac{36000A}{kv_z} \right)^2} \quad (4)$$

Afterwards, calculate the valve flow coefficient using Eq. (3). Then, calculate the valve friction coefficient using Eq. (4). For the specific valve installed on the experimental apparatus, the calculated curve of valve friction coefficient versus valve opening is shown in Figure 2. Obviously, the valve characteristic is equal percentage.

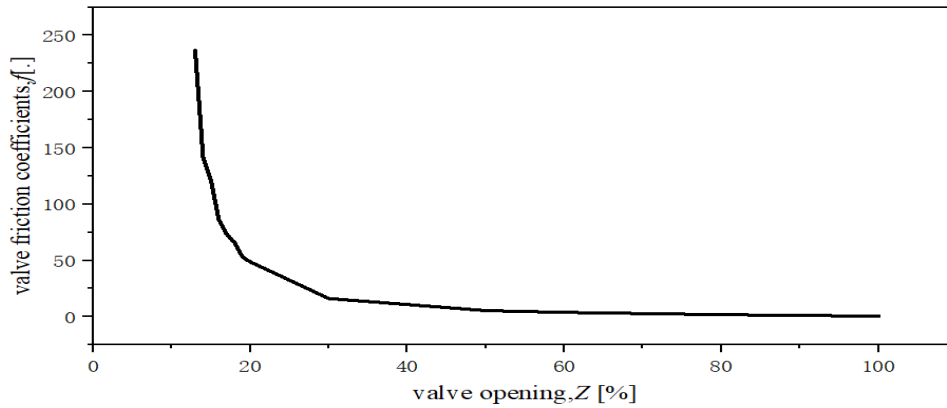


Figure 2. Valve friction coefficients characteristic curve

Use Eq. (3), Eq. (4), Eq. (5) to control valve friction coefficients, so that the valve openings is indirectly controlled.

$$u_k = K_p e_k + K_i \sum_0^k e_k + K_d (e_k - e_{k-1}) \quad (5)$$

$$K_i = K_p T / T_i, \quad K_d = K_p T_d / T \quad (6)$$

4. EXPERIMENTAL VALIDATION

Experimental validation was carried out for Case 1 with superficial gas velocity of 0.15 m/s (standard condition) and superficial liquid velocity of 0.05 m/s, and Case 2 with superficial gas velocity of 1 m/s (standard condition) and superficial liquid velocity of 0.05 m/s.

Case 1 is typical SS1 regime, and the experimental results are shown in Fig. 3. Severe slugging was eliminated after six slugging periods and six times of valve opening adjustments. Case 2 is a typical SS2 regime, in which the phase of liquid outflow is absent. The experimental results are shown in Fig. 4. Severe slugging was eliminated after five times of valve opening adjustments. The stabilizing time of the control process was faster than conventional control methods which need more than 30 slug periods to settle (Pedersen et al. 2014).

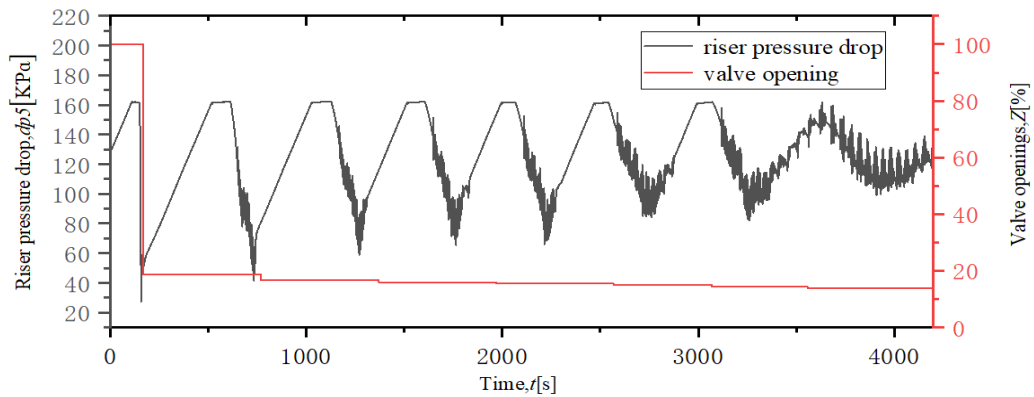


Figure 3. Experimental result – Case 1.

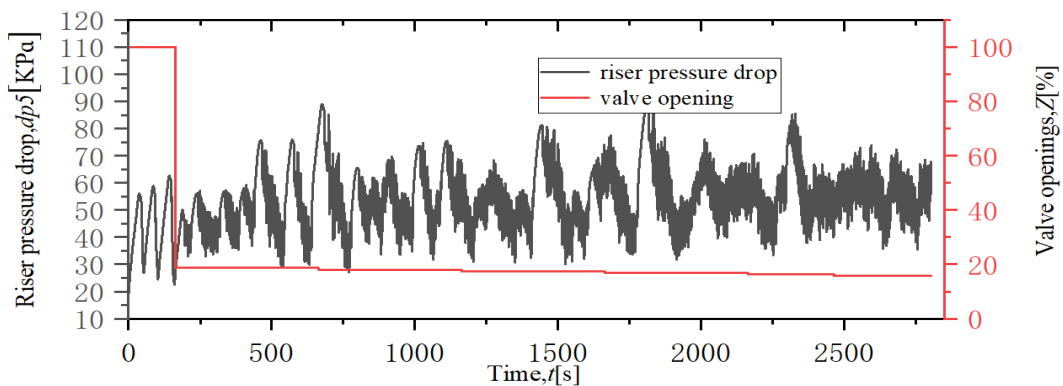


Figure 4. Experimental results – Case 2.

5. CONCLUSIONS

In this paper, a new anti-slug control scheme was experimentally studied and designed. Distinguished from conventional schemes, this scheme processed the choke pressure drop to detect the slug flow online, while using a PID controller to regulate the valve friction coefficients instead of directly controlling the valve openings. The experimental validation showed a quick control process, and severe slugging could be achieved within six slugging periods, even for conditions for which no a priori knowledge existed.

6. REFERENCES

- Jahanshahi, E., Skogestad, s., 2013. “Closed-loop model identification and PID/PI tuning for robust anti-slug control”. *IFAC Proceedings Volumes*, Vol. 46, pp. 233-240,
- Oliveira, V.D., Jäschke, J., and Skogestad, s., 2015. “An autonomous approach for driving systems towards their limit: an intelligent adaptive anti-slug control system for production maximization”. *IFAC-PapersOnLine*, Vol. 46, Issue 6, pp.104-111.
- Park, K.H., Kim, T.W, Kim, Y.J, Lee, N., and Seo, Y.,2021. “Experimental investigation of model-based IMC control of severe slugging”. *Journal of Petroleum Science and Engineering*, Vol. 204.
- Pedersen, S., Durdevic, P., and Yang, Z.Y., 2017“Challenges in slug modeling and control for offshore oil and gas productions: A review study”. *International Journal of Multiphase Flow*. Vol. 88, pp. 270–284.
- Pedersen, S., Durdevic, P., and Yang, Z.Y., 2014“Learning control for riser-slug elimination and production-rate optimization for an offshore oil and gas production process”. *IFAC Proceedings Volumes*. Vol. 47, pp. 8522-8527.

ACKNOWLEDGMENT

This work is financially supported by National Key Research and Development Program of China (Grant Number 2022YFC2806200).

EXPERIMENTAL STUDY ON INSTABILITIES OF DROPLETS SUBJECTED TO AN EXTERNAL ELECTRIC FIELD

Alekos Ioannis Garivalis*, Giorgio Donolo, Paolo Di Marco

Department of Energy, Systems, Territory, and Constructions Engineering, University of Pisa, Largo Lucio Lazzarino 1, 56122, Pisa, Italy
*alekos.garivalis@unipi.it

Keywords: Sessile droplet, Interface instabilities, Electric field.

1. INTRODUCTION

The issue of the evaporation of sessile droplets under an electric field is of fundamental importance for many applications, particularly due to its low cost. In the presence of gravity, the evaporation of droplets depends on the three heat transfer mechanisms and vapor diffusion in the surrounding environment, which predominate over other phenomena along with convection (Gibbons *et al.*, 2021). By activating an electric field around a droplet, various geometric parameters influencing its evaporative process, such as the contact angle, can vary. For this reason, this process is influenced by the field itself. This phenomenon is particularly crucial for technologies such as “electrospraying” and for cooling in the absence of gravity (Dehaeck *et al.*, 2023), which is essential in space applications where convective processes cannot occur due to the absence of gravitational field. This can be addressed by “replacing” the gravitational field with an electric field.

An important application of our experiment involves the electrospinning process, reviewed by Haider *et al.* (2018). Electrospinning is a technique used to produce nanomaterials with advantageous properties compared to other technologies, especially in the fabrication of nanofibers. These nanofibers find applications in various fields; for example, when produced with biocompatible polymers, they are utilized in the biomedical field to construct Drug Delivery Carriers, create synthetic human tissues, and produce bandages. Additionally, they are used to manufacture air filtration systems or for water filtration and desalination. Electrospinning is based on the instability of droplets of certain liquefied materials subjected to an electric field. The materials used are generally polymeric, and due to their high viscosity and other characteristics, a continuous jet emerges from the droplets. By varying the involved parameters, such as the field intensity, fluid flow rate, and distance from the collector, it is possible to obtain fibers with very small diameters, so much so that they are called nanofibers.

In this work, sessile droplets of different materials were studied under the action of a nearly uniform electric field. The effects on the interface shape and instabilities have been quantified. An attempt to generalize the instability occurrence and consequent jet formation has been carried out.

2. EXPERIMENTAL APPARATUS

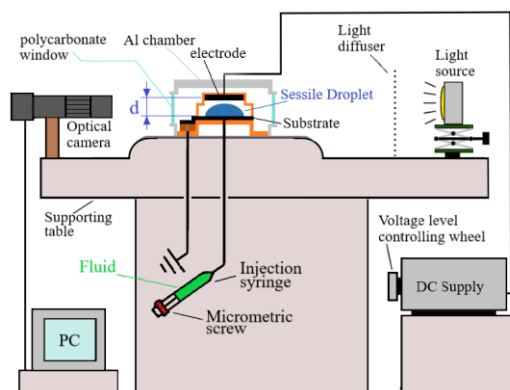


Figure 1. Experimental apparatus schematic.

The experimental setup is shown in Figure 1. It is mainly composed of a metallic substrate on which the droplet is deposited. The substrate is positioned under a washer-shaped electrode, and electrically grounded. The electrode distance from the substrate is $d = 6$ mm. The assembly is enclosed within a sealed chamber, onto which diffused light is directed, and a video camera is focused. A computer is connected to the camera (Ximea xiQ MQ022CMMG-CM) for video acquisition, and a high-voltage DC power supply, with an adjustable potential difference up to 30 kV, is connected to the

electrode to generate the electric field. A small tube allows the pumping of the analyzed fluid into the chamber through a hole in the substrate; the injected volume is calibrated using syringe connected to a micrometric screw to form the droplet as slowly as possible. Two concentric circular grooves, etched around the hole in the substrate, enable the formation of droplets with fixed base diameters of 4 mm and 8 mm, respectively.

Table 1. Properties of the fluids used.

	HFE-7100	Novec-649	FC-72	Water	Alcohol
ρ [kg/dm ³]	1.53	1.60	1.68	0.997	0.789
σ [mN/m]	13.7	10.8	10.0	72.8	23.2

Five different fluids were analyzed in the experiments, and their properties, measured under standard conditions, are reported in Table 1. Here, ρ represents density, and σ represents surface tension. As the first three fluids are similar, for the sake of brevity only one of them will be discussed in the results. Regarding the level of potential difference generated between the electrodes, cases of 7 kV and 10 kV were analyzed for all fluids except for alcohol and water, for which cases of 5 kV and 7 kV were considered (higher levels would have generated electric arcs). The chosen potential difference levels, ΔV , were selected since the electric force acting on the droplet is proportional to the square of the magnitude of the average electric field ($E = \Delta V/d$). Therefore, with these ΔV levels, the magnitude of this force is approximately doubled when transitioning from the case with lower potential to the one with the higher value.

The evolution of the droplet shape has been recorded by the camera. Fluid was injected slowly (quasi-static conditions) since the instability occurred. A code developed in the Matlab software was used to track the droplet interface and calculate the geometrical properties (such as volume, contact angle, etc.). Identifying the droplet profile was sufficient for our evaluations, given the assumed axisymmetric shape of the droplets. From it, all the geometric properties necessary for force calculations were obtained, varying with time.

3. RESULTS

According to Vancauwenberghe *et al.* (2013), two important dimensionless groups for the analysis are the Bond number, $Bo = (\rho g H R_b)/\sigma$, where σ is the surface tension, g is the acceleration of gravity, H the droplet height, R_b the droplet base radius) and the electric Bond number, $Bo_{el} = (\epsilon_0 E^2 R_b)/\sigma$, where ϵ_0 is the vacuum electric permittivity and E the average electric field intensity). Their values for each case with a base diameter of 4 mm are reported in Table 2. The Bond number represents the ratio of the forces acting on the droplet due to gravity and surface tension. Given the small value of Bo , in cases without an electric field it is permissible to approximate the shape of the droplets of all fluids with a spherical cap. The electric Bond number represents the ratio between the electric force and that due to surface tension.

Table 2. Bond numbers.

	HFE-7100	Novec-649	FC-72	Water	Alcohol
Bo	4.83E-03	5.81E-03	6.59E-03	5.37E-04	1.33E-03
Bo_{el} 5 kV	-	-	-	0.17	0.53
Bo_{el} 7 kV	1.76	2.23	2.41	0.33	1.04
Bo_{el} 10 kV	3.59	4.55	4.92	-	-

An elongation of the droplet shape in the direction of the electric field is observed for all droplets. Particularly, from the experiments on droplets with a diameter of 4 mm, two different behaviors are observed: some assume a cone-like shape, while others an oval shape. The first behavior is observed in the cases of HFE, NOVEC, and FC, while the second in the cases of alcohol and water. This difference, shown in Figure 2a, is likely related to the different value of the contact angle, which manages to surpass the right angle in the latter two cases.

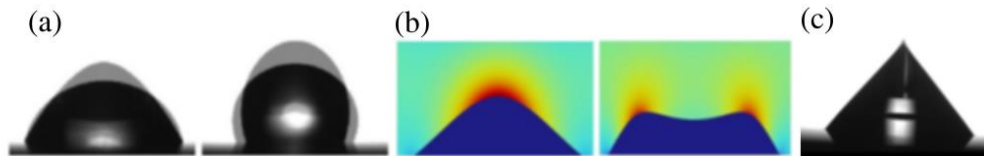


Figure 2. (a) Different droplet shapes with and without electric field. (b) Electric field distributions for droplets with $R_b = 4$ and 8 mm, respectively. (c) Instability (Taylor cone) occurrence.

Increasing the volume of the droplet under an electric field leads to a critical value (V_{cr}) at which instability on the surface is observed. This phenomenon is named “Taylor cone”, after G.I. Taylor (1964). This instability causes the formation of small fluid jets at the apex of the droplet, which are ejected towards the upper electrode. Additionally, the

cone-like droplets tend to assume a perfect cone shape, as depicted in Figure 2c which shows the moment when instability occurred in the case of alcohol, with a diameter of 4 mm and $\Delta V = 7$ kV. Similar phenomena would be observed by fixing the droplet volume and increasing the electric field intensity.

In Figure 3 the value of the dimensionless critical volume normalized to the volume of a sphere with radius R_b (V^*) is represented as a function of the electric Bond number (Bo_{el}). In some conditions, the issue of the formation of a central depression at droplet top was encountered (shown in Figure 2b), whose shape cannot be determined through the digitization of the profile performed by our code due to the camera setup (Garivalis *et al.*, 2023). Due to the central depression, accurate measures of the volume for droplets with an 8 mm diameter of HFE, NOVEC, and FC without numerical simulation is impossible. For these three fluids, only values for a 4 mm diameter are reported. However, for alcohol and water, the critical volume can be estimated even for larger droplets using the measured geometric parameters. In fact, from the videos, for these fluids, the crater does not seem to form. From this graph, it is possible to observe a power-law relationship connecting the two dimensionless groups: the lower the Bo_{els} , the greater the effect of σ compared to the electric field, and the greater the V_{cr} .

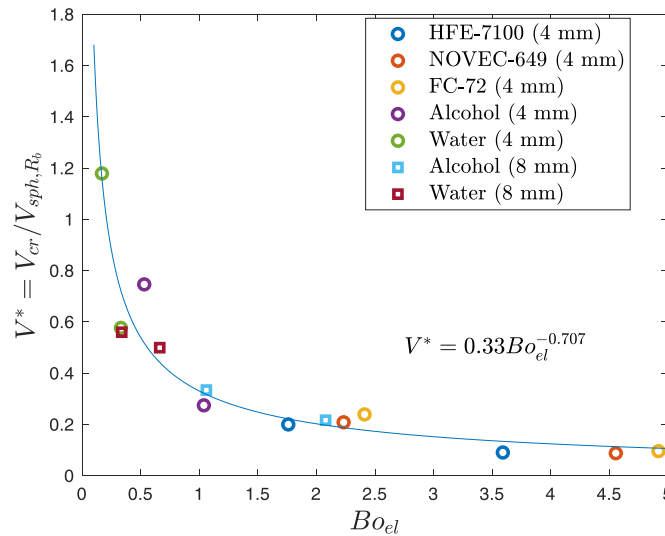


Figure 3. Non-dimensional critical volume V^* vs electric Bond number.

4. CONCLUSIONS

An experimental investigation has been conducted on sessile droplets of different liquids under the action of an external electric field. The interface instabilities, originating a Taylor cone, were quantified and successfully correlated to the electric Bond number. An empirical power law to fit the results was proposed. This correlation is valid since the droplets retain a convex shape. Because of combined action of electric field and gravity, for liquids with high density and low surface tension, a concave depression can be observed in correspondence of the droplet axis.

5. REFERENCES

- Dehaeck, S., Rednikov, A.Y., Machrafi, H., Garivalis, A.I., Di Marco, P., Parimalanathan, S.K., and Colinet, P., 2023. "Active Role of Vapor Clouds around Evaporating Sessile Droplets in Microgravity: Marangoni Jets and Electroconvection". *Langmuir*, 39(27), 9343-9357.
- Garivalis, A.I., Lobianco, S., Rednikov, A., and Di Marco, P., 2023. "Numerical evaluation of large sessile drops interface under gravity and electric fields". In *Proceedings of the 11th International Conference on Multiphase Flow*. Kobe, Japan.
- Gibbons, M.J., Garivalis, A.I., O'Shaughnessy, S., Di Marco, P., and Robinson, A.J., 2021. "Evaporating hydrophilic and superhydrophobic droplets in electric fields". *International Journal of Heat and Mass Transfer*, 164, 120539.
- Haider, A., Haider, S., and Kang, I.K., 2018. "A comprehensive review summarizing the effect of electrospinning parameters and potential applications of nanofibers in biomedical and biotechnology". *Arabian Journal of Chemistry*, 11(8), 1165-1188.
- Taylor, G.I., 1964. "Disintegration of water drops in an electric field". *Proceedings of the Royal Society of London. Series A. Mathematical and Physical Sciences*, 280(1382), 383-397.
- Vancauwenberghe, V., Di Marco, P., and Brutin, D., 2013. "Wetting and evaporation of a sessile drop under an external electrical field: A review". *Colloids and Surfaces A: Physicochemical and Engineering Aspects*, 432, 50-56.

INVESTIGATING CONDENSATION WITH R1233zd(E) IN A MINICHANNEL DURING A PARABOLIC FLIGHT CAMPAIGN

Nicolò Mattiuzzo^a, Arianna Berto^a, Marco Azzolin^{a,*}, Stefano Bortolin, Andrey Glushchuk^c, Patrick Queeckers^c, Pascal Lavieille^b, Marc Miscevic^b

^aUniversity of Padova, Department of Industrial Engineering, Via Venezia 1, 35131 – Padova (Italy)

^bUniversité Paul Sabatier, Laboratoire Plasma et Conversion d’Energie, CNRS, INPT, UPS – Toulouse (France)

^cUniversité Libre de Bruxelles, Center for Research and Engineering in Space Technologies (CREST)

Av. F. Roosevelt 50, CP 165/62, 1050 – Brussels, (Belgium)

*marco.azzolin@unipd.it

Keywords: condensation, microgravity, parabolic flight, R1233zd(E)

1. INTRODUCTION

The complexity of future space missions is expected to increase, as well as the electrical power requirements and the heat to be dissipated by the thermal control systems. Two-phase heat transfer processes have gained a huge interest in thermal management, since they allow to remove high heat fluxes with systems having small volume and weight (Lee et al., 2013). The condenser is a key component in two-phase cooling systems (e.g. mechanically pumped loops). During the condensation phase-change processes, the presence of volume forces such as gravity is expected to modify the distribution of the liquid and gas phases inside the tube and thus to affect the heat transfer. Limited works investigating condensation in micro-gravity conditions are available in the literature (Zhang et al., 2019; Berto et al., 2022). More experimental studies are needed to better understand the occurring physical mechanisms, assess the validity of existing heat transfer models and develop new correlations. In this work, condensation heat transfer measurements are performed inside a 3.38 mm diameter channel with hydrochlorofluoroolefin R1233zd(E) ($GWP_{100\text{-years}} = 1$, nearly zero ODP (IPCC, 2023)). Data are taken during the 84th ESA Parabolic Flight Campaign on board the Novespace Airbus A-310. The experimental heat transfer coefficients and flow pattern visualizations, obtained at saturation temperature of 40 °C and mass flux smaller than 50 kg m⁻² s⁻¹, are here presented and analyzed.

2. EXPERIMENTAL SETUP AND DATA REDUCTION PROCEDURE

In Fig. 1 a schematic of the test rig specifically designed for the parabolic flight campaign is reported. The experimental apparatus allows heat transfer coefficient measurements, evaluation of the liquid film thickness inside a glass tube and simultaneously recording of the flow regimes with a high-speed camera.

The experimental test rig consists of a primary loop filled with R1233zd(E) and three auxiliary water circuits. Considering the refrigerant circuit, the subcooled liquid coming from the post-condenser is moved by a gear pump (Cole-Parmer® EW07003-90 Ismatec® REGLO-ZS) and sent to the turbine volumetric flow meter M4 (NATEC® Sensors GmbH FTO-1). The M4 flow meter operates in the range 13 - 100 mL min⁻¹. After the flow meter, the operative fluid enters a cylindrical stirring evaporator and it exits as saturated vapor. Two electrical heaters (H2 and H3) are installed in the pipeline between the evaporator and the test section to feed the test section with superheated vapor. Then, the fluid R1233zd(E) is condensed in the test section, which is composed of two tube-in-tube heat exchangers connected by a 70 mm borosilicate glass tube. The first heat exchanger is divided into 3 sub-sectors, while the second presents only one sub-sector. The internal tube is made of copper and it has an inner diameter equal to 3.38 mm. The external water annulus is realized by a LEXAN® tube. In each sub-sector, the coolant water flows in counter-flow inside the annulus between the external surface of the copper tube and the LEXAN® tube. The copper tube has been machined on the water side to realize several fins that increase the heat transfer area and allow the insertion of wall thermocouples. Each sub-sector is equipped with 6 wall thermocouples (drilled in the tube wall 0.6 mm far from the internal surface of the copper tube), a thermopile to measure the water temperature difference in each sub-sector and two water thermocouples (inlet and outlet) to double-check the temperature difference on the water side. The first sub-sector is connected to the first water loop, while second and third sub-sectors are connected in series to the second loop. Lastly, the fourth sub-sector is connected to the third water circuit. All the thermocouples and thermopiles used in the test section are T-type (copper-constantan). Two T-type thermocouples are used to measure the temperature of R1233zd(E) at the inlet and outlet of the test section. Furthermore, an absolute pressure transducer (Keller® Series PAA 33X, 0-2.5 bar measuring range) is placed at the inlet of the test section, while a differential pressure transducer (OMEGA® Engineering Inc., 0-150 mbar measuring range) allows to get the outlet pressure. Finally, the refrigerant is subcooled in the post condenser, which is an air-cooled thermoelectric assembly (TEA). The TEA modules are composed by Peltier cells and they are used for both the post condenser and the coolant water line temperature control. The TEA goal is to stabilize the temperature during the different gravity conditions encountered during the parabolic flight. The Peltier cells are cooled by an air fan placed on the hot side. Each water circuit

includes a peristaltic pump (Diaphragm pump Thomas[®] 5002F Twin BLDC), a turbine volumetric flow meter (BIO-TECH[®] FCH-m-PP-LC, operating in the range 0 - 160 mL min⁻¹), T-type thermocouples and a TEA. Peristaltic pumps have been chosen for their small sensitivity to the changing gravity level.

The last part of the setup is the optical system used for flow visualizations and liquid film thickness measurements. The liquid film thickness is obtained by combining different optical methods: the shadowgraph technique, applied to the flow images acquired with the high-speed camera, the chromatic confocal imaging, and interferometry. The glass tube has been machined (for an axial length of 15 mm) on the external side to realize a special shape of the tube consisting of two curved parts (lenses) separated by two flat sides. The curved portions of the glass tube guarantee a magnification of the liquid film thickness observed with the high-speed camera, while the flat parts allow the accurate measurement of the liquid film thickness by means of optical sensors (chromatic confocal sensor and interferometer) without light defocus. The optical setup includes a telecentric backlight illuminator (TECHSPEC[®] telecentric backlight illuminator), three mirrors and the high-speed camera (Digital Camera Optronis[®] CL600x2). More information regarding the systems employed in the experimental campaign are available in Berto et al. (2022).

The quasi-local condensation heat transfer coefficient is calculated in each subsector as follows:

$$HTC_i = \frac{\dot{m}_{w,i} \cdot c_{w,i} \cdot \Delta T_{w,i}}{A \cdot (T_{sat} - T_{wall})_i} \quad (1)$$

where the numerator is the heat flux measured on the water side (mass flow rate of the water $\dot{m}_{w,i}$, specific heat of the water $c_{w,i}$, water temperature difference $\Delta T_{w,i}$ in the i -th sub-sector) and the denominator is the product of the heat transfer area A in and the temperature difference in between the refrigerant T_{sat} and the wall T_{wall} in the i -th sub-sector. The enthalpy at the outlet of each i -th sub-sector $h_{out,i}$ is evaluated from an energy balance considering the heat flow rate exchanged on the water side Q_w , the refrigerant mass flow rate \dot{m}_{ref} and the inlet enthalpy of the condensing fluid (or superheated vapor in the first sub-sector) $h_{in,i}$, which is computed from the measured pressure and temperature using REFPROP 10 (Lemmon et al., 2018). The outlet enthalpy from the i -th sub-sector is considered as the inlet enthalpy of the following sub-sector. The thermodynamic vapor quality $x_{out,i}$ at the outlet of a sub-sector, and thus at the inlet of the following one, can be determined from the outlet enthalpy and the latent heat of vaporization:

$$x_{out,i} = \frac{h_{out,i} - h_L}{h_V - h_L} \quad (2)$$

where h_L and h_V are respectively the liquid and vapor specific enthalpy at the saturation pressure.

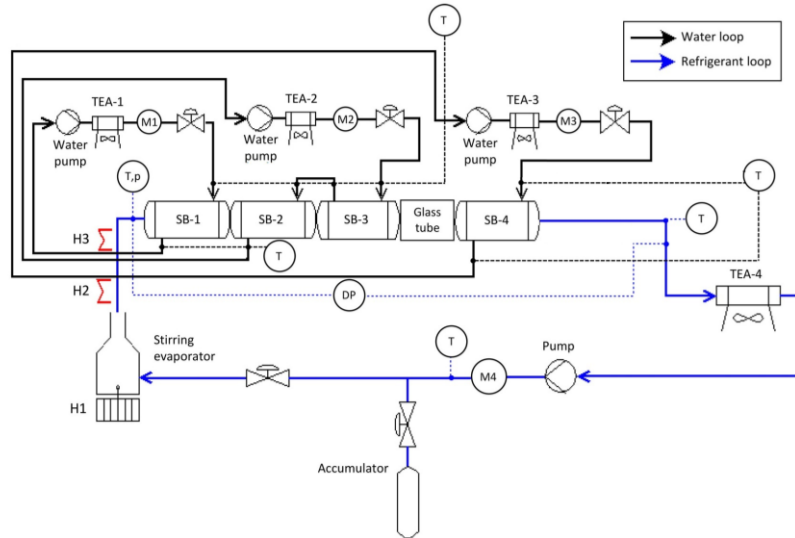


Figure 1. Experimental setup (SB sub-sector; TEA thermoelectric assembly; T temperature sensor; p pressure sensor; DP differential pressure sensor; M flow meter (M4 for refrigerant); H1-3 electric heater).

3. CONDENSATION HEAT TRANSFER COEFFICIENTS AND FLOW VISUALIZATIONS

Fig. 2 presents some of the experimental results obtained during the 70th ESA Parabolic Flight Campaign in terms of heat transfer coefficient measurements and flow pattern visualizations when varying the gravity level. In this case, the refrigerant was HFE-7000. In Fig. 2a), a comparison between the HTC in normal gravity and microgravity conditions is reported as function of the vapor quality and the mass flux. Generally, the HTC in microgravity condition is lower than the heat transfer coefficient measured in horizontal configuration and ground conditions (Berto et al., 2022). The heat

transfer coefficient reduction is more marked when the mass flux is reduced (40% at 30-40 kg m⁻² s⁻¹), while at higher mass fluxes the difference is smaller (12% at 100 kg m⁻² s⁻¹). At low mass flux, the higher the vapor quality, the more the heat transfer coefficient in microgravity is closer to the one measured on ground (at 30 kg m⁻² s⁻¹ and $x = 0.4$ the HTC measured in microgravity conditions is 44% lower compared to the one measured on ground, whereas at $x = 0.7$ a HTC reduction equal to 35% is found).

Fig. 2b) shows a comparison between the flow regime observed in the glass tube with the high-speed camera at $G = 50 \text{ kg m}^{-2} \text{ s}^{-1}$ and $x = 0.28$ respectively under normal gravity (1g), hypergravity (2g) and microgravity conditions (μg). From the visualization the liquid distribution in the tube changes with the gravity condition. In fact, the liquid film is thicker at the bottom of the tube during the hypergravity phase compared to the other conditions. Furthermore, no detectable liquid is present in the upper portion of the tube. During normal gravity conditions, the liquid is mostly present at the bottom of the tube, but a thin film can be seen on the top. Instead, the microgravity condition completely modifies the liquid distribution, with a continuous film of condensate all around the internal circumference of the glass tube.

With the new experimental data with R1233zd(E), we expect to enhance our understanding regarding the heat transfer under reduced gravity conditions, as the properties of the fluid are different from those of HFE-7000. Furthermore, we expect to conduct a more detailed investigation into the phenomenon of condensation at low flow rates, which is also relevant for applications like two-phase pumped loops.

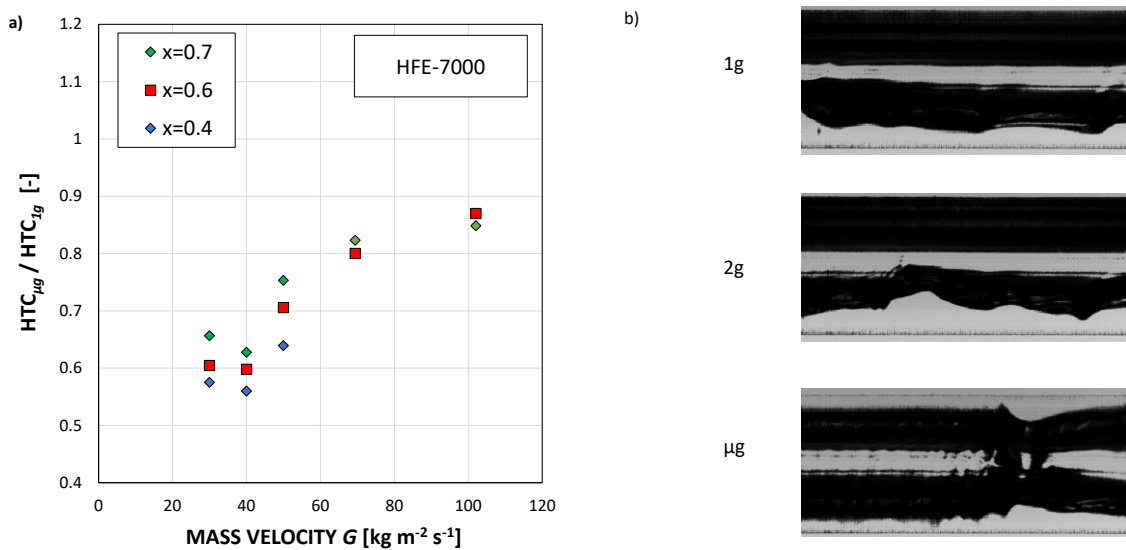


Figure 2. Main results obtained with HFE-7000 during the 70th parabolic flight campaign. a) Comparison between the heat transfer coefficient measured in microgravity condition and during the normal gravity phase; b) Comparison between the flow regimes at $G = 50 \text{ kg m}^{-2} \text{ s}^{-1}$ and $x = 0.28$ at different gravity levels (normal gravity 1g, hypergravity 2g and microgravity condition μg).

4. REFERENCES

- Berto, A., Azzolin, M., Lavieille, P., Glushchuk, A., Queeckers, P., Bortolin, S., Saverio, C., Miscovic, M., Del, D., 2022. Experimental investigation of liquid film thickness and heat transfer during condensation in microgravity. *Int. J. Heat Mass Transf.* 199. <https://doi.org/10.1016/j.ijheatmasstransfer.2022.123467>
- Lee, H., Mudawar, I., Hasan, M.M., 2013. Experimental and theoretical investigation of annular flow condensation in microgravity. *Int. J. Heat Mass Transf.* 61, 293–309. <https://doi.org/10.1016/j.ijheatmasstransfer.2013.02.010>
- Lemmon, E.W., Bell, I.H., Huber, M.L., McLinden, M.O., 2018. NIST Standard Reference Database 23: Reference Fluid Thermodynamic and Transport Properties-REFPROP, Version 10.0, National Institute of Standards and Technology. <https://doi.org/https://doi.org/10.18434/T4/1502528>
- UNEP, 2023. Climate Change 2023: Synthesis Report | UNEP - UN Environment Programme 35–115. <https://doi.org/10.59327/IPCC/AR6-9789291691647>
- Zhang, L., Xu, B., Shi, J., Chen, Z., 2019. Experimental study on condensation heat transfer of FC-72 in a narrow rectangular channel with ellipse-shape pin fins : Ground and microgravity experiments. *Int. J. Heat Mass Transf.* 141, 1272–1287. <https://doi.org/10.1016/j.ijheatmasstransfer.2019.06.055>

HEAT TRANSFER ENHANCEMENT OF IMPINGEMENT COOLING WITH DIFFERENT SHAPED RIBS TARGET SURFACE

Xinlei Li^a, Hui ren Zhu^{a,*}, Cunliang Liu^a, Zhipeng Xu^a, Guodong Li^a

^a School of Power and Energy, Northwestern Polytechnical University, Xi'an, Shaanxi 710072, China

*zhuhr@nwpu.edu.cn

Keywords: Impingement cooling, Shaped ribs, Heat transfer characteristics, Jet-to-crossflow interactions

1. INTRODUCTION

Jet impingement cooling, as a technology that can effectively improve the heat transfer effect, is widely used in the internal cooling structure of aeroengine turbine, which has been researched at home and abroad. It is found that there are many factors affecting the impact heat transfer, including flow factors and geometric factors, such as the Reynolds number(Prevost et al., 2022), crossflow(Leo'n De Paz & Jubran, 2010), impact hole geometry(Rakhsha et al., 2023), impact target surface structure. Arranging perturbation structures on the impact target plate is an important method to enhance heat transfer. The arrangement of spoiler structure on the target plate also has many forms, such as the arrangement of different shapes and sizes of spoiler columns(Ravanji & Zargarabadi, 2020), spoiler ribs, tiny spoiler structures(Vr et al., 2021), pits to increase the roughness of the target surface.

Rao et al(Rao et al., 2016) experimentally and numerically studied jet impingement heat transfer performance on roughened plates with micro-W-shaped ribs (1mm in height and 1mm in width). According to their results, the micro-W-shaped ribs efficiently increased turbulent mixing in the near-wall region, significantly improving heat transfer performance without introducing additional pressure losses. He et al(He et al., 2022). proposed a corrugated target wall and numerically investigated the effect of corrugation depth on jet impingement heat transfer. They observed that the fluctuation of surface made the deflected jets impinge orthogonally on the target wall, ameliorating the adverse effects of crossflow. In addition, with the increase of corrugation depth, the overall thermal performance is increased and reached its peak at a depth of 0.8 times the jet hole diameter.

In this study, for the internal cooling structure in the region of the suction surface of the turbine blade, different shapes of raised structures are arranged on the target plate of the impact structure in order to enhance the intensity of impact heat transfer in this region. The effect and Mechanism of various parameters on the aerodynamic characteristics as well as the heat transfer characteristics, including the shape of rib, the jet Reynolds number and the constant flow ratio, have been investigated in this paper.

2. EXPERIMENTAL METHODS AND PARTIAL RESULTS

In this paper, the geometrical models of single-row impact structure is meshed respectively, as shown in Fig. 1. For the single-row structure, non-structural meshing is used for the impact hole channel and the impact target plate channel, with the aim of improving the meshing efficiency of different structures when studying the target surface with shaped ribs. The surface meshes of the impact hole surface, impact target surface and disturbance structure are encrypted, and the boundary layer division is carried out on the target and rib surfaces of special interest, with a boundary layer number of 15. Due to the SST turbulence model selected for the computational simulation in this paper, it is necessary to appropriately set up the boundary layer parameters so that the Y_{plus} value of the wall is around 1. For the geometric model of the multi-row structure, the mesh delineation is similar to that of the single-row structure, but in order to reduce the number of meshes in the impact channel, which is a large and simple structural region, local mesh encryption is carried out in the region near the target surface using BOI.

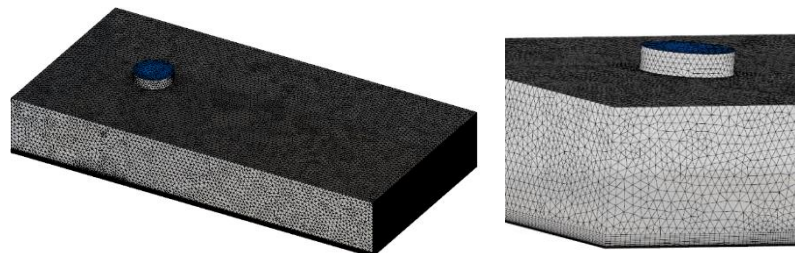


Figure 1. The mesh of single-row impact structure.

In order to determine the prediction accuracy of the numerical calculation method for the current model, a validation experiment based on the baseline structural dimensional parameters is carried out in the range of $Re=12000-24000$. The

test system for the jet impingement structural experiment in this paper is shown in Fig. 2. The test system mainly consists of an air intake system, a flow regulation system, an air intake section, an experimental section, and a data acquisition system. The impact target plate in the experiment is made of purple copper material, which is installed on the fixed plate through the prominent ear-shaped fixed thread. On the back of the target plate, a heat film is arranged to provide a stable heat source for the copper block, and the power supply of the heat film is provided by an adjustable DC regulated power supply, which can be used to change the output thermal power by adjusting the voltage at both ends of the heat film, which is calculated according to the measured values of the ammeter and voltmeter. Insulation cotton is pasted on the back of the fixed plate to minimize heat loss. In the air inlet cavity and near the impact plate upstream of the airflow channel arranged in the total pressure probe to measure the airflow pressure. Five temperature measurement points are set up on the impact target plate to measure the surface temperature, and the data are transmitted to the computer by the temperature acquisition module.

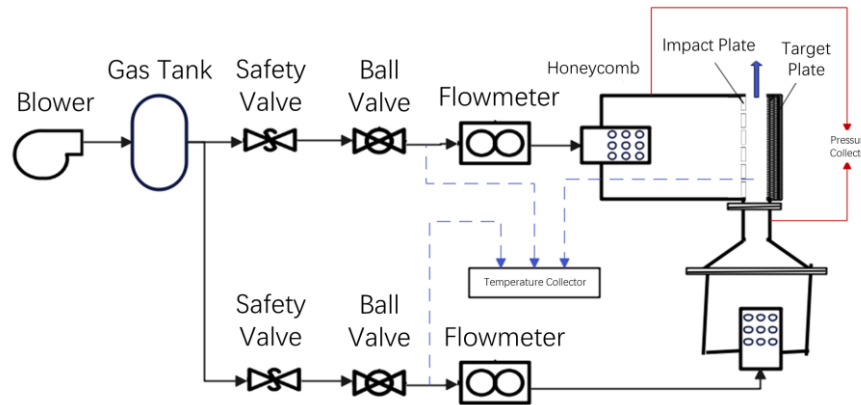


Figure 2. Experimental system.

3. CONCLUSIONS

Figure 3 shows the Nu number distribution of different target surface structures, local Nu number changes mainly occur in the rib and its nearby region. The rib is facing the centre of the impact hole, which is equivalent to the reduction of the impact distance, the heat transfer coefficient of its stagnation region is higher than that of the plane target plate. Meanwhile the second peak disappears completely and the surface heat transfer coefficient reaches its highest value near the stationary point.

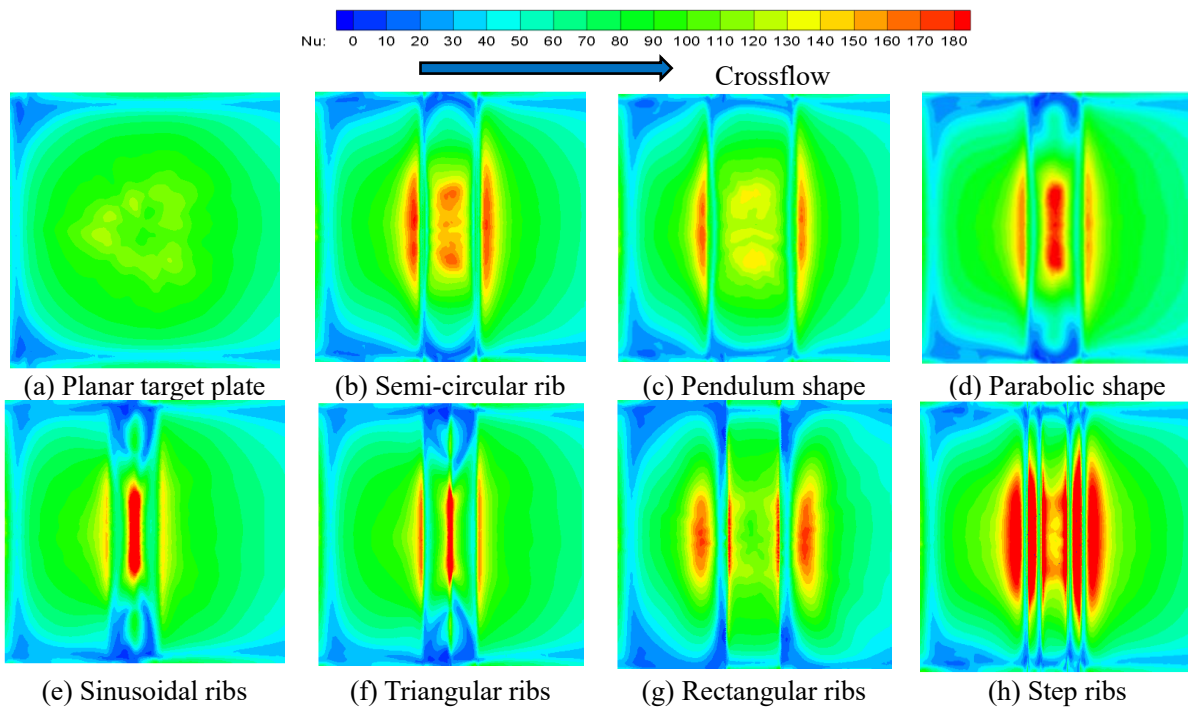


Figure 3. Nu number distribution of different target plates

Figure 4 shows the Nu number distribution for different target plates at Reynolds number of 20000. For the ribbed target plates with pendulum, semicircular, parabolic, sinusoidal, and triangular ribs, the Nu number distribution patterns in the impact region are similar, and there are three maxima in all of them. For the Nu maxima near the stationary point, this is caused by the direct impact of the jet on the target surface of the perturbation structure. The pendulum rib has the smallest Nu maxima, but has the smoothest Nu change in the stationing area; the triangular rib has the largest Nu peak, but has the most drastic change in value.

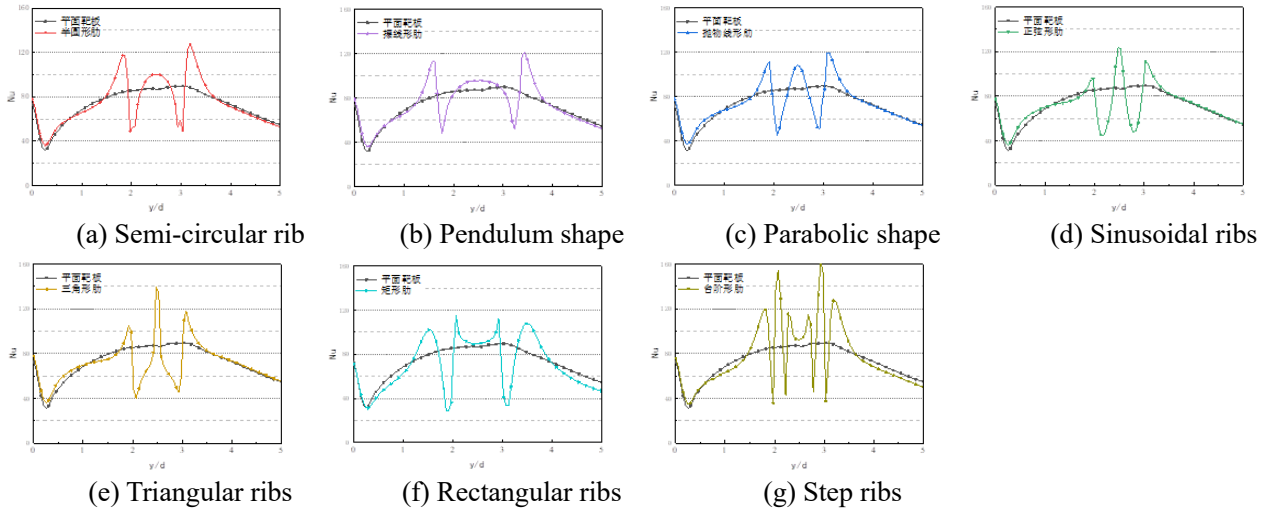


Figure 4. Spread-mean distribution of Nu numbers for different target plates.

Setting up the shaped spoiler structure directly under the impact hole can significantly improve the heat exchange effect of the target surface, while the flow loss brought by the spoiler structure is very small.

By studying the flow heat transfer characteristics of different shaped spoiler structures for jet impingement, it is found that reasonable flow separation and secondary impingement can enhance the ability of enhanced heat transfer. Based on this, this paper proposes a step-shaped perturbation structure, which brings significantly greater heat transfer gain than other shaped perturbation structure, compared with the plane target plate, the overall heat transfer increased by about 23.7%, followed by semi-circular, so that the heat transfer is increased by 13.8%; rectangular ribs have the weakest heat transfer enhancement effect.

4. REFERENCES

- He, J., Deng, Q., & Feng, Z. 2022. "Heat transfer enhancement of impingement cooling with corrugated target surface" . *International Journal of Thermal Sciences*, 171, 107251-.
- Leo'n De Paz, M., & Jubran, B. A. 2010. "A Numerical Study of an Impingement Array Inside a Three Dimensional Turbine Vane." ASME Turbo Expo 2010: Power for Land, Sea, and Air,
- Prevost, T., Battaglioli, S., Jenkins, R., & Robinson, A. J. 2022. "Enhancing Jet Array Heat Transfer: Review of Geometric Features of Nozzle and Target Plates" . *International Journal of Thermofluids*, 16, 100203.
- Rakhsha, S., Rajabi Zargarabadi, M., & Saedodin, S. 2023. "The effect of nozzle geometry on the flow and heat transfer of pulsed impinging jet on the concave surface" . *International Journal of Thermal Sciences*, 184, 107925.
- Rao, Y., Chen, P., & Wan, C. 2016. "Experimental and numerical investigation of impingement heat transfer on the surface with micro W-shaped ribs" . *International Journal of Heat and Mass Transfer*, 93, 683-694.
- Ravanji, A., & Zargarabadi, M. R. 2020. "Effects of pin-fin shape on cooling performance of a circular jet impinging on a flat surface" . *International Journal of Thermal Sciences*, 161.
- Vr, A., Yh, A., Sr, A., Cong, H., Nf, A., Cla, B., Ks, B., Sns, A., & Bgs, A. 2021. "Multi-objective optimization of a chip-attached micro pin fin liquid cooling system" . *Applied Thermal Engineering*.

Visualization Measurement of Mixing Process of Viscous Liquid Contained in a Rotating Cylindrical Vessel

Tomoya Taguchi^{a,*}, Tetsuro Yanaseko^a, Masaki Hiratsuka^a, Koji Hasegawa^a

^aDepartment of Mechanical Engineering, Kogakuin University, Tokyo 163-8677, Japan

*am23041@g.kogakuin.jp

Keywords: multiphase flow, self-healing structural ceramics, mixing, visualization

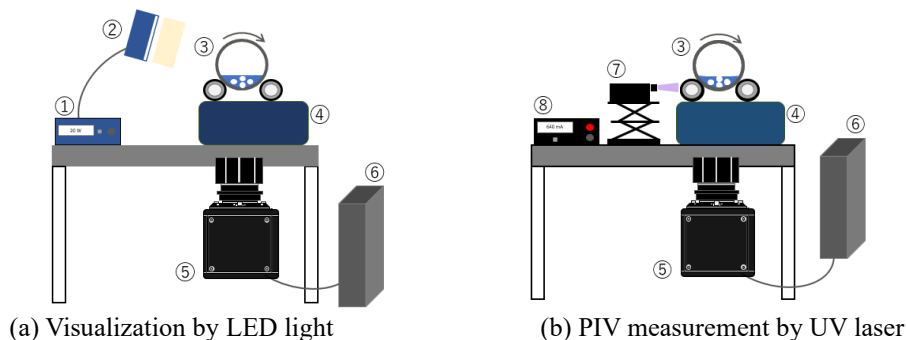
1. INTRODUCTION

The aircraft industry is tasked with reducing carbon dioxide emissions associated with flight, which requires the development of lighter and more efficient engines. One option for weight reduction is the use of turbine blades, which are a crucial component of jet engines. Currently, nickel superalloy, a metallic material with high heat resistance, is commonly used. Ceramics are gaining attention as alternatives to metallic materials due to their lightweight, heat-resistant properties, and high energy conversion efficiency. However, their brittleness has prevented practical use. Self-healing ceramics that repair cracks are now being explored. However, the manufacturing of these products is largely dependent on the knowledge of engineers. Therefore, a better understanding of the mixing processes involved in their production is necessary. The purpose of this study is to investigate the mixing phenomena associated with the interaction between a viscous fluid and solid spheres enclosed in a rotating cylindrical vessel from a hydrodynamic perspective. This paper examines the impact of the number of solid spheres and the height of the liquid surface on solid-liquid mixing in a vessel.

2. EXPERIMENTAL METHOD

Figure 1(a) depicts the experimental apparatus used to visually observe the mixing process of viscous fluid and solid spheres sealed inside a rotating cylindrical vessel. The vessel had the same size (inner diameter 113 mm) as the ball mill used for mixing the ceramic powder and solvent when preparing self-healing ceramics. Acrylic cylinder was used as the material to visualize the inside of the vessel. The experiment used glycerin, with a density of 1260 kg/m³ and the same viscosity as the slurry used for ceramics preparation, as the simulated fluid in the vessel. Solid spheres of alumina, with a diameter of 15 mm and a density of 3800 kg/m³, were used as well. The cylindrical vessel was rotated using a rotating ball mill table. The number of balls (15, 30, and 45) and the glycerin level height (20, 50, and 75 mm) were varied for systematic experiment in the present study. Images of the inside the rotating acrylic pods were captured using a high-speed camera with LED backlighting.

The experimental setup used for PIV measurements is shown in Fig. 1(b). To visualize the flow fields in the vessel, a sheet UV laser was irradiated at 1.40 A and acrylic particles of a UV-excited phosphor luminescent particle of 10 μm in diameter were added to glycerin for PIV measurements. The obtained images were processed using commercial software (Flownizer) for PIV analysis.



1	Light power supply	5	High-speed camera
2	LED light	6	Computer
3	Cylindrical vessel	7	UV laser
4	Rotating ball mill table	8	Laser power supply

Fig. 1 Schematic of the experimental setup.

3. RESULTS AND DISCUSSIONS

Figure 2 displays the impact of the number of balls on solid-liquid mixing in the vessel. The number of balls was varied between 15, 30, and 45 at a liquid level of $h = 50$ mm and a vessel rotation speed of $n = 70$ rpm. As the number of balls increased, they moved from their initial position at the bottom of the vessel to the sides and then to the top, confirming the frequent dropping of the balls from the top of the vessel. According to the text, as the balls move to the top of the vessel, their kinetic energy increases due to the impact on the liquid surface, which is expected to enhance solid-liquid mixing.

Figure 3 provides an example of the effect of the initial glycerin level on the solid-liquid mixing process in a vessel. The experiment was conducted with 30 balls, a rotational speed of 70 rpm, and varying liquid surface heights of $h = 20, 50,$ and 75 mm. The number of balls falling from the top of the container decreased as the liquid surface height increased. This may be due to the balls remaining in the liquid as the liquid surface height increased. These results suggest that increasing the liquid surface height has a limited effect on promoting solid-liquid mixing in the container.

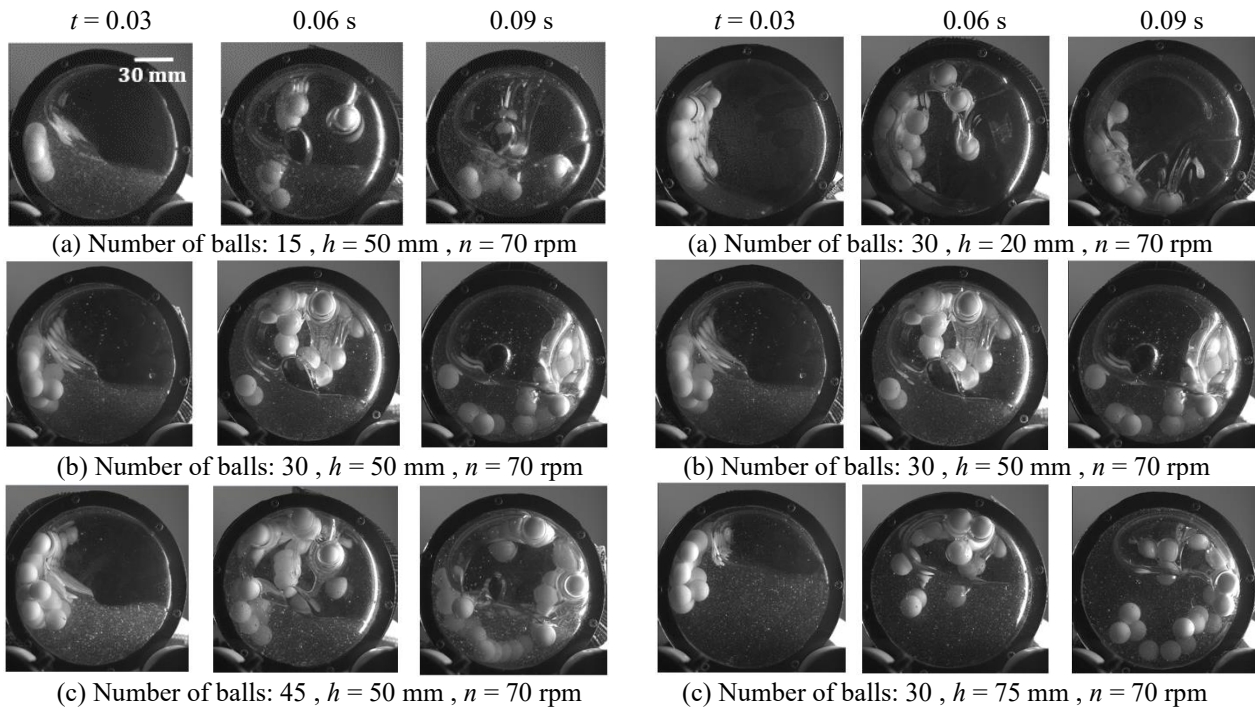


Fig. 2 Effect of the number of balls.

Fig. 3 Effect of liquid level.

PIV analysis was used to measure the flow field of a viscous fluid enclosed in a vessel, including the interaction with solid spheres. However, the presence of multiple solid spheres complicates the flow field and makes quantitative evaluation difficult. In this study, we analyzed the flow field in a rotating cylindrical vessel without solid spheres, as well as the flow field when a single solid sphere impinged on a stationary viscous fluid.

Figure 4 displays the results of PIV measurements when the solid spheres were not enclosed. The liquid-level height was set to $h = 15$ mm, which refers to the conditions described in the previous section and is expected to promote mixing. The vessel rotation speed was set at 70 rpm.

Figure 4(a) displays the average velocity vector field, while Figure 4(b) shows the velocity variation over time measured every 2-10 mm from the wall surface in the h -direction, as indicated by the white arrow in Figure 4(a). The solid purple line represents the rotational velocity of the vessel, and the solid gray line represents the average velocity of each vector. These results confirm an increase in flow velocity near the vessel wall as the vessel rotates. The velocity of the fluid inside the container was deemed to have decreased due to the shear stress.

Figure 5 represents the PIV measurement results obtained when a solid sphere penetrated a stationary viscous pool. The liquid surface was set at a height of 30 mm, and the solid sphere was dropped from three different heights (40, 80, and 110 mm). The maximum height of the solid sphere was limited to 110 mm due to the inner diameter of the above-mentioned cylindrical vessel is 113 mm. The results showed that the velocity vector near the solid sphere boundary surface increased as the initial position of the sphere increased, and the area of the flow field showing changes expanded. It is assumed that the penetration velocity of the solid sphere into the viscous fluid increases as its initial position increases, resulting in a more complex flow field of the viscous fluid.

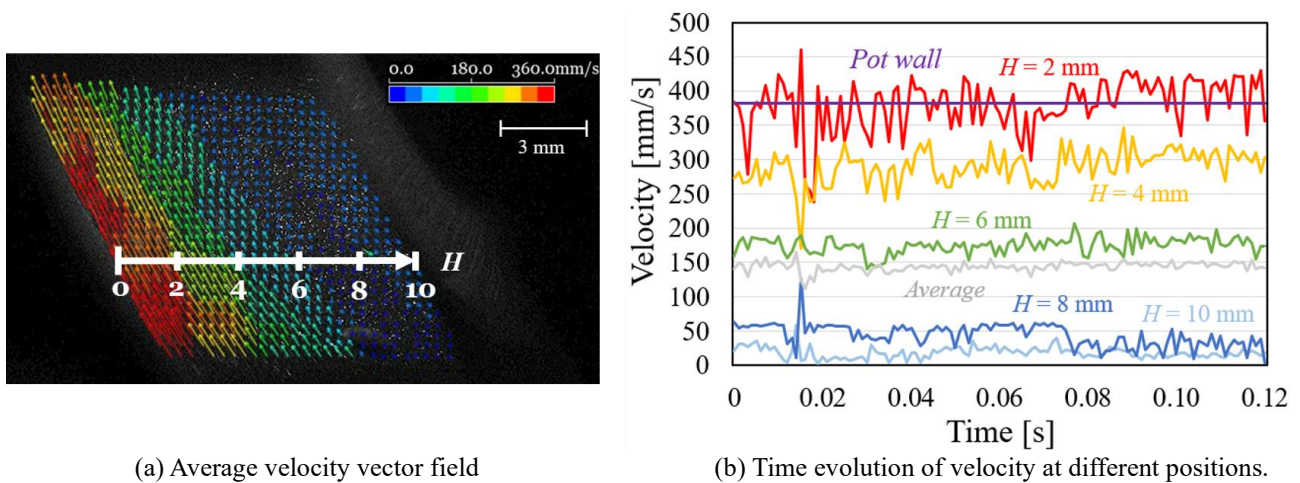


Fig. 4 PIV measurement results without balls in the cylindrical container.

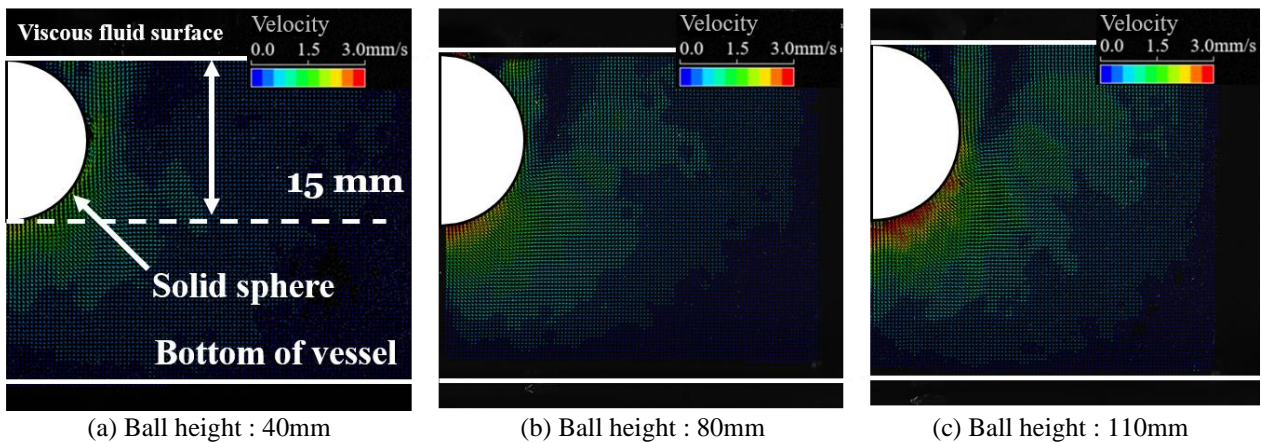


Fig.5 PIV measurement for a penetrating single solid sphere into stationary viscous pool.

4. CONCLUSIONS

This study presents an experimental investigation of the interaction between a viscous fluid and solid spheres enclosed in a rotating cylindrical vessel. The effects of mixing conditions, such as the number of solid spheres and liquid level height of the solvent, on the flow field were visualized. As the quantity of balls increased, so did the number of balls falling from the top of the vessel, indicating the possibility of improved mixing. However, as the height of the liquid surface increased, the number of balls falling from the top of the vessel decreased, suggesting that their contribution to mixing was limited. PIV measurements were used to visualize the flow field of a viscous fluid enclosed in a vessel. Under the condition of a no-ball, the flow velocity reaches a maximum near the vessel wall due to the velocity of the rotating vessel wall. The fluctuation range of the flow field varies depending on the initial position of the ball. A higher initial position of the falling ball enhance the mixing of the flow fields of the viscous fluid.

5. REFERENCES

- Ichikawa, Y., Kobayashi, H., Takehara, I. and Tatsumi, T.,1999. "Development Summary of the 300 kW Ceramic Gas Turbine CGT302." *Turbo Expo: Power for Land, Sea, and Air*. American Society of Mechanical Engineers. Vol. 78583, 99-GT-105, V001T04A002.
- Ando, K., Osada, T., Takahashi, K. and Wataru, N., 2014. "Self-crack-healing behavior in ceramic matrix composites." *Advances in Ceramic Matrix Composites*, Woodhead Publishing, pp. 515-544.

EXPERIMENTAL INVESTIGATION ON THE INFLUENCE OF THE FLOW REGIME ON FLOW BOILING HEAT TRANSFER UNDER TEMPORALLY VARYING HEAT LOADS

Jana Rogiers^{a*}, Jari Raeymackers^a, Jera Van Nieuwenhuysen^a, Hendrik Vansompel^{a,b}, Michel De Paepe^{a,b}

^aGhent University, Sint-Pietersnieuwstraat 41, 9000 Gent, Belgium

^bFlandersMake@UGent Core Lab MIRO, Leuven, Belgium

*Jana.Rogiers@UGent.be

Keywords: flow boiling, heat transfer, time-varying, two-phase

1. INTRODUCTION

Flow boiling heat transfer is a promising technique to improve the heat transfer in numerous applications, but questions remain about the physical phenomena taking place. Compared to liquid flow convective heat transfer, flow boiling offers a higher heat transfer rate at a lower temperature difference between the surface and the working fluid. Another important benefit is that a highly uniform surface temperature can be obtained. Those advantages make flow boiling very interesting for cooling of electronics, nuclear reactors, chemical plants, and for heat exchange in power plants, air conditioning systems, concentrated solar power systems, etc. There are, however, also disadvantages related to flow boiling heat transfer. Three of the most important ones are dry-out after the critical heat flux is exceeded, the occurrence of different types of flow instabilities, and the insufficient knowledge about the occurring physical phenomena during flow boiling.

Past research has mainly focused on flow boiling in tubes with a constant and uniform heat flux boundary condition. Many of the possible applications, however, feature a non-constant and/or non-uniform heat flux. Some examples are the time-varying heat flux due to the sun in concentrated solar power plants, start-up and acceleration of electric cars causing a non-constant power dissipated in the power electronics, ... Only very limited research has been performed on the effect of temporal variations in heat flux on flow boiling heat transfer. The relevant works can be divided into two categories: microscale and macroscale flow boiling. The threshold between both is debatable and ambiguous. Thome *et al.* (2017) suggested using the Bond number (Bo) to find a threshold value. A high Bond number corresponds to a flow which is largely influenced by gravitational forces and little by surface tension forces. Thome *et al.* mention that in literature values of $Bo = 2 - 4$ are commonly suggested threshold values. This paper will focus on macroscale flow boiling. In some works, macroscale flow boiling under non-constant heat flux conditions has been considered (Wang *et al.* (2012), Chen *et al.* (2017, 2021), Li *et al.* (2022), Rogiers *et al.* (2023)). The few researchers that performed tests on macroscale flow boiling agreed that if the oscillation periods of the periodically varying heat flux signal are long enough, periodic oscillations in bubble parameters (departure diameter, departure frequency and number of active nucleation sites) and heat transfer parameters (heated wall temperature and heat transfer coefficient) are induced with the same oscillation frequency as the heat flux signal. A higher amplitude, longer period and higher average value of the heat flux signal cause larger oscillation amplitudes in the resulting bubble and heat transfer parameters. Furthermore, the heated wall temperature oscillation follows the heat flux signal with a time lag due to the heat capacity of the tube and/or heater. The available measurement data is, however, very limited and the system response of different experimental campaigns is difficult to compare due to different tube geometries and heat flux waveforms used. Furthermore, most studies consider a saturated or subcooled inlet condition. This, however, means that the effect of the flow regime on the response has not yet been validated. Therefore, in this paper, the influence of the flow regime on the heat transfer characteristics response to a periodically varying heat flux is experimentally evaluated.

2. EXPERIMENTAL FACILITY

In order to experimentally evaluate the effect of the flow regime on flow boiling heat transfer under temporally varying heat flux conditions, an experimental facility was developed and built. Fig. 1 shows the piping and instrumentation diagram (P&ID) of the setup, consisting of a working fluid (refrigerant) loop and a water-glycol cooling loop. The refrigerant is in subcooled liquid state at the inlet of the pump, after which the mass flow rate is measured by a Coriolis flow meter. The state can thereafter be determined by a pressure and temperature measurement. Then follows an electrical preheater which adds heat such that the wanted vapor quality at the inlet of the test section is reached. Between the preheater and the test section, a pressure relief valve, flow visualization section with high speed camera, and pressure and temperature measurement are installed. The test section, of which a schematic is given in Fig. 2, is a stainless steel horizontal tube with a 7.75 mm internal diameter, which is heated by Joule heating of the tube itself. This means that a voltage is put over the test section, causing a current flow through the test section and because of the electrical resistance of the tube, a certain power is generated. After the test section, again a pressure and temperature measurement and flow

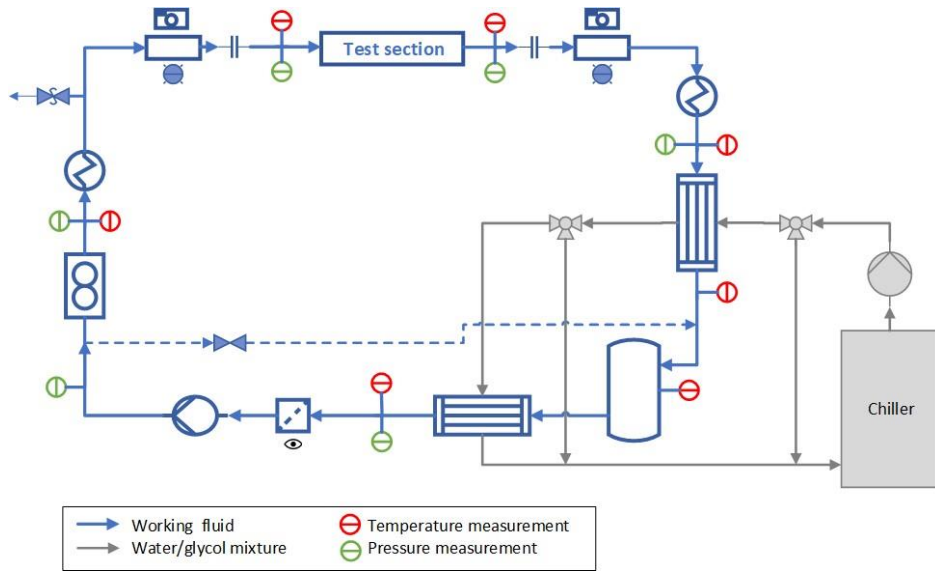


Figure 1: P&ID of experimental facility

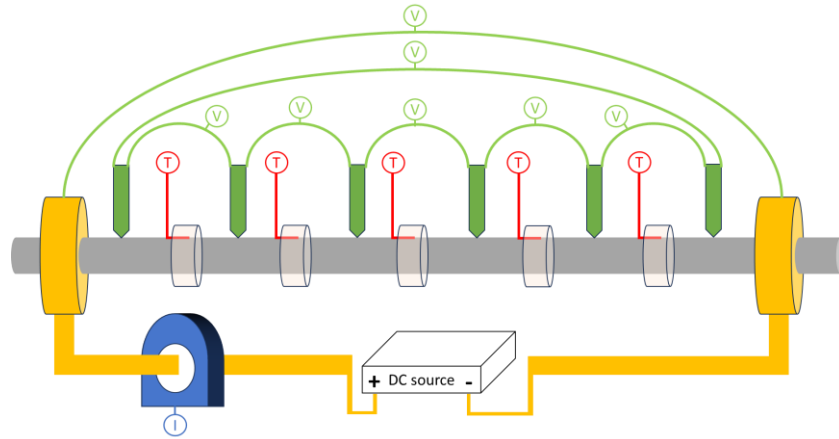


Figure 2: Schematic of test section

visualization section follow. The electrical post-heater evaporates and then superheats the flow, such that afterwards, the vapor state can be determined by the pressure and temperature sensors. The flow is then cooled down in the condenser and ends up in a liquid receiver, where both liquid and vapor are present (in equilibrium). The pressure in the system is controlled by a trace heater around this liquid receiver. Finally, the flow is subcooled and filtered to ultimately return to the pump and as such close the loop.

Figure 2 shows a schematic of the test section with the relevant measurement equipment indicated. The current through the test section is delivered by an EA-PSI 9080-340 DC source and measured by a DS400UB current sensor. Along the test section, five T-type thermocouples measure the outer wall temperature of the stainless steel tube. Furthermore, seven voltage drop measurements take place which are also used to determine the tube temperature.

3. DATA ANALYSIS

The heat transfer coefficient (htc) from the tube to the refrigerant is defined as:

$$htc = \frac{q}{T_i - T_{sat}} \quad (1)$$

Therefore, the heat flux (q), inner wall temperature (T_i) and (local) refrigerant saturation temperature (T_{sat}) should be known. The heat flux can be deduced from the voltage (V) – and current (I) measurements as:

$$q = \frac{V \cdot I}{A} \quad (2)$$

with A the inner tube wall area corresponding to the distance between the two ends of the voltage measurement. The saturation temperature is assumed to increase linearly throughout the test section and is measured before and after the test section. The inner wall temperature can be determined based on either thermocouple or voltage drop measurements. The relevant one dimensional conduction equation to calculate the inner wall temperature then becomes:

$$\frac{1}{r} \cdot \frac{d}{dr} \left(k_{ss}(T) \cdot r \frac{dT}{dr} \right) + \dot{q}_v = 0 \quad (3)$$

with r the radius, k_{ss} the temperature-dependent thermal conductivity of the stainless steel test section, and \dot{q}_v the volumetric heat generation within the tube. For both cases, the outer wall of the test section is insulated and it is thus assumed there are no heat losses to the environment, which is the first boundary condition used to solve the differential equation. The second boundary condition then depends on whether the thermocouple – or voltage measurement is used. With the thermocouple measurement (T_{meas}), the boundary condition simply states the temperature on the outer diameter of the tube should equal T_{meas} . When using the voltage measurement on the other hand, an area-averaged temperature can be determined from the resistance of the tube, which varies linearly with temperature.

$$R(T) = R_0 \cdot (1 + \alpha \cdot (T - T_0)) \quad (4)$$

Here, T_0 is the reference temperature, R_0 the electrical resistance corresponding to that temperature, and α the temperature coefficient. The (local) resistance can be calculated from the voltage – and current measurements. Using Equation (4) the local area-averaged tube wall temperature can then be obtained. The radius to which this local tube wall temperature corresponds depends on the tube geometry and is in this case 4,260 mm.

4. RESULTS AND DISCUSSION

The refrigerant used during the tests described in this work is R1233zd(E), which has a near zero ozone depletion potential and a global warming potential as low as 1. Furthermore, it has a boiling point at 18.32°C at atmospheric pressure. Validation of the correct functioning of the test section happened through single-phase (liquid) convective flow heat transfer measurements, which were compared to the Dittus-Boelter correlation. Furthermore, the energy balance over the test section and from before the preheater until after the post-heater were checked to estimate the heat losses and evaluate whether or not these should be taken into account. Next to the single-phase validation tests, validation of the two-phase heat transfer under constant heating conditions were performed and compared to the correlations of Kattan-Thome-Favrat (1998), Gungor-Winterton (1986) and Jung *et al.* (1989).

For the experiments on flow boiling heat transfer under time-varying heat loads, three flow regimes were considered: slug flow, intermittent flow and annular flow. The considered saturation temperatures are in the range of 65 – 85°C and mass fluxes are within 200 – 800 kg/m²s.

Note to reviewers: *The tests will be performed in the coming weeks, which leaves enough time to finish the final manuscript by the deadline of 1st of July 2024.*

5. CONCLUSIONS

Flow boiling is a very interesting technique for applications where efficient heat transfer is needed. Past studies mainly focused on constant and uniform heat flux boundary conditions, which is not an accurate representation of many real-life applications. Therefore, an experimental setup was designed and built, which allows evaluating the influence of time-varying heat fluxes on the heat transfer coefficient and inner wall temperature during flow boiling of a refrigerant. The inlet conditions at the test section are chosen in three different flow regimes (annular, intermittent and slug flow), such that it can be verified whether the flow regime affects the response to a time-varying heat flux boundary condition.

6. REFERENCES

- Thome, J.R., Cioncolini, A., 2017. “Chapter Four – Flow Boiling in Microchannels”. *Advances in Heat Transfer*, Vol. 49, pp.157-224
- Wang, S.L., Chen, C.A., Lin, Y.L., Lin, T.F., 2012, “Transient oscillatory saturated flow boiling heat transfer and associated bubble characteristics of FC-72 over a small heated plate due to heat flux oscillations”. *International Journal of Heat and Mass Transfer*, Vol. 55, pp.864-873
- Chen, C.A., Lin, T.F., Yan, W.M., 2017. “Time periodic saturated flow boiling heat transfer of R-134a in a narrow annular duct due to heat flux oscillation”. *International Journal of Heat and Mass Transfer*, Vol. 106, pp.35-46
- Chen, C.A., Lin, T.F., Yang, T.F., Li, W.K., Yan, W.M., 2021. “Experimental study on influence of oscillatory heat flux on heat transfer of R-134a time-periodic subcooled flow boiling in annular duct”. *International Journal of Heat and Mass Transfer*, Vol. 167
- Li, W.K., Hsu, S.H., Lin, T.F., Chen, C.A., Yan, W.M., 2022. “Assessment on R-410A saturated flow boiling heat transfer subject to periodic oscillating heat flux inside an annular duct”. *International Journal of Thermal Sciences*, Vol. 179
- Rogiers, J., Martin, A.T., Dirker, J., De Paepe, M., 2023. “Experimental study on saturated flow boiling in a horizontal cylinder under temporally varying heat loads”. *International Heat Transfer Conference Digital Library*
- Kattan, N., Thome, J.R., Favrat, D., 1998. “Flow boiling in horizontal tubes: part 3—development of a new heat transfer model based on flow pattern”. *Journal of Heat Transfer*, Vol. 120, pp.156-165
- Gungor, K.E., Winterton, R.H.S, “A general correlation for flow boiling in tubes and annuli”. *International Journal of Heat and Mass Transfer*, Vol. 29, pp. 351-358
- Jung, D.S., McLinden, M., Radermacher, R., Didion, D., 1989. “A study of flow boiling heat transfer with refrigerant mixtures”. *International Journal of Heat and Mass Transfer*, Vol. 32, pp. 1751-1764

THERMAL FIELD IN MONTI SABATINI VOLCANIC LITHOSTRATIGRAPHIC SUCCESSIONS

Colacino L.^{a,*}, Violante A. C.^b, Trinchieri R.^b, Habib E.^a

^aDipartimento di Ingegneria Astronautica, Elettrica ed Energetica, Sapienza Università di Roma, via Eudossiana 18

^bENEA Centro ricerche Casaccia, via Anguillarese 301, Anguillara Sabazia (RM)

* leonardo.colacino@uniroma1.it

Keywords: heat conduction, shallow geothermal, geothermal gradient, volcanic lithostratigraphic successions, optical fiber

1. INTRODUCTION

A detailed knowledge of the backdrop geothermal heat flux is relevant for modelling the performance of borehole heat exchangers (BHE). The measurement and assessment of heat flux in volcanic and geothermal areas are reported in the review paper from Wang and Pang (2023) that illustrates the current state of the art of the methods used to target the geothermal resources. The estimation of the ground thermal field has been object of few site-specific studies, due to the strong dependency between thermal and the ground properties. Deep thermal field data has been used by Fuchs *et al.* (2020) to define a 3D numerical crustal temperature model by inverse optimization methodology for the conductive thermal field of the Danish onshore subsurface. Also, Cherubini *et al.* (2013) previously investigated the deep thermal profile of a basin in a North German site. Toth *et al.* (2020) highlighted the effects of anisotropy and asymmetry of basin groundwater flows has a critical role in discharge and accumulation patterns when using the ground as an inertial tank.

The heat transfer affecting the volcanic lithostratigraphic succession under analysis is attributed to three primary phenomena: advection from the external environment, lateral advection contingent upon the presence of aquifers, which may result in heat supply or discharge, and conduction from the underlying strata due to the deep geothermal heat flux. In this paper the heat conduction in the substrates is investigated through the measurements of the temperature in five wells. The survey relates to volcanic substrates, as a prior investigation (Violante *et al.*, 2021) documented the presence of the Sabatini volcanic succession in the ground domain utilized for the boreholes field.

2. METHOD

At the ENEA-Casaccia Research Centre, north of Rome (Italy), a pilot plant using low-enthalpy geothermal energy was installed in 2021. Ground temperatures are measured in 5 wells by using an optic fibers system as shown in Fig. 1.

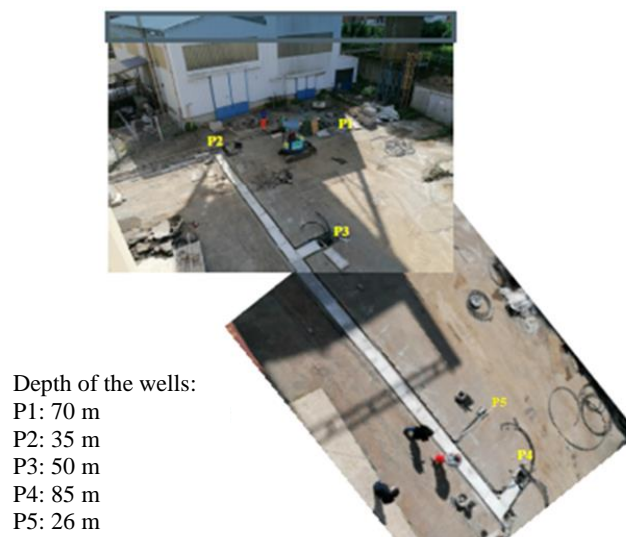


Figure 1: View from above of the borehole field including the depth of wells.

The installed optical fiber is a DiTeSt (Distribuite Temperature Sensing – DTS) cable, manufactured by Smartec SA (Switzerland). This cable has a polyamide (Nylon) outer sheath and a steel core. The core tube is hermetically sealed and contains four optical fibers that can be used for measurements, each measuring 9 μm. They are insensitive to bending, with a double-layer acrylate coating to improve micro-curving performance. The cable offers high resistance to tensile strength, crushing, lateral waterproofing, chemicals, and abrasion. The operating temperature range is 233.15 °K to 358.15 °K. The DTS system, which acquires by Raman effect, detects temperature values in a distributed manner over the entire length of the fiber, with a set spatial resolution of 2 m and a thermal resolution of 0.1 °K.

In particular, the current analysis focuses on the evolution of the deep thermal field during the period immediately succeeding the installation when the borehole field is still inoperative, starting from two weeks after the end of the Ground Response Test (GRT), whose activity was used also to measure the thermal properties of the ground along each probe. The thermophysical properties: thermal conductivity, thermal resistance and the undisturbed temperature of the ground have been firstly extrapolated experimentally by the thermal profiles of the probes obtained after the GRT test.

Afterwards, these data were corrected according to the measures on rock samples taken from the ground simultaneously with the installation of piezometers near the existing BHEs field. This allowed for the creation of a detailed lithostratigraphic sequence, enabling the determination of the thickness of each lithotype, the changes, and heteropies of facies in each layer.

3. RESULT AND DISCUSSION

Seasonal fluctuations have an impact on the first layers, with the amplitude of the thermal solicitation which gradually decreases with depth., while the presence of basement heat fluxes suggests the presence upwellings of hydrothermal fluids from the bottom, as shown in Fig. 2.

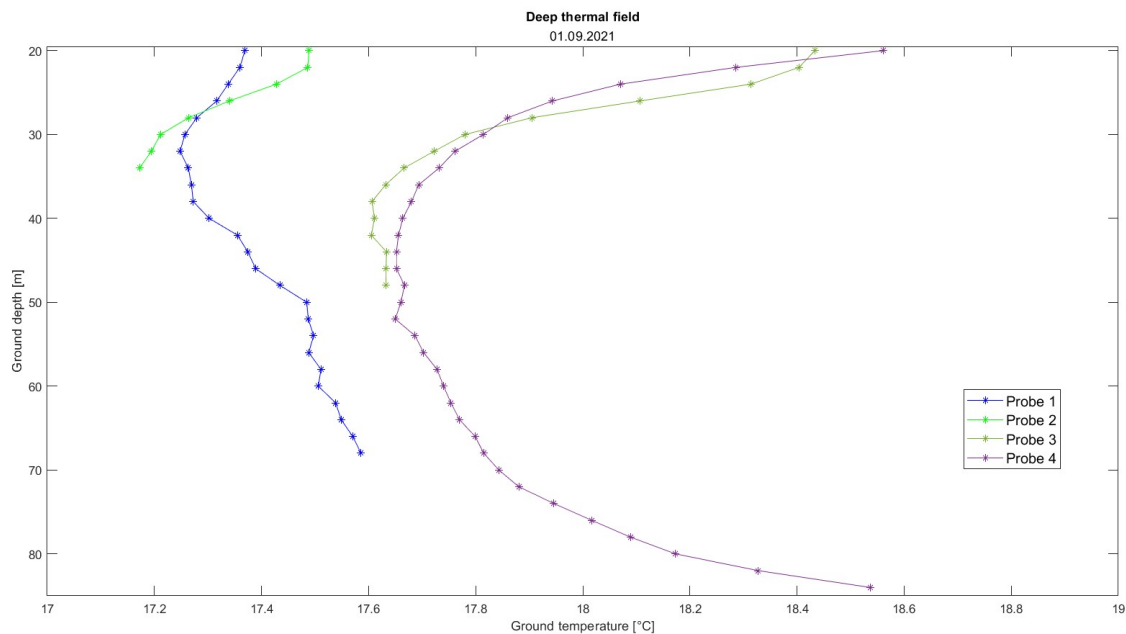


Figure 2: Temperature along 4 probes in function of depth.

The gradient regularizes into the underlying layers, compatible with the presence of an aquifer. The deepest layer, in correspondence of well P4, consisting of sandy silt, presents higher temperatures at the bottom, as it is near the bed of the aquifer composed of clays where it is affected by the deep ground geothermal heat flux.

The comparison of the data from different wells shows a horizontal gradient at depths where surface effects are not relevant. This implies that the lithologies are not perfectly parallel between themselves, evidencing the significant impact of the different thermophysical properties of the material on the heat transfer (Violante *et al.*, 2024).

Moreover, the time evolution of the temperature at the deepest measure point, at the depth of 85 m, over a 1-year time period shows unexpected fluctuations. These may be due to fluctuations in the upwellings of hydrothermal fluids from the bottom.

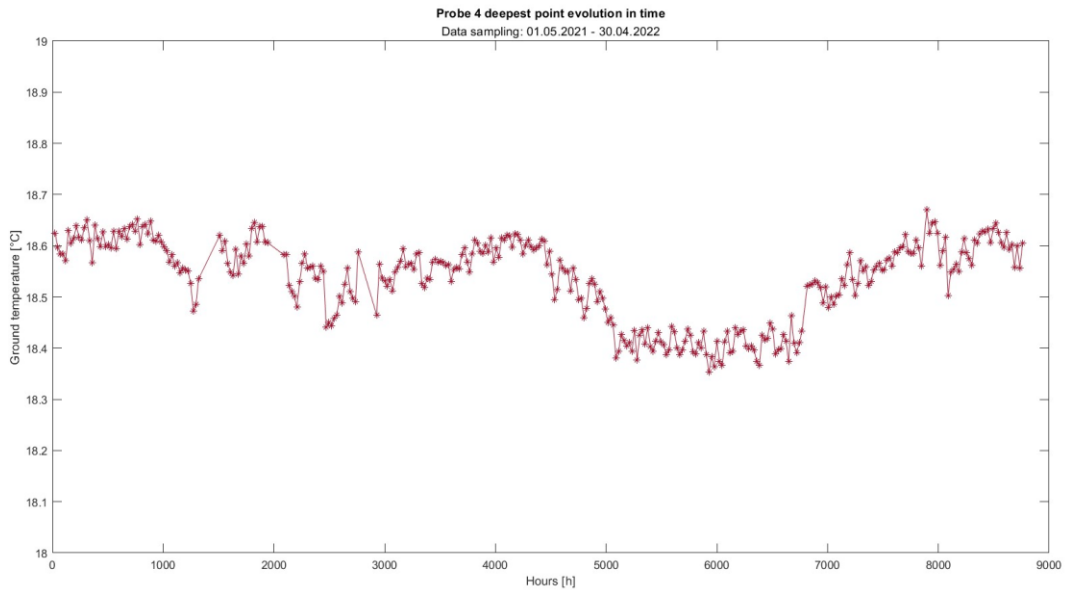


Figure 3: Time evolution of temperature in well P4 at 85 m depth.

4. CONCLUSIONS

The temperature in the Sabatini volcanic lithostratigraphic successions is far from being constant and uniform even at depths where the influence of surface heat transfer is not relevant.

5. REFERENCES

- Cherubini Y., Cacace M., Sheck-Wenderoth M., Moeck I., Lewerenz B., 2013, "Controls on the deep thermal field: implications from 3-D numerical simulations for the geothermal research site Groß Schönebeck", *Environmental Earth Sci* 70, pp. 3619-3642
- Fuchs S., Balling N., Mathiesen A., 2020, "Deep basin temperature and heat-flow field in Denmark – New insights from borehole analysis and 3D geothermal modelling", *Geothermics* 83
- Toth A., Galsa A., Madl-Szonyi J., 2020, "Significance of basin asymmetry and regional groundwater flow conditions in preliminary geothermal potential assessment – Implications on extensional geothermal plays", *Global and Planetary change* 195
- Violante A. C., Proposito M., Donato F., Guidi G., Falconi L. M., 2021, "Preliminary study of a closed loop vertical ground source heat pump system for an experimental pilot plant (Rome, Italy)", *Renew. Energy* 176, pp. 415–422
- Violante A. C., Guidi G., Proposito M., Mataloni S., Spaziani F. 2024. "Use of Distributed Temperature Sensing (DTS) Coupled to Ground Source Heat Exchangers for Geological Thermo-Stratigraphic Correlation", *Renewable Energy*, In press
- Wang Y., Pang Z., 2023, "Heat flux in volcanic and geothermal areas: Methods, principles, applications and future directions", *Gondwana research* 122, pp. 260-278

PHASE CHANGE FRONT MOVEMENT CHARACTERIZATION AND CORRELATION DEVELOPMENT

Kenny Couvreur^{a,b,*}, Maité Goderis^{a,b}, Wim Beyne^{a,b}, Michel De Paepe^{a,b}

^aDepartment of Electromechanical, Systems and Metal Engineering – UGent, Ghent, Belgium

^bFlandersMake@UGent – Core lab EEDT-MP, Leuven, Belgium, www.flandersmake.be

*Kenny.couvreur@ugent.be

Keywords latent thermal energy storage, heat exchanger, liquid fraction, energy fraction

1. INTRODUCTION

Latent thermal energy storage (LTES) systems have proven to be an efficient way to store energy. In these systems, Phase Change Materials (PCMs) are used as storage materials and undergo a phase change while storing or releasing energy. LTES systems have achieved notable development for cold storage and large-scale ice or aqueous salt solutions, especially for domestic refrigeration. Despite numerous promising applications, the widespread adoption of LTES systems remains pending.

LTES heat exchangers can be seen as classical, steady-state heat exchangers where one of the two working fluids is replaced by a stationary material, i.e. the PCM. Classical heat exchangers are characterized by traditional, low-computational methods such as the logarithmic mean temperature difference or the effectiveness-number of transfer units method. The goal of these methods is acquiring the outlet temperature of the HTF, given the inlet HTF temperature and HTF mass flow rate. However, in LTES systems, the phase change taking place during the charging and discharging, introduces a moving-boundary problem that needs to be solved. Because of this transient behavior, design methods used for regular heat exchangers are not applicable for LTES systems. As a result, general characterization and design methods for LTES systems are still under development, due to their transient nature caused by the varying energy content of the system during charging or discharging (Beyne *et al.* 2023).

To establish a practical sizing approach, it is essential to possess a thorough understanding of the melting and solidification processes occurring during the charging and discharging of LTES systems. Specifically, insights into the temporal evolution of the heat transfer between the HTF and PCM are crucial. Current research on LTES systems has focused on a narrow range of parameters, such as HTF inlet temperature, HTF mass flow rate, geometry dimensions, and PCM properties. This limited applicability underscores the need for a universally applicable design and sizing method that transcends these specific conditions and is founded on a deep understanding of the underlying physics governing phase change processes.

In a recent analytical method developed by Beyne *et al.* (2021) the phase change front location (as a function of time) is used to determine the local phase change fraction over time. This local phase change fraction is integrated to determine the overall phase change fraction as a function of time for the complete heat exchanger. The method showed good agreement with a numerical simulation of a planar geometry and has been expanded to other geometries in a follow-up study (Beyne *et al.* 2023).

According to these analytical studies the moving speed of the solid liquid interface at the boundary interface is supposed to be constant. The analytical solution predicts the movement of the phase front and the time required to reach the position of the phase front at a distance x from the inlet of the heat exchanger is given

The design model further allows to predict the liquid fraction as a function of time based on geometric and material parameters. Based on the liquid fraction, the outlet temperature as a function time can be determined.

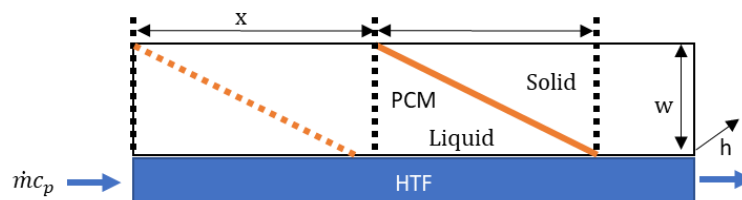


Figure 1. Schematic of a planar heat exchanger with the PCM solid-liquid interface indicated in orange.

While for planar heat exchangers the design model is validated to a numerical model, in this paper the position and movement of the phase change front in shell and tube LTES heat exchanger is investigated both experimentally and numerically to understand the relation between the process conditions and the liquid fraction and outlet temperature as a function of time. The derivation of the analytical model assumed the starting temperature of the LHTES heat exchanger

is uniform at the PCM phase change temperature. In these experiments the PCM is initially subcooled and the influence of neglecting the sensible heat capacity is further investigated.

2. EXPERIMENTAL SET-UP

The storage system is composed of a rectangular enclosure with 36 steel tubes of 6 m length. The storage material used is a binary eutectic mixture of KNO_3 and NaNO_3 with mass ratio 54-46% and a melting temperature between 221-223 °C. The shell side has been filled with a total amount of 3637 kg. To improve the heat transfer rate, each tube is fitted with 545 radial hexagon shaped aluminum fins with a circumradius of 5 cm. The LTES unit is depicted in Figure 2 together with a cross sectional schematic of the LTES unit. At 26 different axial positions the PCM temperatures are measured at positions 1, 2, 3, 4 indicated on the cross sectional view of the LTES unit. A comprehensive summary of the design parameters of the LTES system is given in the work of Couvreur *et al.* (2023). The LTES unit is interconnected via a thermal oil circuit with a 250 kW electrical heater providing the energy required for charging. The thermal oil, being the heat transfer fluid (HTF), flows through the tubes and exchanges thermal energy with the PCM. Different HTF mass flow rates and inlet temperatures can be tested.

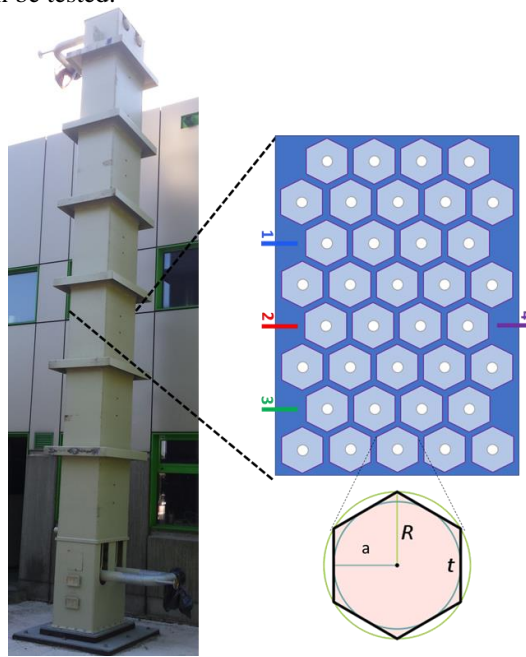


Figure 2. Cross sectional view of the shell-and-tube LTES battery. At 26 different axial positions the PCM temperatures are measured at positions 1, 2, 3, 4 indicated on the cross sectional view of the LTES unit

3. FRONT MOVEMENT CHARACTERIZATION AND CORRELATION

The intention of this work was to experimentally validate the analytical models derived in the work of Beyne *et al.* (2021). However, the number of experiments (total of 4 charging experiments with a constant inlet temperature of 250 °C but 4 different mass flow rates) which could be performed were limited due to mechanical failure of the storage system. As such, in this work these experiments are briefly analyzed and discussed but the front movement characterization and correlation development will be done numerically. For the experiments, the phase change front location could be determined at fixed locations related to the position of the thermocouples. For each thermocouple (or location) the time required to reach the upper melting limit of 223 °C is selected. A linear function as in Eq. 1 with x [m] the front location is fitted to the experimental data by use of non-linear least squares. The resulting best fits are also shown on Figure 3. The initial non-linear part of datapoints of each dataset are excluded from the fitting process and only the linear part is fitted. The results of the fitting process with give the lowest RMSE are given in Table 1. A clear influence of the HTF mass flow rate can be seen, both on the *Slope* and the *Intercept* values.

$$t_c(x) = \text{Intercept} + \text{Slope} \cdot x \quad 1$$

$$v_{pc} = \frac{U_l}{\dot{m} c_{htf} \Delta T_0} \quad 2$$

The *Slope* is in fact the moving speed of the phase change front, v_{pc} [s/m] as in Eq. 2, With ΔT_0 the initial temperature difference between the HTF inlet, $T_{htf,in}$ and the phase change temperature, T_m . U_l [J/m] is the internal energy change per meter tube. The *Intercept* is the time required for the phase change front to reach the boundary interface (t_0) and is the solution of the Stefan problem. When the experimental results are compared to the analytical expression of Eq. 2 one has to consider the total internal energy change of all constituents and not only the latent heat of phase change as shown in Figure 3. Although the experimental results already show some interesting results, it is not possible with the small dataset to derive an accurate analytical expression for the phase change front movement and especially does not allow for predicting the total LTES behavior. As such, a numerical model will be further used for a more detailed analysis of the front movement.

Table 1. Phase change front location fitting parameters

Experiment	<i>Slope</i> [s/m]	<i>Intercept</i> [s]
1	1241	7456
2	974	6244
3	836	5622
4	803	5308

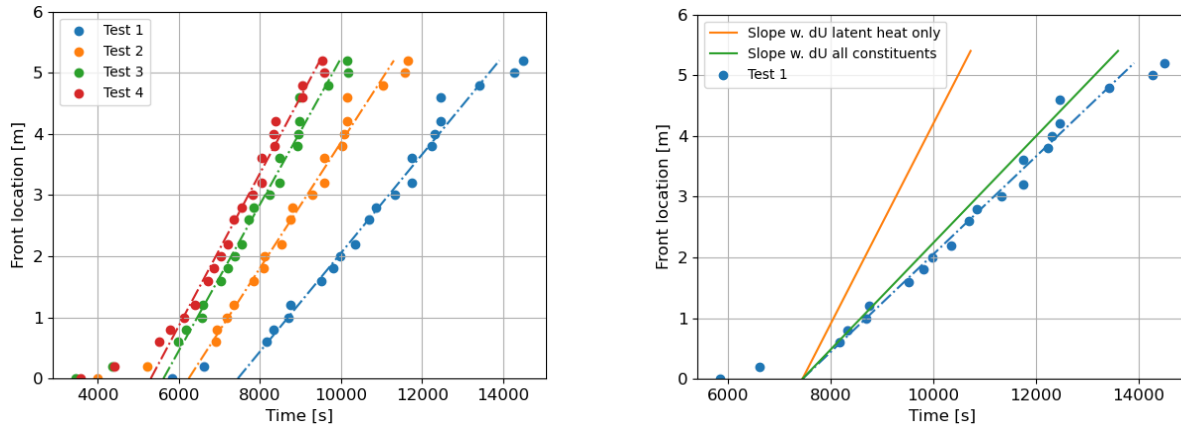


Figure 3. (Left) Tracking of the phase change front movement for the four different experiments. (right) Comparison of the moving speed of the phase change front obtained with $U_l = h_{lat}$ and the slope obtained with $U_l = \Delta U(T_{start}, T_{htf,in})$.

4. CONCLUSIONS

The experimental results of a large scale LTES unit show the constant movement of the phase change front which depends on the operational conditions. The number of real experiments however do not allow for further development of a predictive analytical model. Therefore a numerical model is made. The numerical results show good agreement with the experimental results and allow for a more detailed correlation development without considering the experimental uncertainties. The correlation development however is still ongoing work and results will be included in the full paper.

5. REFERENCES

- Beyne, W., S. Lecompte, K. Couvreur and M. De Paepe (2021). An analytical solution for solidification in planar latent thermal energy storage heat exchanger. *Proceedings of the 15th International Conference on Heat Transfer, Fluid Mechanics and Thermodynamics (HEFAT2021)*. J. Meyer. Online: 213–217.
- Beyne, W., I. T'Jollyn, S. Lecompte, L. F. Cabeza and M. De Paepe (2023). "Standardised methods for the determination of key performance indicators for thermal energy storage heat exchangers." *Renewable & Sustainable Energy Reviews* **176**.
- Beyne, W., R. Tassenoy, M. Goderis, V. Van Riet and M. De Paepe (2023). "A predictive method for pipe in pipe, cylindrical modules and spherical packed bed latent thermal energy storage systems." *Journal of Energy Storage* **68**.
- Couvreur, K., W. Beyne, R. Tassenoy, S. Lecompte and M. De Paepe (2023). "Characterization of a latent thermal energy storage heat exchanger using a charging time energy fraction method with a heat loss model." *Applied Thermal Engineering* **219**

EFFECT OF AMMONIA COMPOSITION ON FLAME STRUCTURE AND BLOWOUT LIMITS OF NON-PREMIXED AMMONIA-HYDROGEN-NITROGEN-AIR FLAMES

Santhosh Rudrasetty^{a,*}, Rajneesh Kumar Yadav^a, Binita Pathak^a

^aDepartment of Mechanical Engineering, IIT (BHU) Varanasi, Varanasi, Uttar Pradesh 221005, India

*rsanthosh.mec@iitbhu.ac.in

Keywords: Ammonia-hydrogen-nitrogen flame, non-premixed flame, flow regime map, blowout limits

1. INTRODUCTION:

Ammonia (NH_3) has been established as a reliable green hydrogen (H_2) carrier. At the destination site, this ammonia is only partially thermally cracked [1] to save the energy required to convert entire ammonia back into hydrogen. The partially cracked ammonia is a mixture of ammonia-hydrogen-nitrogen which is combustible. All the works on promising $NH_3/H_2/N_2$ -air mixtures reported are for premixed combustion [2]. All the reported non-premixed swirl combustors' investigations are with either NH_3 -air or NH_3/CH_4 -air flames. Thus, for adopting $NH_3/H_2/N_2$ -air mixtures in non-premixed combustion systems, relevant to many industry burners and gas turbines, the present work aims to construct a full stability map of $NH_3/H_2/N_2$ -air mixtures to determine favorable stable operating conditions and blowout limits in a non-premixed swirl combustor.

2. EXPERIMENTAL SETUP:

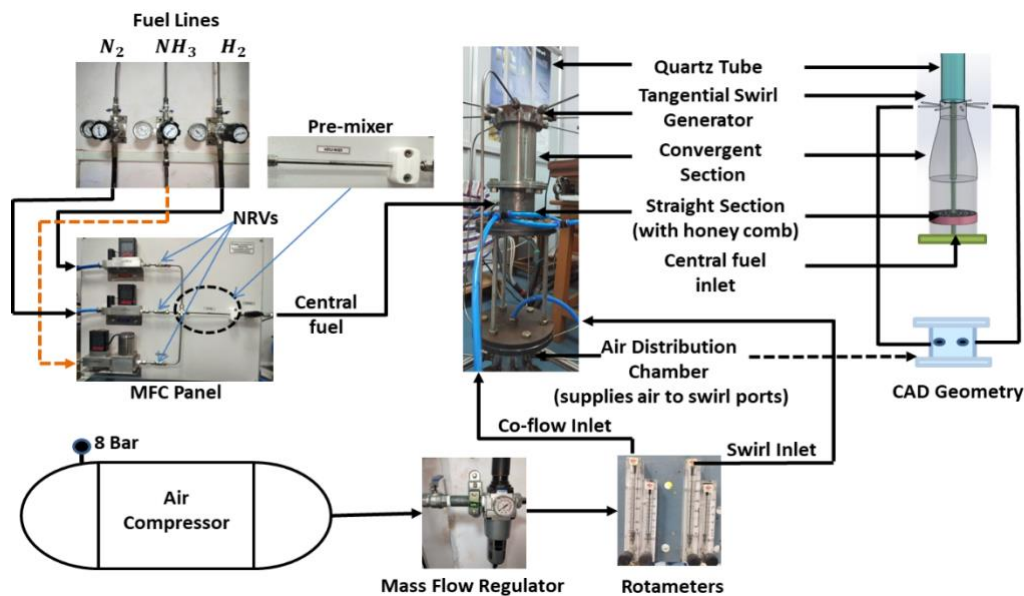


Fig. 1: Experimental setup

The experimental setup consisting of an atmospheric tangential-swirl combustor and related fuel and flow lines is shown in Fig. 1. It consists of fuel flow lines of NH_3 , H_2 , and N_2 that are connected to three different mass flow controllers (Alicat: 0-100 lpm, 0-50 lpm, and 0-50 lpm respectively with an accuracy of 0.8% of the reading as per manufacturer specification). These mass flow controllers are used to regulate the fuel flows to obtain different blends of $NH_3-H_2-N_2$. This fuel blend is then directed through the central jet. The central jet is surrounded by a swirling coaxial air jet. The atmospheric air is compressed with the help of a compressor (make: ELGi) rated for a flow rate of 1500 lpm at a maximum working pressure of 12 kgf/m² with a tank capacity of 500 liters. It is then fed to (a) coannular jet and (b) tangential-swirl generator block. Both streams are regulated through the rotameters of 0-1000 lpm and 0-500 lpm (accuracy: 3% of full scale) respectively. The setup facilitates independent control of fuel, coannular and swirl ports' mass flow rate. A quartz tube of a diameter of 80 mm and 500 mm length is used as confinement. The quartz tube is further connected to the exhaust system.

3. METHODOLOGY:

Keeping a constant Reynolds number for fuel in the central jet ($Re_f = U_f d_f / \nu_f$ where U_f , d_f , ν_f denote velocity of fuel, diameter of central jet and kinematic viscosity of fuel, respectively), three test cases with different ammonia compositions are selected for this study as shown in Table 1. The $NH_3/H_2/N_2$ blend is aimed to represent partially-cracked ammonia. Therefore, H_2/N_2 is maintained in 3:1 ratio as partial cracking of 1 mole of NH_3 produces 3 moles of H_2 and 1 mole of N_2 . For each Re_f , different coannular Re_a are established. For each (Re_f , Re_a), swirl is increased from 0 to a value where flame blowsout. The intensity of swirl imparted is characterised by geometric swirl number $S_G = \frac{\pi r_0 d_0}{2A_t} \left[\frac{m_\theta}{m_\theta + m_A} \right]^2$, where r_0 denotes the radial distance for tangential swirl port, d_0 denotes the co-annular diameter of burner annulus, A_t denotes the total area of swirling ports, m_θ denotes the mass flow rate of tangential air input ports and m_A denotes combined fuel and co-annular mass flowrates. The flame regime maps are then constructed based the flame structures in the parameter space of Re_a and S_G . The NH_2^* chemiluminescence (wavelength~ 630 ± 10 nm) images are then captured using CCD camera of 2048×2048 pixels. The images are then binarized using in-house written MATLAB code to identify flame topology.

Table 1: Test cases for NH_3, H_2 and N_2 blend in central jet for fuel flow

$NH_3:(H_2:N_2)$	Total volumetric flow (m^3/s)	Reynolds number for central fuel (Re_f)	Geometric swirl number (S_G)	Annular flow Reynolds number (Re_a)
70:30	9.67×10^{-6}	~115	0 - 19.75	0 - 11637 (blow out)
50:50	1.16×10^{-5}		0 - 19.45	0 - 15189 (blow out)
20:80	1.61×10^{-5}		0 - 19.42	0 - 15189 (blow out)

4. RESULTS AND DISCUSSION:

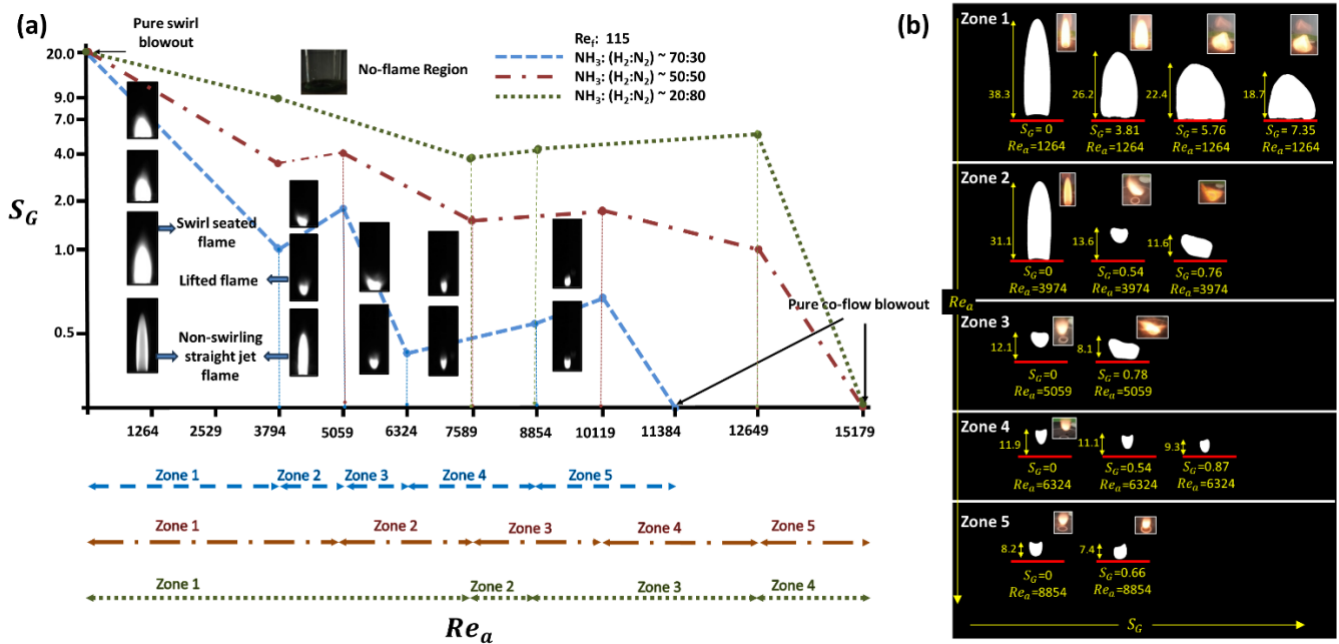


Fig. 2: (a) Flame regime map for $NH_3:(H_2:N_2) \sim 70:30; 50:50$ and $20:80$ at $Re_f: 115$
(b) NH_2^* chemiluminescence images for $NH_3:(H_2:N_2) \sim 70:30$

Fig. 2a represents regime map of three different blends of $NH_3/H_2/N_2$ - air flames in the parameter space of Re_a and S_G . Three different blowout modes are depicted in the regime map (Fig. 2a). The first one appears when the flame is blown out with pure swirl, i.e., with no co-flow air. This is shown as uppermost point on y-axis. This S_G is determined by the geometrical dimension of combustor. This is because $S_G = \frac{\pi r_0 d_0}{2A_t} \left[\frac{m_\theta}{m_\theta + m_A} \right]^2$ and for pure-

S_G blowout the $m_A=0$. Therefore, the pure- $S_G = \frac{\pi r_0 d_0}{2A_t}$. It is noted that pure- S_G depends only on combustor geometry. This value of this pure- S_G in the present combustor is ~ 19.75 . The second limit one appears with $S_G=0$ and at maximum Re_a (this is shown at the extreme right side of x-axis). It is observed that this blowout limit with pure co-flow increases as the NH_3 volume fraction decreases in the fuel blend and highest blowout limit occurs as $Re_a = 15179$. The third blowout is observed at multiple combinations of Re_a and S_G . These are represented as ‘dotted’ lines in the parameter space of Re_a and S_G (Fig. 2a). The region below the dotted lines indicate ‘flame regime’ and ‘no-flame region’ beyond it. It is observed that the ‘flame regime’ increases as volume fraction of NH_3 decreases (with an associated increase in H_2). This may be due to wider flammability limit of H_2 .

Based on careful observation, the ‘flame regime’ in the regime maps is divided into five different zones. In Zone 1, the jet flame at $S_G=0$ is shortened on increase in S_G . At sufficient higher S_G , the burner-attached flame blowsout. The sequence of these events are shown in Fig. 2b which represents binary images of NH_2^* chemiluminescence snapshots. The blowout limit is shown in Fig. 2a. In Zone 2, the burner-attached flame at $S_G=0$ lifts-off. With a further increase in S_G , the flame interestingly retraces back towards the burner exit plane and reattaches to it and blowsout at higher S_G . Meanwhile, in Zones 3 & 4, at $S_G=0$ a lifted flame is initially observed instead of burner-attached flame. With a further increase in S_G , it reattaches to the burner exit and blowsout. The difference between Zones-3 & 4 is that in Zone 4, the flame is narrower as compared to Zone 3. In Zone 5, initial lifted flame has shorter lift-off height than Zone 3 & 4 (Fig. 2b). The further blowout sequence is same as Zones 3 & 4.

With regards to the blowout limits (dotted lines in Fig. 2a), the limits collapse onto a single curve (linear) when plotted against Re_θ . This is shown in Fig. 3. As defined in coaxial swirling flame literature, $Re_\theta = U_\theta d_\theta / \nu_{air}$, where $U_\theta = U_a \cdot S_G$ is characteristic velocity magnitude of swirl imparted to co-flow jet and the d_θ is defined as the area averaged diameter which is calculated as: $d_\theta = (A_a d_a + A_t d_t) / (A_a + A_t)$ where A_a and A_t is defined as the cross-sectional area of co-annular pipe and total area of all swirl inducing port respectively. d_a and d_t are the corresponding diameters of co-annular pipe and swirl ports. The magnitude of U_θ is directly proportional to the intensity of swirl imparted to co-airflow annulus. For a particular fuel blend, Re_θ represented in Fig. 3 is the mean of all combinations if Re_a and S_G at which blowout occurs. The error bars show the deviation from this mean. The map is quite useful in determining the blowout limits in terms of a single input parameter Re_θ . It is indicative of swirling strength of co-airflow stream surrounding the central fuel jet. The positive slope of the curve implies that as NH_3 volume fraction decreases, the representative swirling strength of the coflow annulus (indicated by Re_θ) required to blowout the flame is higher. Similar blowout collapse was observed for methane flame in one of the authors’ previous works [3].

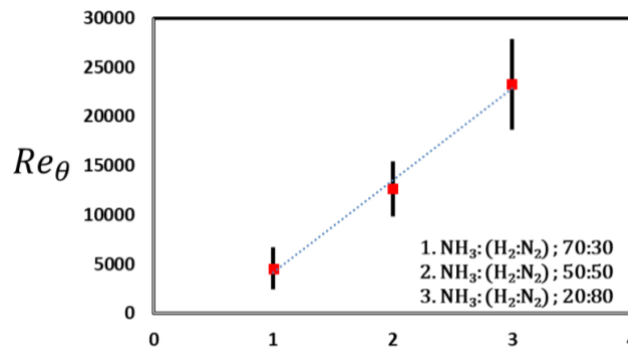


Fig. 3: Collapsed Blow out limit for the three different blends used in the present experiments

5. REFERENCES:

1. B. Mei, J. Zhang, X. Shi, Z. Xi, Y. Li, Enhancement of ammonia combustion with partial fuel cracking strategy: Laminar flame propagation and kinetic modeling investigation of $NH_3/H_2/N_2$ /air mixtures up to 10 atm, Combust Flame, 231 (2021) 111472.
2. A.A. Khateeb, T.F. Guiberti, Z. Xuren, Y. Mourad, A. Jamal, W.L. Roberts, Stability limits and NO emissions of technically premixed ammonia-hydrogen-nitrogen-air swirl flames, Int J Hydrogen Energy 45 (2020) 22008-22018.
3. Santhosh, R., and Saptarshi Basu. "Transitions and blowoff of unconfined non-premixed swirling flame." Combustion and Flame 164 (2016): 35-52.

EXPERIMENTAL CHARACTERIZATION OF A SOLAR BOILER AS A SENSIBLE THERMAL ENERGY STORAGE SYSTEM

Alixé Degelin^{a,b*}, Sophie Vercammen^a, Wito Plas^a, Maité Goderis^a, Wim Beyne^a, Michel De Paepe^{a,c}

^aDepartment of Electromechanical, Systems and Metal Engineering, Ghent University, Sint-Pietersnieuwstraat 41, 9000 Ghent, Belgium

^bEMIB, Faculty of Applied Engineering, University of Antwerp, Groenenborgerlaan 171, 2020 Antwerp, Belgium

^cFlandersMake@UGent – Core lab EEDT-MP, flandersmake.be, Belgium

*alixe.degelin@ugent.be

Keywords: sensible thermal storage system, charging time energy fraction method, experimental predictive model

1. INTRODUCTION

For characterizing heat exchangers, many methods already exist, such as the e-NTU and the LMTD method. These methods however are based on the assumption of a heat exchanger in steady state while latent thermal energy storage (LTES) and sensible thermal energy storage (STES) do not operate in steady state. This is why Beyne et al. (2021) recently developed a new method for quantitatively studying these systems: the charging time energy fraction (CTEF) method. The main benefit of the CTEFM is that the outlet state can be predicted as a function of time, which allows for capturing of the non-steady state behavior. The predictive value of this method has been demonstrated in the study of Beyne et al. (2021) on a latent storage heat exchanger. The characterization of a STES system on the other hand has not been conducted before. It is important to be able to predict the outlet state as a function of time of STESs, not only because it is an upcoming application in domestic households, but also because water tank storage is the cheapest and most widely used type of TES (Denehkar et al., 2022). In this paper the water tank of a solar boiler is characterized using the CTEF method and the predicted outlet temperature is compared to the measured outlet temperature.

2. CHARGING TIME ENERGY FRACTION METHOD

This section focusses on the characterization of a thermal storage system using the CTEF method. For a more extensive explanation of the method, readers are referred to Beyne et al. (2021). The CTEF method is a characterization method to predict the heat transfer fluid outlet temperature as a function of time, based on the heat transfer fluid inlet temperature and mass flow rate. The outlet temperature of the heat transfer fluid is correlated with the inlet conditions by the net efflux of energy \dot{Q}_f as in Eq. (1).

$$\dot{Q}_f = \dot{m}(h_{out} - h_{in}) \quad (1)$$

With \dot{m} the mass flow rate and h the specific enthalpy of the heat transfer fluid. During a charging cycle, with the storage tank at uniform temperature at the start and with negligible losses to the environment, the integrated efflux of energy $Q_f(t)$ can be written as an energy fraction $\alpha(t)$ of the total internal energy ΔU of the tank (Eq. (2)).

$$\alpha(t)\Delta U = \int_{t_{start}}^t \dot{m}(h_{out} - h_{in})dt = Q_f(t) \quad (2)$$

The integrated efflux of energy $Q_f(t)$ can be determined from measurements on the heat transfer fluid inlet and outlet while the total stored internal energy ΔU is known for the chosen charging cycle. The outlet temperature can be predicted by correlating the function $\alpha(t)$ as a function of time, initial conditions and inlet conditions. As the parametrizing of $\alpha(t)$ is difficult due to different dominant heat transfer processes in a latent thermal energy storage system, the fitting problem is rewritten as the charging time t_c in function of several energy fraction levels α_i instead of the energy fraction in function of the charging time (Eq. 3).

$$t_c(\alpha_i) \text{ for which } Q_f(t) = \alpha_i \max_t Q_f(t) \quad (3)$$

The prediction of the outlet state thus requires defining a set of functions f to relate a set of parameters p to the heat transfer fluid inlet conditions \dot{m} and h_{in} for every energy fraction α_i by comparing the measured charging time (Eq. (3)) with the predicted charging time (Eq. (4)).

$$t_c(\alpha_i) = f(\dot{m}; h_{in}; p(\alpha_i)) \quad (4)$$

In Beyne et al. (2021) Eq. (5) was proposed as a the charging time correlation for a latent thermal energy storage system with A, B C and D the fitting coefficients and ΔT the temperature difference of heat transfer fluid inlet and the peak PCM phase change temperature. For sensible thermal energy storage systems, the temperature difference ΔT can be defined as the difference between the heat transfer fluid inlet temperature and the initial tank temperature.

$$t_c(\alpha_i) = \underbrace{\left(A(\alpha_i) + \frac{B(\alpha_i)}{\dot{m}} \right) \frac{1}{\Delta T}}_{Slope} + \underbrace{\left(C(\alpha_i) + \frac{D(\alpha_i)}{\dot{m}} \right)}_{Intercept} \quad (5)$$

The mean efflux of energy $\overline{Q}_f^{\alpha_1, \alpha_2}$ between fractions α_1 and α_2 can now be calculated as in Eq. (6).

$$\overline{Q}_f^{\alpha_1, \alpha_2} = \frac{\alpha_1 - \alpha_2}{f(\dot{m}; h_{in}; p(\alpha_1)) - f(\dot{m}; h_{in}; p(\alpha_2))} \Delta U \quad (6)$$

The mean outlet state can be determined between fractions α_1 and α_2 as in Eq. (7) where h_{in} and \dot{m} are the measured inlet state and mass flow rate and evaluated at the average time $t_m^{\alpha_1, \alpha_2}$.

$$\bar{h}_{out}^{\alpha_1, \alpha_2} = h_{in}(t_m^{\alpha_1, \alpha_2}) - \frac{\overline{Q}_f^{\alpha_1, \alpha_2}}{\dot{m}(t_m^{\alpha_1, \alpha_2})} \text{ with } t_m^{\alpha_1, \alpha_2} = \frac{f(\dot{m}; h_{in}; p(\alpha_1)) + f(\dot{m}; h_{in}; p(\alpha_2))}{2} \quad (7)$$

3. EXPERIMENTAL SET-UP AND MEASUREMENTS

In order to validate the correlation function as proposed in Eq. (5) for a STES system, measurements are performed on the thermal storage system of a solar boiler. The storage system is an open, pressure free ROTEX Sanitube INOX water storage tank. Inside the tank, there is a corrugated helical coil made of cross-linked polyethylene (PEX) with an aluminum layer inside a polymer matrix. This coil is placed in the middle of the tank and consists of two parallel helical coils of 51 and 46 m. The total length of the coils is 97 m. The outer diameter of the tube of the coil itself is 32 mm and the wall has a thickness of 2 mm (Bokisova et al. 2017). The inside dimensions of the solar boiler are 138.5 x 48 x 48 cm. The boiler has a storage capacity of 300 l and has a double walled jacket made of polypropylene with PUR hard foam heat insulation. All thermocouples in the circuit are K-type thermocouples.

Six charging tests are performed to fit the coefficients (A, B, C and D) of the charging time energy fraction method. The heat transfer fluid inlet temperature and mass flow rate are kept constant throughout the charging test and are displayed in Table 1. The tests are started with a uniform tank temperature of 20 °C and stopped when the temperature difference in coil inlet and outlet remains constant.

Table 1. Charging test matrix for the characterization using the charging time energy fraction method.

Mass flow rate	Inlet temperature		
	30 °C	40 °C	50 °C
150 kg/s	X	X	X
300 kg/s	X	X	
450 kg/s	X		

4. CHARACTERIZATION AND OUTLET TEMPERATURE PREDICTION

The fitting coefficients A, B C and D as described in Eq. (5) are defined using the charging time energy fraction method and displayed in Fig. 1. The *Slope*, defined by coefficients A and B, is related to the ratio of the stored energy to the average heat transfer rate as explained by Beyne et al. (2021). Coefficient B is negative as the charging time descends more with decreasing mass flow rates. As a result, the *Slope* is overall negative. This can be explained by the fact that the total stored energy is smaller when the initial temperature difference is smaller such that the charging time is shorter. A non-linear behavior in the coefficients A and B is visible. This indicates that there is a decreased heat transfer rate at higher charging fractions. The main reason is the reduced temperature difference between the tank and the heat transfer fluid.

Coefficients C and D together form the *Intercept* and are not linked to the average heat transfer coefficient. Since the heat transfer mode is sensible heating, the curves of C and D show the same non-linear behavior as A and B due to the reduced temperature difference and thus reduced heat transfer rate.

The characterization is evaluated by comparing the predicted with the measured heat transfer fluid outlet temperature. The result for the charging test with a HTF inlet temperature of 30 °C and mass flow rate of 450 kg/s is shown in Fig. 2. (Absolute temperature difference, error analysis and model evaluation to be included in full paper).

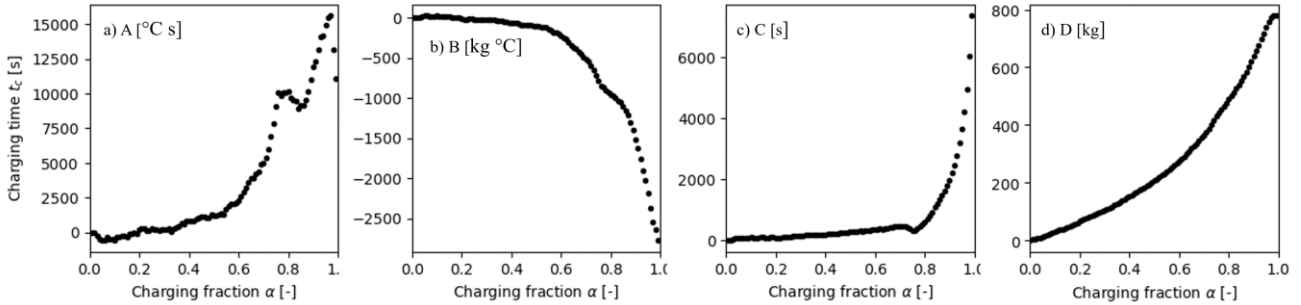


Figure 1. Fitting coefficients A, B, C and D for the charging time correlation as proposed in Eq. (5) as a function of the energy fraction α .

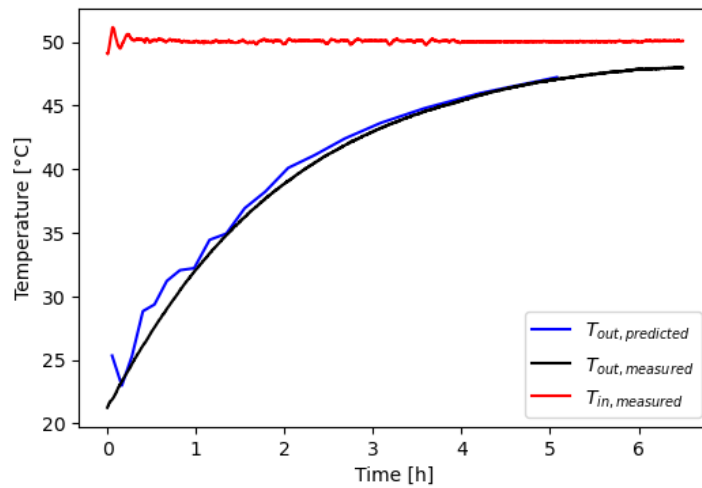


Figure 2. Measured (blue) and predicted (black) heat transfer fluid outlet temperature as a function of time for an inlet temperature (red) of 50 °C and mass flow rate of 150 kg/s.

5. CONCLUSIONS

This paper presented the use of the charging time energy fraction method on a sensible thermal storage system using the water tank of a solar boiler. Characterizing the TES with the CTEF method allows to predict the stored energy and heat transfer outlet temperature as a function of the inlet mass flow rate and temperature. The results of the prediction of the outlet temperature of the heat transfer fluid show good correspondence with the measured values, which indicates that the proposed correlation for charging time is suited for STESs.

6. REFERENCES

- W. Beyne, K. Couvreur, I. T' Jollyn, R. Tassenoy, S. Lecompte and M. De Paepe, 2021. "A charging time energy fraction method for evaluating the performance of a latent thermal energy storage heat exchanger". *Applied thermal energy*, Vol. 195, 117068
- W. Beyne, K. Couvreur, S. Lecompte and M. De Paepe, 2021. "A technical, financial and CO2 emission analysis of the implementation of metal foam in a thermal battery for cold chain transport". *J. Storage Mater.* Vol. 35, 102324
- L. Bokisova, Ö. Bağcı, A. Sharif, D. Daenens, W. Beyne, & M. De Paepe, 2017. "Thermal analysis of a plastic helical coil heat exchanger for a domestic water storage tank". Proceedings of the 9th World Conference on Experimental Heat Transfer, Fluid Mechanics and Thermodynamics (ExHFT-9), PT72.
- S. Danekar, H. Yousefi, 2022. "A comprehensive overview on water-based energy storage systems for solar applications". *Energy Reports*, 8, 8777-8797

Study on Multiphase flow Measurement in Large-diameter Metal Pipe using Ultrasonic Velocity Profiler

Masataka Teshigawara^a, Hiroshige Kikura^a, Naruki Shoji^b, Hideki Kawai^b,

Kazunori Takeuchi^c, Koji Mochizuki^c and Norio Tenma^d

^aTokyo Institute of Technology, ^bMuroran Institute of Technology,

^cMODEC, Inc, ^dNational Institute of Advanced Industrial Science and Technology

*kikura.h.aa@m.titech.ac.jp

Keywords: Flow measurement, Gas-liquid two-phase flow, Multiphase flow, Ultrasonic velocity profiler

1. INTRODUCTION

Flow measurement of solid-gas-liquid three-phase flow in a large-diameter metallic pipe used in nuclear power plants, chemical plants, and recovery technologies for rare metals, methane hydrates, etc., is difficult. Although several measurement methods have been developed for the multiphase flow, for instance, the fiber optic probe method (Jones Jr, O. C., & Delhaye, J. M., 1976) or wire mesh tomography (Prasser, H. M., Scholz, D., & Zippe, C., 2001) are not applicable to the multiphase flow containing solid phase. Also, optical measurement techniques such as particle image velocimetry, particle tracking velocimetry, and Laser Doppler velocimeter are not suitable for opaque metallic pipes and fluids. Therefore, we have focused on ultrasonic fluid measurement technology, which is non-invasive and can be applied to opaque pipes and fluids. Among the ultrasonic measurement techniques, we have investigated the ultrasonic velocity profiler (UVP), which was developed by Takeda Y. et al in 1987. UVP has already been applied to single-phase and gas-liquid two-phase flows (Aritomi, M., et al., 1996, Kotzé, R., Wiklund, J., Haldenwang, R., & Fester, V., 2011), however, it has not yet been studied for a solid-gas-liquid three-phase flow. Also, no applications to large-diameter metal pipe have been reported because of the challenge of ultrasonic transmittance for the metal pipe. In this paper, we conducted flow velocity measurements of rising bubbles and solids in a large-diameter steel pipe to demonstrate the feasibility of clamp-on UVP measurements on large-diameter steel pipe.

2. Ultrasonic Velocity Profiler

As shown in Figure 1, UVP is a method to measure the flow velocity distribution along the ultrasonic beam axis. The ultrasonic pulse with a center frequency f_c is irradiated from the ultrasonic transducer onto the fluid. Doppler frequency f_D corresponding to the moving velocity of the reflectors is obtained by analyzing the reflected echo signals. The Doppler frequency is then converted to velocity to obtain the velocity distribution using the following equation.

$$v(x) = \frac{c f_D(x)}{2 f_c \sin \theta} \quad (1)$$

where c is sound velocity in fluid, and x is the measurement position that can be obtained by following equation.

$$x = \frac{c\tau}{2} \quad (2)$$

where τ is the receiving time of reflected ultrasound from transmission. There are several methods for extracting Doppler frequency from echo signals (Shoji N, et al., 2019, Wongsaroj W, et al., 2020). This study used an autocorrelation method (Kasai C, et al., 1987), which can calculate velocity with relatively few pulse repetitions.

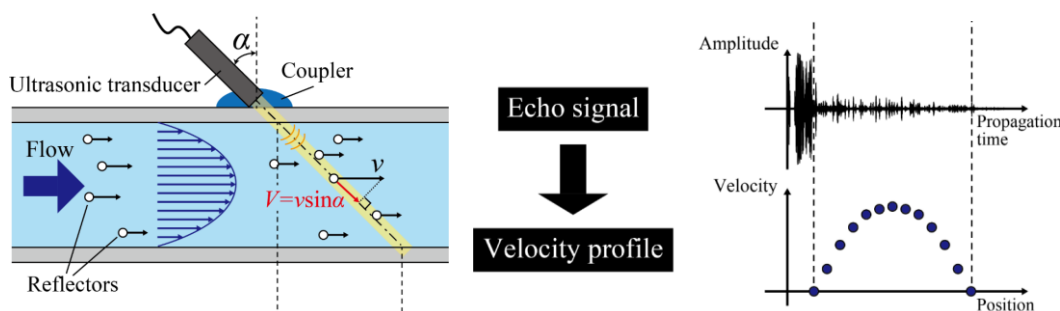


Figure 1. Principle of the UVP.

3. Experiments

In order to verify whether ultrasonic echo signals from the reflector can be obtained to calculate the flow velocity, ultrasonic pulses were transmitted to a gas or solid-phase reflectors in a large-diameter steel pipe by an ultrasonic transducer installed outside the pipe. In this experiment, the steel pipe with a wall thickness of 25.4 mm and an inside diameter of 710 mm was submerged in a pool approximately 2 m in diameter. In addition, the steel pipe cut 1/6 in circumferential direction was submerged in an acrylic water tank to visualize internal flows. As shown in Figure 2, an ultrasonic transducer installed outside the pipe was used to transmit ultrasonic pulses to reflectors (bubbles and ice) and the reflected echo signals from the reflectors were received by the same transducer. Rising bubbles (about 5 mm in diameter, gas phase) and rising ice (30 mm cubes, solid phase) were used as the reflectors, respectively.

The UVP system consist of an ultrasonic transducer, an ultrasonic pulser/receiver (JPR-600C, Japan Probe Co, Ltd.), an A/D converter (PXIe-5170R, National Instruments Co, Ltd.), and a computer for signal processing. The ultrasonic transducer with ultrasonic element diameter of 13 mm and a center frequency of 1 MHz was installed outside the pipe at angle of 16 degrees to maximize the ultrasonic transmittance. The detail of measurement conditions is shown in Table 1.

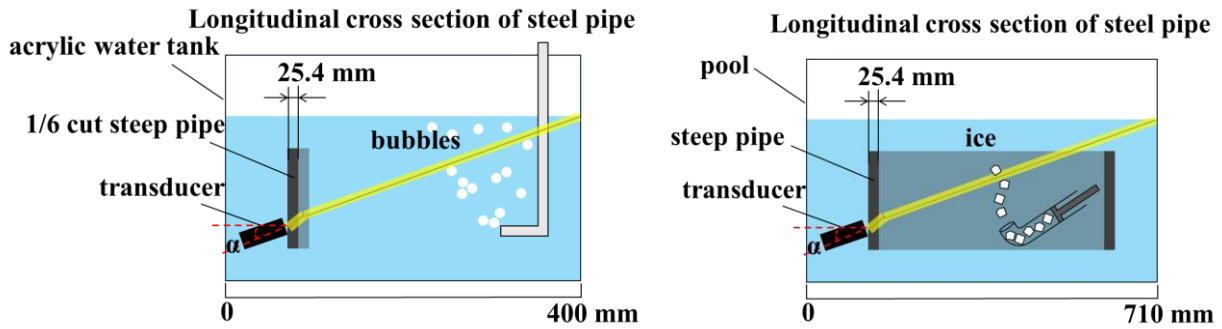


Figure 2. Gas and solid phase velocity measurement in the large-diameter steel pipe with UVP method.

Table 1. Measurement conditions for UVP measurement applied to large-diameter steel pipe.

Parameter	Value
Ultrasonic frequency	1.02 MHz
Ultrasonic element diameter	13 mm
Number of wave cycles in single pulse	4
Applied voltage	200 V _{pp}
Ultrasonic incident angle	16 degrees
Sound velocity in water	1482 m/s
Spatial resolution in the direction of ultrasonic propagation	2.96 mm
Time resolution	128 ms
Sampling speed of ultrasonic waveform	25 MS/s
Bubble diameter	≈ 5 mm
Ice diameter	≈ 30 mm

4. Results

Figure 3 shows the measurement result of bubble rising velocity profiles using the UVP technique. Each profile represents the time-averaged value derived from 1000 instantaneous measurements. These findings demonstrate the feasibility of obtaining gas-phase velocity distribution within the steel pipe using an external ultrasonic transducer. The velocity measurement results for ice are shown in Figure 4, with each profile similarly representing time-averaged velocities. These results suggest that ultrasonic reflection signals can be captured from the solid phase, allowing for the measurement of rising velocity profiles at various radial positions along the pipe's direction. The suitability of the UVP method for multiphase flow within large-diameter steel pipes has been affirmed.

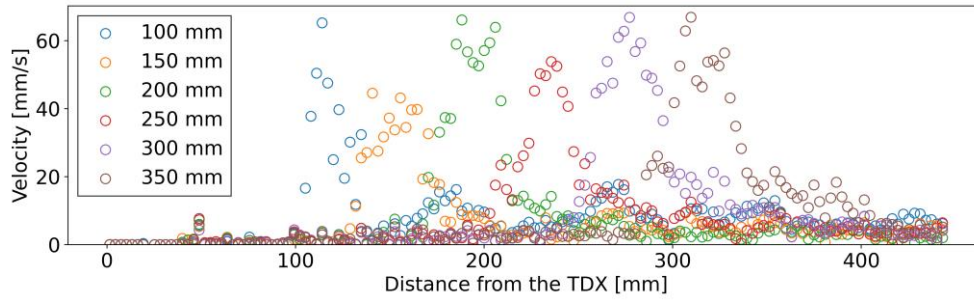


Figure 3. Time-averaged velocity profiles of bubbles while changing the injection position. Values in legend represent distance from steel pipe wall.

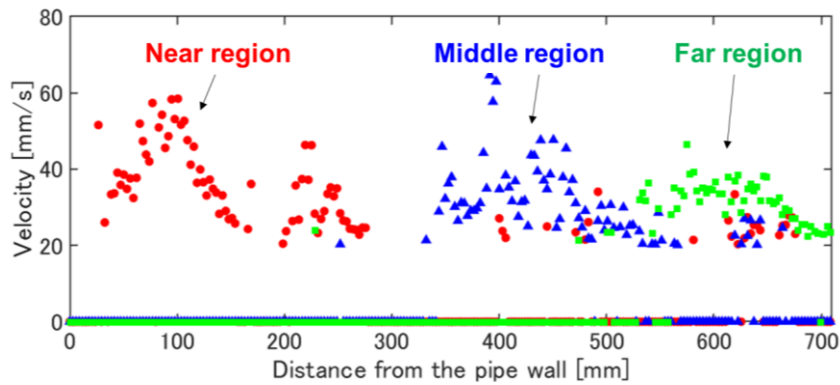


Figure 4. Time-averaged velocity distribution of ice at each ice feeding position in a large-diameter steel pipe.

5. Conclusion

We introduced a measurement technique for the solid-gas-liquid three-phase flow within a large-diameter metallic pipe using UVP, confirming its suitability for large-diameter steel pipes. The UVP method was employed in the large-diameter steel pipe to measure velocity profiles of gas and solid phases. The findings indicated that ultrasonic reflection signals could be obtained from both gas and solid phases externally, allowing the measurement of rising velocity profiles at different positions along the radial pipe direction. Future work involves comparing UVP results with those of PTV or PIV to evaluate the validity of experimental results.

References

- Aritomi, M., Zhou, S., Nakajima, M., Takeda, Y., Mori, M., & Yoshioka, Y. (1996). Measurement system of bubbly flow using ultrasonic velocity profile monitor and video data processing unit. *Journal of Nuclear Science and Technology*, 33(12), 915-923.
- Jones Jr, O. C., & Delhaye, J. M. (1976). Transient and statistical measurement techniques for two-phase flows: a critical review. *International Journal of Multiphase Flow*, 3(2), 89-116.
- Kasai C, et al: Real-time two-dimensional blood flow imaging using ultrasound doppler, *Japanese Journal of Applied Physics*. 26 (1987), 9-13.
- Kotzé, R., Wiklund, J., Haldenwang, R., & Fester, V. (2011). Measurement and analysis of flow behaviour in complex geometries using the Ultrasonic Velocity Profiling (UVP) technique. *Flow Measurement and Instrumentation*, 22(2), 110-119.
- Prasser, H. M., Scholz, D., & Zippe, C. (2001). Bubble size measurement using wire-mesh sensors. *Flow measurement and Instrumentation*, 12(4), 299-312.
- Shoji N, et al.: Novel Algorithm for High Flowrate Metering with Ultrasonic Pulsed Doppler Method, Proc. Of 15th International Conference on Fluid Control, Measurements and Visualization. (2019), 298.
- Takeda, Y. (1995). Velocity profile measurement by ultrasonic Doppler method. *Experimental thermal and fluid science*, 10(4), 444-453.
- Wongsaraj W, et al.: De-aliasing of ultrasonic velocity profiler on bubbly flow beyond the Nyquist limit, *Acoust. Sci. & Tech.* 41 (2020), 917-920.

Acknowledgement

This study was conducted as a part of the methane hydrate research project funded by METI (the Ministry of Economy, Trade and Industry, Japan)

A STUDY OF THE VORTICES MERGING OVER A NONPLANAR CRANKED LAMBDA WING MODEL AT SUBSONIC SPEED

Hassan Aleisa^{a,*}, Konstantinos Kontis^a, Melike Nikbay^b

^aUniversity of Glasgow, Glasgow, G12 8QQ, UK

^bIstanbul Technical University, Istanbul, 34469, Turkey

*hsn.aleisa@gmail.com

Keywords: experimental, numerical, nonplanar, lambda wing, subsonic speed

1. INTRODUCTION

Nonplanar cranked lambda wing planform of moderate-aspect-ratio has been the subject of experimental and numerical investigations by academic collaboration between the University of Glasgow and Istanbul Technical University within the framework of the NATO AVT-SP-002 project titled "Turbulence and the Aerodynamic Optimization of Nonplanar Lifting Systems". The present study experimentally and computationally investigates the development of wing flows and their subsequent impact on flight mechanics performance for military aircraft configurations involving a specific near lambda flying-wing UCAV concept. Low-speed wind tunnel tests of the model are performed in the DeHavilland low-speed wind tunnel facility at the University of Glasgow. Furthermore, the model is also evaluated numerically using OpenFOAM 8.0. The complex flow structure, vortices formation, interaction, and breakdown behavior over the wing model were illustrated as how the angle of attack influences them. Finally, the flow topology was correlated with the aerodynamic loads to demonstrate how the flow structures affect the aerodynamic performance of the wing model. The flowfield analyzes were reported using post-processed figures.

2. CRANKED-LAMBDA WING MODEL

The fundamental geometric features of a highly swept flying wing model are an edge-aligned delta wing with large strakes (inboard wing) and a swept constant chord wing with nonplanar tapered wingtips (outboard wing) (Figure 1). Table 1 provides the geometrical specifications of the wing model used for the present study.

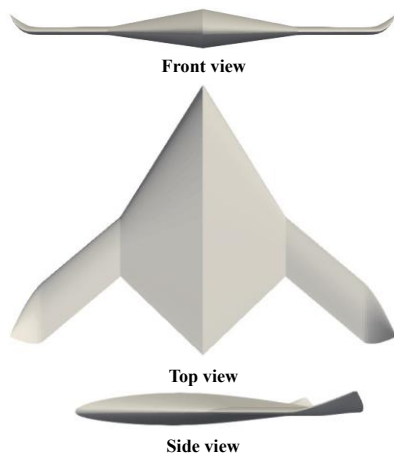


Table 1. Geometrical parameters

Parameter	Value
Wing Area, S m ²	0.145
Wingspan, b m	0.75
Aspect ratio, AR	3.879
LE inboard sweep angle, Λ_{LEI} °	58
LE outboard sweep angle, Λ_{LEO} °	40
TE sweep angle, Λ_{TE} °	40
Airfoil profile	NACA 64 ₁ 212

Figure 1. Nonplanar cranked lambda wing planforms

3. METHODOLOGY

The aerodynamic characteristics and flowfield of a nonplanar cranked lambda wing planform experimentally and computationally were investigated using deHavilland low-speed wind tunnel facility and OpenFOAM 8.0, respectively. The experimental test facility is a closed return atmospheric low-speed wind tunnel with a maximum speed of 70 m/s. The dimensions of the tunnel test section are 2.65 m × 2.1 m × 5.4 m. In this study, the wind tunnel free-stream velocity was adjusted to approximately 30 m/s, and the flow range of angle of attack (AOA) was from 0 to 40° with a step of 5° to measure aerodynamic loads using a six-component balance (Figure 2). Furthermore, the simpleFOAM solver and blockMesh + snappyHexMesh [Greenshields, 2020] are used for the flow analysis and flow domain discretization (Figure 3), respectively. The two-equation k- ω SST model was chosen for the closure of the turbulence.

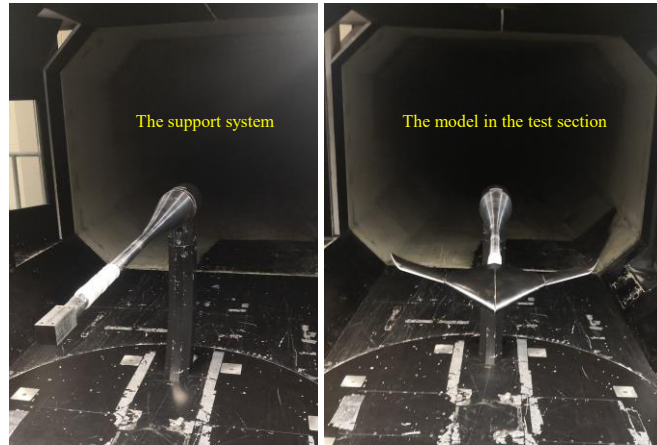


Figure 2. The support system and model in the wind tunnel test section

3. RESULTS AND DISCUSSION

Aerodynamic Coefficients

The aerodynamic characteristics of the UAV model were analyzed using various parameters such as coefficients of lift (C_L), drag (C_D), and pitching moment (C_{PM}) (Figure 3). As evident in the C_L plot, the lift increases nonlinearly, the C_L slope decreases with AOA due to flow separation for $AOA \approx 10^\circ$ and the stall occurs at a critical AOA ($\approx 35^\circ$). The C_D slowly increases for lower values of $AOA = 10^\circ$ and then rapidly increases because of flow separation. The C_{PM} curve is vulnerable to minor changes in the forces, and it can cause an unstable phenomenon such as a pitch-up or -break condition. The C_{PM} plot shows a pitch up occurs at 10° AOA, the plot increases up to 15° AOA and then decreases with an increase in AOA.

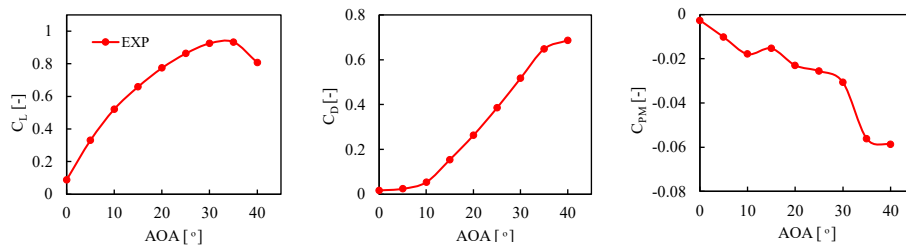


Figure 3. Aerodynamic characteristics of the UAV model from wind tunnel test.

Flowfield Analyses

Surface pressure distributions were computed along the non-dimensional chordwise distance at different spanwise locations (Figure 4) for selected moderate to high AOA values (10° , 15° , 20° and 25°) are provided in Figure 5. A small rise in the suction pressure occurs with an increase in AOA at station $Y = 0.50b$. At station $Y = 0.69b$ for 10° and 15° AOA, a higher suction is visible. However, a reduction in suction pressure is observable for 20° and 25° AOA. The C_p distribution for station $Y=0.90b$ provides the flow behavior near the wingtip area. A further comparison of the flow structure using the C_p distribution and wall shear streamlines on the upper surface of the model at various moderate to high AOA is shown in Figure 7.

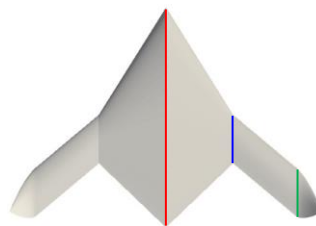


Figure 4. Location of spanwise slices for the model.

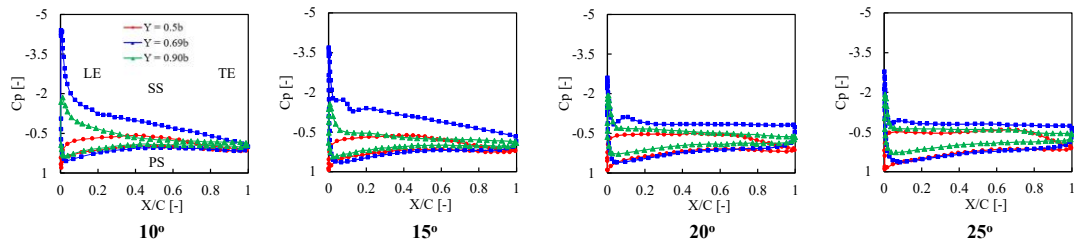


Figure 5. Cp distribution at different spanwise locations for various AOA.

The vortex flow was visualized using Cp with wall shear streamlines and iso-surface of the Q-criterion to explain the vortex flow behavior, such as evolution, attachment, separation, and vortex breakdown over the wing upper surface. Figures 6 show the flow structure behavior employing the Cp distribution and wall shear streamlines on the suction surface of the model at various moderate to high AOA. There is a higher suction zone on the leading edge with a medium suction intensity at the mid-outboard and the central part of the wing; however, the wing trailing edge reveals higher pressure at 10° AOA. The suction pressure area moves to the inboard wing, whereas most outboard wing suffers stall at 15° AOA. The suction pressure and the outboard vortex strength cut down, and the vortex breaks down at 20° AOA. On the other hand, the suction and inboard vortex strength rise, breaking down at AOA greater than 25°.

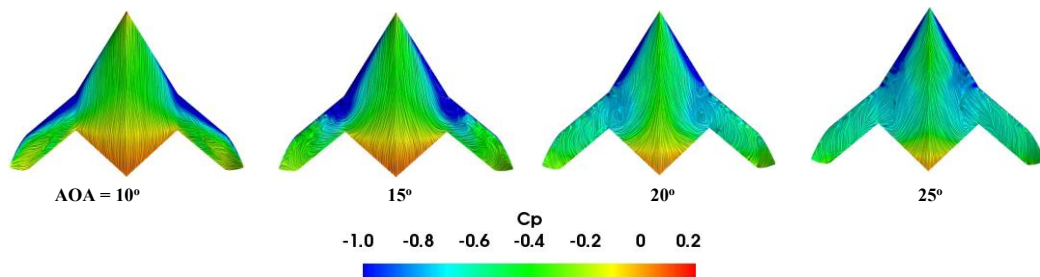


Figure 6. Cp distribution with wall shear streamlines for various AOA.

The Q-criterion colored by non-dimensionalized velocity was used to show the vortex body, regions, and separating from a shear layer over the wing model (Figure 7)—higher velocity magnitude at the leading edge at 10° AOA. The outboard vortex creation is detectable at 15° along the outboard section. With the rise of the AOA, the outboard leading edge vortices separate from the leading edge and shift downstream.

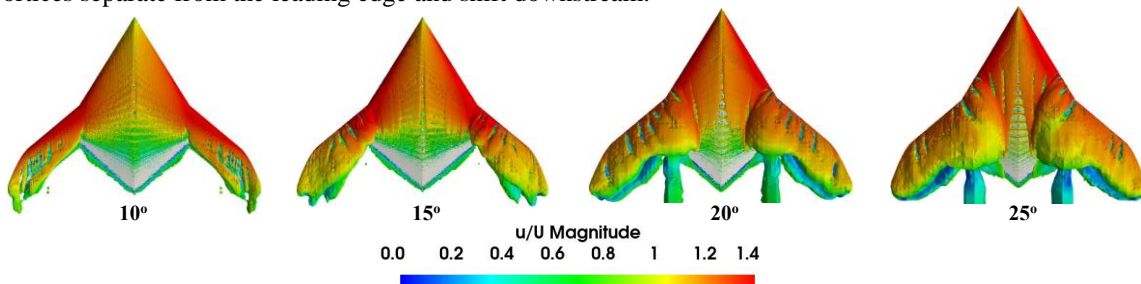


Figure 7. The iso-surface of Q criterion ($=35000 \text{ s}^{-2}$) colored by velocity magnitude for various AOA.

4. CONCLUSIONS

A combination of experimental and numerical investigations was performed to investigate the aerodynamic characteristics of a nonplanar cranked lambda wing configuration at various angles of attack. The leading edge vortex's aerodynamic features and the local suction pressure provide an additional lift in the form of a vortex lift. The vortex movement results in an overall nonlinear aerodynamic behavior. The wing model has undergone an unstable pitching moment characteristic at 10° AOA due to flow separation. This wing planform exhibits challenging aerodynamic behavior due to complex nonlinear flowfields such as mixed attached/separated flow, formation, interaction vortices, and vortex breakdown, impacting the aerodynamic stability and control significantly.

5. REFERENCES

Greenshields, C. J. OpenFOAM Version 8 User Guide, The OpenFOAM Foundation, London, UK 2020.

ANALYSIS OF THE STORAGE AND RELEASE OF THERMAL SOLAR ENERGY FOR THE PRODUCTION OF DOMESTIC HOT WATER USING ENCAPSULATED PCM

C Bianqui,^{a,*}, A Viedma^a, A Egea^a and A García^a

^a Universidad Politécnica de Cartagena, Departamento de Ingeniería Térmica y de Fluidos, Escuela Técnica Superior de Ingeniería Industrial. Campus Muralla del Mar, Calle Doctor Fleming, s/n, 30202 Cartagena, España.

*cristina.bianqui@edu.upct.es

Keywords: encapsulated PCM, thermal energy storage, solar systems efficiency, solar energy, domestic hot water

1. INTRODUCTION

In recent years, the importance of energy storage in solar thermal systems for domestic hot water (DHW) production has increased due to the intermittent nature of this kind of energy, making them less effective in adverse weather or at night. Thermal energy storage (TES) systems, particularly those using phase change materials (PCM), have been developed to enhance DHW system efficiency. Hybrid accumulators, which combine water and PCM, have been designed and manufactured, with the PCM encapsulated in containers. These systems are known for their easy manufacturing, quick DHW acquisition, suitability for domestic use, and cost-effectiveness. Hybrid accumulators commonly incorporate macroencapsulated PCM in a packed bed configuration.

In the literature, numerical studies have been found regarding hybrid packed bed accumulators. Veerappan et al. (2009) studied phase change processes of various PCMs in spherical capsules for a solar energy system. Experimental tests are rarely conducted. In the research group, the design and manufacturing of a hybrid accumulator with cylindrical capsules stainless-steel capsules have previously been done (Hernández Ballester, 2023). Paraffins with different melting points are chosen as PCM. The capsules are placed vertically, as shown in Fig. 1.

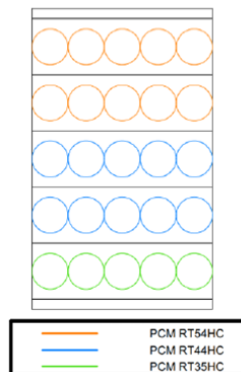


Figure 1. Scheme of hybrid accumulator developed by the research group (Hernández Ballester, 2023).

Beyond studies about accumulators, understanding the performance of individual capsules is crucial to comprehend the behavior and properties of encapsulated PCMs. An example is the study of Li et al. (2015), who experimentally examined the temperature field of paraffin inside a glass sphere using embedded thermocouples.

Given the limited experimental data on the behavior of encapsulated PCM, in this study melting and solidification tests are conducted on a cylindrical stainless-steel capsule intended for the storage and recovery of energy in DHW systems. The chosen PCM is the paraffin RT35 from Rubitherm. To analyze the processes, thermocouples are placed inside the capsules.

2. MATERIALS AND METHODS

Figure 2 shows the configuration of the capsule. It is a cylinder with a diameter of 60 mm and a height of 20 mm. It is filled with RT35 paraffin until its maximum volume, 40 cm³. Inside it, thermocouples are placed, arranged in a semicircular shape and also in its centre.

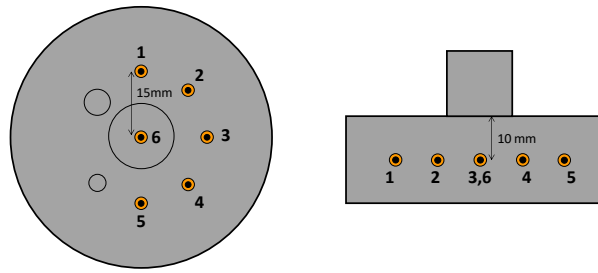


Figure 2. Configuration of the capsule.

Thermal properties of the paraffin RT35 are detailed in Table 1. The melting and solidification temperature ranges have been experimentally determined by DSC (Differential Scanning Calorimetry) analysis, as well as the heat storage capacity and the specific heat capacity. Solid density was measured with a helium stereopycnometer, while liquid density was obtained by measuring mass and volume values with a syringe.

Table 1. Thermal properties of the paraffin RT35.

Thermal characteristics [units]	Values
Melting temperature [°C]	32-38
Solidification temperature [°C]	34-27
Heat storage capacity [kJ/kg]	235
Specific heat capacity [kJ/(kg·K)]	1.9
Solid density at 25°C [kg/l]	0.88
Liquid density at 45 °C [kg/l]	0.79

The facility for conducting the tests is depicted in Fig. 3. On the one hand, the melting tests simulate the charging processes of the accumulator, when the energy is stored. First, the encapsulated PCM is placed in the cylindrical thermal bath, which is full of water at ambient temperature. Then, it is placed in the rectangular thermal bath, where water has been previously heated to 45 °C. On the other hand, solidification tests represent the opposite process. In other words, the capsule is preheated in the rectangular thermal bath until it reaches 45°C and then immersed in the other bath. In both cases, temperature values measured by the thermocouples inside the capsule are obtained by using the data acquisition system.

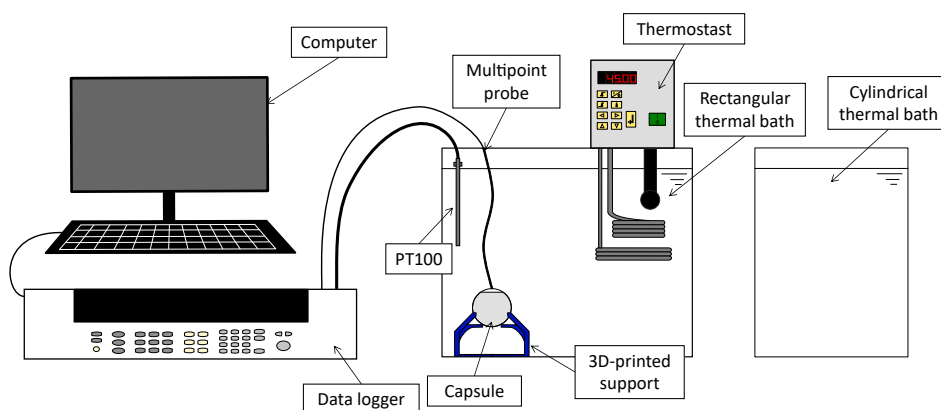


Figure 3. Facility for melting and solidification tests.

3. RESULTS

In Fig. 4, the results of the melting test of the encapsulated PCM are presented. It is observed how the PCM inside the capsule melts from the points in the upper area to the ones in the lower area. This is due to the lower density of the PCM in its liquid state, which accumulates at the top of the capsule. The total melting time is about 40 minutes.

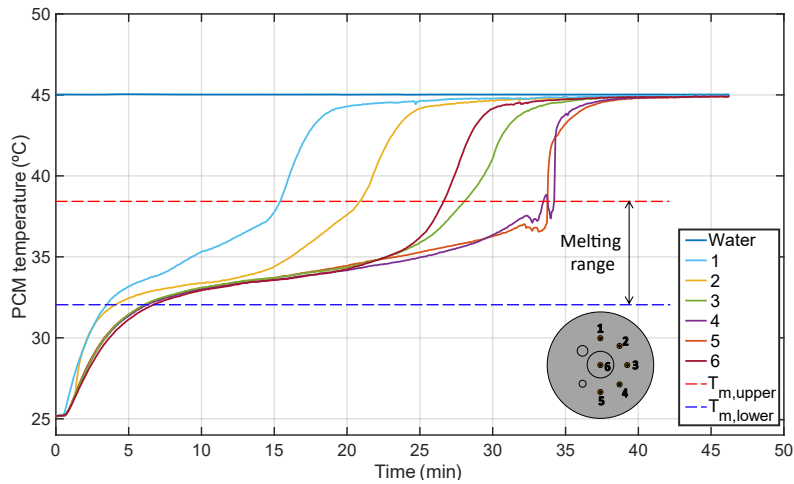


Figure 4. PCM temperature over time during the melting test at a constant water temperature.

The results of the solidification test are shown in Fig. 5. It is observed that the PCM at the measurement points solidifies at the same time approximately, instead of visualising a clear time gap between the different points as seen in the melting test. The total solidification time is around 45 minutes.

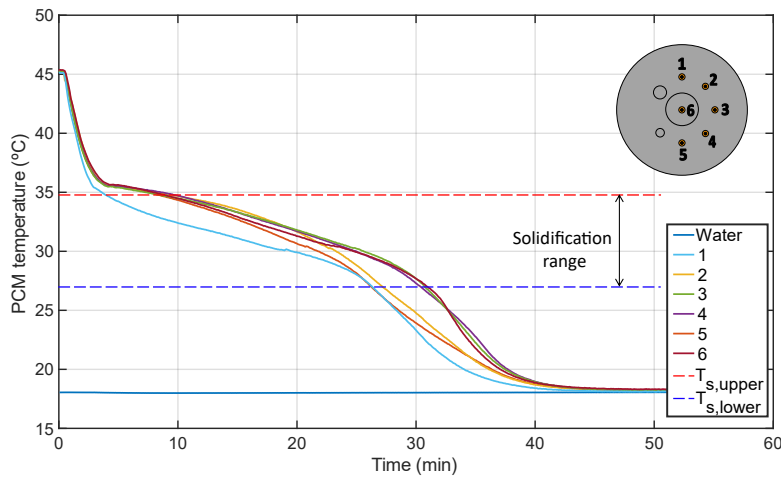


Figure 5. PCM temperature over time during the solidification test at a constant water temperature.

4. CONCLUSIONS

To optimize the storage and recovery of solar thermal energy in hybrid accumulators in DHW systems, it is essential to first understand the phase change processes of the encapsulated PCM. In this study, melting and solidification tests of the encapsulated PCM in a stainless-steel cylinder have been conducted. Thermocouples have been placed inside it in order to study the temperature field of the PCM. Subsequently, the temperature values over time have been graphically represented. In the melting tests, it is observed that the PCM melts from the top to the bottom of the encapsulation due to density differences between the solid and liquid states. During the solidification tests, the PCM temperature decreases almost simultaneously at all measurement points.

5. REFERENCES

- Veerappan, M., Kalaiselvam, S., Iniyan, S, and Goic, R., 2009. "Phase change characteristic study of spherical PCMs in solar energy storage", *Solar Energy*, vol. 83, pp. 1245-1252.
- Hernández Ballester, Marta, 2023. "Diseño, construcción y caracterización experimental de un prototipo de almacenamiento de energía térmica híbrido con material de cambio de fase encapsulado", Final Master Project. Repositorio UPCT.
- Li, W., Wang, Y.- H., and Kong, C.- C., 2015. "Experimental study on melting/solidification and thermal conductivity enhancement of phase change material inside a sphere", *International Communications in Heat and Mass Transfer*, vol. 68, pp. 276-282.

Effect of Characteristic Length on Natural-convection-driven Evaporation-based Solar Evaporators for Desalination Applications

Debartha Chatterjee, Umesh Madanan*, K. Muralidhar

Department of Mechanical Engineering, Indian Institute of Technology Kanpur, India

*umadhanan@iitk.ac.in

Keywords: Solar thermal desalination, interfacial vapor generation, characteristic length, natural convection

1. Introduction

Water stress is gradually becoming one of the most rapidly advancing global crises and is projected to affect more than 5.7 billion people by 2050. Cost-effective, potable, decentralized, small to medium-scale desalination technologies look promising for underdeveloped and remote locations. Photothermal-based interfacial solar-vapor generation systems, utilizing the idea of heat localization, have received tremendous attention from the perspective of desalination applications. Equation (1) below outlines the relevant parameters that must be tweaked for optimizing the performance of such systems (Vaartstra et al., 2020).

$$A\alpha q_{solar}'' = \dot{m}h_{lv} + A\varepsilon\sigma(T_{int}^4 - T_{\infty}^4) + Ah_a(T_{int} - T_{\infty}) + q_{cond} \quad (1)$$

where, A is the evaporating surface area, α is the solar absorptivity, q_{solar}'' is the solar influx, h_{lv} is the total enthalpy of phase change, ε is the emissivity of the evaporating surface, σ is the Boltzmann constant, T_{int} and T_{∞} are the evaporating surface temperature and bulk water temperature, respectively, and q_{cond} is the conduction heat loss into the bulk water. \dot{m} can be evaluated as $h_m(\rho_{w,s} - \rho_{w,a})$; where $\rho_{w,s}$ and $\rho_{w,a}$ are the densities of water vapor at the evaporating surface and the ambient air, respectively, and h_m is the mass transfer coefficient which can be obtained using Sherwood-Rayleigh relation (Zhang et al., 2021).

A majority of the studies reported in the literature have proposed novel photothermal-based materials having very high solar absorptivity (α) and heat localization strategies (minimizing q_{cond}) leading to high thermal efficiency. However, heat and mass transport coupling from such evaporators pose a serious constraint to the efficiency of vapor generation. Vapor transport resistance, which is a function of the effective boundary layer thickness (Vaartstra et al., 2020), is greatly influenced by the geometry of the evaporator. Any reduction in the evaporator size leads to a consequent decrease in the effective boundary layer thickness and, thereby, in the vapor transport resistance (Zhang et al., 2021). Some researchers have numerically analyzed and proposed innovative evaporator geometries that can yield thin effective boundary layer and, in turn, a reduced vapor transport resistance. The existing literature has generally employed a Sherwood-Rayleigh power-law relationship to predict evaporation rates for natural convection-driven evaporation (Bower and Saylor, 2009). However, these relationships are highly sensitive to operating conditions and the geometry of the evaporating surface (Poós and Varju, 2019). Moreover, all these power-law relationships have been developed considering evaporation from water bodies with a finite water depth. Such heated-from-below systems develop natural convection on the water-side owing to the presence of an unstable density stratification. This water-side convection influences the temperature of the evaporating surface and, in turn, the air-side natural convection and evaporation rate (Bower and Saylor, 2009). However, the configuration of photothermal-based interfacial solar-vapor generation systems is substantially different from those employed for developing the aforementioned power-law relationships. Such systems involve evaporation of water from porous structures (such as fabric, wicking materials, and foams), which typically offer an enhanced evaporation rate when compared to a normal surface due to thin film evaporation sites along their interface region. Furthermore, heat localization demands the depth of the evaporating surface to be much smaller than its width.

Based on the review of the existing literature, there are two areas which require further investigation: (i) a Sherwood-Rayleigh power-law relationship based on rigorous experiments under controlled environmental conditions to accurately predict the evaporation rate from photothermal-based interfacial solar-vapor generation systems and (ii) systematic experimental investigations under controlled environmental conditions that solely consider the effect of evaporator geometry on vapor generation efficiency. Therefore, the present study aims to bridge these gaps in the literature by investigating three different evaporator geometries (triangular, square, and circular) with similar projected areas inside a controlled environmental chamber (with varying far-field conditions) for different input heat fluxes (1000 W/m² to 4000 W/m²). Infrared thermography will be employed to measure the temperature of the evaporating surface. The experimentally obtained evaporation rate (measured using a digital weighing balance) will be non-dimensionalized and compared against the existing Sherwood-Rayleigh power-law relationships. Furthermore, a new Sherwood-Rayleigh power law relationship will be proposed, with modified coefficients, exponent values, and newly defined characteristic length, for better and more reliable prediction of evaporation rates for photothermal-based interfacial solar-vapor generation systems.

2. Experimental setup

The proposed investigations are carried out using a controlled environmental chamber, which can maintain a relative humidity range of 30 – 80% and a far-field ambient temperature range of 25 – 45°C. An IR transparent glass is used to facilitate the IR thermographic imaging of the evaporating surface. The temperature of the evaporating surface is used for computing the theoretical Sherwood number. A digital weighing balance (with continuous monitoring and data logging capability) is used for measuring the actual evaporation rate. Since the photothermal coating in such interfacial solar-vapor generation systems is meant to enhance the solar absorptivity (α) and solar-to-heat conversion, the heat and mass transport on the air side in such systems are independent of such coatings (Zhang et al., 2021). Also, decoupling of the vapor generation surface and the solar-absorbing surface is shown to have several practical advantages (Chatterjee et al., 2023). A controlled thermal bath is used to maintain a uniform and constant temperature boundary condition using aluminum heat sinks below the evaporating surface. A non-woven fabric, which is used as the wicking and evaporating test material, is hung from both ends of the heat sink with proper thermal insulation on the back end of the heat sink (see Fig. 1). This ensures that the transport phenomena of the evaporator configuration mimic that of a photothermal-based interfacial solar-vapor generation system. Three different evaporator geometries (as shown in Fig. 1) are used for the present study to understand the role of evaporating surface geometry on heat and mass transport.

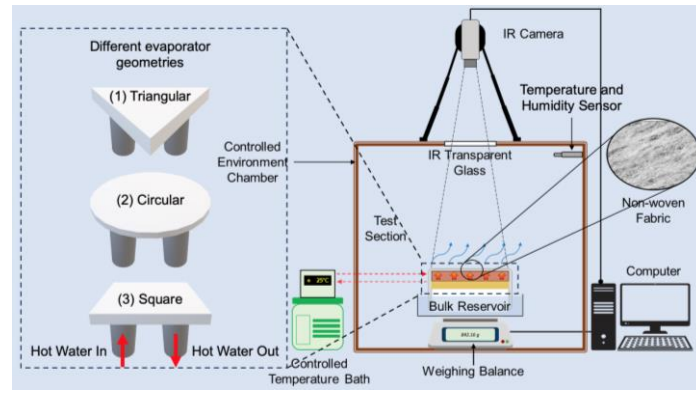


Figure 1. Schematic of the experimental setup and the different evaporator geometries employed in the present study

3. Data Reduction

$$(\eta) = \frac{\dot{m} \times h_{lv}}{q_{in}} \quad (3)$$

$$(h_{lv}) = h_{fg} + h_L \quad (4)$$

$$(h_{fg}) = 1.92 \times 10^6 \left[\frac{T_{Savg} + 273.15}{(T_{Savg} + 273.15) - 33.91} \right]^2 \quad (5)$$

$$(h_L) = c_p (T_{Savg} - T_W) \quad (6)$$

where, η is the solar-to-vapor conversion efficiency, h_{lv} is the total enthalpy of phase change, q_{in} is the input power density \dot{m} is the evaporation rate, c_p ($J/kg \cdot K$) is the specific heat of water, h_{fg} is the latent heat of phase change, h_L is the sensible heat of phase change, T_{Savg} ($^{\circ}C$) is the average temperature of the cotton cloth, T_W ($^{\circ}C$) is the bulk water temperature at the time of experiment (Zhang et al., 2021).

$$Sh = ARa^m Sc^n \quad (7)$$

The general power-law relationship between Sherwood number and Rayleigh number is given as: Equation (7). Where, A , m , and n are constants.

$$Ra = \frac{\Delta\rho_G L_c^3 g}{\nu_G \rho_G D_{LG}}, \quad \text{and} \quad Sh = \frac{h_m L_c}{D_{LG}}$$

Where, $\Delta\rho_G$ is the difference in density of the bulk environment (kg/m^3), ν is the kinematic viscosity (m^2/s), ρ_G is the density (kg/m^3), and D_{LG} is the diffusion coefficient of the bulk environment (m^2/s), where $L_c = A_e/\wp$ is the characteristic length (m), A_e is the evaporation area (m^2), \wp is the perimeter of the evaporating surface (m) (Goldstein et al., 1973).

3. Results and discussion

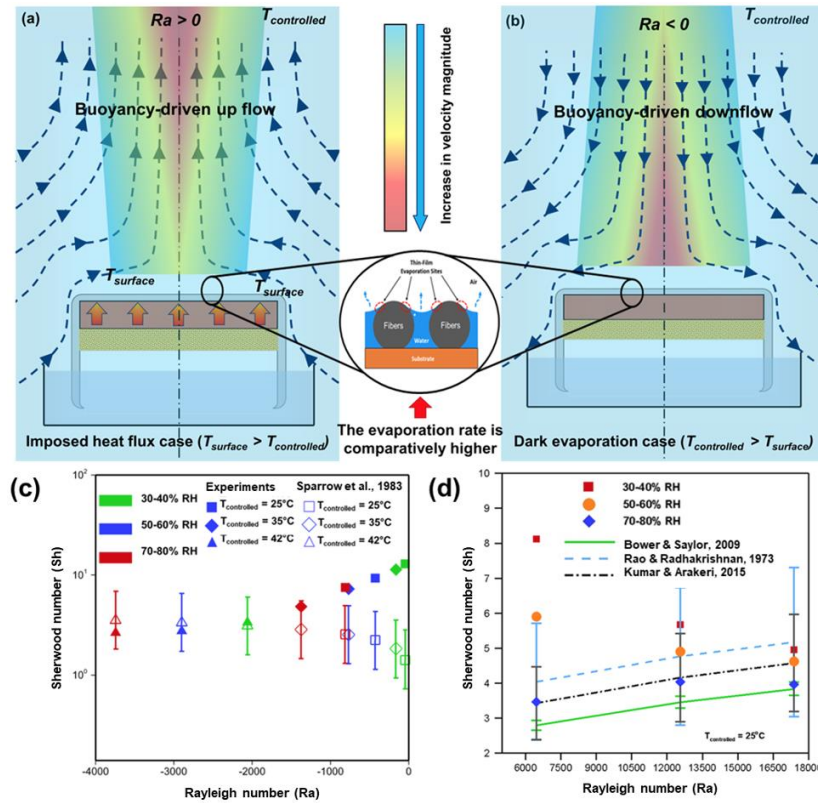


Figure 2. Schematic showing the transport process (buoyancy-driven up flow and down flow) in the air-side of the evaporator with (a) and without (b) imposed heat flux cases for the far-field conditions maintained in the present study.

Plot of Sherwood (Sh) number against Rayleigh (Ra) number: for dark evaporation case (c) for different far-field conditions and different ambient RH ranges viz. 30-40%, 50-60%, and 70-80% (d) and comparison with corresponding literature for a square geometry.

4. Conclusions

The present study investigates the evaporation rate for a square geometry under controlled environmental conditions. The effect of dark evaporation for different far-field ambient conditions and the impact of far-field ambient conditions on the evaporation rate for a square geometry for different input heat fluxes are reported in this paper. The experimentally-obtained evaporation rates, after converting to non-dimensional forms, are utilized for comparison against the existing Sherwood-Rayleigh correlations. Similar investigations will be carried out for triangular and circular geometries with varied projected evaporator areas and reported in the final paper.

5. References

- Bower, S. M., Saylor, J. R. 2009. A study of the Sherwood–Rayleigh relation for water undergoing natural convection-driven evaporation. *International Journal of Heat and Mass Transfer*, 52(13-14): 3055-3063.
- Chatterjee, D., Kulshrestha, T., Khandekar, S. 2023. Continuous vapor generation for thermal-desalination applications using a thermosyphon based heat localization strategy. *Desalination*, 555: 116492.
- Goldstein, R. J., Sparrow, E. M., Jones, D. C. 1973. Natural convection mass transfer adjacent to horizontal plates. *International Journal of Heat and Mass Transfer*, 16: 1025–1035.
- Kumar, N., Arakeri, J. H. 2015. Natural Convection Driven Evaporation from a water surface. In: *Proceedings of International Union of Theoretical and Applied Mechanics Symposium*, 15: 108-115.
- Poós, T., Varju, E. 2019. Review for prediction of evaporation rate at natural convection. *Heat and Mass Transfer*, 55: 1651-1660.
- Rao, V. K., Radhakrishnan, P. P. 1977. Evaporation of water from pools. *Journal of the Indian Institute of Science*, 59(3): 106.
- Sparrow, E.M, Kratz, G. K., Schuerger, M. J. 1983. Evaporation of water from a horizontal surface by natural convection, *Journal of Heat and Mass Transfer*, 105: 469–475.
- Vaartstra, G., Zhang, L., Lu, Z., Díaz-Marín, C. D., Grossman, J. C., Wang, E. N. 2020. Capillary-fed, thin film evaporation devices. *Journal of Applied Physics*, 128(13): 130901.
- Zhang, L., Xu, Z., Zhao, L., Bhatia, B., Zhong, Y., Gong, S., Wang, E. N. 2021. Passive, high-efficiency thermally-localized solar desalination. *Energy & Environmental Science*, 14(4): 1771-1793.

EXPERIMENTAL STUDY OF THERMAL-HYDRAULIC PERFORMANCE IN RECTANGULAR DUCT WITH WIRE COIL INSERTS AND NON-UNIFORM HEAT FLUX

F.Z. Benouis*, A. García, R. Herrero-Martín, A. Egea
Polytechnic university of Cartagena, Spain
*fatima,benouis@upct.es

Keywords: Heat transfer, pressure drop, rectangular duct, wire coil inserts, non-uniform heat flux.

1. INTRODUCTION

Heat transfer and fluid flow within channels or ducts constitute fundamental aspects across various engineering applications, including heat exchangers, chemical reactors, electronic systems, solar collectors, and power generation plants. This study addresses both the scientific and industrial aspects of this phenomenon, particularly focusing on the physical behavior of flow in rectangular ducts with wire coil inserts and understanding various flow patterns and their role in transitioning to turbulence.

Considering the varied shapes and designs of heat exchanger pipes customized for particular applications, extensive numerical and experimental investigations have been conducted on various pipe geometries to evaluate their impact on heat transfer. Prior research has examined flow behavior in rectangular ducts with corrugated surface [1-4], as well as ducts with triangular, trapezoidal, rhombic, and other cross-sectional geometries [5-6] However, there is limited literature available on the transition from laminar to turbulent flow within rectangular ducts, indicating a need for additional research and analysis in this area. While smooth tubes are common in most heat exchangers, the adoption of enhancement techniques has facilitated the development of more compact and efficient designs. Notably, the use of wire coils inserts, Feng et al. [7] underscore wire coil inserts as economically feasible enhancement methodologies. Numerous authors have investigated various coil geometries in circular section ducts aimed at enhancing heat transfer efficiency[8-9].

To the best of the authors knowledge, the utilization of wire coil inserts within a rectangular duct, subjected to non-uniform heat flux, has not been previously explored. This investigation has yielded promising results with significant implications for industrial applications.

2. EXPERIMENTAL SETUP

Performance assessments were carried out in a 2.5m long rectangular duct with dimensions of 25*10mm and 1mm thickness (1), under non-uniform heat flux conditions induced by a metal strip connected to a power supplier, generating a heat flux of 16666W/m². Figure 1. shows the test rig used in the current investigation. Water served as the working fluid, spanning a continuous range of Reynolds numbers from 500 to 10000, covering laminar, transition, and turbulent flow regimes comprehensively to facilitate accurate identification of various flow patterns. This flow is driven by a variable speed centrifugal pump (8) to the test section. The corresponding mass flow rate is regulated by an electro- valve (11) and measured with a Coriolis mass flow-meter (6). Pressure drop is acquired using differential pressure sensors (9-10) of different ranges to cover the full range. Two differential pressure transducers of different full scales are duly employed to assure the accuracy of the experiments. Inlet and outlet tube temperatures are measured by RTD Pt-100 sensors (3) and (4) to obtain fluid properties. Inlet fluid temperatures range from 40 °C to 60 °C were tested. All the experimental data are collected through an Agilent® data acquisition model 34980A.

For the heat transmission experiments, 6 sections were crafted at various length along the tube to ascertain the temperature distribution throughout its length, as illustrated in fig 2. In each of the 6 sections under investigation, 8 thermocouples were positioned according to the arrangement depicted in the same figure. The duct made of brass while wire inserts (3 coils) are of stainless-steel.

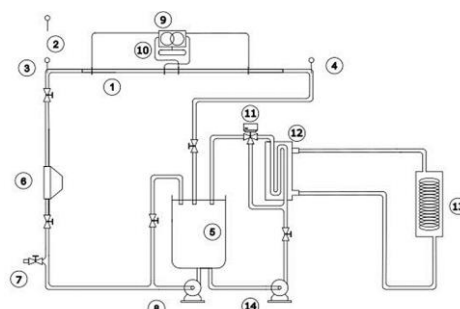


Figure 1. experimental setup.

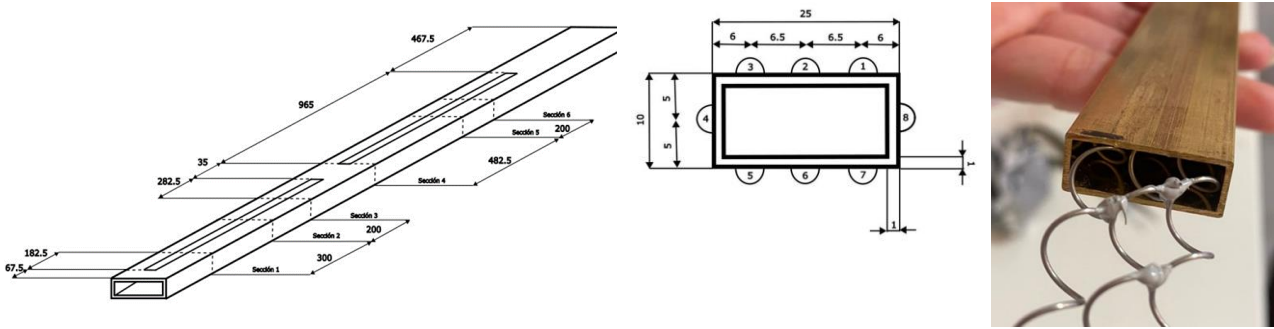


Figure 2. schematic of the test section with thermocouples position.

3. RESULTS AND DISCUSSION

Pressure drop tests

To validate the experimental procedure, isothermal flow tests were conducted to ascertain the friction factor for both empty tubes and tubes with wire coil inserts across Reynolds numbers ranging from 500 to 10000, covering laminar, transition and low turbulent flow regime. The experimental results are compared with the analytical solution for laminar flow $f_{LS} = 16/Re$ and the Blasius equation for turbulent flow $f_{TS} = 0.0791(Re^*)^{-0.25}$. Results are illustrated in Fig3. Three zones can be distinguished based on the trend of the data points: Zone 1 corresponds to the laminar regime, characterized by Reynolds numbers (Re) below 2000. In Zone 2, the transitional region is observed, spanning Reynolds numbers between 2000 and 2200. Finally, Zone 3 represents the turbulent regime, where Reynolds numbers exceed 2200. In the wire coil tests, denoted by the black diamonds, no discernible distinction was observed among the three zones, suggesting that turbulent flow prevailed across all tested Reynolds numbers owing to the presence of these elements. Moreover, the introduction of wire coil inserts resulted in a notable increase in pressure drop, ranging between 2 and 10 times higher compared to the configuration without such inserts.

$$f = \frac{\Delta P}{(2\rho v^2)(\frac{D_h}{L})} \quad (1)$$

$$Re^* = \frac{\rho v^* D_h}{\mu} \quad (2)$$

$$v^* = \frac{v}{(0.5\alpha)^{0.16}} \quad (3)$$

$$\alpha = \frac{width}{height} \quad (4)$$

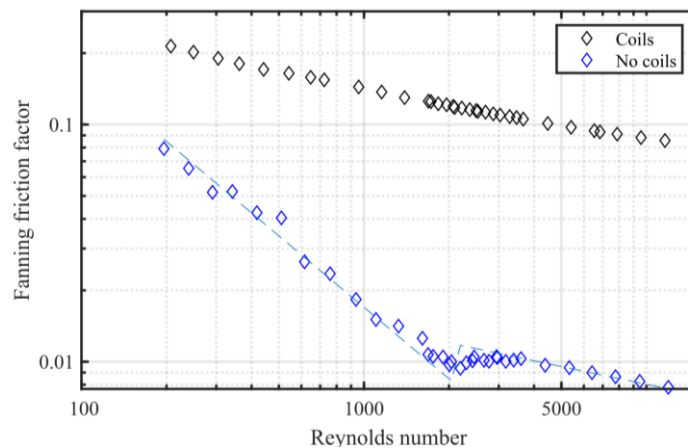


Figure 3. Friction factor results in the tube with and without wire-coil inserts.

Heat transfer tests

Figure 4. illustrates the temperature distribution along the metal strip across different sections. Furthermore, it presents the estimated fluid temperature in each section, as well as at the inlet and outlet temperatures. Despite minimal differences in fluid temperature, whether coils are inserted or not (depicted in red for the case without inserted elements and blue with inserted elements), a distinct advantage in wall temperature is observed in the presence of wire coils. When using

wire coils, wall temperatures decrease until they align with fluid temperatures, demonstrating maximum cooling potential. It is noteworthy that fluid temperature variations do not follow a linear trend due to non-uniform distances between sections (Figure 2).

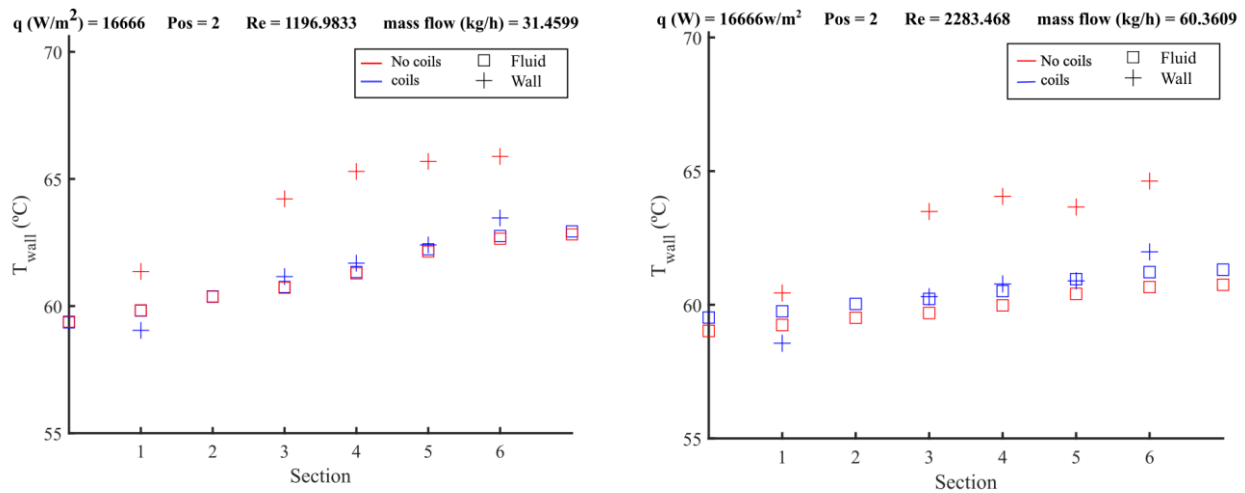


Figure 4. Temperature distribution at position 2 for different sections and for two different Reynolds numbers.

4. CONCLUSIONS

A preliminary characterization of heat transfer in the geometry has been performed, and pressure drop in the geometry with the acquired inserted elements has been analyzed. wire-coils show better performance as an enhancement passive technique in tube heat exchanger applications $Re = [500-10000]$. Although the insertion of elements in the tube resulted in a notably higher pressure drop, particularly evident at higher flow rates, the observed values remained relatively low, typically below 10 mbar for Reynolds numbers below 2000. It is worth noting that these pressure drop values pertain solely to the test section, representing a small proportion compared to the total system losses. Consequently, it can be inferred that at elevated flow rates, the overall pressure drop would be substantially higher. Conversely, at lower flow rates where the total system experiences reduced pressure drop, the enhanced heat transfer facilitated by the insertion of elements becomes more advantageous. These findings underscore the substantial decrease in wall temperature, approximately 4 degrees lower compared to configurations lacking coil inserts, thus emphasizing the efficacy of coil integration in augmenting heat transfer efficiency.

5. REFERENCES

- [1] E. A. M. Elshafei, M. M. Awad, E. El-Negiry, and A. G. Ali, "Heat transfer and pressure drop in corrugated channels," *Energy*, vol. 35, no. 1, pp. 101–110, Jan. 2010, doi: 10.1016/j.energy.2009.08.031.
- [2] E. A. M. Elshafei, M. M. Awad, E. El-Negiry, and A. G. Ali, "Heat transfer and pressure drop in corrugated channels," *Energy*, vol. 35, no. 1, pp. 101–110, Jan. 2010, doi: 10.1016/j.energy.2009.08.031.
- [3] P. Naphon, "Laminar convective heat transfer and pressure drop in the corrugated channels," *International Communications in Heat and Mass Transfer*, vol. 34, no. 1, pp. 62–71, Jan. 2007, doi: 10.1016/j.icheatmasstransfer.2006.09.003.
- [4] S. Zahran, A. A. Sultan, M. Bekheit, and M. R. Elmarghany, "Heat transfer augmentation through rectangular cross section duct with one corrugated surface: An experimental and numerical study," *Case Studies in Thermal Engineering*, vol. 36, Aug. 2022, doi: 10.1016/j.csite.2022.102252.
- [5] H. H. Ting and S. S. Hou, "Numerical study of laminar flow and convective heat transfer utilizing nanofluids in equilateral triangular ducts with constant heat flux," *Materials*, vol. 9, no. 7, 2016, doi: 10.3390/MA9070576.
- [6] M. Khoshvaght-Aliabadi, S. E. H. Rad, and F. Hormozi, "Al₂O₃-water nanofluid inside wavy mini-channel with different cross-sections," *J Taiwan Inst Chem Eng*, vol. 58, pp. 8–18, Jan. 2016, doi: 10.1016/j.jtice.2015.05.029.
- [7] Z. Feng, X. Luo, F. Guo, H. Li, and J. Zhang, "Numerical investigation on laminar flow and heat transfer in rectangular microchannel heat sink with wire coil inserts," *Appl Therm Eng*, vol. 116, pp. 597–609, 2017, doi: 10.1016/j.applthermaleng.2017.01.091.
- [8] Z. Feng *et al.*, "Combined influence of rectangular wire coil and twisted tape on flow and heat transfer characteristics in square mini-channels," *Int J Heat Mass Transf*, vol. 205, May 2023, doi: 10.1016/j.ijheatmasstransfer.2023.123866.
- [9] Z. Feng *et al.*, "Hydrothermal and energy-saving performances in a mini-channel heat sink under different wire coil inserts induced swirling flow," *Int J Heat Mass Transf*, vol. 216, Dec. 2023, doi: 10.1016/j.ijheatmasstransfer.2023.124515.

EFFECTS OF THE NOZZLE EXIT SECTION SHAPE ON THE VELOCITY FIELD AND HEAT TRANSFER OF IMPINGING SYNTHETIC JETS

G. Longobardo^{a*}, G. Paolillo^a, T. Astarita^a, G. Cardone^a, C. S. Greco^a
Dept. of Industrial Engineering, University of Naples “Federico II”, Napoli, Italy
*giosue.longobardo@unina.it

Keywords: synthetic jets, particle image velocimetry, infrared thermography

1. INTRODUCTION

Impinging synthetic jets (SJs) have proven to be an effective and reliable alternative to continuous jets for surface cooling, while simultaneously arousing researcher’s interest both in the fluid dynamics community as well as in the heat and mass transfer community. Crucial benefits are associated with SJs if compared to continuous jets: the simplicity of the design allows for reduced dimensions and high reliability. In fact, a SJ is produced by the periodic and controlled oscillation of an actuator (e.g., as actuator it could be used the diaphragm of a loudspeaker, like in the present work, or a piezoelectric membrane or even an alternating piston) placed inside a cavity provided with an opening (Carlomagno *et al.* 2014, Bhapkar *et al.* 2014, Valiorgue *et al.* 2009, Chaudhari *et al.* 2010, Greco *et al.* 2014). A key aspect of the working principle of SJs is that the jet is generated starting from a quiescent ambient fluid with zero net mass flux across the opening, that is why sometimes they are also referred to as zero net mass flux (ZNMF) jets. The core mechanism for the generation of such ZNMF jets is the periodic oscillation of pressure within the cavity, driven by the periodic movement of the actuator. Such alternating pressure field in turn produces alternating phases of suction/ejection from the opening of the cavity. During the ejection phase, vortices form due to the flow separation at the exit of the orifice/nozzle, which then propagate downstream under their self-induced velocity. The working conditions of the SJ are identified by two dimensionless parameters: the Reynolds number, $Re = U_0 D / \nu$, and the Strouhal number, $Sr = f D / U_0$, where U_0 is a characteristic velocity scale (generally related to the volume flow rate during the ejection phase), D is the exit section diameter, ν the kinematic viscosity of air and f the operating frequency. In the current work the authors are interested in investigating the behavior of impinging SJs, therefore it is appropriate to introduce an additional operating parameter: the non-dimensional impingement distance, H/D , with H being the exit section-to-plate distance. The effects of Re , Sr , H/D have been intensively investigated over the course of the last decade, like in Greco *et al.* (2014) and in Greco *et al.* (2017), both in terms flow structure of the jet as well as in terms of heat transfer capabilities of the different configurations. Additional work has been done to leverage the potentiality of such devices by developing innovative configurations to further increase heat transfer capabilities and to reduce the acoustic signature of the device. On the topic, Chaudhari *et al.* (2010) paved the way for such innovative configurations, suggesting that the modification of the orifice/exit section shape of the nozzle may play a significant role in defining the performance of SJ. Their work focused on the performance assessment of different exit section shapes at multiple nozzle-to-plate distances and proved that for $H/D > 5$ the square orifice is more effective than the rectangular or the circular one. While at smaller nozzle-to-plate distances, $3 < H/D < 5$, the circular nozzle proved to be the most effective. Further work on exit section shapes was done by Bhapkar *et al.* (2014), which proved that at short impingement distances, the shape to be preferred is the elliptical one, outputting even better performances than the square orifice. While Jeyalingam and Jabbal (2016) found that lobed orifices are able to reduce broadband noise over mid to high frequencies when compared to circular orifices.

2. EXPERIMENTAL SETUP

The current work focuses on the effects of the exit section shape on the velocity flow field as well as the heat transfer capabilities of impinging SJs. As previously mentioned, the chosen actuator for the SJ consists of a loudspeaker oscillating inside a cavity with an orifice fitted with interchangeable nozzles, all with a fixed circular entry section and a different exit section shape. To keep the dimensionless parameters constant among different nozzle geometries, the hydraulic diameter has been fixed to 20mm for every case. The experimental campaign focuses on four different exit section shapes (in addition to the circular one): the square, the triangle, the rectangle with aspect ratio 2:1, the rectangle with aspect ratio 4:1, which are presented in Figure 1. The experimental setup, shown in Figure 2, is set to perform both velocimetry and heat transfer measurements. More specifically, a planar Particle Image Velocimetry (PIV) setup has been developed to capture the flow field produced by the synthetic jet in terms of both its time-averaged as well as its phase-averaged evolution. To characterize the heat transfer performance of the configuration, the 2D distribution of the convective heat transfer coefficient h is measured on the plate via infrared (IR) thermography and the heated thin foil sensor. The mentioned plate consists of a rectangular 50 μ m thick constantan foil. The foil is steadily and uniformly heated by applying

a voltage difference, provided by a stabilized DC power supply, to the edges of the plate (*i.e.*, by means of Joule heating). One side of foil the is cooled by the impinging SJ, while the other one is imaged by an IR camera. The same side seen by the IR camera is coated with a thin film of black paint with high emissivity. The previously mentioned convective heat transfer coefficient is then computed enforcing a local steady energy balance.

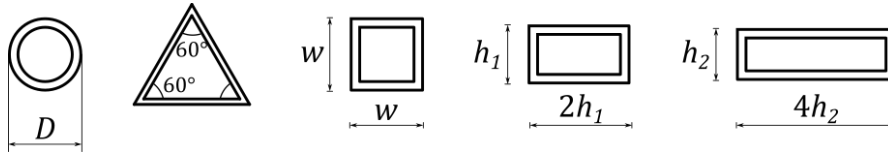


Figure 1 - Shapes of the synthetic jet nozzle exit section investigated in the current work.

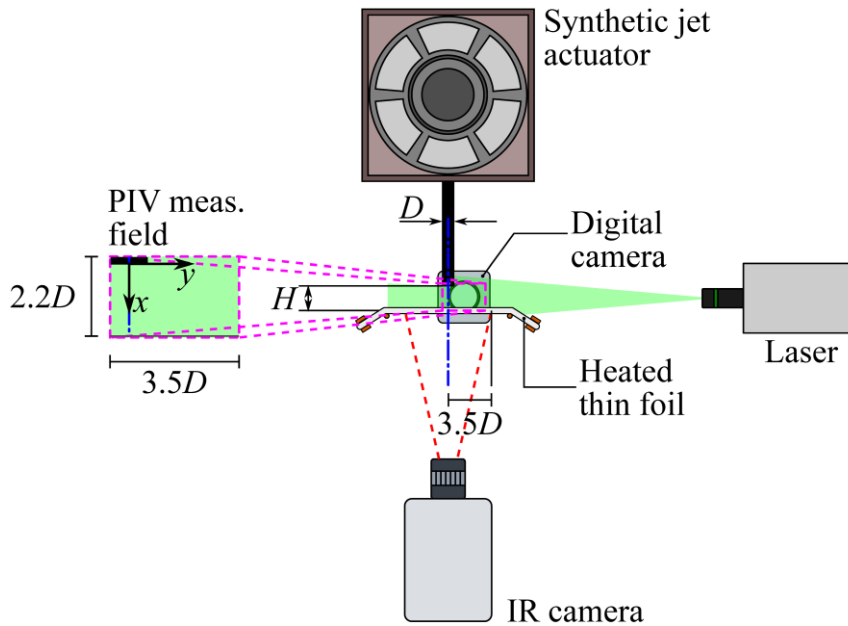


Figure 2 - Schematic of the experimental apparatus.

3. RESULTS

At the current stage, preliminary measurements have been made on the baseline exit section nozzle shape configuration, *i.e.*, the circular one. Figure 3 shows the evolution of the phase averaged PIV flow fields for the baseline configuration with $Re = 3000$, $Sr = 0.062$ and $H/D = 2$. The middle-top subfigure ($\varphi = 36^\circ$) in Figure 3 shows the buildup of the large-scale vortex which drives the ejection phase, such large-scale vortex is convected downstream, impinges onto the plate, spreads across the plate and then finally propagates outside the PIV field of view. The combination of the Reynolds and Strouhal number, as well as the nozzle-to-plate distance selected, produces the so-called trailing jet configuration, *i.e.*, a column of fluid that follows the vortex, characterized by relatively high velocities. On the other hand, the suction phase can be identified with the displacement of the saddle point from approximately $0.5D$ from the impingement plate back to the exit section with low velocities near the wall.

Since the evolution of the mentioned large-scale vortices is greatly influenced by the shape of the exit section, in the final work, a systematic analysis of the SJ performance is carried out comparing the different exit section shapes. The final goal would be to elucidate on the core mechanisms responsible for the increase/decrease in heat transfer performance among different geometries and provide a better understanding of the complex fluid dynamics involved, by combining velocimetry as well as heat transfer measurements.

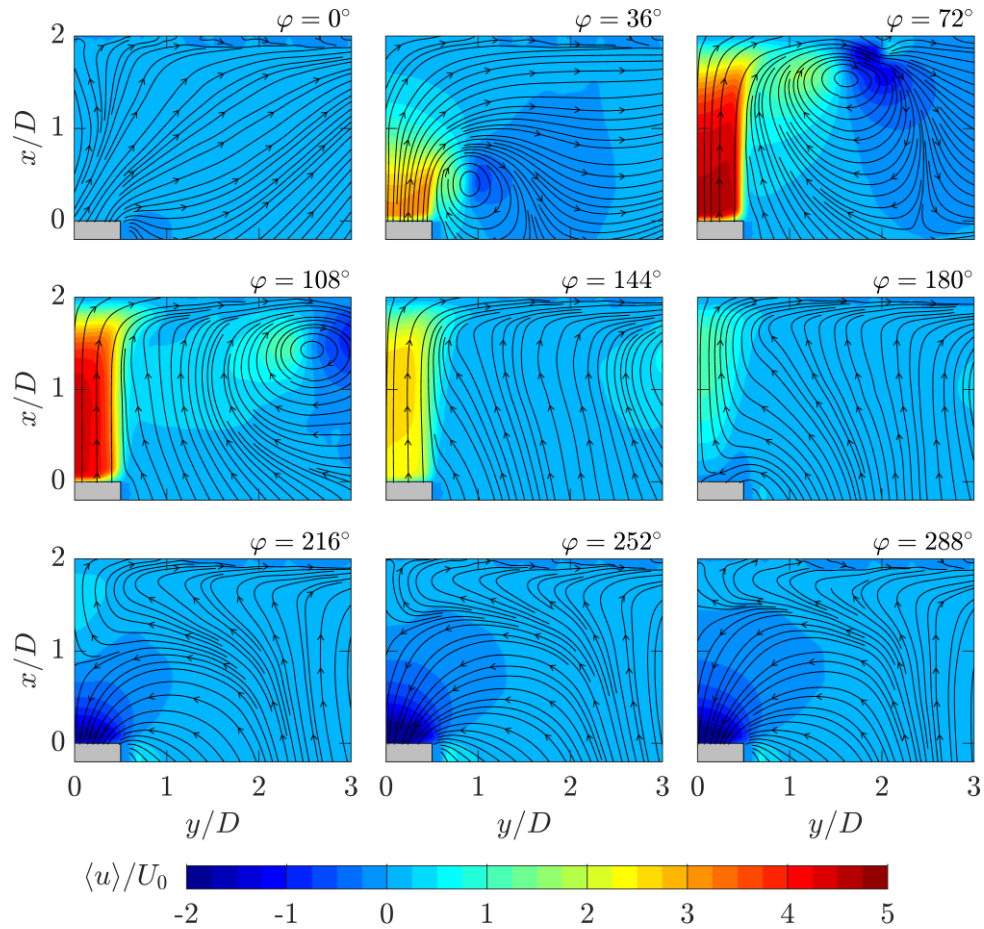


Figure 3 - Evolution of the phase-averaged velocity field for a synthetic jet issuing from a circular nozzle with $St=0.062$, $Re = 3000$ and $H/D = 2$. Maps of the axial velocity with 2D streamlines superimposed.

4. REFERENCES

- Bhaskar, U. S., Srivastava, A., & Agrawal, A., 2014. "Acoustic and heat transfer characteristics of an impinging elliptical synthetic jet generated by acoustic actuator". *International Journal of Heat and Mass Transfer*, 79, 12-23.
- Carlomagno, G. M., & Ianiro, A., 2014. "Thermo-fluid-dynamics of submerged jets impinging at short nozzle-to-plate distance: a review". *Experimental Thermal and Fluid science*, 58, 15-35.
- Celata, G.P. and Zummo, G., 2009. "Flow boiling heat transfer in microgravity: Recent progress". *Multiphase Science and Technology*, Vol. 21, pp. 187–212.
- Chaudhari, M., Puranik, B., & Agrawal, A., 2010. "Heat transfer characteristics of synthetic jet impingement cooling". *International Journal of Heat and Mass Transfer*, 53(5-6), 1057-1069.
- Greco, C. S., Ianiro, A., & Cardone, G., 2014. "Time and phase average heat transfer in single and twin circular synthetic impinging air jets". *International Journal of Heat and Mass Transfer*, 73, 776-788.
- Greco, C. S., Cardone, G., & Soria, J., 2017. "On the behaviour of impinging zero-net-mass-flux jets." *Journal of Fluid Mechanics*, 810, 25-59.
- Jeyalingam, J., & Jabbar, M., 2016. "Optimization of synthetic jet actuator design for noise reduction and velocity enhancement". *Proceedings of 8th AIAA Flow Control Conference* (p. 4236).
- Valiorgue, P., Persoons, T., McGuinn, A., & Murray, D. B., 2009. "Heat transfer mechanisms in an impinging synthetic jet for a small jet-to-surface spacing". *Experimental Thermal and Fluid Science*, 33(4), 597-603.

Interaction of Incident shock and compressible vortex ring with a grooved cone mounted on a flat plate with a coaxial hole

Amar Yadav^{a,*}, Pawan Kumar Karn^{b,*}, Debopam Das^{a,b}

^aDepartment of Aerospace Engineering, Indian Institute of Technology, Kanpur

^bDepartment of Sustainable Energy Engineering, Indian Institute of Technology, Kanpur

*Amar Yadav: amary20@iitk.ac.in; Pawan Kumar Karn: pkkarn@iitk.ac.in

Keywords: Compressible vortex ring, Grooved cone, Wine Glass Shock structure, Tent Shock

A compressible vortex ring is generated at the exit of the open shock tube for a starting jet. Thangadurai (2008) and Dora et al.(2014) did extensive experiments and numerical simulations to characterize the compressible vortex ring. The interaction of Incident Shock (IS) and compressible vortex ring (Primary vortex ring, PVR) with a body provides many interesting flow phenomena. In the past many researchers did experiments and numerical simulations for the shock-body interaction and shock-vortex-body interaction. Most of the researchers used solid walls, perforated wedges and walls, and a solid cone mounted on a plate. Thangadurai (2008), Thangadurai and Das (2012) conducted experiments on PVR interacting with a solid wall positioned perpendicular to the jet axis and they described the ramification of the flow due to reflected shock and lift-off phenomena of the vortex rings. Lamont and Hunt (1976) investigated the individual interaction of impinging axisymmetric supersonic jets on three different symmetric triangular wedges. Centerline Mach number, wedge angle, jet shock strength and distance between nozzle and wedge, affect the flow pattern formed near the wedge. Mehta and Prasad (1997) did the experiments and numerical simulation for supersonic jet impinging on axisymmetric deflector and they observed vortex formation near the vicinity of the deflector. Nuvvula (2022) and Nuvvula et al. (2021) did the numerical simulation on a solid cone mounted on a flat plate to minimise the ramification effect of reflected shock and reported some new flow structures like Tent shock and corrugated Mach disk. Nuvvula et al. (2022) conducted shadowgraph experiments to validate their numerical observations.

Skews and Takayama (1996) performed schlieren experiments for the incident shock moving over a perforated plate. The IS diffracts at the perforation corners forming expansion waves and vortex ring inside the perforation. Skews (2005) demonstrated that the maximum stagnation pressure loss across the perforated plate occurs when the blockage ratio and Mach number are maximum, and the wall angle is minimum. Yadav et al. (2023) performed numerical simulations on a perforated axisymmetric cone mounted on a flat plate and firstly, reported a new shock structure formation named Wine Glass shock structure and secondly, reported a decrement in overall average pressure as compared to an axisymmetric solid cone case mounted on a flat plate.

In the present study, we investigate the interaction process of an incident shock (IS) and compressible vortex ring with a grooved axisymmetric cone mounted on a flat plate with different coaxial plate hole sizes. The plate has a coaxial hole, allowing the air from the grooves to go outside.

The numerical simulations are performed using commercial software ANSYS Fluent. Numerical setup is given in “Figure 1” along with the dimensions and boundary conditions. Axisymmetric, 2-D, transient laminar flow conditions and AUSM+ scheme along with explicit time stepping are adapted to perform the numerical simulation. Structured Mesh is prepared using the ANSYS Meshing tool. Air is used as the working fluid. The pressure ratio of the driver to driven section is kept at 8.85 such as to obtain an exit Shock speed of Mach number 1.57.

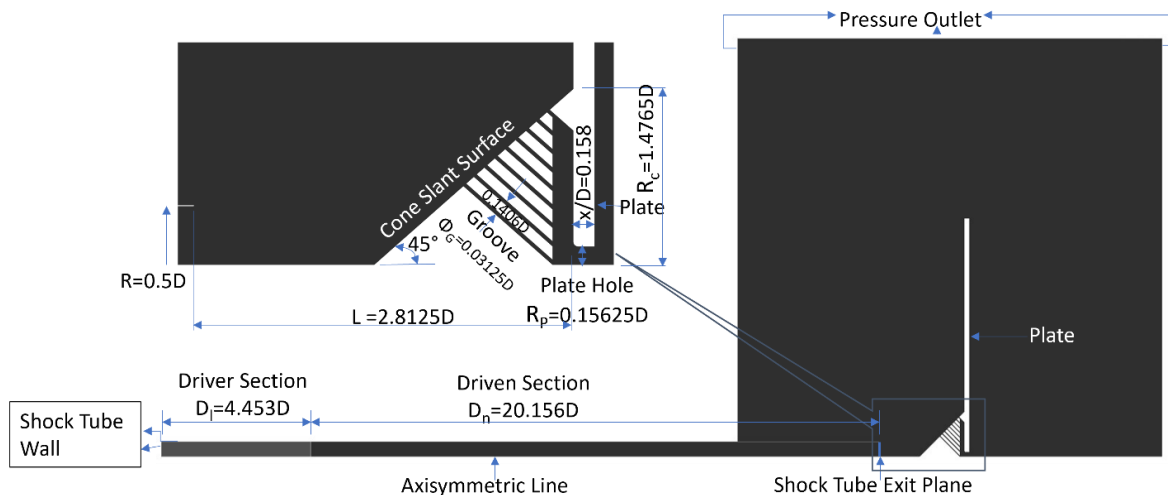


Figure 1. Numerical setup.

Three different plate hole radii are considered, i.e. $0.15625D$, $0.3125D$, and $1.1269D$, by keeping other dimensions fixed. When the IS comes out of the shock tube exit, it diffracts, and the flow behind the IS forms a compressible vortex ring (also named primary vortex ring, PVR).

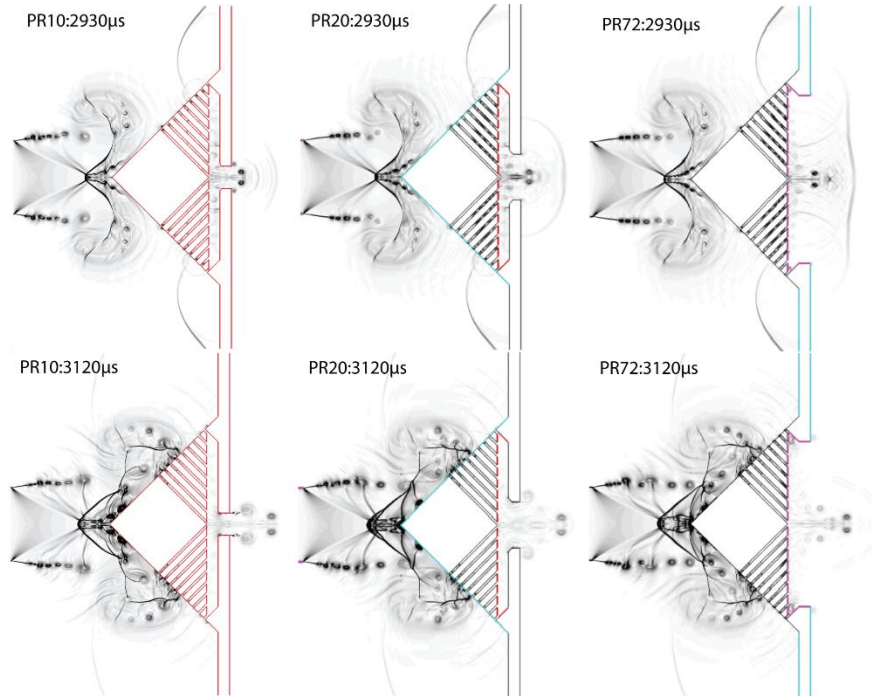


Figure 2. Numerical schlieren for Plate holes 10, 20, and 72.1248 mm radius.

The diffraction process, formation of PVR, embedded shock (ES), Mach disk (MD), counter-rotating vortex ring (CRVR) and jet shear layer vortices are well studied by Dora et al. (2014) and Thangadurai (2008). As the IS interacts with the cone, it reflects as regular reflection (RR) which is named as primary reflection (PR). The IS moves along the cone surface and its incidence angle changes with respect to the reflection point and the RR changes to Mach reflection (MR); Nuvvula et al.(2021). Meanwhile, the PR interacts with the PVR and MD. The outer periphery destabilizes forming vortices as it interacts. PR is absorbed by the MD, which corrugates the MD (Nuvvula et al.2022). When the IS passes over the grooves, it diffracts at the groove corners and expansion waves at each corner, which move upstream of the flow, and vortex at the corner inside the groove (Skew and Takayama 1996, Yadav et al.2023). The IS reflects from the flat plate as secondary reflection (SR), which moves along the cone surface and further shock goes through MR to RR at the flat plate. In the meantime, when the IS diffracts from the groove corner and it moves all along the length of the groove length. Further, it diffracts at the exit of the groove and starts reflecting from the plate. The compression waves move through the groove towards the upper surface of the cone and as they come out of the groove, they diffract and interact with the SR. This interaction forms a new shock structure, Wine Glass Shock (WGS) structure, see Figure 2 at $2930\mu\text{s}$ (PR10, PR20). This shock structure predominantly depends on the plate hole diameter. When the backside plate is removed, WGS does not form since there is no reflecting compression wave travelling towards the upper surface, see Figure 2 at $2930\mu\text{s}$ (PR72). With time, WGS disintegrates, and SR starts interacting with the PVR. The part of SR between PVR and cone surface separates from the rest of SR, forming a secondary embedded shock (SES). The SES, ES, and MD combined form a shock structure named Tent Shock (TS) sitting at the apex of the cone (Nuvvula et al. 2021, Nuvvula et al. 2022); see Figure 2 at $3120\mu\text{s}$ (PR10, PR20, PR72). Here, the orientation of SES is slightly different as compared to the solid cone mounted on the flat plate case because of the presence of shear layer vortices, and also, the flow is at some angle at the groove inlet. It is also observed that plate hole radius also affects the merging of shear layer vortices (SLV). SLVs start merging much earlier than the others for lower plate hole radius. More distinct SLVs are observed for higher plate hole radii. The pressure plot (Figure 3b) shows a similar trend but with relatively decreased pressure till the TS disintegration and when the PVR reaches the flat plate and starts moving radially. As the PVR lifts-off, the flow between the PVR and the cone surface becomes locally supersonic forming multiple shocklets. Similarly, as the PVR moved away from the cone and the flat plate, SLVs moved over the cone surface forming shocklets which move towards the cone-plate junction resulting in large pressure fluctuations (Figure 3b). Figure (3a) shows the overall average pressure trend at different points of the cone and flat plate for all three sizes of plate hole cases. Till point 3 (Pt3, between groove 5 and groove 6; w.r.t. cone apex),

the overall pressure decreases, and after that, till cone-plate junction (Pt6), the overall pressure increases. The case PR72 shows a very distinct feature as shown in Figure 3(a), i.e. it is minimum at Pt3 but increases to a maximum at Pt6 thus predicting an optimal radius case between PR20 and PR 72. We will present a detailed analysis in future.

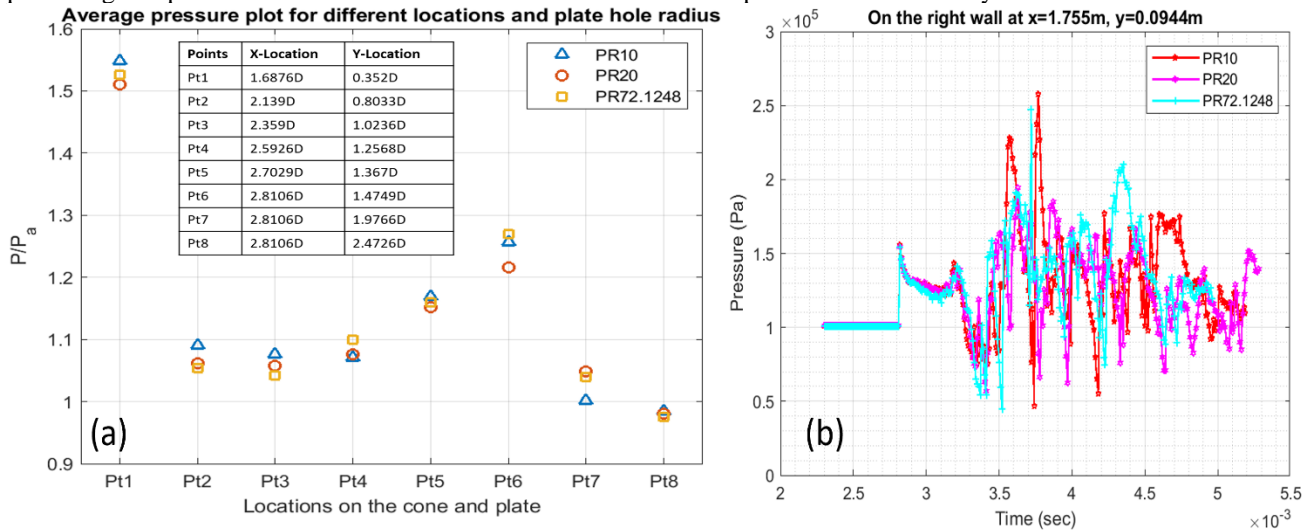


Figure 3. (a) Overall average pressure at different points on the cone and flat plate. Distances are with respect to the shock tube exit. (b) Pressure vs time plot at the cone-plate junction point.

References:

- Dora, C.L., Thangadurai, M., De, S., Das, D., 2014. "Role of slipstream instability in formation of counter-rotating vortex rings ahead of a compressible vortex ring". *Journal of Fluid Mechanics*, Vol. 753, pp. 29–48.
- Lamont, P.J., Hunt, B.L., 1976. "The impingement of underexpanded axisymmetric jets on wedges". *Journal of Fluid Mechanics*, Vol. 76, pp. 307-336.
- Mehta, R.C., Prasad, J.K., 1997. "Flow structure of a supersonic jet impinging on an axisymmetric deflector". *Indian Journal of Engineering and Materials Sciences*, Vol. 4(5), pp.178-188.
- Nuvvula, P.K., Javed, M., Thangadurai, M., Das, D., 2021. "Video: Story of shock-vortex interaction during compressible vortex ring and trailing jet impingement on a cone". 74th Annual Meeting of the APS Division of Fluid Dynamics-Gallery of Fluid Motion. American Physical Society.
- Nuvvula, P.K., 2022. *Compressible vortex ring interaction with a cone mounted on a flat plate*. M.Tech. thesis, Indian Institute of Technology, Kanpur, India.
- Nuvvula, P.K., Yadav, A., Karn, P.K., Rajan, R., Javed, M., Das, D., 2022. "Experiments on Compressible Vortex Ring Interaction with a Cone Mounted on a Flat Plate". *Fluid Mechanics and Fluid Power, Select Proceedings of FMFP 2022*, Vol. 2, pp. 739-745, DOI:10.1007/978-981-99-5752-1.
- Skews, B.W., Takayama, K., 1996. "Flow through a permeable surface due to shock wave impact". *Journal of Fluid Mechanics*, Vol. 314, pp. 27–52.
- Skews, B.W., 2005. "Shock wave interaction with porous plates". *Experiments in Fluids*, Vol.39, pp.875–884.
- Thangadurai, M., 2008. *Flow and acoustic characteristics of high mach number vortex rings during evolution and wall-interaction: an experimental investigation*. Ph.D. thesis, Indian Institute of Technology, Kanpur, India.
- Thangadurai, M., Das, D., 2012. "Experimental study on a compressible vortex ring in collision with a wall". *Journal of visualization*, Vol.15, pp. 321–332.
- Yadav, A., Nuvvula, P.K., Karn, P.K., Murugan, T., Das, D., 2023. "Compressible vortex ring interaction with perforated cone mounted on a flat plate". *ISSW34, 34th International Symposium on Shock Waves, Daegu, South Korea*.

Experimental Sensitivity Analysis on Flip-Flop Synthetic Jet Parameters

P. Scavella^{1*}, G. Paolillo¹, G. Cardone¹, T. Astarita¹, C. S. Greco¹

1. Department of Industrial Engineering, University of Naples “Federico II”, Naples, Italy

* Corresponding author: piergiorgio.scavella@unina.it

Keywords Active flow control, sweeping jets, parametric analysis, Infrared thermography.

1. INTRODUCTION

Unsteady excitation, unlike continuous jet flows, has emerged as a powerful tool for exerting control over critical fluid phenomena such as transition, separation, shear-layer mixing and appears to have great potential in the area of heat transfer enhancement.

Many fluidic devices generate such an unsteady excitation in the external free flow field of a jet by the presence of a fluid dynamic instability or by forcing the jet itself.

Fluidic oscillators operate by directing fluid into the jet stream, generating pulses or swirling patterns, exhibiting a wide array of configurations ranging from essential to intricate designs. One of the most promising solutions, for their simplicity due to the absence of moving parts, is the device based on self-sustained oscillation presented by Viets [1] and, from here, successively developed and analyzed (e.g. [2, 3]).

Crow and Champagne [4], with their analysis on orderly structure of jet turbulence, had suggested that the dominant coherent structure, serving as the principal mode, is characterized by a Strouhal number of 0.3. To broaden the span of the mixing layer, the proposed strategy involved enhancing this primary coherent structure by manipulating its intrinsic frequency. Subsequent studies [5] have indicated that this preferred mode frequency is not universally applicable and depends on the specific application. Thus, there is a need for a more adaptable and controllable device to address a wider range of applications effectively. Ad hoc designed geometries strongly predetermine the self-sustained flow oscillator controlling capabilities, and it is not straightforward to control changing flow conditions.

Here, the use of aiding secondary jet is introduced and then developed in a wide range of declinations. An example of coupling the main jet with a second continuous jet perpendicular to the main one is explored by Tamburello and Amitay in [6], while the coupling with a synthetic jet is considered in [7], in which one of the results findings is the high receptivity of the primary continuous jet to the control jets. As presented by Glezer [8], a synthetic jet, or zero net mass-flux jet, could be used as a direct device for fluidic excitation that operates by altering the pressure within a tiny opening, causing periodic intake and expulsion of fluid from the passing flow.

In this work, an innovative configuration with a steady jet controlled at its nozzle exit with synthetic jet technology is presented. The synthetic jets do not operate directly on the external flow field but serve as a control mechanism on the primary jet. Such an innovative device allows to specifically control and influence both the temporal and the spatial oscillations of the jet itself differently from what present in the literature. In particular, the periodic disturbances induced by synthetic jets allow for more precise and dynamic adjustment of the main jet temporal/spatial oscillations, potentially satisfying several requirements in the field of heat transfer applications [9].

The presence of two opposite synthetic jets allows to operate on their actuation frequency (Strouhal number), exit velocity (Reynolds number), and phase shift; all of these quantities are principal responsible of the control mechanism.

To evaluate and understand the full capabilities of this device, a comprehensive parametric study is carried out by ranging their governing parameters. Infrared Thermography techniques are used to analyze and characterize the fluid dynamic and heat transfer behavior.

2. EXPERIMENTAL SETUP

In Figures 1 and 2, the device is shown. The device is 3D printed and has two lateral square plates where the loudspeakers are mounted. These loudspeakers are placed opposite to each other on both sides of the flip-flop nozzle structure. The primary flow comes from the rear attached tube, which collects airflow from a centrifugal blower. Before reaching the device, a heat exchanger is used to keep the jet air temperature equal to the ambient one.

The internal design of the device is sketched in Figure 2. The primary jet flows through a converging nozzle, characterized by an area contraction ratio of 8, with a squared exit width of 10 mm. The two synthetic jets influence the primary flow only in the external field, where the two constant area nozzles convey the flow outside in the same direction as the flow of the main jet. They have a rectangular exit, with an area ratio of 2, where the lower side dimension visible in the section reported in Figure 2, is 5 mm.

A sketch of the experimental setup is depicted in Figure 3.

The flip-flop jet, depicted in Figure 1, expels the flow that impinges the foil on its bottom face. An infrared camera looks at the face of the foil opposite to the jet impingement. The convective heat transfer coefficient is computed by using the heated thin foil heat flux sensor [11]. Nozzle-to-plate distances ranging between 0.5 w and 10 w, with w being the nozzle slot-exit width, have been investigated.

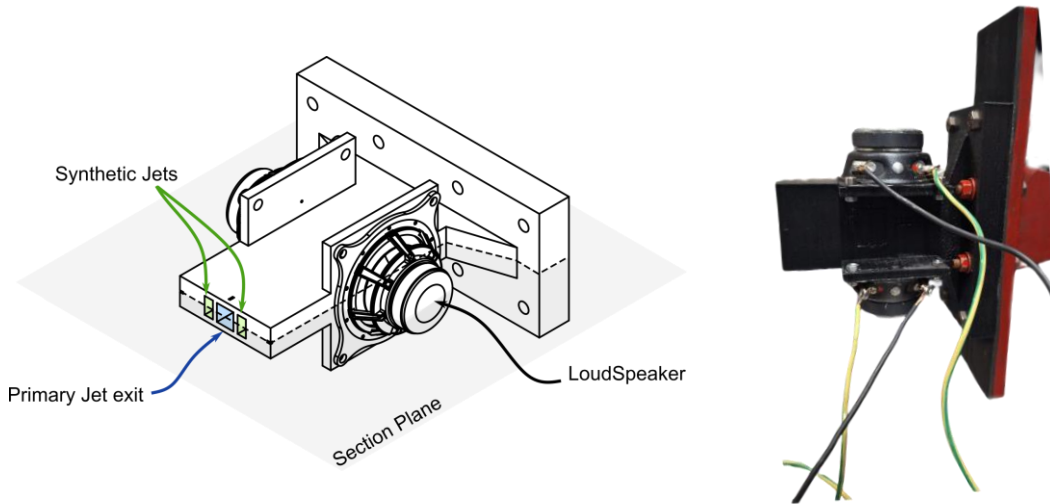


Figure 1. Sketch of the experimental setup (left) and actual prototype (right).

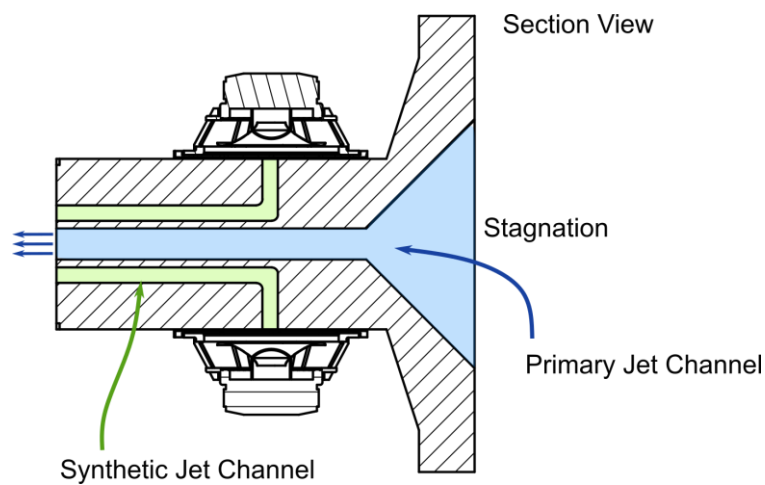


Figure 2 Section view of the flip-flop nozzle.

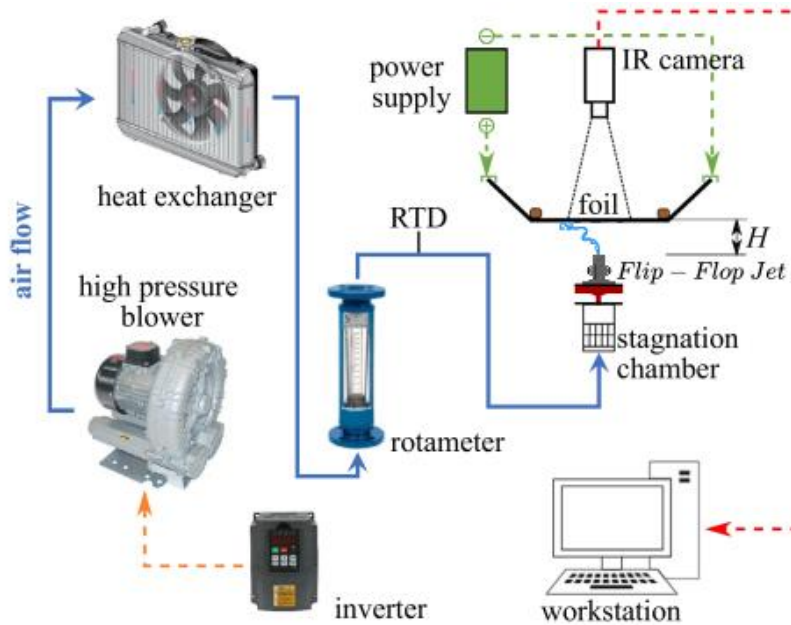


Figure 3 Sketch of experimental setup

4. RESULTS AND CONCLUSION

The investigation has focused on examining the impact of the control frequency and phase of synthetic jets, the main flow Reynolds number, and the distance between the nozzle and the plate on the heat transfer performances of impinging flip-flop jet. It has been observed that as the nozzle-to-plate distance increases, there is a corresponding decrease in the Nusselt number, accompanied by a noteworthy alteration in its distribution. Still, a change in frequency and phases will control the jet width of the flip-flop jet, changing the impinging area and thus generating different Nusselt number distributions.

5. REFERENCES

- [1] Viets H (1975) Flip-flop jet nozzle. *AIAA J* 13:1375–1379
- [2] Raman, G., Rice, E. J., & Cornelius, D. M. (1994). Evaluation of flip-flop jet nozzles for use as practical excitation devices
- [3] Camci, C., & Herr, F. (2002). Forced convection heat transfer enhancement using a self-oscillating impinging planar jet. *J. Heat Transfer*, 124(4), 770-782.
- [4] Crow, S. C., & Champagne, F. H. (1971). Orderly structure in jet turbulence. *Journal of fluid mechanics*, 48(3), 547-591.
- [5] Gutmark, E., & Ho, C. M. (1983). Preferred modes and the spreading rates of jets. *The Physics of fluids*, 26(10), 2932-2938.
- [6] Tamburello, D. A., & Amitay, M. (2007). Interaction of a free jet with a perpendicular control jet. *Journal of Turbulence*, (8), N21.
- [7] Tamburello, D. A., & Amitay, M. (2007). Dynamic response of a free jet following the activation of a single synthetic jet. *Journal of Turbulence*, (8), N48.
- [8] Glezer, A., & Amitay, M. (2002). Synthetic jets. *Annual review of fluid mechanics*, 34(1), 503-529..
- [9] Chaudhari, M., Puranik, B., & Agrawal, A. (2010). Heat transfer characteristics of synthetic jet impingement cooling. *International Journal of Heat and Mass Transfer*, 53(5-6), 1057-1069.
- [10] Reynolds, W. C., & Hussain, A. K. M. F. (1972). The mechanics of an organized wave in turbulent shear flow. Part 3. Theoretical models and comparisons with experiments. *Journal of Fluid Mechanics*, 54(2), 263-288.
- [11] Carlomagno G.M., Cardone G., Infrared thermography for convective heat transfer measurements, *Experiments in fluids*, Vol. 49, no.6, pp. 1187-1218, 2010.

Experimental investigation of asynchronous bubble growth in mini channels using machine learning image processing

Valentin Scheiff^{a,*}, Konstantinos Kyprianidis^a, Rebei Bel Fdhila^{a,b}

^aMälardalen University, Västerås, Sweden

^bHitachi Energy, Västerås, Sweden

*valentin.scheiff@mdu.se

Keywords: Nucleate boiling, mini channel experiment, convolutional neural network, oscillation, bubble tracking

1. INTRODUCTION

Enhancing the efficiency of traditional energy system devices presents a significant challenge, particularly due to the compactness of electrical systems. This compactness necessitates high power density, resulting in substantial heat release and thereby requiring efficient cooling mechanisms. Among various cooling methods employed for thermal management, nucleate boiling stands out as an efficient heat transfer technique. This efficiency is due to a mixed effect of bubbly-induced convection and latent heat transport. However, the heat transfer characteristics and fluid flow dynamics during boiling are dependent on several numerous parameters from macroscopic factors such as flow velocities, fluid-wall interactions, and surface roughness, as shown by *O'Hanley et al. (2013)* but also from microscale behaviors with local bubble interaction such as coalescence, oscillation, or bubble frequency. Furthermore, it's important to note that these conditions vary significantly in mini or narrow channels compared to other geometric configurations due to the confinement of bubbles, as discussed by *Kromer et al. (2016)*.

This distinction is particularly pertinent considering that mini channels have been widely utilized in nuclear reactors and electrical equipment heat sinks for their enhanced heat performance. Still, the understanding of subcooled boiling in such configurations remains to be studied since models are made for specific experiments and are not generic. The aim of this study is to analyze bubble generation at microscale with local bubble interaction from an experimental mini channel with high aspect ratio and heated with cartridges to control the heat flux at the wall. To achieve this, a high-speed camera is utilized as a visualization tool to catch Onset of Nucleate Boiling generated on the wall. After acquiring images, the application of image processing techniques becomes necessary to track the bubbles and their edges, enabling the determination of their location and deformation over time, regardless of any noise or irregular shapes present.

Furthermore, the integration of Convolutional neural networks (CNNs) has enabled automatic and scalable image analysis due to their unique feature of capturing the spatial structure of the input data. CNN is then used in the study to determine the principal characteristics of boiling such as the bubble density, detachment frequency or apparition, and how they interact between them as well as nucleation site's locations with high accuracy. The algorithm is based on image data that play a vital role in understanding microscale boiling physics since boiling images are richly embedded with bubble statistics, which are quantitative measurements of the dynamic boiling phenomena *Zhou et al. (2020)*. A focus is placed on how bubbles generated from two or more close nucleation sites disturb the flow and others bubbles formation.

2. BACKGROUND - OBJECTIVES

Boiling in mini channels is one promising technique presented as an alternative for thermal management of future power systems, but current models are insufficient. The heat flux transferred to the fluid is determined as a function of an average superheat temperature on boiling curve. These curves give information on the appearance of nucleated boiling on the wall and make it possible to characterize boiling with its transition where the heat flux transferred to the fluid is determined as a function of an average superheat temperature. These boiling transitions are closely related to the fluid properties in contact with the solid, the formation of the thermal boundary layer near the wall during the formation and the development of vapor bubbles. Then different heat transfer occurs during each boiling regime (conduction through the vapor phase during film boiling or forced convection) that can be visualized by high-speed cameras. It is then a powerful system for cooling but needs to be controlled. Each of these events depends on the operating conditions such as wall surface condition or generated heat flux for example. Local bubble behaviors are important to understand how boiling transition is triggered, with bubble motion, and coalescence *Wei et al. (2011)*. The use of performant technologies such as high-speed cameras that could not be used for practical application, and powerful image processing is essential. This is a challenge to overcome that doesn't facilitate development of generalized methods to optimize cooling technologies.

However, local behaviors can be analyzed only if bubbles generated on the wall are followed over time with their exact position. Each bubble edge is then determined with a Convolutional Neural Network as image processing to support a versatile experiment with high accuracy. CNN has been widely used in research for many applications including computer vision and image recognition, etc. It can provide efficient and accurate solutions if applied to bubble detection, tracking, and properly dealing with large amounts of data to extract statistics with a post processing algorithm that follows the bubbles over time *Suh et al. (2021)*. Conventional methods to process these data require extensive users' involvement, which is time-consuming and increases the chances of introducing user bias. Such drawbacks of the conventional techniques refuel the motivation of devising a non-destructive and automated optical technique that can provide accurate

quantification of boiling dynamics to determine microscopic factors which are part of how boiling is spreading in the channel.

3. METHODS

a- Experimental set-up

The experimental set-up is described in *Scheiff (2022)*. The test section is a mini channel designed to let a fluid thickness of 3mm with the possibility to vary and study other cases with smaller thickness. The heated wall is made of aluminum and is in contact with deionized water to create the same conditions that are applied in many electrical real applications. The test object's front section size is 400x84mm with a hydraulic diameter of 5.8mm. A flat heater was used to reach boiling and impose a uniform heating. Finally, the test section is insulated and connected to a hydraulic loop where a micro pump provides the liquid flow, and a bath heater can control its temperature. All experimental characteristics are presented in Table 1 and set-up is represented in Fig. 1.

Table 1. Characteristics of test section

Parameters	Value	Parameters	Value
Channel Width / Length (mm)	84 / 400	Heat Flux (kW/m ²)	4.45
Channel Depth (mm)	3	Frequency	5000
Hydraulic diameter (mm)	5.8	T _{liq} (Celsius)	40
Plate thickness (mm)	20	T _{sat} (Celsius)	99.6
Heating area (m ²)	0.0168	Reynolds number	150

A visualization box allows to catch boiling phenomenon on the wall thanks to a high-speed camera Phantom SpeedSense2012a with a resolution of 1280x800 pixels and a framerate range imposed in this study at 5000 Hz. The camera is placed in front of the heated test section with front lighting. The experiment shows a good repeatability for the same test with a maximum deviation of 1.2°C for generated heat flux of 4450W/m² and a Reynolds number of 150. Results are taken after a flow establishment length of about 20cm.

b- Computer vision method

The image processing method is shown in *Soibam (2023)*. An image segmentation algorithm based on CNN is used to study bubble dynamics from images obtained with the experiment to study every bubble on the image. The model is shown in Fig. 1. This model is a one stage object detection, it can regress the objects directly to predict the bubbles and their position. The current algorithm focuses on extracting the bubble's mask to post-process them with MATLAB code. CNN is known for its ability in handling multi-dimensional data imbued with spatial information and its ability to optimize fewer parameters compared to a feed-forward neural network. Object detection typically employs two methods: the one-stage method and the two-stage method. The primary contrast lies in their approach to detecting objects. The one-stage method, such as You Only Learn Once - YOLO, concurrently detects object positions and classifies them. Conversely, the two-stage method initially predicts object positions and subsequently classifies them. The method here focuses on implementing a one-stage detection method, which offers the advantages of swift inference speed and the capacity for real-time prediction without sacrificing accuracy.

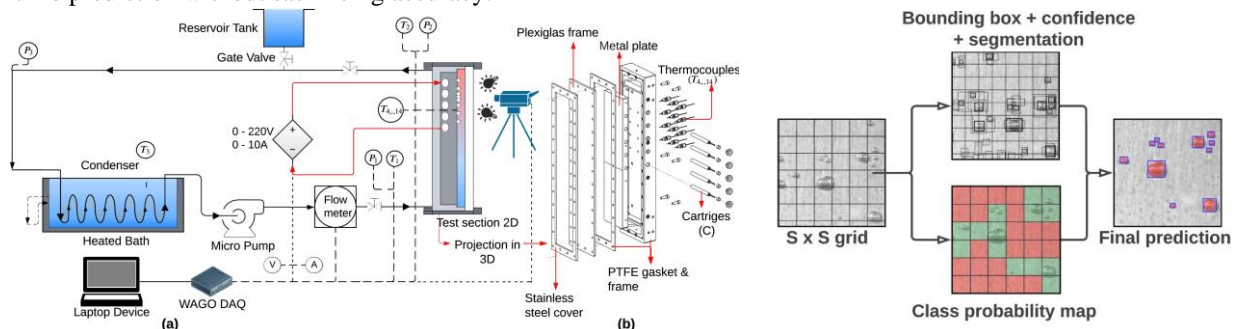


Figure 1: Experimental set-up with Grid to estimate bounding box, segmentation and to calculate the matrices with CNN.

In total 600 images were labeled with an average of 20 bubbles per image, with 80% are used for training (480 images) and 20% for validation (120 images). The mask is given on each image and is then binarized to give the edge of every bubble. Tracking of these bubbles enable to study the key dynamics such as bubble position, coalescence, oscillation, velocity, and so Reynold's bubble number or Weber number. Furthermore, this technique allows us to study bubble history such as breakage, collision, and coalescence which play a major role in subcooled boiling heat transfer.

4. RESULTS - DISCUSSION

In our experimental setup, due to experimental limitations, only front lighting was employed that implies the creation of shadows with bubbles that disturb the images. Despite these challenges, the algorithm is trained to recognize bubbles formation without shadows/noise. The generated mask is then used with a post-processing code to get the position and exact shape of the bubble. It allows to study each bubble at the initial stage, estimate the center and so the deformation of the bubbles over time as shown in Fig. 2. The robustness of this approach in extracting meaningful data from imperfect experimental conditions underscores its effectiveness in capturing the dynamics of bubble behavior.

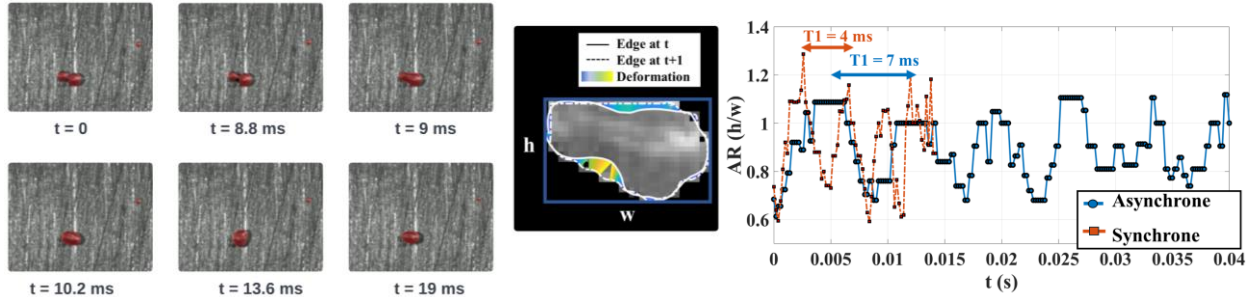


Figure 2. Coalescence of two bubbles generated on two different nucleation sites. Deformation of the bubble edges (white) with the edge at $t+1$ (white dash line) for first instant of merging and Aspect Ratio after coalescence.

The aspect ratio AR is defined as the minimum rectangular area which fits best the bubble and that gives the height (h) and the width (w). In this scenario, where bubbles grow asynchronously (with different diameters when merging), they combine with nearby bubbles to form larger ones. The diameter ratio (D_{b1}/D_{b2}) between these 2 bubbles was 0.66 (Asynchrone) which gives enough impulsion for the bubble to leave the nucleation site but remain on the wall. During the process of bubble coalescence, the smaller bubble, initially at a higher pressure, is drawn into the larger bubble with lower pressure, showing an oscillation period of 7 ms at the outset. But when the bubbles grow at the same time with a diameter ratio close to 1 (Synchrone), the new bubble formed after merging leaves its nucleation site and the wall earlier to condense in the flow with an oscillation period that can reach 4 ms. The dynamics of bubble growth and coalescence in this scenario are influenced by the asynchronous bubble growth at two different nucleation sites with a distance lower than the maximum diameter a bubble can reach in this configuration. The variations in diameter ratios detected by the image can lead to different oscillation periods and will affect the capacity of the bubble to remain on the wall.

5. CONCLUSION

Boiling is a promising cooling process, but its performance depends on parameters that challenge potential boiling control and make system integration challenging. Therefore, there is a strong focus on this area to address the uncertainties associated with two-phase cooling and so, an experimental set-up has been built to reproduce a mini channel and trigger the boiling process. Image processing with automated detection of bubble life thanks to a convolutional neural network has been developed to determine major process in boiling propagation with a statistical approach, especially at the ONB. As a result, it becomes possible to catch with high accuracy every bubble to follow the propagation of nucleate boiling in any situation such as two growing bubbles in a mini channel. The deformation of bubbles during boiling processes contributes to the understanding of the larger bubble's generation, which can insulate the wall and lead to critical situations where Coalescence-induced bubble deformation can alter the local flow dynamics within a system. This advancement allows for the identification of key processes involved in the propagation of boiling phenomena, from ONB toward nucleate boiling with higher interactions between bubble generation, motion, and deformation.

6. REFERENCES

- H. O'Hanley, C. Coyle, J. Buongiorno, T. McKrell, L.-W. Hu, M. Rubner, and R. Cohen, "Separate effects of surface roughness, wettability, and porosity on the boiling critical heat flux," *Applied Physics*, vol.103, no.2, p.24-102 (2013).
- H. Kromer, T. Laneryd, H. Anglart, L. Al-Maeni, and R. Bel Fdhila, "Experimental investigation of flow nucleate boiling heat transfer in a vertical minichannel," *PRTEC*, (2016).
- Zhou, H. J. & Niu, X. J. "An image processing algorithm for the measurement of multiphase bubbly flow using predictor-corrector method." *Int. J. Multiphase. Flow* (2020).
- Wei, J. H., Pan, L. M., Chen, D. Q., Zhang, H., Xu, J. J., & Huang, Y. P. "Numerical simulation of bubble behaviors in subcooled flow boiling under swing motion". *Nuclear engineering and design*, 241(8), p.2898-2908. (2011).
- Suh, Y., Bostanabad, R., & Won, Y. Deep learning predicts boiling heat transfer. *Scientific reports*, 11(1), 5622 (2021).
- Scheiff, V., Aslanidou, I., Kyprianidis, K., & Bel Fdhila, R. "Experimental study of nucleate boiling dynamics in a rectangular mini-channel set-up". In 8th Thermal and Fluids Engineering Conference (TFEC). (2023).
- Soibam, J., Scheiff, V., Aslanidou, I., Kyprianidis, K., & Fdhila, R. B. Application of deep learning for segmentation of bubble dynamics in subcooled boiling. *Int. J. Multiphase. Flow*, 169, 104589. (2023)

LIQUID FILM THICKNESS MEASUREMENT IN HFC134A-GAS ETHANOL SYSTEM SIMULATING TWO-PHASE FLOW PHENOMENA UNDER HIGH PRESSURE CONDITIONS

Shoji Mori^{a,b}, Huacheng Zhang^a and Yutaro Umehara^{a,b}

^aDepartment of Mechanical Engineering, Graduate School of Engineering, Kyushu University, 744 Motooka, Nishi-ku, Fukuoka 819-0395, Japan

^bInternational Institute for Carbon-Neutral Energy Research, Kyushu University, 744 Motooka, Nishi Ward, Fukuoka 819-0395, Japan

* morisho@mech.kyushu-u.ac.jp

Keywords: Annular flow, Two-phase flow, Disturbance wave, Film thickness

1. INTRODUCTION

Annular flow is a two-phase flow regime that is encountered in many industries, such as nuclear reactors. Since a large amount of liquid is transported by the disturbance waves travelling over the base liquid film and dryout occurs at the base liquid film between two successive disturbance waves (Mori and Fukano, 2006), it is of great significance to fully understand the liquid film behaviors including film thickness and wave height to avoid the burnout of the fuel rods surface in nuclear reactors. Several researchers have investigated the liquid film and disturbance waves through experimental and analytical approaches. However, most experimental data and analysis available in the literature are limited to the air–water system under near atmospheric and room temperature while the physical properties of working fluids in these studies are very different from those of the steam–water annular flow in BWRs.

In this study, we employ the HFC134a gas and 95% ethanol aqueous solution, whose properties under comparatively low pressure and temperature conditions (0.7 MPa, 40 °C) are similar to those of steam and water under BWR operating conditions (7 MPa, 285 °C) as the working fluids. Meanwhile, the liquid film thickness was carefully measured with respect to time in the vertical upward annular flow experiments. Moreover, the film thickness from current experimental data is evaluated by the correlation proposed in our previous research.

2. EXPERIMENTAL APPARATUS AND PROCEDURES

The physical properties of HFC134a–ethanol and other systems in our previous work (Zhang et al., 2023) are summarized in Table 1, including information on density of gas and liquid, surface tension, and viscosity of gas and liquid, denoted by ρ_G , ρ_L , σ , μ_G , and μ_L , respectively. The electrical conductivity of the 95% ethanol aqueous solution is 800 ± 100 S/cm and is measured before and after each experiment. The superficial liquid velocity, denoted by j_L , at the test section is set at 0.1 and 0.4 m/s for each experimental condition. It should be mentioned that the vaporization of working fluids has minor effect on electrical conductivity and flow behavior which is confirmed by repeating experiments with same working fluids.

Table 1 Summary of the properties of the working fluids.

System	Pressure [MPa]	Temperature [°C]	ρ_G [kg/m ³]	ρ_L [kg/m ³]	σ [mN/m]	μ_G [μPaS]	μ_L [μPaS]	ρ_L/ρ_G [–]
Steam–Water (BWR operating condition)	7.0	285	37.1	738.1	17.4	19.7	90.8	20
HFC134a–95% Ethanol	0.7	40	31.5	850.0	31.0	12.3	983.0	27
Nitrogen–Water	0.2	25	2.3	997.0	67.4	17.7	850.0	434
HFC134a–Water	0.7	40	31.5	992.0	59.0	12.3	570.0	32
Nitrogen–95% Ethanol	0.2	25	2.3	850.0	30.7	17.7	1420.0	370

To obtain the liquid film time trace in annular two-phase flows, the conductance probe method is used to measure the time-varying liquid film thickness (Fukano, 1998). Two sets of sensors with an accuracy of $\pm 5\%$ are installed in the test section for the film thickness measurement (Fig. 1). Each sensor comprises one pair of conductance probes. The axial

distance between one pair of conductance probes is 5.0 mm. The constant electric current of the main circuit is fixed at 1.0 mA, which is provided by the constant current power source and measured using a standard electric resistance of 1 k Ω . The time-varying voltage and current output from these sensors are recorded simultaneously using a YOKOGAWA DL850E digital oscilloscope with an accuracy of $\pm 0.5\%$ at a sampling frequency of 5 kHz over the length of the 10,000 data points (2 s). An isolation amplifier is placed between the sensors and oscilloscope, to protect the oscilloscope from high voltage. As shown in the cross-sectional view of the test section in Fig. 2, four M1 screws fixed vertically to the channel are connected on the outside.

From the obtained film thickness time trace, the frequency of film thickness is calculated. We define the film thickness with the highest frequency as the base film thickness denoted by t_{Fbase} and the film thickness with the 99% cumulative frequency as the maximum film thickness denoted by t_{Fmax} . Then, the disturbance wave height, H , is defined as the difference between the base and maximum film thicknesses. The average film thickness, t_{Fave} , is the arithmetic mean value of film thickness.

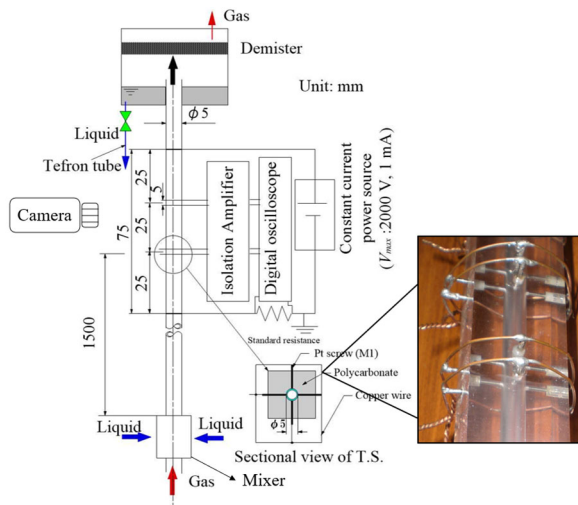


Fig. 1. Schematic of the test section.

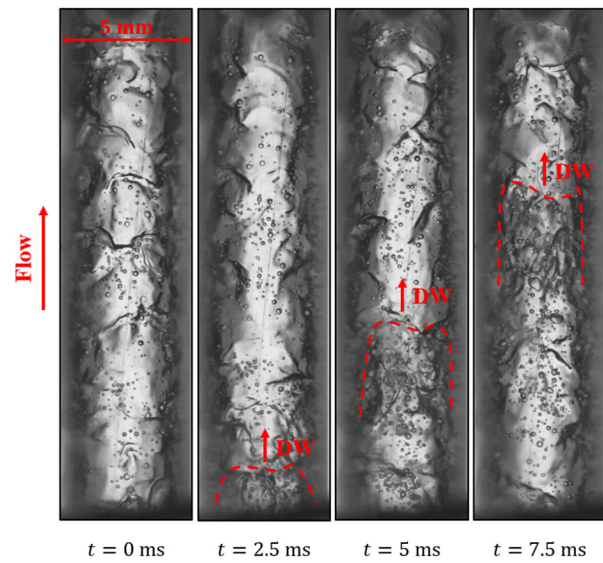


Fig. 2 Flow pattern of HFC134a–95% ethanol annular flow under $j_L = 0.1$ m/s and $j_G = 3$ m/s. The red dotted line indicates the front of the disturbance wave (DW).

3. RESULTS AND DISCUSSIONS

Conventionally, the wavy interfacial structure in annular flows is classified by large-scale disturbance waves and small-scale ripple waves. Disturbance waves move on the base film yet ripple waves travel either on the base film or over the disturbance waves. Moreover, compared with ripple waves, disturbance waves usually possess larger wave height, velocity, longitudinal size, and lifetime. It is shown in Fig. 2 that the ripple waves coexist with disturbance waves. The disturbance waves could be distinguished from the ripple waves by their circumferential coherence and larger wave velocity and longitudinal size.

Fig. 3 (a) and (b) shows the comparison between measured t_{Fbase} , t_{Fave} , and t_{Fmax} , and H of HFC134a–95% Ethanol and other systems respectively. It is shown that t_{Fbase} , t_{Fave} , t_{Fmax} , and H are almost the same under the same liquid flow rate when plotted against the following gas Weber number, which is consistent with our previous report (Zhang et al., 2023):

$$We_G = \frac{\rho_G j_G^2 D}{\sigma} \quad (1)$$

The probable reason is that the surface tension force tends to maintain the shape of the gas–liquid interface against the drag force acting on the disturbance wave and We_G converges the effect of surface tension force and drag force.

Several correlations regarding t_{Fave} (Anderson and Mantzouranis, 1960; Henstock and Hanratty, 1976; Ju et al., 2015; Pan et al., 2015; Zhang et al., 2023) and H (Cuadros et al., 2019; Han et al., 2006; Ju et al., 2015; Zhang et al., 2023) are evaluated with current experimental data of HFC134a–95% Ethanol system as shown in Fig.4. It is readily apparent that the correlations by Ju et al. (2015) and Zhang et al. (2023) can provide the best predictive results of t_{Fave} while the correlations by Zhang et al. (2023) can provide the best predictive results of H .

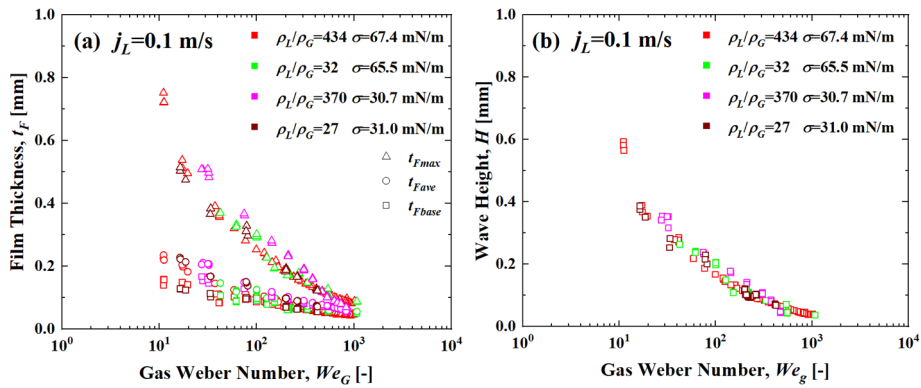


Fig. 3 Comparison of (a) t_{Fave} and (b) H against We_G under $j_L = 0.1$ m/s.

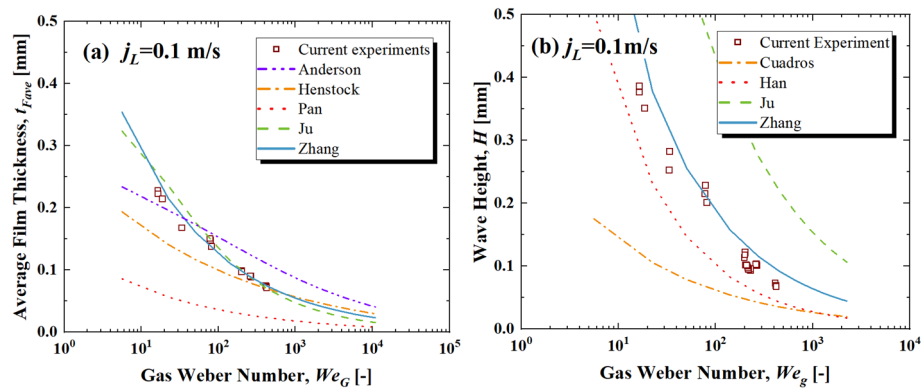


Fig. 4 Comparison of measured and predictive value of (a) t_{Fave} and (b) H under $j_L = 0.1$ m/s.

4. CONCLUSIONS

In the present study, the experiments of HFC134a–95% Ethanol annular flows with fluid properties that are close to the steam and water under the BWR operating condition are performed. The obtained film thickness and wave velocity are compared with the previous experimental investigation. Similar to our previous observation of annular flow with different density ratios and surface tension, the base, average, maximum film thickness, and wave height of HFC134a–95% Ethanol system also collapse onto a single curve when plotted with gas Weber number. Several predictive correlations are evaluated with current experimental data.

5. REFERENCES

- Anderson, G.H., Mantzouranis, B.G., 1960. Two-phase (gas—liquid) flow phenomena—I Pressure drop and hold-up for two-phase flow in vertical tubes. *Chemical Engineering Science*, Vol. 12, PP. 109–126.
- Cuadros, J.L., Rivera, Y., Berna, C., Escrivá, A., Muñoz-Cobo, J.L., Monrós-Andreu, G., Chiva, S., 2019. Characterization of the gas-liquid interfacial waves in vertical upward co-current annular flows. *Nuclear Engineering and Design*, Vol. 346, PP. 112–130.
- Fukano, T., 1998. Measurement of time varying thickness of liquid film flowing with high speed gas flow by a constant electric current method (CECM). *Nuclear Engineering and Design*, Vol. 184, PP. 363–377.
- Han, H., Zhu, Z., Gabriel, K., 2006. A study on the effect of gas flow rate on the wave characteristics in two-phase gas-liquid annular flow. *Nuclear Engineering and Design*, Vol. 236, PP. 2580–2588.
- Henstock, W.H., Hanratty, T.J., 1976. The interfacial drag and the height of the wall layer in annular flows. *AIChE Journal*. Vol. 22, PP. 990–1000.
- Ju, P., Brooks, C.S., Ishii, M., Liu, Y., Hibiki, T., 2015. Film thickness of vertical upward co-current adiabatic flow in pipes. *International Journal of Heat and Mass Transfer*. Vol. 89, PP. 985–995.
- Mori, S., Fukano, T., 2006. Relation between the occurrence of Burnout and differential pressure fluctuation characteristics caused by the disturbance waves passing by a flow obstacle in a vertical boiling two-phase upward flow in a narrow annular channel. *Nuclear Engineering and Design*. Vol. 236, PP. 985–992.
- Pan, L., He, H., Ju, P., Hibiki, T., Ishii, M., 2015. Experimental study and modeling of disturbance wave height of vertical annular flow. *International Journal of Heat and Mass Transfer*. Vol. 89, PP. 165–175.
- Zhang, H., Mori, S., Hisano, T., Yoshida, H., 2023. Effect of gas density and surface tension on liquid film thickness in vertical upward disturbance wave flow. *International Journal of Multiphase Flow*. Vol. 159, PP. 104342.

CONCENTRATION, THERMAL AND POLYDISPERSITY EFFECTS ON THE PHASE AND FLOW BEHAVIOR OF SODIUM LAURYL ETHER SULFATE-WATER SYSTEMS

Rosalia Ferraro^{a,b}, Sergio Caserta^{a,b,*}, Gerardino D'Errico^{c,d}, Stefano Guido^{a,b}

^aDICMaPI, Università di Napoli Federico II, P.le V. Tecchio 80, 80125 Napoli, Italy

^bCEINGE Advanced Biotechnologies Franco Salvatore, Via Gaetano Salvatore, 486, 80131 Napoli, Italy

^cDSC, Università degli Studi di Napoli Federico II, Via Cintia, 21, 80126 Napoli, Italy

^dCSGI, Consorzio Interuniversitario per lo Sviluppo dei Sistemi a Grande Interfase, Via della Lastruccia 3, I-50019 Sesto Fiorentino, Florence, Italy

*sergio.caserta@unina.it

Keywords: Surfactants; Sodium Lauryl Ether Sulfate; Molecular polydispersity; Phase behavior; Industrial applications.

1. BACKGROUND

Surfactants play a fundamental role in numerous aspects of everyday life (Blagojević *et al.*, 2019). These versatile compounds are widely present in household and personal care products (Lee *et al.*, 2016; Cornwell, 2018) and find extensive applications as stabilizers in paints, plastics, and corrosion inhibitors (Bilgin *et al.*, 2022; Huang *et al.*, 2019; Deyab, 2015). Moreover, surfactants hold promise for revolutionizing biological processes such as drug extraction and delivery (Hasheminasab and Fakhari, 2015; Ge *et al.*, 2019; Chen *et al.*, 2014; Budinčić *et al.*, 2021; Mariani *et al.*, 2020; Keshvari *et al.*, 2021), owing to the formation of mesophases in aqueous solutions.

Understanding the phase and flow behavior of surfactant systems and their modulation by concentration and temperature is crucial not only for tailoring product properties (El-Dossoki *et al.*, 2019; Wand *et al.*, 2020; Finizio *et al.*, 2020), but also for essential processes like dissolution in water (Li *et al.*, 2016). In addition, while most studies focus on monodisperse surfactants, industrial practices often involve commercial surfactants with significant molecular polydispersity, a factor frequently overlooked.

2. OBJECTIVES

This work underscores the pivotal role of molecular polydispersity in governing the phase and flow behaviors of surfactants, which may diverge substantially from those of their monodisperse counterparts. Our comprehensive investigative approach entails: (i) Employing Time-Lapse dissolution experiments in microchannel geometries to observe the dissolution and phase transitions; (ii) Utilizing polarized light microscopy, confocal microscopy, and Small Angle X-ray Scattering for microstructure identification and concentration assessments; (iii) Conducting rheological evaluations at various concentrations and temperatures to determine their effects on the surfactant properties.

3. METHODS

We focus on Sodium Lauryl Ether Sulfate (SLES), one of the most widely used surfactants globally, known for its cost-effectiveness and eco-friendliness. Although the phase behavior of SLES has been investigated previously (Miyake and Yamashita, 2017; Castaldo *et al.*, 2019), the role of polydispersity has been largely overlooked. The surfactant sample used in this study is described by the average chemical formula $C_{12}H_{25}(OCH_2CH_2)_3OSO_3Na$, indicating an average ethoxylation degree of approximately three (SLE₃S). Using Gas Chromatography–Mass Spectrometry (GC-MS) and Nuclear Magnetic Resonance (NMR) spectroscopy, we quantified the polydispersity of SLE₃S samples and compared them with those obtained for SLE₁S. Time-lapse dissolution experiments in a microchannel geometry were conducted to examine phase transitions induced by polydispersity. As a result, we observed that SLE₃S exhibited one additional microstructure that was absent in SLE₁S.

To identify the specific concentration and type of microstructure, we employed a combination of experimental techniques, including polarized light visual inspections, confocal microscopy, and Small Angle X-ray Scattering (SAXS). Furthermore, to quantify differences in terms of viscoelastic properties, we conducted rheological characterizations at varying concentrations of SLE₃S as a function of temperature.

4. RESULTS

Figure 1A illustrates the dissolution of SLE₁S at 72%wt and 30 °C. Over 30 minutes, three distinct strips emerged: a dark strip on the left indicating the micellar phase, L₁, at low surfactant concentration, a brighter central strip representing

the hexagonal phase (H), and a rightmost strip with Maltese crosses showing the concentrated lamellar phase, L_α . Yellow dotted lines in the figure demarcate the phase boundaries. Conducting the same experiment under identical concentration and temperature conditions with SLE₃S, as depicted in B, revealed four distinct strips, indicating an additional phase absent in SLE₁S. From left to right, the sequence begins with the dark L_1 , followed by the more birefringent H and then a phase likely corresponding to the isotropic cubic phase, distinguished by alternating dark and bright horizontal bands. This suggests a coexistence of birefringent structures alongside the cubic phase. The final strip, also in this case, is a L_α , characterized by typical Maltese cross patterns, as reported in the insets.

Extending our analysis to examine temperature effects on these microstructures, we conducted the SLE₃S dissolution experiment at higher temperatures (Fig. 1C). The POM images in C show that while the L_1 and L_α phases remain largely unchanged at 60°C, the multi-structured phase darkens, hinting at a potential phase transition. This comprehensive analysis underscores the significant role of both polydispersity and temperature in influencing the microstructural behavior of these surfactant systems.

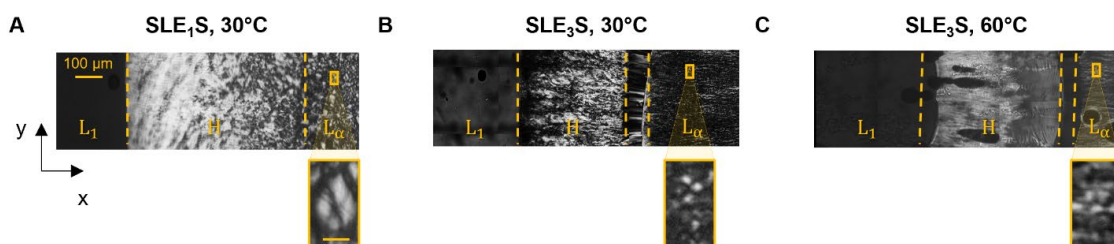


Figure 1. Phase behavior of surfactant systems. Polarized Optical Microscopy (POM) images of SLE₁S at 30°C (A), SLE₃S at 30°C (B), and SLE₃S at 60°C (C). Insets provide a magnified view of the Maltese cross, indicative of the lamellar phase. The scale reported in the figure is 50 μm .

To explore how the structural features of the SLE₃S aqueous mixtures affect the flow behavior, a rheological characterization was performed. Figure 2 presents viscosity measurements as a function of surfactant concentration at four temperatures examined (30, 40, 50, and 60 °C) and at a fixed shear rate ($\dot{\gamma}=10$ 1/s), aiming to identify and characterize various phases.

Figure 2A shows a significant increase in viscosity when transitioning from a 20%wt to a 35%wt (H) mixture across all temperatures. The viscosity remains relatively constant for the hexagonal (H) and lamellar (L_α) phases. However, a noticeable reduction in viscosity is observed in the 50%wt SLE₃S solution with increasing temperature, while the 20%wt solution shows a slight increase from 0.02 to 0.12 Pa·s, likely due to the formation of longer worm-like micelles at higher temperatures (Kalur *et al.*, 2005). Remarkably, the sample at 60%wt displays a significant temperature-dependent viscosity change, dropping from 40 to 4 Pa·s between 40 and 50°C.

A similar pattern in the relationship between viscosity and concentration is observed for both moduli, G' and G'' , as depicted in Fig. 2B and C, respectively. In the 60%wt solution, both moduli radically decrease with temperature; specifically, at $\omega = 10$ rad/s, G' falls from $3.7 \cdot 10^5$ to $6 \cdot 10^3$ Pa and G'' from $2 \cdot 10^4$ to $8.40 \cdot 10^2$ Pa. Conversely, for other phases (L_1 , H, and L_α), both moduli increase by about a factor of two.

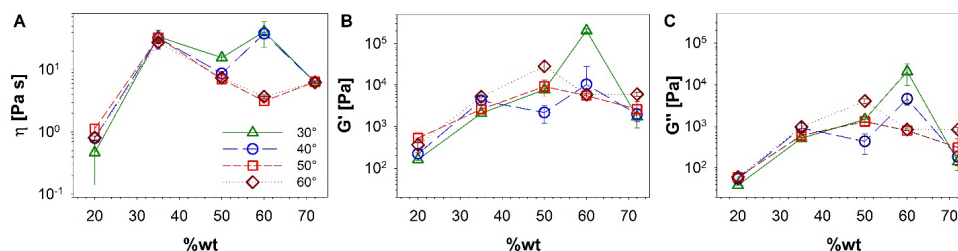


Figure 2. Temperature and Concentration effects on rheological properties of SLE₃S. Viscosity (η , A), elastic (G' , B) and viscous (G'' , C) moduli as a function of SLE₃S concentration (%wt), across different temperatures. The symbols and lines represent measurements at 30°C (triangles, solid line), 40°C (circles, dashed line), 50°C (squares, dash-dot line), and 60°C (diamonds, dotted line).

5. CONCLUSIONS

Our study comprehensively examines the influence of molecular polydispersity on SLES surfactants' phase behavior, addressing a literature knowledge gap. We hypothesize polydispersity significantly shapes phase behavior, impacting fundamental understanding and industrial applications, notably in detergent and personal care product formulations. Through Gas Chromatography–Mass Spectrometry and Nuclear Magnetic Resonance spectroscopy, we quantitatively characterize polydispersity in SLE₃S, revealing diverse ethoxylation degrees and distinct microstructural behaviors

compared to SLE₁S. Time-lapse dissolution experiments and rheological assessments elucidate phase transitions and flow properties, highlighting the coexistence of hexagonal, cubic, and lamellar phases in SLE₃S. In detail, the findings reveal that SLE₃S, being more polydisperse, demonstrates complex phase behavior not observed in the less polydisperse SLE₁S. Notably, SLE₃S exhibits a unique concentration domain, corresponding to a concentration of 60%wt, where hexagonal (H), cubic, and lamellar (L_α) phases coexist, resulting in highly viscoelastic heterogeneous mixtures. This behavior is attributed to the local segregation of surfactant components with varying polarity, underscoring the crucial role of molecular polydispersity in the phase behavior of SLES surfactants.

Our findings emphasize the profound influence of molecular polydispersity on surfactant self-assembly, providing insights crucial for optimizing product attributes and minimizing environmental impacts across various applications.

6. REFERENCES

- Bilgin S, Bahraeian S, Liew M L, Tomovska R and Asua J M 2022 Surfactant-free latexes as binders in paint applications *Progress in Organic Coatings* **162** 106591
- Blagojević S M, Erić N, Nešović M and Blagojević S N 2019 Micellization and Foamability of Sodium Laureth Sulfate and Polysorbate Surfactant Mixtures *Russian Journal of Physical Chemistry A* **93** 2804-11
- Budinčić J M, Petrović L, Đekić L, Fraj J, Bučko S, Katona J and Spasojević L 2021 Study of vitamin E microencapsulation and controlled release from chitosan/sodium lauryl ether sulfate microcapsules *Carbohydrate Polymers* **251** 116988
- Castaldo R I, Pasquino R, Villone M M, Caserta S, Gu C, Grizzuti N, Guido S, Maffettone P L and Guida V 2019 Dissolution of concentrated surfactant solutions: from microscopy imaging to rheological measurements through numerical simulations *Soft matter* **15** 8352-60
- Chen Y, Ma P and Gui S 2014 Cubic and hexagonal liquid crystals as drug delivery systems *BioMed research international* **2014**
- Cornwell P A 2018 A review of shampoo surfactant technology: consumer benefits, raw materials and recent developments *International journal of cosmetic science* **40** 16-30
- Deyab M A 2015 Application of nonionic surfactant as a corrosion inhibitor for zinc in alkaline battery solution *Journal of Power Sources* **292** 66-71
- El-Dossoki F I, Gomaa E A and Hamza O K 2019 Solvation thermodynamic parameters for sodium dodecyl sulfate (SDS) and sodium lauryl ether sulfate (SLES) surfactants in aqueous and alcoholic-aqueous solvents *SN Applied Sciences* **1** 1-17
- Finizio A, Patrolecco L, Grenni P, Galli E, Muzzini V G, Rausedo J, Rizzi C and Caracciolo A B 2020 Environmental risk assessment of the anionic surfactant sodium lauryl ether sulphate in site-specific conditions arising from mechanized tunnelling *Journal of hazardous materials* **383** 121116
- Ge X, Wei M, He S and Yuan W-E 2019 Advances of non-ionic surfactant vesicles (niosomes) and their application in drug delivery *Pharmaceutics* **11** 55
- Hasheminasab K S and Fakhari A R 2015 Application of nonionic surfactant as a new method for the enhancement of electromembrane extraction performance for determination of basic drugs in biological samples *Journal of Chromatography A* **1378** 1-7
- Huang Z, Jia H, Muyden A P v, Fei Z and Dyson P J 2019 Sustainable, Reshapable Surfactant–Polyelectrolyte Plastics Employing Water as a Plasticizer *ACS applied materials & interfaces* **11** 31311-6
- Kalur G C, Frounfelker B D, Cipriano B H, Norman A I and Raghavan S R 2005 Viscosity increase with temperature in cationic surfactant solutions due to the growth of wormlike micelles *Langmuir* **21** 10998-1004
- Keshvari M A, Afshar A, Daneshi S, Khoradmehar A, Baghban M, Muhaddesi M, Behrouzi P, Miri M R, Azari H and Nabipour I 2021 Decellularization of kidney tissue: comparison of sodium lauryl ether sulfate and sodium dodecyl sulfate for allotransplantation in rat *Cell and Tissue Research* **386** 365-78
- Lee S, Lee J, Yu H and Lim J 2016 Synthesis of environment friendly nonionic surfactants from sugar base and characterization of interfacial properties for detergent application *Journal of Industrial and Engineering Chemistry* **38** 157-66
- Li H, Dang L, Yang S, Li J and Wei H 2016 The study of phase behavior and rheological properties of lyotropic liquid crystals in the LAS/AES/H₂O system *Colloids and Surfaces A: Physicochemical and Engineering Aspects* **495** 221-8
- Mariani L, Grenni P, Barra Caracciolo A, Donati E, Rausedo J, Rolando L and Patrolecco L 2020 Toxic response of the bacterium *Vibrio fischeri* to sodium lauryl ether sulphate residues in excavated soils *Ecotoxicology* **29** 815-24
- Miyake M and Yamashita Y 2017 *Molecular structure and phase behavior of surfactants*: Elsevier: Amsterdam
- Wand C R, Panoukidou M, Del Regno A, Anderson R L and Carbone P 2020 The relationship between wormlike micelle scission free energy and micellar composition: The case of sodium lauryl ether sulfate and cocamidopropyl betaine *Langmuir* **36** 12288-98

EFFECTS OF THE RHEOLOGICAL PROPERTIES OF A VISCOPLASTIC FLUID ON THE SLUG FLOW PATTERN

Daiane Mieko Iceri^{a,*}, Gláucio Kenji Matoba^b, Roney Leon Thompson^c, Annie Fidel-Dufour^d, Marcelo Souza Castro^{a,b}

^aCenter for Energy and Petroleum Studies (CEPETRO), Universidade Estadual de Campinas (UNICAMP), Campinas, São Paulo, Brazil, 13083-896

^bSchool of Mechanical Engineering, Universidade Estadual de Campinas, Mendeleyev Street, 200, Campinas, 13083-860, São Paulo, Brazil

^cDepartment of Mechanical Engineering, Federal University of Rio de Janeiro, Centro de Tecnologia, Rio de Janeiro, 21941-909, Rio de Janeiro, Brazil

^dTotalEnergies, CSTJF Avenue Larribau, PAU, Cedex 64018, France.

*daianeiceri@cepetro.unicamp.br

Keywords: Two-phase flow, Viscoplastic fluid, Carbopol solution, slug flow pattern, non-Newtonian fluid

1. INTRODUCTION

Multiphase flow, both in the environment and in the industrial process, is commonly observed. An important one among these scenarios is in processes related to oil extraction and transportation. Oils extracted in deep offshore developments with low temperature conditions can present non-Newtonian behavior with yield stress characteristic. Furthermore, during the transport of these oils, the decompression process can release free gases resulting in a two-phase flow. However, the available literature on multiphase flows primarily focuses on fluids exhibiting Newtonian behavior. Research studies concerning two-phase flow with viscoplastic behavior fluids remain limited.

The first investigation involving two-phase flow with non-Newtonian fluids were related to those with power-law characteristics (Chhabbra and Richardson, 1984). These studies focused their attention on flow patterns and not on the behavior of stresses and velocity profiles. Experimental data on two-phase flow involving a liquid exhibiting non-Newtonian behavior and a gas are scarce in the literature. Xu *et al.* (2007) observed good agreement between the flow patterns experimentally observed for a gas-non-Newtonian fluid flow compared with Barnea (1987) flow pattern map for a 60mm diameter pipe and -5° slope.

Studies in the literature lack investigations into fluids exhibiting yield stress and characterized by the Herschel-Bulkley model. Therefore, the current study aims to present initial tests conducted with a Carbopol solution and a neutralizer to simulate two-phase experimental tests within a pipeline.

2. MATERIAL AND METHODS

The experimental apparatus is located at the Center for Energy and Petroleum Studies (CEPETRO), situated at UNICAMP. Figure 1 illustrates the layout of the experimental apparatus. The test section features a 53 mm diameter in the horizontal direction. The test section is after a development length of 20 meters.

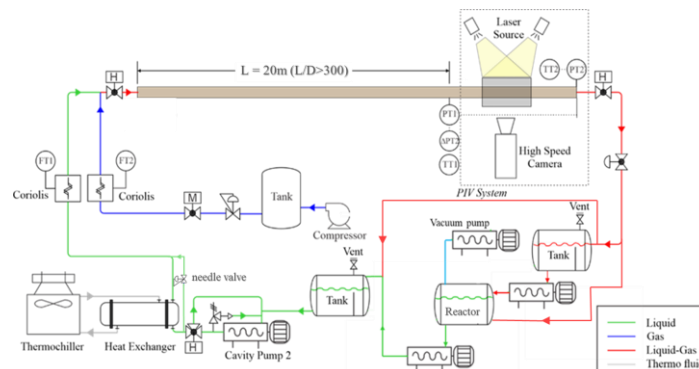


Figure 1. Experimental apparatus

The experimental apparatus includes a positive displacement pump and a heat exchanger for regulating fluid temperature (operating through a thermo chiller system using water). A Coriolis mass flow meter is used to obtain liquid and air flow measurements. Additionally, temperature and pressure data at the inlet and outlet and differential pressure measurements at a distance of 2.4 meters in the test section were collected. A high-speed camera captures the flow pattern. The experimental apparatus incorporates a vacuum pump to remove trapped air from the fluid. This system includes a reactor equipped with internal temperature control and an agitator to aid air elimination. Furthermore, we utilize the

reactor for large-scale sample preparation. This experimental apparatus can operate with liquid velocities of 0.08 up to 1.5 m/s and gas velocities between 0.8 and 2 m/s.

A challenge in studying a fluid characterized by a Herschel-Bulkley-type model is to prepare a solution capable of consistently reproducing viscoplastic conditions. Prior small-scale studies were crucial to determine the components, concentrations, and experimental procedure, developed by Iceri *et al.* (2023). The sample utilized in this study consists of an aqueous solution of Carbopol and a neutralizer agent (Triethanolamine). In the following, this solution is referred to a Carbopol solution.

During each test, a sample of the solution was collected for rheological measurements. These tests employed a Mars II rheometer, which utilized serrated parallel plates to prevent slip with a 1mm gap, as described in Iceri *et al.* (2023). One challenge encountered during the tests was to maintain the rheological properties within the standard deviation of the tests conducted on the rheometer. Critical degradation was observed during the tests caused by the shear in the pump. Hence, the results presented below are preliminary and part of an ongoing research.

3. RESULTS

The experimental apparatus described in the previous section initially validated through single-phase and two-phase tests using water. These experimental conditions are represented in Figure 2(a), indicating the experimental condition on Barnea (1987) map. The superficial velocities examined with water were replicated with the Carbopol solution. While a stratified flow pattern was observed during the water tests, the flow pattern verified with Carbopol was slug. Figure 3 shows two snapshots of a Taylor bubble capture in a two-phase flow with a Carbopol solution.

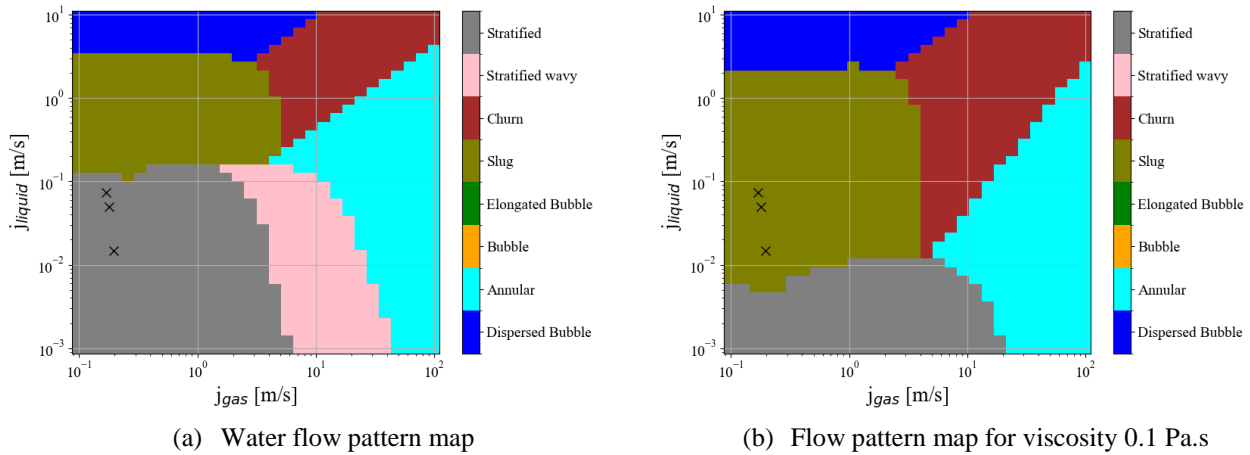


Figure 2. Flow pattern map from Barnea (1987) for a horizontal pipe with 53 mm diameter for different liquid viscosities.

Due to Carbopol degradation, only three feasible experimental conditions were selected for comparison in the present study. To monitor this effect, we took rheological measurements after each experimental test. Consequently, when the yield stress value fell below the standard deviation of the rheological data, the tests with this solution were finished.

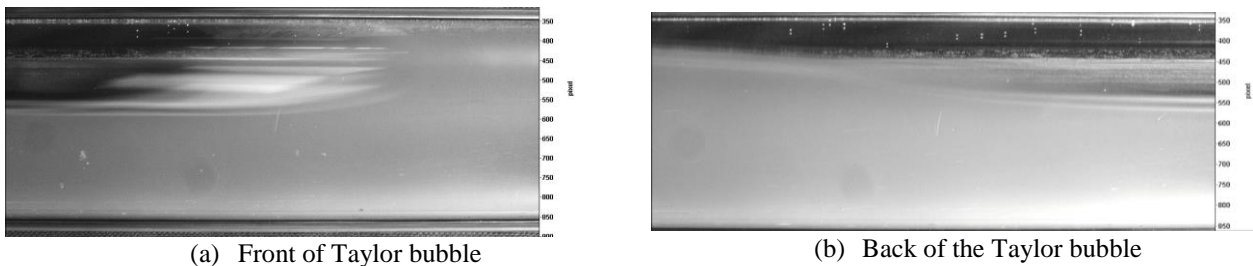


Figure 3. Slug flow pattern, for Carbopol solution, with liquid velocity 0.09m/s and gas velocity 0.16m/s

In another front of this research, preliminary tests involving single-phase flow obtained the velocity profile with a Particle Image Velocimetry (PIV) technique. These tests indicated that the stress rate profile below the yield stress varied from 10^{-2} to 10^0 s^{-1} . The equivalent viscosity region, determined by the flow curve obtained from the rheometer, ranged between 10^3 and 10^1 Pa.s . The flow curve is presented in Figure 4. From the flow curve, rheological data can be obtained (yield stress $3.9 \pm 1.6 \text{ Pa}$, the consistency index 1.3 Pa.s^n and flow behavior index as 0.5).

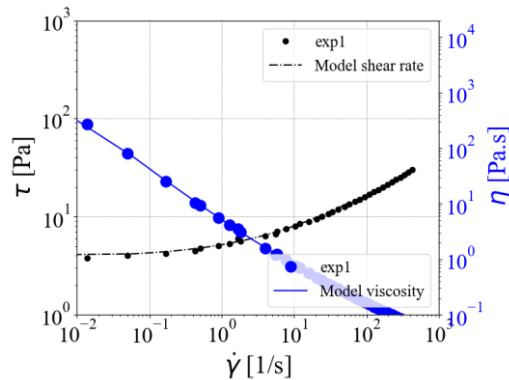


Figure 4. Flow curve of the solution taken from experimental tests.

However, according to the literature of power-law fluids, (see Xu *et al.*, 2007), the apparent viscosity (an average value) is indicated to obtain the flow pattern map. In this case, for the viscosity evaluated at the shear rate for the liquid in single-phase, a churn flow pattern should be obtained for the velocities imposed in the present study. Even when considering the lowest value of this viscosity range, the corresponding conditions remained in the churn region. However, observing the absence of scattered bubbles in the Taylor bubble exit region in the image, a slug flow pattern is noted. The experimental results were compared with different viscosity conditions, with the limit of 1 Pa.s being the viscosity that includes the experimental conditions within the observed flow pattern, as shown in Figure 3(b).

This work speculates that fluids exhibiting yield stress in two-phase flow cannot be classified in the same way as a Newtonian fluid or as proposed in the literature for a non-Newtonian fluid without yield limit stress. Therefore, this study highlights the necessity for a more detailed examination of flow patterns for fluids with yield stress while also investigating the impacts of rheological properties on the flow pattern map.

4. CONCLUSIONS

The experimental tests conducted in this research, focusing on a two-phase flow involving a fluid characterized by Herschel-Bulkley-type behavior, revealed a lack of the classification of flow patterns analyzing the effect of the rheological properties of non-Newtonian fluids. Existing literature often relies on apparent viscosity to assess flow pattern maps, where the lack of tests for non-Newtonian fluids with yield stress might correspond to the differences in the observed flow patterns. In this way, Barnea's flow pattern map cannot be directly applied in the same manner as the other types of non-Newtonian fluid. It is necessary to create a database of flow patterns encompassing various velocities, from which maps for different fluid behavior can be evaluated.

5. ACKNOWLEDGEMENTS

We gratefully acknowledge the support of the ALFA - Artificial Lift and Flow Assurance Research Group, hosted by the Center for Energy and Petroleum Studies (CEPETRO) at the Universidade Estadual de Campinas (UNICAMP), Brazil. We also thank TotalEnergies EP Brazil for their funding and support, as well as the ANP (Brazil's National Oil, Natural Gas, and Biofuels Agency) for assistance through the R&D levy regulation. Special thanks to the CEPETRO-UNICAMP and FEM-UNICAMP for their collaboration, and to the Alberto Luiz Coimbra Institute (COPPE-UFRJ) for their contributions.

5. REFERENCES

- Barnea, D. (1987). "A unified model for predicting flow-pattern transitions for the whole range of pipe inclinations." *International journal of multiphase flow*, 13(1), 1-12.
- Chhabra, R.P., Richardson, J.F., 1984. Prediction of flow pattern for the co-current flow of gas and non-newtonian liquid in horizontal pipes. *Can. J. Chem. Eng.* 62, 449–454. <https://doi.org/10.1002/cjce.5450620401>.
- Iceri, Daiane Mieko, Jorge Luiz Biazussi, Charlie van der Geest, Roney Leon Thompson, Thierry Palermo, e Marcelo Souza Castro. "The yielding behavior of aqueous solutions of Carbopol and triethanolamine and its prediction considering the fractal nature of the formed aggregates." *Rheologica Acta* 62 (July 2023): 405–416.
- Xu, J., Wu, Y., Shi, Z., Lao, L., Li, D., 2007. Studies on two-phase co-current air/non-Newtonian shear-thinning fluid flows in inclined smooth pipes. *Int. J. Multiph. Flow* 33, 948–969. <https://doi.org/10.1016/j.ijmultiphaseflow.2007.03.008>

Experimental Measurement Technique for the Determination of Flow and Heat Transfer Characteristics of Impinging Jets in Industrial Thermoprocessing Plants

Jan Erik Menzler^a, Eileen Trampe^{a,*}, Nico Rademacher^{a,*},
Dominik Büschgens^a, Herbert Pfeifer^a

^aDepartment for Industrial Furnaces and Heat Engineering, RWTH Aachen University
*trampe@iob.rwth-aachen.de

Keywords: Jet impingement cooling, Heat transfer coefficient (HTC), Infrared thermography (IRT), Particle image velocimetry (PIV)

1. INTRODUCTION

Nozzle systems are utilized in metal production to heat and cool material in continuous strip processing lines and in chamber furnaces for the heat treatment of steel, aluminum and copper strip. They are also used in the production and finishing of flat glass, in the drying of paper tapes and in textile technology. The nozzles are directed onto the strip in such a way that the resulting impingement flow ensures the highest possible and most homogeneous heat or mass transfer. In addition, the pressure pad that forms on the surface can ensure that the strip floats through the plant if intended.

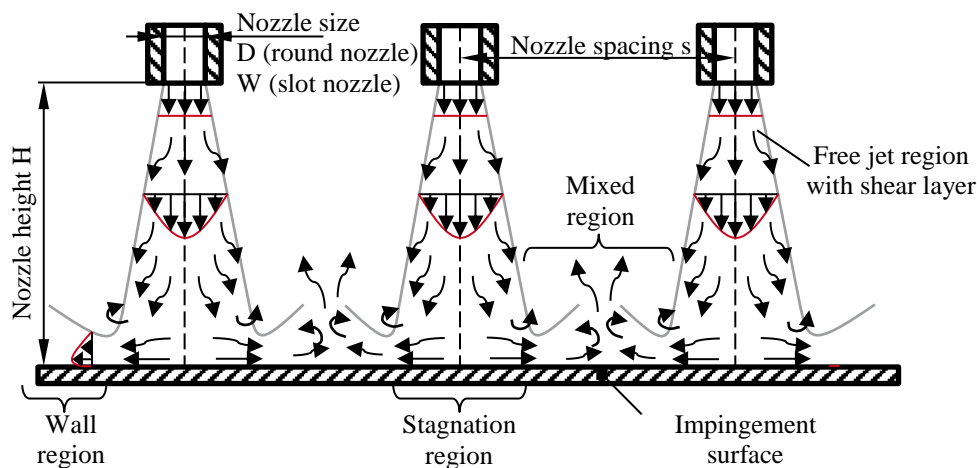


Figure 1. Flow field of an impinging jet.

In Figure 1, the flow field and relevant geometric sizes of an impinging jet are shown. The flow leaves a round or slot nozzle and initially spreads out like a free jet. A stagnation zone is built up near the wall, in which the jet is slowed down and deflected. Downstream of the deflection, the jet spreads out in a wall boundary layer. In the case of cooling, heat is transferred from the surface with the flow by the forced convection.

The flow and therefore also heat transfer characteristics of an impingement jet depend on the geometric design of the nozzle, the distance of the nozzle from the impingement surface resp. the metal strip, the distance between the nozzles in an array of multiple nozzles, the angle at which the jet hits the surface, the jet velocity and the thermal properties of the fluid. For this reason, it is essential to investigate nozzle systems in different geometric configurations in order to optimize the design of heat treatment plant sections and achieve the highest and most uniform heat transfer with the lowest possible energy input.

With a test rig at the Department for Industrial Furnaces and Heat Engineering at the RWTH Aachen University, it is possible to investigate both the flow and heat transfer properties of impingement jet systems using state-of-the-art measurement technology.

2. EXPERIMENTAL SETUP AND MEASUREMENT MEHTOD

The experimental setup for the simultaneous investigation of forced convective heat transfer and the flow properties of impact jets is shown in Figure 2. The test setup consists of a fan, an inlet section with volume flow measurement, a distribution chamber, an exchangeable nozzle field and an electrically conductive *Constantan*[®] (55 % Cu, 45 % Ni) strip.

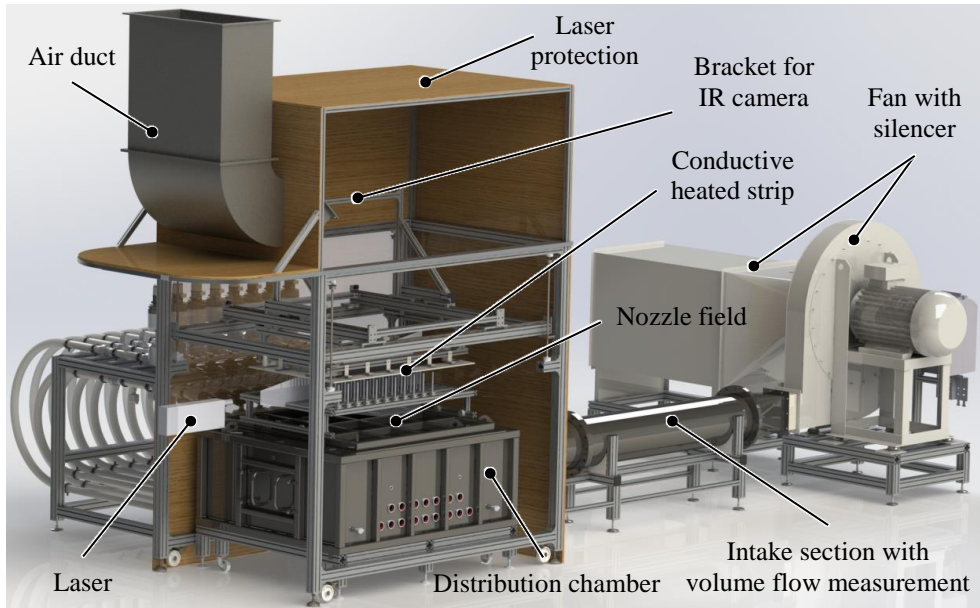


Figure 2. Test rig, dimensions: 8 m x 5 m x 4 m.

Air is drawn in by the fan, which can achieve a maximum pressure increase of $\Delta p = 22,800$ Pa and a maximum volumetric flow rate of $Q = 10,800$ m³/h at a fan speed of $r = 3000$ rev/min. The fan is connected to a pipe that leads into the distribution chamber. A Wilson grid is installed in the pipe to measure the volume flow. Various nozzle systems can be mounted on the distribution chamber in order to investigate different nozzle geometries. The nozzle field can have dimensions of up to 1480 mm x 1560 mm. The *Constantan*[®] strip above the nozzle field, measuring 630 mm x 1160 mm, serves as the impingement surface, its distance to the nozzle system can be adjusted between $H = 0 \dots 250$ mm using an electric motor. The thin *Constantan*[®] strip is resistance-heated by three transformers, each with an electrical output of $P = 12.5$ kVA. The heat generated by the electric supply is transported away convectively by the flow. An infrared camera with a resolution of 640 x 480 pixels (~ 0.3 mega pixels) above the strip measures the temperature distribution on the reverse surface.

Laser measurement technology is utilized to analyze the flow characteristics (see below). For this reason, the entire experimental setup is enclosed in wooden paneling or laser protection curtains. The air drawn in by the fan can escape again through an air duct.

The impingement jet cooling of the *Constantan*[®] strip creates a temperature distribution on the strip surface. Due to the small thickness of the strip ($t = 0.1$ mm), it is thermally thin with Biot numbers in the range of $Bi = 0.0001 \dots 0.001$. Therefore, it can be assumed that the temperature distribution on the impingement surface and the averted surface is the same. The resulting temperature distribution is measured using the infrared camera. Each pixel of the camera represents a square section of the strip with a side length of approximately $a = 1$ mm. The strip is thus divided into square elements with a certain temperature $T_{x,y}$. The local heat transfer coefficient can be determined using an energy balance around each element.

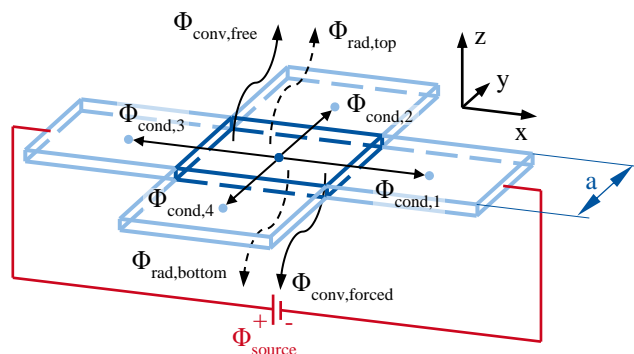


Figure 3. Schematic representation of the heat flows of one strip element.

In steady state, the supplied heat source is balanced by conductive, convective and radiative heat transfer. The energy balance according to equation 1 results from the heat flows shown in Figure 3. The individual heat flows are calculated as a function of the measured temperatures of the strip ($T_{x,y}$), the surrounding air (T_∞) and the impingement jet (T_{fluid}),

the strip's thermal conductivity k and emissivity ϵ as well as an assumed free convective heat transfer coefficient h_∞ . By rearranging the equation, the heat transfer coefficient h can be determined experimentally. The resulting measurement error was estimated using an error propagation analysis. Depending on the test parameters, it amounts to around 4 %.

$$\Phi_{\text{source}} = \Phi_{\text{conv, forced}} + \Phi_{\text{conv, free}} + \Phi_{\text{rad,top}} + \Phi_{\text{rad,bottom}} + \sum_{k=1}^4 \Phi_{\text{cond,k}} \quad (1)$$

with Φ_{source}	$= P_{\text{eff}}/a^2$	(electrically generated effective heat)
Φ_{cond}	$= k(T_{x,y} - T_{x\pm 1,y\pm 1})$	(conducted heat to neighboring elements)
Φ_{rad}	$= \epsilon\sigma(T_{x,y}^4 - T_\infty^4)$	(radiated heat, top / bottom side)
$\Phi_{\text{conv,free}}$	$= h_\infty(T_{x,y} - T_\infty)$	(natural convection top side)
$\Phi_{\text{conv,forced}}$	$= h(T_{x,y} - T_{\text{fluid}})$	(forced convection bottom side)

The flow characteristics of impact jets have a direct impact on its heat transfer properties. They are investigated using laser measurement technology. Particle Image Velocimetry (PIV) or Laser Doppler Anemometry (LDA) can be used to determine the velocity distribution of the flow within a 2D laser section. Secondary variables, such as the local turbulence intensity or the formation of vortices, can be determined from the temporal course of the velocity field.

3. CONCLUSION

The flow field of impact jets and their heat transfer properties can be measured using the presented experimental setup. With the help of temperature measurement technology, the distribution of the local heat transfer coefficient on the impingement surface can be determined with a resolution of 1 mm. Figure 4 shows the result of the evaluation of a nozzle system consisting of 5 slot nozzles, each with a width of $W = 5$ mm, arranged at a distance of $s = 70$ mm to each other. The nozzle box pressure during the test was $p = 1254$ Pa, which corresponds to a nozzle exit velocity of $v = 46.3$ m/s ($Re_{D_H} = 31,518$).

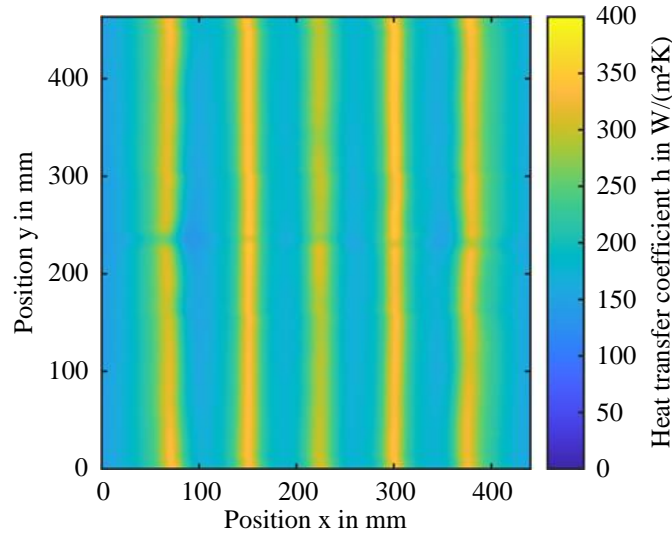


Figure 4. Heat transfer coefficient distribution of a slot nozzle array.
 $W = 5$ mm, $H = 30$ mm, $s = 70$ mm, $p = 1254$ Pa.

In addition to heat transfer, the velocity field of the impingement flow can be recorded using laser measurement technology. This allows conclusions to be drawn as to which flow phenomena have which influences on the heat transfer. Nozzle systems can then be optimized with regard to these flow characteristics.

REMARK

The Laser test equipment is still being put into operation. More details and results are going to be presented on the final poster.

THERMOSENSITIVE COATINGS FOR FAST TRANSIENT HEAT TRANSFER CHARACTERIZATION

Donato Fontanarosa^{a,*}, Yanshen Zhu^b, Matevž Vodopivec^a, Erin Koos^b, Maria Rosaria Vetrano^a

^aKU Leuven, Department of Mechanical Engineering, Celestijnenlaan 300A, 3001 Leuven, Belgium

^bKU Leuven, Department of Chemical Engineering, Celestijnenlaan 200J, 3001 Leuven, Belgium

[*donato.fontanarosa@kuleuven.be](mailto:donato.fontanarosa@kuleuven.be)

Keywords: fast transient heat transfer, thermosensitive coatings, thermography

1. INTRODUCTION

The recent advancements in micro-manufacturing technology have attracted new research focused on enhancing the performance of two-phase heat transfer systems (e.g., direct liquid cooling) by modifying the micro- and nano-surface structures to locally alter the wettability and/or the thermal conductivity. However, a complete mechanistic understanding of the rapid fluid-solid heat transfer dynamics occurring at micro- and submicrometric scales in the proximity of the solid wall and its relation to the inner surface structure is largely unexplored. This results in a large discrepancy among studies on the heat transfer performance of enhanced surfaces and the subsequent impossibility of exploiting the manufacturing potentials. Overcoming these limitations requires efforts in developing new measurement techniques to capture the surface temperature dynamics with submicron (in space) and submillisecond (in time) resolution. In this regard, there are two approaches: contact measurement (e.g., thermocouples and MEMS sensors) and optical measurement (e.g. IR cameras). Even though it can reach a very high acquisition speed (10 kHz or more), the former is local and intrusive. On the contrary, the latter is extensive and non-intrusive, making it ideal and preferred to the former. It is generally based on high-speed IR imaging, thanks to the recent introduction of advanced and expensive long-distance IR cameras that detect medium and long wavelengths with a spatial and temporal resolution of 30 $\mu\text{m}/\text{px}$ and 500 μs in the best-case scenario. A promising alternative to IR imaging is represented by thermosensitive coatings, also known as temperature-sensitive paints (TSPs), where luminescent particles immobilized into a polymeric binder are excited with light of a specific wavelength, emitting light of a longer wavelength whose intensity depends on the actual temperature of the structure containing the luminescent particles (Al Hashimi *et al.*, 2021, Đačanin Far and Dramićanin, 2023). Excitation and emission wavelengths typically range in the UV and VIS spectra, respectively, making TSP-based thermography exploitable using general-purpose high-speed cameras at a lower cost than the most advanced high-speed IR cameras. Nowadays, Ruthenium complexes and quantum dots (QDs) define the current frontiers of thermosensitive coatings thanks to their fast response and the large temperature ranges (Li *et al.*, 2022, Zhu *et al.*, 2023). In this work, we will show the potentialities of TSPs for the measurements of transient heat transfer phenomena, and we will use them to monitor the surface temperature during pool boiling.

2. METHODS

The experimental setups are shown in Figure 1. The first enables pure conduction investigations in air at ambient conditions (Figure 1a), and the second allows pool boiling tests at atmospheric pressure (Figure 1b). For both setups, the test cell consists of an aluminum plate equipped with ceramic support with an $8 \times 10 \text{ mm}^2$ hole milled in the center to allow thermographic observations of transient temperature fields. A 25 μm -thickness Inconel 600 foil of size $8 \times 30 \text{ mm}^2$ is mounted on the ceramic support with epoxy adhesive and connected with two copper electrical contacts to generate Joule heating and control the temperature of the foil. The bottom side of the foil is spin-coated with TSP, and an optical cage system is installed on the bottom of the test cell to illuminate the deposited TSP with a 1.1 W UV lamp (model: Hamamatsu LC-L1 V5) via a long-pass dichroic beam splitter with a cut-on wavelength of 490 nm. The light emitted by the TSP coating is recorded with a high-speed camera (model: Photron SA3) equipped with a Sigma Macro lens 105 mm set at $f/2.8$ aperture, together with a 72 mm extension tube. In pure conduction experiments, the foil is painted on the top face with high emissivity (97.5%) black paint allowing for simultaneous high-speed IR imaging (model: InfraTec ImageIR 5300).

Concerning the TSP preparation, polyacrylic acid (PAA) is used as a binder, while $\text{Ru}(\text{phen})_3\text{Cl}_2$ and $\text{Eu}(\text{TTA})$ are used as fluorescent dyes. The fluorophore-in-binder concentrations by weight are reported in Table 1, together with their working relative UV intensity. The TSP spin-coating is performed at 1000 rpm for 60 s (final thickness $< 3 \mu\text{m}$).

Table 1. Properties of the investigated TSP coatings. Binder: polyacrylic acid.

Test case	Fluorophore	Fluor./Binder [%wt]	UV intensity [%]	T_{ref} [K]	$T_{max,c}$ [K]	A [K^2]	B [K]	R^2
Ru(phen)	$\text{Ru}(\text{phen})_3\text{Cl}_2$	36.8	8	304.4	374.3	1357978	2783	0.9993
Eu(TTA)	Eu(TTA)	20.1	40	307.0	331.3	2312906	3404	0.9969

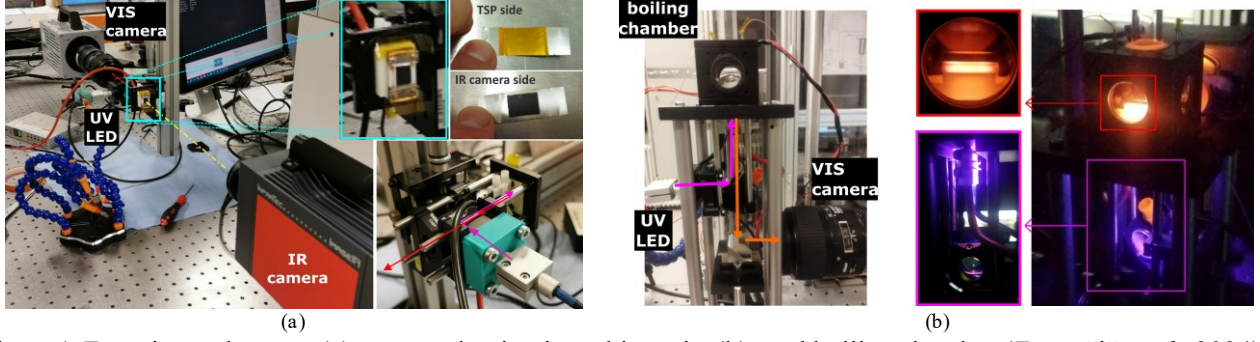


Figure 1. Experimental setups: (a) pure conduction in ambient air; (b) pool boiling chamber (Zupančič *et al.*, 2024).

TSP calibration is performed via pure conduction in the air at ambient conditions tests using synchronized IR (spatial resolution: 0.156 mm/px) and TSP thermography (spatial resolution: 0.0265 mm/px) at 2000 Hz, and then averaging the measurements in space (window size: 1 mm²) and time (window size: 0.25 s). The calibration curve is obtained by 2nd order polynomial fitting as $\ln\left(\frac{I_{ref}}{I}\right) = A\left(\frac{1}{T_{ref}} - \frac{1}{T}\right)^2 + B\left(\frac{1}{T_{ref}} - \frac{1}{T}\right)$, where T_{ref} is the average reference temperature and I_{ref} is the average TSP intensity corresponding to T_{ref} . The polynomial coefficients A and B , the maximum temperature used for calibration $T_{max,c}$, T_{ref} and the fit goodness R^2 are summarized in Table 1 for each investigated TSP. Figure 2 shows the calibration data, the calibration curves and one validation point.

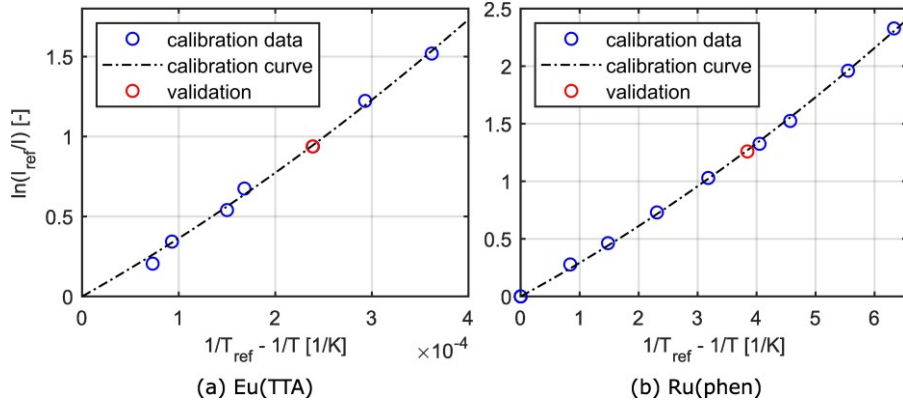


Figure 2. TSP calibration curves: (a) Eu(TTA); (b) Ru(phen).

3. RESULTS

As shown in Figure 3, the dynamic response has been first assessed in pure conduction tests by imposing on the metal foil low (cases a and c) and high power (cases b and d) steps, as well as a power pulse (case e). Such power inputs correspond to four temperature ramps and one pulse with average heating slopes of 2.3 K/s (case a), 23.15 K/s (case b), 0.65 K/s (case c), 28.3 K/s (case d), and 402.6 K/s (case e).

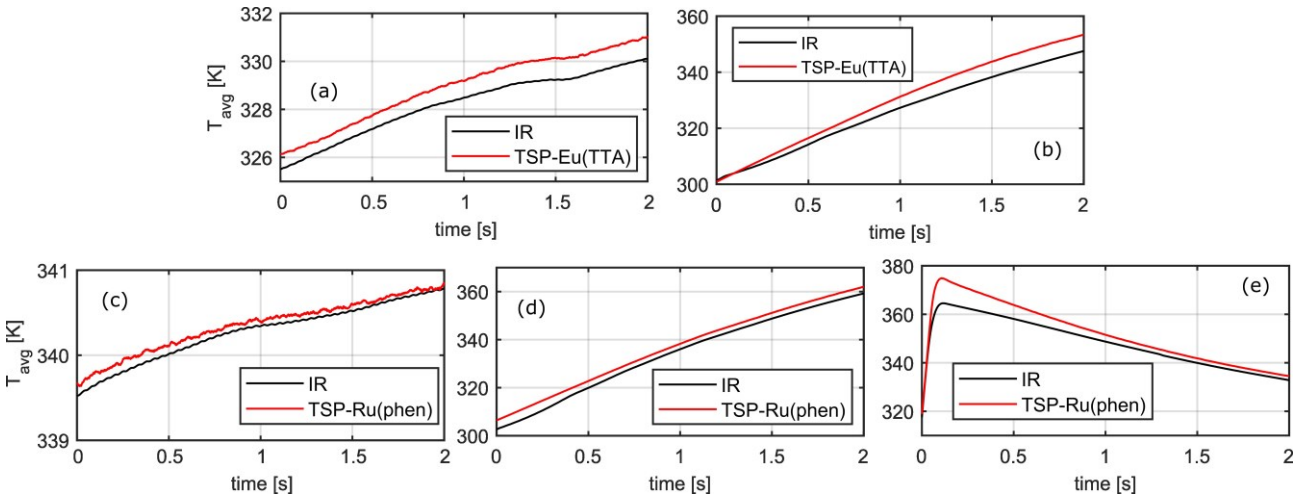


Figure 3. Pure conduction tests and TSP dynamic responses. Eu(TTA): (a) and (b). Ru(phen): (c), (d) and (e).

Both Eu(TTA) and Ru(phen) follow the heating dynamics, with the TSP side which is hotter than the IR side, due to the insulating effect induced by the ceramic holder and the lower thermal conductivity of the TSP. Eu(TTA) exhibits the poorest performance with increasing deviations from IR measurements up to a maximum of 1 K for case a and 5.8 K for case b. On the contrary, Ru(phen) exhibits a constant deviation from the IR signals, equal to about 2.8 K for case d and almost negligible (< 0.35 K) for case c; such a deviation reduces in the absence of Joule heating (see case e), meaning the observed deviations between the TSP and the IR signals are partially related to an actual temperature difference between the two imaged foil faces. TSPs have been then applied to pool boiling of the dielectric fluid 3M Novec 7000 (boiling temperature of 307.15 K) undergoing constant heat flux at atmospheric pressure. Figure 4 shows the TSP thermography recorded at 4 and 10 kHz after increasing the relative UV intensity to 40 (with recalibration) and 90%, (without calibration) respectively. Active nucleation sites with bubble footprints smaller than $400\ \mu\text{m}$ are detected, as shown in the instantaneous spatial maps on the left. After identification of the main nucleation regions (coloured windows in Fig. 3), the temporal dynamic of the average temperature in each region is plotted (see graphs on the right). Different bubble dynamics are detected, with decreasing nucleation activity when moving from nucleation region 1 to nucleation region 3.

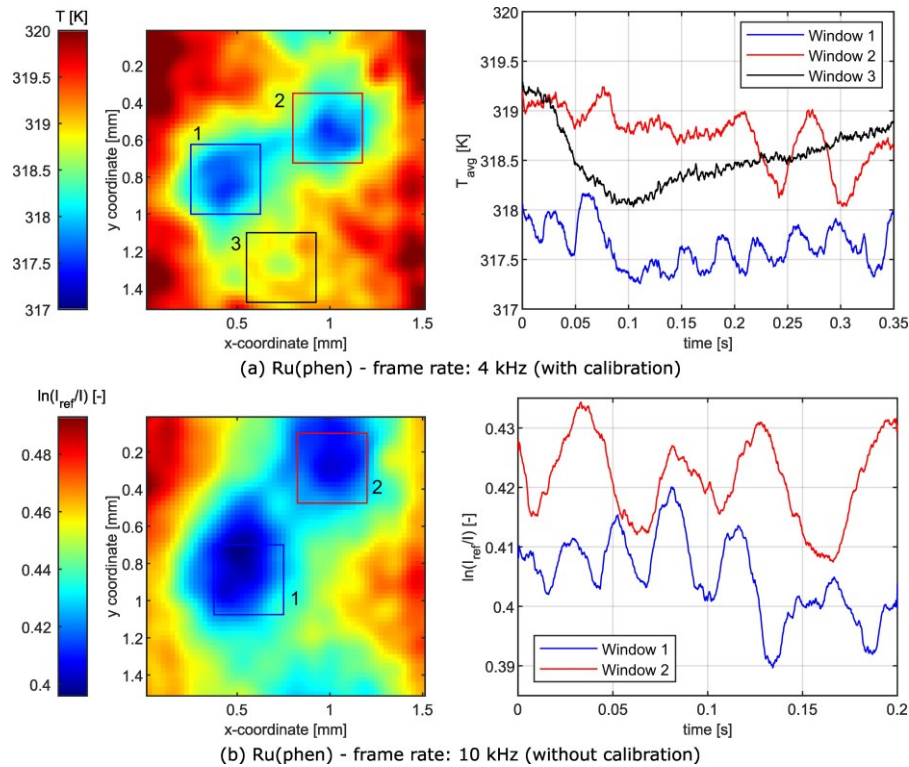


Figure 4. Pool boiling tests and TSP dynamic responses with Ru(phen): (a) 4 kHz; (b) 10 kHz.

4. CONCLUSIONS

The present work provides an experimental assessment of the performance of different TSPs made of acrylic binders and different fluorescent dyes. The dynamic response is assessed by imposing power steps and pulses on the metal foil in pure conduction and to pool boiling tests. The preliminary results prove the TSP potential in overcoming the current limitations of IR thermography and enabling spatio-time-frequency modal analyses of the heat transfer dynamics at the micro-scale for a deeper understanding of two-phase heat transfer processes in the presence of fast transients.

5. REFERENCES

- Al Hashimi, H., Chaalal, O., Chaalal, M., Muhamed, H., 2021. Review of Temperature Measurement Techniques. *Biomed J Sci & Tech Res* 40(3).
- Đačanin Far, L. and Dramićanin, M.D., 2023. Luminescence Thermometry with Nanoparticles: A Review. *Nanomaterials*, 13(21), p.2904.
- Li, S., Zhai, Y., Pan, X., Jin, Y. and Wang, M., 2022. High-sensitive luminescence thermometer using Ruphen-based temperature-sensitive paint. *Infrared Physics & Technology*, 123, p.104151.
- Zhu, Y., Buitenhuis, J., Förster, B., Vetrano, M.R. and Koos, E., 2023. Development of Perovskite Quantum Dots for Two-Dimensional Temperature Sensors. *ACS Applied Nano Materials*, 6(6), pp.4661-4671.
- Zupančič, M., Fontanarosa, D., Može, M., Bucci, M., Vodopivec, M., Nagarajan, B., Vetrano, M.R., Castagne, S. and Golobič, I., 2024. Enhanced nucleate boiling of Novec 649 on thin metal foils via laser-induced periodic surface structures. *Applied Thermal Engineering*, 236, p.121803.

TEMPERATURE DEPENDENCE OF CLUSTER FORMATION BEHAVIOR OF TEMPERATURE SENSITIVE MAGNETIC MICROCAPSULES

Keiko Ishii^{a*}, Koji Fumoto^b

^aCollege of Science and Engineering, Chuo University,
1-13-27, Kasuga, Bunkyo-ku, Tokyo, 112-8551, Japan

^bCollege of Science and Engineering, Aoyama Gakuin University,
5-10-1, Fuchinobe, Chuo-ku, Sagamihara, Kanagawa, 252-5258, Japan

*k.ishii@mech.chuo-u.ac.jp

Keywords: Magnetic Fluid, Thermal Fluid, Optical visualization, Microcapsule

1. INTRODUCTION

A magnetic fluid is a unique material that behaves as if the liquid itself possesses magnetism, and its usage as a refrigerant is expected to realize unprecedentedly smart and highly efficient heat transport devices. Among them, temperature-sensitive magnetic fluids are expected to realize a more functional heat removal system because their magnetization is temperature-dependent near room temperature (Fumoto et al., 2007). In particular, because magnetic particles respond to magnetism, the internal flow may be controlled by applying an external magnetic force, in addition to increasing the thermal conductivity of the refrigerant itself, and functional heat transport is expected (Alam and Kin, 2018). Since the magnetization of temperature-sensitive magnetic fluids decreases as the temperature rises, it is expected that the magnetic particles attracted to the wall surface by the magnetic force will leave the wall surface after receiving heat. Hence, researchers have focused on using temperature-sensitive magnetic fluids as refrigerants (Fumoto et al., 2009). The heat transport efficiency of a magnetic fluid is known to increase when a magnetic field is applied, which is considered to arise from cluster formation inside the flow path and a unique velocity distribution. Measurements have been conducted using an ultrasonic Doppler current meter, visual inspection of diluted magnetic fluid, and observation of the magnetic fluid flow field by particle image velocimetry (PIV) particles, but the detailed flow has not been understood. There are few experimental reports that clearly demonstrate the flow characteristics of magnetic clusters near the wall surface affected by the flow field. Hence, quantitative visualization measurements of the flow field by encapsulating magnetic particles in fluorescently labeled microcapsules were conducted (ishii et al. 2020). In this study, we used this method to visualize the formation of temperature-sensitive magnetic clusters affected by forced convection fields and temperature.

2. EXPERIMENT

In this experiment, microcapsules were synthesized using the solvent evaporation method (ishii et al. 2019). Poly-IBM (poly isobutyl methacrylate), temperature-sensitive magnetic particles (Mn-Zn ferrite, Ichinen Chemicals, particle diameter: 23.9 nm), Nile Red, Span20 (sorbitan monolaurate) dissolved and dispersed in 1-2 dichloromethane were used as the organic phase. Water in which gum arabic was dispersed was used as the aqueous phase. The organic phase was added dropwise to the aqueous phase, and an O/W emulsion was prepared using a homomixer. The organic solvent in the oil droplets was completely vaporized to obtain a solid microcapsule. The particle size can be controlled by varying the stirring speed. In this study, the stirring speed was 14000 rpm, and a microcapsule with an average particle size of 2 μm was used.

Figure 1 shows a schematic of the equipment used in this experiment. The experimental equipment consists of an optical system such as a microscope, camera, syringe pump, and flow path for visualization containing a magnetic field supply unit. A syringe pump (ASONE, SPDC1) ensures that the microcapsule suspension flows a predetermined rate ($2.98 < \text{Re} < 50.6$). The observation section is irradiated with a laser (532 nm) to excite the fluorescent dye in the capsule. The emission wavelength of the capsule was observed by a CMOS camera (FLIR, GS3-U3-32S4MC) using a dichroic mirror and long-pass filter. The visualization channel (40 x 140 x 10 mm) is made of a cycloolefin polymer with low fluorescence, and a rectangular channel (whose width, depth, and length are 1 mm, 1 mm, and 100 mm, respectively) is created 8 mm from the top surface. The magnetic field was applied perpendicular to the direction of the flow path. Neodymium magnets (30 mm x 35 mm x 5 mm) were used, and the magnetic flux density at the flow path observation position was adjusted from 72 -- 158 mT by stacking multiple magnets. The center of the magnetic circuit is the center of the flow path, and this position was the observation area. In the magnetic circuit, magnets were installed on each of the two sides. A single magnet was installed on one side of the circuit, while 2-4 magnets were installed on the other side. This prevented the magnetic flux from spreading and caused the clusters to accumulate strongly on one side of the flow path.

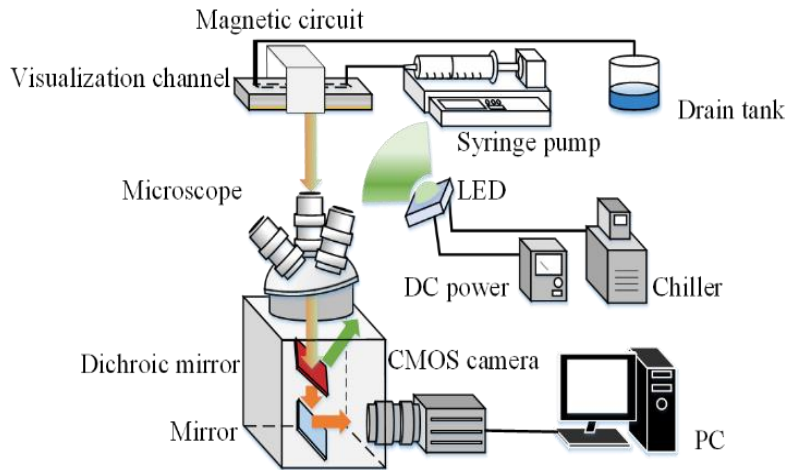


Figure 1. Experimental setup for visualizing the flow field

3. RESULTS AND DISCUSSIONS

Figure 2 shows an example of a fluorescence image of magnetic cluster taken by the microscope. It can be confirmed that the magnetic microcapsules fluorescence and are attracted to the magnet to form clusters near the wall surface. In this study, we describe the observation results of cluster formation and movement by observing the image itself and investigate the relationship between the spatial average length of the cluster and various parameters. The cluster length was calculated by binarizing the image and dividing by the width of the image to calculate the average cluster length per space. The experimental parameters were the time from magnetic field application, flow velocity and temperature, and the effect of these parameter on the cluster length was investigated.

Figure 3 shows the cluster length under each flow velocity condition. Here, the viscosity of the liquid was $5.72 \text{ mPa}\cdot\text{s}$, the magnetic flux density was 142.3 mT , and the measurement timing was 500 s from the application of the magnetic field. Multiple experiments were performed for each parameter. Red circles (\bullet) show a tendency for clusters to increase monotonically during the measurement time, black crosses (\times) when no clusters are formed on the wall surface, and blue triangles (\blacktriangle) for cases showing unstable behavior.

The cluster length tends to decrease as the flow velocity increases. When the flow velocity is 70 mm/s or more, the cluster tends to be shorter than other conditions. This is because the fluid shear force exceeded the bonding force between the magnetic capsules, causing the cluster to collapse or detach from the wall surface. On the other hand, it should be noted that the error bar of the data becomes large when the flow velocity is in the range of 45 to 65 mm/s . In the range just before the shear force at which the cluster collapses, the cluster formation behavior tends to become unstable, and there are cases where the cluster becomes longer than other conditions, and there are cases where the cluster collapses and is hardly detected. In the range of 40 mm/s or less, the cluster length gradually decreases as the flow velocity increases. It can be said that the cluster formation characteristics change depending on the flow velocity.

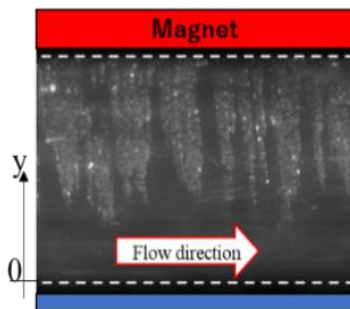


Figure 2. The appearance of the cluster formed on the wall surface.

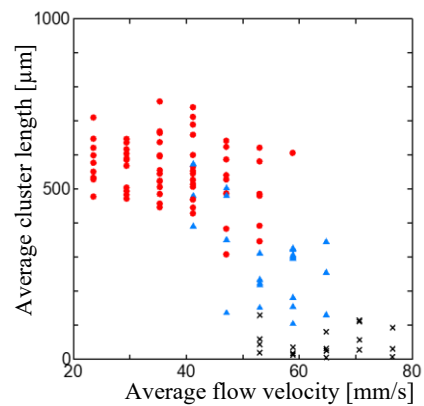


Figure 3. Average cluster length at each flow velocity ($B=142.3\text{mT}$, $\mu=5.72\text{mPa}\cdot\text{s}$, Particle : Mn-Zn ferrite).

The capsule dispersion adjusted to a predetermined temperature was injected into the temperature-controlled flow path, and the temperature dependence of the cluster formation characteristics was investigated. Magnetite, which has a small temperature dependence of magnetization, and manganese-zinc ferrite, which has temperature-sensitive magnetism were compared. Figure 4 shows the relationship between the shear stress at the boundary where the cluster collapses and the temperature. The horizontal axis is the temperature at the outlet of the flow path near the observation part. The black dotted line and the green range in the graph show the average and variation of the boundary shear stress at which the cluster collapses when the magnetic flux density is 142.3 mT, respectively. In magnetite particles, the clusters collapsed at a constant shear stress regardless of temperature. On the other hand, in the temperature-sensitive magnetic particles, the fluid shear force required for cluster decay decreased as the temperature increased. By applying this feature, clusters with heat may be released, and clusters without heat may be able to perform functional heat transfer by staying on the wall surface to absorb heat.

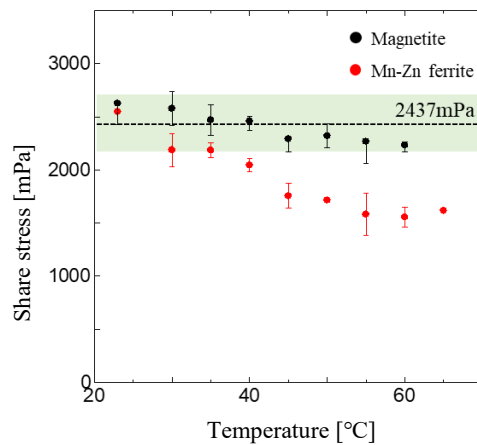


Figure 4. Shear stress as the cluster detaches from the wall surface by changing the fluid temperature.

4. CONCLUSIONS

Fluorescent magnetic microcapsules were prepared, and cluster formation and collapse behavior were visualized at the magnetic field application position in a forced convection field. Overall, larger flow velocities were associated with shorter clusters owing to the fluid shear force. When the applied fluid shear force exceeded a certain level, the magnetic clusters did not grow on the wall surface. However, when the fluid shear force was low, the clusters grew on the wall surface, and moved owing to the flow. In the region shortly before this critical shear force, the average length of the cluster became unstable. In the temperature-sensitive magnetic capsule, the shearing force at which the cluster collapses depend on the temperature.

5. REFERENCES

- Alam, T. and Kim, M.H. 2018. "A comprehensive review on single phase heat transfer enhancement techniques in heat exchanger applications" *Renew. Sustain. Energy Rev*, Vol.81 pp.813–839.
- Fumoto, K., Yamagishi, H. and Ikegawa, M., 2007. "A Mini Heat Transport Device Based On Thermo-Sensitive Magnetic Fluid" *Nanoscale and Microscale Thermophysical Engineering*, Vol. 11, pp. 201-210.
- Ishii, K., Aizawa, R. and Fumoto, K., 2019. "Synthesis of Temperature-Sensitive Magnetic Microcapsules and Visualization of Cluster Formation". *IEEE Magnetics Letters*. Vol.10, pp. 575–580.
- Ishii, K., Aizawa, R. and Fumoto, K., 2020. "Two-Dimensional Flow Field Visualization of Temperature-Sensitive Magnetic Fluids Using a Luminescent Microcapsule" *IEEE Magnetics Letters*, Vol. 11, pp.2994559.

EXPLORING RHEOLOGICAL CHARACTERISTICS: A COMPARATIVE ANALYSIS OF RHEOLOGICAL MEASUREMENTS AND THE REAL DATA IN PIPELINE FLOW

Gláucio K. Matoba^a, Daiane M. Iceri^b, Helder L. Moura^b, Miguel M Valheros^a, Roney L. Thompsom^c, Annie Fidel-Dufour^d, Marcelo S. Castro^{a,b}

^aSchool of Mechanical Engineering, Universidade Estadual de Campinas (UNICAMP), Campinas-SP, Brazil.

^bCenter for Petroleum studies (CEPETRO), Universidade Estadual de Campinas (UNICAMP), Campinas-SP, Brazil.

^cDep. of Mechanical Engineering, COPPE, Federal University of Rio de Janeiro, Centro de Tecnologia, Ilha do Fundão, 21945-970, Rio de Janeiro, RJ.

^dTotalEnergies, CSTJF Avenue Larribau, PAU, Cedex 64018, France.

*kenji.matoba@gmail.com

Keywords: Non-Newtonian fluid, yield-stress, PIV, rheometer

1. INTRODUCTION

Non-Newtonian fluids are prevalent in various industrial sectors, including cosmetics, food processing, and petroleum industries (Balmforth, Frigaard e Ovarlez 2014). In many instances, the behavior of these fluids can be effectively described by the Herschel-Bulkley (HB) equation ($\tau = \tau_y + k\dot{\gamma}^n$) for $\tau \geq \tau_y$, and $\dot{\gamma} = 0$ for $\tau < \tau_y$, where τ and $\dot{\gamma}$ represent scalar quantities that capture the intensity of the corresponding tensors. Here, τ_y represents the yield stress, while k and n denote the consistency coefficient and power-law index, respectively. Accurate determination of these rheological parameters is crucial for estimating dimensionless numbers, friction factors, pressure drop, and consequently sizing pipelines and pumps in industrial installations.

Traditional rheometric measurements, including flow curves, oscillatory, and creeping flow tests, are commonly employed to determine the yield stress of HB fluids (Iceri, et al. 2023). However, discrepancies in rheological parameter values suggest that these conventional methods, designed to minimize fluid slippage, tend to overestimate these parameters (García-Blanco, et al. 2022). An alternative approach involves using Particle Image Velocimetry (PIV) to estimate velocity profiles, offering reliable insights into yield stress determination (Pérez-González, et al. 2012). This study aims to compare yield stress values obtained through these different methods. The findings reveal a difference of less than 10% between the methodologies employed.

2. METHODOLOGY

2.1 Experimental apparatus

The experimental setup employed a closed-loop flow system consisting of a 20-meter-long pipeline with a circular pipe with diameter of 0.053m in horizontal direction. At the end of the pipeline, a transparent acrylic viewing section was installed for the PIV system measurements. Continuous fluid circulation throughout the system was ensured by a positive displacement pump. The experimental fluid utilized in this study comprises an aqueous solution incorporating Carbopol (Polyacrylic Carbomer 940) and triethanolamine (TEA) as a neutralizer (85% neutralization in water). The Carbopol concentration was 0.15wt%, while the TEA concentration was 750 ppm. The solution preparation protocol followed the methodology outlined by (Iceri, et al. 2023).

This study utilized Particle Image Velocimetry (PIV) for flow visualization and measurement. The PIV system comprised a pulsed laser head emitting 200mJ pulses at 5Hz with a wavelength of 532nm. A high-speed camera equipped with a 1376 x 1040 CCD chip, and a Zeiss Milvus 2/50M lens with a 50mm focal length (F/5.6). The PIV operated in a double-frame mode, with the interframe time adjusted for each experimental condition. The tracer particles were Polyamide Seeding Particles (PSP) provided by Dantec Dynamics, each with a diameter of 50 μ m. A detailed description of the experimental apparatus and the PIV procedure will be provided in the full article.

2.2 Theoretical analysis

The analytical solution for the velocity profile was derived following the methodology outlined by (Chhabra e Richardson 2008) for a fully developed, steady-state flow of an incompressible HB fluid. The velocity profile is segmented into two distinct regions within a circular cross-section for laminar flow. The first region corresponds to shear stress exceeding the yield stress, as delineated by Eq.(1). The second region represents a scenario where the shear stress is lower than the yield stress, this type of motion is commonly referred to as plug flow.

$$u(r/R) = \frac{n}{n+1} R \left(\frac{\tau_y}{\phi k} \right)^{(1/n)} \left\{ (1 - \phi)^{(n+1)/n} - \left(\frac{r}{R} - \phi \right)^{(n+1)/n} \right\} \quad (1)$$

where ϕ denotes the ratio between the yield stress and the wall shear stress (τ_y/τ_w) and radius ratio (r_p/R), with r_p as the plug radius. Extending the Hagen-Poiseuille formula enables the calculation of the local shear stress as:

$$\tau(r/R) = \frac{r}{R} \frac{\Delta P D}{L 4} \quad (2)$$

3. RESULTS AND DISCUSSIONS

Figure 1 presents the findings concerning the velocity ($u(r/R)$), shear rate ($\dot{\gamma}$), and shear stress (τ) profiles under the mean velocity condition of 0.27 m/s. In Figure 1(a), the analytical velocity profile is depicted by the blue dashed line (Eq.(1)) using rheological data obtained from the rheometer. Equation 1 is valid for $0 < r/R < 1$; therefore, it was mirrored for the region with $r < 0$, under the assumption of flow symmetry. Notably, this profile indicates a region of plug flow at the center of the pipe. Additionally, the black open circles in the same figure depict the PIV experimental data, fitted with a polynomial curve shown as a solid black line. The polynomial fit resulted in an average error of -4.9×10^{-6} . Additionally, a distinct segment of the curve is highlighted in red, indicating the "real shear" region, bounded by non-slip conditions near the wall and shear rate values exceeding 1×10^{-2} . This red line is also depicted in Figs.1(b) and (c), representing the same region.

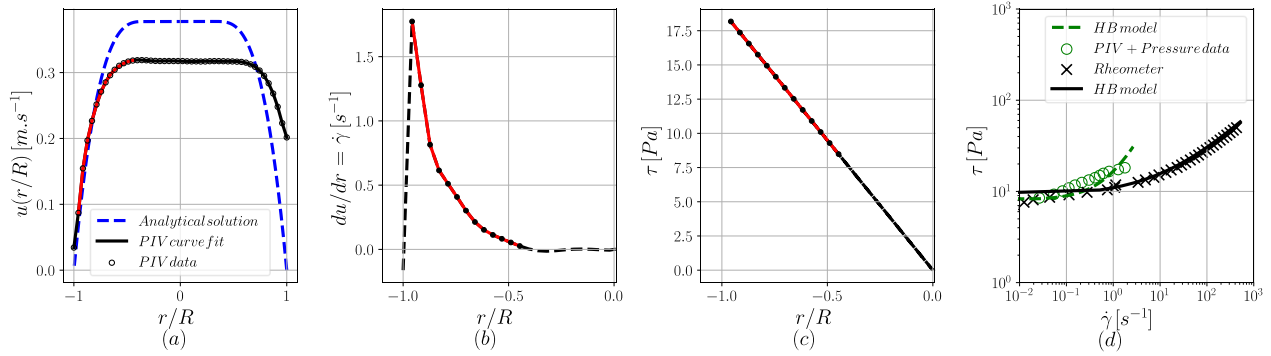


Figure 1. (a) Velocity profile from PIV data and the analytical solution from Eq.(1); (b) First derivative of PIV velocity profile ($\dot{\gamma}$); (c) Shear stress profile from differential pressure data, Eq.(2); (d) Flow curve comparison.

The velocity profile adjusted by the PIV experimental data displays asymmetry, with the bottom portion of the horizontal pipeline ($r/R < 0$) differing from the upper region ($r/R > 0$), contrary to the expected symmetry of the theoretical velocity profile. This asymmetry is attributed to greater light scattering in the upper region of the pipe during testing, caused by the high fluid's turbidity. This scattering hampers uniform laser light distribution to the uppermost particles, resulting in compromised image cross-correlations and higher uncertainty in PIV measurements in this region. To mitigate uncertainty, subsequent analyses will focus solely on the bottom region ($r/R < 0$).

Figure 1(b) illustrates the first derivative of the velocity profile, which leads to the shear rate. This figure exclusively depicts the bottom region from the centerline, with the abscissa axis ranging from $-1.0 < r/R < 0.0$, the same as in Fig.1(c). The dashed line depicts the shear rate function, and the filled black circles indicate the derivative values corresponding to the PIV velocity points. Analyzing the shear rate values facilitates the determination of the plug radius (r_p), where $\dot{\gamma} < 1 \times 10^{-2}$ was defined as the cutoff limit of the shear rate data, similar to rheometric tests, thus establishing the plug radius. The plug radius value determined by PIV is $\phi = 0.45$, whereas the theoretical plug ratio is $\phi = 0.34$.

Figure 1(c) displays the shear stress profile from differential pressure sensor data, as given by Eq. (2), represented by the dashed line. The red line overlays the region corresponding to the "real shear" rate. The black dots correspond to the PIV points. In practical terms, the yield stress (τ_y) can be calculated by using the pressure sensor data and the plug ratio (r_p/R), as indicated by Eq.(2), with $r = r_p$. In this case, the determined yield stress was found to be 8.49 Pa. This approach, referred to as "Plug ratio from PIV and pressure data," is illustrated in Tab.(1). However, this approach does not enable the estimation of the consistency coefficient (k) or the power-law index (n).

Utilizing the data extracted from the shear rate and shear stress curves depicted in Figs.1(b) and (c) respectively, it becomes feasible to reconstruct a flow curve mirroring the rheometer flow curve illustrated in Fig.1(d). By correlating the PIV data with the differential pressure sensor data, the reconstructed flow curve was meticulously aligned concerning the positions (r/R) shared between these two profiles. It is noteworthy that this curve signifies a slip-free region, following the findings of (Pérez-González, et al. 2012) (García-Blanco, et al. 2022). The resultant flow curve, depicted by open green circles, was subsequently refined through adjustment using the Herschel-Bulkley curve fit. This approach is referred to as "Flow curve from PIV and pressure data," and the outcomes are presented in Tab.(1). The rheological flow curve

data is illustrated in Fig.1(d) with "x" markers, and the Herschel-Bulkley model is represented by the black continuous line. This approach is referred to as "Rheometer – Parallel plates" and the corresponding results are presented in Tab.(1).

The yield stress (τ_y) values demonstrate remarkable consistency across all methods, with a deviation of less than 10%, as shown in Table 1. However, the value of the consistency coefficient (k) estimated by combining PIV with data from the differential pressure sensor was significantly overestimated, approximately by 298%, compared to the value obtained from the rheometer. This discrepancy arises from the flow conditions, particularly low velocities, resulting in a region with low shear rate data and, consequently, a non-precise fitting of the Herschel-Bulkley model curve.

Table 1. Results of yield-stress from different techniques.

Method	τ_y [Pa]	k [Pa.s ⁿ]	n	Relative error of τ_y [%]
Rheometer – Parallel plates	8.81 ± 2.00	2.16	0.5	-
Plug ratio from PIV and pressure data	8.49	-	-	-3.76
Flow curve from PIV and pressure data	8.08	8.60	0.5	-8.23

3. CONCLUSION

In this study, an experimental investigation was conducted using an aqueous solution of Carbopol, showcasing the non-Newtonian fluid behavior of the Herschel-Bulkley type. The velocity profile data obtained from Particle Image Velocimetry (PIV) and data from the differential pressure sensor during laminar flow in the circular pipeline were utilized to determine the rheological properties of the fluid and compare them with measurements obtained from a parallel plate rheometer.

The findings indicate a convergence in the yield stress values obtained through the three methodologies, with a relative error of less than 10%. However, the consistency coefficient values showed divergence, suggesting the need for additional experimental points to refine the analysis. These insights underscore a methodology for further investigation aimed at enhancing the understanding and characterization of the rheological behavior of non-Newtonian fluids under flow conditions.

4. ACKNOWLEDGEMENTS

We gratefully acknowledge the support of the ALFA - Artificial Lift and Flow Assurance Research Group, hosted by the Center for Energy and Petroleum Studies (CEPETRO) at the Universidade Estadual de Campinas (UNICAMP), Brazil. We also thank TotalEnergies EP Brazil for their funding and support, as well as the ANP (Brazil's National Oil, Natural Gas, and Biofuels Agency) for assistance through the R&D levy regulation. Special thanks to the CEPETRO-UNICAMP and FEM-UNICAMP for their collaboration, and to the Alberto Luiz Coimbra Institute (COPPE-UFRJ) for their contributions.

4. REFERENCES

- Balmforth, Neil J., Ian A. Frigaard, e Guillaume Ovarlez. "Yielding to Stress: Recent Developments in Viscoplastic Fluid Mechanics." *Annual Review of Fluid Mechanics* (Annual Reviews) 46 (January 2014): 121–146.
- Chhabra, Raj P., e John Francis Richardson. *Non-Newtonian flow and applied rheology - engineering applications*. Butterworth-Heinemann, 2008.
- García-Blanco, Yamid J., Vitor Y. Urazaki, Ángel. D. J. Rivera, Luis H. Quitian, Eduardo M. Germer, e Admilson T. Franco. "Rheological characterization of viscoplastic fluid flow in a pipe with wall slip using in situ particle image velocimetry." *Rheologica Acta* 62 (December 2022): 93–110.
- Herschel, Winslow H., e Ronald Bulkley. "Konsistenzmessungen von gummi-benzollösungen." *Kolloid-Zeitschrift* (Springer) 39 (1926): 291–300.
- Iceri, Daiane Miekko, Jorge Luiz Biazussi, Charlie van der Geest, Roney Leon Thompson, Thierry Palermo, e Marcelo Souza Castro. "The yielding behavior of aqueous solutions of Carbopol and triethanolamine and its prediction considering the fractal nature of the formed aggregates." *Rheologica Acta* 62 (July 2023): 405–416.
- Pérez-González, José, Juan Javier López-Durán, Benjamín M. Marín-Santibáñez, e Francisco Rodríguez-González. "Rheo-PIV of a yield-stress fluid in a capillary with slip at the wall." *Rheologica Acta* (Springer Science and Business Media LLC) 51 (September 2012): 937–946.

Evaporation-induced emulsification and phase separation dynamics of ternary droplets in acoustic levitation

Misaki Mitsuno^{a,*}, Koji Hasegawa^b

^a Graduate School of Engineering, Kogakuin University, Tokyo, 163-8677, Japan

^b Department of Mechanical Engineering, Kogakuin University, Tokyo 163-8677, Japan

*am23059@ns.kogakuin.ac.jp

Keywords: acoustic levitation, droplet, evaporation, Ouzo effect, core-shell structure

1. INTRODUCTION

In recent years, contactless sample manipulation technology in midair has been attracting great attention in the fields of biochemistry and pharmaceutical science. One of the promising methods is the acoustic levitation (Foresti, D *et al.*, 2013). This method enables us to levitate, transport, mix, and evaporation of samples in resonant acoustic fields (Yarin, A. L *et al.*, 1998). Acoustic levitation offers a unique advantage by mitigating undesirable wall effects like nucleation and contamination, which are common in conventional container-based methods. However, it has been pointed out that this method causes nonlinear and dynamic behaviors such as unsteady translational motion (Hasegawa, K and Kono, K. 2019) and evaporation behavior (Maruyama, Y and Hasegawa, K., 2020) in the levitated sample. Although there are many previous studies on the evaporation behavior of one or two component droplets, experimental studies on the evaporation behavior of three or more component droplets are still in the development stage. In this study, we aim to understand the evaporation dynamics of spontaneous emulsification and phase separation of Ouzo droplets (Tan, H *et al.*, 2016) premixed with water, ethanol and anise oil upon evaporation. To achieve this, the spontaneous emulsification and phase separation process of Ouzo droplets upon evaporation was visualized and analyzed.

2. EXPERIMENTAL METHOD

Figure 1 (a) shows a schematic diagram of the experimental setup used in this study (Maruyama, Y and Hasegawa, K. 2020). A sinusoidal signal generated by a function generator was input to an ultrasonic transducer. Ultrasonic wave is emitted from the bottom horn connected to the ultrasonic transducer and is reflected by the top reflector, which is placed at a multiple of half the wavelength distance to form an acoustic standing wave between the horn and the reflector, as shown in Fig. 1 (b). To levitate the droplet, a liquid droplet was manually injected using a syringe and needle near the acoustic pressure node of the acoustic standing wave. A high-speed camera with backlight illumination was used to visualize the levitated droplets. The interface temperature of the levitated droplet was simultaneously captured using an IR camera. The images obtained by the high-speed camera were processed using a computer and in-house code.

The reflector shape used in this experiment has a radius of curvature of 36 mm (R36). The frequency was 19.3 kHz and the wavelength λ was 18 mm. The width of the horn and reflector is 36 mm ($\approx 2\lambda$). The distance between the horn and reflector is 48 mm ($\approx 5\lambda/2$), and a droplet was levitated near the third pressure node ($\approx 3\lambda/2$ from the bottom reflector). The ambient temperature is $23\pm 2^\circ\text{C}$ and the humidity is $55\pm 5\%$.

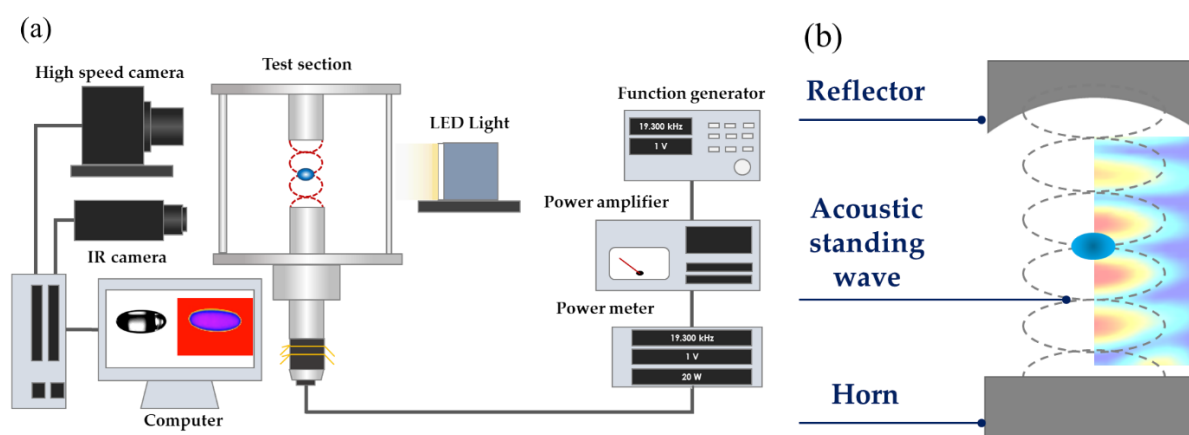


Figure 1. Schematic of acoustic levitator: (a) experimental setup and (b) levitation principle.

3. RESULTS AND DISCUSSIONS

Figure 2 shows the evaporation process of the Ouzo droplets with concentrations of 70 vol%, 29 vol%, 1 vol% of ethanol, water, and anise oil, respectively. Fig. 2 (a) shows that the droplet diameter decreased with time, with the ouzo effect occurring 60 s after levitation. During the Ouzo effect, the droplets became cloudy (black) because the backlight could not penetrate through the generated myriad micro-oil droplets. Figure 2 (b) depicts the time evolution of the droplet diameter and aspect ratio in Fig. 2 (a). The aspect ratio $AR (=b/a)$ is defined as the equatorial-to-polar ratio of the major diameter b and minor diameter a . The red area highlighted in Fig. 2 (b) represents the time when each droplet experienced the Ouzo effect, which lasted until approximately 30 s. The experimental results showed that the levitated droplet evaporated and nonlinearly decreased the droplet diameter. During the evaporation process, the droplet gradually changed shape and became more spherical ($AR \approx 1$). This nonlinear behavior is due to the preferential evaporation of the volatile ethanol component (~ 200 s), and following the evaporation of water (200 s~). After the preferential evaporation of ethanol, the higher surface tension of water maintains the spherical shape of the droplet interface.

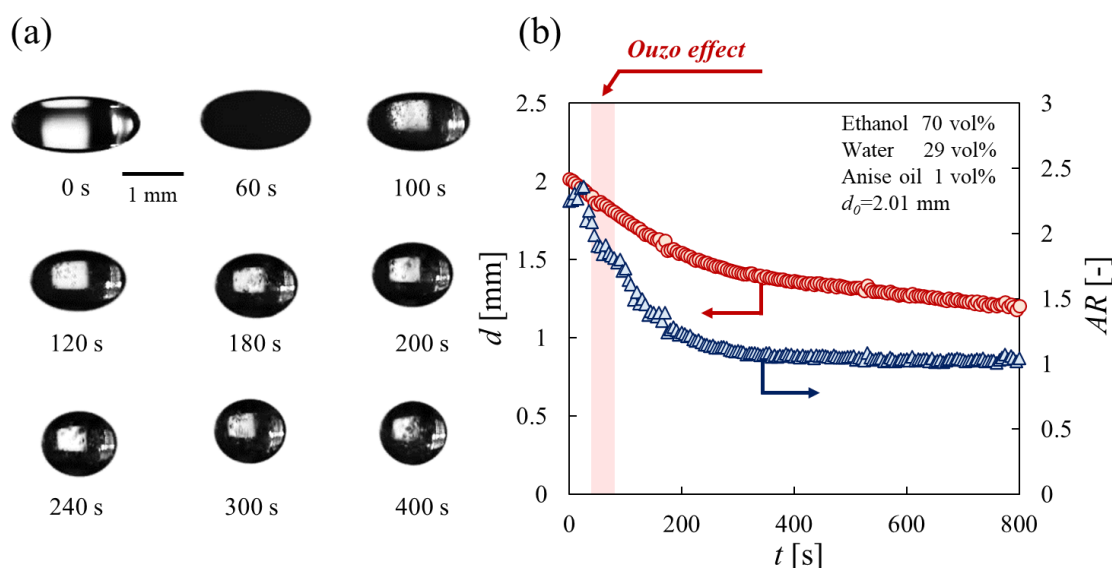


Figure 2. Evaporation process of Ouzo droplets (ethanol: 70 vol%, water: 29 vol%, anise oil: 1 vol%). (a) Snapshot of Ouzo droplet during evaporation and (b) time evolution of d and AR . The highlighted red area in (b) indicates the occurrence of the Ouzo effect.

The transition time and duration of the Ouzo effect were then investigated by changing the ethanol concentration. These results indicate that the Ouzo effect occurs during droplet levitation when the ethanol concentration is 40–90 vol%. However, no clear changes were observed in the levitated droplets below 30 vol% ethanol, and the onset of the Ouzo effect could not be confirmed. We also found that higher ethanol concentrations delayed the onset and shortened the duration of the Ouzo effect. Therefore, as the concentration of ethanol increases, the proportion of volatile components in the droplet also increases, resulting in a decrease in the initial water component for the Ouzo effect and a shorter duration. The highly volatile droplets also condense ambient water vapor, so the effect of relative humidity is also thought to be responsible for the onset of the Ouzo effect. For the relative humidity of 50% and 80%, it was confirmed that the termination time of the Ouzo effect was delayed at 80% humidity due to the increase in ethanol concentration. The duration of the Ouzo effect also became longer. This was thought to be due to an increase in the amount of condensation caused by the increase in humidity. Therefore, it is suggested that the water component inside the droplet is important in the onset of the Ouzo effect.

Based on these results, the evaporation of Ouzo droplets in acoustic levitation with four distinct phases based on our experimental results is illustrated in Fig. 3 (Mitsuno, M and Hasegawa, K, 2024): (1) preferential evaporation of ethanol, (2) onset of emulsification with myriad tiny oil droplets (Ouzo effect), (3) phase separation with the core-shell structure due to coalescence of oil droplets, and (4) evaporation completion resulting in the remaining oil droplets. It is noteworthy that a core-shell structure was observed as shown in the third phase. The oil droplet in the water droplet floated near the top of the droplet interface owing to the density difference. These findings can facilitate our understanding of the surfactant-free oil-in-water emulsion in levitated ternary droplets, paving the way for contactless droplet manipulation for airborne microfluidics.

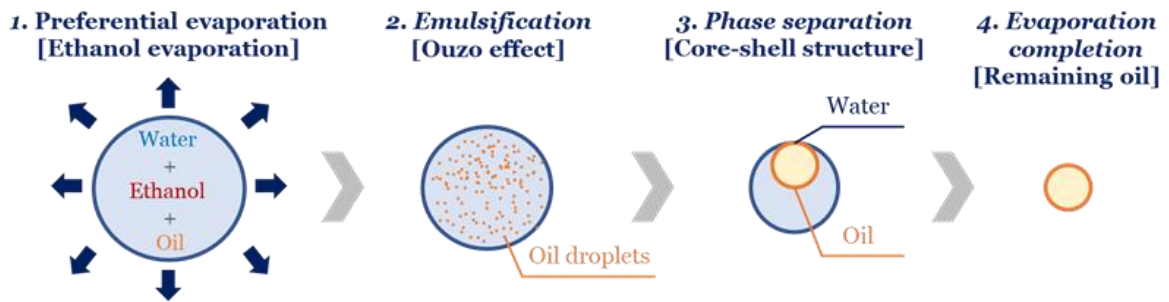


Figure 3. Evaporation, spontaneous emulsification, and phase separation processes of Ouzo droplet in acoustic levitation

4. CONCLUSIONS

The aim of this study is to understand the evaporation dynamics of spontaneous emulsification and phase separation associated with evaporation of Ouzo droplets. To achieve this, we visualized and quantified the spontaneous emulsification and phase separation processes. The obtained results and discussion are summarized as follows:

- 1) The Ouzo effect can be observed even under contactless conditions by acoustic levitation.
- 2) The Ouzo effect occurred between 40 vol% and 90 vol% ethanol concentrations. At higher ethanol concentrations, the onset of the Ouzo effect was delayed, and its duration time was shorter.
- 3) When the relative humidity increased, the termination time of the Ouzo effect was delayed and the duration of the ouzo effect was extended.
- 4) The evaporation of ouzo droplets in acoustic levitation can be divided into four stages. These findings pave the way for non-contact droplet manipulation in airborne microfluidics.

5. REFERENCES

- Foresti, D., Nabavi, M., Klingauf, M., Ferrari, A. and Poulikakos, D., 2013. "Acoustophoretic contactless transport and handling of matter in air". *Proceedings of the National Academy of Sciences*, Vol. 110, pp. 12549–12554.
- Frohn, A. and Roth, N., 2000. *Dynamics of droplets*. Springer Berlin, Heidelberg.
- Hasegawa, K. and Kono, K., 2019. "Oscillation characteristics of levitated sample in resonant acoustic field". *AIP Advances*, Vol. 9, pp. 035313.
- Maruyama, Y. and Hasegawa, K., 2020. "Evaporation and drying kinetics of water-NaCl droplets via acoustic levitation". *RSC advances*, Vol. 10, pp. 1870-1877.
- Mitsuno, M. and Hasegawa, K., 2023. "Airborne Ouzo: Evaporation-induced emulsification and phase separation dynamics of ternary droplets in acoustic levitation". *Physics of Fluids*, Vol. 36, pp. 033328.
- Tan, H., Diddens, C., Lv, P., Kuerten, J. G., Zhang, X. and Lohse, D., 2016. "Evaporation-triggered microdroplet nucleation and the four life phases of an evaporating Ouzo drop". *Proceedings of the National Academy of Sciences*, Vol. 113, pp. 8642-8647.
- Yarin, A. L., Pfaffenlehner, M. and Tropea, C., 1998. "On the acoustic levitation of droplets". *Journal of Fluid Mechanics*, Vol. 356, pp. 65-91.

TURBULENT MIXING IN A SMALL ASPECT RATIO RECTANGULAR FREE JET

Mohammad Azad*, Willie Quinn

St. Francis Xavier University, Antigonish, Nova Scotia, Canada
*mazad@stfx.ca

Keywords: Rectangular, Orifice, Turbulence, Jet, Turbulent Mixing

1. INTRODUCTION

Rectangular turbulent free jets have been studied extensively over the past few decades (Sforza *et al.* 1966, Sfeir 1979, Quinn 1992). Quinn (1992) did experiments in jets issuing from rectangular orifices with aspect ratios of 2, 5, 10, and 20 and found that mixing in the near field increased with the aspect ratio of the rectangular orifice, as long as the flow was three dimensional. However, the difference in the far-field mixing rates of the rectangular jets with aspect ratios of 2 and 5 was insignificant. The mean streamwise centerline velocity decay rate increased significantly in the rectangular jets with aspect ratios of at least 10. Zaman (1999) conducted an experimental study on rectangular jets with aspect ratios of 1, 2, 4, 8, 16, and 32. His results showed no distinct difference among the rectangular jets with aspect ratios of 1, 2, 4, and 8. These jets did not even have an increased mixing over the round jet. However, the rectangular jets with aspect ratios of 16 and 32 had higher mixing rates than the smaller aspect ratio rectangular jets and the round jet. Some authors have reported that rectangular jets with small aspect ratios had higher mixing rates than a round jet (Mi *et al.* 2000, Mi and Nathan 2010). This finding contradicts the results of Quinn (1992) and Zaman (1999). The quantities measured in previous studies were limited to the jet centerline and major or minor axis planes. It appears that no detailed measurements, especially those in cross-planes have thus far been made in a rectangular jet issuing from a small aspect ratio orifice, except some cross-stream mean streamwise velocity contour maps. In this paper, the mean streamwise centerline velocity decay, spreading, entrainment, and mean streamwise velocity contour maps are presented. Also, the streamwise and spanwise turbulence intensities and the mean static pressure on the jet centerline, mean streamwise vorticity and mean static pressure contours on the cross-planes and secondary flow velocity vectors are presented.

2. EXPERIMENTAL SET-UP AND EQUIPMENT

A detailed description of the flow facility and equipment has been given in Quinn (2006). Very briefly, a blow down flow facility, consisting of a centrifugal fan, a diffuser, a settling chamber, and a contraction, was used. The centrifugal fan, supported on anti-vibration neoprene pads, drew air and delivered it via a flexible duct to the orifices through the diffuser, settling chamber and the contraction. A three-dimensional traversing system, also supported on anti-vibration neoprene pads, was used to move the measuring probes in the flow field. A pitot-static tube with an ellipsoidal head and four circumferentially located static pressure holes and a DANTEC P51 x-array hot-wire probe were used to make the measurements. The hot-wire probe was calibrated for velocity and yaw in situ online according to Bradshaw (1975). The temperature was monitored by a thermocouple placed close to the hot-wire probe and the pitot-static tube and corrections for temperature drift were made in the data reduction software following Bearman (1971). The signals from the hot-wire probe and the thermocouple were linearized and digitized as described in Quinn (2006).

3. RESULTS AND DISCUSSION

The normalized mean streamwise centerline velocity decay results are shown in Fig. 1. U_{bulk}/U_{cl} starts at a value slightly larger than 1 at the exit of the orifice and decreases slightly afterwards due to vena contracta effect in both rectangular and round jets. U_{bulk}/U_{cl} remains constant up to 3.22 and 4.14 diameters downstream in the rectangular and round jet, respectively, indicating a higher mixing rate in the rectangular jet. Soon after, U_{bulk}/U_{cl} increases monotonically in both jets. The mean streamwise centerline velocity decay rates have been calculated from this linear decay region. The decay rates are 0.165 and 0.157 for the rectangular and round jets, respectively. These values are close to the respective values (0.161 and 0.156, respectively) of Mi and Nathan (2010). These results also revealed that the kinematic virtual origin is located upstream of the rectangular jet exit and downstream of the round jet exit.

The mean static pressure distribution on the jet centerlines is shown in Fig. 2. The mean static pressure starts at a value higher than atmospheric pressure at the exit and decreases gradually, due to the vena contracta effect, and becomes atmospheric downstream of the exit plane before decreasing further caused by increase in turbulence intensity. The mean static pressure reaches its minimum value and starts recovering to the atmospheric pressure approximately at 5 and 7 diameters downstream in the rectangular and round jet, respectively, indicating a higher mixing rate in the rectangular jet.

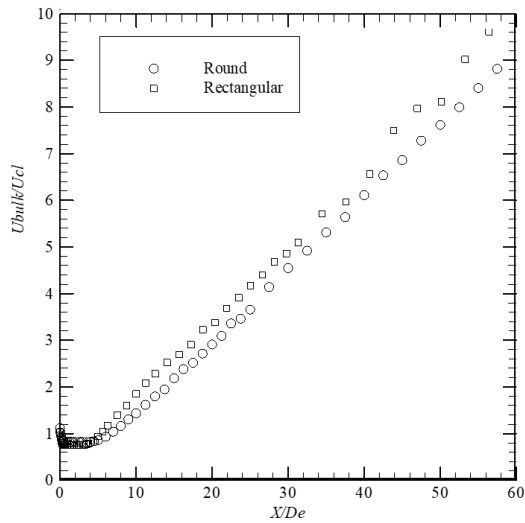


Figure 1. Mean streamwise centerline velocity decay.

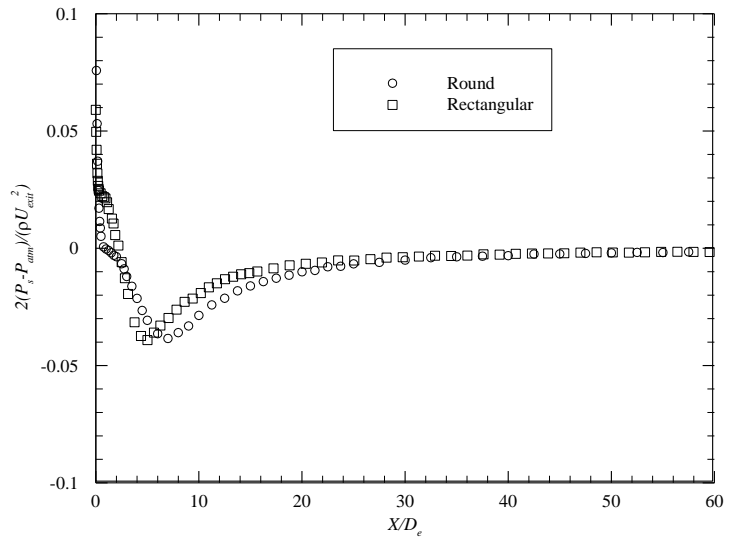


Figure 2. Mean static pressure on the jet centerline.

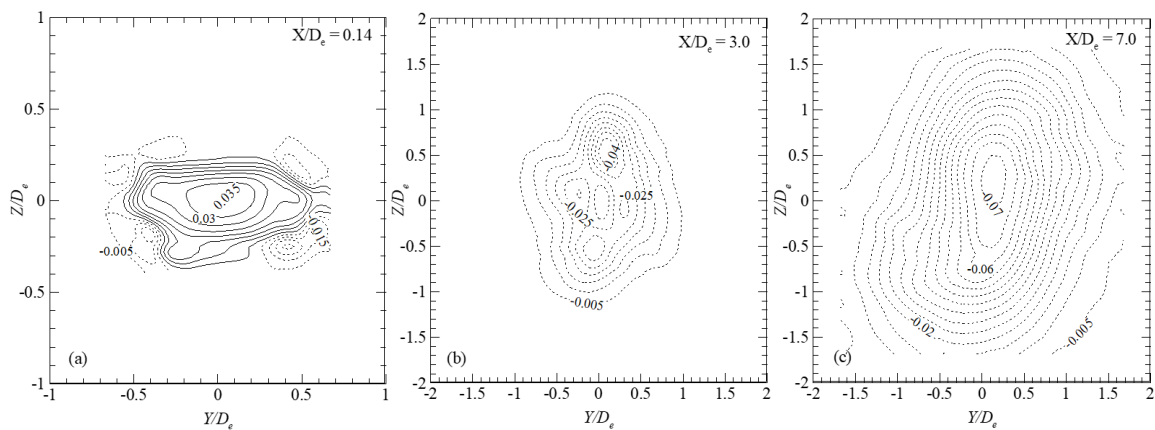


Figure 3. Mean static pressure contour maps.

The mean static pressure contour maps $(2(P_s - P_{atm})/\rho U_{cl}^2)$ for the rectangular jet at 0.14, 3 and 7 diameters downstream are shown in Fig. 3. The continuous and dashed lines represent positive and negative pressures, respectively. At 0.14 diameter downstream, the pressure in the central region of the jet is positive, consistent with the mean static pressure distribution on the jet centerline shown in Fig. 2, and negative in the corner regions. Flow is, therefore, induced from the corners into the central region. Also, the higher than ambient pressure in the central region pushes the jet fluid to the ambient through the sides of the rectangle. At 3 and 7 diameters downstream, the pressure is negative everywhere, which brings more ambient fluid into the jet and the pressure keeps increasing toward the atmospheric value.

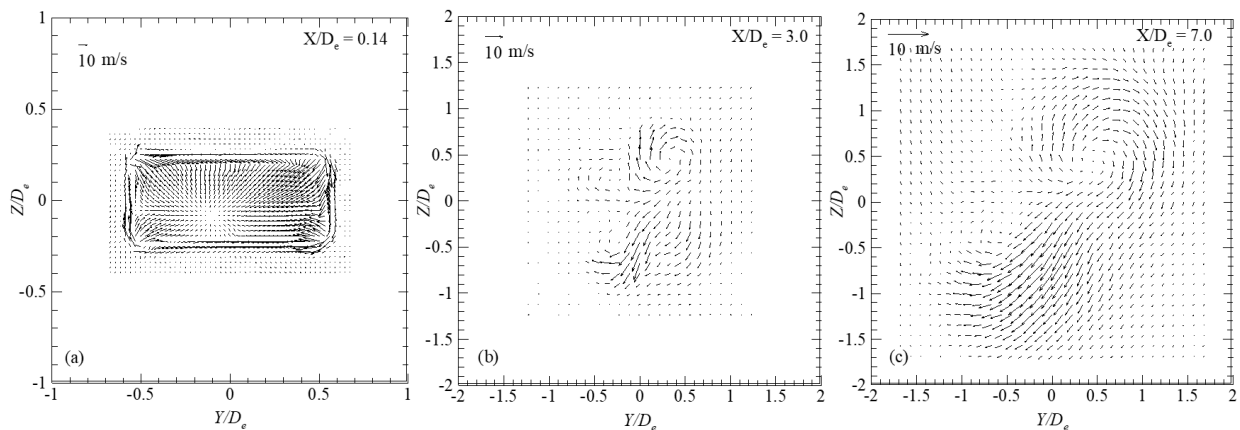


Figure 4. Secondary flow velocity vectors.

The secondary flow velocity vectors for the rectangular jet at the corresponding locations are shown in Fig. 4. The secondary flow velocity vectors at 0.14 diameter downstream show that the ambient fluid flows into the jet through the corners, as was indicated by the mean static pressure contour maps. Three diameters downstream, two clockwise rotating cells align approximately with one of the diagonals of the rectangular orifice. Further downstream, these two cells merge into a single cell covering the whole jet.

The normalized mean streamwise vorticity ($\Omega_x D_e / U_{cl}$) contour maps at the corresponding locations of the rectangular jet are presented in Fig. 5. The continuous and dashed lines represent positive and negative rotating vortices, respectively. At 0.14 diameter downstream, four pairs of positive and negative rotating vortices are aligned with the corners of the jet. Orientations of the vortex pairs are such that flow of the ambient fluid into the jet occurs through the corners and outflow of the jet fluid to the ambient occurs through the sides of the jet, consistent with the other results discussed above. Four pairs of rotating cells are still present 3 diameters downstream, although they appear tilted. These cells merge into a single vortex 7 diameters downstream and still appear to be tilted by 45°.

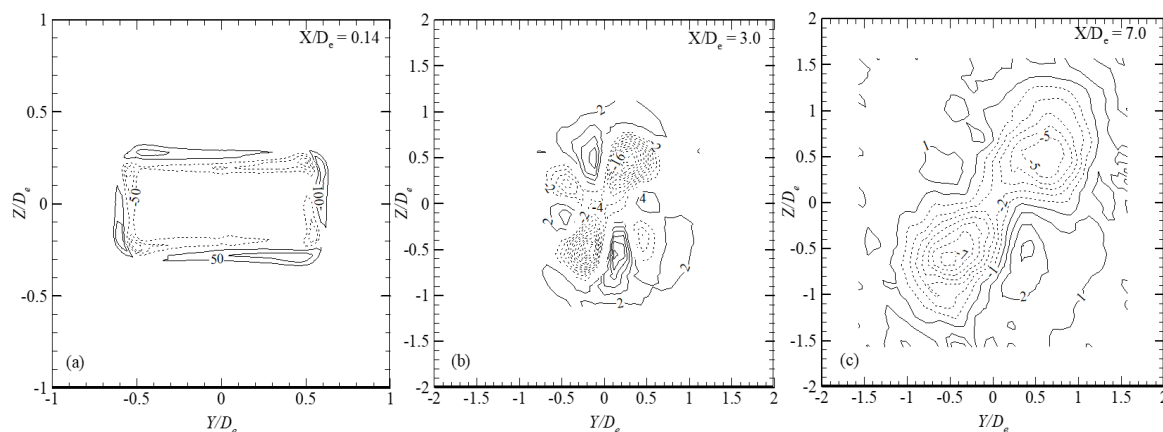


Figure 5. Mean streamwise vorticity contour maps.

4. CONCLUSIONS

An isothermal, incompressible, and unforced rectangular jet issuing from a sharp-edged orifice with an aspect ratio of 2 was investigated experimentally. The Reynolds number, based on the equivalent diameter of the rectangular orifice (same as the diameter of the round orifice), was 1.61×10^5 . Some results from experiments in a sharp-edged round jet are also presented. The mean streamwise centerline velocity decay rate shows that mixing in the rectangular jet is higher than the round jet. Also, the mean static pressure on the centerline starts to recover from a negative value toward the ambient pressure earlier in the rectangular jet than in the round jet. The mean streamwise vorticity contour maps of the rectangular jet show that four pairs of counter-rotating vortices generate at the four corners, which draw air from the ambient into the jet through the corners and push out to the ambient through the sides. This finding is complemented by the mean static pressure contour maps and the secondary flow velocity vectors.

5. REFERENCES

- Bearman, P. W., 1971 "Corrections for the Effect of Ambient Temperature Drift on Hot-wire Measurements in Incompressible Flow," *DISA Info*, Vol. 11, No. 11, pp. 25-30.
- Bradshaw, P., 1975. *An Introduction to Turbulence and its Measurement*, Pergamon Press, Oxford.
- Mi, J., and Nathan, G. J., 2010. "Statistical Properties of Turbulent Free Jets Issuing from Nine Differently-Shaped Nozzles," *Flow, Turbulence and Combustion*, Vol. 84, No. 4, pp. 583-606.
- Mi, J., Nathan, G. J., and Luxton, R. E., 2000. "Centreline Mixing Characteristics of Jets from Nine Differently Shaped Nozzles," *Experiments in Fluids*, Vol. 28, No. 1, pp. 93, 94.
- Quinn, W. R., 1992. "Turbulent Free Jet Flows Issuing from Sharp-edged Rectangular Slots: The Influence of Slot Aspect Ratio," *Experimental Thermal and Fluid Science*, Vol. 5, No. 2, pp. 203-215.
- Quinn, W. R., 2006 "Upstream Nozzle Shaping Effects on Near Field Flow in Round Turbulent Free Jets," *European Journal of Mechanics B/Fluids*, Vol. 25, No. 3, pp. 279-301.
- Sfeir, A. A., 1979. "Investigation of Three-Dimensional Turbulent Rectangular Jets," *AIAA Journal*, Vol. 17, No. 10, pp. 1055-1060.
- Sforza, P. M., Steiger, M. H., and Trentacoste, N., 1966. "Study on Three-Dimensional Viscous Jets," *AIAA Journal*, Vol. 4, No. 5, pp. 800-806.
- Zaman, K. B. M. Q., 1999. "Spreading Characteristics of Compressible Jets from Nozzles of Various Geometries," *Journal of Fluid Mechanics*, Vol. 383, pp. 197-228.

SELF-SIMILARITY OF A TRIANGULAR TURBULENT FREE JET

Mohammad Azad

St. Francis Xavier University, Antigonish, Nova Scotia, Canada
mazad@stfx.ca

Keywords: Turbulent jet, Triangular, Orifice, Self-similarity

1. INTRODUCTION

The self-similarity of turbulent jets is a subject of extensive research due to its significance in unravelling the complexities inherent in turbulent flows. Numerous studies have highlighted that turbulent free jets tend to lose their distinctive characteristics far downstream from their origin, exhibiting similar behaviors (Dowling and Dimotakis 1990, Antonia and Zhao 2001). Some suggest that this region is not entirely independent of initial conditions (George 1989, Mi *et al.* 2001). Some researchers have emphasized that the collapse of mean velocity profiles to a single curve, when it is plotted using a velocity scale and a length scale, doesn't necessarily imply independence from initial conditions but rather indicates a streamwise dependence on normalizing scales (George and Davidson, 2004). This discrepancy was addressed by defining strong self-similarity, called self-preserving, and weak self-similarity (Sciamarella *et al.* 2012). In self-preserving flow, all the velocity profiles and other quantities can be normalized using a single velocity and length scale. On the other hand, a weak self-similarity exists when each dependent variable is allowed to have its own scale.

This paper aims to explore the self-similarity of a jet issuing from an isosceles triangular orifice with an apex angle of 70° . In the far field, self-similarity will be explored for jets issuing from a sharp-edged round orifice and an isosceles triangular orifice with an apex angle of 10° . The scope of this study is restricted to streamwise and spanwise first and second-order quantities.

2. EXPERIMENTAL SET-UP AND EQUIPMENT

A detailed description of the flow facility and equipment has been given in Quinn (2006). Very briefly, a blow down flow facility, consisting of a centrifugal fan, a diffuser, a settling chamber, and a contraction, was used. The centrifugal fan, supported on anti-vibration neoprene pads, drew air and delivered it via a flexible duct to the orifices through the diffuser, settling chamber and the contraction. A three-dimensional traversing system, also supported on anti-vibration neoprene pads, was used to move the measuring probes in the flow field. A pitot-static tube with an ellipsoidal head and four circumferentially located static pressure holes and a DANTEC P51 x-array hot-wire probe were used to make the measurements.

3. RESULTS AND DISCUSSION

The near field spanwise profiles of mean streamwise velocity, streamwise turbulence intensity, spanwise turbulence intensity, and spanwise Reynolds primary shear stress are presented in Fig. 1. The mean streamwise velocity profile 0.25 diameter downstream exhibits off-center peaks. As the jet evolves downstream, the off-center peaks flatten. Seven diameters downstream, the velocity profile transforms into a 'bell shape' with wide tails. The mean streamwise velocity profiles are not self-similar in this near-field region. Both streamwise and spanwise turbulence intensity profiles are characterized by off-center peaks and low turbulence intensities in the central region. Spanwise Reynolds primary shear stress is zero at the center of the jet and exhibits off-center peaks when turbulence intensities have their peaks. As the jet evolves, the peaks in the Reynolds shear stress profiles move toward the jet centerline. As evident from Fig. 1, none of the profiles reaches self-similarity in this near flow field.

The mean streamwise velocity, streamwise turbulence intensity, spanwise turbulence intensity, and spanwise Reynolds primary shear stress profiles in the far flow field are presented in Fig. 2. The mean streamwise velocity profiles, normalized by the local centerline velocity and the local half-velocity width, collapse into a single curve represented by a Gaussian distribution. As mentioned by Afriyie (2017), based on the collapse of the mean streamwise velocity profiles into the Gaussian distribution, it can be said that the mean streamwise velocity profiles reach self-similarity 10 diameters downstream the jet exit plane. The spanwise turbulence intensity and Reynolds primary shear stress achieve self-similarity 15 diameters downstream of the jet exit plane.

The mean streamwise velocity, streamwise turbulence intensity, spanwise turbulence intensity, and spanwise Reynolds primary shear stress profiles 25 diameters downstream of the jets issuing from 10° and 70° isosceles triangular orifices and a sharp-edged round orifice are presented in Fig. 3. The mean streamwise velocity profiles of all the jets collapse into a Gaussian distribution indicating self-similarity in those profiles. This indicates that the jets have forgotten their initial conditions, at least for the mean streamwise velocity profiles. The other profiles of these jets do not collapse

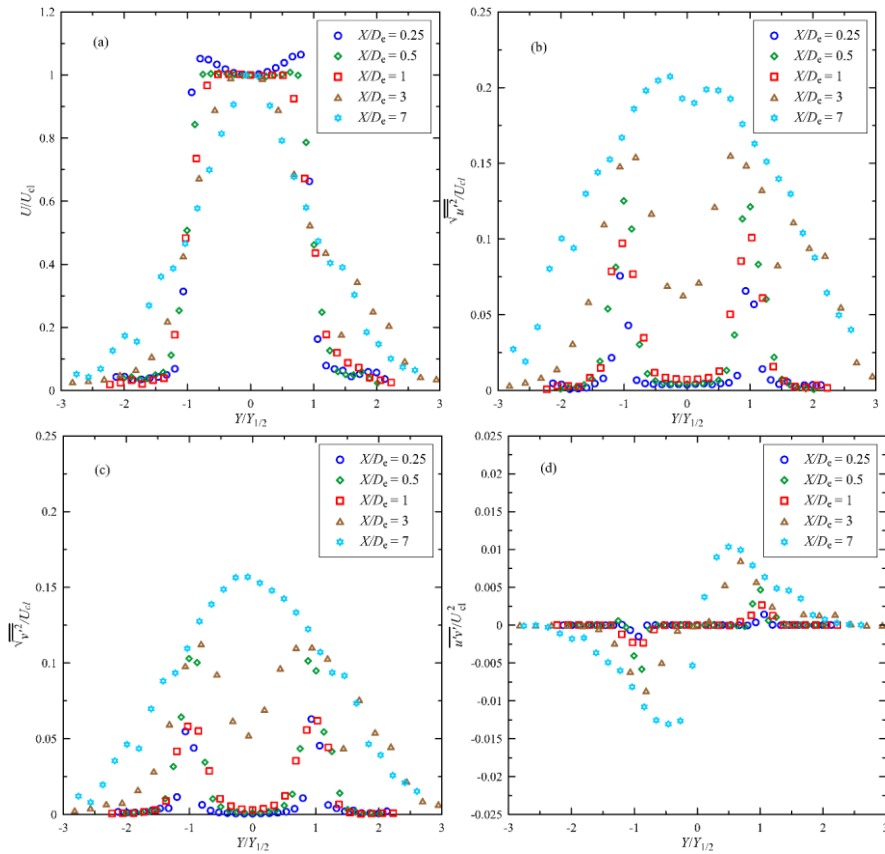


Figure 1. Near field profiles of the 70° triangular jet: (a) mean streamwise velocity, (b) streamwise turbulence intensity, (c) spanwise turbulence intensity, and (d) Reynolds primary spanwise shear stress.

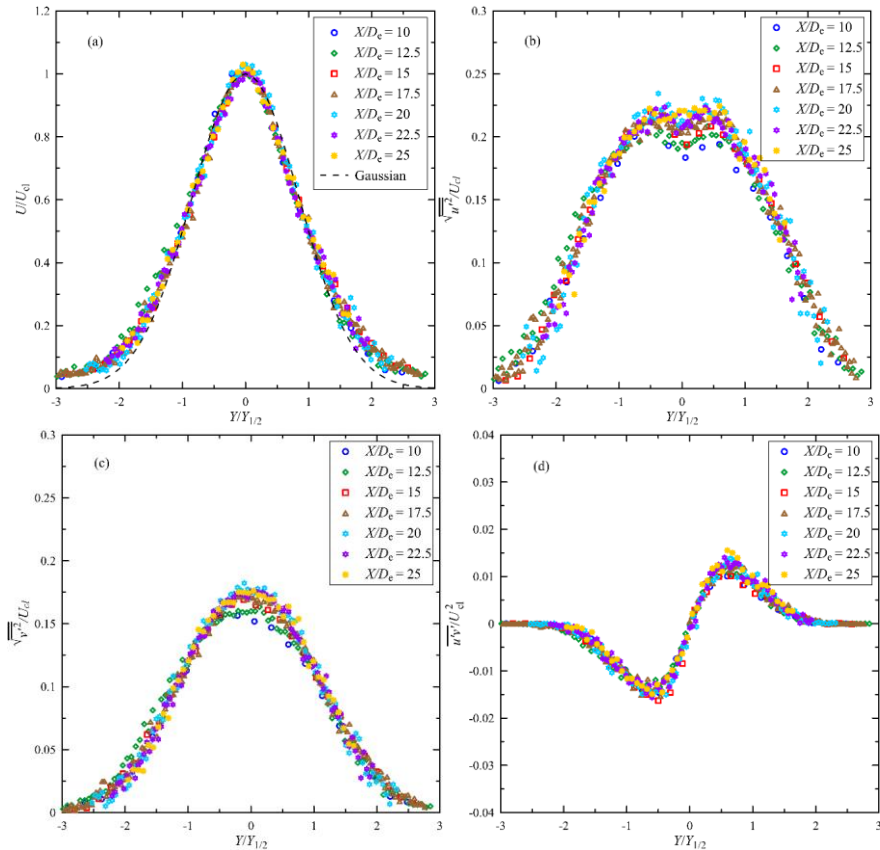


Figure 2. Far-field profiles of the 70° triangular jet: (a) mean streamwise velocity, (b) streamwise turbulence intensity, (c) spanwise turbulence intensity, and (d) Reynolds primary spanwise shear stress.

onto a single curve, indicating that the jets are not self-preserving, at least in the range tested in the present study.

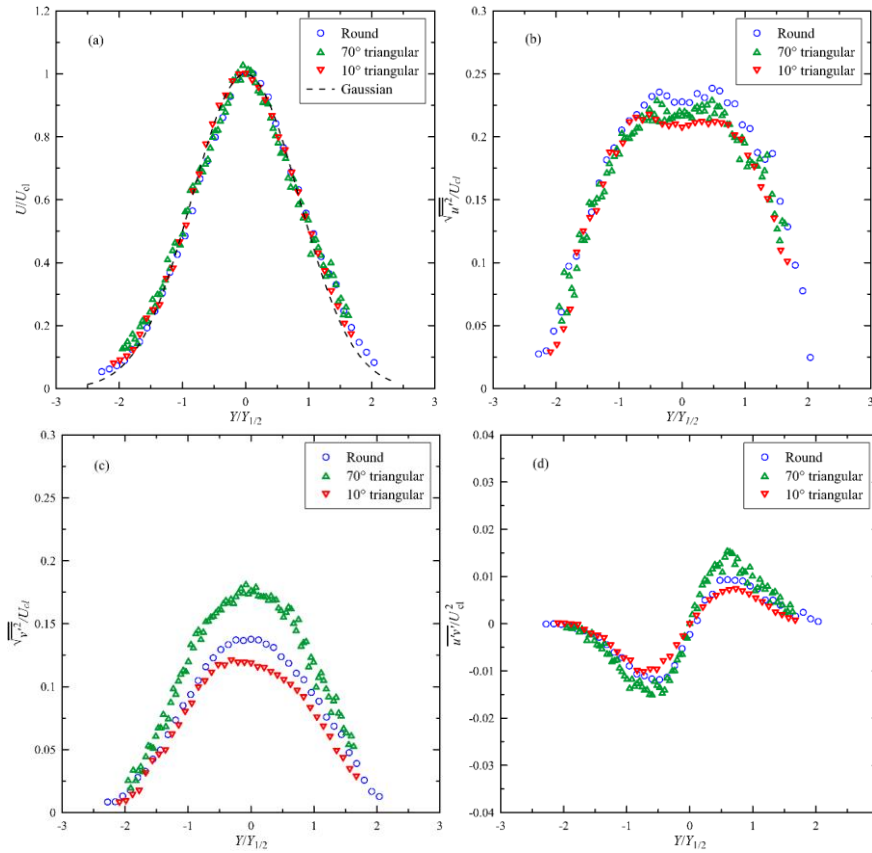


Figure 3. Far-field profiles of different jets: (a) mean streamwise velocity, (b) streamwise turbulence intensity, (c) spanwise turbulence intensity, and (d) Reynolds primary spanwise shear stress.

4. CONCLUSIONS

A turbulent jet issuing from an isosceles triangular orifice with an apex angle of 70° has been thoroughly studied for self-similarity. The mean velocity field of this jet achieves self-similarity 10 diameters downstream from the jet exit plane. The spanwise turbulence intensity and Reynolds primary shear stress reach self-similarity 15 diameters downstream from the jet exit plane. The trace of jet initial conditions cannot be observed in the mean flow field of the 10° and 70° triangular and round jets at 25 diameters downstream from the jet exit plane. However, the effects of initial conditions (geometry of the orifice) are present in the streamwise and spanwise turbulence intensities and the Reynolds primary shear stress of these jets even 25 diameters downstream of the jet exit plane.

5. REFERENCES

- Afriyie, Y. Y., 2017. "Effect of Nozzle Geometry on Mixing Characteristics of Turbulent Free Orifice Jets," M.Sc. Thesis, Dept. Mech. Eng., *University of Manitoba*, Manitoba.
- Antonia, R. A., and Zhao, Q., 2001. "Effect of initial conditions on a circular jet," *Exp. Fluids*, vol. 31, pp. 319–323.
- Dowling, D. R., and Dimotakis, P. E., 1990. "Similarity of the concentration field of gas-phase turbulent jets," *J. Fluid Mech.*, vol. 218, pp. 109–141.
- George, W. K., 1989. "The self-preservation of turbulent flows and its relation to initial conditions and coherent structures," *Advances in Turbulence*, Hemisphere, New York, pp.39-73.
- George, W. K., and Davidson, L., 2004. "Role of Initial Conditions in Establishing Asymptotic Flow Behavior," *AIAA J.*, vol. 42, no. 3, pp. 438- 446.
- Mi, J., Nobes, D. S., and Nathan, G. J., 2001. "Influence of jet exit conditions on the passive scalar field of an axisymmetric free jet," *J. Fluid Mech.*, vol. 432, pp. 91-125.
- Sciamarella, D., Silva, F., and Artana, G., 2012. "Similarity analysis of a glottal-like jet," *Exp. Fluids*, vol. 53, pp. 765–776.
- Quinn, W. R., 2006 "Upstream Nozzle Shaping Effects on Near Field Flow in Round Turbulent Free Jets," *European Journal of Mechanics B/Fluids*, Vol. 25, No. 3, pp. 279–301.

DROPWISE CONDENSATION OF SATURATED VAPOR ON SUPER-DEWETTING SURFACES FABRICATED THROUGH NOVEL COATING TECHNIQUE

^aBünyamin Polat, ^aMete Budakli, and ^{a,b}Mehmet Arik

^aÖzyeğin University, Istanbul, Türkiye

^bAuburn University, Auburn, Alabama, USA

mete.budakli@ozyegin.edu.tr

Keywords: Condensation, Phase-change heat transfer, Drop size distribution, Thermal management

1. INTRODUCTION

Condensation plays a pivotal role in industrial applications such as in cryogenic cooling systems, heat recovery devices used in power plants, heat pumps as well as in distillation columns. The vapor-to-liquid phase-change can occur in two distinct modes: filmwise (FWC) (Rainieri et al., 2009) or dropwise condensation (DWC). While FWC involves the formation of a continuous liquid film entirely covering the surface, DWC is characterized by the formation of separated small droplets, offering significant advantages in heat transfer efficiency but has been challenging to maintain over extended periods and to implement industrially. Since the seminal work of Schmidt et al. in 1930, which first experimentally demonstrated the superior heat transfer capabilities of DWC, there has been a concerted effort in research to achieve and sustain DWC. Thereby the realization of DWC is greatly influenced by surface free energy (Khalil et al., 2019) and hence the de-wetting ability (Chu et al., 2017). Surfaces with low surface free energy named as hydrophobic surfaces are more conducive to DWC. Furthermore, DWC offers lower thermal resistance due to sweeping of droplets and release of solid surface area and thus leading to higher heat transfer coefficients than FWC. Recent research has increasingly emphasized the role of surface modifications such as coating (Goswami et al., 2021), chemical etching, utilizing nano-grass (Xie et al, 2018), among others in augmenting heat transfer efficiencies by fostering DWC on a variety of materials, including copper, aluminum and stainless-steel. These techniques are designed to modify the surface energy and texture it to promote DWC, though their effectiveness can vary. Notably, some investigations have revealed that nano-structured surfaces do not consistently improve condensation heat transfer (Miljkovic et al, 2013). This variability in performance can be attributed to the intricate dynamics of droplet behavior, to blistering of the coating layer as well as to the formation of an oxide layer. This indicates that a thermally long-lasting surface coating should be designed in order to guarantee high heat transport for extended operation time. Concurrently, the material compatibility coupled among the working fluid, coating and substrate material should be indemnified. Given that DWC involves complex interactions between the surface and the condensing droplets, the characteristics of droplet formation and expansion are crucial in determining the overall heat transfer efficiency (Kim and Nam, 2016). Understanding these interplays represents key insights into optimizing condensation processes for advanced thermal management devices.

Our study diverges from the conventional reliance on complex and often unsustainable surface treatments like electrochemical etching, lubricant infusion or Polydimethylsiloxane (PDMS) (Ge et al., 2020) coating. These traditional methods, aside from being time-consuming and costly due to multi-stage processes as well as the use of harmful chemicals, also suffer from durability issues or by the utilization of a second liquid (oil as lubricant) in the system. Moreover, in most studies, they have been typically operated rather below 100°C, which is far from real applications encountered in the industry. In this study, we introduce a set of experimental heat transfer data with surface wetting results obtained for water vapor condensation at 100°C on surfaces embossed with long-term durable superhydrophobic coating which were fabricated by means of a novel approach. DWC was achieved for varying subcooling on several copper substrates, while the thermal performance was up to 120% larger than those predicted through Nusselt theory. The long-term durability tests over 24 hours have shown approximately a 15% decrease of heat transfer coefficient.

2. EXPERIMENTAL METHOD AND DATA ANALYSIS

An experimental setup (see Fig. 1a) is used for condensation studies demonstrably comprehensive, featuring dual circulating pipelines dedicated to vapor delivery and the ingratiation of wall cooling, respectively. This system undergoes pre-experimental boiling and evacuation with purge to ensure vapor purity and reduction of non-condensable gases. Integral to the system's precision are a high-accuracy chiller, a mass flow meter, and T-type thermocouples at the cooling water's inlet and outlet as well as within the heat sink for substrate cooling, which collectively regulate the subcooling condition of the wall and ascertain cooling rates via the application of cooling water circulation (see Fig. 1b). Heat flux and heat transfer coefficient values were determined by assuming one-dimensional heat conduction from vapor through the test specimen towards a copper heat sink which was cooled by a temperature-controlled chiller. The droplet dynamics was captured by a high-speed camera (18µm/pix.) frontally focused on the condensing surface area at a frame rate of 1000 Hz.

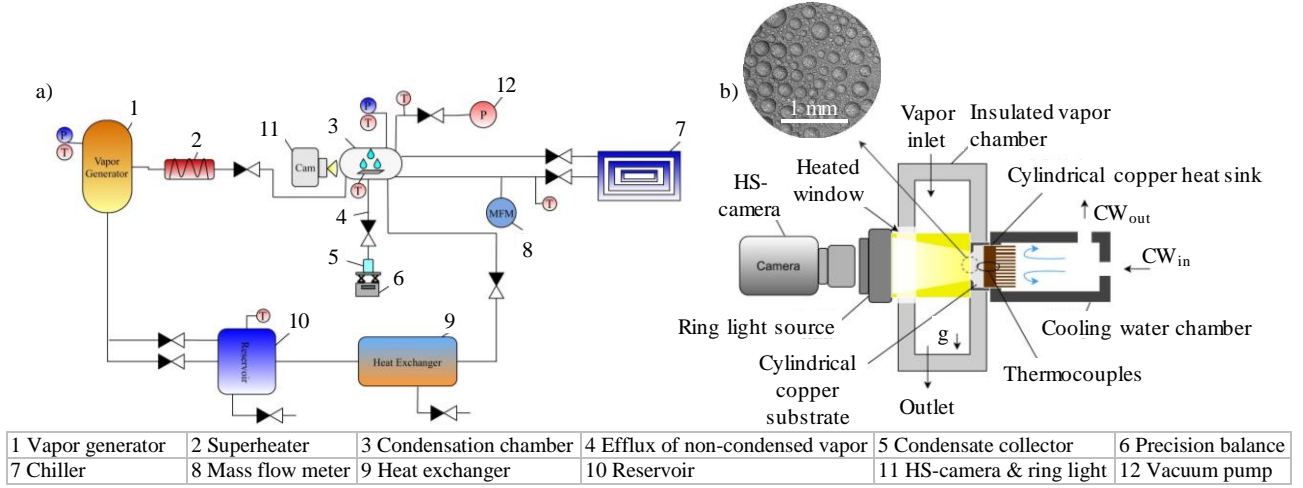


Figure 1. Experimental setup for condensation investigation: a) Process flow diagram of the condensation test system, b) Cross-section of condensation chamber.

By applying the in-house developed coating method, three copper test specimens with superhydrophobic surface property were tested for varying surface micro-pattern. Data recording was carried out at steady state condition for a vapor pressure of 1.02 bar and temperature of 100.1°C. A one-dimensional heat conduction has been considered for the heat transfer calculation of experimentally measured data as follows:

$$q = k\Delta z_2^{-1}(T_2 - T_3) \quad (1)$$

$$HTC = q[T_V - (T_1 + [(\Delta z_1)(\Delta z_2)^{-1}](T_2 - T_3))]^{-1} \quad (2)$$

The measured data have been compared with the modified Nusselt theory (Eq. 4) for disc-shape substrates (O'Neill and Westwater, 1984).

$$HTC_{disc} = 0.83404 (k^3 \rho^2 g \lambda \mu^{-1} R^{-1} \Delta T^{-1})^{0.25} \quad (3)$$

Moreover, the following expressions have been used for a second comparison by utilizing the DWC model (Rose and Glicksman, 1973):

Table 1. Equations for Dropwise condensation model.

$q = \int_{r_{min}}^{r_e} n(r)Q_d(r)dr + \int_{r_e}^{r_{max}} N(r)Q_d(r)dr \quad (5)$		
$A1 = \frac{\Delta T}{\rho L_{lv}(2-3\cos\theta_{adv} + \cos^3\theta_{adv})} \quad (6)$	$A2 = \frac{\theta}{4k_l \sin\theta_{adv}} \quad (7)$	$A3 = \frac{\delta_{coat}}{k_{coat}\sin^2\theta_{adv}} + \frac{1}{2h^i(1-\cos\theta_{adv})} \quad (8)$
$n(r) = \frac{1}{3\pi r_{max}^2 r_e^2} \left(\frac{r_e}{r_{max}}\right)^{-\frac{2}{3}} \frac{(r_e - r_{min})r(A2r + A3)}{(r - r_{min})r_e(A2r_e + A3)} e^{B(r) + C(r)} \quad (9)$	$N(r_e) = \frac{1}{3\pi r_{max}^2 r_e^2} \left(\frac{r_e}{r_{max}}\right)^{-\frac{2}{3}} \quad (10)$	
$B(r) = \frac{A3}{A1\tau} \left[(r_0 - r) - r_{min} \ln\left(\frac{r_0 - r_{min}}{r - r_{min}}\right) \right] \quad (11)$		
$C(r) = \frac{A2}{A1\tau} \left[\frac{(r_0^2 - r^2)}{2} + r_{min}(r_0 - r) - r_{min}^2 \ln\left(\frac{r_0 - r_{min}}{r - r_{min}}\right) \right] \quad (8)$		
$r_{min} = \frac{2\sigma_{lv}T_{sat}}{\Delta T\rho_v L_{lv}} \quad (9)$	$r_{max} = \sqrt{\frac{6c(\cos\theta_{rec} - \cos\theta_{adv})\sin\theta\sigma_{lv}}{\pi(2-3\cos\theta + \cos^3\theta)\rho_l g}} \quad (10)$	$r_e = \left(\frac{0.148}{r_{min}^2}\right)^{-\frac{1}{2}} \quad (11)$

The thermophysical properties for the fluid and solid have been considered according to the bulk mean temperature and as copper, respectively.

4. RESULTS AND DISCUSSION

In Figure 2a, the heat transfer coefficient over heat flux is presented for measurements on three substrates named as X-1, X-2, and X-3. Generally, it can be concluded that the heat transfer coefficient diminishes once larger subcooling was adjusted. However, an enhancement of up to 120% was achieved over predictions made by the classical Nusselt theory

for varying subcooling conditions. This significant increase in efficiency can be attributed to the strong droplet formation on the surfaces as indicated in Figure 2b. X-1 and X-2 show a trend predicted by the DWC model for most of the heat flux spectrum. Another feature is that a gradually reducing thermal performance can be identified starting from X-1 to X-3, while X-3 shows the lowest efficiency in heat transport.

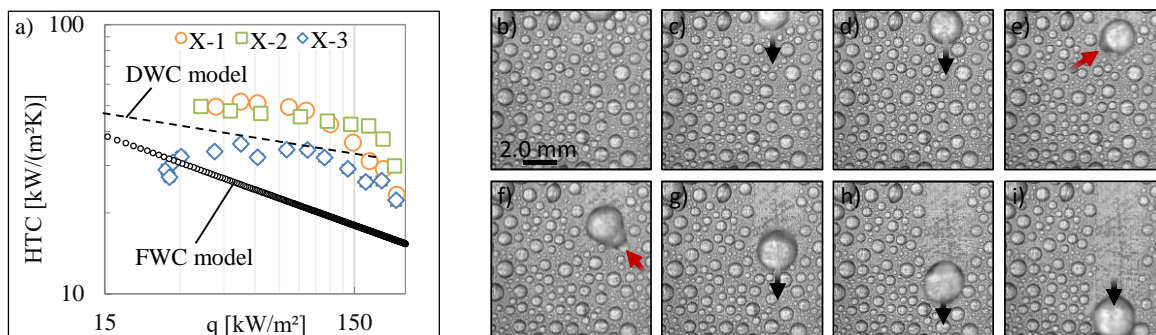


Figure 2. Heat Transfer performance and surface wetting: a) HTC versus heat flux obtained on superhydrophobic substrates at saturated vapor conditions for 1.02 bar, b) - i) Dropwise condensation on X-2, time step between each image is 10 milliseconds, $\Delta T = 15$ K, field of view is 9.2×9.2 mm, scale bar represents 2.0 mm.

High-speed images show a distinct formation of droplets on the superhydrophobic surface (see Figs. 2b-i), while these are presented for X-2, solely. Heterogeneous droplet size and distribution can be identified while the maximum radius of sweeping droplet has been estimated to be 1.92 mm for this case, saturated vapor conditions for 1.02 bar with a subcooling of 15 K. The average sweeping velocity of the droplet shown in the images has been determined to be 115.2 mm/s. While the droplet was slipping downwards, it soaked (red arrows) smaller-sized sessile droplets in the vicinity of its path and concurrently, it gained on speed due to increase of liquid mass. This process might be one of the influential mechanisms contributing to the enhancement of HTC.

5. CONCLUSIONS

In this study, we have developed superhydrophobic surfaces in order to increase the thermal performance of condensation of water vapor at saturated conditions. We compared the measured results by using theoretical models used to describe filmwise and dropwise condensation heat transfer which are available in the literature. The experiments revealed that approximately a 120% increase in HTC compared to FWC could be achieved with the coating method we have developed in this study, whereas the measured HTC shows a good agreement with the theory for DWC. Furthermore, the role of droplet size distribution in enhancing the efficiency of dropwise condensation has been evaluated by using high-speed imaging technique.

6. REFERENCES

- S. Rainieri, F. Bozzoli, G. Pagliarini, 2009. "Effect of a hydrophobic coating on the local heat transfer coefficient in forced convection under wet conditions". *Exp. Heat Transfer* 22 163–177.
- Schmidt, E., Schurig, W. and Sellschopp, W., 1930. "Versuche über die Kondensation von Wasserdampf in Film- und Tropfenform". *Forsch. Ingenieurwes.*, 1(2), pp. 53-63.
- K. Khalil, D. Soto, T. Farnham, A. Paxson, A.U. Katmis, K. Gleason, K.K. Varanasi, 2019. "Grafted nanofilms promote dropwise condensation of low-surface-tension fluids for high-performance heat exchangers". *Joule* 3 1377–1388.
- F. Chu, X. Wu, Q. Ma, 2017. "Condensed droplet growth on surfaces with various wettability" *Applied Thermal Engineering*, 1101-1108, 115.
- A. Goswami, S. C. Pillai, G. McGranaghan, 2021. "Surface modifications to enhance dropwise condensation". *Surfaces and Interfaces*.
- J. Xie, J. Xu, W. Shang, K. Zhang, 2018. "Dropwise condensation on superhydrophobic nanostructure surface, part II: Mathematical model". *International Journal of Heat and Mass Transfer* 127 1170-1187.
- N. Miljkovic, R. Enright, Y. Nam, K. Lopez, N. Dou, J. Sack, E.N. Wang 2013. "Jumping droplet-enhanced condensation on scalable superhydrophobic nanostructured surfaces" *Nano Lett.* 13 179–187.
- H. Kim, Y. Nam, 2016. "Condensation behaviors and resulting heat transfer performance of nano-engineered copper surfaces", *Int. J. Heat Mass Transfer* 93 286–292.
- Q. Ge, A. Raza, H. Li, S. Sett, N. Miljkovic, and T. Zhang, 2020. "Condensation of Satellite Droplets on Lubricant-Cloaked Droplets". *ACS Applied Materials and Interfaces*, 22246-22255, 12(19).
- O'Neill G, Westwater J, 1984. "Dropwise condensation of steam on electroplated silver surfaces". *Int. J. Heat Mass Transfer*. Vol. 27, No. 9, pp. 1539-1549.
- Rose, J. W., Glicksman, L. R. 1973. "Dropwise condensation, the distribution of drop sizes". *International Journal of Heat and Mass Transfer* 16(2), 411–425.

APPLICATION OF THE OPTICAL FLOW METHOD IN PIV IMAGES: NON-NEWTONIAN FLUID FLOW IN A HORIZONTAL PIPE

**Helder L. Moura^{a,*}, Gláucio K. Matoba^b, Daiane M. Iceri^b, Miguel M Valheros^b, Roney L. Thompson^c,
Annie Fidel-Dufour^d, Marcelo S. Castro^{a,b}**

^aCenter for Petroleum studies (CEPETRO), Universidade Estadual de Campinas (UNICAMP), Campinas-SP, Brazil.

^bSchool of Mechanical Engineering, Universidade Estadual de Campinas (UNICAMP), Campinas-SP, Brazil.

^cDep. of Mechanical Engineering, COPPE, Federal University of Rio de Janeiro, Centro de Tecnologia, Ilha do Fundão, 21945-970, Rio de Janeiro, RJ.

^dTotalEnergies, CSTJF Avenue Larribau, PAU, Cedex 64018, France.

*heldermoura08@gmail.com

Keywords: Optical flow, PIV, Non-Newtonian fluid

1. INTRODUCTION

Optical flow (OF) is a technique for evaluating the velocity field based on the change in light intensity in consecutive images. For applications in fluid mechanics, it has been demonstrated that some of the OF based methods can determine velocity fields with high accuracy in different scenarios obtained from synthetic PIV (Particle image velocimetry) images (Mendes *et al.*, 2022). A major advantage of the OF methodology is that the velocity fields are output at the same resolution as the input, i.e. the information is provided for each pixel of the image. Although OF, as a differential approach, should be more appropriate for continuous objects than for small particles, Mendes *et al.* (2022) concluded that OF algorithms are promising and can enable the extraction of denser velocity fields, even if the imaging conditions are not ideal for PIV (integral approach).

Although long prevalent in the computer vision industry, OF methods are not widely known and applied to real PIV images by the fluid mechanics community (Zhang and Chanson, 2018). Specifically, in analyzing non-Newtonian flows, there are still no studies on the application of OF methods to synthetic and real PIV images. Therefore, the aim of this work is to compare the velocity profiles obtained experimentally by PIV, OF and the analytical solution for a non-Newtonian fluid flowing in a horizontal pipe according to the Herschel-Bulkley (HB) model.

2. METHODOLOGY

2.1 Experimental apparatus

The PIV experiments were conducted in 20 m horizontal galvanized steel pipes with internal diameter $D = 0.053$ m. At the end of the pipeline, a transparent acrylic box ($8.8 \times 8.8 \times 24.8$ cm) with an internal diameter corresponding to that of the pipe was installed. The flow was conducted in a closed circuit using a positive displacement pump (rotation of 80 rpm and average flow velocity of 0.076 m/s). The experimental fluid utilized in this study comprises an aqueous solution incorporating Carbopol (Polyacrylic Carbomer 940) and triethanolamine (TEA) as a neutralizer (85% neutralization in water). The Carbopol concentration was 0.15wt%, while the TEA concentration was 750 ppm. The solution preparation protocol followed the methodology outlined by (Iceri, *et al.* 2023).

2.2 Measurement system

The PIV system from LaVision was used in the Classic PIV configuration (2D-2C). The PIV system comprised an Nd:YAG laser (532 nm, 200 mJ), which provided a 2 mm thick light sheet, and an Imager Intense camera (1376×1040 px CCD sensor) positioned at 90° to the normal plane of the laser light sheet. A Canon objective lens with a focal length of 50 mm (f/5.6) was used on the camera. The acquisition frequency was 5 Hz. The particle used was polyamide with a diameter of 50 μm.

2.3 Data acquisition and processing PIV

Data acquisition was carried out using Davis 8 software. To ensure the statistical reliability of the PIV measurements, 1400 pairs of images were recorded in double-frame mode. The interframe time was 4650 μs.

The processing step was carried out using the Matlab[®] language. The image pre-processing methodology is described in detail in Barbutti *et al.* (2021). The images were processed using the standard cross-correlation (SCC) method. Multigrid analysis with a discrete window shift (Scarano, 2001) was applied. Five passes were made. The final interrogation window (IWf) for each pass was 36, 32, 24, 16 and 10 px (in this work IWf = 10px). In addition, simple post-processing was carried out at the end of each stage using the methodology described by Westerweel and Scarano

(2005). The PIV uncertainty and its propagation for the time-averaged profile were calculated using the definitions proposed by Xue *et al.* (2014) and Sciacchitano and Wieneke (2016), respectively.

2.4 Optical flow processing

The OF algorithm selected for processing the PIV images was that proposed by Farneback (2003). This method approximates sets of pixels belonging to the same region using quadratic polynomials in two consecutive frames. In brief: the calculation of spatial gradients (partial derivatives in relation to x and y) are obtained using finite differences; in this step, the magnitude and direction of the gradient at each point is obtained; a Gaussian pyramid is then generated from the input images to represent different scales of resolution; for each level of the Gaussian pyramid, the coefficient polynomials that approximate the movement between the frames are calculated; the polynomial coefficients are used to calculate the optical flow between the frames; optimization methods, for example Levenberg-Marquardt, can be used to improve the accuracy of the OF.

The input parameters for the algorithm were: image scale = 0.5, number of pyramid layers = 5, mean filter size = 25 px, number of iterations of search per pyramid level = 5, pixel neighborhood size = 5 px and Gaussian standard deviation = 1.1.

2.5 Theoretical analysis

According to Chhabra and Richardson (2008), for the laminar flow of HB model fluids it is possible to obtain the analytical solution of the velocity profile for two distinct regions: (i) Eq. (1) delimited by $R_p < r \leq R$ (where R_p is the plug radius and R is the pipe) and (ii) Eq. (2) delimited by $0 \leq r < R$.

$$u(r/R) = \frac{nR}{(n+1)} \left(\frac{\tau_w}{k} \right)^{1/n} \left[(1-\phi)^{(n+1)/n} - \left(\frac{r}{R} - \phi \right)^{(n+1)/n} \right] \quad (1)$$

$$u(r/R) = \frac{nR}{(n+1)} \left(\frac{\tau_w}{k} \right)^{1/n} (1-\phi)^{(n+1)/n} \quad (2)$$

In Eq.(1) and Eq.(2), ϕ denotes the ratio between the yield stress (τ_y) and the wall shear stress (τ_w) and radius ratio ($\tau_y / \tau_w = R_p / R$) and was calculated iteratively using the equations presented from Hou et al. (2020). For the configuration used in this work, $\phi \cong 0.5813$ was found. The parameters consistency index (k), power-index (n) and τ_y , were obtained using a rheometer and presented values of 1.3818 Pa.sⁿ, 0.5 and 9.6783 Pa, respectively.

3. RESULTS AND DISCUSSIONS

Figure 1a presents the time-average velocity profile obtained using the PIV technique and Fig. 1b the velocity profile calculated using the Farneback algorithm (2003). A comparison is made for the two profiles with the analytical solution of Eqs. (1) and (2) using the mean absolute error (MAE).

The uncertainty in the PIV velocity profile shows a tendency to increase from the $r/R > 0$ region (Fig. 1a). This is experimentally justified by observing the turbidity of Carbopol. The laser light-sheet showed a more dispersed behavior from the center of the duct, creating a "blurred" effect in the images. As a result, the particle images followed the same effect: loss of intensity and a decrease in the signal-to-noise ratio represented from the primary peak ratio (PPR). The velocity, which in this region should behave symmetrically in relation to the profile in the lower portion, showed an overestimated value close to the wall (at $r/R > 0.75$). For OF, the loss of particle intensity is not relevant as long as there is no significant change in intensity patterns in the same area in the consecutive frame. In addition, the ideal concentration range of the reconstructed particle image (N_p) in OF is greater than in PIV, i.e. it is possible to obtain significant results from the OF method even with a low N_p value (Mendes *et al.*, 2022). This is evident in Fig. 1b considering the symmetry of the profile obtained in relation to the analytical profile and for the MAE value (6.2%) in relation to the PIV profile (MAE = 7.7%). Also, according to Mendes *et al.* (2022), the authors observed in their results that the accuracy of the OF method is sensitive in regions where the velocity is zero at the wall and the gradients are high. Comparing only the region of the velocity profile for $-1 < r/R < 0$ for the two methods, the MAE error near the OF wall at some points is double that of the PIV (especially in the region $-0.9 < r/R < -0.75$). This proves that there is a need for further research into the accuracy of OF methods or a hybrid approach with PIV.

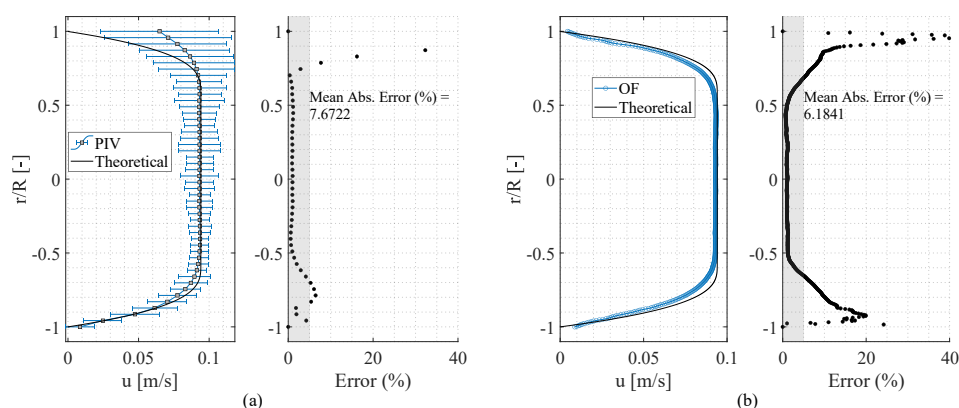


Figure 1. (a) Velocity profile obtained from the PIV technique; (b) velocity profile using OF processing. Comparison of both with the analytical solution of Eqs. (1) and (2) and calculation of MAE.

4. CONCLUSIONS

In this study, the optical flow (OF) methodology was used on PIV images with flow data of a non-Newtonian fluid in a horizontal pipeline. As a result of the turbidity, the velocity profile obtained by the PIV technique deviated from the analytical solution due to the high dispersion of the laser light-sheet. The application of the OF methodology enabled the symmetry of the curve to be restored, a denser profile to be obtained and a lower mean absolute error (MAE) compared to the PIV data (overcoming areas where the PIV uncertainty was considerably high). However, there was a loss of information in the regions near the wall. This demonstrates that the OF method applied needs to be further studied in conjunction with other algorithms or even included as a PIV post-processing step.

5. ACKNOWLEDGEMENTS

We gratefully acknowledge the support of the ALFA - Artificial Lift and Flow Assurance Research Group, hosted by the Center for Energy and Petroleum Studies (CEPETRO) at the Universidade Estadual de Campinas (UNICAMP), Brazil. We also thank TotalEnergies EP Brazil for their funding and support, as well as the ANP (Brazil's National Oil, Natural Gas, and Biofuels Agency) for assistance through the R&D levy regulation. Special thanks to the CEPETRO-UNICAMP and FEM-UNICAMP for their collaboration, and to the Alberto Luiz Coimbra Institute (COPPE-UFRJ) for their contributions.

6. REFERENCES

- Barbutti, A. D., Amaral, R de L., de Moura, H.L., Oliveira Júnior, F. de A, Nunhez, J.R. and de Castilho, G.J., 2021. "A new field correction method for PIV measurements based on mutual information: Case study on a stirred tank flow". *Measurement*, Vol. 186, pp. 110–130.
- Farneback, G., 2003. "Two-frame motion estimation based on polynomial expansion". In: *Bigun J, Gustavsson T (eds) Image analysis*. Springer, Berlin, Heidelberg, pp 363–370.
- Hou, L-T., Liu, S., Zhang, J. and Xu J-y., 2020. "Evaluation of the Behavioral Characteristics in a Gas and Heavy Oil Stratified Flow According to the Herschel–Bulkley Fluid Model". *ACS Omega*, Vol. 5, pp. 17787-17800.
- Iceri, D. M., Biazussi, J. L., van der Geest, C., Thompson, R. L., Palermo, T. and Castro, M. S., 2023. "The yielding behavior of aqueous solutions of Carbopol and triethanolamine and its prediction considering the fractal nature of the formed aggregates." *Rheologica Acta*, Vol. 62, pp. 405–416.
- Liu, T. and Shen, L., 2008. "Fluid flow and optical flow". *Journal of Fluid Mechanics*. Vol. 614, pp. 253-291.
- Mendes, L.P.N., Ricardo, A.M.C., Bernardino, A.J.M. and Ferreira R.M.L., 2022. "A comparative study of optical flow methods for fluid mechanics". *Experiments in Fluids*, Vol. 63, pp. 7.
- Scarano, F., 2001. "Iterative image deformation methods in PIV". *Measurement Science and Technology*, Vol. 13, pp. R1–R19.
- Sciaccitano, A., Wieneke, B., 2016. "PIV uncertainty propagation". *Measurement Science and Technology*. Vol. 27, pp. 8.
- Westerweel, J., Scarano, F., 2005. "Universal outlier detection for PIV data". *Experiments in Fluids*, Vol. 39, pp. 1096–1100.
- Xue, Z., Charonko, J.J., Vlachos, P.P., 2014. "Particle image velocimetry correlation signal-to-noise ratio metrics and measurement uncertainty quantification". *Measurement Science and Technology*, Vol. 25., pp. 115301.
- Zhang, G. and Chanson, H., 2018. "Application of local optical flow methods to high-velocity free-surface flows: Validation and application to stepped chutes". *Experimental Thermal and Fluid Science*, Vol. 90, pp. 186-199.

ETHANOL FLAT PLATE PULSATING HEAT PIPE: EFFECT OF THE FILLING RATIO

Luis Betancur-Arboleda^{a,*}, Pamela Hulse^a, Larissa Krambeck^b, Kelvin Guessi Domiciano^b, Guilherme Carpes Zonta^b, Marcia Barbosa Henriques Mantelli^b

^aTechnological Units of Santander, Calle de los Estudiantes # 9-82 Bucaramanga-Colombia

^bHeat Pipe Laboratory, Department of Mechanical Engineering, Federal University of Santa Catarina, Florianopolis, Brazil

* labetancur@correo.uts.edu.co

Keywords: pulsating heat pipe, filling ratio, ethanol, sharp grooves

1. INTRODUCTION

Nowadays, technological advances enable the manufacturing of high-performance electronic components, which generate heat during operation, making the thermal management a critical issue for electronic gadgets, from satellites to computer processors (Ayel et al., 2015). The exceeding heat demands for more efficient heat removal processes. The heat pipe technology is a family of two-phase devices that offer cooling alternatives for low and high thermal fluxes, including ground or space applications (Mantelli, 2021). Among them, the pulsating heat pipes (PHPs) are highlighted because of their simplicity of manufacture and their heat transfer capabilities, with or without gravity assistance. In addition, this device exhibits low thermal resistance at high heat loads (Bastakoti et al., 2018). PHPs use a confined small channel to promote the working fluid motion instead of a porous media. The working fluid changes of phase inside these channels, creating a pattern of liquid plugs and vapor bubbles, which transfer heat in a chaotic behavior (Nikolayev, 2021).

Among other fabrication techniques, flat plate PHP can be fabricated by diffusion bonding of machined plates. Despite meandering a small diameter tube forming interconnected parallel channels is a simple fabrication process of PHPs, the flat plate PHPs are more suitable for thermal control of electronics due to their flat geometry, which reduces the thermal contact resistance with the heat source, improving the heat exchange.

The diffusion bonding technology allows for the creation of any internal structure inside the PHP. Therefore, PHP with any number of turns, different channel sizes, grooved channels (Krambeck et al., 2022), porous media (Betancur et al., 2021), and different roughness (Betancur et al., 2020) can be easily fabricated. Although these factors strongly influence the device capacity, the final design should also include the working fluid selection and its volume, which may depend not only on the operation temperature and heat transfer characteristics, but also of the selected geometry and fabrication process.

In this context, Krambeck et al. (Krambeck et al., 2022) studied two diffusion-bonded PHPs for the thermal management of large-scale electronic devices, one with a simple round cross-section channel and another with ultra-sharp lateral grooves in the evaporator section. Despite water being an excellent working fluid for copper PHPs, the authors related that water delayed the startup in both PHPs, as it operated in typical slug-plug flow mode, which limited their heat transfer range. In order to anticipate the startup of the slug-plug flow in the PHPs, Betancur-Arboleda (Betancur-Arboleda et al., 2023) tested the same PHPs filled with ethanol, considering a filling ratio (FR) of 60 %, observing an early startup in the horizontal and against-gravity positions. However, the results indicated that the filling ratio might be too high for the working fluid ethanol, in both PHPs, despite being the FR recommended in the literature. Therefore, a study of the best filling ratio must be carried out in order to obtain the best PHP performance.

This experimental study expands the results obtained by Betancur-Arboleda et al. (Betancur-Arboleda et al., 2023), investigating the impact of the ethanol amount on the thermal performance of two diffusion-bonded flat plate PHP, made of copper. In one the PHPs, the evaporator's cross-section consisted of round channels with ultra-sharp lateral grooves, and in the other the cross section was a round channel. These authors followed the procedure reported by Krambeck et al. (Krambeck et al., 2022) to examine the working fluid filling ratio on the thermal behavior of the PHP with ethanol at different filling ratios follows, particularly in the startup and evaporator temperatures, in the horizontal orientation.

2. METHODS

In this study, two pulsating heat pipes designed for electronic cooling are experimentally investigated. In each device, two copper plates, 2.2 mm thick, with 13 U-turn half round channels (machined by CNC) were diffusion bonded, forming 26 interconnected parallel channels with round geometry. The grooved PHP, features a unique cross-section with a round channel (1.25 mm radius) and chamfers on both lateral sides, fabricated before the thermal cycle (Betancur-Arboleda et al., 2020). These chamfers after the bonding forms two ultra sharp grooves in the lateral fo the channels. The thermal performance of the PHPs are estimated using the overall thermal resistance parameter, calculated by:

$$R_t = \frac{\Delta T}{Q} \quad (1)$$

where ΔT is the difference between the average temperature of the evaporator and condenser, and Q is the applied heat load. Each test last around 900 s, which guarantees the pseudo steady-state conditions. The power inputs used in the evaporator section were 20, 40, 60, 80, 100, 140, 180, 230, 290, and 350 W. In the condenser, cooling water from a thermal bath is used as the heat sink. Ethanol was the working fluid with the filling ratios (FRs) of 20, 30, 40, 50, 60, and 70%. In this work, FR is defined as the ratio between the volumes of the charged working fluid and the void channel.

3. RESULTS AND DISCUSSION

Figure 1 presents the thermal resistances as a function of the heat loads, for the grooved (Figure 1a) and for the round PHP (Figure 1b) at the horizontal position, considering filling ratios from 20 to 70%, with steps of 10%. In general, as thermal load increases, thermal resistance decreases. The devices work successfully with all FRs. According to the plots, the grooved PHP showed an odd behavior at low powers (up to 80W) that depended on the filling ratio. This behavior was less notable in the round PHP. However, at higher power inputs, the grooved PHP was less affected by the filling ratio reaching lower thermal resistance values quicker than observed for the round PHP, although with the appropriate FR for the round channel (30%, 9 ml of ethanol), both devices tended to attain basically the same resistance.

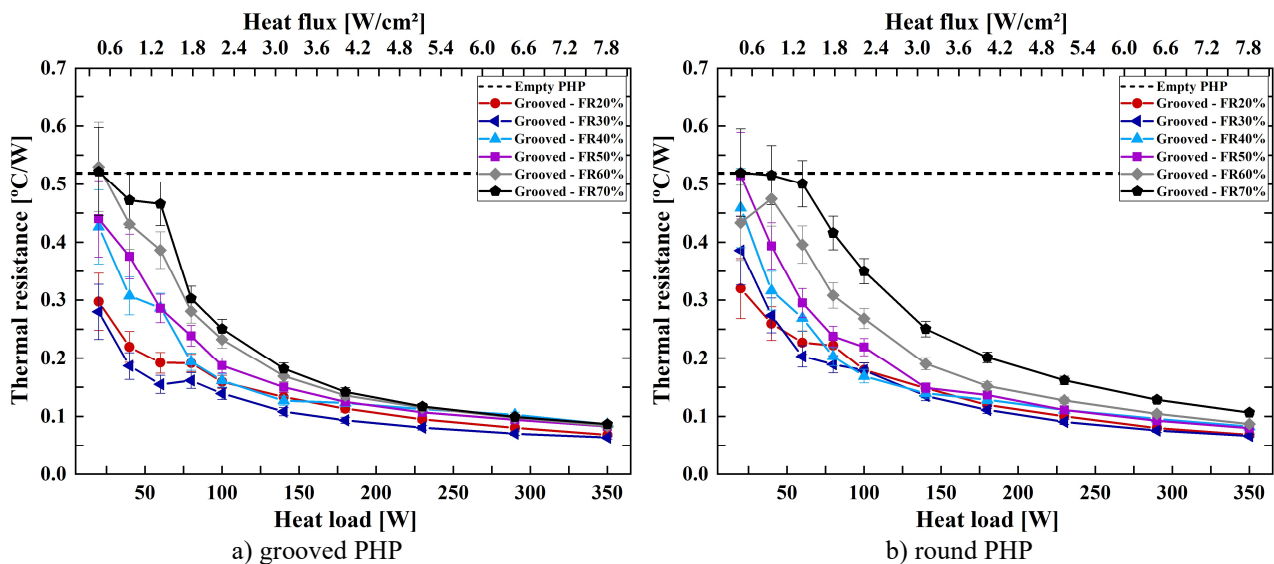


Figure 1. Thermal resistance comparison for both PHPs operating with different filling ratios

Figure 2 presents the distribution of temperatures as a function of time for the two PHPs with the best FR, i.e., 30%. Through this graph, it is possible to identify the exact startup instant, i.e., the when the device starts operating in the pulsating mode, which happened at 40 W. Before that, the round PHPs transfer heat by conduction through the case material and the working fluid while the grooved one worked as a heat pipe (the grooves were the porous media), with smaller thermal resistances. Besides, the grooved PHP showed more intense oscillations in the condenser region for heat loads between 40 and 100 W, demonstrating more efficient working fluid movement.

4. CONCLUSION

A filling ratio study of two flat plate PHPs, manufactured by diffusion bonding, was accomplished in this research under several heat loads. The main difference among the PHPs was the channel geometry, round and round with lateral grooves in the evaporator section. The conclusions obtained from the preliminary results are:

- The round and the grooved PHPs were able to operate successfully in a slug-plug flow for the tested conditions.
- Although most studies indicate that the best filling ratios for PHPs are between 50 and 70% for the horizontal, this study showed that the PHPs operating with ethanol worked with a better thermal performance with a significantly lower filling ratio, of 30%.
- The sharp grooves improved the startup and the working fluid movement, as the grooves maintained the liquid film on the evaporator, intensifying the oscillations, as it provides liquid for phase change during the whole operation, avoiding local dryouts. Furthermore, the grooves reduced the thermal resistances to low heat loads.

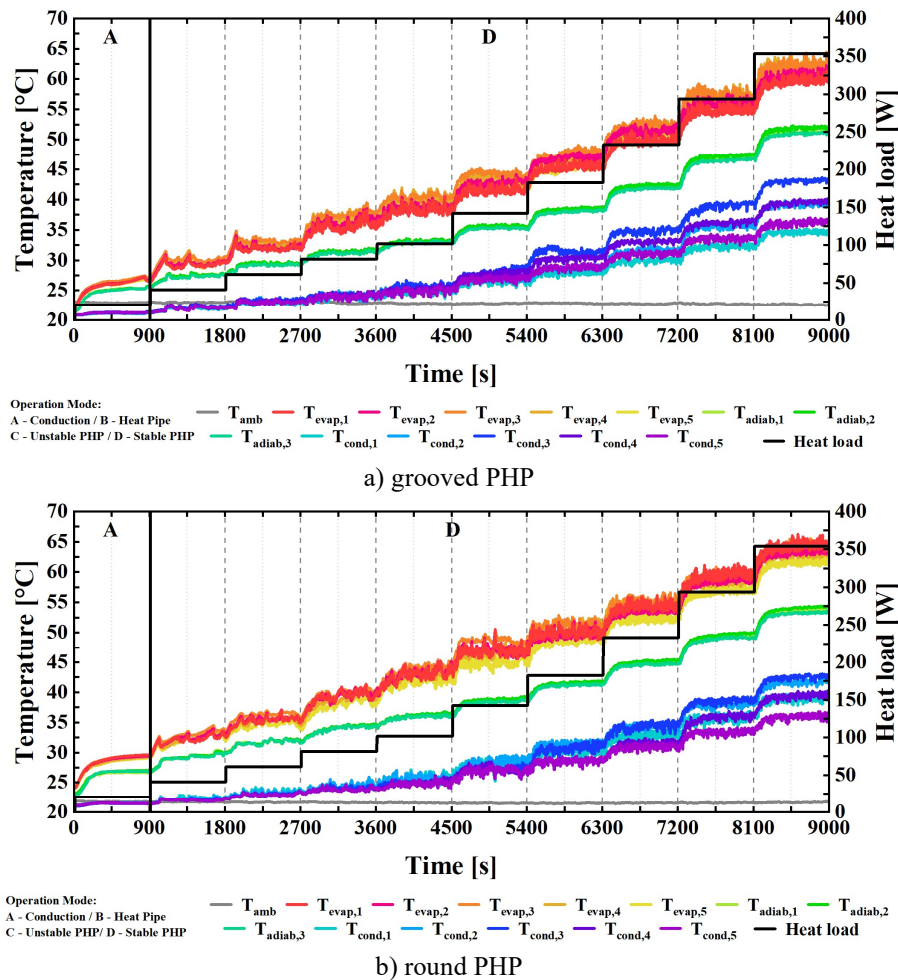


Figure 2. Temperature distribution of both PHPs operating with the best filling ratio

5. REFERENCES

- Ayel, V., Araneo, L., Scalambra, A., Mameli, M., Romestant, C., Piteau, A., Marengo, M., Filippeschi, S., Bertin, Y., 2015. "Experimental study of a closed loop flat plate pulsating heat pipe under a varying gravity force." *International Journal of Thermal Sciences*, Vol. 96, pp. 23–34.
- Bastakoti, D., Zhang, H., Li, D., Cai, W., Li, F., 2018. "An overview on the developing trend of pulsating heat pipe and its performance." *Applied Thermal Engineering*, Vol. 141, pp. 305–332.
- Betancur, L., Facin, A., Paiva, K., Mantelli, M., Gonçalves, P.P., Nuernberg, G., Paiva, K., Mantelli, M., Nuernberg, G., 2021. "Study of diffusion bonded flat plate closed loop pulsating heat pipes with alternating porous media." *IOP Conference Series: Materials Science and Engineering*, Vol. 1139, pp. 012001.
- Betancur, L.A., Flórez-Mera, J.P., Mantelli, M., 2020. "Experimental study of channel roughness effect in diffusion bonded pulsating heat pipes." *Applied Thermal Engineering*, Vol. 166, pp. 114734.
- Betancur-Arboleda, L., Hulse, P., Melian, I., Mantelli, M.H., 2020. "Diffusion bonded pulsating heat pipes: fabrication study and new channel proposal." *Journal of Brazilian Society of Mechanical Engineers*, Vol. 42, pp. 466.
- Betancur-Arboleda, L.A., Krambeck, L., Domiciano, K.G., Zonta, G., Barbosa, M., Mantelli, M.B.H., 2023. "Flat Plate Pulsating Heat Pipe for Electronics Cooling," in: *Proceeding of 27th International Congress of Mechanical Engineering (27th COBEM)*. Florianopolis, Brazil.
- Krambeck, L., Domiciano, K.G., Betancur-arboleda, L.A., Mantelli, M.B.H., 2022. "Novel flat plate pulsating heat pipe with ultra sharp grooves." *Applied Thermal Engineering*, Vol. 211, pp. 118509.
- Mantelli, M.B.H., 2021. *Thermosyphons and Heat Pipes: Theory and Applications*, Thermosyphons and Heat Pipes: Theory and Applications. Springer International Publishing.
- Nikolayev, V.S., 2021. "Physical principles and state-of-the-art of modeling of the pulsating heat pipe: A review." *Applied Thermal Engineering*, pp. 117111.

HEAT TRANSFER CHARACTERISTICS OF WATER-OIL PLUG FLOW IN A HORIZONTAL CIRCULAR TUBE

Takashi Morimoto^{a,*}, Toshikazu Esaki^a, Takato Kimura^a and Hiroyuki Kumano^a

^aDepartment of Mechanical Engineering Aoyama Gakuin University, 5-10-1 Fuchinobe, Chuo-ku, Sagami-hara, Kanagawa, 252-5258, Japan

*morimoto@me.aoyama.ac.jp

Keywords: Plug flow, Liquid-liquid two phase flow, Heat transfer, Laminar flow, Circular tube

1. INTRODUCTION

In recent years, the increasing heat generation density in high-performance electronic devices has led to the problem of electronic device failures caused by temperature rise (Khattak and Ali, 2019). Therefore, highly efficient cooling systems for electronic devices are now required, and many studies have been conducted to improve the heat transfer performance of cooling systems. There are several approaches to improve the heat transfer performance of cooling systems, one of which is to improve the heat transfer performance of the fluid flowing in the cooling system. Water has been widely used as a cooling medium in the past, but liquid-liquid plug flow is expected to replace water as a cooling medium. Liquid-liquid plug flow is a flow state in which two immiscible liquids form a continuous phase or a dispersed phase, respectively, and flow alternately, as shown in Fig. 1. Previous studies (Asthana et al., 2011, Abdollahi et al., 2020) on liquid-liquid plug flow have reported that the Nusselt number of liquid-liquid plug flow is 4 to 7 times higher than that of a single-phase fluid. Therefore, it is expected to be utilized as a new cooling medium. However, the effects of the kinematic viscosity of each fluid and the type of fluid forming the continuous or dispersed phase on the Nusselt number of the liquid-liquid plug flow have not been identified.

In this study, water and silicon oil are selected as the liquids that form the liquid-liquid plug flow to investigate the effects of kinematic viscosity on the heat transfer characteristics and how the characteristics change when the continuous and dispersed phases are switched.

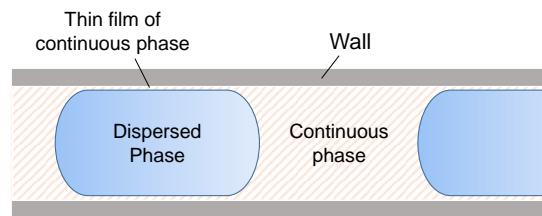


Figure 1. Schematic of liquid-liquid plug flow.

2. EXPERIMENTAL SECTION

Table 1 shows physical properties of fluids used for the experiment. Water and silicone oil (KF-96L-1cs, KF-96L-10cs, Shin-Etsu Chemical Co., Japan) were used immiscible liquids.

Table 1. Physical properties of test fluids ($T = 25\text{ }^{\circ}\text{C}$).

	Water	KF-96L-10cs
Density, kg/m^3	997	935
Specific heat, kJ/kg/K	4.2	1.7
Thermal conductivity, W/m/K	0.61	0.14
Kinematic viscosity, m^2/s	0.893×10^{-6}	10×10^{-6}

The schematic diagram of the experimental apparatus is shown in Figure 2. The experimental apparatus consists of storage tanks for silicone oil and water, a gear pump, solenoid valves, a flowmeter, a Y-shaped confluence section, the observation sections, and a heating section. The observation sections are made of acrylic or glass allowing observation of the flow state of the plug flow. The detailed diagram of the heating section is shown in Fig. 3. The heating section is made of a stainless steel pipe with a length of 1.0 m and an inner diameter of 6 mm. A nichrome heater, insulated over a length

of 0.9 m, is wound around the pipe wall, allowing for electrical heating under constant heat flux conditions using a direct current stabilized power supply. T-type thermocouples were used to measure the temperatures of the pipe wall and the fluid flowing through the pipe. The pipe wall temperature was measured using three thermocouples embedded at 90° intervals around the circumference of the cross-sections at positions $x = 275, 575,$ and 875 mm from the start of the heating section, and the average temperature measured by three thermocouples at each position was used for data reduction.

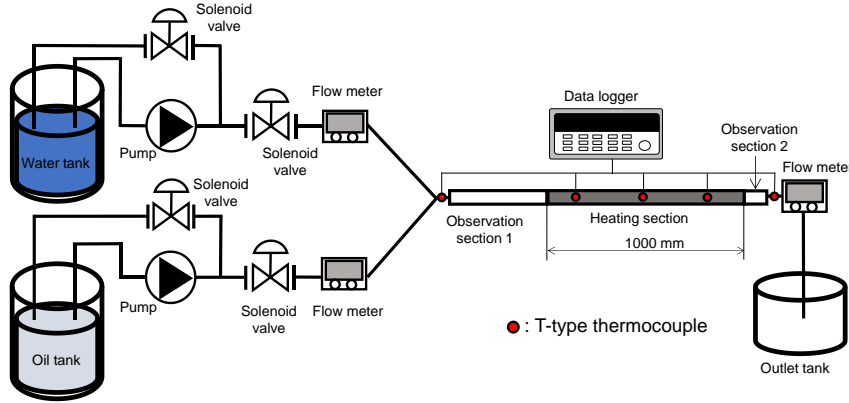


Figure 2. Schematic of the experimental apparatus.

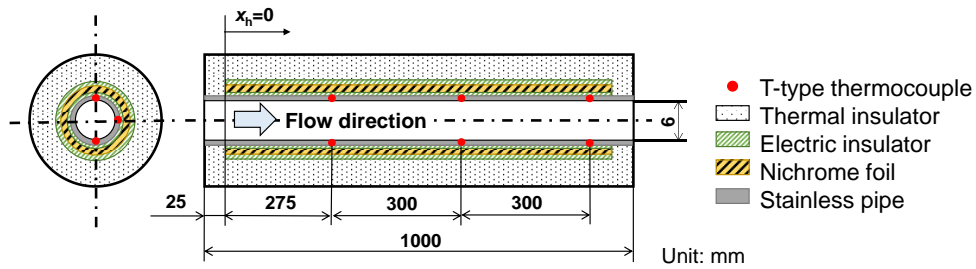


Figure 3. Detail of heating section.

The experimental conditions are shown in Table 2. The experimental procedure involves first forming plug flow by alternately pumping water and oil into the confluence section. After the formation of the plug flow, the plug flow moving through the heating section is heated at a predetermined heat flux. The local heat transfer coefficient α_x ($\text{W/m}^2/\text{K}$) is calculated using Eq. (1) from the wall temperature when a steady state is reached.

$$\alpha_x = \frac{q}{T_{w,x} - T_{b,x}} \quad (1)$$

where, q (W/m^2), $T_{w,x}$ ($^{\circ}\text{C}$) and $T_{b,x}$ ($^{\circ}\text{C}$) are the wall heat flux, wall temperature and bulk mean temperature, respectively. In this study, the bulk mean temperature at each heating position was calculated by linearly interpolating the temperatures measured at the inlet and outlet of the heating section. The experimental results were evaluated by Nusselt number and Graetz number:

$$Nu = \frac{\alpha_x D_{in}}{k} \quad (2)$$

$$Gz = \frac{xk}{\rho c u_m D_{in}^2} \quad (3)$$

where, k (W/m/K), ρ (kg/m^3), c (J/kg/K) and u_m (m/s) are the thermal conductivity, the density, the specific heat and mean velocity, respectively.

In this study, it is assumed that the density of the plug flow obeys the principle of additivity, and the values for each physical property were calculated by weighting them with the mass flow rate. However, the thermal conductivity does not obey the principle of additivity. Nonetheless, in this study, since each plug of water and silicone oil is heated by an equal heat flux in a horizontal pipe, and thus the heat is applied equally to each fluid. Therefore, in the same way as

density and specific heat, the thermal conductivity was also calculated using the weighted sum of the physical properties of both fluids, weighted by their respective mass flow rates.

This study also investigated whether the heat transfer characteristics of plug flow change depending on whether water acts as the dispersed phase or the continuous phase. Therefore, when forming plug flow with water as the dispersed phase, the material for the confluence section and the observation section is acrylic; when water acted as the continuous phase, the materials is glass.

Table 2. Experimental conditions.

Inlet temperature, °C	18
Flow velocity, m/s	2.0
Water / oil velocity ratio	1
Heat flux, W/m ²	1000 – 3000
Pipe material	Acrylic, Glass

3. RESULTS AND DISCUSSION

Figure 4 shows flow state of plug flow moving in the observation section 1 (Fig. 2). The plug length represents total length of water and oil plug. As it can be seen from Fig. 4, water is the dispersed phase in the acrylic pipe and it is the continuous phase in the glass pipe. It was confirmed that the continuous and dispersed phases of the plug flow did not switch when the plug flow passed through observation section 2, suggesting that the condition observed in observation section 1 was maintained even in the heating section made of the stainless steel.

Figure 5 shows Nusselt number of the water, oil and plug flow at each Graetz number. The continuous phase of the plug flow is oil. The solid line in the figure shows the value of the empirical equation for the Nusselt number when a fluid flowing in a circular tube in a laminar flow is heated under constant heat flux condition:

$$Nu_{emp} = 5.364 \left[1 + \left(\frac{220}{\pi} Gz \right)^{-10/9} \right]^{3/10} - 1.0 \quad (4)$$

As shown in the Fig. 5, the results for water and oil are in good agreement with the empirical value. In the case of the plug flow, the Nusselt number is relatively constant regardless of the value of the Gretz number. This may be due to the immediate development of the thermal boundary layer in the case of plug flow. Figure 6 shows the Nusselt number for the plug flow in which the continuous phase is the oil and the kinematic viscosity of the water (dispersed phase) is varied. As it can be seen from Fig. 6, there is no significant difference in the Nusselt number when the kinematic viscosity of the dispersed phase is changed, indicating that the effect of the kinematic viscosity of the dispersed phase on the heat transfer is relatively small.

Figure 7 shows the Nusselt number of plug flow when the continuous phase and the dispersed phase are switched. The Nusselt number represents the value calculated from the temperature measured at the position of $x_h = 575$ mm. The convergence value of 4.364 for Eq. (4) is also shown, since it was suggested that the development of a thermal boundary layer in the plug flow. As it can be seen from Fig. 7, the Nusselt number of the plug flow with water as continuous phase is significantly higher than that of the plug flow with oil as the continuous phase. Furthermore, the Nusselt number of the plug flow with water as the continuous phase increases as the dimensionless plug length decreases.

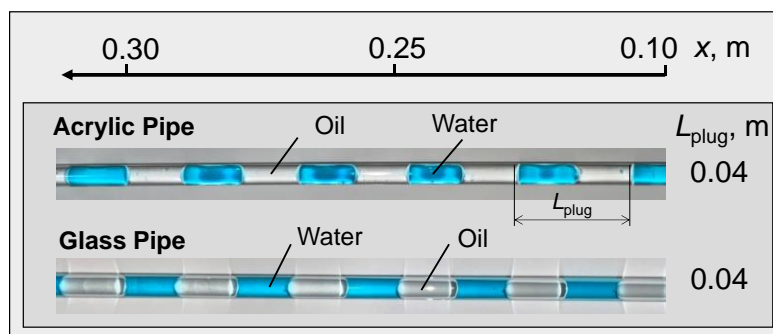


Figure 4. Flow appearance of plug flow moving in the acrylic pipe and glass pipe.

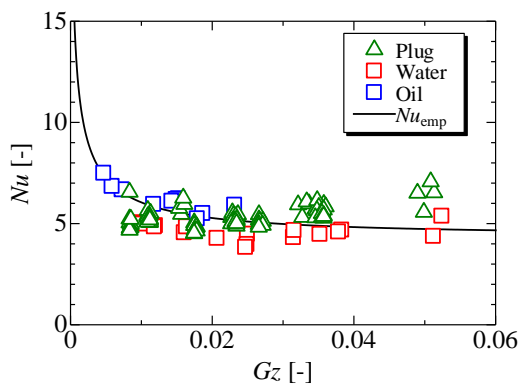


Figure 5. Nusselt number vs. Graetz number. The continuous phase of plug flow is the oil

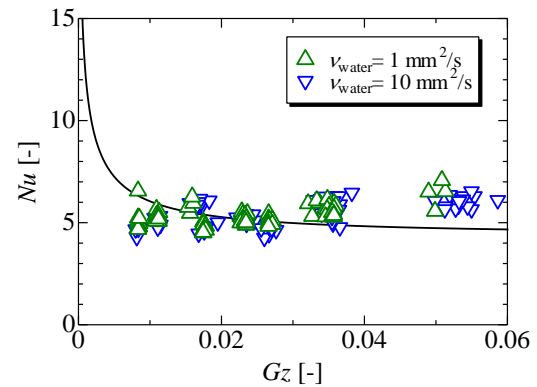


Figure 6. Nusselt number vs. Graetz number for plug flow with oil as the continuous phase. The kinematic viscosity of water is varied.

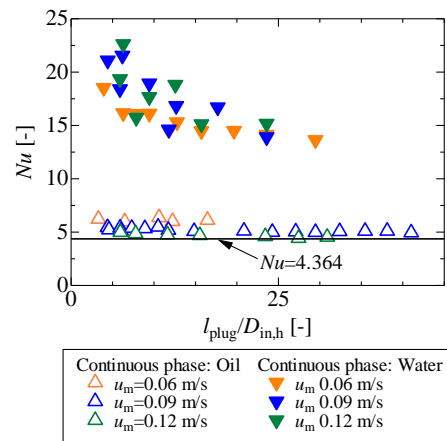


Figure 7. Nusselt number for the plug flow with various dimensionless plug length.

4. CONCLUSIONS

In this study, a liquid-liquid plug flow was formed using water and silicone oil, and the effects of the kinematic viscosity of the liquid and the type of fluid forming the continuous or dispersed phase on the heat transfer characteristics of the liquid-liquid plug flow were investigated. Experimental results showed that the effect of kinematic viscosity of the dispersed phase on the heat transfer of the plug flow was relatively small. On the other hand, when the continuous phase was water instead of oil, the Nusselt number changed significantly, increasing 3 to 5 times that of the single-phase fluid. In the conference, the effects of fluid kinematic viscosity and plug length on the heat transfer of the plug flow will be discussed in more detail.

5. REFERENCES

- Khattak, Z. and Muhammad, H.A., 2019. "Air cooled heat sink geometries subjected to forced flow: A critical review". *International Journal of Heat and Mass Transfer*, Vol. 130, pp. 141–161.
- Asthana, A., Zinovik, I., Weinmueller, C. and Poulikakos, D., 2011. "Significant Nusselt number increase in microchannels with a segmented flow of two immiscible liquids: An experimental study". *International Journal of Heat and Mass Transfer*, Vol. 54, pp. 1456–1464.
- Abdollahi, A., Norris, E.S. and Sharma, N.R., 2020. "Fluid flow and heat transfer of liquid-liquid Taylor flow in square microchannels". *Applied Thermal Engineering*, Vol. 172, 115123.

CURRENT AND TEMPERATURE MEASUREMENTS OF NANOWIRE NETWORK USING THERMOREFLECTANCE IMAGING

Kazuya Tatsumi^{a,*}, Yuta Sugihara^a, Yuki Wakamatsu^a, Reiko Kuriyama^{a,b}

^aKyoto University, Kyotodaiagku-katsura, Nishikyo-ku, Kyoto 615-8540, Japan

^bJapan Science and Technology Agency PRESTO, 5-3, Yonbancho, Tokyo, 102-8666, Japan

*tatsumi@me.kyoto-u.ac.jp

Keywords: Silver nanowire, Two-dimensional measurement, Thermoreflectance imaging, Inverse problem

1. INTRODUCTION

A sheet consisted of Ag-NWs which is randomly dispersed and forming a network can be applied to electronic devices and wearable devices as flexible and transparent conductive film material and heater (Lee et al., 2012, Araki et al., 2014). To evaluate the performance and reliability of the sheet and device, it is necessary to understand the characteristics of the current and temperature distributions of the Ag-NW network (Sadeque et al., 2018). Further, the current path is based on the dispersed pattern of the Ag-NWs and the electric and thermal resistances of the Ag-NWs and contact point at the Ag-NW junction. These resistances change depending on the properties of the polymer coating of the Ag-NW and contact conditions at the junction. Although, the contact electric resistance at a single point of two Ag-NWs have been investigated (Bellew et al., 2018), the variation of the resistance and its effect in the Ag-NW network is unknown. The challenges to investigate and reveal these matters are threefold: (1) to measure the electric current and contact resistance distribution, (2) to evaluate the effect of the contact resistance variation on the current and temperature distributions, (3) to model the current and heat transfer paths, and the effect of the contact resistance variation. In this work, we exploit a technique to obtain the current, contact resistance, and heat transfer characteristics of the Ag-NW network by combining the thermoreflectance imaging (TRI) technique and numerical simulation. From the measured temperature distribution, we estimated the current and contact resistance distribution. Once the method was validated, the effects of the Ag-NW density and the contact resistance variation on the current path and temperature pattern are discussed based on stochastic and statistic modeling.

2. METHODS

Thin layer of Ag-NWs (Sigma-Aldrich: #739448) was dispersed on the glass substrate between parallel Au-electrodes using vacuum filtration. Diameter and length of the Ag-NWs were $D=120\text{-}150\text{ nm}$ and $L_{NW}=20\text{-}50\text{ }\mu\text{m}$, respectively. The number density was approximately 240 per $100\text{ }\mu\text{m}$ square.

Thermoreflectance imaging technique was utilized to measure the two-dimensional temperature distributions of the Ag-NW network. Current was applied to the Au-electrodes in a square pulse form of $10\text{ }\mu\text{s}$ width with period of $250\text{ }\mu\text{s}$. Reflectance was measure by LED flash light with width of $1.5\text{ }\mu\text{s}$ and high sensitive-high resolution camera. The nominal wavelength of the LED light was 530 nm . Timing of irradiation was adjusted to the phases at which the Ag-NW gave the temperature equal to room temperature and the maximum temperature, respectively. We measured and aligned 5,000 pairs of these images and averaged the reflectance change. The reflectance was converted to temperature using the thermoreflectance coefficient C_{TR} of $8.96 \times 10^{-5}\text{ K}^{-1}$, which we obtained from our calibration measurement for Ag sheet.

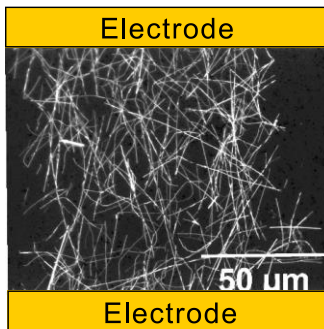


Figure 1. Photograph of the Ag-NWs dispersed on glass substrate forming a network in $100\text{ }\mu\text{m}$ square area between a pair of Au electrodes.

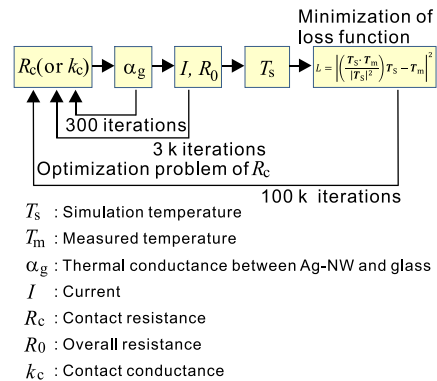


Figure 2. Numerical procedure to derive the temperature and current distributions, and contact resistance of the Ag-NW junctions by matching the temperature to the TRI measurement.

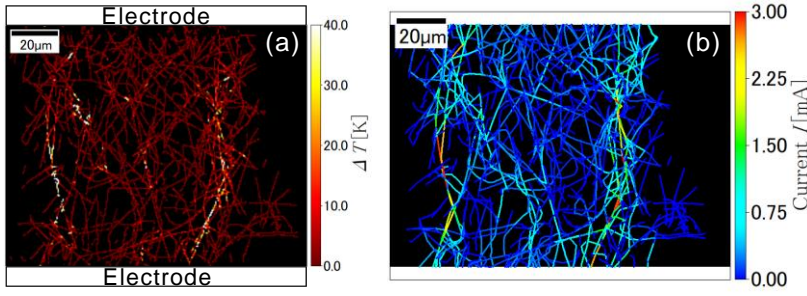


Figure 3. Distribution of (a) temperature change ΔT of the Ag-NW network measured by TRI, and (b) current with contact resistance at the junctions solved to match the temperature with measurement.

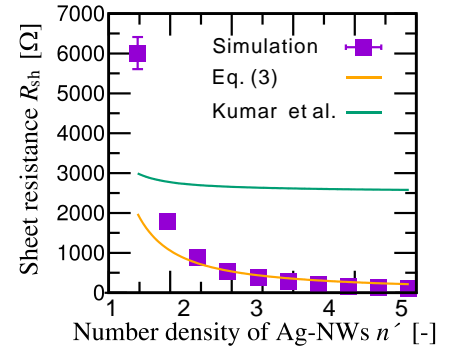


Figure 4. Relation of the sheet resistance to the dimensionless nanowire number density.

We conducted a numerical simulation solving the current and energy (heat transfer) conservation equations of the Ag-NWs in the network to obtain the current and temperature distributions. The voltage and total current applied to the electrode were set equal to those of the measurement. Heat transfer between the Ag-NW and glass substrate was also considered. The current and contact electric resistances of the Ag-NW junctions were derived by finding the condition which makes the temperature distribution of the simulation match with that of the measurement: namely, we solved the minimization problem of the loss function for the temperature difference between the simulation and measurement at all Ag-NWs. The heat transfer between Ag-NW and glass, current flow, and the contact electric resistance were updated and obtained through the iteration process (Fig. 2).

3. RESULTS AND DISCUSSION

The temperature distribution of Ag-NWs obtained by the measurement is shown in Fig. 3(a). Temperature was not uniform, and high temperature regions and hot-spots were generated in the network. Figure 3(b) shows the current distribution. Current did not flow uniformly through the network, and formed certain paths in which high current density regions existed. Contact resistance gave a wide range of variation. From the sensitivity analysis for the temperature distribution to each contact resistance, the number of junctions to which the temperature distribution was highly sensitive was 178 out of the total number of junctions 2,358. Resistance of these key junctions varied in the range of 3.7Ω to $1.4 \times 10^5 \Omega$. Combination of low and high contact resistances of these key junctions produced the current path. This was confirmed by comparing the distributions with the case when equal contact resistance was given to the junctions, and the probability density function for the temperature of the two cases. From these results, the number of paths increases and the area of high temperature and current decreases representing a more uniform distribution was obtained in the case of equal contact resistance.

The relationship between the Ag-NW concentration and the overall resistance of the Ag-NW network (sheet resistance, R_{sh}) is shown in Fig. 4. The area of the network was 2 mm square and several samples were simulated to obtain sufficient data for statistical analysis. The contact resistance R_c was 2 k Ω which was larger than the resistance of an Ag-NW. The value n' is the ratio between the number of wires per L_{NW} square n and the critical percolation number n_c , $n' = n/n_c$. To discuss the effect of limited current path on the sheet resistance, the results of the model of Kumar et al. (2017), which assuming the junctions to appear stochastically at the NWs and the current to flow through the NWs and junctions with equal probability and under constant voltage gradient in the region between the electrodes, are shown in the figure. The present results show that R_{sh} increases as n' decreases. The increase of R_c and the decrease of n' made the limitation of the current paths stronger, which increased the local current density and the resulting overall resistance.

To further validate this discussion, we modified the model of Kumar et al. so as the current flows preferentially through Ag-NWs and not equally over junctions in the Ag-NW. The sheet resistance of the modified model is given as Eq. (1).

$$R_{sh} = \frac{\pi L_{NW}}{2\sqrt{N_{NW}}} \left(\frac{4\rho}{\pi D^2} + \frac{cnR_c}{L_{NW}(2(e^{-cn} - 1) + cn(1 - e^{-cn}))} \right) \quad (1)$$

where ρ is the electric resistivity of Ag, N_{NW} is the number of NWs per area, and $c=2/\pi$. The model agrees well with the simulation. This shows that the current flows mainly along the Ag-NW if the R_c is relatively large, and that contact resistance indeed controls the current path. Obviously, if specific current paths become dominant for the current flow in the network with respect to the overall current distribution, the model based on uniformity and isotropy can no longer be applied. This can be confirmed also by the results that the simulation gives larger R_{sh} than the models in the region of small n' .

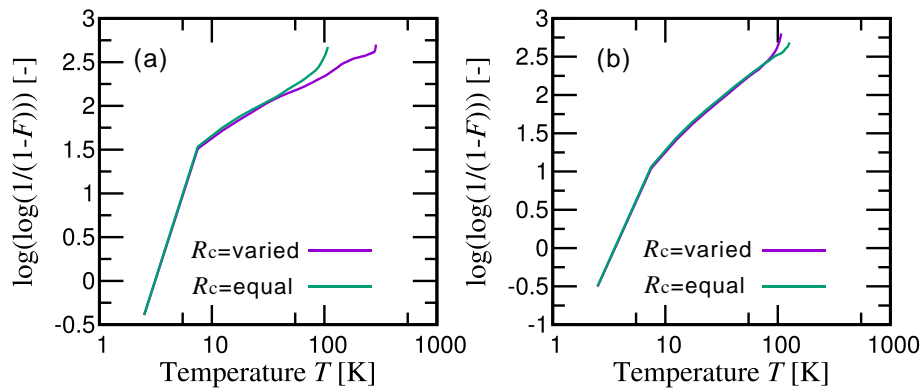


Figure 5. Weibull plot of the temperature of the Ag-NWs for the case of randomly varied contact resistance and the case when equal resistance was applied. (a) Ag-NW number density of $n'=1.3$ and (b) $n'=2.16$. F is the cumulated distribution function of the Weibull distribution.

Further analysis was conducted to evaluate the effect of the contact resistance variation on the current and temperature distributions: namely, junctions with equal contact resistance and randomly applied resistance with the average value being equal were performed for $n'=1.3$, 1.73 and 2.16. We applied the curvilinear progression using the Weibull distribution to represent the path pattern of the current (Das et al., 2016). Discussing the obtained shape parameter in relation to n' , the case of random contact resistance gave larger current than the case of equal contact resistance indicating that variation of contact resistance decreases the uniformity of the current distribution and generates high concentration regions. This was more conspicuous for smaller n' as limited number of paths could be formed in this case.

The results of temperature and heat transfer exhibited different characteristics. As shown in Fig. 5, the Weibull plot with two slopes were obtained. The two shape factors of these slopes were attributed to the Joule heating for the high temperature region, and to the effect of heat transfer for low temperature region, respectively (Tamai et al., 2023). The ratio of these two changed with the elapse time after the start of heating, having the heat transfer effect increase as elapse time increased. Therefore, the temperature distribution needs to consider the timescale of the heat transfer in addition to the Joule heating represented by the current path.

4. CONCLUSIONS

The contact electric resistance of the Ag-NW junction varied in the network, and played an important role in generating specific current paths and hot-spots. This tendency appeared significantly in smaller Ag-NW number density case. The performance and reliability analysis of conductive sheets and heaters using Ag-NWs need to consider the variation and reliability of the contact electric resistance. The heat transfer affected the temperature differently from the current path, showing the impact of diffusion. The variation of contact thermal resistance can affect the reliability of the network similar to the electric resistance and is considered as future work.

5. REFERENCES

- Lee, P., Lee, J., H. Lee, J. Yeo, S. Hong, K. H. Nam, D. Lee, S. S. Lee, and S. H. Ko, S.H., 2012. "Highly stretchable and highly conductive metal electrode by very long metal nanowire percolation network". *Advanced Materials*, Vol. 24, pp. 3326-3332.
- Araki, T., Jiu, J., Nogi, M., Koga, H., Nagao, S., Sugahara, T., and K. Sukanuma, K., 2014. "Low haze transparent electrodes and highly conducting air dried films with ultra-long silver nanowires synthesized by one-step polyol method". *Nano Research*, Vol. 7, pp. 236-245.
- Sadeque, S., Gong, T., Maize, K., Ziabri, A. K., Mohammed, A. M. S., Shakouri, A., and Janes, D. B., 2018. "Transient thermal response of hotspots in graphene-silver nanowire hybrid transparent conducting electrodes". *IEEE Trans. on Nanotechnology*, Vol. 17, pp. 276-28.
- Bellew, A. T., Manning, H. G., da Rocha, C. G., Ferreira, M. S., and Boland, J. J., 2015. "Resistance of single Ag nanowire junctions and their role in the conductivity of nanowire networks". *ACS Nano*, Vol. 9, pp. 11422-11429.
- Kumar, A., Vidhyadhiraja, N. S., and Kulkarni, G. U., 2017. "Current distribution in conducting nanowire networks". *J. Applied Physics*, Vol. 122, 045101.
- Das, S. R., Mohammed, A. M. S., Maize, K., Sadeque, S., Shakouri, A., Janes, D. B., and Alam, M. A., 2016. "Evidence of universal temperature scaling in self-heated percolating networks". *Nano Letters*, Vol. 16, pp. 3130-3136.
- Tamai, K., Sugihara, Y., Tatsumi, K., Kuriyama, R. and Nakabe, K., 2023. "Analysis of joule heating characteristics in nanowire networks measured by thermoreflectance imaging method". In *Proceedings of the 8th Thermal and Fluids Engineering Conference (TFEC)*, Maryland, U.S.A.

Rapid cooling mechanism in liquid nitrogen using porous copper material

Yutaro Umehara^{a, b*}, Shoji Mori^{a, b},

^aDept. of Mech. Eng., Kyushu Univ., 744, Motoooka, Nishi ward, Fukuoka, 819-0395

^bInternational Institute for Carbon-Neutral Energy Research, Kyushu Univ., 744 Motoooka, Nishi ward, Fukuoka 819-0395, Japan

*umehara@mech.kyushu-u.ac.jp

Keywords: Liquid nitrogen, Electrolytic deposition, Porous material, Quenching, Wickability

1. INTRODUCTION

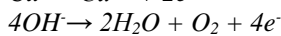
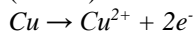
Cryogenic liquid is used in a wide range of fields, such as the rocket fuel (T. M. Tomsik, 2020), coolant for superconducting magnets (Y. Shirai *et al.*, 2011) and freezing food (H. Davidge, 1981) etc., while cryogenic liquid is a challenging substance to handle due to the very low saturation temperature at atmospheric pressure. To use the cryogenic liquid in the various fields, all the components and pipelines should be cooled down to the saturation temperature of the cryogenic liquid. However, since the cryogenic liquid easily undergoes a phase change, the precooling requires a large amount of cryogenic liquid. To reduce the amount of the cryogenic liquid for the precooling, the various researches have been carried out to improve the heat transfer. D. He *et al.* (2019) reported that the nanopore structure improves the quenching characteristics in the liquid nitrogen. Y. Kikuchi *et al.* (1985) used the additional layer which has low thermal conductivity on the sample to reduce the cooling time in the liquid nitrogen. In this study, we conduct the quenching experiment using the liquid nitrogen as the coolant. To enhance the cooling characteristics, the copper porous plate which made using the electrolytic deposition was attached to the surface of test specimen.

2. EXPERIMENTAL

2.1 Fabrication of the copper porous plate

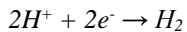
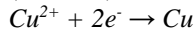
Electrolytic deposition method was used to fabricate the copper porous on the copper plate. The fabrication included four steps. First, copper plate (99.96%) with 20mm in diameter and 0.3mm in thickness was cleaned up in acetone. Electropolishing process was maintained for 10s. Second, this copper plate was used as a cathode in the acid solution (CuSO₄ 0.4mol/L and H₂SO₄ 1.5mol/L, 200ml). A square copper plate with sides of 40mm and thickness of 1mm was used as the anode. Fig. 1(a) shows the schematic design of the electrolytic deposition apparatus. The distance between the two plates was 20mm. Third, direct current (6A) was supplied through both plates. This duration was called deposition time and was changed (3 and 5, 7min). The electrochemical reaction at each electrode is as follows,

(Anode)

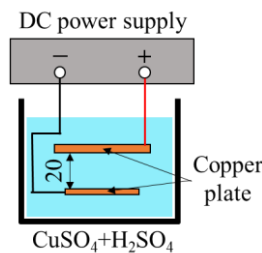


(1)

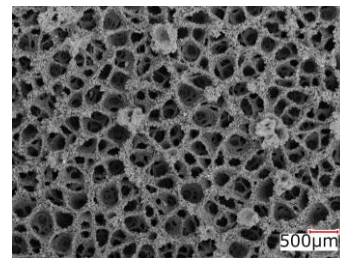
(Cathode)



(2)



(a) Electrolytic deposition equipment



(b) SEM image (6A 3min)

Fig. 1 Fabrication method of copper porous plate by electrolytic deposition

Copper porous was formed on the cathode. Finally, copper porous plate was sintered in vacuum furnace at 950°C for 30 min. Fig. 1(b) shows SEM image. Table 1 shows the copper porous condition (thickness, porosity and average pore size)

with the difference deposition time. The thickness and average pore size increased with the increase of the deposition time, while the porosity did not change.

Table 1 Copper porous condition

Deposition time [min]	Thickness [mm]	Porosity [-]	Average pore size [μm]
3	0.751	0.918	305
5	1.007	0.915	418
7	1.216	0.925	512

2.2 Quenching experiment

Figure 2 shows the schematic design of experimental apparatus and copper block. Copper block ($\phi 30\text{mm}$ and 30mm in the height) had a M3 hole to keep the height. To reduce the edge effect for quenching characteristics, R5 chamfering applied to the edge of bottom surface. Two K-type thermocouples ($\phi 0.5\text{mm}$) were inserted at 5 and 10mm from the bottom of the copper block. Copper porous plate was fixed on the bottom surface using solder. The temperature data was recorded every 0.1s . Liquid nitrogen (-196°C , atmospheric pressure) was stored in glass Dewar bottle which was put on the lifting platform.

The experimental procedure is as follows; First, copper block was heated up by heat gun to 45°C . Then, the Dewar bottle was lifted up until $2\sim 3\text{mm}$ of the bottom of the copper block was immersed. This immersion depth was maintained manually until the wall temperature was equal to the saturation temperature of liquid nitrogen. The above procedure was repeated three times on the same surface. Wall temperature and heat flux were calculated from the inverse analysis of one-dimensional heat conduction (Eq. (3)) (P.L. Woodfield *et al.*, 2006).

$$\rho c \frac{\partial T}{\partial t} = k \frac{\partial^2 T}{\partial z^2} \quad (3)$$

where, ρ , c , k is the density, thermal capacity and thermal conductivity, respectively. Properties used for calculation is summarized in Table 2. These properties are the value at the average temperature between initial temperature and saturation temperature of liquid nitrogen.

Table 2 Copper properties at 200 K

Density ρ [kg/m^3]	Specific heat c [$\text{J}/\text{kg K}$]	Thermal conductivity k [$\text{W}/\text{m K}$]
8970	362	391

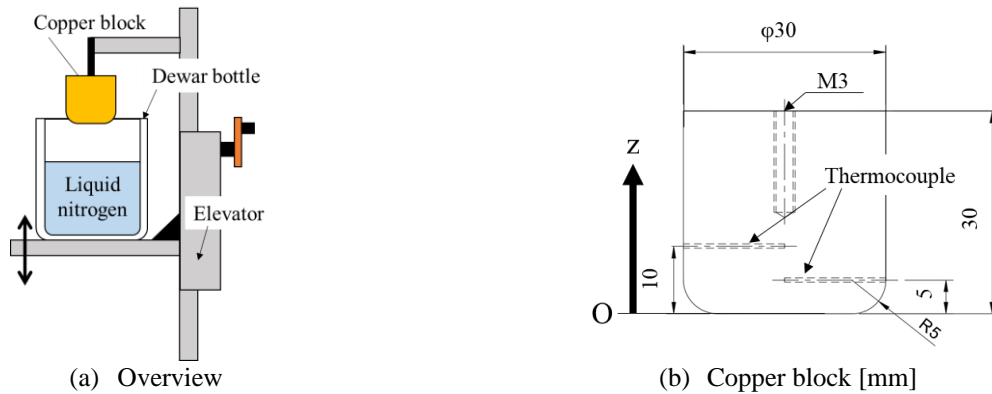


Fig. 2 Experimental apparatus

3. RESULTS AND DISCUSSIONS

The cooling curves are shown in Figure 3. The cooling time of bare and copper porous of different deposition time (3 and 5, 7 min) was 1814 and 329, 171.5, 141.6 s, respectively. All copper porous plate can reduce the cooling time in liquid nitrogen. And also, the cooling time decreases with the increase of the deposition time. Fig. 4 shows the boiling curves. Since the results of the inverse analysis were unstable at the beginning of cooling, the boiling curves were shown from 200K . And, the minimum wall temperature was defined from the minimum heat flux point. In Fig. 4, the heat flux of the bare surface was almost same with the film boiling heat transfer. On the other hand, the heat flux of the whole copper porous plate (deposition time: 3, 5, 7 min) was 1.62, 4.47, 4.85 times higher than that of the bare surface, respectively. Since the film boiling heat transfer can not realize the high heat flux, it is considered that the boiling

transition was occurred at the beginning of the cooling. Y. Kikuchi *et al.* (1985) reported that the low thermal conductivity layer caused the early collapse of the film boiling. In fact, as the copper porous has low thermal conductivity due to the high porosity, it is believed that the early collapse of the film boiling was induced. The reason why the heat flux is different on the copper porous plate with the different deposition time can be related to the wickability of the surface. Wickability was defined by Rahman *et al.* (2014) to explain the critical heat flux of the pool boiling and indicates the capillary performance (=the absorption rate of water contained in a capillary tube) of the surface. Lee *et al.* (2019) reported that the wickability does not affect the film boiling heat transfer, but does affect the transition boiling heat transfer. Therefore, it is considered that the transition boiling heat transfer increases with the wickability as the deposition time increases. After the transition boiling regime, nucleate boiling started from the minimum heat flux point. The all the surface condition shows the same minimum heat flux temperature at around 10K. Based on these results, the boiling transition on the all the surface condition occurred on the bottom surface of copper block.

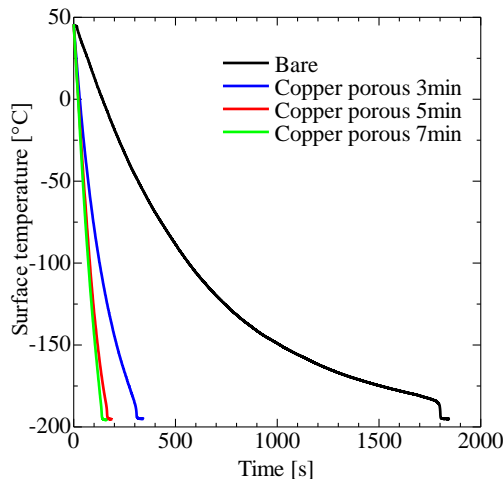


Fig. 3 Cooling curves

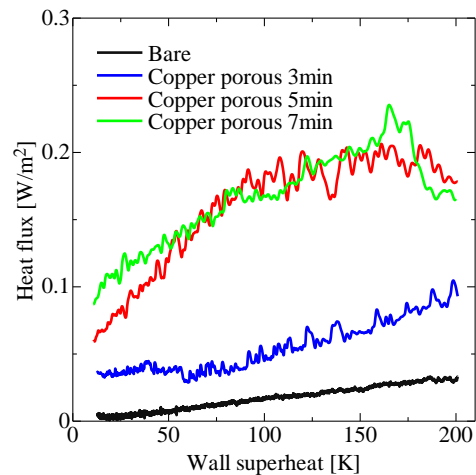


Fig. 4 Boiling curves

4. CONCLUSIONS

In the present study, the quenching experiments were conducted with the copper porous plate which was fabricated by the electrolytic deposition in liquid nitrogen. The different deposition times reflect the different shape of the copper porous plate (thickness, porosity and average pore size). From the cooling curves, all the copper porous plates reduce the cooling time compared to the bare surface. The boiling curves show that the heat flux on the copper porous plate is higher than on the bare surface. As the copper porous plates cause the early collapse of the film boiling, the heat flux at the beginning of the cooling is higher than on the bare surface. Furthermore, since the wickability of the surface affects the transition boiling heat transfer, it is considered that the different deposition time affects the wickability of the copper porous plate and shows the different transition boiling heat transfer.

5. REFERENCES

- Davidge, H., 1981. "Cryogenics in the food industry". *Cryogenics*, 21(5), 287-290.
- He, D., Zhang, P., Lv, F., Wang, S., and Shu, D., 2019. "Cryogenic quenching enhancement of a nanoporous surface". *International Journal of Heat and Mass Transfer*, 134, 1061-1072.
- Kikuchi, Y., Hori, T., and Michiyoshi, I. 1985. "Minimum film boiling temperature for cooldown of insulated metals in saturated liquid". *International journal of heat and mass transfer*, 28(6), 1105-1114.
- Lee, G. C., Kim, S. H., Kang, J. Y., Kim, M. H., and Jo, H., 2019. "Leidenfrost temperature on porous wick surfaces: Decoupling the effects of the capillary wicking and thermal properties". *International Journal of Heat and Mass Transfer*, 145, 118809.
- Rahman, M.M., Olceroglu, E., and McCarthy, M., 2014. "Role of wickability on the critical heat flux of structured superhydrophilic surfaces". *Langmuir*, 30(37), 11225-11234.
- Shirai, Y., Tatsumoto, H., Shiotsu, M., Hata, K., Kobayashi, H., Naruo, Y., and Kinoshita, K., 2011. "Forced flow boiling heat transfer of liquid hydrogen for superconductor cooling." *Cryogenics*, 51(6), 295-299.
- Tomsik, T.M., 2020. "Recent advances and applications in cryogenic propellant densification technology." *Intersociety Cryogenic NAS 1.15*: 209941.
- Woodfield, P. L., Monde, M., and Mitsutake, Y. 2006. "Improved analytical solution for inverse heat conduction problems on thermally thick and semi-infinite solids". *International journal of heat and mass transfer*, 49(17-18), 2864-2876.

EXPLORING PHASE SEPARATION DYNAMICS IN BLOCK COPOLYMER SOLUTIONS: INNOVATIVE EXPERIMENTAL TECHNIQUES WITH THERMODYNAMIC ANALYSIS

Irene Perna^a, Gaia Paradiso^b, Rosalia Ferraro^{a,c}, Marta Gamberoni^b, Salvatore Coppola^b, Sergio Caserta^{a,c*}

^aDepartment of Chemical, Materials and Production Engineering, University of Naples Federico II, P.le V. Tecchio 80, 80125 Naples, Italy

^bElastomers, Research and Development Centre, Versalis S.p.A (Eni), I-48100 Ravenna, Italy

^cCEINGE Advanced Biotechnologies Franco Salvatore, Via G. Salvatore 436, 80131 Naples, Italy

*sergio.caserta@unina.it

Keywords: block copolymers, phase separation dynamics, solvent selectivity, rheological analysis, thermodynamics

1. BACKGROUND

According to the definition given by Bates F.S. and Fredrickson G.H. (1990), block copolymers are unique macromolecules comprised of distinct sequences or blocks of repeating units. Block copolymers find wide-ranging applications thanks to the integration of desirable properties from the different monomer units, which gives rise to materials with hybrid properties (Scott A.J., Penlidis A., 2017). In general, according to Hanley K.J. *et al.* (2000), almost all applications involve mixtures, such as blends with a parent homopolymer, low molecular weight “tackifying” resins and plasticizers, or solvent. The self-organization phenomenon exhibited by block copolymers (BCPs) in solution is nowadays an active area of research and has been a central focus of extensive scientific investigation for several decades (Olvera de la Cruz M., 1989). This interest arises from the need to elucidate the mechanism driving the self-assembly behavior of BCPs when dissolved in solvents. Indeed, the properties of the solvent, such as selectivity (Cloitre M. and Vlassopoulos D., 2011), play a crucial role in comprehending the potential applications of block copolymers across various fields. Consequently, constructing a phase diagram of copolymer solutions is a pivotal step in understanding the stability and behaviour of these complex systems. As stated by Bates C.M. *et al.* (2014), Flory-Huggins block–block interaction parameter(s) χ , the volume fraction of each block and the architecture are fundamental parameters in determining the bulk morphology of block copolymers. Furthermore, in a recent work, Taylor L.W. *et al.* (2024) also found out that the monomer sequency has a fundamental impact on the phase behaviour of the system. The study of block copolymer phase separation results in the investigation of the transition from an isotropic system, such as a homogeneous block copolymer melt or solution, to a spatially discrete state characterized by periodic ordered structures. In fact, under a certain critical temperature, called the order-disorder transition temperature T_{ODT} , microphase separation occurs, and a diverse range of microstructures emerges within block copolymer systems (Matsen M.W. and Bates F.S., 1996). Extensive theoretical and experimental efforts have been dedicated to characterizing and identifying the factors that govern phase separation in polymeric solutions.

2. OBJECTIVES

This study stems from the need to enhance the industrial process associated with the large-scale production of these specific materials in order to reduce their environmental impact.

Specifically, in this work, we focus our attention on two different types of Styrene-Butadiene block copolymers, one possessing nearly monodisperse molar mass distribution and the other displaying polydisperse molar mass distribution and heterogenous chain composition. Specifically, we investigated the interactions of these polymers with a solvent which is selective specifically with the elastomeric part. To this end, we subjected the polymer solutions to temperature sweep analysis to assess the relevant rheological changes related to phase separations. In parallel, in order to integrate and confirm the rheological results, we also conducted an experimental campaign based on microscopy analysis, involving visual inspection and polarised microscopy, to highlight optical evidence of phase separation at varying temperature. From a thermodynamical point of view, it is possible that the system, under a certain range of temperatures and compositions, is metastable, favoring the mechanism phase separation through nucleation and growth. Specifically, in the metastable region, once surpassed a certain critical size, the nuclei start to expand, and the phase separation occurs. From our first results we found out that the type and the concentration of copolymer, as well as the quality and the selectivity of the solvent can impact phase separation at various polymer concentrations.

3. METHODS

Rheological analysis is done using a controlled-stress rheometer (Anton Paar MCR301) equipped with a dual Peltier system to ensure precise temperature regulation. A coaxial cylinder geometry with a diameter of 17mm is utilized. To minimize sample evaporation, a custom-made cap is placed on top. Dynamic mechanical analysis is carried out under static conditions to assess the relevant rheological changes related to phase separations as functions of the temperature, concentration of the polymer and the solvents.

As regard the optical microscopy analysis visual inspection and time lapse microscopy are performed. Visual inspection is an experimental technique used to observe the phase transition of the solution at a macroscopic level through changes in its optical properties, by naked eye. This technique was implemented in recent works (Ferraro R. *et al.*, under review) to investigate the phase behavior of surfactant solutions at different concentration of the surfactant. The set-up consists of a rectangular glass pool previously filled with silicon oil (100 cSt). The samples are loaded in small cylindrical glass bottles (volume ~ 4 mL), fixed into a custom-made support, and placed in a glass box. Silicon oil, with a refractive index close to that of glass (1.40 and 1.51, respectively), is used to minimize curvature effects arising from the cylindrical shape of the bottles. Two flat sheet polarizers are crossed and stuck to two opposite walls of the pool. The pool, containing the samples in the silicon oil bath, is placed on an electric hotplate to perform thermal annealing. The temperature is measured with a thermocouple immersed in the silicon oil and recorded as a function of time using a LabVIEW software. Within the same pool, two bottles containing bi-distilled water and air are also included as control samples. The entire pool, including the bottles, is imaged using a Canon EOS 60D camera connected to a Time-Lapse controller, with an objective Canon EF-S 60mm f/2.8 Macro USM, placed on a tripod and carefully aligned to be orthogonal to the front wall of the pool.



Figure 1. Visual inspection set-up.

On the other hand, an independent setup is used to investigate samples phase evolution on microscopic scale, as a function of concentration and temperature. Time-lapse polarized light microscopy has proven to be a powerful tool for studying and analyzing sample morphology. It has indeed been utilized by Castaldo R. I. *et al.* (2019) and Capaccio A. *et al.* (2020) to study the morphology of a surfactant solution (SLE₃S) in water during the dissolution process. Sample morphology is investigated using an automated Time-Lapse Microscopy (TLM) workstation based on an inverted microscope (Zeiss Axiovert 200, Carl Zeiss, Jena Germany). Several independent fields of view are acquired by a high-resolution high-sensitivity monochrome CCD video camera (Hamamatsu Orca AG, Japan) using several objectives (10x, 5x) and crossed polarizers to visualize the internal microstructure. The microscopy workstation is also equipped with a motorized stage and focus control (Marzhauser) for automated sample positioning that allows to iteratively image the same pre-selected sample regions. A circulating water bath and a thermocouple are used to control sample temperatures. The sample consists of a small quantity of polymer solution sealed between two glass slides separated by 1.2 mm spacers.

4. CONCLUSIONS

The study of block copolymers represents a key topic in polymer science, with applications spanning various industries and research areas. As highlighted, the behavior of block copolymers in solvent remains a focal point of investigation,

reflecting the complexity and importance of understanding their interactions in solution. Our experimental findings underscored the substantial influence of copolymer type and solvent quality on phase separation dynamics across different polymer concentrations. This observation sheds light on the intricate interplay between copolymer characteristics, solvent properties, and phase behavior, offering valuable insights for the design and optimization of polymer systems. By elucidating the factors governing phase separation in polymeric solutions, this study is intended to contribute to advancing our understanding of block copolymer behavior in solvent environments. The integration of rheological and microscopy analyses enhances our capability to probe complex fluid dynamics, paving the way for future research endeavors aimed at refining polymer synthesis and application methodologies.

5. REFERENCES

- Bates C.M., Maher M.J., Janes D.W., Ellison C.J. and Willson C.G., 2014. "Block copolymer lithography". *Macromolecules*, vol. 47, no. 1, pp. 2-12.
- Bates F.S., Fredrickson G.H., 1990. "Block Copolymer Thermodynamics: Theory and Experiment". *Annual Review of Physical Chemistry*, vol 41, p. 525
- Capaccio A., Caserta S., Guido S., Rusciano G., Sasso A., 2020. "Dissolution of a surfactant-water lamellar phase investigated by combining time-lapse polarized light microscopy and confocal Raman spectroscopy". *Journal of Colloid and Interface Science*.
- Castaldo R. I., Pasquino R., Villone M. M., Caserta S., Gu C., Grizzuti N., Guido S., Maffettone P. L., Guida V., 2019. "Dissolution of concentrated surfactant solutions: from microscopy imaging to rheological measurements through numerical simulations." *Soft matter*.
- Cloitre M, Vlassopoulos D., 2011. "Block Copolymers in External Fields: Rheology, Flow-Induced Phenomena, and Applications". *Applied Rheology of Polymeric Fluids* (M. Kontopoulou Ed.) John Wiley & Sons Inc. Chapter 7, pp. 209-239.
- Ferraro R., Salvatore M.M., Esposito R., Murgia S., Caserta S., D'Errico G., Guido S., Under submission. "Impact of surfactant polydispersity on the phase and flow behaviour in water: the case of Sodium Lauryl Ether Sulfate". *Journal of Molecular Liquids*.
- Hanley K.J., Lodge T.P., Huang C-I., 2000. "Phase Behavior of a Block Copolymer in Solvents of Varying Selectivity" *Macromolecules*.
- Matsen M.W., Bates F.S., 1996. "Unifying Weak- and Strong-Segregation Block Copolymer Theories". *Macromolecules*.
- Olvera de la Cruz M., 1989. "Theory of microphase separation in block copolymer solutions". *The Journal of Chemical Physics*.
- Scott A.J., Penlidis A., 2017. Chapter "Copolymerization". *Reference Module in Chemistry, Molecular Sciences and Chemical Engineering*. Elsevier
- Taylor L.W, Priestley R.D and Register R.A, 2024. "Control of Solution Phase Behavior through Block–Random Copolymer Sequence". *Macromolecules*.

NOVEL OPTICAL METHODOLOGY UNVEILS IMPACT OF POLYMERIC POUR POINT DEPRESSANT ON PHASE MORPHOLOGY OF WAXY CRUDE OILS

Irene Perna^a, Rosalia Ferraro^{a,b}, Consiglia Carillo^a, Salvatore Coppola^c, Sergio Caserta^{a,b*}

^aDepartment of Chemical, Materials and Production Engineering, University of Naples Federico II, P.le V. Tecchio 80, 80125 Naples, Italy

^bCEINGE Advanced Biotechnologies Franco Salvatore, Via G. Salvatore 436, 80131 Naples, Italy

^cElastomers, Research and Development Centre, Versalis S.p.A (Eni), I-48100 Ravenna, Italy

*sergio.caserta@unina.it

Keywords: Waxy crude oils, Pour point depressants, Phase morphology

1. BACKGROUND

Crude oil, often denoted as petroleum, stands as an essential asset, assuming a pivotal role in global economies, political landscapes, and technological progressions. Its significance has notably surged due to widespread applications in industrial organic chemistry, encompassing the synthesis of plastics, fertilizers, solvents, adhesives, and pesticides. Despite apprehensions concerning its environmental ramifications, as highlighted by Martinez-Palou R. *et al.* (2011), petroleum and its derivatives are poised to persistently meet a substantial portion. Nonetheless, because of the decrease of readily accessible and economically viable oil reservoirs it is imperative to explore unconventional resources. Among these unconventional resources Li H. *et al.* (2015) underlay heavy and extra-heavy oil which are characterized by a high concentration of long-chain linear alkanes and, according to Eissa Mohyaldinn M. *et al.* (2019), pose distinct complications owing to their intricate composition and elevated viscosity. Indeed, crude oil comprises a complex blend of hydrocarbons with diverse molecular weights, alongside additional organic compounds. Typically, the elemental breakdown reveals an approximate composition of 84%–86% carbon, 10%–14% hydrogen, and marginal proportions of sulfur, nitrogen, and oxygen (Nolan D.P., 2019). As highlighted by Martínez-Palou R. *et al.* (2011) the extraction, transportation, and refinement of heavy and extra-heavy oils is complicated because of the high viscosity and intricate composition. It is also known from literature (Ghannam M.T. *et al.*, 2012) that with decreasing temperatures, the precipitation of high molecular weight paraffins and asphaltenes precipitates a transition from Newtonian fluid behavior to a non-Newtonian fluid, including thixotropic and shear-thinning tendencies coupled with yield stress. The conventional recourse to overcome the challenges associated with heavy oil transportation via pipelines proposed by Ghanaei, E. (2022) is heating. However, this approach causes high capital and operational expenses over extended distances and contends with issues stemming from the cooling influence of ambient water and the upkeep of pumping and heating facilities. An alternative avenue for ameliorating flowability concerns entails the deployment of pour point depressants (PPD). These chemical adjuncts modulate nucleation, adsorption, or solubility, thereby curtailing wax precipitation. The comprehension of waxy crude oil properties, such as the wax appearance temperature (WAT), assumes paramount importance in the formulation and execution of effective mitigation strategies.

2. OBJECTIVES

For several years (Japper-Jaafar A. *et al.*, 2016) it has emerged that cross polar microscopy (CPM), standard rheology, and differential scanning calorimetry (DSC) emerged as advanced techniques to determine WAT. In this research, a comparative analysis was conducted on three distinct types of waxy crude oils, labeled as I, II, and III, differing in their extraction sources, paraffin concentrations, and the presence of PPD. The objective was to determine the WAT of each sample through rigorous experimentation employing various methodologies. While rheological analysis effectively identifies crystallization, its real-time detection capability is limited. Initially, when crystal concentration is low, rheological properties remain largely unchanged. However, as the crystal content increases, noticeable alterations in rheological behavior emerge. Interestingly, our study revealed disparities in WAT identified through rheological analysis compared to those determined by DSC. Conversely, CPM with image analysis demonstrated an impressive ability to identify WAT consistent with DSC results, highlighting the potential of microscopy as a novel and potentially more sensitive method for investigating such phenomena. By integrating these diverse analytical approaches, this study not only advances our understanding of waxy crude oil behavior but also underscores the potential for microscopy to enhance our ability to probe complex fluid dynamics in real-time.

3. METHODS

In this investigation, three distinct crude oils (CO) were subjected to examination. In detail, CO II and CO III were sourced from the same oil field but extracted at different times, with CO II obtained earlier than CO III. CO I, distinguished as the lightest variant among the trio due to its prior extraction, functioned as control. Furthermore, CO II underwent treatment with two unique PPDs, identified as ADD-I and ADD-II. This experimental setup facilitated the comparative analysis of physical attributes and chemical compositions across the crude oils, along with an evaluation of the efficacy of specific additives on their performance. In parallel, CO I was subjected to examination at three distinct concentrations (5%, 10%, and 20% w/w) of paraffin, utilizing Paraffin Wax sourced from Fluka Analytical, serving as a reference standard.

The study regarded the response of waxy crude oil to fluctuations in temperature. Precisely, the experimentation involved both cooling and heating procedures spanning a temperature range from 4°C to 50°C, with a consistent rate of 1°C per minute.

CPM was utilized to analyze the dynamic evolution of microcrystalline structures, with a particular emphasis on wax crystallization. This technique has previously been employed by Castaldo R. I. *et al.* (2019) and Capaccio A. *et al.* (2020) to examine the morphology of a surfactant aqueous solution (SLE₃S) during the dissolution process. CPM is advantageous in the context of waxy crude oils due to the optical anisotropy present in non-cubically structured crystalline materials, leading to birefringence. For experimentation, an optical inverted microscope (Zeiss Axiovert 200) equipped with 20x magnification and polarized microscopy is employed. The microscope is situated on an anti-vibration table and features a focusing mechanism and motorized stage capable of precise and automated adjustments within the sample's field of view. Additionally, the microscope stage incorporates an incubator with a water circulation system connected to a water bath, ensuring precise temperature regulation within the incubator to impose specific thermal profiles on the samples.

Rheological measurements are conducted using a Controlled-Stress Rheometer (Anton Paar, MCR 301) equipped with a dual Peltier system for precise temperature control. A coaxial cylinder geometry with a 17mm diameter is employed to enhance torque signal intensity and minimize sample evaporation. To prevent sample loss and saturate the surrounding environment effectively, a custom-made cap with a cotton-wool disk soaked in crude oil is placed on top. Temperature sweep tests are performed under static conditions. A low deformation of 0.03% is maintained throughout the tests to ensure static conditions and minimize slippage concerns.

Finally, crystallization analysis is also conducted using a Q1000 TA Instruments DSC equipped with a Liquid Nitrogen Cooling System (LNCS) equipped with two identical pans.

4. RESULTS

Figure 1 presents the microscopy findings for CO I at three distinct concentrations of paraffin (5%, 10%, and 20% w/w, denoted as samples B, C and D) at different temperatures (points 1 to 6). The application of crossed polarized light is crucial in this context as it reveals birefringence within the samples, which is indicative of their structural organization. Specifically, crystals appear luminous against the dark background of liquid oil, allowing for the tracking of the wax appearance process. Analysis of the results obtained through CPM indicates that several factors significantly influence the structures of the samples under observation, including the type of crude oil, the concentration and quality of additives, as well as temperature.

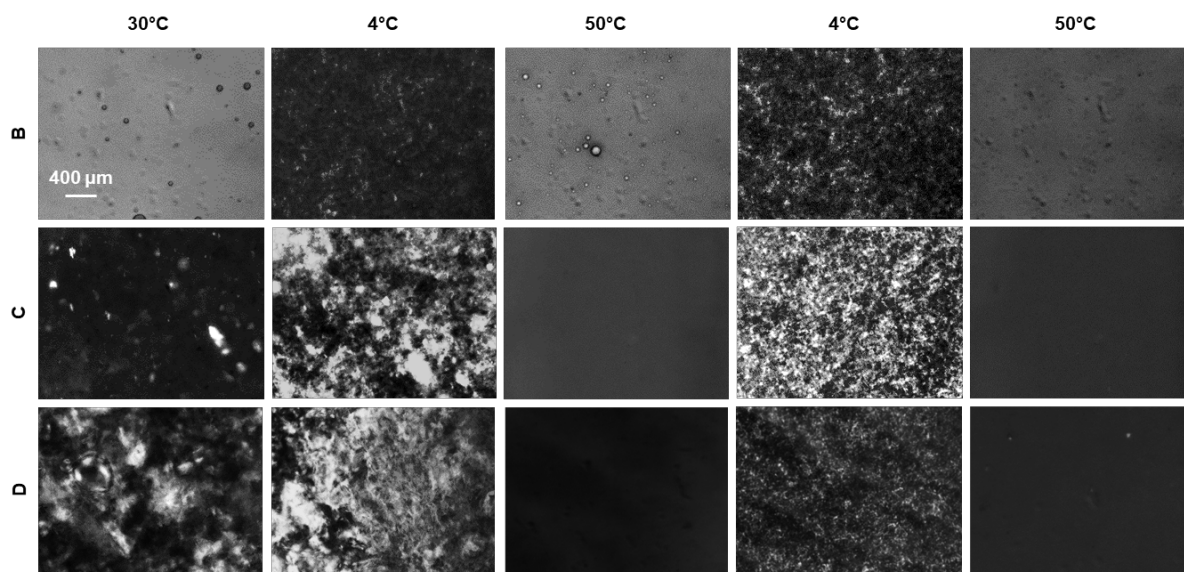


Figure 1. Representative phase-contrast microscopy images depicting the morphological alterations of CO I samples.

5. CONCLUSIONS

In this work we found out that, while rheological analysis effectively identifies crystallization, its capability for real-time detection is constrained. Conversely, CPM combined with image analysis showcased an impressive ability to identify WAT consistent with DSC results. This underscores the potential of microscopy as a novel and potentially more sensitive method for investigating such phenomena. By integrating these diverse analytical approaches, our study not only advances our understanding of waxy crude oil behavior but also highlights the potential for microscopy to enhance our ability to probe complex fluid dynamics in real time.

5. REFERENCES

- Capaccio A., Caserta S., Guido S., Rusciano G., Sasso A., 2020. "Dissolution of a surfactant-water lamellar phase investigated by combining time-lapse polarized light microscopy and confocal Raman spectroscopy". *Journal of Colloid and Interface Science*.
- Castaldo R. I., Pasquino R., Villone M. M., Caserta S., Gu C., Grizzuti N., Guido S., Maffettone P. L., Guida V., 2019. "Dissolution of concentrated surfactant solutions: from microscopy imaging to rheological measurements through numerical simulations." *Soft matter*.
- Eissa Mohyaldinn M, Husin H, Hasan N, M.B. Elmubarak M, M.E. Genefid A, E.A. Dheeb M., 2019. "Challenges during Operation and Shutdown of Waxy Crude Pipelines". *Processing of Heavy Crude Oils - Challenges and Opportunities*, IntechOpen.
- Ghanaei, E., 2022. "Newtonian and Non-Newtonian Viscosity of Waxy Crude Oils and Condensates: A Noncompositional Model". *Industrial & Engineering Chemistry Research*, vol 61, pp. 6703-6721.
- Ghannam M.T., Hasan S.W., Abu-Jdayil B., Esmail N., 2012. "Rheological properties of heavy & light crude oil mixtures for improving flowability". *Journal of Petroleum Science and Engineering*.
- Hongying L., Jinjun Z., Chaofan S., Guangyu S., 2015. "The influence of the heating temperature on the yield stress and pour point of waxy crude oils". *Journal of Petroleum Science and Engineering*, vol. 135, pp.476-483.
- Japper-Jaafar A., Bhaskoro P.T., Mior Z.S., 2016. "A new perspective on the measurements of wax appearance temperature: Comparison between DSC, thermomicroscopy and rheometry and the cooling rate effects". *Journal of Petroleum Science and Engineering*, vol. 147, pp. 672-681.
- Martínez-Palou R., M. de Lourdes Mosqueira, Zapata-Rendón B., Mar-Juárez, C. Bernal-Huicochea E., J. de la Cruz Clavel-López, Aburto J., 2011. "Transportation of heavy and extra-heavy crude oil by pipeline: A review", *Journal of Petroleum Science and Engineering*, vol 75, pp. 274-282.
- Nolan, D.P., 2019. "Physical Properties of Hydrocarbons and Petrochemicals". *Handbook of Fire and Explosion Protection Engineering Principles for Oil, Gas, Chemical, and Related Facilities*, 4th Edition, Chapter 4, pp. 65-88.

STRAIGHT CROSS FLOW PRINTED CIRCUIT HEAT EXCHANGER: PROPOSAL OF THERMAL MODELS AND COMPARISON WITH DATA

Pamela Hulse^a, Luis Betancur-Arboleda^a, Marcia Mantelli^b

^aFaculty of Natural Sciences and Engineering, Technological Units of Santander

^bHeat Pipe Laboratory, Department of Mechanical Engineering, Federal University of Santa Catarina

*phulse@correo.uts.edu.co

Keywords: Printed Compact Heat Exchanger, Thermal Analysis, Machine Learning

1. INTRODUCTION

Heat exchangers play a fundamental role in many industries, from cooling electronic systems to power generation. They promote the heat transfer between two or more fluids at different temperatures, typically separated by a surface, but, sometimes in direct contact with each other. Among all technologies available in the market, the shell-and-tube heat exchanger is the most popular in the industry. This device can be designed for a wide range of operations (from cryogenic to over 1000°C), for almost any temperature difference between the fluids, and for pressures ranging from vacuum to over 100 MPa. Additionally, these devices have a relatively simple manufacturing process compared to other equipment with similar purposes and relatively low cost (Shah & Sekulic, 2003).

However, in special applications such as aerospace and for offshore oil platform exploration, where space and weight constraints are increasingly severe, compact heat exchangers show to be an attractive option. One of the most important characteristics of these devices is large ratio between the heat transfer area to the volume, resulting in reduced dimensions and weight, compared to conventional heat exchangers (Hesselgreaves et al., 2016; Shah & Sekulic, 2003).

The printed circuit heat exchanger (PCHE) can be considered a variation of compact heat exchangers (Hesselgreaves et al., 2016), being a relatively new technology that lately has deserved the attention of several researchers. Many of these works were directed in the development of new channel geometry configuration, to improve the thermal performance with minimum pressure drops. Among them, Yang et al.,(2024) studied the thermal-hydraulic performance of PCHEs with different channel shapes; Wu & Xiao (2023) studied numerically a new configuration of crossed airfoil fins aimed to improve the heat exchange, while reducing de pressure drop; Han et al. (2023) not only conducted numerical analysis but also experimental work regarding these novel airfoil fins, comparing them to straight and zigzag channels. Some very recent work also are considering the use of artificial intelligence as an equipment designing, Wen et al. (2024) studied a combination of CFD simulations and machine learning to conduct optimization research on the airfoil PCHE; the authors concluded that machine learning proves to be beneficial for the design and optimization of PCHEs with S-CO₂ mixtures as working fluids, providing insights into their thermal-hydraulic performance under varying conditions.

Their manufacturing process can be considered an advantage of PCHEs as it allows for better control of the geometry and finishing of the channels. Basically, the fabrication includes the manufacturing of channels in flat plates that are diffusion bonded. The channels are machined through photochemical etching, using ultraviolet light and chemical energy for slot fabrication, resulting in high-quality, precise channels with complex geometries and no burrs (Rathod et al., 2017). The present study aims to discuss the experimental results obtained from a printed circuit heat exchanger, perform thermo-hydraulic analysis, and compare heat transfer data with models, one based on available literature correlations (briefly discussed in this abstract) and another simple model still under development, based on machine learning.

2. METHODS

The data used in this work was obtained from a PCHE with straight channels in a crossflow configuration. It was designed with channels of 2.5 mm of depth and fin thickness of 0.9 mm, fabricated from 3 mm thick stainless steel. The total core dimensions were 173 x 173 x 113 mm, with a heat exchange width of 113 mm and height of 160 mm.

The experimental setup can be seen in Figure 1. Tests were performed with water at ambient temperature (~20°C) on the cold side and air at 100°C on the hot side; the mass flow rate varied from 0.60 to 2.60 kg/s on the cold side and from 0.020 to 0.070 kg/s on the hot side. At the inlet of each branch, a rectifier was positioned to distribute the flow along the cross-section area and make sure that the mass flow rate passing through each channel would be approximately the same.

The measurement of the mass flow rate was made using an electromagnetic flow meter for the water and a Coriolis ELITE CMF200M for the air. The temperature was measured using Pt100 RTDs and pressure was measured with a pressure transducer on the water side and a U-tube manometer on the hot side. Additionally, Type K thermocouples were positioned for ambient temperature control and to measure surface temperature at strategic points. Data were acquired by National InstrumentsTM model NI cDAQ-9178 and processed by Labview software. The data was collected in steady-state condition, considered achieved when the temperature did not vary by more than 0.15°C for 300 seconds.



Figure 1. Experimental setup.

After the tests were conducted, the thermal and hydraulic data were analyzed and compared with correlations predictions proposed by Sarmiento et al. (2020). Using both data and literature correlations, a simple model, using machine learning is under development and preliminary results will be presented at the final paper. Both the experimental data and machine learning model are, for the first time being presented, out of the context of the Master's Science dissertation of the first author of the present paper.

3. RESULTS

Figure 2 shows the plots of the global coefficient of heat transfer as a function of the Re number for the hot stream, for several water Reynolds numbers. A close to linear behavior of the global coefficient with the hot stream Re can be observed. However, the data shows that they are not very sensitive to the mass flow rate of the water. This can be expected as the specific heat of water is almost four times higher than that of the air.

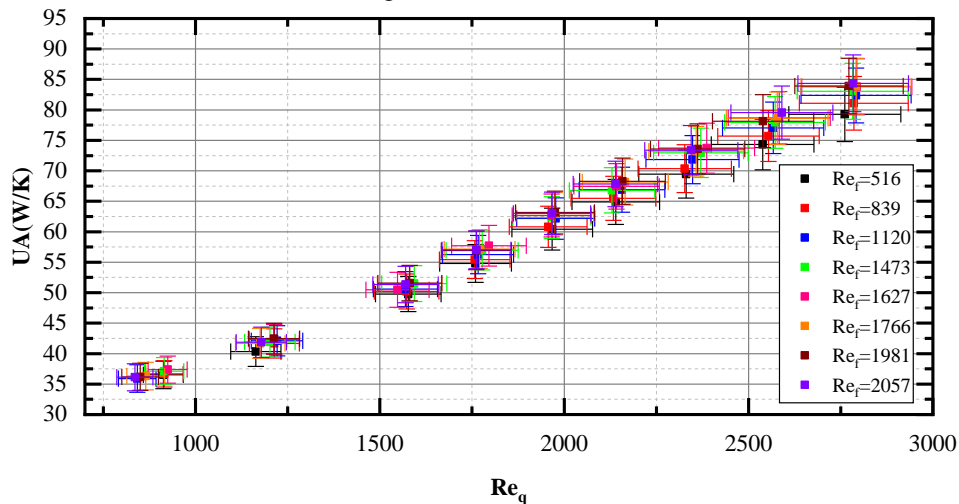


Figure 2. Conductance vs. Reynolds of the hot side

Figure 3.a illustrates the comparison between the theoretical (from a simple model using Sarmiento et al. (2020) correlation predictions) and experimental heat exchanged and Figure 3.b the theoretical and experimental Nusselt number. The model describes well the performance of the device for high power inputs (and so high Reynolds numbers, greater than 2,500). For lower Reynolds' number, the difference is up to 30%, for the constant wall heat flux conditions (black square symbols) and to 20% considering constant wall temperature (red square symbols) in the determination of the Nusselt number. According to Shah & Sekulic (2003), for the case of a liquid-gas heat exchanger with a much higher mass flow rate of the liquid, the boundary condition that best describes the problem is that of uniform wall temperature. However, the comparison between the predictions of the Nusselt numbers are not so good, as it will be discussed in the final paper.

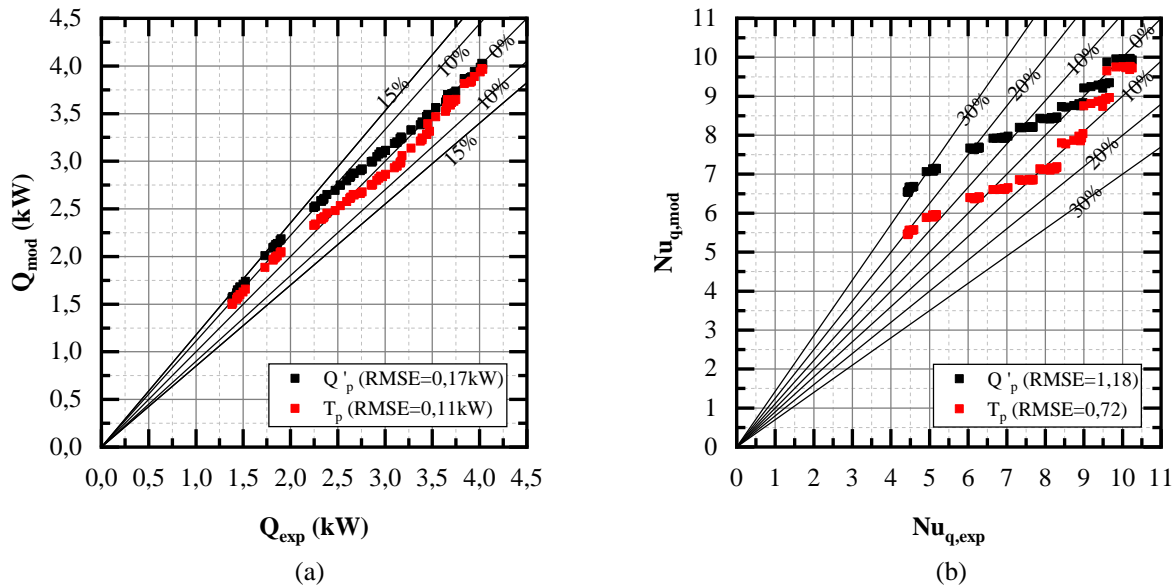


Figure 3. Comparison between the experimental data and the mathematical model of Sarmiento et al. (2020) (a) to heat exchanged and (b) Nusselt number to the hot side.

4. CONCLUSIONS

Main conclusions until now are:

- Due the difference of specific heat and mass flow rates between water and air, the effect of water Reynolds number on the thermal performance is small, resulting in a temperature gradient in the cold branch of practically zero and so the ΔP_{cold} (pressure drop) in this branch is lower than the instruments measurement uncertainties, in most experiments, and so the calculated heat transfer rate by the cold side has a high uncertainty.
- The maximum value obtained for the heat transfer rate in the hot side was of 4.03 ± 0.22 kW. The maximum value of the Nusselt number for the hot side was 10.25 ± 0.97 for the test at the maximum flow rates of both air and water.
- When compared with theoretical results, using a model from the literature, it was observed that the boundary condition that best describes the problem is that of uniform wall temperature. The mean square error decreased from 0.17 kW for uniform wall heat flux condition to 0.11 kW for uniform wall temperature condition. And using the uniform wall temperature condition, the model describes this class of heat exchangers with a maximum average percentage error of 8.4% for the heat transfer rate, 21.5% for conductance, and 20% for Nusselt.
- It is mandatory to find a model that describes the thermal behavior on laminar region.

5. REFERENCES

- Han, Z., Cui, X., Guo, J., Zhang, H., Zhou, J., Cheng, K., Zhang, H. & Huai, X. (2023). Experimental and numerical studies on the thermal-hydraulic performance of a novel airfoil fins printed circuit heat exchanger. *International Journal of Heat and Mass Transfer*, 217(September), 124655. <https://doi.org/10.1016/j.ijheatmasstransfer.2023.124655>
- Hesselgreaves, J., Law, R. & Reay, D. (2016). *Compact Heat Exchangers: Selection design and operation*. Elsevier Ltd.
- Sarmiento, A. P. C., Milanez, F. H. & Mantelli, M. B. H. (2020). Theoretical models for compact printed circuit heat exchangers with straight semicircular channels. *Applied Thermal Engineering*, 115435. <https://doi.org/10.1016/j.applthermaleng.2020.115435>
- Shah, R. K. & Sekulic, D. P. (2003). *Fundamentals of heat exchanger design* (John Wiley & Sons (ed.)). <https://doi.org/10.1007/bf00740254>
- Wen, Z. X., Wu, J. L., Wang, S. S., Cheng, J. Q. & Li, Q. (2024). Numerical study and machine learning on local flow and heat transfer characteristics of supercritical carbon dioxide mixtures in a sinusoidal wavy channel PCHE. In *International Journal of Heat and Mass Transfer* (Vol. 223). <https://doi.org/10.1016/j.ijheatmasstransfer.2024.125278>
- Wu, J. & Xiao, J. (2023). Numerical study of crossed airfoil fins in a printed circuit heat exchanger. *Applied Thermal Engineering*, 230(PA), 120646. <https://doi.org/10.1016/j.applthermaleng.2023.120646>
- Yang, X., Zhang, Z., Tian, K., Wang, J., Ma, T. & Sundén, B. (2024). Thermal-hydraulic performance of printed circuit heat exchangers with various channel shapes under rolling conditions. *Applied Thermal Engineering*, 244(February). <https://doi.org/10.1016/j.applthermaleng.2024.122779>

IMPACT OF SURFACE TEXTURING ON HYDROGEN PRODUCTION VIA PEM ELECTROLYSIS

Jakob Raeymaekers^{a,*}, Klara Arhar^b, Matic Može^b, Pierre Colinet^c, Iztok Golobič^b, Maria Rosaria Vetrano^a and Johan Steelant^d

^a KU Leuven, Department of Mechanical Engineering, TME Division, Heat and Mass Transfer group, 3001 Leuven, Belgium

^b University of Ljubljana, Faculty of Mechanical Engineering, SI-1000 Ljubljana, Slovenia

^c Université Libre de Bruxelles, Transfers, Interfaces and Processes (TIPs), 1050 Brussels, Belgium

^d KU Leuven, Department of Mechanical Engineering / ESA ESTEC, 2201 AZ Noordwijk, Netherlands

*jakob.raeymaekers@kuleuven.be

Keywords: Electrolysis, Wettability, Laser Surface Texturing

1. INTRODUCTION

Water electrolysis systems play an essential role in manned space travel. With the recently renewed interest in long-term space exploration missions toward the Moon and, eventually, Mars, these systems will remain vitally important. Electrolysis of water can provide a secure supply of breathable oxygen for crew life support. Alternatively, the produced hydrogen can be used as a propellant or fuel for transportation or power generation [Brinkert et al., 2018]. The main obstacle to the in-space operation of a water electrolysis system is the near-absence of buoyancy forces. On Earth, gravitational acceleration gives rise to buoyancy, leading to the detachment of oxygen and hydrogen gas bubbles from the electrodes and, eventually, the separation of the bubbles from the liquid electrolyte. On the contrary, in reduced- or micro-gravity environments, buoyancy forces are nearly absent, and detachment, as well as separation and collection of product gases, are severely hindered [Akay et al., 2022]. This causes gas bubbles to remain on the electrodes longer, thus blocking nucleation sites, which leads to a decrease in the effective electrocatalytic area as well as increase in ohmic resistances [Lomax et al., 2022]. Together, both effects significantly increase the cell overpotential [Darband et al., 2019]. Additionally, the mass transfer of products away from and reactants towards the electrode surface decreases. Consequently, the near absence of buoyancy significantly lowers the efficiency of electrolysis systems. Therefore, rapid and efficient removal of gas bubbles from the electrodes is the major challenge in microgravity environments.

Numerous ways exist to enhance the bubble detachment mechanism. These methods can be passive, i.e., without energy consumption during operation, which mainly pertains to electrode surface functionalization, or active, such as an externally imposed flow or field. Alternative approaches to artificially establish gravitation and phase separation, e.g., using centrifugal force due to rotation, have also been examined [Sakurai et al., 2013]. Still, these systems are typically associated with significant additional energy costs [Akay et al., 2022]. The preferred approach to design an efficient (photo-)electrochemical cell for application in a microgravity environment is, therefore, first the consideration of surface functionalized electrodes, which can then be further assisted by shear, electromagnetic, or other forces [Akay et al., 2022]. In this communication, we investigate the increase in electrolysis efficiency and gas production rate achieved when using laser-textured electrodes with functionalized wettability in Proton Exchange Membrane (PEM) water electrolysis.

2. MATERIALS AND METHODS

Surface preparation and characterization. In this work, five electrode pairs with different modified surface structures, and hence wettability, are investigated. High purity platinum foils (Advent Research Materials Ltd., 100 μm thickness, 99,95% purity) are the material of choice for this study, as Pt is the most common material used for electrodes in PEM electrolysis due to its excellent stability in acidic environments and favorable catalytic properties. The final dimensions of the electrodes exposed to the electrolyte (0,5 M H_2SO_4) are $10 \times 10 \text{ mm}^2$. Four pairs of electrodes were textured using a nanosecond pulsed fiber laser (FL-mark-C with JPT Opto-electronics Co., Ltd. “M7 30 W” MOPA source), creating different patterns of parallel or crosshatched grooves on the surface. The pulse frequency was set to 110 kHz, the pulse duration to 45 ns, the speed to 170 mm s^{-1} and the focal beam diameter to $\sim 25 \mu\text{m}$. The average laser pulse fluence was calculated to be $\sim 17 \text{ J cm}^{-2}$ at lower (30%) and $\sim 33 \text{ J cm}^{-2}$ at higher (60%) power. One electrode pair remained untextured and is considered as the reference. Resulting surface topographies are measured using a Sensofar S Neox 3D optical profiler, which allows to determine the depth, width, and spacing of the micro-scale geometries on the surface. Wettability is characterized through the static contact angle using a DataPhysics Instruments OCA50 optical contact angle measuring system. The resulting characteristics of the different surfaces are reported in Table 1, and a visual representation of the laser-textured ones is shown in Figure 1b-e. It can be observed that low laser power (Pt 35.3, 60.3, and cr60.3) leads to clearly distinguishable and spatially separated features. In contrast, higher power (Pt 60.6) induces more overlap between adjacent grooves and, hence, a higher surface roughness due to higher amounts of remelted material during laser-modification.

Table 1. Characteristics of the electrodes.

Surface name ⁽¹⁾	Characteristics	Roughness ratio r [-] ⁽²⁾
Pt Flat	Flat untextured surface	1
Pt 35.3	Parallel grooves, 35 μm spacing, 36 μm depth	2,90
Pt 60.3	Parallel grooves, 60 μm spacing, 28 μm depth	2,12
Pt 60.6	Parallel grooves, 60 μm spacing, 56 μm depth	4,54
Pt cr60.3	Crosshatched grooves, 60 μm spacing, 60 μm depth	4,11

⁽¹⁾: The first number indicates the groove spacing; the second number indicates whether a low (30%) or high (60%) laser power setting was used. ⁽²⁾: r is defined as the ratio of the actual over the projected surface area. Measurements were performed at 20x magnification over a projected surface area of 872,8 μm x 657,2 μm (= 0,574 mm²).

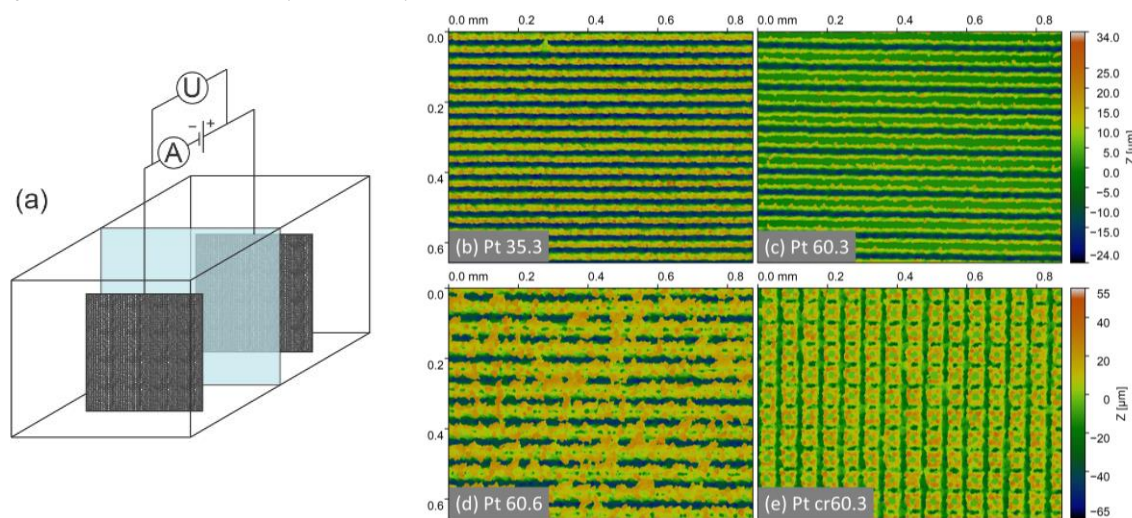


Figure 1. (a) Schematic of the PEM electrolysis cell; (b-e) Images of the microstructure of the different surfaces as obtained by the Sensofar S Neox 3D optical profiler.

Experimental setup. All experiments were carried out in a custom-made PMMA cell (68x42x43 mm³) with separate anodic and cathodic chambers (see Figure 1a). A NafionTM 117 membrane was placed in the middle to allow proton (H⁺) transport between the chambers while preventing any product gas crossover. The Pt foil electrodes were clamped inside PTFE holders with a gold-plated copper wire feedthrough and suspended in the cell. They were positioned parallel to the membrane with an inter-electrode distance of 21 mm. A Delta Elektronika[®] SM-15-100 DC power source supplied power to the electrodes. At the same time, voltage and current were recorded using two digital multimeters with accuracies of 1 mA and 0,01 V. Lastly, a glass measuring syringe (Fortuna Optima[®], 20 mL) was attached to a cell outlet port to measure the hydrogen production rate.

Experimental procedure. In a first step, the electrodes were laser-textured and cut to size. Before testing, they were thoroughly rinsed with de-ionized water. A 0,5 M H₂SO₄ electrolyte solution was prepared by mixing 450 mL ultrapure water (Chem-Lab NV, < 1 $\mu\text{S}/\text{cm}$) with 50 mL 5 M sulfuric acid (Chem-Lab NV). The solution was degassed in a Branson 3510 ultrasonic cleaner for 20 minutes and then poured into the electrolysis cell. Additional in-situ degassing was performed by running the reaction for 5 minutes at 3,0 V, ensuring that all air had escaped the cell before taking any measurements. The current was then discontinued to let all bubbles escape from the electrode surfaces. After the preparatory work was finished, the measurement campaigns were started. First, the voltage was gradually increased until the minimal value at which a small current started to flow, was found (denoted V_0). Then, the voltage was increased in steps of 0,25 V until 5,00 V was reached, while the current was recorded at each step (upward run). The maximal value of 5,00 V was chosen as preliminary tests at higher voltages showed a considerable increase in the system's temperature, which would reduce the reliability of the results and the efficiency calculations. To evaluate the effects of hysteresis, the voltage was then again decreased using the same 0,25 V steps until the reaction stopped (downward run). Similar to boiling systems, slightly higher current densities are expected during downward runs compared to upward runs due to an increased number of activated nucleation sites. Up- and downward runs were repeated thrice, and recorded currents were averaged over the three measurements. For the gas production measurements, the electrolysis reaction was operated for exactly 5 minutes at a fixed voltage while the produced hydrogen was captured in the glass measuring syringe. The total resulting volume yield was then read from the syringe. Supply voltages were increased from 2,00 to 5,00 V in steps of 0,50 V. All measurements were again repeated three times and averaged. The resulting H₂ volume yield was also used to

estimate the electrical efficiency of the cell by comparing the total energy content of the captured H₂ (higher heating value of 142 MJ/kg) to the energy supplied to the cell over the 5 minutes duration of the experiment.

3. RESULTS AND DISCUSSION

Figure 2 shows the results for (a) the current density-voltage characteristic, (b) the hysteresis between up- and downward measurement runs, and (c) the hydrogen production rate as a function of current for each of the platinum surfaces. As shown in Figure 2a, the measured current density is the lowest for the untextured surface over the whole range of supply voltages. Thus, all textured surfaces achieve an enhancement over the unmodified reference case. The best performance (approx. +45% compared to reference) was found on the surface with deep and widely spaced grooves (Pt 60.6), which is in line with it being the surface with the highest roughness. Shallow grooves show enhancements of approximately 25% (Pt 35.3) to 30% (Pt 60.3). The crosshatched structure (Pt cr60.3) shows the least improvement (+ 10%) despite exhibiting a relatively large surface area. Figure 2b illustrates the hysteresis on the current density at the measured voltages. Overall, hysteresis effects are small. Only the crosshatched surface shows a relatively significant hysteresis effect of up to 6-7%. It is also interesting to note that all textured surfaces show a positive hysteresis effect. In contrast, the untextured surface shows a negative hysteresis, i.e., the recorded current density values are smaller in the downward measurement run than in the upward run. Lastly, Figure 2c shows the production rate of hydrogen as a function of current. All values fall along a linear curve, as is proven by fitting a straight line through the data points, and is also expected based on Faraday's law of electrolysis. This means that if a higher current density is measured for the same supply voltage, the H₂ production rate will also be higher. Thus, the process will more efficiently create hydrogen gas from electric power.

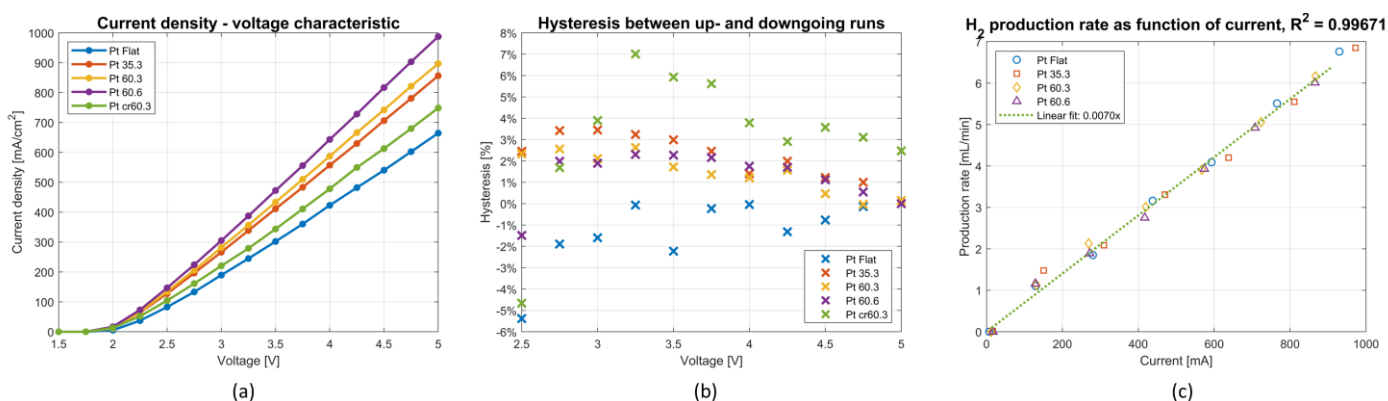


Figure 2. Quantitative results of the measurement campaigns: (a) Current density-voltage characteristic; (b) Hysteresis on the current density between up- and downward measurement runs (positive values represent a higher current density in the downward run than in the upward run); (c) Hydrogen production rate as a function of the current.

4. CONCLUSIONS

All textured surfaces tested in this study enhanced the performance of PEM electrolysis. The highest enhancement was achieved on a surface with deep and widely spaced grooves. Hysteresis effects are small and are positive for textured surfaces due to a higher number of nucleation sites during decreasing voltage than during increasing voltage, and negative for untextured surfaces. Gas production experiments prove that an increase in current density at a given voltage can be directly translated to an increase in production rate and, hence, in electrolysis efficiency.

5. REFERENCES

- Akay, O., Bashkatov, A., Coy, E., Eckert, K., Einarsrud, K., Friedrich, A., Kimmel, B., Loos, S., Mutschke, G., Röntzsch, L., Symes, M., Yang, X., Brinkert, K., 2022. "Electrolysis in reduced gravitational environments: current research perspectives and future applications", *npj Microgravity*, Vol. 8, 1-11.
- Brinkert, K., Richter, M., Akay, O., Liedtke, J., Giersig, M., Fontaine, K., Lewerenz, H.-J., 2018. "Efficient solar hydrogen generation in microgravity environment", *Nature Communications*, Vol. 9, 2527.
- Darband, G. B., Aliofkhazraei, M., Shanmugam, S., 2019. "Recent advances in methods and technologies for enhancing bubble detachment during electrochemical water splitting", *Renewable and Sustainable Energy Reviews*, Vol. 114, 109300.
- Lomax, B. A., Just, G. H., McHugh, P. J., Broadley, P. K., Hutchings, G. C., Burke, P. A., Roy, M. J., Smith, K. L., Symes, M. D., 2022. "Predicting the efficiency of oxygen-evolving electrolysis on the moon and mars", *Nature communications*, Vol. 13, 583.
- Sakurai, M., Sone, Y., Nishida, T., Matsushima, H., Fukunaka, Y., 2013. "Fundamental study of water electrolysis for life support system in space", *Electrochimica Acta*, Vol. 100, 350-357.

BLOCKAGE RATIO EFFECTS ON TURBULENT FLOWS AROUND RECTANGULAR PRISMS AT A MODERATE REYNOLDS NUMBER

Fati Bio Abdul-Salam^{a,*}, Kumahor Sedem^a, Xingjun Fang^{a,b}, and Mark F. Tachie^a

^aDepartment Of Mechanical Engineering, University of Manitoba, Winnipeg, Manitoba, R3T 5V6 Canada

^bInstitute of Mechanics, Chinese Academy of Sciences, Beijing, 100190, People's Republic of China

*abdulsa8@myumanitoba.ca

Keywords: blockage ratio, vortex shedding, flow separation

1. INTRODUCTION

Turbulent flow separation induced by bluff bodies has been a major research topic due to its prevalence in diverse engineering and environmental applications. Canonical bluff body cross-sections that have been extensively studied include square, circular, rectangular, and triangular prisms, owing to their resemblances to engineering structures such as high-rise buildings, bridges, and offshore structures. Despite their geometric simplicity, the flow dynamics around rectangular prisms are intricate. There has been extensive studies on the effects of streamwise aspect ratio ($AR = L/h$, where L and h are the streamwise length and thickness of the prism, respectively), Reynolds number ($Re = U_e h/\nu$, where U_e is the incoming flow velocity and ν is the kinematic viscosity), and turbulence intensity on rectangular bluff bodies in a uniform flow (Moore *et al.*, 2019, Mashhadi *et al.*, 2021). However, an important parameter that has not received much attention is the blockage ratio (BR), defined as the ratio of the frontal area of the prism to the other non-blocked flow passage. There exists significant scatter in the literature especially for rectangular prisms between $AR = 2$ and 3.5 . For instance, for the $AR = 3$ prism, at a similar Reynolds number of 3000, the studies by Liu *et al.* (2023) at $BR = 7\%$ and Nakagawa *et al.* (1999) at $BR = 20\%$ showed mean flow reattachment in the latter but not the former. These discrepancies are often attributed to the differences in BR among various studies without direct exploration. Thus, the goal of the present study is to address these discrepancies by systematically investigating the effects of blockage ratio on the spatiotemporal dynamics of the separated flow around a rectangular prism with $AR = 3$ using a time-resolved particle image velocimetry.

2. EXPERIMENTAL SET-UP AND MEASUREMENT PROCEDURES

The experiments were performed in an open recirculating water channel in the Turbulence and Hydraulic Engineering Laboratory (THEL) at the University of Manitoba. The interior dimension of the test section is 6000 mm long, 450 mm deep and 600 mm wide. To isolate the effects of blockage ratio, the Reynolds number (based on the incoming flow velocity and thickness of the prism) was kept at 7500. The designated blockage ratios were achieved by varying both the channel width and the thickness of the prisms. As summarized in Table 1, three rectangular prisms with thicknesses (h) of 15 mm, 24 mm, and 30 mm were fabricated from smooth acrylic plate and painted with non-reflective paint to avoid reflection from the laser. The streamwise length (L) of each prism was three times its thickness ($L/h = 3$). Four blockage ratios ($BR = 2.5\%$, 4% , 5% , and 10%) were investigated. For blockage ratios of 2.5% , 4% , and 5% , the prism thicknesses were 15 mm, 24 mm, and 30 mm, respectively, and the width of the test section was 600 mm. A false wall was made by firmly screwing a 9 mm thick acrylic plate to the base of the test section. This was done to decrease the width of the test section (S) from its original 600 mm to 300 mm. For the 10% blockage ratio, the prism thickness was 30 mm and the width of the test section was 300 mm.

Table 1. Summary of test parameters

Notation	U_e (m/s)	h (mm)	S (mm)	BR %
BR2.5	0.50	15	600	2.5
BR4	0.31	24	600	4.0
BR5	0.25	30	600	5.0
BR10	0.25	30	300	10.0

A time-resolved particle image velocimetry system (TR-PIV) was used for velocity measurements at half water depth. The seeding particles used were silver-coated hollow glass spheres. The specific gravity and mean diameter of the particles were 1.4 and $10\ \mu\text{m}$, respectively. The seeding particles were illuminated by a diode pumped dual-cavity high speed neodymium doped yttrium lithium fluoride (Nd:YLF) Photonics Industries DM30-527DH laser. Two high-speed 12-bit complementary metal oxide semiconductor (CMOS) cameras, each with a resolution of $2560\ \text{pixels} \times 1600\ \text{pixels}$ were used to simultaneously capture images of the illuminated particles into two fields of views (FOV). The cameras were positioned side-by-side and placed above the test section to capture the images. An overlap of 15 mm in the

streamwise direction was ensured between the two fields of view. A total number of 60000 images were captured at a sampling frequency of 800 Hz for each test case. A commercial software (Davis version 10.0.5) supplied by LaVision, Inc was employed for data acquisition, image-processing, and velocity vector calculations. A graphic processing unit accelerated multi-pass cross-correlation algorithm was used for the instantaneous velocity vectors calculations. An initial interrogation area (IA) of 128 pixels \times 128 pixels with 50% overlap followed by four final passes with interrogation area of 24 pixels \times 24 pixels with 75% overlap was used.

3. RESULTS AND DISCUSSION

Figure 1 presents contours of the streamwise mean velocity fields superimposed with mean streamlines to visualize the mean flow. For brevity, results for BR2.5, BR5 and BR10 are shown to highlight the effects of blockage ratios. Regardless of the blockage ratio, the incoming flow separates at the sharp leading edge and accelerates over the prism, resulting in a local maximum velocity above the prism. The maximum velocity increases with blockage ratio due to mass conservation. Two distinct recirculation bubbles, hereafter referred to as the primary and wake vortices, are formed over and behind the prism, respectively. A relatively small secondary separation bubble is formed near the leading edge of the prism, exhibiting a recirculation opposite to the primary vortex. The formation of the secondary recirculation bubble is due to the effects of an adverse pressure gradient on the reversed boundary layer over the prism. For the lower blockages (BR2.5 and BR4), the separated flow does not reattach onto the surface of the prism but is instead entrained into the wake, resulting in a large wake vortex. As blockage ratio increases, there is an augmented tendency of mean flow reattachment signified as the increased curvature of the separated shear layer. As quantitatively shown using the isopleth of $U = 0$, the mean flows in BR5 and BR10 cases reattach prior to the trailing edge at $x/h = 2.9$ and 2.4 , respectively. This clearly shows the significant role blockage ratio plays and explains why mean flow reattachment was observed by Nakagawa *et al.* (1999) (BR = 20%) but not Liu *et al.* (2023) (BR = 7%). The recirculation length is defined as the streamwise distance from the trailing edge to the point of intersection of the $U = 0$ line and the centreline of the prism. The recirculation length gives a quantitative measure of the wake vortex. The recirculation length, L_R , is significantly larger for the unattached test cases (BR2.5 and BR4) compared to the reattached cases (BR5 and BR10). For instance, $L_R = 2.6$ for BR2.5 compared to $L_R = 0.9$ for BR10.

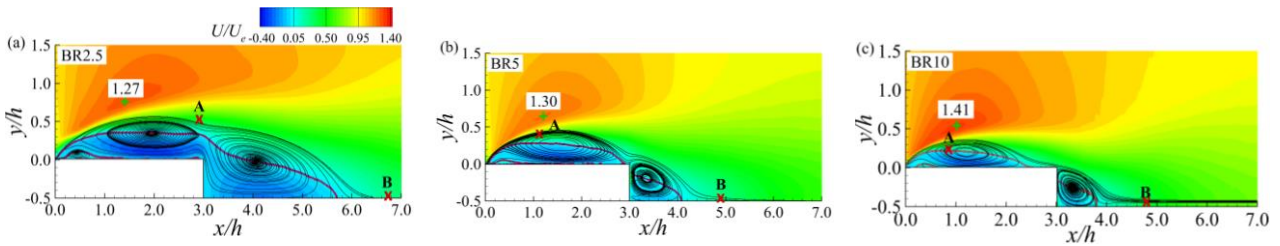


Figure 1. Contours of the streamwise mean velocity (U) superimposed with mean streamlines (black continuous lines) and the isopleth of $U = 0$ (red line). (a) BR2.5, (b) BR5 and (b) BR10.

Figure 2 presents the premultiplied frequency spectra of the streamwise and normal velocity at the maximum location of $\overline{u'u'}$ (A) and $\overline{v'v'}$ (B), respectively. The frequency spectra of the unattached test case (Fig. 2(a)) reveal multiple peaks at low and high frequencies. The presence of the multiple frequencies for the unattached test cases are evidence of different scaled coherent structures that modulate the shear layer. Meanwhile, for the reattached test cases (Fig. 2(b) and (c)), a single distinct dominant peak which corresponds to the von Kármán shedding frequency is observed.

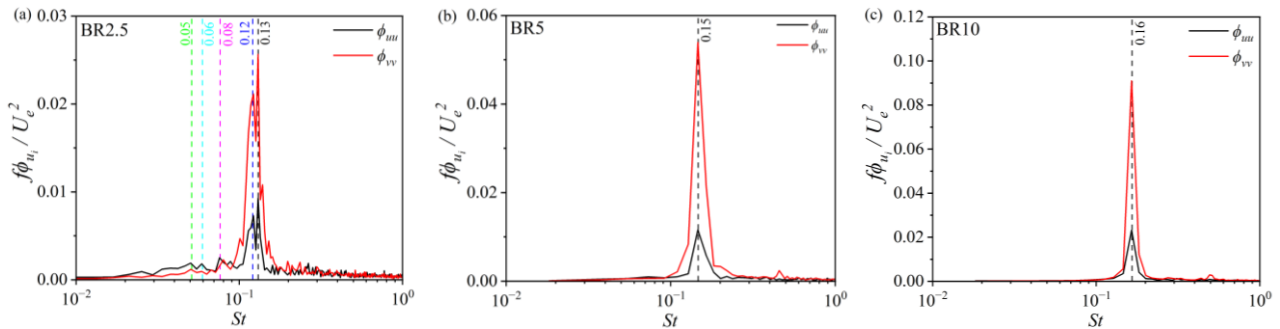


Figure 2. Premultiplied frequency spectra of the streamwise and normal velocity fluctuations for (a)BR2.5, (b) BR5 and (c) BR10.

Taking advantage of the availability of whole-field time-resolved data, contours of the integral time scales are presented in Fig. 3 to examine the effects of blockage ratio on the time scales of the prisms. The integration was carried out over the time displacement range from zero to the first zero crossing point of the temporal autocorrelation of R_{uu} . In general, relatively small integral time scale is concentrated in a distinct area emanating from the leading edge. However, in the region above and in the first half of the separation bubble for BR2.5, excessively high levels of integral time scale are observed. Meanwhile, the integral time scale for the reattached test cases in Figs. 3(b) and (c) are evidently disrupted by the mean flow reattachment. The high levels of integral time scale suggest low-frequency flapping motion of the reverse flow region. In fact, the integral time scale in Fig. 3(a) does not vary strongly downstream of the centre of the mean separation bubble over the body. This shows that for the unattached test cases, there is a global feature of the low-frequency flapping motion and suggests a strong interaction between the separation bubble over in the wake of the prism.

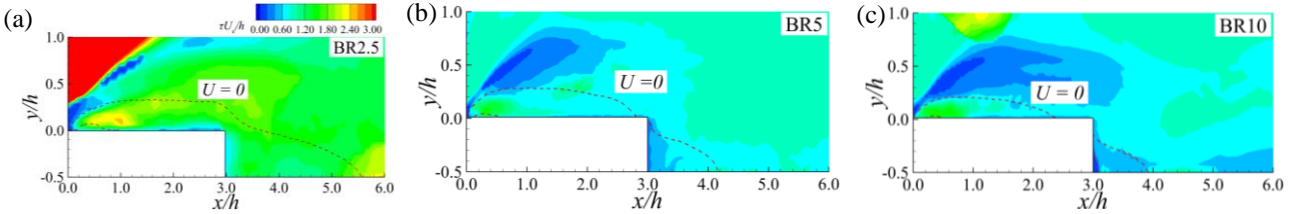


Figure 3. Contours of the integral time scale for (a)BR2.5, (b) BR5 and (c) BR10. The dashed lines are the isopleths of $U = 0$.

The unsteady characteristics of the turbulent flow separation are further analyzed using the instantaneous reverse flow area, which is calculated by summing the areas with negative u values. Figure 4 presents the premultiplied frequency spectra of the total reverse flow area to further investigate the time scales of the separation bubble. For the BR2.5 prism, multiple competing frequencies are observed with similar energy levels, highlighting a complex flow dynamic for the unattached test case. The low frequencies are consistent with the typical flapping motion frequencies observed in the literature and is also consistent with the conclusion from Fig. 3(a). This flapping motion ceases to exist in the reattached cases. Instead, the spectra for BR5 shows a dominant peak at $St = 0.15$ as well as its subharmonic ($St = 0.07$). For the BR10 prism, a single dominant peak is observed at $St = 0.16$ which corresponds to the shedding frequency. These results are consistent with the observation from the contours of integral time scale in Fig. 3. It is noteworthy that the distinct peaks observed using the reverse flow area are consistent with those obtained from the spectra of the velocity fluctuations.

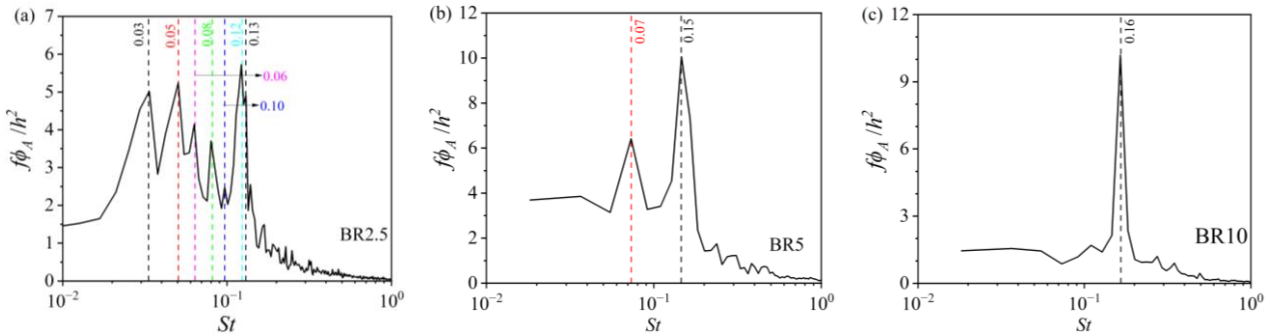


Figure 4. Premultiplied frequency spectra of the reverse flow area for (a)BR2.5, (b) BR5 and (c) BR10.

The full paper will include a comprehensive literature review, experimental and measurement procedure. Turbulent kinetic energy and proper orthogonal decomposition will be performed to further elucidate the kinematic and structural effects of blockage ratio on the separating flows.

5. REFERENCES

- Liu, M., Kumahor, S., and Tachie, M. F., 2023. "Reynolds number effects on turbulent wakes generated by rectangular cylinders with streamwise aspect ratio between 1 to 4". *Journal of Fluids Engineering*, Vol. 146, 21 pages.
- Mashhadi, A., Sohankar, A., and Alam, M. M., 2021. "Flow over rectangular cylinder: Effects of cylinder aspect ratio and Reynolds number". *International Journal of Mechanical Sciences*, Vol. 195, 25 pages.
- Moore, D. M., Letchford, C. W., and Amitay, M., 2019. "Energetic scales in a bluff body shear layer". *Journal of Fluid Mechanics*, Vol. 875, pp. 543–575.
- Nakagawa, S., Nitta, K., and Senda, M., 1999. "An experimental study on unsteady turbulent near wake of a rectangular cylinder in channel flow". *Experimental in Fluids*, Vol. 27, pp. 284–294.

UNSTEADY DYNAMICS OF FLOW SEPARATION AROUND TRAPEZOIDAL PRISMS

Fati Bio Abdul-Salam^{a,*}, Smit Shah^a, Amir Sagharichi^a, Xingjun Fang^{a,b}, and Mark F. Tachie^a

^aDepartment Of Mechanical Engineering, University of Manitoba, Winnipeg, Manitoba, R3T 5V6 Canada

^bInstitute of Mechanics, Chinese Academy of Sciences, Beijing, 100190, People's Republic of China

*abdulsa8@myumanitoba.ca

Keywords: trapezoidal prism, flow separation, asymmetric wake

1. INTRODUCTION

Turbulent flow separations around bluff bodies remain an active research topic in the fluid engineering community due to their occurrence in nature and many engineering applications. Examples include flow around high-rise buildings, bridges, and vehicles. Previous studies have demonstrated that the flow dynamics around these bodies depend on several parameters such as body geometry, Reynolds number, aspect ratio, blockage ratio, and incoming turbulence intensity (Nakagawa, 1999, Abdul-Salam *et al.*, 2023, Liu *et al.*, 2023). Depending on the test conditions, the wake behind the body may be symmetric or asymmetric. Significant information on the effects of these test conditions for symmetric wake flows are available in the literature. However, knowledge on asymmetric wake flows is still lacking despite their prevalence in many engineering applications. A common feature of symmetric wake flows is the alternating vortices of opposite signs and equal strengths formed about the centreline behind the prism, namely the von Kármán (VK) vortex street. On the effects of streamwise aspect ratio (AR, ratio of lower length to height of prism), previous investigations have shown that for aspect ratios less than 2.0, the separated shear layer is shed directly into the wake while mean flow reattachment is observed for streamwise aspect ratio greater than 3.5. Between aspect ratio 2.0 and 3.5, there is intermittent reattachment of the separated shear layer onto the surface of the prism, resulting in a massive recirculating region in the wake of the prism (Nakagawa *et al.*, 1999, Abdul-Salam *et al.*, 2023). For AR 0.5 to 1.2, the shedding frequency ($St = fh/U_e$, where f is the frequency) varies between 0.13 – 0.15. Meanwhile, for AR 2 to 3.5, the shedding frequency falls within the ranges of 0.03 – 0.20. In the present study, we experimentally investigate the spatiotemporal dynamics of asymmetric wake flows generated by trapezoidal prisms with different lower streamwise lengths using time-resolved particle image velocimetry (TR-PIV).

2. EXPERIMENTAL SET-UP AND MEASUREMENT PROCEDURES

The experiments were performed in an open recirculating water channel located at the Turbulence and Hydraulic Engineering Laboratory (THEL) at the University of Manitoba. The test section has a streamwise length of 6000 mm, a spanwise width of 600 mm, and a vertical height of 450 mm. A centrifugal pump and a 30 kW variable speed drive motor are used to drive the recirculating water in the test section. The flow velocity in the channel can be varied from 0.03 m/s to 2.00 m/s. Three trapezoidal prisms with fixed vertical height, $h = 20$ mm, upper streamwise length, $S = 12$ mm ($0.6h$), and spanwise width, $B = 588$ mm ($29.4h$) but with different lower streamwise lengths, of $L = 20$ mm, 40 mm, and 60 mm, corresponding to $AR (\equiv L/h) = 1, 2,$ and $3,$ respectively, were tested. The prisms were secured in place between two acrylic plates, each with a thickness of 6 mm and clamped to the side walls of the test section. The prisms were coated with non-reflective black paint to minimize glare from laser illumination. The water depth (D) in the test section was maintained at a constant level of 430 mm. The prisms were positioned at half water level, ensuring that their mid-height was 215 mm above the bottom wall of the test section. The resulting blockage ratio (h/D) was 5%, so that its effects on the flows were negligible. The incoming flow velocity was set at 0.50 m/s and the Reynolds number defined based on the incoming flow velocity and vertical height of the prism was $Re = 10000$.

Velocity measurements were conducted using a time-resolved particle image velocimetry system (TR-PIV). Silver-coated hollow glass spheres with specific gravity and mean diameter of 1.4 and 10 μm , respectively, were used as seeding particles. A diode pumped dual-cavity high speed neodymium doped yttrium lithium fluoride (Nd:YLF) Photonics Industries DM30-527DH laser was used to illuminate the seeding particles. Two high-speed 12-bit complementary metal oxide semiconductor (CMOS) cameras with resolutions 2560 pixel \times 1600 pixel were used to capture images of the illuminated particles into two fields of views (FOV) simultaneously. For each test case, 60000 images were captured at a sampling frequency of 800 Hz. Data acquisition, image-processing, and velocity vector calculations were performed using a commercial software (Davis version 10.0.5) supplied by LaVision, Inc (Göttingen, Germany). A GPU-accelerated multi-pass cross-correlation algorithm was used for the velocity vectors calculations. A single initial interrogation area (IA) of 128 pixel \times 128 pixel with 50% overlap and four final passes with interrogation area of 24 pixel \times 24 pixel and with 75% overlap was used.

3. RESULTS AND DISCUSSION

Figure 1 (a,d,g) presents contours of the streamwise mean velocity superimposed with mean streamlines (black continuous lines) and isopleth of $U = 0$ (red line) to visualize the mean flow around the prisms. The results show that, regardless of the aspect ratio, the incoming flow separates at the leading edge and is shed into the wake without reattaching onto the surface of the prisms. The mean streamlines reveal two recirculation bubbles formed on both sides of the centreline in the wake of the prisms. The sizes of the wake bubbles are similar for the AR1 prism. However, due to the more asymmetric geometry of the AR2 and AR3 prisms, the wake bubble above these prisms is comparably larger than the lower bubble. The streamwise extent of the recirculation region (L_R/h) is measured as the streamwise distance between the leading edge and the most downstream point in the isopleth of $U = 0$. The value of L_R/h is significantly shorter for AR1 ($L_R/h = 1.7$) compared to AR2 ($L_R/h = 4.5$) and AR3 ($L_R/h = 5.6$). The larger recirculation region for AR2 and AR3 is attributed to the intermittent detachment and reattachment of the separated shear layer onto the surface of the prism. The peak value of the mean streamwise velocity occurs over the AR1 prism but in the wake of AR2 and AR3 prisms. The location of peak U for the AR1 prism is similar to those reported for rectangular prisms (Liu *et al.*, 2023). This similarity can be attributed to the body geometry of the AR1 prism. The magnitude of the local maximum velocity decreases with an increase in aspect ratio.

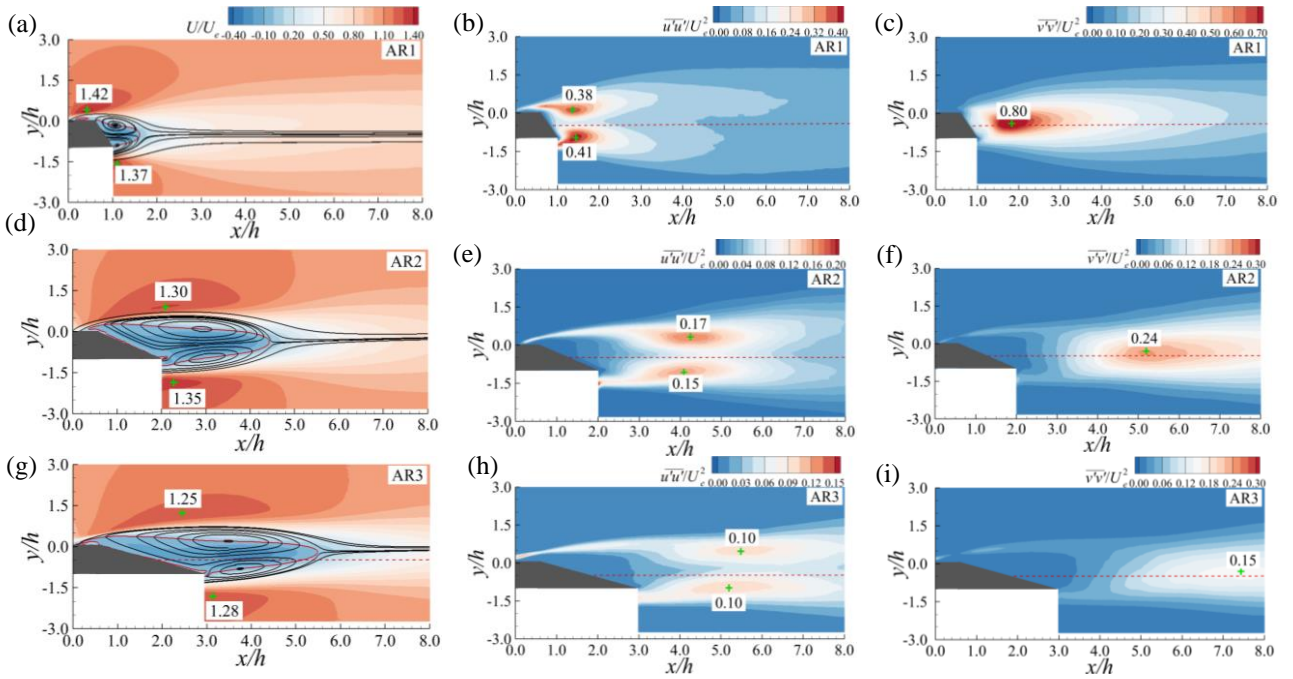


Figure 1. Contours of the streamwise mean velocity (U) (left column), streamwise $\overline{u'u'}$ (middle column) and vertical $\overline{v'v'}$ (right column) Reynolds normal stress. Due to the laser being shot from the top of the test section, the flow fields beneath the prisms were obscured in the shadow of the prisms.

Contours of the streamwise Reynolds normal stress ($\overline{u'u'}$) presented in Fig. 1 (b,e,h) shows that irrespective of the aspect ratio, dual peaks of elevated $\overline{u'u'}$ are formed in the wake region of the prisms. For a given test case, the magnitudes of peak $\overline{u'u'}$ above and below the horizontal centreline are comparable. However, the peaks are closer to the trailing edge of the AR1 prism but further in the wake for the AR2 and AR3 prisms. It can also be seen that as the aspect ratio increases, the maximum $\overline{u'u'}$ decreases. For instance, the maximum $\overline{u'u'}$ for the AR1 is 59% higher than AR2 prism and 74% higher than the AR3 prism. The difference in peak magnitude and location highlights the effects of aspect ratio on the turbulent motions. Contours of the vertical Reynolds normal stress ($\overline{v'v'}$) shown in Fig. 1(c,f,i) reveal a single distinct peak in the wake region, in contrast to the dual peaks observed for the streamwise normal stress. The high intensity of the vertical fluctuation in the wake of the prism is as a result of the von Kármán vortex shedding. However, similar to $\overline{u'u'}$, the location of maximum $\overline{v'v'}$ moves closer to the trailing as the aspect ratio decreases. The streamwise location of maximum $\overline{v'v'}$ are respectively, $x/h = 1.9, 5.3,$ and 7.5 for AR1, AR2, and AR3. Owing to the asymmetric nature of the flow, the vertical location is slightly offset above the centreline of the prisms. The maximum value of $\overline{v'v'}$ decreases monotonically with an increase in aspect ratio. Similar aspect ratio effects were made by Nakagawa *et al.* (1999) and Liu *et al.* (2023). The relatively lower magnitude of the vertical Reynolds normal stress for AR2 and AR3 is due to the large recirculation

bubble in the wake region of these prisms. As stated by Nakagawa *et al.* (1999), the existence of a substantial recirculation bubble in the wake region corresponds to weaker vortex shedding. This is consistent with the findings in the present study.

The premultiplied frequency spectra of the streamwise and vertical fluctuating velocities at the maximum location of $\overline{u'u'}$ and $\overline{v'v'}$, respectively, are presented in Fig. 2. The fundamental von Kármán vortex shedding frequencies manifest as distinct peaks in the frequency spectra. The dimensionless vortex shedding frequencies (St) for the AR1 and AR2 prisms are 0.13 and 0.11, respectively. The shedding frequency for the AR1 trapezoidal prism is in good agreement with the values of 0.13 reported for AR0.6 and AR1 rectangular prisms, while that of the AR2 trapezoidal prism is mean of those reported for AR0.6 ($St = 0.13$) and AR2 ($St = 0.09$) rectangular prisms. Meanwhile for the AR3 prism, two distinct peaks are observed at $St = 0.05$ and 0.12. The appearance of multiple peaks has been linked to the intermittent reattachment of the separated shear layer for rectangular prisms (Abdul-Salam *et al.* 2023). The spectra also show less distinct peaks at higher frequencies. These frequencies correspond to the second and third harmonics of the fundamental shedding frequency.

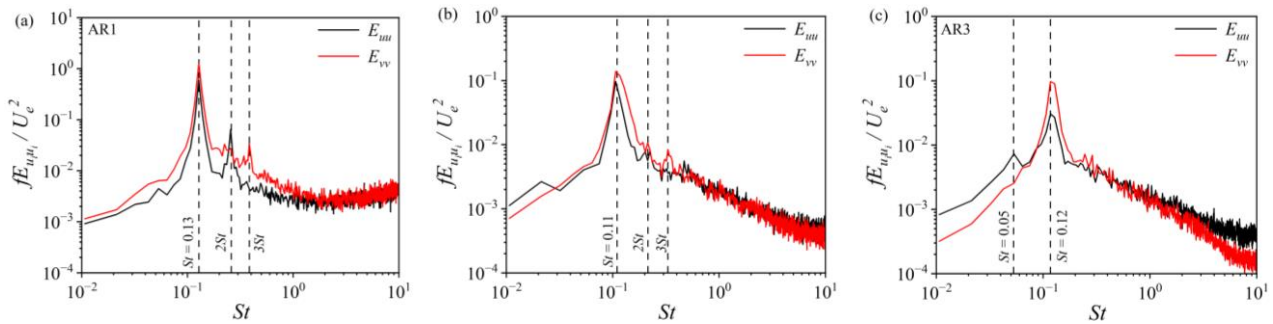


Figure 2. Premultiplied frequency spectra of the streamwise and vertical fluctuating velocities at the location of maximum Reynolds normal stresses. (a) AR1, (b) AR2, and (c) AR3.

The effects of aspect ratio on the spatial structures are examined in Fig. 3 using two-point autocorrelation of the streamwise fluctuating velocity (R_{uu}). Two reference points are selected at $0.1h$ above the upper trailing edge and $0.1h$ in the streamwise direction away from the lower trailing edge. For brevity, the results are shown for AR1 and AR3 to highlight the effects of aspect ratio. For the AR1 prism (Fig 3a,b), regardless of the reference point, significant correlations are observed far from the body in the wake region, even near the separation point upstream of the reference point. This suggests global instability encompassing both upstream and downstream of the prism. It is also interesting to see negative correlations near the lower trailing edge in Fig. 3a. Figures 3 a,b show that the shear layer from the upper trailing edge tend to affect the shear layer from the lower trailing edge (opposite in phase). On the other hand, for the AR3 prisms (Figs. 3c,d), the correlations gradually decays while exhibiting streamwise elongation. This pattern is the manifestation of shed vortices passing the reference point. The global instability exhibited in the AR1 case does not occur in the AR3 case. Indeed, the interactions of the shear layers downstream the upper and lower trailing edges are not distinct either.

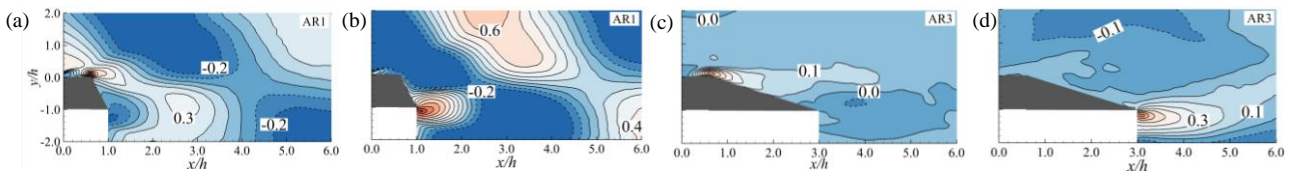


Figure 3. Two-point autocorrelation of the streamwise fluctuating. The contour levels are from -0.2 to 1 at intervals 0.1.

In the full paper a more comprehensive literature review and detailed description of the experimental set-up will be provided. Proper orthogonal decomposition and analyses of the reverse flow area will be performed to further evaluate the effects of aspect ratio on the spatiotemporal characteristics of asymmetric wake flow induced by trapezoidal prisms.

5. REFERENCES

- Abdul-Salam, F. B., Fang, X., and Tachie, M. F., 2023. "Blockage ratio and Reynolds number effects on flows around a rectangular prism". *Physics of Fluids*, Vol. 35, 23 pages.
- Liu, M., Kumahor, S., and Tachie, M. F., 2023. "Reynolds number effects on turbulent wakes generated by rectangular cylinders with streamwise aspect ratio between 1 to 4". *Journal of Fluids Engineering*, Vol. 146, 21 pages.
- Nakagawa, S., Nitta, K., and Senda, M., 1999. "An experimental study on unsteady turbulent near wake of a rectangular cylinder in channel flow". *Experimental in Fluids*, Vol. 27, pp. 284–294.

EFFECTS OF POROSITY VARIATION OF PIN-FIN HEAT SINKS WITH VAPOR PATHS ON FLOW BOILING PERFORMANCE

Juhyeon Lee^{a,*}, Sung Jin Kim^a

^aKorea Advanced Institute of Science and Technology, Daejeon, Republic of Korea

*juhyeonlee@kaist.ac.kr

Keywords: flow boiling, two-phase flow, pin-fin heat sink

1. INTRODUCTION

As the power density of electronic devices increases while the size of those decreases, thermal management for high heat flux becomes a significant factor affecting performance and reliability. Thus, two-phase cooling has been studied due to its high heat transfer coefficient (HTC) and good uniformity of temperature. Among them, flow boiling in microchannels is a promising candidate having the advantages of both small passages of microchannels and latent heat transfer of phase change.

Recently, flow boiling in pin-fin heat sinks with vapor paths is reported to promote boiling heat transfer performance by facilitating vapor venting introducing dedicated vapor pathways [1,2]. Li et al. [2] achieved a CHF of 345 W/cm² using HFE 7100 and decreased pressure drop using pin-fin heat sinks with vapor pathways. However, although dimensions of vapor pathways are major factors on flow boiling performance, there are no consideration about vapor pathways. Furthermore, in spite of vapor pathways, vapor blankets are still stuck inside pin-fin heat sinks, resulting in local dry-out and high-pressure drop as shown in flow visualization images. It is because it is difficult for vapor bubbles in pin-fin heat sinks to escape from pin-fin region to vapor pathways.

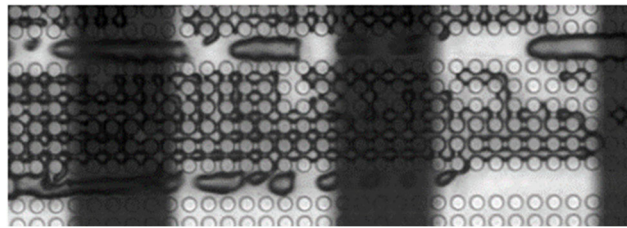


Fig. 1 Vapor blankets stuck in pin-fin arrays [1]

The object of the present study is to investigate the flow boiling heat transfer performance depending on geometries of a pin-fin heat sink with vapor pathways. A unit cell with a vapor pathways and pin-fin regions is selected as an experimental domain. To figure out the effect of vapor pathways on flow boiling performance, test chip with various width of vapor pathways are fabricated and tested. Furthermore, to figure out the effect of the porosity variation on vapor venting, pin-fin heat sinks with variable porosity and pin-fin heat sinks with constant porosity are compared. The dielectric working fluid, HFE 7100, is used as the working fluid with mass fluxes of $G = 247 \text{ kg/m}^2\text{s}$ and heat fluxes of $q'' = 5 - 160 \text{ W/cm}^2$. High-speed photography and IR thermometry are used to investigate flow characteristics and thermal characteristics.

2. EXPERIMENTS

Fig. 2(a) shows the schematic of a test section, which consists of a 500 μm thick silicon wafer and a 500 μm thick glass. The pin-fins are etched on the silicon wafer using deep reactive ion etching (DRIE), and the glass is bonded onto the etched silicon wafer for flow visualization. On the other side, a serpentine heater of 2.5 mm x 1 cm and RTD sensors are deposited. The heater and RTD sensors are calibrated in a convection oven from 25°C to 250°C. The height of pin-fins is 50 μm and all other dimensions are specified in Fig. 2(a). The experimental setup is shown in Fig. 2(b). Prior to the flow boiling experiments, the working fluid is degassed in the reservoir tank. Under ambient conditions, the dissolved oxygen (DO) content is 366 ppm, equivalent to 53% of air by volume in HFE-7100. For comparison, DO content in water under same conditions is only 8.25 ppm. Therefore, when using HFE-7100 as the working fluid, degassing process is crucial for high

repeatability of each experiment. Degassing process is conducted by vigorous boiling for 1.5 hours using cartridge heaters located in the reservoir tank. After that, the dissolved oxygen (DO) content is measured to be less than 3 ppm, which is equivalent to 0.37% by volume. The degassed working fluid is pumped by a micro gear pump (mzr-7501, HNP mikrosysteme) from the reservoir tank to the test section. A Coriolis flow controller (M14, Bronkhorst) is used to not only measure the flow rates but also control the desired mass flow rate. Pressure transducers (PX1004, Omega), and K-type thermocouples measure the absolute pressures, and temperatures at inlet/outlet during the experiments, respectively. The two-phase mixture leaving from the test section enters a flat plate heat exchanger, cooled with ethylene-glycol/water pumped by chiller. The condensed liquid is returned to the reservoir tank.

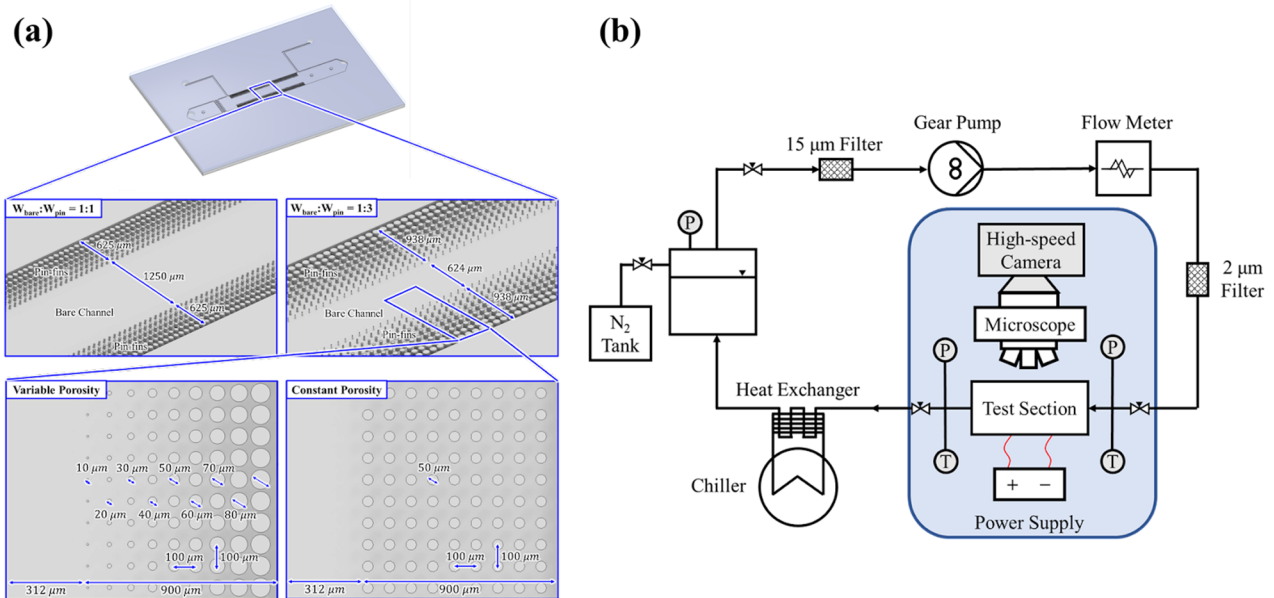


Fig. 2 (a) The schematic of a test section (b) the experimental setup

3. CONCLUSIONS

In this study, flow boiling heat transfer performance depending on the dimensions of a pin-fin heat sink with vapor pathways experimentally is investigated. Two-phase heat transfer coefficients (HTC) and critical heat fluxes (CHF) of pin-fin heat sinks with vapor pathways are measured and compared. Flow boiling experiments are conducted using HFE-7100 as the working fluid with mass flux of 247 $\text{kg}/\text{m}^2\text{s}$. Due to the vapor venting, the local dry-out is prevented in pin-fin regions, resulting in high flow boiling heat transfer performance. In conclusion, it is confirmed that inducing active vapor venting from the heat transfer area during two-phase heat transfer is one of major design factors.

4. REFERENCES

- Li, W. and Joshi, Y., 2020. "Capillary-assisted evaporation/boiling in PDMS microchannel integrated with wicking microstructures". *Langmuir*, Vol. 36, pp. 12143-12149.
- Li, W., Luo, K. and Joshi, Y., 2022. "A remarkable CHF of 345W/cm² is achieved in a wicked-microchannel using HFE-7100". *International Journal of Heat and Mass Transfer*, Vol. 187, pp. 122527.

CHARACTERISTICS OF PHASE CHANGE FRONT MOVEMENT IN VERTICAL TUBE AND TUBE LATENT THERMAL ENERGY STORAGE HEAT EXCHANGERS

Julie Van Zele^{a,b}, Maité Goderis^{a,b,*}, Kenny Couvreur^{a,b}, Wim Beyne^{a,b}, Michel De Paepe^{a,b}

^aDepartment of Electromechanical, Systems and Metal Engineering – UGent, Ghent, Belgium

^bFlandersMake@UGent – Core lab EEDT-MP, Leuven, Belgium, www.flandersmake.be

*julie.vanzele@ugent.be

Keywords: Latent thermal energy storage, phase change material, tube-in-tube heat exchanger, phase change front movement, characterisation

1. INTRODUCTION

The essential role of thermal energy storage systems in shaping a sustainable and carbon-neutral future cannot be highlighted enough, as they serve as a crucial link between heat demand and supply (Karami 2020). Among the various thermal storage options, latent thermal energy storage (LTES) stands out for its use of phase change to store thermal energy, with a remarkable capacity to store 4 to 10 times more energy per unit mass than its sensible equivalent at similar temperature differences (Regin 2008).

Despite the considerable potential of LTES systems, their widespread adoption has been hindered by challenges in sizing. The non-linear and transient nature of LTES systems precludes conventional heat exchangers theories, requiring extensive experimental and numerical testing (A. Castell and C. Solé 2015). Hence, extensive experimental and numerical testing is primarily performed nowadays. Although recent efforts have focused on predictive methods for sizing LTES heat exchanger systems, existing approaches often fall short in fully capturing the dynamics of system performance over time.

A recent analytical method, developed by Beyne et al. (Beyne 2023), offers a promising approach for sizing LTES systems, linking the evolution of the phase change front to the (instantaneous) internal energy change of the phase change material (PCM) volume and consequently, to the heat transfer rate between the heat transfer fluid (HTF) and PCM. This analytical method provides a comprehensive characterization of LTES systems based on a deeper understanding of the phase change process.

Nevertheless, regardless the potential of analytical models describing the phase change front movement, literature remains scarce on phase change front dynamics. Therefore, this study aims to enhance our understanding of phase change front dynamics, with a particular focus on comparing melting and solidification experiments and analysing the effects of operating conditions on its movement.

2. SET-UP DISCRIPTION

The experimental set-up comprises a tube-in-tube heat-exchanger with a length of 1 metre, wherein water serves as the heat transfer fluid flowing through an inner copper tube, while phase change material occupies the outer tube. The copper inner tube, with an outer diameter of 15 mm and a wall thickness of 2 mm, is concentrically positioned within a transparent polycarbonate tube, measuring 60 mm in outer diameter and 3 mm in wall thickness. The PCM utilized is the paraffin RT35HC from Rubitherm, exhibiting a phase change range between 34 to 36 °C (Rubitherm GmbH 2023). In total, the heat exchanger system accommodates 1.497 kg of PCM, providing a latent heat capacity of 360 kJ.

Table 1. Properties of paraffin RT35HC.

Melting area	34-36	°C
Congeaing area	36-34	°C
Heat storage capacity	240	kJ/kg
Specific heat capacity	2	kJ/kgK
Density solid (at 25°C)	0.88	kg/l
Density liquid (at 40°C)	0.77	kg/l
Heat conductivity (both phases)	0.2	W/mK
Max. operating temperature	70	°C

To observe the phase change front evolution along the entire length of the tube, a camera mounted on a linear slider is positioned in front of the heat exchanger. Using a motor, the camera can be positioned at an inclined angle to the PCM

tube. This enables visual observation of the phase change front at the outer diameter of the PCM tube during a solidification experiment. Lastly, the entire assembly is enclosed within a large box filled with insulation granules, to minimize thermal losses (Vermiculite 2023). Figure 1 is a schematic representation of the full set-up.

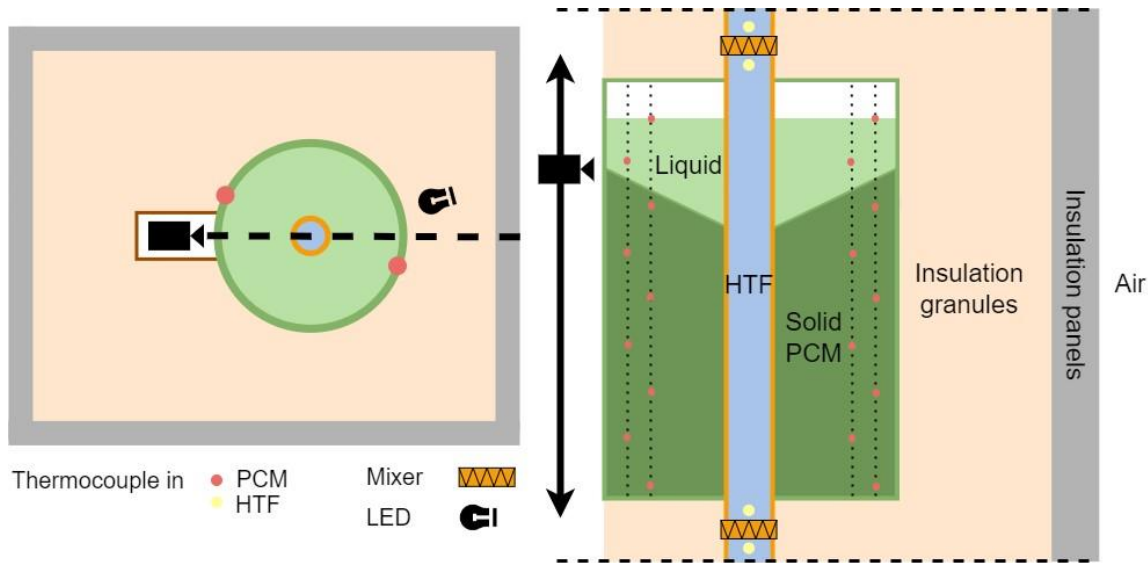


Figure 1. Schematic illustration of the PCM heat exchanger unit.

Temperature measurements of the heat transfer fluid at the inlet and outlet of the heat exchanger are conducted using two mixers and a total of four normal and two differential 1.5-mm K-type thermocouples. The HTF mass flow rate is quantified utilizing a coriolis flowmeter of the type Proline Promass F 300. Additionally, temperature distribution within the PCM is monitored through the deployment of 18 K-type thermocouples situated at nine varying heights and two depths. All thermocouples are calibrated to an accuracy of 0.15 °C.

3. METHODOLOGY

A series of melting and solidification experiments are performed in which the HTF mass flow rate (\dot{m}_{HTF}) and HTF inlet temperature ($T_{inlet,HTF}$) were varied. Table 2 represents all 18 conducted experiments and the initial PCM temperature is always 26°C.

Experiment	\dot{m}_{HTF} [kg/h]	$T_{inlet,HTF}$ [°C]
MELT 1	20	50
MELT 2	20	55
MELT 3	20	65
MELT 4	30	50
MELT 5	30	55
MELT 6	30	65
MELT 7	55	50
MELT 8	55	55
MELT 9	55	65
SOLID 1	20	20
SOLID 2	20	15
SOLID 3	20	5
SOLID 4	30	20
SOLID 5	30	15
SOLID 6	30	5
SOLID 7	55	20
SOLID 8	55	15
SOLID 9	55	5

Table 2. The experimental matrix.

During each experiment, the vertical position of the phase change front at the outer diameter of the PCM tube is tracked over time by the camera. The front position is defined as the vertical distance covered by the phase change front, beginning at the inlet of the HTF tube.

4. RESULTS AND DISCUSSION

The experimental setup is currently undergoing refinements to improve precision. A part of the melting experiments have already been performed and the remaining experiments will be carried out soon. Upcoming experiments include variations in the inlet temperature of the HTF and the HTF mass flow rate, while simultaneously observing the temporal evolution of the phase change front, as described in the previous section.

First, the characteristics of the phase change front during melting and solidification experiments will be compared. Afterwards, the data obtained from these experiments will be compared with the theoretical framework proposed by Beyne et al (Beyne 2023).

5. CONCLUSIONS

A series of melting and solidification experiments have been performed in which the HTF mass flow rate, HTF inlet temperature were varied. During each experiment, the movement of the phase change front was tracked over time using a camera.

6. REFERENCES

- A. Castell and C. Solé. 2015. "11 - design of latent heat storage systems using phase change materials (PCMs)." In *Advances in Thermal Energy Storage Systems*, by ed. L. F. Cabeza, 285–305. Woodhead Publishing.
- Beyne, W. 2023. "An approximate analytical solution for the movement of the phase change front in latent thermal energy storage heat exchangers." *Energy Storage* 106132.
- Karami, R. 2020. "Experimental investigation of the effect of perforated fins on thermal performance enhancement of vertical shell and tube latent heat energy storage systems." *Energy Conversion and Management* 112679.
- Lipnicki, Z. 2012. "An experimental and theoretical study of solidification in a free convection flow inside a vertical annular enclosure." *International Journal of Heat and Mass Transfer* 655-664.
- Raud, R. 2017. "Design optimization method for tube and fin latent heat thermal energy storage systems." *Energy* 585-594.
- Regin, A. F. 2008. "Heat transfer characteristics of thermal energy storage system using pcm capsules: A review." *Renewable and Sustainable Energy Reviews* 2438–2458.
2023. *Rubitherm GmbH*. December 19. <https://www.rubitherm.eu/en/productcategory/organische-pcm-rt>.
- Tay, N. H. S. 2012. "An effectiveness-NTU technique for characterising tube-in-tank phase change thermal energy storage systems." *Applied Energy* 309-319.
2023. *Vermiculite*. December 16. <https://shop.deschacht.eu/nl-be/7921/vermiculite-g3-medium-9kg-100l>.

EXPERIMENTAL INVESTIGATION ON THE INFLUENCE OF ETHANOL/WATER MIXTURE ON NUCLEATE POOL BOILING FOR STRUCTURED SURFACES.

Yiota Xanthopoulou^{a,*}, Axel Sielaff^a, Peter Stephan^a

^a Technical University of Darmstadt, Institute for Technical Thermodynamics, Darmstadt

*xanthopoulou@tttd.tu-darmstadt.de

Keywords: Pool boiling, Binary mixture, Nucleate boiling, Microstructured surface, Heat transfer

1. INTRODUCTION

Over the last decade, significant research efforts have focused on enhancing heat transfer in nucleate pool boiling by selectively (micro-)structuring heater surfaces. Microstructured surfaces have demonstrated the capability to improve the heat transfer coefficient (HTC) compared to technically smooth surfaces. However, a common observation is the reduction in the critical heat flux (CHF). Former studies predominantly employed pure, single-component fluids. In our investigations, we utilize the binary fluid mixture ethanol-water, to investigate the influence of the material properties of the fluid and its dynamic wetting characteristics with the corresponding wall material. Altering the composition of the mixture allows for specific variations in fluid properties like surface tension, wettability, and boiling point, directly influencing heat transfer during boiling and bubble dynamics.

Unlike pure fluids, mixtures typically exhibit a lower heat transfer coefficient (Fujita et al. 1997, Inoue et al. 2004, Xanthopoulou et al. 2023). This reduction is attributed to local concentration differences in the thermal boundary layer, affecting a.o. the local saturation temperature, the diffusive mass transport resistance, and Marangoni flows induced by surface tension gradients [Dang et al. 2018]. Our current focus is on exploring mixture effects during boiling on differently microstructured heater surfaces. We analyze bubble dynamics, heat transfer coefficient, and critical heat flux for various concentrations of the ethanol-water mixture. The overarching objective is to unravel interactions between binary mixtures and microstructured surfaces, identifying strategies to enhance heat transfer in such systems.

2. EXPERIMENTAL SETUP

Experiments are conducted in a setup enabling precise pressure control, continuous in-situ monitoring of the mixture concentrations, and optical observations of the bubbles' lifecycle. The upper part of this heater module is exchangeable, allowing the use of different surfaces as boiling surfaces. It consists of a copper cylinder and the upper side of it serves as the boiling surface. Four types of surfaces have been manufactured for comparison purposes and are presented in Table 1.

Table 1. Types of used heater surfaces

Surface	Abbreviation
Smooth copper surface	Tcu
Microneedles \varnothing 1 μ m and 10 μ m height	10cu
Microneedles \varnothing 1 μ m and 20 μ m height	20cu
Hierarchical surface: microneedles in a striped pattern	Opt

Our findings in this study utilize pure ethanol and a range of 10 - 90 vol% ethanol-water mixture at system pressures of 0.4 bar and 1 bar. Comparative analyses involve the completely smooth copper surface (Tcu) and the hybrid microstructured surface (Opt) as the most efficient surface. The microstructure consists of a 0.48 mm wide structure similar to the 20cu surface and 0.26 mm wide uncoated strips (Fig. 2).

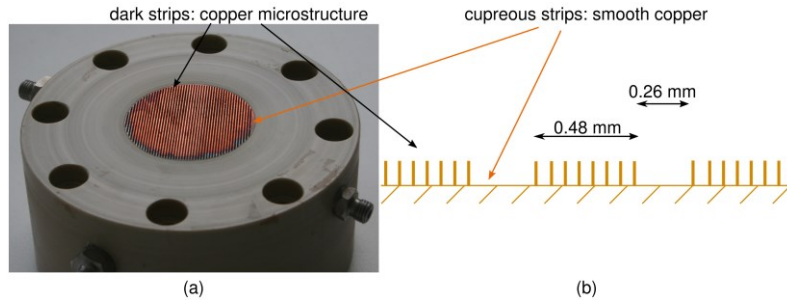


Figure 2. Image (top) and sketch (bottom) of the optimized, hierarchical boiling surface.

3. RESULTS

In Fig. 3 the heat transfer coefficient is shown versus the heat flux for different surfaces and fluid compositions.

The surfaces 20cu and 10cu demonstrated increased Heat Transfer Coefficients (HTCs) but decreased Critical Heat Flux (CHF) values for pure ethanol (Zimmerman, 2022). This phenomenon is attributed to hindered rewetting of the microstructure. Conversely, the hierarchical surface (Opt) exhibits an enhancing effect on both HTC and CHF attributed to an improved flow of fresh fluid to the microstructure. However, with ethanol-water mixtures, the impact is less promising, especially for the 50% vol. mixture. Heat transfer performance improved for pure ethanol, but the 90% vol. mixture showed minimal response to the optimized surface. The rise in heat transfer coefficients for mixtures follows a linear increment until reaching the critical heat flux.

The hierarchical microstructure enhanced heat transfer through increased surface area and improved nucleation. CHF increased for pure ethanol and the 10% vol. mixture, possibly due to vapor outflow and liquid inflow separation. This facilitated easier rewetting, potentially delaying irreversible dry spot formation. For mixtures, mass diffusion and rewetting issues persisted, leading to lower HTC and CHF values compared to pure ethanol. Concentration fluctuations, mass transfer resistance (Dang et al. 2018, Fazel et al. 2013), the Marangoni effect (Armijo & Carey 2010), and effective superheat loss (Fazel et al. 2013) contributed to this.

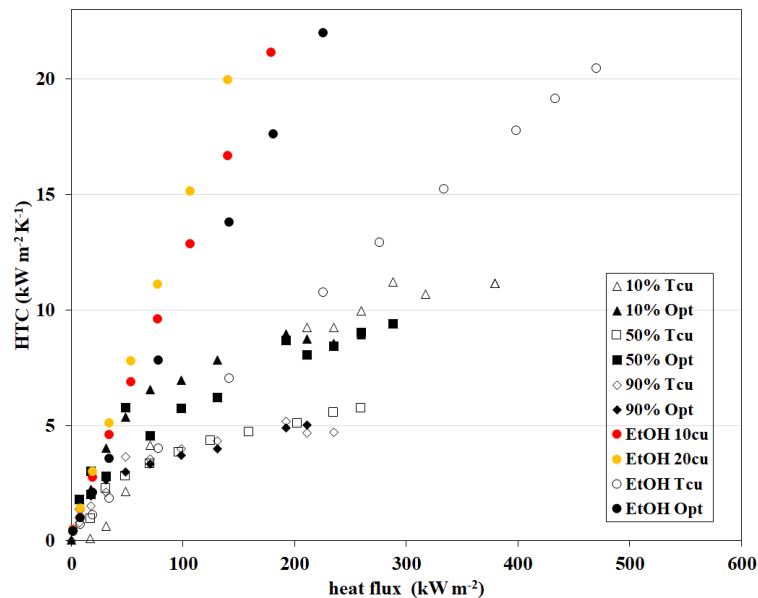


Figure 3. Heat transfer coefficient curves at various system pressures using ethanol and ethanol-water mixture in concentrations of 10%, 50%, and 90% vol. as boiling fluid.

The heat transfer coefficient enhancement ratios and critical heat flux enhancement ratios for the Opt surface compared to the Tcu surface are presented in Tables 2 and 3. While the hierarchical microstructure enhances heat transfer, mass diffusion, and surface rewetting limitations emerge, especially with mixtures. The exact explanation for this phenomenon is not entirely clear, and further investigations into concentration fluctuation effects, mass transfer resistance, and the Marangoni effect are suggested.

Table 2. Heat transfer coefficient enhancement ratios at various system pressures using ethanol and ethanol-water mixture in three concentrations as boiling fluid.

	$\dot{a}_{max,Opt} / \dot{a}_{max,Tcu}$			
	EtOH	10% vol. EtOH/H ₂ O	50% vol. EtOH/H ₂ O	90% vol. EtOH/H ₂ O
1 bar	2.49	1.2	1.47	0.97
0.4 bar	2.29	1.08	1.68	1.1

Table 3. Critical heat flux enhancement ratios at various system pressures using ethanol and ethanol–water mixture in three concentrations as boiling fluid.

	CHF_{Opt} / CHF_{Tcu}			
	EtOH	10% vol. EtOH/H ₂ O	50% vol. EtOH/H ₂ O	90% vol. EtOH/H ₂ O
1 bar	1.01	1.04	1.12	0.9
0.4 bar	1.2	1.28	0.9	0.82

Figure 3, shows a vapor outflow and liquid inflow separation, particularly at low heat flux conditions. While hypothesized to persist at high heat flux levels, conclusive evidence is challenging due to abundant bubbles obstructing visibility. The separated vapor outflow and liquid inflow concept contributes to increased CHF for pure fluids and the 10% vol. mixture. The discontinuous microstructure may facilitate easier rewetting, delaying irreversible dry spot emergence at higher heat flux levels. This configuration also impedes complete vapor envelopment, mitigating the Cassie–Baxter state.

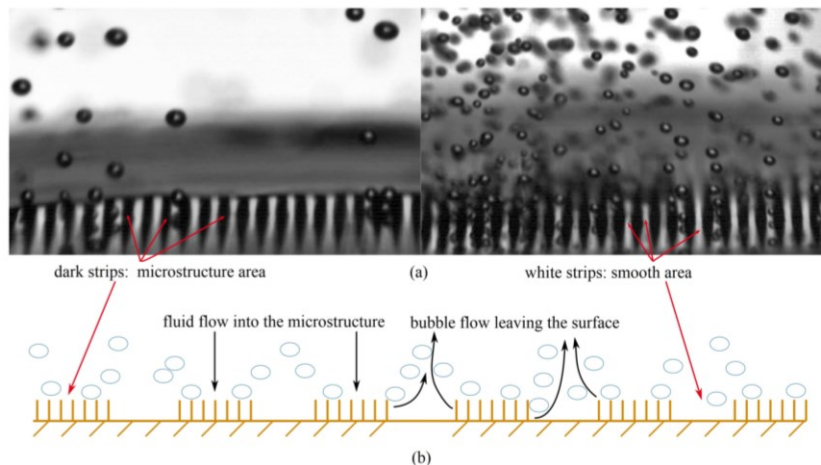


Figure 3. B&W images (a) and sketch (b) show the boiling phenomenon at low heat fluxes on the microstructure surface.

Future research could delve into the growth and dynamics of single bubbles on hierarchical microstructured surfaces in diverse fluid scenarios. Understanding the interplay between surface structure, fluid composition, and bubble behavior would contribute to optimizing heat transfer in various applications.

4. REFERENCES

- Armijo, K., & Carey, V. (2010). Prediction of binary mixture boiling heat transfer in systems with strong Marangoni effects. *Frontiers in Heat and Mass Transfer (FHMT)*, 1(2).
- Dang, C., Jia, L., Peng, Q., Huang, Q., & Zhang, X. (2018). Experimental and analytical study on nucleate pool boiling heat transfer of R134a/R245fa zeotropic mixtures. *International Journal of Heat and Mass Transfer*, 119, 508-522.
- Fazel, S. A., & Jamialahmadi, M. (2013). Semi-empirical modeling of pool boiling heat transfer in binary mixtures. *International journal of heat and fluid flow*, 44, 468-477.
- Fujita, Y., & Tsutsui, M. (1997). Heat transfer in nucleate boiling of binary mixtures: development of a heat transfer correlation. *JSME International Journal Series B Fluids and Thermal Engineering*, 40(1), 134-141.
- Inoue, T., Teruya, Y., & Monde, M. (2004). Enhancement of pool boiling heat transfer in water and ethanol/water mixtures with surface-active agent. *International Journal of Heat and Mass Transfer*, 47(25), 5555-5566.
- Xanthopoulou, Y., Sielaff, A., Stephan, P.: Experimental investigation of the influence of water/ethanol mixtures on microstructure surfaces during nucleate boiling. In: *Proc. 17th International Heat Transfer Conference (IHTC-17)*, 10.1615/IHTC17.360-20, 2023.
- Zimmermann, M.: Experimental investigation of nucleate boiling on microstructured and smooth surfaces. *Technische Universität Darmstadt, Dissertation*, 10.26083/tuprints-00019673, 2022.

DESIGN AND CONSTRUCTION OF A TEST RIG FOR THE QUALIFICATION OF A ROTATING MAGNETIC REFRIGERATOR PROTOTYPE

Johan Augusto Bocanegra^{a*}, Daniele Petrarulo^a, Luis David Misale^b, Annalisa Marchitto^a, Federico Scarpa^a, Luca Antonio Tagliafico^a

^aDepartment of Mechanical, Energy, Management, and Transportation Engineering, University of Genoa, Genoa, Italy

^b University of Bologna, Bologna, Italy

* augusto.bocanegra@unige.it

Keywords: AMR, magnetocaloric, solid-state refrigeration, Gadolinium, GWP

1. INTRODUCTION

Magnetic refrigeration offers a promising alternative to conventional vapor-compression refrigeration, eliminating refrigerant fluids with high Global Warming Potential (GWP) and potentially achieving higher efficiencies (Kamran et al., 2020). Magnetic refrigerators can obtain higher efficiencies than vapor compression machines thanks to eliminating dissipative components such as the compressor and the lamination valve (Kamran et al., 2020). In an active magnetic regenerative (AMR) refrigerator, the strong environmental impact of the refrigerant fluids is avoided by using a solid-state material as a refrigerant. These kinds of refrigerants are magnetocaloric materials (MCM) because a temperature change is induced by a change in the applied magnetic field, the magnetocaloric effect (MCE). An additional heat transfer fluid is used to achieve regeneration in the AMR cycle. The heat transfer or secondary fluid could be a gas (like air or helium) or a liquid, such as a water-glycol micelle (glycol addition avoids freezing and corrosion).

The experimental facilities or test rigs built over time to study different magnetic refrigerator prototypes change depending on the type of regenerator (linear or rotary), the type of MCM (Gadolinium or its alloys), the type of heat transfer fluid (air, water, or oils), the type of end heat exchanger at the hot and cold side (HHEX and CHEX), and the controlled operative parameters (for example the cycle frequency, or the mass flow rate of the heat transfer fluid) (Yu et al., 2010).

As can be figured out, the design and construction of a test rig to perform an experimental characterization of an active magnetic refrigerator prototype must consider the specific characteristics of the regenerator and combine multiple subsystems, such as the mechanical, hydraulic, and thermal subsystems, but also must consider the possible procedures to study the performance of the AMR; this put conditions on the data acquisition and control system. This study presents insights into designing and constructing a test rig tailored for a new rotary magnetic refrigeration prototype developed at the University of Genoa.

2. METHODS

The constructed magnetic refrigeration device involves rotating a magnetocaloric material arranged on a matrix around a fixed permanent magnet assembly into the Active Magnetic Regenerator (AMR); an image of the regenerator is shown in Fig. 1(a). The regenerator consists of a permanent magnet array capable of generating a magnetic field near 1 T in air and a matrix filled with magnetocaloric material (MCM) that rotates around the magnetic field using a motor (M) to do it. The MCM is Gadolinium in the form of thin plates forming straight channels. Two heat exchangers could allow the heat flux associated with the refrigeration cycle; the cold heat exchanger (CHEX) is used to impose the cooling load, and the hot heat exchanger (HHEX) is used to accomplish the heat rejection. Note that it is necessary to use a pump to circulate the working (heat transfer) fluid. The selection of the specific hardware elements to construct the test bench was based on multiple simulations using a numerical model of the refrigerator that allowed to determine the operational limits, for example, the required torque and rotation frequency of the motor, the flowrate imposed by the pumps or the heat transfer characteristics of both HEXs. A schematic of the test rig divided into one primary circuit and two secondary circuits is presented in Fig. 1 (b). As can be seen, the secondary circuits are used to connect the primary circuit with the two thermal baths (TB). The problem linked to establishing or controlling the heat transfer at both ends is not trivial because a precise selection of the heat exchangers is necessary to ensure the device's optimum performance (Bocanegra et al., 2023). A bypass circuit using a 3-way valve is implemented at the secondary side, controlling the effective flow rate of the fluid coming from each TB.

The test rig's design requires determining which components are fundamental for its operation in the different operating conditions required to characterize the device and optimize its operation. The test rig will allow testing of two operative modes: imposed temperature span or free heat exchange with the environment (called *free running*). Under any

of those operative modes, two operation parameters, the utilization factor (proportional to the working fluid flow rate) and the rotation frequency, must be adjusted to ensure optimum regenerator performance. The test rig was designed under those requirements.

The data acquisition of different temperature, mass flow rate, pressure, and torque measurements is necessary to study the AMR's transitory and steady-state performance. From those acquired values are derived performance indicators such as the cooling load or the coefficient of performance (COP). Moreover, the acquired data serve as feedback signals that help to control the main operative parameters. The data acquisition system was projected using type A sensors and industrial interfaces connected with Modbus protocol to a computer running dedicated software for data acquisition and control of the magnetic refrigerator prototype.

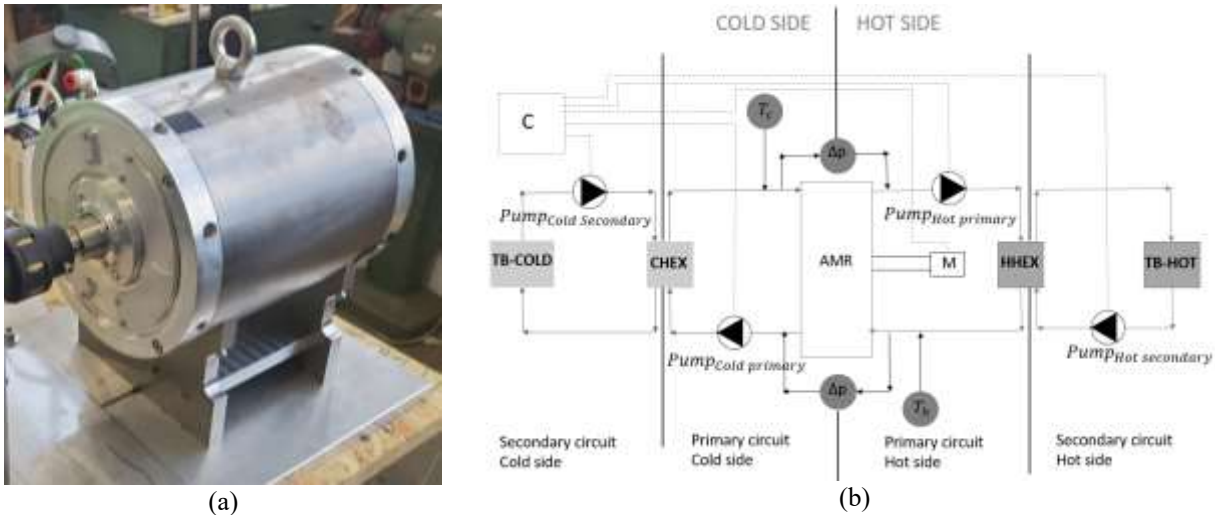


Figure 1. The Rotary Active Magnetic Regenerator (AMR) is mounted in a simplified test bench with two heat end exchangers (CHEX and HHEX) and a motor (M). (a) rotary Active Magnetic Regenerator (AMR); (b) simplified scheme of the test rig.

3. RESULTS

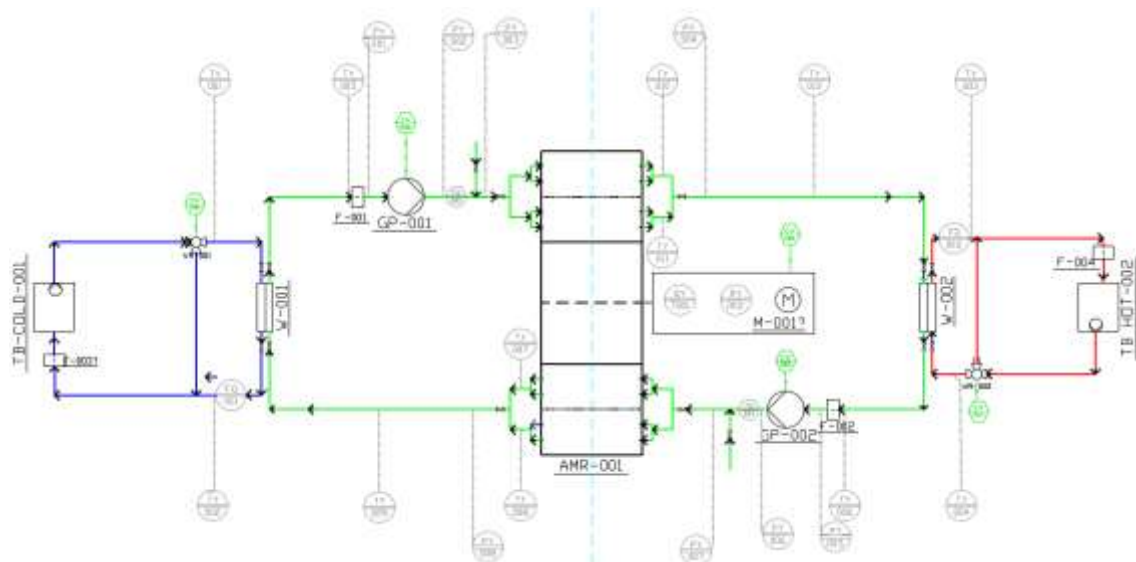


Figure 2. Test-rig diagram. Primary circuit (green pipes), Secondary circuits (blue and red pipes). Sensors (greys) and controls (green).

Appropriate operative ranges of the elements in the rig (such as pumps, motors, and sensors) were established after developing several simulations. Temperatures, pressures, fluid flow rate, torque, and rotation frequency are quantities of interest that must be measured. All the elements presented in the simplified design were included in the constructed test rig with the addition of the bypass and the acquisition and control system; a more precise diagram of the test rig is

presented in Fig. 2. Figure 3 presents a photo of the constructed test rig; flexible pipes were used to connect all the components. A computer is connected to the test rig to acquire and control the prototype, the protocol Modbus TCP/IP is used to interface a programmable logic Programmable Logic Controller (PLC) that receives the signals from each acquisition module (12 thermistors PT1000 were used as temperature sensors and were acquired by dedicated Modbus modules, generic current I/O modules were used for the acquisition of other signals, as those coming from four fluid rate ultrasonic meters. The control system was constructed to regulate the by-pass valves, to adjust the heat exchange, and the pumps to adjust the utilization factor, and the rotation frequency of the motor directly linked to the AMR frequency.

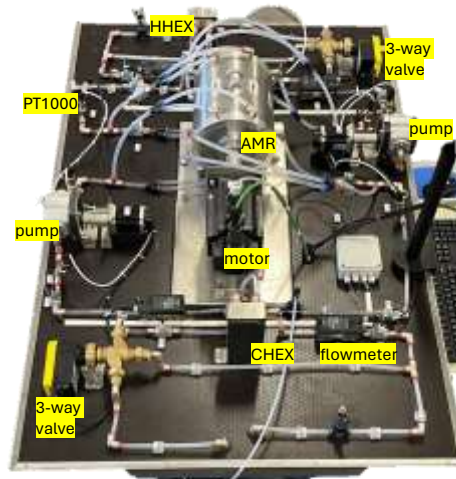


Figure 3. Constructed test rig. The magnetic regenerator (AMR) is mounted in this test bench designed for a versatile performance characterization of the prototype under different operative conditions (imposed temperature span or free heat exchange with the ambient).

4. CONCLUSIONS

This work shows the design of a test rig capable of evaluating the performance of an active magnetic refrigerator under different operative modes (imposed temperature span or free running), allowing the selection of the main operating parameters (rotation frequency and utilization factor) and conditions (reference temperature and heat exchange conditions). The test rig was designed to test a new rotary active magnetic regenerator developed at the University of Genoa. Some key aspects are:

- The design and plant components were determined and supported by numerical simulations of the considered prototype. The adopted methodology can be extended to other prototypes.
- The numerical simulations of the AMR refrigerator help to understand the system's requirements and guide the choice of pumps and heat exchangers.
- A bypass system based on three-way valves controls the cooling load and heat rejection during the two operative modes.
- Measurement systems such as resistance temperature detectors, pressure sensors, ultrasonic flow meters, and a control system have been installed to allow experimentation with the prototype.
- A dedicated software interface was also designed to connect a PC to the test rig using industrial communication protocols and a PLC.

5. REFERENCES

- Bocanegra, J.A., Scarpa, F., Tagliafico, L.A., 2023. "The role of external heat exchangers in the performance of active magnetic refrigerator". *International Journal of Refrigeration*, Vol. 154, pp. 168–181. <https://doi.org/10.1016/j.ijrefrig.2023.07.019>
- Kamran, M.S., Ahmad, H.O., Wang, H.S., 2020. "Review on the developments of active magnetic regenerator refrigerators – Evaluated by performance". *Renewable and Sustainable Energy Reviews*, Vol. 133, pp. 110247. <https://doi.org/10.1016/j.rser.2020.110247>
- Yu, B., Liu, M., Egolf, P.W., Kitanovski, A., 2010. "A review of magnetic refrigerator and heat pump prototypes built before the year 2010". *International Journal of Refrigeration*, Vol. 33, pp. 1029–1060. <https://doi.org/10.1016/j.ijrefrig.2010.04.002>

Impact and Boiling of Single and Multiple Droplets on a Heated Solid Surface

Tianhan Chen^{a,*}, Koji Hasegawa^a

^aDepartment of Mechanical Engineering, Kogakuin University, Tokyo 163-8677, Japan

*am23045@g.kogakuin.jp

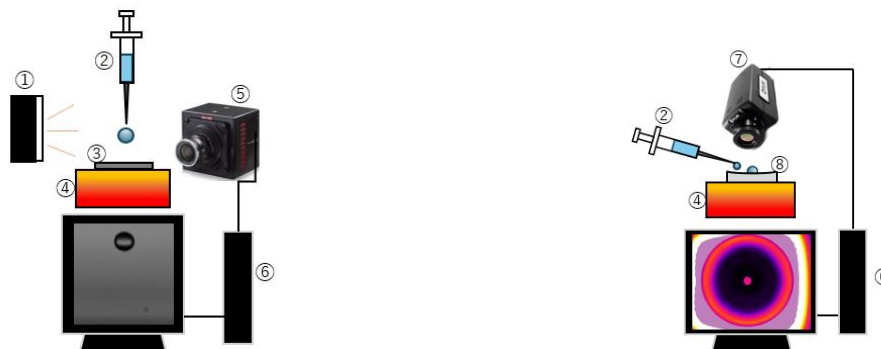
Keywords: droplet impact, heated solid substrate, boiling, Leidenfrost effect, evaporation

1. INTRODUCTION

There are various types of impact behaviors between droplets and the surfaces of liquids and solids. In recent years, one of these behaviors, the impact of droplets with heated solid surfaces, has been widely applied in fields such as industrial steelmaking cooling and fuel injection for internal combustion engines. However, the impact behavior of a single droplet on a heated solid surface varies rapidly depending on conditions such as droplet diameter, drop height, and substrate temperature, substrate properties, and surrounding gas conditions. The Leidenfrost (LF) effect is an important phenomenon that occurs when a droplet impacts on a sufficiently heated solid surface. Although many researchers have investigated the dynamics of the LF droplets, there are yet many challenges due to the complex multiphase, multiscale, and multiphysics problem. We aim to systematically understand the droplet dynamics impacted on the heated substrate to clarify the LF conditions for single and multiple droplets. To achieve this, we visualized and quantified the droplet behavior using a high-speed or IR camera.

2. EXPERIMENTAL METHOD

Figure 1 represents the schematics of the experimental setup for (a) single droplet and (b) multiple droplets visualized high speed camera and IR camera, respectively. For a single droplet as shown in Fig. 1 (a), the stainless-steel surface with a flat surface was heated and an ethanol droplet was released from directly above. The entire droplet impact process was recorded using a high-speed camera with a backlight illumination by LED. The spatial resolution of obtained images by a high-speed camera was 25.9 $\mu\text{m}/\text{pixel}$. The heated solid surface temperature ranged from 100 to 400°C, while the drop height varied between 5 and 100 mm.



(a) Setup for single droplet with high-speed camera

(b) Setup for multiple droplets with IR camera

①	LED light	②	Syringe
③	Target surface made by stainless steel with flat top	④	Heating plate
⑤	High-speed camera	⑥	Computer
⑦	IR camera	⑧	Target surface made by aluminum with concave top

Figure 1. Schematics of the experimental setup.

For multiple droplets as shown in Fig. 1 (b), the water droplet was gently placed near the center of the heated solid surface, which is made of aluminum with a concave shape (curvature radius of 300 mm). When a water droplet become stable LF condition at the center of a concave surface, a second droplet of ethanol was carefully dropped close to the levitating water droplet. The temperature of the solid surface and boiling point of the droplets play an important role in the LF condition for two different droplets. The boiling point of water and ethanol are 100 and 78°C, respectively. In the present study, the target substrate temperature ranged from 140°C to 260°C (every 20°C) to realize the triple Leidenfrost

effect (TLF) (Pacheco-Vázquez, F *et al.* 2021). The volume of the water droplet is also a changed between 0.05 ml and 0.3 ml. The spatial resolution of obtained images by a IR camera was 199 $\mu\text{m}/\text{pixel}$.

3. RESULTS AND DISCUSSION

Figure 2 displays the various types of impact behavior of a single droplet, which are influenced by the temperature of the heated solid surface (T_s) and the Weber number (We) (Staat, H.J.J *et al.* 2015). The substrate temperature measured by the thermal sensor was between 100°C and 400°C. We is calculated as the ratio of inertia force to surface tension force, with the density and surface tension of ethanol at saturation temperature ($\rho = 727 \text{ kg/m}^3$ and $\sigma = 17.4 \text{ mN/m}$). The drop height ranged from 5 mm to 100 mm, while the droplet diameter varied from 2.05 mm to 3.24 mm. Therefore, We changes from 6 to 400. As shown in Fig. 2, when T_s is lower than about 160°C, impact behavior tends to be deposition. Film-splash occurs when We is more than about 130 meanwhile T_s is more than around 180°C. The most significant behavior, bounce occurs in the range of small We and T_s is above about 180°C or higher. Therefore, within this range, occurrence of LF effect can be observed.

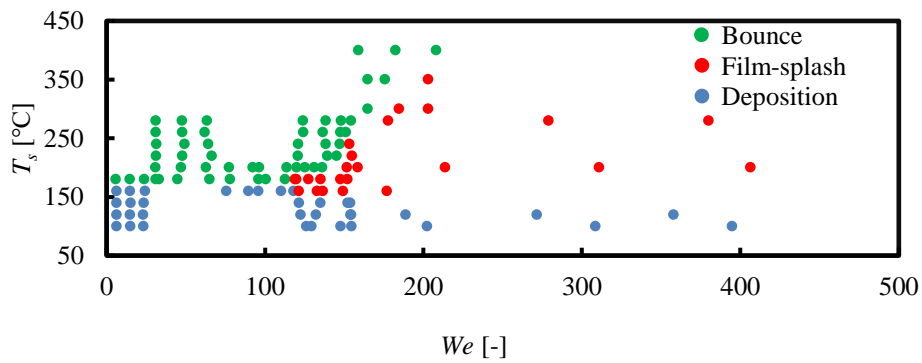


Figure 2. Phase diagram of droplet impact on heated solid substrate with different We and temperature T_s .

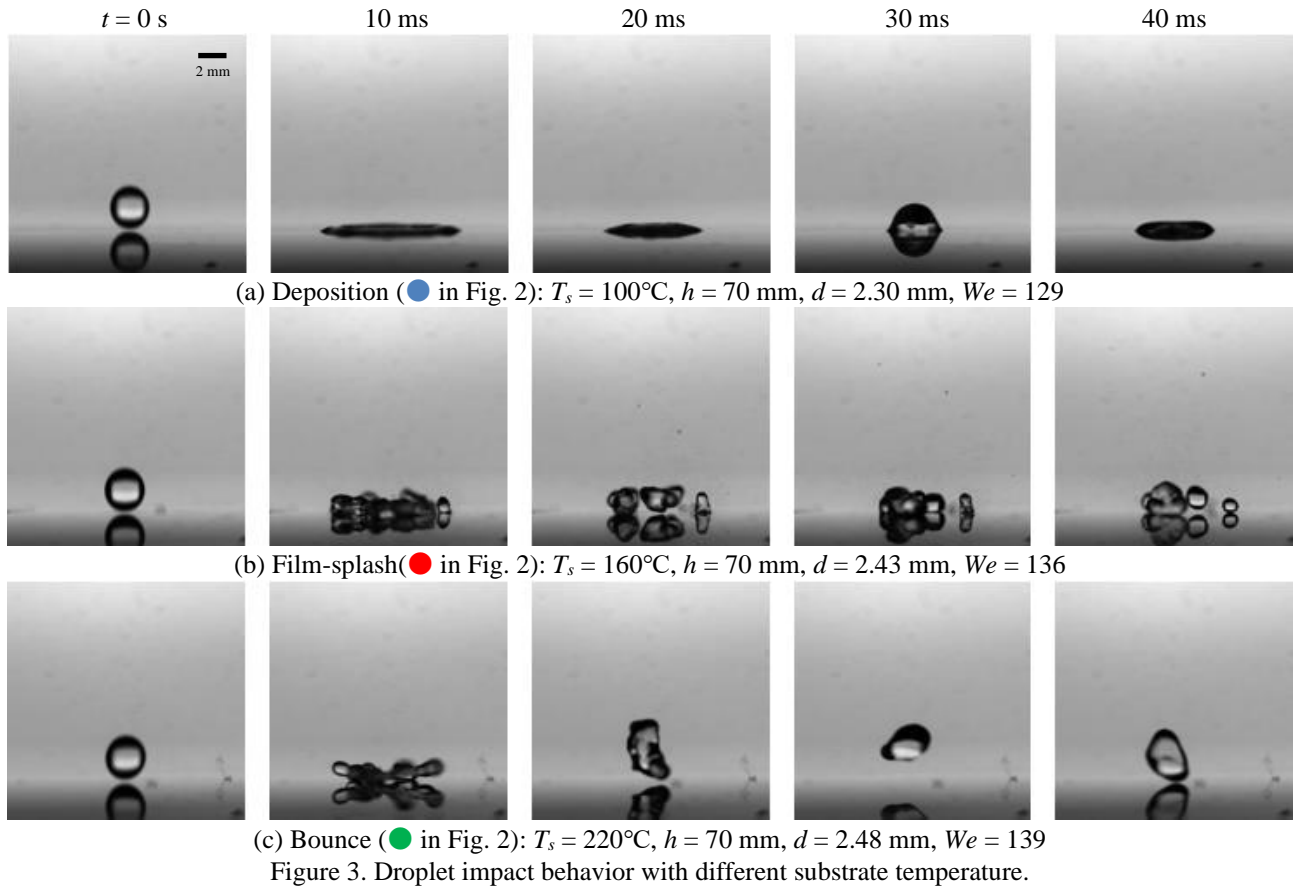


Figure 3. Droplet impact behavior with different substrate temperature.

Figure 3 represents a comparison of droplet impact behavior with different substrate temperature. All these cases are the same drop height $h = 70$ mm, therefore, We were turned to be almost constant. Here, time $t = 0$ s indicates the time just before droplet impact. Comparison between Fig. 3 (a) and (b), droplet impact behavior was different. In Fig. 3 (b) impacted ethanol droplet split into many small droplets. For Fig. 3 (c), the impacted droplets dramatically deformed, but contracted and bounced on the heated substrate due to the difference of T_s . After confirming the bounce behavior, which indicates the conditions for the LF effect, the next step is to investigate the TLF effect with multiple droplets. For the preliminary experiment, we analyzed the dynamic behavior of water and ethanol droplets with changing the volume (V) of water droplet.

Fig. 4 shows the connections between V and T_s , as well as the probabilities of the TLF effect. The four plots used in Fig. 4 indicate whether the TLF effect occurred. The \times mark indicates that no LF effect of the water droplet, as well as the TLF effect, did not occur. The \blacksquare mark indicates that the LF effect of water droplets has been observed, but the TLF effect has not been observed. When the droplet released, the ethanol and water droplet coalesced immediately. In the view of TLF effect, these two marks seem to be same, however we distinguished these two cases in Fig. 4 by indicating 0% of the occurrence of TLF effect. The \blacktriangle mark indicates an experimental data with a TLF effect with a note on the probability of occurrence (not observed in all cases). The \bullet mark indicates that the TFL effect was observed in all cases. However, there may be a measurement error. More experiments should be performed to increase the precision of the probability. Nevertheless, the experimental results shown in Fig. 4 remain informative. The boundary between the \times mark and the \blacksquare mark may indicate that when the water droplet changes from film splashing behavior to bouncing behavior on a heated aluminum surface, in the range of 140 to 180°C, which is relevant with the results shown in Fig. 2. When V is larger than 0.2 ml, while T_s is around 260°C, the probability of TLF effect becomes close to 100%.

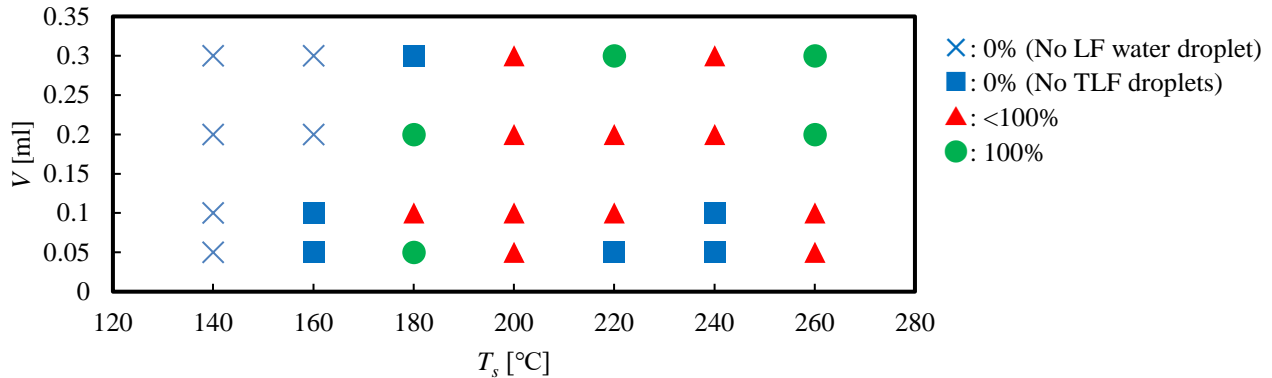


Figure 4. Phase diagram of TLF droplet on heated concave substrate with different water volume V and temperature T_s .

4. CONCLUSIONS

In this study, the LF effect was investigated by studying the impact behavior between ethanol and a heated solid surface, and the TLF effect of water and ethanol droplets on the heated concave substrate. The obtained results and discussion are summarized below:

- 1) When a droplet of saturated ethanol hits a solid surface, the Weber number is affected by the diameter of the droplet and the falling height.
- 2) The impact behavior of the droplet on a heated solid surface is determined by the Weber number and the surface temperature, resulting in either bouncing, film splashing, or deposition behavior. Bouncing behavior is observed over a range of small Weber numbers and temperatures of about 180°C and above, confirming the LF effect.
- 3) The TLF effect of water and ethanol droplets was confirmed at low Weber numbers and a surface temperature above 180°C. The larger the water droplet, the more likely the TLF effect was observed.

5. REFERENCES

- Biance, A.L., Clanet, C. and Quéré, D., 2003. "Leidenfrost drops". *Physical Review Letters*, Vol. 15, pp. 1632–1637.
- Pacheco-Vázquez, F., Ledesma-Alonso, R., Palacio-Rangel, J.L. and Moreau, F., 2021. "Triple Leidenfrost Effect: Preventing Coalescence of Drops on a Hot Plate". *Physical Review Letters*, Vol. 127, 204501.
- Staat, H.J.J., Tran, T., Geerdink, B., Riboux, G., Sun, C., Gordillo, J.M. and Lohse, D., 2015. "Phase diagram for droplet impact on superheated surfaces". *Journal of Fluid Mechanics*, Vol. 779, R3.

DROPWISE-TO-FILMWISE TRANSITION DURING CONDENSATION OF STEAM ON HYDROPHILIC SURFACES

**Marco Tancon^{a,*}, Antonio Abbatecola^a, Stefano Bortolin^a, Lorenzo Facco^{a,b},
Riccardo Parin^b, Davide Del Col^a**

^a Department of Industrial Engineering, University of Padova, Via Venezia 1, 35131, Padova, Italy

^b TerraXcube, Eurac Research, Via Ipazia 2, 39100, Bolzano, Italy

* marco.tancon@unipd.it

Keywords: dropwise condensation, heat transfer, hydrophilic surface, transition mode, droplet removal

1. INTRODUCTION

Dropwise condensation (DWC) is a phase-change process that involves the formation and rapid removal of randomly distributed drops on the condensing surface. It is well-established that promoting DWC can significantly improve the heat transfer performance as compared to filmwise condensation (FWC). The resulting condensation mode (FWC or DWC) depends on the operating conditions (e.g. heat flux) and the interaction between condensing fluid and surface (wettability). Hydrophobic coatings (static contact angle $\sim 90^\circ$) are usually employed to promote DWC on metallic surfaces. Recent studies have suggested that DWC on hydrophilic surfaces can provide additional advantages such as reduced thermal resistance associated with conduction through the droplets, enhanced nucleation and thus higher heat transfer coefficients (HTC). However, due to limitations in materials science, there are few experimental data about DWC of pure steam on hydrophilic surfaces, and the actual advantage of promoting DWC on such surfaces is still unclear.

Another aspect that requires further study is the transition from dropwise to filmwise condensation. Since the ratio of DWC heat transfer coefficient to FWC heat transfer coefficient can be close to 10 (Bortolin *et al.*, 2022), identifying the key parameters (e.g. wall subcooling, surface characteristics, fluid properties) involved in the transition from DWC to FWC and understanding their role in the condensation process is very important. Stylianou and Rose (1983) and Utaka *et al.* (1985) conducted studies to clarify the transition mechanism, but no definitive conclusions were drawn. The transition could be linked to one or both of the following mechanisms. First, for sufficiently high wall subcooling, the rate at which new portions of the surface are cleaned by coalescence and sweeping events becomes unable to sustain the increasing condensation rate. Second, considering that the radius of the smallest thermodynamically viable drop is inversely proportional to the subcooling, increasing the saturation-to-wall temperature difference activates smaller nucleation sites, potentially resulting in the formation of a continuous film. Nevertheless, it is accepted that DWC can only be maintained up to a certain value of subcooling and heat flux, which is strongly dependent on surface properties and operating conditions.

The present work addresses understanding of DWC promotion and sustainability over vertical surfaces that present a relatively high wettability. Sol-gel coated aluminium samples with hydrophilic behaviour (advancing contact angle $\theta_a \approx 50^\circ$) and reduced contact angle hysteresis ($\Delta\theta < 30^\circ$) were tested during DWC of pure steam at constant saturation temperature ($T_{sat} = 107.5^\circ\text{C}$). Two types of tests were performed: endurance tests at fixed heat flux to evaluate the evolution of the coating wettability and tests at variable coolant inlet temperature (20-90 $^\circ\text{C}$) to assess the effect of wall subcooling and heat flux on the DWC phenomenon and HTC. To support the heat transfer data, characterisation of the developed surfaces was carried out based on contact angles, film thickness and microscopic images.

2. MATERIALS AND METHODS

The apparatus used to study condensation is a two-phase thermosiphon loop: steam generated in a boiling chamber (with a maximum power of 6 kW) flows into the test section, it is partially condensed over a vertically mounted aluminium sample, then the mixture leaving the test section is fully condensed and sub-cooled in a secondary condenser before returning to the boiling chamber. The boiling chamber and the test section are connected using stainless-steel tubes heated by electrical resistances wrapped around the outer wall. By adjusting the power supplied to the heaters, pure steam ($T_{sat} = 107.5^\circ\text{C}$) with a slight superheating ($\approx 4\text{ K}$) is obtained at the test section entrance. Inside the test section, the vapor flows downward over the front side of the sample (heat transfer area of $20 \times 50\text{ mm}^2$) and condenses, rejecting the heat to the cooling water on the back side.

Samples are made of high purity aluminium (AW 1050), mirror-polished on the condensation side before the deposition of the coating. The surface over which condensation takes place was functionalized with a sol-gel silica film obtained by acid catalyzed hydrolysis and condensation of TEOS (tetraethylorthosilicate), MTES (methyltriethoxysilane), OTES (octyltriethoxysilane) in alcoholic media. The solution was prepared by mixing TEOS, MTES, OTES, EtOH, HCl

1 M and H₂O in molar ratios of (TEOS + MTES + OTES):EtOH:HAc:HNO₃ (0.1 M) = 1:0.01:2.9:150 respectively, with molar fractions of silane precursors TEOS:MTES:OTES = 0.35:0.6:0.05. The deposition was performed at controlled air humidity (25%) by dip coating the aluminum substrate into the obtained solution with a withdraw speed of 12 cm min⁻¹. Then the samples were heat-treated in air inside a furnace at 450 °C for 1 h. Dynamic contact angles measured by sessile drop method, coating thickness measured by ellipsometry, and optical images were used for the characterizations of the fabricated surfaces.

Six thermocouples are embedded inside the sample at two depths from the surface ($z_1 = 1.3$ mm and $z_2 = 2.8$ mm). Based on the thermocouples readings, the Fourier law can be applied to obtain the local heat flux (q_{loc}) at three longitudinal locations and the local surface temperature ($T_{w,loc}$). Thus, the local HTC is defined as the ratio of q_{loc} to ($T_{sat} - T_{w,loc}$). The local measurements at the middle position are considered in the present work to describe the average thermal behavior of the surface. The average heat flux exchanged during condensation is checked by evaluating the thermal balance at the cooling side of the test section. Each experimental data reported here is the average of 480 readings taken at 1 Hz frequency. Uncertainty bars are calculated with a coverage factor $k = 2$. In addition to thermal measurement, a high-speed camera combined with a macroscopic lens and LED as a light source is used for the visualization of the phenomenon. Additional information on the experimental apparatus, data reduction technique and measurement uncertainty can be found in Tancon *et al.* (2022).

3. EXPERIMENTAL RESULTS

The mirror polished sample exhibited an advancing contact angle $\theta_a = 60^\circ$ and a receding contact angle $\theta_r < 10^\circ$. After coating deposition, the surface wettability slightly changed: $\theta_a = 51 \pm 5^\circ$ and $\theta_r = 22 \pm 3^\circ$. Thus, the developed surfaces were hydrophilic with reduced contact angle hysteresis compared to the baseline aluminium. The present study will demonstrate that achieving stable DWC on hydrophilic surfaces is possible, provided that the droplet mobility is sufficiently high (meaning low contact angle hysteresis), as hypothesized in Cha *et al.* (2018). Optical images confirmed homogeneous film deposition on the substrate, while ellipsometry measurements indicated a coating thickness of approximately 370 nm. After condensation, the film thickness slightly decreased (≈ 350 nm) and the contact angles remained almost the same ($\theta_a = 53 \pm 3^\circ$ and $\theta_r = 19 \pm 2^\circ$). These small variations in coating characteristics are not expected to affect the heat transfer measurements.

Figure 1 shows the condensation curve measured for the hydrophilic coated surface when varying the inlet temperature of the cooling water from 90 °C to 20 °C. The saturation temperature ($T_{sat} = 107.5$ °C) and vapor velocity ($v_{vap} = 2.5$ m s⁻¹) were maintained constant. In Fig. 1a and Fig. 1b, the local heat flux (q_{loc}) and HTC obtained at the center of the sample are respectively plotted versus surface subcooling (ΔT). The obtained condensation curve can be divided into three regions. In the first region ($\Delta T < 2$ K), the heat flux increases with subcooling and the HTC remains constant. In the second region ($2 \text{ K} < \Delta T < 14 \text{ K}$), the heat flux increases sublinearly with subcooling until it reaches a maximum value of about 530 kW m⁻²; this results in a decrease of the HTC. In the third region ($\Delta T > 14$ K), both HTC and heat flux decrease. From the results of Fig. 1, two further aspects can be noted. First, the HTC measured during DWC (≈ 190 kW m⁻² K⁻¹) is approximately 7 times higher than the value obtained during FWC (≈ 25 kW m⁻² K⁻¹). Second, the HTC measured during DWC on such hydrophilic surfaces is much higher even when compared to DWC on hydrophobic surfaces. For comparison, the HTC measured on aluminum samples functionalized by sol-gel coatings with similar thickness (400 nm) but higher contact angles ($\theta_a = 87^\circ$, $\theta_r = 64^\circ$) was around 90 kW m⁻² K⁻¹ (Tancon *et al.*, 2024). Thus, the advantage of promoting DWC on hydrophilic surfaces is clear.

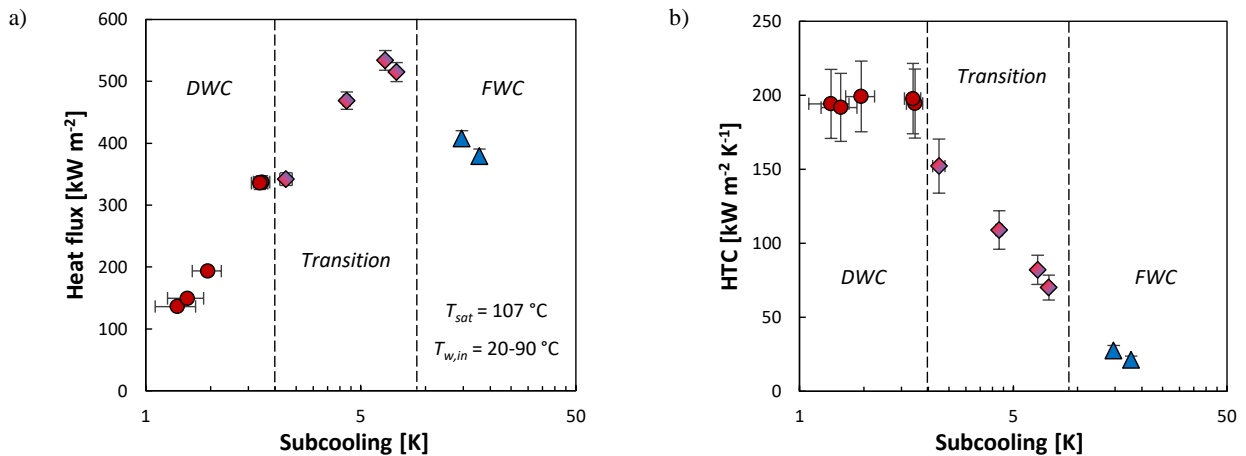


Figure 1. Heat transfer measurements during condensation of steam on the hydrophilic vertical surface at constant saturation temperature: a) heat flux and b) heat transfer coefficient vs degree of subcooling.

High-speed video recordings were used to correlate heat transfer data with condensation modes (Fig. 2). Pure DWC occurred at low values of subcooling ($\Delta T < 2$ K, $q < 300$ kW m⁻²), whereas FWC covered more than 50% of the surface at high subcooling ($\Delta T > 15$ K). Intermediate ΔT conditions resulted in DWC with an increasing presence of rivulets and flooded zones as heat flux increased. The transition from DWC to FWC appears to occur when the condensation rate exceeds the one obtained from droplet removal by coalescence and sweeping. Data in Fig. 1 was collected by decreasing the coolant temperature from 90 °C to 20 °C (left to right on the condensation curve). Once partial flooding of the surface was achieved at the maximum wall subcooling, reversion to pure DWC was observed when increasing the coolant temperature and thus reducing wall subcooling and the heat flux. The ramp from the highest to lowest coolant temperature and vice versa was repeated twice during the test run.

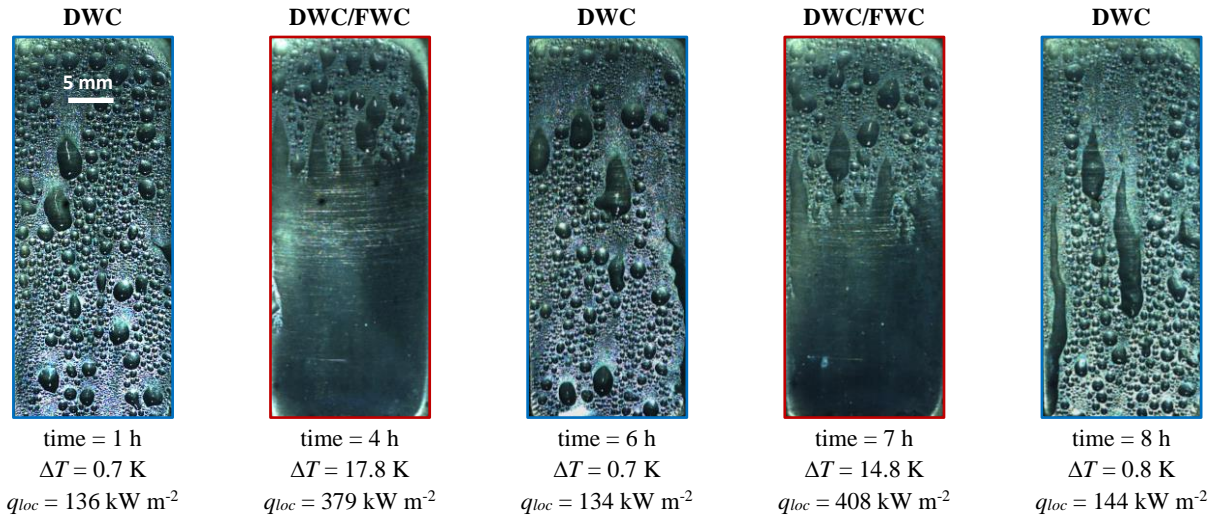


Figure 2. Images of one continuous condensation test run recorded on the hydrophilic surface with reduced contact angle hysteresis for different cooling water inlet temperatures: between 90 °C and 20 °C. The corresponding time, wall subcooling and heat flux are reported.

4. CONCLUSIONS

Condensation of pure steam was studied on hydrophilic coated aluminum vertical samples ($\theta_a \approx 50^\circ$) that present reduced contact angle hysteresis ($\Delta\theta < 30^\circ$) compared to the untreated aluminum. Heat transfer measurements and video analysis were performed at constant saturation temperature (107.5 °C) and vapor velocity (2.5 m s⁻¹) while varying the inlet temperature of the cooling water in the range 20-90 °C, and thus the wall subcooling. At low values of subcooling ($\Delta T < 2$ K) and heat flux ($q < 300$ kW m⁻²), the fabricated hydrophilic surface promoted pure dropwise condensation (DWC) with heat transfer coefficient (HTC) equal to 190 kW m⁻² K⁻¹. When the subcooling was increased from 2 K to 14 K, the heat flux continued to increase up to a maximum value of about 530 kW m⁻², although the HTC decreased due to the formation of rivulets and flooded areas. For subcoolings above 14 K, both HTC and heat flux decreased as flooding occurred on more than 50% of the surface. Reducing the wall subcooling, and thus heat flux, resulted in a reverse transition from FWC to pure DWC. Video analysis suggested that the transition from DWC to FWC takes place when the droplet removal rate due to both coalescence and sweeping events is exceeded by the condensation rate.

5. REFERENCES

- Bortolin, S., Tancon, M., Del Col, D., 2022. "Heat Transfer Enhancement During Dropwise Condensation Over Wettability-Controlled Surfaces". In *The Surface Wettability Effect on Phase Change*, pp. 29–67.
- Cha, H., Vahabi, H., Wu, A., Chavan, S., Kim, M.K., Sett, S., Bosch, S.A., Wang, W., Kota, A.K., Miljkovic, N., 2020. "Dropwise condensation on solid hydrophilic surfaces". *Science Advances*, Vol. 6, eaax0746.
- Stylianou, S.A., Rose, J.W., 1983. "Drop-to-filmwise condensation transition: Heat transfer measurements for ethanediol". *International Journal of Heat and Mass Transfer*, Vol. 26, pp. 747–760.
- Tancon, M., Abbatecola, A., Mirafiori, M., Bortolin, S., Colusso, E., Martucci, A., Del Col, D., 2024. "Investigation of surface inclination effect during dropwise condensation of flowing saturated steam". *International Journal of Thermal Sciences*, Vol. 196, 108738.
- Tancon, M., Mirafiori, M., Bortolin, S., Basso, M., Colusso, D. Del Col, 2022. "Dropwise condensation mechanisms when varying vapor velocity". *Applied Thermal Engineering*, Vol. 216, 119021.
- Utaka, Y., Saito, A., Tani, T., 1985. "Study on dropwise condensation curves". *Bulletin of JSME*, Vol. 28, n. 240.

SLUG FREQUENCY FOR A GAS-LIQUID VISCOUS FLOW IN VERTICAL PIPES

Keziah Magit^a, Buddhika Hewakandandamby^{a*}, David Hann^a, Wigdan Kisha^a

^aFaculty of Engineering, University of Nottingham, University Park, Nottingham, NG7 2RD, UK.

^{a*} buddhika.hewakandamby@nottingham.ac.uk

Abstract

In designing industrial installations that may encounter intermittent gas-liquid flows, slug frequency is a vital parameter that must be considered. Empirical correlations and experimental investigations abound in the literature to predict this parameter. However, most of these studies have focused on air and water, leaving little data available for viscous liquid phases. Understanding the impact of liquid viscosity on slug flow is crucial for pipeline sizing and equipment design. This study explores the effects of high oil viscosity on slug frequency in vertical pipes through experimental investigation. Non-intrusive Electrical Capacitance Tomography (ECT) was employed to measure time series void fraction, with air-silicon oil (ranging from 4.8 to 234 cP) as the operating fluid in a vertical pipe with a 68 mm ID and 4.5 m length. The experiment utilized superficial gas velocities ranging from $0.07 \leq U_{sg} \leq 2.4 \text{ m/s}$ and liquid velocities ranging from $0.15 \leq U_{sl} \leq 0.53 \text{ m/s}$. The results reveal that slug frequency is notably affected by liquid viscosity. While existing empirical models based on Strouhal number and input liquid fraction, as well as the Lockhart Martinelli parameter, provide good predictions for experimental slug frequency, they are limited to a close range of data conditions. Therefore, a new empirical correlation has been developed based on an extended range of available experimental data.

Keywords: Slug frequency. Viscous flow, vertical pipes, gas-liquid flow

1. Introduction

Gas-liquid mixtures have different flow patterns in vertical flow. Among these, slug flow is the most common and is encountered in industries like nuclear, chemical, petroleum, and energy production. Slug frequency is a crucial parameter when studying intermittent flow, and it is defined as the number of liquid slugs passing through a point in the pipe within one second. Slug frequency is required for accurately predicting slug-flow characteristics like pressure gradient and liquid holdup. However, only a few studies have explored the effect of high-viscosity behaviour on slug characteristics. (Gokcal et al. 2009) found that slug flow was the dominant flow pattern for high-viscosity-oil and -gas flows. (Gregory and Scott 1989) also observed that the frequency was dependent on the form of the Froude number. Based on these observations, a correlation for the frequency in horizontal flows has been proposed:

$$f^h = 0.0226 \left[\frac{U_{ls}}{gD} \left(\frac{19.75}{U_{ms}} + U_{ms} \right) \right]^{1.2} \quad (1)$$

Few correlations have been reported for vertical slug flow, among which is the work of (Hernandez-Perez 2008) who adjusted his data in 32 and 67 mm pipes to Gregory and Scott correlation modifying the empirical parameters.

(Heywood and Richardson 1979) proposed a first slug frequency correlation mathematical model in horizontal flow using a test section. The model of the latter for vertical slug flow is reported in (Saidj et al. 2018).

(Zabaras 2000), proposed a correlation for slightly inclined pipes based on experiments from 0° to 11° . This correlation corrects Gregory "Eq. (1)" by multiplying it by an angle-dependent term.

$$f^h = 0.0226 \left[\frac{U_{ls}}{gD} \left(\frac{19.75}{U_{ms}} + U_{ms} \right) \right]^{1.2} (0.836 + 2.75 \sin^{0.25} \alpha) \quad (2)$$

In the study by (Fossa, Guglielmini, and Marchitto 2003), it was found that the frequency of slugs in a pipeline can be correlated with a dimensionless Strouhal number and liquid volume fraction. (Liu and Wang 2008) and (Abdulkadir et al. 2016) later confirmed this criterion and applied it to independent frequency data.

More recently, (Al-Safran, Kora, and Sarica 2016) reviewed correlations developed for high-viscosity flows and identified the random nature of slug frequency due to dissipation, merging, and regeneration of liquid slugs along the pipeline. To predict the probability of a certain slug frequency occurring, he proposed a model based on the Poisson probability theory. The mean slug frequency, required as input to this model, was correlated with the pipe diameter, liquid superficial velocity, and slip ratio. Details of the correlation can be found (Al-Ruhaimani et al. 2018).

Although previous studies improved our understanding of slug frequency dynamics, most of the available correlations for predicting it in vertical flow are either mathematical models with unknown variables or simple empirical correlations for a limited range of flow conditions. To develop a more general correlation, several parameters, including physical properties of phases such as liquid viscosity and pipe geometry, should be considered in addition to the variables already accounted for.

2. Methodology

Experiments were conducted in a flow rig (Figure 1) to investigate the flow of the air-silicone oil mixture. The flow facility included a liquid tank, a liquid centrifugal pump, a mixing section, a vertical riser, two horizontal sections, two 90° bends, air and liquid flowmeters, temperature sensors, and pressure transmitters. The mixing section had inlets for air and liquid, with diameters of 28 mm and 42 mm, respectively, while the main pipe section had an average internal diameter of 68mm. The silicone oil was pumped from the storage tank into the mixing section using the centrifugal pump. To improve liquid flow control and boost flow stability, a bypass line with an appropriate valve arrangement was installed. The air was supplied from a central compressed air line. The temperature and pressure of both the liquid and gas streams were measured using sensors and transmitters before the mixing section. Within the mixing section, the silicone oil and air were thoroughly mixed, and the mixture flowed along a vertical riser of 4.5 m before reaching the bend. This provided a 66-pipe diameter length, which is considered enough for flow development (Abdulkadir et al., 2012; Azzi & Friedel, 2005; Benbella et al., 2009).

An Electrical Capacitance Tomography (ECT) probe was installed upstream of the bend as illustrated in Figure 1 for flow measurements around the vertical bends. During the measurements, the ECT was placed 5D immediately upstream. The density of the air and silicone oil used was 1.18 and 915 kg/m^3 , respectively. The velocity range for the air and silicone oil were (0.07- 2.4) and (0.15 – 0.53) m/s , respectively. The facility ran at ambient temperature and atmospheric pressure.

Data analysis and processing were carried out using the method proposed by Hazuku et al. (2008) to estimate the frequency of the structures. This was done by applying two thresholds, with the lower threshold being the mean of the void fraction time series and the upper threshold being the mean of the values that are higher than the lower threshold. A gas structure was identified whenever the time series values rose above the upper threshold. Figure 2 shows a sample of the structure using the above method.

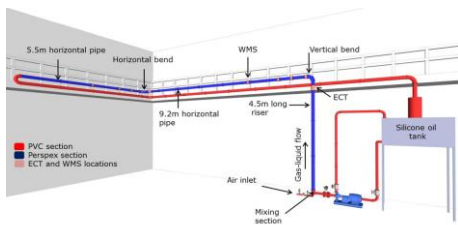


Figure 1 Experimental flow facility (Omar et al. 2018)

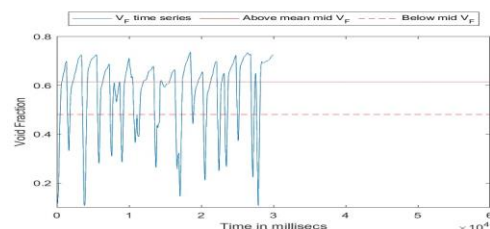


Figure 2 Structure identification (Hazuku, Takamasa, and Matsumoto 2008) method.

3. Results

The slug frequency is a crucial parameter that refers to the number of slugs passing through a defined pipe cross-section in a 60-second timeframe. This parameter is related to the inherent instability of slugging conditions, and an accurate estimation of slug frequency can help reduce the risk of several operational issues, such as flooding of two-phase separators, pressure pulsations, and pipe failure due to severe vibration. Additionally, it is essential to accurately predict this parameter due to its inclusion as a closure relation in many slug flow models.

In this study, the frequency of liquid slugs was estimated using the modified method of Hazuku et al. (2008) for large structures. The frequency of slugs was determined for 4.8cP oil and 234 cP oil in the vertical pipe section for liquid superficial velocities ranging from 0.15 m/s to 0.46 m/s . Figure 3 shows how the frequency of slugs varies with an increase in gas superficial velocities and viscosity of the oil used. As the gas superficial velocity increases, slug frequency also increases for liquid superficial velocities of 0.15 m/s and 0.23 m/s , which agrees with the work of (Abdulkadir et al. 2010). However, at higher liquid superficial velocities, slug frequency shows an inconsistent trend. An increase in viscosity from 4.8 cP to 234 cP oil results in a decrease in slug frequency. This is due to the dominating effect of viscous forces over inertia forces, which increases drag force and decreases the bubble rise velocity. As a result, the length of the slug unit increases due to the coalescence of bubbles, leading to a decrease in bubble frequency as liquid viscosity increases. This is contrary to what was proposed by (Gokcal et al. 2009), which could be due to the use of horizontal pipe.

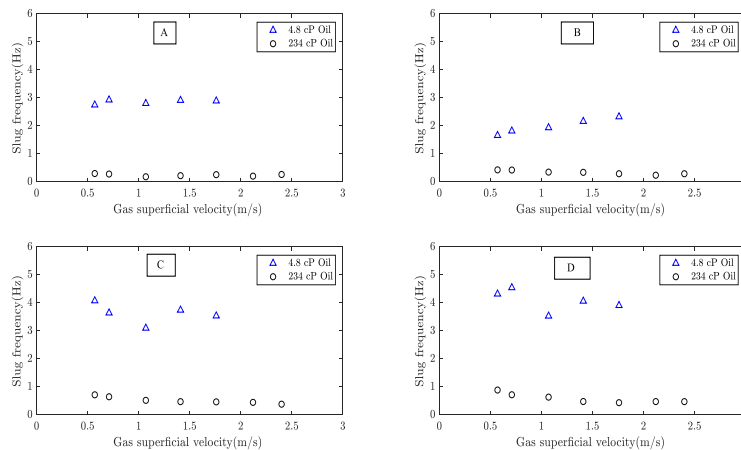


Figure 3: Slug frequency for (A) $U_{sl} = 0.15 \text{ m/s}$, (B) $U_{sl} = 0.23 \text{ m/s}$, (C) $U_{sl} = 0.38 \text{ m/s}$, and (D) $U_{sl} = 0.46 \text{ m/s}$

For the analysis of oscillating unsteady fluid flow dynamics problems, a dimensionless value useful is the Strouhal number. It represents a measure of the ratio of inertial forces due to the unsteadiness of the flow to the inertia forces ($S_t = fD/U_{SG}$) due to changes in velocity from one point to another (Saidj et al. 2018).

In Figure 3(A), the Strouhal number based on the gas superficial velocity is shown for 234cP oil as a function of input liquid fraction on a log-log plot, $X = \frac{U_{SL}}{U_{SL}+U_{SG}}$.

The relationship between Strouhal number and the Lockhart -Martinelli parameter is shown in Figure 3(B) again on a log-log plot for 234cP oil. The Lockhart-Martinelli parameter, X , is defined as the square root of the pressure drops for the liquid part of the flow flowing alone in the pipe divided by that for the gas and it is approximately equal to the ratio of liquid and gas superficial velocities times the square root of the liquid to gas density ratio; $X = \sqrt{\frac{\rho_L U_{SL}}{\rho_G U_{SG}}}$

The relationship between Strouhal number based on gas superficial velocity with liquid quality and Lockhart-martinelli parameter X is positive.

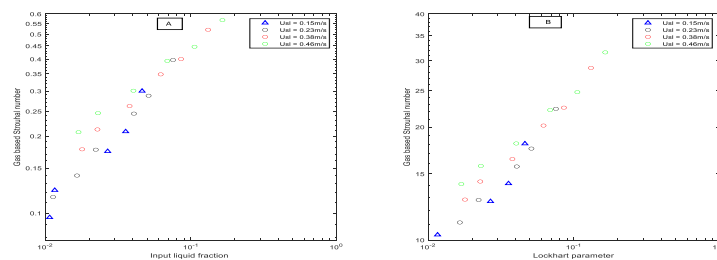


Figure 4: Log-log plot of the dimensionless Strouhal number versus Input liquid fraction (A) and the Lockhart-Martinelli (B) parameter for 234cP Oil

4. Conclusion

In this paper, experimental data from 68mm ID vertical pipe section, in which an air-silicon oil of viscosities 4.8cp and 234cp mixture flow is presented. Electrical Capacitance Tomography (ECT) was used to provide a cross-sectional averaged void fraction at 5D before the vertical pipe section for two different oil viscosities. Slug frequency was estimated from the void fraction time series of the ECT. Slug frequency was found to decrease with increases in viscosity due to the dominating effect of viscous forces over inertia forces with an increase in drag force. The available slug frequency correlations for gas-liquid flow are essentially based on air-water experiments developed for horizontal flow for low-viscosity data. Therefore, the accuracy of these available models was diverse.

5. References

Abdulkadir, M., V. Hernandez-Perez, I. S. Lowndes, B. J. Azzopardi, and E. Sam-Mbomah. 2016. "Experimental Study of the Hydrodynamic Behaviour of Slug Flow in a Horizontal Pipe." *Chemical Engineering Science* 156: 147–61. <https://doi.org/10.1016/j.ces.2016.09.015>.

Abdulkadir, M., V. Hernandez-Perez, S. Sharaf, I. S. Lowndes, and B. J. Azzopardi. 2010. "Experimental Investigation

- of Phase Distributions of Two-Phase Air-Silicone Oil Flow in a Vertical Pipe.” *World Academy of Science, Engineering and Technology* 61 (January 2019): 52–59.
- Al-Ruhaimani, F., E. Pereyra, C. Sarica, E. Al-Safran, S. Chung, and C. Torres. 2018. “A Study on the Effect of High Liquid Viscosity on Slug Flow Characteristics in Upward Vertical Flow.” *Journal of Petroleum Science and Engineering* 161. <https://doi.org/10.1016/j.petrol.2017.11.047>.
- Al-Safran, Eissa, Ceyda Kora, and Cem Sarica. 2016. “Prediction of Slug Liquid Holdup in High Viscosity Liquid and Gas Two-Phase Flow in Horizontal Pipes.” *Journal of Petroleum Science and Engineering* 133: 566–75. <https://doi.org/10.1016/j.petrol.2015.06.032>.
- Fossa, M., G. Guglielmini, and A. Marchitto. 2003. “Intermittent Flow Parameters from Void Fraction Analysis.” *Flow Measurement and Instrumentation* 14 (4–5): 161–68. [https://doi.org/10.1016/S0955-5986\(03\)00021-9](https://doi.org/10.1016/S0955-5986(03)00021-9).
- Gokcal, B., A. S. Al-Sarkhi, C. Sarica, and E. M. Al-Safran. 2009. “Prediction of Slug Frequency for High Viscosity Oils in Horizontal Pipes.” *Proceedings - SPE Annual Technical Conference and Exhibition* 2 (October): 903–15. <https://doi.org/10.2118/124057-ms>.
- Gregory, G. A., and D. S. Scott. 1989. “Correlation of Liquid Slug Velocity and Frequency in Horizontal Cocurrent Gas-liquid Slug Flow.” *AIChE Journal* 15 (6): 933–35. <https://doi.org/10.1002/aic.690150623>.
- Hazuku, Tatsuya, Tomoji Takamasa, and Yoichiro Matsumoto. 2008. “Experimental Study on Axial Development of Liquid Film in Vertical Upward Annular Two-Phase Flow.” *International Journal of Multiphase Flow* 34 (2): 111–27. <https://doi.org/10.1016/j.ijmultiphaseflow.2007.10.008>.
- Hernandez-Perez, V. 2008. “Hernandez Perez, Valente (2008) Gas-Liquid Two-Phase Flow in Inclined Pipes. PhD Thesis, University of Nottingham.” no. September.
- Heywood, N. I., and J. F. Richardson. 1979. “Slug Flow of Air-Water Mixtures in a Horizontal Pipe: Determination of Liquid Holdup by γ -Ray Absorption.” *Chemical Engineering Science* 34 (1): 17–30. [https://doi.org/10.1016/0009-2509\(79\)85174-X](https://doi.org/10.1016/0009-2509(79)85174-X).
- Liu, Dingsheng, and Shudong Wang. 2008. “Flow Pattern and Pressure Drop of Upward Two-Phase Flow in Vertical Capillaries.” <https://doi.org/10.1021/ie070901h>.
- Omar, Rajab, Buddhika Hewakandamby, Abdelwahid Azzi, and Barry Azzopardi. 2018. “Fluid Structure Behaviour in Gas-Oil Two-Phase Flow in a Moderately Large Diameter Vertical Pipe.” *Chemical Engineering Science* 187: 377–90. <https://doi.org/10.1016/j.ces.2018.04.075>.
- Saidj, Faiza, Abbas Hasan, Hiba Bouyahiaoui, Ammar Zeghloul, and Abdelwahid Azzi. 2018. “Experimental Study of the Characteristics of an Upward Two-Phase Slug Flow in a Vertical Pipe.” *Progress in Nuclear Energy* 108 (March): 428–37. <https://doi.org/10.1016/j.pnucene.2018.07.001>.
- Zabaras, G J. 2000. “Prediction of Slug Frequency for Gas/Liquid Flows .” *SPE J* 5: 252–258.

HEAT TRANSFER AND PRESSURE DROP MEASUREMENTS OF A NOVEL BAFFLE HEAT SINK FOR POWER ELECTRONICS COOLING

Ilya T'Jollyn^{a,b,c,*}, Jana Rogiers^{b,c}, Jasper Nonneman^{b,c}, Michel De Paepe^{b,c}

^aUniversity of Antwerp, Groenenborgerlaan 171, Antwerp, Belgium

^bGhent University, Sint-Pietersnieuwstraat 41, Ghent, Belgium

^cFlandersMake@UGent – Core lab MIRO, Gaston Geenslaan 8, Leuven, Belgium

*Ilya.TJollyn@UAntwerpen.be

Keywords: Heat transfer, Electronics cooling, E-Fluid, Oil cooling

1. INTRODUCTION

Electric vehicles (EVs) are experiencing rapid adoption in the automotive sector due to their reduced environmental impact, primarily attributed to lower emissions (Pevac et al., 2019). However, a significant drawback of current-generation EVs is their limited driving range (Kempton, 2016). One potential solution is to improve the compactness of the drivetrain, as a more compact and lighter drivetrain contributes to overall system efficiency. Nonetheless, this adjustment leads to increased power dissipation per unit volume, which presents challenges in cooling the drivetrain components. Typically, the drivetrain comprises the battery, motor, gearbox, and power electronics (Rajashekara, 2013). The power electronics convert DC voltage and current from the battery into an AC waveform to drive the electric motor.

Traditionally, forced liquid cooling using a water-glycol mixture is utilized to cool the power electronics (Rogiers et al., 2022). Consequently, two separate liquid circuits are integrated into the drivetrain: an oil lubrication circuit and a water-glycol coolant circuit. An approach to enhance drivetrain compactness involves merging these circuits by using lubrication oil to cool both the power electronics and the motor. However, the fluid properties of oil (lower thermal conductivity and specific heat capacity and higher viscosity) are inherently worse than those of water-glycol in terms of heat transfer efficiency. This presents significant challenges for cooling the power modules in the power electronics unit, as very high heat fluxes are encountered here. Conventional heat sink designs (for water-glycol) are not optimized for oil flows, as the flows tend to be laminar compared to the turbulent flows of water-glycol. The 3D flow behaviour inherent to turbulent flows needs to be induced by the heat sink geometry for laminar flow to prevent the buildup of thermal boundary layers that impede effective heat transfer. In this study, a novel geometry incorporating baffles in four directions is proposed. Two baffle heat sinks with different geometrical parameters are tested and compared to a state-of-the-art benchmark heat sink design.

2. EXPERIMENTAL SETUP

The setup to determine the baffle heat sink performance has been used and described in previous work for other heat sinks (Rogiers et al., 2022). The description of the setup is summarized here for the comprehension of the reader.

A conditioning circuit is used to provide a controlled oil flow to the heat sink. The inlet temperature is set to 65 °C, while the flow rate is varied from 2 to 13 l/min. The e-fluid used in the setup is Evogen5191SA and its thermophysical properties at 65 °C are given in Table 1.

Table 1. Fluid properties at 65 °C.

Density	Specific heat capacity	Thermal conductivity	Kinematic viscosity
797 kg m ⁻³	2200 J kg ⁻¹ K ⁻¹	0.14 W m ⁻¹ K ⁻¹	17 10 ⁻⁶ m ² s ⁻¹

To evaluate the heat sinks, a test section is designed with the intention of precisely applying the required heating power and accurately determining the heat sink base temperature. The illustration in Fig. 1 depicts the test section comprising two polyoxymethylene (POM) components (labelled as 1 and 2) secured together with bolts (labelled as 4), enclosing an aluminium heater block (labelled as 3). The lower part of this heater block is machined to achieve the desired heat sink geometry. Within this heater block, three cylindrical cartridge heaters simulate the heat dissipation from the power electronics, which is set to 500 W. O-rings are used to avoid oil leakage (at the locations labelled as 6 and 7). The direction of oil flow is indicated by solid white arrows, passing through a flow straightener (labelled as 5), beneath the base of the heater block, and again through another flow straightener.

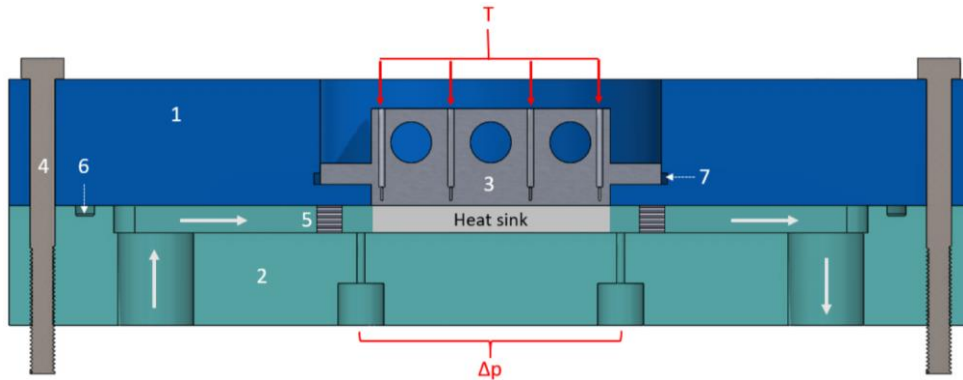


Figure 1. Test section.

Several measurements are done to evaluate the heat sink performance. Notably, the pressure drop across the heat sink (Δp) is gauged using two small pressure tappings positioned before and after the heat sink. Additionally, eight K-type thermocouples measure the temperature (T) immediately above the base of the heater block. Upstream and downstream of the test section, the oil temperature is measured after the flow passes a mixer segment, ensuring uniform temperature distribution of the oil across the tube. Moreover, the oil flow rate is determined by a Coriolis flow meter.

The innovative baffle heat sink features numerous parallel channels with baffles oriented in four directions. These baffles direct the flow to the right, bottom, left, and top, inducing a swirling motion to prevent the accumulation of thick thermal boundary layers. Additionally, the baffles increase the heat transfer area, effectively acting as fins. The heat sink is made by milling, which allows to generate the baffles parallel to the base and pointing away from the base. For the baffles pointing towards the base, a separate part is made which fits onto the main part. Both parts are shown in Fig. 2. A close-up of the baffles after assembly of both parts is shown in Fig. 3.

Two variations of the baffle heat sink are tested. The base area is for both cases equal to 56 mm (streamwise width) by 57 mm (streamwise length) and the used material is aluminium with a thermal conductivity of 140 W/mK. The dimensions of these heat sinks are given in Table 2 and the letters used for the dimensions are indicated in Fig. 3.

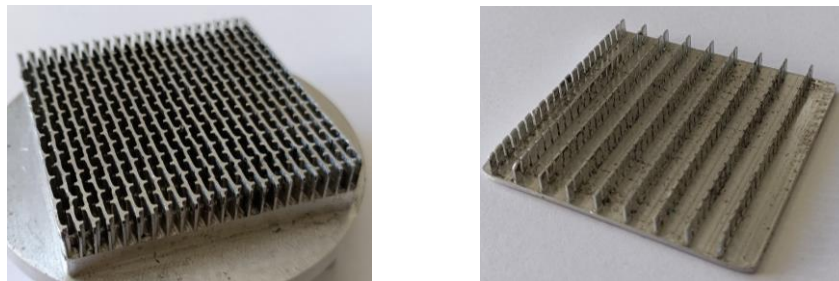


Figure 2. Heat sink with baffles parallel to and pointing away from the base (left) and separate part with baffles pointing towards the base.

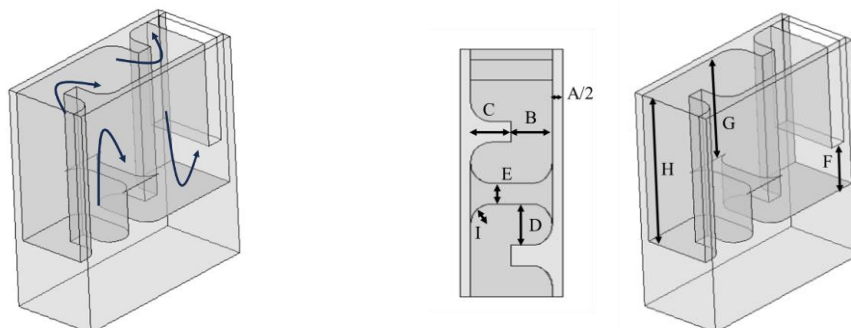


Figure 3. Close-up of the repetitive baffle section with oil flow indicated (left) and its geometric parameters (middle and right).

Table 3. Geometric parameters of the baffle heat sinks.

Parameter	A	B	C	D	E	F	G	H
Baffle 1	0.3 mm	1.2 mm	1 mm	1.2 mm	0.3 mm	2.6 mm	4 mm	6.5 mm
Baffle 2	0.5 mm	0.5 mm	0.5 mm	0.8 mm	0.7 mm	1.8 mm	2.1 mm	4 mm

3. MEASUREMENT RESULTS

Both baffle heat sink designs are tested experimentally and compared to a state-of-the-art benchmark heat sink. This benchmark heat sink is a pin fin heat sink, optimized for laminar oil flows (Vander Heyde et al., 2021) and tested on the same setup (Rogiers et al., 2022). A trade-off is at work for the optimal heat sink design: pressure drop and pumping power should be as low as possible, while also base temperature and thermal resistance are preferably minimized. Pumping power is calculated as the product of volumetric flow rate and pressure drop, while the thermal resistance (R) is determined using the following equation, taking into account the conductive temperature drop in the aluminium:

$$R = \frac{T_{TC,avg} - T_{in}}{Q} - \frac{d}{kA} \quad (1)$$

In Eq. (1), $T_{TC,avg}$ is the area-weighted average of the temperatures measured by the thermocouples, T_{in} is the oil inlet temperature, Q is the heat dissipation, d is the distance between the thermocouple tip and the heat sink base, k is the aluminium thermal conductivity and A is the base area.

The measured pressure drop of the baffles heat sinks and the pin fin benchmark as a function of flow rate are shown in Fig. 4 (left). As expected, pressure drops are significantly higher for the baffle heat sinks, as they inherently disturb the flow more and also have a much larger wetted area. Although the flow is laminar, pressure drop increases more than linearly with flow rate due to the swirling motion induced by the perturbation on the flow. The thermal resistance of the heat sinks as a function of flow rate is shown in Fig. 4 (middle). Both baffle heat sinks exhibit significantly lower thermal resistances than the pin fin heat sink. The thermal resistance of all heat sinks decreases considerably with the flow rate.

To evaluate the trade-off between hydraulic and thermal performance, Fig. 4 (right) shows the thermal resistance as a function of the pumping power for all three heat sinks. The best performing heat sinks will have a curve closer to the origin of the axis, indicating both low thermal resistance and low pumping power. The first baffle heat sinks performs slightly worse than the benchmark pin fin heat sink, but the second baffle heat sink clearly outperforms the benchmark. This indicates both that the novel baffle heat sink has potential to be a highly effective solution and that the design of the geometrical parameters of the baffle heat sink is crucial for thermohydraulic performance.

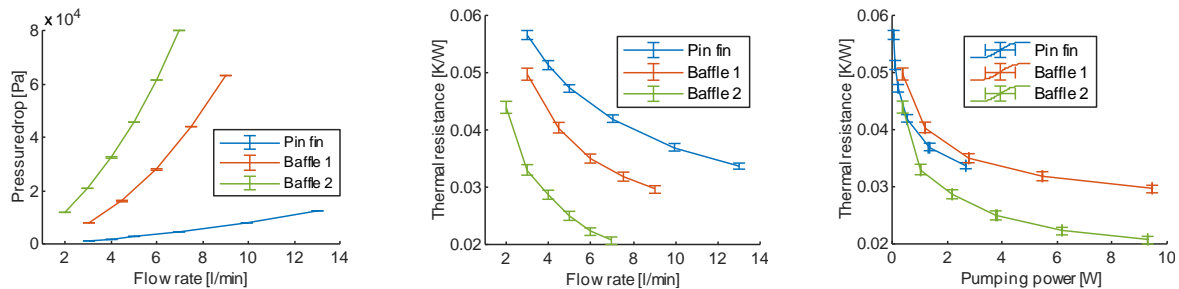


Figure 4. Thermal resistance (left) and pressure drop (middle) as a function of flow rate and thermal resistance as a function of pumping power (right).

4. CONCLUSIONS

A novel baffle heat sink for power electronics cooling using laminar oil flows is proposed and experimentally tested in this work. The baffles in four directions produce a swirling motion to break up thermal boundary layers and enhance heat transfer. The baffle heat sink can outperform an optimized pin fin heat sink with a lower thermal resistance at equal pumping power, but a proper design of the baffle geometric parameters is required.

5. REFERENCES

- Kempton, W., 2016. "Electric vehicles: Driving range". *Nature Energy*, Vol. 1, pp. 1–2.
- Pevec, D., Babic, J., Podobnik, V., 2019. "Electric Vehicles: A Data Science Perspective Review". *Electronics*, Vol. 8, pp. 1190.
- Rajashakara, K., 2013. "Present Status and Future Trends in Electric Vehicle Propulsion Technologies". *IEEE Journal of Emerging and Selected Topics in Power Electronics*, Vol. 1, pp. 3–10.
- Rogiers, J., T'Jollyn, I., Schoonjans, T., Nonneman, J., De Paepe, M., 2022. "Experimental Study on the Thermohydraulic Performance of Oil-Cooled Heat Sinks for Power Electronics". In *Proceedings of the 2022 28th International Workshop on Thermal Investigations of ICs and Systems (THERMINIC)*. Edinburgh, United Kingdom.
- Vander Heyde, J., T'Jollyn, I., Rogiers, J., Schoonjans, T., Nonneman, J., Schlimpert, S., De Paepe, M., 2021. "A Comparison of the Thermohydraulic Performance of Oil-Cooled Heat Sink Geometries for Power Electronics". In *Proceedings of the 2021 27th International Workshop on Thermal Investigations of ICs and Systems (THERMINIC)*. Berlin, Germany.

2C-2D PIV/PTV Measurements of High Reynolds Number Turbulent Channel Flow with Sub-Viscous-Length Wall-Normal Resolution

Julio Soria^a, Bihai Sun^{*}, Callum Atkinson

^aLaboratory for Turbulence Research in Aerospace & Combustion (LTRAC), Department of Mechanical and Aerospace Engineering, Monash University, VIC 3800, Australia

*Bihai.sun@monash.edu

Keywords: Particle Image Velocimetry, High Spatial Resolution, Turbulent Channel Flow

1. INTRODUCTION

Fully-developed turbulent channel flow is a canonical wall-bounded turbulent shear flow that is highly significant to the study of wall-bounded turbulence. The flow is statistically homogeneous in both the spanwise and streamwise directions, resulting in no spatial growth of the shear flow in the flow direction. Nevertheless, experimental studies of the turbulent channel flow are less common compared to other canonical flow configurations like turbulent boundary layer and fully developed pipe flow, partially due to the required larger footprint of the experimental facility (Monty and Chong, 2009). To maintain nominally two-dimensional flow in the channel centreline, the experimental facility requires a high aspect ratio, leading to an order of magnitude larger cross-sectional area in comparison to a turbulent pipe flow experimental facilities with the same Reynolds number (Schultz and Flack, 2013). The high spatial resolution PIV measurement along the channel centreline also presents some complexities in the experiment as the high spatial resolution measurement necessitates a high magnification of more than unity, as well as a long working distance of the lens so that the optical system can be placed outside the tunnel. None of the commercially available macro lenses offer the ability to meet both criteria, requiring a unique optical setup for this experiment. Furthermore, the tunnel needs to be heavily seeded to ensure sufficient particles in each PIV interrogation window for high-fidelity measurements. However, this heavy seeding results in the seeding particles between the measurement plane and the lens scattering the light from the laser sheet, which results in a reduction of the measurement's signal-to-noise ratio. This paper presents a two-component, two-dimensional hybrid particle image/tracking velocimetry (2C-2D PIV/PTV) for the turbulent channel flow that overcomes these obstacles to enable high spatial resolution measurement.

2. EXPERIMENTAL METHODOLOGY

The experiment was conducted in the LTRAC high-speed water channel. The test section of the water channel is 1.6 m long in the streamwise direction, 700 mm wide in the spanwise direction and 20 mm high in the wall-normal direction, corresponding to a channel half-height, h , of 10 mm. Due to the high aspect ratio of the cross-section, the side walls have a negligible effect on the flow along the centreline of the channel flow, and the flow along the centreline of the channel nominally is two-dimensional in the mean (Vinuesa et al., 2014). The water channel is constructed using a stainless steel frame with glass on all four sides, providing full optical access to the channel flow. The water channel is powered by a 5.5 kW motor driving a centrifugal water pump. The water from the pump flows into a settling chamber, which holds 200 litres of water and contains four grids and a honeycomb flow straightener to reduce the turbulence level of the inflow. The flow then goes through a 10-to-1 contraction and a boundary layer trip before entering the channel test section. The PIV measurement domain is 1.5 m ($150 h$) downstream of the trip to ensure a fully developed channel flow. At this location, the frictional Reynolds number, Re_{τ} , is estimated to be 1,400, and the viscous length scale, l^+ , is estimated to be $8 \mu\text{m}$. The field of view of the experiment is in the wall-normal -- streamwise direction along the centreline of the channel, which extends the full wall-normal extent of the channel and is 24.5 mm ($2.45 h$) in the streamwise direction. The field of view is illuminated by an InnoLas Compact 400 PIV lamp pumped Nd:YAG laser, with the flow seeded using hollow glass spheres of $11 \mu\text{m}$ diameter.

The PIV image pairs were obtained using two Emergent HZ-100-G-M cameras. These cameras have a CMOS sensor measuring 36.1 mm wide and 29.4 mm high, with a total of 103 million ($11,276 \times 9,200$) pixels. As these cameras do not have a double shutter, a beam splitter is used to match the fields of view of the two cameras, which capture each of the single-exposed PIV images. The large image sensor of these cameras presents a challenge for camera position calibration, as the error introduced by lens distortion near the corners of the imaging sensor can be of the order of 10 pixels. To avoid unacceptable uncertainties caused by lens calibration, a lens-less imaging registration system based on a holographic technique was developed. Unlike conventional imaging, holography belongs to the class of coherent imaging, where the illumination light is a coherent light with a planar wavefront provided by a laser. When a target is placed in the light path, the interference pattern between the scattered light of the camera and the illumination light is recorded by the camera, resulting in the recording of a hologram. Using this technique, it is possible to trace back the incident angle of the imaging

light as well as the relative position between the target and each of the two cameras without distortion introduced by a lens. With this method, the relative position in all three translational axes can be estimated and obtained with low uncertainty and high precision.

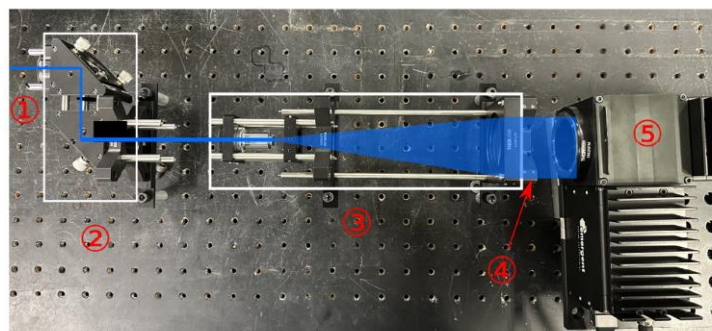
The magnification of the imaging system is 1.47, and the object plane is 350 mm away from the side wall of the water channel, which is longer than the working distance of any available macro lens. Therefore, a telephoto lens was used in the experiment, with the lens located just outside the water channel and the camera positioned about 500 mm away from the lens, as shown in figure 1(b). This optical setup greatly reduces the numerical aperture of the imaging system. Therefore, a large aperture lens, Nikon 400mm f/2.8, is used for the optical PIV imaging system. To increase the signal-to-noise ratio of the PIV images and, at the same time, ensure the measurement volume is adequately seeded, a selective seeding device is used to seed near the central line of the tunnel only. The PIV images are analysed using an in-house multigrid/multipass PIV/PTV algorithm (Soria, 1996), and the PTV velocity vectors are organised into bins that are 0.6 viscous length in height and cover the whole streamwise domain of the measurement. The PTV velocity vectors are corrected for lens distortion using the method described by Sun et al. (2021) before being used for statistics calculation.



(a)



(b)



(c)

Figure 1. (a) A photo of the LTRAC high-speed water channel. 1: settling chamber 2: contraction 3: test section 4: seeding chamber 5: particle filter 6: axillary pump for the filter 7: main pump.
 (b) A photo of the imaging optical setup. 1: first camera 2: second camera 3: (inside the mount) beam splitter 4: 400mm f/2.8 lens 5: mirror to image inside the channel.
 (c) Holographic calibration setup for the two cameras behind a beam splitter. Notice that the illumination light incidents directly onto the imaging sensors of the cameras without a lens. 1 (not shown): solid-state laser 2: beam tilting optics 3: beam expanding and collimating optics 4 (in mount): calibration target 5: cameras

3. RESULTS

The first and second-order statistics of the turbulent channel flow in-plane velocity components in the streamwise and wall-normal direction are presented in figure 2. Due to the symmetry of the flow, the velocity fields from both walls contribute to the velocity statistics. The measured profiles are compared with the first and second-order velocity statistics calculated from a DNS dataset of $Re_\tau = 1,000$ (Lee and Moser 2015).

Since the measurement point closest to the wall is within the viscous sublayer, the mean velocity gradient at the wall can be directly computed from the mean velocity profile. The positions of the walls and the half channel height can be accurately determined by identifying the reflection point in the mean velocity profile, as particles mirrored by the wall are also in the field of view. As a result, the friction Reynolds number for the flow can be accurately determined.

More data are being processed for higher spatial resolution profiles, and further results and discussion will be presented at the conference.

Table 1. Experimental measurements of the flow condition

Re_τ	1,427
U_{CL}	3.01 m/s
h	11.41 mm
u_τ	0.13 m/s

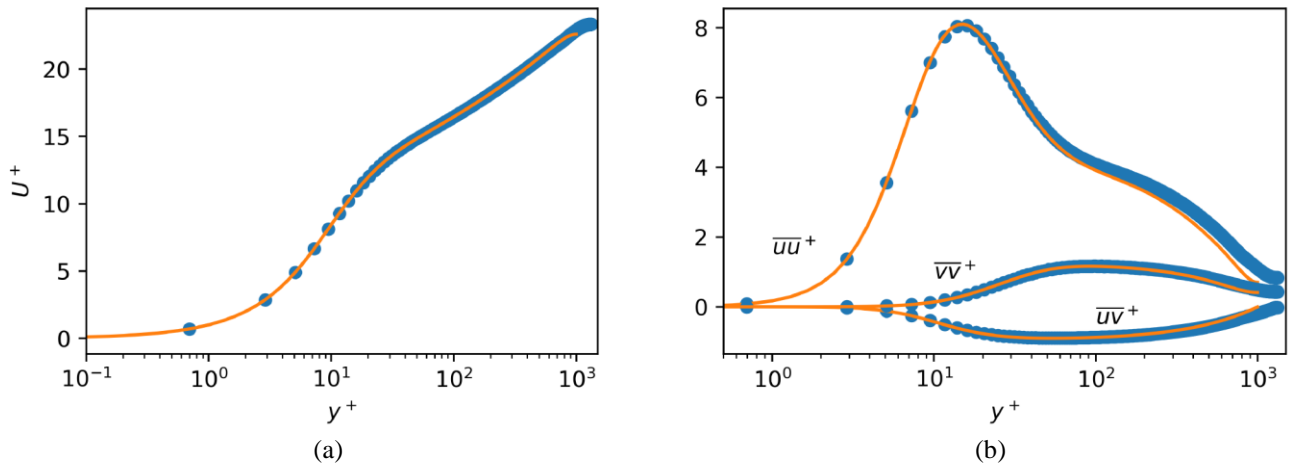


Figure 2. — Profile from DNS of $Re_\tau = 1,000$ (Lee and Moser 2015). ● experimental measurement.
(a) mean velocity profile. (b) Reynolds stress profiles.

5. REFERENCES

- Myoungkyu Lee and Robert D. Moser., 2015 “Direct numerical simulation of turbulent channel flow up to $Re_\tau \approx 5200$ ”. *Journal of Fluid Mechanics*, Vol. 774, pp. 395–415.
- J. P. Monty and M. S. Chong., 2009 “Turbulent channel flow: comparison of streamwise velocity data from experiments and direct numerical simulation”. *Journal of Fluid Mechanics*, Vol. 633, pp. 461–474.
- M. P. Schultz and K. A. Flack., 2013 “Reynolds-number scaling of turbulent channel flow”. *Physics of Fluids*, Vol. 25, pp. 025104.
- Julio Soria., 1996 “An investigation of the near wake of a circular cylinder using a video-based digital cross-correlation particle image velocimetry technique”. *Experimental Thermal and Fluid Science*, Vol. 12, pp. 221–233.
- Bihai Sun, Muhammad Shehzad, Daniel Jovic, Christophe Cuvier, Christian Willert, Yasar Ostovan, Jean-Marc Foucaut, Callum Atkinson, and Julio Soria., 2021 “Distortion correction of two-component two-dimensional PIV using a large imaging sensor with application to measurements of a turbulent boundary layer flow at $Re_\tau = 2386$ ”. *Experiments in Fluids*, Vol. 62, pp. 183.
- Ricardo Vinuesa, Azad Noorani, Adrián Lozano-Durán, George K. El Khoury, Philipp Schlatter, Paul F. Fischer, and Hassan M. Nagib., 2014 “Aspect ratio effects in turbulent duct flows studied through direct numerical simulation”. *Journal of Turbulence*, Vol. 15, pp. 677–706

DEVELOPMENT OF FILM-TYPE SURFACE TEMPERATURE SENSOR BASED ON FLUORESCENCE POLARIZATION

Reiko Kuriyama^{a,*}, Takao Ueda^a, and Kazuya Tatsumi^a

^a Kyoto University, Kyotodaiagku-katsura, Nishikyo-ku, Kyoto 615-8540, Japan

*kuriyama.reiko.2m@kyoto-u.ac.jp

Keywords: Surface temperature, Film-type sensor, Fluorescence polarization, Brownian rotation

1. INTRODUCTION

Surface temperature measurement plays an important role in a variety of situations, such as detecting abnormal heat generation in electronic devices, evaluating heat transfer in heat exchanger piping and monitoring temperature in the manufacturing process. It is, however, not easy to measure surface temperature distribution with high accuracy and high spatial resolution. For example, infrared thermography can visualize surface temperature in non-contact manner, but it is difficult to accurately determine the emissivity of the object to be measured. A sheet-type sensor made of thermochromic material, which changes its hue at a specific temperature, is powerful tool for easily visualizing surface temperature (Eiamsa-ard *et al.*, 2015). However, the temperature range of color change is usually narrow (~ 10 °C) and accuracy remains an issue. Another method is to use an array of point sensors such as thermocouples and thermistors (Huang *et al.*, 2013), but the spatial resolution is relatively low depending on their sensor size.

In the present study, we propose a new film-type sensor for surface temperature measurement (Fig. 1). The sensor consists of two transparent polydimethylsiloxane (PDMS) films, between which a fluorescent dye solution is sealed. By attaching this sensor to the surface to be measured and measuring the temperature of the fluorescent dye solution inside the sensor using fluorescence polarization method (Suzuki *et al.*, 2017, Tatsumi *et al.*, 2017, Kuriyama *et al.*, 2021), the temperature distribution of the target surface is measured. The sensor is approximately 400 μm thick, flexible, and self-adhesive. Therefore, it can be applied to curved surfaces and can be attached and detached easily. This paper experimentally investigates the temperature sensitivity of the sensor by polarization measurement to examine the feasibility of the proposed method. We also attempt to visualize surface temperature distribution of a cover glass where a linear temperature gradient is formed.

2. MEASUREMENT PRINCIPLE

Fluorescence polarization method exploits the depolarization phenomenon due to the rotational Brownian motion of fluorescent molecules. When randomly oriented fluorescent molecules are irradiated by a linearly polarized excitation light, the probability of the absorption is proportional to the value $\cos^2\theta$, where θ is the angle between the directions of excitation polarization and absorption moment of the molecules. If the excited molecules are suspended in liquid, they experience rotational Brownian motion during the fluorescence lifetime. Consequently, the directions of emission moments, which are generally parallel to the absorption moments, are randomized. Depolarization of fluorescence is therefore observed with the degree according to the extent of their rotation.

The degree of polarization can be evaluated by polarization degree $P = (I_{\parallel} - I_{\perp}) / (I_{\parallel} + I_{\perp})$, where I_{\parallel} and I_{\perp} are the fluorescence intensities of the components that are parallel and perpendicular to the excitation polarization, respectively.

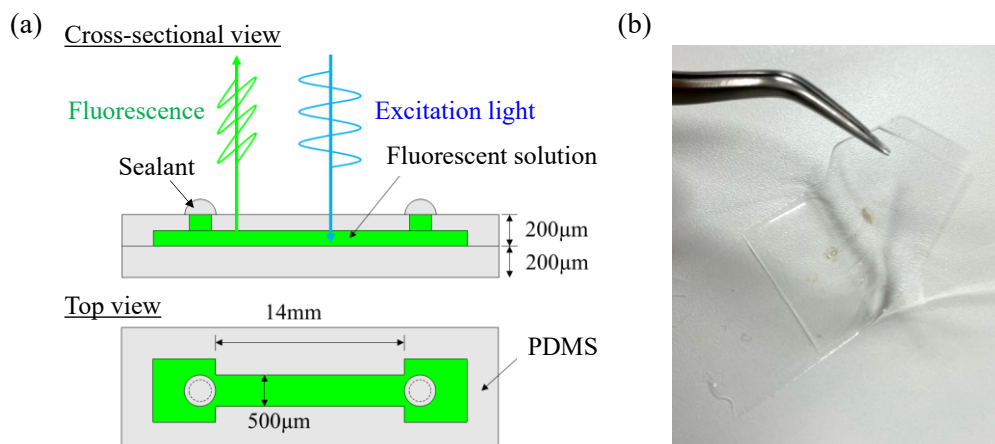


Figure 1. (a) Structure and (b) photograph of film-type surface temperature sensor.

Since P is normalized by the total fluorescence intensity and follows the rotational motion of the molecules only, fluorescence polarization measurement is robust to the spatio-temporal variation in fluorescence intensity. Perrin (1926) theoretically derived the equation which relates P to the fluorescence lifetime τ and the rotational diffusion of fluorescent molecules as:

$$\left(\frac{1}{P} - \frac{1}{3}\right) = \left(\frac{1}{P_0} - \frac{1}{3}\right) \left(1 + \frac{k_B T}{\mu V} \tau\right) \quad (1)$$

where P_0 is the intrinsic polarization (generally ~ 0.5), k_B is the Boltzmann constant, and V is the hydrodynamic volume of the fluorescent molecule. T and μ are the absolute temperature and viscosity of the fluid, respectively. From Eq. (1), the reciprocal of P shows a linear relation with T/μ , if V and τ remains constant during the measurement.

3. EXPERIMENTAL METHODS

Figure 2 shows the experimental setup for fluorescence polarization measurement. The light from LED (Thorlabs; M490L4) was linearly polarized by a polarizer and focused to the sample placed on a temperature controlling stage. The fluorescence was collected by an objective lens (Olympus; LMPlanFLN, 10 \times) and detected by a polarization camera (Baumer; VCXG-50MP). Fluorescence mirror unit (Olympus, U-MWIB3) was used for the measurement. The exposure time and the frame rate were set at 750 ms and 1 fps, respectively, and 100 images were collected for each condition.

In the present study, aqueous glycerol solution containing uranine was used in the sensor. Uranine was dissolved in 80 wt% aqueous glycerol solution at a concentration of 100 mM. Since the fluorescence intensity of uranine depends on pH and is higher when $\text{pH} \geq 9$, the pH of the solution was maintained around 10 by adding 3 mM carbonate-bicarbonate buffer solution. PDMS sheets were made by spin-coating method. Mixture of liquid PDMS and cure agent was poured onto a bare glass and a glass with SU-8 micro-pattern, and spin coated at 500 rpm. After curing, the plain and patterned PDMS sheets were peeled off from the glass and bonded together. The uranine solution was introduced between the PDMS sheets with a syringe, and the inlet was sealed with sealant. The thickness of each PDMS sheet and solution layer was about 200 μm and 100 μm , respectively.

4. RESULTS AND DISCUSSION

The relationship between temperature and polarization degree P was obtained by polarization measurement. A cover glass was placed on the temperature controlling stage and a film-type sensor was attached on the glass surface. The stage temperature was changed in the range of 20–40 $^{\circ}\text{C}$ and monitored by thermocouples. Polarization degree was calculated for each super-pixel, which is a set of 2 \times 2 neighboring pixels with different polarization orientations, and averaged.

Figure 3 shows the measurement result. Each plot shows the spatially averaged value of the polarization degree and different colors indicate different experimental days. Note that a new sensor was prepared for each day. The solid line in Fig. 3 shows the fitting line obtained by least squares regression for all experimental data and the dotted line represents the theoretical curve calculated by Eq. (1). The measured P values generally agree well with the theoretical value and decrease almost linearly with temperature in the range of 20–40 $^{\circ}\text{C}$. The decreasing rate of P with T was about 1.7%/ $^{\circ}\text{C}$, which is slightly smaller than the theoretical prediction. The estimated standard error of the measured P to the fitting line is about 2.6 $^{\circ}\text{C}$.

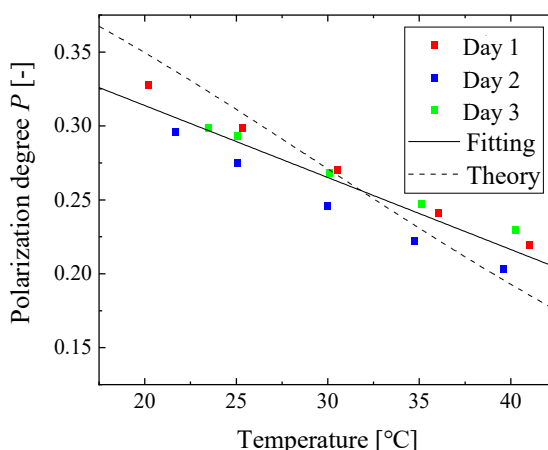
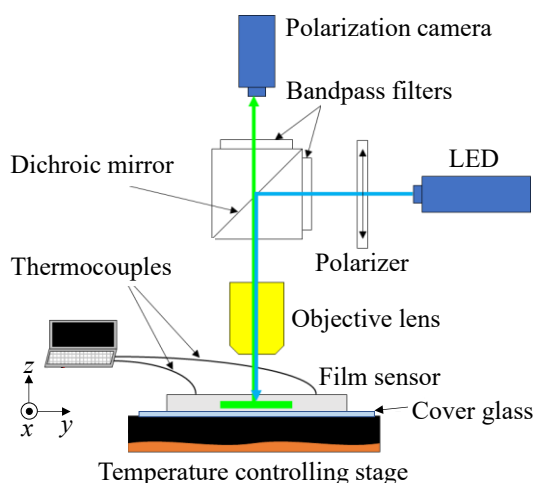


Figure 2. Schematic of the experimental setup.

Figure 3. Relationship between temperature and polarization degree.

Figure 4(a) shows the top view of the test section of the temperature distribution measurement. A cover glass was placed across the two stages with different temperatures: one stage was heated to 40 °C using a Peltier element, while the other stage was left unheated. There was a 2.4 mm gap between the two stages, and thus a temperature gradient was formed in the cover glass in this region. The film-type sensor was attached onto the cover glass and polarization measurement was conducted after the temperature reached steady state. The polarization degree distribution was converted to temperature distribution by applying the calibration result which was previously obtained pixel-by-pixel using the same film sensor.

Figure 4(b) shows the measurement result. The temperature gradient in the y direction is visualized successfully by using the film-type sensor. The spatial resolution was $0.69\ \mu\text{m} \times 0.69\ \mu\text{m}$, which was calculated from system magnification and the size of a super-pixel. However, the temperature measured by the film-sensor was lower than that expected from thermocouple measurements by 5–10 °C. This may be attributed to the effect of reflection of excitation light at the stage surface. In the calibration experiment, the sensor (on a cover glass) was placed in the center of the heating stage, whereas in the temperature distribution measurement, it was placed between the two stages. This may have caused a difference in measured P value due to a difference in the reflection of excitation light from the stage surface. Another possible cause is the effect of evaporation of the solution. The temperature distribution in Fig 4(b) was measured about 20 minutes after the start of stage heating. Therefore, the viscosity of the solution inside the sensor may have increased due to evaporation during heating, resulting in a larger polarization degree.

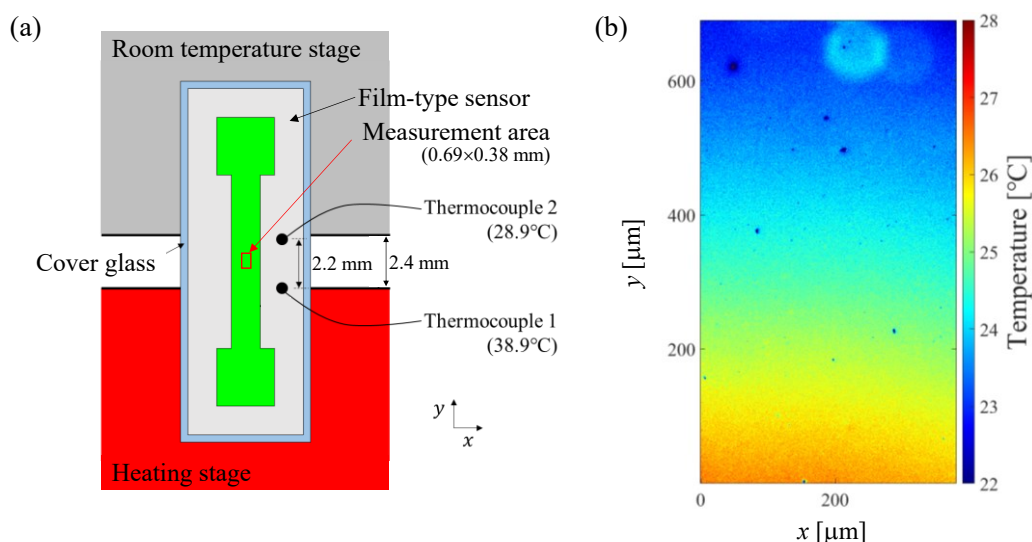


Figure 4. (a) Top view of the test section and (b) surface temperature distribution obtained by using film-type sensor.

5. CONCLUSIONS

The present study proposed a new film-type surface temperature sensor based on fluorescence polarization measurement and examined the feasibility of the method. The polarization degree of uranine glycerol solution decreased with temperature with the sensitivity of $1.7\%/^{\circ}\text{C}$ in the range of 20–40 °C. The linear temperature gradient formed in a cover glass was visualized by the proposed method, but the measured temperature was lower than the measurement result of thermocouples. We will examine the effects of excitation light reflection from the target surface and solution evaporation on the polarization degree.

6. REFERENCES

- Eiamsa-ard, S., Nanan, K., and Wongcharee, K., 2015. "Heat transfer visualization of co/counter-dual swirling impinging jets by thermochromic liquid crystal method," *Int. J. Heat Mass Trans.*, Vol. 86, pp. 600–621.
- Huang, C.-C., Kao, Z.-K., and Liao, Y.-C., 2013. "Flexible miniaturized nickel oxide thermistor arrays via inkjet printing technology," *Appl. Material Interfaces*, Vol. 5 pp. 12954-12959.
- Suzuki, A., Tatsumi, K., Horii, S., Kuriyama R., and Nakabe, K., 2017, "Temperature measurement in microchannel liquid flow by measuring fluorescence polarization," *Trans. JSME, B* (in Japanese), Vol. 83, No.853, 17-00200.
- Tatsumi, K., Hsu, C.-H., Suzuki, A., and Nakabe, K., 2017, "Liquid temperature measurement method in microchannels by using fluorescence polarization," *Heat Mass Trans.*, Vol. 54, No. 8, pp. 2607-2616.
- Kuriyama, R., Nakagawa, T., Tatsumi, K., and Nakabe, K., 2021, "Two-dimensional fluid viscosity measurement in microchannel flow using fluorescence polarization imaging," *Meas. Sci. Technol.*, Vol. 32, No. 9, 095402 (14pp).
- Perrin, F., 1926, "Polarisation de la lumière de fluorescence. Vie moyenne des molécules dans l'état excité. Vie moyenne des molécules dans l'état excité," *Journal de Physique.*, Vol. 7, No. 12, pp. 390–401.

INTERMITTENCY OF FLOW MEANDERING IN A GAP OF A MODEL OF A PERIPHERAL SUBCHANNEL OF A FUEL ROD ASSEMBLY

Maxim Shestakov^a, Mikhail Tokarev^{a,*}

^aInstitute of Thermophysics SB RAS, Lavrentyev ave. 1, 630090 Novosibirsk, Russia

*mikxael@gmail.com

Keywords: turbulent flow, channels of complex shape, PIV, POD, flow meandering, fuel rod assembly, tight lattice, narrow gap, coolant hydrodynamics

1. INTRODUCTION

In the field of nuclear energy, heat exchangers based on a bundle of tubes or rods, such as steam generators or fuel assemblies, are widely used. The fuel assembly typically consists of a bundle of fuel elements in the form of cylindrical rods. The free space between the rods forms a system of subchannels connected by gaps between the rods. Fuel assemblies (FA) with tight lattice rod bundles are considered promising for increasing the conversion rate and heat transfer in small modular reactors. One of the key challenges in the design of small modular reactors is minimizing the reactor core, and a tight lattice could offer a potential solution to this problem.

The arrangement of a tight lattice rod bundle is characterized by the relative pitch of the rods, which is the ratio of the distance between the rod centers (P) to the rod diameter (D). With a longitudinal flow around a rod bundle, the main part of the coolant flows in the subchannels, and the exchange of coolant between the subchannels is ensured by gaps. Studies of the flow structure in these gaps have revealed a significant influence of the P/D ratio on the flow structure, particularly on turbulence intensity, shear stress, and kinetic energy. Large-scale quasi-periodic oscillations of longitudinal and transverse velocities have been observed in the gaps between the rods (Meyer, 2010). Depending on the relative P/D ratio, the amplitude of transverse velocity oscillations can reach 10% or more of the mean flow rate velocity, which is notably higher than that of the secondary flow. The frequency of large-scale velocity oscillations in the gap increases with the flow velocity, while it decreases with the gap width. The Strouhal number, calculated from the rod diameter and the friction velocity ($Sh = fD/u^*$), is independent of the Reynolds number

The generation of large-scale velocity oscillations in the gap is studied in (Möller, 1991), which proposes a flow model where these oscillations occur due to the formation of large-scale vortex structures moving in a staggered order along the gap. According to this model, large-scale vortex structures are formed as a result of flow instability development at the gap boundaries. Numerical modeling of vortex structures in a tight lattice, conducted using the URANS approach and anisotropic turbulence models, demonstrated that the flow structure and the characteristics of vortex structures in the gap are influenced by the Re number and the relative P/D pitch (Yu et al., 2011; Yan et al., 2012). It was observed that as the relative P/D pitch increases, the scale of coherent vortex structures becomes smaller, and the location becomes irregular. Additionally, the coherent vortex structures are less discernible at $P/D = 1.2$. In Yu et al. (2011), a critical value of the relative pitch was proposed: $P/D = 1.03$; with an increase or decrease in P/D relative to this value, the coherence of vortex structures weakened.

The generation of large-scale quasi-periodic oscillations in the gap results in an increased mixing of the flow between the subchannels and enhanced heat transfer from the fuel element to the coolant, contributing to a more uniform transverse distribution of the coolant temperature in the fuel assembly. Large-scale quasiperiodic oscillatory cross-stream velocity in gaps, caused by the propagation and merging of vortex structures, can lead to the synchronization of inter-subchannel exchange (Tavoularis, 2011). The emergence of large-scale quasiperiodic vortex structures enhances inter-subchannel exchange (mixing) between subchannels.

This study presents findings from a comprehensive experimental and numerical investigation of the unsteady hydrodynamic structure of flow within a gap formed by a cylinder and a flat wall, which models the peripheral cell of a fuel assembly. The experiments were conducted using high temporal resolution particle image velocimetry (PIV) techniques (Shestakov and Tokarev, 2023), while high-fidelity numerical data (Li et al., 2024) was employed for machine learning calibration methods of enhanced RANS models for complex geometries.

2. METHODS AND RESULTS

The experiments were carried out on a test setup in the form of a rectangular plexiglass channel with three plexiglass tubes, representing the cases of dense ($D = 13$ mm) and sparse ($D = 10$ mm) packing, as shown in Fig. 1. The formed channel sections are schematically illustrated in Fig. 1b. The channel has a length of 400 mm, while the plexiglass tube measures 295 mm in length. The distance between the tube centers is $P = 14$ mm, resulting in relative pitches of $S = P/D = 1.077$ and 1.4, respectively. The gap between the channel wall and the tubes measures 2 mm for $S = 1.077$ and 4 mm for $S = 1.4$. Distilled water is used as the working fluid. The temperature of the working fluid is consistently maintained at 25 ± 0.1 °C. The Reynolds number is determined by the hydraulic diameter d_h and the mean flow rate

velocity $U_Q = Q/S_{set}$, calculated as the ratio of the flow rate to the cross section of the test section, and has the form $Re = d_h U_Q / \nu$, where ν is the kinematic viscosity. The range of Reynolds numbers varies from 6 300 to 18 900 .

Instantaneous velocity fields were measured using an in-house measuring system with high time resolution (Time-Resolved Particle Image Velocimetry). The measuring system included: dual New Wave Pegasus Nd:YLF laser, four Photron FASTCAM SA5 cameras, two mirrors with the possibility of precise adjustment. The layout of the measuring system is shown in Fig. 1b. The measuring area was illuminated through an optical window mounted in the output collector using two mirrors. The laser sheet in 2D PIV configuration was parallel to the working channel wall.

The spatial structure and dynamics of the flow within the gap between the rods and the flat wall were investigated using high-resolution PIV and Tomographic PIV methods. It is important to highlight several challenges associated with employing PIV methods for studying the flow in a gap formed by curvilinear stacks of tubes and a flat wall. Due to the pronounced flow direction, a complex three-dimensional anisotropic turbulent flow is generated in the gap.

The flow within the gap is characterized by quasiperiodic multiscale pulsations of longitudinal and transverse velocities. To identify the primary motion scales associated with velocity fluctuations in the gap, we analyzed the temporal dynamics of velocity along the channel. The dynamics of such a complex flow were described using the Proper Orthogonal Decomposition (POD) method applied to the time-resolved experimental data. The spatiotemporal flow structure associated with the dynamics of the most energetic flow structures was analyzed based on POD modes and temporal expansion coefficients.

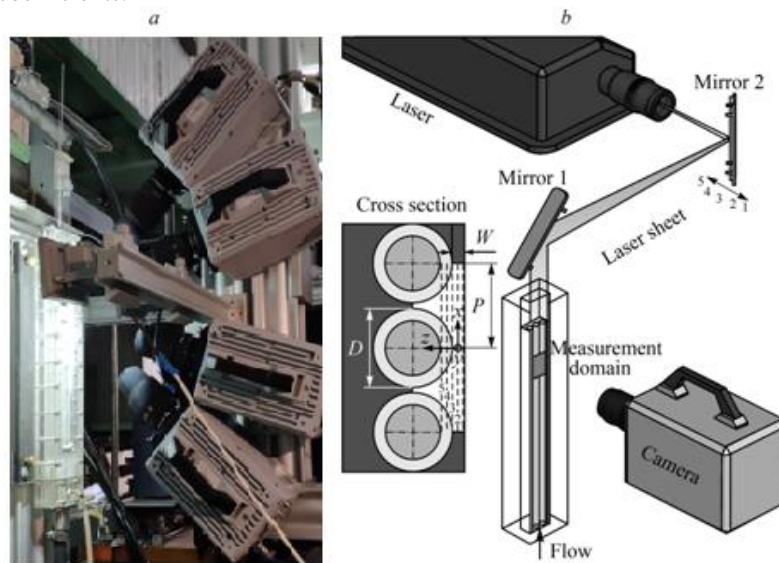


Figure 1. Photograph of the test section and the measuring system (a), location of the measuring system components and positions of the measuring planes in 2D PIV configuration (b).

The experimental data demonstrates that for a fixed S , the longitudinal velocity profiles exhibit similarity across the studied range of Re (Fig. 2, left). Furthermore, altering the parameter S results in a notable variation in the longitudinal velocity profile (Fig. 2, left), despite the visual similarity of the longitudinal velocity distributions (Fig. 2, right). Decreasing S leads to heightened longitudinal velocity gradients and the emergence of an oscillatory flow pattern within the gap (Fig. 2, left). Within the Re range of 9,100 to 18,900, the distributions of the dimensionless longitudinal velocity component remain unaffected by the Re number, with the exception of the flow corresponding to $Re = 6,300$, which reveals a distinct flow structure for both packings (Fig. 2, left). An analysis of the oscillatory nature of the flow in the gap was conducted based on data obtained using POD decomposition.

To illustrate the nature of the flow, Figure 3 (left) depicts the instantaneous distributions of the longitudinal velocity component reconstructed from the first 15 POD modes at various time points within a single sample. The flow within the gap exhibits a complex, unsteady nature, characterized by variations in the length and amplitude of the oscillations, as well as the occurrence of a phase featuring a complete cessation of oscillations (Fig. 3, left).

3. CONCLUSIONS

The spatial flow structure within the gap between the flat wall and three rods, simulating a peripheral cell of the fuel assembly, was experimentally investigated across a broad range of Reynolds numbers, spanning from 6300 to 18900, and two relative pitches $S = 1.077$ and 1.4 . Within the studied parameter range, the normalized profiles of averaged velocity, velocity oscillations, and Reynolds tangential stresses display a mild dependence on the Reynolds number. A reduction in S leads to the emergence of intermittency in the quasiperiodic flow oscillations within the gap. Employing POD decomposition enabled the identification of modes with varying wavelengths and demonstrated that the structure of the most energy-containing eigenmodes remains consistent across all Reynolds numbers examined. The acquired

data offer new insights into the unsteady nature of the flow in the subchannel gap, particularly regarding the influence of Reynolds number and S on the modulation of intermittency in the quasiperiodic flow oscillations and flow meandering within the gap. These experimental findings can serve as a foundation for validating innovative numerical approaches aimed at reproducing the intricate unsteady hydrodynamics within tightly packed lattice rod bundles.

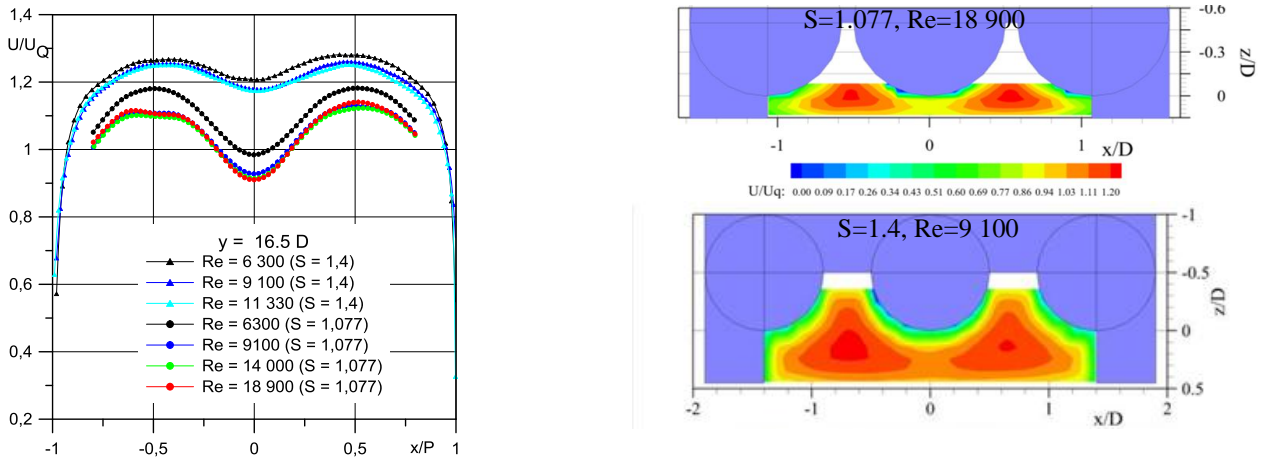


Figure 2. Comparison of average velocity distributions of the longitudinal velocity component in central plane (left) and transverse section (right) at the position $y/D=16.5$ for the set Reynolds numbers, profiles with triangular symbols correspond to the packing $S=1.4$, round ones with $S=1.077$.

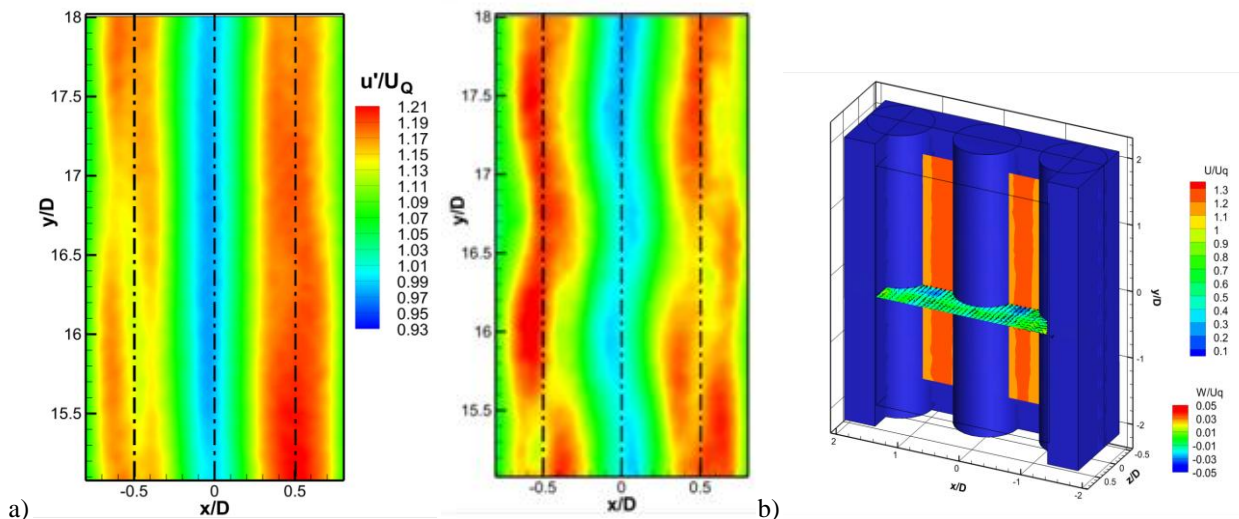


Figure 3. Distributions of (a) the longitudinal component of instantaneous velocity, reconstructed from the first 15 POD modes at two different points in time $S=1.077, Re = 6300$, (b) mean velocity components from Tomographic PIV.

4. REFERENCES

- Li, H., Yakovenko, S., Ivashchenko, V., Lukyanov, A., Mullyadzhyanov, R. and Tokarev, M., 2024. "Data-driven turbulence modeling for fluid flow and heat transfer in peripheral subchannels of a rod bundle". *Phys. Fluids*, Vol. 36, 025141.
- Meyer, L., 2010. "From discovery to recognition of periodic large scale vortices in rod bundles as source of natural mixing between subchannels — A review". *Nuclear Engng Design*, Vol. 240, pp. 1575–1588.
- Möller, S.V., 1991. "On phenomena of turbulent flow through rod bundles". *Exp. Thermal. Fluid Sci.*, 1991, Vol. 4, Iss. 1, pp. 25–35.
- Shestakov, M. and Tokarev, M., 2023. "Modulation of flow meandering in the gap of a model of a peripheral subchannel of a fuel rod assembly". *Thermophys Aeromech*, Vol. 30, No. 6, pp. 1041-52.
- Tavoularis, S., 2011. "Rod bundle vortex networks, gap vortex streets, and gap instability: A nomenclature and some comments on available methodologies". *Nuclear Engng Design*, Vol. 241, pp. 2624–2626.
- Yan B.H., Gu H.Y. and L. Yu, 2012. "Numerical simulation of the coherent structure and turbulent mixing in tight lattice". *Prog. Nuclear Energy*, 2012, Vol. 54, pp. 81–95.
- Yu, Y.Q., Yan, B.H., Cheng X. and Gu, H.Y., 2011. "Simulation of turbulent flow inside different subchannels in tight lattice bundle". *Annals Nuclear Energy*, Vol. 38, pp. 2363–2373.

Investigating the thermal-hydraulic performance of a chaotic heat exchanger: an experimental study

Nouhaila El Hani^{a,*}, Tom Lacassagne^a, Souria Hamidouche^a, Loic Le Bihan^b, André Bontemps^c, S. Amir Bahrani^a

^aIMT Nord Europe, Institut Mines Télécom, Univ. Lille, Center for Energy and Environment, F-59000 Lille, France

^belm.leblanc, Bosch Group France, 29410 Saint-Thégonnec, France

^cUniversité Paris Diderot, Sorbonne Paris Cité, LIED, UMR 8236, CNRS, 75013, Paris, France

*nouhaila.elhani@imt-nord-europe.fr

Keywords: Heat exchanger, heat transfer, chaotic advection, experimental approach

1. INTRODUCTION

Among the various techniques for improving heat transfer, chaotic advection stands out for its efficiency for mixing complex flow in confined geometries. For the same exchange surface as a helical heat exchanger, for example, heat transfer is always more efficient in the presence of a chaotic regime, characterized by complex, unpredictable and irregular flows, as compared to laminar flows. Although turbulence is generally associated with chaos at high Reynolds numbers, chaotic behavior can in fact occur in laminar or transient flows under specific conditions. In these circumstances, small disturbances can produce significant and unpredictable changes in flow patterns, the presence of multiple flow structures, irregular and random trajectories of fluid elements, vortex formation, stretching and bending of fluids. The present experimental work follows on from a previous study in which 4 heat exchangers with 4 different geometries creating chaotic flows were evaluated (Bahrani *et al.* (2019)). To improve heat exchanger efficiency, we investigated a new geometry, for an industrial application. This paper presents a comparative experimental study involving two types of heat exchangers: a helical (HHE) and a chaotic (CHE), of similar internal diameter and exchange surface area, both immersed in a temperature-controlled bath. In order to focus solely on the impact of chaotic advection on internal heat transfer, we consider the laminar regime for the Reynolds number range studied. Their overall performance is assessed by measuring the temperature and pressure difference between the water inlet and outlet of the heat exchanger, which is used to calculate the evaluation performance criterion PEC.

2. EXPERIMENTAL SET-UP

The chaotic heat exchanger (CHE) studied consists of a succession of 18 bends (Radius of curvature $R_c=50$ mm), each bend rotated by 90 degrees and its plane of curvature at a 90-degree angle to the one following it, and has been compared to a helical heat exchanger (HHE). These two geometries have the same inner diameter ($D=2r=23.4$ mm), the same length ($L=2.9$ m), the same pitch ($b=70$ mm) and therefore the same exchange surface. The temperature measurements made on both configurations are carried out over a range of inner flow Reynolds numbers ranging from 400 to 2500, expressed as $Re = \frac{\rho DV}{\mu}$, with V the characteristic flow velocity, ρ the fluid density and μ the viscosity at film (both evaluated at film temperature). The heat exchanger under test, with vertical axis, is immersed in a cylindrical tank filled with water maintained at a temperature of 18°C by means of a thermostatic bath. The water circulating inside the heat exchanger is maintained at 30°C and stored in a tank coupled with a thermostatic bath. This tank is linked to a centrifugal pump to provide a permanent flow with a flow velocity varying between $0.02 < V < 0.1$ m/s. The flow rate of this permanent flow is measured using an electromagnetic flowmeter. The heat exchanger is equipped with 5 type K thermocouples. Two of these thermocouples are used to accurately measure the fluid temperature at the heat exchanger inlet and outlet (T_i and T_o). These measurements are made by inserting the thermocouples into holes previously drilled into the wall of the heat exchanger. This configuration enables the temporal monitoring of fluid temperature variations inside the heat exchanger. Three additional thermocouples are used to measure the temperature of the heat exchanger's outer wall (T_w) at various points. These measurements provide accurate indication of the temperature variation at the exchanger surface.

3. RESULTS AND DISCUSSION

Heat transfer performance and pressure drops for both heat exchangers are evaluated using the Nusselt number Nu , expressed as $Nu = \frac{hD}{k}$, with k the fluid thermal conductivity, and the friction factor f , expressed as $f = \frac{2\Delta p D}{L\rho V^2}$, with Δp the pressure drops and L the exchanger length. The experimental results obtained for the HHE geometry are compared

with the Nu -correlations and f -correlations available in the literature. Tables 1 and 2 summarize some experimental and theoretical correlations of heat transfer and friction factor in the curved tubes used in our study.

The heat transfer coefficient h for each geometry is determined using the wall heat flux density Q and the $LMTD$ method, which is the logarithmic mean temperature difference between the inlet and outlet of the heat exchanger, and is expressed as $h = \frac{Q}{A \times LMTD}$ where $LMTD$ is defined as $LMTD = \frac{(T_i - T_w) - (T_o - T_w)}{\ln\left(\frac{T_i - T_w}{T_o - T_w}\right)}$, with T_i the fluid inlet temperature, T_o is the fluid outlet temperature and T_w is the heat exchanger wall temperatures close to the inlet/outlet.

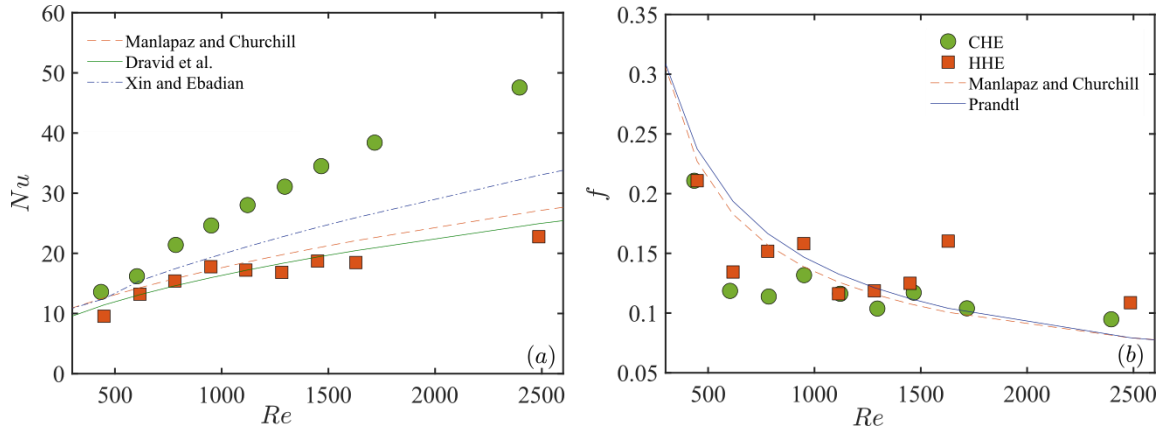


Figure 1. For the two configurations: HHE and CHE: (a) Nusselt number Nu as a function of Reynolds number, (b) Friction coefficient as a function of Reynolds number.

The results, in Fig. 1 (a), show the variation of the Nusselt number as a function of the Reynolds number in both geometries and for Reynolds numbers up to around 2500. For both configurations, the Nusselt number increases with the Reynolds number due to the increase in the internal convection heat transfer coefficient, leading to higher heat transfer efficiency.

For the HHE geometry, it can be seen that the results are in agreement with the correlations listed in Table 1 (in which De is the Dean number, defined as $De = Re\sqrt{r/R_c}$, with R_c the coil radius) for the evaluation of the Nusselt number, starting from $Re=600$. Also, for HHE geometry, at lower Reynolds numbers, the Nusselt number increases with increasing Reynolds number. However, after reaching a Reynolds number of around 1000, the Nusselt number reaches a plateau, then continues to rise. Over the whole range of Reynolds numbers studied, the Nusselt number for the CHE is higher than for the HHE, and from $Re=700$ onwards, it becomes significantly higher than both the HHE experimental measurements and correlation predictions. Figure 1 (b) shows the friction factor versus Reynolds number for the two configurations and for helical coil correlation in Table 2. Our results show that the friction coefficient for the helical configuration and the chaotic one are similar.

Table 1. Nusselt number correlations used for comparison with the helical coil studied. For the HHE studied: $13 < De < 710$, $6 < Pr < 7$, $R_c/r = 12.3$

References	Nu correlations	Conditions
Xin and Ebadian, 1997	$(0.318De^{0.643} + 2.153)Pr^{0.177}$	$20 < De < 2000$, $0.7 < Pr < 175$
Manlapaz and Churchill, 1981	$\left[\left(3.657 + \frac{4.343}{\left(1 + \frac{957}{He^2 Pr}\right)^2} \right)^3 + 1.158 \left(\frac{He}{1 + \frac{0.477}{Pr}} \right)^{\frac{3}{2}} \right]^{\frac{1}{3}}$	$R_c/r > 5$
Dravid et al., 1971	$(0.76 + 0.65De^{0.5})Pr^{0.175}$	$50 < De < 2000$

Table 2. Friction coefficient correlations used for comparison with the helical coil studied.

References	f correlations	Conditions
Prandtl, 1949	$0.29De^{0.36}$	$De > 40$

Manlapaz and Churchill, 1980	$\sqrt{1 + \left(1 + \frac{r/R_c}{3}\right)^2 \left(\frac{De}{88.33}\right)}$	$R_c/r > 5$
------------------------------	-------------------------------------------------------------------------------	-------------

In order to compare these two geometries and quantify the improvement in their heat transfer, while considering the pressure losses, a thermo-hydraulic improvement factor, called PEC (Performance Evaluation Criterion), which was introduced by Webb and Eckert (1972), is used. This criterion is used to compare the Nusselt number and the coefficient of friction of the tube studied with a reference tube (with index is 0 in Eq. (1)), which is the HHE geometry in our study. The PEC is defined as follows:

$$PEC = \frac{Nu/Nu_0}{(f/f_0)^{1/3}} \quad (1)$$

Figure 2 shows the enhancement factor of CHE relative to the HHE used as reference. For all Reynolds number values considered in the laminar regime, the PEC increases with the Reynolds number. A significant improvement in performance is demonstrated for $400 < Re < 1700$, with PEC rising from 1.4 to 2.4.

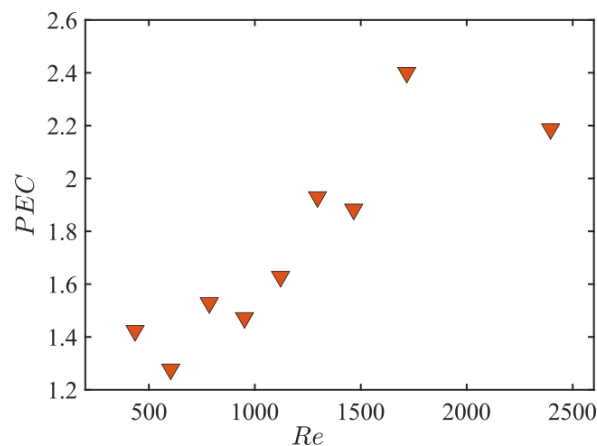


Figure 2. PEC versus Reynolds number.

4. CONCLUSION

The thermo-hydraulic performance of a chaotic heat exchanger (CHE) was experimentally studied and compared to the helical configuration (HHE) with the same exchange area, using the PEC criterion. The results showed that chaotic advection significantly improved heat transfer of the internal flow of the CHE, especially in the transitional Reynolds number regime, with a dramatic increase between $Re=600$ and 1000 , and a plateauing of the enhancement at $Re > 1000$. A more complete study will be undertaken by further increasing the Reynolds number in order to depict the influence of high Reynolds numbers on the heat exchanger performance.

5. REFERENCES

- Bahrani S. A., Humberst L., Osipian R., Royon L., Azzouz K., and Bontemps A., 2019. "How thermally efficient are chaotic advection mixers? an experimental assessment". *International Journal of Thermal Sciences*, Vol. 145, pp. 106046.
- Dravid, A. N., Smith, K. A., Merrill, E. W., Brian, P. L. T. (1971). "Effect of secondary fluid motion on laminar flow heat transfer in helically coiled tubes". *AIChE Journal*, Vol. 17, pp. 1114–1122.
- Manlapaz, R., Churchill, S. (1980). "Fully developed laminar flow in a helically coiled tube of finite pitch". *Chemical Engineering Communications*, Vol. 7, pp. 57–78.
- Manlapaz, R. L., Churchill, S. W. (1981). "Fully developed laminar convection from a helical coil". *Chemical Engineering Communications*, Vol. 9, pp. 185–200.
- Prandtl, L. (1949). "Erzeugung von Zirkulationen beim Schütteln von Gefäßen". *Zeitschrift für Angewandte Mathematik und Mechanik*, Vol. 29, pp. 8–9.
- Webb R.L. and Eckert E.R.G., 1972 "Application of rough surfaces to heat exchanger design". *International Journal of Heat and Mass Transfer*, Vol. 15, pp. 1647–1658.
- Xin, R. C., Ebadian, M. A. (1997). "The effects of Prandtl numbers on local and average convective heat transfer characteristics in helical pipes". *Journal of Heat Transfer*, Vol. 119, pp. 467–473.

Mixed convection in microfluidic channels for flow manipulations (part 2): Thermofluidic analysis with data-driven CFD modelling

Azzini Filippo^{a*}, Pulvirenti Beatrice^a, Rojas-Cardenas Marcos^b, Massimiliano Rossi^a and Morini Gian Luca^a

^aDepartment of Industrial Engineering, Alma Mater Studiorum Università di Bologna, Viale Risorgimento 2, 40136 Bologna, Italy.

^bInstitut Clément Ader (ICA), Université de Toulouse, CNRS-INSA, ISAE-SUPAREO, Mines Albi, UPS, 31400 Toulouse, France

*filippo.azzini2@unibo.it

Keywords: Micro-fluidic, mixed convection, micro-PIV

1. INTRODUCTION

The analysis of mixed convection at the micro-scale is not fully explored yet and can present some interesting applications, especially in the field of micro-mixing or heat-transfer enhancement. Even though at the microscales heat exchange is facilitated due to the large surface-to-volume ratio, the same cannot be said for mass transfer (Guo et al. 2003). Achieving rapid mixing in micro-channel presents challenges due to the low Reynolds number. For this reason, significant interest has been directed to investigating the influence of vortex (Meis et al. 2010) and swirling flows (Lee et al. 2024) in the heat and mass transfer enhancement in microchannels.

This work aims to analyze a regime of mixed convection in square microchannels with transverse temperature gradients. Figure 1-a gives a qualitative description of the phenomena under investigation. It is possible to appreciate that the water flowing inside the micro-channel starts to swirl when entering the region where a temperature gradient is present, and the swirl direction changes from anti-clockwise to clockwise when the direction of the temperature gradient is reversed. The fluid flow characterization of this phenomenon was performed with a 3D particle tracking technique and presented in a companion paper (“Mixed convection in microfluidic channels for flow manipulation (part 1): Fluid-dynamic characterization with 3D PTV”).

The present contribution focuses on the results of CFD simulations with special emphasis on the calibration of the model with experimental measurements based on the micro-PIV technique. In fact, a direct measurement of the temperature field inside the device is not possible with conventional thermometric techniques, therefore, a hybrid experimental and numerical approach was used. Starting from the data obtained experimentally (velocity field and temperature measurement near the wall of the microchannel), it is possible to calibrate the numerical simulation and obtain information on the temperature field, the heat fluxes and the pressure losses that would otherwise be impossible to obtain experimentally. With this combined approach, it is possible to characterize both the thermal and fluid dynamic aspects.

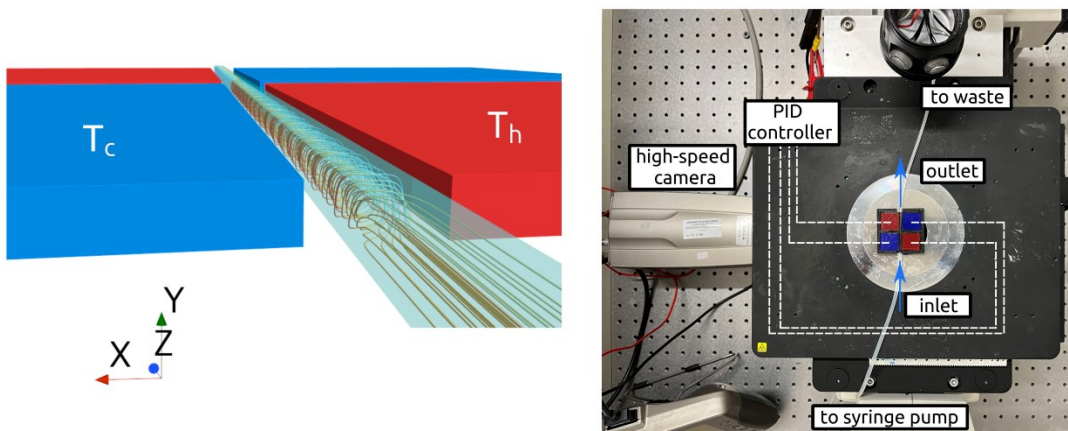


Figure 1: (a) Sketch of the microfluidic chip composed of a square section capillary microchannel and four Peltier modules used to manipulate the temperature gradient. (b) Picture of the experimental setup composed of an inverted microscope, a high-speed camera and an in-house PID controller used to manage the Peltier system.

The experimental apparatus considered in this work is presented in Fig. 1-b. Four Peltier cells connected with an in-house PID controller, are used to induce the temperature gradient that is at the origin of the buoyancy phenomena. With

this system, it is possible to evaluate not only the asymptotic behaviour of the system in different configurations (such as staggered gradient direction or uniform gradient direction) but also the time-related phenomena that occur when the temperature gradient is activated or when an inversion of the direction of the gradient occurs. With the PID controller is possible not only to manage the temperature of the Peltier but also to extrapolate the temperature measurements near the wall of the microchannel that are used in the calibration of the numerical simulation. Another important aspect is that once the simulations are validated, it becomes easier to test new flow conditions and different geometries.

2. DESCRIPTION OF THE MICROFLUIDIC CHIP.

The system is composed of a glass capillary channel with a square cross-section. The hydraulic diameter is equal to 800 μm and the length is 50 mm. Four different Peltier modules are used to impose the temperature gradient inside the channel. Each Peltier module is connected to a thermocouple, which is, in turn, connected to a control system. This setup is used to regulate the temperature and control the direction of the temperature gradient. The figure shows the two possible steady-state configurations, uniform (a) and staggered (b). With this setup, it is also possible to study the transient behaviour of the buoyancy forces when the gradient is activated or reversed.

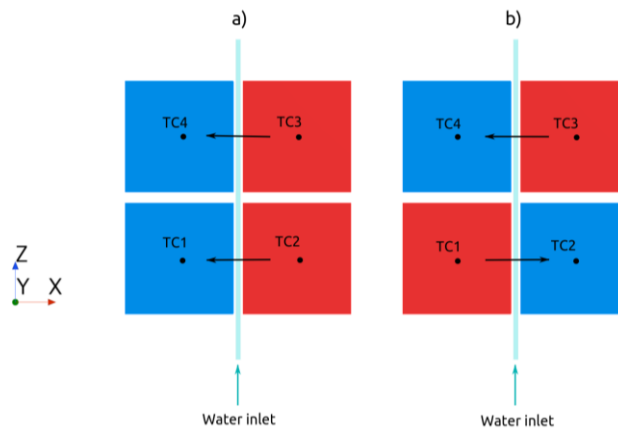


Figure 2: Layout of the microfluidic chip composed of a capillary micro-channel, 4 Peltier modules and 4 control thermocouples (TCs) in the two possible steady-state configurations. a) Uniform thermal gradient along the length of the channel and b) staggered thermal gradient with an inversion in the middle. The direction of the gradient is expressed with the black arrows.

3. NUMERICAL SIMULATION

From the experimental measurements, it is possible to extract all the boundary conditions used to calibrate the numerical simulations (Fig. 3). To account for buoyancy phenomena during the simulation, all fluid properties are considered temperature-dependent. The IAPWS model is used to determine these properties as a function of the temperature. The simulations are carried out using the software STARCCM+, which is a finite-volume-based software used for thermal fluid dynamics simulation. The laminar Navier-Stokes equations are solved in steady-state, and the SIMPLE method is used for pressure-velocity coupling.

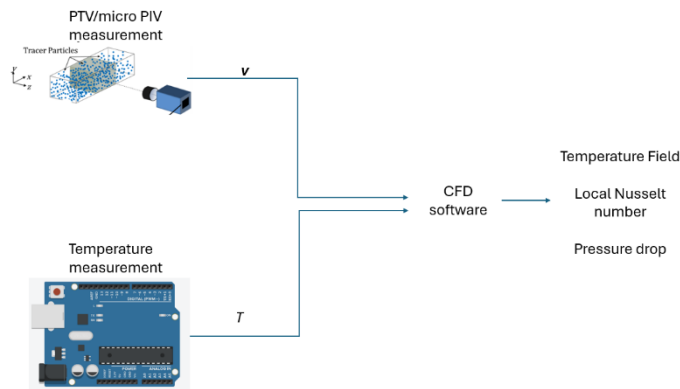


Figure 3: Schematic work-flow used to impose the boundary conditions in the CFD simulations

3. RESULTS AND CALIBRATION

An experimental measurement was performed to validate the numerical simulations using the micro-particle image velocimetry (micro-PIV) technique (Lindken et al. 2009). The water was seeded with polystyrene spheres with a diameter of $1.19 \mu\text{m}$, and a high-speed camera connected to the microscope with a $10\times$ objective lens with $\text{NA} = 0.25$ was used to record a sequence of images. The images were processed using the open-source software *DefocusTracker* to determine the average planar velocity field in the focal plane of the microscope objective, this velocity is imposed as an inlet condition for the simulation. The temperature values measured for the cold and hot sides are used as Dirichlet boundary conditions at the wall of the micro-channels, in this reference case the evaluated temperature was $T_c = 20 \text{ }^\circ\text{C}$ and $T_h = 60 \text{ }^\circ\text{C}$.

Figure 3-a presents the velocity profiles for different parallel horizontal planes (scanning along the y direction) obtained from the numerical simulation (red lines) and experimental measurements (black dots), a good agreement between numerical and experimental results can be observed.

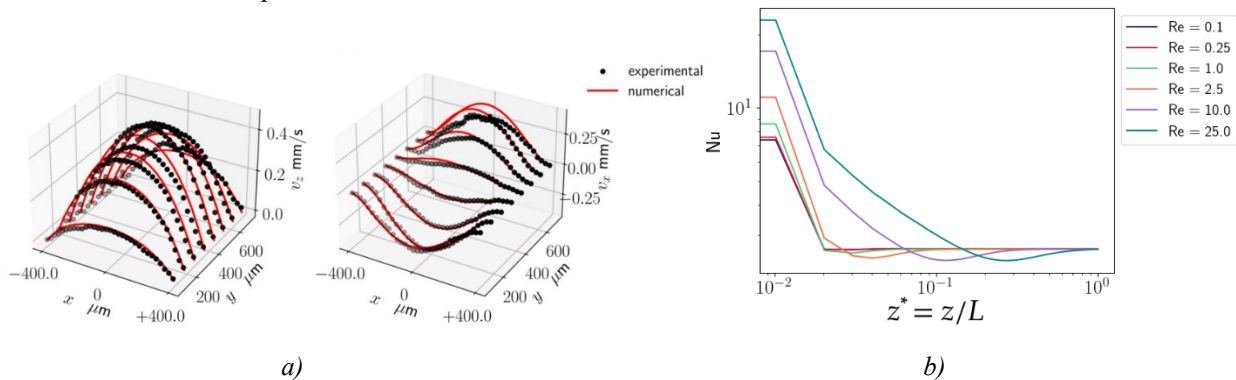


Figure 1: a) Comparison between the numerical and experimental results of the velocity profiles along z and x -direction b) Local Nusselt number trend obtained for different values of the Reynolds number.

The validated numerical model allows to evaluate the Nusselt number trend inside the channel and to examine multiple cases with different flow conditions. In Fig. 3-b the local Nu number as a function of the normalized streamwise coordinate is plotted for different values of the Reynolds number. As the Re number is increased, the entrance length increases but the asymptotic value remain constant. Buoyancy affects the shape of the curve; in fact, it can be observed that the Nusselt number drops below the asymptotic value before stabilizing.

4. CONCLUSIONS

In this work, the mixed convection inside a square section microchannel was investigated numerically and experimentally. The results obtained from the experimental campaign are used to calibrate the numerical model, showing a good agreement between the results. The swirling flow can be used inside systems, such as micromixers, to increase the mixing efficiency, especially for low Reynolds numbers. The dynamics of the buoyancy effects will be investigated using a numerical approach and PTV techniques to better characterise this kind of phenomenon and to identify a way to manipulate the flow inside microchannels.

REFERENCES

- Z.-Y. Guo and Z.-X. Li 2003. "Size effect on single-phase channel flow and heat transfer at microscale". *International Journal of Heat and Fluid Flow*, 24, 284–298.
- M. Meis, F. Varas, A. Velázquez, and J. Vega 2010. "Heat transfer enhancement in micro-channels caused by vortex promoters". *International Journal of Heat and Mass Transfer* 53, 29–40.
- S. Lee, J. Lee, M. Lee, H. Kim, G. Cho, and J. Lee 2024. "Rapid mixing achieved using Coriolis force and grooves in rotating microchannels". *Chemical Engineering Science* 283, 119395.
- R. Lindken, M. Rossi, S. Große, and J. Westerweel 2009. "Micro-particle image velocimetry (μPIV): recent developments, applications, and guidelines". *Lab on a Chip* 9, 2551–2567.

Mixed convection in microfluidic channels for flow manipulation (part 1): Fluid-dynamic characterization with 3D PTV

Massimiliano Rossi^{a,*}, Filippo Azzini^a, Marcos Rojas Cardenas^b, Beatrice Pulvirenti^a and Gian Luca Morini^a

^aDepartment of Industrial Engineering, Alma Mater Studiorum Università di Bologna, Viale Risorgimento 2, 40136 Bologna, Italy

^bInstitut Clément Ader (ICA), Université de Toulouse, CNRS-INSA, ISAE-SUPAREO, Mines Albi, UPS, 31400 Toulouse, France

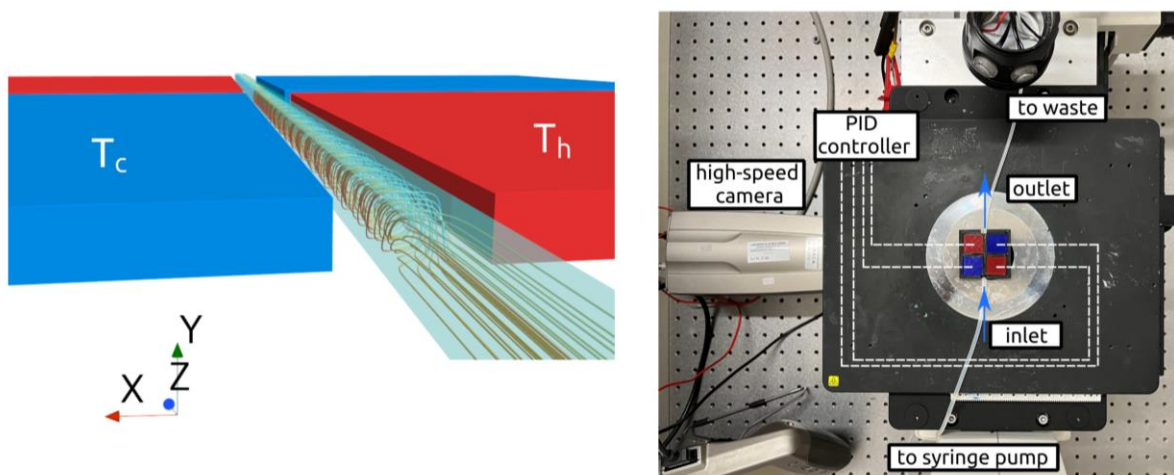
*massimiliano.rossi13@unibo.it

Keywords: mixed convection, microfluidics, 3D PTV, defocus particle tracking, flow manipulation

1. INTRODUCTION

Buoyancy effects are often neglected in microfluidic systems since viscous forces typically dominate over volume forces such as inertia or gravity. However, in cases where the channel dimensions are not too small (typically $> 400 \mu\text{m}$) and a moderate transverse temperature gradient can be established (in the order of 10-50 K/mm), the onset of a consistent transverse buoyance-driven swirling motion can be observed in the fluid (Ishii *et al.* 2020). In combination with a pressure-driven Poiseuille flow, this phenomenon establishes a regime of mixed convection in such microfluidic systems, which is still relatively unexplored both theoretically and experimentally. The characterization of this regime is relevant to the fundamental understanding of heat transfer in these systems, but it may also have important technological implications as a possible flow manipulation mechanism for mixing or particle separation in microfluidic systems. The buoyancy-driven swirls can be easily controlled with Peltier elements put in contact with the side walls of the capillary (Fig. 1). Furthermore, the reduced dimensions of the system allow a fast time response of the swirl as a consequence of temperature changes imposed by the Peltier modules, thus making this approach suitable for real-time applications.

In this work, we present a systematic experimental characterization of the fluid dynamics of this phenomenon in a microfluidic channel with an $800 \times 800 \mu\text{m}^2$ cross-section. The analysis is performed for different Reynolds and Grashof numbers by varying the flow rate and the temperature gradient. In the results section, we present preliminary results obtained with multiplanar micro-particle image velocimetry (micro-PIV) for one experimental condition. In the final presentation, three-dimensional velocity fields measured with the General Defocusing Particle Tracking technique (Barnkob *et al.*, 2020) for different experimental conditions will be shown. The thermofluidic analysis of the phenomenon, including the determination of relevant parameters such as the Nusselt number, will be performed with the support of CFD simulations calibrated on the velocity measurements and presented in a companion paper (“Mixed convection in microfluidic channels for flow manipulations (part 2): Thermofluidic analysis with data-driven CFD modeling”).



(a)

(b)

Figure 1: (a) Sketch of the microfluidic device. The temperature of the side walls of a glass microchannel with a squared cross-section is controlled with Peltier modules to establish controlled convective flows for flow manipulation. (b) Picture of the experimental setup. The microfluidic device is placed on an inverted microscope and high-speed recordings are performed with a high-speed camera. The Peltier modules are driven with in-house PID controller.

2. MATERIAL AND METHODS

The microfluidic system, roughly sketched in Fig. 1a, is composed of a glass capillary with a squared cross-section of $800 \times 800 \mu\text{m}^2$ (VitroTubes, VitroCOM) and a total length of 50 mm. Four $10 \times 10 \text{ mm}^2$ Peltier modules with a thickness of 3 mm are put in contact with the side wall of the microchannel channel through a thermally conductive paste. The modules are managed with a custom-made PID controller. Two configurations are considered: (1) Uniform gradient: The Peltier modules on the same side of the channel have the same temperature. (2) Staggered gradient: The Peltier modules on the same side switch temperature (as shown in Fig. 1).

A 3D-printed plastic housing is realized to assemble the Peltier modules together with the glass capillary. The inlet and outlet of the glass capillary are connected to a syringe pump (Harvard Instruments PHD 400) and to a waste reservoir, respectively. The working fluid is water, seeded with $5\text{-}\mu\text{m}$ -diameter fluorescent polystyrene beads (microparticles GmbH) at low concentrations used as passive tracer particles. The flow is observed using an epi-fluorescent inverted microscope (Nikon Eclipse TE2000-U), and high-speed digital recordings are obtained with a high-speed camera (Olympus I-Speed I). A picture of the experimental setup is shown in Fig. 1-b.

The measurement principle of GDPT is summarized in Fig. 2. The tracer particles dispersed on a fluid volume and observed through the microscope result in defocused particle images, with the defocusing pattern depending on the optical systems used and the depth position of the particle. After a suitable calibration procedure, it is possible to obtain a reference set of images linked to a corresponding depth position. A pattern recognition algorithm based on the normalized cross-correlation function is then used to match a target experimental particle image with the corresponding reference calibration image and retrieve the depth position. The in-plane position is identified in a straightforward fashion by locating the centroid of the particle images. More details on the method and references to further refine the accuracy and reduce bias errors due to optical aberration can be found in Coutinho et al. (2023).

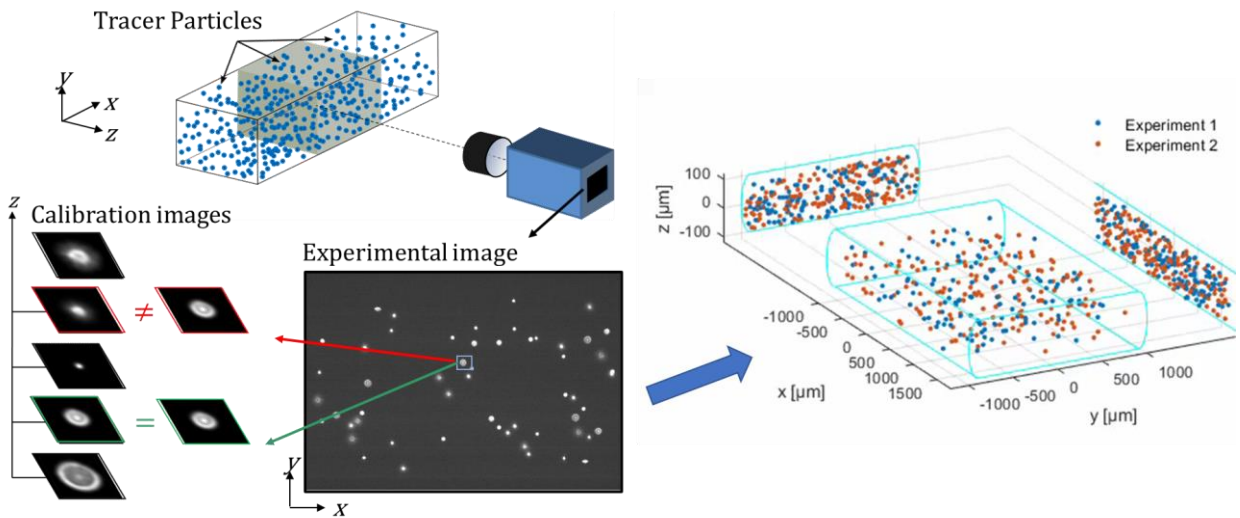


Figure 2: The measurement principle of GDPT. Monodispersed tracer particles, observed with an optical system with a low depth of field, result in defocused particle images. The defocusing pattern depends on the depth position of the particles. A pattern recognition algorithm is used to link the defocused shape with the corresponding depth position previously obtained through a calibration procedure.

3. RESULTS

The fully three-dimensional velocity fields, measured with GDPT for different mixed convection regimes, will be presented at the conference. A summary of the measurement conditions that will be investigated is reported in Table 1.

	Uniform gradient		Staggered gradient	
	Min	Max	Min	Max
Flow rate (ml/h)	0.2	1	0.2	1
Temperature gradient (K/mm)	10	40	10	40

Table 1. Grid of the different operating conditions of the mixed-convection device that will be investigated with 3D PTV.

In Figure 3, we present preliminary results obtained with multi-planar micro-PIV measurements (Santiago et al. 1998). Micro-PIV provides a two-dimensional measurement of the flow field in the focal plane of the microscope objective. To analyze the entire flow field in the channel, a scanning procedure was used through 8 parallel planes, approximately $88 \mu\text{m}$ apart (Figure 3a), with a thickness of the measurement plane (depth of correlation) of approximately $20 \mu\text{m}$. In the

figure, the x , y , and z -axis correspond to the transverse, depth, and streamwise direction, respectively. The experiment is performed with a nominal wall temperature difference of 40 K ($T_c = 20\text{ }^\circ\text{C}$, $T_h = 60\text{ }^\circ\text{C}$) and a flow rate of 0.5 ml/h.

The measured velocity fields shown in Fig. 3, observed from bottom ($y = 0$) to top ($y = L$), show the swirling motion induced by natural convection. In the lower planes, the transverse motion is directed toward the hot wall as the less dense hot fluid moves upwards. In the upper planes, the transverse motion is directed toward the cold wall as the denser cold fluid moves downwards. The streamwise velocity, corresponding to forced convection, has the same order of magnitude as the transverse velocity, corresponding to natural convection, with maximum absolute values of approximately 0.4 mm/s and 0.3 mm/s, respectively.

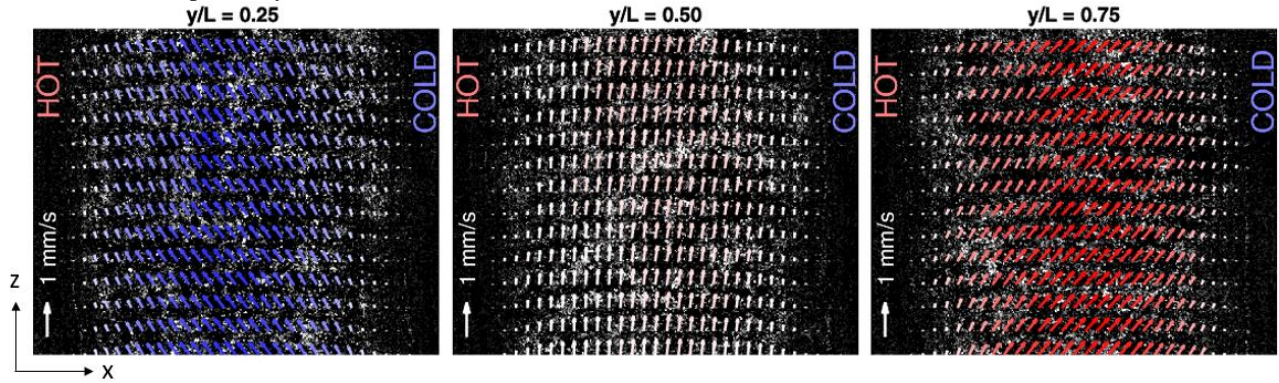


Figure 3: Preliminary measurements of the mixed-convection flow in the microfluidic channel obtained with multiplanar micro-PIV measurements. The colormap (blue to red) represents the values of the velocity component v_x (min value -0.35 mm/s , max value 0.35 mm/s).

In the final presentation, systematic measurements performed with GDPT will be reported for the different cases reported in Table 1. The mixed convection will be characterized in terms of Reynolds number, Grashof number, Richardson number (Gr/Re^2), and a non-dimensional parameter v^* defined as the ratio between maximum absolute transverse velocity $|v_x|$ and maximum absolute streamwise velocity $|v_z|$. It is interesting to notice that although the large Ri number indicates fully natural convection, the ratio between transverse and streamwise flow is in the same order of magnitude, indicating that a mixed convection regime is established in the system.

	Re	Gr	Ri	v^*
$Q = 0.5\text{ ml/h}$, $\Delta T = 40\text{ K}$	0.2	80	2000	0.75

Table 2. Re number, Gr number, Ri number, and velocity ratio v^* for the investigated experimental condition.

4. CONCLUSIONS

We present an experimental analysis of a mixed-convection flow regime established on a microfluidic glass capillary with a squared cross-section of $800 \times 800\text{ }\mu\text{m}^2$. The convective flow is established by means of Peltier modules put directly in contact with the microchannel side walls. With flow rates around 0.2-1 ml/h and temperature gradients around 10-40 K/mm, it is possible to obtain a flow regime characterized by a stable swirling motion that can precisely be controlled by adjusting the temperature of the Peltier modules. The fully three-dimensional extent of the phenomenon for different conditions (flow rates and temperature gradients) is characterized by the GDPT technique, a 3D particle tracking method based on defocusing. Preliminary results obtained at one experimental condition with multiplanar micro-PIV technique are shown in the extended abstract. Interestingly, although the flow is characterized by a large Ri number, the comparison between transverse and streamwise flow velocity indicates the presence of a mixed convection regime. Further results obtained with support of numerical simulations to describe the temperature distribution and heat transfer phenomena are presented in a companion paper.

REFERENCES

- Ishii, K., Hihara, E., and Munakata, T. 2020. "Mechanism of temperature-difference-induced spiral flow in microchannel and investigation of mixing performance of a non-invasive micromixer". *Applied Thermal Engineering*, 174, 115291.
- Barnkob, R., and Rossi, M. 2020. "General defocusing particle tracking: fundamentals and uncertainty assessment". *Experiments in Fluids*, 61, 1-14.
- Coutinho, G., Moita, A., Ribeiro, A., Moreira, A., and Rossi, M. 2023. "On the characterization of bias errors in defocusing-based 3D particle tracking velocimetry for microfluidics". *Experiments in Fluids*, 64(5), 106.
- Santiago, J. G., Wereley, S. T., Meinhart, C. D., Beebe, D. J., and Adrian, R. J. 1998. "A particle image velocimetry system for microfluidics". *Experiments in fluids*, 25, 316-319.

MACHINE LEARNING OF SCATTERING SIGNALS IN OPTICAL FIBER TO IDENTIFY COOLANT LEAKAGE LOCATION OF FUSION REACTOR

Shun Nukaga^{a,*}, Daiki Mori^a, Tsuyoshi Kodera^a, Masahiro Furuya^a, Takuya Katagiri^b

^aWaseda University, 3-4-1, Okubo, Shinjuku-Ku, Tokyo, 169-8555, Japan

^bNational Institutes for Quantum Science and Technology, 2-166, Obuchiomotedate, Kamikitagun Rokkasho-mura, Aomori, 039-3212, Japan

* lucullus@akane.waseda.jp

Keywords: Fusion, LOCA, OFDR, Optical Fiber, Deep Learning

1. BACKGROUNDS

Japanese fusion reactor, JA-DEMO employs a water-cooling system. In the same manner, the test blanket module (TBM) of the international thermonuclear experimental reactor (ITER) employs Water-Cooled Ceramic Breeding (WCCB) as a Japanese port (Kawamura *et al.*, 2020). One must consider the loss of coolant accident (LOCA) as a design base accident for the water at high pressure (15.5 MPa) and temperature (325 °C). Differential pressure measurement systems have been commonly used in nuclear power plants to detect coolant leakage in most power plants. Alternative measure is preferable to measure not only leakage event but also measurement location to work in the high magnetic field environment.

2. OBJECTIVES

We have proposed analyzing scattering signals in an optical fiber to detect and identify the location of high-pressure and temperature water leakage from the coolant piping system under a high magnetic field. It has been verified by the experiments of Liu *et al.* (2003) that optical fibers can be used even under the radiation environment inside a nuclear reactor. We acquired the scattering signals on the basis of the Optical Frequency Domain Reflectometry (OFDR) method. Since the acquired signals were noisy and complicated, we applied a machine learning approach to the signals to identify the leakage location. We hypothesized that this method could enable not only the detection of leaks but also the identification of their locations.

3. METHODS

3.1 Experiments simulating LOCA in ITER TBM

In the ITER Test Blanket Module (TBM), cylindrical TBM sub-modules are arranged in a series, and coolant is circulated within these sub-modules to extract heat (Kawamura *et al.*, 2020). Figure 1 shows the schematic of experimental vessel to simulate a TBM sub-module. The vessel is cylindrical, with four U-shaped tubes running through it. Figure 2 shows schematic of four different defects with a 3 mm diameter hole in each U-shaped tube to simulate defects, which we referred to as defects A, B, C, and D. We then simulated a LOCA within the TBM by ejecting steam into each U-shaped tube. The measurement system for the LOCA and the optical fiber sensor are the ODiSI-B from Luna Innovations and the FBI-Gauge from Fuji Technical Research, respectively. The FBI-Gauge is a sensor that coats the optical fiber with polyimide, and it can measure changes in the stress and temperature of the optical fiber at intervals of 2.6 mm as frequency changes. The optical fiber was laid on the outer surface of the vessel, as shown in Figures 1 and 2.

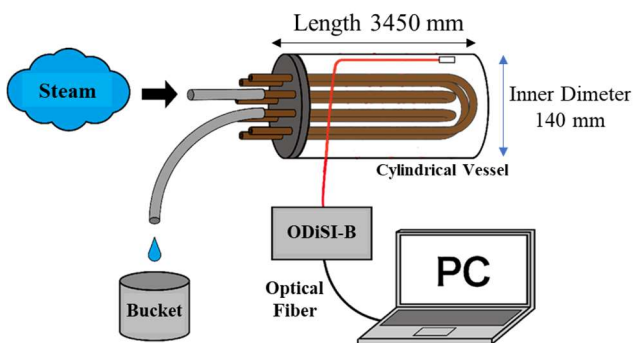


Figure 1. Schematic of the simulated TBM apparatus

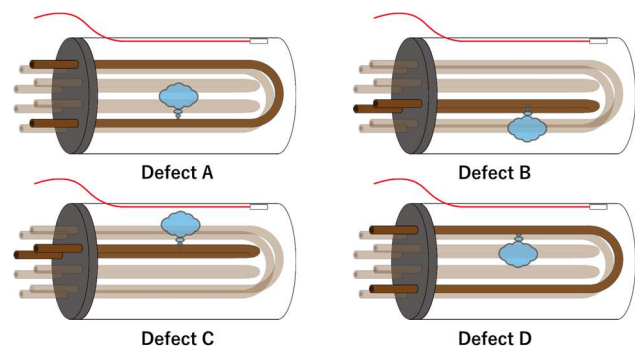


Figure 2 Schematic of four different defect locations.

In the experiment, a steam leakage tests were conducted for four defect locations. Measurements last for 60 s. Number of scattered signals in the optical fiber, ODiSI-B are 6000 at the measurement frequency of 100 Hz. Steam leakage from U-tube was initiated after the waterproof seal was broken. The measurements were repeated for 20 times. In addition, three types of optical fiber installation methods are tested in this experiment. The installation methods are as follows:

(a) Straight-line installation: The optical fiber is affixed in a straight line on the upper part of the container.

(b) π installation: The optical fiber is fixed on the left end wall of the container lid and is installed so that it reaches the right end wall of the bottom surface by going halfway around the container.

(c) 2π installation: The optical fiber is fixed on the upper part of the container lid and is affixed around the container so that it reaches the bottom surface in one round.

Since each installation method is experimented 20 times, totally 60 experiments are conducted

3.2 Leak detection and leak location classification using deep learning

In the experiment, the data measured is converted into a text file using dedicated software and then converted into a csv file using MATLAB 2023b. From the csv files, the portions corresponding to the parts used for measurement are extracted and divided into 3 seconds data. In this process, they are overlapped every 2.5 seconds, resulting in 114 csv files per experiment. The divided csv files are then output as a colormap using MATLAB 2023b. Using the images obtained, classification learning is performed using MATLAB 2023b. The networks used are pre-trained networks, namely AlexNet, GoogLeNet, and ResNet18. The use of pre-trained networks is to compensate for the lack of data, and by changing the network, the impact of factors such as layer thickness is examined.

4. RESULTS AND DISCUSSION

A series of experiments were conducted for 60 signal sets. However, due to an error in converting to a text file, some of the data was corrupted and lost. For instance, in the case of (a) straight-line installation, the pattern with no leakage had 3 data instead of 4. The results obtained from (c) were converted into images, as shown in the following Figure 3.

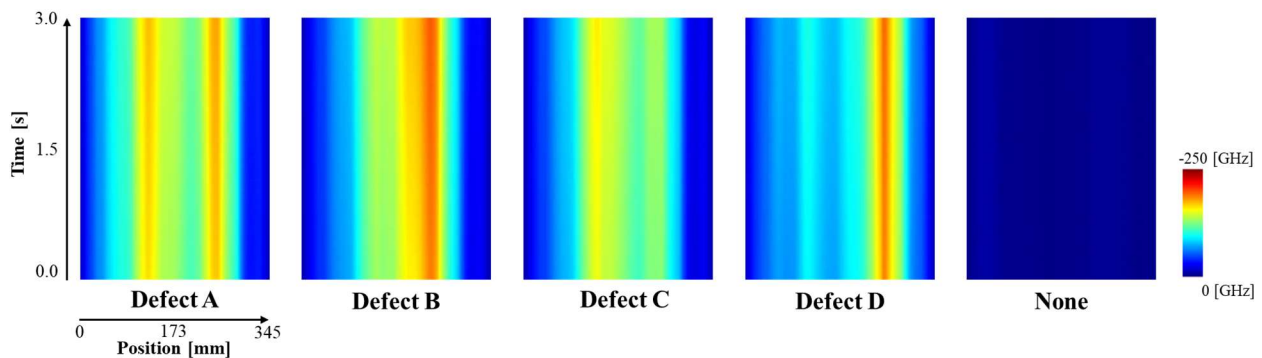


Figure 3. Images of measurement results for each leakage location.

The x-axis of the image represents the position of the fiber. The left edge of the image corresponds to the signal from the point closest to the lid of the container, while the right edge corresponds to the signal from the part closest to the bottom of the container. The y-axis of the image signifies time. As mentioned earlier, the data is divided into 3-second intervals, so the top edge of the image represents data from 3 seconds after the time represented by the bottom edge. Therefore, if you want to observe the change in the signal at a certain measurement point, you should focus on the vertical lines in the image. If you want to observe the signal at a certain time, you should focus on the horizontal lines in the image. During the process of image creation, a color map was used. However, due to the presence of outliers, an appropriate value was chosen for the range of the color bar to capture changes due to leakage.

Upon examining Figure 3, it can be observed that the image contains areas that appear reddish and bluish. The data obtained from the current measurements were visualized such that areas with large frequency changes appear red. In this study, a large frequency change indicates a large temperature change, hence the red areas represent proximity to high-temperature steam. The results of the classification learning conducted for each installation method using three networks are presented in Table 1. Hyperparameter tuning was performed for each learning, and the validation accuracy for the best case is displayed.

Table 1. Results of Classification Learning for Each Installation Method and Network.

Installation Method	AlexNet [%]	GoogLeNet [%]	ResNet18 [%]
(a) Straight-line	99.07	98.14	100.00
(b) π	99.78	100.00	100.00
(c) 2π	100.00	100.00	100.00

As per Table 1, it was possible to identify the leakage location with high accuracy of over 99% in all installation methods and networks. Particularly in case (c), it was possible to classify with 100% accuracy in all networks, indicating that the characteristics of the signal due to leakage from each defect could be captured. The difference in (c) versus (a) and (b) can be attributed to the size of the data derived from the installation method. In case (c), the length of the fiber optic sensor used for measurement is 56 cm, which is larger compared to 30 cm in (a) and 36 cm in (b). Furthermore, while in cases (a) and (b) the measurement is almost completed only on the upper side of the container, in case (c) it was possible to obtain information in the cylindrical direction of the container, such as going around the circumference of the container. On the other hand, it is noteworthy that even in case (a), it was possible to classify with a high accuracy of over 99%. When the fiber installation method is a straight line, the installation is overwhelmingly easier compared to when it is wound like in cases (b) and (c). Other advantages include the fiber being less likely to be subjected to stress and the reduced possibility of damage.

5. CONCLUSIONS

We conducted an experiment simulating a Loss of Coolant Accident (LOCA) using a container that mimics the TBM sub-module, and measurements were made using Optical Frequency Domain Reflectometry (OFDR) with a fiber optic sensor. During this process, we changed the installation method of the optical fiber to evaluate the impact of the installation method. The results of the measurements were converted into images and classification learning was performed using three types of pre-trained networks. As a result, we were able to successfully identify the leakage location with a high accuracy of over 99% in all cases.

6. REFERENCES

- Kawamura, Y., Gwon., H., Guan, W., Tanigawa, H., Hirose, T., Wakasa, A., Yoshino, S., Ouchi, T., Hattori, K., Chiba, N., Kushida, T., Mori, S., Iida, H., Yamamoto, T., Yamanishi, T., Uto, H., Someya, Y., Ochiai, K., Sakasegawa, H., Kim, J., Nakamura, H., Tanigawa, H., Ohira, S. and Hayashi, T., “Progress of water cooled ceramic breeder test blanket module system”. *Fusion Engineering and Design*, Vol. 161, 112050.
- Liu, H., Talnagi, J., Miller, D.W., 2003. “Neutron radiation effects on Fabry–Perot fiber optic sensors”. *Equipment*, Vol. 507, pp. 691-702.

Acknowledgement

This research is partly the result of a commissioned research project in the fiscal year 2023. The authors gratefully acknowledge National Institutes for Quantum Science and Technology (QST).

FLOW BOILING OF R1336MZZ(Z) IN A COPPER MICROGAP WITH TAPERED MANIFOLD

Debora C. Moreira^{a,*}, Alexandre G. Costa^a, Valter S. do Nascimento Jr.^b, Gherhardt Ribatski^a

^aHeat Transfer Research Group - São Carlos School of Engineering, University of São Paulo, São Carlos, São Paulo, 13566-590, Brazil

^bINCT NAMITEC, Institute of Electrical and Computational Engineering – State University of Campinas (FEEC/UNICAMP)

*dcmoreira@usp.br

Keywords: Microchannel, High-speed visualization, Cooling, Low-GWP, HFO.

1. INTRODUCTION

New challenges related to high-performance heat sinks have been proposed due to the development of new materials and micro and nano manufacturing techniques, which enabled the concentration of billions of nanotransistors in a microchip and the development of high-concentration photovoltaic cells, applications that can demand the dissipation of heat fluxes greater than 10 MW/m². In addition, the operating temperatures of these components usually fall into restricted limits, thus requiring an increase in heat transfer coefficient (HTC). During the last decades, many studies have addressed high heat flux dissipation with techniques such as jet impingement, spray cooling and microchannel flow boiling, which has favorable characteristics like relatively stable operating temperature allied to high heat transfer efficiency (Ribatski, 2013). Despite the desirable characteristics of flow boiling heat transfer in microchannel heat sinks, some challenges have been faced in the development of these devices, such as instabilities, flow reversal, high pressure drop and low critical heat flux (CHF) (Kandlikar, 2012).

Significant effort has been put to improve the performance of flow boiling in microchannel heat sinks, with the proposition of diverse geometries and surface structuration, and most investigations comprise experiments with water and refrigerants (Benam *et al.*, 2021). Although water has advantages like good thermal properties, low-cost and prompt availability, the use of refrigerants is preferable in low-temperature applications, since their saturation temperatures at ambient pressure are much lower than that of water. However, traditionally used refrigerants are associated with negative environmental impacts, which motivated the substitution of these fluids by modern options with lower global warming potential (GWP) and null ozone depleting potential (ODP), but extensive investigation on the flow boiling behavior of these new fluids in microchannels heat sinks is required to contribute to a thorough understanding of their boiling mechanisms (Lv *et al.*, 2022). Recently, Marchetto and Ribatski (2020) evaluated the flow boiling heat transfer in polymeric microchannels heat sinks with inlet restrictors using R1336mzz(Z) as working fluid and reported the dissipation of up to 21.2 kW/m², with wall temperature that reached 55°C corresponding to HTC of up to 2.6 kW/m²K and pressure drop of only 1.5 kPa. In order to extend the heat flux and temperature range of experiments, Moreira *et al.* (2023) analyzed the flow boiling behavior of the same fluid in a copper microchannel heat sink combined with an open tapered manifold that had been previously tested with water as working fluid (Moreira *et al.*, 2022) and reported the dissipation of up to 728 kW/m² with HTC that reached 16.7 kW/m²K and pressure drop lower than 10 kPa.

Due to the lack of experimental boiling heat transfer data for R1336mzz(Z) in the literature, in the present study the flow boiling behavior of a plain copper surface was combined to the previously used tapered manifold, forming a tapered microgap, and the experiments comprising mass fluxes from 400 to 1000 kg/m²s and heat fluxes up to 461 kW/m² were carried out in order to serve as benchmark data for future investigations with this relatively new fluid. Values of heat transfer coefficient and pressure drop are reported and their relations to the flow patterns observed with a high-speed camera are discussed.

2. EXPERIMENTAL FACILITY

Detailed information regarding the experimental apparatus that was used in the current experiments can be found in previous works (Marchetto and Ribatski, 2020; Moreira *et al.*, 2023). Heat was supplied to the test section by a copper block containing eight embedded cartridge heaters powered by a DC source. The heated footprint is a square with 10 mm x 10 mm, and polysulfone housing and cover served as manifold and defined the flow area. The cover was milled to create a gap with minimum height equal to 180 μm and a taper corresponding to 6% of the gap length aligned to the heated footprint, so the gap height at the outlet was 780 μm. Figure 1 illustrates the copper chip test section, the diverging gap over the heated surface, and a simplified schematic of the flow loop. An absolute pressure transducer indicated the pressure at the inlet of the test section, and a differential pressure transducer measured the pressure drop. Two K-type thermocouples measured inlet and outlet fluid temperatures, and three K-type thermocouples were lodged in the copper chip below the heated surface, shown in Fig. 1(b) as T_1 , T_2 and T_3 , which were used in wall temperature calculations.

e)

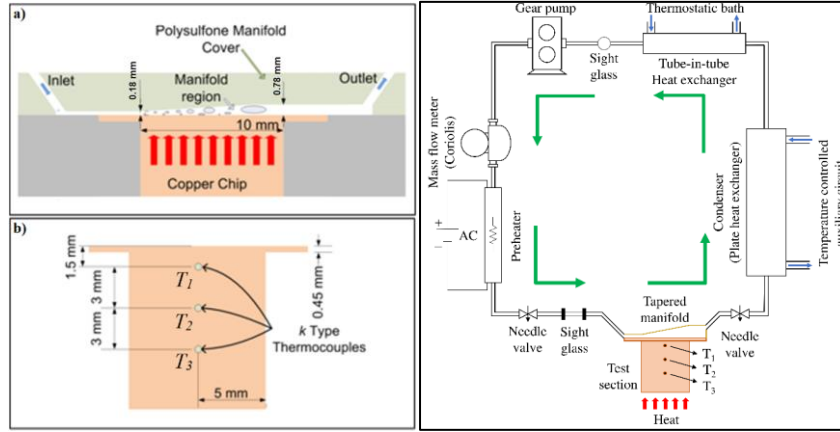


Figure 1: Schematics of the test section showing the (a) flow path and (b) heated copper chip and (c) a simplified diagram of the flow loop.

The input power applied to the cartridge heaters and the pump were controlled using LabView, which also provided the data acquisition. The saturation temperature of the working fluid R1336mzz(Z) was set to 41 °C, and the experimental conditions are summarized in Tab. 1. Heat losses were estimated based on energy balances for single-phase experiments and extrapolated to flow boiling experiments, so the heat flux effectively transferred to the fluid could be calculated. The wall temperature was calculated considering one-dimensional heat conduction through the neck of the copper chip combined with the temperature measurements T_1 , T_2 and T_3 .

Table 1: Experimental Conditions for flow boiling tests.

G_{in} (kg/m ² s)	ΔT_{sub} (°C)	q'' (kW/m ²)
400	20	105-456
600	20 / 20 - 1	136-461 / 110-447
800	20	145-451
1000	20	156-431

3. RESULTS AND CONCLUSIONS

The Boiling curves and pressure drop from experiments at four mass fluxes with inlet subcooling (ΔT_{sub}) of 20 °C are shown in Fig. 2. The critical heat flux was not reached during this experimental campaign, and the applied heat flux was limited by the maximum temperature of the cartridge heaters ($T_{max}=160^\circ\text{C}$).

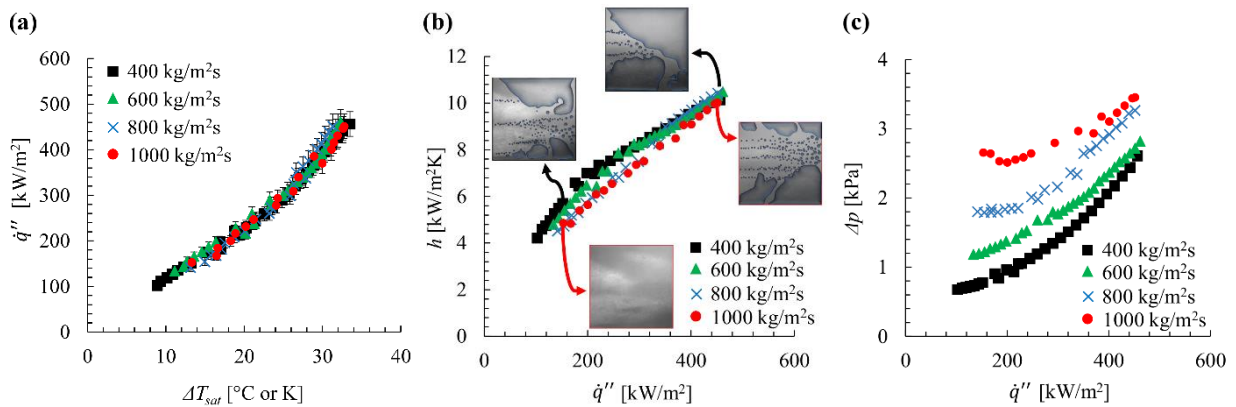


Figure 2: (a) Boiling curves, (b) heat transfer coefficient and (c) pressure drop variation with heat flux for flow boiling of R1336mzz(Z) with fixed inlet and saturation temperatures ($T_{in} = 21^\circ\text{C}$ and $T_{sat} = 41^\circ\text{C}$).

Although the differences in the boiling curves are marginal, it is possible to observe in Fig. 2(a) that for heat fluxes lower than 30 W/cm², the wall superheat increases with the mass flux, as supported by the HTC data seen in Fig. 2(b), which is directly related to the higher heat flux required to the onset of nucleate boiling and lower exit vapor qualities achieved at higher flow rates. As also seen in Fig. 2(b), the density of active nucleation sites decreases as the mass flux rises, which deteriorates nucleate boiling heat transfer and results in the increase of wall superheat, a behavior that is in accordance with that observed by Kalani and Kandlikar (2015). Based on the trends observed in Fig. 2(a,b), it can be speculated that under conditions of greater heat flux than those reached in the present experiments higher mass fluxes

would correspond to lower wall superheats, resulting in higher values of HTC, as reported in our previous investigation (Moreira et al., 2023). The increase in pressure drop with heat and mass fluxes seen in Fig. 2(c) can be attributed to variations in inertia forces and void fraction, due to the rising two-phase specific volume. Moreover, it is possible to notice a change in the slope of the pressure drop curve linked to changes in flow pattern. Nevertheless, it should be remarked that the reported values of pressure drop are low and do not imply in significant increase in the required pumping power nor in relevant variation of the saturation temperature along the microgap.

A negative effect of increasing the inlet degree of subcooling was observed in the calculated HTC, which is directly related to the increase of the dominance of single-phase flow mechanisms, with shorter two-phase flow length in the microgap for higher degrees of subcooling. Fig. 3 shows the flow patterns observed during tests at a fixed heat flux of 305 kW/m² and it is clear that the reduction in the degree of subcooling is directly related to the activation of nucleation sites, increase of two-phase length and significant changes in flow pattern.

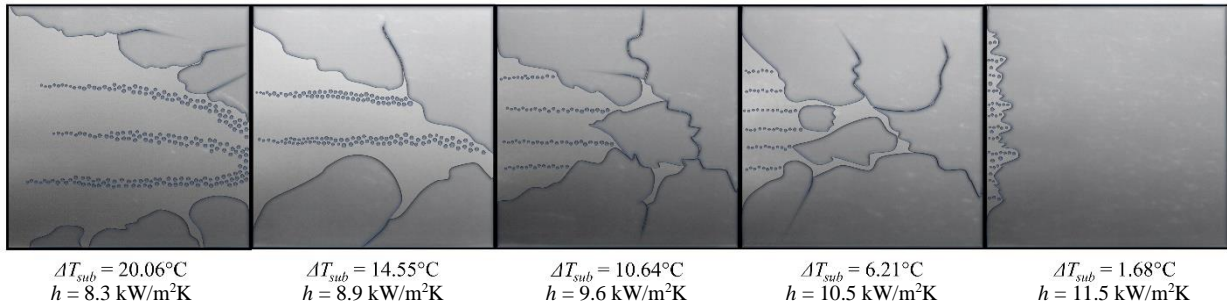


Figure 3: Flow patterns during flow boiling experiments conducted at varying inlet degrees of subcooling for R1336mzz(Z) with inlet mass flux fixed at $G_{in} = 600 \text{ kg/(m}^2\text{s)}$ and saturation temperature of $T_{sat} = 41 \text{ }^\circ\text{C}$ dissipating a heat flux of 305 kW/m².

This work presented experimental results of flow boiling heat transfer and pressure drop for the HFO R1336mzz(Z) over a plain copper surface in a tapered microgap. The saturation temperature was set to $\sim 41 \text{ }^\circ\text{C}$. Effects of mass flux and inlet degree of subcooling were investigated, and significant influence of the activation of nucleation sites and changes in flow patterns could be observed in the heat transfer coefficient and pressure drop values, which was corroborated with the aid of high-speed images of the flow patterns during the experiments. The maximum dissipated heat flux that was achieved during the current experimental campaign was 460 kW/m² without reaching the CHF, with a corresponding HTC of 10.4 kW/m²K, for an inlet degree of subcooling of 20 °C and mass flux equal to 800 kg/m²s. Nevertheless, higher values of HTC could be obtained for lower degrees of subcooling, and the highest value of HTC achieved in the current experimental campaign was 11.5 kW/m²K, with an inlet degree of subcooling of 1.7 °C and an inlet mass flux of 600 kg/(m²s), while dissipating 305 kW/m². The highest value of pressure drop that was measured during the current experiments was 6 kPa, which is a relatively low value when compared to results of flow boiling in microchannels.

4. ACKNOWLEDGEMENTS

The authors would like to acknowledge the financial support provided by FAPESP (Processes #2015/24834-3, #2016/09509-1, #2018/23538-0, and #2022/06392-7), CNPq and CAPES. The technical support given by Mr. Jorge Nicolau dos Santos and Mr. José Roberto Bogni is also recognized and deeply appreciated.

5. REFERENCES

- Benam, B. P., Sadaghiani, A. K., Yağcı, V., Parlak, M., Sefiane, K. and Koşar, A., 2021. Review on high heat flux flow boiling of refrigerants and water for electronics cooling. *International Journal of Heat and Mass Transfer*, 180, 121787.
- Kalani, A. and Kandlikar, S. G., 2015. Flow patterns and heat transfer mechanisms during flow boiling over open microchannels in tapered manifold (OMM). *International Journal of Heat and Mass Transfer*, 89, 494-504.
- Kandlikar, S. G., 2012. History, advances, and challenges in liquid flow and flow boiling heat transfer in microchannels: a critical review. *Journal of heat transfer*, 134(3).
- Lv, H., Ma, H., Mao, N. and He, T., 2022. Boiling heat transfer mechanism of environmental-friendly refrigerants: A review. *International Journal of Refrigeration*, 133, 214-225.
- Marchetto, D. B. and Ribatski, G., 2020. An experimental study on flow boiling heat transfer of HFO1336mzz (Z) in microchannels-based polymeric heat sinks. *Applied Thermal Engineering*, 180, 115815.
- Moreira, D. C., Nascimento Jr, V. S., Kandlikar, S. G., & Ribatski, G. (2023). Flow boiling of R1336mzz (Z) in tapered microgaps with asymmetric dual-V microchannels. *Applied Thermal Engineering*, 228, 120440.
- Moreira, D. C., Nascimento Jr, V. S., Ribatski, G., & Kandlikar, S. G. (2022). Combining liquid inertia and evaporation momentum forces to achieve flow boiling inversion and performance enhancement in asymmetric Dual V-groove microchannels. *International Journal of Heat and Mass Transfer*, 194, 123009.
- Ribatski, G., 2013. A critical overview on the recent literature concerning flow boiling and two-phase flows inside micro-scale channels. *Experimental Heat Transfer*, 26(2-3), 198-246.

EFFECT OF SURFACE MICRO/NANOSTRUCTURE ON FLOW BOILING IN MICROCHANNEL BASED HEAT SINKS

Pedro Pontes^a, Mariana Perez^a, António Moreira, Ana Moita^{a*}

^aIN+, DEM, Instituto Superior Técnico, Universidade de Lisboa

*anamoita@tecnico.ulisboa.pt

Keywords: microchannel based heat sink, two-phase flows, microstructured surfaces

1. INTRODUCTION

There has been a growing interest in designing more compact and efficient cooling devices, which urge to be developed, to cope with the need to dissipate high heat loads, present in numerous applications. In this context, microchannel liquid-based heat sinks are pointed out as a promising solution, as they depict low thermal resistances in comparison with other technologies (Royne *et al.*, 2005). Studies reported in the literature have been focusing in alternative geometries, or working conditions promoting liquid phase change, as a way to improve the performance of the heat sinks. Indeed, the potential of two-phase flows lies in the additional latent heat removed during evaporation. However, this is also a highly unstable flow condition and pressure losses can be significant, overcoming the potential benefits of using two-phase flows. Hence, to better understand the boiling phenomena inside the microchannels, visualization techniques may provide advantages and improve the analysis. Mohammadi and Sharp (2013) made a review on the different techniques used for bubble dynamics analysis in microchannels, including high-speed imaging, fluorescent microscopy and magnetic resonance. Liu and Pan (2016) also explored the use of infrared thermography. Their results evidenced that this technique could help identify temperature distribution in the two-phase region.

Most of the existing studies on microchannel two-phase flow are analyzed solely based on high-speed imagery, while infrared techniques can complement the analysis. The combination of both techniques can provide valuable insight into the heat transfer mechanisms present inside the channels.

Different studies also use surface micro/nano structuring (*e.g.* roughness, cavities and fins) to improve heat transfer. However, a systematic design of the surface characteristics to allow for better control of the flow instabilities have not been achieved yet. In this context, the present work aims to infer the influence of surface cavities in improving heat transfer in microchannels flow boiling and flow stability by controlling where nucleation sites appear. To cope with this, a transparent single channel configuration was used with a combination of high-speed imaging and infrared thermography with high temporal resolution. A smooth surface was used as a reference to compare with the results obtained for surfaces with two and N cavities, under different working conditions.

2. MATERIALS AND METHODS

2.1 EXPERIMENTAL SETUP

A single microchannel was assembled on top of an AISI304 stainless-steel sheet and pressure sealed with an acrylic plate. The stainless-steel sheet (20 μ m thick) was heated by Joule effect, being fed by a DC current digital power supply (AX-3010DS Axiomet). A type K thermocouple with an accuracy of $\pm 0.5^\circ\text{C}$ was assembled between the stainless-steel foil and the microchannel, to register the temperature of the sheet. The working fluid (3M NOVEC HFE7100) was firstly degassed in a degasification station, and then heated in a syringe pump (Harvard Apparatus Model 22) using electrical resistance. The fluid then passed through a thermal bath of oil, to be heated before entering the microchannel, close to the saturation temperature of the working fluid (at ambient pressure). After leaving the thermal bath, the fluid entered the test section and returned to a reservoir, also at atmospheric pressure. A high-speed camera (Phantom V4.2, Vision Research) was placed directly above the microchannel, to record images from the two-phase flow, at 2200fps, with an image resolution of 250x250 pixels. An Onca MWIR-InSb-320 high-speed infrared (IR) thermographic camera recorded the evolution of the temperature distribution of the stainless-steel sheet at 1000fps. Two additional type K thermocouples located at the entrance and exit of the microchannel, registered the fluid temperature. The signals read by the thermocouples were sent to a DT9828 data acquisition device. The pressure drop between the entrance and exit of the microchannel was also measured, using an Omega PX409-001DWUV differential pressure sensor connected to another DT9828 data acquisition device.

2.1 MICROCHANNEL FABRICATION AND SURFACES PREPARATION

The microchannel was made from PDMS – Polydimethylsiloxane, following the procedure described in Marseglia *et al.* (2024). The microchannel used in this study has a rectangular cross section with a hydraulic diameter of 1mm^2 .

The stainless-steel sheets were smooth (as verified using a profilometer, Dektak 3 from Veeco, with a vertical resolution of 20nm). As microstructured surfaces, one used these sheets with cavities with a diameter of $100\ \mu\text{m}$. The distance between cavities is $200\ \mu\text{m}$. The cavities were fabricated by laser etching (FB20-1, New Industries, China). The system parameters were assessed based on the depth and diameter of laser-ablated pits on the laser beam power and on the number of marks of the beam in the same pit. The diameters of pits on the laser beam power and on the number of marks of the beam in the same pit were measured. Periodic pit structures could be fabricated on the metal surface by changing the experimental conditions of scanning interval (100, 200, 300, 400, 600) under the same laser pulses power (20w) and scanning velocity (200 mm/s).

2.2 EXPERIMENTAL PROCEDURE AND WORKING CONDITIONS

As aforementioned, the working fluid used in this study was 3M NOVEC HFE-7100. The main thermophysical properties of this fluid can be found, for instance in Marseglia *et al.* (2024).

For the experiments, the inlet temperature range was set to be 45°C - 55° . For temperature values higher than this range, fluid evaporation is already very intense, and the fluid is closer to a slug flow regime. Below this temperature range, boiling is very difficult to achieve in the microchannels. For working conditions like those reported in [12-13], two main heat fluxes were imposed, which lead to different temperature values on the stainless-steel foil. The minimum foil temperature was close to 61°C to allow bubble formation, close to the saturation temperature of the fluid, at atmospheric pressure. This was achieved for an imposed heat flux of $1346\ \text{W}/\text{m}^2$. The maximum temperature of the sheet was set to 80°C (to protect the acrylic), corresponding to an imposed heat flux of $1637\ \text{W}/\text{m}^2$.

The volumetric flow rate was defined to $1.114\text{mL}/\text{min}$ and $1.119\text{mL}/\text{min}$ corresponding to Reynolds number values of 70 and 120, respectively associated with one channel. All flow rates correspond to a laminar flow regime. These flow rates were determined following the working conditions studied in Marseglia *et al.* (2024), which are relevant for the model studied and for the heat flux requirements, to identify between bubbly flow and conditions leading to the formation of slugs (the two main regimes of interest to explore in the context of the study).

3. SAMPLE RESULTS AND DISCUSSION

The flow inside the microchannel was qualitatively and quantitatively characterized. The effect of surface cavities was addressed comparing a smooth surface with structured surfaces with two microcavities, and with a regular pattern of N microcavities. First, the flow boiling regimes observed for the working conditions tested here were identified. Then pressure drop and heat flux maps were obtained, combining pressure sensors with high-speed imaging and time resolved thermography. Overall, the results obtained for the flow in the microchannel on the smooth surface agree with the theoretical and expected trends. The use of structured surfaces with microcavities showed that the pattern with N cavities promoted nucleation and lead to more stable flows.

As an example, one can discuss the results obtained by combining high-speed imaging with time resolved infrared thermography. The results highlight, for the flow on the smooth surfaces, the promotion of the occurrence of slug flows, for the highest heat fluxes ($1346\ \text{W}/\text{m}^2$), which have a negative impact to the cooling effect, as dry areas are formed as the slug flows, creating hot regions on the surface.

Regarding the microstructured surfaces, the sheet with 2 cavities presented a similar behaviour with slug presence, as observed for the smooth surface. The same behaviour is observed for the sheet with N cavities, however, for the latter, the increased number of nucleation sites located in the cavities leads to a more efficient cooling, since dry areas have a reduced impact. Here, slug flow is followed by other bubbles formed along the microchannel, which are responsible for a faster rewetting of the surface.

Figure 2 depicts the heat flux maps (A), high-speed images (B) and temperature maps (C) obtained when testing the surface with N cavities under maximum heat flux, for each of the volumetric flow rates $1.114\ \text{mL}/\text{min}$ and $1.910\ \text{mL}/\text{min}$, respectively Figures 2a) and 2b). On a first analysis, it is clear from the temperature scales that the surface corresponding to the lowest flow rate has lower temperature. In the Figure, the number of active nucleation sites is higher than for higher flow rate, with even some of the nucleation sites being visible by the center of the microchannel, on the temperature map (C).

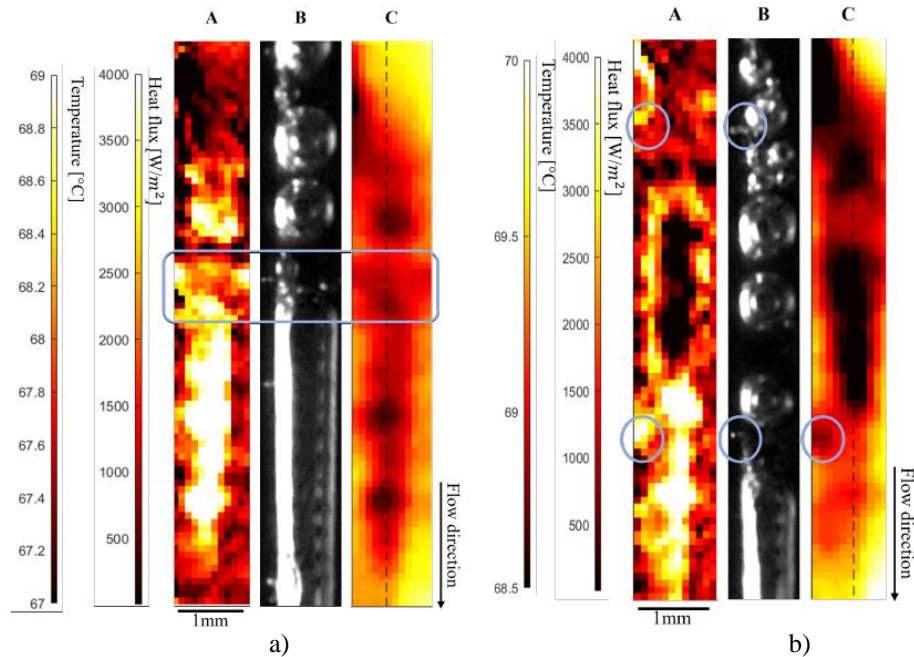


Figure 2. Images of A: Heat flux map; B: High-speed image; C: Temperature map, obtained from testing the stainless-steel sheet with N cavities, for an imposed heat flux of 1637 W/m^2 . a) Flow rate: 1.114 mL/min. ; b) Flow rate: 1.910 mL/min.

4. CONCLUSIONS

The aim of this work was to understand the impact of surface modifications, namely the use of micrcavities, on two-phase flow inside a microchannel. For this, analysis of pressure and temperature variations inside the microchannel is combined with high-speed imaging and infrared thermography.

Through analyzing high-speed images synchronized with infrared images, it was possible to confirm that the presence of cavities had no effect on the performance of the system with respect to the surface with 2 cavities although the surface with N cavities played visible influence in all parameters analyzed.

The heat flux and temperature maps allowed to detect differences on the impact of each flow pattern observed, on the cooling of the heated surface. Moreover, from the heat fluxes and flow rates tested, one had a significant improved performance comparing with the remaining conditions tested: 1637 W/m^2 and 1.114 mL/min

ACKNOWLEDGEMENTS

Authors are grateful to Fundação para a Ciência e Tecnologia (FCT) for partially financing the research through project PTDC/EMETED/7801/2020 and UIPD/50009/2020-FCT and UIDB/50009 – FCT. A.S. Moita also acknowledges FCT for partially financing her contract through CEECINST/00043/2021/CP2797/CT0005, doi: 10.54499/CEECINST/00043/2021/CP2797/CT0005 and for supporting Mr. Pedro Pontes’s PhD fellowship (Ref. SFRH/BD/149286/2019).

5. REFERENCES

- Royne, A., Dey, C.J. and Mills, D.R., 2005. “Cooling of photovoltaic cells under concentrated illumination: a critical review”, Solar energy materials and solar cells, Vol. 86, no. 4, pp. 451–483.
- Mohammadi, M. and Sharp, K.V., 2013. “Experimental techniques for bubble dynamics analysis in microchannels: a review”. Journal of fluids engineering, vol. 135, no. 2, pp. 021202, 2013.
- Liu, T-L. and Pan, C., 2016 “Infrared thermography measurement of two-phase boiling flow heat transfer in a microchannel”. Applied thermal engineering, vol. 94, pp. 568–578.
- Marseglia, G., De Giorgi, M.G., Carvalho, D.S., Pontes, P., Souza, R.R., Moreira, A.L.N and Moita, A.S., 2024.”” Appl Thermal Eng., vol. 236, pp. 121479.

Preliminary Experimental and Computational Investigation of a Laboratory Gas Turbine Combustor

Gonçalo P. Pacheco^{*,a}, Afonso Santoalha^a, Bruno M. Pinto^a, Miguel A. A. Mendes^a and Pedro J. Coelho^a

^aIDMEC, Mechanical Engineering Department, Instituto Superior Técnico, Universidade de Lisboa,

*(E-mail: sousappacheco@gmail.com, miguel.mendes@tecnico.ulisboa.pt, pedro.coelho@tecnico.ulisboa.pt)

Keywords: Gas turbine combustor, Eddy dissipation concept, Flamelet model, Pollutant Emissions

1. INTRODUCTION

Present concerns on climate change, which is largely due to greenhouse gas emissions, a significant part of which result from the combustion of fossil fuels, motivate the need to shift from the combustion of traditional fossil fuels to cleaner fuels and to renewable energy sources. In this context, hydrogen and ammonia are promising fuels, because they do not contain carbon in their composition, but their combustion poses several challenges (Valera-Medina *et al.*, 2018, Noble *et al.*, 2021). These difficulties may be overcome by burning blends of hydrogen and/or ammonia with natural gas. The present work reports preliminary experimental and computational results for the combustion of natural gas in a laboratory gas turbine combustor. This study is the first step in the subsequent investigation of the combustion of natural gas, hydrogen, and ammonia blends. A unique feature of the combustor is the injection of secondary air from holes at the exit section in a direction opposite to the fuel and primary air flow through a swirl burner with a thermal power input ranging from 5 to 6.7 kW. This approach aims at establishing a mild combustion regime, which offers several advantages when compared to traditional combustion strategies. Primarily, it involves a distributed reaction zone instead of a localized flame front, resulting in more uniform distributions of temperature and species concentrations. Consequently, this characteristic leads to decreased combustor temperatures compared to conventional flames. As a result, the formation of nitrogen oxides (NO_x) is significantly reduced, contributing to low emissions.

2. MATERIALS AND METHODS

The combustion chamber is composed of a vertical cylindrical quartz-glass wall with inner diameter of 100 mm, length of 300 mm, and 10 mm thickness, which is insulated with a glass-fiber blanket. The burner has a central tube surrounded by an annular swirler with the vanes aligned at 45° with the axial direction. Primary air is injected through the burner, and secondary air from a piece mounted on the top of the chamber with eight holes. The schematic of the experimental setup can be observed in Fig. 1(a). This design was developed with the goal of aiding inner liner cooling and promoting recirculation, a crucial factor when operating under the mild combustion regime. During the tests, the fuel and the primary air were injected through the swirler and the central tube of the burner, respectively, as displayed in Fig. 1(b). An electric air heater was used to preheat the primary air. There is no preheat of the secondary air, although due to the design of the top piece, there is heat transfer from the exhaust gases to the secondary air through the wall shown in Fig. 1(a).

Measurements of species concentrations were performed by collecting flue gas at the exhaust of the combustor with the aid of a probe attached to a movable arm. The gas sample was drawn through the probe and part of the system by an oil-free diaphragm pump. To prevent any chemical reactions in the sampling gas, the samples were rapidly cooled by the high-water cooling rate in the surrounding annulus upon being drawn into the central tube of the probe. A condenser removed the main particulate burden and condensate. A filter and a drier removed any residual particles and moisture so that a constant supply of clean dry combustion gases was delivered to the gas analyzers Horiba CMA-331 A (CO₂, CO, O₂) and Horiba pg-250 (NO_x). The data obtained for gas species was repeatable, with an average concentration standard deviation of only 2% from the mean value.

Five different operating conditions have been considered so far, as summarized in Table 1. Measurements were grouped based on the global excess air ratio (λ) and thermal input. Additional operating conditions will be considered in the near future with the aim to operate the combustion chamber with alternative fuels, namely ammonia and hydrogen. Numerical simulations were performed using the Ansys-Fluent software. The results obtained so far were obtained using two-equations RANS turbulence models and the eddy-dissipation concept or the steady laminar flamelet model for combustion. Additional simulations are in progress to assess the influence of the physical models and chemical reaction mechanism on the results.

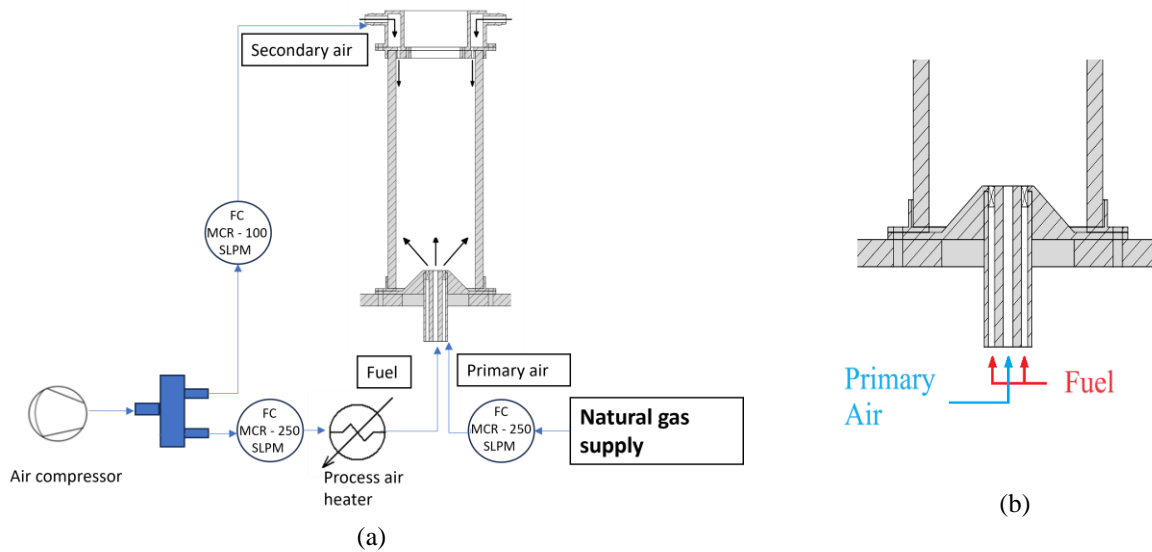


Figure 1. Schematic of the experimental setup.

3. RESULTS AND DISCUSSION

The combustion chamber operates stably in all the test conditions presented in this work. Before the tests and after ignition, the combustion chamber was left to operate for approximately 1 hour to reach stable operating conditions, to minimize the transient heat losses during the measurements. The mass flow rates of the fuel was kept constant for each flame, to keep the thermal input constant. The theoretical O_2 and CO_2 molar fractions (dry volume, %) are displayed in Table 1 for complete combustion, assuming the fuel properties of pure CH_4 , which can account for the deviation from experimental and theoretical results. Figure 2 shows the experimental measurements of species (O_2 , CO_2 , CO , and NO_x) molar fractions at the exit of the combustion chamber for all flames employed in this study.

The measurements of CO show that the overall combustion efficiency is not significantly affected by changing the studied parameters, since combustion was approximately complete for all flames. Flame C strayed further from complete combustion, given the notable increase in the CO measurements, which are above the limits allowed by the most recent legislation. However, it is expected that the addition of heated air mitigates the CO emissions. Regarding NO_x emissions, all the studied flames presented low values that are compliant with the current legislation. It can be observed that the addition of heated air up to $100^\circ C$ to the primary air caused a negligible increase in the NO_x emissions while creating a significant reduction in the CO emissions, with flame B presenting the most significant reduction. Additionally, it should be noted that Flame C presented the lowest NO_x emissions, with only 19 ppm in the exhaust. On operation, the combustion chamber presented a stable lifted flame along the centerline for all the operating conditions.

Table 1. Test conditions.

Flame	A	A-100	B	B-100	C
Thermal Input (kW)	5	5	6.7	6.7	6.7
Air inlet temperature	$20^\circ C$	$100^\circ C$	$20^\circ C$	$100^\circ C$	$20^\circ C$
Global air excess ratio	1.5	1.5	1.5	1.5	2.0
Primary air excess ratio	1.0	1.0	1.0	1.0	1.0
Theoretical O_2 (dry volume, %)	8.9	8.9	8.9	8.9	12.4
Theoretical CO_2 (dry volume, %)	8.9	8.9	8.9	8.9	6.2

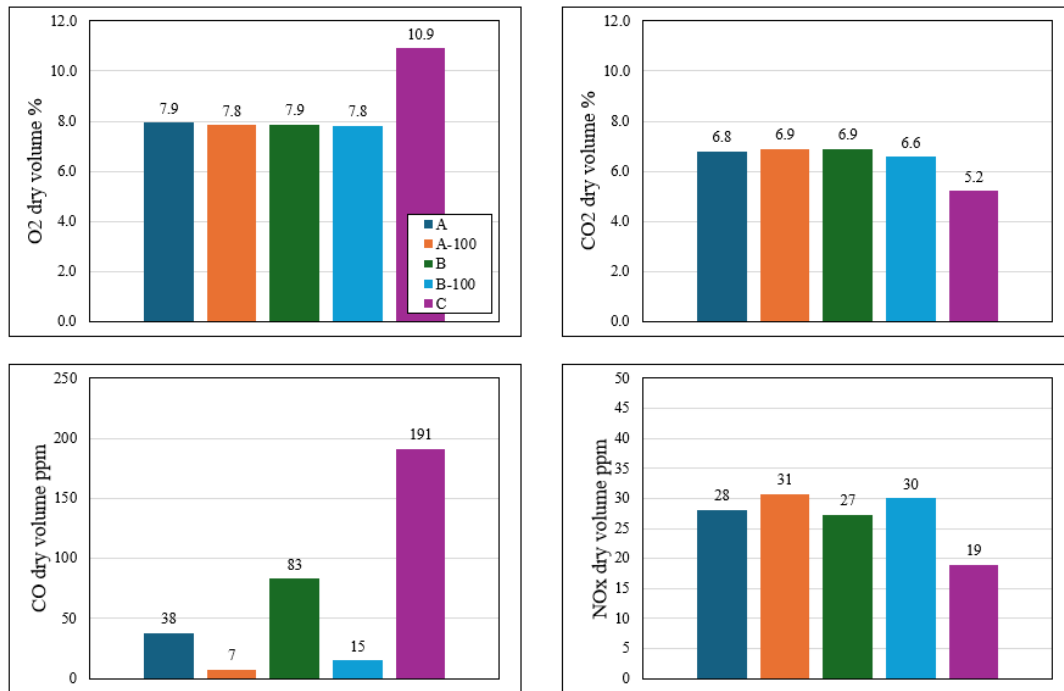


Figure 1: Dry volume molar fraction measurements at the exit of the combustor.

4. CONCLUSIONS

The performance of the combustion chamber was evaluated in terms of flame stability and combustion efficiency through measurements of the exhaust gas analysis. The main conclusions can be summarized as follows:

- Flames A and B, which differ only by the thermal input, exhibited a diluted lifted flame displaying a soft color transition along the centerline of the combustion chamber. However, flame B presented higher CO levels, which were mitigated in flame B-100 with the addition of heated air.
- The combustion chamber is able to operate up to an excess air ratio of 2.0, although the flame presented levels of CO emissions that were above the limit allowed by the legislation.
- Flame A-100 presented the best performance overall. It yields low NO_x emissions compared to a conventional swirl burner flame while keeping CO emissions at minimum values.
- All the studied flames, except flame C, yielded emissions below the legislation limits (DIRECTIVE (EU) 2015/2193.).

Measurement for additional operating conditions and temperature measurements will be included in the full paper. In future studies, the injection of preheated primary air at higher temperatures should be studied, as it is expected to promote a more stable combustion process, leading to a more complete oxidation of CO and a reduction in combustion delay at higher air excess ratios. Additionally, it is planned to fire the burner with blends of natural gas and alternative fuels.

5. ACKNOWLEDGEMENTS

This work was supported by FCT, through IDMEC, under LAETA, projects no. 2022.08675.PTDC (<http://doi.org/10.54499/2022.08675.PTDC>) and UIDB/50022/2020. Gonalo Pacheco acknowledges FCT for the provision of Scholarship 2021.04674.BD. Afonso Santoalha and Bruno Pinto acknowledge IDMEC for the provision of scholarships in the framework of project no. 2022.08675.PTDC.

6. REFERENCES

- Valera-Medina, A., Xiao, H., Owen-Jones, M., David, W.I.F. and Bowen, P.J., 2018, “Ammonia for power”. *Progress in Energy and Combustion Science*, Vol. 69, pp. 63–102.
- Noble, D., Wu, D., Emerson, B., Sheppard, S., Lieuwen, T. and Angello, L. 2021, “Assessment of current capabilities and near-term availability of hydrogen-fired gas turbines considering a low-carbon future”. *Journal of Engineering for Gas Turbines and Power*, Vol. 143, 041002.

VITRIFICATION OF BIOLOGICAL MATERIAL BY IMMERSION IN LIQUID NITROGEN AND SLUSH: AN EXPERIMENTAL STUDY

Alisson S. Silva^a, Jacqueline B. Copetti^{a*}, Matheus Chanan^a, André C Monteiro^a, Jeferson D. Oliveira^b, Elaine M. Cardoso^{c,d}, Mario H. Macagnan^a, Henrique Vidaletti^a, Karolyn Ogliari^e

^aUNISINOS - University of Vale do Rio dos Sinos; Polytechnic School, Unisinos Av., 950, São Leopoldo, RS, 93022-750, Brazil.

^bUSP - University of São Paulo, Polytechnic School, SISEA - Renewable and Alternative Energy Systems Laboratory, SP, Brazil

^cUNESP - São Paulo University State, School of Engineering, Av. Brasil, 56, Ilha Solteira, SP 15385-000, Brazil.

^dUNESP - São Paulo University State, School of Engineering, São João da Boa Vista, 13876-750, SP, Brazil.

^eHemoCord - Umbilical Cord Blood Bank, Unisinos Technology Park- Tecnosinos/UNITEC. 93022718 - São Leopoldo, RS – Brazil

* jcopetti@unisinos.br

Keywords: Cryopreservation, Vitrification, Slush nitrogen

1. INTRODUCTION

Cryopreservation of biological material (BM) has evolved as a technology for various applications in human and veterinary medicine and experimental biology, such as stem cell therapy, tissue engineering (Arav, 2022), assisted reproduction, disease treatment, conservation of ovarian tissues (Dalman et al., 2017), semen (Le et al., 2019), and embryos (Rienzi et al., 2017). The cryopreservation of living cells aims to conserve the material at cryogenic temperatures (from -80 to -196 °C) to suppress biological aging while maintaining its viability and functions (Yang et al., 2019). The viability of living systems depends primarily on the presence of water, and its removal from tissues, cells, or biomolecules through freezing can lead to cellular damage, causing osmotic stress or conformational changes that affect their structure and function. Additionally, ice formation can cause mechanical stresses on BM. One way to preserve cells' life during freezing is to develop formulations and strategies focused on protecting these materials (Wolkers et al., 2021). Cryoprotective agents (CPAs) can minimize osmotic damage and prevent the formation of intracellular and extracellular ice crystals, reducing cryo-injuries in cells (damage to the membrane and cellular structures) and increasing the efficiency of cell preservation (Yang et al., 2019). Cryoprotective agents (CPAs) can be either permeable (organic solvents), which stabilize the plasma membrane (dimethyl sulfoxide - DMSO, glycerol, ethylene glycol (EG), and propanediol - PROH), or non-permeable, which minimize intracellular ice formation and provide extracellular protection, enhancing the efficacy of permeable CPAs (such as trehalose, sucrose, proteins). The freezing method is important for the procedure's success, the viability of cellular functions post-thaw, and the safety associated with CPA toxicity. It depends on factors such as the nature of the cellular material, type and concentration of CPA solution, freezing rate, exposure time to CPA, transport, and thawing protocol (Li et al., 2019). Vitrification is a rapid freezing process in which the biological sample directly transitions from the liquid state to the vitrified and amorphous state without crystallization. This process results in high cooling rates, reaching rates greater than 10,000 °C/min, depending on the sample volume. However, in order to overcome ice formation and prevent recrystallization/devitrification of ice during rewarming, vitrification practices are generally subject to limitations such as CPA concentration and small sample volume (Arav and Yehudit, 2019). Cryoprotective agents (CPAs) have high viscosity and hydrophilicity, reducing the ice formation temperature and increasing the glass transition temperature as their concentration increases, thereby reducing the probability of nucleation and crystallization. On the other hand, the cooling/heating rate and the concentration required for vitrification are inversely related (Isachenko et al., 2012). One of the rapid freezing methods involves immersing the sample using straws with small volumes directly into liquid nitrogen (LN2). However, the main issue for increasing the cooling rate is that LN2 vaporizes near the surface of the sample due to the large temperature difference, forming a 'vapor blanket' around it (Leidenfrost effect), which acts as a thermal insulator, hindering the heat transfer process. In order to prevent the vaporization of LN2, the temperature is reduced to -210 °C (63K) by applying negative pressure. Evaporative cooling causes the nitrogen to partially solidify, thus creating Slush or SN2 (Lee et al., 2007). In this context, the current work presents the results of an experimental comparative study of cryopreservation applied to biological material (MB) using liquid (LN2), subcooled liquid (SC-LN2) and slush (SN2) nitrogen.

2. EXPERIMENTAL APPARATUS AND MEASUREMENT CONDITIONS

The experimental work was carried out to evaluate the method of immersion of samples in three cryogenic fluids: liquid nitrogen (LN2), slush nitrogen (SN2) and subcooled liquid nitrogen (SC-LN2). A mixture of glycerol (CPA) and PBS (buffer solution) was tested, with 30% CPA concentration and 150 μ l of volume. A styrofoam reservoir with a volume of 1 L of nitrogen at 77 K was used for tests with LN2. For the SN2 and SC-LN2 tests, a styrofoam reservoir with 600 ml of liquid nitrogen is inserted into a sealed vacuum chamber to produce the slush, with connections for suction of the vacuum pump and measurements of pressure (Keller PA33X transducer) and temperature. The temperatures at the center of the sample and the cryogenic fluid were measured. For immersion in LN2, thermocouples of type-T (Ω mega) were used and for tests with SN2 and SC-LN2, the type-J, due to the greater measurement range for low temperatures. The data recording is carried out every 0.1 seconds through a data acquisition module (NOVUS- Fieldlogger model) with 8 channels. The layout of the experimental bench is shown in Figure 1.

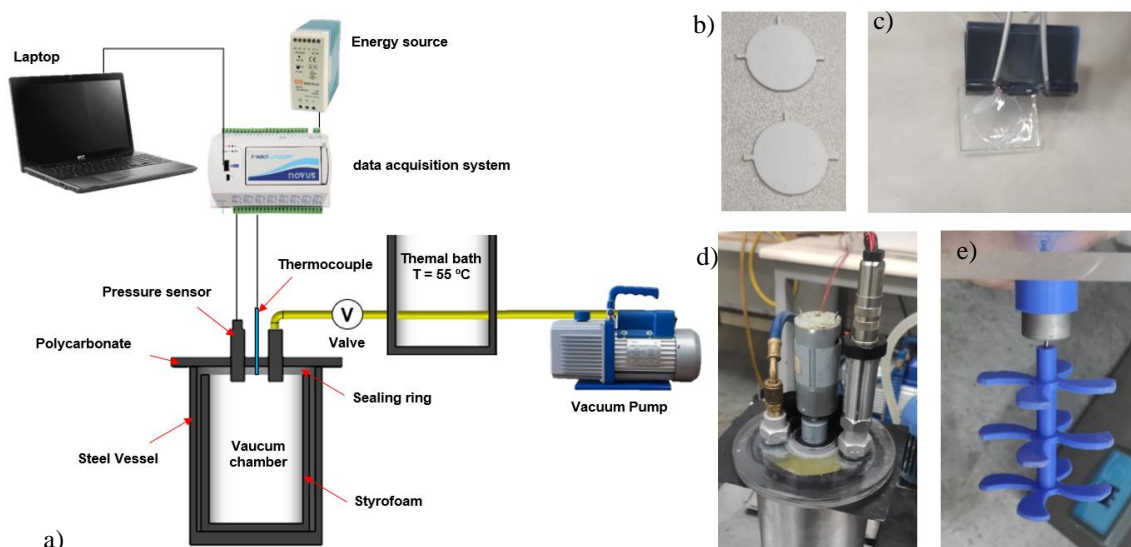


Figure 1. Experimental bench: a) Tests chamber and acquisition system; b) devices molds; c) PDMS devices for samples; d) vacuum chamber and e) stirrer used to produce SN2.

Slush Nitrogen (SN2) is formed by maintaining nitrogen pressure close to the triple point, approximately 12.5 kPa (Wang et al., 2022). The system pressure is gradually reduced to 8 kPa in approximately 20 min and then maintained at this pressure for another 10 min, in order to homogenize all the solid phase formed at a temperature of 61 K. During the production of SN2, a stirrer is used to break up the solid mass of nitrogen that is formed. The temperature of the medium remains stable at -210 $^{\circ}$ C until the entire mass of solid nitrogen melts, a process that takes around 5 minutes. In this step subcooled liquid nitrogen is obtained.

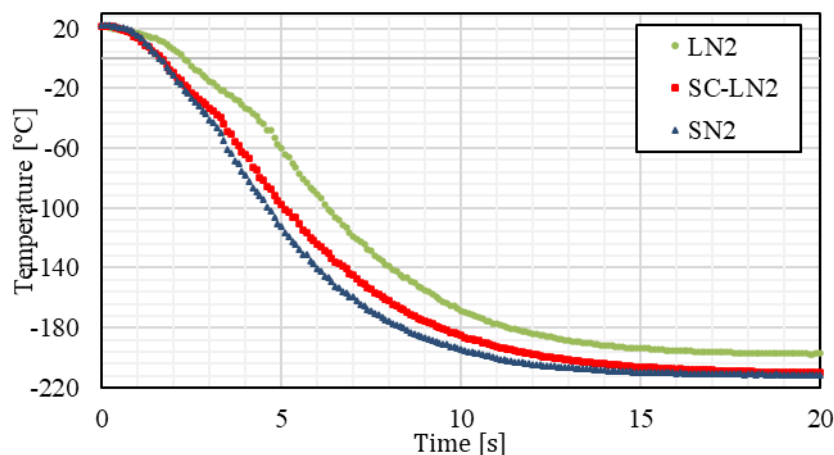
3. RESULTS

The literature uses several ways to analyze the cooling rate (CR). The most common is the beginning of devitrification and critical cooling rate (CCR), the beginning of curve stabilization and the region of curve linearization. Table 1 shows the comparison of rates according to each region analyzed.

Table 1. Cooling rates achieved during que freezing process.

Temperature Ranges [$^{\circ}$ C]	LN2 [$^{\circ}$ C/min]	SC-LN2 [$^{\circ}$ C/min]	SN2 [$^{\circ}$ C/min]
+ 20 \rightarrow - 60 (devitrification start)	1005.23	1422.46	1680.23
- 38 \rightarrow - 137 (CCR pure water)	1652.167	1756.306	2007.56
0 \rightarrow -180 (stabilization starts)	1186.563	1388.815	1590.326
- 60 \rightarrow - 140 (linear cooling rate)	1572.368	1622.359	1925.952

The critical cooling rate is delimited by the type and amount of CPA, calculated within the thermodynamically unstable region, *i.e.*, from the homogeneous nucleation temperature, $T_h = -38$ $^{\circ}$ C to the glass transition temperature, $T_g = -137$ $^{\circ}$ C for pure water (Akiyama et al., 2019). During the experiments, it was observed that for a concentration of 30% glycerol diluted in PBS, the devitrification temperature is close to -60 $^{\circ}$ C. Figure 2 presents the cooling profiles of different freezing mediums, LN2, SN2 and SC-LN2.



. Figure 2. Freezing curves behavior for LN2, SC-LN2 and SN2.

SN2 increased the cooling rate by 67.15% compared to LN2 (devitrification criterion), from 1005.23 to 1680.23 °C/min. The highest CR achieved was 2007.56 °C/min (CCR criterion) for slush. SC-LN2 was also more efficient than LN2 in terms of cooling rate, with an increase of 41.5% (devitrification criterion).

4. CONCLUSIONS

The study conducted an evaluation of different cryogenic fluid immersion methods, including liquid nitrogen (LN2), slush nitrogen (SN2), and subcooled liquid nitrogen (SC-LN2), for samples vitrification containing a mixture of glycerol (CPA) 30% in PBS. Results indicated that cooling rates (CR) varied with each method showing distinct profiles regarding devitrification onset and critical cooling rate (CCR). Successful formation of SN2 was achieved through careful pressure control and stirring, resulting in subcooled liquid nitrogen production. Overall, the study provides valuable insights into optimizing cryopreservation techniques and underscores the importance of selecting appropriate cryogenic fluids and experimental parameters for effective sample preservation in biomedical and biotechnological applications.

5. REFERENCES

- Akiyama et al., 2019, “Cryoprotectant-free cryopreservation of mammalian cells by superflash freezing”. Proceedings of the National Academy of Sciences of the USA, Vol. 116(16), pp. 7738–7743.
- Arav A., Yehudit N., 2019. “The Near Future of Vitrification of Oocytes and Embryos: Looking into Past Experience and Planning into the Future”. *Transfusion Medicine and Hemotherapy*. Vol. 46, pp. 182–186.
- Arav, A., 2022. “Cryopreservation by Directional Freezing and Vitrification Focusing on Large Tissues and Organs”. *Cells*, Vol.11, pp.1072.
- Dalman, A. et al., 2017. “Slow freezing versus vitrification technique for human ovarian tissue cryopreservation: an evaluation of histological changes, WNT signaling pathway and apoptotic genes expression”. *Cryobiology*, Vol. 79, pp. 29–36.
- Isachenko, V. et al., 2012. “Vitrification of human ICSI/IVF spermatozoa without cryoprotectants: new capillary technology”, *Journal of Andrology*. Vol. 33, pp. 462–468.
- Le, M. T., et al., 2019. “Cryopreservation of human spermatozoa by vitrification versus conventional rapid freezing: effects on motility, viability, morphology and cellular defects”. *European Journal of Obstetrics and Gynecology and Reproductive Biology*, Vol. 234, pp. 14–20.
- Lee, D.R., et al., 2007. Effect of using slush nitrogen (SN2) on development of microsurgically manipulated vitrified/warmed mouse embryos. *Human Reproduction*, Vol.22(9), pp.2509-2514.
- Li, Y-X., et al., 2019. “Vitrification and conventional freezing methods in sperm cryopreservation: a systematic review and meta-analysis”. *European Journal of Obstetrics and Gynecology and Reproductive Biology*, Vol. 233, pp. 84–92.
- Rienzi L, et al. 2017 “Oocyte, embryo and blastocyst cryopreservation in ART: systematic review and meta-analysis comparing slow-freezing versus vitrification to produce evidence for the development of global guidance”. *Human Reproduction Update*, Vol. 23(2): pp.139–55
- Yang, J., et al., 2019. “Advanced Biotechnology for Cell Cryopreservation”. *Transactions of Tianjin University*. Vol.26, pp. 409–423.
- Wang et al., 2022 “Experimental study on the pool boiling heat transfer of slush nitrogen under triple point to atmospheric pressure”, *IOP Conf. Series: Materials Science and Engineering*, 1240, 012153.
- Wolkers F.W.; Oldenhof, H., 2021. *Cryopreservation and Freeze-Drying Protocols*. Springer Protocols. Humana Press, 4th edition.

FLOW BOILING HEAT TRANSFER OF PROPANE (HC-R290) IN MULTI-PORT MINICHANNELS

Jeferson D. Oliveira^a, Jacqueline B. Copetti^{b,*}, Priscila F. Silva^c, Mario H. Macagnan^b, Elaine M. Cardoso^d

^aSISEA - Renewable and Alternative Energy Systems Laboratory, Polytechnic School of the University of São Paulo, Brazil

^bUniversity of Vale do Rio dos Sinos, Mechanical Engineering Graduate Program, LETEF, Laboratory of Thermal and Fluid Dynamic Studies, Unisinos Ave., 950, São Leopoldo, 93022-750, RS, Brazil

^cTTI Lab - Research and Development - R & D, 684, Rue Jean-Neveu, Longueuil, Qc, Canada, J4G 1P1

^dUNESP - São Paulo State University, School of Engineering, Campus of São João da Boa Vista, SP, Brazil

*jcopetti@unisinos.br

Keywords: propane, flow boiling, heat transfer, flow patterns, multiport minichannel

1. INTRODUCTION

Because of the environmental concerns associated with traditional chlorinated refrigerants, finding suitable substitutes in the refrigeration industry has become a pressing priority. Propane is considered an eco-friendly and promising alternative to replace R22 and R502. Lillo et al. (2018) investigated two-phase flow boiling heat transfer, pressure drop, and dry-out vapor quality for refrigerant R290 (propane) in a circular channel. The experiments were conducted using a single horizontal stainless-steel tube with specific dimensions and heated using direct current. The study varied parameters such as mass flux, heat flux, and saturation temperature to observe their effects on the experimental results. According to their results, nucleate boiling is the primary heat transfer mechanism observed. Heat transfer coefficients remain relatively consistent throughout evaporation until dry-out occurs, leading to a sudden deterioration in heat transfer performance. Local vapor quality has a weak effect on heat transfer coefficients, primarily noticeable at high mass fluxes, low heat fluxes, and low saturation temperatures.

De Oliveira et al. (2018) investigated flow patterns and heat transfer characteristics during the flow boiling of R-290 within a tube with a 1.0 mm inner diameter. Their experiments covered different ranges of heat and mass fluxes at a consistent saturation temperature of 25 °C. Significant impacts of both mass and heat flux on the heat transfer coefficient were observed, and predominant flow patterns such as slug, churn, wavy-annular, and smooth-annular flow regimes were identified. Additionally, a new method for flow pattern identification based on boiling number and slip ratio was proposed. Their study noted the prevalence of convective boiling for most flow patterns and the occurrence of dryout, even under lower mass velocities and higher heat flux conditions. Furthermore, it was found that the heat transfer coefficient increased with increasing vapor quality.

Hu et al. (2019) investigated the heat transfer behavior of mixed hydrocarbon refrigerants within spiral wound heat exchangers (SWHEs). In this case, the researchers focus on ethane/propane mixtures across varying ethane concentrations, observing how changes in vapor quality affect the heat transfer coefficient. They found an initial increase in heat transfer coefficient with rising vapor quality, peaking at 0.6 – 0.8 vapor quality before sharply declining. Additionally, the influence of ethane content on the heat transfer coefficient is examined, with notable fluctuations observed.

Oliveira et al. (2021) investigated the characteristics of different refrigerants in air-conditioning and refrigeration systems, specifically focusing on finding replacements for R134a. They tested three types of refrigerants — R290, R600a, and R1270 — and new mixtures by combining them. By doing experiments in a tube with certain conditions, like how fast the liquid flows and how hot it gets, they found that the pure hydrocarbon refrigerants generally transferred heat better than R134a, with R600a slightly better in some situations. They also noticed that the heat transfer improves when the liquid moves faster and gets hotter. These findings suggest that these hydrocarbon refrigerants and their mixtures could be good alternatives to R134a in air-conditioners and refrigerators. Zhao et al. (2023) investigated the heat transfer characteristics of R290 flowing through a horizontal micro-fin tube. Experimental analyses were conducted under various conditions, including different saturation pressures, mass fluxes, heat fluxes, and vapor qualities. Four distinct flow patterns were observed: bubbly, plug, slug, and annular flow. The onset of dry-out was found to occur when the liquid film thickness equaled the fin height, happening earlier at high heat fluxes and low saturation pressures. The maximum heat transfer coefficient and friction pressure drop were noted at the onset of dry-out, with the heat transfer coefficient showing a significant correlation with heat flux. In fact, other authors have focused on characteristics of R290 in flow boiling (Quenel et al. (2023); Fenouche and Ouadha (2023) and Zhao et al. (2023)) due to interesting thermodynamics characteristics for flow boiling.

In the current work, we intend to investigate the heat transfer characteristics and flow patterns during two-phase flow boiling of propane (R290) in various geometries and conditions. Additionally, understand the effects of parameters such

as mass flux, heat flux, and vapor quality on heat transfer coefficient and pressure drop during flow boiling of propane, including channel flow distribution and how it affects heat transfer and flow patterns.

2. EXPERIMENTAL APPARATUS

A research facility was made to study the flow boiling and pressure drop in multiport mini channels, as depicted in Fig. 1a. The setup comprises a loop for controlling mass flux and is designed to assess various fluids across various flow conditions. The primary circuit includes a pre-heater (PH), a test section (TS), and a visualization section (VS). The secondary circuit encompasses a condenser, a refrigerant reservoir, a vessel for liquid refrigerant, a magnetically driven micro gear pump, and a subcooler. The pre-heater (PH), a horizontal stainless-steel tube with a 4.4 mm inner diameter and 500 mm length, is uniformly heated via the Joule effect, establishing the experimental conditions entering the test section (TS) just downstream (Fig. 1b). Refrigerant flows into the PH as subcooled liquid and reaches saturation at the exit, determining the vapor quality at the TS inlet, which varies based on the heat flux applied to the PH. The TS comprises an extruded aluminum tube with seven parallel rectangular channels, each 300 mm in length and an average hydraulic channel diameter of 1.47 mm. Following the test section (TS), there is a visualization section (VS) with a length of 32 mm (refer to Fig. 1c). This section comprises a multiport tube that is open and mounted within a polycarbonate structure, enabling visualization of the flow pattern. During the tests, high-speed cameras were employed to capture images and videos of the flow.

3. RESULTS

The tests were conducted considering a mass flux G ranging from 35 to 170 kg/(m²s) and a heat flux q'' varying from 3.5 to 20 kW/m². Figure 2(a) presents the influence of G on the heat transfer coefficient, h , for a heat flux of $q'' = 20$ kW/m². In general, h increases with the increase of G and vapor quality, x , for $G > 35$ kg/(m²s). For $G \geq 100$ kg/(m²s), h increases even at low vapor quality conditions ($x < 0.3$), indicating a greater influence of convective boiling on heat transfer. For $G = 70$ kg/(m²s), h increases starting from $x > 0.4$. For $G \geq 55$ kg/(m²s), nucleate boiling predominates in heat transfer, even for $x > 0.7$. Indeed, for $G = 35$ kg/(m²s), heat transfer is fully governed by nucleate boiling due to the constant behavior of h with respect to x .

Mass flux is a principal factor that profoundly influences the process, particularly in convective boiling scenarios. Figure 2(b) illustrates how h varies with different q'' conditions, with G held constant at 70 kg/(m²s). Here, h demonstrates a notable reliance on q'' , even under low vapor mass conditions ($x < 0.3$). However, the dependence on q'' is irrelevant from $x \approx 0.55$, although h increases with x .

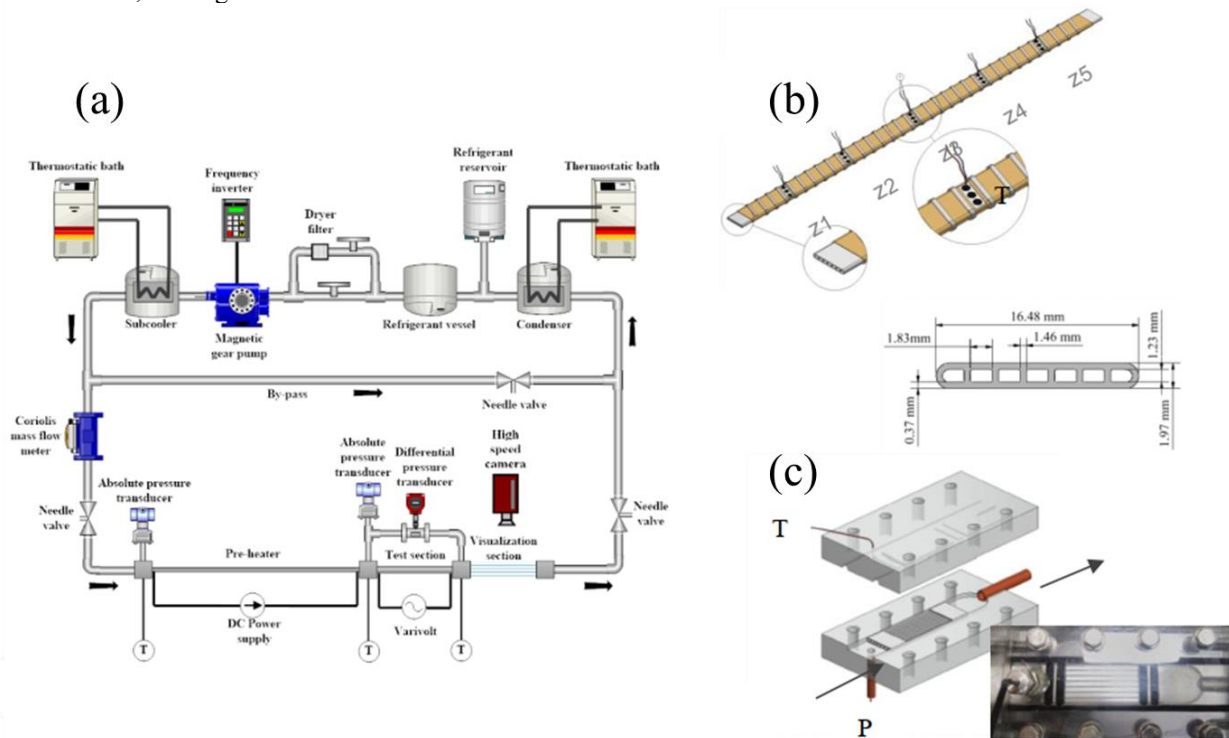


Figure 1. (a) Schematic view of the experimental facility; (b) Test section, TS – multiport minichannels and dimensions and (c) Visualization section, VS.

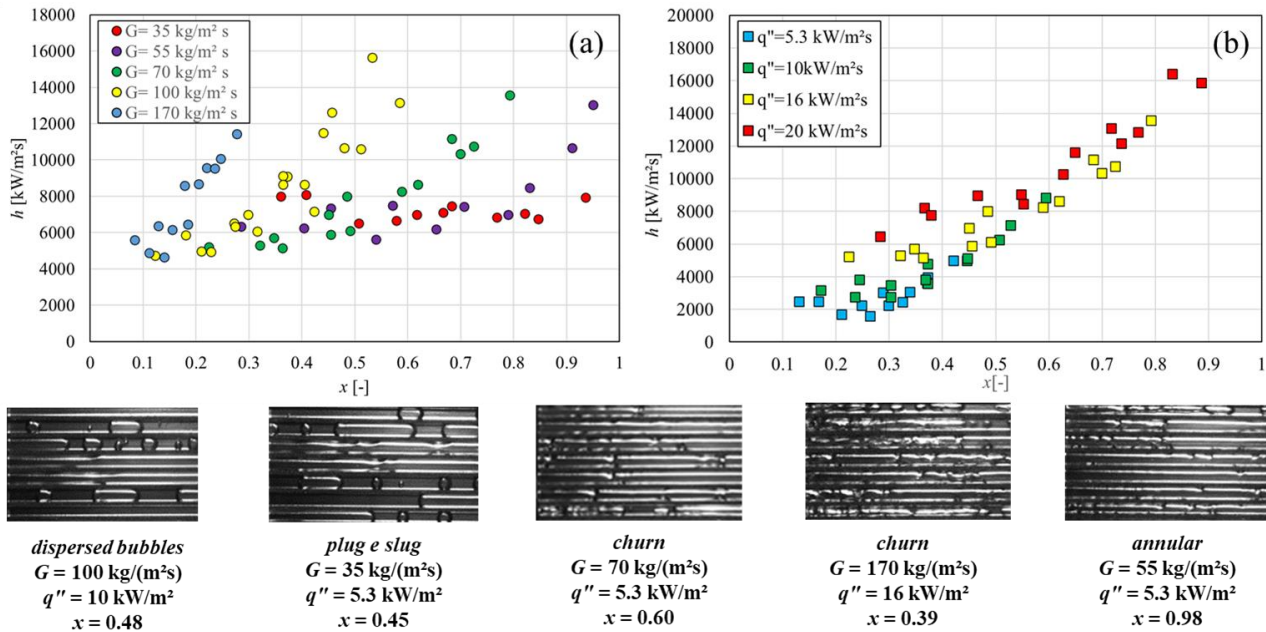


Figure 2. (a) Effect of G for a heat flux of 20 kW/m^2 ; (c) Effect of q'' for a mass flux of $70 \text{ kg/m}^2\text{s}$; (c) Flow patterns.

Figure 2(c) displays some samples of flow patterns encountered during the tests. Nucleate boiling is characterized by the presence of dispersed bubbles (bubbly flow) and plug flow. On the other hand, slug, churn and annular flows are found in conditions where h increases with the increase of x ; they are usually associated with higher h values, especially for $G > 35 \text{ kg/m}^2\text{s}$.

4. CONCLUSIONS

In summary, this study delves into heat transfer dynamics in flow boiling across varied mass and heat fluxes. Mass flux emerges as a critical factor, notably affecting convective boiling. The heat transfer coefficient, h , strongly depends on mass flux and vapor quality. Convective boiling predominates at higher mass fluxes, influencing heat transfer even at low vapor qualities. Conversely, nucleate boiling governs heat transfer at lower mass fluxes. Flow pattern analysis further elucidates the relationship between heat transfer and flow regimes. These findings offer insights for optimizing heat transfer systems in diverse engineering applications.

5. REFERENCES

- De Oliveira, J. D., Passos, J. C., Copetti, J. B., and van der Geld, C. W. M., 2018. "Flow boiling heat transfer of propane in 1.0 mm tube. *Experimental Thermal and Fluid Science*, Vol. 96, pp. 243–256.
- Fenouche, R., & Ouadha, A., 2023. Flow and heat transfer features during propane (R290) and isobutane (R600a) boiling in a tube. *International Journal of Thermofluids*, Vol. 20, pp. 100428.
- Hu, H., Ding, C., Ding, G., Chen, J., Mi, X., & Yu, S. 2019. Heat transfer characteristics of two-phase mixed hydrocarbon refrigerants flow boiling in shell side of LNG spiral wound heat exchanger. *International Journal of Heat and Mass Transfer*, Vol. 131, pp. 611–622.
- Lillo, G., Mastrullo, R., Mauro, A. W., and Viscito, L., 2018. "Flow boiling heat transfer, dry-out vapor quality and pressure drop of propane (R290): Experiments and assessment of predictive methods". *International Journal of Heat and Mass Transfer*, Vol. 126, pp. 1236–1252.
- Oliveira, G. H. S., Moreira, T. A., Ayub, Z. H., & Ribatski, G., 2021. "Flow boiling of hydrocarbons and their zeotropic binary mixtures under pre- and post-dryout conditions". *Applied Thermal Engineering*, Vol. 198, pp. 117483.
- Quenel, J., Anders, M., and Atakan, B., 2023. Propane-isobutane mixtures in heat pumps with higher temperature lift: An experimental investigation. *Thermal Science and Engineering Progress*, Vol. 42, pp. 101907.
- Zhao, C., Guo, H., Xue, H., Nie, F., Gong, M. and Yang, Z. 2023. Boiling heat transfer and pressure drop of R290 in a micro-fin tube. *International Journal of Refrigeration*, Vol. 155, pp. 195–206.

EXPERIMENTAL STUDY OF FLOW CONDENSATION HEAT TRANSFER OF R1233ZD(E) AT MODERATE AND HIGH SATURATION TEMPERATURES

Stanisław Gluch^{a*}, Dariusz Mikielwicz^a

^aGdansk University of Technology

*stanislaw.gluch@pg.edu.pl

Keywords: Thermodynamic critical point, Flow condensation, Heat transfer coefficient, Pressure drop, Heat pump

1. INTRODUCTION

High temperature heat pumps (HTHP) are one of the key technologies needed for the green energy transition. They provide an opportunity to utilize low and medium temperature waste heat for industrial processes with use of electricity from zero-emission sources. The key process of HTHP performance is flow condensation under high saturation temperature. Most literature condensation studies were executed for conventional conditions where saturation temperatures range from -20°C to 40°C . Moreover, many studies examining high saturation temperature condensation utilize refrigerants which are banned in the European Union for new applications due to ozone-depleting potential ODP and global warming potential GWP (Garimella et al., 2016; Jiang et al., 2007; Jiang & Garimella, 2003). The paper presents the results of an experimental study of flow condensation of R1233zd(E) in minichannel at moderate and high saturation temperatures. R1233zd(E) is an eco-friendly fluid with ODP 0 and GWP 1. The heat transfer coefficient and pressure drop were measured for flow condensation in a horizontal copper tube with a 3 mm internal diameter and a length of 50 mm. The experiment has been conducted for saturation temperatures ranging from 83°C to 145°C which corresponds to values of reduced pressures ranging from 0.2 to 0.7. Reduced pressure is the ratio of saturation pressure and critical pressure. Mass velocities ranged from 600 to 1000 kg/m²s. The effects of reduced pressure, mass velocity, heat flux, vapor quality, and flow regime were analyzed. The main objective of the research is to obtain new experimental data which allows to validate and develop prediction methods for heat transfer coefficient during condensation at high saturation temperatures.

2. Experimental Facility

The experimental facility is the development of testing stand designed for the measurement of heat transfer coefficient during flow boiling under high saturation temperatures used in research (Gluch et al., 2023; Pysz et al., 2023). A new condensation test section was added with two cooling loops. The condensation test section is pipe in pipe heat exchanger which is presented in Figure 1. The measurement method in principle is the same as in (Jiang & Garimella, 2003) with an improvement of temperature control in cooling loops. That testing facility used municipal water for cooling and could not control the temperature of the cooling water. The new testing rig utilizes an ultra-thermostat Julabbo f33 which allows setting the desired temperature between -30°C and 200°C (water is limited from 5°C to 99°C). Control of cooling fluid temperature allows for an increase or decrease in cooling heat duty and a change in heat flux during condensation. The scheme of the condensation testing facility is presented in the figure 1. The internal pipe diameter is 3 mm and the length of heat transfer is 50 mm. Measurement points of temperature and pressure are highlighted in Figure 2. Water flowing in the first cooling loop has a high mass flow which ensures a high heat transfer coefficient on the side of water, but heat duty measurement would have an unacceptable error in loop I. Mass velocity in Loop II is relatively small which allows accurate heat duty measurement. After the condensation test section, there is a visualization section. High speed camera Photron UX100 is used for the capture of two-phase flow structures.

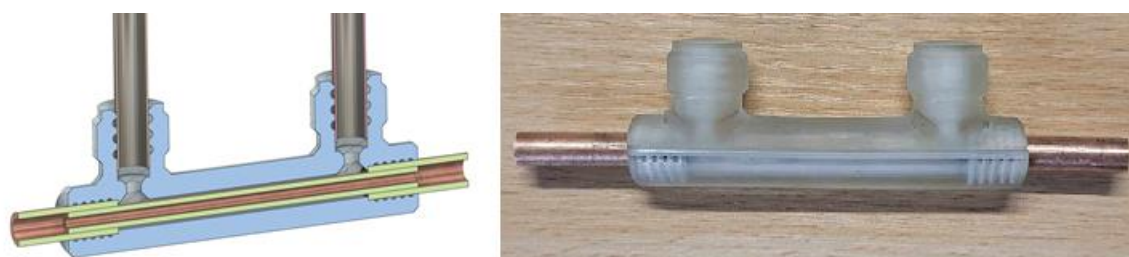


Figure 1. Drawing and photograph of condensation test section

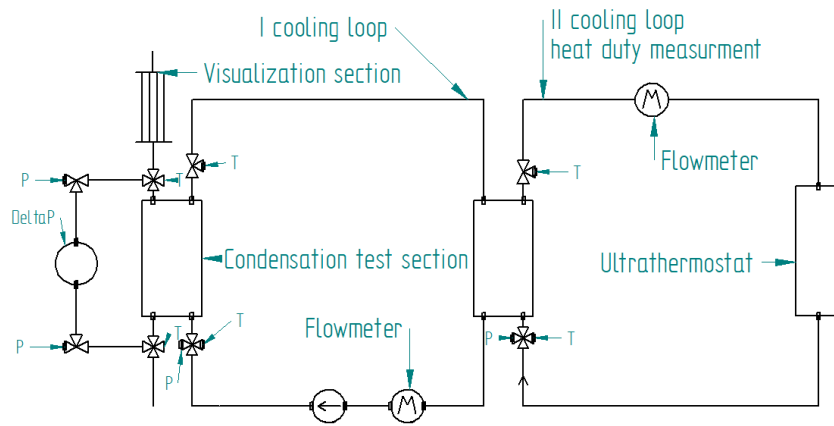


Figure 2. Scheme of condensation test section with cooling loops

3. Experimental results

Experiment results for two mass velocities are presented in the figure 3. Both diagrams present results for saturation temperature 83°C. Results are compared with the Mikielewicz prediction method (Mikielewicz & Mikielewicz, 2011). The full paper features experimental results for saturation temperatures up to 145°C which correspond to reduced pressure 0.7 compared with 7 prediction methods. Despite a saturation temperature of 83°C reduced pressure is only 0.2 Experimental data for a relatively well-predicted low value of reduced pressure is presented in Table 1.

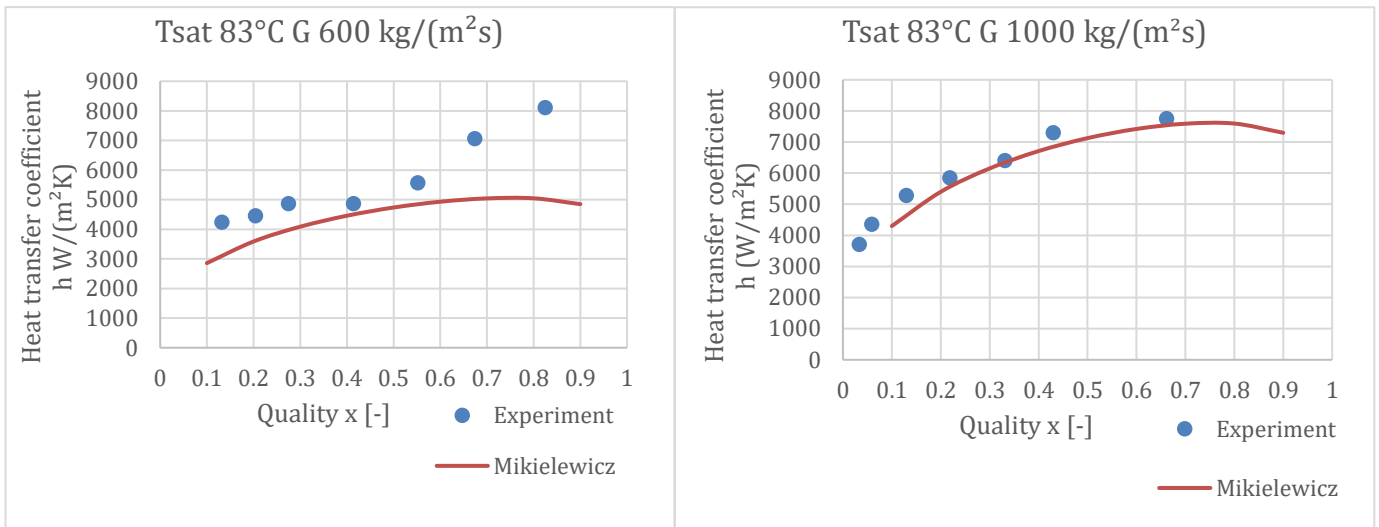


Figure 3. Results of the experiment for saturation temperature 83°C which corresponds to reduced pressure 0.2 for mass velocities 600 kg/(m²s) and 1000 kg/(m²s)

Table 1. Results of calculations for different modeling methods

Model	MAE Mean Absolute Error	Number of points within $\pm 30\%$	Percentage of points within $\pm 30\%$
Mikielewicz (Mikielewicz & Mikielewicz, 2011)	14.85%	13	92.86%
Shah 1979 (Shah, 1979)	15.03%	13	92.86%
Cavallini 2006 (Cavallini et al., 2006)	15.21%	13	92.86%

Horizontal flow structures are presented in the figure 4. On the top bubbly flow could be observed. The middle photograph features a wavy-annular flow and on the bottom is a fully developed annular flow. Vapor quality in the first photo is 11,98%, in the middle is 19.2% and in the third is 40.6%. Full paper feature flow maps for measured data.



Figure 4. Flow structures of R1233zd(E) in 3mm horizontal pipe under saturation temperature 83°C, saturation pressure 0.71 MPa, reduced pressure 0.2, and mass velocity 1000 kg/(m²s)

4. CONCLUSIONS

Experimental data for heat transfer coefficient during flow condensation of R1233zd(E) in a horizontal 3mm diameter minichannel are presented. Data covers two mass velocities, 600 kg/(m²s) and 1000 kg/(m²s), for saturation temperature 83°C. Literature prediction methods managed to predict experimental data with high accuracy for two-phase heat transfer. Experimental data for higher values of reduced pressure are needed to further validate literature prediction methods. Three flow structures are presented, which are bubbly, wavy-annular, and annular flow.

5. REFERENCES

- Cavallini, A., Del Col, D., Doretti, L., Matkovic, M., Rossetto, L., Zilio, C., & Censi, G. (2006). Condensation in horizontal smooth tubes: A new heat transfer model for heat exchanger design. *Heat Transfer Engineering*, 27(8), 31–38. <https://doi.org/10.1080/01457630600793970>
- Garimella, S., Andresen, U. C., Mitra, B., Jiang, Y., & Fronk, B. M. (2016). Heat Transfer During Near-Critical-Pressure Condensation of Refrigerant Blends. *Journal of Heat Transfer*, 138(5). <https://doi.org/10.1115/1.4032294>
- Gluch, S., Pysz, M., & Mikielewicz, D. (2023). Flow maps and flow patterns of R1233zd(E) in a circular minichannel at low, medium and high values of saturation pressure. *36th International Conference on Efficiency, Cost, Optimization, Simulation and Environmental Impact of Energy Systems, ECOS 2023*, 402–413. <https://doi.org/10.52202/069564-0037>
- Jiang, Y., & Garimella, S. (2003). Heat Transfer and Pressure Drop for Condensation of Refrigerant R-404A at Near-Critical Pressures. *ASHRAE Winter Meetings CD, Technical and Symposium Papers, 2003*, 667–677.
- Jiang, Y., Mitra, B., Garimella, S., & Andresen, U. C. (2007). Measurement of condensation heat transfer coefficients at near-critical pressures in refrigerant blends. *Journal of Heat Transfer*, 129(8), 958–965. <https://doi.org/10.1115/1.2401618>
- Mikielewicz, D., & Mikielewicz, J. (2011). A common method for calculation of flow boiling and flow condensation heat transfer coefficients in minichannels with account of nonadiabatic effects. *Heat Transfer Engineering*, 32(13–14), 1173–1181. <https://doi.org/10.1080/01457632.2011.562728>
- Pysz, M., Gluch, S., & Mikielewicz, D. (2023). Experimental study of flow boiling pressure drop and heat transfer of R1233zd(E) at moderate and high saturation temperatures. *International Journal of Heat and Mass Transfer*, 204. <https://doi.org/10.1016/j.ijheatmasstransfer.2023.123855>
- Shah, M. M. (1979). A general correlation for heat transfer during film condensation inside pipes. *International Journal of Heat and Mass Transfer*, 22(4), 547–556. [https://doi.org/10.1016/0017-9310\(79\)90058-9](https://doi.org/10.1016/0017-9310(79)90058-9)

EFFECT OF POROUS STRUCTURE OF NI-BASED OXYGEN CARRIER ON REACTION CHARACTERISTICS IN CHEMICAL LOOPING COMBUSTION

Masashi Kishimoto^{a*}, Kota Ike^a, Yuting Guo^a, Hiroshi Iwai^a

^aDepartment of Mechanical Engineering and Science, Kyoto University, Nishikyo-ku, Kyoto 615-8540, Japan

*kishimoto.masashi.3m@kyoto-u.ac.jp

Keywords: chemical looping combustion, porous media, microstructure, gas diffusion

1. INTRODUCTION

Reducing emissions of greenhouse gases such as carbon dioxide (CO₂) is considered urgent to curb global climate change. Currently, the combustion of fossil fuels is the main source of CO₂ emission; therefore, various technologies for carbon capture and storage (CCS) have been under investigation. Since the combustion gas contains a large amount of nitrogen from the air, absorbents such as amine-based materials (Dutcher et al., 2015) are used to selectively capture CO₂ in the combustion gas. However, these materials need to be regenerated after the CO₂-capturing process by supplying heat, which requires additional energy and complicates the entire system design. Oxygen combustion (oxy-combustion) (Nemitallah et al., 2017) is also proposed to prevent nitrogen from mixing into the exhaust gas; however, obtaining pure oxygen from ambient air requires additional processes and energy.

As an alternative way to utilize energy from the combustion of hydrocarbon fuels, chemical looping combustion (CLC) was proposed (Abuelgasim et al., 2021). The CLC system consists of two reactors, i.e., fuel and air reactors. Metal oxides, called oxygen carriers, circulate between these two reactors, and they offer oxygen to oxidize hydrocarbon fuels in the fuel reactor. Subsequently, they are regenerated (oxidized) by reacting with oxygen in the supplied air in the air reactor. Since the exhaust gas from the fuel reactor is a mixture of CO₂ and H₂O, CO₂ can be easily separated by simply removing H₂O through condensation.

Research on CLC is preceded by material exploration. It was found that metallic materials such as Ni, Fe, Cu, and Mn can smoothly offer oxygen to combust fuels (Fang et al., 2009), and ceramic materials such as Al₂O₃ can offer structural stability during the redox cycles. Therefore, the common oxygen carriers are composite porous materials of metal and oxide. Therefore, it is expected that the porous microstructure of the oxygen carriers has an influence on the gas transport and reaction within the particle. Hence, revealing the correlation between the microstructure and reactivity of the oxygen carrier is desired.

In this study, therefore, we experimentally investigate the influence of the porous microstructure of Ni-based oxygen carriers on their reactivity for methane combustion. Several oxygen carriers with different microstructures are fabricated and tested. From the exhaust gas analysis, the reaction characteristics and oxygen utilization ratio are quantified and compared among the fabricated oxygen carriers.

2. EXPERIMENTAL

Ni-based oxygen carrier was fabricated and tested. To increase the reactivity of the oxygen carrier and improve the structural stability during the redox cycle, nickel oxide was supported by ceramic particles to form a porous structure. To obtain various oxygen carriers with different porous microstructures, the solid volume ratio of Ni to support was varied as Ni: support = 25: 75, 35: 65, and 50: 50. Also, to increase the porosity in the porous structure, pore former (acrylic beads with a diameter of 1.5 μm) was added with a weight ratio of 10% and 30% for the oxygen carrier of Ni: support = 25: 75. First, the oxide (NiO), support (Al₂O₃), and pore former particles were mixed with planetary ball milling with isopropanol. After evaporating the isopropanol, the resultant powder was sieved with a mesh with size of 53 μm to remove agglomerates. Subsequently, the powder was uniaxially pressed in a mold to form a disk with a diameter of 30 mm and sintered at 1400°C for five hours. Finally, the sintered pellet was crushed into a coarse powder with a diameter of 250–500 μm. The obtained oxygen carrier was filled in a glass tube with an inner diameter of 8 mm. The amount of oxygen that can be utilized for combustion was maintained the same at the initial state (oxidized state) among the various oxygen carriers.

Figure 1 shows the schematic image of the experimental setup. The temperature of the oxygen carrier was maintained with an electric furnace. The reactant gas mixture was supplied using mass flow controllers, and the effluent gas was analyzed using a gas chromatograph and a film flow meter.

The porous microstructure of the oxygen carriers was analyzed using scanning electron microscopy (SEM). The oxygen carriers used in the experiment were first impregnated with epoxy resin and then cut and polished to expose the cross-section. The obtained SEM images were segmented into NiO (or Ni), support, and pore phases, and their volume fractions were quantified based on the area fraction on the images.

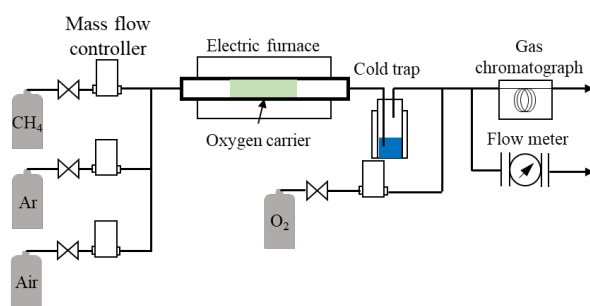


Figure 1. Schematic image of the experimental setup.

3. RESULTS AND DISCUSSION

Figure 2 shows the effluent gas flow rate during the methane combustion process. The black lines represent the amount of solid carbon deposited in the oxygen carrier in the unit of sccm (standard cubic centimeter per minute), which was evaluated from the atomic balance of carbon. Similarly, the purple lines represent the amount of steam, which was evaluated from the atomic balance of hydrogen. The existence of H_2 and solid carbon suggests the methane cracking reaction at the oxygen carrier. The generated H_2 and carbon are subsequently oxidized using the oxygen in the oxygen carrier, forming CO and CO_2 . Formation of CO, CO_2 , and H_2O continued for about 20 min in the oxygen carrier with Ni: support = 25: 75 solid volume ratios, whereas about 60 min in 50: 50 and 30 min in 25: 75 with 30% pore former. Since the total amount of nickel oxide in the oxygen carrier was the same among the three oxygen carriers tested, the difference in the duration of the reaction is considered to be a result of their microstructure.

Figure 3 compares the oxygen utilization during the combustion process among the oxygen carriers with different microstructures. The oxygen utilization is defined as the ratio of oxygen utilized during the reaction to the total amount of oxygen in NiO. The amount of oxygen utilized during the reaction was evaluated from the flow rates of CO, CO_2 , and H_2O in the effluent gas. It can be observed that oxygen utilization increases as the amount of NiO in the oxygen carrier increases and as the amount of pore former used in the fabrication process is higher. It is also found that not all the NiO in the oxygen carrier released oxygen during the supplied methane. This suggests that some NiO particles in the oxygen carriers were inaccessible to the supplied methane.

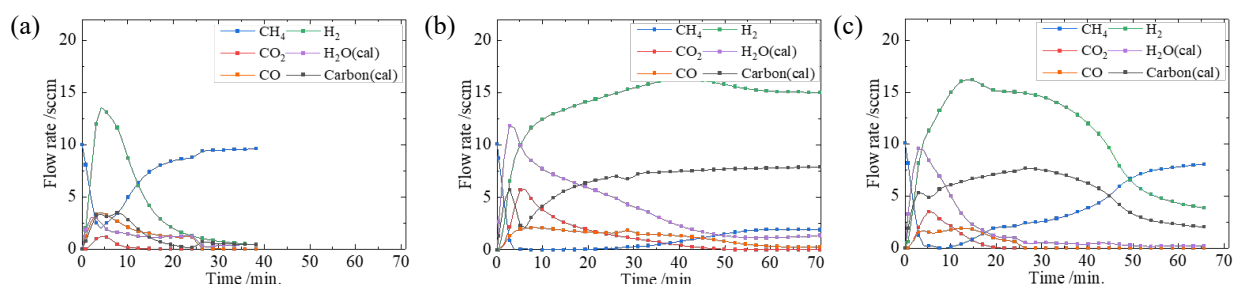


Figure 2. Effluent flow rate of gas species during methane combustion process. Ni: support = (a) 25: 75, (b) 50:50, and (c) 25: 75 with 30 wt.% pore former.

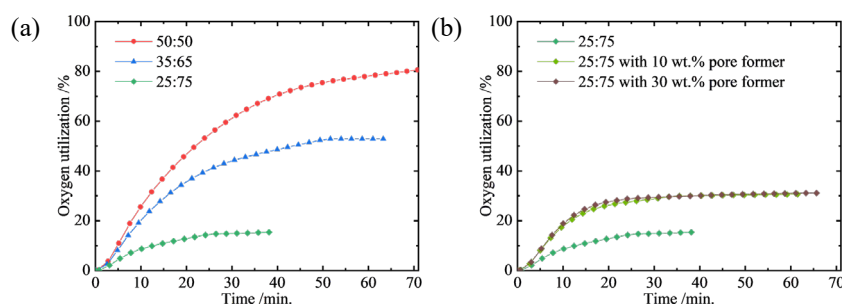


Figure 3. Oxygen utilization in oxygen carriers during methane combustion process. (a) Effect of solid volume fraction, and (b) effect of amount of pore former.

Figure 4 shows the cross-sectional micrograph of the oxygen carriers after the methane combustion process. White, gray, and black phases correspond to NiO (or Ni), support, and pore phases, respectively. It can be observed that the amount of pore phase (porosity) increases as the Ni ratio in the oxygen carrier is higher. Similarly, the porosity increases as the amount of pore former used during fabrication was higher.

Since the oxygen carriers were prepared using the uniaxial pressing process, the porosity in the oxygen carriers is expected to be marginal unless a pore former was added. Therefore, the reaction of NiO is considered to be initiated from the outer surface of the oxygen carriers of Ni: support = 25: 75, 35: 65, and 50: 50. As the reaction proceeds, NiO is reduced to Ni, and its volume shrinks to form additional pores in the oxygen carrier. Such pores help the gaseous methane diffuse into the oxygen carriers and further react with NiO. As the amount of NiO in the oxygen carrier is larger, the NiO particles are more likely to be interconnected with each other, resulting in the forming of percolated pores after reduction. This is the possible reason oxygen utilization increases as the solid ratio of NiO increases in the oxygen carrier, as shown in Fig. 3(a). On the other hand, when the oxygen carriers are prepared by adding pore former, they tend to have larger pores even in the fully oxidized state. Therefore, the pores that lead the supplied methane into the oxygen carriers are formed more easily. This results in the larger oxygen utilization in the oxygen carriers fabricated with pore formers, as shown in Fig. 3(b).

In addition to the oxygen utilization, the reaction rate can also be roughly estimated from the slope of the graph in Fig. 3. Since the chemical loop combustion process is inherently a slower process than the gas-phase combustion process, enhancement of the reaction rate is desired. In this sense, adding the pore former is found to be effective in increasing the porosity in the oxygen carrier at the oxidized state and, hence, offering larger reaction sites.

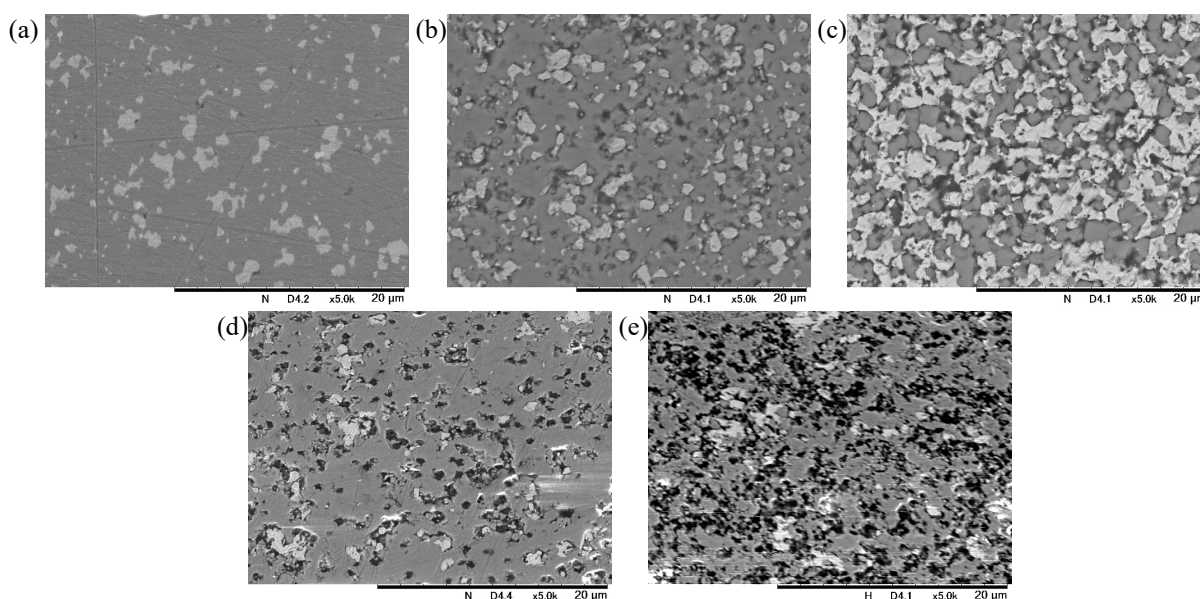


Figure 4. Cross-sectional SEM images of oxygen carriers after methane combustion process. Ni: support = (a) 25: 75, (b) 35: 65, (c) 50: 50, (d) 25: 75 with 10 wt.% pore former, and (e) 25:75 with 30 wt.% pore former.

4. CONCLUSIONS

The effect of the porous microstructure of Ni-based oxygen carriers on their reaction characteristics has been experimentally investigated. Several oxygen carriers with different internal porous media were fabricated by varying the solid volume ratio and the amount of pore former added in the starting material. Oxygen utilization was evaluated based on the effluent gas analysis. It has been revealed that the oxygen utilization increases as the solid volume ratio of nickel increases and the amount of pore former is larger. The SEM observation of the oxygen carrier revealed that significant differences in the amount and morphology of the pore phase were identified. The oxygen utilization and reaction rate of the oxygen carrier were enhanced by increasing the initial porosity inside the carrier to offer smoother gas transport and a larger reaction surface.

5. REFERENCES

- Abuelgasim, S., Wang, W. and Abdalazeez, A., 2021. "A brief review for chemical looping combustion as a promising CO₂ capture technology: Fundamentals and progress". *Sci Total Environ*, Vol. 764, pp. 142892.
- Dutcher, B., Fan, M. and Russell, A. G., 2015. "Amine-based CO₂ capture technology development from the beginning of 2013-a review". *ACS Appl Mater Interfaces*, Vol. 7, pp. 2137-2148.
- Fang, H., Haibin, L. and Zengli, Z., 2009. "Advancements in Development of Chemical-Looping Combustion: A Review". *International Journal of Chemical Engineering*, Vol. 2009, pp. 1-16.
- Nemitallah, M. A., Habib, M. A., Badr, H. M., Said, S. A., Jamal, A., Ben-Mansour, R., Mokheimer, E. M. A. and Mezghani, K., 2017. "Oxy-fuel combustion technology: current status, applications, and trends". *International Journal of Energy Research*, Vol. 41, pp. 1670-1708.

LDV AND PIV MEASUREMENTS OF TURBULENT BOUNDARY LAYER FLOW OVER TRAVELING WAVY WALL FOR DRAG REDUCTION

Yasuhiro YOSHIDA^a, Tomohiro NIMURA^a, Akira MURATA^a, and Kaoru IWAMOTO^{a*}

^aDepartment of Mechanical Systems Engineering, Tokyo University of Agriculture and Technology
2-24-16, Nakacho, Koganei, Tokyo, 184-8588, Japan

*iwamotok@cc.tuat.ac.jp

Keywords: Turbulence Control, Drag Reduction, Turbulent Boundary Layer Flow, PIV, LDV

1. INTRODUCTION

Reducing energy consumption of transportation equipment is an important issue for sustainable development in society. One effective way to solve this problem is to reduce frictional drag in boundary layers that develop on aircraft and vehicles by suppressing their turbulence. To achieve this, many researchers have demonstrated that passive or active wall deformations can reduce the drag. In this study, we focus on a periodic (open-loop) active wall deformation in the form of a traveling wave, where the wall deforms in the normal direction and travels in the streamwise direction. The wall deformation at the given time t and the streamwise location x is formulated as

$$y_{wall} = \eta \sin\left(\frac{2\pi}{\lambda}(x - ct)\right), \quad (1)$$

where η , λ , and c are the amplitude, the wavelength, and the wave speed. The traveling wave can substantially reduce the drag of internal turbulent flows, as reported in studies of direct numerical simulations (DNS) (Nakanishi *et al.*, 2012) and experiments (Suzuki *et al.*, 2019). They have achieved reductions in the drag by 60% and 10%, respectively, compared to plane walls. However, it remains to be investigated whether the traveling wave can reduce the drag in turbulent boundary layer flows.

Coherent structures in the near-wall region play a significant role in sustaining turbulence (Robinson, 1991). Turbulent controlling methods of wall turbulence for drag reduction affect the nature of the coherent structures so that they lead to reductions in the Reynolds shear stress (RSS). While many studies have been devoted to observing such modifications to understand their mechanisms to suppress turbulence, research on the effects of the traveling wavy wall is limited.

We have two main objectives in this study. One is to quantify the drag reduction effect of turbulent boundary layer flow due to the traveling wavy wall. The other is to observe modifications of the coherent structure in terms of streaky structures, which are involved in maintaining turbulence. We perform measurements with a laser Doppler velocimetry (LDV) for the former objective, and a particle image velocimetry (PIV) for the latter.

2. EXPERIMENTAL SETUP AND PROCEDURE

An open-loop wind tunnel is used for this study, and its test section for turbulent boundary layer flow is shown in Fig. 1a. A cross section of the upstream edge of the test section is $200 \times 200 \text{ mm}^2$, whose height is expanded in the streamwise direction to adjust the pressure gradient in the streamwise direction to zero. A trip wire with a diameter of 3 mm is placed in the inlet of the wind tunnel to promote the transition of the flow into turbulence. In this paper, the origin of the Cartesian coordinate system is on the wall where the trip wire is placed. The wall consists of a stable acrylic wall for the development of the flow in the range $x < 0.9 \text{ [m]}$, and a flexible rubber sheet to generate the traveling wave on it in the range $x \geq 0.9 \text{ [m]}$. In this study, a condition with the traveling waves is referred to as “wavy”, while a condition without the wave is

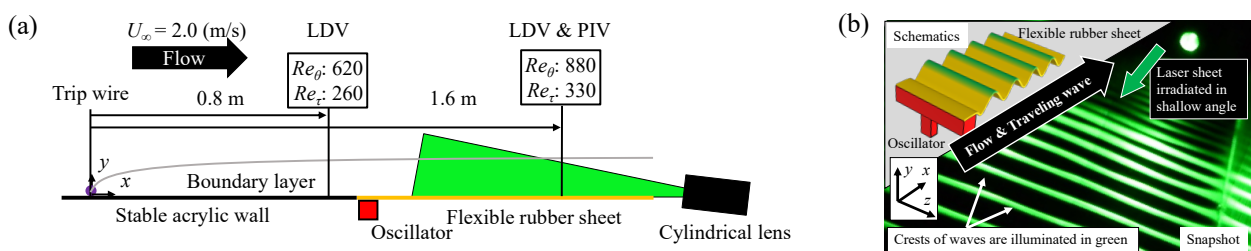


Figure 1. Schematics of experimental apparatus: (a), test section of the zero-pressure-gradient boundary layer wind tunnel with the flexible rubber sheet and their lighting for the PIV measurements; (b), schematics and snapshot of the visualization of generated traveling wave.

“flat”. A schematic of the generating method and a snapshot of a visualization experiment are shown in Fig. 1b. The upstream edge of the rubber sheet is oscillated so that the wave propagates on the rubber sheet with attenuation in the streamwise direction. The visualization experiment was performed by illuminating crests of the waves with a laser sheet irradiated in a shallow angle to discern the wave was uniform in the spanwise direction. The wave is generated so that their parameters η , λ , and c are within the range of the condition for the relaminarization proposed by Nakanishi *et al.* (2012). Streamwise distributions of these parameters are measured by a laser displacement meter, and it was within the appropriate range, as shown in a previous study by Suzuki *et al.* (2019).

All experiments are carried out with free stream velocity $U_\infty = 2.0$ m/s, whose turbulent intensity is less than 1.0%. The Reynolds numbers based on the momentum thickness (Re_θ) and that based on the friction velocity (Re_τ) are 620 and 220 in $x = 0.8$ [m] and 880 and 330 in $x = 1.6$ [m], respectively. A seeding was operated with silicon oil with a diameter of 1 μm for both LDV and PIV measurements. LDV measurements are performed at $x = 0.8$ [m] and $x = 1.6$ [m] to obtain wall-normal profiles in each location. We utilized a back-scattering two-component LDV (Artium, Inc.) to obtain the streamwise and the wall-normal components of the flow velocities. PIV measurements are performed at $x = 1.6$ [m] with an area of 80 (streamwise) \times 70 (wall-normal) mm^2 , which corresponds to 510×440 wall units, by a high-speed CCD camera with a resolution of 1280×1024 pixel². We obtained 2590 pairs of images at the recording rate of 15 Hz, which is strictly one-tenth of the frequency of the wall deformation, with a pulse delay of 200 μs . Velocities are yielded by spatial cross-correlation of seeded images with a window size of 32×8 pixel² with an overlap of 50%.

3. RESULTS AND DISCUSSION

Total drag coefficients between $x = 0.8$ [m] and $x = 1.6$ [m] are evaluated by the streamwise integral of the von Kármán momentum integral equation

$$C_D = \frac{2}{L} \Delta\theta - \frac{2}{L} \int_0^h \frac{\Delta \overline{u'u'}}{U_\infty^2} dy + \frac{2}{L} \int_0^h \frac{\Delta P}{\rho U_\infty^2} dy, \quad (2)$$

where θ is the momentum thickness, h is a wall-normal height that is greater than 99% boundary layer thickness, and P is the pressure. Here, Δ denotes a difference between $x = 0.8$ [m] and $x = 1.6$ [m], which are separated by $L = 0.8$ [m]. Note that we calculated P from the Reynolds averaged boundary layer equation in the wall-normal direction, i.e., $P(y) = \overline{v'v'}(y) + P_\infty$, instead of a measurement of the pressure. A drag reduction rate due to the traveling wave is evaluated as

$$R_D = \frac{C_D^{\text{flat}} - C_D^{\text{wavy}}}{C_D^{\text{flat}}} \times 100[\%], \quad (3)$$

where C_D^{flat} and C_D^{wavy} are the total drag coefficients in Eq. (2) for the flat and the wavy cases. It was estimated as 12.2 % with an uncertainty of ± 3 %. The error is evaluated by the propagation from the statistical error and an uncertainty due to an adjustment of the pressure gradient in the free stream.

This study operates a three-component decomposition for instantaneous velocities \mathbf{u} as $\mathbf{u} = \bar{\mathbf{u}} + \tilde{\mathbf{u}} + \mathbf{u}''$, where $\bar{\mathbf{u}}$ denotes the time average, $\tilde{\mathbf{u}}$ denotes the periodic fluctuation accompanied by the traveling wavy motion, and \mathbf{u}'' denotes the stochastic fluctuation. The wall-normal profiles of the streamwise velocity \bar{u} , the streamwise stochastic Reynolds normal stress $\overline{u''u''}$, and the stochastic RSS $-\overline{u''v''}$ are shown in Fig. 2. Here, superscript ()⁺ indicates the normalization by the kinematic viscosity and the friction velocity for the flat wall case. The mean velocity shown in Fig. 2a is reduced in the near-wall region while it is enhanced in the outer region. This modification is known as the typical response of the turbulent suppression that leads the drag reduction. Fluctuating quantities shown in Fig 2b and 2c directly indicate that the turbulence is well suppressed in a wide wall-normal range of the boundary layer.

Figure 3 shows the typical instantaneous flow field of the stochastic fluctuation in the streamwise direction u'' obtained

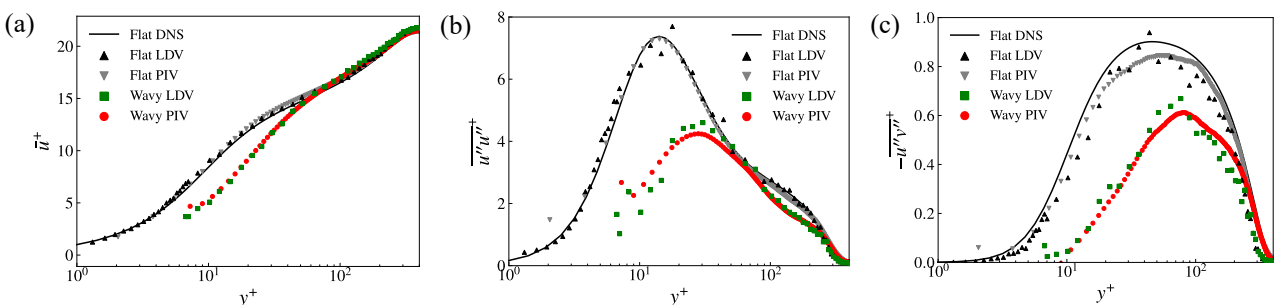


Figure 2. Wall-normal profile of turbulent statistics in $x = 1.6$ [m]: (a) mean streamwise velocity; (b) streamwise stochastic Reynolds normal stress; (c) stochastic RSS. The DNS data is taken from the data base of KTH (Schlatter and Örlü., 2010) at $Re_\theta = 1000$.

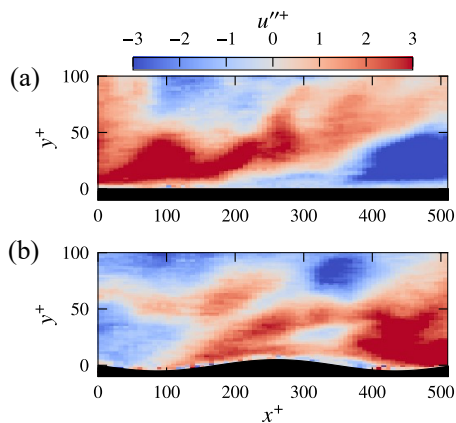


Figure 3. Typical instantaneous field of stochastic streamwise velocity fluctuation: (a) flat; (b) wavy. The region inside the wall is colored with black.

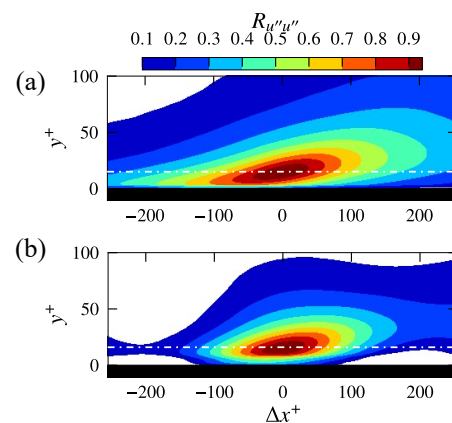


Figure 4. Map of two-point correlation of stochastic streamwise velocity fluctuation: (a) flat; (b) wavy. Dot-dashed lines in white indicate $y_{ref}^+ = 15$.

by the PIV measurements. In the flow over the flat wall, it can be observed that clusters of high- and low-momentum fluids, which are elongated in the streamwise direction (Fig.3a). The structures with similar features can be found in the wavy case (Fig. 3b), which indicates that the typical near-wall structures exist even in the flow over the wavy wall. To extract average structural features in the buffer layer, we utilize the two-point correlation, which is defined as

$$R_{u''u''}(\Delta x, y) = \frac{\overline{u''(x, y_{ref}) u''(x + \Delta x, y)}}{\sqrt{\overline{u''^2}(y_{ref})} \sqrt{\overline{u''^2}(y)}}, \quad (4)$$

where the Δx is the spatial separation in the streamwise direction, y_{ref} is the wall-normal reference location. Here, we assumed the statistically homogeneous in the streamwise direction within the measurement area. Fig. 4 shows the map of the two-point correlation with $y_{ref}^+ = 15$. Here, the streamwise length satisfying $R_{u''u''} > 0.2$ was shortened from 600 to 300 by the traveling wave.

The Reynolds normal stress shown in Fig. 2b is notably reduced in their peak. This peak in the flat wall is known that their fluctuating energy is mainly comprised of the streaky structure, whose representative streamwise length scale of approximately 1000 in wall units (Robinson, 1991). That structure is well captured by the correlation (Fig. 4a), while its streamwise extent is reduced in the wavy condition (Fig. 4b). This phenomenon may indicate that the streamwise extent of the streaks is shortened due to the wavy wall.

4. CONCLUSIONS

We performed LDV and PIV measurements of the turbulent boundary layer flow over the traveling wavy wall deformation generated on the flexible rubber sheet. The LDV measurements in two streamwise locations confirmed that the drag reduction rate $R_D = 12.2\%$ with the von Kármán integral equation. Turbulent fluctuations were reduced in the wavy wall case, and it is considered a cause of the drag reduction. We observed the instantaneous flow fields and the two-point correlations with the PIV to understand the near-wall coherent structures in the drag-reduced flow. Even in the flow over the wavy wall, the near-wall coherent structures can be found as the case of the flat wall, however, their spatial features are different. The correlation with the reference height $y_{ref}^+ = 15$ was reduced for the case of the wavy wall, as it indicates that the streaky structures in the buffer layer are shortened. We will present extensive discussion by observing the correlation in various reference locations in the phase direction at the conference.

5. REFERENCES

- Nakanishi, R., Mamori, H., and Fukagata, K., 2012. "Relaminarization of turbulent channel flow using traveling wave-like wall deformation". *International Journal of Heat and Fluid Flow*, Vol. 35, pp. 152–159.
- Robinson, S. K., 1991. "Coherent motions in the turbulent boundary layer". *Annual Review of Fluid Mechanics*, Vol. 23, pp. 601–639.
- Schlatter, P., and Örlü, R., 2010 "Assessment of direct numerical simulation data of turbulent boundary layers". *Journal of Fluid Mechanics*. Vol. 659, pp. 116–126.
- Suzuki, I., Shimura, T., Mitsuishi, A., Iwamoto, K., and Murata, A., 2019. "Experimental study on drag reduction effect with traveling wave control using PIV measurement". In *Proceedings of ASME - JSME - KSME Joint Fluids Engineering Conference 2019*, pp. 48-55.

Thermographic Sensing of Benard-Cell Convection: Investigating Heat Transfer and Fluid Dynamics in Rectangular Containers with Free Surfaces

Shashi Rastogi, Parthkumar Sohaliya, and Chirodeep Bakli*

Thermofluidic and Nanotechnology for Sustainable Energy Systems Laboratory, School of Energy Science and Engineering, Indian Institute of Technology Kharagpur, Kharagpur 721302, India

* chirodeep@iitkgp.ac.in

ABSTRACT

The Rayleigh-Bénard convection (RBC) phenomenon occurring within an enclosure remains a compelling example of a complex fluid system, characterized by the interplay of buoyancy forces, thermal gradients, and fluid motion. Theoretical exploration of Rayleigh-Bénard convection has long been challenging due to the intricate nature of these unstable stratified flows, where small perturbations can lead to significant changes in flow patterns. In this study, we employ infrared thermography to experimentally investigate Rayleigh-Bénard convection within a fluid layer heated from below, enabling precise measurements of the temperature field at the solid-liquid interface. Through careful analysis, we unveil the intricate dynamics governing the convection process, including the formation of convective rolls and the emergence of coherent structures. Our findings underscore the pivotal role played by the geometry of the closed containers and the thickness of the fluid in shaping the convection patterns, highlighting the complex interplay between boundary conditions and fluid dynamics. This work not only deepens our fundamental understanding of RBC but also carries broad significance for diverse fields, including geophysics, astrophysics, and engineering, where convection is paramount for heat and mass transport.

Keywords: Rayleigh-Bénard convection, Benard cells, thermal imaging, fluid instability.

1. INTRODUCTION

Thermal convection, broadly defined as the transfer of heat between two points facilitated by fluid motion, represents a fundamental aspect of fluid dynamics. Natural convection emerges when heat transfer is driven solely by buoyancy forces, arising from density variations within the fluid induced by temperature gradients [1]. This phenomenon often exhibits inherent instabilities within the fluids, leading to complex flow patterns and dynamic behavior. A notable manifestation of this instability is observed in Rayleigh-Bénard convection [2], where a fluid layer heated from below experiences spontaneous flow instabilities, resulting in the formation of characteristic convective cells known as Benard cells. In this particular family of instability when we focus on the thin layer of liquid whose upper layer is open to the atmosphere, the surface tension forces also play an important role which results in a phenomenon called Rayleigh-Benard- Marangoni instability or Benard-Marangoni instability [3]. The occurrence of the Benard-Marangoni instability at the surface of a fluid heated from below presents an accessible experimental phenomenon. However, visualizing and analyzing the data for such occurrences can prove challenging [4]. In these experiments, when the temperature surpasses a certain threshold, a spatio-temporal pattern comprising Benard cells emerges [5], defining the regime as Benard convection. Moreover, the size and number of these Benard cells are contingent upon the thermophysical properties of the fluid [6] and the shape of the container in which the fluid resides. At times, these patterns elude direct observation with the naked eye, necessitating thermal imaging for comprehensive analysis.

In this study, we conducted a thermographic examination of Rayleigh-Benard convection within a square enclosure. Our investigation aimed to comprehensively characterize the temperature distribution and flow dynamics within the system under varying experimental conditions. By employing advanced thermal imaging techniques, we aimed to elucidate the subtle nuances of the convective patterns, shedding light on the underlying mechanisms driving the Benard-Marangoni instability. Additionally, we sought to explore the influence of different fluid properties and container geometries on the formation and evolution of Benard cells, providing valuable insights into the intricate interplay between thermophysical parameters and convection behavior.

2. EXPERIMENTAL SETUP

The experimental setup comprises a rectangular acrylic box with dimensions outlined in **Table 1**. A base aluminum sheet of thickness 6mm is affixed, directly in contact with the hot plate. The box is filled with silicon oil to a specified depth (δ) and remains open at the top, as depicted in **Figure 1**. We employ the FLUKE Ti480 PRO IR Fusion thermal camera (temperature range $-20\text{ }^{\circ}\text{C}$ to $+650\text{ }^{\circ}\text{C}$), renowned for its precision and versatility. This cutting-edge instrument provides high-resolution thermal images, facilitating detailed analysis and interpretation of heat transfer phenomena at the solid-liquid interface. Both the schematic and the physical experimental setups are illustrated in **Figure 1**. (a) and (b).

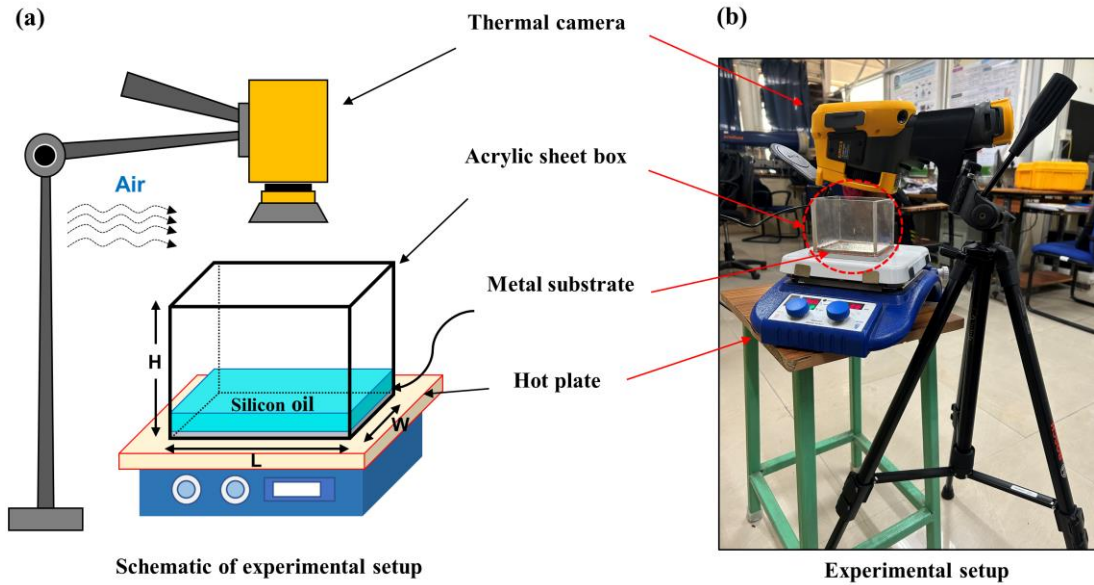


Figure 1. (a) Schematic of experimental setup and (b) actual experimental setup.

Table 1. Dimensions of the acrylic boxes used in the experiment.

Box	Length (L)	Width (W)	Height (H)
Box I	88mm	88mm	80mm
Box II	120mm	80mm	80mm

Two different box sizes are taken in which the length (L), and width (W) are varied. Boxes with different aspect ratios affect the convection phenomenon and hence the Bernard cells pattern. Furthermore, we have also varied the oil thickness δ between 5 to 15mm in order to see its effect on the size and the number of convection cells. The camera height is fixed and it is the same for each experiment.

We initiate our experiment using Box I and a 5mm thick layer of oil heated at the base through a hotplate and observing the formation of Bernard cells. Subsequently, we vary the oil thickness to 10mm and 15mm to assess how the oil height impacts Bernard cell formation. We then replicate the experiment using Box II to explore the influence of box shape on cell size and quantity. Since our experiment is in its preliminary stages and the heat provided by the hot plate is non-uniform, distinguishing Bernard cell size and shape proves challenging. To enhance precision, we plan to uniformly heat the box bottom in future trials. Additionally, we intend to affix thermocouples to the base to monitor temperature differentials at which Bernard cells form across all cases.

3. RESULTS & DISCUSSIONS

At an initial oil thickness of 5mm ($\delta = 5\text{mm}$), Bernard cell formation occurs at approximately a temperature of 50.1°C ($\pm 0.1^{\circ}\text{C}$), as depicted in Figure 2 (a). Notably, the cells appear small, randomly distributed, and numerous. As the temperature rises to around 61.3°C ($\pm 0.1^{\circ}\text{C}$), these cells begin to disintegrate, leading to a uniform heating of the entire system until a steady temperature is attained. Moreover, with an increase in oil thickness to 10mm ($\delta = 10\text{mm}$), we note the initiation of Bernard cell formation at 33.6°C ($\pm 0.1^{\circ}\text{C}$), indicating a somewhat more uniform cell structure as compared to the previous case. Additionally, there is a reduction in the number of cells, and the destruction of cells commences at 100.8°C ($\pm 0.1^{\circ}\text{C}$). Upon further increasing the oil thickness to 15mm ($\delta = 15\text{mm}$) (depicted in Figure 2. (c)), there is a decrease in the number of cells, resulting in a slightly larger pattern compared to the other two cases. From our preliminary experiments, we can infer that the formation of Bernard cells is significantly influenced by the fluid

height. In forthcoming experiments, we will investigate how the enclosure's shape impacts Bernard cell formation and elucidate the underlying physics governing such pattern formation.

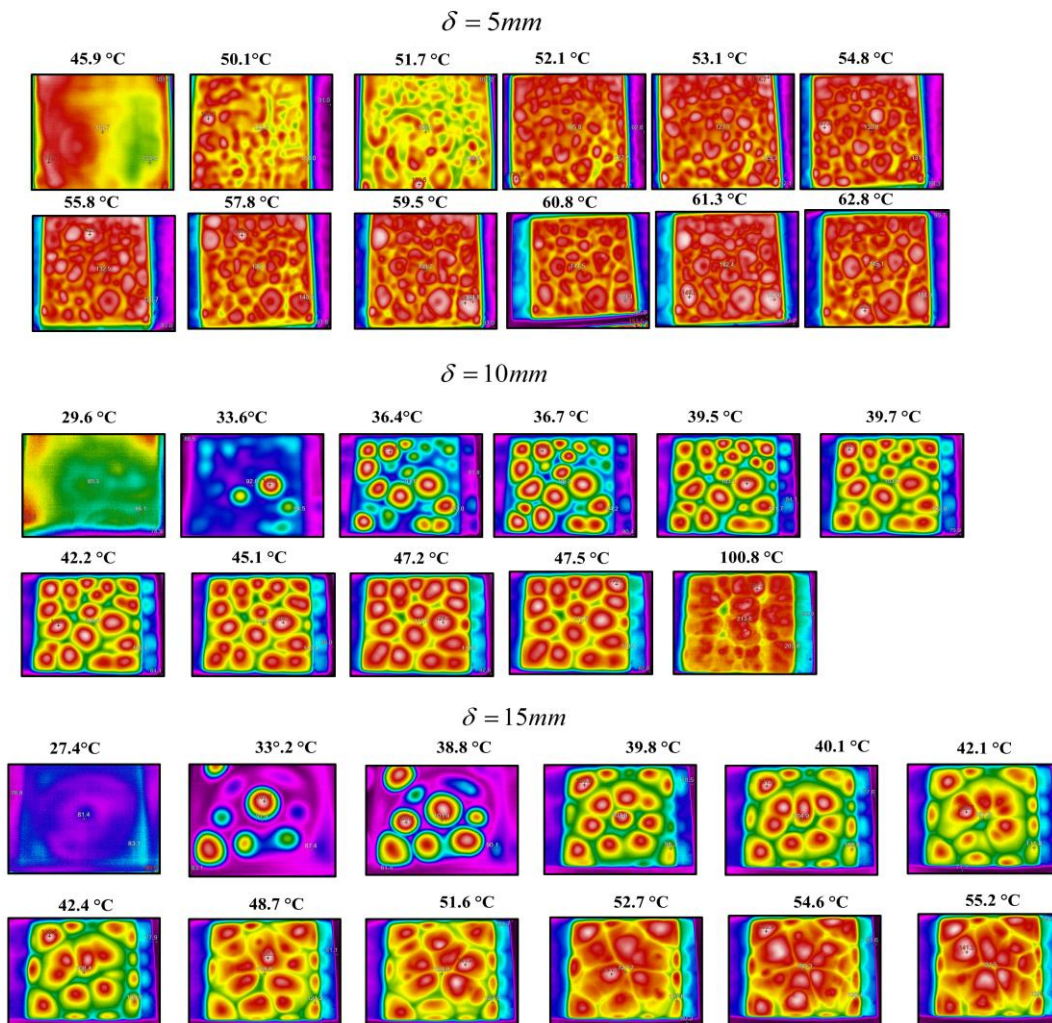


Figure 2. Benard cell formation for oil thickness (a) 5mm (b) 10mm and (c) 15mm.

5. REFERENCES

- [1] K.B. Saleem, A.H. Marafie, K. Al-Farhany, W.K. Hussam, G.J. Sheard, Natural convection heat transfer in a nanofluid filled l-shaped enclosure with time-periodic temperature boundary and magnetic field, *Alexandria Eng. J.* 69 (2023) 177–191. <https://doi.org/10.1016/j.aej.2022.12.030>.
- [2] Lord Rayleigh, LIX. On convection currents in a horizontal layer of fluid, when the higher temperature is on the under side, *London, Edinburgh, Dublin Philos. Mag. J. Sci.* 32 (1916) 529–546. <https://doi.org/10.1080/14786441608635602>.
- [3] R. Es Sakhly, K. El Omari, Y. Le Guer, S. Blancher, Rayleigh–Bénard–Marangoni convection in an open cylindrical container heated by a non-uniform flux, *Int. J. Therm. Sci.* 86 (2014) 198–209. <https://doi.org/10.1016/j.ijthermalsci.2014.06.036>.
- [4] R. Guido, M. Dutra, M. Monteiro, A.C. Martí, Seeing the invisible: convection cells revealed with thermal imaging, *Eur. J. Phys.* 44 (2023) 055102. <https://doi.org/10.1088/1361-6404/ace80e>.
- [5] T. Inagaki, M. Hatori, T. Suzuki, Y. Shiina, Heat transfer and fluid flow of benard-cell convection in rectangular container with free surface sensed by infrared thermography, *J. Vis.* 9 (2006) 145–160. <https://doi.org/10.1007/BF03181758>.
- [6] W. Waris, M. Lappa, Thermographic analysis of topographically controlled Marangoni–Rayleigh–Bénard convection in a fluid with temperature-dependent properties, *Int. J. Therm. Sci.* 196 (2024) 108718. <https://doi.org/10.1016/j.ijthermalsci.2023.108718>.

ADVANCING EXPERIMENTAL THERMAL ANALYSIS OF ELECTRIC MACHINES BY AVERAGE WINDING TEMPERATURE MEASUREMENTS

Jasper Nonneman^{a,b,*}, Ilya T'Jollyn^{a,b,c} and Michel De Paepe^{a,b}

^aGhent University, Sint-Pietersnieuwstraat 41, Ghent, Belgium

^bFlanders Make@UGent – Core lab MIRO, Gaston Geenslaan 8, Leuven, Belgium

^cUniversity of Antwerp, Groenenborgerlaan 171, Antwerp, Belgium

*Jasper.Nonneman@UGent.be

Keywords: Electric machine, Average winding temperature measurements, Experimental investigation

1. INTRODUCTION

An experimental approach is commonly employed to assess and analyse the thermal performance of specific electric machine designs. These evaluations often focus on various design aspects, such as geometry and cooling methods. The experiments are often conducted on subcomponents or subassemblies, such as motorette setups (Yang et al., 2017). Motorette setups typically consist of a symmetrical portion of the machine with one or more windings assembled, excluding rotating components. This configuration allows for a precise application and measurement of heat sources within targeted components. Traditionally, the DC resistance of the windings serves as the primary method for dissipating heat using DC currents. Accurately measuring the thermal performance necessitates the placement of local temperature sensors at strategic locations, such as where the highest temperatures are expected. However, accurate local temperature measurements are challenging by the high thermal gradients caused by low thermal conductivities, anisotropy of the materials and high contact and interface resistances e.g. at the winding-liner-core interface. The accuracy of the local temperature measurements is therefore compromised by the exact location and thermal contact between sensor and machine part (Boglietti et al., 2019). Moreover, the presence of local temperature sensors can further influence these gradients due to limited space in high-power density machine designs (Nonneman et al., 2020). Additionally, temperature sensor measurements only provide discrete data, potentially offering a skewed representation of the overall temperature distribution within machine components.

Within this study, a novel method is proposed to enhance thermal measurements on motorette setups by leveraging the machine winding resistance as average temperature sensor. This approach capitalizes on utilizing the winding as a DC heat source and exploits the dependency of its DC resistance on the average temperature. Consequently, this enables the precise determination of the average winding temperature.

2. METHODOLOGY

The DC resistance $R_c(T_c)$ of an electrical conductor is dependent on the conductor temperature T_c . This resistance at a given temperature can be calculated using Eq. 1, where R_0 represents the resistance at a reference temperature T_0 and α denotes the temperature coefficient.

$$R_c(T_c) = R_0 [1 + \alpha (T_c - T_0)] \quad (1)$$

During the application of DC current to the windings in motorette testing, the current I_c and voltage V_c across the conductor are measured to determine the electrical power dissipated within it. These measurements can further determine the conductor resistance using Eq. (2).

$$R = V/I \quad (2)$$

Consequently, the average conductor temperature T_c can be derived from its electrical resistance. Various factors contribute to the precision of the average conductor temperature. Firstly, it is needed to measure the current I_c and voltage V_c precisely. Additionally, knowledge of the initial resistance R_0 and temperature coefficient α at a reference temperature T_0 is required. These parameters are determined ahead of the experiments through a calibration process of the conductor resistance with respect to temperature. During calibration, the conductor is subjected to different temperatures T_0 and T_m in an oven, with the resistances $R_{c,0/m}$ determined using Eq. 2 and by measuring the voltage $V_{cal,0/m}$ and current $I_{cal,0/m}$ through the conductor. To minimize heat dissipation within the conductor during calibration, a small current $I_{cal,0/m}$ is employed. This current is determined using a precise shunt resistance R_{sh} in series with the conductor, with the voltage V_{sh} across it being measured. The final expression for the average conductor temperature T_c is provided by Eq. (3). The total uncertainty in the conductor average temperature can be determined based on the uncertainty associated with each

property using the propagation of uncertainty. This aids in selecting the appropriate measurement equipment and shunt resistance to achieve the desired accuracy in T_c .

$$T_c = \left[\left(\frac{V_c V_{sh,0}}{I_c V_{cal,0} R_{sh}} - 1 \right) (T_m - T_0) \right] / \left[\frac{V_{cal,m} V_{sh,0}}{V_{sh,m} V_{cal,0}} - 1 \right] + T_0 \quad (3)$$

3. DEMONSTRATION ON MOTORETTE SETUP

The method for measuring the average conductor temperature is demonstrated on a motorette setup, which comprises a cooling body with a laminated iron core featuring two parallel-sided slots. A rectangular copper wire winding with eight turns is inserted into these slots, as illustrated in Fig. 1. Voltage taps are soldered onto the winding leads to exclusively measure the voltage across the winding, eliminating any additional electrical (contact) resistances within or connections with the supply cables. To validate the average temperature measurement, eight 0.5 mm mineral insulated T-type thermocouple temperature sensors are strategically placed at various locations on the winding, as indicated in Fig. 1. These sensors are attached to the winding using a UV-curing adhesive. The labels denote both the axial location (L – lead side, M – middle, T – turn side) and the turn number (1-8).

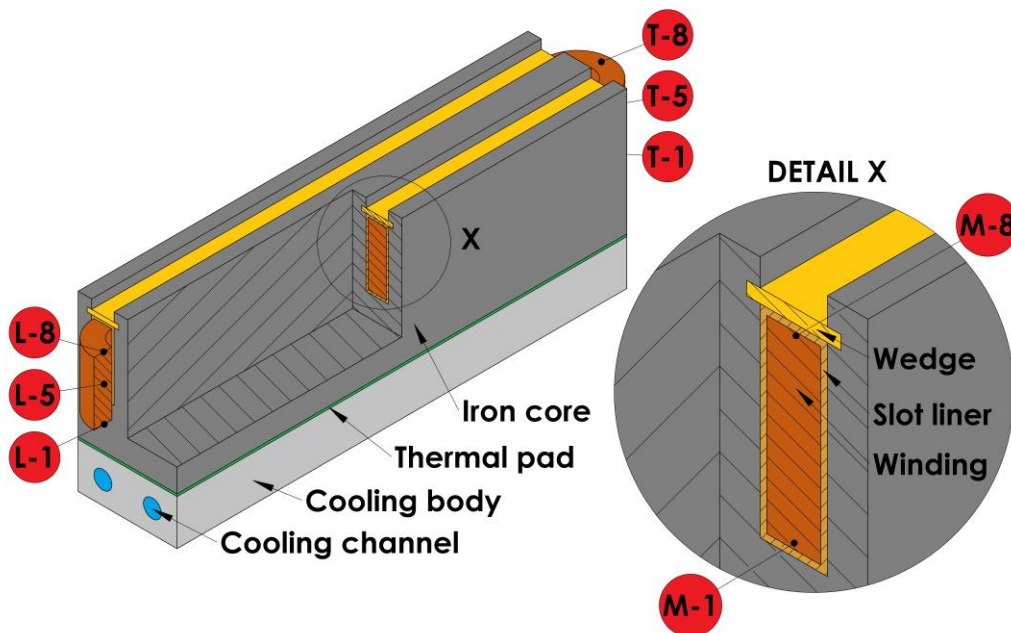


Figure 1. Overview of the motorette assembly and local winding sensor locations.

The winding is calibrated ahead of the experiments at $T_0 = 18.93 \pm 0.10$ °C and $T_m = 148.42 \pm 0.24$ °C, as measured by the eight thermocouples. The thermocouples exhibit an accuracy of 0.1 °C following an in-house thermocouple calibration. However, due to observed temperature differences among the eight sensors during conductor calibration, the standard deviation among the sensors is included in the temperature uncertainty. A PCN RXM50 shunt resistance R_{sh} of 50 ± 0.025 m Ω is used to determine the current $I_{cal,0/m}$, supplied by an Aim TTI PLH120 power supply. The voltages across the shunt resistance $V_{sh,0/m}$ and winding $V_{cal,0/m}$ are measured by a Keithley 2701 DAQ with an accuracy of 3.5×10^{-6} V and 3×10^{-3} % for voltages below 100 mV. This resulted in a calibration current $I_{cal,0/m}$ of 567 mA which is sufficiently low to avoid causing a temperature increase in the winding. The determined initial resistance R_0 of the winding is 3.66 m Ω and the temperature coefficient α is 3.889×10^{-3} .

Using the results of the calibration procedure, the average winding temperature can be determined in the experiment. A DC current I_c of 147.10 ± 0.42 A is measured and supplied to the winding by an EA-PS 9200-210 DC source. At steady-state, the voltage across the winding is determined to be 0.807 V, resulting in a heat dissipation of 118.69 W. Subsequently, the winding resistance R_c is calculated using Eq. 2 as 5.49 m Ω , from which the average winding temperature T_c is determined as 147.14 ± 0.83 °C.

Figure 2 presents the average winding temperature with uncertainty, compared to the thermocouple sensors. As anticipated, the sensor closest to the wedge side (turn 8) and the end windings (lead and turn side) of the motorette exhibit the highest temperatures. Additionally, the lead side of the winding generally experiences higher temperatures than the turn side, attributed to additional losses in the lead wires and supply cable connections. Analysis of the temperatures measured by the thermocouples on the lead and turn side reveals a steeper temperature gradient near the cooling body (turn 1) compared to the wedge side (turn 1), attributed to uniform volumetric heat generation within the winding. This

explains why the average winding temperature aligns closer to the wedge side, rather than precisely midway between turn 1 and 8. These results underscore the significance of utilizing the average winding temperature measurements to gain insights in the thermal behaviour of electric machines.

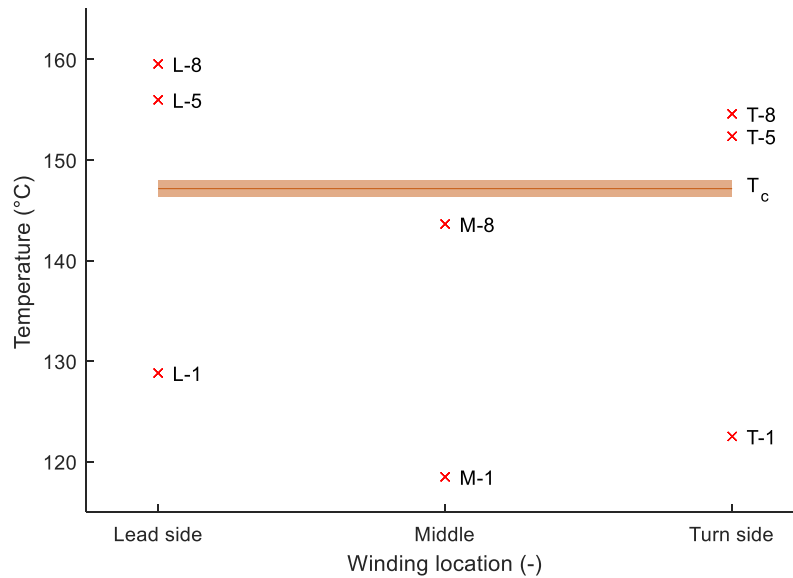


Figure 2. Thermocouple temperatures at various locations and average winding temperature with associated uncertainty.

4. CONCLUSIONS

A method is proposed and demonstrated in this study to accurately determine the average winding temperature in motorette setups of electric machines. This method capitalizes on the relationship between DC electrical resistance and temperature, complemented by the consideration of excited DC losses. To ensure precise average winding temperature measurements, a calibration procedure is introduced, along with a careful selection of instrumentation. The effectiveness of this approach is demonstrated through experiments conducted on a motorette setup and compared with data obtained from local thermocouple sensors. In this demonstrator case, the average winding temperature measurement exhibits an uncertainty of 0.83 °C, highlighting the accuracy of the method. The results underscore the reliability of the proposed method in offering comprehensive insights into the temperature distribution within electric machine windings.

5. REFERENCES

- Boglietti, A., Cossale, M., Popescu, M., & Staton, D. A. (2019). "Electrical machines thermal model: Advanced calibration techniques". *IEEE Transactions on Industry Applications*, 55(3), 2620-2628.
- Nonneman, J., Schlimpert, S., T'Jollyn, I., & De Paepe, M. (2020). *Modelling and Validation of a Switched Reluctance Motor Stator Tooth with Direct Coil Cooling*. Paper presented at the 2020 19th IEEE Intersociety Conference on Thermal and Thermomechanical Phenomena in Electronic Systems (ITherm).
- Yang, Y., Bilgin, B., Kasprzak, M., Nalakath, S., Sadek, H., Preindl, M., et al. (2017). "Thermal management of electric machines". *IET Electrical Systems in Transportation*, 7(2), 104-116.

EXPERIMENTAL STUDY ON BOILING HEAT TRANSFER OF DIELECTRIC FLUID NOVEC 7100 AT LOW PRESSURE/TEMPERATURE CONDITIONS

Jiatong Yu^{a,b}, Zhihao Chen^{a,b,*}, Yoshio Utaka^{a,b}
^aSchool of Mechanical Engineering, Tianjin University
^bState Key Laboratory of Engines, Tianjin University

*zhchen2015@tju.edu.cn

Keywords: Nucleate pool boiling, Critical heat flux, Low saturation pressure, Novec 7100

1. INTRODUCTION

Recently, the boiling of dielectric fluid has been widely applied in cooling technology for electrical/electronic devices. The boiling performances of dielectric fluids have been studied, including the influence of surface orientation [1–2], surface roughness [1,3], subcooling of the liquid [1,2], and confinement conditions [4,5]. However, although in low-temperature environments in closed systems, the boiling characteristics are needed especially at low pressure/temperatures, the saturation conditions, which should influence the boiling heat transfer [6–8], were still not well elucidated for dielectric fluid. It should be noticed that the knowledge of boiling heat transfer under low saturation conditions is essential for a cooling system using two-phase flow since the system may operate at low ambient temperature. Therefore, Novec 7100, a typical dielectric fluid, was used as the test fluid in this study. The boiling heat transfer characteristics for dielectric fluid at low saturation conditions were experimentally studied.

2. EXPERIMENTAL SYSTEM AND METHOD

The experimental apparatus, as shown in Figure 1, includes a boiling vessel, temperature control system, and data acquisition system. The boiling vessel is an airtight cylindrical container wrapped in a water sleeve to control the saturation temperature/pressure of the test fluid. A pressure transducer and two thermocouples were used to monitor test fluid saturation.

A heat transfer plate made of copper was set in the boiling vessel and immersed in the test fluid. A ceramic heater with a size of 20 × 20 mm was attached to one side of the heat transfer plate. The other side of the plate was used as the boiling surface. Moreover, the heat transfer plate and heater, except for the boiling surface, were entirely enwrapped in an insulating sleeve made of polyetheretherketone (PEEK). The insulating sleeve ensured that most of the heat was transferred through the boiling surface and helped realize one-dimensional heat conduction through the copper plate. The heat flux on the boiling surface was calculated based on the heating power of the heater and the surface area. The surface temperature was determined based on the temperature in the heat transfer plate and the heat flux.

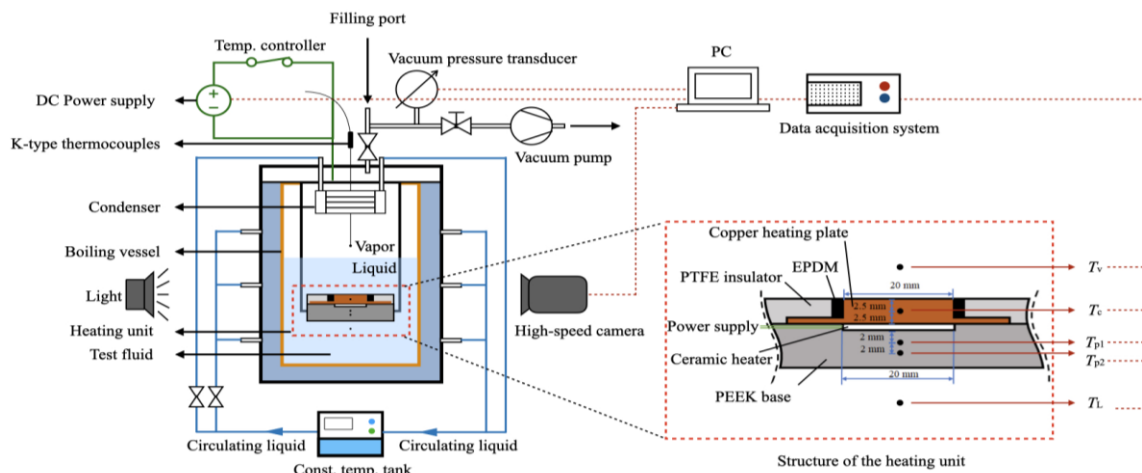


Figure 1. Experimental apparatus and heating unit

3. EXPERIMENTAL RESULTS AND DISCUSSION

The experiments were carried out under different saturation temperatures of -40°C – 60°C . Figure 2 shows the experimentally measured boiling curves, and the predicted boiling curves based on the correlations proposed by Rohsenow [9] and Kutateladze [10] are also compared. First, at a particular saturation temperature, the experimentally measured boiling curves exhibited a qualitatively normal tendency — that is, the heat fluxes increased with an increase in the surface superheat until the Critical Heat Flux (CHF) point was reached. There was also a hysteresis from the maximum superheat of the single-phase heat transfer to the onset of nucleate boiling under each condition. In other words, the temperature difference between these increased with decreasing temperature. In the range of this study, it was approximately two $^{\circ}\text{C}$ under relatively high temperature conditions but reached 8°C at -40°C .

In each curve's low heat flux region, the qualitative trends between the measured data and the correlations agreed relatively well. However, in the medium and large heat flux regions, the measured values showed a relatively steep increase with increasing superheat, whereas the correlations exhibited a relatively gradual increasing trend. Around atmospheric pressure (saturation temperature of 61°C), Rohsenow's equation is relatively well approximated to the experimental data. However, with the decrease of the saturation pressure/temperature, the two correlations differ significantly from the experimental data. In addition, the experimental heat fluxes are broadly higher than the correlations, especially for low saturation pressure/temperature conditions and in the high superheat range. Due to the complexity of the boiling phenomenon, it can still be concluded that the two correlations have a certain level of reliability for predicting boiling heat transfer under a high saturation temperature. Meanwhile, for saturation temperature conditions lower than 0°C , those correlations underestimated the boiling heat transfer.

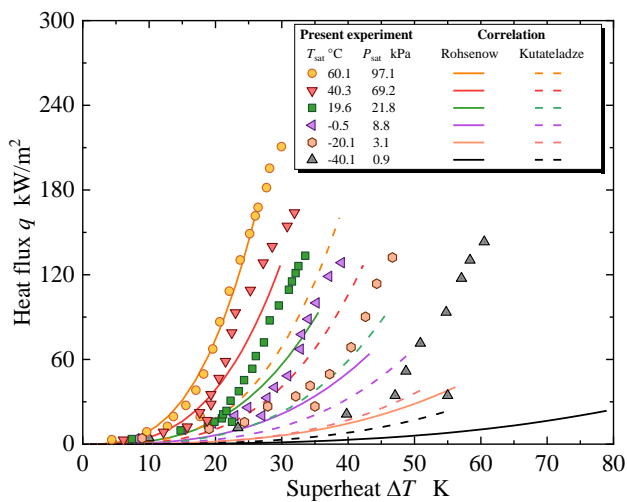


Figure 2. Boiling curves under different saturation pressures/temperatures for Novec7100

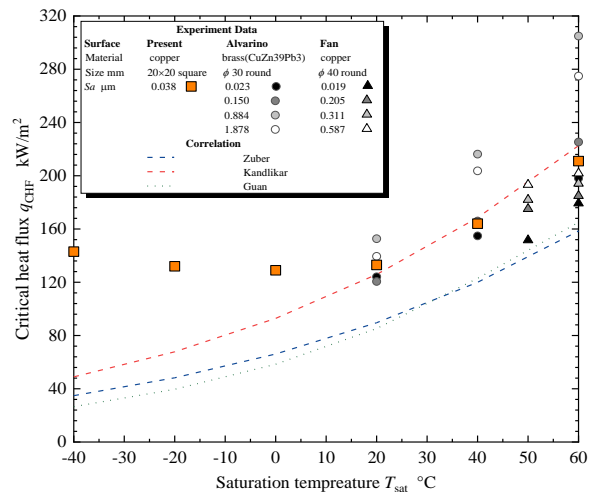


Figure 3 Critical heat flux of Novec7100 under different saturation temperature/pressures

To demonstrate the influence of the saturation temperature on the CHF, the experimental results are summarized in Figure 3, which shows the trend of the CHF variation with the change in saturation temperature. The experimental data of Novec 7100 obtained by Alvarino et al. [8] and Fan et al. [11] and the predicted values based on Zuber [12], Kandlikar [13], and Guan [14] are shown for comparison. The previous experiments in the literature were under normal pressures corresponding to a saturation temperature of 20°C – 80°C . In that range, the results obtained in this study agree well with the literature values and correlations. Different researchers' experimental results had some discrepancies possibly induced by different surface roughness conditions. Therefore, it was confirmed that CHF values decrease with decreasing saturation temperature until 20°C , as shown in Figure 3. However, with a further decrease in saturation temperature to less than 20°C , the CHF showed a tendency to rise slightly rather than decline, which is the opposite of the predictions. In addition, the difference between the experimental results and predicted values of CHF became more significant with the decrease in saturation temperature, indicating the underestimation of the CHF by the current correlations. This particular tendency was first shown for Novec 7100. The low-pressure boiling of water observed by McGillis [15] showed nearly constant values of CHF in the pressure range of approximately 2–20 kPa, which differs from Zuber's trend and is quite similar to the results of this study. This indicates that the CHF mechanism may dramatically change at low saturation temperatures. However, there is currently an insufficient theoretical explanation; a possible reason is inferred and discussed in the next section.

4. CONCLUSIONS

An experimental study was performed to explore the influence of saturation pressure/temperature in the wide range of 0.89 kPa/−40°C to 97.1 kPa/60°C on the CHF of Novec 7100 with an airtight experimental system to control the saturation conditions. Overall, the boiling heat transfer performance (heat flux) of Novec 7100 deteriorated with decreasing saturation temperature. However, the trend differed at very low saturation pressures. The primary results are summarized as follows.

(1) For saturation temperatures larger than 20°C, the CHF decreased with the saturation temperature, which can be predicted reasonably well by conventional correlations.

(2) At saturation temperatures lower than 20°C, the CHF showed a trend of slight increase with a decrease in saturation temperature. At saturation temperatures around 0°C, the CHF showed minima, and the difference between experimental results and conventional correlations increased significantly with decreasing pressure/temperature. The CHF value at −40°C was approximately five times higher than the correlation obtained by Zuber.

(3) The phenomenon of self-induced subcooled boiling caused by the static pressure of the liquid layer on the heating surface under a low saturation pressure was investigated for CHF enhancement. Visual observations of the boiling aspect also characterize self-induced subcooled boiling, in which bubbles disappear quickly with condensation in the subcooled liquid near the heating surface.

Acknowledgment/Funding

This work was supported by the National Key Research and Development Program of China, MOST-JICA International Research Project (2021YFE0192800).

5. REFERENCES

- [1] A. Priarone, Effect of surface orientation on nucleate boiling and critical heat flux of dielectric fluids, *Int. J. Therm. Sci.* 44 (2005) 822–831.
- [2] A. Suszko, M.S. El-Genk, Dielectric liquids natural convection on small rough Cu surfaces at different orientations, *Int. J. Heat Mass Transf.* 81 (2015) 289–296.
- [3] M. El-Genk, Combined effects of subcooling and surface orientation on pool boiling of HFE-7100 from a simulated electronic chip, *Exp. Heat Transf.* 16 (2003) 281–301.
- [4] J.P. McHale, S.V. Garimella, Bubble nucleation characteristics in pool boiling of a wetting liquid on smooth and rough surfaces, *Int. J. Multiph. Flow.* 36 (2010) 249–260.
- [5] K.J.L. Geisler, A. Bar-Cohen, Confinement effects on nucleate boiling and critical heat flux in buoyancy-driven microchannels, *Int. J. Heat Mass Transf.* 52 (2009) 2427–2436.
- [6] A. Kalani, S.G. Kandlikar, Enhanced pool boiling with ethanol at subatmospheric pressures for electronics cooling, *J. Heat Transf.* 135 (2013) 111002.
- [7] I. Mudawar, T.M. Anderson, Parametric investigation into the effects of pressure, subcooling, surface augmentation and choice of coolant on pool boiling in the design of cooling systems for high-power-density electronic chips, *J. Electron. Packag.* 112 (1990) 375–382.
- [8] P. Fariñas Alvariño, M.L. Sánchez Simón, M. dos Santos Guzella, J.M. Amado Paz, J.M. Sáiz Jabardo, L. Cabezas Gómez, Experimental investigation of the CHF of HFE-7100 under pool boiling conditions on differently roughened surfaces, *Int. J. Heat Mass Transf.* 139 (2019) 269–279.
- [9] W.M. Rohsenow, A method of correlating heat transfer data for surface boiling of liquids, *Trans. ASME* (1951).
- [10] S.S. Kutateladze, Heat transfer in condensation and boiling, US Atomic Energy Commission, *Technical Information Service*, 1959.
- [11] X. Fan, S. Gu, J. Lei, G. Luo, F. Meng, L. Wu, S. Gu, Experimental and analytical study on the influence of saturation pressure and surface roughness on pool boiling CHF of HFE-7100, *Int. J. Chem. Eng.* 2022 (2022) 1–18.
- [12] N. Zuber, On the stability of boiling heat transfer, *Trans. ASME* 80 (1958) 711–714.
- [13] S.G. Kandlikar, A theoretical model to predict pool boiling CHF incorporating effects of contact angle and orientation, *Journal of Heat Transfer* 123 (2001) 1071–1079.
- [14] C.K. Guan, J.F. Klausner, R. Mei, A new mechanistic model for pool boiling CHF on horizontal surfaces, *Int. J. Heat Mass Transf.* 54 (2011) 3960–3969.
- [15] R. McGillis, V.P. Carey, J.S. Fitch, W.R. Hamburg, Pool boiling on a small heat dissipating element in water at low pressure, *ASME/AIChE National Heat Transfer Conference*, Minneapolis, Minnesota, 1991.

Flow Characteristics of Amplifier in Curved Pipe Using Response Surface Method

Dong-Sin Lee^a, Hyun-Su Jeong^a, Hwan-Gyo Kim^a, Youn-Jea Kim^{b,*}

^aGraduate School of Mechanical Engineering, Sungkyunkwan University, Suwon 16419, South Korea

^bSchool of Mechanical Engineering, Sungkyunkwan University, Suwon 16419, South Korea

*yjkim@skku.edu

Keywords: Coanda Effect, Ejector, Pipe Flow, Discrete Phase Model, Computational Fluid Dynamics

1. INTRODUCTION

When a branch pipeline joins the main pipeline at the downstream of a hydrogen gas supply line, a reduction in transport energy usually occurs, and additionally at points where the pipeline makes sudden bends, erosion occurs due to the collision of some particles. In particular, when hydrogen gas transport at low temperatures for reliability, which can cause erosion as solid particles, such as ice particles, colliding with the pipe walls. This phenomenon can cause hydrogen gas transport efficiency and reliability issues. A mass flow amplifier utilizing the Coanda effect is a fluidic machine that utilizes the velocity of the Coanda flow to generate suction to amplify the main flow. If set up a mass flow amplifier on the main pipeline as joined branch line, it can amplify the main flow and change the particle erosion rate through additional pipe flow characteristics. In this study, a mass flow amplifier was set in a curved pipe model, and the amplification rate of main flow and erosion rate of pipe changed according to a mass flow amplifier's position.

2. METHODOLOGY

In this study, a mass flow amplifier was combined with an 90° elbow with a diameter of 40 mm. The flow domain and parameters are shown in Fig. 1. The secondary flow is injected through the mass flow amplifier shape with generating the Coanda effect, and then it flows along the wall surface and generates velocity-driven suction force inside the pipe. Finally suction force is delivered to the primary flow inlet and used for amplifying the primary flow.

For the numerical analysis, the commercial code ANSYS FLUENT 2023 R1 was used. And the boundary conditions and geometrical parameters applied in this study are summarized and shown in Tables 1~2 in detail. Hydrogen was used as the working fluid, and to accurately simulate the Coanda flow of hydrogen, the $k-\omega$ model was used for turbulence flow, which is known to accurately simulate the flow in walls. In addition, the discrete phase model(DPM) was used to inject 10,000 inert spherical particles into the primary flow inlet and calculate the erosion rate by the particles. The variable parameter is the gap distance(G) of the amplifier from the 90° curved location at the pipe. The response surface method(RSM) built in ANSYS was used to check the changes in the amplification rate and erosion rate with according to all G values including uncalculated values.

Table 1. Boundary conditions applied in this study

Name	Type	Value
Secondary inlet	Mass flow inlet	0.0003 [kg/s]
Primary inlet	Pressure inlet	1 atm (Open)
Outlet	Static pressure	1 atm (Open)
Fluid	Hydrogen (ideal gas)	273K
Particle	Inert sphere particle	273K / 998 [kg/m ³]

Table 2. Geometrical parameters

Parameters	Value [mm]
Primary inlet diameter (D)	40
Secondary inlet diameter (d)	10
Clearance (C)	0.4
Horizontal length of pipe (L_1)	317
Horizontal length of amplifier (L_2)	27
Vertical length of pipe (L_3)	220
Gap distance (G)	0, 30, 60, 90, 120

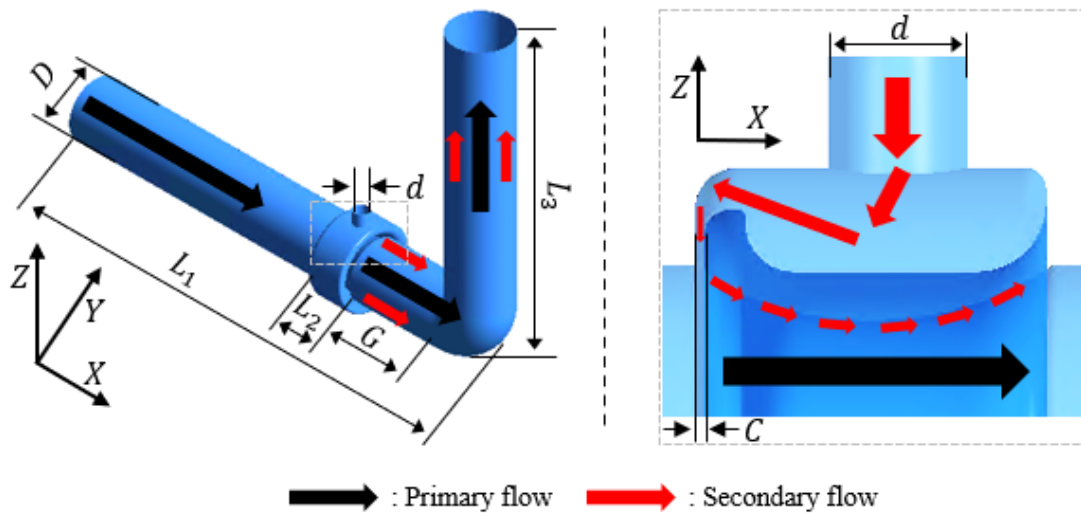


Figure 1. Flow domain of amplifier and 90° elbow

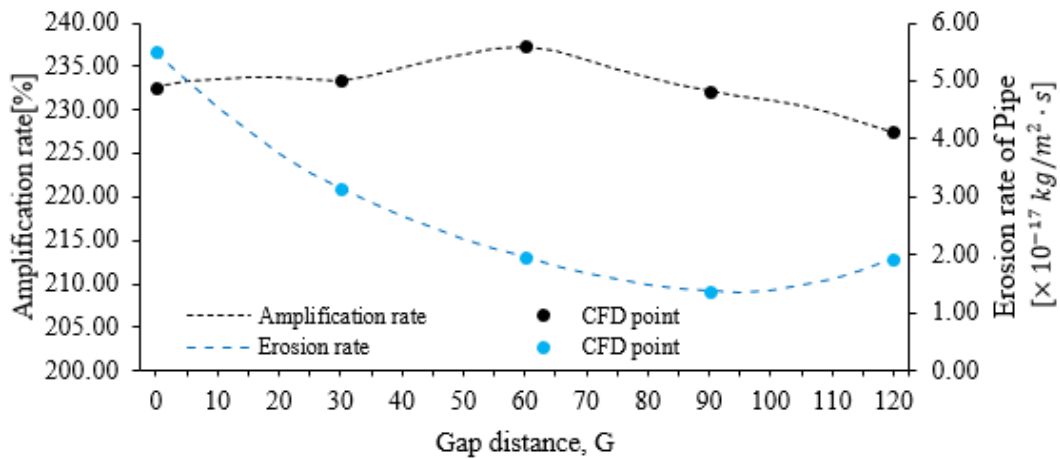


Figure 2. Amplification rate and erosion rate of pipe predicted value by RSM with CFD values

3. CONCLUSIONS

As shown in Fig. 2, the gap distance(G) of the mass flow amplifier from the curve point of the pipe had little effect on the amplification rate. An average value of the amplification rate is about 233.37%. The maximum value is about 1.71 % higher than average value and the minimum value is about 2.52% lower than it. On the other hand, the gap distance(G) had a relatively large effect on the erosion rate. An average value of the erosion rate is about $2.51 \times 10^{-17} \text{ kg/m}^2 \cdot \text{s}$. The maximum value is about 118.46% higher than an average value and the minimum value is about 45.47% lower than it, with a decreasing trend as G increased. So, it is possible to obtain a high amplification rate and a relatively low erosion rate by adjusting location of the amplifier flow. And if we utilize the mass flow amplifier geometry at the point where the branch pipeline joins the main pipeline, it also can similarly affect on the amplification of the main flow and the erosion rate of pipe.

ACKNOWLEDGEMENT

This study was supported by the Korea Agency for Infrastructure Technology Advancement (KAIA) grant funded by the Ministry of Land, Infrastructure, and Transport, grant number (RS-2022-00142936).

REFERENCES

- Chen, J., Wang, Y., Li, X., He, R., Han, S., & Chen, Y., 2015, "Erosion prediction of liquid-particle two-phase flow in pipeline elbows via CFD–DEM coupling method," *Powder Technology*, Vol. 275, p. 182–187.
- Del Rio, J. a. S., Marín, J. G. A., García, S. V., Londoño, D. M., & Zuluaga, D. a. H., 2016, "Simulation analysis of a Coanda-Effect ejector using CFD," *Tecciencia*, Vol. 12, No. 22, p. 17–25.
- Reba, I., 1966, "Applications of the Coanda effect," *Scientific American*, Vol. 214, No. 6, p. 84–92.

Experimental study on freezing of supercooled water droplet impacting on curved cold surfaces

Sun Zhaoyang^a, Chang Shinan^a, Zhang Shuyi^a

^aSchool of Aeronautic Science and Engineering, Beihang University

*zhaoyangsun@buaa.edu.cn

Keywords: Curved cold surface, supercooled water droplet, impact, freezing

Abstract: The impact of supercooled water droplets(SCWD) on the cold surface of aircraft is the cause of aircraft icing, which seriously threatens the safety of aircraft flight. In order to develop safe, efficient and energy-saving anti-icing method, it is necessary to deeply study the icing mechanism of supercooled water droplets impacting on curved cold surfaces. In this paper, the freezing of SCWD impacting on cold surfaces with different curvature is studied experimentally. The effect of the We number($We = 459-650$) and the impact surface temperature($T_w = -30^\circ\text{C} - 0^\circ\text{C}$) on the impact freezing process was investigated. It is found that with the increase of We , the water droplet spreading factor(WDSF) increases and the freezing times decrease gradually. In addition, the lower surface temperature reduces the rate of droplet retraction, thus shortening the freezing time. When the T_w is below -25°C , the droplets splash at the moment of impact and freeze directly during the spreading stage. Meanwhile, the WDSF increases significantly with the surface curvature increases from 0 to 125, the freezing time decreases. And the ice ring formed by the freezing of the droplet changes from raised crown shape to concave cake shape in the center. When the impact position of the droplet was changed, the WDSF of the droplet increased sharply, the freezing time was shortened significantly, and the lower part of the droplet was frozen into strip icicles. Finally, the results of this study can provide experimental support for the development of anti-icing technology for aircraft.

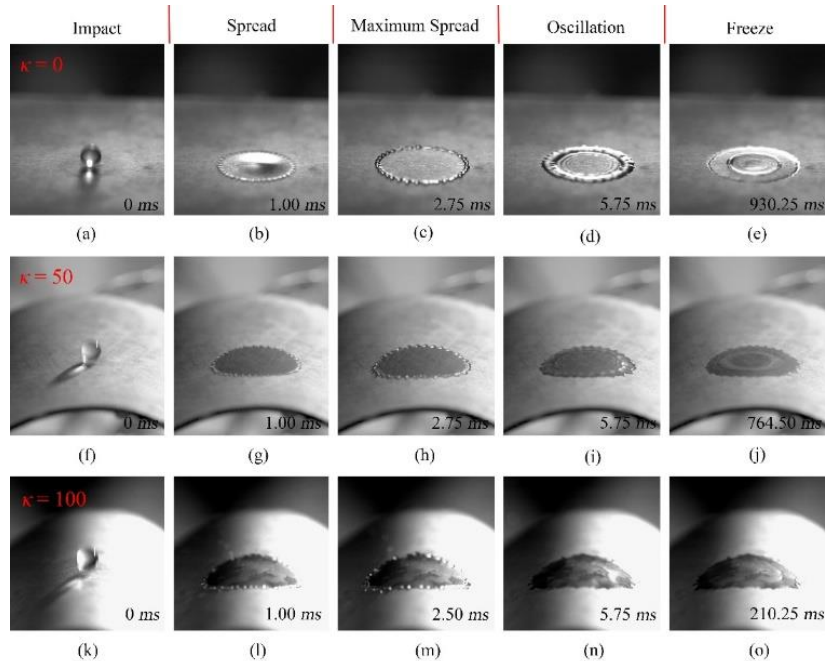


Figure 1. Morphological evolution of droplet impact freezing($\kappa=0, 50, 100$).

EXPERIMENTAL EVALUATION OF SHELL AND PLATE HEAT EXCHANGER

Dijane Ferreira^{a*}, Marcia Mantelli^{b*}, Fernando Milanese^c

^{a, b, c} Universidade Federal de Santa Catarina, Florianópolis, Santa Catarina, Brasil

^{a*}ferreira.dijane@labtucal.ufsc.br, ^{b*}marcia@labtucal.ufsc.br, ^{c*}fernando.milasene@labtucal.ufsc.br

Keywords: Shell and plate, Heat exchanger, Heat transfer, Nusselt number, friction factor

1. INTRODUCTION

Corrugated plate heat exchangers are widely used in the industry due to their high thermal performance, associated with the relative ease of fabrication, assembly, and maintenance. However, conventional types of equipment are limited to applications that do not require high operating temperatures and pressures, which led to the development of the shell and plate heat exchanger, especially to address this deficiency in mechanical resistance. (D. dos S. Ferreira, 2019; Wang et al., 2007)

Shell and plate heat exchangers (SPHE) use stacked circular plates that are welded together. The plates are then inserted into a cylindrical shell, capable of withstanding high operating pressures. The circular shape reduces stress concentration areas, protecting against potential failures. Shell and plate heat exchangers have the main advantages of conventional plate exchangers, such as ease of installation and maintenance, in addition to reduced volume and mass, while maintaining the mechanical robustness of shell and tube units. (Gavelin, 2009; Kapustenko et al., 2020; Wang et al., 2007)

When analyzing the existing technologies of plate heat exchangers, it is noted that the studies are restricted to each specific experiment, resulting in correlations and theoretical models specific to each experimental condition evaluated and leading to the need for adjustments when considering new operation conditions.

Thus, the objective of this article is to experimentally evaluate the thermal and hydraulic behavior of shell and plate-type heat exchangers. The results will be expressed in terms of Nusselt numbers and friction factors. A commercial shell and plate-type heat exchanger is under-tested in the laboratory using water and commercial thermal oil as the working fluids.

2. METHODOLOGY

The experimental procedure was carried out on a pressurized bench, Figure 1, where heat exchanger experiments are conducted using commercial thermal oil as the working fluid, and water as the cooling fluid. The bench consists of a hot gas line and a pressurized liquid line with a maximum working pressure of 10 bar.

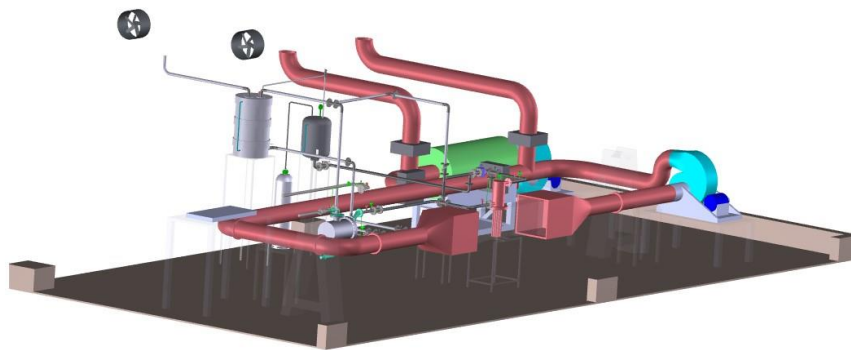


Figure 1. Experimental set-up

The composition of the experimental bench is shown in Figure 2. The hot branch consists of a gas burner, a fuel source, two fans, four damper-type valves (represented by D), a fuel valve and the piping. The liquid branch is composed of a pressurized liquid ring, a pressure relief valve, control valves, a gear pump, a gas/liquid heat exchanger (which works as a heater), and a liquid/liquid heat exchanger (SPHE), which comprises the test section.

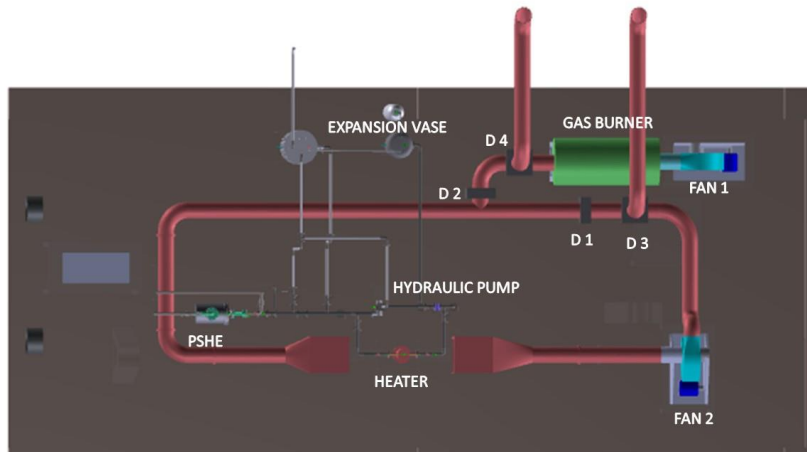


Figure 2. Detailed experimental set-up

The general operation of the bench works as follows: fuel feeds the gas burner through a control valve, which adjusts the flow of fuel to be consumed, and the fan 1 promotes the injection of the primary gas, assisting in the control of gas combustion. The dampers D2 and D4 regulate the direction of a share of the gas, heated by the burner, directing it to the line or the environment. Fan 2 promotes negative manometric pressure in the heater region, ensuring the permanency of gases in this section. The dampers D1 and D3 act in the control of gas recirculation. The hot gases pass through a shell-type heat exchanger and the heater, which is a two-phase thermosiphon heat exchanger. As for the liquid branch, the working fluid, previously heated by the hot gas branch, propelled by the hydraulic pump, circulated along the branch, and was cooled by the SPHE. The heat is removed by a water cooling circuit.

Data acquisition systems collected the following data: temperature, pressure, and mass flow. The collected data is then used to evaluate the thermal and hydraulic behavior of the heat exchanger.

3. RESULTS

The data discussed in this section was obtained in steady-state flow conditions. Besides, it is considered that all the heat transfer between fluids happens through the walls of the heat exchanger, no losses to the external environment were considered. Using the collected data such as: mass flows, temperatures, and pressure drops over time, heat transfer coefficients and heat exchanger effectiveness are obtained.

Heat transfer is evaluated in terms of the equivalent thermal resistance of the heat exchanger. The Wilson-plot method (Figure 3), previously described in (Ferreira et al., 2020) work was applied. The method consisted of splitting the global thermal resistance of the heat exchanger in the thermal resistance of the hot fluid, which in this case is the thermal oil, and the remaining resistances (cooling fluid and the walls of the heat exchanger). This data is useful for getting “clean” data for the proposal correlations of the hot fluid analysis. A plot of the overall thermal conductance (inverse of the thermal resistance) as a function of the inverse of hot fluid velocity (v^{-n})

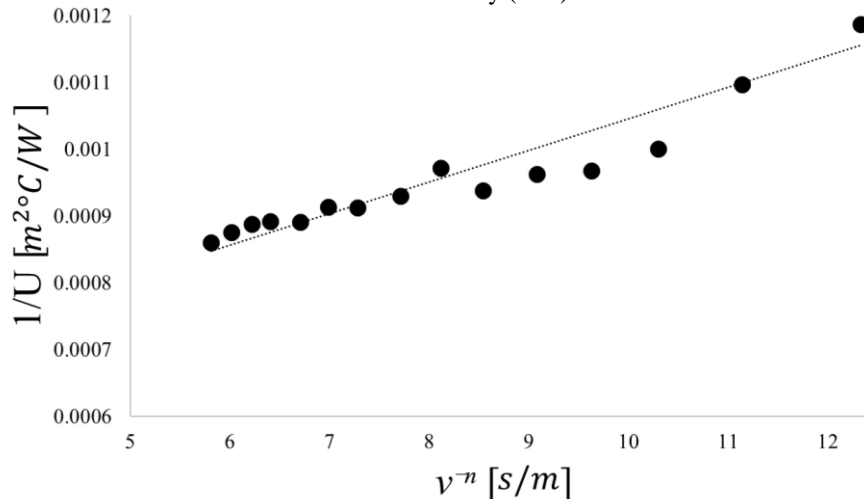


Figure 3. Wilson-plot method applied to PSHE heat transfer analysis

The next results will contemplate the evaluation of the thermal behavior of the hot fluid flow through the heat exchanger, based on the Nusselt number, for different flows and temperatures. In addition, conclusions about the behavior of the devices will be presented.

5. REFERENCES

- Ferreira, D. dos S. (2019). *ANÁLISE EXPERIMENTAL DO COMPORTAMENTO TERMO- HIDRÁULICO DE UM TROCADOR DE CALOR DO TIPO PLACAS CORRUGADAS*. Universidade Federal de Santa Catarina.
- Ferreira, D., Mantelli, M., & Milanese, F. (2020). WILSON PLOT METHOD TO OBTAIN NUSSOLT NUMBER FOR A PLATE HEAT EXCHANGER. *Thermal Engineering*, 19(2), 25–30.
- Gavelin, S. (2009). Improve gas compression systems with all-welded shell-and-plate heat exchangers. *Hydrocarbon Processing*, 88(8).
- Kapustenko, P. O., Klemeš, J. J., Arsenyeva, O. P., Kusakov, S. K., & Tovazhnyansky, L. L. (2020). The influence of plate corrugations geometry scale factor on performance of plate heat exchanger as condenser of vapour from its mixture with noncondensing gas. *Energy*, 201. <https://doi.org/10.1016/j.energy.2020.117661>
- Wang, L., Sundén, B., & Manglik, R. M. (2007). *Plate Heat Exchangers: Design, Applications and Performance* (1st ed.). Wit Press.

STUDY OF STABILITY OF A DENTAL AIROTOR COOLING JET

Binita Pathak^{a,*}, Santhosh Rudrasetty^a

^aDepartment of Mechanical Engineering, Indian Institute of Technology, IIT-BHU Varanasi

*binita.mec@itbhu.ac.in

Keywords: stability, jet spray cooling, dental airotor

1. INTRODUCTION

Dental airotors are frequently used tools in dentistry for various procedures like root canal treatment, scaling, etc. [Offner et. al]. These airotors operates at very high speed and requires continuous cooling. The cooling is usually maintained using a water spray system [Allison et. al]. The spray system is very complicated and has not been explored completely yet, except a few [Sergis et. al]. We investigated a dental airotor cooling system which employs a water jet which is destabilized using an air jet at an angle of $\sim 28^\circ$. We employed linear stability analysis to understand the effect of the governing parameters on the growth of the instabilities at the water-air interface and validated the model with our experimental results.

2. EXPERIMENTAL SETUP

The experimental setup is schematically shown in Fig. 1. The water jet is ejected through the nozzle exit at '0' and the air at 'a' respectively. The air jet makes an angle of 28° with the axis of the water jet. The dynamics of the system is captured using a high speed camera (Photron Fastcam Mini AX100) attached with a zoom lens. The jets are illuminated using back light (Veritas Constellation 120e).

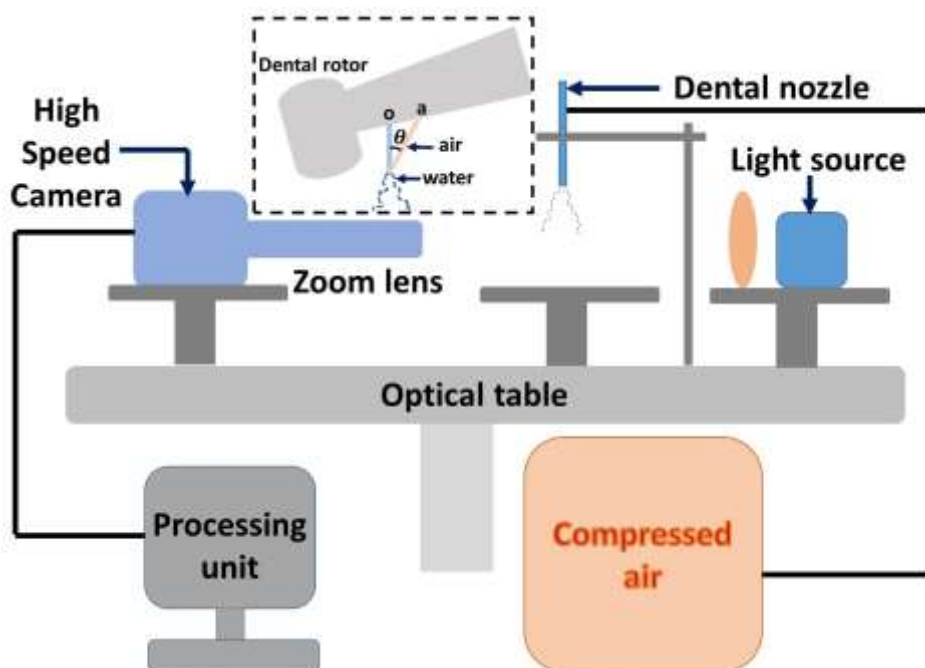


Figure 1: Schematic of the experimental setup (inset: dental air-rotor).

3. RESULT AND DISCUSSION

As the liquid jet interacts with the air $\sim 1.5\text{mm}$ from the jet exit 'o' (Fig. 2(i)), disturbances are developed on the interface (Fig. 2(ii)). The wave-like disturbances grow and eventually lead to complete break-up of the jet. The liquid jet (of radius R) propagated with a uniform base velocity U_w in the axial direction (Z -axis) and the air with a velocity U_a

at an angle of θ with the z-axis respectively. The base velocities are: $\bar{V}_i = U_w \hat{i}_z$ and $\bar{V}_0 = U_a \cos\theta \hat{i}_z + U_a \sin\theta \hat{i}_r$ respectively (here, i and 0 refer to the water jet and the air respectively). We employed viscous potential theory for our analysis and hence the velocities can be expressed by a potential function ϕ_j . The system is perturbed axially in the form $e^{\omega t + ikz}$ (ω is the growth rate of the perturbation and k is the wave number respectively) such that the continuity equation for the perturbed potentials are given as $\nabla^2 \hat{\phi}_j = 0$. We solve the Laplace equation to get the potential as: $\hat{\phi}_j = (A_j I_0(kr) + B_j K_0(kr)) e^{\omega t + ikz}$ (here, I_0 and K_0 are the modified Bessel function of first and second kind respectively. '^' represents perturbed quantities). The water-air interface is perturbed as: $\eta = \hat{\eta}_0 e^{\omega t + ikz}$. The perturbed interface is described as: $F_j = r - R_0 - \eta$. We apply the kinematic boundary condition for each phase: $\frac{DF}{Dt} = 0$ and the dynamic boundary conditions as: $\hat{P}_i - \hat{P}_0 = \sigma \nabla \cdot \mathbf{n} + 2\mu_i \frac{\partial^2 \phi_i}{\partial r^2} - 2\mu_0 \frac{\partial^2 \phi_0}{\partial r^2}$ (σ is the surface tension). The pressures are estimated using Bernoulli's equation. The final dispersion relation is obtained as:

$$\omega^{*2} \left\{ -\frac{I_0(k^*)}{k^* I_1(k^*)} + \frac{K_0(k^*)}{K_1(k^*) k^*} \hat{\rho} \right\} + \omega^* \left\{ -2 \frac{I_0(k^*)}{I_1(k^*)} i + 2 \frac{K_0(k^*)}{K_1(k^*)} \hat{u} \hat{\rho} \cos\theta - i \frac{K_0(k^*)}{K_1(k^*)} \hat{u} \hat{\rho} \sin\theta - \frac{k^* I_0 + I_2}{\text{Re} I_1} - \frac{k^* (K_0(k^*) + K_2(k^*))}{\text{Re} I_1(k^*)} \right\} + \left\{ \frac{I_0(k^*)}{I_1(k^*)} k^* + i \hat{\rho} \hat{u}^2 k^* \sin\theta \cos\theta \frac{a_1}{K_1(k^*)} - \hat{\rho} \hat{u}^2 k^* \cos^2\theta \frac{k^* K_0(k^*)}{K_1(k^*)} - \frac{k^{*2} - 1}{\text{We}} - i \frac{I_0(k^*) + I_2(k^*) k^2}{I_1(k^*) \text{Re}_i} - (K_0(k^*) + K_2(k^*)) \hat{u} \cos\theta \frac{k^{*2}}{\text{Re}} i \right\}$$

(here, I_1 , I_2 and K_1 , K_2 are the modified Bessel function of first and second kind respectively (index denotes the order of the function). The growth rate (ω) and wave number (k) are non-dimensionalised using (R/U_w) and R respectively. The Reynolds number: $\text{Re} = \frac{\rho_i U_w R}{\mu_i}$ and Weber number: $\text{We} = \frac{\rho_i U_w^2 R}{\sigma}$ are based on the jet density (ρ_i) and viscosity (μ_i). σ is the surface tension.

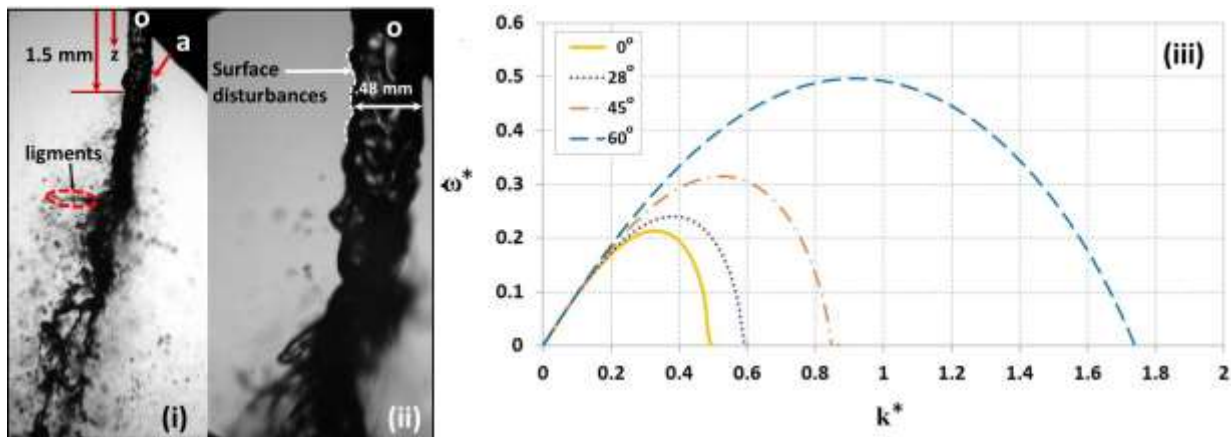


Figure 2: (i) Instability of the water jet leading to the spray formation, (ii) zoomed view of the jet and (iii) the effect of the air with water jet angle (θ) on the jet instability growth rate (ω^*).

The figure 2(iii) depicts the variation of the disturbance growth rate with different wave numbers. The rate increases with an increase of the angle made by the air with the water jet (θ). We have also analyzed the effect of jet Weber number and Reynolds number on the stability (not shown here). Although the Reynolds number do not have significant effect on the jet, the Weber number is extremely crucial for the stability of the jet. Both the increase in inertia and a decrease in surface tension (i.e., an increase in Weber number) stabilize the jet. The largest growing wavelength estimated using the model is ~ 6 mm which is validated with our experimental results.

4. CONCLUSIONS

In summary, we have studied the stability of a water spray-type cooling system for a dental airtor by employing linear stability analysis (LSA) and validated our analysis with the experimental results. We found significant influence of the angle made by the air jet with the water jet axis (θ) and the Weber number on the stability of the jet. The jet can be destabilized by increasing the angle (θ) which will require an alteration of the nozzle design. Alternatively, the other governing parameters like air-water density ratio and jet velocity can be controlled to control the stability of the jet and acquire the required atomization.

5. REFERENCES

- Allison, J.R., Edwards, D.C., Bowes, C., Pickering, K., Dowson, C., Stone, S.J., Lumb, J., Durham, J., Jakubovics, N. and Holliday, R., (2021). The effect of high-speed dental handpiece coolant delivery and design on aerosol and droplet production. *Journal of Dentistry*, 112, pp103746.
- Offner, D., Brisset, L. and Musset, A.M., (2019). Evaluation of the mechanical cleaning efficacy of dental handpieces. *Journal of Hospital Infection*, 103(1), pp.e73-e80
- Sergis, A., Wade, W.G., Gallagher, J.E., Morrell, A.P., Patel, S., Dickinson, C.M., Nizarali, N., Whites, E., Johnson, J., Addison, O. and Hardalupas, Y., (2021). Mechanisms of atomization from rotary dental instruments and its mitigation. *Journal of dental research*, 100(3), pp.261-267

EXCESS LIQUID MANAGEMENT FOR A HIGH HEAT FLUX SPRAY EVAPORATOR INTEGRATED IN A VAPOR COMPRESSION REFRIGERATION SYSTEM

Marcus V. P. Carneiro, Jader R. Barbosa Jr.*

POLO - Research Laboratories for Emerging Technologies in Cooling and Thermophysics
Department of Mechanical Engineering, Federal University of Santa Catarina
Florianópolis, SC, 88040-900, Brazil, Phone/Fax: (+55) 48 3721-7900
*jrb@polo.ufsc.br

Keywords: spray cooling, vapor compression, heat exchanger, electronics cooling

1. INTRODUCTION

Thermal management has always been a must in any electronic device. Therefore, several cooling schemes and systems have been proposed over the past decades to cope with their performance and operating temperature requirements. However, the increasing performance and continual miniaturization of electronic packages impose several new challenges to thermal engineers due to rising heat flux densities. Some examples worth mentioning are related to the avionics of airplanes (Kellermann et al., 2020), the Li-ion batteries of electric cars (Lei et al., 2020), the processors and memories of supercomputers and data centers (Liu et al., 2020), and the IGBTs of power modules (Choi et al., 2019). Although aluminum and copper heat sinks with natural or forced air convection remain frequently used, thermal designers and manufacturers already consider more complex and costly schemes, particularly liquid and two-phase cooling, to enable the proper operation of their devices. Moreover, such cooling schemes can be easily combined with different technologies to further enhance their heat removal capability. For instance, mechanical vapor compression enables cooling temperatures below that of the ambient while allowing great potential for heat recovery (Liang et al., 2019).

To the best of our knowledge, a direct comparison of different refrigeration system architectures to assess the use of excess liquid in high heat flux thermal management solutions has not yet been done. Therefore, this work aims to provide a quantitative and qualitative analysis of two different refrigeration loop solutions based on the cooling system thermodynamic performance (compressor power, coefficient of performance) and steady-state heat transfer parameters (heat transfer coefficient and critical heat flux). The first solution uses an electrical trace heater to superheat the excess liquid by Joule effect. The second uses an internal heat exchanger (IHX) to superheat the excess liquid with the subcooled liquid exiting the condenser, as in an indirect regenerator heat exchanger. To that end, the multiple colliding jets strategy investigated in a refrigeration system as a spray cooling solution by Carneiro and Barbosa (2021) is considered as the high heat flux evaporator.

2. EXPERIMENTAL WORK

The schematic diagram of the experimental apparatus with its main components is presented in Fig.1(a). It contains a small-scale, oil-free, linear-motor compressor (1), a Coriolis effect mass flow meter (2), a brazed plate counterflow heat exchanger that acts as the refrigeration system condenser (3), a spray cooling unit (4), and an electrical trace heater (5) which controls the minimum superheating degree at the compressor inlet. Additionally, auxiliary components are used, a thermal bath (6) to control the hot-end temperature, a paddle wheel flow meter (7) to measure the secondary fluid flow rate, and a charging unit (12) with a load cell (11) and two electrical valves (13) to measure and control the refrigerant inventory in the refrigeration system. The excess liquid management solution assessed is selected by means of a three-way ball valve that connects the cooling unit to the refrigeration system through the refrigerant loop configuration of interest. Configuration (i) directly connects the cooling unit exit to the electrical trace heater that controls the superheating degree at the compressor inlet and the cooling unit inlet to the condenser outlet. On the other hand, configuration (ii) connects the cooling unit to the refrigeration loop through a regenerator. The regenerator is a brazed plate heat exchanger that allows the high-pressure and high-temperature liquid exiting the condenser to exchange heat with the low-pressure and low-temperature two-phase mixture exiting the spray cooling unit. For configuration (ii), the electrical trace heater (5) is used only if the superheating degree (10 °C) is not reached. Fig.1(b) presents the ph -diagram for both vapor compression refrigeration loop configurations under consideration in this work.

The working fluid enters as a subcooled liquid in the cooling unit for both loop configurations and it expands in the orifices section of the spray cooling unit. The orifice section not only expands the refrigerant but atomizes it in three colliding jets. A low-pressure spray is produced through the single-point impact of the three colliding jets that impinge on the top heated surface of a copper block that emulates an electronic device. Heat is dissipated using a NiCr heater placed at the bottom of an insulated copper block. This heat is transferred from the top surface to the refrigerant, exiting the

spray cooling unit as a two-phase mixture through the drainage channels. This two-phase mixture is either superheated to the minimum superheating degree by means of electrical trace heater for configuration (i) and the IHX for configuration (ii). For certain experimental data, mainly for setups with large refrigerant inventory, the electrical trace heater is used to guarantee the minimum superheating degree that is not reached with only the IHX.

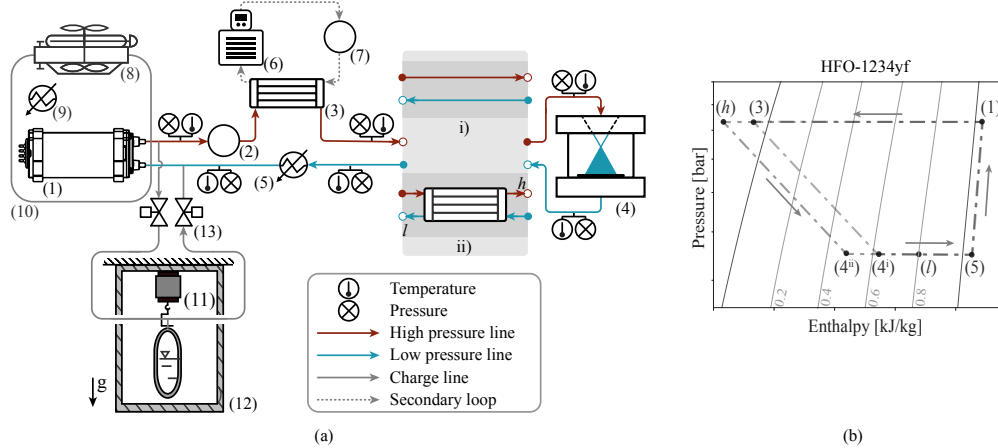


Figure 1. (a) Schematic diagram of the experimental facility and (b) ph -diagram of the vapor compression refrigeration loop.

The experiments were conducted to investigate the influence of the applied thermal load (cooling capacity), refrigerant mass in the system (refrigerant charge) and the excess liquid loop configuration on the heat transfer performance. The minimum superheating degree at the compressor inlet was set to be 10 °C for all the experiments. The hot reservoir (ambient) temperature was controlled to 25 °C. As for the experimental procedure, different refrigerant charges were evaluated for each refrigeration loop configuration, however, it was kept fixed while the cooling capacity was increased. Therefore, different boiling curves for each setup operating at distinct refrigerant charge can be built. R-1234yf was the refrigerant of choice as it presents low GWP and considerable dielectric and thermophysical properties.

3. DATA REGRESSION

The heater surface temperature, T_s , the heat transfer coefficient, \bar{h}_s , and the refrigeration system coefficient of performance, COP, are among the key parameters used to evaluate the different refrigeration loop configurations. The general expressions for these parameters are, respectively,

$$T_s = \bar{T}_{\text{RTD}} - \frac{\dot{q}_s l_s}{k_c}, \quad \bar{h}_s = \frac{\dot{q}_s}{(T_s - T_{\text{evap}})} \quad \text{and} \quad \text{COP} = \frac{\dot{Q}_c}{(\dot{W}_{\text{comp}} + \dot{W}_{\text{fans}} + \dot{W}_{\text{sh}})}. \quad (1)$$

The surface temperature was determined through a linear extrapolation of Fourier's law considering 1-D heat conduction whereas the temperatures were measured right underneath the heat transfer surface for these steady-state experimental tests. From the surface temperature expression, \bar{T}_{RTD} is the arithmetic average temperature measured by the five RTD probes located at a distance l_s from the base of the heat transfer surface, k_c is the copper thermal conductivity and \dot{q}_s is the average heat flux at the heated surface.

The heat transfer coefficient was calculated based on its definition using the average heat flux, the surface temperature and the evaporation temperature, T_{evap} . It is important to highlight that the average heat flux at the top surface of the copper block was calculated based on the electrical power supply at the NiCr heater and a thermal analysis of the insulation and drainage unit. A detailed description of the numerical assessment is presented in Oliveira (2016), which indicates the fraction of the electrical power dissipated at the heater that reaches the top surface of the copper block is 95% or more for the range of imposed thermal load. Therefore, a conservative approximation of the heat flux was performed as $\dot{q}_s = 0.95\dot{Q}_c/A_s$, where \dot{Q}_c is the thermal load and A_s is the cross-section area of the copper block.

The coefficient of performance was computed as the ratio of the cooling capacity to the sum of the electrical powers required to run the compressor, \dot{W}_{comp} , the cooling fans placed inside the compressor calorimeter (which are mandatory to cool the compressor as per its supplier), \dot{W}_{fans} and the suction line trace heater, \dot{W}_{sh} . The suction line trace heater is considered as an extra electrical power required to run the compressor since vapor compression refrigeration systems require a minimum vapor quality to safely operate. Therefore, the line trace heater power consumption is considered for both refrigeration loop configurations, being minimal for the configuration including the IHX to guarantee the superheating degree of 10 °C.

4. RESULTS

To correctly compare both loop configurations, the same evaporation temperature is imposed at a heat load of 25 W for both solutions by varying the refrigerant charge. The same evaporation temperature for the cooling unit at the starting point of the boiling curve of each loop configuration allows the evaluation of the applied heat load effect as it is increased with a fixed refrigerant charge until the last stable temperature point is reached. This point is defined as the setup critical heat flux, CHF, and limits the solution heat transfer ability. Figure 2(a) presents the resulting surface temperature as a function of the applied thermal load for the refrigeration loop configuration (i) for different evaporation temperature. In this refrigeration loop configuration, the surface temperature was kept below 45 °C and sustained up to 200 W of thermal load. Figure 2(b) shows that the heat transfer coefficient is greatly affected by the refrigerant charge. This is a direct consequence of the liquid film formation by the spray atomization over the heated surface. Lastly, Figure 2(c) shows the resulting COP for the same refrigeration loop configuration. For this loop configuration, the superheating degree is reached by means of the electrical trace heater. It is important to notice that the COP is virtually the same for the different imposed evaporation temperatures and increases linearly until the CHF is reached.

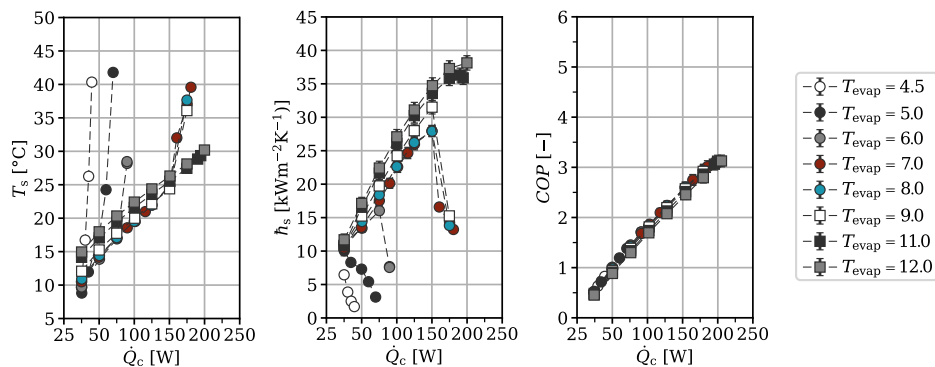


Figure 2. Refrigeration loop (i) parameters. (a) Boiling curves, (b) surface temperature, (c) heat transfer coefficient.

5. CONCLUSIONS

Two loop configurations have been assessed as liquid management solutions of the excess liquid exiting a high heat flux spray cooling unit integrated in the miniaturized vapor compression refrigeration system. The experiments carried out with R1234yf allow a quantitative evaluation of the heat transfer performance in each refrigeration loop configuration considering different corresponding evaporation temperatures enforced at a heat load of 25 W. For the full manuscript, these results are compared to ones obtained for the refrigeration loop (ii). The manuscript discusses the effect of higher subcooling degrees obtained for configuration (ii) and how it impacts the liquid film formation over the heated surface. Furthermore, the linear COP increasing trend for the loop configuration (i) is discussed and compared once a minimal superheating heat load is required for configuration (ii). Additionally, the full experimental result analysis is complemented by high-speed video sequence of the liquid film over the heated surface and discusses its effect on the heat transfer coefficient and CHF.

6. REFERENCES

- Carneiro, M. V. P. and Barbosa, J. R. (2021), 'A comparison of parallel and colliding jet arrays in a compact vapour compression heat sink for electronics cooling', *Applied Thermal Engineering* **195**, 117217.
- Choi, U.-M., Jorgensen, S. and Blaabjerg, F. (2019), 'Impact of cooling system capacity on lifetime of power module in adjustable speed drives', *IEEE Journal of Emerging and Selected Topics in Power Electronics* **7**(3), 1768–1776.
- Kellermann, H., Habermann, A. L., Vratny, P. C. and Hornung, M. (2020), 'Assessment of fuel as alternative heat sink for future aircraft', *Applied Thermal Engineering* **170**, 114985.
- Lei, S., Shi, Y. and Chen, G. (2020), 'A lithium-ion battery-thermal-management design based on phase-change-material thermal storage and spray cooling', *Applied Thermal Engineering* **168**, 114792.
- Liang, K., Li, Z., Chen, M. and Jiang, H. (2019), 'Comparisons between heat pipe, thermoelectric system, and vapour compression refrigeration system for electronics cooling', *Applied Thermal Engineering* **146**, 260–267.
- Liu, L., Zhang, Q., Zhai, Z. J., Yue, C. and Ma, X. (2020), 'State-of-the-art on thermal energy storage technologies in data center', *Energy and Buildings* **226**, 110345.
- Oliveira, P. A. (2016), Development of a Two-Phase Jet Heat Sink Integrated with a Compact Refrigeration System for Electronics Cooling, Dr. Eng. Thesis, Federal University of Santa Catarina.

ELECTROSTATIC OIL-REFRIGERANT SEPARATION

**Vivek S. Garimella^a, Donghyeon Yoo^a, Tarek Gebrael^a, Haoyun Qiu^a, Syed Angkan Haider^a,
Nenad Miljkovic^{a,*}**

^aDepartment of Mechanical Science and Engineering, University of Illinois Urbana-Champaign, Urbana, IL

*nmiljkov@illinois.edu

Keywords: Air Conditioning, Oil Management, Compression, Refrigeration

1. INTRODUCTION AND OBJECTIVES

As global efforts to decarbonize key emitting sectors continue, opportunities to decrease the carbon emissions of heating, ventilation, air conditioning, and refrigeration (HVAC&R) systems can aid in making significant progress towards a net-zero carbon grid. These systems are estimated to account for 48.7% of total building energy use, with a large portion of these needs met using vapor-compression systems (Garimella *et al*, 2022). In these vapor-compression systems, oil plays a necessary role in lubrication of the compressor. This oil, however, gradually becomes entrained as a mist in the refrigerant stream exiting the compressor and its transport to other components lowers the heat transfer coefficient, increases pressure drop, and enhances the potential of compressor failure. Due to these adverse effects, the separation of the lubricant from refrigerant streams has been a topic of scientific interest over the recent years (Toyama *et al*, 2006). Most oil separators today retain this mist using a mechanical separator, where the refrigerant-oil mixture flows through a barrier, usually a mesh, and the droplets, upon impact with the mesh, coalesce with each other and fall under the effect of gravity. Though mechanical separators are attractive due to the simplicity of their mechanism, they become inefficient at high mass flow rates, partially because more oil droplets are entrained along the streamlines of the vapor and escape the mesh when the inertia of the flow and its drag forces become higher (Xu and Hrnjak, 2019). A recent study by Damak and Varanasi (2019) addressed this for water mist by adding an electrical force that overcomes the drag of the flow and attracts the droplets to the mesh. Their method ionizes the air through corona discharge at high voltages and imparts a net charge on the flowing water droplets. The charged droplets are attracted to the mesh due to the electric field applied between the ion emitter and the mesh, overcoming the inertia of the vapor flow. While this method could be translated into applications in oil-refrigerant separation, the application of a corona discharge is highly hazardous in systems that rely on flammable refrigerants, which are becoming increasingly prevalent in the transition towards low global warming potential refrigeration (Goetzler *et al.*, 2014). It is, thus, critical to develop systems in which there is no risk of refrigerant ignition due to a corona discharge and potential oxygen leaks into the system.

We study electrostatic oil-refrigerant separation to enhance the separation efficiency compared to mechanical coalescence separators and to enable use with both flammable and non-flammable refrigerants. Rather than using a corona discharge to impart charge on the oil droplets, this separator leverages the inherent electrostatic charge of the oil (accumulated via tribocharging as the oil travels through piping systems and valves) and use it to direct the oil droplets towards the separation mesh, where a potential difference is applied between the mesh and the a secondary electrode in the oil stream. A system based on a similar idea has been investigated by Ohno *et al* (2019) to separate oil from CFCs using parallel plates instead of meshes, showing that this method is effective in increasing separation efficiency without the use of a corona discharge. The objectives of this work are to characterize the mechanisms by which oil droplets within streams of refrigerant can be collected via tribocharging of the droplets and application of an electric field, characterizing the increase in separation efficiency achievable via these electrostatic forces. Additionally, the mechanisms governing the droplet motion are explored, where scaling analyses and experimental studies are conducted to estimate a relationship between the flow rate of the working fluid and the electric field intensity which must be applied to overcome the drag imposed on the droplets by the stream of working fluid in which they are entrained. Insights are developed and presented which discuss the challenges which may be present in developing closed-loop components which leverage these electrostatic forces to develop higher-efficiency oil separators with low pressure drop.

2. METHODS

To characterize the oil flow within the system, we use a variety of analytical, experimental, and simulation methods. Experimentally, we construct a system, shown in Fig. 1, in which compressor oil (Parker F442 Oil) is deposited into a stream of nitrogen (which we use as a substitute for refrigerant here to allow for easier visualization in an open-loop system) using a commercial lubricator. The flow rate of nitrogen is measured using a gas flowmeter prior to the deposition of oil. As the droplet is entrained into the stream of nitrogen, the droplet is broken up into a mist. The oil-nitrogen mist then travels through a tygon tube where it enters the visualization chamber. Inside the visualization chamber, a ring electrode is connected to the mist line. The separation mesh serves as the second electrode, where the potential difference is applied using a digital power supply between the ring and the mesh to generate the electric field. There are multiple

configurations possible for this facility such that the electric field intensity can be fine-tuned via a combination of the position of the mesh in one of the two slots, the position of the ring electrode on the oil line, and the potential difference applied between the two electrodes.

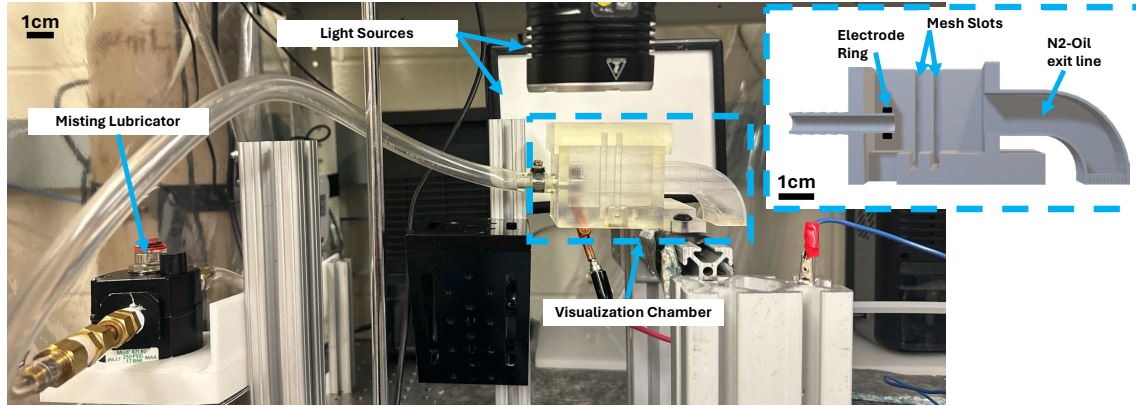


Figure 1. Photograph of the experimental test facility.

To determine the separation efficiency of the system, a stream of nitrogen is sent through the system for 15 seconds, allowing for a consistent amount of oil to be deposited into the nitrogen stream. The mesh electrode is weighed before each experimental run, and then weighed once more following each test run to determine the amount of oil retained in the mesh. The mesh electrode is cleaned using both compressed air and isopropyl alcohol between each test. These tests were run at volumetric flow rates ranging from 500 cm³/s to 2500 cm³/s, and at electric field intensities between 0 kV/mm and 0.8 kV/mm. We also use COMSOL Multiphysics to simulate the electric field intensity and profile between the ring and the mesh electrode. We use high-speed imaging to track the path lines of the oil droplets and determine whether the oil droplets follow a trajectory similar to the profile of the electric field lines. Analytically, we characterize the forces imposed on the droplet by both the stream of nitrogen (a drag force) and the electric field. The conservation of momentum equation used for this analysis can be seen in Eq. (1), where m represents the droplet mass, du/dt represents the acceleration of the droplets, q represents the charge of the droplet (Coulombs), E represents the electric field intensity (kV/mm), μ_{refg} represents the dynamic viscosity of the working fluid (Pa-s), Q represents the volumetric flow rate (m³/s) of the working fluid, A represents the cross-sectional area of the tubes (m²), and U_{particle} represents the velocity of the oil droplet (m/s).

$$m \frac{du}{dt} = qE + 6\pi\mu_{\text{refg}} [(Q/A) - U_{\text{particle}}] \quad (1)$$

3. RESULTS AND CONCLUSIONS

Figure 2 shows the simulated electric field lines (leftmost panel) as well as the captured droplet flow paths for two representative cases—one where no potential difference, and thus no electric field, is applied between the two electrodes (middle panel) and one where a potential difference of 6 kV is applied between the two electrodes (rightmost panel). The results shown in Fig. 2 indicate that the application of an electric field creates a greater distribution of droplets in the flow, while also increasing the rate at which droplets are ejected from the ejector, and that the applied voltage between the two electrodes does in fact begin to pull the droplets along the electric field lines between the two electrodes.

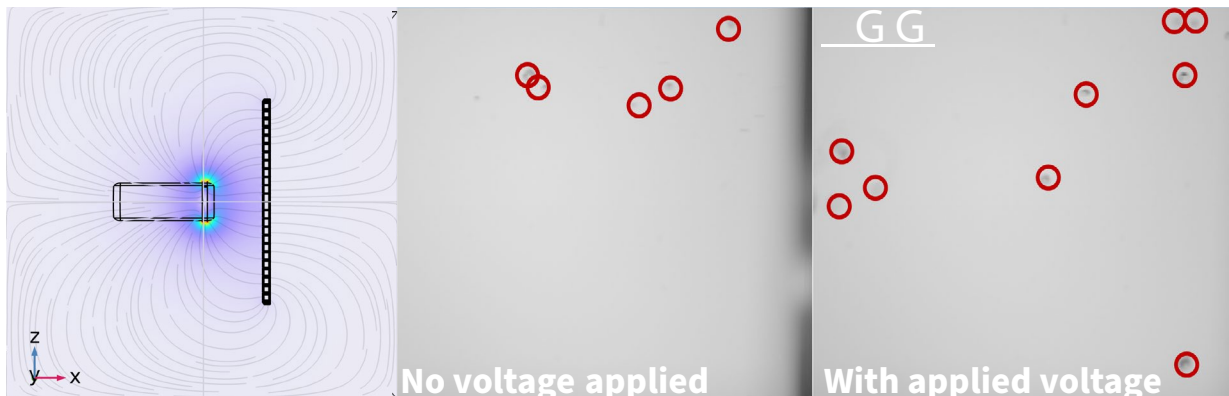


Figure 2. Electric field lines in COMSOL (left); High-speed imaging of droplets with no applied voltage (middle); High-speed imaging of droplets with a 6 kV potential difference (right)

The separation efficiencies shown in Fig. 3 indicate that the electrostatic effects imposed on the oil droplets in the flow lead to a higher fraction of oil droplets being driven towards the mesh nodes. The behavior of the oil droplets seen via high-speed imaging indicate three distinct regimes in which the oil droplets interact with the electric field. In the first regime, at low electric field intensities where the magnitude of the electric force is not significant enough to overcome the drag force imposed on the droplets by the working fluid, the oil remains in a fine mist, and largely follows the working fluid streamlines around the mesh nodes. As the electric field intensity increases, however, the droplets begin to be pulled from the working fluid and begin to coalesce as they are directed towards pathlines as defined by the electric field lines. At even higher electric field intensities, the droplets form a liquid bridge in between the ejector and the mesh, and an asymptotic behavior is seen, where there is a saturation of oil along the electric field lines and further increases in the electric field intensity do not contribute to an increase in separation efficiency. The impact of the electric field can also be seen numerically, as the asymptotic limit approached in these experimental analyses was a nearly 7× increase in separation efficiency compared to the tests run where no potential difference was applied.

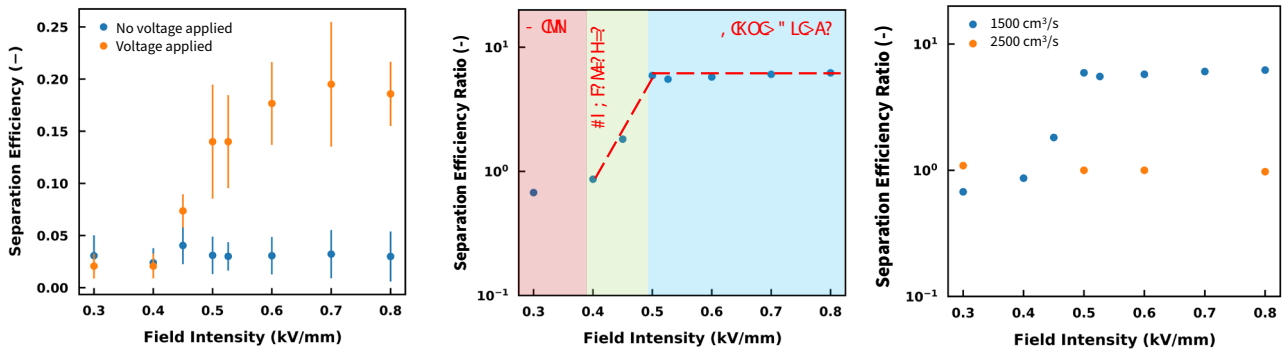


Figure 3. Separation efficiency at 1500 cm³/s with and without applied electric field (left); Ratio of separation efficiencies (Voltage/No Voltage) (middle); Comparison of separation efficiency effects between 1500 cm³/s and 2500 cm³/s (right)

The final effect seen in Fig. 3 is that an increase in the volumetric flow rate of the working fluid had a substantial effect on the ability of the applied electric field to pull the droplets from the streamlines of the working fluid. While, at the intermediate flow rate of 1500 cm³/s, the maximum voltage which could be applied by the generator was more than sufficient to achieve the asymptotic effects in separation efficiency, at the highest-tested flow rate of 2500 cm³/s, the maximum applicable voltage was not sufficient to begin observing an appreciable increase in the separation efficiency compared to the separation efficiency of the system with no applied voltages. This shows the relationships which govern a value for the “critical” electric field intensity (E_{crit}), i.e., the electric field intensity where, for a given flow rate, increased separation efficiency is seen for a system operating with an applied potential difference compared to a system operating with no applied potential difference. This “critical” electric field value can be determined, to scale as shown in Eq. (2).

$$E_{crit} \sim 6\pi\mu_{refg}Q(qA)^{-1} \quad (2)$$

While future work is necessary to integrate this technology into real-device components, the increase in separation efficiency seen in these electrostatically driven separation mechanisms can aid in decreasing the overall footprint of separators, allowing for more compact HVAC&R systems as well as decreased pressure drop.

5. REFERENCES

- Garimella, S., Lockyear, K., Pharis, D., El Chawa, O., Hughes, M.T. and Kini, G., 2022. “Realistic pathways to decarbonization of building energy systems”. *Joule*, Vol. 6, pp. 956–971.
- Toyama, T., Matsuura, H. and Yoshida, Y., 2006. “Visual techniques to quantify behavior of oil droplets in a scroll compressor”. In *Proceedings of the 2006 International Compressor Engineering Conference*. West Lafayette, USA.
- Xu, J. and Hrnjak, P., 2019. “Coalescing oil separator for compressors”. *International Journal of Refrigeration*, Vol. 106, pp. 41-53
- Damak, M. and Varanasi, K.K., 2018. “Electrostatically driven fog collection using space charge injection”. *Science Advances*, Vol. 4
- Goetzler, W., Zogg, R., Young, J. and Johnson, C., 2014. “Alternatives to Vapor-Compression HVAC Technology”. *ASHRAE Journal*, Vol. 56, pp. 12-23
- Ohno, M., Ozawa, Y. and Mizuno, A., 2019. “Recovery and Regeneration of CFCs Using Electrostatic Separation”. *International Journal of Plasma Environmental Science and Technology*, Vol. 13

Nonuniform Stratification of Hydrogen-Methane Gas Mixtures Inside a Vertical Pipeline in a Gravity Field

Jaeyong Sung^a, Tae Kyun Kim^b

^aDept. of Mechanical and Automotive Engineering, Seoul National University of Science and Technology
232 Gongneung-ro, Nowon-gu, Seoul 01811, Korea

^bGraduate School, Seoul National University of Science and Technology
232 Gongneung-ro, Nowon-gu, Seoul 01811, Korea
jysung@seoultech.ac.kr; heksim1@naver.com

Keywords: Hydrogen-methane gas mixture, Stratification, Volume fraction, Vertical pipe, CFD

1. INTRODUCTION

In contemporary society, fossil fuels are the primary energy sources, whose combustion results in the emission of byproducts such as CO₂ and NO_x. These gases are recognized as major contributors to environmental pollution and the greenhouse effect [1,2]. In contrast, hydrogen, characterized by its high calorific value, broad flammability limits and low ignition energy, is emerging as a promising clean alternative energy source. Predominantly producing water vapor during combustion, hydrogen is anticipated to play a significant role in reducing the environmental energy consumption [3].

In response to the urgent need for sustainable energy solutions, the United States and the European Union have initiated projects like Energy Earthshots-Hydrogen Shot, leveraging urban gas infrastructures for hydrogen transition. Some researches [4,5] demonstrated significant carbon emission reductions of 2.36% when hydrogen constitutes 20% of the gas mixture. This progress towards hydrogen incorporation in urban gas supplies prompts extensive research into the dynamics of hydrogen stratification within pipelines, the combustion characteristics of hydrogen-enriched gas, and the associated risks of hydrogen leakage. Notable studies by Ren and Zhang [6], Boulahlib *et al.* [7], Marangon and Carcassi [8], and Vudumu and Koylu [9] have devoted to the combustion phenomena of household gas appliances using hydrogen-blended natural gas, as well as the abnormal diffusion and stratification behaviors of hydrogen-methane mixtures, and the potential for explosive combustion in high-hydrogen scenarios.

This study aims to investigate the nonuniform stratification of methane-hydrogen gas mixtures inside a vertical pipeline in a gravity field utilizing the computational fluid dynamics (CFD) method. The gas mixtures assumed to be initially stationary and the temporal behaviors of stratification are considered for various initial concentrations of hydrogen. The evolution of hydrogen velocity fields within the pipe over time and the variations of hydrogen volume fraction according to the pipe length are discussed.

2. NUMERICAL METHOD

When valves of urban gas pipeline are closed during the summer months, there is no flow within the pipe system. Thus, the initial conditions were set to be stationary with a given hydrogen concentration in the gas mixture. The vertical pipeline has a diameter of 20 mm and a length of 100 mm, while maintaining the gas temperature of 300K at an atmospheric pressure of 101,325 Pa.

For the numerical analysis, a mixture model which is one of multiphase models, was employed. The flows are assumed to be 3D, compressible and transient. In addition, the flow is laminar since it is primarily driven by gravitational and buoyancy forces resulting in very slow velocities. The SIMPLE algorithm, coupled with body force weighting, was utilized for the solution method. The method of body force weighting enhances accuracy in analyzing such phenomena as the natural convection and stratification. The present numerical method has been validated using the data of Ren and Zhang [6] and the governing equations are as follows;

$$\frac{\partial \rho_m}{\partial t} + \nabla \cdot (\rho_m \vec{u}_m) = 0 \quad (1)$$

$$\frac{\partial}{\partial t} (\rho_m \vec{u}_m) + \nabla \cdot (\rho_m \vec{u}_m \vec{u}_m) = -\nabla p + \nabla \cdot [\vec{\mu}_m (\nabla \vec{u} + \nabla \vec{u}_m^T)] + \rho_m \vec{g} + \nabla \cdot (\sum_{k=1}^n \alpha_k \rho_k \vec{u}_{dr,k} \vec{u}_{dr,k}) \quad (2)$$

$$\frac{\partial}{\partial t} (\alpha_k \rho_k) + \nabla \cdot (\alpha_k \rho_k \vec{u}_m) = -\nabla \cdot (\alpha_k \rho_k \vec{u}_{dr,k}) \quad (3)$$

$$\vec{u}_{dr,k} = \vec{u}_k - \vec{u}_m \quad (4)$$

Equations (1~3) represent the continuity, momentum and volume fraction equations, respectively. Here, ρ , v , p , μ , and α denote the density, velocity, pressure, viscosity, and volume fraction, respectively. The subscript m denotes the

properties of the mixed gas, while the subscript k denotes the properties of individual gases. The total number of individual gases, n is 2 since the gas is a mixture of hydrogen and methane. The continuity and momentum equations govern the flow of the mixed gas, whereas the volume fraction equation, influenced by the drift velocity, acts as a continuity equation for individual gas. The drift velocity as defined in equation (4) represents the relative velocity of a specific gas with respect to the mixed gas velocity, which is caused by the different movement of individual gas within the mixed gas due to gravity, pressure or thermal effects. The relationship between the physical quantities of the mixed gas and those of individual gases is as follows.

$$\rho_m = \sum_{k=1}^n \alpha_k \rho_k, \quad \overline{u}_m = \frac{\sum_{k=1}^n \alpha_k \rho_k \overline{u}_k}{\rho_m}, \quad \overline{\mu}_m = \sum_{k=1}^n \alpha_k \mu_k \quad (5)$$

3. RESULTS AND DISCUSSION

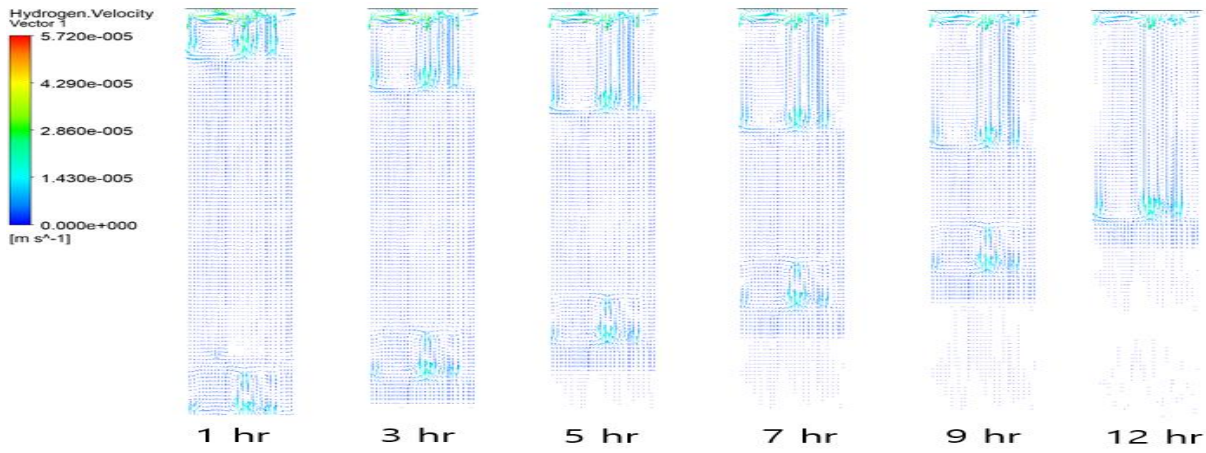


Figure 1. The evolution of hydrogen velocity fields within the pipe over time ($H_2 = 20\%$, $D = 20$ mm, $L = 100$ mm)

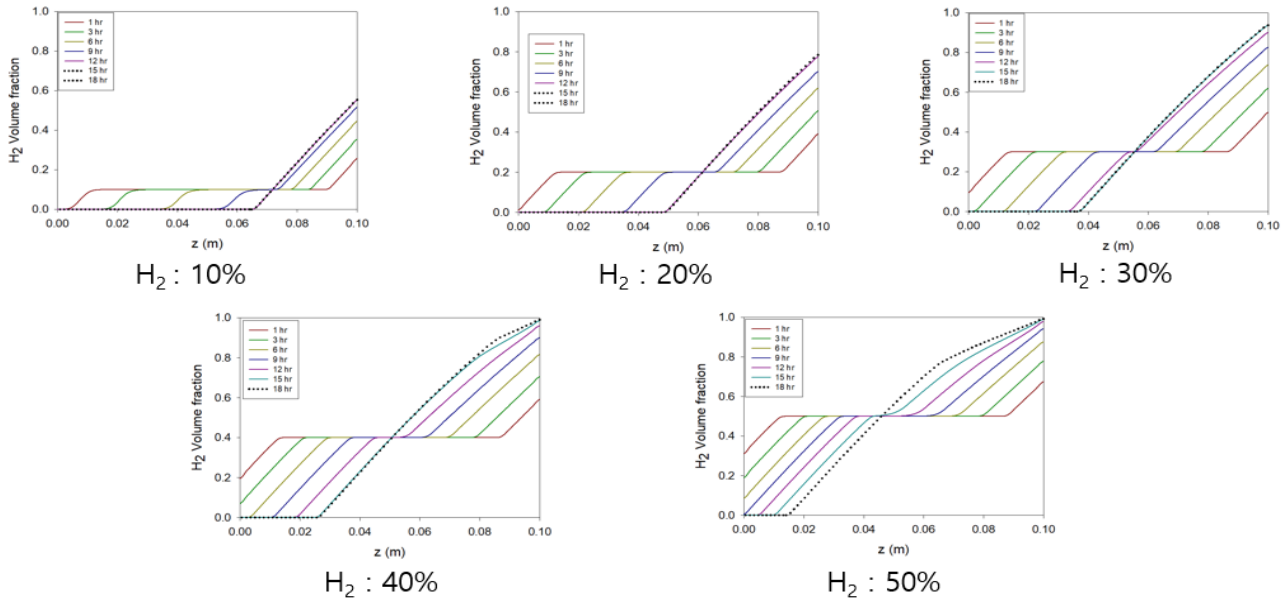


Figure 2. Variations of hydrogen volume fraction according to the pipe length for various initial hydrogen concentrations ($D = 20$ mm, $L = 100$ mm)

Figure 1 shows the evolution of the hydrogen velocity field within the pipeline over time when the initial hydrogen concentration is 20%. Due to the natural convection caused by the density difference between the two gases in a gravity field, the lighter hydrogen gas rises towards the upper section and the heavier methane gas moves downward. At the earlier stage of the stratification, there exists two vortices. One is formed at the top of pipe and the other is formed at the bottom of pipe. As time goes on, the upper vortex expands downward with the size increasing. However, the lower vortex remains relatively constant in size then gradually ascends towards the upper region. After 12 hours, the two vortices merge, exhibiting a combined structure. With the lower vortex moving upward, the hydrogen near the bottom of pipe

significantly disappears, which indicates that the heavier methane is accumulated at the bottom of pipe.

In figure 2, the variations of hydrogen volume fraction according to the pipe length for various initial hydrogen concentrations are plotted. The pipe diameter D is 20 mm, and the length L is 100 mm. Due to the stratification, the hydrogen in the upper section of the pipe becomes dense, whereas it in the lower section becomes dilute. However, the distribution of hydrogen is nonuniform along the pipe length and the temporal behavior of stratification strongly depends on the initial hydrogen concentration. At a certain time, the hydrogen concentration at the bottom of the pipe is reduced to zero, and then the no-hydrogen region expands with time. In the upper section of the pipe, the hydrogen concentration increases linearly along the pipe length having a peak at the top of the pipe, which increases significantly with the initial hydrogen concentration. At the final stage of the stratification (an equilibrium state), the hydrogen concentration below a certain position of the pipe approaches zero. The positions are $z/L = 0.63$ and 0.18 for the initial concentration of 10% and 50%, respectively. Above these positions, the hydrogen concentration increases linearly along the pipe length. Although the effect of pipe length is not shown in this figure, it is also observed that the time required for hydrogen to reach an equilibrium state increases with the pipe length. Once the concentration of hydrogen stabilizes, it remains consistent even as more time elapses.

4. CONCLUSIONS

In this study, the nonuniform stratification of initially stationary hydrogen-methane gas mixtures in a vertical pipeline has been investigated. The stratification occurs due to natural convection caused by gravity and the density difference between the two gases. During the stratification, two vortices are formed at the upper and lower section of the vertical pipe. The upper vortex expands downward with the size increasing, whereas the lower vortex moves towards the upper region keeping the size constant, which results in merging of both the vortices and disappearing of hydrogen in the bottom region of the pipe. the heavier methane is accumulated at the bottom of pipe.

During the stratification, the distribution of hydrogen is nonuniform along the pipe length and the temporal behavior of stratification depends on the initial hydrogen concentration. As the initial concentration of hydrogen increases, the no-hydrogen region formed in the lower section of the pipe decreases at the final stage of the stratification. In the upper section of the pipe, the hydrogen concentration increases linearly along the pipe length having a peak at the top of the pipe, which increases significantly with the initial hydrogen concentration.

5. ACKNOWLEDGEMENT

This work was supported by the Korea Institute of Energy Technology Evaluation and Planning (KETEP) grant funded by the Korea government (MOTIE) (RS-2023-00237341, Safety Verification and Development of Safety Technology for Combustion Performance of Residential/Industrial Combustors and Gas Equipment)

6. REFERENCES

- [1] Kovač, A., Matej, P. and Doria, M., 2021. "Hydrogen in Energy Transition: A Review". *International Journal of Hydrogen Energy*, Vol. 46(16), pp. 10016–10035.
- [2] Ogden, J., Daniel, S., Zane, M. and Marshall, M., 2018. "Natural Gas as a Bridge to Hydrogen Transportation Fuel: Insights from the Literature". *Energy Policy*, Vol. 115, pp. 317–329.
- [3] Shin, Y. and Cho, E. S., 2021. "Numerical Study on H₂ Enriched NG Lean Premixed Combustion". *Journal of the Korean Society Combustion*, Vol. 26(1), pp. 51–58.
- [4] Talibi, M., Balachandran, R. and Ladommatos, N., 2017. "Influence of Combusting Methane-Hydrogen Mixtures on Compression-Ignition Engine Exhaust Emissions and in-Cylinder Gas Composition". *International Journal of Hydrogen Energy*, Vol. 42(4), pp. 2381–2396.
- [5] Park, H. Y., Yoon, S. H., Rho, B. S., Lee, W. J. and Choi, J. H., 2019. "Effect of Hydrogen (H₂) Addition on Flame Shape and Combustion Products in Mixed Coflow Diffusion Flames of Methane (CH₄), Ethane (C₂H₆) and Propane (C₃H₈)". *Journal of the Korean Society of Marine Environment & Safety*, Vol. 25(6), pp. 780–787.
- [6] Ren, S. and Zhang, Q., 2015. "Influence of Concentration Distribution of Hydrogen in Air on Measured Flammability Limits". *Journal of Loss Prevention in the Process Industries*, Vol. 34, pp. 82–91.
- [7] Boulahlib, M. S., Medaerts, F. and Boukhalifa, M. A., 2021. "Experimental Study of a Domestic Boiler using Hydrogen Methane Blend and Fuel-Rich Staged Combustion". *International Journal of Hydrogen Energy*, Vol. 46(75), pp. 37628–37640.
- [8] Marangon, A. and Carcassi, M. N., 2014. "Hydrogen–Methane Mixtures: Dispersion and Stratification Studies". *International Journal of Hydrogen Energy*, Vol. 31(11), pp. 6160–6168.
- [9] Vudumu, S. K. and Koylu, U. O., 2009. "Detailed Simulations of the Transient Hydrogen Mixing, Leakage and Flammability in Air in Simple Geometries". *International Journal of Hydrogen Energy*, Vol. 34(6), pp. 2824–2833.

Study of Droplet Motion and Freezing under Shear of Cold Air Streams

Xibo Qiao, Shinan Chang* and Shuoshuo Wang

School of Aeronautic Science and Engineering, Beihang University, Beijing 100191, China

* sn_chang@buaa.edu.cn

Keywords: Air streams, Shear, Droplet, Freezing

1. INTRODUCTION

The phenomenon of freezing and frosting of water in nature has a very serious impact on human industrial production and daily life. Especially in the field of aviation, the problem of anti-icing/de-icing of aircraft has become a major problem to be solved urgently.

Therefore, in order to reduce the harm caused by icing, it is of great significance to study the freezing phenomenon of liquid droplets on the plane and explore the influence of cold air flow on the icing of liquid droplets for the study of the icing mechanism on the plane surface and the prediction of subsequent ice growth, which can provide an important reference for the design of aircraft anti-icing/de-icing system.

2. Experimental Method

In this paper, the droplet freezing observation platform of the research group of Beihang University was used in the experiment. The platform includes low-speed wind tunnel, temperature control system, image acquisition system and droplet generation system, etc. The experimental conditions of cold surface temperature as low as -25°C , air flow velocity as low as $0\sim 40\text{m/s}$, and air flow temperature as low as -20°C can be changed, and the dynamic movement of the frozen phase interface of the droplet and the change process of the contour with time can be recorded

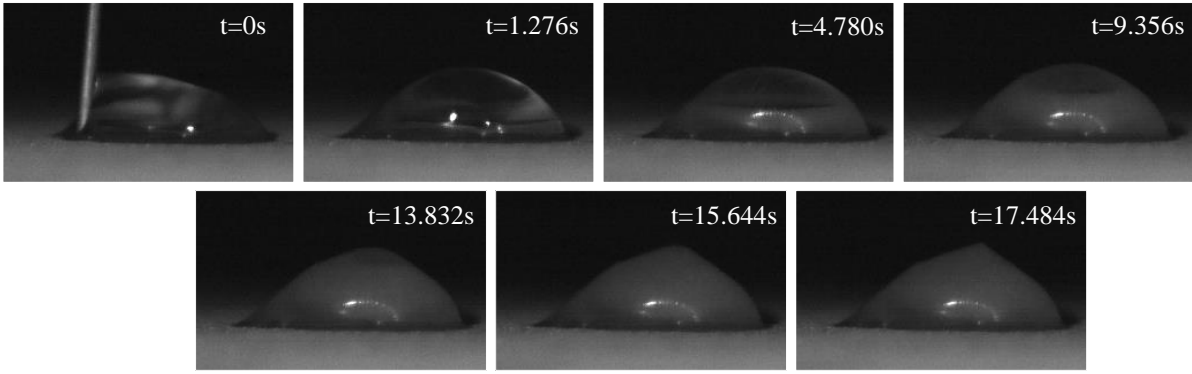
In order to explore the effects of cold airflow shear and solid-liquid interface heat transfer on droplet movement and freezing, the following experimental conditions were set for research.

Table 1. Experimental Cases

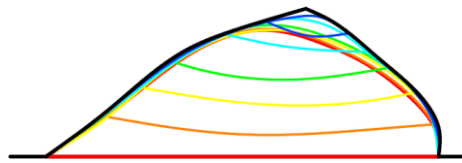
Case	Drop volume (μl)	Air velocity (m/s)	Droplet temperature ($^{\circ}\text{C}$)	Air temperature ($^{\circ}\text{C}$)	Surface temperature ($^{\circ}\text{C}$)
1	20	8	5	-8	-20
2	20	12	5	-8	-20
3	20	15	5	-8	-20
4	20	18	5	-8	-20
5	20	20	5	-8	-20
6	20	15	5	10	-20
7	20	15	5	-5	-20
8	20	15	5	-12	-20
9	20	15	5	-17	-20
10	20	15	5	-8	-8
11	20	15	5	-8	-10
12	20	15	5	-8	-14
13	20	15	5	-8	-18

3. Result and Discussion

The freezing process of droplet under the action of airflow shear was observed by a high-speed camera in the experiment. Figure 1 shows the original image of droplet freezing (a) The trend of the front during droplet freezing(b)



(a) The droplet freezing process(air velocity=15m/s, surface temperature= -20°C, air temperature= -8°C)



(b) Variation trend of droplet freezing front
(The fronts are red, orange, yellow, green, cyan, blue and purple in that order)
Figure 1. Droplet freezing image

Under the action of cold air flow, the length of droplet will spread out, and the distance of tip deviation will also change with the increase of air flow speed. For specific droplet, the droplet morphology and freezing characteristics under different air flow speeds will be recorded.

Figure 2 shows the influence of air velocity on the spread length and tip deviation distance of the droplet. With the increase of air velocity, under the action of air shear force, the droplet will spread longer on the cold surface and form a larger icing area. The frozen shape is also affected by the change of air flow, and the tip will shift to different degrees, and the shift will be more obvious with the increase of air flow speed.

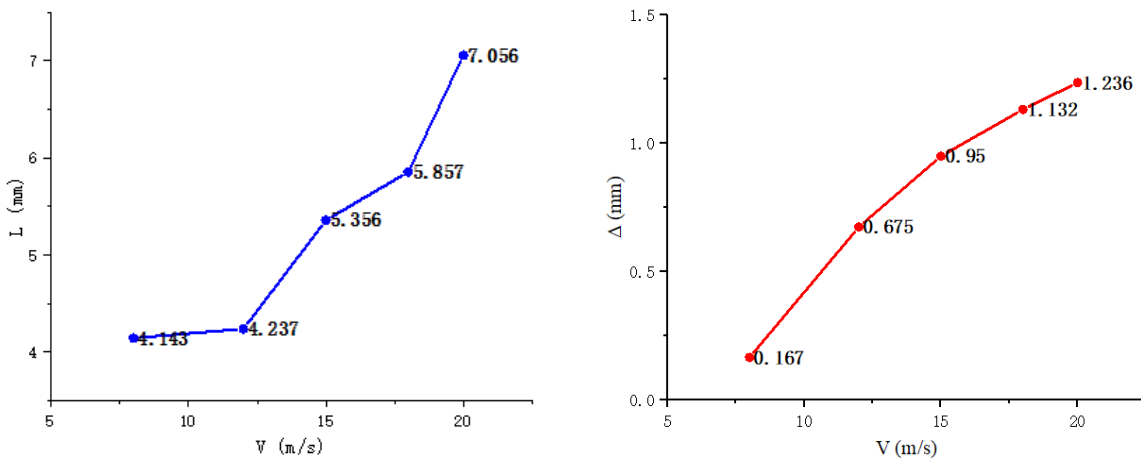


Figure 2. Variation of droplet length(left) and tip offset distance(right) with airflow velocity
(L-droplet length, V-air velocity, Δ-tip offset distance)

The freezing speed mainly depends on the heat conduction of the cold plate and the air convection of the surrounding environment. The heat transfer on the surfaces of the two media can be described by the following equation

$$\frac{dQ}{dt} = -hA(T_2 - T_1) \quad (1)$$

In the equation, $\frac{dQ}{dt}$ is the thermal conductivity, h is the surface heat transfer coefficient, A is the contact area between water drop and surface, T_2 and T_1 are the temperature of water drop and cold surface respectively.

It can be seen from the formula that the heat conduction at the solid-liquid interface is related to the temperature difference between the solid and the liquid. When the droplet temperature is constant, the lower the cold surface temperature is, the greater the thermal conductivity will be, resulting in the shortening of the freezing time. Figure 3 shows the freezing time as the cold surface temperature decreases.

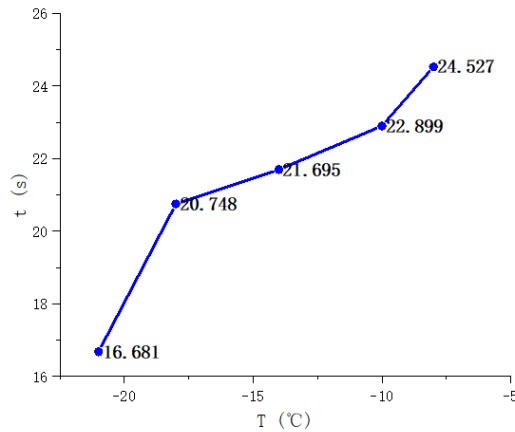


Figure 3. Variation of freezing time with surface temperature (t-freezing time, T-surface temperature)

4. CONCLUSIONS

The effect of cold air flow on droplet movement behavior and freezing characteristics was studied. The shear effect of cold air flow on liquid made droplet spread length larger, and its shape also changed, which had an important influence on the subsequent ice growth. In addition, the effect of cold surface temperature on droplet freezing was also studied. Lower surface temperature increased the heat transfer efficiency at the solid-liquid interface, resulting in faster freezing rate and shorter freezing time.

5. REFERENCES

- Su, Qian, et al. "A Review of Loop Heat Pipes for Aircraft Anti-Icing Applications." *Applied Thermal Engineering*, vol. 130, Feb. 2018, pp. 528–40. EBSCOhost.
- Tianwei Lai, et al. "Experimental Study on Frost Crystal Morphologies and Frosting Characteristics under Different Working Pressures." *Applied Sciences*, vol. 12, no. 8, Apr. 2022, p. 4025. EBSCOhost.
- Shinan, C., et al. "Heat Transfer Characteristics of Micron Ultrathin Shear-Driven Water Film Flowing on a Horizontal Metal Surface." *International Journal of Heat and Mass Transfer*, vol. 148, Feb. 2020. EBSCOhost.
- Ober li, Linda, et al. "Condensation and Freezing of Droplets on Superhydrophobic Surfaces." *Advances in Colloid and Interface Science*, vol. 210, Aug. 2014, pp. 47–57. EBSCOhost.
- Strub, M., et al. "Experimental Study and Modelling of the Crystallization of a Water Droplet." *International Journal of Refrigeration*, vol. 26, no. 1, Jan. 2003, pp. 59–68. EBSCOhost.
- Jung, S., et al. "Mechanism of Supercooled Droplet Freezing on Surfaces." *Nature Communications*, vol. 3, Jan. 2012. EBSCOhost.

Study of castor oil/diesel emulsified fuels: Behavior of a single droplet in high temperature environments using image analysis methods and combustion characteristics of emulsions in diesel engines

Shuhn-Shyurng Hou ^{1,2,*}, Chun-Ta Chen ³, Wei-Cheng Chiu ^{1,2}, Ming-Da Lai ²

¹Green Energy Technology Research Center, Kun Shan University
No.195, Kunda Rd., Yongkang Dist., Tainan 710303, Taiwan

²Department of Mechanical Engineering, Kun Shan University
No.195, Kunda Rd., Yongkang Dist., Tainan 710303, Taiwan

³Department of Mechatronic Engineering, National Taiwan Normal University
No. 162, Sec. 1, Heping East. Rd., Taipei 10610, Taiwan

* Corresponding Author: sshou@mail.ksu.edu.tw

Abstract

The behavior of a single droplet in castor oil/diesel blends was investigated using a suspended-droplet heating device. The castor oil used in the experiment was obtained through the cold pressing process of castor seeds. During the experiment, we varied the heating temperature and the mixing ratio of castor oil/diesel blends. High-speed video recordings captured drop size variations and vaporization, expansion, bubbling, ejection, swelling, and micro-explosion phenomena, which were subsequently analyzed using an imaging analysis method. Additionally, a K-type thermocouple monitored droplet temperature history throughout the heating process. Notably, the droplet's evaporation rate, determined by the slope of the d^2 -law, increased with rising heating temperature. Furthermore, an increase in heating temperature or castor oil blending ratio resulted in faster expansion and shorter droplet lifetimes. Interestingly, micro-explosions did not occur in the castor oil/diesel blended fuel. Engine tests were conducted with varying castor oil percentages (0%, 5%, and 10%) in the castor oil–diesel emulsion. Stability was maintained during these tests, and the use of 5% and 10% castor oil showed comparable maximum pressure in the combustion chamber and exhaust gas temperature compared to petroleum diesel. While brake-specific energy consumption (BSEC) slightly decreased, brake thermal efficiency (BTE) increased. The addition of castor oil to petroleum diesel led to a slight increase in NO_x emissions and a slight decrease in CO₂ emissions and smoke opacity. Moreover, the 5% and 10% blending ratios of castor oil in the castor oil/diesel emulsions reduced PM_{2.5} by 20% and 23%, respectively, compared to petroleum diesel.

Keywords: Diesel engine, Bio-fuel, Castor oil, Castor oil/diesel blends, Engine performance, Emissions

Prediction of Boiling Heat Transfer Coefficients with Uncertainty under Upward Flow Conditions using Deep Neural Networks and Gaussian Process Regression

Tomihiko Kinjo^{a,b,*}, Koji Enoki^b, Yuichi Sei^b, Hayato Nakano^b

^a Japan Aerospace Exploration Agency, 3-1-1 Yoshinodai, Sagami-hara Kanagawa, Japan, 252-5210

^b The University of Electro-Communications, 1-5-1 Chofugaoka, Chofu, Tokyo, Japan, 182-8585

*kinjoh.tomihiko@jaxa.jp

Keywords: Heat transfer, Two-phase flow boiling, Deep learning, Gaussian process regression, Thermoinformatics

1. INTRODUCTION

In recent years, the increase in the size of spacecraft and the increased performance of electronic devices has led to a rising trend in heat generation. Moreover, there is a growing demand for enhancing heat dissipation capabilities within limited heat dissipation areas, particularly for long term activities in lunar environments. Additionally, addressing greenhouse gas emissions to combat global warming has become an urgent task on Earth.

In response to these challenges, the application of boiling two-phase flow for thermal control technology is being considered, with a focus on refrigerants and heat exchangers. For instance, in the air conditioning sector, refrigerants with high greenhouse effects, such as fluorocarbon refrigerants, have historically been used. However, the Kigali Amendment to the Montreal Protocol aims to gradually reduce the production and consumption of hydrofluorocarbon (HFC) refrigerants by 85% in terms of global warming potential (GWP) by 2036 in advanced countries. Therefore, the development of refrigeration and air conditioning technologies using low-GWP refrigerants has become an urgent issue. Low-GWP refrigerants have been identified as potential solutions, but evaluation of the boiling heat transfer coefficients of these new refrigerants is limited.

Furthermore, cooling technologies utilizing two-phase flow heat transfer are also being considered for application in spacecraft, with efforts underway to understand heat transfer rates in microgravity environments (H.J van Gerner, et al., 2015). However, experiments in microgravity environments are difficult to develop in a short period of time due to the long timelines and costs involved. Consequently, there is a need for methods to predict heat transfer rates in microgravity environments on Earth gravity (Baba et al., 2012).

In this study, we are evaluating the influence of gravity direction on boiling heat transfer coefficients for low-GWP refrigerants and developing prediction techniques using experiments and deep learning. Low-GWP refrigerants, often referred to as low-pressure refrigerants, have lower pressures compared to commonly used refrigerants R245fa. As it is a relatively new refrigerant, there is limited research on the evaporation heat transfer coefficient within the tube. Additionally, many studies have focused on horizontal experimental setups concerning gravity, with few studies investigating the effect of the angle between the flow direction and gravity, such as upward and downward flows. Therefore, in this study, we have developed a new experimental apparatus to obtain heat transfer coefficients for upward and downward flows to experimentally evaluate the influence of gravity direction on heat transfer coefficients. Furthermore, we have organized the dominance regions of forces based on dimensionless numbers and conducted experiments under conditions where the effects of gravity and inertial forces can be compared.

In addition, we are investigating the application of deep learning to predict boiling heat transfer rates from limited data (Sei, et al., 2022). Prediction methods using artificial intelligence can be considered as alternative techniques to existing methods by treating heat transfer rates obtained from multiple conditions as big data. In existing studies, utilizing deep learning for heat flow phenomena in two-phase fluids have been identified, focusing on the classification of flow patterns and prediction of heat transfer rates under boiling conditions. However, there is currently no established method for prediction using deep learning, and examples of predicting the influence of gravity direction on heat transfer rates using deep learning have not been confirmed. Through our research, we have found that predicting heat transfer rates using deep learning can achieve higher accuracy compared to existing studies. Furthermore, while conventional deep learning-based prediction methods cannot evaluate uncertainties in the obtained results, we propose a novel method combining DNN and Gaussian process regression to predict heat transfer rates (Sei, et al., 2021). DNN and Gaussian process regression can predict not only heat transfer coefficients with high accuracy but also the uncertainties of the predicted heat. We are currently working on various thermal engineering and informatics issues, including multiphase flow, and we refer to this. We are currently working on various thermal engineering and informatics issues, including multiphase flow, and we refer to this research area as "thermoinformatics," a new field that combines thermal engineering and informatics.

For this reason, in this study, we experimentally evaluated the influence of gravity direction on boiling heat transfer rates for low-GWP refrigerants and assessed the prediction of heat transfer rates using DNN and Gaussian process regression, as well as the uncertainty of prediction accuracy.

2. Experimental apparatus and measurement

Figure 1 depicts a schematic diagram of the experimental setup. The experimental apparatus mainly consists of a pump, inverter, Coriolis flowmeter, preheater, test section, and condenser. The preheater and test section are directly heated by applying a predetermined amount of heat to electrodes provided on the flanges. Heating the preheater allows control of the quality at the inlet of the test section. Temperature sensors and absolute pressure gauges are attached to the inlet and outlet of the preheater, as well as the inlet and outlet of the test section. The refrigerant flow rate can be adjusted by a valve at the pump inlet or frequency control by the inverter. The test section consists of stainless-steel tubes with outer diameters of 1/4 inch and 1/2 inch and a total length of 500 mm. Additionally, K-type thermocouples are attached to the test section wall for measuring wall temperatures. To experimentally evaluate the influence of gravity direction on heat transfer rates, an assessment of the dominant regions using dimensionless numbers is performed. Figure 2 depicts the results of organizing the dominant regions using Weber number (We), Bond number (Bo), and Froude number (Fr) for each pipe diameter under conditions of heat input and mass flow rate. The use of dimensionless numbers represents the dominant regions of inertia, gravity, and surface tension. From the dominant regions, it has been reported that as the pipe diameter decreases, surface tension becomes relatively dominant, and the effects of gravity and inertia decrease. In this study, experiments were conducted under conditions focusing on gravity and inertia in which the influence of surface tension is minimal.

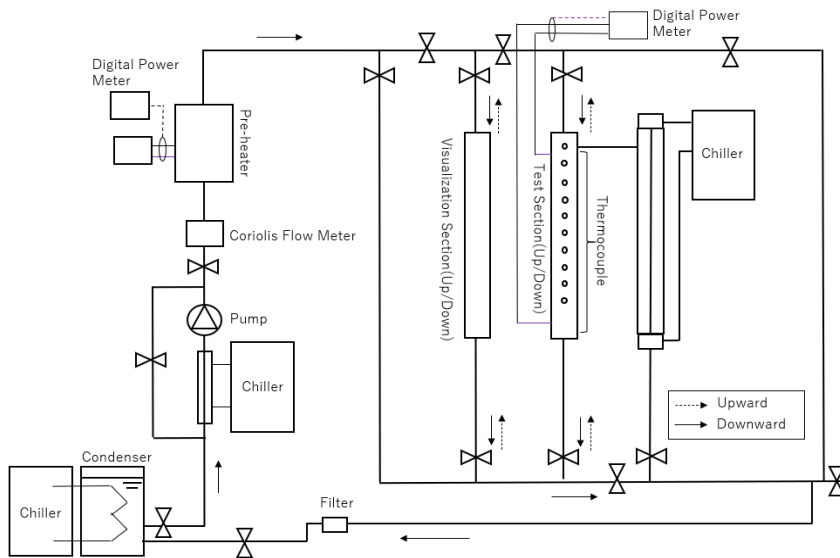


Fig.1 Experimental apparatus

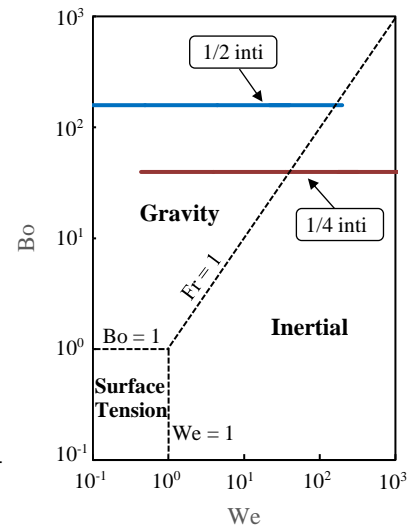


Fig.2 Dominant force regime map pip diameter

3. Deep Neural Networks and Gaussian Process regression

In existing studies, research predicting flow regimes and heat transfer rates can be found, but no established methods have been confirmed yet. Additionally, prediction results focusing on the direction of gravity in the flow have not been observed. Therefore, we addressed the prediction of heat transfer rates for upward flow, including uncertainties, using a novel approach that combines DNN and Gaussian process regression. Fig. 3 depicts the overall structure of the DNN, while Fig. 4 depicts the learning process. Our proposed system iterates between a training phase and a prediction phase multiple times. During each prediction phase, our system outputs a predicted heat transfer coefficient and its associated uncertainty. Finally, based on these uncertainties, the system generates a final predicted heat transfer coefficient that minimizes the expectation of the prediction error and its uncertainty.

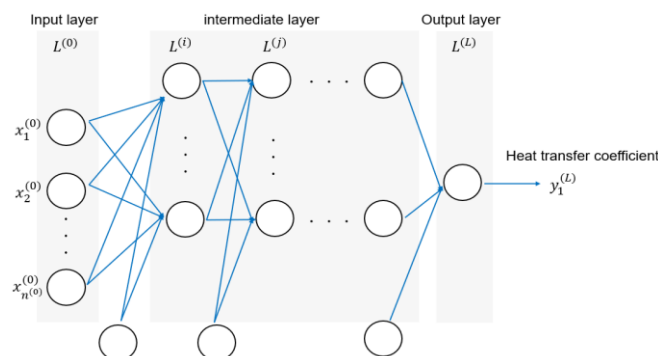


Fig.3 Overall structure of deep neural networks.

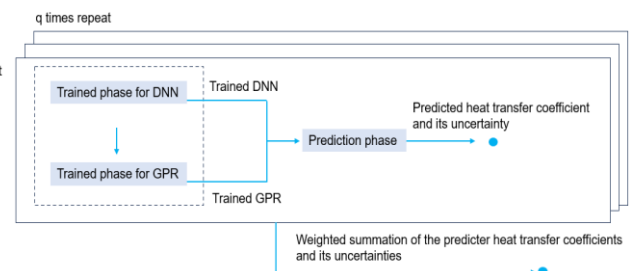


Fig.4 Overall architecture

4. Databases and Evaluation

We used a database containing upward flow data (Miyata et al., 2008; Ayeba et al., 2023). Table 1 presents a summary of the database. Additionally, we have compiled 12 physical properties, and representative data are shown in Table 2. Our investigation into prior research revealed a scarcity of data regarding heat transfer in upward flows compared to horizontal flows. Therefore, we plan to assess the outcomes of training combined with experimental data in the future. However, as an initial step, we conducted training using existing data. The relationships between the physical experimental values (ground truth value) and the predicted values are depicted in Figure 5. In Figure 5, R20, and R30, which represent the percentages by which the predicted values are within ± 20 and ± 30 of the ground truth, respectively, are depicted. As a result, prediction accuracy is high in regions with high heat transfer coefficients and low in regions with low heat transfer coefficients. By refrigerant, most of the HFE-7000 data falls within the R30 range, with R410A having lower prediction accuracy.

Table.1 Experimental conditions of data points obtained from existing studies for upward flow

Source	Fluid	Quality	Saturation Pressure MPa	Inside Diameter mm	Mass Flux kg/m-2/s-1	Heat Flux kW.m-2	N
Miyata et.al	R410A	0.1-0.9	0.135	1.0	30-200	1-16	546
Ayeba et.al	HFE-7000	0.15-0.7	0.12 – 0.15	6.0	75-400	15-25	64

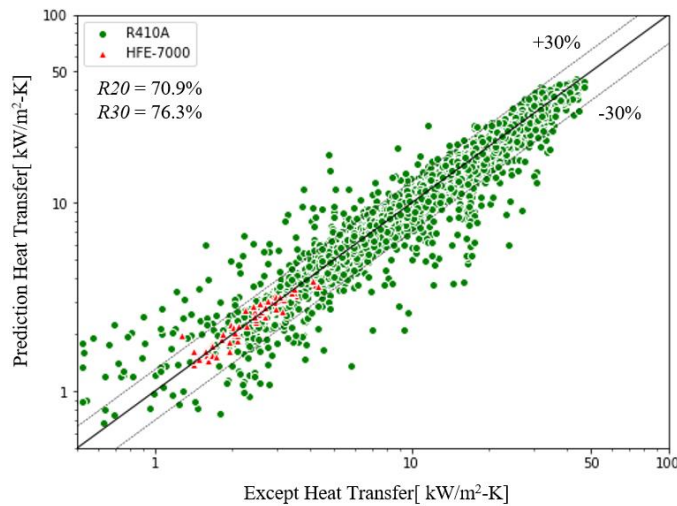


Fig.5 Comparison of predictions and experimental data

5. CONCLUSIONS AND FUTURE WORK

We are conducting experiments and using deep learning to evaluate the effect of gravity direction on the upward boiling heat transfer coefficient of low GWP refrigerants. Additionally, we are employing a combination of DNN and Gaussian process regression to predict the heat transfer coefficient and evaluate the uncertainty of the predictions. In the future, we plan to report on the results of training with additional experimental data and discuss the findings based on experimental results.

6. REFERENCES

- H.J van Gerner, et al., 2015, "A heat pump for space applications", 45th International Conference on Environmental Systems 12-16, July, Bellevue, Washington
- Sei, et al., 2022, "Prediction of boiling heat transfer coefficients for mini-channels", Multiphase Science and Technology, 34(2), 43–65
- Sei, et al., 2021, "Prediction of Heat Transfer Coefficients with Uncertainty in Mini-Channels Using Deep Neural Networks and Gaussian Process Regression", International Journal of Heat and Mass Transfer, March 2
- Baba, et al., 2012, "Thermal Hydraulic Characteristics in Two-phase Flow Loop Driven", Japanese J, Multiphase Flow, Vol.25, No.5(Japanese)
- Miyata., et al., 2008, "Boiling Heat Transfer and Pressure Drop of Refrigerant Flowing Vertically Upward in a Small Diameter Tube", Japan Society of Refrigerating and Air Conditioning Engineers, Vol.23, 359-369, No.4(Japanese)
- Ayeba, et al., 2023, "Theoretical modeling of heat transfer in vertical upward and downward annular flow boiling". Heat Transfer Engineering, Pages 381-398

THE EFFECT OF AIR INJECTION ON PRESSURE GRADIENT IN HORIZONTAL OIL-IN-SALINE-WATER EMULSION (O/W) FLOWS

Alex Roger Almeida Colmanetti^{a,*}, Andres Felipe Eslava Sarmiento^a, Davi Pereira Carvalho^a, Maria de Fátima Rodrigues da Cunha^b, Aloisio Euclides Orlando Junior^b, Gherhardt Ribatski^a

^aHeat Transfer Research Group, São Carlos School of Engineering, University of São Paulo, EESC – USP
Av. Trabalhador São-carlense, 400 – Centro 13566-590. São Carlos – SP – Brasil

^bCentro de Pesquisas, Desenvolvimento e Inovação Leopoldo Américo Miguez de Mello – CENPES/PETROBRAS
Av. Horácio Macedo, 950 – Cidade Universitária da Universidade Federal do Rio de Janeiro, Rio de Janeiro – RJ,
21941-915

*alex.colmanetti@usp.br

Keywords: Three-phase flow, horizontal flow, flow patterns, pressure drop, produced water.

1. INTRODUCTION

Multiphase flows are present in several industrial applications, e.g., chemical, pharmaceutical, food, and petroleum industries (Brandt et al., 2020, Descamps et al., 2006). In the oil and gas industry, three-phase flows are present in many processes found in oil exploration and processing, e.g., effluents treatment (Piccioli et al., 2020). Notably, an abundant effluent found in oil exploration is the produced water, which consists of an emulsion characterized by oil droplets (with a diameter of 10 – 50 microns) dispersed in saline water (Piccioli et al., 2020). The treatment of produced water in offshore fields often involves the use of unitary operations (flotation) to separate the oil drops dispersed in saline water. Induced gas flotation (IGF) is one of the technologies employed in the treatment of produced water (Rawlins, 2009, Piccioli et al., 2020). This technique induces the removal of oil droplets (with a diameter of 10 – 50 microns) from saline water through the injection of a gas into the emulsion. In this context, the injection of gas into the oil-in-water emulsion (O/W) may induce the oil-water separation. Pressure drop during air-water-oil flows under conditions of produced water treatment are not completely understood until now. There is a lack of studies concerning the pressure drop evaluation for in-tube horizontal three-phase flows (oil-water emulsion and gas) under conditions close to those found in the treatment of produced water. Although there are studies in the literature on three-phase horizontal flow, most of them deal with high oil concentration, which characteristics and, consequently, flow behaviors are significantly different from those of oil-in-water emulsion (O/W) at low oil concentration (Dehkordi et al, 2019, Hewitt, 2005, Lahey et al., 1992, Shean, 1976, Spedding et al., 2005, Taitel et al., 1995).

The present study concerns an investigation of the effect of air injection in horizontal flows of an emulsion of oil-in-saline-water (O/W) with reduced oil concentration (below 300 ppm). Experiments were performed for liquid superficial velocity (J_L) from 1.75 m/s to 3.30 m/s, for gas superficial velocity (J_G) from 0.0 m/s to 18.05 m/s, for temperature (T) from 70.8°C to 79.8°C, water salinity (C_{sal}) from 0 to 29.7 g/L, oil concentration (C_{oil}) from 37.6 to 308.7 ppm and drop size distribution (DSD) from 16.2 to 22.2 μm .

2. EXPERIMENTAL SETUP

Figure 1.a illustrates a diagram of the experimental apparatus. The setup allows experiments of two-phase flow and three-phase flow in a horizontal pipe 9.25 m long with an internal diameter of 14.8 mm. The development of oil-in-water (O/W) emulsions is performed by injecting oil into the water flow through a “mixing T device” (MTD), highlighted in red in Fig. 1.a (oil injector). The MTD was developed seeking the development of emulsions (O/W) with monodisperse droplets and reduced oil concentration (below 500 ppm). This device has a restriction to the flow that induces an increase in water velocity (v_w) and consequently an increase in turbulent fluctuations, leading to drop breakage (Hinze, 1955). A globe valve is installed downstream of the MTD which aperture is used to define the oil droplet size distribution (DSD). The oil droplet size distribution (DSD, see Fig. 1.b) is evaluated in real-time by an online particle size analyzer (PSA) (model Insittec Wet, Malvern-Panalytical®). This equipment allows the evaluation of DSD and oil concentration (C_{oil}) through the laser diffraction technique. The globe valve acts as an oil droplet-breaking device, imposing a local pressure drop associated with high shear stresses in the flow. Such a pressure drop is monitored by the differential pressure transducer ΔP_6 (Figure 1). The application of the MT device for this purpose was validated in previous studies by the group (HTRG) aiming to generate stable oil-in-water (O/W) emulsions (Colmanetti et al, 2022). Samples of water were extracted upstream the oil injection into the water and its salinity evaluated through a Hanna Salinity Tester model HI98319 with resolution of 0.1 g/L and precision of ± 1.0 g/L.

The test section is segmented into four subsections (2.0 meters long each, $L_S = 2.0$ m), and five transparent viewing sections ($L_V = 0.25$ m), as indicated in Figure 1. The viewing sections were positioned at a distance of 2.0 meters (between subsections) to enable recognition and capture of flow images throughout the test section. Furthermore, four differential pressure transducers ($\Delta P1$, $\Delta P2$, $\Delta P3$, and $\Delta P4$) are used to measure the pressure drop (ΔP) along the subsections. The experimental uncertainties of measured and calculated parameters are presented in Table 1.

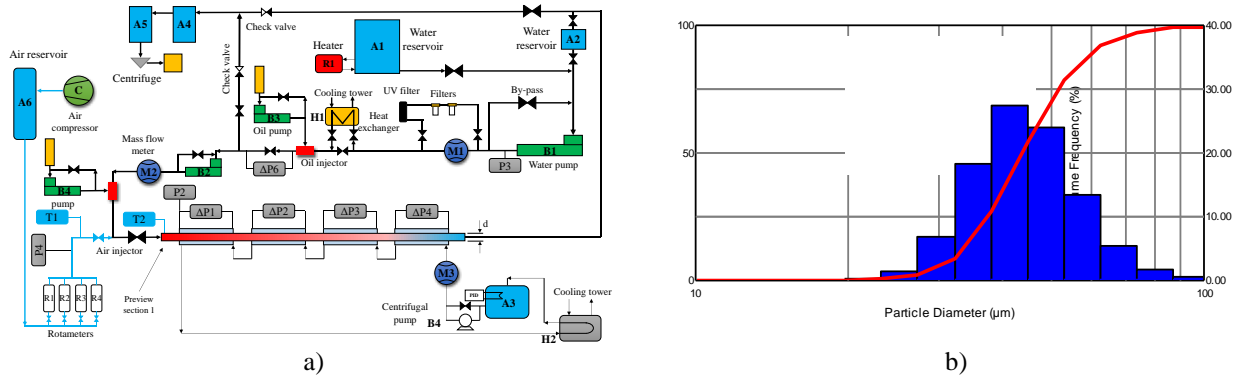
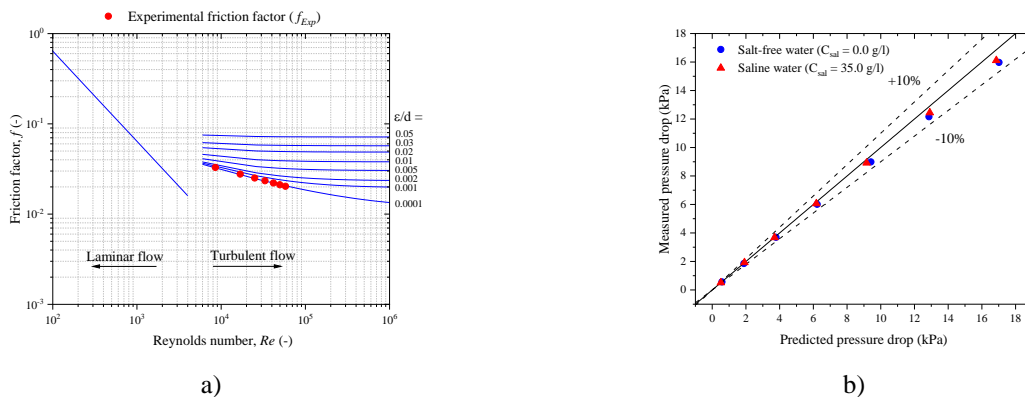


Table 1. Experimental uncertainties found of calculated and measured parameters.

Liquid superficial velocity (J_L , m/s)	Gas superficial velocity (J_G , m/s)	Pressure drop (ΔP , kPa)	Temperature ($^{\circ}C$)	Water salinity (g/L)	Drop size distribution (DSD, μm)
0.01	0.01	0.10	0.15	1.0	1.4

Figure 2 presents the setup validation performed for water single-phase flow. The predictions of friction factor (f) and pressure drop (ΔP) were obtained according to Colebrook (1939). Figure 2.a show that the experimental friction factor agrees with Colebrook (1939). Figure 2.b gives the measured pressure drop as a function of predicted pressure drop for salt-free water (blue) and saline water ($C_{sal} = 35.0$ g/l, in red). For both conditions, a spread of less than 10% was obtained.



3. RESULTS AND DISCUSSIONS

Figure 3.a shows the pressure gradient (dp/dx) as a function of the ratio (J_G/J_L) of the superficial gas velocity and the superficial liquid velocity for temperatures from $72.3^{\circ}C$ to $79.7^{\circ}C$. The pressure gradient data obtained for liquid superficial velocity (J_L) of 3.10 with tap water (Fig. 3.a, blue ball) are close to the pressure gradient obtained for conditions with salinity of 28.4 g/L (Fig. 3.a, red triangle). The same behavior is observed for liquid superficial velocity from 1.75 m/s to 1.80 m/s (Fig. 3.a), indicating that water salinity (C_{sal}) does not affect the pressure gradient. Figure 3.b shows a comparison of the measured pressure gradient and the corresponding calculated values according to the homogeneous model, with the two-phase viscosity (emulsion+gas) given by Dukler et al. (1964), and the drift-flux model (Wallis, 1969). Differences greater than 40% are observed between calculated and measured values. The homogeneous model seems a

reasonable approach since most of the data concerns bubbly flow. The oil-in-water emulsion (O/W) was modelled as an homogeneous mixture with its properties weighted according to the mixture composition taking into account the properties of the pure fluids and the oil concentration. Salinity was not considered in the modeling.

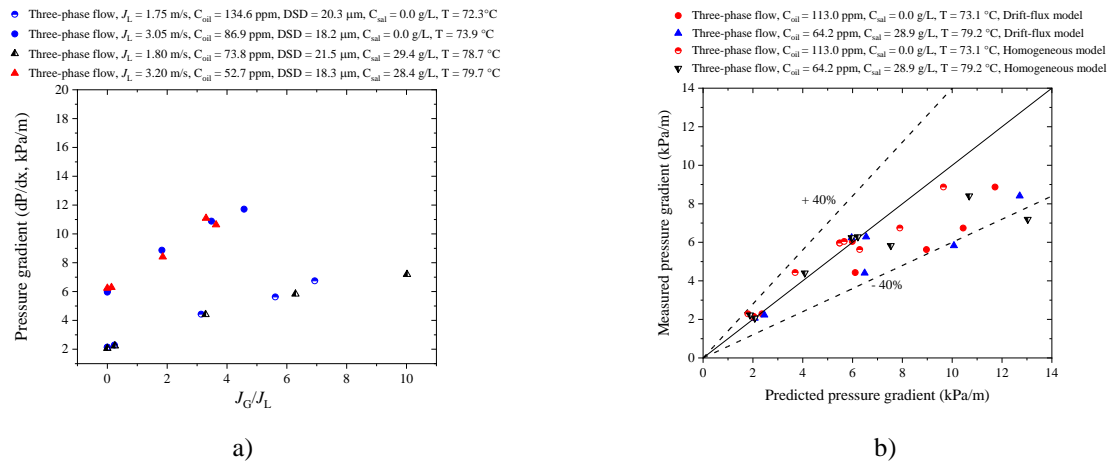


Figure 3. a) Pressure gradient as a function of the ratio of superficial velocity of gas and liquid (J_G/J_L), b) measured pressure gradient as function of predicted pressure gradient.

4. CONCLUSIONS

The conclusions gathered from this study are the following: (i) salinity did not affect the pressure gradient for three-phase horizontal flow for superficial liquid velocities (J_L) ranging from 1.75 m/s to 3.20 m/s, (ii) the pressure gradient predictions provided by the drift-flux model were more accurate ($\pm 20\%$) than the predictions provided by the homogeneous model ($\pm 40\%$), (iii) the use of the homogeneous model to model the oil-in-water emulsion (O/W) proved promising, (iv) the effect of oil addition to the water on the pressure gradient for the rate of concentrations evaluated in the present study is not significative.

5. REFERENCES

- Brandt, A., Czernek, K., Płaczek, M., and Witzczak, S., 2020. "Downward Annular Flow of Air–Oil–Water Mixture in a Vertical Pipe". *Energies*, Vol. 14, pp. 1- 30.
- Colebrook, C.F., 1939. "Turbulent Flow in Pipes, with Particular Reference to the Transition Region between the Smooth and Rough Pipe Laws". *Journal of the Institution of Civil Engineers*, Vol. 11, pp. 133-156
- Dehkordi, P. B., Colombo, L. P. M., Mohammadian, E., Shahrabadi, A., and Azdarpour, A., 2019. "A mechanistic model to predict pressure drop and holdup pertinent to horizontal gas-liquid-liquid intermittent flow". *Chemical Engineering Research and Design*, Vol. 149, pp. 182-194.
- Descamps, M., Oliemans, R. V. A., Ooms, G., Mudde, R. F., and Kusters, R., 2006. Influence of gas injection on phase inversion in an oil–water flow through a vertical tube. *International journal of multiphase flow*, Vol. 32(3), pp. 311–322.
- Dukler, A. E., Wicks, M. III, and Cleveland, R. G., 1964. "Frictional pressure drop in two-phase flow: An approach through similarity analysis", *AIChE journal*, Vol. 10, pp. 44-51.
- Hewitt, G. F., 2005. "Three-phase gas–liquid–liquid flows in the steady and transient states". *Nuclear engineering and design*, Vol. 235, pp. 1303-1316.
- Hinze, J. O., 1955. "Fundamentals of the hydrodynamic mechanism of splitting in dispersion processes". *AIChE journal*, Vol. 1, pp. 289–295.
- Lahey Jr, R. T., Açıkgöz, M., and Franca, F., 1992. "Global volumetric phase fractions in horizontal three-phase flows". *AIChE journal*, Vol. 38.7, pp. 1049-1058.
- Piccioli, M., Aanesen, S. V., Zhao, H., Dudek, M., and Øye, G., 2020. "Gas flotation of petroleum produced water: a review on status, fundamental aspects, and perspectives". *Energy & Fuels*, Vol. 34(12), pp. 15579-15592.
- Rawlins, C. H., 2009. "Flotation of fine oil droplets in petroleum production circuits". *Recent Advances in Mineral Processing Plant Design*, Vol. 232, pp. 232–246.
- Shean, A.R., 1976. *Pressure drop and phase fraction in oil-water-air vertical pipe flow*. Master thesis, Massachusetts Institute of Technology, USA.
- Spedding, P. L., Donnelly, G. F., & Cole, J. S., 2005. "Three phase oil-water-gas horizontal co-current flow: I. Experimental and regime map". *Chemical Engineering Research and Design*, Vol. 83(4), pp. 401-411.
- Taitel, Y., Barnea, D., and Brill, J. P., 1995. "Stratified three phase flow in pipes", *International Journal of Multiphase Flow*, Vol 21, pp. 53-60.
- Wallis, G. B., 1969. *One-dimensional two-phase flow*. McGraw-Hill, New York, 1rd edition

EXPERIMENTAL AND NUMERICAL STUDY TO INVESTIGATE SUBCOOLED BOILING IN MINICHANNELS

Beata Maciejewska^{a,*}, Magdalena Piasecka^b

^aFaculty of Management and Computer Modelling, Kielce University of Technology

^bFaculty of Mechatronics and Mechanical Engineering, Kielce University of Technology, Al. Tysiaclecia Panstwa Polskiego 7, 25-314 Kielce, Poland

*beatam@tu.kielce.pl

Keywords: flow boiling, minichannel, heat transfer coefficient, FEM, time-dependent Trefftz functions

1. INTRODUCTION

This study aims to explore flow boiling heat transfer in a group of minichannels with varying numbers, focusing on determining the heat transfer coefficient during subcooled flow boiling. To address this, an experimental and numerical approach was employed.

Experimentally, the work investigates the effectiveness of minichannel heat exchangers and utilizes infrared thermography to measure external temperatures, aiding in the estimation of heat transfer coefficients.

Numerically, a finite element method (FEM) based on Trefftz functions was applied to solve the time-dependent heat transfer problem. The numerical calculations were aimed to complement the experimental findings by providing a deeper insight into the heat transfer characteristics during subcooled flow boiling, with the numerical results verified against a simple 1D approach based on Newton's law of cooling, showing satisfactory agreement.

2. EXPERIMENT

Experimental studies focused on boiling heat transfer in parallel minichannels with flowing fluid Fluorinert FC-72. The test section utilized a Haynes-230 alloy foil for heating, with channels 1 mm deep and varying widths. Experiments observed the fluid's temperature, pressure, flow patterns, and heat flux with infrared thermography and a high-speed camera through a glass panel. Measurements were taken at 1-second intervals, covering single-phase convection and subcooled boiling. Data acquisition stations monitored the fluid's inlet and outlet temperatures, pressure, mass flow rate, and electrical parameters to calculate the heat flux. The experiment aimed to understand the heat transfer processes in minichannels, crucial for enhancing thermal management in various engineering applications.

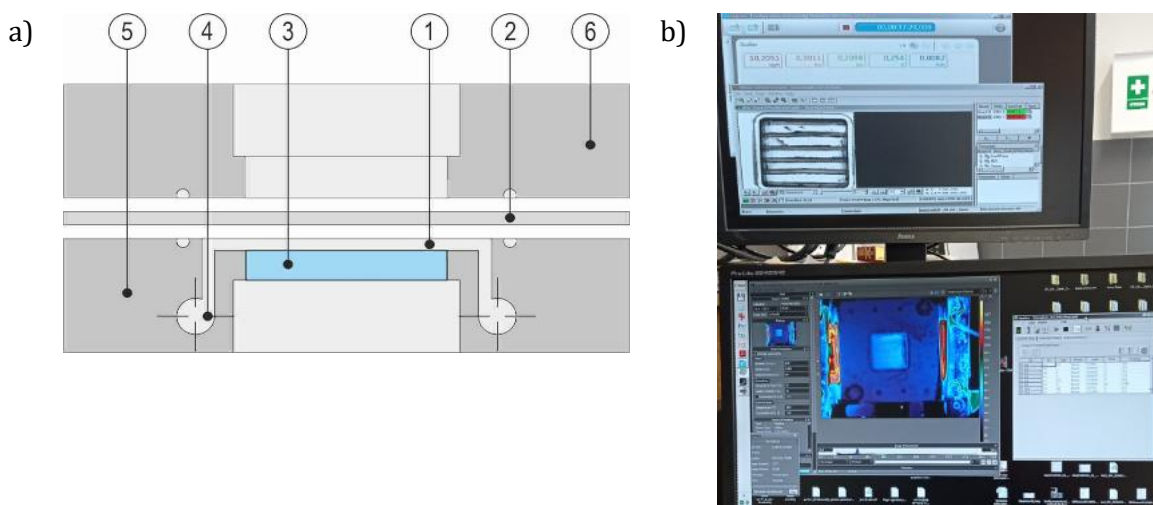


Figure 1. Test section with minichannels:

- a) longitudinal section: 1- minichannel, 2- heated foil, 3- glass panel, 4- thermocouple, 5- top cover, 6- channel body;
- b) a view of the of data and image acquisition system when thermographic image and two phase flow image are illustrated during experiments.

3. MATHEMATICAL MODEL OF HEAT TRANSFER

The mathematical model represents a nonstationary, two-dimensional heat transfer problem within a group of minichannels, focusing on a central channel for analysis. It assumes laminar flow of an incompressible fluid (Fluorinert FC-72) and temperature-independent material properties. The model disregards temperature variability along the minichannel width, aligning fluid flow with the x -axis and considering the y -axis as the minichannel depth.

The computational domain divides into two regions: the heater domain (Ω_H) and the fluid domain (Ω_M), in which the governing differential equations are formulated.

In Ω_H , the heat equation is:

$$\kappa_H \nabla^2 T_H - \frac{\partial T_H}{\partial t} = - \frac{q_w(t)}{\delta_H \cdot \lambda_H} \quad (1)$$

in Ω_M , the Fourier-Kirchhoff equation is modified to:

$$\kappa_F \nabla^2 T_F - v_x \frac{\partial T_F}{\partial x} - v_y \frac{\partial T_F}{\partial y} - \frac{\partial T_F}{\partial t} = 0 \quad (2)$$

where where $\kappa_H = \frac{\lambda_H}{\rho_H c_{p,H}}$, λ_H – the heated wall thermal conductivity, ρ_H – the heated wall density, $c_{p,H}$ – the heated wall specific heat, $\kappa_F = \frac{\lambda_F}{\rho_F c_{p,F}}$, λ_F – the fluid thermal conductivity, ρ_F – the fluid density, $c_{p,F}$ – the fluid specific heat, q_w – the heat flux, $q_w(t) = \frac{I(t)\Delta U(t)}{A}$, A – cross-sectional area of the heated wall, I – the current, ΔU – the voltage drop across the heated wall.

Differential equations are supplemented with appropriate boundary and initial conditions. The boundary conditions take into account the measurements of the heated foil temperature conducted using infrared thermography.

The local heat transfer coefficients at the heated wall–fluid interface are obtained from the Robin boundary condition:

$$\alpha_{2D}(x, t) = \frac{-\lambda_H \frac{\partial T_H(x, \delta_H, t)}{\partial y}}{T_H(x, \delta_H, t) - T_F(x, y_{ref}, t)} \quad (3)$$

and Newton's law of cooling as:

$$\alpha_{1D}(x, t) = \frac{I(t)\Delta U(t)}{A \cdot (T_{H,IR}(x, t) - T_{F,bulk}(x, t))} \quad (4)$$

where $T_{F,bulk}(x, t)$ is the fluid temperature changing linearly from the inlet to the outlet of the minichannel, $T_{H,IR}(x, t)$ represents temperature measurements taken with an IR camera.

The mathematical model effectively combines physical principles and mathematical equations to predict heat transfer dynamics within minichannels.

4. COMPUTATIONAL METHOD

The Finite Element Method (FEM) with time-dependent Trefftz-type basis functions (Maciejewska and Piasecka 2017) is employed to solve the heat transfer problem in a minichannel, as depicted by equations (1) and (2), along with boundary and initial conditions. This approach involves segmenting the time-space domain into subdomains, where the unknown temperature function within each 8-node cuboidal subdomain is interpolated using Trefftz functions, pertinent to the heat equation in the heated wall and the Fourier-Kirchhoff equation in the flowing fluid.

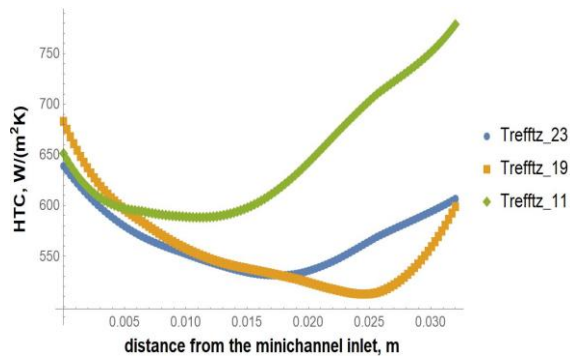
Temperature values at Lagrange interpolation nodes are determined by minimizing functionals expressing mean square error of the approximate solution at the edge of the area and at common edges between elements, with temperature at the end of a period serving as the initial temperature for the next period of time (Maciejewska and Piasecka 2019).

4. RESULTS AND CONCLUSIONS

The research focused on the subcooled boiling area identified through detailed analysis of boiling curves.

Numerical calculations based on the FEM with time-dependent Trefftz-type basis functions provided a comparative analysis of heat transfer coefficients along the minichannel length over time. The results for the test section with 11, 19 and 23 minichannels are shown in Figure 2.

a)



b)

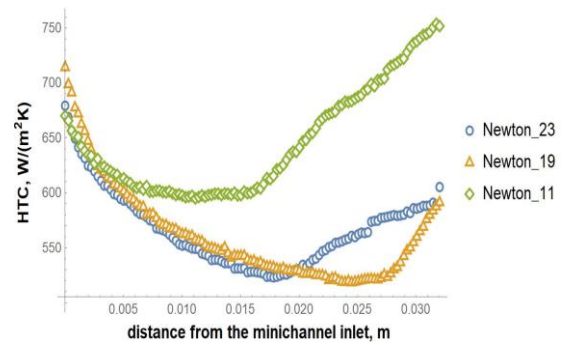


Figure 2. The heat transfer coefficient (HTC) versus distance from the minichannel inlet calculated using the FEM with Trefftz-type basis functions (a) and Newton's law of cooling (b) based on data for the test sections with 11, 19, 23 minichannels, at the average heat flux of $q_w = 22.2 \text{ kW/m}^2$.

The obtained results indicate first a decrease and then an increase in heat transfer coefficients with the distance from the minichannel inlet, which is a phenomenon observed in various minichannel configurations. Moreover, comparisons of results obtained from Newton's law of cooling with those obtained from FEM with Trefftz functions highlighted the effectiveness and reliability of the latter method in capturing the nuances of subcooled boiling heat transfer.

In conclusion, the adoption of Trefftz-type functions within the FEM framework for analyzing subcooled boiling phenomena in minichannels has demonstrated significant potential. It not only aligns closely with experimental data but also provides a robust tool for predicting thermal behaviors in complex fluid dynamics scenarios.

Numerical calculations based on the FEM with time-dependent Trefftz-type basis functions provided a comparative analysis of heat transfer coefficients along the minichannel length over time. The results indicate a consistent increase in heat transfer coefficients with distance from the minichannel inlet, a pattern observed across different minichannel configurations. Furthermore, comparisons between results obtained from Newton's law of cooling and those derived from the FEM with Trefftz functions underscored the efficacy and reliability of the latter method in capturing the nuances of subcooled boiling heat transfer.

In conclusion, the adoption of Trefftz-type functions within the FEM framework for analyzing subcooled boiling phenomena in minichannels has demonstrated significant potential. It not only aligns closely with experimental data but also provides a robust tool for predicting thermal behaviors in complex fluid dynamics scenarios.

5. REFERENCES

- Maciejewska, B., Piasecka, M., 2017. "Trefftz Function-Based Thermal Solution of Inverse Problem in Unsteady-State Flow Boiling Heat Transfer in a Minichannel." *International Journal of Heat and Mass Transfer*, Vol. 107, pp. 925–33.
- Maciejewska, B., Magdalena Piasecka M., 2019. "Time-Dependent Study of Boiling Heat Transfer Coefficient in a Vertical Minichannel." *International Journal of Numerical Methods for Heat and Fluid Flow*, Vol. 30(6), pp. 2953–69.

BOILING HEAT TRANSFER RESEARCH DURING FLOW IN RECTANGULAR MINICHANNELS

Magdalena Piasecka^{a,*}, Sylwia Hozejowska^b, Artur Piasecki^c

^a Kielce University of Technology, Faculty of Mechatronics and Mechanical Engineering

^b Kielce University of Technology, Faculty of Management and Computer Modelling

^c Kielce University of Technology, Faculty of Environmental Engineering, Geomatics and Renewable Energy

^{a,b,c} Al. Tysiaclecia Panstwa Polskiego 7, 25-314 Kielce, Poland

*tmpmj@tu.kielce.pl

Keywords: heat transfer, flow boiling, minichannel, infrared thermography, Trefftz method

1. INTRODUCTION

Heat exchangers play a critical role in various industries where energy transfer is involved. There is a significant emphasis on research related to compact small-scale heat exchangers with a configuration of minichannels. This emphasis arises from their widespread use in cooling electronic components. The cooling of these components, essential for temperature reduction, remains a key focal point in research.

This work focusses on heat transfer in a model compact heat exchanger with a group of minichannels positioned vertically with fluid upward flow. On the basis of the experimental data, calculations with the use of T-functions were performed. As a result, local heat transfer coefficient values were determined to evaluate the heat transfer process's intensity and, consequently, the heat exchanger's efficiency.

2. EXPERIMENTAL STAND AND METHODOLOGY

The experimental setup is shown in Figure 1. The working fluid flow loop includes: a test section with minichannels, flow pump, mass flow meter, pressure sensor, compensating tank, heat exchanger, air separator and filters. The data acquisition system comprises data acquisition stations with expansion cards and PC software. The following data were acquired: dedicated to: (i) acquiring thermograms of the outer surface of the heated wall of the minichannel using an infrared camera, (ii) capturing two-phase flow patterns and (iii) recording of fluid temperature, pressure, mass flow rate, current intensity and voltage drop across the heated wall of the minichannels. Detailed information on the experiment stand and methodology can be found in previous works by the authors (Piasecka *et al.*, 2023, 2024, 2021).

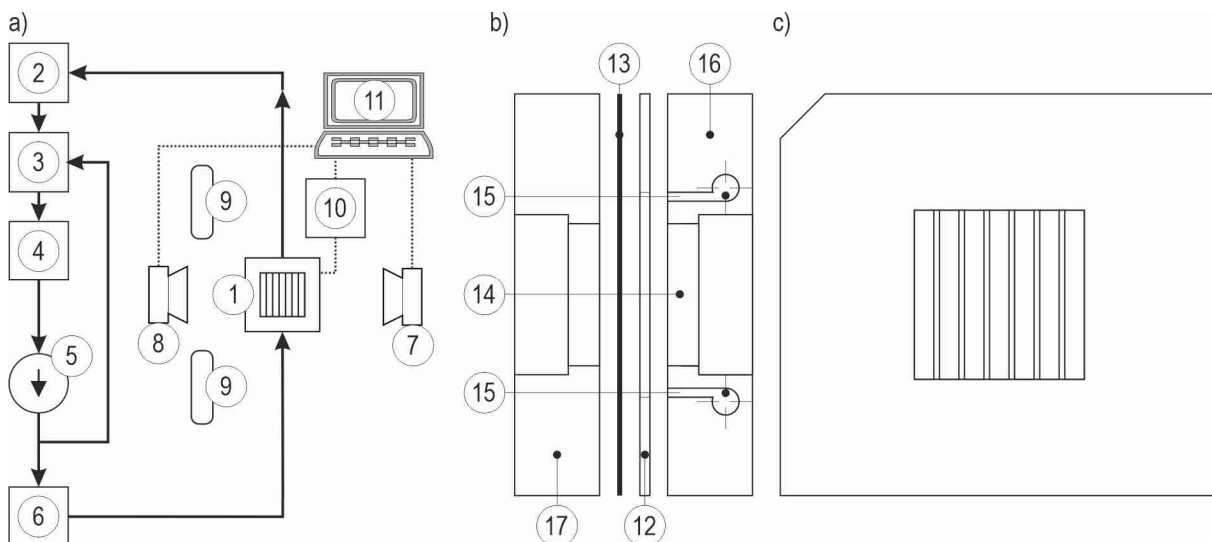


Figure 1. a) Schematic diagram of the main loops implemented in the test stand: 1 - test section; 2 - heat exchanger; 3 - pressure regulator; 4 - filter; 5 - circulating pump; 6 - Coriolis mass flow meter; 7 - infrared camera; 8 - high-speed camera; 9 - lighting system; 10 - DAQ stations; 11 - PC; b) longitudinal section showing its main components separated: 12 - spacer with group of seven minichannels, 13 - heating plate, 14 - glass plate, 15 - inlet/outlet chamber, 16 - body, 17 - front cover, c) view of the test section from the front cover side.

Experiments were performed for Fluorinert FC-72 flow boiling in a group of seven minichannels. Dimensions of a single minichannel were as follows: 1 mm (depth), 6 mm (width) and 32 mm (length). The test section was vertically with upward flow. A 0.1 mm thick plate, made of Haynes-230 alloy, was a heating wall for the flowing fluid. Other main parts of the test section, i.e. the cover and body, were made of aluminium. The sides were produced in a Teflon spacer. The temperature of the outer surface of the plate (in contact with ambient air) was measured by infrared thermography (FLIR A655sc infrared camera). The foil on the outer side was coated with a black paint of known emissivity (0.98). Flow patterns were observed through the glass plate and recorded by a high-speed camera.

During the experimental series, there was a laminar flow of FC-72 along the minichannels. It was accompanied by a gradual increase in the electric power supplied to the heating plate. Investigations were conducted under similar stable thermal and flow stationary conditions for two boiling regions (subcooled and saturated), as follows:

- temperature of the working fluid at the inlet (average): 301.8 K;
- overpressure at the inlet (average): 119 035 Pa;
- heat flux density $q = 7.94 \div 56.97 \text{ kW/m}^2$;
- mass flow rate (average): $Q_m = 21.23 \text{ kg/h}$.

3. MATHEMATICAL APPROACH AND CALCULATIONS

The approach is a modification of the mathematical model presented in (Piasecka *et al.*, 2021). The central minichannel from group of seven were taken into consideration. The following assumptions were made in the model:

- the heat exchange process is time-independent;
- the physical parameters of the minichannel elements are independent of temperature;
- the heat exchange occurring on the sidewalls of the minichannel does not affect the thermodynamic parameters of its central part;
- the fluid flow in the minichannel is steady and laminar (Reynolds number < 2300) with a constant mass flow rate;
- the temperature of the fluid changes with the distance from the inlet to the minichannel (x) and the depth of the channel (y);
- the temperature of the heating plate changes with its width (y).

The temperature of the heating plate T_h satisfies the following equation

$$\frac{d^2 T_h}{dy^2} = -\frac{qv}{\lambda_h} \quad (1)$$

where qv means the volumetric heat flux, λ_h - thermal conductivity. Knowing the measurements of the temperature of the outer surface of the plate and neglecting heat exchange with the environment allows us to solve equation (1).

The temperature of the fluid T_f satisfies the energy equation in the form

$$\lambda_f \nabla^2 T_f = v(y) c_p \rho_f \frac{\partial T_f}{\partial x} \quad (2)$$

where ∇^2 denotes the Laplace operator, $v(y)$ is the velocity of the fluid parallel to the heating plate, c_p, ρ_f means the specific heat capacity and density respectively. The Trefftz method was used to solve equation (2) with the following boundary conditions: (i) the fluid temperature and pressure at the inlet and outlet to/from the minichannel are known, (ii) the temperature and heat flux are equal on the contact wall between the plate and the fluid.

Knowing the distribution of the heating plate temperature allows us to determine the local heat transfer coefficient as a function of the distance from the inlet to the minichannel

$$\alpha(x) = \frac{-\lambda_h \frac{\partial T_h}{\partial y}(x, \delta_h)}{T_h(x, \delta_h) - T_{f,ave}(x)} \quad (3)$$

where L means length of the minichannel, δ_h - heating plate thickness and the fluid reference temperature $T_{f,ave}$ is computed by analogy to (Piasecka *et al.*, 2021).

4. RESULTS

The heating plate temperature measurements obtained due to the IR camera as a function of distance from the minichannel inlet are illustrated in Figure 2a. The two-dimensional fluid temperature distributions obtained by the Trefftz method for selected heat fluxes are shown in Figure 2b. The heat transfer coefficient versus the distance from the inlet is shown in Figure 3a. Example boiling curves constructed for three distances from the inlet are shown in Figure 3b.

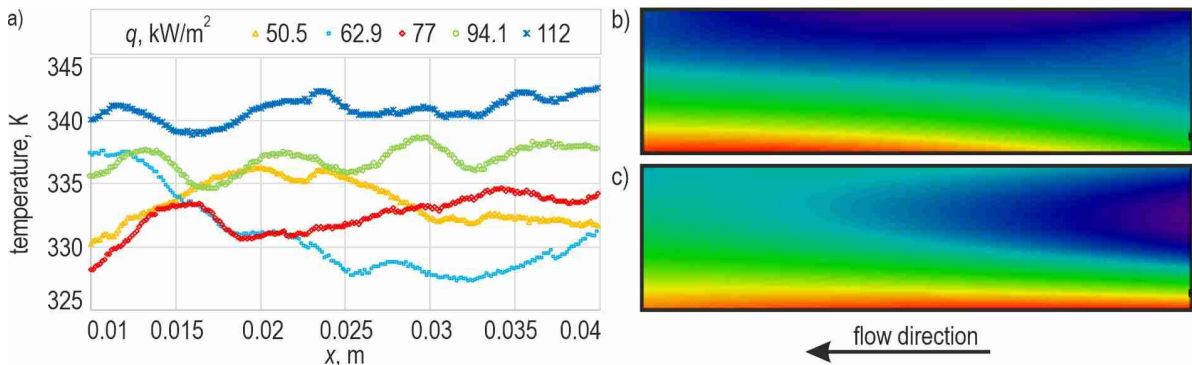


Figure 2. a) Temperature measurements of the heating plate obtained due to the IR camera as a function of distance from the minichannel inlet; b,c) two-dimensional fluid temperature distribution obtained by the Trefftz method for: $q = 28.3 \text{ kW}/(\text{m}^2 \text{ K})$ (b) and $q = 62.8 \text{ kW}/(\text{m}^2 \text{ K})$ (c).

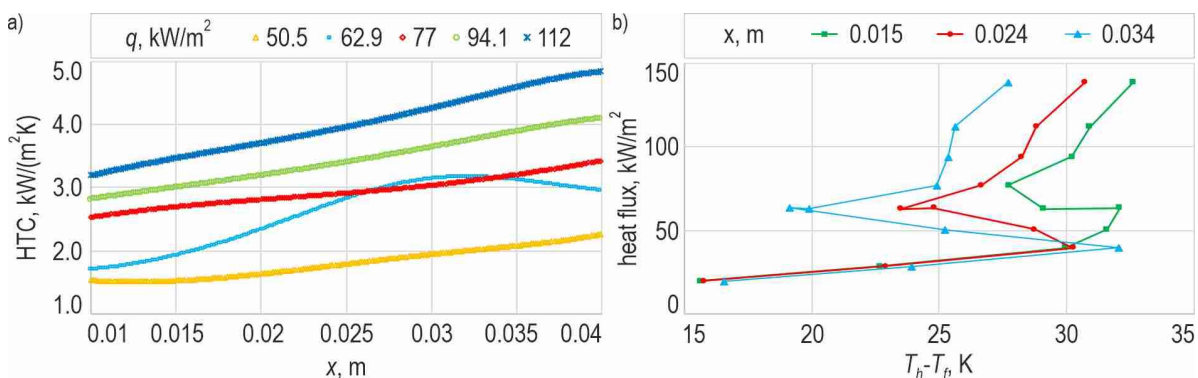


Figure 3. a) Heat transfer coefficient as a function of distance from the minichannel inlet; b) boiling curves constructed for three distances from the inlet: 0.015 m, 0.024 m and 0.034 m.

When analysing the data presented in Figure 2 it was observed that:

- The temperature of the fluid slightly increased with the distance from the minichannel inlet, Figure 2a;
- The two-dimensional fluid temperature distribution reveals a near-wall layer adjacent to the heating foil, as well as an expanding heating zone within the fluid as the heat flow increases, Figure 2b;
- The values of local heat transfer coefficients ranged between 0.8 and 5.6 $\text{kW}/(\text{m}^2 \text{ K})$; the heat transfer coefficient increases with the distance from the channel inlet and reaches higher values for higher heat fluxes, Figure 3a;
- In the boiling curves plotted as the heat flux density versus the temperature difference, the ‘temperature overshoot’ also known as ‘nucleation hysteresis’ was recognisable; it was observed that with increasing distance from the inlet, the temperature drops characteristic of boiling initiation were higher, Figure 3b.

4. CONCLUSIONS

This work presents results of investigations concerning FC-72 flow boiling heat transfer in a group of seven parallel minichannels. In experiments, the test section was vertically orientated with upward flow. Infrared thermography was used to measure the temperature distribution on the outer side of the heating plate. Local values of the boiling heat transfer coefficient were calculated from the Robin boundary condition with the help of Trefftz functions. The results were presented as plate temperature, fluid temperature and heat transfer coefficient dependences as a function of the distance from the channel inlet (or local distribution). Example boiling curves are also illustrated. The results were analysed.

5. REFERENCES

- Piasecka M., Hożejowska S., Pawińska A., 2023. „Trefftz Functions Methods in Analysis of the Effect of Enhanced Heated Surface on FC-72 Flow Boiling in Minichannels”. *Applied Thermal Engineering*, Vol. 236, Part C, Paper Number: 121689, pp. 1-13.
- Piasecka, M., Maciejewska, B., Michalski, D., Dadas, N., Piasecki, A., 2024. “Investigations of Flow Boiling in Mini-Channels: Heat Transfer Calculations with Temperature Uncertainty Analyses”. *Energies*, Vol. 17(4), Paper Number: 791, pp. 1-33.
- Piasecka, M., Hożejowska, S., Maciejewska, B., Pawińska, A., 2021. “Time-Dependent Heat Transfer Calculations with Trefftz and Picard Methods for Flow Boiling in a Mini-Channel Heat Sink”. *Energies*, Vol. 14 (7), Paper Number: 1832, pp. 1-24.

Experimental evaluation of nozzle microfabrication methods on the sizing and dynamics of water sheet jets

Alexandros Petimeinaris^{*,a}, Priyanka Sinha^a, Julian Schmid^b, Alexandros Terzis^a

^aThermo-Fluids & Interfaces Laboratory, Faculty of Aerospace Engineering, Technion – Israel Institute of Technology, Haifa, 3200003, Israel

^bDepartment of Mechanical and Process Engineering, ETH Zurich, Sonneggstrasse 3, CH8092 Zurich, Switzerland
*alexandros@campus.technion.ac.il

Keywords: Liquid sheet jets, Microfluidic nozzle, Lithography, Etching

1. INTRODUCTION

Liquid sheet jet applications are found everywhere across the scientific spectrum; spanning from physics and biology to engineering. Liquid sheet physical foundations were set by early studies on their formation (Taylor, 1960), identification of instability mechanisms (Crapper et al., 1975; Squire, 1953) and comprehension of liquid sheet disintegration and atomization (Dombrowski & Fraser, 1954; Ibrahim & Przekwas, 1991; Ryan et al., 1995). However, nowadays liquid sheets are employed in applied studies performing various forms of spectroscopy (Buttersack et al., 2023; Ekimova et al., 2015; Kondoh & Tsubouchi, 2014). Furthermore, liquid sheets serve as wall-free continuous reactors. In engineering applications, they are exploited for their superior fluid-mixing abilities. They enable the control of micro-mixing scales of reacting fluids and the precise selection of the induced reactions in liquid propellant rocket engines, while in bioengineering studies they are utilized to understand the kinetics of folding proteins (Erni & Elabbadi, 2013; Hertzog et al., 2006).

The primarily established method to produce liquid sheets demands two identical and coplanar jets to collide at an oblique angle (Bremond & Villermaux, 2006; Bush & Hasha, 2004). Drawbacks of this experimental setup that have been reported, as minor asymmetrical mispositioning of the jets obstructs the acquisition of the desired liquid sheet structures (Jung et al., 2010), while the fixed design of the jet discharging probes reduces the testing flexibility. Recently, however, an alternative approach implementing a convergent nozzle channel in a microfluidic device has emerged, due to the operational simplicity and quick model production (Ha et al., 2018). The latter design consists of two glass layers which are separated by a thin Kapton polyimide layer, incorporating the nozzle geometry. Alternatively, other studies have opted to use lithographic techniques and engrave the nozzle geometries on glass wafers through etching to generate liquid sheet jets (Crissman et al., 2022; Hoffman et al., 2022).

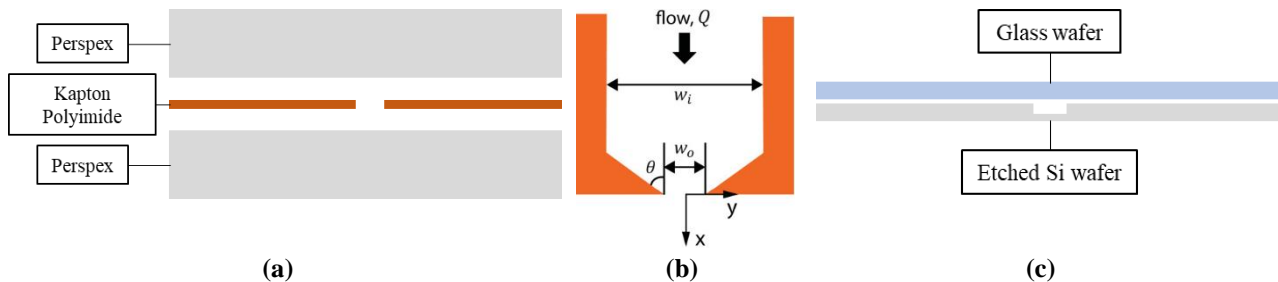


Figure 1. (a) Front view of the vertically stacked Perspex and polyimide nozzle configuration (b) Description of nozzle geometry and its respective parameters as per (Ha et al., 2018) & (c) Front view of the chip with an etched nozzle geometry on the Silicon wafer using lithographic methods (Deep Reactive-Ion Etching, DRIE)

This study aims to compare fabrication approaches of the microfluidic chips and phenomenologically evaluate the structure and stability of water sheets. Herein, as it is illustrated in Figure 1a, a microfluidic device resembling Ha et al. (2018) is reduced to a thick three-layer chip consisting only of Perspex and Kapton polyimide layers. It is, then, compared to a millimeter-thin chip of bonded Si and glass wafers containing an engraved nozzle using deep reactive-ion etching (DRIE), as shown in Figure 1c. Shadowgraph imaging is applied to demonstrate the size changes of water sheets when the nozzle convergent angle θ , channel's depth d and outlet width w_o are varied along with the flow rate Q , as they are schematically explained in Figure 1b.

2. RESULTS & DISCUSSION

Figure 2 qualitatively demonstrates the size variation of the liquid sheet's primary link for a converging nozzle of $2\theta=120^\circ$ nozzle angle. The increase of the flowrate -in the range of 50 to 250 ml/min- results in a gradual increase of the length and the width of the liquid sheet. At 50 ml/min, apart from the primary link, another smaller liquid sheet is formed perpendicular to the imaging plane, before it coalesces into vertically impinging droplets. Simultaneously with the size

increase, higher flow rates alter the liquid sheet structure. At 100 and 150 ml/min the liquid sheet is composed of a single link before it breaks down to a column of droplets. Early signs of fragmentation become visible in this range, as semi-detached droplets appear on liquid sheet rims. Further flow rate increase moves the onset of these instabilities closer to the generating apex of the liquid sheet. Consequently, before the rims of the primary link merge downstream, instabilities have propagated inside the liquid sheet leading to its breakup.

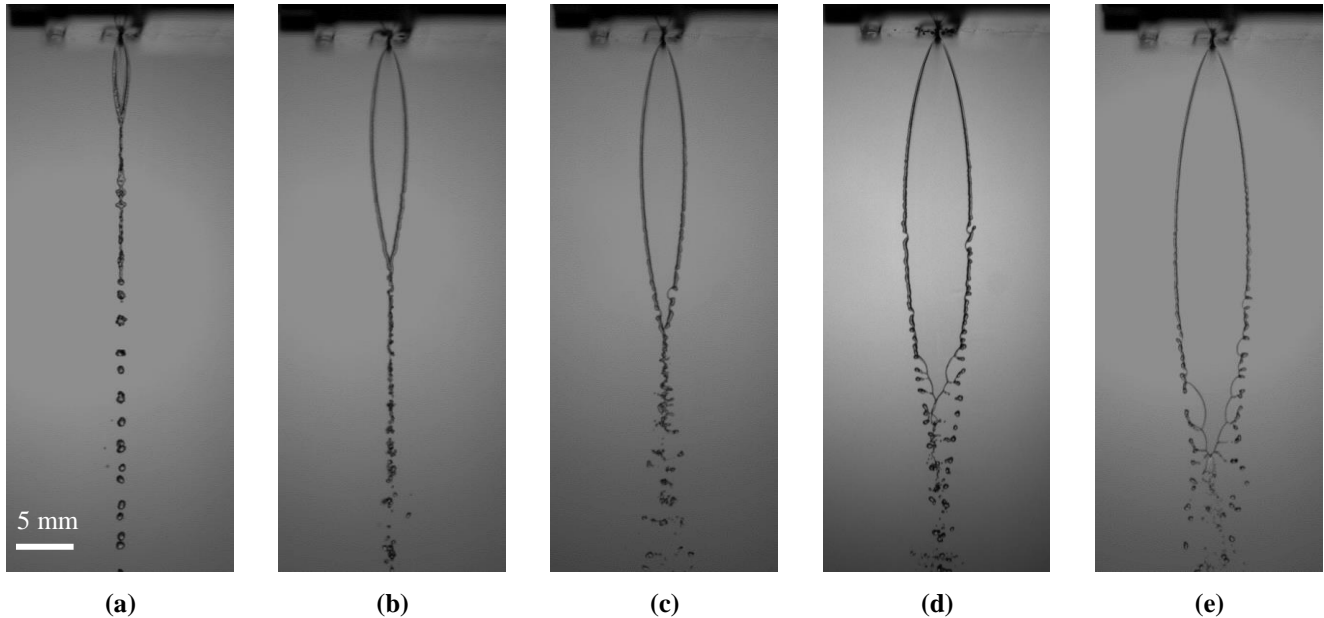


Figure 2. Primary liquid sheet link size variation with increasing flowrates of: (a) 50 ml/min, (b) 100 ml/min, (c) 150 ml/min, (d) 200 ml/min & (e) 250 ml/min of a $2\theta=120^\circ$ convergent nozzle angle.

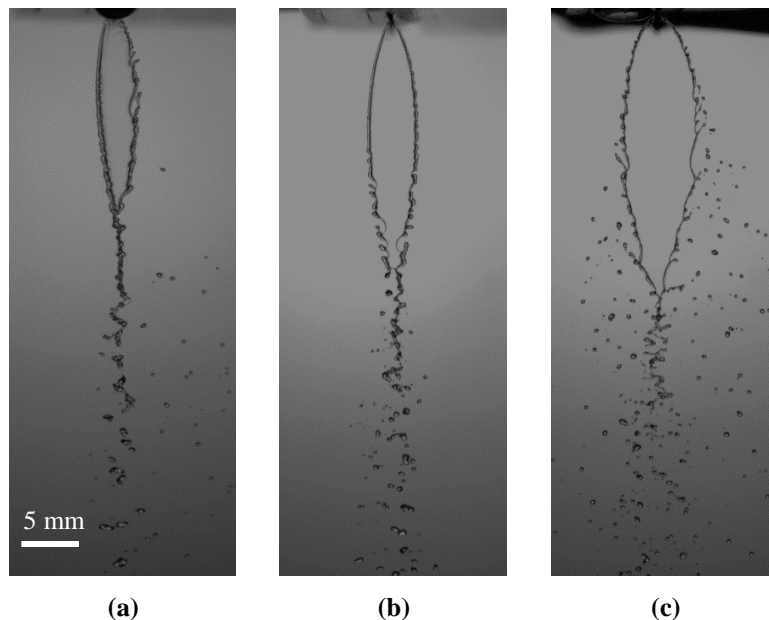


Figure 3. Primary liquid sheet link size variation with increasing convergent nozzle angle of (a) $2\theta=120^\circ$, (b) $2\theta=120^\circ$ & (c) $2\theta=120^\circ$ at a 150 ml/min flow rate.

The disintegration of the liquid sheet is also promoted by geometrical variations, as it is indicated in the images of Figure 3. By maintaining constant flow conditions and varying the nozzle geometry of the chip, the influence of the nozzle angle is evaluated. Alongside a small upsizing of the liquid sheet, the increase in the nozzle angle augments the lateral over the axial momentum component leading to a profound increase of the liquid sheet width. Furthermore, the onset of shedding droplets is detected closer to the liquid sheet origin. This is particularly evident in Figure 3c. Consequently, higher nozzle angles also promote the liquid sheet disintegration, as lateral momentum exceed curvature forces which cause the rims to retract, eventually leading to droplet detachment and the generation of a two-dimensional spray close to the nozzle outlet.

3. CONCLUSIONS

This study emphasizes on presenting two fabrication approaches for convergent micronozzles which are used for the generation of water sheet jets. Both the influence of the manufacturing methods on the sheet jet production and the effect of geometrical attributes and flow conditions variations on the liquid sheet sizing are investigated. The results reveal that the length of the liquid sheet is primarily affected by the flow rate variation. The width increase is also strongly influenced by the geometrical features of the convergent nozzle which are also found to control the stability of the liquid sheet.

Under identical conditions, the fabrication method can result in minor differences on the produced water sheet jets. The bonded wafers with the etched nozzle geometry deliver more consistently symmetrical water sheets. This superior performance arises from the precise wafer alignment before bonding and the accurate outlet edge dicing, while the laser-cut polyimide nozzles comparatively lack slightly in dimensional accuracy and demand more extensive preparation of the outlet surface.

4. REFERENCES

- Bremond, N., & Villermaux, E. (2006). Atomization by jet impact. *Journal of Fluid Mechanics*, 549, 273–306. <https://doi.org/10.1017/S0022112005007962>
- Bush, J. W. M., & Hasha, A. E. (2004). On the collision of laminar jets: Fluid chains and fishbones. *Journal of Fluid Mechanics*, 511, 285–310. <https://doi.org/10.1017/S002211200400967X>
- Buttersack, T., Haak, H., Malerz, S., Seidel, R., Hergenbahn, U., Meijer, G., Thürmer, S., Winter, B., Buttersack, T., Haak, H., Malerz, S., Schewe, H. C., Trinter, F., Mudryk, K., Pugini, M., & Credidio, B. (2023). Photoelectron spectroscopy from a liquid flatjet. *The Journal of Chemical Physics*, 158. <https://doi.org/10.1063/5.0155182>
- Crapper, G. D., Dombrowski, N., & Pyott, G. A. D. (1975). Large Amplitude Kelvin-Helmholtz Waves on Thin Liquid Sheets. *Proceedings of the Royal Society of London. Series A, Mathematical and Physical Sciences*, 342, 209–224. <https://doi.org/10.1098/rspa.1975.0021>
- Crissman, C. J., Mo, M., Chen, Z., Yang, J., Huyke, D. A., Glenzer, S. H., Ledbetter, K., F. Nunes, J. P., Ng, M. L., Wang, H., Shen, X., Wang, X., & DePonte, D. P. (2022). Sub-micron thick liquid sheets produced by isotropically etched glass nozzles. *Lab on a Chip*, 22(7), 1365–1373. <https://doi.org/10.1039/d1lc00757b>
- Dombrowski, N., & Fraser, R. P. (1954). A photographic investigation into the disintegration of liquid sheets. *Philosophical Transactions of the Royal Society of London*, 247(924), 101–130.
- Ekimova, M., Quevedo, W., Faube, M., Wernet, P., & Nibbering, E. T. J. (2015). A liquid flatjet system for solution phase soft-x-ray spectroscopy. *Structural Dynamics*, 2(5). <https://doi.org/10.1063/1.4928715>
- Erni, P., & Elabbadi, A. (2013). Free impinging jet microreactors: Controlling reactive flows via surface tension and fluid viscoelasticity. *Langmuir*, 29(25), 7812–7824. <https://doi.org/10.1021/la401017z>
- Ha, B., DePonte, D. P., & Santiago, J. G. (2018). Device design and flow scaling for liquid sheet jets. *Physical Review Fluids*, 3(11), 1–14. <https://doi.org/10.1103/PhysRevFluids.3.114202>
- Hertzog, D. E., Ivorra, B., Mohammadi, B., Bakajin, O., & Santiago, J. G. (2006). Optimization of a microfluidic mixer for studying protein folding kinetics. *Analytical Chemistry*, 78(13), 4299–4306. <https://doi.org/10.1021/ac051903j>
- Hoffman, D. J., Van Driel, T. B., Kroll, T., Crissman, C. J., Ryland, E. S., Nelson, K. J., Cordones, A. A., Koralek, J. D., & DePonte, D. P. (2022). Microfluidic liquid sheets as large-area targets for high repetition XFELs. *Frontiers in Molecular Biosciences*, 9(December), 1–15. <https://doi.org/10.3389/fmolb.2022.1048932>
- Ibrahim, E. A., & Przekwas, A. J. (1991). Impinging jets atomization. *Physics of Fluids A*, 3(12), 2981–2987. <https://doi.org/10.1063/1.857840>
- Jung, S., Hoath, S. D., Martin, G. D., & Hutchings, I. M. (2010). Atomization patterns produced by the oblique collision of two Newtonian liquid jets. *Physics of Fluids*, 22(4), 1–10. <https://doi.org/10.1063/1.3373513>
- Kondoh, M., & Tsubouchi, M. (2014). Liquid-sheet jets for terahertz spectroscopy. *Optics Express*, 22(12), 14135. <https://doi.org/10.1364/oe.22.014135>
- Ryan, H. M., Anderson, W. E., Pal, S., & Santoro, R. J. (1995). Atomization characteristics of impinging liquid jets. *Journal of Propulsion and Power*, 11(1), 135–145. <https://doi.org/10.2514/3.23851>
- Squire, H. B. (1953). Investigation of the instability of a moving liquid film. *British Journal of Applied Physics*, 4(6), 167–169. <https://doi.org/10.1088/0508-3443/4/6/302>
- Taylor, G. (1960). Formation of thin flat sheets of water. *Mendel, Darwin, and Fisher*, 259(1931), 523–529.

Droplet Wall Interactions

Michael Ushakov, Mario Del Mastro, Alexandros Terzis

Thermo-Fluids & Interfaces Laboratory, Faculty of Aerospace Engineering

Technion – Israel Institute of Technology, Haifa 3200003, Israel

*e-mail: ush.michael@campus.technion.ac.il

Keywords: *Drop impact, thermal atomization, microstructures, lithography*

1. THEORETICAL BACKGROUND

The interaction of droplets with surfaces exhibiting different wettability, and under different environmental conditions plays a crucial role across a broad spectrum of engineering applications. These range from spray cooling, and ink-jet printing to the creation of powders, encapsulation processes, and the dynamics of droplet-wall interactions in internal combustion engines, fuel atomization, aircraft icing/de-icing systems, as well as cooling of hypersonic leading edges.

The field of droplet dynamics has evolved significantly, driven by technological advancements that demand a deeper understanding of interface kinetics and thermodynamics at the micro-scale, alongside the development of tailored engineered surfaces for specific applications. This evolution is supported by breakthroughs in optical diagnostics at the micro-scale and micro-fabrication methods that enable precise modifications of key factors influencing the drop impact process outcomes.

Upon impact with a heated surface, a droplet can exhibit one of four distinct behaviors: *film evaporation*, *nucleate boiling*, *transition boiling*, and *film boiling* which leads to thermal atomization. Each regime possesses unique microscopic dynamic and thermodynamic characteristics that affect the outcome of the process. For drop impact on flat heated surfaces, these behaviors are mainly determined by the Weber number (We) which couples the aerodynamic drag forces with the cohesion forces associated with the surface tension as follows:

$$We = \frac{\rho u^2 D}{\sigma} \quad (1)$$

where ρ is the fluid density (kg/m^3), u is the drop velocity (m/s), D , is the droplet diameter (m) and σ is the surface tension of the droplet (N/m).

In recent years, the advancement of manufacturing techniques at the nano/micro level has led to the modification of surface properties. Nano/micro-structures in the form of circular or square pillars have been incorporated on the target surfaces to control the drop impingement process. The surface properties of a micro-structured surface can be characterized using the surface roughness factor (r) and the solid packing fraction (ϕ) defined as follows:

$$r = 1 + \frac{\pi d h}{p^2} \quad \phi = \frac{\pi d^2}{4p^2} \quad (2)$$

where h is the height of the pillars, d is the hydraulic diameter of the pillars and p is the pitch distance spacing between the centroids of two adjacent pillars.

The behavior of a droplet upon impingement varies with the surface's unique combination of r and ϕ , affecting the observed impact regimes across different Weber numbers and surface temperatures. On micro-structured surfaces with pillars, a droplet can either adopt the Wenzel state, penetrating voids between pillars for maximal liquid-surface contact, or the Cassie-Baxter state, resting at the top of the pillars without void penetration. These states are differentiated by the critical contact angle, categorizing surfaces into distinct r and ϕ regions.

2. OBJECTIVE

This study aims to explore how various combinations of droplet diameter (D), pillar height (h), diameter (d), and spacing (p) - leading to identical roughness (r/D) and packing fraction (ϕ/D) factor ratios - influence droplet behavior upon impact on a superheated surface. We present diverse phase maps illustrating outcomes when experimental surfaces result in either the Wenzel or Cassie-Baxter states, with one surface showcasing behavior in a transitional zone between these states. The physical size of droplet diameter (D), varying between 0.5 mm to 3 mm is also examined. Moreover, achieving very high Weber numbers (>1500) and surfaces temperature far above the Leidenfrost point (~ 500 °C), is a pivotal aspect of our research, facilitated through the use of an advanced newly designed drop impact vertical tunnel.

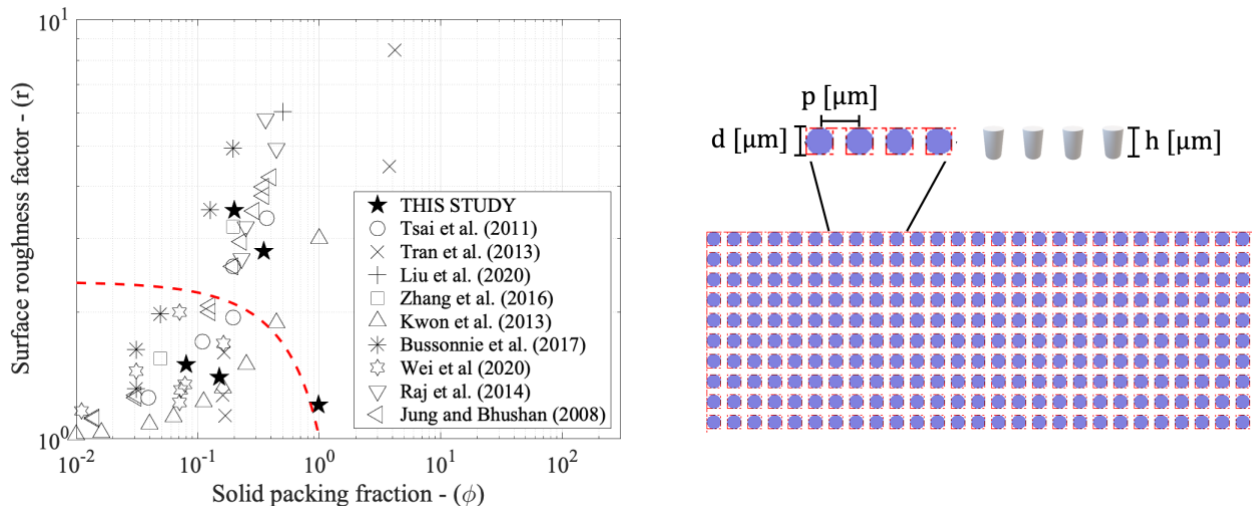


Figure 1 (left) Solid packing fraction and roughness factor used in existing literature. (right) Micro-structured schematic design used in this study.

3. EXPERIMENTAL METHODS

The tailored engineered surfaces used in this study were produced using standard lithography techniques on the surface of 2-inch silicon wafers. This process typically involves several key steps. First, the surface of the silicon wafers is coated with a photoresist material where the thickness of this layer can be precisely controlled to influence the height of the resulting micro-pillars. A mask with the desired pattern of micro-pillars is then placed directly in contact with the photoresist-coated substrate. The assembly is then exposed to ultraviolet (UV) light and the areas of photoresist exposed to the light undergo chemical changes, while the areas shielded by the opaque parts of the mask remain unchanged. After exposure, the substrate is treated with a developer solution. The development process reveals a pattern that matches the mask, with the remaining photoresist forming the structure of the micro-pillars. In this study, the photoresist itself is not the desired material for the micro-pillars, hence, an etching process was then employed. This was done through a reactive ion etching (RIE) technique, which uses plasma to selectively remove substrate material.

The region of engineered surface on the 2-inch silicon wafers consisted of a $35 \times 35 \text{ mm}^2$ rectangle area in the center of the wafer, which is approximately 57% of the region of the wafer and at least 15 times larger than the droplet maximum diameter used in this study ($\sim 3 \text{ mm}$). Table 1 summarizes the physical dimensions of pillar height (h), diameter (d), and spacing (p) used in this study to achieve the same $r = 1.2$ and $\phi = 0.98$.

h [μm]	d [μm]	p [μm]
0.3	2	3
5.0	5	20
40.0	10	80

Table 1 Summary of micro-pillar dimensions used in the present study.

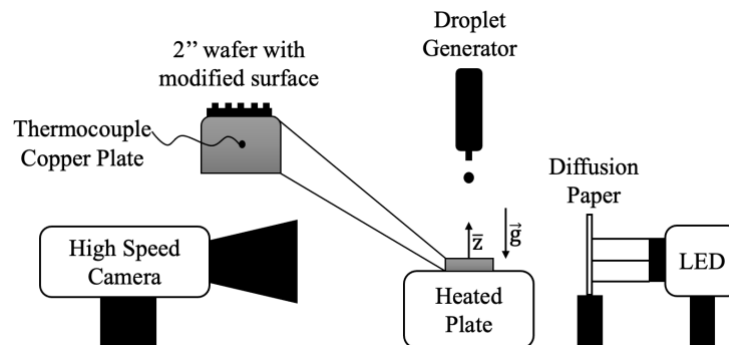


Figure 2 Schematic representation of the experimental setup

High-speed shadowgraph experiments were designed to investigate the effects of droplet impacts on heated engineered surfaces. Figure 2 shows a schematic representation of the experimental setup. The experiments utilized a high-speed

camera (Mini UX100, Photron) paired with a high-intensity LED light source (GS Vitec QX) and a GX8 controller, which were aligned opposite each other. A diffusion paper was placed in between in order to provide uniform illumination of the drop impact region. To heat the silicon wafers to the desired temperature, a constant temperature plate capable of reaching up to 550 °C was employed (SCI550-Pro). This heating setup ensures the surface temperature exceeds the Leidenfrost point for water droplets. Droplet generation was achieved using a peristaltic pump (PP-XLE-1600) operating with deionized water that offers a wide range of flow rates, from 0.006 to 1690 mL/min. By employing hydrophobic PTFE needles of varying gauges (18-30 size), droplets of different sizes were produced (0.8 to 3 mm). Various Weber numbers were explored by adjusting the height of the droplet generator mounted on an aluminum rail, ranging from 0.3 to 1.8 meters from the target surface. To prevent unwanted air currents from affecting the droplets' fall, an acrylic tube was used to encapsulate the droplet's path, effectively creating an isolated vertical tunnel for the droplets.

4. RESULTS

Figure 3 shows an example of drop impact on a flat heated SI surface. The droplet placed on the sample measures 2 mm in diameter and falls from a height of 1 m, resulting in a Weber number (We) of 550. This, coupled with a surface temperature of 300°C, leads to a droplet thermal atomization regime, wherein the droplet disintegrates into numerous smaller droplets that evaporate rapidly due to the high temperature and kinetic energy. This experiment is part of a series conducted to develop a comprehensive droplet impact phase map for any tested surface. Through the maps and data collected from these experiments, an analysis is performed, and conclusions are drawn regarding the varying effects of the pillar properties on the droplet impact regimes upon contact with a hot wall.

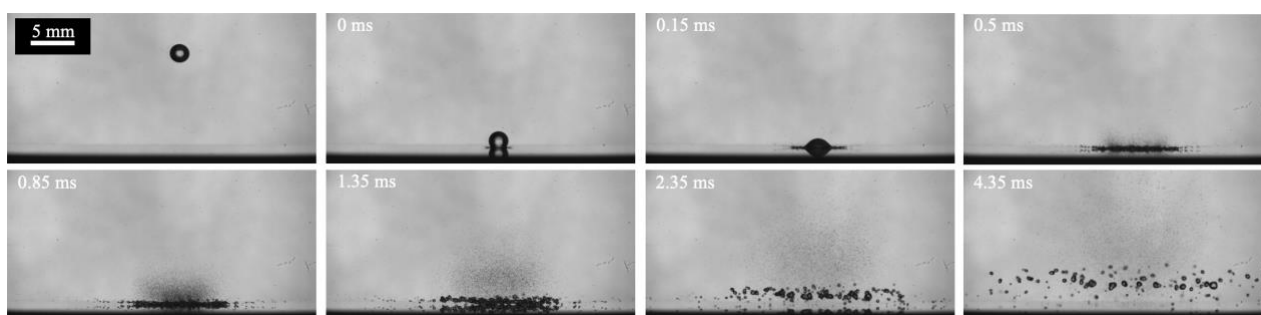


Figure 3 Drop impact on a flat silicone surface heated to 300°C

5. REFERENCES

- Bussonnière, A. *et al.* (2016) “Universal wetting transition of an evaporating water droplet on hydrophobic micro- and nano-structures,” *Soft Matter*, 13(5), pp. 978–984.
- Jung, Y.C. and Bhushan, B. (2008) “Wetting behavior during evaporation and condensation of water microdroplets on superhydrophobic patterned surfaces,” *Journal of Microscopy*, 229(1), pp. 127–140.
- Kwon, H. *et al.* (2013) “Increasing Leidenfrost point using micro-nano hierarchical surface structures,” *Applied Physics Letters*, 103(20), p. 201601.
- Liu, L., Cai, G. and Tsai, P.A. (2020) “Drop Impact on Heated Nanostructures,” *Langmuir*, 36(34), pp. 10051–10060.
- Raj, R. *et al.* (2014) “High-resolution liquid patterns via three-dimensional droplet shape control,” *Nature Communications*, 5(1), p. 4975.
- Tran, T. *et al.* (2013) “Droplet impact on superheated micro-structured surfaces,” *Soft Matter*, 9(12), pp. 3272–3282.
- Tsai, P. *et al.* (2011) “Microscopic structure influencing macroscopic splash at high Weber number,” *Soft Matter*, 7(24), pp. 11325–11333.
- Wei, M. *et al.* (2020) “Heat transfer suppression by suspended droplets on micro-structured surfaces,” *Applied Physics Letters*, 116(23), p. 233703.
- Zhang, W. *et al.* (2016) “Droplet impact behavior on heated micro-patterned surfaces,” *Journal of Applied Physics*, 119(11), p. 114901.

TWO-PHASE FLOW IN A CENTRIFUGAL ROTOR USING PARTICLE IMAGE VELOCIMETRY

Ofuchi, E. M., Stel, H., Mancilla, E., and Morales R.E.M.

Multiphase Flow Research Center – NUEM, Graduate Program in Mechanical and Materials Engineering – PPGEM, Federal University of Technology of Paraná, Curitiba, PR, Brazil

edgarofuchi@alunos.utfpr.edu.br

Keywords: centrifugal pump, two-phase flow, PIV, turbulence enhancement, turbulence suppression

1. INTRODUCTION

Centrifugal pumps have been the subject of extensive research regarding their behavior under two-phase flow conditions. One notable challenge associated with two-phase flow in centrifugal pumps is the performance degradation induced by the presence of gas. This degradation manifests as a sudden drop in the pump's pressure rise, commonly referred to as the “surging” phenomenon. During surging, the pump's ability to efficiently handle the two-phase mixture is severely compromised (Lea and Bearden, 1982).

The literature has presented numerous factors that contribute to this performance decline. These include gas and liquid flow rates, pump geometry, liquid viscosity, surface tension, and rotational speed (Duran and Prado, 2003; Gamboa and Prado, 2012; Monte Verde et al., 2017; Murakami and Minemura, 1974; Trevisan and Prado, 2011). Visualization techniques have been employed to examine the flow patterns within the pump channels to gain further insights (Cubas et al., 2020; Gamboa and Prado, 2010; Monte Verde et al., 2017). For example, Cubas et al. (2020) demonstrated that the formation of gas pockets within these channels directly correlates with the occurrence of surging.

Previous investigations have primarily focused on understanding the impact of the gas phase on overall pump performance. However, the specific interactions between the gas phase and the liquid flow field remain an open question. Computational Fluid Dynamics (CFD) has been employed to analyze the liquid flow field (Stel et al., 2020). Nevertheless, these simulations rely on interfacial models to calculate the interaction between liquid and gas phases, which are typically derived from studies of two-phase flows in pipes.

This work presents an experimental study on two-phase flow in a centrifugal rotor through Particle Image Velocimetry (PIV). The study was performed using two capillary banks that promote bubbles of different sizes. This work aims to understand better how the bubbles affect the liquid velocity, turbulent kinetic energy (TKE), and Reynolds shear stress (RSS).

2. EXPERIMENTAL SETUP

The experiments were carried out in the Multiphase Flow Research Center (NUEM) facilities. Figure 1 shows the schematics of the test section (a), a picture of the experimental loop (b), and bubbles from the visualization section in the intake pipe (c).

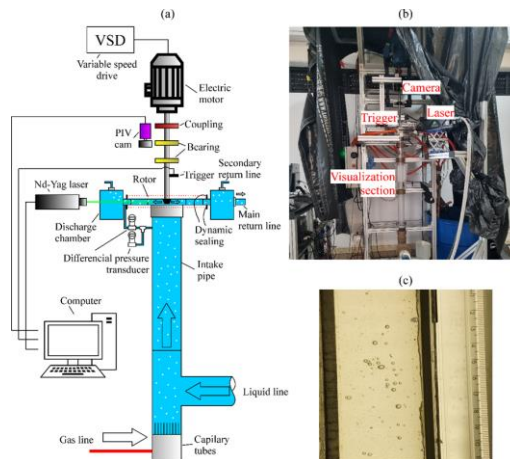


Figure 1. Schematics of the test section (a), picture of the experimental loop (b), and bubbles from the visualization section in the intake pipe (c).

Gas bubbles are generated through the capillary bank located below the intake pipe. They mix with water and are carried to the rotor test where PIV measurements are performed using the phase-locking technique. The two-phase flow mixture is collected in the discharge chamber and returned to the water tank through the main and secondary return lines.

In this study, fluorescent tracer particles were employed to investigate the behavior of fluid flow. When combined with a high-pass filter, these tracer particles effectively mitigate the impact of light scattering caused by the presence of bubbles. A double-frame approach was used to calculate the liquid velocity through cross-correlation. The presence of bubbles in PIV images was effectively mitigated using an algorithm designed to exclude their influence from the velocity calculation. Moreover, bubble size distribution was extracted from the intake pipe and PIV images.

The experiments were carried out at a rotating speed of 300 rpm, different intake liquid and gas flow rates, and using two capillary banks, namely C1 and C2.

3. RESULTS

The two-phase flow experiments were performed for low gas flow rates due to experimental setup limitations regarding the gas pocket formation. It was observed that single and two-phase flow presented similar liquid flow fields. Therefore, the difference between single and two-phase flow fields was performed as:

$$\phi_{dif}(x, y) = \frac{\phi_{TP}(x, y) - \phi_{SP}(x, y)}{U_2} \quad (1)$$

where, ϕ can be the velocity (W), the turbulent kinetic energy (\sqrt{k}) or the Reynolds shear stress ($\sqrt{u'v'}$).

Figure 2 shows the contours of several variables on a midspan plane for cases tested at 300 rpm rotating speed, 0.75·QBEP flow rate, 0.030 l/min intake gas flow rate ($\gamma = 0.065$), and capillaries C1 and C2. In (a) and (b), the average gas volume fractions for two-phase flow tests with capillaries C1 and C2, respectively, are shown. The corresponding single-phase flow fields of velocity, turbulence kinetic energy, and Reynolds shear stress are shown in (c), (f), and (i), while the corresponding flow fields obtained by calculating the difference between the variables measured for single and two-phase flow are shown in (d), (g) and (j) for C1 and in (e), (h) and (k) for C2.

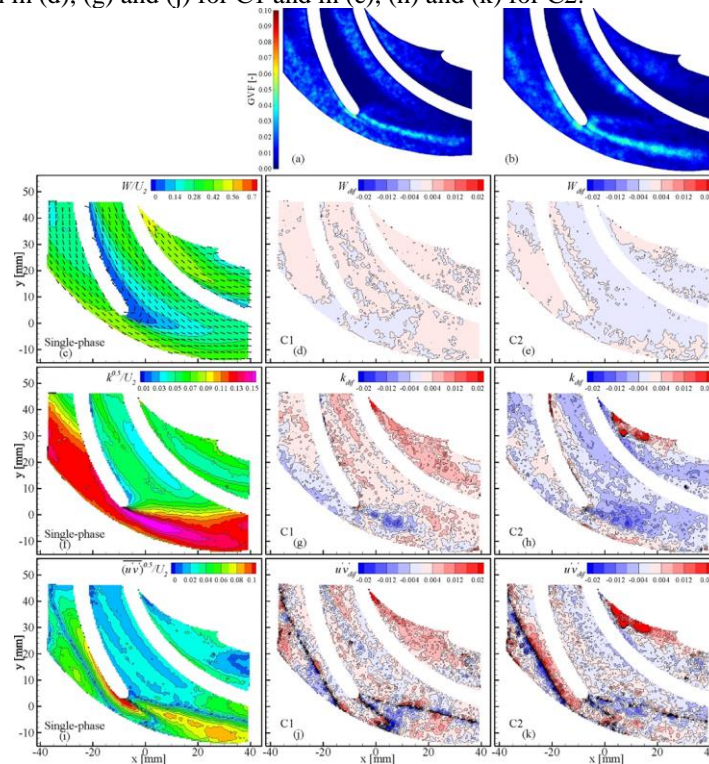


Figure 2. Contours of several variables on a midspan plane for cases tested at 300 rpm rotating speed, 0.75· Q_{BEP} liquid flow rate, 0.03 l/min intake gas flow rate and two capillary banks: average gas volume fraction for a two-phase flow test (a) using C1, (b) using C2; (c), (f), and (i): dimensionless velocity, turbulence intensity and dimensionless RSS fields for single-phase flow; (d), (g), and (j): corresponding contours obtained by calculating the difference between the variables measured for single and two-phase flows using C1; (e), (h), and (k): corresponding contours obtained by calculating the difference between the variables measured for single and two-phase flows using C2.

It can be observed that, in general, the flow fields of all variables are somehow affected by the capillary used as the gas injection system. As for the volume fraction, it can be observed a lack of bubbles behind the blade suction side occurs

for both C1 and C2 cases owing to higher liquid velocity near the blade pressure side. Regarding the single-phase to two-phase velocity differences, the velocity difference has mainly increased for C1, while it reduced for C2. Conversely, using C1 caused an increase in the turbulence kinetic energy and the Reynolds shear stress levels compared to the single-phase case, while a significant decrease was observed for the case with C2, especially on TKE. These two distinct behaviors are believed to be related to the bubbles suppressing the velocity fluctuations. The increased diameter from the C2 case could reduce further the turbulence owing to the larger surface area where the turbulence is suppressed.

4. CONCLUSIONS

This investigation presents a comprehensive two-phase flow study focusing on the gas phase's influence on the liquid flow field. The liquid flow field for single-phase and two-phase flows was characterized by utilizing particle image velocimetry (PIV). The results demonstrate that the presence of the gas phase significantly impacts the liquid flow field, particularly in terms of turbulent variables. Furthermore, alterations in the capillary bank configuration lead to either an augmentation or reduction of turbulent kinetic energy and Reynolds shear stress.

5. REFERENCES

- Cubas, J.M.C., Stel, H., Ofuchi, E.M., Marcelino Neto, M.A., Morales, R.E.M., 2020. Visualization of two-phase gas-liquid flow in a radial centrifugal pump with a vaned diffuser. *J Pet Sci Eng* 187, 106848. <https://doi.org/10.1016/j.petrol.2019.106848>
- Duran, J., Prado, M., 2003. ESP Stages Air-Water Two-Phase Performance-Modeling and Experimental Data. *SPE Journal* 13.
- Gamboa, J., Prado, M., 2012. Experimental study of two-phase performance of an electric-submersible-pump stage. *SPE Production and Operations* 27, 414–421. <https://doi.org/10.2118/163048-PA>
- Gamboa, J., Prado, M.G., 2010. Visualization Study of Performance Breakdown in Two-Phase Performance of an Electrical Submersible Pump. *Proceedings of the Twenty-Sixth International Pump Users Symposium*.
- Lea, J.F., Bearden, J.L., 1982. Effect of Gaseous Fluids on Submersible Pump Performance. *JPT, Journal of Petroleum Technology* 34, 2922–2930. <https://doi.org/10.2118/9218-PA>
- Monte Verde, W., Biazussi, J.L., Sassim, N.A., Bannwart, A.C., 2017. Experimental study of gas-liquid two-phase flow patterns within centrifugal pumps impellers. *Exp Therm Fluid Sci* 85, 37–51. <https://doi.org/10.1016/j.expthermflusci.2017.02.019>
- Murakami, M., Minemura, K., 1974. Effects of Entrained Air on the Performance of Centrifugal Pumps : 2nd Report, Effects of number of blades. *Bulletin of JSME* 17, 1286–1295. <https://doi.org/10.1299/jsme1958.17.1286>
- Stel, H., Ofuchi, E.M., Chiva, S., Morales, R.E.M., 2020. Numerical simulation of gas-liquid flows in a centrifugal rotor. *Chem Eng Sci* 221, 115692. <https://doi.org/10.1016/j.ces.2020.115692>
- Trevisan, F., Prado, M., 2011. Experimental investigation of the viscous effect on two-phase-flow patterns and hydraulic performance of electrical submersible pumps. *Journal of Canadian Petroleum Technology* 50, 45–52. <https://doi.org/10.2118/134089-PA>

Micro-PIV measurements in a free flow and porous medium coupled system: Effects of Reynolds number and porosity

Mario Del Mastro*, Alexandros Terzis

Thermo-Fluids & Interfaces Laboratory, Faculty of Aerospace Engineering
Technion – Israel Institute of Technology, Haifa, Israel

*mario.del@campus.technion.ac.il

Keywords: Transport in porous media, micro-PIV, REV-scale, interface processes.

1. DESCRIPTION OF THE PROBLEM

Transport phenomena in porous media are ubiquitous across nature, industry, and over widely disparate length scales. Drug delivery, point-of-care diagnostics, groundwater remediation, soil water evaporation, fuel cells, and CO_2 capture are just some examples in our daily lives. Nevertheless, the determination of the transport process for such complex systems remains a challenge. An intricate example is encountered across the interface of a free-flow and porous-medium coupled systems, as depicted in Figure 1.1. In these systems, the exchange of mass and energy is contingent upon the fluid-fluid interfaces, and on top of the porous medium a boundary layer forms, implicating the diffusion of mass and energy, as well as advection. The use of the Navier-Stokes equations over the entire domain to resolve all fine-scale heterogeneities is infeasible for practical applications due to the computational cost of the problem. On the other hand, pore-scale effects, which may globally affect the exchange fluxes, cannot be resolved on the REV scale. Further, processes at the free flow level are highly dynamic and occur on much smaller time scales than processes in the porous domain. The quantification of mass, momentum and energy transport at the interface is thus a challenging task that depends on appropriate coupling conditions between two distinct regions.

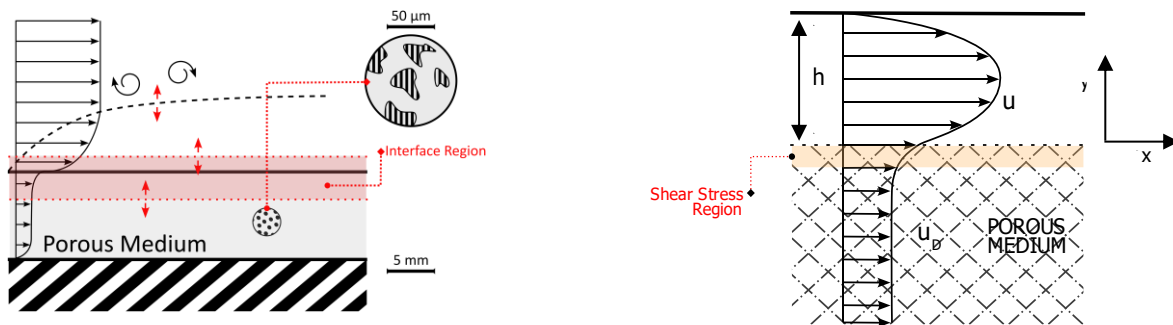


Figure 1.1: (Left) Free flow and porous-media coupled system: Representative Elementary Volume (REV) visualization. Average interface and exchange processes. (Right) Expected axial velocity profile on REV scale.

2. OBJECTIVE

The main objective of this work is to experimentally study the complex dynamics of the interface in the free-flow and micro-porous media coupled system depicted in Figure 1.1. The system is characterized by the isothermal flow condition and the exclusive employment of a single component fluid, flowing in the streamwise direction. The porous medium, with its intricate network of pores, presents a unique set of flow that significantly affect the overall system behaviour. The velocity field is influenced by a wide range of parameters, including the Reynolds number, the porosity, the tortuosity, the geometry of the pores, the shape of the interface, and the ratio between the height of the free-flow channel and the height of the porous material. Among these parameters, the focus has been directed towards examining the impact of the Reynolds number and the porosity, while maintaining constancy across other geometric and fluid parameters. By varying the Reynolds number and the porosity of the material, this study aims to elucidate their effects on the micro scale and how their repercussions at the REV scale.

The novelty of this study lies in the innovative examination of the problem at the micrometric scale by mean of Micro-PIV technique, resolving the velocity field on a very high measurement resolution, i.e. 5.2 [$\mu\text{m}/\text{vector}$]. Additionally, this investigation encompasses a detailed discussion on the model fabrication methods, along with a comprehensive discussion on the necessary precautions for ensuring proper functionality, as will be delineated in the methods section. This approach not only marks a significant advancement in the experimental investigation of micro-scale fluid dynamics but also contributes to the refinement of fabrication techniques for microfluidic devices, thereby paving the way for enhanced precision and control in the manipulation of fluid flows at microscopic levels.

3. METHODOLOGY

The experimental tasks are carried out using micromodels fabricated with combined photolithography and soft lithography techniques. First, the voids of the porous domain were photolithographically formed in bas-relief, and then, the resulting master mould used as a template for the replica moulding of polydimethylsiloxane PDMS microfluidic models. In very general terms, the process involves laser-printing a pre-designed geometric pattern onto a photomask, which is then transferred to a photoresist layer spin-coated to a clean silicon wafer. Following a soft-baking phase, the photoresist is exposed to UV, creating a pattern that serves as a mold for fabricating PDMS models via soft lithography. The PDMS, mixed with a curing agent, is poured over the mold and then baked to facilitate polymer cross-linking, resulting in the formation of the micromodel.

The steady state velocity flow is measured by mean of micro-PIV, with particular emphasis placed on the interface region between the free-flow and the porous medium. Micro-PIV presents several challenges, including visualizing tracer particles smaller than the wavelength of light, minimizing errors caused by the Brownian motion of tracer particles, and capturing particle images with short exposure times to prevent particle streaking in the image field. To achieve spatial resolution on the micron scale, careful selection of particles was necessary to ensure they were of an appropriate size, i.e the maximum particle diameter was chosen to stay smaller than 3 pixels, to correctly track the flow without clogging the device or generating additional uncertainties during the measurements. Additionally, these particles must be large enough to scatter sufficient light for detection, reduce Brownian motion, and avoid adhesion to surfaces due to the dominating surface forces present at this scale. For this purposes the selected particles were the 860 [nm] diameter particles.

The setup system used for this study and the schematic representation of the micromodel are shown in Figure 3.1. The study involves the use of three different models having different porosities. The reference frame of each micro-model is fixed, i.e. the height of the free channel of the porous material are fixed as well as the the pillar edge is fixed at 100 [μm]. Different porosities are achieved altering the spacing of the pillars from 50 [μm] to 150 [μm] to cover the porosities: 55%, 75% and 83%. Complete saturation of the micromodel was achieved by removing air from the model by CO_2 rinsing, at controlled pressures, and subsequently filled with water and properly sealed to prevent air from re-entering the model through the in and out ports.

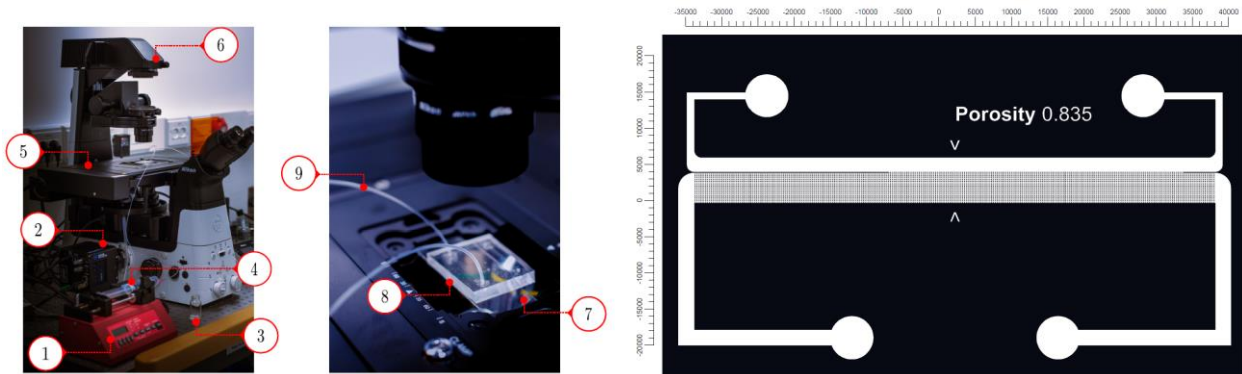


Figure 3.1: (Left) An illustrative schematic representation of the experimental set-up. It consists of the following elements: (1) Syringe pump, (2) Back-illuminated Kinetix Scientific CMOS (sCMOS) camera, (3) Discharge reservoir, (4) Injection reservoir, (5) Stage, (6) Nikon Eclipse Ti2 Series inverted microscope, (7) Objectives, (8) Micromodel, and (9) Micro-tubes. (Right) The Micro model designed for porosity 83.5%.

4. SAMPLE OF RESULTS & CONCLUSIONS

The flow field was evaluated for the three different models at three distinct volumetric flow rates: 10 [$\mu\text{L}/\text{min}$], 20 [$\mu\text{L}/\text{min}$], and 30 [$\mu\text{L}/\text{min}$] that respectively correspond to Reynolds 0.16, 0.31 and 0.47. Following the measurements, a statistical convergence analysis was conducted on selected points within the domain to ascertain the number of images required per ROI to achieve results with low uncertainty values. Subsequently, an analysis of the measurement errors was undertaken. These errors remained stable and were found limited in the free-flow region and slightly higher in the porous region. The uncertainties were calculated using the Steele and Coleman method. Once the repeatability and reliability of the results were confirmed, the study progressed from a micrometric scale to a Representative Elementary Volume (REV) scale through averaging processes. From the REV scale, the calculation of specific problem-related parameters was undertaken, such as the Beavers and Joseph coefficient defined in the Equation (4.1) – left side, and other related parameters like the Ochoa-Tapia and Whitaker's stress jump coefficient, defined in Equation (4.1) – right side. These were compared with the values currently available in the literature to benchmark the study's findings against established data. This step not only validates the experimental approach and methodologies employed but also extend the availability of these coefficients to the micro-fluidic scale.

$$\frac{1}{\varphi} \left(\frac{\partial u}{\partial y} \right)_{y=0^+} - \frac{1}{\varphi} \left(\frac{\partial u}{\partial y} \right)_{y=0^-} = \left(\frac{\beta}{\sqrt{k}} u \right)_{y=0} ; \quad \vec{u} - \vec{u}_D = \frac{\sqrt{k}}{\alpha_{BJ}} \frac{du}{dy} \quad (4.1)$$

The study concludes with an analysis conducted on the flow at the microscopic level, which demonstrates how, with the coupled effects of porosity and Reynolds number, the transport processes between the main flow and the flow within the microporous material change drastically. This transition ranges from Stokes flow, characterized by the presence of the classical U-shaped velocity profile, to the emergence of secondary flows and vortices at the interface region and below as shown in Figure 4.1. These structures influence the velocity distribution at the interface and the boundary layer is depicted in Figure 4.1, right side. More in detail, analyzing these figures, it is possible to observe how the fluid, flowing above and below the pillars, with high momentum, generates two counter-rotating vortices, i.e. due to shear flows. Additionally, a boundary layer develops immediately above this interface, which is, in turn, influenced by the presence of these vortices. This evolution in flow behavior underscores the significant impact of porous medium geometry and Reynolds number on the dynamics of fluid interaction between the free-flow and the porous domains.

In conclusion, it can be stated that certain parameters exert a significant impact on both the microscopic and macroscopic flow fields, such as the porosity and the Reynolds number. With an increase in porosity, the penetration depth of the main flow into the porous material also rises; This parameter similarly affects the formation or not of vortical structures within the porous material, just as the Reynolds number does. Concluding, the aim of this study is to elucidate how such structures influence the dynamics of flow on a macroscale or Representative Elementary Volume (REV) scale, thereby contributing additional insights and advancing the resolution of this still open physical problem.

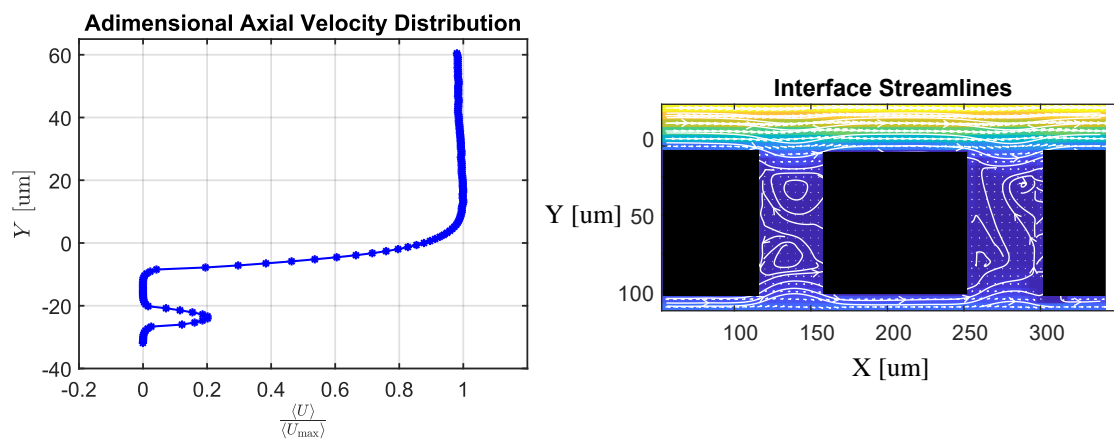


Figure 4.1: (Left) Axial Distribution of the average velocity at the interface on a macroscale or Representative Elementary Volume (REV) scale. (Right) Axial velocity field and corresponding streamlines highlight the formation of stationary vortices at the system's interface.

5. REFERENCES

- Arthur, J.K. (2019) "Experimental investigation of porous medium structural effects on a coupled porous media-free zone laminar flow," *SN Applied Sciences*, 1(9), p. 1062.
- Beavers, G.S. and Joseph, D.D. (1967) "Boundary conditions at a naturally permeable wall," *Journal of Fluid Mechanics*, 30(1), pp. 197–207.
- Ochoa-Tapia, J.A. and Whitaker, S. (1995) "Momentum transfer at the boundary between a porous medium and a homogeneous fluid—I. Theoretical development," *International Journal of Heat and Mass Transfer*, 38(14), pp. 2635–2646.
- Saffman, P.G. (1971) "On the Boundary Condition at the Surface of a Porous Medium," *Studies in Applied Mathematics*, 50(2), pp. 93–101.
- Terzis, A. et al. (2019) "Microscopic velocity field measurements inside a regular porous medium adjacent to a low Reynolds number channel flow," *Physics of Fluids*, 31(4), p. 042001.

THERMAL IMAGING OF CONDENSATION USING TEMPERATURE SENSITIVE PAINTS

Yutaku Kita*

Department of Engineering, King's College London, Strand, London WC2R 2LS, United Kingdom
International Institute for Carbon-Neutral Energy Research (WPI-I²CNER), Kyushu University, 744 Motoooka,
Nishi-ku, Fukuoka 819-0395, Japan
*yutaku.kita@kcl.ac.uk

Keywords: Condensation, Temperature sensitive paints, Thermal imaging

1. INTRODUCTION

Condensation is a fundamental process found in a variety of industrial operations including power generation, distillation, air conditioning and water harvesting and plays a crucial role in their energy efficiency. Dropwise condensation has therefore been of considerable interest due to the potential of achieving higher heat transfer coefficients than those of filmwise condensation. Although research is underway for the industrial application of dropwise condensation, numerous researchers have focused on droplet evolution and shapes, departure mechanisms and jumping phenomena without completing the task of evaluating local and transient heat transfer which should come along with the droplet behaviour (El Fil *et al.* (2020)). Understanding of such microscopic and transient nature of dropwise condensation heat transfer is paramount for the development of a comprehensive predictive model.

To the best of our knowledge, however, experimental research reporting quantitative data of transient heat transfer distributions during condensation has been limited. This is probably due to the difficulty in measuring temperature distributions on condensing surfaces using conventional techniques. While infrared (IR) thermometry has recently become popular in boiling research, its application to condensation research is generally challenging due to the optical characteristics of IR. More specifically, in condensation experiments, the backside of a condensing surface must be continuously cooled by coolant fluids. The coolant fluid, which is normally liquids and opaque to IR, blocks the emission from the surface, disabling access to the thermal information at the location of interest.

To overcome this problem, we develop a technique capable of simultaneously monitoring droplet behaviour and measuring temperature distributions on a heat transfer surface using temperature sensitive paints (TSPs). TSPs are fluorescent paints that are excited by ultraviolet (UV) light and emit light at a longer wavelength with its intensity varying depending on the temperature. As it uses visible lights, we were able to measure the surface temperature through materials that are opaque to IR with high spatial and temporal resolutions. In the present contribution, we demonstrate the feasibility of transient heat transfer measurement during condensation using TSP.

2. METHODOLOGY

In the present work, ruthenium tris (1, 10-phenanthroline) dichloride was chosen as a temperature sensitive fluorophore which has a peak emission at a wavelength of ca. 560 nm when excited by a UV irradiation. The TSP solution was prepared with 40 mg ruthenium compound and 100 mg polyacrylic acid dissolved within 0.5 mL ethanol as suggested by Al Hashimi *et al.* (2018).

As illustrated in Fig. 1 (a), the substrate for condensation experiments consisted of a titanium sheet attached to a sapphire window via an adhesive. The TSP solution was spin-coated on the bottom side (facing the adhesive) of the Ti sheet. On top of the sapphire window (facing the adhesive), TSP dots of 1 mm in diameter were deposited and then covered with a thin aluminium layer. The thickness of each layer are indicated in Fig. 1 (a). Since the thermophysical properties of the adhesive are known, the heat flux across the adhesive can be determined by solving heat equation with temperatures of the two layers probed by the TSP.

Fig. 1 (b) shows the schematic of the condensation setup. The substrate was placed vertically in the test section, separating the steam path (Ti surface side) from the coolant path (sapphire surface side). The pressure inside of the condensation chamber was reduced by a vacuum pump. The temperature of the coolant water was regulated by a chiller. Steam generated from a vacuum evaporator entered the test section and partially condensed on the Ti surface.

A UV-LED was used to illuminate the sample from the water side to excite the TSP. The emitted light from the TSP was detected by a CMOS camera. A long pass filter was placed to block any background or reflected UV light from reaching the camera. We also used another CMOS camera to capture the behaviour of condensing drops from the steam side. Both cameras captured images every 0.1 seconds, and the spatial resolutions of TSP side and surface side were 15 $\mu\text{m}/\text{pixel}$ and 25 $\mu\text{m}/\text{pixel}$, respectively.

To obtain temperature values, correlations between the temperature and the intensity of TSP emission must be known. Therefore, we took images of the TSP layer at different surface temperatures without condensation. The surface temperature was controlled by the coolant water which was allowed to flow both sides of the substrate to ensure a uniform temperature distribution. Then, we obtained correlations between the surface temperature (assumed to be identical to the water temperature) and the intensity of TSP for each pixel.

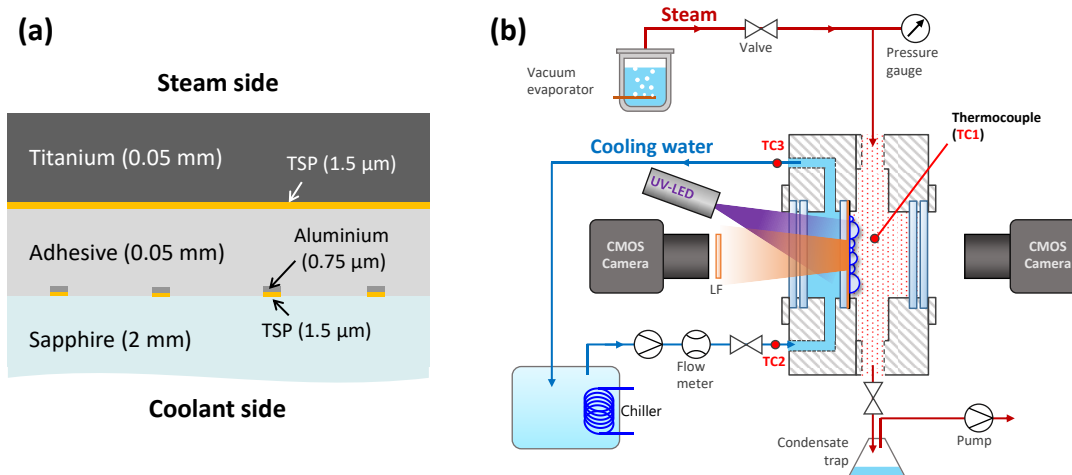


Figure 1. Schematic diagram of (a) the substrate and (b) experimental setup.

3. RESULTS

Fig. 2 presents exemplary snapshots of visual and temperature images captured in the experiments. For the presented case, the system pressure was 6.2 kPa (corresponding saturation temperature of steam was 36.9 °C). The coolant water at inlet temperature 10 °C was introduced at 6.5 L/min. The surface was coated with a hydrophobic monolayer to promote dropwise condensation.

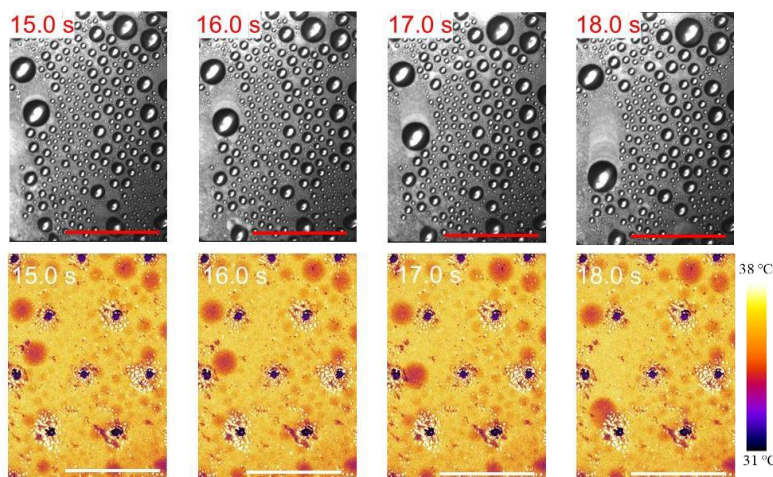


Figure 2. Snapshots of visual (upper) and temperature (bottom) images during steam condensation on a titanium surface coated with a hydrophobic monolayer. The system pressure was 6.2 kPa, and the coolant inlet water temperature and flow rate were 10 °C and 6.5 L/min, respectively. The scale bar is 10 mm.

As a result, temperature variations following droplet motion were clearly visible. A lower temperature was found in regions of large droplets due to the large thermal resistance to the heat flow from the steam. The regions of no droplet or small droplets, on the other hand, showed higher temperatures. The spatial resolution of the temperature distribution is subject to thermal diffusion within the titanium sheet as well as the TSP layer. As a result of lateral thermal diffusion within those layers, the temperature distribution indicated by the TSP should be blurred compared to the actual surface temperature distribution at the very surface. In the present experimental configuration, droplets larger than ca. 1.2 mm were distinguishable in the thermal images.

4. CONCLUSIONS

In this contribution, the potential of TSP-based local heat transfer measurement for condensation has been demonstrated. Further investigations using this technique are underway to determine, for example, the relationship between droplet size and heat flux and the conditions for the transition from dropwise to filmwise condensation.

5. REFERENCES

- Al Hashimi, H., Hammer, C.F., Lebon, T.M., Zhang, D. and Kim, J., 2018. "Phase-change heat transfer measurements using temperature-sensitive paints". *Journal of Heat Transfer*, Vol. 140, No. 3, 031601.
- El Fil, B., Kini, G. and Garimella, S., 2020. "A review of dropwise condensation: Theory, modeling, experiments, and applications". *International Journal of Heat and Mass Transfer*, Vol. 160, 120172.

STEAM EXPLOSION RETARDANT FOR MOLTEN LEAD-BISMUTH TO STABILIZE VAPOR FILM

Masahiro Furuva^{a,b,*}, Takahiro Arai^b

^a Waseda University, 3-4-1, Okubo, Shinjuku-Ku, Tokyo, 169-8555, Japan

^b Central Research Institute of Electric Power Industry (CRIEPI)
2-6-1 Nagasaka, Yokosuka, Kanagawa 240-0196, Japan

* mfuruya@waseda.jp

Keywords: Steam Explosion, Triggering, Retardant, LBE, Film Boiling Quenching, Cloud Point, Polymer

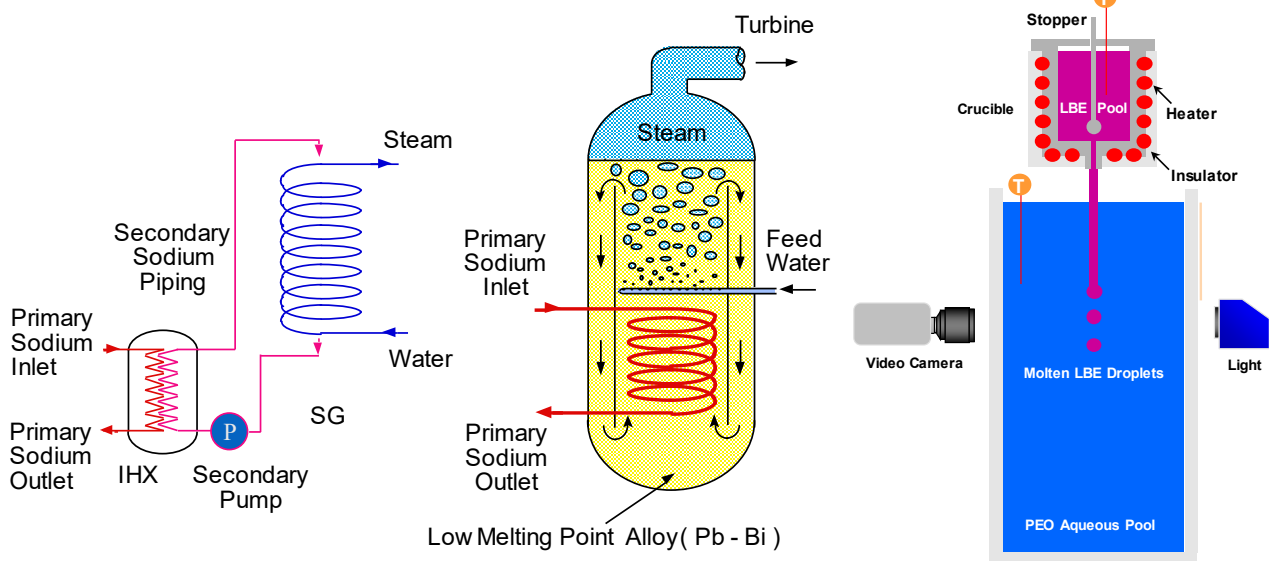
1. INTRODUCTION

Steam explosions are considered industrial disasters in many industries, including the metal and paper industries. For instance, Kinoshita *et al.* (1995) devised a direct-contact heat-transfer steam generator for a sodium-cooled fast-breeding nuclear reactor. Figure 1 illustrates the concept of injecting water into molten lead-bismuth eutectic (LBE) alloy to gain heat-transfer area and simplify the reactor cooling system by replacing the two vessels. There are many applications of LBE, such as direct contact heat transfer (Grachev *et al.*, 1999) and an LBE-cooled fast reactor (Buongiorno, 2001). Effective measures should be taken to avoid steam explosion when the molten LBE is in contact with water.

The authors have developed a steam explosion retardant, which is polyethylene oxide (PEO), in the water, and demonstrated its effectiveness for high temperature (up to 1700°C) molten tin (Furuva and Arai, 2017). The authors concluded that PEO may be precipitated in the liquid side due to the cloud-point phenomenon to suppress steam explosions even for the molten droplets at 1700 °C without producing by-products. The paper addresses the effectiveness of steam explosion retardant for LBE as a function of molecular weight and concentration.

2. STEAM EXPLOSION FACILITY

Figure 2 is a schematic of the steam explosion facility (not to scale). The molten LBE is heated in the crucible at 450 °C. This target temperature is selected as it is well above the melting temperature (124 °C) and the oxidation is less significant. A series of molten LBE droplets is released from the nozzle (i.d. 4 mm) at the bottom of the crucible by withdrawing the stopper. The molten LBE droplets are immersed into a PEO aqueous solution pool. The internal dimensions of the pool container are 100 mm^W × 100 mm^L × 200 mm^H. The solution level is 190 mm. The distance from the nozzle exit to the solution surface is 20 mm. The initial pool temperature was maintained at 20 °C. The steam explosion behavior is visualized using a video camera on the basis of the backlighting method.



(a) conventional SG (b) direct-contact SG
Figure 1. Direct-contact SG concept with LBE.

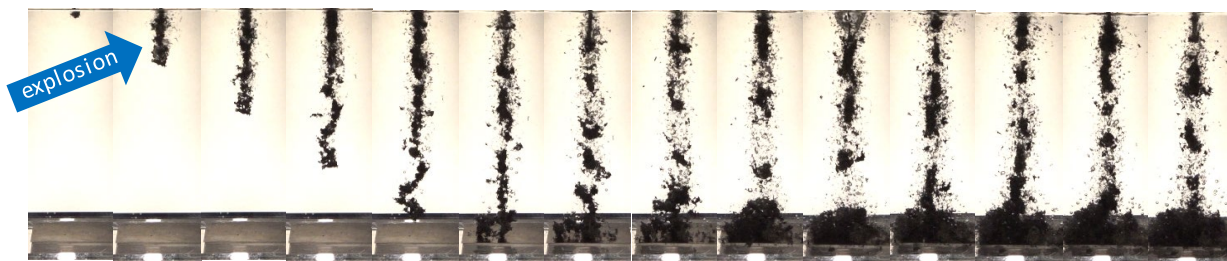
Figure 2. Schematic of Steam Explosion Facility.

3. RESULTS AND DISCUSSION

Figure 3 shows successive stages of molten LBE droplets at 450 °C immersed into water and 0.03 wt% PEO at initially 20 °C. Each frame was taken after the first droplet immersion into the pool, as shown at the top of the figure. In Figure 3(a), a steam explosion occurred for the whole molten LBE volume in the water pool. This state is classified as exploded ('yes' exploded in the later discussion). In Figure 3(b), the molecular weight of PEO is 20 kg/mol. Although several precursor droplets did not explode, the droplets exploded in the upper part of the frame at 734 ms after immersion. The explosion occurred intermittently in the limited region. This state is classified as 'partly' exploded. Subsequent droplets exploded intensely and repeatedly. In Figure 3(c), the molecular weight of PEO is 4000 kg/mol. None of the droplets exploded throughout the experiment. This state is classified as a 'no' explosion.

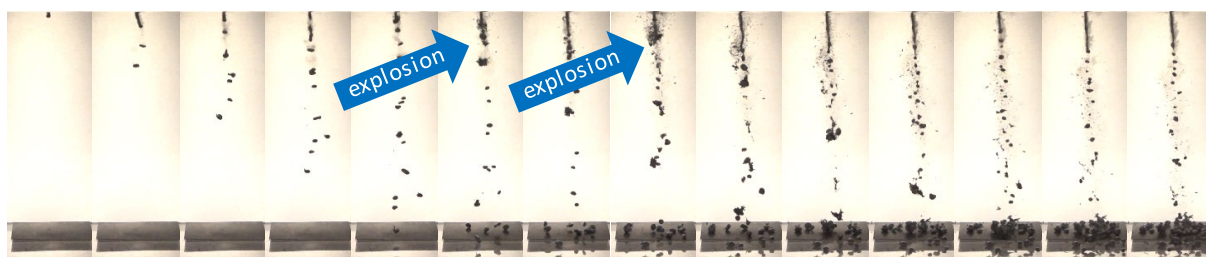
Table 1 summarizes the steam explosion severity of molten LBE droplets immersed in PEO aqueous solution in terms of molecular weight and PEO solution. The severity classification is defined above in Figure 3. Steam explosion occurs for the PEO molecular weight of 20 kg/mol. This is because the cloud-point temperature is higher than the saturation temperature to precipitate near the vapor-liquid interface. Above this molecular weight, the cloud-point temperature is a few degrees Celsius below the saturation temperature to precipitate near the vapor-liquid interface to stabilize the vapor film. Another limit is PEO concentration. The steam explosion did not occur above a PEO concentration of 0.03 wt%. Therefore, PEO concentration must be thicker enough to increase viscosity near the vapor-liquid interface and stabilize the vapor film.

Time: 0 67 133 200 267 334 400 467 534 601 661 734 801 868 ms

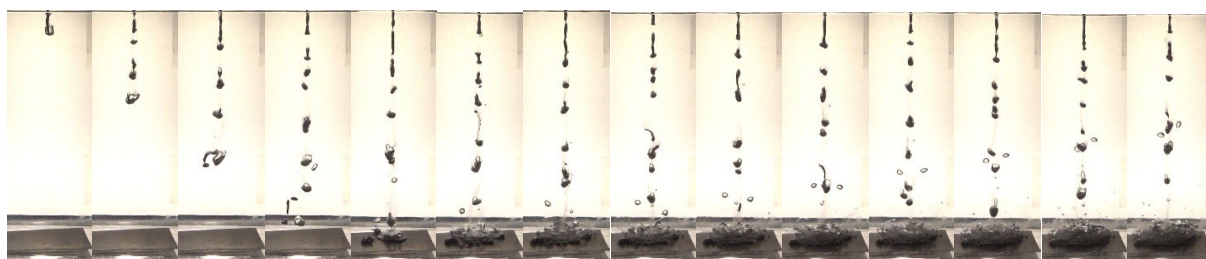


(a) Water (classified as 'Yes': exploded)

0 50 mm
|||||



(b) Molecular weight of PEO: 20 kg/mol (0.03 wt%) (classified as 'partly': partly exploded)



(c) Molecular weight of PEO: 4000 kg/mol (0.03 wt%) (classified as 'no': not exploded)

Figure 3. Successive stages of molten LBE droplets at 450 °C immersed into water and 0.03 wt% PEO aqueous pool at 20 °C.

Table 1. Steam explosion severity of molten LBE droplets immersed in PEO aqueous solution in terms of molecular weight and concentration of PEO.

		Molecular Weight of PEO (kg/mol)					
		20	400	1000	2000	4000	5000
PEO Concentration (wt%)	0.005	-	-	-	-	partly	-
	0.01	yes	partly	partly	partly	partly	partly
	0.03	Partly	no	no	no	no	no
	0.06		-	-	-	no	-
	0.1	partly	no	no	-	no	-
	0.3	-	-	-	-	no	-
	0.5	Partly	-	-	-	-	-
Water	0	yes					

Severity classification: ‘yes’: exploded, ‘partly’: exploded locally (not entirely), ‘no’: not exploded.

4. CONCLUSIONS

Steam explosion experiments were conducted for the molten LBE droplets at 450 °C into PEO aqueous solution at 20 °C. Steam explosion occurs for the PEO molecular weight of 20 kg/mol. This is because the cloud-point temperature is higher than the saturation temperature to precipitate near the vapor-liquid interface. Above this molecular weight, the steam explosion did not occur above a PEO concentration of 0.03 wt%. Therefore, PEO concentration must be thicker enough to increase viscosity near the vapor-liquid interface and stabilize the vapor film.

5. REFERENCES

- Buongiorno, J., 2001. “Conceptual Design of a Lead-Bismuth Cooled Fast Reactor with In-Vessel Direct-Contact Steam Generation,” *Ph.D. dissertation*, MIT, USA.
- Furuya, M., Arai, T. 2017, “Applicability of Steam-Explosion Retardant for Molten Nickel and Tin at High-Temperature,” In *Proceedings of 17th International Topical Meeting on Nuclear Reactor Thermal Hydraulics (NURETH-17)*, Xi’an, Shaanxi, China, Sept. 3-8.
- Grachev, N. S., Kirillov, P. L., Martynov, P. N. 1999. “Steam generators with direct contact between liquid metal and water,” In *Proceedings of Ninth International Topical Meeting on Nuclear Reactor Thermal Hydraulics (NURETH-9)*, San Francisco, California, October 3-8.
- Kinoshita, I., Nishi, Y., Furuya, M., 1995. “Direct-contact heat-transfer characteristics between a melted alloy and water,” *Heat Transfer – Japanese Research*, Vol. 24, No. 4, pp. 397-407.

6. ACKNOWLEDGMENT

The authors are grateful for many constructive suggestions from Professor Emeritus Takeo Takashima of Oyama National College of Technology. The authors thank Mr. Kouji Suzuki and Mr. Takeo Yoshioka for their assistance in these experiments.

INVESTIGATION OF CRITICAL HEAT FLUX IN NITROGEN FLOW BOILING AND REDUCED GRAVITY

F. Chavagnat^a, M. Graffiedi^a, J. Hartwig^b, Baglietto Emilio^a and M. Bucci^a

^aDepartment of Nuclear Science and Engineering, Massachusetts Institute of Technology, Cambridge, MA, USA

^bNASA Glenn Research Center, Cleveland, OH, USA

*mbucci@mit.edu

Keywords: heat transfer, cryogenic boiling, phase-detection, critical heat flux

1. BACKGROUND AND OBJECTIVES

The use of cryogenic mixtures (e.g., LH₂/LOx or LCH₄/LOx) as rocket fuel led to a significant leap forward in rocket engine efficiency, producing high thrust per mass of burned fuel. However, NASA's recent hydrogen leak during fueling of Artemis stresses the complexity of dealing with the large volumes of cryogenic fuel necessary (LH₂ having the lower density of any liquid), even for relatively short-range objectives like the Moon. The difficulties related to fuel management is motivating new research to optimize fuel usage in rockets which would allow farther space exploration and more cost-effective missions. The on-going research focuses on the storage of cryogenic fuel in low earth orbit as fuel depot, and the increase of propulsion engines efficiency (e.g., with nuclear thermal propulsion). However, in both cases, engineers have to deal with the inherent challenges of cryogenic fuel, esp. their low boiling temperature. Whether it is about storing or transferring cryogenes, only a small heat leak from the environment or residual superheat in structural components suffice to boil the fuel with detrimental consequences (unstable flow in transfer line, vibration in pumps, tank over-pressurization, etc.). Our inability to provide reliable predictions of boiling heat transfer of cryogenic fuel, in particular in reduced gravity conditions, remains a major roadblock in the development of new technologies in low-Earth orbit (see review from Hartwig et al. (2016)).

Predicting the boiling crisis is a task that have tormented the research community for decades irrespective of the fluid of interest. Several published studies have presented measurement of critical heat flux (i.e., the heat flux at which the boiling crisis occurs) of cryogenes in various conditions with mild success (e.g., see Hartwig et al., 2016). Despite the complexity of boiling phenomena, the development of new experimental studies allowing for finer characterization of boiling leveraging optical diagnostics (see Richenderfer et al., 2016; Kossolapov, 2021 and Chavagnat, 2024) opened the possibility of providing mechanistic models of boiling heat transfer (Gilman and Baglietto, 2017). Naturally, one could ask whether the boiling crisis can also be mechanistically determined? More precisely, can it be determined by the sole knowledge of the different boiling parameters (bubble sizes, nucleation site density, etc.)?

Recently, the work of Zhang et al. (2023) has shed light on the percolative nature of the departure from nucleate boiling (DNB) transition. This finding led to uncover a relationship between the boiling crisis and the product of a triplet of boiling parameters (the average bubble footprint radius A_f , the probability of having a bubble on an active nucleation site ft_g and the nucleation site density N''). As the boiling system approaches DNB, the product $N''ft_gA_f$ tends to ~ 1 , consistently in both pool boiling and flow boiling, across difference boiling surfaces and different fluids (including liquid nitrogen in pool boiling only), all in normal gravity conditions.

In this study, we explore the effect of flow velocity and reduced gravity on the critical heat flux of cryogenic boiling. Both effects lead to complications in using Zhang et al.'s model. First, the low surface tension of cryogen makes bubbles and larger vapor patches very mobile on the boiling surface, whereas the model was developed assuming non-sliding bubbles. Physically, the nucleation frequency becomes also much more challenging to evaluate, as the time necessary for a site to produce a bubble partially depends on the complex movement of the vapor on the surface. Second, in absence of effective forces that help detaching bubbles (i.e., at low flow velocity and reduced gravity), the boiling process becomes unstable with larger fluctuations observed in the boiling parameters.

To assess whether the percolation model proposed by Zhang et al. (2023) can be leveraged to treat such situations, we developed a modular boiling setup that allows to perform non-intrusive optical diagnostics of nitrogen boiling in pool and flow boiling conditions under normal gravity and reduced gravity. The optical methods allow tracking liquid and vapor phases on the boiling surface through phase-detection (Kossolapov et al., 2020) and characterization of boiling parameters using synchronized phase-detection and shadowgraphy. Even with phase-detection, evaluating nucleation site density and bubble nucleation frequency is an incredibly difficult task due to bubbles sliding. Therefore, another approach to the calculation of the boiling parameters triplet (i.e., $N''ft_gA_f$) which circumvent the issue of sliding bubbles, proposed by Wang et al. (2024), is also explored in this work.

2. EXPERIMENTAL METHODS

The experimental setup consists of a test-section containing pressurized liquid nitrogen with optical accesses. Nitrogen is used here as a proxy for cryogenic fuels, such as hydrogen and oxygen. Figure 1 shows a simplified schematic of our experimental apparatus in its pool boiling configuration (that can be seen by the presence of head space above the heating surface). Liquid nitrogen (99.995% mol pure) is boiled on a heating element which consist of a 700 nm-thick Joule-heated Indium Tin Oxide (ITO) thin film coated on a sapphire substrate. The transparency of both the sapphire substrate and ITO thin-film allow us to obtain very detailed optical imaging of the boiling surface. In flow boiling configuration, the headspace standing above the heating surface is removed and instead the nitrogen flows through a square channel of 11 mm by 11 mm. The P&ID is then more complicated. Auxiliary systems controlling vacuum insulation, supply and venting of liquid nitrogen, and an instrumentation system gathering heat input, temperature, and pressure data. A frame supports the integrality of the equipment. The nitrogen flows from the dewar, continuously run through the test-section and is evacuated to the atmosphere. The mass flow rate is controlled by the nitrogen pressure at the dewar and a flow regulating valve, and measured with Coriolis flow meter upstream of the test-section.

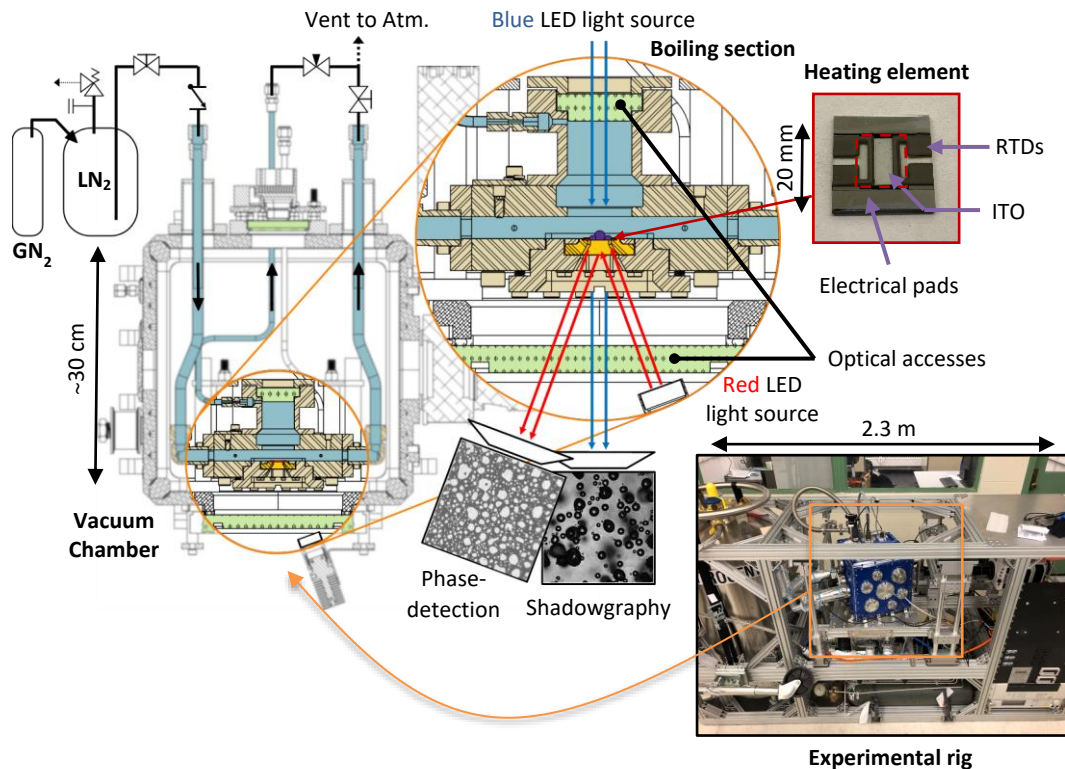


Figure 1: Schematic of the experimental apparatus for saturated LN₂ pool boiling. Liquid nitrogen is shown in teal.

Our typical sapphire substrate has a nano-smooth surface finish with only a handful micron-sized cavities (similar than shown by Richenderfer et al., 2018). The power input in the ITO is determined by measuring the current and voltage drop across the thin film. The temperature of the heating surface is measured by two thin-film RTD sensors directly coated on the sapphire substrate. Nitrogen boiling on the heating substrate is recorded using two imaging techniques: backlit shadowgraphy and, importantly, a phase-detection based on partial internal reflection (details shown in Kossolapov et al., 2020).

3. RESULTS

Figure 2 (left) shows the critical heat flux measured in pressurized nitrogen boiling at different flow and gravity conditions. Dots in blue are measurements performed in normal gravity, while red dots are obtained in microgravity condition. As shown, in normal gravity conditions there are three possible regimes. For very low flow rates, the DNB is practically independent of the flow rate (i.e., it is constant, as indicated by the horizontal straight black line). Conversely, for very high flow rates, the DNB increases with the flow (the curved line in the plot indicates a proportionality to the flow rate to the power 0.4, which is rather usual). The boiling data obtained each of the conditions shown in Figure 2 (at the exception of pool boiling-like in reduced gravity) shows the sign of criticality observed by Zhang et al. (2023), i.e., a

probability distribution function (PDF) of the bubble footprint area given by a power law with a negative slope coefficient <3 , in our case near -2 (i.e., $p(A_f) \propto A_f^\gamma$, here with an exponent γ of -2) at DNB. Figure 2 (right) shows measurement of the PDF at different heat flux, near ONB (in blue) and near DNB (in red), for nitrogen pool boiling in Earth gravity. Phase-detection imaging are shown as well in Figure 2 near ONB (framed in blue) and DNB (in red) illustrating the typical output of the experiment. Vapor appears as light gray while liquid appears dark gray. The heating surface is horizontal with quiescent nitrogen. On these images, only bubble footprints are visible. After identifying and tracking each bubble on the heating surface, we can construct a database of bubbles and derives the quantities of interest including the PDFs shown in Figure 1, but also assess the Zhang et al. (2023) boiling crisis criterion. Both PDF curves shows that the probability of finding a bubble with footprint area A_f decreases with increasing A_f , irrespective of the heat flux. However, the rate of decrease of the PDFs with increasing A_f changes with the heat flux. When bubbles are isolated such that no significant number of coalescence events occur (e.g., near ONB), the probability of having a large bubble depends on the probability that the bubble lifts off from the surface or slide out of the heating surface during growth. As the bubble gets larger and larger with time, the probability of the bubble leaving the surface increases (buoyant forces, lift and drag forces all increase with the increasing size of the bubble faster than capillary forces retaining the bubble). However, as the number of bubbles increases on the surface with increasing heat flux, the probability of finding large bubble naturally increases due to coalescence (e.g., shown by the PDF plotted in red).

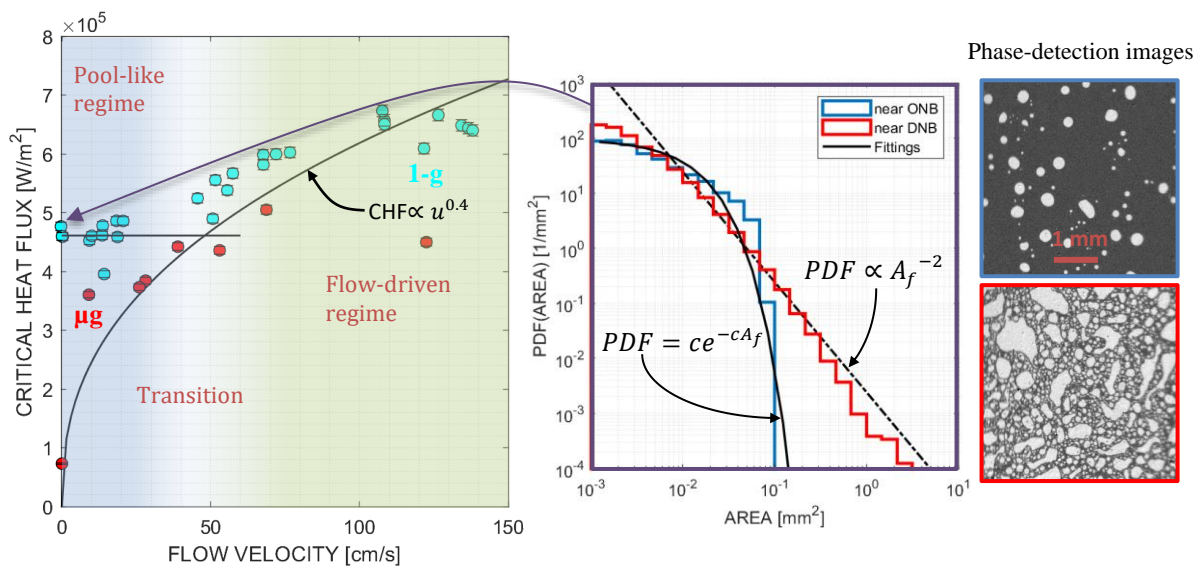


Figure 2: Left – plot of the critical heat input against flow velocity at 1-g and in reduced gravity, right – plot of the PDF of the bubbles’ footprint near ONB (in blue) and near DNB (in red) for saturated nitrogen pool boiling on horizontal upward-facing surface.

4. CONCLUSIONS

Our experimental investigation shows the critical heat flux could be determined using the percolation model proposed by Zhang et al. (2023). However, bubbles sliding on the surface makes the criterion originally proposed by the author (i.e., using nucleation frequency and nucleation site density) difficult to use in nitrogen boiling due to the frequent sliding of bubble on the surface, irrespective of the flow velocity. Instead, we showed that the more practical criterion proposed by Wang et al. (2024) is applicable to flow-driven DNB as well as pool-like regime in normal gravity conditions. We show that with our measurements of bubble density and average bubble footprint area, and Wang et al.’s DNB criterion, one can recover the typical trend of CHF with flow velocity in $u^{0.4}$. In micro-gravity, the situation is more complex due to the emerging transient behavior of the boiling system. In particular, we show that temporary supercritical distribution of the bubble footprint area distribution can exist while remaining in the nucleate boiling regime.

5. REFERENCES

- Hartwig, J., Darr, S., & Asencio, A., 2016. “Assessment of existing two-phase heat transfer coefficient and critical heat flux correlations for cryogenic flow boiling in pipe quenching experiments”. *International Journal of Heat and Mass Transfer*, Vol. 93, pp. 441–463.
- Richenderfer, A., Kossolapov, A., Seong, J. H., Saccone, G., Demarly, E., Kommajosyula, R., Baglietto, E., Buongiorno, J., & Bucci, M., 2018. “Investigation of subcooled flow boiling and CHF using high-resolution diagnostics”. *Experimental Thermal and Fluid Science*. Vol. 99, pp. 35-58.

- Kossolapov, A., 2021. "Experimental Investigation of Subcooled Flow Boiling and CHF at Prototypical Pressures of Light Water Reactors", Ph.D. thesis, Massachusetts Institute of Technology.
- Chavagnat, F., 2024. "High-Resolution Experimental Measurements and Mechanistic Modelling of Saturated Cryogenic Pool Boiling Heat Transfer", Ph.D. thesis, Massachusetts Institute of Technology.
- Gilman, L and Baglietto, E., 2017. "A self-consistent, physics-based boiling heat transfer modeling framework for use in computational fluid dynamics". *International Journal of Multiphase Flow*. Vol. 95, pp. 35-53.
- Zhang, L., Wang, C., Su, G. et al., 2023. "A unifying criterion of the boiling crisis". *Nat Commun* 14, 2321. <https://doi.org/10.1038/s41467-023-37899-7>
- Chi Wang, Guanyu Su, Olorunsola Akinsulire, Limiao Zhang, Md Mahamudur Rahman & Matteo Bucci, 2024 "Investigation of critical heat flux enhancement on nanoengineered surfaces in pressurized subcooled flow boiling using infrared thermometry", *Heat Transfer Engineering*, 45:4-5, 417-432, DOI: 10.1080/01457632.2023.2191441
- Kossolapov, A., Phillips, B., & Bucci, M., 2021. "Can LED lights replace lasers for detailed investigations of boiling phenomena?". *International Journal of Multiphase Flow*. Vol. 135, 103522.

SINGLE SESSILE BUBBLE GROWTH BEHAVIOR IN MICROGRAVITY

**Fedor Ronshin^{a,*}, Alexey Rednikov^b, Anastasia Zorkina^a, Julie Jambert^{b,c}, Irina Graur^d, Oleg Kabov^a,
Pierre Colinet^b, and Lounes Tadrist^d**

^aKutateladze Institute of Thermophysics, Av. Lavrentyev, 1, Novosibirsk 630090, Russia

^bUniversité libre de Bruxelles, TIPs Laboratory, CP 165/67, 50 Av. F.D. Roosevelt, Brussels 1050, Belgium

^cInstitut de Mécanique des Fluides de Toulouse, 2 All. Prof. Camille Soula, Toulouse 31400, France

^dAix Marseille Université, CNRS, Laboratoire IUSTI, UMR 7343, Technopole de Château-Gombert, 5 rue Enrico Fermi, Marseille 13453, France

*f.ronshin@gmail.com

Keywords: boiling, microgravity, single bubble growth

1. INTRODUCTION

Investigation of boiling phenomena holds significant importance in various scientific and engineering disciplines due to its fundamental role in heat transfer processes, phase change dynamics, and energy conversion systems. Boiling is a complex multiphase phenomenon that occurs in a wide range of natural and industrial contexts, influencing the efficiency and performance of numerous technological applications. Understanding the underlying physics of boiling is crucial for optimizing heat transfer rates, enhancing thermal management strategies, and improving the design and operation of thermal systems.

Boiling plays a critical role in the cooling of electronic devices, power generation in thermal power plants, refrigeration systems, and propulsion systems in aerospace applications. The ability to control and manipulate boiling processes can lead to advancements in energy efficiency, sustainability, and reliability across various industries. Moreover, the study of boiling phenomena contributes to the development of predictive models, computational simulations, and innovative technologies that enable the optimization of heat transfer performance and the mitigation of thermal challenges.

Despite extensive research efforts, the physics of boiling remains incompletely understood due to the involvement of numerous influencing factors. Further experimental investigations are required to validate the existing models and develop more precise physical frameworks applicable across a wide range of parameters. Microgravity experiments offer a valuable avenue for advancing this research, as they allow for the observation of boiling phenomena on larger spatial and temporal scales with enhanced resolution by eliminating the effects of gravity-induced bubble detachment and buoyancy convection.

To address these challenges, an international scientific team, supported by the European Space Agency, conducted a microgravity boiling research program onboard the International Space Station, which included the Reference mULTiscale Boiling Investigation (RUBI) experiment using FC-72 as the working liquid. This study focused on pool-boiling dynamics, specifically examining the smooth growth of single bubbles generated at artificial nucleation sites under near-saturation conditions and minimal heater power settings within the RUBI setup. Detailed information regarding the experimental setup and methodology can be found in previous publications (Sielaff *et al.*, 2022; Oikonomidou *et al.*, 2022; Ronshin *et al.*, 2024).

2. EXPERIMENTAL SETUP AND NUMERICAL MODEL

A comprehensive exposition of the experimental configuration and methodologies employed are provided by Sielaff *et al.* (2022). Herein, we outline the principal components of the RUBI experiment and the model description employed in the present investigation. The experimental setup (cf. Figure 1) includes a boiling cell maintained at a constant pressure P adjustable between 0.5 and 1 bar. Thermal control mechanisms allow for the initial thermalization of the boiling cell using N-perfluorohexane (FC-72) as the working fluid at a temperature T_{set} ranging from 30 °C to 70 °C in the beginning of each experimental run. The subcooling degree ΔT_{sub} is determined as the difference between the saturation temperature T_{sat} corresponding to the pressure P and T_{set} , i.e., $\Delta T_{sub} = T_{sat} - T_{set}$. A thin-foil heater with a chromium layer approximately 400 nm thick is deposited on top of a 5 mm thick BaF₂ plate acting as the substrate. The mean power q of the heater can be varied within the range of 0.25 to 2 W/cm². Bubble initiation occurs after a waiting time t_{wait} (a few seconds) following the activation of the heater. The initiation process involves locally superheating an artificial nucleation site extending approximately 100 μm deep within the BaF₂ substrate using a focused laser pulse (as BaF₂ is transparent). The pulse duration t_{pulse} can be set to either 10 or 20 ms. Infrared thermography is employed to assess the temperature distribution along the heating foil from below, while high-speed camera imaging from a side angle (approximately 5°

with respect to the horizontal) is used to monitor bubble shapes. The data from black and white images has been subjected to postprocessing using custom software (Oikonomidou *et al.*, 2022).

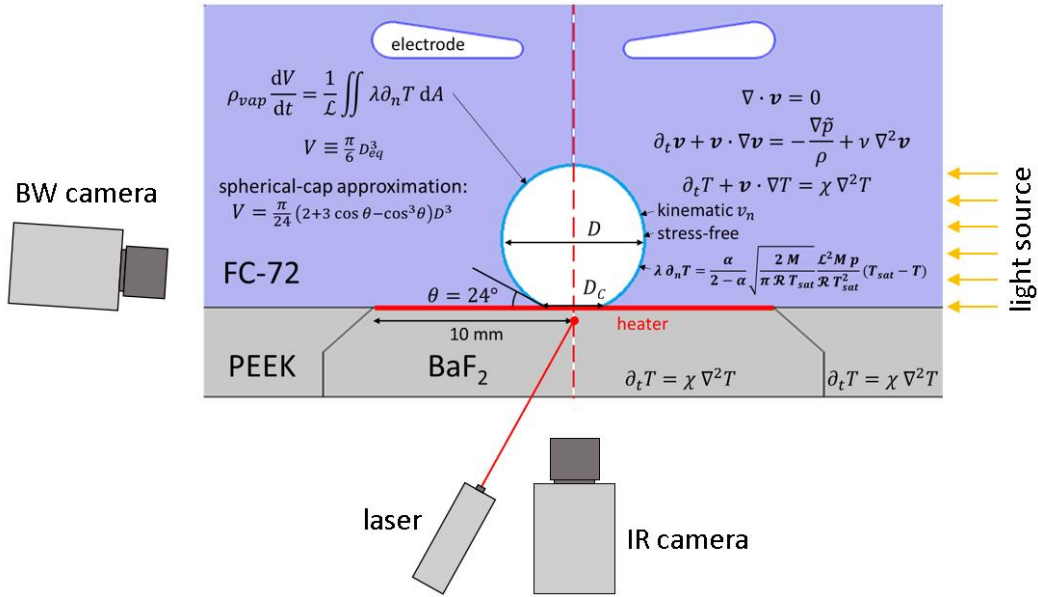


Figure 1. Schematic diagram of the experimental setup and the numerical model.

To elucidate the experimental observations, a simplified axisymmetric model has been constructed as depicted in Figure 1. The model represents a sessile bubble in the shape of a spherical cap, which is considered a suitable approximation for the pool boiling experiments after initial shape fluctuations. The contact angle θ is predetermined and constant. Its value is set to a representative average value obtained from the experiment (e.g., 24°), with studies indicating that the bubble diameter evolution over time is minimally affected by this parameter. The interior of the bubble is assumed to be inert dynamically, and heat transfer through it is neglected. The growth of the bubble, or more broadly the evolution of its size, is governed by heat transfer mechanisms within the surrounding liquid. The model employs a complete set of Navier-Stokes equations and convective heat transfer equations to describe this process. Additionally, an equation for the evolution of bubble size is included, where the vapor mass changes over time based on the integral heat flux from the liquid divided by the latent heat. At the bubble interface, a Schrage-type kinetic equation with an accommodation coefficient α set to unity is utilized. This results in the bubble surface temperature being nearly equal to the saturation temperature T_{sat} except for a small region near the contact line (of the order of tens of nm) where evaporation kinetics play a significant role due to high local flux densities. In numerical simulations, a non-uniform mesh with nanometer-scale resolution near the contact line is employed to capture kinetic effects accurately. No additional nano/microscopic effects at the contact line are considered apart from the kinetic effect. Heat transfer within the solid substrate, consisting of a BaF₂ plate and adjacent PEEK layer, is fully accounted following RUBI specifications. The heat generation distribution on the BaF₂ plate, facilitated by a not fully axisymmetric sub-micrometric coated joule heater (assumed to be of zero thickness in the model), is axisymmetrized by averaging values at each concentric circle (Ronshin *et al.* 2024). The non-uniform heat generation density on the heater, attributed to varying electric currents in this configuration, is integrated into the axisymmetrization process using the data from Schinnerl *et al.* (2023). The nucleation process is not explicitly modeled; instead, a small initial bubble (diameter is equal to the first experimentally observed one at 500 fps) is introduced at the onset of the laser pulse at experimental nucleation time. The laser pulse is simulated as a localized heat source distributed uniformly within a $30 \mu\text{m}$ sphere and acting at a depth of $100 \mu\text{m}$ in BaF₂ for either 10 ms or 20 ms (as specified by RUBI guidelines). The simulations are conducted using the COMSOL Multiphysics software. Nevertheless, the presence of systematic errors may be the primary factor at play, as the calculated ΔT_{sub} value necessary for the model turns out to be consistently lower by approximately the same magnitude (roughly 1.5°C) than the officially declared ΔT_{sub} in RUBI. This discrepancy is corroborated by additional cases examined subsequently in this study, as well as by analogous observations reported by RUBI partners in Toulouse and Darmstadt (private communication, Torres *et al.* 2024).

3. RESULTS AND DISCUSSION

In this study, we have selected specific parameters for analysis in a reference case: a low heat flux ($q = 0.5 \text{ W/cm}^2$), a low subcooling degree ($\Delta T_{sub} = 1^\circ\text{C}$), pressure ($P = 500 \text{ mbar}$), a low waiting time ($t_{wait} = 2 \text{ s}$), and the typical laser pulse duration ($t_{pulse} = 20 \text{ ms}$). The time evolution of various process characteristics is depicted in Figure 2(a-e) from

$t = 0$ s (start of the laser pulse) to $t = 9$ s (end of observation), divided into three distinct stages (1st, 2nd, and 3rd). The growth of the equivalent diameter (and consequently the volume) is observed to exhibit a smooth progression, despite displaying a complex behavior, as shown in Figure 2. The model, limited to sessile spherical-cap bubbles, effectively captures this growth pattern. However, the evolution of the contact diameter (Figure 2d) during the 1st stage is irregular before stabilizing at a spherical cap.

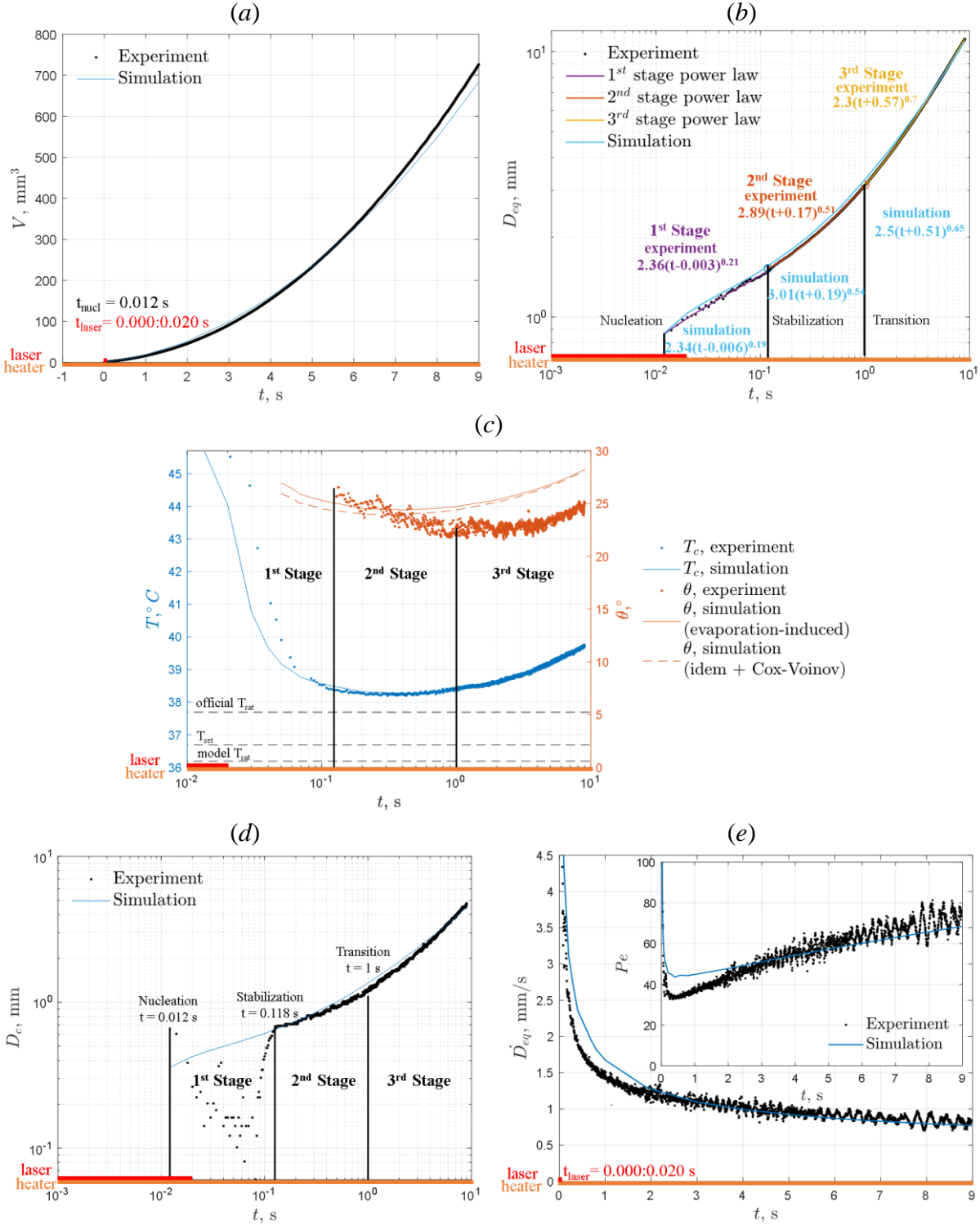


Figure 2. Experimental and simulation results for the evolution of various quantities during bubble growth. $P = 500$ mbar, $q = 0.5$ W/cm², $t_{\text{wait}} = 2$ s, $t_{\text{laser}} = 20$ ms, $T_{\text{set}} = 36.7^\circ\text{C}$, $\Delta T_{\text{sub}} = 1^\circ\text{C}$. Additional model settings: model $\Delta T_{\text{sub}} = -0.5^\circ\text{C}$, $\alpha = 1$, $\theta = 24^\circ$, spherical-cap bubble, initial condition at the first bubble appearance in experiment. Three stages are distinguished. (a) Bubble volume V . (b) Equivalent diameter of the bubble D_{eq} with power laws at each stage. (c) Temperature at the contact line T_c and contact angle θ . (d) Contact diameter of the bubble D_c . (e) $\dot{D}_{eq} \equiv dD_{eq}/dt$ and the Pelet number $Pe \equiv D_{eq}\dot{D}_{eq}/4\chi_l$.

Analysis of the contact-line temperature results in Figure 2(c) reveals significant initial superheating effects due to the laser during the 1st stage, dissipating towards the end of this phase. The power-law approximation exponent for bubble growth during this stage is approximately 0.2, indicating an initial explosive growth followed by deceleration due to decreasing superheating. This leads to a decrease in the Peclet number of bubble growth initially. The onset of the 2nd stage is characterized by stabilization at a spherical-cap shape, resulting in regular evolution of the contact diameter (Figure 2d) and a plateau in the contact-line temperature (Figure 2c). The power-law exponent approaches 0.5, and the Peclet number reaches a minimum during this phase. The contact angles remain relatively constant over time (Figure 2c), supporting the model's simplification with a fixed experimentally derived value of $\theta = 24^\circ$. Posterior application of the microregion approach yields contact angle results that align well with experimental measurements. During the 3rd stage up to $t = 9$ s, increasing substrate temperature leads to accelerated bubble growth, reflected in a power-law exponent of approximately 0.7 (Figure 2b) and a rising Peclet number (Figure 2e). Despite the bubble extending beyond the thermal boundary layer towards the liquid at ambient temperature, evaporation flux is predominantly influenced by the small contact-line vicinity near the heated substrate. Through recalibration of only ΔT_{sub} (by 1.5°C here), simulations closely reproduce measured quantities, particularly demonstrating good agreement for the Peclet number (Figure 2e). In Figure 2(e), the time derivative of the experimental data for the equivalent diameter growth rate, \dot{D}_{eq} , is computed using central finite differences as $\dot{D}_{eq}^k = \frac{D_{eq}^{k+s} - D_{eq}^{k-s}}{t^{k+s} - t^{k-s}}$, where the superscript numbers denote data points. A step size s is employed for each point k , with an optimal value of $s = 7$ chosen to reduce noise without losing signal information. Notably, the time derivative is sensitive to uncertainties, particularly during the initial two seconds of bubble growth when there is a relatively high deviation between experimental and simulated \dot{D}_{eq} and Peclet number (Pe). Characteristic pulsations are observed in the experimental data for \dot{D}_{eq} and Pe , attributed to bubble shape oscillations. The time scales evaluated at $D \sim 5$ mm and $D \sim 10$ mm suggest periods of oscillations for \dot{D}_{eq} at approximately 0.14 s and 0.4 s, corresponding to a double period in terms of Pe . Regarding the results for the contact angle in Figure 2(c), theoretical curves are plotted for the evaporation-induced contact angle θ_{mic} obtained from the microregion model equations (Rednikov and Colinet, 2017). The superheat ΔT is determined as the difference between the contact-line temperature T_c calculated within the bubble growth model over time and the saturation temperature T_{sat} . The theoretical curve for the contact angle also considers a contribution from the receding motion of the contact line during bubble growth. While this effect is initially present, it becomes weak after stabilization, with contact-line velocities below 1 mm/s. Thus, for simplicity, the theoretical contact angle is evaluated as $\theta = \theta_{mic}$. The simulations show that the contact angle and contact-line temperature reach minima simultaneously, while in experiments, these minima are slightly shifted. This discrepancy may be attributed to the simplifications in the microregion model and measurement inaccuracies.

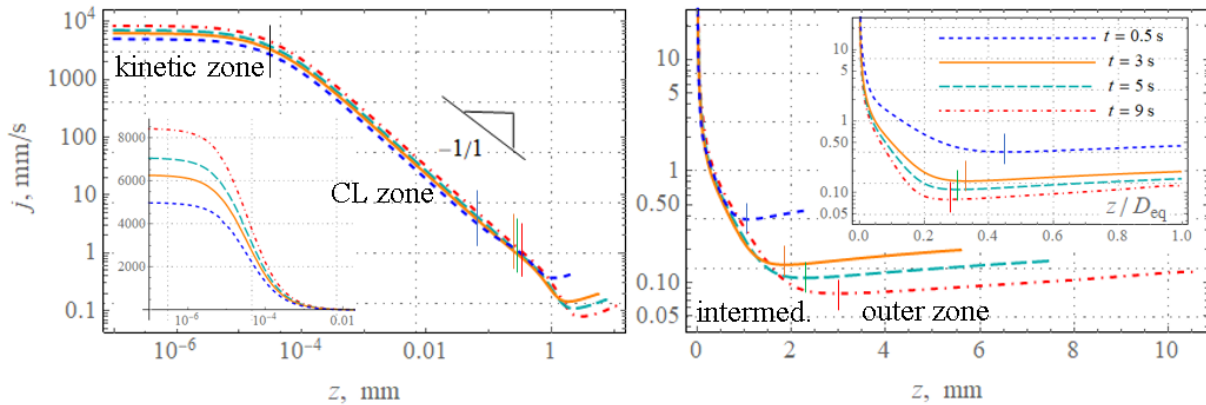


Figure 3. Computed evaporation flux density along the bubble surface at various times as a function of z between the substrate at $z = 0$ and the bubble apex at $z = \frac{1}{2}D(t)(1 + \cos \theta)$. Several representations (including the insets) of the same results are provided to discern various details.

Figure 3 illustrates the evaporation flux density distribution along the bubble surface as determined by simulations. The disparity in this quantity spans five orders of magnitude between the contact line and the top of the bubble. Various distinct zones with specific flux behaviors are identifiable. Initially, there is a kinetic zone where the flux remains at a high level due to the resolution of the contact line singularity by kinetic effects. Subsequently, a 'wedge-conducting' zone (referred to as the contact-line, CL zone) is observed slightly away from the contact line, exhibiting a (quasi) inversely linear behavior $j \sim z^{-1}$ characteristic of heat conduction across a wedge with differing constant temperatures on each side. The size of this zone is notably smaller than the bubble radius, indicating wedge and conduction-dominated heat transfer despite high overall Peclet numbers. The outer boundary of this CL zone is not precisely defined but is chosen where the observed behavior visibly diminishes. Following this, an intermediate zone is identified where bubble surface curvature, advective heat transfer, and the development of a thermal boundary layer at the substrate are considered to influence the

flux. Subsequently, the flux reaches a minimum and begins to increase with z , marking an outer zone extending to the apex of the bubble where it meets the liquid at the original temperature T_{set} beyond the substrate's thermal boundary layer. In this region, $j > 0$ (evaporation) is observed based on the model $\Delta T_{sub} = T_{set} - T_{sat} = -0.5^\circ\text{C}$ (superheat) derived from model T_{sat} . The official value of $\Delta T_{sub} = 1^\circ\text{C}$ would indicate vapor condensation ($j < 0$) in the outer zone. Heat transfer in this region is dominated by advection, with the increase in j with z attributed to a rise in velocity (the highest normal velocity due to bubble growth occurs at the apex). Although occupying a minor fraction of the bubble's surface area, the contribution of the kinetic and contact-line (CL) zones to the total evaporation flux is disproportionately significant.

4. CONCLUSIONS

A physical analysis of a pool-boiling experiment with single bubbles on a predetermined laser-ignited nucleation site in microgravity was conducted to investigate bubble growth dynamics over a relatively long period of time (~ 9 s) and up to large sizes (~ 1 cm). By eliminating buoyancy effects, the study focused on mild cases of stably onward bubble growth selected from numerous runs conducted onboard the International Space Station (ISS). Specifically, near-saturation cases with low heater power values (0.5 W/cm^2) were examined.

The analysis integrated four tools, including post-processing of bubble images from a side-view black-and-white camera, temperature profile evolution retrieval using a bottom-view infrared camera, a global numerical model describing bubble growth, and a microregion model to estimate contact angle values. The study revealed four distinct stages of bubble growth under different operating conditions:

1. Zeroth stage: Bubble nucleation and explosive growth under the laser pulse, attributed to 'shock vaporization' from the nucleation site upon laser impact.

2. First stage: Bubble shape oscillations moderated by inertia and surface tension, leading to stabilization at a sessile spherical-cap shape. Bubble growth rate slows down as the substrate cools after the laser pulse, characterized by a power law with an exponent 0.2.

3. Second stage: Transition phase lasting up to 1 s, marked by a minimum in the contact-line temperature evolution and Peclet number. The power-law exponent approaches the classical 'established-growth' value of 0.5 during this stage.

4. Third stage of bubble growth extends until the end of the observation period ($t = 9$ s), during which the bubble reaches a size of approximately one centimeter. The contact-line temperature gradually rises, aligning with the ongoing increase in substrate temperature due to the continued heating. Consequently, local superheating intensifies over time, leading to a higher power-law exponent for bubble growth (0.7).

The global model effectively replicates the collective measurement outcomes, encompassing bubble diameter evolution, temperature profiles, and stages of growth. However, achieving precise quantitative agreement necessitates a pre-calibration or readjustment of subcooling (or superheating) values ΔT_{sub} . The simulation outcomes are notably sensitive to these values, typically within a few degrees in this study, highlighting the potential impact of uncertainties or inhomogeneities in ambient temperature values (T_{set}) or known thermodynamic data (saturation temperature T_{sat}). Adjusting ΔT_{sub} by approximately 1.5°C is often required for optimal agreement.

The model elucidates a non-uniform distribution of heat and evaporation flux along the bubble surface, with a small contact-line region comprising a minor percentage of the surface area contributing significantly to the overall flux. The measured contact angle, approximately 25° , exhibits slight variations during the second and third growth stages. These measurements align well with the predictions from a classical microregion model when incorporating contact-line superheat values from the global bubble-growth model simulations. The contact angle predominantly arises from evaporation effects, unaffected substantially by contact-line motion.

Manipulating the accommodation coefficient in evaporation kinetics from 1 to 0.7 enhances agreement for contact angles without significantly impacting computed bubble growth. Analysis underscores the critical role of subcooling ($\Delta T_{sub} = T_{sat} - T_{set}$ or superheating if negative) in bubble evolution. While this study focused on near-saturation cases with minimal subcooling, future investigations should prioritize scenarios with substantial subcooling (common in the majority of runs in the aforementioned space experiment) for a comprehensive parametric exploration.

The study was supported by the Russian Science Foundation grant No. 24-79-10251, <https://rscf.ru/en/project/24-79-10251/>

5. REFERENCES

- Kind, J. and Sielaff, A. 2024. *Private communication*.
- Oikonomidou, O., Evgenidis, S., Argyropoulos, C., Zabulis, X., Karamaoynas, P., Raza, M.Q., Sebilliau, J., Ronshin, F., Chinaud, M., Garivalis, A.I., Kostoglou, M., Sielaff, A., Schinnerl, M., Stephan, P., Colin, C., Tadrist, L., Kabov, O., Di Marco, P., and Karapantsios, T. 2022. "Bubble growth analysis during subcooled boiling experiments on-board the international space station: Benchmark image analysis". *Adv. Colloid Interface Sci.*, Vol. 308, No. 102751.

- Rednikov, A. Ye. and Colinet, P. 2017. "Asymptotic analysis of the contact-line microregion for a perfectly wetting volatile liquid in a pure-vapor atmosphere." *Physical Review Fluids*, Vol. 2, No. 124006.
- Ronshin, F., Kabov, O., Rednikov, A., and Tadrist, L. 2024. "Preliminary physical analysis of a single-bubble pool-boiling experiment in space: Effect of subcooling and possible non-condensable residuals" *International Communications in Heat and Mass Transfer*, Vol. 150, No. 107188.
- Schinnerl, M., Sielaff, A., Zabulis, X., Evgenidis, S., Oikonomidou, O., and Stephan, P. 2023. "Heat transfer in single bubble nucleate boiling within the multiscale boiling project onboard the International Space Station" In *International Heat Transfer Conference Digital Library*. Begel House Inc.
- Sielaff, A., Mangini, D., Kabov, O., Raza, M. Q., Garivalis, A. I., Zupančič, M., ... and Tadrist, L. 2022. "The multiscale boiling investigation on-board the International Space Station: An overview" *Applied Thermal Engineering*, Vol. 205, No. 117932.
- Torres, L., Urbano, A., Colin, C., and Tanguy, S. 2024. "On the coupling between direct numerical simulation of nucleate boiling and a micro-region model at the contact line". *Journal of Computational Physics*, Vol. 497, No. 112602.

EXPERIMENTAL INVESTIGATION ON CONVECTIVE HEAT TRANSFER OF HEAT EXCHANGER COMPOSED OF PARAFFIN/COPPER FOAM COMPOSITE MATERIAL

Ratiba S. Ferfera^{a,*}, Brahim Madani^a

^a Laboratory of Multiphase Transport and Porous Media (LTPMP), University of Sciences and Technology Houari Boumediene (USTHB), Algiers, Algeria.

* sferfera@usthb.dz / s.ferfera@hotmail.com

Keywords: PCM, metal foam, heat transfer, Nusselt number, heat exchanger

1. INTRODUCTION

PCMs are widely studied by researchers and used in the different industry fields, such as in heat exchangers (Mahdi et al., 2021), solar thermal (Kazem et al., 2023), electronic devices thermal management (Ferfera et al., 2020a) (Ferfera et al., 2020b), etc. its due to their large capacity to store thermal latent heat (Martínez et al., 2023). On the other hand, they present a very slow thermal response due to their poor thermal conductivity. Several studies have been carried out to improve the thermal performance of PCM, as the addition of fins (Safari et al., 2024; Sodhi and Muthukumar, 2021), nano particles (Al-Aasam et al., 2023). Several anterior experimental and numerical studies carried out on heat transfer and thermal conductivity enhancement of composite PCM/metal foam. (Ferfera and Madani, 2020) found that the metal foam improves the heat transfer and thermal conductivity of the PCM but the latent thermal storage capacity of the PCM decreases. (Huang et al., 2021) realized that the metal foam accelerated the PCM melting process, the melting front was less uniform due to the natural convection of liquid PCM. (Noghrehabadi et al., 2021) found that the melting interface advancement was less uniform and curved from high porosities due the natural convection of the liquid PCM and melting front became more uniform and vertical for low porosities. This shows that the liquid PCM natural convection has a very large influence on the phase change and melting font. Many studies in the literature have been carried out on the open cell metal foam geometric characteristics influence on the PCM melting front and on thermal conductivity the improvement. However, there is lake information on the metal foam influence on the convective transfer characteristics of liquid PCM.

In this paper, experimental study is carried out on paraffin and PCM/metal foam composite samples. The aim of this study is to explore the pore density effect on the conductive and convective heat transfer. Thus, five different samples are tested: pure paraffin, PCM/Cu foam with pore densities varying from 10 PPI to 40 PPI. The metal foam pore density effect on the phase change paraffin and convective heat transfer of liquid paraffin are studied.

2. SAMPLES PREPARATION

In the present work, the PCM used is Paraffin with a latent heat of fusion of 160 kJ/kg.K measured in a melting temperature range of 42 to 48 °C. In order to obtain a paraffin/metal-foam composite sample, an impregnation process is adopted consisting of immersing the metal foam, provided by the supplier POROMETAL®, in a bath of molten paraffin. Five samples, with dimensions of 80 x 50 x 5 mm³, are obtained as part of this study: A pure paraffin sample, and four Paraffin/Cu-foam composite samples with pore density of 10, 20 and 40 PPI and at porosity of 96.1 % and pore density of 30 PPI at porosity of 95.5 %. An image processing series using the Scanning Electron Microscopy (SEM) (JEOL JSM-6360LV) is carried out on the studied metal foam samples. Figure 1 shows SEM image of an open-cell copper foam sample (Figure 1a) and composite paraffin/Copper foam sample (Figure 1b) with porosity and pore density of 96,1% and 40 PPI, respectively. As shown in Figure 1a, the metal foam structure consists of multiple cells randomly distributed in space and limited by the ligaments and pores. Figure 1b shows that paraffin occupies the cell void in the nickel foam.



Figure 1. Samples SEM image (a) copper foam (b) paraffin/Cu-foam composite ($\epsilon = 96.1\%$, $\omega = 40$ PPI)

3. EXPERIMENTAL PROCEDURE

Figure 2 is a schematic representation of the experimental setup and the thermocouples location used in the present study. The experimental setup is composed of four major parts shown in Figure 2a: a test section, a direct current generator, a data acquisition center and a microcomputer for storing and processing data (Ferfera and Madani (2019)).

The test section consists of a cavity, a closed Plexiglas container, vertical and transparent. The cavity contains the paraffin/metal foam composite sample placed vertically in contact with an electrical heat source made of a duralumin plate. An empty space of 1 cm is left above the sample due to paraffin volume expansion during the phase change. A low voltage direct current generator “constant DC 0-12V from PHYWE®” supply the heat source by an electrical power. Twelve type K thermocouples (Chromel-alumel), with a diameter equal to 0.5 mm, are used to measure the heat source and the sample studied transient temperature. Six of them are placed in the middle of the Duralumin plate and the others in the middle of the sample. The location of the thermocouples is shown in Figure 2b. The experimental installation is equipped with a “NI SCXI-1001” DAQ acquisition system developed by National Instrument® (NI), a computer equipped with an analog acquisition card and LabVIEW is used for processing, visualization and storage of signals.

The uncertainty on the heat flow derived from the Fourier law, measurements taken as follows: thermocouples ($\pm 0.1^\circ\text{C}$) (given by the manufacturer), caliper (0.05mm), power supply ($\pm 0.1\text{V}$), and that of thermal conductivity ($\pm 0.1\text{W/m.K}$). The uncertainty in the flow is estimated at 12.55%.

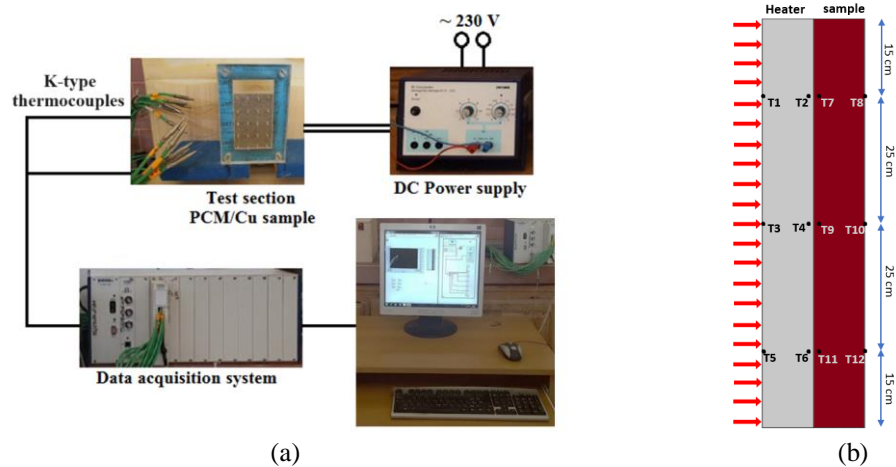


Figure 2. Experimental setup (a) Schematic illustration of the experimental setup (b) location of the thermocouples

4. RESULTS AND DISCUSSION

Figure 3 shows the transient temperature of Paraffin/Cu-foam composite sample with porosity and pore density of 96.1 % and 40PPI, respectively. During the charging process, shows in Figure 1a, the heater transient temperature curves (T1-T6) are confused, that means the temperature distribution on the heater is uniforme, contraly of the composite sample, it's shows that the transient temperature distribution is not uniforme through the sample. paraffin melting phase can be distinguished between $t=2000\text{s}$ and $t=7000\text{s}$, the temperature gradient has decreased and the transient temperature variation slowdown, during this phase paraffin melts and stores thermal energy in latent heat form. Figure 3b shows the paraffin solidification process. the heater power supply is turned off and the composite sample is no longer subjected to a uniforme heat flow. the figure shows that the temperature curves (T1 to T12) are all combined, this shows that the temperature distribution is uniforme and paraffin solidification process is uniforme trough the sample.

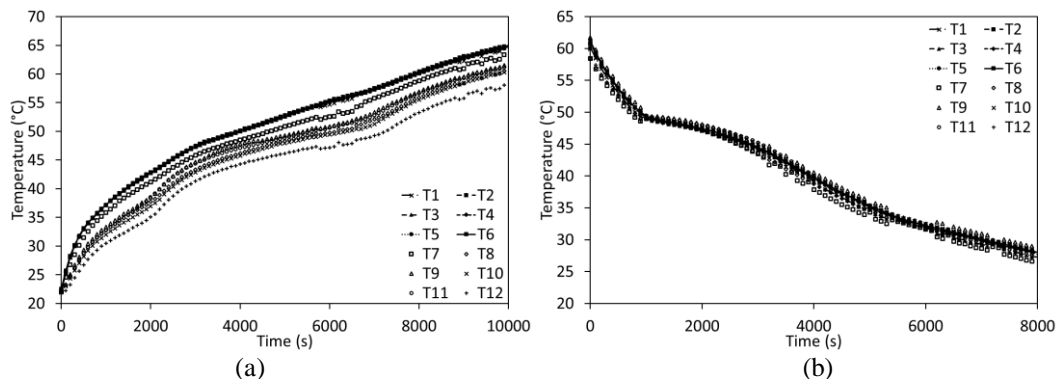


Figure 3. Paraffin/Cu-foam (96.1 %, 40PPI) sample transient temperature (a) charging and (b) discharging process
Figure 4 shows the Nusselt number based on the fiber diameter variation with pore density. It shows that the metal foam pore density influences the natural convection of liquid paraffin. The nusselt number based on fiber diameter decreases

with when the PPI increased. Because, when the number of PPI increases the pores decrease, hence the interstitial surface between the copper foam ligaments and the paraffin increases, this leads to conductive heat transfer is more dominant for higher pore densities than convective heat transfer.

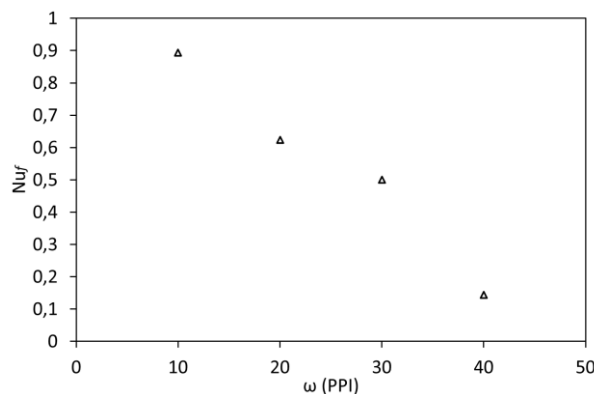


Figure 4 the Nusselt number based on the fiber diameter variation with pore density.

5. CONCLUSIONS

In this study, paraffin/copper foam composite samples of different pore density are prepared by the impregnation process. an experimental procedure is carried out on the study of heat transfer on composite samples. Transient temperatures were measured for the melting (charging) and solidification (discharging) process of paraffin. the Nusselt number based on the fiber diameter is studied, and it is found that the conductive transfer is more dominant for higher pore numbers.

6. REFERENCES

- Al-Aasam, A.B., Ibrahim, A., Sopian, K., Abdulsahib M, B., and Dayer, M. (2023). Nanofluid-based photovoltaic thermal solar collector with nanoparticle-enhanced phase change material (Nano-PCM) and twisted absorber tubes. *Case Studies in Thermal Engineering* 49, 103299.
- Ferfera, R.S., and Madani, B. (2020). Thermal characterization of a heat exchanger equipped with a combined material of phase change material and metallic foams. *International Journal of Heat and Mass Transfer* 148, 119162.
- Ferfera, R.S., Madani, B., and Serhane, R. (2020a). Investigation of heat transfer improvement at idealized microcellular scale for metal foam incorporated with paraffin. *International Journal of Thermal Sciences* 156, 106444.
- Ferfera, R.S., Madani, B., and Serhane, R. (2020b). Investigation of Heat Transfer Performance of PCM/Copper Foam Composite Heat Sink for Electronic Devices. In *Proceedings of the 11th International Conference on Porous Metals and Metallic Foams (MetFoam 2019)* (Springer), pp. 161-170.
- Huang, X., Sun, C., Chen, Z., and Han, Y. (2021). Experimental and numerical studies on melting process of phase change materials (PCMs) embedded in open-cells metal foams. *International Journal of Thermal Sciences* 170, 107151.
- Kazem, H.A., Al-Waeli, A.A., Chaichan, M.T., Sopian, K., Ahmed, A.-A., and Wan Nor Roslam, W.I. (2023). Enhancement of photovoltaic module performance using passive cooling (Fins): A comprehensive review. *Case Studies in Thermal Engineering* 49, 103316.
- Mahdi, J.M., Mohammed, H.I., Talebizadehsardari, P., Ghalambaz, M., Sh. Majdi, H., Khan, A., Yaïci, W., and Giddings, D. (2021). Simultaneous and consecutive charging and discharging of a PCM-based domestic air heater with metal foam. *Applied Thermal Engineering* 197, 117408.
- Martínez, A., Carmona, M., Cortés, C., and Arauzo, I. (2023). Experimentally based testing of the enthalpy-porosity method for the numerical simulation of phase change of paraffin-type PCMs. *Journal of Energy Storage* 69, 107876.
- Noghrehabadi, A., Samimi Behbahan, A., Wong, C., and Behbahani-Nejad, M. (2021). Investigation on the effect of metal foam properties on the PCM melting performance subjected to various heat fluxes. *Journal of Computational Applied Mechanics* 52, 320-331.
- Safari, V., Kamkari, B., Hewitt, N., and Hooman, K. (2024). Experimental comparative study on thermal performance of latent heat storage tanks with pin, perforated, and rectangular fins at different orientations. *Thermal Science and Engineering Progress* 48, 102401.
- Sodhi, G.S., and Muthukumar, P. (2021). Compound charging and discharging enhancement in multi-PCM system using non-uniform fin distribution. *Renewable Energy* 171, 299-314.

EFFECTS OF REFRIGERANT CHARGE IN HEAT PUMP ON THERMOHYDRAULIC PERFORMANCE OF MICROCHANNEL EVAPORATOR

Georges El Achkar^{a,b,*}, Jalal Faraj^{b,c}, Mahmoud Khaled^{b,c}

^aInternational Center in Fundamental and Engineering Thermophysics, Tianjin University of Commerce, Tianjin, China

^bEnergy and Thermo-Fluid Group, Lebanese International University (LIU), Bekaa, Lebanon

^cEnergy and Thermo-Fluid Group, The International University of Beirut (BIU), Beirut, Lebanon

*georges_elachkar@hotmail.com

Keywords: Heat pump, microchannel evaporator, heat transfer, pressure drop, coefficient of performance

1. INTRODUCTION

The use of microchannel heat exchangers (MCHEs) is considered as one of the most efficient thermal control solutions in the 21st century thanks to their high compactness, represented by the high ratio of their heat transfer surface area to their volume (Kadam and Kumar, 2014). Therefore, numerous research works were lately conducted on single-phase and two-phase flows in MCHEs in order to characterise and optimise their thermohydraulic performance (Asadi *et al.*, 2014).

The studies on the MCHEs available in the literature were mostly focused on the effects of the configurations and the boundary conditions on the flow distribution and pattern, heat transfer and pressure drop. Dang and Teng (2011) experimentally studied the influence of the substrate thickness, cross-sectional area and inlet/outlet locations on the thermohydraulic performance of counter-flow MCHEs, and found that the I-type heat exchanger had the best performance. El Achkar *et al.* (2011,2012,2013,2014) experimentally investigated the flow and heat transfer laws during flow condensation in horizontal circular and square cross-section single microchannels and the effects of the hydrodynamic coupling between four horizontal microchannels on the flow distribution. Huang *et al.* (2016) experimentally determined the heat transfer and pressure drop during flow boiling of a new environmentally friendly refrigerant R1233zd(E) in a parallel microchannel evaporator. Nevertheless, much fewer studies were conducted on MCHEs operating in heat pumps (Kim and Braun, 2012), where several parameters (particularly the refrigerant charge) have significant effects on their thermohydraulic performance.

In this work, the effects of the refrigerant charge in a heat pump on the thermohydraulic performance of a microchannel evaporator are experimentally investigated. The experimental setup and procedure are first introduced, and the determined thermohydraulic parameters of the microchannel evaporator (temperature distribution, pressure drop) are then presented and analyzed.

2. EXPERIMENTAL SETUP AND PROCEDURE

The experimental setup (Figure 1a) mainly consists of a compressor (Tecumseh, model TFH2480Z), an air-cooled condenser (M3 Technology, model 783670-1), a homemade reservoir, a filter drier (Emerson, model EK 053), a Coriolis mass flow meter (U-ideal, model DMF-1), a thermostatic expansion valve (Sporlan, model KT-43-RZ), a test section, a temperature-controlled chamber and a data acquisition system (Yokogawa, model MX100).

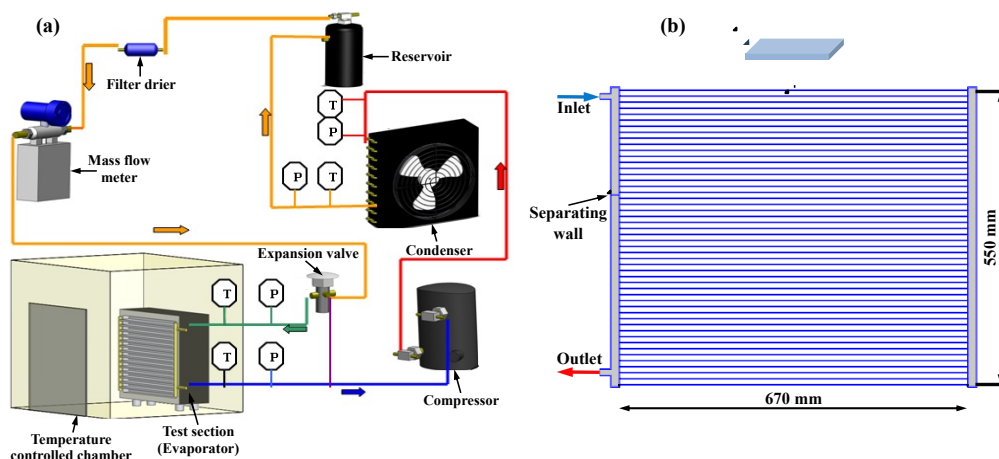


Figure 1. Schematic diagrams of (a) the experimental setup and (b) the microchannel evaporator.

Prior to the experiments, the refrigerant (R404A) is first perfectly degassed, while the loop of the heat pump is put under vacuum, and then released in the reservoir with the desired charge.

When the heat pump is turned on, the liquid R404A leaving the reservoir passes through the filter dryer, the Coriolis mass flow meter and the thermostatic expansion valve, where its pressure decreases. Downstream the expansion valve, the R404A passes through the test section placed in the thermally insulated temperature-controlled chamber. This test section is an aluminum evaporator consisting of 52 parallel rectangular cross-section microchannels, whose ends are connected to two vertical cylindrical manifolds of inner diameter 20 mm (Figure 1b). These microchannels have an inner height of 0.7 mm, an inner width of 15 mm and a length of 670 mm. The gap between two adjacent microchannels is 10 mm and filled with aluminium fins. The R404A inlet and outlet ports are located respectively in the upper and lower parts of one manifold, in which a horizontal wall is fitted to separate the incoming and outgoing fluid. The microchannels are heated thanks to a ventilator blowing air at a rate of $4350 \text{ m}^3 \cdot \text{h}^{-1}$ across them. The vapour leaving the evaporator passes through the compressor, where its pressure increases, and the condenser before returning into the reservoir.

Calibrated T-type thermocouples of 0.5 mm diameter are implemented in the temperature-controlled chamber, at the inlet and the outlet of the evaporator and the condenser, and at the middle and the ends of the microchannels. Absolute pressure transducers (model ET-1000) are implemented at the inlet and the outlet of the evaporator and the condenser in order to measure the pressure drop inside them. The measurements ranges and uncertainties of the sensors are reported in Table 1. All data are collected using a data acquisition system consisting of a data logger, an interface card and a computer.

Table 1. Measurements ranges and uncertainties of the sensors.

Sensor	Range	Uncertainty
Mass flow meter	0–500 $\text{kg} \cdot \text{h}^{-1}$	$\pm 0.2 \%$
T-type thermocouple	-185–300 $^{\circ}\text{C}$	$\pm 0.5 \text{ }^{\circ}\text{C}$
Absolute pressure transducer	0–120 bar	$\pm 1 \%$

3. RESULTS AND ANALYSIS

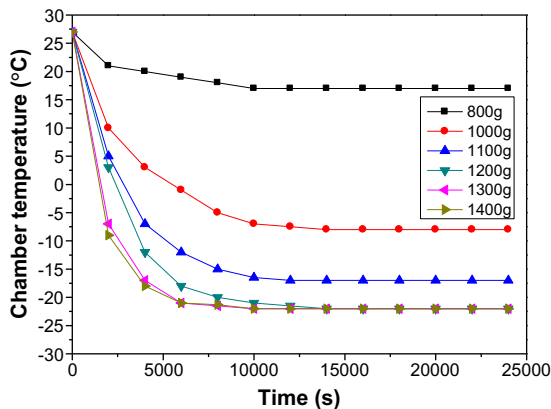


Figure 2. Evolutions of the chamber temperature as a function of time for an ambient chamber temperature of $27 \text{ }^{\circ}\text{C}$ and different R404A charges.

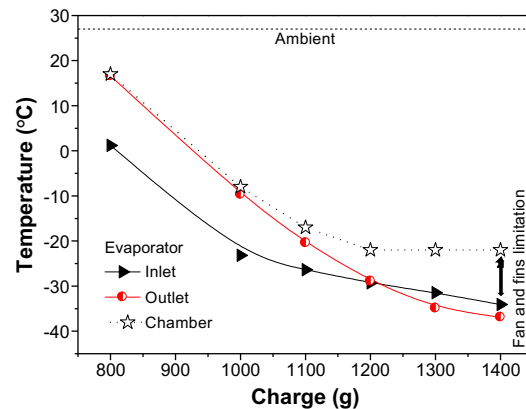


Figure 3. Evolutions of the evaporator and the chamber steady state temperatures as a function of R404A charge.

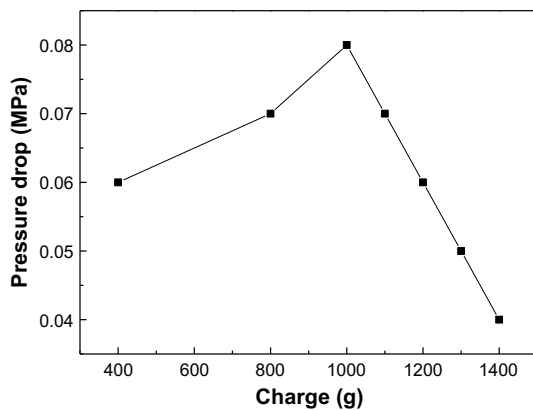


Figure 4. Evolution of the evaporator pressure drop as a function of R404A charge.

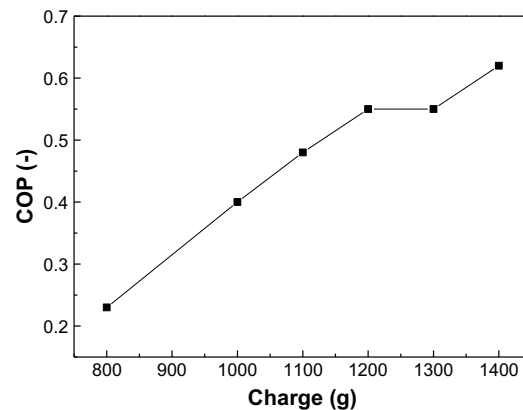


Figure 5. Evolution of the heat pump COP as a function of R404A charge.

Figure 2 shows the evolutions of the chamber temperature as a function of time for an ambient chamber temperature of 27 °C and different R404A charges. The chamber refrigeration rate increases and the time needed to reach a steady state chamber temperature (i.e., characteristic time) decreases with the R404A charge increase regardless of the ambient chamber temperature (chosen to be greater than the R404A saturation temperature in the evaporator). These two aspects are due to the increase of the heat power recovered by the R404A. However, for a R404A charge greater than 1200 g, the steady state chamber temperature reaches a plateau of -23 °C (Figure 3) because of the limitation of the evaporator refrigeration capacity due to the limiting external heat transfer coefficient between the air and the external surface of the evaporator.

Figure 4 shows the evolution of the evaporator pressure drop as a function of the R404A charge. This pressure drop first increases and then decreases with the R404A charge increase, with a maximum value obtained at a R404A charge of 1000 g. This trend can be explained by the two-phase flow patterns in the channels, which strongly depend on the refrigerant mass flux and have a significant effect on its pressure drop. Indeed, for a low mass flux, the flow pattern in a microchannel is annular, while for a high mass flux, the flow pattern becomes slug/plug and/or bubbly.

Figure 5 shows the evolution of the heat pump coefficient of performance (COP) as a function of the R404A charge. Although this COP is maximum at a charge of 1400 g, the optimal thermohydraulic performance of the evaporator can be considered at a charge of 1200 g, which corresponds to its thermal limitation.

4. CONCLUSIONS AND PERSPECTIVES

The effects of R404A charge in a heat pump on the thermohydraulic performance of a microchannel evaporator were experimentally investigated. Proportional and inversely proportional relationships were respectively found between the chamber refrigeration rate and the characteristic time, on the one hand, and the R404A charge, on the other hand. An increasing then decreasing pressure drop with the R404A charge increase was found, with a maximum value obtained at a R404A charge of 1000 g. An optimal operating point of the evaporator was obtained at a R404A charge of 1200 g, for which the COP of the heat pump is 0.55.

As perspectives to this work, the effects of R404A charge in the heat pump on the thermohydraulic performance of the same MCHE but used as a condenser will be investigated.

REFERENCES

- Asadi, M., Xie, G. and Sunden, B., 2014. "A review of heat transfer and pressure drop characteristics of single and two-phase microchannels". *International Journal of Heat and Mass Transfer*, Vol. 79, pp. 34–53.
- Dang, D. and Teng, J.-t., 2011. "The effects of configurations on the performance of microchannel counter-flow heat exchangers—An experimental study". *Applied Thermal Engineering*, Vol. 31, pp. 3946–3955.
- El Achkar, G., Lavieille, P., Lluç, J. and Miscevic, M., 2011. "Heat transfer and flow distribution in a multichannel microcondenser working at low mass fluxes". *International Journal of Heat and Mass Transfer*, Vol. 54, pp. 2319–2325.
- El Achkar, G., Lavieille, P. and Miscevic, M., 2012. "Loop heat pipe and capillary pumped loop design: about heat transfer in the isolated bubbles zone of condensers". *Applied Thermal Engineering*, Vol. 33-34, pp. 253–257.
- El Achkar, G., Miscevic, M. and Lavieille, P., 2013. "Flow patterns and heat transfer in a square cross-section micro condenser working at low mass flux". *Applied Thermal Engineering*, Vol. 59, pp. 704–716.
- El Achkar, G., Miscevic, M. and Lavieille, P., 2016. "An experimental study on slug-bubbly condensation flows at low mass velocity in a square cross-section micro-channel". *Heat Transfer Engineering*, Vol. 37, pp. 1181–1189.
- Huang, H., Borhani, N. and Thome, J. R., 2016. "Experimental investigation on flow boiling pressure drop and heat transfer of R1233zd(E) in a multi-microchannel evaporator", *International Journal of Heat and Mass Transfer*, Vol. 98, pp. 596–610.
- Kadam, S. T. and Kumar, R., 2014. "Twenty first century cooling solution: microchannel heat sinks". *International Journal of Thermal Sciences*, Vol. 85, pp. 73–92.
- Kim, W. and Braun, J. E., 2012. "Evaluation of the impacts of refrigerant charge on air conditioner and heat pump performance". *International Journal of Refrigeration*, Vol. 35, pp. 1805–1814.

ENHANCEMENT USAGE OF THERMOELECTRIC GENERATOR MODULES FOR HYBRID SYSTEMS: EXPERIMENTS AND ANALYSIS

Jalal Faraj^{a,b}, Georges El Achkar^{a,c,*}, Hicham El Hage^a, Rani Taher^d, Mahmoud Khaled^{a,b}

^aEnergy and Thermo-Fluid Group, Lebanese International University, LIU, Bekaa, Lebanon

^bEnergy and Thermo-Fluid Group, The International University of Beirut BIU, Beirut, Lebanon

^cInternational Center in Fundamental and Engineering Thermophysics, Tianjin University of Commerce, Tianjin, China

^dCollege of Engineering and Technology, American University of the Middle East, Kuwait

*georges_elachkar@hotmail.com

Keywords: Thermoelectric module, hybrid system, heat recovery, renewable energy, experiments

1. INTRODUCTION

Thermoelectric generators (TEGs) are a promising technology that can be used in a variety of industries to transform heat differentials into electrical power. (TEGs) are highly suitable for waste heat recovery in industrial processes, automobile exhaust systems, and renewable energy systems. They work mainly by the Seebeck effect to create electricity from a temperature gradient. TEGs effectively convert heat into electricity without the need for moving components or emissions, which improves energy efficiency and lessens the impact on the environment. The relatively low power output of thermoelectric generators (TEGs) is one of the main problems that deals with this type of technology. Even though TEGs can convert heat differentials into energy, they frequently have low power generation capacities, which can prevent them from being widely used in some applications. In this context, the present paper discusses an experimental enhancement of usage of TEG modules for outdoor situations where the heating source is the sunlight. For this reason, an experimental setup is developed where four experimental configurations that describe the usage enhancement of TEG modules are considered. The first configuration is considered as the reference one in the present paper, where the TEG module that is used is not modified. The second configuration consist of adding a film of black body to the surface of TEG that is exposed to the sun light. The third configuration is the reference one but adding a container of oil on the surface that is exposed to the sunlight. The fourth one consist of combining the oil tank and the black body surface together and then compared with only black body surface. Noting here that the black body film is cold asphalt oil and the cold source in the present study is provided by a water circulation system. Finally, the experimental measurements in each modified configuration is compared with the reference one. Based on these measurements, the output power is measured using a digital multimeter and it was noticed that the TEG output power is enhanced remarkably when the black body and the oil container are used. In addition, it was noticed that the black body film and the oil container could store energy which permits to increase the temperature difference and also enhance the efficiency of the TEG modules by increasing the output power.

2. MATERIALS AND METHODS

Different experiments were performed in 4 consecutive days in order to maintain a similar weather condition during the measurements. The measurements are performed from 8:00 AM till 8:00 PM during the summer days. The figure 1 summarizes the studied configurations and shows the oil tank used in figure 1.a where the TEG modules with black body surface is shown in Figure 1.b. The Figure 1.c shows the last configuration of combining oil tank and the black body film to be compared with the black body case. This case is essential to clarify the effect of oil tank. The water circulation was used in these experiments in order to maintain the cold surface of TEG modules at 20 °C. This is provided by a water tank and piping system where the water is circulating through the plate. Accordingly, the TEG modules were placed at the upper surface of the cold plate. The water flow rate is ensured by the hydrostatic pressure. The TEG used in the present study are Bismuth Tin type (BiSn) and their dimensions are 40x40 mm².

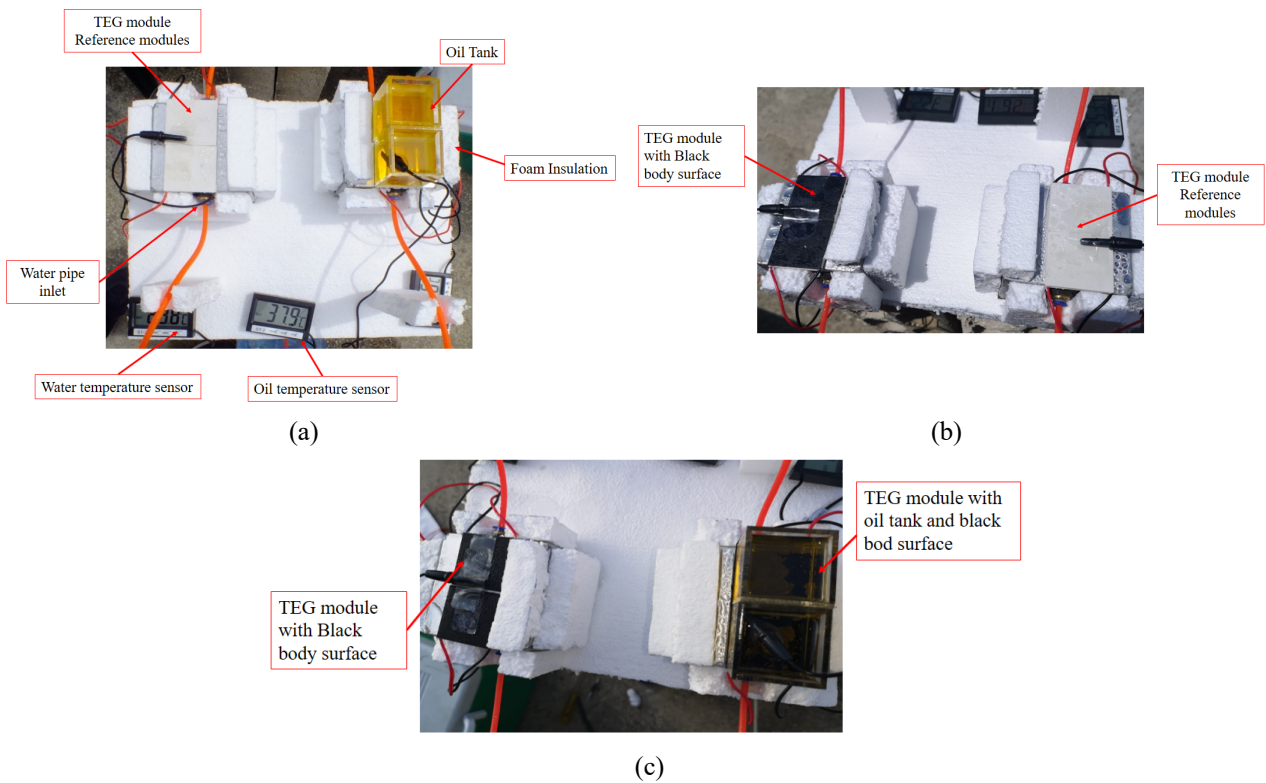


Figure 1: (a) TEG with oil tank (b) TEG with black body surface (c) TEG with black body and oil tank.

3. MAIN RESULTS

In this part, the authors would present the main important results obtained from the present study whereas in the extended version all obtained results will be presented and discussed. The figures below (2, 3 and 4) present the output power obtained by the TEG modules for each configuration presented in the previous section. It could be noticed that a remarkable enhancement of the TEG usage is observed. Accordingly, at peak time (14:00), the black body surface increases the output power 6 times when it is compared with reference TEG module. Moreover, the oil surface increases the output power 3 times when it is compared with reference TEG module. Finally, the output power of combined system (Oil Tank and Black surface) compared with the only black surface is presenting more advantages. In addition to these brief results, an energy analysis will be discussed in the extended version because the time plays an important variable in each configuration.

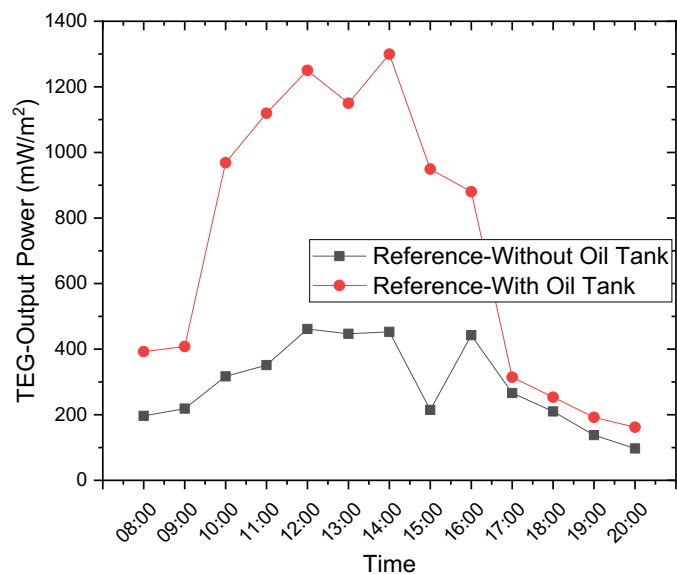


Figure 2. Comparison of the variation of output power of TEG with respect to time for TEG with and without oil Tank.

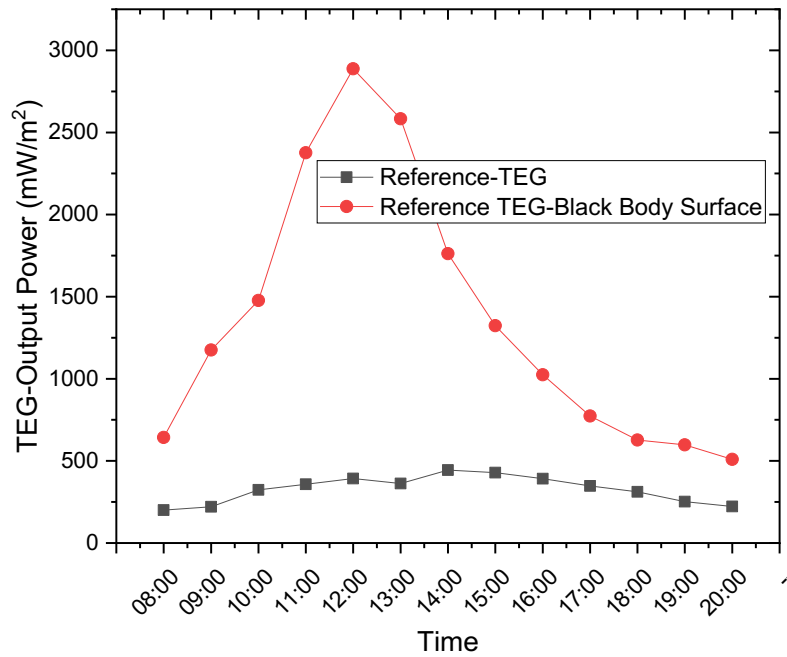


Figure 3. Comparison of the variation of output power of TEG with respect to time for TEG black and white surfaces.

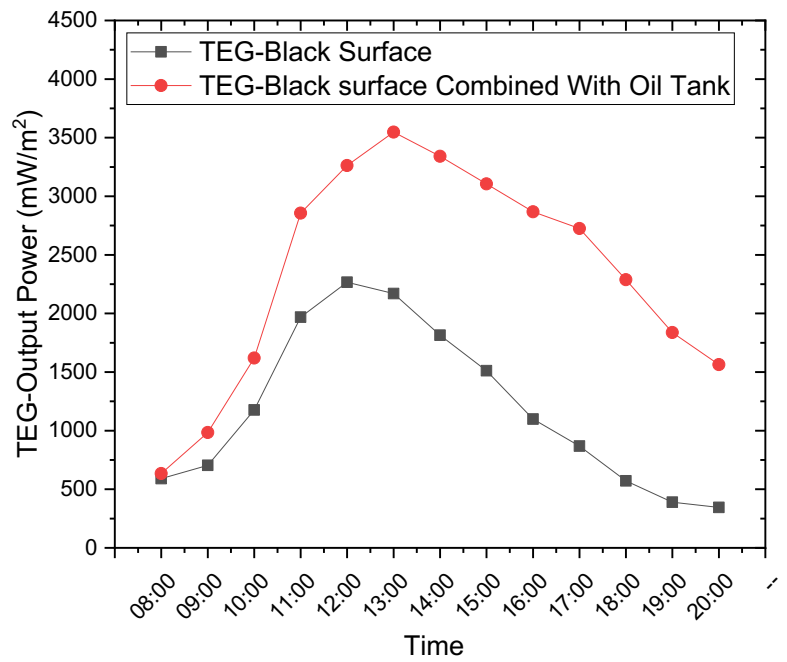


Figure 4. Comparison of the variation of output power of TEG with respect to time for TEG with black surface and TEG module with oil tank combined with black surface.

OPTIMIZING CONCRETE CONDUCTIVITY WITH COPPER AND BRASS FILLERS IN UNDER FLOOR HEATING

Ahmad Al Takash^{a,b}, Georges El Achkar^{a,c,*}, Jalal Faraj^{a,b}, Mahmoud Khaled^{a,b}

^aEnergy and Thermo-Fluid Group, Lebanese International University, LIU, Bekaa, Lebanon

^bEnergy and Thermo-Fluid Group, The International University of Beirut BIU, Beirut, Lebanon

^cInternational Center in Fundamental and Engineering Thermophysics, Tianjin University of Commerce, Tianjin, China

*georges_elachkar@hotmail.com

Keywords: Underfloor heating, heat transfer, sustainability, material selection, thermal conductivity

1. ABSTRACT

This study focuses on the impact of material composition and thermal conductivity on the heat transfer behavior in underfloor heating systems. With an emphasis on their various heating techniques, the two main categories of underfloor heating systems are hydronic and electric. By assessing the effect of various filler materials on thermal conductivity, the study seeks to improve the efficiency of heat transmission. A customized experimental setup was used to mix concrete specimens with brass and copper at various percentages, and then to investigate the thermal behaviors of the results. The findings showed that specimens with 20% copper had the highest thermal conductivity (5.357 W/m K) among other specimens which had lowest temperature difference (45 K) and reached steady state in time less than other specimens (4000 s). This emphasized how important material composition and choice are to maximizing heat transmission. The study offers recommendations for improving energy-efficient underfloor heating solutions and helps create useful design standards for such systems, which ultimately increase comfort and energy efficiency in commercial and residential areas.

2. MATERIALS AND METHODS

2.1. CONCRETE SPECIMENS AND THERMAL CONDUCTIVITY MEASUREMENT

The specimens are composed of concrete. Brass and copper filler are applied at various percentages of cement mass (0%, 10%, 15%, and 20%). This experiment employed a linear heat conduction module. Cool water is pushed through the intake and circulated around the specimens to absorb heat and maintain a steady temperature during the experiment. The hot water drains out of the outlet. In addition, thermocouples are connected to a heat transfer service unit that reads and monitors temperature fluctuation across the specimen. Specimens and insulation preparation is shown in Figure 1.



Figure 1. Specimens, fillers and thermal insulation preparation.

2.2. MAIN GOVERNING EQUATIONS

The main equation that will be used is the heat transfer rate of conduction (q) in (W) (Fourier's law of conduction):

$$q = -kA \frac{\Delta T}{\Delta Y} \quad (1)$$

Where k is the thermal conductivity in ($\text{W m}^{-1} \text{K}^{-1}$), A is the cross-sectional area of the specimen in (m^2), ΔT is the temperature difference between the thermocouples in (K), ΔY is the height of the specimen in (m).

The electric power to the heater (P) in (W) is calculated using the following equation:

$$P = VI \quad (2)$$

Where V is the voltage in (V) and I is current in (A).

The percentage of enhancement in thermal conductivity (% e) is calculated using the following equation:

$$\%e = \frac{K_f - K_{ref}}{K_{ref}} \times 100 \quad (3)$$

K_{ref} is the conductivity for the reference specimen (100% concrete) and K_f denotes the conductivity of the specimen containing fillers.

2.3. SAMPLE COMPOSITION AND MASS CALCULATION

The specimen's composition, including the concrete, brass, and copper used, is displayed in Table 1. The mass of each material is found based on the specimen's total mass (50 g) and the associated percentages. Each sample's element composition is indicated in the following table.

Table 1. Composition and mass distribution of specimens.

Samples	% of Concrete	% of Brass	% of Copper	Mass of Brass	Mass of Copper	Mass of Concrete
Sample 1	100	0	0	0	0	50
Sample 2	90	10	0	5	0	45
Sample 3	85	15	0	7.5	0	42.5
Sample 4	80	20	0	10	0	40
Sample 5	90	0	10	0	5	45
Sample 6	85	0	15	0	7.5	42.5
Sample 7	80	0	20	0	10	40
Sample 8	85	10	5	5	2.5	42.5
Sample 9	85	5	10	2.5	5	42.5

3. RESULTS AND ANALYSIS

As illustration of the results, the temperature variations of the reference concrete sample and concrete sample with 20% copper over time are depicted in figure 2, showing steady increases at specific intervals. 100% concrete sample starts at $\Delta T = 0$ and stabilizes at 58 °C after 8000 seconds while 20% copper concrete sample stabilizes at 46 °C after 4000 seconds. The ΔT values for specimens measured at 2000 seconds are 30 °C for concrete, 35 °C for 20% copper. This underscores the impact of copper content on heat transfer rates and material heat conduction properties. These behaviors were also noticed for the other enhanced copper and brass filled samples.

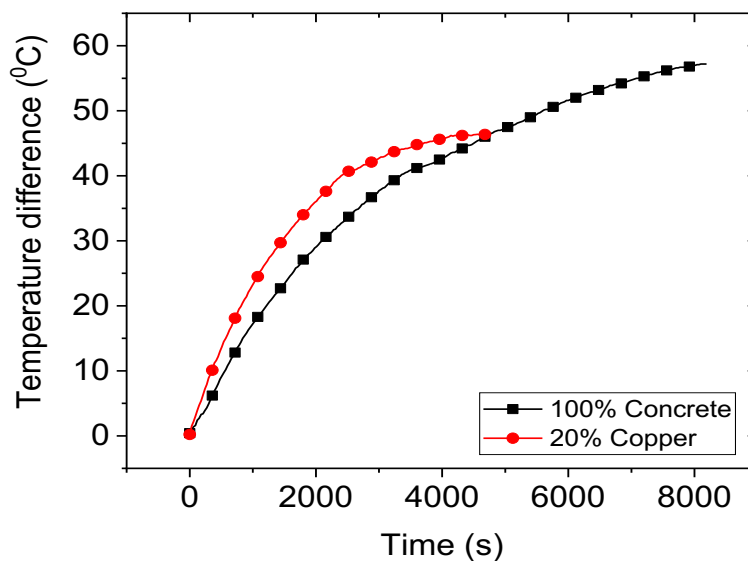


Figure 2. Variation of temperature over time: copper (20%) versus concrete (100 %)

The findings highlight the influence of material composition and thermal properties on heat conduction behavior. Higher thermal conductivity materials facilitate quicker heat transfer. Moreover, the improvement in thermal conductivity as a percentage for each specimen over 100% concrete, the reference material, percentage of enhancement in thermal

conductivity for the specimens are also shown in Figure 3. This improvement % offers information on the effects of various materials and compositions on heat transfer efficiency. This figure shows the percentage of enhancement in thermal conductivity for each specimen compared to the 100% Concrete reference. The relationship between temperature difference (ΔT) and thermal conductivity (k) is evident, with higher thermal conductivity values exhibiting lower temperature differences. This indicates that materials with higher thermal conductivity are more effective at conducting heat and maintaining smaller temperature gradients along their length. Comparing ΔT values and enhancement percentages across specimens highlights the importance of material choice and composition in designing systems with optimized heat conduction properties. As a result, this specimen (20% Copper) had the biggest increase in thermal conductivity (17.32%) when compared to the reference material. The fact that the measured ΔT was lower indicates that the copper addition greatly increased heat conduction, making it the most efficient of all the examples.

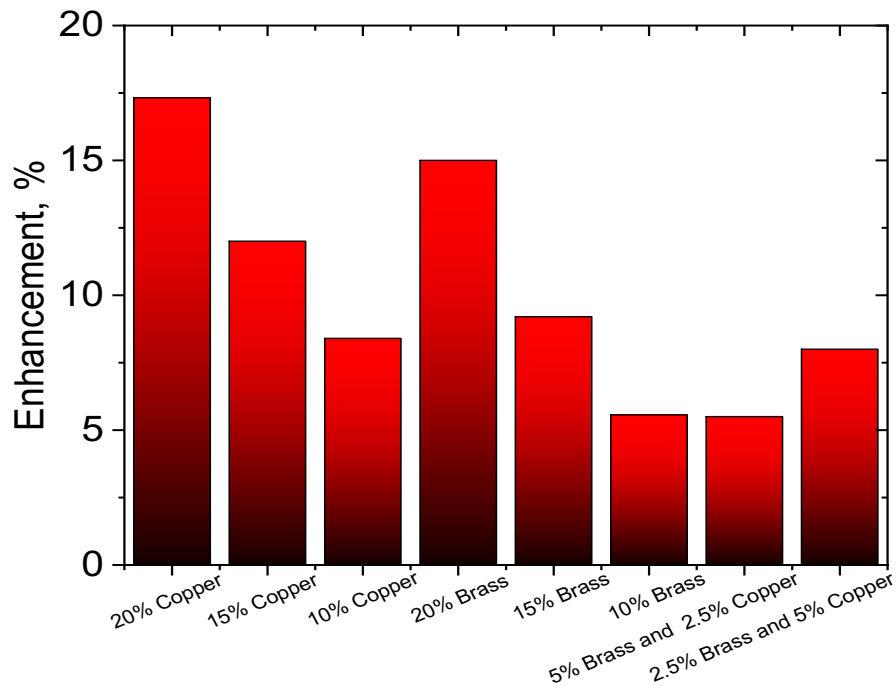


Figure 3. Enhancements in thermal conductivity.

Based on the experimental study outcomes, a case study using 20% copper configuration is considered in a real under floor heating enhancement and compared to a reference case of 100% concrete (Table 3). The main note from Table 3 is that the heat rate increased by 7.45W for each $1m^2$.

Table 3. Resistance of flooring by using 100% concrete and concrete with copper.

	L (mm)	A (m^2)	K ($\frac{W}{m.K}$)	R ($\frac{m^2.K}{W}$)	Q (W)
Tile	55 (mm)	1	1.7	0.03	
Tile plastering	50 (mm)	1	1.1	0.04	
Concrete	85 (mm)	1	4.566	0.019	213.48
Concrete with Copper	85 (mm)	1	5.357	0.016	220.93

4. CONCLUSION

In conclusion, the experimental study of the linear heat transfer unit's behavior and heat transfer properties yielded important new information on the influence of material composition and thermal conductivity on heat conduction efficiency. The findings showed that materials with increased thermal conductivity, such as those with copper or brass additions, display more effective heat transmission with fewer temperature variations throughout their length. This emphasizes how crucial material composition and selection are when building systems for the best possible heat conduction. The results offer useful information for engineering applications where regulating heat transport is essential.

THERMODYNAMIC ANALYSIS OF A COMPRESSED CO₂ ENERGY STORAGE SYSTEM WITH NON-INSULATED TANKS

Florent Dewevre^{a,b*}, Clément Lacroix^a, Khaled Loubar^a, Sébastien Poncet^b

^a Joint CNRS Unit GEPEA, IMT Atlantique, Nantes, France

^b Department of Mechanical Engineering, Université de Sherbrooke, Sherbrooke, Canada

*florent.dewevre@imt-atlantique.fr

Keywords: Carbon dioxide, Energy storage, Renewable Energy, Compressed gas

1. INTRODUCTION

In order to decarbonize the energy production, renewable energies are spreading all over the world. For electricity production, solar and wind energy sources appear as a necessary solution in the energetic mix (Gallo et al., 2016). To palliate for their intermittent nature, energy storage systems are deemed necessary. Among them, Compressed CO₂ Energy Storage (CCES) show good potential to be non-geographical constrained large-scale energy storage with low environmental impact and cost. They have been proposed to cope with some issues of compressed air energy storage and liquid air energy storage. Indeed, CO₂ allows a better energy density than CAES, allowing aboveground reservoirs without operating at cryogenic temperatures (Wang et al., 2015). This new kind of energy storage are at the earliest stage of research. Currently, there is a lack of dynamic studies to better understand their behavior. To begin to bridge this gap, a thermodynamic analysis of a CCES is conducted in this paper, assuming the dynamic behavior and considering heat exchanges with the surroundings.

2. CCES description and thermodynamic modelling

The CCES studied in this paper is represented in Figure 1 and is working as follows:

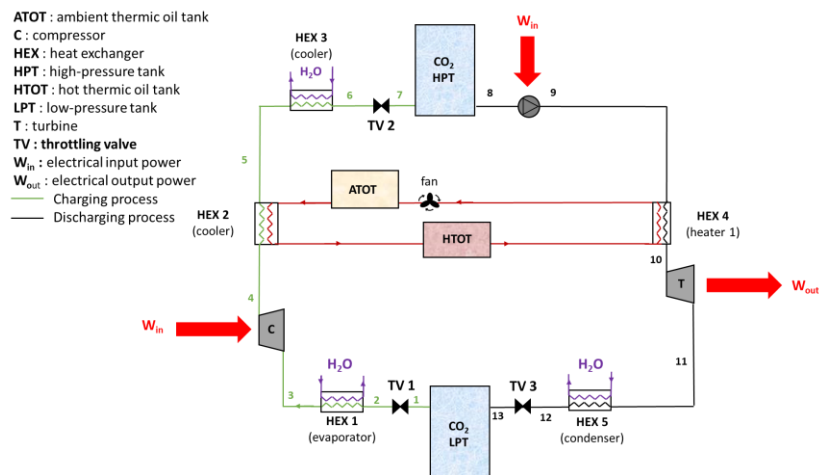


Figure 1 : Layout of the studied CCES

Charging process: Liquid CO₂ leaving the LPT is expanded and evaporated in HEX1. Then, the gaseous CO₂ is compressed by the compressor using the available electricity. The hot supercritical CO₂ at the outlet is cooled in HEX2 and the heat is stored through an oil thermal storage. Before entering the HPT, the supercritical CO₂ is cooled under the critical temperature in HEX3.

Discharging process: The CO₂ leaving the HPT is pumped to the targeted turbine inlet pressure and is heated up by the compression heat recovered in the charging phase. The hot supercritical CO₂ is then expanded by the turbine and liquefied in HEX5 before entering LPT.

For simplicity, the following assumptions are considered in the thermodynamic model: thermodynamic equilibrium in the CO₂ tanks, pressure neglected in the pipes and heat exchangers, thermal exchanges are considered only with the CO₂ tanks, inlet water flow and oil in the ATOT are considered at the ambient temperature, and turbomachineries operate with a constant isentropic efficiency.

In this paper, complete charges and discharges will be investigated. A charge is set as finished when the maximum pressure is reached or when there is liquid CO₂ in the LPT yet. A discharge is set as finished when there is no liquid remaining in the HPT.

CO₂ tanks are modelled by applying the mass conservation and the energy conservation based on the first law of thermodynamics:

$$V_{\text{tank}} \frac{d\rho_{\text{CO}_2}}{dt} = -\dot{m}_{\text{CO}_2,\text{out}} + \dot{m}_{\text{CO}_2,\text{in}} \quad (1)$$

with ρ_{CO_2} the CO₂ density inside the tank (kg/m³), V_{tank} the tank's volume (m³) and \dot{m}_{CO_2} the CO₂ mass flow rate (kg/s).

$$\frac{d(m_{\text{CO}_2} u_{\text{CO}_2})}{dt} = -\dot{m}_{\text{CO}_2} h_{\text{out}} + \dot{m}_{\text{CO}_2} h_{\text{in}} + \dot{Q} \quad (2)$$

with u_{CO_2} the CO₂ internal energy (kJ/kg), h_{out} the outlet enthalpy (kJ/kg), h_{in} the inlet enthalpy (kJ/kg) and \dot{Q} the heat power of the heat exchange between the CO₂ tanks and the ambient.

The heat transfer coefficient to calculate \dot{Q} is calculated with the Nusselt number through a vertical wall (Bergman et al., 2018). HEX 2 and 4 are modeled with a heat exchange efficiency of 85%, while HEX1 and HEX5 with 95% efficiency. The heat transfer fluid mass flow rate is set to have a minimum of 5 K pinch point temperature. Turbomachineries are modeled with an 85% isentropic efficiency. The expansion in throttling valves is assumed as isenthalpic. The outlet pressure of TV1 is fixed at 4 MPa. If the pressure in the LPT is below 6.5 MPa, the outlet pressure of TV3 is fixed to this value, otherwise the outlet pressure is set to the LPT pressure one.

Two evaluation criteria will be examined in this work. The RTE is defined as the output electricity during the discharging phase over the input energy during the charging phase. It represents the energy efficiency of the system:

$$RTE = \frac{W_T - W_p}{W_C} \quad (3)$$

with W_T (kWh) the output turbine energy, W_p (kWh) the pump energy consumption, W_C (kWh) the compressor energy consumption.

The EVR is defined as the output energy to the storage volume. It represents the energy density of the system:

$$EVR = \frac{W_T - W_p}{V_{\text{HPT}} + V_{\text{LPT}} + V_{\text{oil}}} \quad (4)$$

with V_T (m³) the thermal oil tanks volume, V_{LPT} (m³) the LPT volume and V_{HPT} (m³) the HPT volume.

The aim of this analysis is to evaluate such CCES configuration (simplest CCES configuration), to point out the main sources of irreversibility and to quantify the effect of the ambient temperature.

3. Results and discussion

Simulations of the CCES base case are performed for 10 complete charge / discharge cycles with random waiting time (time between charge and discharge or inversely). For the base case, tanks' volume has been chosen to have a maximum pressure of 200 bar and the ambient temperature is equal to 288K. Figure 2 depicts the tanks' pressure and the exergy destructions of the CCES.

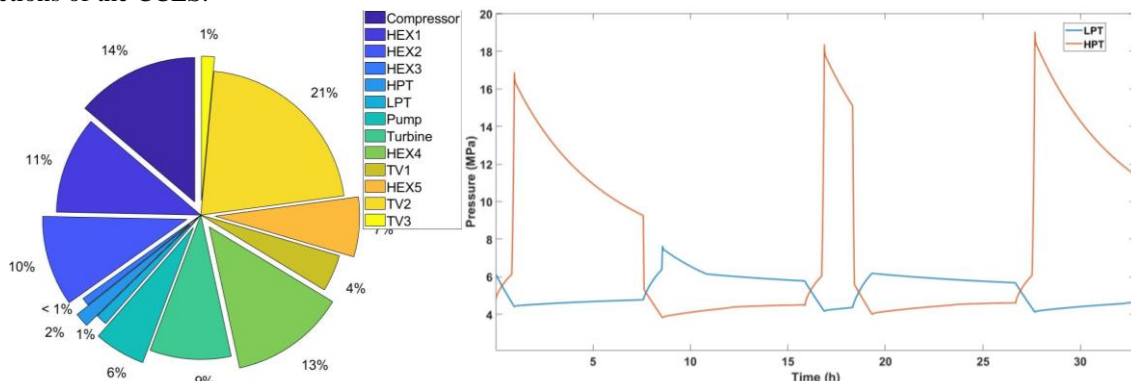


Figure 2 : Exergy destruction in the CCES and pressure changes in the LPT and HPT.

From Figure 2, it can also be seen that the component with the greatest exergy destruction is TV2 (21%) which is the throttling valve just before the HPT. In fact, at the beginning of each charge, the HPT pressure is low (around 4 MPa) implying large pressure losses through TV2. A liquid expander recovering these energy losses can be a way to improve the efficiency. Heat exchangers are responsible for 41% of the total exergy destruction with the greatest amount for HEX2 and HEX4. Then turbomachineries are responsible for 36% with most of the exergy destruction coming from the compressor (14%) and the turbine (13%). Isobaric tanks assumption considered in most of analyses in the literature, remove exergy destruction for TV2 and for the pump (30% of the total exergy destruction).

From the pressure curves in Fig.2, one can notice 2 main parts during the filling or emptying of a tank, depending of the CO₂ state. If the CO₂ is liquid or in a supercritical state, the pressure rises or decreases quickly due to the high density and low compressibility. Then, if the tanks contain gas and liquid, the slope is smoother because of the lower density and higher compressibility of the gas state. Although the targeted high pressure can be reached in the HPT in the charging mode, the non-isothermal process of the charging phase implies a reduction of the stored energy, affecting the EVR. To store more energy, more CO₂ in the system is needed. It means to charge the system several times, by waiting that the pressure decreases thanks to the thermal exchange with the ambient.

The pressures and temperatures in LPT and HPT strongly depend on the inlet / outlet enthalpy. As the water and oil are assumed at ambient temperature, a rise of the ambient temperature may have significant effects. During a filling, the warmer the ambient temperature, the higher the pressure. It means a reduce expansion ratio during the discharging phase implying a lower performance. Moreover, the complete charge and discharge of the CCES is shorter as the pressure buildup is faster, reaching the maximum pressure quicker. Another issue is also that an ambient temperature closer to the CO₂ critical temperature implies a path close to the critical point in the LPT filling process. It means higher mass flow rate to avoid pinch point in HEX5 which limits the efficiency of the heat exchange.

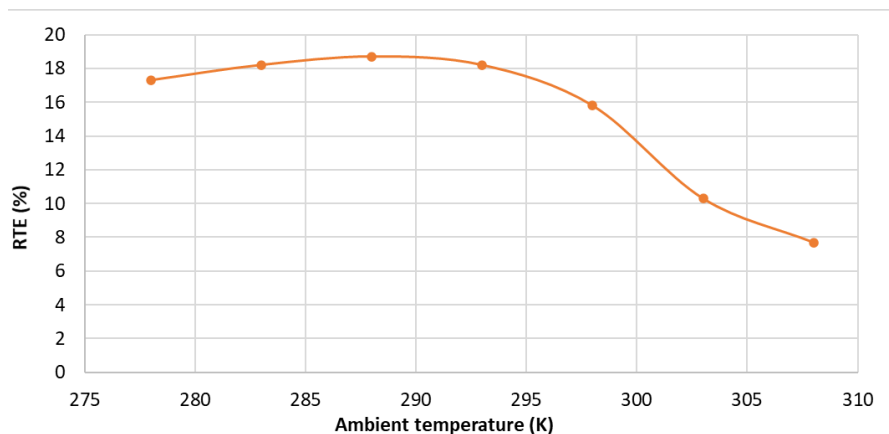


Figure 3 : RTE as a function of the ambient temperature

4. CONCLUSIONS

Thermomechanical energy storage systems like CCES are presented in the scientific literature like a promising way to store excess energy from renewable sources. In order to assess better the opportunities of such systems, a thermodynamic analysis of a CCES considering its dynamic behavior was realized. It considered a simple CCES configuration with liquefaction using ambient water. The results indicated a low RTE, especially due to the use of a pump in the discharging phase (but essential to maximize the EVR if isochoric tanks are assumed). Also, the way to use ambient source as water to liquefy CO₂ is a cheap method but the performances of the CCES can be heavily degraded if this source become too hot. One solution to limit this issue, is to have an insulated close cycle to evaporate and liquefy CO₂. Thus, the configurations of CCES operating in such way to use ambient water, should use thermal storages like in CCES working with lower pressures and temperatures.

F.D. and S.P. acknowledge the financial support of the NSERC chair established in 2014 at Université de Sherbrooke and funded by Hydro-Québec, Natural Resources Canada and Copeland Canada Inc.

5. REFERENCES

- A.B. Gallo, J.R. Simões-Moreira, H.K.M. Costa, M.M. Santos, E. Moutinho dos Santos, 2016, "Energy storage in the energy transition context: A technology review". *Renewable and Sustainable Energy Reviews*, Vol. 65, pp. 800-822.
- M. Wang, P. Zhao, Y. Wu, Y. Dai, 2015, "Performance analysis of a novel energy storage system based on liquid carbon dioxide". *Applied Thermal Engineering*, Vol. 91, pp. 812-823.
- T.L. Bergman, A.S. Lavine, F.P. Incropera, D.P. DeWitt, 2018. "Fundamentals of Heat and Mass Transfer", Wiley, 8th edition.

TAILORING SURFACE CHEMISTRY AND SURFACE ROUGHNESS TO ENABLE THE LONG-TERM STABLE DROPWISE CONDENSATION

Muhammad Jahidul Hoque^a, Nenad Miljkovic^{a,b,c,d*}

^aDepartment of Mechanical Science and Engineering, University of Illinois, Urbana, IL, USA

^bMaterials Research Laboratory, University of Illinois, Urbana, IL, USA

^cDepartment of Electrical and Computer Engineering, University of Illinois, Urbana, IL, USA

^dInternational Institute for Carbon Neutral Energy Research, Kyushu University, 744 Motoooka, Nishi-ku, Fukuoka 819-0395, Japan

*Corresponding Author: nmiljkov@illinois.edu

Keywords: climate change, hydrophobic, durable, sustainable, energy, condensation, droplet, DLC

1. INTRODUCTION

Seventy percent of global electricity is generated by steam-cycle power plants. A hydrophobic condenser surface within these plants could boost overall cycle efficiency by 2% (Champlin, 2018). This enhancement equates to an additional 1,000 TWh per year annually, or 83% of the global solar electricity production. Furthermore, this efficiency increase reduces CO₂ emissions by 460 million tons /year with a decreased use of 2 trillion gallons of cooling water per year (IEA, 2021). However, the main challenge with hydrophobic surfaces is their poor durability. Here, we show that solid microscale-thick fluorinated diamond-like carbon (F-DLC) possesses mechanical and thermal properties that ensure durability in moist, abrasive, and thermally harsh conditions. The F-DLC coating achieves this without relying on atmospheric interactions, infused lubricants, self-healing strategies, or sacrificial surface designs. Through tailored substrate adhesion and multilayer deposition, we develop a pinhole-free F-DLC coating with low surface energy and comparable Young's modulus to metals. In a three-year steam condensation experiment, the F-DLC coating maintains hydrophobicity, resulting in sustained and improved dropwise condensation on multiple metallic substrates. Our findings provide a promising solution to hydrophobic material fragility and can enhance the sustainability of renewable and non-renewable energy sources.

2. A DURABLE COATING DESIGN STRATEGY

The rational design of the multi-layer F-DLC coating was guided by our physics-based understanding of condensation-induced blistering. The quantitative parameter that describes blistering, Ω , demonstrates that delamination of a hydrophobic coating will occur if $\Omega > 1$. Specifically, the blistering parameter Ω is governed by the pinhole size, R_d , the base radius of the pinhole-adjunct delaminated region, R_{b0} , the liquid-vapor surface tension of the working fluid (water) γ , as well as the coating intrinsic properties including its wet adhesion G , Young's modulus E and coating thickness h :

$$\Omega = \left(\frac{1.04R_{b0}}{R_d} \right) \left(\frac{\gamma^4}{EG^3h} \right)^{\frac{1}{4}}. \quad (1)$$

For a typical 100-nm thick fluoropolymer deposited on a smooth metal substrate ($R_{b0} \approx 5R_d$, $E \approx 1$ GPa, $G \approx 10$ mJ.m⁻²), $\Omega \approx 3.6$. Hence, polymers are unable to prevent delamination, unless their thicknesses exceed 10 μ m (where $\Omega \approx 1$). Our multi-layer F-DLC coating decreases Ω by using several synergistic approaches. By co-depositing short-chain PFCs (perfluorinated compounds) with the top DLC (a-C:H) surface (fDLC), we enable high Young's modulus of $E = 78$ GPa and low surface energy of ~ 24 mJ.m⁻². By deploying a well-established titanium (Ti) bonding layer, we enable an interfacial toughness of ~ 10 J.m⁻². Utilizing our Ti-DLC-fDLC multilayer, we eliminate pinholes, ensuring $\Omega < 4.2 \times 10^{-3}$ via the design of a 1- μ m thick multi-layer F-DLC coating.

While the Ti-DLC-fDLC multilayer focuses primarily on blistering and delamination, satisfying abrasion resistance and high temperature stability requires further stack modification. In addition to the aforementioned three-layer design, we included an additional layer composed of co-deposited DLC and silica (a-C:H:Si:O, amorphous hydrogenated carbon films containing silicon and oxygen) between the DLC layer and the Ti adhesion layer, which we term DLN. The added DLN layer is well-adapted in conventional DLC multilayers to: 1) enhance adhesion with the Ti layer by silica infusion, 2) provide good thermal stability and act as a stress reliever, and 3) further decrease the pinhole density. As a result, the multilayer F-DLC coating designed here not only promises reliable adhesion between the coating and a variety of arbitrary substrates, but it also decreases interfacial stresses from abrasion or thermal expansion by increasing the numbers of layered interfaces.

The F-DLC fabrication process is a rationally developed and optimized multi-layer film comprised of a primary adhesion layer deposited via physical vapor deposition (PVD) sputtering followed by plasma assisted physical vapor deposition (PACVD) to build the remaining three layers (Fig. 1a). The PACVD coating is done in a vacuum chamber at 250°C, maintaining localized filaments to assist in homogenous plasma conditions throughout the vessel. Hydro-carbonated DLN gases which give the elemental structure were introduced in the system which was deposited on the Ti-coated substrate. Then a fluorine precursor as a liquid form is introduced to the system which was vaporized and co-deposited with the DLC layer at the end of the deposition process. Cross-sectional SEM of the coating shows a total thickness of $\sim 1.65 \pm 0.05 \mu\text{m}$.

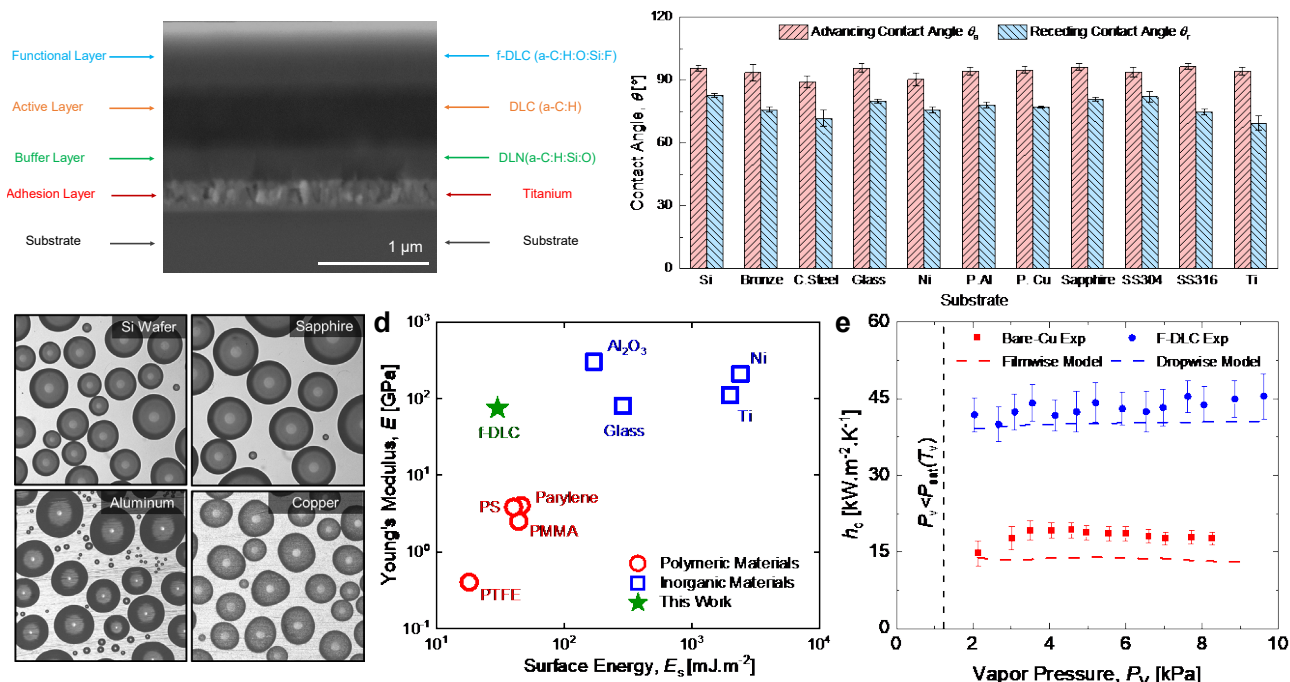


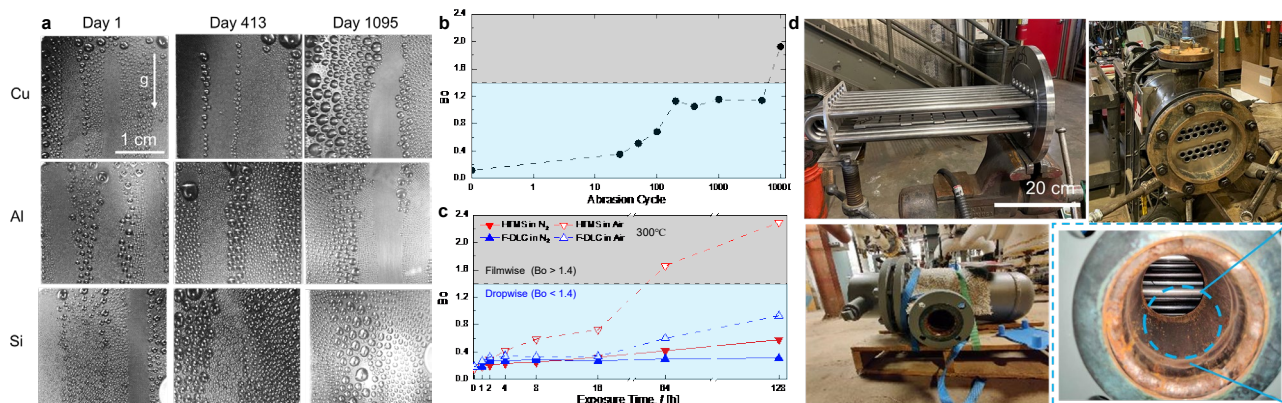
Figure 1. (a) The multi-layer design architecture of F-DLC. (b) DI water contact angle on various substrates coated with F-DLC. (c) Optical microscopy images showing condensation of atmospheric water vapor on different F-DLC coated substrates. (d) Surface energy and Young's modulus comparison of FDLC with other engineering materials. (e) Condensation heat transfer coefficient on F-DLC coated and bare Cu tubes under varying steam vapor pressure conditions.

To demonstrate versatility, we deposited F-DLC on a variety of substrates, showing substrate-independent wetting (Fig. 1b). The wettability of the F-DLC coated substrates were determined by performing water contact angle measurements using a microgoniometer (MCA-3, Kyowa Interface Science). The apparent advancing contact angle on an F-DLC coated smooth silicon wafer (University Wafer) is, $\theta_a = 97.5 \pm 1^\circ$ (Fig. 2b). Figure 2c shows top view optical microscopy images of atmospheric water vapor condensation on the different F-DLC coated substrates demonstrating spherical droplet morphologies with highly mobile contact lines, key to attaining high quality hydrophobicity. Although the surface energy is 25% higher when compared to Teflon-like materials having surface energy of $\sim 20 \text{ mJ}\cdot\text{m}^{-2}$, the F-DLC coating maintains a $\sim 20\text{X}$ higher Young's modulus. Figure 2d shows the surface energy and Young's modulus of many commonly used engineering materials, demonstrating that F-DLC combines the merits of both low surface energy and high mechanical modulus. To determine the overall condensation heat transfer performance, an F-DLC coated copper (Cu) tube was fabricated following the same process described for the flat coupons and condensation heat transfer experiments were performed in a chamber with a controlled environment (Hoque et. al., 2023). Condensation heat transfer behavior was benchmarked by comparison to an uncoated Cu tube sample having identical diameter and length. Figure 1e shows calculated and predicted heat transfer coefficient as a function of vapor pressure. The F-DLC coated Cu sample showed a $\sim 3\text{X}$ higher condensation heat transfer compared to the uncoated Cu tube over a wide range of vapor pressures. To compare the experimental results to theoretical predictions, we calculated the dropwise condensation heat transfer coefficient (blue dotted line in Fig. 1e) using the droplet growth and distribution model and the filmwise condensation heat transfer coefficient using the Nusselt condensation model on a horizontal tube.³ The experimentally measured dropwise and filmwise heat transfer coefficient are in good agreement with the well-validated dropwise and filmwise condensation models, respectively.

3. PERFORMANCE OF FDLC

To evaluate the long-term durability of the F-DLC coating during steam condensation, we built a separate vacuum-compatible condensation chamber (Hoque et. al., 2023). The environmental chamber was first evacuated to $P < 5 \text{ Pa}$ to

remove non-condensable gases, then, hot steam was injected into the chamber from a boiler after following a detailed degassing procedure. Cold water at $\sim 10^{\circ}\text{C}$ was supplied to the cold plate inlet via a chiller, which reduces the surface temperature of the mounted samples. As the steam comes in contact with the F-DLC surfaces it forms water droplets and initiates dropwise condensation. Figure 2a shows time-lapse images of condensation on various FDLC coated surfaces, even after the long-term exposure (> 1095 days) to saturated steam conditions, the F-DLC coating exhibited continued



dropwise condensation during tests, regardless of the base substrate.

Figure 2. (a) Pure steam condensation durability of FDLC for over 3 years. (b) Mechanical (abrasion) and (c) thermal robustness of FDLC showing the transition point from dropwise to filmwise condensation. (d) A prototype shell-tube heat exchanger design with FDLC-coated tubes, which is ready to be tested in a real power plant environment at UIUC.

To evaluate long-term mechanical durability of the F-DLC film against abrasion and wear, cyclic abrasion resistance tests were performed on a Taber abrasion tester and based on wettability change a prediction model for dropwise- to filmwise is developed. Figure 2b shows that F-DLC surface is predicted to maintain dropwise condensation even after 5000 abrasion cycles due to the maintenance of low droplet Bond number ($Bo < 1.4$). Calculations of Bo for each tested surface based on the abraded surface contact angle measurements reveal a maximum $Bo \sim 1.14$ after 5000 abrasion cycles. To characterize the effects of potential oxidation in air, we heated the F-DLC surface in an atmospheric pressure oven (Lindberg/Blue M Moldatherm Box Furnace) over a variety of temperature ranges (Hoque et al., 2023). The thermal stability of the F-DLC coating was compared to a control sample consisting of a HTMS SAM hydrophobic coating deposited on identical substrates. As shown in Fig. 2c, even after 128 hours of exposure to hot air (300°C) the F-DLC coating maintain dropwise condensation ($Bo \sim 0.9 < 1.4$).

To scale up the application of FDLC coating, a prototype shell-and-tube heat exchanger has been developed in collaboration with Abbott Power Plant at the University of Illinois (Fig. 2d). The prototype features 13 U-shaped carbon steel tubes, each approximately 0.5 m long and 0.0254 m diameter. This prototype will be integrated as a small condenser unit in the cycle and subjected to testing under power plant conditions (high pressure and high-temperature pure steam).

4. CONCLUSIONS

In summary, our developed a multilayer F-DLC coating has low surface energy characteristic of non-polar polymers, with a high Young's modulus approaching that of metals. We demonstrate the versatility of F-DLC on a wide range of substrates including crystalline, non-crystalline and common engineering metals, all showing similar surface energy after coating. The F-DLC not only demonstrates enhanced dropwise condensation heat transfer, but also durability in moist environments for a period of more than three years. Characterization of the compatibility of F-DLC in elevated temperature environments exceeding 300°C and sustainability after 5000 mechanical abrasion cycles demonstrates resiliency. The outcomes of our work not only develop a low surface energy coating capable of implementation for a plethora of versatile applications, it overcomes the challenge of generating hydrophobic surfaces that can achieve extended lifetime during exposure to harsh thermo-mechanical environments. Furthermore, F-DLC coatings have the potential to enhance the sustainability of non-renewable energy generation sources, thus helping societies reach their climate change goals through carbon emissions reduction and lower utilization of environmentally harmful fossil fuels.

5. REFERENCES

- Champlin, P. A. *Techno-Economic Evaluation of Cross-Cutting Technologies for Cost Reduction in Nuclear Power Plants* Masters of Science thesis, Massachusetts Institute of Technology, (2018).
 IEA. *World Energy Outlook 2021*. (Paris. France, 2021).
 Hoque, M. J. L., L.; Ma, J.; Cha, H.; Sett, S.; Yan, X.; Rabbi, K. F.; Ho, J. Y.; Khodakarami, S.; Suwala, J.; Yang, W.; Mohammadmoradi, O.; Ince, G. O.; Miljkovic, N. Ultra-resilient multi-layer fluorinated diamond like carbon hydrophobic surfaces. *Nat Commun* **14**, 4902, doi:10.1038/s41467-023-40229-6 (2023).

On the Quenching of Spray Cooling - When does it occur? -

Yasuyuki Takata^{a,b}

^aInternational Institute for Carbon-Neutral Energy Research, Kyushu University, Japan

^bSchool of Engineering, The University of Edinburgh, UK

*takata@mech.kyushu-u.ac.jp

Keywords: Spray cooling, Droplet impingement, Quenching, Oxide layers

1. INTRODUCTION

When we cool down a hot steel with water spray, the sample temperature decreases gradually first and then rapidly at a certain point. The point is called “*quenching point*” where rapid cooling starts by the direct contact between liquid and the hot surface. The temperature of the quenching point varies widely from ~200°C to ~800°C depending on the surface and spray conditions. It is of great importance to predict the quenching point. Despite a number of previous studies, the mechanism of onset of quenching has not yet been clearly understood. One of the reasons is due to the presence of the oxide layers formed on the hot surface. These oxide layers have non-uniform porous structures and low thermal conductivity and hence raise the quenching temperature. In the present study, we try to explain the quenching temperature based on the assumption of the transient heat conduction for a contact between two semi-finite bodies. We used several different artificial oxide layers and made a series of experiments on spray cooling and observation of single individual droplet impinging onto the hot oxide surfaces. As a result, the onset of quenching always seems to happen at the contact surface temperature of around 250°C regardless of the composition and thickness of the oxide layer.

2. EXPERIMENTS AND TRANSIENT HEAT CONDUCTION MODEL

We conducted the following two experiments^[1]. (a) Spray cooling of hot samples with several artificial oxide layers, and (b) Observation of single droplet impinging on to the hot surfaces. In the experiment (a), cooling curves are obtained and in (b), a contact time and a maximum spreading diameter of the droplet during the collision with the hot surfaces are obtained by analyzing images of high-speed video.

Five test samples with artificial oxide layer were prepared for the experiments. These oxide layers are made by flame spray on the SUS304 base sample. The thermophysical properties of these five oxide layers are shown in Table 1 which were measured by TGA-DSC and laser flash.

Table 1. Thermophysical properties of test samples

	Density, ρ (kg/m ³)	Spec heat, c (J/(kg·K))	Therm cond, k (W/(m·K))	Therm diff, α (mm ² /s)
SUS304	7920	547	19.05	4.410
Fe ₃ O ₄	5170	868	2.975	0.663
TiO ₂	4160	823	3.756	1.097
Al ₂ O ₃	3380	1140	2.293	0.595
SiO ₂ -ZrO ₂	3680	794	1.441	0.493

@RT @280 ° C measured by TGA-DSC and laser flash

Layer thickness: 50, 100, 150, 200 μ m
Surface roughness (Ra): 1.82 \pm 0.48 μ m
Contact angle @RT: 70 \pm 18°

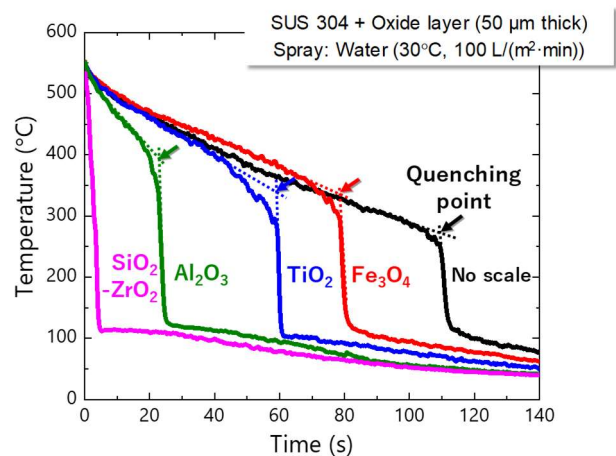


Figure 1. Cooling curve

Figure 1 shows the cooling curves of these five test samples. The cooling curve of the base sample (SUS304) with no oxide layer is plotted in the figure for the reference. Each quenching point is indicated by arrow. It is found that the SiO₂-ZrO₂ does not have a quenching point in this figure and its quenching temperature is much higher than 560°C which is the starting temperature of the spray experiment. Quenching temperatures of the other samples are about 380°C, 340°C, 335°C and 280°C for Al₂O₃, TiO₂, Fe₃O₄ and no oxide sample, respectively. The cooling rate becomes faster in the order of SiO₂-ZrO₂, Al₂O₃, TiO₂, Fe₃O₄ and no oxide sample.

To understand the mechanism of quenching we observed behaviors of individual droplet impinging onto the hot surfaces by high-speed video and then we analyzed the images of the impacting droplets to obtain the maximum spreading diameter, D_{max} , and the contact time with the hot surface, t_c , as shown in Figure 2. The experimental data of t_c and D_{max} are plotted in Figures 3 and 4, respectively. t_c and D_{max} decrease with surface (wall) temperature, T_w , except for SiO₂-ZrO₂. However, it seems difficult to correlate the data from these figures.

Here, we introduce a physical model of transient heat conduction of two infinite solids. During the droplet impact, typical contact time, t_c , lies in the order of 1ms. Considering the thickness of oxide layer of 100 μ m, we can regard both water droplet and oxide layer as infinite solids for 1ms. Based on this model, the contact surface (interfacial) temperature, T_s , at the collision of water droplet with the hot surface is given by the following equation.

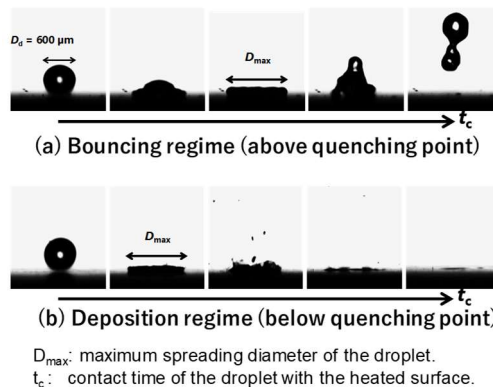


Figure 2. Droplet behavior characterization

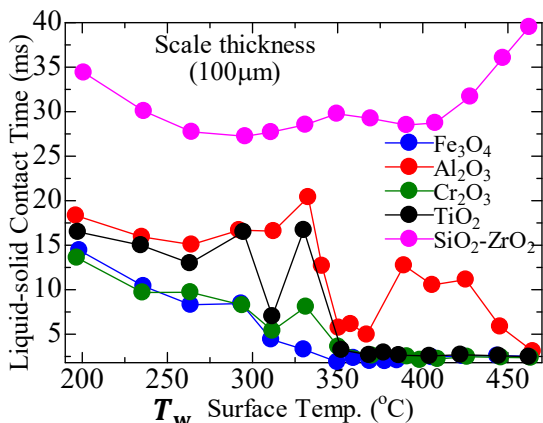


Figure 3. Contact time

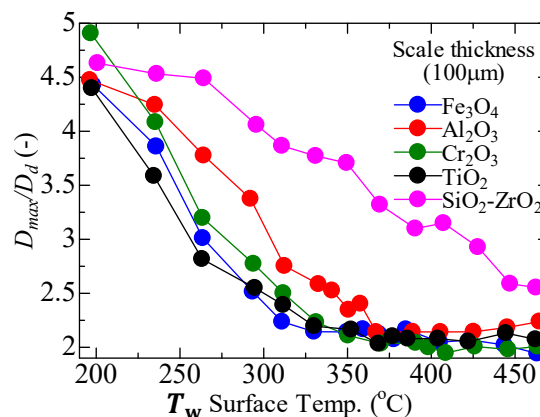


Figure 4. Maximum spreading diameter

$$T_s = \frac{T_w \sqrt{(\rho ck)_w} + T_l \sqrt{(\rho ck)_l}}{\sqrt{(\rho ck)_w} + \sqrt{(\rho ck)_l}} \quad (1)$$

where T_l is the liquid temperature, $\sqrt{(\rho ck)_w}$ and $\sqrt{(\rho ck)_l}$ are thermal effusivities of oxide layer and water droplet, respectively. We convert horizontal axis of Figures 3 and 4 from T_w to T_s by equation (1). Converting the horizontal axis from T_w to T_s , Figures 3 and 4 are re-plotted as Figures 5 and 6, respectively.

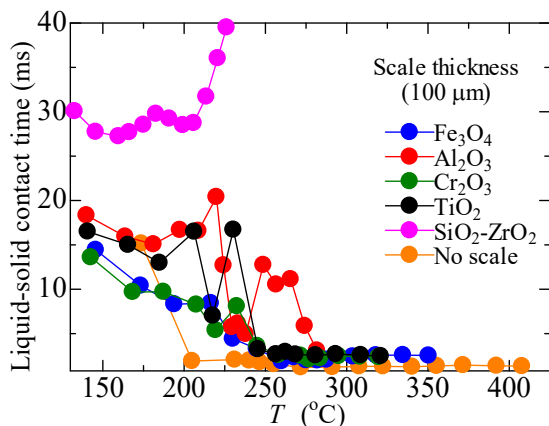


Figure 5. Contact time in relation to the contact surface temperature

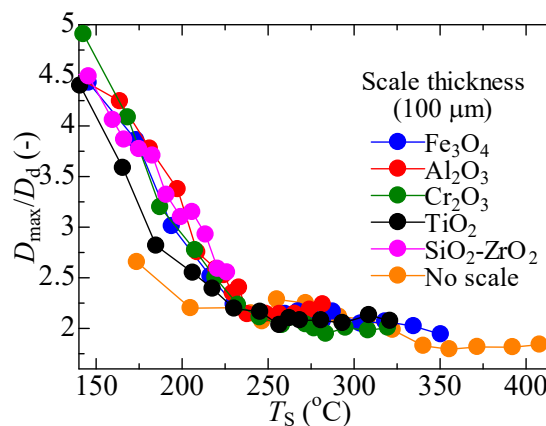


Figure 6. Maximum spreading diameter in relation to the contact surface temperature

In Figures 5 and 6, most of data seem to be correlated with a common single curve and the data can be divided into two regions at around $T_s=250^\circ\text{C}$. This temperature does not exceed the superheat limit temperature.

When we apply this model (equation (1)) to the results of Figure 1, the quenching temperatures, T_w , are converged approximately to $\sim 250^\circ\text{C}$. This means that T_w at quenching is the *apparent* quenching temperature and T_s is the *actual* quenching temperature.

To understand the meaning of T_s , we changed the system pressures between 0.1MPa and 0.5MPa^[2]. The quenching temperatures, T_s , is shown in Figure 7 with wall temperature, T_w , saturation temperature, T_{sat} , superheat limit temperature, $T_{spinodal\ limit}$ and temperatures at minimum heat flux point, $T_{MHF(Berenson)}$ and $T_{MHF(Cai\ et\ al.)}$. The data of T_s are most close to $T_{MHF(Cai\ et\ al.)}$ predicted by the following equation^[3].

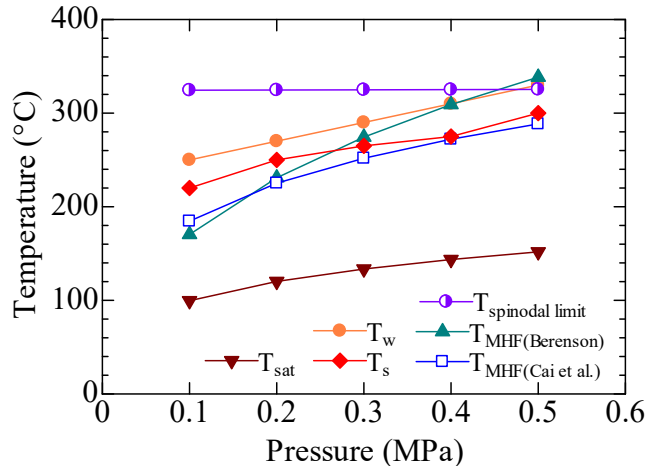


Figure 7. Quenching temperature with system pressure

$$T_{MHF} = T_{sat} + 0.1223 \left(\frac{\rho_l}{\rho_v} \right)^{-0.2029} \frac{\rho_v L_w}{Nuk_v} \left[\frac{\sigma^3}{g \rho_v^2 (\rho_l - \rho_v)} \right]^{1/4} \quad (2)$$

where Nu is estimated by Klimenko's equation^[4].

3. CONCLUSIONS

The conclusions of the present study are summarized as below.

- (1) Quenching temperature scatters from experiment to experiment. They are *apparent* quenching temperatures. *Actual* quenching temperature is given by contact surface temperature, T_s , based on transient heat conduction of two semi-infinite bodies.
- (2) Quenching always occurs at around $T_s=250^\circ\text{C}$ for atmospheric pressure. The actual quenching temperature can be approximately predicted by temperature at minimum heat flux point that is given by equation (2).

ACKNOWLEDGEMENTS

The author would like to thank to his collaborators, Prof. M. Kohno, Dr. S. Hidaka at Kyushu University, and Dr. Y. Kita at King's College London. The present work was financially supported by Kakenhi Grant KIBAN(B) 23H01357 by MEXT and JFE Steel Corp.

REFERENCES

- [1] K. Tsukamoto, Y. Kita, S. Inoue, T. Hamanosono, S. Hidaka, S. Ueoka, H. Fukuda, M. Kohno, Y. Takata, On the onset of quench during spray cooling: The significance of oxide layers, *Applied Thermal Engineering*, Vol.179, 115682, 2020
- [2] Y. Kita, M. Nakamatsu, S. Hidaka, M. Kohno, Y. Takata, Quenching mechanism of spray cooling and the effect of system pressure, *International Journal of Heat and Mass Transfer*, Vol. 190, 122795, 2022
- [3] C. Cai, I. Mudawar, H. Liu, Mechanistic method to predicting minimum heat flux point wall temperature in saturated pool boiling, *International Journal of Heat and Mass Transfer*, Vol. 156, 119854, 2020
- [4] V.V Klimenko, Film boiling on a horizontal plate - new correlation, *International Journal of Heat and Mass Transfer*, Vol. 24, pp. 69–79, 1981

BOILING HEAT TRANSFER FOR ELECTRONICS COOLING AT HIGH HEAT FLUXES

Zan Wu^{a,b,*}, Zhen Cao^c, Xiangbo Huang^a, Junye Li^b, Weiyu Tang^a

^a College of Electrical Engineering, Zhejiang University, Hangzhou 310027, China

^b ZJU-Hangzhou Global Scientific and Technological Innovation Center, Hangzhou 311200, China

^c Department of Thermal and Fluid Engineering, University of Twente, 7500 AE Enschede, the Netherlands

*wuzan@zju.edu.cn

Keywords: High heat flux, boiling heat transfer, electronics cooling, manifold microchannel, micro/nanostructured surface

1. INTRODUCTION

Integrated Circuits (ICs) have been a keystone of electronics in digitalization and electrification, including cloud computing, smart electric grid, electric vehicles. Currently, ICs are developing to be miniaturized and integrated towards more powerful chips, but simultaneously resulting in serious heat production. For electronics cooling, it poses severe thermal challenges to dissipate high heat flux within a low temperature budget and limited space. It is reported that when the chip surface temperature reaches 70~80 °C, chip reliability decreases by 5% with the temperature increasing by 1°C, and more than 55% of the electronics failures are caused by excessive temperatures. Therefore, chip cooling becomes one of the bottlenecks of next-generation electronics development. Up to now, numerous cooling technologies have been developed, mainly including air cooling, liquid cooling, and phase-change cooling. Concerning the ever-increasing heat load, the two-phase cooling by coolant boiling (i.e., immersion cooling and embedded two-phase cooling) is advantageous over the others due to its higher heat transfer capacity and relatively low power consumption. This study aims to provide comprehensive insights into pool boiling enhancement by micro/nano structures and manifold microchannel flow boiling.

2. POOL BOILING ON MICRO/NANO-STRUCTURED SURFACES FOR IMMERSION COOLING

The electrophoretic deposition method (EPD) and the electrochemical deposition method (ECD) were developed to fabricate micro/nanostructured coatings, and micro-pin-fin surfaces (PF) were fabricated using the etching method. The coating and pin fins considerably change the surface-liquid interactions and then tailor boiling performance. Figure 1 shows the boiling curves of several liquids on the modified surfaces, including dielectric liquids and water. It is seen that the boiling curve is shifted to the left, meaning that boiling is significantly enhanced. The modified surface could also initiate boiling at a lower superheat. Critical heat flux is enhanced on the modified surface except the EPD surface (Fig. 1(a)), and further measurements indicate that the surface wickability of HFE-7200 is not intensified.

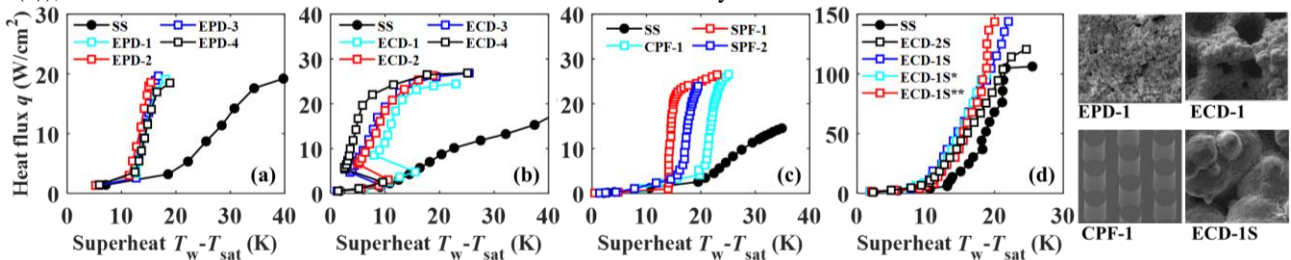


Figure 1. Pool boiling curves on the modified surfaces: (a) HFE-7200, (b) NOVEC-649, (c) FC-72, (d) water

Bubble departure diameter was compared on the smooth surface and the modified surface, concerning dielectric liquids and water, as shown in Fig. 2. It is seen that the bubble departure diameter on the modified surface is smaller than that on the smooth surface, meaning that the modified surface accelerates bubble departure. In addition, the active nucleation site density was also quantitatively compared. The coated surface has the nucleation site density of 1-2 orders of magnitude higher than the smooth surface.

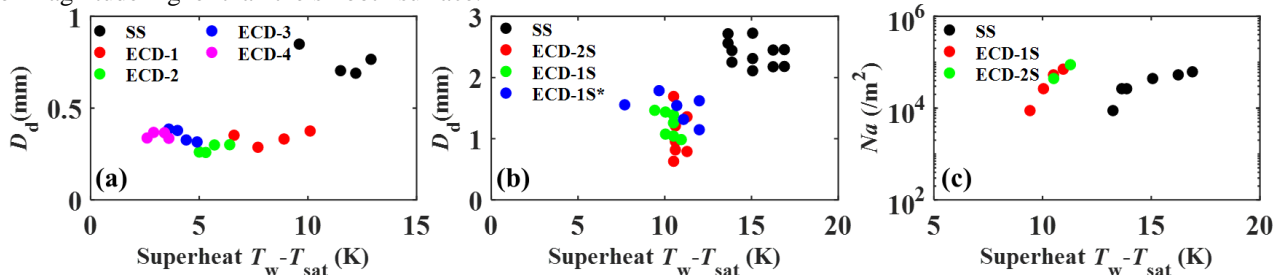


Figure 2. Bubble departure diameters: (a) NOVEC-649, (b) water; (c) active nucleation site density

Based on the experimental analysis of bubble dynamics, a mechanistic model was established to predict pool boiling curve. It is indicated that the model coincides with the experiment well, especially at low-to-moderate heat flux (Fig. 3).

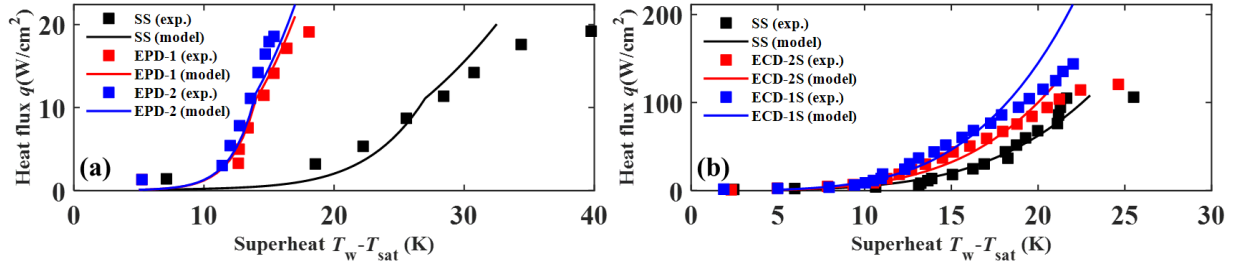


Figure 3. Comparison of boiling curve between experiment and model: (a) HFE-7200, (b) water

The mechanism of critical heat flux enhancement was extensively explored, from the perspective of capillary wicking, structure-induced evaporation, and coalescence bubble lateral moving. A revised force-balance model was proposed, which further considers a micro/nanostructure-dependent surface tension force and a micro/nanostructure-induced wicking force, as shown in Fig. 4. The model shows a better prediction of CHF.

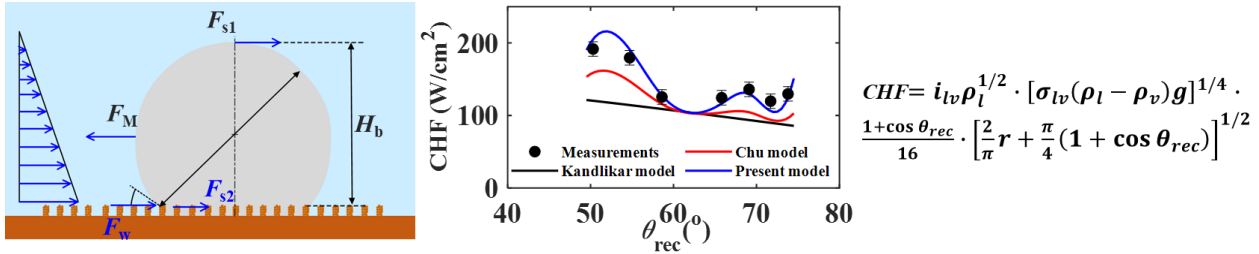


Figure 4. Revised force-balance CHF model and the model evaluation

4. COOLING PERFORMANCE OF MANIFOLD MICROCHANNELS FOR POWER ELECTRONICS

The embedded microchannel cooling has been proposed to dissipate ultra-high heat fluxes. We conducted a subcooled flow boiling test on the proposed Z-MMC cooler with a subcooling degree of 10 K with water as the working fluid. As the power density of the chip rises, the fluid flow state in manifold microchannels changes accordingly, as shown in Fig. 5, the coolant reaches the ONB (onset of nucleate boiling) point at 641 W/cm² and a small number of bubbles begin to appear in the inlet manifold when the power density reaches 948 W/cm². It can be seen that when ONB occurs, the slope becomes larger as the wall superheat rises, and the heat transfer coefficient tends to increase.

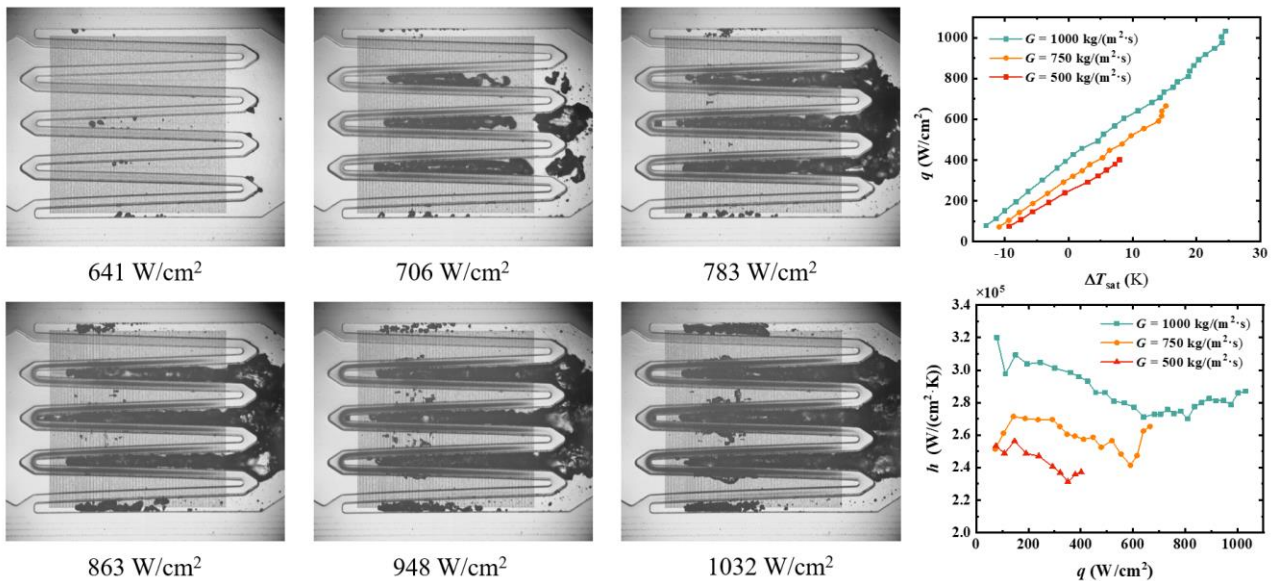


Figure 5. Flow boiling patterns under different heat fluxes at 1000 kg/(m²·s) and detailed data plots at different mass flow rates

For multi-chips power modules, reliable packaging and thermal management are of great importance for substantially realizing the full excellent electrical performance of SiC MOSFETs. We proposed integrated manifold microchannels on

the DBC substrate of SiC power module using nano-Ag sintering, and the high pressure drop and temperature nonuniformity along the flow path associated with microchannels are suppressed by specified manifold designs (tapered manifold, and cascaded manifold). Both of them are compared against widely used pin-fin heat sinks, and three simulated SiC power modules are fabricated following the same packaging process to investigate the thermal characteristics. Then, their junction-to-fluid thermal resistances are experimentally and numerically compared to provide a comprehensive understanding of thermal-hydraulic performance of different heat sinks. Three thermal test vehicles (TTVs) for SiC power devices were then fabricated following the same packaging process, and experiments were performed to compare their overall performance using water at four different fluid flowrates (6 cm³/s [0.36 L/min] to 36 cm³/s [2.16 L/min]). An ultra-high die-heat-flux of over 1000 W/cm² could be managed with the junction temperature T_j less than 110 °C using the serial-connected MMCHS, and thermal resistance as low as 10.25 mm² K/W has been achieved at the maximum flowrate. The detailed data for the performance of single-phase water cooling is shown in Fig. 6.

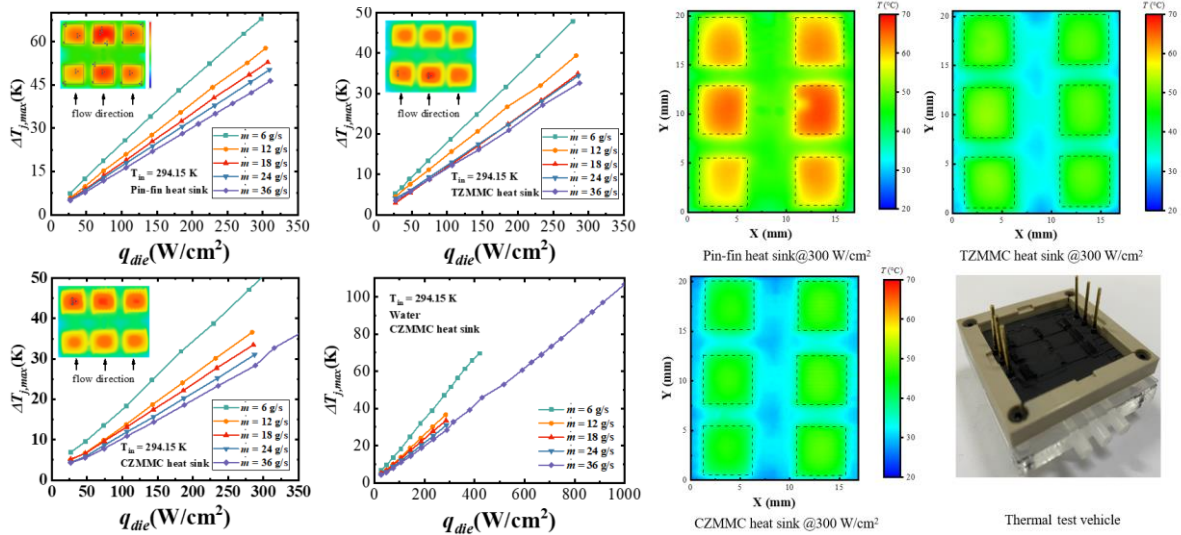


Figure 6. The junction temperature difference relative to the cooling water inlet temperature versus the average heat flux of six chips and comparison of typical chip surface temperature map at an effective heat flux of 300 W/cm²

Figure 7 illustrates the two-phase heat transfer results of this structural module and the temperature distribution of different chip heat flow densities at a mass flow rate of 12 g/s. Since two-phase heat transfer utilizes the latent heat of vaporization of the cooling fluid, it significantly improves the heat transfer performance compared to single-phase heat transfer at low mass flow rates. The vertical near U-shaped manifold structure can give a uniform coolant distribution in the manifold microchannel heat sink, in addition to the high heat transfer efficiency of flow boiling. Thus, the thermal resistance is greatly reduced and the temperature uniformity between the multi-chips is excellent. For example, in the case of power density of 470 W/cm², the maximum difference in the junction temperature of different chips is only 1.6 K

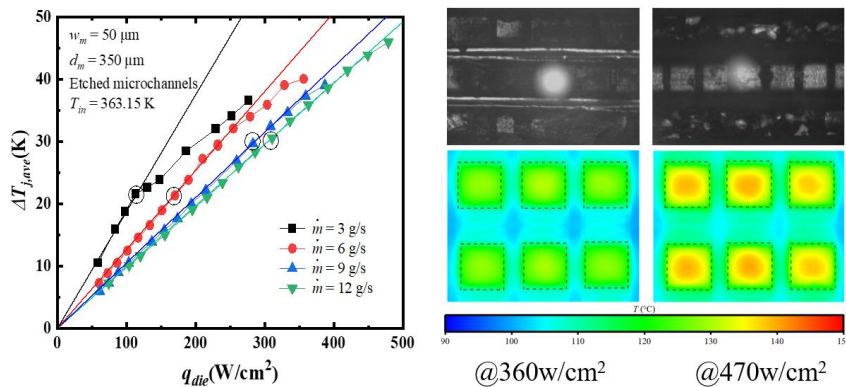


Figure 7. Results of water flow boiling heat transfer and typical chip surface temperature map at 12 g/s

6. CONCLUSIONS

This work experimentally investigated pool boiling heat transfer on micro/nanostructured surfaces, which may have a potential for immersion cooling of electronics. Then, results for single-phase and flow boiling heat transfer in manifold microchannel heat sinks were presented, which is promising for cooling power electronics of ultra-high heat fluxes. More details and additional data will be presented later.

FILM CHARACTERISTICS AND HEAT TRANSFER DURING CONDENSATION IN A SMALL DIAMETER CHANNEL

Davide Del Col and Stefano Bortolin

University of Padova, Department of Industrial Engineering, Via Venezia 1, 35131 Padova, Italy
davide.delcol@unipd.it

Keywords: In-tube condensation, Heat transfer coefficient, Liquid film thickness, Microgravity, Numerical simulations

1. INTRODUCTION

Condensation process is common in many applications, including energy plants, heat pumps, electronics cooling, and spacecraft thermal control (Del Col *et al.*, 2023). Concerning in-tube condensation, annular regime is one of the most recurrent flow patterns. A deep understanding of the condensation heat transfer phenomenon is essential to develop accurate models, in particular at low values of mass velocity, when it is more difficult to predict heat transfer coefficients, due to the combined effects of vapor shear stress, gravity force and surface tension (Toninelli *et al.*, 2019). Condensers operating at low mass velocity can be found for instance in heat pipes but also in refrigeration systems and heat pumps when working at partial loads. Annular condensation is controlled by the thermal resistance across the film of condensate, which in general depends on the film thickness, the presence of interfacial waviness and turbulence in the liquid film. Even at low mass velocity and laminar liquid film conditions, the liquid-vapor interface can be rippled by waves and deviations are observed with respect to the classical Nusselt theory for film condensation. In the present work, heat transfer coefficient (HTC) and liquid film thickness (LFT) are investigated during annular flow condensation inside a 3.4 mm diameter channel, considering three fluids with different thermodynamic and transport properties. Optical sensors are used to measure the LFT and temperature sensors are embedded in the wall to measure the HTC. Heat transfer data are analyzed together with the condensate characteristics. The effect of gravity is investigated. Numerical simulations for the prediction of liquid-vapor interface evolution are performed to get a deeper insight of the phenomena.

2. HEAT TRANSFER COEFFICIENT AND LIQUID FILM THICKNESS MEASUREMENTS

The test section designed for the study of in-tube condensation is composed of two diabatic parts for HTC measurements separated by a glass tube for flow pattern visualizations and LFT measurements. The diabatic sections are divided in sub-sectors, where the refrigerant flows inside a circular cross-section copper channel having an inner diameter equal to 3.4 mm. Distilled water streaming in an external annulus is used to extract the heat. A finned geometry on the external side of the copper tube was realized to reduce the coolant side heat transfer resistance and to allow the installation of wall thermocouples. A sketch of the optical system is shown in Fig. 1a: it consists of a borosilicate tube, a LED source, a high-speed camera and a chromatic confocal sensor. The external surface of the glass tube was machined to obtain a special external shape consisting of two curved parts that work as a lens. The acquired images of the two-phase flow (Fig. 1b) are then processed by means of shadowgraph technique.

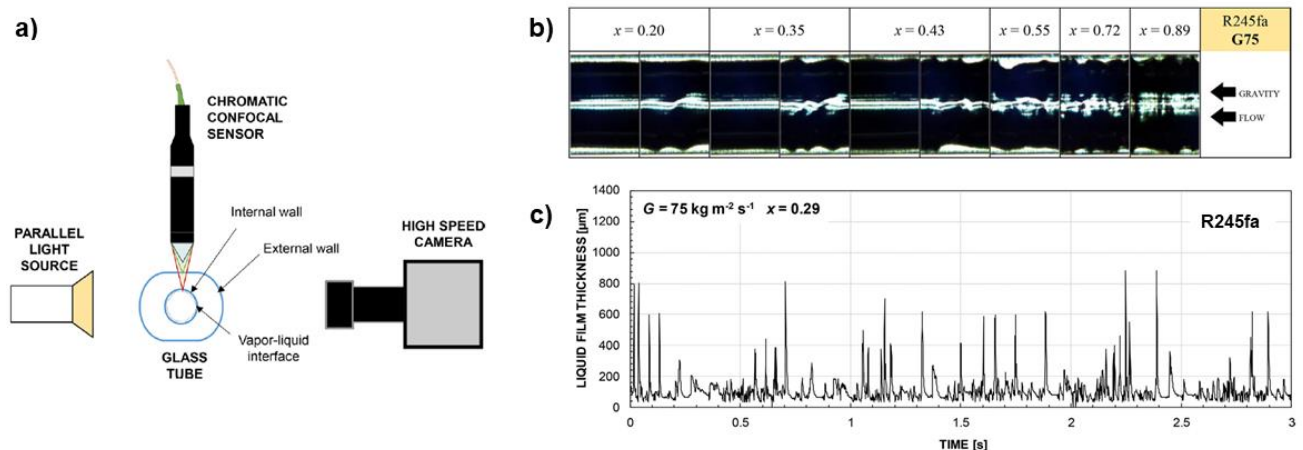


Figure 1. a) Optical system for LFT measurement. b) Flow pattern visualizations during R245fa downflow condensation inside the 3.4 mm inner diameter tube at mass velocity $G = 75 \text{ kg m}^{-2} \text{ s}^{-1}$ and varying vapor quality x . c) Temporal evolution of the local LFT.

Due to the shape of the tube, the LFT observed by the high-speed camera is not equal to the real LFT inside the tube. Using a ray tracing model, the relationship between the apparent LFT observed with the high-speed camera and the real LFT inside the tube can be calculated (Berto *et al.*, 2021). The external shape of the glass tube was designed with two flat parts in correspondence to the confocal chromatic sensor position for punctual LFT measurements (Fig. 1c).

HTC and LFT measurements were performed with three different fluids (R245fa, R134a and HFE-7000) during vertical downflow condensation, at mass velocity G from $30 \text{ kg m}^{-2} \text{ s}^{-1}$ to $150 \text{ kg m}^{-2} \text{ s}^{-1}$, and $30 \text{ }^\circ\text{C}$ - $40 \text{ }^\circ\text{C}$ saturation temperature. The effects of mass flux and vapor quality on the LFT and interfacial waviness are discussed by means of both statistical and spectral analyses. In general, the LFT is found to decrease with increasing mass velocity under the effect of vapor shear stress. But, at low mass velocity, an increase of the LFT has been observed when increasing the mass velocity (in the case of R134a varying G from $30 \text{ kg m}^{-2} \text{ s}^{-1}$ to $50 \text{ kg m}^{-2} \text{ s}^{-1}$). This trend is opposite to the one found at high mass velocity and this is due to the transition from shear stress-driven to gravity-driven downward flow condensation (Berto *et al.*, 2022b). Furthermore, HFE-7000 LFT measurements are compared against independent data (Berto *et al.*, 2023) measured at LAPLACE laboratory at the same operative conditions inside a diabatic sapphire tube coupled with an infrared camera, a chromatic confocal sensor and an interferometer. Comparable LFT, wave heights and frequencies are obtained in the two experimental test sections at the same working conditions ($G = 20 - 30 \text{ kg m}^{-2} \text{ s}^{-1}$).

3. MEASUREMENTS IN MICROGRAVITY CONDITIONS

The 3.4 mm diameter test section was installed in a rack to perform measurements with HFE-7000 at different gravity conditions on board Novespace Airbus A310 (70th ESA Parabolic Flight Campaign). Condensation tests were performed at $40 \text{ }^\circ\text{C}$ saturation temperature and mass velocity from $30 \text{ kg m}^{-2} \text{ s}^{-1}$ to $50 \text{ kg m}^{-2} \text{ s}^{-1}$. The condensation process was studied by simultaneously measuring the HTC (Fig. 2a) and the LFT.

A criterion based on the dimensionless inclination parameter Y is proposed to identify the regions (Fig. 2b) where the condensation HTC is affected by the gravity level and where it is not (Berto *et al.*, 2022a).

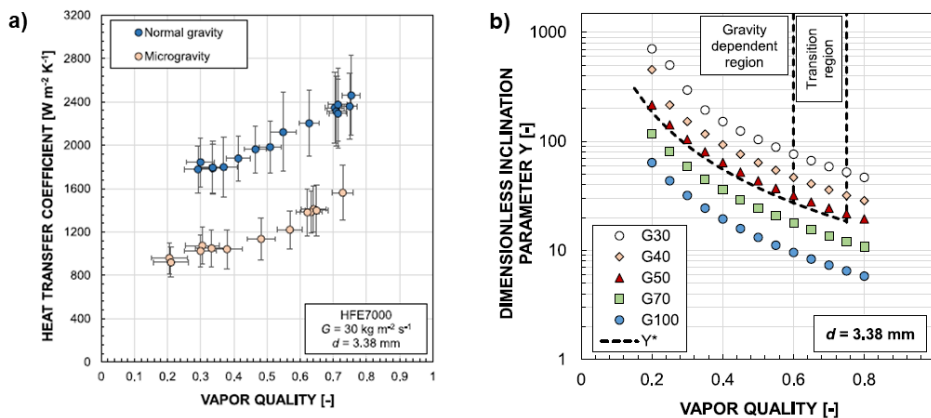


Figure 2. a) HTC with HFE-7000 at $G = 30 \text{ kg m}^{-2} \text{ s}^{-1}$ in normal gravity (horizontal flow) and microgravity conditions. Dimensionless inclination parameter Y for the transition from gravity-dependent to gravity-independent region.

4. NUMERICAL SIMULATIONS

An OpenFOAM solver based on the Volume of Fluid (VOF) method is used to predict the LFT of R245fa flowing inside the 3.4 mm channel (Zanetti *et al.*, 2023).

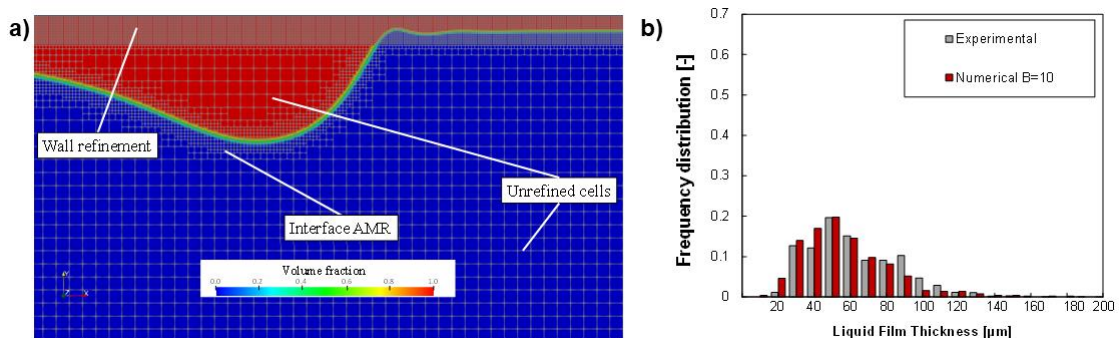


Figure 3. a) Mesh size variations in the computational domain during the passage of a liquid wave. b) Experimental and numerical frequency distribution of the LFT (R245fa, $G = 100 \text{ kg m}^{-2} \text{ s}^{-1}$, $x = 0.77$).

The numerical setup consists of a 2D axisymmetric domain with Adaptive Mesh Refinement (AMR) applied at the liquid/vapor interface (Fig. 3a). The Reynolds-Averaged Navier Stokes (RANS) with the $k-\omega$ SST model are adopted for simulating the turbulence in both the liquid and vapor phases. A turbulence damping parameter B is introduced to damp the turbulence at the interface. The numerical results are compared against LFT measurements during vertical annular flow (Fig. 3b).

4. CONCLUSIONS

To understand the underlying condensation mechanisms and develop physical models, HTC measurements must be combined with quantitative measurements of the LFT and waves characteristics. In this work, optical techniques are coupled with temperature measurements to study annular condensation inside a 3.4 mm inner diameter channel with R245fa, R134a and HFE-7000 in vertical downflow. The following conclusions can be drawn.

- Instantaneous LFT data are employed to characterize the condensate flow, introducing the definition of mean and base LFT. Both these parameters are found to decrease when increasing vapor quality and mass velocity, showing an opposite trend with respect to the measured HTCs. HFE-7000 generally displays lower film thickness values compared to R245fa and R134a due to the smaller vapor density. The appearance of high-amplitude waves and the resulting thinning of the liquid film between two consecutive disturbance waves enhance the heat transfer.

- The accuracy of several models for the prediction of HTC, LFT and void fraction is assessed against experimental data. Even at low mass velocity (e.g. R245fa, $G = 30 \text{ kg m}^{-2} \text{ s}^{-1}$, $x = 0.7$), when comparing experimental results with the Nusselt theory, measured data show higher HTCs due to the presence of waves at the vapor-liquid interface.

- Condensation tests are carried out with HFE-7000 in two separate laboratories (adiabatic glass tube in one case, diabatic sapphire test section in the other): the measured LFT at the same vapor quality and mass flux basically does not depend on the condensation heat transfer process, but only on hydrodynamics, at least for the working conditions (for example, heat flux) of the present experiments.

- In-tube condensation heat transfer under microgravity is penalized compared to normal gravity conditions (horizontal flow), especially when the vapor shear stress decreases (i.e. decreasing mass flux and vapor quality).

- VOF numerical simulations show good agreement with the experimental measurements in terms of mean/base liquid film thickness and waves frequency distribution. However, these parameters are strictly related to the use of a turbulence damping parameter, whose optimum value (capable of reproducing the experiments) has been found to be dependent from the working conditions.

There are still open questions regarding in-tube annular flow condensation: more accurate heat transfer models for low mass velocities are needed; criteria for laminar-to-turbulent transition in the liquid film must be validated; in the presence of interfacial waves, the mean LFT is not enough to explain the measured values of HTCs, thus further work is needed to link waves characteristics to heat transfer data.

ACKNOWLEDGEMENTS: The contributions of Arianna Berto and Marco Azzolin (University of Padova, Italy), Marc Miscevic and Pascal Lavieille (Université de Toulouse, France), Emanuele Zanetti (Delft University of Technology, the Netherlands) and Mirco Magnini (University of Nottingham, UK) are greatly acknowledged.

5. REFERENCES

Berto, A., Azzolin, M., Lavieille, P., Glushchuk, A., Queeckers, P., Bortolin, S., Iorio, C.S., Miscevic, M. and Del Col, D., 2022a. "Experimental investigation of liquid film thickness and heat transfer during condensation in microgravity". *Int. J. Heat Mass Transf.*, Vol. 199, 123467.

Berto, A., Beaumale, M., Lavieille, P., Azzolin, M., Bortolin, S., Miscevic M. and Del Col, D., 2023. "Inter-laboratory optical measurements of film thickness during annular flow condensation in a small diameter channel". *Experimental Thermal and Fluid Science*, Vol. 148, 110963.

Berto, A., Lavieille, P., Azzolin, M., Bortolin, S., Miscevic, M. and Del Col, D., 2022b. "Film thickness, interfacial waviness and heat transfer during downflow condensation of R134a". *Applied Thermal Engineering*, Vol. 214, 118808.

Berto, A., Lavieille, P., Azzolin, M., Bortolin, S., Miscevic, M. and Del Col, D., 2021. "Liquid film thickness and heat transfer measurements during downflow condensation inside a small diameter tube". *Int. J. Multiph. Flow*, Vol. 140, 103649.

Del Col, D., Berto, A., Azzolin, M., Bortolin, S., Miscevic, M. and Lavieille, P., 2023. "Condensation heat transfer in microgravity conditions". *npj Microgravity*, Vol. 9(1), 32.

Toninelli, P., Bortolin, S., Azzolin, M. and Del Col, D., 2019. "Visualization and numerical simulations of condensing flow in small diameter channels". *Heat Transfer Engineering*, Vol. 40(9-10), pp. 802-817

Zanetti, E., Berto, A., Bortolin, S., Magnini, M. and Del Col, D., 2023. "Study of the vapor-liquid interface during annular flow in a minichannel: OpenFOAM numerical simulations vs optical measurements". *Proceedings of the 8th Micro and Nano Flows Conference*. Padova, Italy.

OVERVIEW OF THERMOSYPHON AND HEAT PIPE TECHNOLOGIES

Marcia Barbosa Henriques Mantelli^a

^aHeat Pipe Laboratory
Federal University of Santa Catarina
Campus Universitário Trindade, 88040-900 Florianópolis, Brazil
[*marcia@labtucal.ufsc.br](mailto:marcia@labtucal.ufsc.br)

Keywords: two-phase heat transfer technologies, heat pipes, thermosyphons, pulsating heat pipes, electronics cooling

1. INTRODUCTION

Thermosyphons and heat pipes are highly efficient heat transfer devices that use two-phase cycles of fluids as the operating principle. Typical thermosyphons and/or heat pipes consist of an evacuated tube casing, within which a controlled amount of a working fluid is introduced. In heat pipes, capillary forces provided by a wick, are responsible for the movement of the fluid through the device. In thermosyphons, gravity forces do this job. Although heat pipes and thermosyphons may have many different geometries and configurations, they are basically composed of three main regions: evaporator, adiabatic section and condenser. In some applications, the adiabatic section may not be present. These devices can be used in applications where heat needs to be transferred with high efficiency or where uniform temperatures are required. These devices are able to manage heat in a myriad of equipment, from very small, such as electronic components, up to very large ones, such as oil storage tanks in petroleum refineries. Thermosyphons are more suitable for industrial applications because, as they do not require porous media to operate, they are easy to construct. Therefore, the fabrication costs are much reduced when compared to heat pipes. Besides, they are able to transport at least one order of magnitude more heat than heat pipes. However, as they need the gravity action to operate, the heat sources (evaporators) necessarily are positioned at below positions relative to the heat sinks (condensers). When this condition cannot be fulfilled, such as in microgravity applications or mobile computers, for instance, heat pipes are the correct technology to be applied. Some major applications of thermosyphons and heat pipes are explored in this talk.

2. TWO-PHASE DEVICES: BRIEF DESCRIPTION OF THE WORKING PRINCIPLES

Figure 1, in the left side, illustrates the physical principles of thermosyphon operation. Heat is delivered to the thermosyphon in the evaporator section, reaching the working fluid, causing liquid-vapor phase change. The generated vapor, due to pressure gradients inside the thermosyphon, crosses the adiabatic region and reaches the condenser, where heat is removed. The vapor contained in the condenser region condenses and the resulting liquid returns to the evaporator by the action of gravity forces. Therefore, the evaporator must be located in a position inferior to the condenser. Due to the surface tension effects between the tube material and the liquid, small rivulets are formed over the tube internal wall.

Heat pipes operate in very similar way, however, the return of the working fluid from the condenser to the evaporator happens due to the capillary forces resulting from the presence of a wick structure located inside the device, as illustrated in Fig. 1, in the right.

Thermosyphons and heat pipes can also be designed to operate in loops. Internally smooth tubes connect evaporators to condensers, within which only vapor or liquid flows. This arrangement avoids the dragging forces between liquid and vapor due to countercurrent flows. Schematics of loop thermosyphons and loop heat pipes are presented in Fig. 2.

In a general sense, the casing and the working fluid are considered the major components of thermosyphons. In heat pipes, besides these two, the wick is another key element. Usually located in the inner tube wall, the wick structure is responsible for the capillary forces that pump the working fluid from the condenser to the evaporator. Casings can be made of metal, ceramic or other material. Besides, several different liquids can be used as working fluids (liquid nitrogen, water, alcohol, naphthalene, liquid sodium, etc). Basically, the selection of these materials depends on the device working temperature and its application. The wick, in heat pipes, can be made of different porous materials such as metal screens, sintered metal powder, longitudinal grooves, corrugated fiber glass, etc. Usually, the design of thermosyphons or heat pipes starts with the selection of the working fluid, which must operate at the required temperature level. After the working fluid is selected, the casing is chosen. The casing material should be chemically compatible with the working fluid, avoiding the formation of non-condensable gases that would block part of the device, decreasing its performance. For heat pipes, the wick structure must provide the necessary liquid pumping capacity and be compatible with the working fluid and with the casing material.

In summary, two-phase technologies are very versatile, as they can operate at basically any temperature level and they can assume multiple shapes.

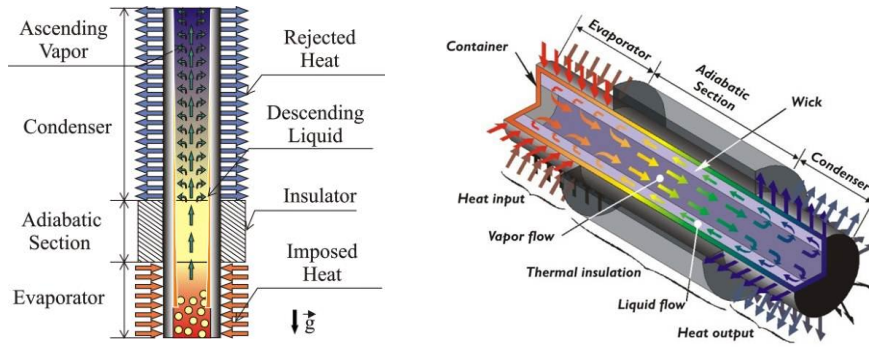


Figure 1. Operational principles of thermosyphons (left) and heat pipes (right).

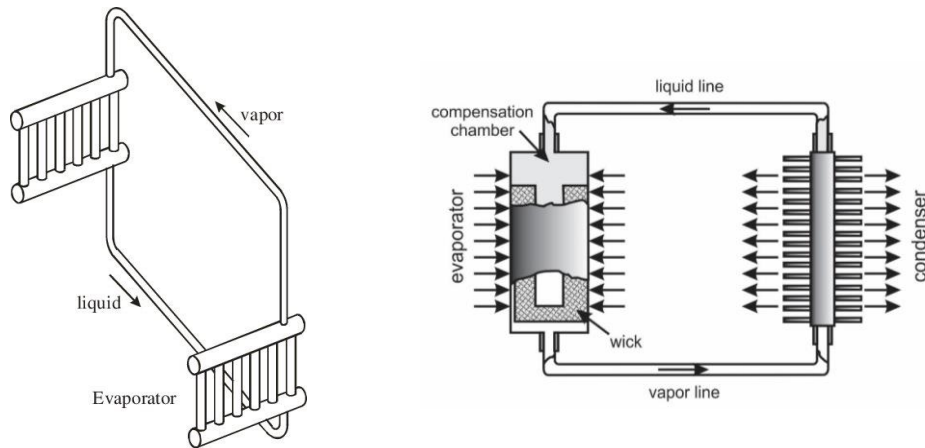


Figure 2. Schematics of loop thermosyphons (left) and loop heat pipes (right).

Basically, a traditional PHP is made from small diameter tubes, meandered in serpentine shape, vacuumed and charged with a controlled amount of working fluid. Figure 3 shows schematics of PHPs. As for other two-phase heat transfer devices, a PHP is composed by three sections: evaporator, adiabatic section and condenser. In the evaporator section, liquid receives heat and evaporates, forming vapor bubbles that grow up to the tube diameter. These bubbles can occupy a considerable volume of the tube. They are intercalated with liquid plugs and the set (vapor slugs and liquid plugs) move together along the tube, as “train wagons” from the evaporator to the condenser, where the working fluid lose heat and the vapor is partially condensed. The expansion (evaporator) and contraction (condenser) of the vapor bubbles results in forces over the working fluid able to force its movement along the tubes. Therefore, heat is transferred from the condenser to the evaporator by two major mechanisms: latent (phase change) and sensible (convection). Actually, PHPs tend to be an isochoric system, and, due this characteristic, the sensible heat transfer by the liquid plugs is the major heat transfer mechanism, representing more than 80% of the total heat transferred.

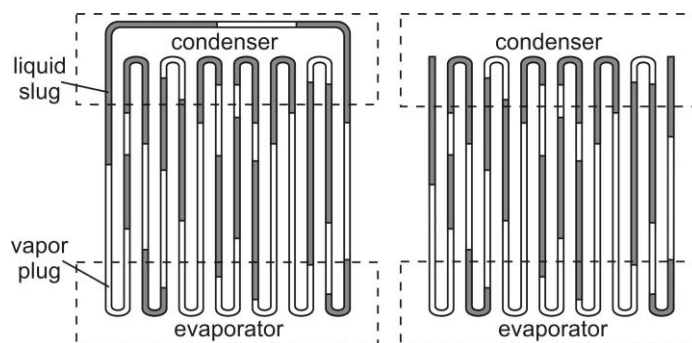


Figure 3. Schematics of pulsating heat pipes: closed circuit (left) and open sealed circuit (right).

2. PHYSICAL PHENOMENA

Several physical phenomena drive the operation of two-phase heat transfer devices. Simple literature available models are used as the basis for modeling their thermal performances, including the heat transfer capacity and pressure drops. These models include, among others: liquid flow in tubes (Hagen-Poiseuille), disjoining pressures and condensation over vertical cooled walls in contact with saturated vapor (Nusselt models), as illustrated in Fig. 4. In the talk, phenomena such as Geyser boiling in thermosyphons will be discussed.

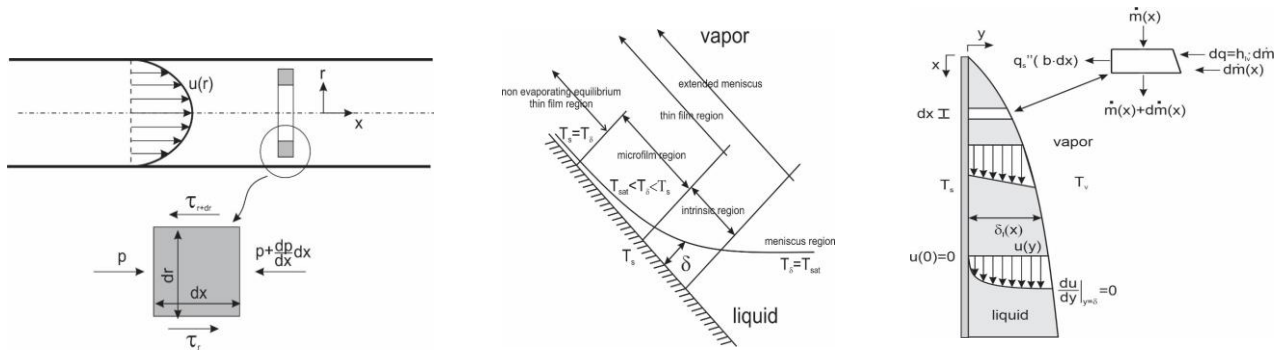


Figure 4. Schematics of important physical phenomena in two-phase devices: Hagen-Poiseuille flow (left) disjoining pressure (center) and Nusselt condensation in vertical cooled walls in the presence of saturated vapor (right).

3. DESIGN AND FABRICATION

The success of the application of a two-phase heat transfer technology starts from the careful design of the device and from the application of the correct fabrication techniques. A flow chart of the design methodology is presented in Fig. 5. The techniques employed for the fabrication of the two-phase devices mentioned will be discussed, with emphasis in diffusion bonding, which can be considered a new process for flat devices.

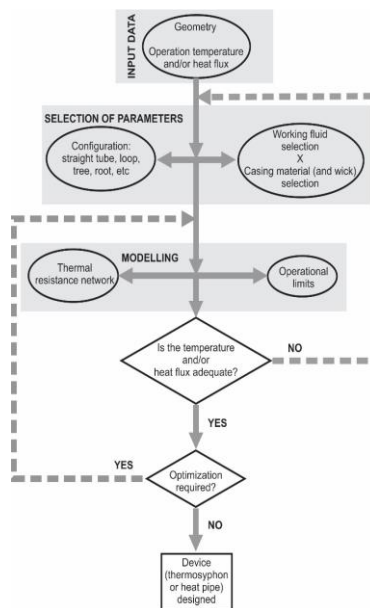


Figure 4. Flow chart of the two-phase heat transfer device design methodology.

4. APPLICATIONS

Several applications of the discussed two-phase devices will be presented, with emphasis in the electronics cooling, avionics, solar, nuclear reactors, converters, cooling towers, heat exchangers, driers, etc., all of them developed in Lactual (UFSC/Brazil) along the years.

5. REFERENCES

Mantelli, M.B.H., 2021. *Thermosyphons and Heat Pipes: Theory and Applications*. Springer Nature, Switzerland.

A RETROSPECTIVE ON EXPERIMENTAL RESEARCH IN UNDERSTANDING MICROLAYER AND CONTACT LINE EVAPORATION

Axel Sielaff^{a,*}, Nishant Sinha^a, Peter Stephan

^a Technical University of Darmstadt, Institute for Technical Thermodynamics, Peter-Grünberg-Str. 10, 64287 Darmstadt, Germany
*sielaff@ttd.tu-darmstadt.de

Keywords: contact line, microlayer, evaporation, boiling, heat transfer

1. INTRODUCTION

It has been known for many years that the region where liquid, wall, and vapor converge in two-phase heat transfer significantly affects the evaporation process. This has been studied by many research groups. This extended abstract presents the experimental investigations carried out at the author's institute. The aim is to provide a basis for the presentation, focusing not only on the results, but also on the experimental methods used, including the question of what worked well and what did not.

2. RESEARCH HISTORY AT TTD ON CONTACT LINE AND MICROLAYER EVAPORATION

Around the year 2000 Höhmann [1] already used thermochromic liquid crystals on a capillary gap with the refrigerant HFE7100 and a thin metallic foil as a heater. His studies showed a temperature difference of approximately 200 mK in the contact region for the stationary contact line. Wagner [2] later used a similar foil heater to investigate the temperature profile under a bubble. He optimized the measurement technique using infrared thermography, which has a lower spatial resolution but can better capture transient processes. Wagner conducted pool boiling studies and calculated the heat flux from the thin foil to the fluid using a simple Fourier heat conduction equation. He identified a region of high heat flux density, which he attributed to the three-phase contact region based on synchronous black-and-white images. Based on the theory of *Contact Line Evaporation*, he did not attribute the broad area of high heat flux density shortly after bubble nucleation to *Microlayer Evaporation* but rather to signal smearing due to the rapid movement of the contact line. However, based on current knowledge, it can be assumed that Wagner was the first to measure *Microlayer Evaporation* at the author's institute. Wagner conducted these measurements similarly to Höhmann, exclusively with refrigerants. Ibrahim [3] extended the methodology for a stationary capillary gap, similar to Wagner, using infrared thermography. He continued to use a thin metallic foil as the heating element and a refrigerant as the test fluid. He found strong cooling in the three-phase contact region and slight oscillation of the contact line. Sielaff continued Wagner's measurements using essentially the same technology and found a clear distinction in bubble growth based on the waiting time for bubble nucleation. Bubbles nucleated after a longer waiting time grow within a hotter thermal boundary layer, leading to rapid spreading. By calculating the heat flux densities, he showed that the different behaviors were attributable to the *Contact Line* and *Microlayer Evaporation*. To study these phenomena independently, Fischer [4] expanded Ibrahim's experimental setup. Fischer used two bellows to move the liquid up and down in the capillary gap in a controlled manner. He also improved the heater design by coating an infrared-transparent crystal with a chromium layer, which is used for Joule heating. This was the first time (at the author's institute) that such studies were conducted without suppressing orthogonal heat conduction from a massive heater to the solid-fluid interface, with simultaneous temperature measurements in close proximity to the liquid interface (distance $< 1 \mu\text{m}$). While previous authors used simpler Fourier heat conduction to calculate the heat flux, Fischer used a numerical 3D calculation for the significantly thicker heater. Fischer described how a receding contact line widened the area of high heat flux, potentially forming a thin film. The heater first used by Fischer and developed by colleagues at the Institute for Material Technology, Surface Technology and Corrosion at the TU Darmstadt [5] is still used in experimental research and has also been used successfully in boiling experiments on the International Space Station [6]. Schweikert extended Fischer's method by moving the heater instead of the fluid and developed a complex in-situ infrared calibration for moving samples [7]. With the optimized measurement technique, Schweikert achieved a breakthrough by clearly identifying the regime boundary between *Contact Line Evaporation* and *Microlayer Evaporation* for the first time [8].

Figure 1 shows that the process tends towards *Contact Line Evaporation* at higher temperatures and slower contact line velocities. In comparison, *Microlayer Evaporation* occurs at lower temperatures and higher velocities. Schweikert also conducted microlayer thickness calculations based on heat flux measurements. Sinha continued Schweikert's work and enhanced the methodology with three-color laser interferometry to directly measure the microlayer thickness and the contact angle.

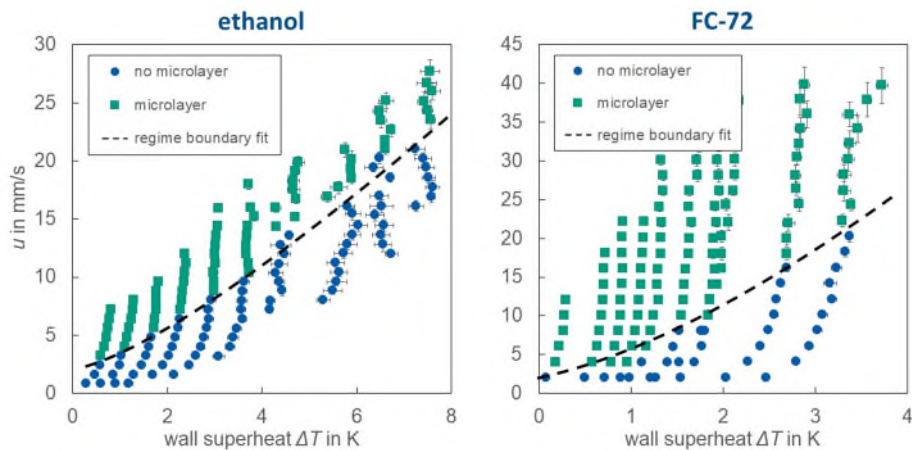


Figure 1: Regime boundary between Microlayer and Contact Line Evaporation for pure ethanol and FC72

3. CURRENT INVESTIGATIONS

Continuing Schweikert’s efforts, ongoing dewetting experiments are being performed with complex surfaces and complex fluids. Two structures with V-grooves (100 μm and 500 μm) were fabricated to perform the dewetting experiments, keeping FC72 as the test fluid. The evaporation regimes change completely by increasing the complexity of the surface. Figures 2a and b show an approximately 6 mm long thin layer of higher heat flux for the 100 μm structure. While the entire area appears to be covered by liquid, the different heat flux ratios caused by the structure can still be seen. In contrast, applying a 500 μm V-grooved surface, the formation of rivulets is observed (see Figures 2c and d). A high heat flux zone is also visible in the area of the three-phase contact line (see Figure 1d). A comparison of the maximum height of the thin film with respect to the liquid level is shown in Figure 2e for the different structures, heat fluxes, and velocities. Comparable to a smooth surface, a higher liquid rise is observed due to the increased dewetting velocity. Conversely, as the heat flux increases, a decrease in liquid rise is observed due to enhanced evaporation. The groove width plays a critical role, especially at lower heating levels where capillary forces dominate the behavior of the liquid. Therefore, narrower 100 μm grooves showed a more significant liquid rise than 500 μm grooves under identical conditions. However, as heating levels increased and evaporation rates accelerated, the differences in liquid rise between the two groove widths diminished.

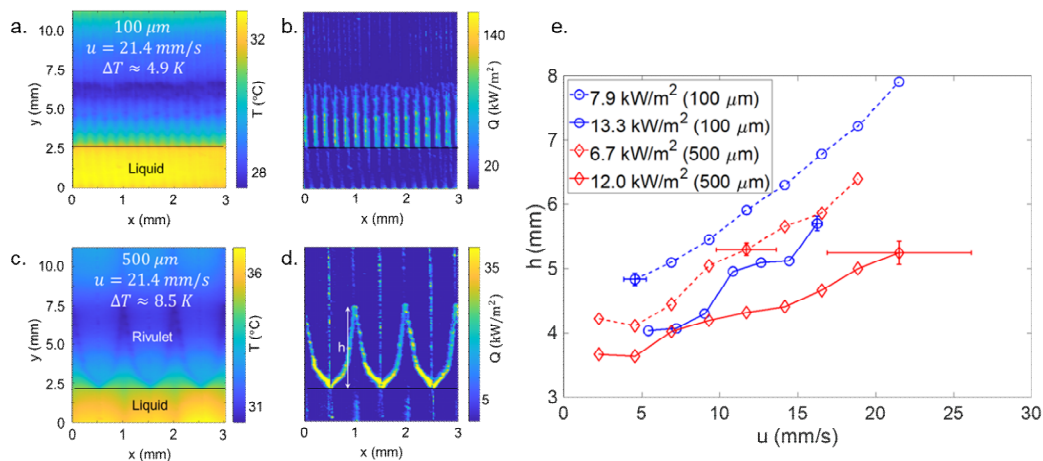


Figure 2: (a,b) Temperature and heat flux profile of the 100 μm V-grooved surface, (c,d) Temperature and heat flux profile of the 500 μm V-grooved surface, (e) Thin film or rivulet height

Further experiments are conducted during evaporation with ethanol/water mixtures (ethanol fractions of 90% w/w and 70% w/w). For these experiments, the height of the contact line position is shown in Figure 3. Interestingly, for an ethanol-water mixture containing 90 wt% ethanol, mainly *Microlayer Evaporation* is observed at the tested wall superheats and dewetting velocities (see Figure 3a). However, as the water concentration was further increased, a multi-stage evaporation process was observed for a 70% ethanol-water mixture and the late stages of the 90% mixture (2.47 mm/s and 4.14 mm/s). First, *Contact Line Evaporation* took place, followed by a period of *Microlayer Evaporation*. Finally, the process became unstable and appeared to return to *Contact Line Evaporation*, also indicated by the dotted line in Figure 3b. Therefore, we currently assume that the regime maps shown in Figure 1 should be extended to include

the influence of concentration in case mixtures are used. However, since the concentration in the thin film changes with time, this poses a significant measurement challenge. According to the authors, the temporal change in the composition of the thin film is also the reason for the instabilities observed in Figure 3b.

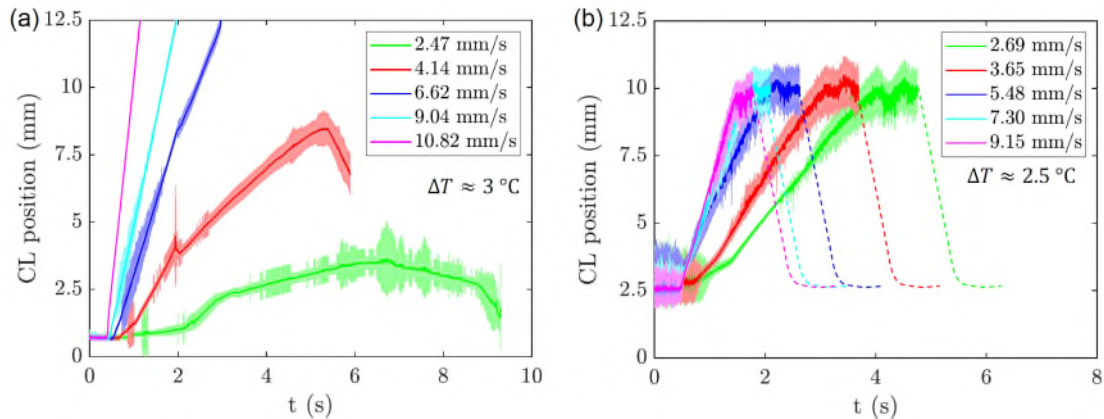


Figure 3: Contact line position during dewetting experiments using water-ethanol mixtures

4. CONCLUSIONS

Experimental investigations of the last 20 years have helped to resolve the controversial discussion as to whether *Microlayer* or *Contact Line Evaporation* predominates in boiling and evaporation processes. It has been shown that both phenomena exist within certain parameter ranges. For some pure substances, both regimes could be precisely distinguished including a regime map showing the dependencies on wall superheat and detwetting velocity. Current research focuses on the influence of structured surfaces and mixtures on such regime boundaries. This is a special experimental challenge because the composition of mixtures changes with time during the evaporation process.

5. ACKNOWLEDGEMENT

The authors gratefully acknowledge the financial support of the German Aerospace Center DLR (Vapor III project, grant no. 50WM2257). They also kindly acknowledge the financial support by the German Research Foundation DFG within the Collaborative Research Center 1194 “Interaction of transport and Wetting Processes” - Project number 265191195.

6. REFERENCES

- [1] Höhmann, C., and Stephan, P., “Microscale temperature measurement at an evaporating liquid meniscus,” *Experimental Thermal and Fluid Science*; Vol. 26, 2-4, 2002, pp. 157–162. doi: 10.1016/S0894-1777(02)00122-X.
- [2] Wagner, E., *Hochauflösende Messungen beim Blasensieden von Reinstoffen und binären Gemischen*, Shaker, Darmstadt, 2009.
- [3] Ibrahim, K., Abd Rabbo, M. F., Gambaryan-Roisman, T., and Stephan, P., “Experimental investigation of evaporative heat transfer characteristics at the 3-phase contact line,” *Experimental Thermal and Fluid Science* [online], Vol. 34, No. 8, 2010, pp. 1036–1041.
- [4] Fischer, S., Batzdorf, S., Gambaryan-Roisman, T., and Stephan, P., “High Resolution Heat Transfer Measurements at the Three Phase Contact Line of a Moving Single Meniscus,” *Proceedings of the 15th International Heat Transfer Conference*, 2014.
- [5] Nejati, I., Sielaff, A., Franz, B., Zimmermann, M., Hänichen, P., Schweikert, K., Krempel, J., Stephan, P., Martin, A., Scheerer, H., Engler, T., and Oechsner, M., “Experimental Investigation of Single Bubble Nucleate Boiling in Microgravity,” *Microgravity Science and Technology* [online], Vol. 32, No. 4, 2020, pp. 597–607.
- [6] Sielaff, A., Mangini, D., Kabov, O., Raza, M. Q., Garivalis, A. I., Zupančič, M., Dehaeck, S., Evgenidis, S., Jacobs, C., Van Hoof, D., Oikonomidou, O., Zabulis, X., Karamaounas, P., Bender, A., Ronshin, F., Schinnerl, M., Sebilleau, J., Colin, C., Di Marco, P., Karapantsios, T., Golobič, I., Rednikov, A., Colinet, P., Stephan, P., and Tadrist, L., “The multiscale boiling investigation on-board the International Space Station: An overview,” *Applied Thermal Engineering*; Vol. 205, 2022, p. 117932.
- [7] Schweikert, K., Sielaff, A., and Stephan, P., “Pixel-wise in situ calibration method for high accuracy infrared thermography of moving targets,” *Infrared Physics & Technology*; Vol. 118, 2021, p. 103862.
- [8] Schweikert, K., Sielaff, A., and Stephan, P., “On the transition between contact line evaporation and microlayer evaporation during the dewetting of a superheated wall,” *International Journal of Thermal Sciences*; Vol. 145, 2019, p. 106025.

DROPLET IMPACT ONTO SUPERHYDROPHOBIC SURFACES

Dongsheng Wen^{a,b*}, Zunru Fu^b, Yan Yan^a, Xiaolong Ma^a and Guice Yao^b

^aInstitute of Thermodynamcis, Technical University of Munich,

^bSchool of Aeronautic Science and Engineering, Beihang Univeristy

*Email: d.wen@tum.de

Keywords: droplet, superhydrophobicity, low pressure, vaporization, bouncing

1. INTRODUCTION

Droplet impact on solid surface bears significant implications to a wide range of applications, such as spray drying/cooling, diesel combustion, plasma spray coating, water proofing and self-cleaning, anti-icing and inkjet printing. Considering its importance, a large number of experimental, theoretical and numerical studies have been conducted on droplet impact. These studies can be clearly demarcated into three categories: droplet impact under adiabatic, under heating conditions and under cooling conditions, where nice reviews/summaries can be found recently (Josserand and Thoroddsen, 2016, Chen et al.2022 and Wang et al. 2023). Within each category, various influential factors have been investigated, including the influence of i) the solid substrate with different structures and wettability, either homogeneously or heterogeneously, ii) the gas environment such as pressure, temperature and moisture, as well different types of gases, and iii) the droplet parameters such as composition (i.e., mixtures of fluids or fluid containing different ingredients ranging from blood cells to nanoparticles) and impact velocities. Different impact patterns have been reported under adiabatic, heating and cooling conditions. To account for different observed phenomena, a number of dimensionless numbers, such as Weber, Reynolds, Ohnesorge and Capillary number have been used to reflect the relative importance among inertial, viscous and capillary forces. Some well-known relationships have been established for droplet dynamics, such as the maximum spreading factor, the droplet contact time, and droplet rebound characteristics on different surfaces.

One interesting phenomenon observed both experimentally and numerically is the droplet skating or bouncing from the surface, which could happen on hydrophilic and smooth surfaces, on superhydrophobic surfaces, and on extremely hot surfaces. The presence of gas, here we include both entrapped air and generated vapor via phase change, governs the droplet dynamics. The gas can be caused by i) air trapped during the droplet impact, ii) air pockets presenting on structured surfaces, and iii) vapor produced during the droplet life time, including evaporation, boiling and sublimation. For instance, the presence of air pockets is the underlying mechanism for surface hydrophilicity that is responsible for various droplet dynamics such as flashing, skating and bouncing. Droplet bouncing on hydrophilic and smooth surfaces is due to the cushion effect from the entrapped air film between the approaching droplet and the surface. The classical Leidenfrost phenomena where droplets dance on hot surfaces is due to the generated vapor film that separate the droplet from the heating surface. It shall be noted that most of the droplet impact studies are primarily focused on atmospheric pressure conditions. Under low pressure environment, it is expected that the amount of entrapped gas would become smaller, while the generated vapor associated with low pressure phase change may become increasingly important.

Quite a few applications are related to low pressure. For instance, most of the steam condensers operate in the range of tens of kPa, achieving stable droplet condensation and reducing contact time still remain as a dream for heat transfer scientists. At similar pressure range, subcooled droplets impacting onto aircraft leads to ice formation with different morphologies, an area of high importance to the aviation safety. At lower pressure (i.e., below 10 kPa), vaporization from water droplet can be used as microthrust for micro-spacecraft, and the concept of vapor chamber operating around 1 kPa pressure has been suggested, and recent advance in thermal spray for thermal barrier coatings operates in 1-5 kPa range (Nishii et al.2021). Our knowledge about droplet impact under low pressure, however, is still insufficient. For impact under adiabatic conditions, a pioneering study observed that under a few kPa range, the typical droplet splash phenomenon can be largely suppressed due to the reduced or disappearance of entrapped gas film upon impact (Xu et al.2005). A few limited low pressure studies under heat transfer conditions are focused on stationary droplets. A typical experiment starts with a stationary droplet at ambient conditions, and the pressure of the chamber is decreased rapidly by a vacuum pump. The vaporization due to depressurization produces a rapid cooling effect that may lead to droplet icing and subsequent bouncing from the substrate. For instance, a droplet trampolining phenomenon was discovered as the pressure was reduced to a few kPa (Schutzius et al.2015), where liquid droplets continuously bounced off from the substrate, like a trampolining. This was explained by a vapor overpressure effect, arising from the fast evaporation between the droplet and the substrate. Using a similar setup, iced droplets jumping away from the substrate was reported as the pressure was reduced to around 0.5 kPa (Yan et al. 2024). It was claimed that intensive surface vaporization from the freezing droplet during the recalescence process induced an upward vapour momentum, which led to the iced droplet jumping. However

due to the lack of proper control of the gas and substrate temperature in these work, droplet experienced a non-equilibrium phase change process during the rapid depressurisation process, from possibly flash vaporisation associated with the depressurization to a quasi-equilibrium phase change due to temperature difference among the droplet, environment gas and the substrate. Such complexities make the interpretation of droplet dynamics difficult.

This work reports our recent work on droplet impact onto different surfaces with varied hydrophilicities, from homogeneous to heterogeneous surfaces. One particular focus will be on droplet impact onto super-hydrophobic surfaces under low pressure, where a unique pancake bouncing phenomenon was observed. In addition, a maximum reduction in the contact time, i.e., 85%, comparing to all reported data has been obtained.

2. EXPERIMENTAL SETUP AND RESULTS

We have performed many droplet impact studies from both experimental and numerical simulation aspects, including droplet dewetting, droplet impact on varied wettability surfaces, droplet icing, entrapped air film effect upon droplet impact and multiscale droplet modelling (Luo et al. 2023). Some of these will be illustrated in the presentation, and here we present only the droplet impact at low pressure conditions. A common impact facility under low pressure is shown in Figure 1. The experiments were performed in a low pressure environment chamber (EC), where the air pressure and moisture level were controlled (Fu et al. 2024). An example of micro-channel structured superhydrophobic surfaces prepared by the laser ablation method is also shown, which has a typical static contact angle (CA) of degassed water of 160° with the CA hysteresis of $<8^\circ$.

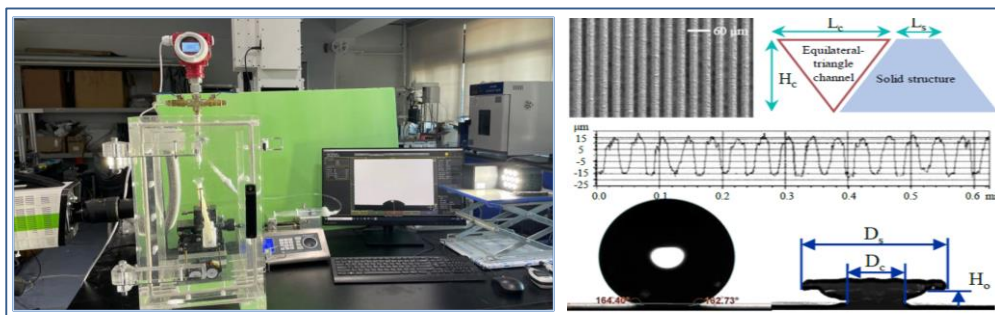


Figure 1 Preliminary low pressure impact experimental setup and substrate characteristics

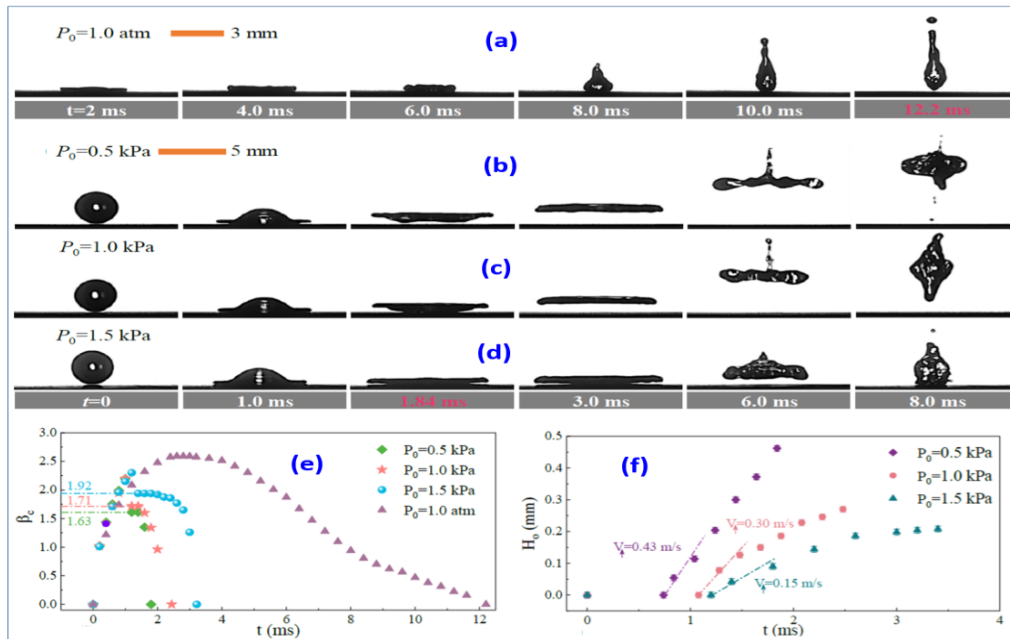


Figure 2 Unique pancake bouncing phenomenon in low pressure (where $\beta_c = D_c/D_0$ is the spreading factor, and H_0 is the lift height of the lamella, initial water droplet size $D_0=2.50$ mm and $We=77$)

Figure 2 displays a typical scenario of a droplet impact in atmospheric and low-pressure environment at $We=77$. A conventional droplet spreading-retracting rebound is clearly observed under 1 atm condition, Figure 2a. However, a unique pancake-bouncing phenomenon is observed at environment pressure < 2 kPa, Figure 2 (b-d), showing three distinctive features: i) Lamella lift-off, which occurs during the spreading period when the out-rim of the droplet is suddenly lifted off the surface, forming a flying-saucer shape. The lift-off induces a sudden stop of the outward spreading of the contact line, Figure 2e. ii) Lamella growth, where the lifted lamella keeps growing both vertically and horizontally,

producing a ‘pulling effect’ that accelerates the retraction of the contact line, Figure 2f. iii) Pancake bouncing, where the droplet detaches from the solid nearly parallelly, forming a flat pancake shape. As the droplet starts bouncing during the spreading stage, i.e., instead of in the receding period under 1 atm, the droplet contact time is significantly reduced in low pressure environment. The shortest contact time is identified as 1.72 ms in 0.5 kPa environment, which is a ~85% reduction comparing to 1 atm condition (12.2 ms). To the best of our knowledge, this represents the maximum reduction of the contact time upon droplet impacts onto a solid surface, either from surface structure design or external energy input.

It should be noted that the pancake bouncing discovered here is fundamentally different from that reported in atmospheric condition (Liu et al.2014), even though they have similarities in droplet morphology and contact time reduction. The atmospheric pancake bouncing is caused by the capillary energy recovery from the penetrated liquid into sub-millimeter-scaled superhydrophobic structures, and the bouncing starts from the center of the droplet, i.e., the recovery of capillary energy lifts the droplet in a pancake form. For smaller structures (<300 μm), no atmospheric pancake bouncing can be observed in the range of $We = [3-64]$. There is no sufficient capillary energy recovery in our study due to much smaller structures, and the spreading lamella always leaves the surface first, which then pulls the central part away from the surface. The result is also different from the low-pressure trampling-type bouncing phenomenon for stationary or quasi-stationary droplets, where a conventional droplet bounce pattern was reported (Schutzius et al.2015). The dynamic pressure resulting from droplet impact at high Weber numbers should be properly accounted.

The key to understand such low-pressure bouncing lies in the proper analysis of the lamella dynamics, i.e., why it can be lifted off during the spreading period? Here, we propose that it is the water vapor overpressure accumulated inside the micro-channel structure beneath the droplet, which is originated from the fast evaporation under rarefied conditions, is the driven power for the lift-up of the lamella. Different to the stationary or the low Weber number case (i.e., the estimated maximum value of $We \sim 1$ due to droplet re-bouncing (Schutzius et al.2015), the kinetic energy effect from high Weber number droplet impact has to be properly accounted in our case. Consequently, we considered three competitive forces that are responsible for the lamella lift-off and the subsequent pancake bouncing phenomenon: i) the vapor overpressure due to the fast evaporation underneath the droplet, ii) the impact pressure effect resulting from the droplet kinetic energy, and iii) the adhesion from the surface. Different to an idealized constant evaporation rate assumption that corresponds to the given environment pressure, we have to consider the variation of evaporation rate under the influence of local vapor pressure distribution along the micro-channels underneath the droplet to better account for the overpressure effect, as below. It is believed that the competition between the water vapor overpressure effect, droplet impact force, and surface adhesion shall determine if the pancake bouncing behavior could occur.

3. CONCLUSIONS

This work reports the droplet impact behaviors on various superhydrophobic surfaces, and a unique pancake bouncing phenomenon was firstly reported at environmental pressure less than 2 kPa with fundamentally different mechanisms from the previous reported pancake bouncing in atmospheric environment. Comparing to the inertial-capillary timescale, the contact time can be reduced by 85%. The restrained flow of the fast-evaporated water vapor inside the micro-channel structures by the viscous force in slip flow regime is identified as the power source that drives the spreading lamella lifting-off the ground. The competition between the vapor overpressure, impact pressure and surface adhesion effects determine the pancake bouncing behavior and the presence of different patterns and variation of contact time. Future work are proposed to address the current limitations of the experimental system, with better control of the heat transfer effect among the droplet, the environmental and the substrate.

4. REFERENCES

- Cheng, X., Sun, T. and Gordillo. L., 2022. “Drop impact dynamics: impact force and stress distribution”. *Annual Review of Fluid Mechanics*, 54:57
- Josserand, C. and Thoroddsen. S., 2016. “Droplet impact on a solid surface”. *Annual Review of Fluid Mechanics*, 48: 365
- Wang, X., Xu, B., Guo, S., Zhao, Y. and Chen, Z., 2023. “Droplet impacting dynamics: recent progress and future aspects”. *Advances in Colloid and Interface Science*, 317:102919
- Nishii, K., Hattori, A., Koizumi, H., and Komurasaki, K., 2021. “Low-pressure-vaporization of water droplets on wall under normal and microgravity conditions”. *Acta Astronautica*, 186: 508
- Bird, J., Dhiman, R., and Varanasi, K., 2013. “Reducing the contact time of a bouncing drop”. *Nature*, 2013, 503:385
- Xu, L., Zhang, W. and Nagel, S., 2005. “Drop splashing on a dry smooth surface”. *Physical Review Letters*, 94: 184505
- Schutzius, T., Jung, S., Martra, T., Graeber, G., Kohme, M. and Poulikakos, D., 2015. “Spontaneous droplet trampolining on rigid superhydrophobic surfaces”. *Nature*, 527: 82
- Yan, X., Samuel, C. etc. 2024. “Unravelling the role of vaporization momentum in self-jumping dynamics of freezing supercooled droplet at reduced pressures”. *Nature Communication*, 15:1567
- Luo, J., Chu, F., Zhang, J. and Wen, D., 2023. “Re-spreading behavior of droplet impact on superhydrophobic surfaces at low Weber numbers”. *Applied Physical Letter*, 123: 061604
- Fu, Z., Jin, H., Zhang, J., Xue, T., Guo, Q., Yao, G., Gao, H., Wang, Z. and Wen, D., 2024. “Low pressure pancake bouncing on superhydrophobic surfaces”. *Small*, 2310200.
- Liu, Y., Moevius, L. etc. 2014. “Pancake bouncing on superhydrophobic surfaces”. *Nature Physics*, 10: 515.

LAMINAR SEPARATION BUBBLES: FROM AIRFOILS TO FINITE WINGS

Serhiy Yarusevych

University of Waterloo, 200 University Ave. W, Waterloo, Ontario, Canada, N2L
syarus@uwaterloo.ca

Keywords: Laminar separation bubbles, airfoils, wings, low Reynolds number aerodynamics, transition.

1. INTRODUCTION

A growing number of practical applications involves lifting surfaces, such as wings and blades, operating at aerodynamically low chord-based Reynolds numbers ($Re_c < 500,000$, e.g., Carmichael, 1981). Examples of relevant applications include micro aerial vehicles, small-to-medium scale wind turbines, gliders, conventional aircraft during take-off and landing, high altitude flyers, last stages of turbojet engines, urban mobility platforms, and many other engineering systems. In aerodynamically low Reynolds number flows, a laminar boundary layer forming on the suction surface is prone to separation. Depending on the operating parameters, namely, the Reynolds number, angle of attack, and free-stream turbulence, the separated shear layer often undergoes a relatively rapid laminar-to-turbulent transition and can reattach in the mean sense, forming a laminar separation bubble (LSB). Although less significant compared to stall, the formation of an LSB has a detrimental effect on lift-to-drag ratio, and its inherently unsteady dynamics can lead to vibrations and noise emissions. Thus, LSBs have been a subject of active research over the past several decades.

Pioneering studies of LSBs largely focused on the mean bubble topology and the effect of bubble formation on surface pressure distribution and airfoil performance (e.g., Tani, 1964). Subsequently, due to its importance to flow reattachment and separation bubble formation, laminar-to-turbulent transition process in the upstream boundary layer and within LSB was explored extensively in both experimental and numerical studies (e.g., Watmuff, 1999; Marxen et al., 2013). The earlier stages of the transition process have been shown to agree well with linear stability theory predictions (e.g., Yarusevych and Kotsonis, 2017); while later stages of transition lead to shear layer roll-up and the formation of coherent structures (Marxen et al., 2013). The shedding of shear layer vortices is argued to play a dominant role in re-energising the near-wall flow and leading to flow reattachment in the mean sense. The strongly periodic nature of these structures can also give rise to tonal noise emissions when an LSB forms close to the trailing edge (Pröbsting and Yarusevych, 2015). Although the shear layer rollers are known to break down in the vicinity of the mean reattachment point, the associated strongly periodic pressure fluctuations have been argued to create a feedback loop by influencing the disturbance environment upstream of separation (e.g., Boiko et al., 2002).

The author, along with multiple collaborators, have contributed to the recent progress in research focused on LSB transition and dynamics. This abstract, and the associated keynote presentation, are meant to elucidate some of this work. In particular, the aim is to provide a comprehensive summary of the transition process for an LSB forming on an airfoil, encompassing initial transition in the attached boundary layer, subsequent flow development in the fore portion of an LSB, and the eventual formation and dynamics of coherent structures. Further, the recent work focused on LSB development on finite wings/blades is highlighted, extending the prior research on two-dimensional airfoils to finite lifting surfaces encountered in practice, as well as LSB development during transient flow events. It should be noted that the foregoing discussion and the subsequent highlights of the findings from the research conducted by the author are by no means meant to providing an exhaustive literature review, and the reader is referred to the associated publications for a more extensive list of references.

2. METHODS OF INVESTIGATION

The overview of the results presented in the subsequent section is based on a series of published papers by the author and colleagues. The details of the associated experiments and analytical modelling are available in the relevant publications, and only a very brief outline is provided here. For the studies concerned with a nominally two-dimensional airfoil geometry, an airfoil model was positioned either between two end plates or spanning the width of the test section to minimize end effects to the immediate vicinity of model mounting locations. An experimental verification was then conducted to ensure nominally two-dimensional flow development, in the mean sense, over the central span of the model where measurements had been conducted. For the studies involving finite models, a removable attachment was designed so that a nominally two-dimensional airfoil model could be converted into a finite wing by removing a portion of the model span, creating a free end.

For all the studies discussed in the next section, wind tunnel experiments were conducted in low free-stream turbulence environment ($Tu \sim 0.06\%$) and the models were polished following a rigorous protocol to ensure uniform, smooth surface

finish. Consequently, a normal mode of transition was observed for all the cases examined. The wind tunnel measurements consisted of different combinations of flow visualisations, surface pressure measurements, and fluid flow velocity measurements via planar and volumetric Particle Image Velocimetry (PIV) selected to provide a comprehensive description of the flow features of interest.

3. OVERVIEW OF MAIN FINDINGS

It is first instructive to provide an overview of the transition process development in the presence of an LSB. Based on the classical receptivity theory, the disturbances developing in the boundary layer on an airfoil are expected to originate in the leading-edge region, where free stream vortical and acoustic perturbations enter the near-wall flow. Through controlled acoustic excitations, Pröbsting and Yarusevych (2021) verified that the receptivity region is situated between the leading edge and the vicinity of the suction peak, i.e., encompassing the favourable pressure gradient region upstream of laminar flow separation. Employing experimental velocity and pressure measurements, Michelis et al., (2017) used a combination of a numerical solution of boundary layer equations well upstream of separation and experimental measurements of an LSB to provide a comprehensive outlook on the combined stability characteristics of the attached boundary layer and the bubble. Their linear stability modelling on the combined mean velocity fields demonstrates the presence of a continuous stability spectrum, namely, continuous evolution of the most unstable perturbations in the unstable flow domain starting from the attached boundary layer. It can thus be deduced that, at sufficiently large Reynolds numbers, the initial disturbances originating from the free-stream perturbations in the receptivity region undergo selective amplification of the unstable packets through Tollmien-Schlichting instability in the boundary layer, which then feed into the separated shear layer where a much stronger amplification takes place through the predominantly inviscid Kelvin-Helmholtz instability. The results of Yarusevych and Kotsonis (2017) show that the amplification rates scale with the shape factor, producing a notably stronger amplification in the separated flow and within taller LSBs. Once the amplified perturbations reach significant amplitudes (~ 0.1 of edge velocity), shear layer is rolled up into vortices shed at the frequency of the most amplified perturbations. Thus, the transition process initiates in the receptivity region and is dictated by the combined stability characteristics of the attached boundary layer and the upstream portion of the LSB. The growth of unstable perturbations in turn lead to formation and determine the characteristics of shear layer vortices that dominated flow dynamics in the aft portion of LSB.

The development of shear layer vortices was a subject of some scientific debate. Their formation was associated with strong spanwise coherence in some studies (e.g., Kirk and Yarusevych, 2017), while strongly distorted structures were observed in other investigations (Burgmann and Schroder, 2008), and different mechanisms that may be responsible for vortex deformations have been identified (Marxen et al., 2013). The investigations of Istvan and Yarusevych (2018) indicate that free-stream turbulence intensity level can significantly affect the development of shear layer vortices, with higher free-stream turbulence levels resulting in notably stronger distortions of vortices shed in LSBs, correlating with higher turbulence intensities in the experimental facilities where such flow development was observed previously. Michelis et al. (2018) performed tomographic PIV measurements to elucidate the development of vortices in LSBs. They employed stability analysis to demonstrate that both normal and oblique modes were amplified in the upstream boundary layer. As expected, normal modes are associated with the highest amplification rates, but non-negligible amplification of oblique waves was also observed. On the basis of combined stability analysis and experimental data, Michelis et al., (2018) postulate that vortex deformations originate from a superposition of normal and oblique waves amplified upstream of LSB, which results in the initial spanwise deformation of the vortex filaments. The degree of the initial vortex deformation depends on the significance of oblique waves relative to the normal mode. This was further substantiated by the observation that forcing the normal mode can serve to suppress vortex deformations observed in the baseline flow. Moreover, Kurelek et al., (2023) showed that naturally amplified spanwise deformations can be triggered artificially by deterministic three-dimensional local forcing applied upstream of separation. Finally, it can be demonstrated that initial spanwise deformations of shear layer vortices are naturally amplified in the LSB due to the joint action of mean shear and Biot-Savart induction.

An extension of the progress made in understanding of LSB physics on airfoils has been made by considering LSBs on finite wings. Toppings and Yarusevych (2021, 2022) conducted detailed experimental measurements to elucidate the mean LSB topology and dynamics on a finite wing. It has been shown that, despite notable changes in the effective angle of attack along the span of a finite wing, the mean bubble topology does not change appreciably along the span, except for the regions adjacent to wing root and tip. Further, an LSB locks onto a common shedding frequency and the shear layer vortices are initially shed in a largely two-dimensional manner outside of the regions influenced by end effects. Their results also show that LSB forms an open separation near the root and tip region with spanwise flow entering the bubble from both ends. Near the wing tip, the separation is suppressed due to the action of the tip vortex, while corner separation at the root and turbulent boundary layer development can influence the transition process in the adjacent LSB region.

Toppings and Yarusevych (2024) considered transient effects associated with bubble bursting and formation on an airfoil and finite wing due to changes in free-stream conditions, e.g., the Reynolds number. Their work indicates that bubble bursting, i.e., transition from LSB to stall, is initiated at a spanwise location associated with a local maximum LSB

height located away from the root and tip regions. The stalled flow region then spreads outward towards wing tip and root. A reverse process is observed when LSB is formed, where reattachment propagates towards midspan from the wing tip and root regions. Notably, the process of bubble bursting and formation takes more than 10 convective time scales, with substantially shorter transient durations observed on an airfoil compared to an equivalent finite wing configuration.

4. CONCLUSIONS

LSB topology and dynamics are largely governed by the formation and evolution of shear layer roll up vortices leading to laminar-to-turbulent transition and shear layer reattachment in the mean sense. Linear stability analysis confirms that there is a continuous stability spectrum spanning laminar boundary layer and separated shear layer regions, linking LSB transition and shear layer vortex shedding to upstream amplification of disturbances that originate from free-stream perturbations in the receptivity region.

Flow development in the aft portion of the bubble is highly three-dimensional even on nominally two-dimensional geometries. It manifests in progressive deformation of shear layer vortices, with subsequent vortex breakdown. The initial deformations may be attributed to the growth of oblique modes in the attached boundary layer, which are inherently amplified in the bubble.

On a finite wing, an open LSB forms due to wing tip and root effects. Away from the affected regions, however, LSB topology and dynamics are quasi two-dimensional, with shedding process locking onto a common frequency despite effective angle of attack variation across the span.

During transients leading to bubble bursting/re-formation, LSB bursting initiates in midspan region and spreads outwards along the span, while a reverse progression is followed during LSB re-formation. These transients last on the order of 10 convective time units and are shorter for the airfoil compared to finite wing.

5. REFERENCES

- Boiko, A. V., Grek, G. R., Dovgal, A. V. and Kozlov V. V. (2002) *The origin of turbulence in near wall flows*. Springer-Verlag, Berlin.
- Burgmann, S. and Schroder, W. (2008) "Investigation of the vortex induced unsteadiness of a separation bubble via time-resolved and scanning PIV measurements," *Experiments in Fluids*, Vol. 45, pp. 675-691.
- Carmichael, B.H. (1981) "Low Reynolds number airfoil survey." NASA CR-165803.
- Istvan, M., and Yarusevych, S. (2018) "Effects of free-stream turbulence intensity on transition in a laminar separation bubble formed over an airfoil," *Experiments in Fluids*, 59:52, pp. 1-20.
- Kirk, T., and Yarusevych, S. (2017) "Vortex shedding within laminar separation bubbles forming over an airfoil," *Experiments in Fluids*, 58:43, 17 p.
- Kurelek, J., Kotsonis, M., and Yarusevych, S. (2023) "Superposition of AC-DBD plasma actuator outputs for three-dimensional disturbance production in shear flows," *Experiments in Fluids*, 64:84, pp. 1-21.
- Marxen, O., Lang, M., and Rist, U. (2013) "Vortex formation and vortex breakup in a laminar separation bubble," *Journal of Fluid Mechanics*, Vol. 728, pp. 58-90.
- Michelis, T., Kotsonis, M., and Yarusevych, S. (2018) "On the origin of spanwise vortex deformations in laminar separation bubbles," *Journal of Fluid Mechanics*, Vol. 841, pp. 81-108.
- Michelis, T., Yarusevych, S., and Kotsonis, M. (2017) "Response of a laminar separation bubble to impulsive forcing," *Journal of Fluid Mechanics*, Vol. 820, pp. 633-666.
- Pröbsting, S., and Yarusevych, S. (2015) "Laminar separation bubble development on an airfoil emitting tonal noise," *Journal of Fluid Mechanics*, Vol. 780, pp 167- 191.
- Pröbsting, S., and Yarusevych, S. (2021) "Airfoil flow receptivity to simulated tonal noise emissions," *Physics of Fluids*, Vol. 33, 044106, pp. 1-16.
- Tani, I. (1964) "Low speed flows involving bubble separations," *Progress in Aerospace Science*, Vol. 5, pp. 70-103.
- Toppings, C.E. and Yarusevych, S. (2022) "Structure and dynamics of a laminar separation bubble near a wing root: towards reconstructing the complete LSB topology on a finite wing", *Journal of Fluid Mechanics*, Vol. 944, A14.
- Toppings, C.E. and Yarusevych, S. (2021) "Structure and dynamics of a laminar separation bubble near a wingtip", *Journal of Fluid Mechanics*, Vol. 929, A29, pp. 1-39.
- Toppings, C.E. and Yarusevych, S. (2024) "Laminar separation bubble formation and bursting on a finite wing", *Journal of Fluid Mechanics*, Vol. 986, A26.
- Watmuff, J. H. (1999) "Evolution of a wave packet into vortex loops in a laminar separation bubble," *Journal of Fluid Mechanics*, Vol. 397, pp. 119-169.
- Yarusevych, S., and Kotsonis, M. (2017) "Steady and transient response of a laminar separation bubble to controlled disturbances," *Journal of Fluid Mechanics*, Vol. 813, pp. 955-990.

Effect of initial ambient pressure on the explosive characteristics of thermobaric explosive

Quan Mai^a, Ying Mai^b, Jian Yao^a, Xianzhao Song^a, Guokai Zhang^a, Dan Zhang^a, Bin Li^a, Lifeng Xie^a, Yongxu Wang^{a,*}

^a School of Safety Science and Engineering, Nanjing University of Science and Technology, Nanjing 210094, Jiangsu, China

^b Luoyang 11th Senior High School, Luoyang 471000, Henan, China

*wangyongxu@njust.edu.cn

Abstract: In order to study the effect of initial ambient pressure on the explosion characteristics of thermobaric explosives, this paper carries out a series of static explosion experiments on different grades of thermobaric explosives under two kinds of initial ambient pressures, and adopts the pressure test system, high-speed camera system and temperature acquisition system to get the explosion process, shock wave overpressure parameter and temperature parameter of thermobaric explosives under different initial ambient pressures, and carry out a comparative analysis. The results show that low-pressure conditions have an inhibitory effect on the peak overpressure of the shockwave generated by the explosion of thermobaric explosives, and that the overpressure decay rate of thermobaric explosives with large charges is higher than that of those with small charges at close range, but the opposite is true at long range. As the initial ambient pressure decreases, the shockwave propagation velocity and TNT equivalent of thermobaric explosives decrease, and this effect is more pronounced for small charge explosives. The shock wave overpressure attenuation rate shows a similar sinusoidal law of change and establishes the shock wave overpressure peak attenuation law equation for warm pressure explosives at different initial ambient pressures. The explosion process and temperature parameters of thermobaric explosives were further analyzed, and it was found that the diameter, height, intensity and duration of the explosive fireball are positively correlated with the quality of the explosive and negatively correlated with the initial ambient pressure, and that the low-pressure environment significantly inhibits the energy release efficiency of thermobaric explosives. As the initial ambient pressure decreases, the maximum temperature of the exploding fireball and the duration of the high temperature decrease significantly, but the effect of quality on these parameters is smaller. These conclusions provide important theoretical support for a better understanding of the explosive behavior of thermobaric explosives under different initial environmental pressures.

Keywords: thermobaric explosive, blast wave, Initial environmental pressure, Explosive fireball temperature, TNT equivalent

1. INTRODUCTION

Thermobaric explosives (TBX) have attracted considerable attention in military and engineering fields in recent years due to the unique explosive properties and efficient energy release mechanism [1-3]. Compared to traditional high explosives, thermobaric explosives can generate higher blast pressure and longer sustained high temperature through the synergistic effect of combustion reaction and blast wave, which makes their destructive effect in enclosed or semi-enclosed environments particularly significant [4-7].

Deepening the study of temperature and pressure explosives efficient energy release process, revealing the explosion reaction mechanism and characteristics of temperature and pressure explosives, mastering its shock wave characteristic parameter law and the principle of high-temperature effect is the key direction of domestic and foreign research [7-10]. The current research on the explosion characteristics of thermobaric explosives evaluation method is mainly focused on the development of explosive formulations, thermobaric explosives detonation characteristics and energy release mechanism, etc. [11-13], the energy release of thermobaric explosives is more complex, which can be mainly divided into three phases [14-15]: 1) rapid decomposition of the explosives and the anaerobic reduction reaction; 2) anaerobic combustion phase, the oxides produced by the explosion and metal particles occur a sharp reaction; 3) aerobic combustion reaction after the explosion, the metal powder in the explosives such as aluminum powder and oxygen in the air to aerobic combustion reaction. The aluminum powder content, granularity and activity of the aluminum powder have an important effect on the energy output characteristics of temperature and pressure explosives, so understanding the explosion characteristics of different temperature and pressure explosives plays a crucial role in the configuration and selection of formulations [16]. The current assessment of the explosion characteristics of thermobaric explosives of different methods, such as Wang B et al [17] on the different equivalents of thermobaric explosives of the shock wave overpressure, explosion of fireballs and other comparative studies, found that with the increase in charge, the maximum temperature of the explosion of the fireball, the fireball size (diameter \times height) and the duration of the explosion of the fireball have a certain degree of increase in the high-temperature range in the fireball range of the percentage of the fireball has also increased. Chen K et al [18] studied the peak overpressure, impulse and quasi-static pressure of aluminum explosives containing different particle sizes, and found that with the increase of aluminum powder particle size, the reflected wave overpressure and impulse showed a tendency to first increase and then decrease, and with the increase of aluminum powder particle size, the reflected wave overpressure and impulse showed a tendency to first increase and then decrease. Zheng B et al [19] u

sed a high speed camera to carry out a comparative analysis of the throw of different explosives to determine the mathematical expression for the time-synchronous change in the radius of throw of the explosion products of thermobaric explosives. Li X et al [20] used infrared thermography to analyze the explosion temperature of thermobaric explosives and found that the temperature of the explosion cloud is higher. The high temperature duration is 2 to 5 times that of TNT. The volume of the high-temperature cloud can be 2 to 10 times that of TNT. Xu W et al [21] studied the shock wave overpressure, impulse and temperature of three typical explosives and found that zinc plated explosives had the largest peak and RDX explosives formed fireballs with the smallest maximum diameter and duration.

Although there are many methods for evaluating the explosive properties of explosives, a systematic and scientific evaluation method has not been established, and the existing evaluation methods and occasions are all carried out under atmospheric conditions, but the actual application environment, the initial environmental pressure may be significantly different due to factors such as geographical location, climatic conditions or man-made operations [22-23]. This makes it particularly important to study the behavior of hot pressure explosives at different initial ambient pressures. However, most of the domestic and foreign research on the explosion characteristics of different initial environmental pressure is established in the confined space simulation of different environments or through simulation methods to open the evaluation [24-25], such as: Li R et al [26] use the theory of magnitude analysis and the Autodyn finite element software to analyze the shock wave parameters of explosives under low temperature and low pressure conditions, and get the altitude increases, the explosion of the near-field shock wave propagation velocity increases, the explosion of the far-field shock wave propagation velocity is reduced. High altitude environment of low pressure on the shock wave peak overpressure and specific impulse greater than the impact of low temperature, the explosion of near-field shock wave propagation speed depends on the impact of low pressure, the explosion of far-field shock wave propagation speed depends on the impact of low temperature. Wang Q et al [27] in a cylindrical explosion tank to conduct implosion experiments under different vacuum conditions. Through the implosion experimental study, the blast wave propagation velocity u , overpressure Δp , specific impulse i , relative pressure factor α and relative specific impulse factor γ and other blast wave parameters were obtained under different vacuum levels. Zhang G et al [28] in the explosion container of J0-8 explosives in the vacuum and atmospheric pressure conditions to study the explosive power, found that the propagation of explosive products in the vacuum environment has a clear directionality, and in the atmospheric pressure conditions than the vacuum conditions have a stronger destructive power. Veldman, R. L. et al [29] studied experimentally and numerically the reflected blast pressure of a 226.8 g spherical C-4 charge under various atmospheric pressure conditions and found that the effect of ambient pressure on the normal reflected impulse decreases with decreasing proportional distance. For shorter distances, the effect of ambient air pressure on the normal reflected pressure is not significant. However, at higher ambient pressures, there is a significant increase in the reflected pressure as the distance between the explosive and the reflecting structure increases.

In summary, domestic and foreign on the temperature and pressure explosives in closed containers under low pressure or vacuum conditions of the energy release characteristics of relatively more, but temperature and pressure explosives in the application of the process, more in the open environment, the relevant experimental data in the open space is less, and different initial environmental pressure temperature and pressure explosives under the explosion characteristics of the study is also because of the experimental conditions, location, safety and other factors to conduct experiments is more difficult, the relevant research also very few. In this paper, through the plains and high altitude areas to carry out different equivalents of thermobaric explosives explosion characteristics research, system of a kind of thermobaric explosives shock wave overpressure peak, the explosion process, the temperature and other parameters of a detailed comparative study, intuitively respond to the thermobaric explosives in the different initial ambient pressures of the explosion process, the overpressure peak, the temperature of the difference between the thermobaric explosives for the subsequent study of thermobaric explosives release characteristics, formula optimization and application scenarios determination. Provide a certain reference value for the subsequent study of the energy release characteristics of temperature and pressure explosives, formulation optimization and application scenarios.

2. EXPERIMENTAL PART

2.1 Test sample

Test selected thermobaric explosives for a formula temperature and pressure explosives (Chongqing Hongyu Precision Industry Co., Ltd.), the main ingredients for 54% of RDX, 37% of aluminum powder, 9% of binder and other ingredients, aluminum powder selected in accordance with the GJB 1738-93 standard for extra-fine aluminum powder, burst heat of about 7500 kJ·mol⁻¹, the density of about 1.86 g·cm⁻³, the length of a cylindrical bare charge with a ratio of 0.8, 8 industrial detonators and 8 g passivation of the passivation of the explosive charge to detonate. Ratio of 0.8 of the column of bare drugs, 8 industrial detonators and 8 g passivated hesperidin transmission Explosives detonation. The basic physical and chemical properties of the samples used in the test are given in Table 1.

Table 1 physical and chemical properties of the test sample

Pilot sample	Density/g·cm ⁻³	Detonation velocity/km·s ⁻¹	Explosion heat/MJ·kg ⁻¹
Thermobaric explosive	1.86	7.53	7.5

2.2 Test system and test method

Experimental site selection of a flat area and a higher altitude area for static explosion experiments, the two experimental sites are using the same cloth field, as shown in figure 1, the flat conditions 1 kg and 10 kg of warm-pressure explosives were 2 rounds each, a total of 4 rounds of experiments; high-altitude areas (the initial ambient pressure of 59.08 kPa) 1 kg and 10 kg of warm-pressure explosives were 3 rounds each, warm-pressure explosives were 6 rounds, a total of 10 rounds! Experiments, in order to avoid experiments due to uneven ground, obstructions hindering the propagation of shock waves and other external factors interfere with the accuracy of the data collected, the site as far as possible to choose a medium hardness and a wide-open view of the flat site as a static explosion test site, to ensure that in the explosion of the fireball and the propagation of the shock wave within the area of no obstructions, no buildings, trees and personnel activities.

The mass of the test specimens was 10 kg and 1 kg, the center of the specimens was tightly bonded with 8 g of passivated black sock and secured with an 8# industrial detonator through the detonator base. The test samples were placed in a special bomb rack, the height from the ground was 0.5 m and 1.5 m, defining the geometric center of the drug column projected on the ground as the center of the explosion, seven ground pressure sensors from the center of the explosion in distance of 2 m, 3 m, 4 m, 6 m, 8 m, 10 m, 12 m, respectively. The data acquisition system consisted of five U.S. PCB piezoelectric pressure transducers (113 B, with ranges from 0.34 to 6.9 MPa, with sensitivity coefficients of 15.5 MPa). 6.9 MPa, sensitivity coefficient 15.489-0.721 mv-kPa-1. produced in the United States) and a 16-channel data collector (Elsys, sampling frequency 100 kHz-s-1, produced in Switzerland) and a computer terminal, which were used to record the shock wave pressure generated by the explosion; a high-speed camera (Photron mini ux100, recording speed 20,000 fps, produced in Switzerland) was used to record the shock wave pressure generated by the explosion. A high-speed camera (Photron mini-ux100, 20,000 fps, manufactured in Shanghai) was used to record the explosion, and an infrared camera (A615 infrared camera, 100 frames per second maximum sampling rate, manufactured in Shanghai) was used to record the temperature field changes.

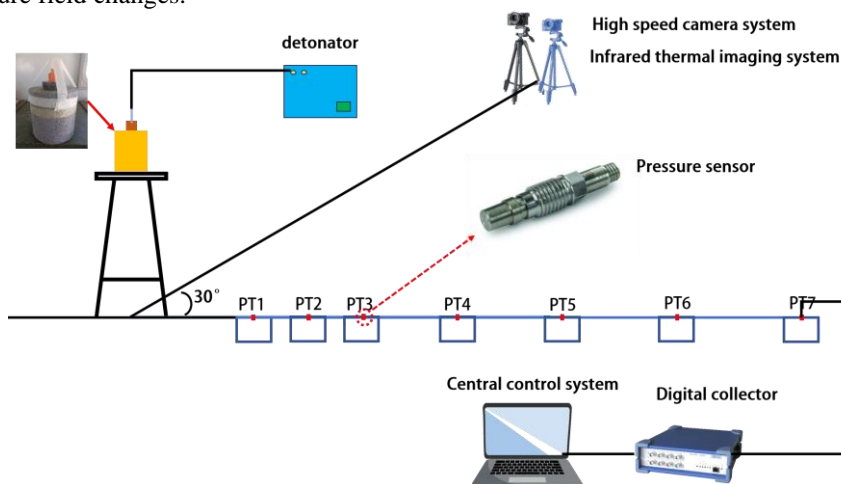


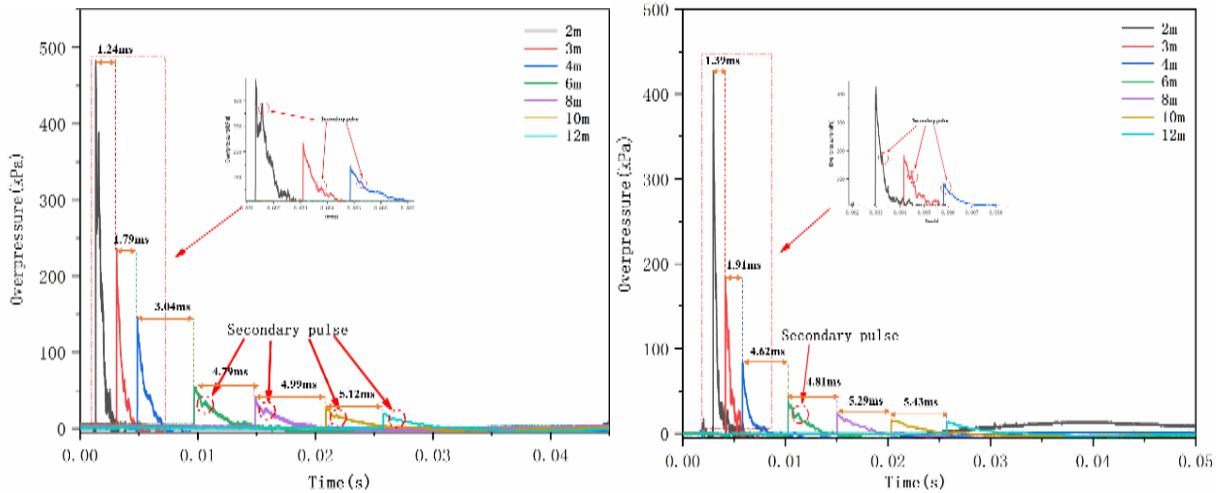
Figure. 1 The layout of the experiment

3. RESULTS AND DISCUSSION

3.1 Analysis of explosion pressure parameters

Figure. 2 shows the ground blast overpressure versus time at different initial positions from the center of the explosion after the deactivation of 1 kg of warm pressure explosives at initial ambient pressures of 101.33 kPa and 59.08 kPa respectively. As can be seen from the figure 2, the experimentally obtained overpressure waveform is clear, stable, with an obvious pressure rise and fall process. Overall, with the increase in propagation distance of the temperature and pressure explosives explosion shock wave, the wavefront surface of the peak overpressure rapidly attenuated, the propagation speed is also smaller with the increase in propagation distance. This is due to the fact that the shock wave front of the blast increases in size as the propagation distance increases, even if there is no other energy loss, the area of the wave front also increases, the energy per unit area also decreases, and secondly, the overpressure zone of the air shock wave also increases as the distance increases, the amount of compressed air continues to increase, so the average energy per unit mass of air continues to decrease. It can be observed that warm pressure explosives, which are present along the rising edge of the explosive shock wave, reach the peak after a gradual decay to the atmospheric state. It is noteworthy that the warm pressure explosives, which are present due to the third stage after the explosion of the afterburning reaction, provide energy for the entire system. This results in the peak of the shock wave being a smaller decline in the peak of the second pulse peak, and then attenuation, repeated attenuation to the atmospheric state. As the initial environmental pressure decreases, the secondary pulse of the thermobaric explosive becomes less pronounced after 6 m, indicating that the decreased pressure of the initial environment has a greater effect on the third stage of the post-ignition reaction of the thermobaric explosives. The initial ambient pressure decreases, resulting in a reduction in the oxygen content per unit of air. This plays a limiting role on the combustion of aluminum powder in thermobaric explosives. With the increase in

distance, the overall energy of the wavefront surface decays more rapidly, and the energy provided by the afterburning reaction of the aluminum powder is insufficient to cause the secondary shockwave pulses. Consequently, with the reduction in the ambient pressure, the secondary pulses of the thermobaric explosives are no longer apparent after 6 m. This also indicates that the reduction in initial ambient pressure exerts an inhibitory effect on the afterburning effect of thermobaric explosives.



a) Waveform curve of 1 kg TBX under plain conditions b) Waveform curve of 1 kg TBX under low pressure

Figure. 2 shows the waveform curve of TBX under different initial environmental pressures

Figure 3 shows the decay curve of the ground surface overpressure with distance, at 2 m from the explosion center. The initial ambient pressure was 101.33 kPa, and the peak shockwave pressure was 518.8 kPa and 2437.5 kPa, respectively, for 1 kg and 10 kg of thermobaric explosives. In contrast, the initial ambient pressure was 59.08 kPa, and the peak shockwave pressure was 436.5 kPa and 1793.2 kPa, respectively, for the same quantities of explosives. As the initial ambient pressure decreased, the peak shock wave pressure of the 1 kg and 10 kg thermobaric explosives decreased by 15.86% and 26.43%, respectively. As the propagation distance of the shock wave increases, the peak pressure of the two explosives declines rapidly within a radius of 2 m to 12 m from the detonation center. At a distance of 12 m, the peak pressure of the 1 kg and 10 kg thermobaric explosives has decreased by 36.25% and 29.58%, respectively. As the distance over which shockwaves propagate increases, the peak pressure of the two types of explosives in question decays rapidly. This is observed to occur at distances of between 2 and 12 m from the center of the explosion. At a distance of 12 m, the peak pressure of 1 kg and 10 kg thermobaric explosives has attenuated by 36.25% and 29.58%, respectively. It is evident that the overpressure attenuation rate is higher than that of 10 kg thermobaric explosive in the region closer to the center of the explosion. Conversely, in the region farther away from the center of the explosion, the overpressure attenuation rate is higher than that of 1 kg thermobaric explosive. Figure 4 presents the attenuation rate and the average attenuation rate of each measurement point under different initial ambient pressures. It can be observed that the overpressure attenuation rate of the shock wave of TBX exhibits a comparable sinusoidal pattern. This phenomenon is related to the complex explosion reaction process of temperature and pressure explosives, which contains a large number of internal combustible metal powder particles. During the explosion reaction process of the whole system at different stages of the combustion additive reaction, these particles undergo a decline in shockwave amplitude and oscillation. The average attenuation rate of 1 kg TBX is slightly higher than that of 10 kg TBX. This is due to the increase in the distance of the shockwave propagation, which occurs after the larger drop. The small quantity of TBX involved in the afterburning reaction of the energy of the whole system means that they are unable to provide more energy, resulting in a larger shockwave overpressure attenuation, particularly at the initial environmental pressure drop. Furthermore, the greater external heat loss exacerbates the attenuation rate of the shockwave at longer distances.

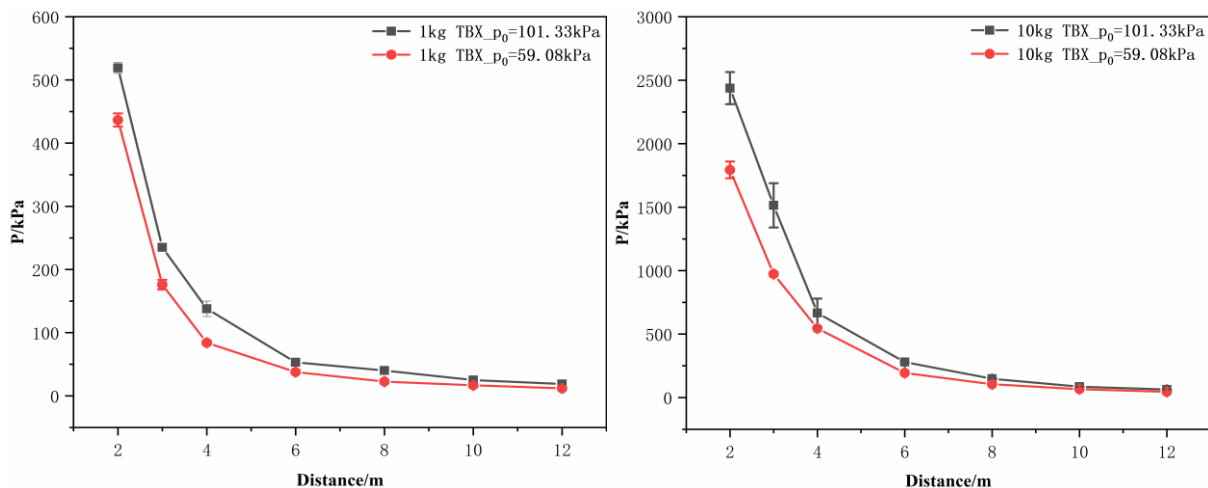


Figure. 3 Attenuation curve of ground overpressure with distance

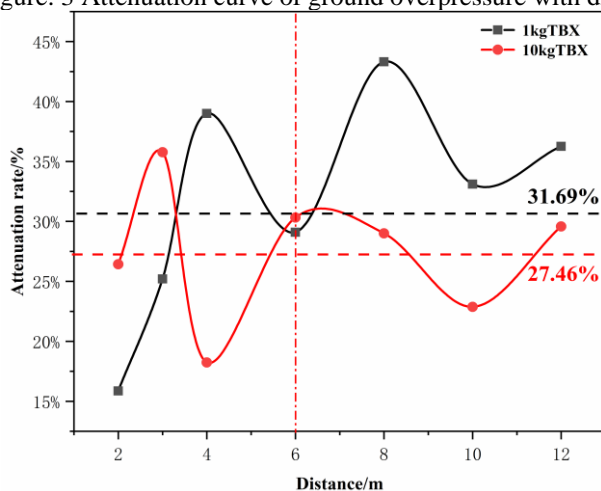


Figure. 4 Attenuation rate and average attenuation rate of each measuring point under different initial environmental pressures

According to the data obtained from the overpressure experiment, the shock wave overpressure equation under different initial environmental pressures can be obtained by fitting the peak value of shock wave overpressure of 1kg and 10kg thermobaric explosives at different detonation center distances. On this basis, the TNT equivalent is calculated by referring to the calculation method in GJB5412-2005:Δ

$$\left\{ \begin{aligned} \Delta p_{p_0=101.33} &= \frac{-408.3}{\bar{r}} + \frac{3357.82}{\bar{r}^{-2}} - \frac{1546.56}{\bar{r}^{-3}}, 0.91m \cdot kg^{-1/3} \leq \bar{r} < 3.65m \cdot kg^{-1/3} \\ \Delta p_{p_0=101.33} &= \frac{184.17}{\bar{r}} - \frac{111.99}{\bar{r}^{-2}} + \frac{3743.01}{\bar{r}^{-3}}, 3.65m \cdot kg^{-1/3} \leq \bar{r} \leq 12m \cdot kg^{-1/3} \end{aligned} \right. \quad (1)$$

$$\left\{ \begin{aligned} \Delta p_{p_0=59.08} &= \frac{-340.57}{\bar{r}} + \frac{2651.33}{\bar{r}^{-2}} - \frac{1266.58}{\bar{r}^{-3}}, 0.91m \cdot kg^{-1/3} \leq \bar{r} < 3.65m \cdot kg^{-1/3} \\ \Delta p_{p_0=59.08} &= \frac{-355.67}{\bar{r}} + \frac{4372.31}{\bar{r}^{-2}} - \frac{7806.17}{\bar{r}^{-3}}, 3.65m \cdot kg^{-1/3} \leq \bar{r} \leq 12m \cdot kg^{-1/3} \end{aligned} \right. \quad (2)$$

Table 2 TNT equivalent of ground shock wave overpressure under different initial environmental pressures

Initial ambient pressure/kPa	Type	TNT equivalent							
		2m	3m	4m	6m	8m	10m	12m	Mean value
101.33	1 kg TBX	1.6	1.6	1.9	1.6	1.6	1.8	1.7	1.7
59.08	1 kg TBX	1.5	1.6	1.3	1.3	1.3	1.4	1.4	1.4
101.33	10 kg TBX	1.1	1.8	1.4	1.4	1.3	1.3	1.6	1.4
59.08	10 kg TBX	1.4	1.4	1.2	1.3	1.3	1.2	1.2	1.3

As shown in Table 2, at an initial ambient pressure of 101.33 kPa, the shockwave overpressure TNT equivalents of 1 kg and 10 kg of thermobaric explosive are 1.7 and 1.4, respectively. However, as the initial ambient pressure decreases to 59.08 kPa, the shockwave overpressure TNT equivalents decrease to 1.4 and 1.3, with a decrease rate of 17.6 per cent and 7.1 per cent, respectively. It can be observed that the initial ambient pressure exerts a discernible influence on the shockwave overpressure TNT equivalent of thermobaric explosives, with a more pronounced impact observed in the case of smaller-quality thermobaric explosives. Up to a certain threshold, the initial ambient pressure does not exert a significant effect on the shockwave overpressure TNT equivalent of thermobaric explosives. It can be observed that the initial ambient pressure exerts a discernible influence on the shockwave overpressure TNT equivalent of thermobaric explosives, with a more pronounced impact observed in the case of smaller-quality thermobaric explosives. Up to a certain threshold, the initial ambient pressure does not exert a significant effect on the shockwave overpressure TNT equivalent of thermobaric explosives.

Figure 5 shows the variation of overpressure peak shockwave velocity with distance for different qualities of thermobaric explosives. It can be observed that the overpressure peak shockwave velocity of thermobaric explosives gradually decays with the increase of distance. Furthermore, it can be seen that with the decrease of the initial ambient pressure, the shockwave velocity of thermobaric explosives decreases. The initial ambient pressure of 101.332 kPa decreased to 59.08 kPa, with both 1 kg and 10 kg shockwave velocities exhibiting the greatest rate of decrease at 5 m. The maximum decrease in shockwave velocity was 34.83% for the 1 kg shockwave and 29.74% for the 10 kg shockwave, with the average decrease in shockwave velocity being 13.48% and 17.2%, respectively. It can be observed that the initial environmental pressure exerted on TBX is considerable. As the quality of the explosives increases, the influence of environmental factors on the reduction of the aforementioned phenomenon can be explained by the attenuation law of shock waves. The analysis presented above demonstrates that the propagation of shock waves in air is affected by various factors, including compression, heat transfer and other processes that contribute to the attenuation of energy as the distance between the source and the receiver increases. The speed of the shock wave increases and then decreases with the distance from the initial explosion. This is due to a reduction in ambient pressure, thinning of the air, and a decrease in air density, which results in a slower propagation speed for the shock wave. Additionally, the temperature and initial energy of the explosives, which contain aluminum powder, are reduced. In low-pressure conditions, the shock wave attenuation is faster due to the propagation of the blast products. The velocity of the shock wave can be calculated by the time difference between the arrival of the shock wave at the ground sensor and the known distance between the ground sensor and the centre of the explosion. It is evident that the temperature and pressure of the explosives are significantly influenced by the initial ambient pressure. The lower the initial ambient pressure, the thinner the air, the lower the density, and the greater the work done by the shock wave, which leads to a more rapid attenuation of the shock wave velocity.

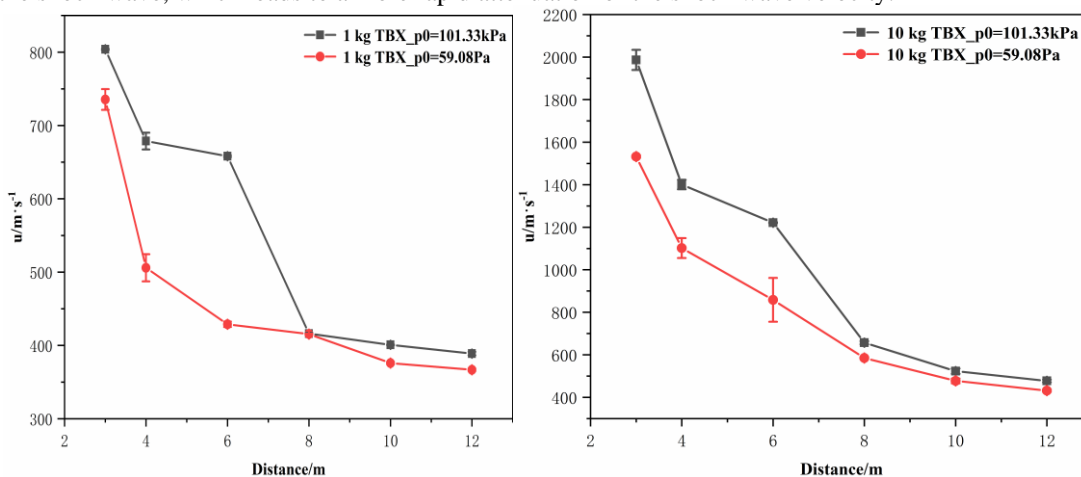


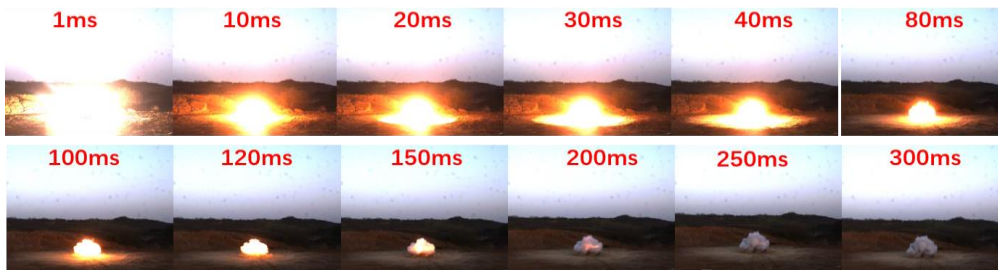
Figure. 5 the variation curve of overpressure shock wave velocity of TBX with distance under different initial environmental pressures

3.2 Explosion process analysis

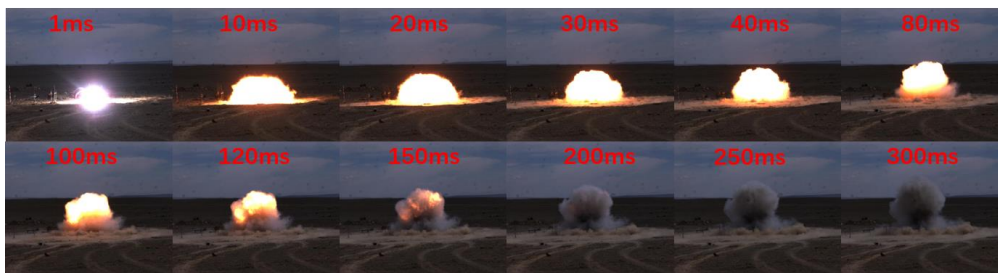
Figure 6(a)-(d) illustrates the evolution of the explosion fireball subsequent to the detonation of 1 kg and 10 kg thermobaric explosives in disparate initial environments, as captured by the high-speed camera system. The initial phase of the explosive and high-temperature expansion process is illustrated in figures 6 (a) - (d). Over the first 30 ms, the detonation device initiates the condensation phase bombardment of the explosives, resulting in the rapid expansion of the explosion products and unreacted components of the mixture. Concurrently, the mixture undergoes a chemical reaction with the air, emitting a strong white light. This process intensifies the fireballs, which become larger. The intensity of the white light is proportional to the temperature of the blast field. The temperature of the warm-pressure explosive white light is the highest, with the longest duration, at approximately 20 ms. Under atmospheric pressure, the duration of the initial pressure reduction is substantial. A high-temperature triggered by compression waves has the potential to catch up with the precursor explosion wave, increasing its impulse. The subsequent phase is the afterburning reaction process, during which the white light disappears, the explosive products and metal particles are ejected, the explosive fireball gradually expands, and the high-temperature combustion of the metal particles provides the subsequent energy for the entire system.

From 30 ms later, as can be observed in the high-speed footage, there is a false light surrounding the exploding fireball. This is due to the influence of the fireball's glare illuminating the surrounding air, as well as the formation of water vapor and microdots caused by the temperature decrease over time. The intensity of the false light is also reduced, and the initial ambient pressure has a weakening effect on the temperature field of the exploding fireball of the explosives. This is evidenced by the fact that the false light is weaker at high altitude than at plain conditions. It is noteworthy that the disappearance of the explosive fireball coincides with the maintenance of a high temperature in the explosion area, particularly in the case of 10 kg thermobaric explosives. The presence of smoke within the interior of a large area of high temperature indicates that afterburning plays a role in the destruction of the explosion.

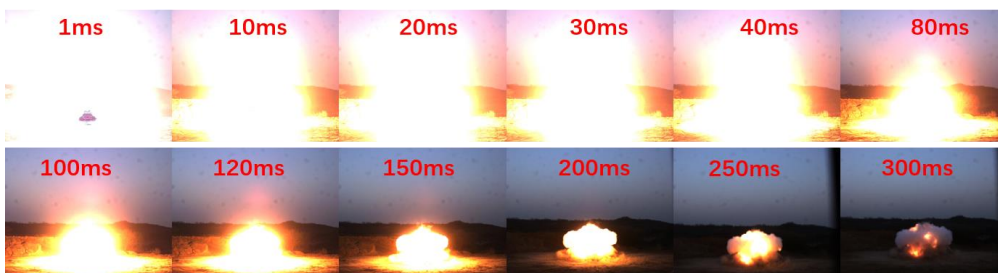
From the perspective of the comprehensive explosion process of thermobaric explosives, the fireball size trend initially exhibits an increase, followed by a decrease (the process is remarkably brief, occurring in approximately 1 ms). Subsequently, the fireball size trend gradually increases, then gradually decreases, and ultimately reaches a point of disappearance. The initial ambient pressure decreased to 59.08 kPa, resulting in a reduction in the explosive response and a shorter duration of the fireball explosion. The initial ambient pressure exerts a discernible influence on the duration of the explosive fireball, particularly with regard to the duration of each stage of change. Overall, as the initial ambient pressure declines, the duration of the high temperature also diminishes. Furthermore, the duration of the explosive fireball is inversely proportional to the initial ambient pressure. In addition, the diameter, height, intensity of light radiation, and duration of the explosive fireball exhibit a positive correlation with mass and a negative correlation with initial ambient pressure. This relationship is contingent upon the composition of warm pressure explosives and the specific characteristics of their explosive reaction process. Thermobaric explosives, which contain internal aluminum powder and other metal powders, are classified as thermobaric explosives. These explosives undergo a deflagration process after the formation of microparticles, which are mixed with air. The larger the mass, the larger the initial energy. The light radiation area and high temperature area are also relatively large, which enables the production of relatively strong light radiation and fireballs. The relative quality of the aluminum powder within the content is also large, and aluminum powder has a good thermal conductivity. The reaction between aluminum powder and oxygen constantly releases heat. Due to the high temperature, the aluminum powder particles become cloudy, reaching the shell-breaking and reaction threshold temperature. This results in heat penetration, redox reaction exothermicity, and subsequent transfer of heat to adjacent aluminum powder, maintaining the subsequent reaction. This attenuates the energy, weakening the duration of the fireball and strengthening the initial drop in ambient pressure, which inhibits the diffusion of the aluminum powder combustion. The introduction of energy into the system exerts a weakening influence, thereby limiting the initial ambient pressure on the thermobaric explosives explosion fireball and high-temperature duration.



(a) 1 kg TBX_{p0=101.33kPa}



(b) 1 kg TBX_{p0=59.08kPa}



(c) 10 kg TBX_{p0=101.33kPa}



(d) 10 kg TBX_{p0=59.08kPa}

Figure. 6 Motion evolution of 1 kg and 10 kg TBX fireball under different initial environments

To analyze the diameter of the fireball under different initial ambient pressures, the images in figure. 6 were subjected to analysis and processing to obtain the maximum diameters recorded at different points in time. figure. 7 illustrates the variation in the maximum fireball diameter over time following the explosion of thermobaric explosives under different initial ambient pressures. As shown in figures 6 and 7, the diameter of the explosive fireball of thermobaric explosives is directly proportional to the mass of the explosive fireball in different initial environmental pressures. However, despite this similarity, there are still differences in the process. As the initial environmental pressure decreases, the thermobaric explosives explosion fireball reach their maximum diameter at a slower rate and then maintain a constant size for a period of time before gradually declining. This indicates that the thermobaric explosives in the initial environmental pressure have a significant impact on the initial environmental pressure. Additionally, as the initial environmental pressure decreases, the air becomes thinner, the oxygen content decreases, aluminum powder is less likely to be thrown and combustion is inhibited, and the reaction process slows down. The overall system energy is diminished, thereby slowing the reaction of thermobaric explosives in a low-pressure environment and reducing the energy available.

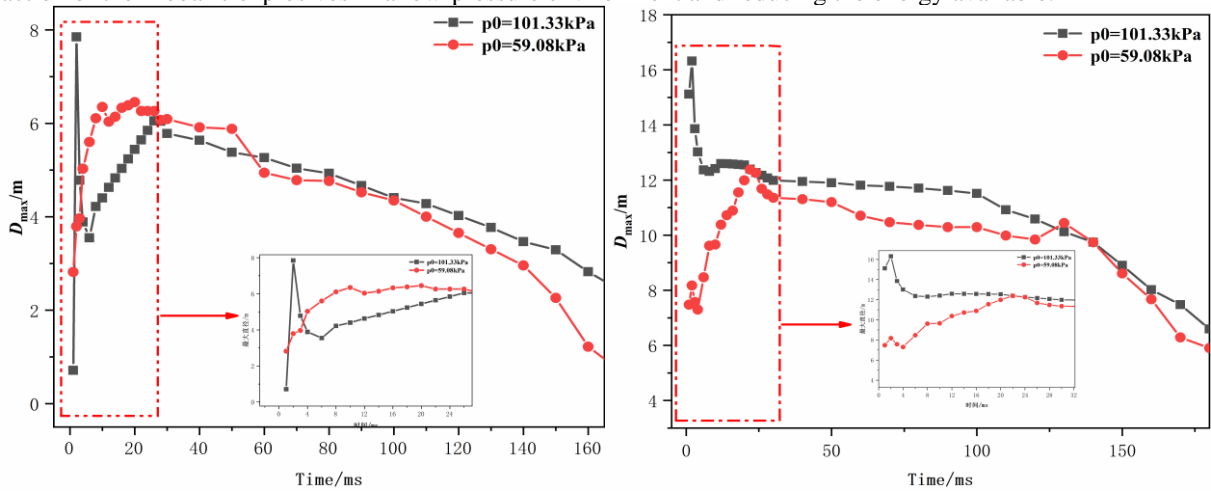


Figure. 7 Variation curve of the maximum diameter of the exploding fireball with time under different initial ambient pressures

3.3 Analysis of explosive fireball temperature

For thermobaric explosives, the temperature and duration of the fireball are also important indicators of their performance. Table 3 presents the explosion temperature parameters of thermobaric explosives. As illustrated in Table 3, the maximum temperature of the fireball for 1 kg and 10 kg of thermobaric explosives in the plains (initial pressure of 101.33 kPa) is 1983°C. The temperature of the fireball in the explosion of 1 kg and 10 kg thermobaric explosives reached 8°C and 2140.5°C, respectively. The duration of the fireball temperature exceeding 1200°C was 181.8 ms and 333.33 ms, respectively, while the duration of the fireball temperature exceeding 500°C was 454.5 ms and 1000 ms, respectively. While the initial ambient pressure declines to 59.08 kPa, the maximum temperature drop rate of 15.95% and 16.68%, the explosion fireball temperature is greater than 1200°C, with a duration drop rate of 31.2% and 38.81%, respectively. Furthermore, the explosion fireball temperature is greater than 500 °C, with a duration drop rate of 38.88% and 40%. It can be observed that the initial ambient pressure, despite exerting a considerable influence on the maximum temperature of the explosive fireball, is less affected by the temperature duration. Conversely, the thermobaric explosives have a more pronounced impact on the temperature and duration of the fireball.

Table 3 Explosion temperature field parameters

Initial ambient pressure /kPa	Type	$T_{max}/^{\circ}C$	$t_{>1200^{\circ}C}/ms$	$t_{>500^{\circ}C}/ms$
101.33	1 kg TBX	1983.8	181.82	454.5
59.08	1 kg TBX	1667.4	125.1	277.79
101.33	10 kg TBX	2140.5	333.3	1000
59.08	10 kg TBX	1783.5	204.0	596.2

4. CONCLUSIONS

The static explosion test of different levels of thermobaric explosives in free space allows for the comprehensive analysis of the explosion process of thermobaric explosives, shock wave parameters, and temperature field parameters. This analysis yields insights into the energy release characteristics of thermobaric explosives under different initial ambient pressures, shock wave parameters, and temperature parameters. The following law describes the relationship between these variables:

- 1) The analysis of high-speed images has revealed that the thermobaric explosives display the characteristics of volumetric explosions, with the fireball undergoing a growth process following its explosion. This growth process is distinct from that observed in other high-explosive explosives, exhibiting a degree of independence. Low initial ambient pressure conditions can impede the energy release efficiency of thermobaric explosives. The diameter, height, intensity and duration of the explosion of the fireball of light radiation exhibit a positive correlation with mass and a negative correlation with initial ambient pressure. The continuation and maintenance of the subsequent deflagration process is dependent upon the persistence of a high-temperature environment and the rapid establishment of a system combustion.
- 2) Low-pressure conditions exert an inhibitory effect on the peak overpressure of the shock wave generated by the explosion of thermobaric explosives. Furthermore, the decay rate of thermobaric explosives with a large dosage is higher than that of thermobaric explosives with a small dosage at closer distances. However, at longer distances, the opposite is true. Furthermore, the study indicates that the shock wave overpressure decay rate of thermobaric explosives exhibits a sinusoidal-like pattern, which is attributed to its intricate explosive reaction process and internal combustible metal powder. Additionally, the empirical formulae for the shock wave overpressure of thermobaric explosives under varying initial ambient pressures are presented.
- 3) As the initial ambient pressure decreases, the shock wave propagation velocity and the TNT equivalent of thermobaric explosives decrease. Furthermore, the initial ambient pressure has a greater effect on the shock wave propagation velocity and the TNT equivalent of thermobaric explosives when a small charge is used.
- 4) The diameter of the fireball produced by thermobaric explosive is proportional to its mass at varying initial ambient pressures. However, a reduction in pressure results in a slower increase in the size of the fireball and a reduction in its energy. The initial ambient pressure of 101.332 kPa, the maximum temperature of the fireball of the explosion of 1 kg and 10 kg of thermobaric explosives were 1983.8 °C and 2140.5 °C, respectively. It was observed that the duration of high temperatures increased with the increase in mass and prolonged duration of the explosion. Upon reduction of the initial ambient pressure to 59.08 kPa, a notable decline was observed in the maximum temperature of the exploding fireball and the duration of the high temperature. However, the quality of the warm-pressure explosives exhibited a relatively minor impact on these parameters.

5. REFERENCES

- [1] WANG B L, Li Y N, Han Z W. Some reflections on the Development trend of thermobaric explosives. *Journal of Explosives and Explosives*, 2023,46(11): Front insertion 1-Front insertion 2.
- [2] Deng Z Y, Wang Y, Qi G Y, et al. The research progress of elemental explosives under high temperature and high-pressure structure evolution. *Energetic Material*, 2022, 30 (6): 622-638.
- [3] Li Y, Li B C. Research progress on killing factors and characteristics of cloud explosive bomb/thermobaric bomb. *Journal of Trauma Surgery*, 2022,24(1): 18-22.
- [4] Yao J X, Xu H X, Yu H J, et al. Development status and prospect of fuel air explosives. *Aerospace Missiles*, 2014(2): 85-89.
- [5] Hu H W, Song P, Deng G Q, et al. Properties and development status of thermobaric explosive. *Advances in Mechanics*, 2022,52(1): 53-78.
- [6] Fan P X, Song F L. The Principle and Development status of thermobaric weapons. *Science and Technology Information*, 2006(27): 36-37.
- [7] Mohamed A K, Mostafa H E, Elbasuney S. Nanoscopic fuel-rich thermobaric formulations: Chemical composition optimization and sustained secondary combustion shock wave modulation. *Journal of Hazardous Materials*, 2015, 301(JAN. 15):492-503.
- [8] Zhang J K, Botterbush K S, Bagdady K, et al. Blast-related traumatic brain injuries secondary to thermobaric explosives: implications for the war in Ukraine. *World neurosurgery*, 2022(167): 176-183.

- [9] Uystepuyst, David, Monnoyer, Francois. A numerical study of the evolution of the blast wave shape in rectangular tunnels. *Journal of Loss Prevention in The Process Industries*. 2015(34): 225-231.
- [10] Xing X L, Zhao S X, Wang Z Y. Discussions on Thermobaric Explosives (TBXs). *Propellant, Explosives, Pyrotechnics*. 2014,39(1): 14-1.
- [11] Liu Q, Yao J, Song X Z, et al. Effect of initial ambient pressure on shock wave overpressure and temperature of RDX based thermobaric explosive. *Journal of Beijing institute of technology*: 1-10 [2024-06-23].
- [12] Zhao X Y, Wang B L, Li X. Shock wave patterns of warm pressure explosives in field near-ground airbursts. *Explosion and Shock*, 2016, 36(1): 38-42.
- [13] Xie Q M, Qu G J, et al. Shock wave characteristics of different components of thermobaric explosive. *Engineering Blasting*, 2017, 23(1): 1-5.
- [14] Kim C K, Lai M C, Zhang Z C, et al. Modeling and numerical simulation of afterburning of thermobaric explosives in a closed chamber. *International journal of precision engineering and manufacturing*, 2017, 18(5): 979-986.
- [15] Jiang Z P, Wang B L, Li X, et al. Comparative study on explosive power characteristics of a solid thermobaric agent and a "Simir" agent. *Pyrotechnics*, 2015(6): 28-29.
- [16] Pei M J, Mao G W, et al. Study on the energy release efficiency of aluminum-containing thermobaric fuel during explosive dispersion. *Journal of University of Science and Technology of China*, 2007, 37(3):276-283.
- [17] Wang C, Li Y N, Li J, et al. Influence of charge amount on explosive damage power of thermobaric explosive. *Explosive Materials*, 2023, 52(4): 37-43.
- [18] Chen K, Xiao W, Han Z W, et al. Effect of aluminum particle size on explosion parameters of HMX-based thermobaric explosive in confined space. *Journal of Explosives and Explosives*, 2019, 43(3): 298-302,307.
- [19] Zheng B, Chen L, Ding Y S, et al. Motion law of explosive dispersion of thermobaric explosive. *Explosion and Shock Waves*, 2008, 28(5): 433-437.
- [20] Li X L, Hui J M. Explosion temperature of thermobaric explosive. *Explosion and Shock Waves*, 2008, 28(5): 471-475.
- [21] Xu W, Wang C, Yuan J, et al. Investigation on energy output structure of explosives near-ground explosion[J]. *Defence Technology*, 2020, 16(2): 290-298.
- [22] Zhang Y L, Zhai H B, Li Z R, et al. Comparative experimental study on explosive fireball surface temperature of TNT and thermobaric explosive. *Explosive Materials*, 2015(5): 23-26.
- [23] Yan J J, Jin P G, Li H B, et al. Experimental study on post-combustion effect of thermobaric explosive in limited space. *Science Technology and Engineering*, 2015(17): 5-7.
- [24] Yan X M, Su J J, Li Z Z, et al. Study on the explosion thermal effect of warm-pressure explosives in trench. *Fireworks*, 2015(1): 22-25.
- [25] Li Z Z, Wang S Q, Gou B W. Research on explosion temperature testing method in confined space. *Fireworks*. 2012, (5) :41-52.
- [26] Li R, Li X C, Wang Qn, et al. Propagation characteristics of explosive shock wave under low temperature and low pressure. *Explosion and Shock Waves*, 2023, 43(2): 16-26.
- [27] Wang Q, Lu J W, Li Z M, et al. Propagation law of explosion wave in cylindrical explosion tank under negative pressure. *Explosion and shock*, 2021,42(6):1250-1256.
- [28] Zhang G H, Li B B, Shen F, et al. Experimental study on explosive characteristics of explosives under vacuum. *Journal of Explosives and Explosives*, 2019,43(3):308-313.

- [29] Veldman R L, Nansteel M W, et al. The Effect of Ambient Pressure on Blast Reflected Impulse and Overpressure. *Experimental Techniques*, 2017, 41(3): 227-236.
- [30] Huang Y F, Tian X, Feng B, et al. Experimental study on explosive properties of thermobaric explosive. *Explosion and Shock Waves*, 2016, 36(4): 573-576.
- [31] Veysiere B, Khasainov B A. A model for steady, plane, double-front detonations (DFD) in gaseous explosive mixtures with aluminum particles in suspension. *Combustion & Flame*. 1991, 85(1-2): 241-253.
- [32] Gurevich M A, Lapkina K I, Ozerov E S. Ignition limits of aluminum particles. *Combustion, Explosion and Shock Waves*. 1970, 6(2). 154-157.
- [33] Benselama, A M, William-Louis, M. J. A numerical study of the evolution of the blast wave shape in tunnels. *Journal of hazardous materials*. 2010, 181(1): 21-34.
- [34] Feldgun V R, Karinski Y S, et al. Prediction of the quasi-static pressure in confined and partially confined explosions and its application to blast response simulation of flexible structures. *International Journal of Impact Engineering*. 2016(4): 46-60.
- [35] Donahue L, Zhang F, Ripley R C. Numerical models for afterburning of TNT detonation products in air. *Shock Waves*. 2013, 23(6): 559-573.
- [36] Kuhl A L, Bell J B, Beckner V E. Heterogeneous Continuum Model of Aluminum Particle Combustion in Explosions. *Combustion, Explosion, and Shock Waves*. 2010, 46(4): 433-448.
- [37] Trzcinski W A, Kicinski W. Calorimetry Studies of Explosion Heat of Non-Ideal Explosives. *Journal of Thermal Analysis & Calorimetry*. 2009, 96(2):14-16.

Effect mechanism of 5-Amino-1*H*-Tetrazole on the pyrolysis and combustion behaviors of Nano-Al@Fe₂O₃ thermite reaction

Author: Jiu Chen

School of Safety Science and Engineering (School of Emergency Management),
Nanjing University of Science and Technology, Nanjing, 210094, Jiangsu, China

ABSTRACT

thermite has been widely applied in military and civilian area due to its excellent performances. However, considering the different actual requirements in the application process, it is necessary to further modify and optimize the thermite formulations to achieve the desired practical purposes. Therefore, in this paper, 5-Amino-1*H*-Tetrazole (CH₃N₅, 5AT) was introduced as a fuel or energetic material to Nano-Al@Fe₂O₃ thermite to modify and enhance the pyrolysis and combustion behaviors due to its outstanding physicochemical properties. Different mass ratio of 5AT was blended with the raw material Nano-Al and Fe₂O₃ powders by wet ball milling method respectively to explore the suitable addition mass ratio. The SEM and XRD characterizations were performed to verify the mixing effect. The results show that it achieves a homogeneous blend accompanied by no obvious reaction occurrence between the raw materials and 5AT. The DSC test and combustion experiment were conducted to measure the pyrolysis and characteristics. Furthermore, to measure the ability of energy output for different thermite formulations, the stainless-steel plate penetration experiment was also operated. The results show that the pyrolysis reaction process is promoted with the presence of 5AT. Moreover, the combustion temperature

presents a relatively steady reduction while the ability of energy output shows an elevation when the addition content of 5AT is 1%~5%. However, both the combustion temperature and the ability of energy output appear a sharp decline when the content of 5AT is over 5%. The conclusions in this paper can offer some valuable information for the design of thermite formulations.

Keywords: Thermite; 5-Amino-1*H*-Tetrazole; Additive; Energy output; Pyrolysis; Combustion;

Experimental study of hydrogen-oxygen catalytic recombination for hydrogen mitigation in a confined pipeline using Pt/C catalyst: Development of temperature and hydrogen concentration

Xuan Li^a, Si-Yuan Zhou^a, Tao-Tao Ye^a, Jing Zhang^{a,*}, Bin Li^a, Dan Zhang^a, Yong-Xu Wang^a, Lifeng Xie^a

^aSchool of Safety Science and Engineering (School of Emergency Management), Nanjing University of Science and Technology, Nanjing 210094, China

*zhangjing116@njust.edu.cn

Keywords: Temperature characteristics, hydrogen-oxygen catalytic recombination, exothermic, Hydrogen mitigation, Hydrogen safety

1. INTRODUCTION

Driven by the new round of scientific and technological revolution and industrial change, the world energy landscape is undergoing a profound adjustment. To respond to global climate change, it has become a consensus among countries to promote a clean and low-carbon energy transition (Shen and Zhang, 2021). Hydrogen, with its wide range of sources, its high calorific value, high utilization rate, and the fact that it does not produce any greenhouse gases or harmful pollutants (Guo and Duan, 2019), is considered to have the potential to be a long-term alternative to fossil fuels. However, the many unsafe characteristics of hydrogen (Li and Bi, 2018) and a series of safety accidents (Yanez and Kuznetsav 2015) are a constant wake-up call for the utilization of hydrogen energy in countries around the world. Therefore, the study of effective protective measures (Cao and Li, 2018, Cao and Li, 2022,) for hydrogen explosion and the reduction of the probability and risk of hydrogen explosion accidents are urgent issues for the development of hydrogen energy.

Hydrogen-oxygen catalytic recombination, or passive auto-catalytic recombiners (PARs) as an effective hydrogen elimination technology is widely used in hydrogen safety protection of nuclear power plant containment. On the one hand, the technique could eliminate leaking hydrogen before an explosion occurs, on the other hand, the technology does not require an external power supply and can also be operated unattended, and thus, it is considered that it can also be applied to a wide range of hydrogen-related sites in non-nuclear power plants. In this paper, the hydrogen leakage phenomenon is simulated in a 905 mL pipe. Based on the Pt/C catalyst, the effects of hydrogen concentration, hydrogen leakage rate, and the position of the catalytic layer on the reaction temperature and the temperature outside the reaction zone are investigated. Furthermore, the feasibility of the hydrogen-oxygen catalytic recombination reaction applied to hydrogen elimination inside a confined gallery is also analyzed. The results of the study can provide a reference for the design of hydrogen elimination in confined spaces.

2. Experimental setup

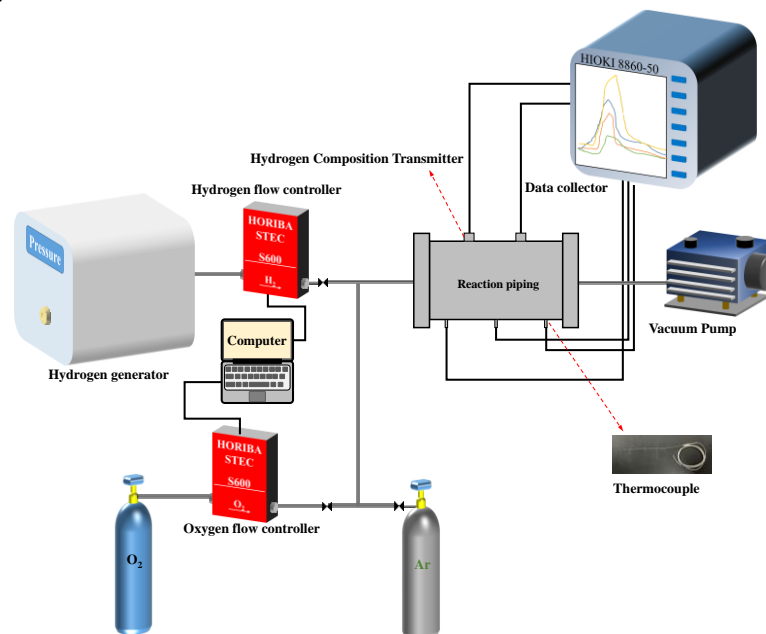


Figure 1. Schematic diagram of the experimental system

Fig. 1 shows the schematic diagram of the experimental system for the hydrogen-oxygen catalytic recombination reaction. The experiment was performed in the 905 mL container. The catalytic layer was placed parallel to the vertical section of the vessel. The hydrogen required for the experiment was supplied by a hydrogen generator capable of producing 99.99% high-purity hydrogen, and the air was provided by a 40 L high-pressure air cylinder. Both hydrogen flow and air flow were controlled by a mass flowmeter (S600, HORIBA Precision Instruments, China) with an accuracy of $\pm 0.5\%$ F.S.. As shown in Fig. 2, three type K thermocouples (measuring range 0-800°C, probe diameter 1 mm) were installed in sequence at point T_3 , T_2 and T_1 , measuring 30 mm, 90 mm, and 150 mm from the inlet side, with the probes located in the axial center of the container to monitor the temperature change. A Vacuum pump and a 40 L high-pressure argon cylinder were applied to pump and wash the gas within the container. During the experiment, temperature data were collected in real-time by an oscilloscope (HIOKI, 8860-50, Japan), and the reaction process was recorded by a DV. At the end of the reaction, the residual hydrogen concentration was detected by two hydrogen transmitters on top of the container.

3. RESULTS

Fig. 2 show the temperature peaks at each temperature measurement point for different hydrogen concentrations, different hydrogen leakage rates and different catalyst positions. The results show that the high-temperature region always exists at the catalyst surface under any conditions, on the contrary, there is no large temperature change at the two symmetric positions away from the catalyst surface. Considering that the temperature change at the catalyst surface is almost exclusively caused by the exothermic hydrogen-oxygen catalytic recombination reaction, it is believed that it can better reflect the reaction temperature trend.

Typical temperature and hydrogen concentration development over time for a hydrogen concentration of 30 vol% is given in Fig. 5a, where the catalyst is located in C_{mid} and the hydrogen leakage rate is 100 mL/min. First, when hydrogen had just leaked into the vessel, it had not diffused to the surface of the catalyst (t_1), and there was no change in hydrogen concentration detected by the hydrogen concentration sensors on either side of the catalyst. Then, the hydrogen concentration at C_1 and C_2 increased, but there was no obvious temperature change on the catalyst surface before t_2 , indicating that the reaction did not take place. On the one hand, fewer hydrogen molecules were adsorbed on the surface of the active metal Pt due to the low hydrogen content, and on the other hand, the mass transfer resistance of hydrogen molecules was higher due to the small concentration gap between the two sides of the catalyst, resulting in the hindered diffusion of hydrogen over the porous phase of the catalyst and the limited reaction. Furthermore, as the hydrogen content increased and the hydrogen concentration gradient on both sides of the catalyst increased, the non-homogeneous phase reaction gradually proceeded on the surface of the catalyst with a gradual increase in temperature, which further increased the diffusion of hydrogen molecules over the porous phase of the catalyst. Until the hydrogen concentration at the right side of the catalyst (C_1) reached a peak (t_3), at which time the rate of hydrogen consumption was greater than the rate of hydrogen leakage, the hydrogen concentration began to decline and the reaction temperature continued to rise.

The reaction process of the above typical reaction is further analyzed as shown in Fig. 6. With the continuous leakage of hydrogen into the vessel, the hydrogen and oxygen adsorbed on the surface of the catalyst reacted and released heat, and the heated gas carried the hot steam generated by the reaction to diffuse upwards, liquefying into a water mist upon contact with the cold wall surface at the upper end of the vessel (35s). The hot vapor gathered above the vessel by thermal buoyancy and more to the left of the catalytic layer by the leftward airflow (50 - 55s). As the reaction continued and the reaction temperature increased, the amount of hot vapor generated and the diffusion rate increased, and gradually spread from the left to the entire vessel.

Fig. 5b shows the maximum reaction temperature and maximum temperature rise for different hydrogen concentrations. When the hydrogen concentration is lower than 15 vol%, as the hydrogen concentration increases, more hydrogen molecules and oxygen molecules involved in the reaction in the vessel release more heat, resulting in higher temperature rises. However, as the hydrogen concentration continued to increase, the maximum temperature rise remained essentially constant and approached the maximum temperature rise at a hydrogen concentration of 15 vol%.

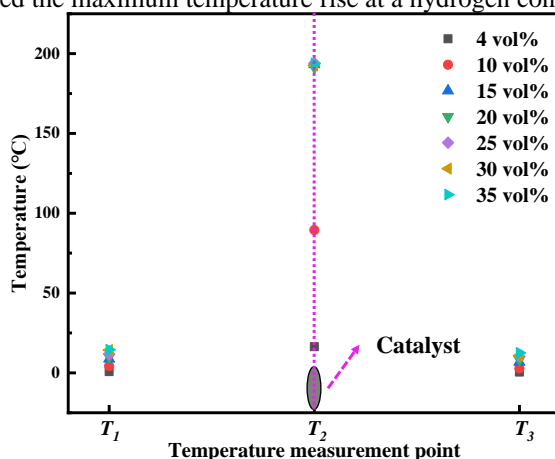


Figure 2. Temperature at each temperature point for different hydrogen concentrations

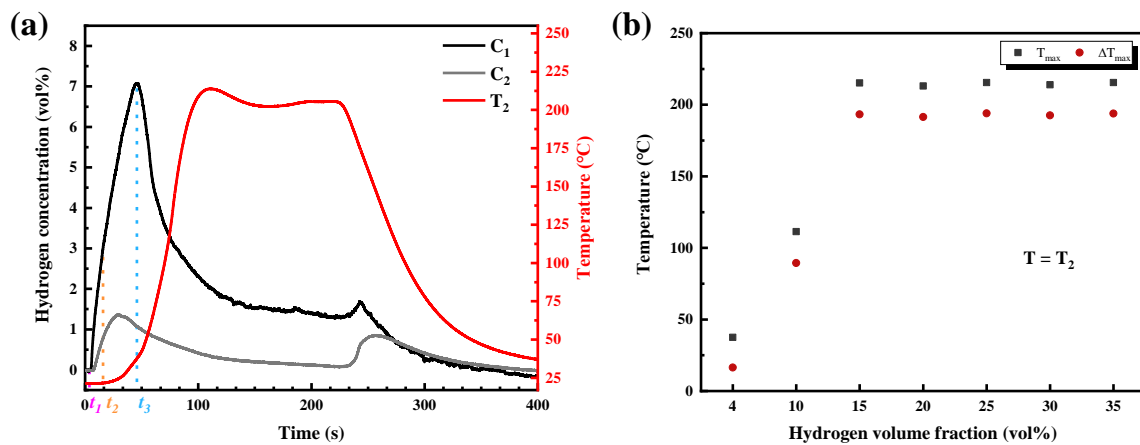


Figure 5. (a) Typical temperature and hydrogen concentration development profile (b) Peak temperature and maximum temperature rise at different hydrogen concentrations

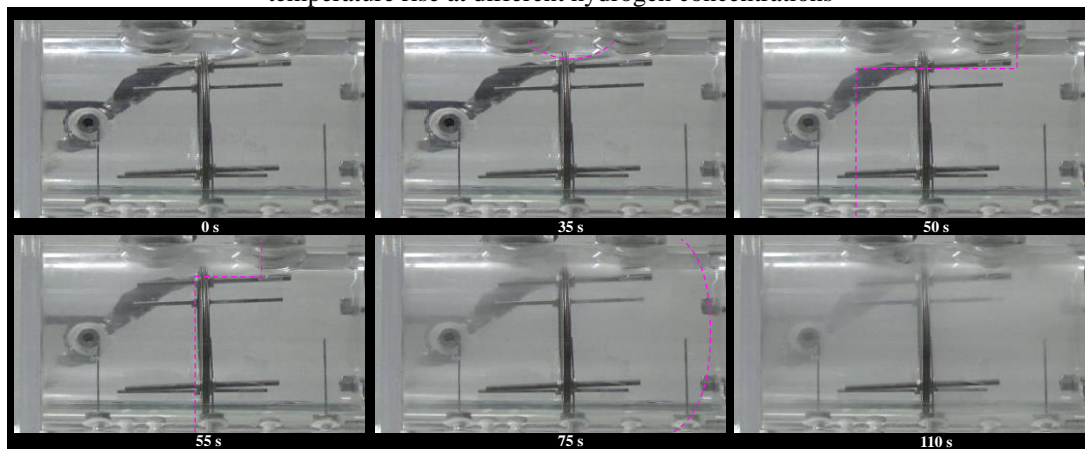


Figure 6. Typical reaction process

4. CONCLUSIONS

It is found that the high temperature zone is always near the catalyst surface. The hot steam spreads under the action of the hydrogen flow first to the left side of the vessel, and then gradually spreads to the whole vessel. It is interesting to note that the reaction temperature first increases and then remains constant with increasing hydrogen concentration, but the corresponding high temperature duration grows and two temperature peaks forms.

5. REFERENCES

- Shen X, Zhang Z, Dou Z, Zhang C. Premixed CO/air combustion in a closed duct with inhibition. *Energy* 2021;230:120782.
- Gong L, Duan QL, Sun JH, Molkov V. Similitude analysis and critical conditions for spontaneous ignition of hydrogen release into the atmosphere through a tube. *Fuel* 2019;245:413-9.
- Li YC, Bi MS, Li B, Zhou YH, Gao W. Effects of hydrogen and initial pressure on flame characteristics and explosion pressure of methane/hydrogen fuels. *Fuel* 2018;233:269-82.
- Yanez J, Kuznetsav M, Souto-Iglesias A. An analysis of the hydrogen explosion in the Fukushima-Daiichi accident. *Int J Hydrog Energy* 2015;40(25):8261-80.
- Cao Y, Li B, Gao K. Pressure characteristics during vented explosion of ethylene-air mixtures in a square vessel. *Energy* 2018;151:26-32.
- Cao Y, Li B, Xie L, Pan X. Experimental and numerical study on pressure dynamic and venting characteristic of methane-air explosion in the tube with effect of methane concentration and vent burst pressure. *Fuel* 2022;316:123311.

Investigation of the effect of nonmetallic oxides on the properties of 5-Amino-1H-Tetrazole: microscopic morphology, kinetics, and thermal safety parameters

Si-Yuan Zhou^a, Xuan Li^a, Dan Zhang^{a*}, Bin Li^a, Li-Feng Xie^a

^a School of Safety Science and Engineering (School of Emergency Management), Nanjing University of Science and Technology, Nanjing 210094, China

*danzhang@njust.edu.cn

Keywords: 5-Amino-1H-Tetrazole, Catalyst, Pyrolysis, Kinetics, Propellant

1. INTRODUCTION

Tetrazoles and their derivatives can rapidly release considerable energy and gas at high temperatures or in explosions, and have very excellent explosive properties (Shingo, 2011). 5-Aminotetrazole (5AT), as a new type of tetrazole high-nitrogen energy-containing compounds with high-nitrogen, low-carbon, and low-hydrogen structural features, has a molecular formula of CH_3N_5 , a nitrogen content as high as 82.3%, and an enthalpy of formation of $208.7 \text{ kJ mol}^{-1}$. 5AT has sufficient thermal stability and high density to produce a large amount of gas upon thermal decomposition, and is often used as an environmentally friendly gas-producing material, which is often mixed with oxidizers and other types of additives widely used in propellants, airbags, space engines, fire extinguishers, and other fields (Zhou, 2023). However, 5-AT propellants suffer from high combustion temperatures (higher than 1200 K) and unstable combustion (larger burn rate pressure index). In addition, the 5AT stepwise pyrolysis and wide pyrolysis temperature range will attenuate the combustion behavior of such propellants (Colonna, 2020). Therefore, in order to increase the general applicability of 5AT applications, scholars have tried to adopt the method of doping different kinds of catalysts in order to achieve the purpose of improving the performance of 5AT and making up for the existing defects. Non-metallic oxides have become a hot research topic due to their low price, wide range of sources, and good catalytic properties (Pragnesh, 2016). Combined with the previous research findings that silica has been widely used and shows vast research prospects in the field of catalysis, therefore, in this paper, SiO_2 was chosen as the catalyst to explore the effect of SiO_2 on various aspects of 5AT performance through scanning electron microscopy (SEM), thermogravimetric analyzer (TG), X-ray diffraction (XRD), kinetic calculations, and the related calculations of thermal safety parameters to provide a theoretical basis for the application of 5AT in the civil and military applications.

2. SAMPLE PREPARATION AND TESTING

Fig. 1 shows the sample preparation as well as the testing procedure, where SiO_2 was added at 3% of the total weight. The 5AT with added SiO_2 with and without added SiO_2 is denoted as sample 5AT, 5AT- SiO_2 , respectively. Tests were carried out using a thermogravimetric analyzer (SDT Q500), in which the samples were homogeneously dispersed in an open alumina crucible and heated at a programmed heating rate $\beta = 5, 10, 15, \text{ and } 20 \text{ }^\circ\text{C min}^{-1}$, respectively, with a set temperature range of $30 \text{ }^\circ\text{C}$ to $800 \text{ }^\circ\text{C}$, and a nitrogen environment with a flow rate of 50 mL min^{-1} . Tests were carried out using a scanning electron microscope (S4800), which was scanned to obtain micrographs of the samples to observe their microscopic morphology and elemental distribution. Tests were performed using XRD (Bruker D8 Advance) to obtain the crystalline structure of each sample. In addition, various kinetic calculation methods such as Flynn-Wall-Ozawa (FWO), Kissinger-Akahira-Sunose (KAS), Straink's method as well as CR method were carried out based on the thermogravimetric test results to calculate and analyze activation energies, and parameters of the reaction model.

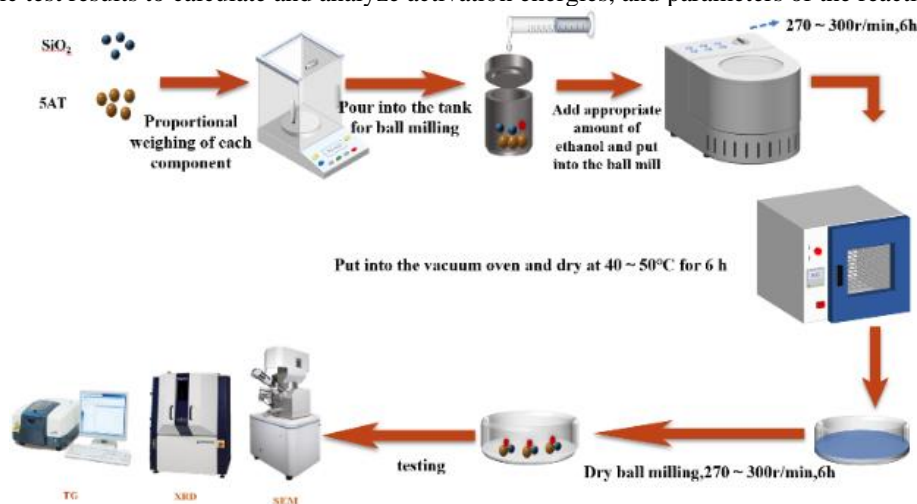


Figure. 1 Sample preparation and testing

3. RESULTS

The microscopic morphology of the two samples is shown in Fig. 2, and the TG-DTG curves of the two samples at four heating rates are shown in Fig. 3. The activation energy-conversion curves obtained based on the FWO method are shown in Fig. 4, and the reaction models for each stage were plotted based on the CR method are shown in Fig. 5. As can be seen from Fig. 2, SiO₂ formed a good composite structure with 5AT. As can be seen from Fig. 3, with the increase of the heating rate, the TG-DTG curves of both samples showed hysteresis phenomenon, and the peak temperatures were shifted to the high temperature direction. This may be due to the thermal hysteresis phenomenon caused by the increase of the heating rate, the heat transfer time between the sample and the environment becomes less, the environment temperature can not be transferred to the sample inside in time, and there exists a large temperature difference between the sample inside and outside, and the time needed to reach the pyrolysis temperature becomes longer. The peak temperature of the first stage of sample 5AT-SiO₂ was delayed by about 15°C compared to the first stage of sample 5AT, and the peak temperature of sample 5AT-SiO₂ was delayed by about 30°C compared to the second stage of sample 5AT, indicating that, the catalyst (SiO₂) shifted the thermal decomposition of 5AT toward high temperature in the third stage, which delayed the peak temperature of decomposition, but the decomposition efficiency of the decomposition still took place. increase, therefore, it can be guessed that the decomposition reaction mechanism of 5AT under the catalytic effect of SiO₂ has been changed. The results of the three methods (FWO, Straink and Kissinger) are relatively close to each other, indicating that the calculations are reliable. The average activation energies of all three samples in the first stage are relatively low, indicating that 5AT pyrolysis in the first stage is the easiest to occur, while the second and third stages are more complex reactions. As can be seen from Fig. 4, the change rule of the two samples is more consistent, in the conversion rate of 0.1 to 0.9, with the increase of the conversion rate, the activation energy decreases. When the conversion rate is 0.1~0.2, with the increase of conversion rate, the activation energy decreases the most. When the conversion rate is 0.1~0.3, the trend of the three samples is more consistent, and the activation energy decreases with the increase of the conversion rate; when the conversion rate is 0.3~0.9, the activation energy of sample 5AT increases with the increase of the conversion rate and the amplitude is increasing, and the activation energy of sample 5AT-SiO₂ decreases, which indicates that the catalyst is functioning from the time when the conversion rate is 0.3. As can be seen in Fig. 5, for the first stage of the reaction, sample 5AT is a secondary reaction model (F2), while sample 5AT-SiO₂ is a tertiary reaction model (F3), suggesting that SiO₂ changes the pyrolysis mechanism of 5AT at that stage.



Figure. 2 SEM diagram

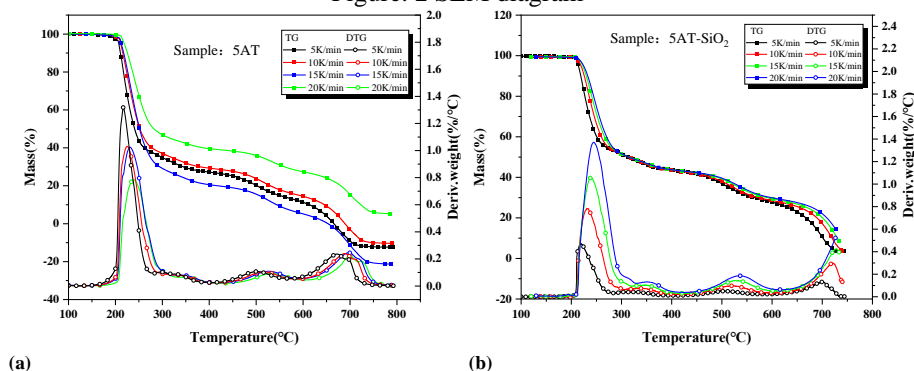


Figure. 3 TG-DTG curves of two samples at four warming rates

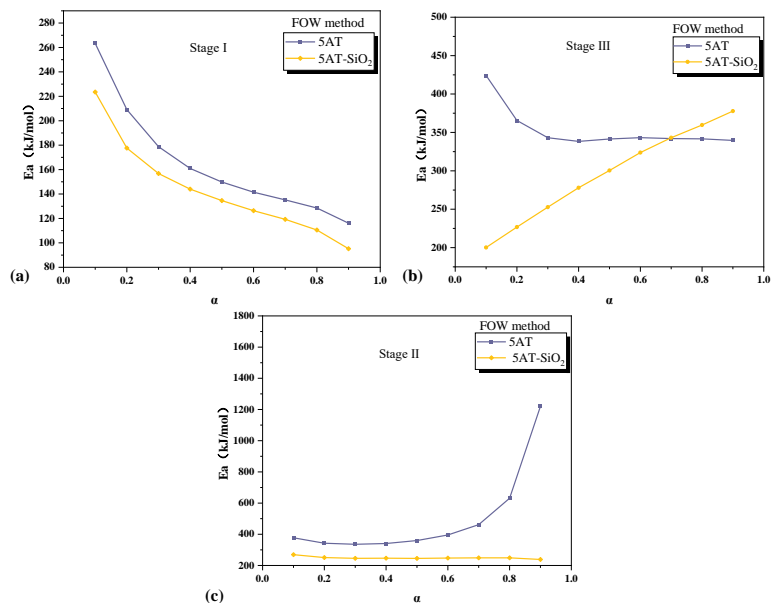


Figure. 4 Activation energy-conversion curve based on the FWO method

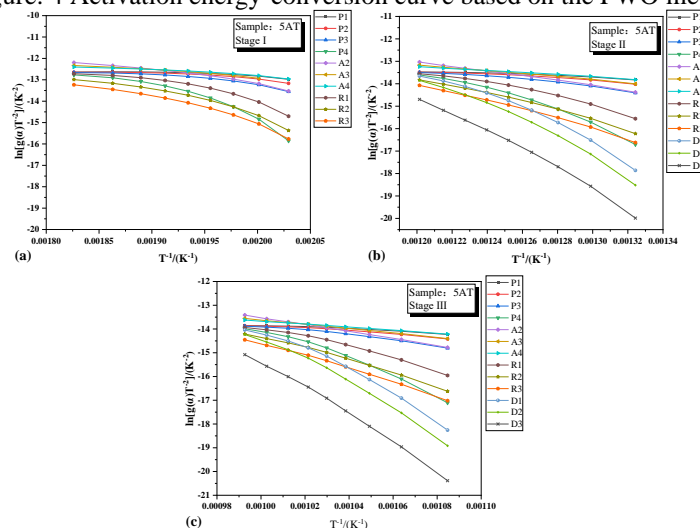


Figure. 5 Modeling the reactions of the three samples at each stage based on the CR method

4. CONCLUSIONS

1. The catalyst SiO_2 compounds well with 5AT when mixed using the mechanical ball milling method.
2. SiO_2 did not shorten the pyrolysis process of 5AT, and the stages were divided into temperature intervals similar to those of 5AT, with the peak temperature shifted back and the activation energy of each stage reduced.
3. The catalyst SiO_2 changes the pyrolysis mechanism of 5AT, and in one stage, the reaction model of 5AT changes from F2 to F3.

Through the experiments and analysis in this paper, it can be inferred that the catalyst (SiO_2) can indeed improve the pyrolysis performance of 5AT, but it will have some effect on the thermal safety behavior of 5AT, but the effect is not significant. The study in this paper can provide further references and suggestions for the application of 5AT in the field of energy-containing materials as well as the study of the combustion performance of 5AT and the influence of catalyst.

5. REFERENCES

- Shingo Date, Takumi Sugiyama, and Norikazu Itadzu. Burning Characteristics and Sensitivity Characteristics of Some Guanidinium 1,5'-bis-1H-Tetrazolate/Metal Oxide Mixtures as Candidate Gas Generating Agent[J]. Propellants, Explosives, Pyrotechnics 36.1(2011):51-56.
- Si-Yuan Zhou, Jiu Chen, Xuan Li, et al. Catalytic pyrolysis of 5-Amino-1H-Tetrazole with copper and its oxide: A deep insight into the combustion mechanism for high nitrogen compound. Fuel 2023;334:126764.
- Colonna P, Bezenine S, Gil R, Synthesis JHJA, Catalysis. Alkene Hydroamination via Earth - Abundant Transition Metal (Iron, Cobalt, Copper and Zinc) Catalysis: A Mechanistic Overview. 2020;362.
- Dave PN, Ram PN, Chaturvedi S. Transition metal oxide nanoparticles: Potential nano-modifier for rocket propellants[J]. Particulate Science and Technology. 2016;34(6):676-80.

From fundamentals of crystallization fouling on nanomaterials to rational design of scalephobic surfaces

Tobias Armstrong^a, Julian Schmid^a, Thomas M. Schutzius^{a,b,*}

^aLaboratory for Multiphase Thermofluidics and Surface Nanoengineering, Department of Mechanical and Process Engineering, ETH Zurich, Sonneggstrasse 3, CH-8092 Zurich, Switzerland

^bDepartment of Mechanical Engineering, University of California, Berkeley, CA 94720, USA

[*tschutzius@berkeley.edu](mailto:tschutzius@berkeley.edu)

Keywords: crystallization fouling, surface nanoengineering, thermofluidics

Crystallization fouling, a process where scale forms on surfaces, is pervasive in nature and technology, negatively impacting the energy conversion and water industries. Despite efforts, rationally designed materials that are intrinsically resistant to crystallization fouling without the use of active methods like antiscalant additives remain elusive. This is because scalephobic surfaces are constructed today without sufficient reliance on an intricate but necessary science-base, of how interfacial thermofluidics, nucleation thermodynamics, and surface nanoengineering control the onset of nucleation and adhesion of frequently encountered scaling salts like calcium carbonate and calcium sulfate. Such scaling salts are common components of fouling deposits in industrial heat exchangers and membranes, which significantly inhibit heat transfer and flow performance. The term “scale” refers summarily to surface deposits of either calcium carbonate or calcium sulfate. Such scaling salts have retrograde solubility in water and are common components of fouling deposits in industrial heat exchangers (Melo 1987) and membranes (Tijing 2015), which significantly inhibit heat transfer and flow performance. Recent experimental studies investigated the effects of surface engineering on bulk surface deposits (consisting of numerous crystals), while theoretical studies have emphasized only one specific surface property (e.g., surface energy) to interpret and rationalize passive scalephobic surface design. This situation makes concrete conclusions and experiments difficult to find and is a significant hurdle to advancing the state-of-the-art. Therefore, we lack fundamental understanding of scale formation on surfaces as a function of the collaborative action of surface texture, surface composition, and substrate stiffness. Therefore, guided by interfacial thermofluidic and thermodynamics theories, and employing advanced experimental methods in the areas of surface nanoengineering and diagnostics, in this work we have developed an integrated knowledge-base for how engineered surfaces can beneficially interact with interfacial transport phenomena in order to advance scalephobic surfaces. We have identified mechanisms for reducing scale nucleation and its adhesion to substrates in order to design and engineer scalephobic materials based on the collaborative action of their composition and topography. The effects of surface texture curvature, surface composition, and substrate compliance on scale nucleation and adhesion have intertwined and sometimes competing impacts. Connected to this are cutting edge materials fabrication techniques and considerations to the development of surfaces for future applications.

For crystallization fouling, the main surfaces where scale forms are in heat exchangers and on membranes, and attention has been given to try to engineer surfaces to passively inhibit scale formation. Scale is thermally insulating and can clog pores, so inhibiting its formation through coating deposition should improve heat transfer and flow performance, however, the coatings themselves should not reduce thermal conductivity or porosity. Approaches to inhibiting scale formation on surfaces include reducing heterogeneous nucleation rates and substrate-scale adhesion. Researchers have studied the effects of confinement and surface energy on scale nucleation. Studies have concluded that the calcification proceeds via a transient amorphous calcium carbonate precursor phase that is initially nucleated in confinement (Stephens 2010, Weiss 2002, Loste 2004, Beniash 1999, Gal 2014). For crystals grown in confinement on a surface where the structure induces low contact area and has low cohesion, it will have low adhesion and can be removed easily by hydrodynamic shear stresses (Cheong 2013). What remains to be seen is if these findings can be translated into an array of rationally engineered surface texture features. Scale formation can be reduced through surface energy modification (Zhao 2005, Al-Hadhrami 2013, Azimi 2014), however, its influence has been shown to be non-specific due to surface texture effects (Chevalier 2014, Zhao 2018). Furthermore, there are still important open questions regarding the effect of substrate wettability on scale nucleation (Azimi 2014, Chevalier 2014, Giuffre 2013). Surface roughness can increase scale adhesion due to enhanced nucleation (higher surface area) (Hui 2015) and mechanical interlocking effects (more crystallites can fill the texture) (Keysar 1994, Herz 2008, Alahmad 2008). However, experimental investigations into surface scaling on nano-textured coatings revealed low fouling rates, which were attributed to low surface energy and higher hydrophobicity (Malayeri 2009). For surface energy, by reducing it one reduces the work of adhesion necessary to remove scale (Zhao 2005, Bornhorst 1999, MacAdam 2004). Models have been used to predict the anti-scaling behavior of a surface based on work of adhesion²⁷ and fracture energy (Förster 1999, Gent 1972), however, these models are valid only for smooth surfaces and cannot explain the influence of surface texture (Bargir 2009, Förster 2000), which is always present and plays an important role. Therefore, predicting scale formation on surfaces based on surface energy

alone is not reliable (Bargir 2009, Santos 2015, Zettler 2005). In addition to surface texture and composition, substrate compliance is also important in controlling the scale crystal particle-substrate adhesion, especially for small particles on soft materials (Style 2013, Xu 2017). Soft materials like polymers membranes are used in many technical applications, where they experience crystallization fouling. Despite the clear importance of understanding the adhesion of scale particles to smooth and textured compliant substrates, studies are missing. Despite recent research into specific aspects of scale formation on surfaces, the combined effects of interfacial thermofluidics, nucleation thermodynamics, and surface texture and composition on scale nucleation and adhesion remain unresolved.

Here we study scale formation on surfaces at the individual and collective crystallite level (micro to nanoscale) by systematically varying the above substrate properties with advanced materials engineering techniques guided by all relevant theories including nucleation thermodynamics and interfacial thermofluidics and aided by advanced experimental measurements. To control scale supersaturation, we have two experimental methods, namely, a microfluidic mixing chamber as well as a parallel plate heat exchanger, both with optical access. We engineer our surfaces with a range of techniques including block copolymer lithography and etching; spin coating and ultraviolet light curing; and wet etching. We use brightfield imaging along with digital holography and total internal reflection imaging. To study scale adhesion, we built a custom-made scanning fluid dynamic gauge system which allows us to impose a known shear stress underwater and to image the crystallite removal process *in situ*. All together, we have advanced the crystallization fouling knowledge-base at the micro- and nano-scale specifically by identifying surface composition and texture features that prevent scale nucleation, and when it does form, to reduce its substrate adhesion such that it can be removed by flowing water. Through this work, we are working towards a rational for the design and creation of a new class of antiscalant surfaces that can be truly termed scale-phobic, significantly advancing the state-of-the-art.

REFERENCES

- Alahmad, M. Factors Affecting Scale Formation in Sea Water Environments – An Experimental Approach. *Chem. Eng. Technol.* 2008, Vol. 31, pp. 149–156.
- Al-Hadhrani, L. M., Quddus, A., Al-Otaibi, D. A., 2013. “Calcium Sulfate Scale Deposition on Coated Carbon Steel and Titanium.” *Desalin. Water Treat.* Vol. 51, pp. 2521–2528.
- Azimi, G., Cui, Y., Sabanska, A., Varanasi, K. K., 2014. “Scale-Resistant Surfaces: Fundamental Studies of the Effect of Surface Energy on Reducing Scale Formation.” *Appl. Surf. Sci.* Vol. 313, pp. 591–599.
- Bargir, S., Dunn, S., Jefferson, B., Macadam, J., Parsons, S., 2009. “The Use of Contact Angle Measurements to Estimate the Adhesion Propensity of Calcium Carbonate to Solid Substrates in Water.” *Appl. Surf. Sci.* Vol. 255, pp. 4873–4879.
- Beniash, E., Addadi, L., Weiner, S., 1999. “Cellular Control over Spicule Formation in Sea Urchin Embryos: A Structural Approach.” *J. Struct. Biol.* Vol. 125, pp. 50–62.
- Bornhorst, A., Müller-Steinhagen, H., Zhao, Q., 1999. “Reduction of Scale Formation under Pool Boiling Conditions by Ion Implantation and Magnetron Sputtering on Heat Transfer Surfaces.” *Heat Transf. Eng.* Vol. 20, pp. 6–14.
- Cheong, W. C., Gaskell, P. H., Neville, A., 2013. “Substrate Effect on Surface Adhesion/Crystallisation of Calcium Carbonate.” *Journal of Crystal. Growth.* Vol. 363, pp. 7–21.
- Chevalier, N. R., 2014. “Do Surface Wetting Properties Affect Calcium Carbonate Heterogeneous Nucleation and Adhesion?” *J. Phys. Chem. C.* Vol. 118, pp. 17600–17607.
- Förster, M., Augustin, W., Bohnet, M., 1999. “Influence of the Adhesion Force Crystal/Heat Exchanger Surface on Fouling Mitigation.” *Chem. Eng. Process. Process Intensif.* Vol. 38, pp. 449–461.
- Förster, M., Bohnet, M., 2000. “Modification of Molecular Interactions at the Interface Crystal/Heat Transfer Surface to Minimize Heat Exchanger Fouling.” *Int. J. Therm. Sci.* Vol. 39, pp. 697–708.
- Gal, A., Kahil, K., Vidavsky, N., Devol, R. T., Gilbert, P. U. P. A., Fratzl, P., Weiner, S., Addadi, L., 2014. “Particle Accretion Mechanism Underlies Biological Crystal Growth from an Amorphous Precursor Phase.” *Adv. Funct. Mater.* Vol. 24, pp. 5420–5426.
- Gent, A. N., Schultz, J., 1972. “Effect of Wetting Liquids on the Strength of Adhesion of Viscoelastic Material.” *J. Adhes.* Vol. 3, pp. 281–294.
- Giuffrè, A. J., Hamm, L. M., Han, N., De Yoreo, J. J., Dove, P. M., 2013. “Polysaccharide Chemistry Regulates Kinetics of Calcite Nucleation through Competition of Interfacial Energies.” *Proc. Natl. Acad. Sci.* Vol. 110, pp. 9261–9266.
- Herz, A., Malayeri, M. R., Müller-Steinhagen, H., 2008. “Fouling of Roughened Stainless Steel Surfaces during Convective Heat Transfer to Aqueous Solutions.” *Energy Convers. Manag.* Vol. 49, pp. 3381–3386.
- Hui, L., Liu, M., Cai, Y., Lv, Y., 2015. “Fouling Resistance on Chemically Etched Hydrophobic Surfaces in Nucleate Pool Boiling.” *Chem. Eng. Technol.* Vol. 38, pp. 416–422.
- Keysar, S., Semiat, R., Hasson, D., Yahalom, J., 1994. “Effect of Surface Roughness on the Morphology of Calcite Crystallizing on Mild Steel.” *J. Colloid Interface Sci.* Vol. 162, pp. 311–319.
- Loste, E., Park, R. J., Warren, J., Meldrum, F. C., 2004. “Precipitation of Calcium Carbonate in Confinement”. *Adv. Funct. Mater.* Vol. 14, pp. 1211–1220.

- MacAdam, J., Parsons, S. A., 2004. "Calcium Carbonate Scale Formation and Control." *Rev. Environ. Sci. Biotechnol.* Vol. 3, pp. 159–169.
- Malayeri, M. R., Al-Janabi, A., Müller-Steinhagen, H., 2009. "Application of Nano-Modified Surfaces for Fouling Mitigation." *Int. J. Energy Res.* Vol. 33, pp. 1101–1113.
- Melo, L. F., Bott, T. R., Bernardo, C. A., 1987. *Fouling Science and Technology*; Kluwer Academic Publishers: London.
- Santos, O., Anehamre, J., Nilsson, M., 2015. "Minimizing Calcium Carbonate Scaling By Modifying the Surface of Heat Exchangers With Flexible Ceramic Coatings." Vol. 2015, pp. 314–319.
- Stephens, C. J., Ladden, S. F., Meldrum, F. C., Christenson, H. K., 2010. "Amorphous Calcium Carbonate Is Stabilized in Confinement". *Advanced Functional Materials.* Vol. 20, pp. 2108–2115.
- Style, R. W., Hyland, C., Boltyanskiy, R., Wettlaufer, J. S., Dufresne, E. R., 2013. "Surface Tension and Contact with Soft Elastic Solids". *Nature Communications.* Vol. 4, pp. 2728.
- Tijing, L. D., Woo, Y. C., Choi, J. S., Lee, S., Kim, S. H., Shon, H. K., 2015. "Fouling and Its Control in Membrane Distillation: A Review". *Journal of Membrane Science.* Vol. 475, pp. 215–244.
- Weiss, I. M., Tuross, N., Addadi, L., Weiner, S., 2002. "Mollusc Larval Shell Formation: Amorphous Calcium Carbonate Is a Precursor Phase for Aragonite". *J. Exp. Zool.*, Vol. 293, pp. 478–491.
- Xu, Q., Jensen, K. E., Boltyanskiy, R., Sarfati, R., Style, R. W., Dufresne, E. R., 2017. "Direct Measurement of Strain-Dependent Solid Surface Stress". *Nature Communications.* Vol. 8, pp. 555.
- Zettler, H. U., Weiß, M., Zhao, Q., Müller-Steinhagen, H., 2005. "Influence of Surface Properties and Characteristics on Fouling in Plate Heat Exchangers." *Heat Transf. Eng.* Vol. 26, pp. 3–17.
- Zhao, Q., Wang, X., 2005. "Heat Transfer Surfaces Coated with Fluorinated Diamond-like Carbon Films to Minimize Scale Formation." *Surf. Coatings Technol.* Vol. 192, pp. 77–80.
- Zhao, J., Wang, M., Lababidi, H. M. S., Al-Adwani, H., Gleason, K. K., 2018. A Review of Heterogeneous Nucleation of Calcium Carbonate and Control Strategies for Scale Formation in Multi-Stage Flash (MSF) Desalination Plants. *Desalination*, Vol. 442, pp. 75–88.

QUANTIFICATIONS ON SUPERCRITICAL FLUID DYNAMICS BY PIXELATED INTERFEROMETRY: CRITICAL PHENOMENA AND PHASE NON-EQUILIBRIUM

Lin Chen^{a, b, *}

^a Institute of Engineering Thermophysics, Chinese Academy of Sciences, Beijing, 100190, China

^b University of Chinese Academy of Sciences, Beijing, 100149, China

* Corresponding E-mail: chenlin2018@iet.cn

Keywords: supercritical fluid, carbon dioxide, interferometry, visualization, thermodynamics

1. INTRODUCTION

The current study extends the fundamental experimental quantifications on supercritical region fluid dynamics under representative geometries, which considers the unique thermophysical properties of such fluid states (Chen 2021). A supercritical fluid can be special due to its large variations of thermal and transport properties that differ from normal fluid or two-phase fluid states as working media in energy systems and/or chemical reaction environment (Carlès, 2010). According to Fig. 1, the critical point set aside different fluid regions while the density parameter shows continuous variations and large gradient in the near-critical region and the specific heat show narrowed steep region across the near-critical gas-liquid region as well as the supercritical region. Such property trends give special advantages of near-critical compressing and heat transfer enhancement (and also possible deterioration) for power systems like Brayton cycle for energy conversions (coal fire, solar, geothermal, etc) (Chen 2021). However, those changes in detailed chamber/channel/compressing/expanding flow situations will cause stability and efficiency problems under sudden changes of transport mechanisms. To understand such basic case trends and general fluid-machinery problems, the current study proposes the application of pixelated interferometry to field-based quantifications on boundary heat transfer flows of supercritical fluid, so as to give new possibilities in correlation upgrading and mechanism understanding for real designs and applications.

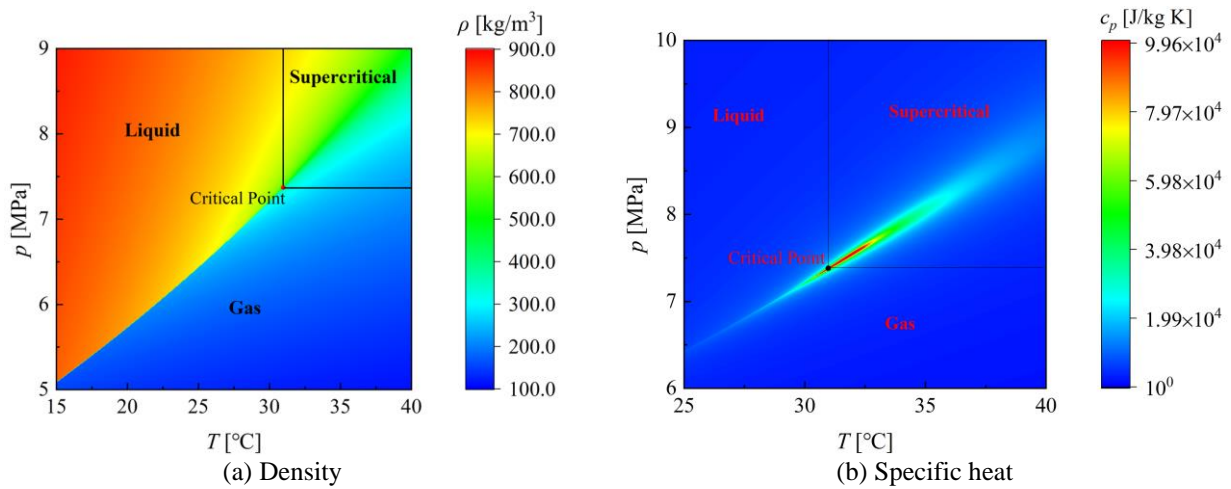


Figure 1. Phase diagrams of carbon dioxide. (a) Density; (b) Specific heat.

2. QUANTITATIVE MEASUREMENT METHOD BY INTERFEROMETRY

Interferometers with phase shifting method are appropriate for sensing displacement, vibration, and physical phenomena (Zhang et al., 2022). It provides interferometric pictures of multi-phase retardation angles using a single device, allowing for the reduction of ambient noise and the measurement of non-static behaviors (Chen 2021). This technique of acquiring multi-phase delay angle images with a single device is called Parallel Phase-shifting Interferometry (PPSI). In this study, optical components were installed in a Self-balancing Vibration Isolation Optical Table (Surface Roughness <math>< 0.6 \mu\text{m}</math>). The polarized light was emitted from a He-Ne laser (R-30991, $\lambda = 633$ nm, 5.0 mW, Newport). The practical optical component configuration and completed construction are shown in Fig. 2.

The PPSI technique is based on the pixelated array masked method which is using a micropolarizer array as a phase mask. The micropolarizer contains a phase-shifting array of four polarizing elements. The interference data map of four polarization angles θ ($0, \pi/2, \pi, 3\pi/2$) in the visualization chamber can be measured simultaneously.

The experiment was conducted in a thermostatic room (range 0-40°C, accuracy $\pm 1^\circ\text{C}$). There are three essential procedures in this experiment: acquisition of sub/supercritical state, phase-shifting interferometric measurement, data processing, as shown in Fig. 2. The carbon dioxide from the gas cylinder is introduced to the buffer tank (150 mL). The parameters change in the target element is characterized through the phase-shifting interferometric measurement. The information about the flow field is then extracted from the interference fringes using proprietary techniques (Zhang et al., 2022). The pressure and temperature in the system are measured precisely through pressure transmitter (3051TA, 0.05%, Rosemount) and thermoelectric cooler (TEC) temperature controller ($\pm 0.01^\circ\text{C}$). Figure 3 shows representative experimental geometries of chamber and channel flow with static/through flow conditions.

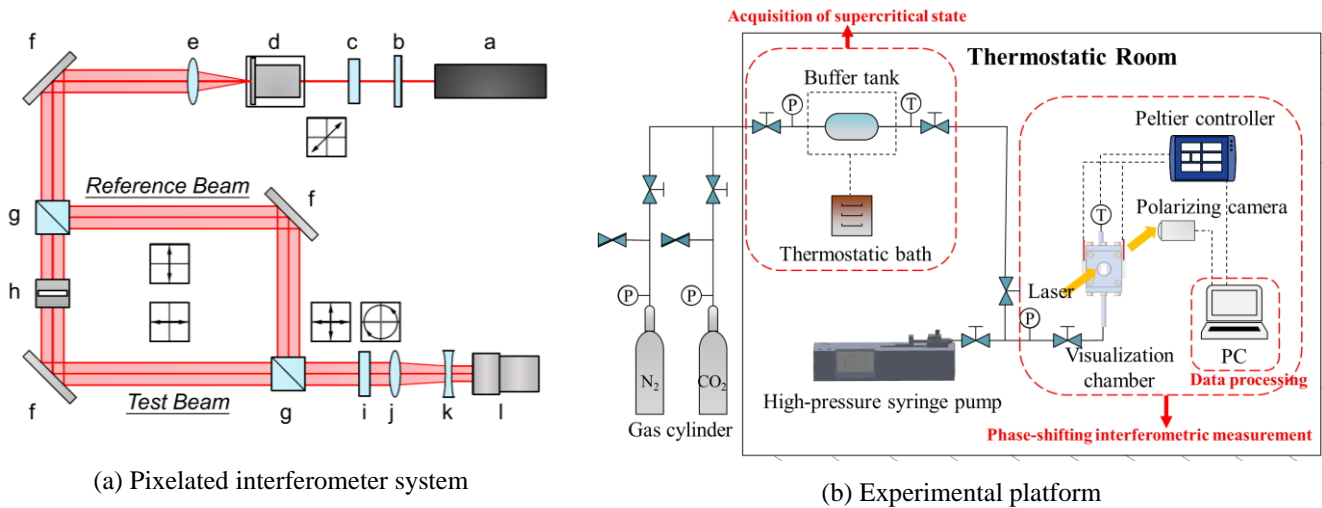


Figure 2. Schematic diagram of the system design. (a) Pixelated interferometer system; (b) Experimental platform.

3. TRANSIENT FIELD ANALYSIS OF CRITICAL REGION THERMODYNAMICS

Figure 3 gives the bottom heating results of a closed chamber under near-critical conditions, such boundary heating gives typical supercritical convection scenario: (1) very small and homogeneous heating up of boundary without obvious thermal plume process; (2) detailed local in-equilibrium of near-critical transport; (3) possibility of quantitative flux and local transport analysis.

Figure 4(a) gives the jet mixing visualization results, which show the new physics of “phase behavior” between the mixing of liquid-like case to gas-like case: (1) mixing layer thickness very thin compared with other cases; (2) large deviations among different positions due to quick phase expansion for such cases.

Figure 4(b) gives the turbulent boundary flow of mini-channel under subcritical and supercritical cases. Local turbulent heat transfer under heat input/perturbation can be extracted from the density and temperature field info, which can help for analysis of transient boundary behaviors of “phase” transitions in supercritical region. Based on those series of experimental quantification analysis, detailed discussions on such unique phase and transportation phenomena can be expected for next step designs and application analysis.

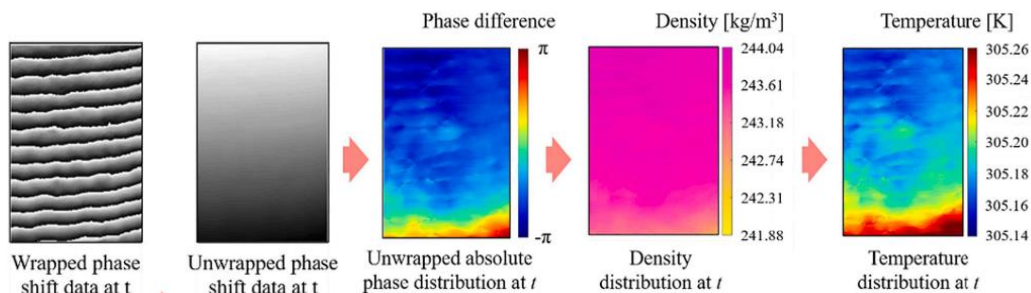
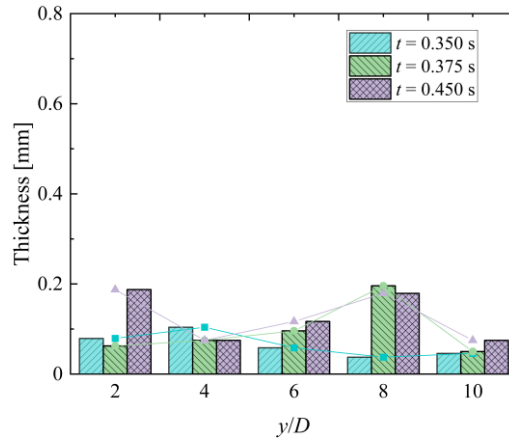
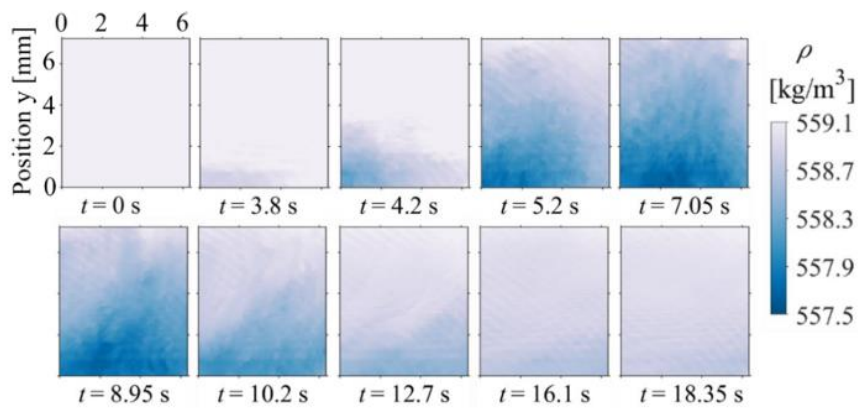


Figure 3. Extraction of field data for near-critical convection (7.02MPa, 32°C, $5.12 \times 10^4 \text{ W/m}^2$) (Zhang et al., 2017).



(a) Liquid-lik to gas-like CO₂ at 35°C, (7.58 to 7.445MPa. (Yang an Chen, 2023)



(b) turbulent channel flow at 7.819MPa, $\Delta p = 14.56$ Pa, 306.17 K, 14057W/m² (Chen et al., 2024)

Figure 4. Dynamics of supercritical jet and turbulent flow results.

4. CONCLUSIONS

This study shows the series of works performed in the Heat and Mass Transfer Research Center of Institute of Engineering Thermophysics, Chinese Academy of Sciences, on the critical dynamics of CO₂ fluid, for the application targets of wide power conversion, carbon capture and sequestration, chemical and environmental sectors. Newly developed system with pixelated array-masked interferometer system has been successfully applied in the quantitative characterization of critical region fluid dynamics, including the cross-critical, pseudo-critical, convection, local heating response, as well as turbulent boundary flow, etc. This study (1) gives for the first time detailed full field information of critical region phenomena and (2) opens the world of interesting critical region for engineering correlations and (3) allows for future in-depth analysis of local-scaling in real application designs.

Thanks to the support from the National Natural Science Foundation of China (52076207), CAS Project for Young Scientists in Basic Research (YSBR-043), CNNC Key Laboratory on Nuclear Reactor Thermal Hydraulics Technology (2020RETHOF-071801) and CAS Key Research Program of Frontier Sciences (ZDBS-LY-JSC018).

5. REFERENCES

- Chen, L., 2021. *Handbook of Research on Advancements in Supercritical Fluids Applications for Sustainable Energy Systems*. IGI Global, Hershey, Pennsylvania.
- Carlès, P. A brief review of the thermophysical properties of supercritical fluids. *J. Supercrit. Fluids*, Vol. 53, p. 2-11 (2010)
- Zhang, Y. Z., Chen, L., Wu, Q. X., Yang, D., Kanda, Y., Zang, J. G., Komiya, A., Huang, Y. P., 2022. "Preliminary measurements of transient boundary heat transfer process under supercritical pressures using pixelated phase-shifting interferometry". *Int. Commun. Heat Mass Trans.* Vol. 138, p. 106396.
- Yang, D., Chen, L., 2023. "Visualization of dynamic phase mixing and equilibrium process in transcritical and supercritical conditions". *Flow Meas. Instrum.* Vol. 92, p. 102399.
- Chen, L., Zeng, G., Yang, D., Yuan, H.Z., Zang, J.G., Huang, Y.P., 2024. "Quantitative Visualization on Boundary Heat Transfer of Supercritical CO₂ Mini-Channel Through-Flow (Re=10⁴) via Pixelated Phase-Shifting Interferometry". *International Journal of Heat and Mass Transfer*, Vol. 223, p. 125258.

Effect of hydrogen concentration, vent area, vent shape, and burst pressure on vented hydrogen-air explosions and its consequence analysis

Qing Chen^a, Bin Li^{a,*}, Yongxu Wang^a, Dan Zhang^a, Rhoda Afriyie Mensah^b, Oisik Das^b, Lifeng Xie^a

^aSchool of Safety Science and Engineering, Nanjing University of Science and Technology, Nanjing 210094

^bDivision of Structural and Fire Engineering, Department of Civil, Environmental and Natural Resources Engineering, Luleå University of Technology, 97187 Luleå, Sweden.

*libin@njust.edu.cn

Keywords: Hydrogen, Explosion venting, Overpressure, Second explosion...

1. Background and Objectives

In recent years, countries around the world have actively formulated strategies for hydrogen energy development. Demand for hydrogen production, transport, and storage has grown gradually^[1-4]. As the infrastructure of the hydrogen industry expands, the likelihood of hydrogen explosions increases accordingly. There are many ways to mitigate or eliminate the hazards caused by explosive accidents to equipment, buildings, and people, such as explosion suppression, explosion protection, explosion resistance and explosion vented. Explosion vented as one of the most cost-effective means, is widely used in various industries in production practice^[5-8]. However, in China, the development of hydrogen long-tube trailers, hydrogen fuel cell vehicles, and comprehensive urban utility tunnels started late, and experience in dealing with related explosions is not yet sufficient. Once an explosion accident occurs, it will lead to serious consequences, so it is important to study the explosion vented of such closed or semi-closed pipeline structure facilities and to provide experience in the design of related explosion relief structures

Vented area, vented shape and burst pressure will be taken into account in the study, and the hydrogen explosion characteristics of the shock tube will be investigated by analyzing the pressure characteristics, the hydrogen explosion release process, and the flame temperature under different release conditions. Further study of the possible consequences of external pipeline pressures and temperatures on people, property, and facilities. This study will provide scientific basis and technical support for facilities such as hydrogen long-tube trailers, hydrogen fuel cell vehicles and urban utility tunnels, ensuring that in an explosion accident, casualties and property damage can be effectively reduced and the overall safety level enhanced.

2. Experimental setup

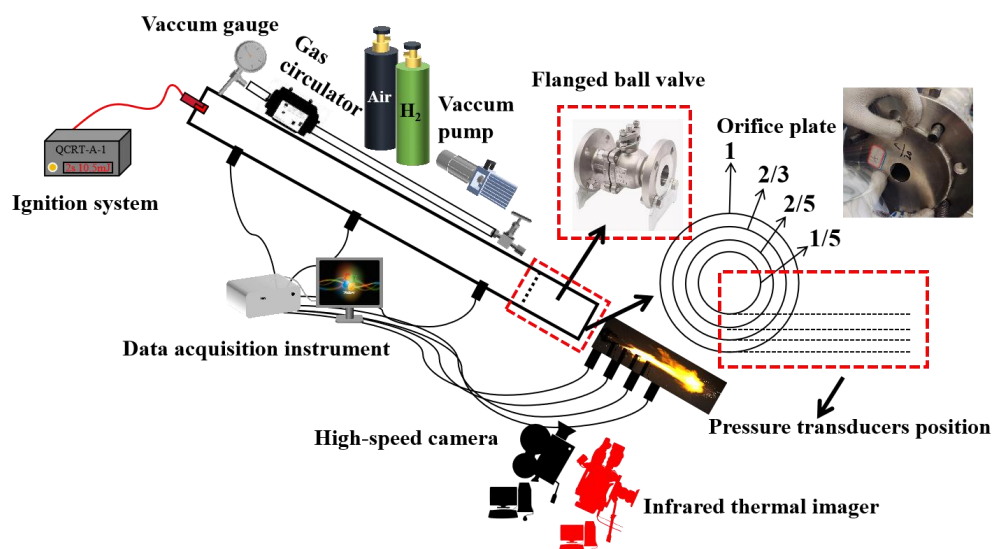


Figure 1. Experiment setup.

All hydrogen explosion vented tests were carried out in a shock tube with a length of 0.25 m ball valve flange, a total length of 2.25 m and internal diameter of 70 mm with an L/D ratio of 32, as shown in Fig. 1. A data acquisition instrument (TRANET FE 404, ELSYS, Switzerland) and seven piezoelectric pressure sensors (113B26, PCB, America, measurement range of 0-6.895MPa, accuracy of 0.01%) were used to record the pressure-time data during the hydrogen explosion vented test. Three piezoelectric pressure transducers were placed inside the pipeline from the upstream

section to the downstream section at 40 cm(PT1), 100 cm(PT2), and 160 cm(PT3), respectively, and four transducers on the outside of the pipeline were located 10 cm(PT4), 20 cm(PT5), 30 cm(PT6), and 40 cm(PT7)away from the orifice plate, respectively. The surface of the external pipeline transducers was always flush with the lower end of the vent port under all texts, for example, the four black dashed lines in the red dashed box in Figure 1. The burst pressure and the vented area and vented shape are adjusted by means of different thicknesses of polyester film and different sizes of orifice plates, respectively. A high-speed camera (Photron UX100 camera, Japan) and an infrared thermal imager ((IRS 669, FOTRIC, China) were used to record the hydrogen explosion vented process and flame temperatures outside the pipeline, with frame rates of 2000 fps and 120 fps, respectively. The tests were conducted at atmospheric pressure and at 25°C. By the way, the rupture pressure of the plastic film was measured by inflating and pressurizing in the shock tube, and the rupture pressure was recorded by the static pressure transducer and the high-speed camera shooting pressure gauge simultaneously for a total of six tests. Results showed the rupture pressures of the two specifications of 0.0125mm (thin film) and 0.1mm (thick film) polyester film were 51kPa and 597kPa, respectively, which are a lot of differences from Song’s prediction formula^[9].

3. Results

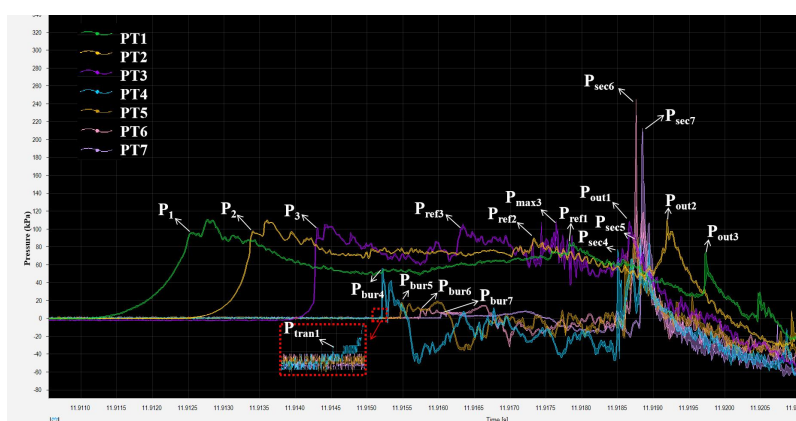


Figure 2. Typical explosion vented pressure-time histories at a hydrogen concentration of 40% with thin film(Thickness 0.0125mm).

Figure 2 demonstrated a typical pressure-time curve for the discharge process of 40% concentration of hydrogen under film conditions, with seven peaks appearing in the history curves a and b respectively. Combined with high-speed camera recording of the venting process and pressure-time data for analysis, P_x (x is the transducers’ number for 1,2 and 3) caused by the precursor wave which is in front of the flame front, $P_{ref\ x}$ is caused by the collision of the precursor wave with the diaphragm to form the first reflected wave, $P_{max\ x}$ represents the maximum explosion pressure inside the pipeline before the secondary explosion outside the pipeline occurs, $P_{out\ x}$ represents the maximum explosion pressure inside the pipeline after the appearance of the second explosion outside the pipeline., P_{trans} is a structural dynamic response (high speed deformation) of the film caused by a precursor wave, which pushes the air outside the pipe to form a secondary shock wave that is transmitted. P_{bur} is the first peak that propagates to the outside of the pipe after the rupture of the polyester film due to a precursor wave and P_{sec} for the external secondary explosion generated by the maximum explosion pressure.

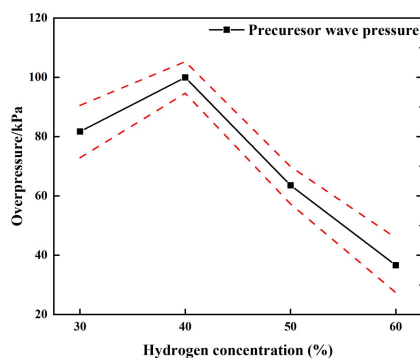


Figure 3. The curve of $P_{(1,2,3)}$ - hydrogen concentration for different vented areas in circular vented.

As shown in Figure 3, the circular vented different vented areas conditions of different concentrations of hydrogen - precursor wave pressure curve, the area formed by the two red dotted lines represents the error interval for all test

results. Analysis of the pressure-time curve found in all the circular vented under the conditions of different vented areas of the hydrogen explosion relief test, the same concentration of the three measurement points in the pipeline of the precursor wave pressure values are basically the same.

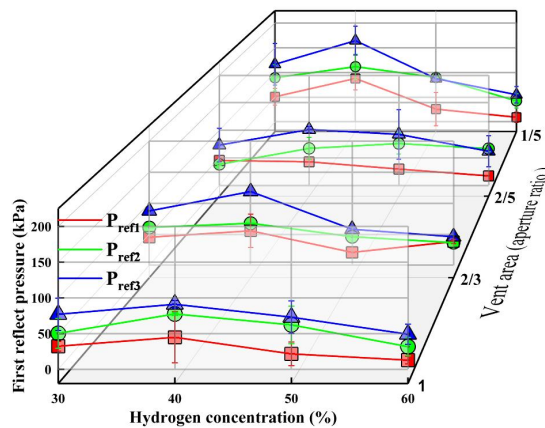


Figure 4. Curves of $P_{ref(1,2,3)}$ -hydrogen concentrations at different vent areas

Figure 4 shows the curves of $P_{ref(1,2,3)}$ -hydrogen concentrations at different vent areas. It can be seen that P_{ref} showed an increasing and then decreasing trend with increasing concentration in the same vented area, whatever the area of the discharge the maximum of P_{ref} occurs at three measurement points inside the pipe at 40% concentration of hydrogen. However, as the vented area decreases, the P_{ref} increases at both four hydrogen concentrations, but the magnitude of the change is small. It is because of the 40% concentration of hydrogen in the optimal equivalence ratio near the explosion generated by the precursor wave is stronger, and with the reduction of the relief area reflected back to the upstream section of the reflected wave intensity gradually weakened, reducing the reflected wave and flame interactions, and further decrease its impact on the internal shock tube.

4. CONCLUSIONS

1. Vented shape, vented area and burst pressure have almost no effect on the peak pressure of the precursor wave, whereas hydrogen concentration has a great effect on the peak pressure of the precursor wave.
2. In the circular vented under different conditions of the vent area, the closer to the vent the greater the impact of the first reflected wave. At 40% hydrogen concentration in all vent area test conditions, the first reflected wave inside the shock tube is affected by the maximum. As the area decreases, the impact gradually becomes more significant, but the change is not noticeable.

5. REFERENCES

- [1] Rasul, M.G., Hazrat, M., Sattar, M., Jahirul, M. and Shearer, M., 2022. "The future of hydrogen: Challenges on production, storage and applications". *Energy Conversion and Management*, 272.
- [2] Mostafaeipour, A., Hosseini, Dehshiri, S. and Hosseini, S., 2020. "Ranking locations for producing hydrogen using geothermal energy in Afghanistan". *International Journal of Hydrogen Energy*. Vol. 45, pp. 15924-15940.
- [3] Gondal, I.A., Masood, S. and Khan, R., 2018. "Green hydrogen production potential for developing a hydrogen economy in Pakistan". *International Journal of Hydrogen Energy*. Vol. 43, pp. 6011-6039.
- [4] Madadi, A.V., Zendejboudi, S., Cata, S. and Dusseault, M., 2022 "A comprehensive review on hydrogen production and utilization in North America: Prospects and challenges". *Energy Conversion and Management*. 269.
- [5] Hu, S., Kang, T., Geng, J., Zhang, M., Wang, Y., Li, H. and Fei, S., 2023 "Explosion Venting Design for a Special Vehicle". *Journal of Physics: Conference Series*. 2478.
- [6] Komarov, A.A., Korolchenko, D., Gromov, N. and Korolchenko, A., 2021 "Specifics of Explosion-Venting Structures Providing Acceptable Indoor Explosion Loads". *Applied Sciences*.12.
- [7] Lv, P., Li, T., Zhang, Y., Pang, L. and Yang, K., 2023 "Influence of the opening pressure of explosion-venting surface on methane deflagration characteristics in municipal sewage confined spaces". *Process Safety Progress*. Vol. 42, pp. 729-736.
- [8] Sun, Y., Zhou, X., Bai, G., Li, A., Xin, T. and Li, D., 2021 "Vent burst doors as an effective method of suppressing the dangers of gas explosions". *AIP Advances*. 11.
- [9] Song, X., Chen, G., Dong, Y., Li, B., Zhang, D. and Xie, L., 2023 "The overpressure and temperature characteristics of hydrogen-air mixtures during a vented explosion in a large L/D ratio duct: Effect of burst pressure". *Fuel*. 350.

EFFECT OF STAINLESS-STEEL SURFACES ON BIOFILM FORMATION: IMPLICATIONS DURING ELECTRICAL IMPEDANCE SPECTROSCOPY MEASUREMENTS

Avgoulas D.I.^{1*}, Petala M.², Kostoglou M.¹, Karapantsios T.D.¹

¹Laboratory of Chemical and Environmental Technology, Department of Chemistry, Aristotle University of Thessaloniki, 54124, Thessaloniki, Greece

²Laboratory of Environmental Engineering and Planning, Department of Civil Engineering, Aristotle University of Thessaloniki, 54124, Thessaloniki, Greece

*dimiavgou@gmail.com

Keywords: electrical impedance device, biofilm formation, *Pseudomonas fluorescens*, stainless steel, cleaning process

1. INTRODUCTION

A novel electrical impedance spectroscopy device has been developed for measuring milk collection rate, temperature and conductivity during goat/sheep milking. The electrical measurements are conducted by stainless steel ring electrodes which are flush-mounted to the inner walls of the test tube (Karapantsios et al., 2016). However, microorganisms could pose a challenge towards this attempt. *Pseudomonas fluorescens* bacterial group is considered among the most significant spoilage bacteria in milk and dairy products due to their ability to adhere to surfaces of milk tanks and dairy processing equipment, proliferate and generate structurally complex and dynamic communities named biofilms. Biofilm growth mode provides protection from harsh conditions such as cleaning-in-place procedures, while it might also attract or serve as a shelter for other pathogens or spoilage microorganisms (Zarei et al., 2022). The objective of this study is to evaluate the early biofilm formation of *P. fluorescens* on stainless steel surfaces either under stagnant or shear stress conditions. The potential attachment of bacteria on metallic electrodes might lead to false electrical signals and misinterpretation of results (Kampouraki et al., 2024), thus affecting the sensitivity of analysis. Furthermore, through the understanding of biofilm formation on these surfaces, a standardization of an effective cleaning protocol can be established.

2. MATERIALS AND METHODS

Two differently treated stainless steel surfaces, a passivated (SS) and a both passivated and electropolished (SSEP), were used as a substrate. Dimensions of each surface corresponding to Length \times Width \times Depth were 76 \times 12.7 \times 1.6 mm, respectively. The analysis of clean surfaces was performed employing confocal microscopy, while the wettability was measured by calculating the contact angle between the surface and a drop (5 μ L) of distilled water. *P. fluorescens* SBW25 was cultured over stainless steel surfaces using fresh, sterile tryptic soy broth (TSB) as a nutrient medium. More specifically, the samples were placed horizontally in sterile Petri dishes, whereas 18 mL of TSB and 2 mL of bacteria at OD₆₀₀ = 0.5 (1:10 dilution) were added to each Petri dish. The experiments were performed for 24 h at 30°C either under stagnant or shaking (100 rpm) conditions. For visualization of bacterial adhesion on stainless steel surfaces, the co-staining method with Syto9/PI for LIVE/DEAD cells was employed and the samples were observed under a fluorescence microscope. Image processing was carried out using ImageJ software. The experimental procedure is described in detail (Avgoulas et al., 2024).

3. RESULTS

3.1 Physicochemical characteristics of the stainless steel surfaces

Among the studied surfaces, SS presented the highest roughness (Sdr = 10.8 \pm 0.5 %), while electropolishing technique led to a final material with a significantly lower roughness (Sdr = 0.06 \pm 0.01 %) (**Fig. 1**). Regarding the wettability of the surfaces, the smoothness of the SSEP led to a constant contact angle of 85.1° \pm 1.8° at both directions. However, SS presented an anisotropic effect dependent on the planar direction. More specifically, when the contact angle was estimated perpendicular to the grooves of SS, it was found 76.3° \pm 3.0°, presenting a hydrophilic nature. On the contrary, when the measurement was performed parallel to the grooves, it was 100.6° \pm 5.5°, displaying hydrophobic properties (**Fig. 2**).

3.2 Evaluation of *P. fluorescens* adhesion on stainless steel surfaces under static conditions

As shown in fluorescence images (**Fig. 3A**), *P. fluorescens* exhibits a higher affinity for SS. From size distribution analysis, a particle size shift to smaller ones for SSEP is observed, indicating that *P. fluorescens* is mainly found at a single cell state or small clusters of odd number of cells after 24 h. On the contrary, SS seems to stimulate the formation of bigger clusters with more prominent the presence of dead cells. Moreover, comparing the number of particles, SS displays approximately threefold increase compared to SSEP (**Fig. 3B**).

3.3 Evaluation of *P. fluorescens* adhesion on stainless steel surfaces under shaking conditions

As shown in fluorescence images (Fig. 4A), shaking mode affects intensively the bacterial adhesion compared to static conditions. This might be attributed either to difficulty of cells to reach and adhere to the wetted surface or to cell growth in planktonic form due to efficient oxygen conduction from the liquid-air interface and local nutrient availability because of mixing conditions. SS displays higher surface coverage (1.1% ± 0.2%) compared to SSEP (0.2% ± 0.04%), while bacteria tend to form bigger clusters in the first case (Fig. 4B). Moreover, bacteria appear oriented along the grooves of SS, suggesting that roughness affects the initial biofilm formation.

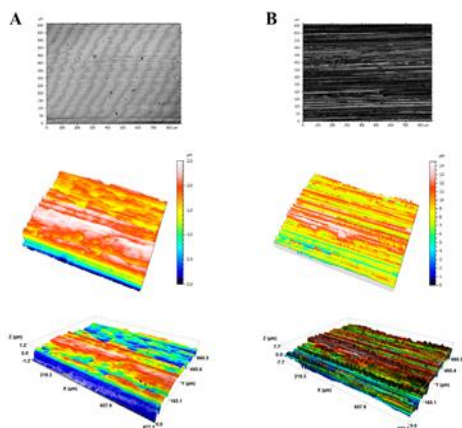


Figure 1. 3D images of clean surfaces (A) SSEP and (B) SS obtained by confocal microscopy.

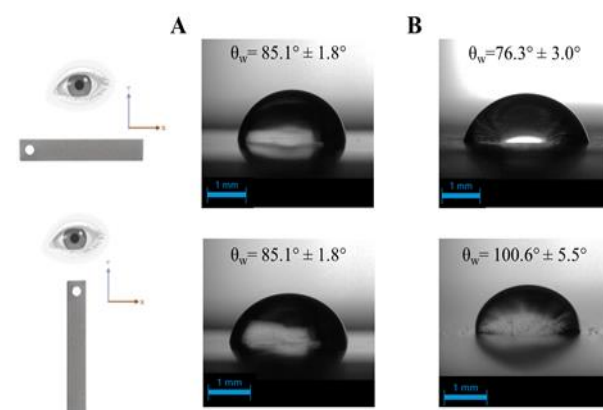


Figure 2. Contact angle of water droplet (A) SSEP and (B) SS.

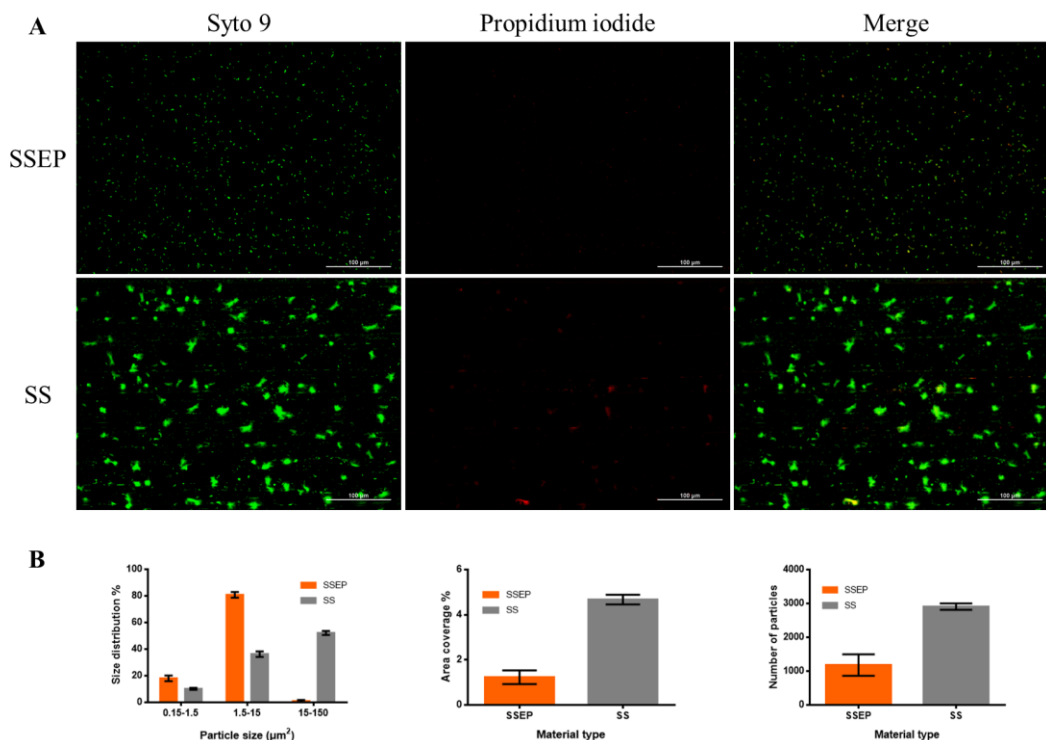


Figure 3. A) Fluorescence images of *P. fluorescens* adhesion on stainless steel surfaces under stagnant conditions after 24h. B) Quantitative analysis derived from image processing with ImageJ software.

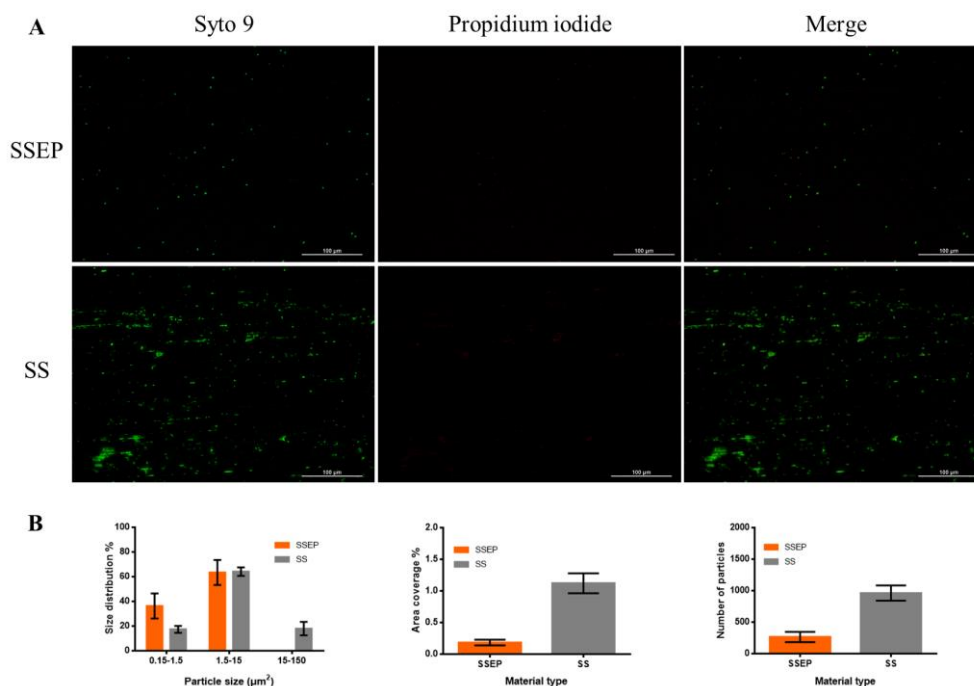


Figure 4. A) Fluorescence images of *P. fluorescens* adhesion on stainless steel surfaces under shaking conditions after 24h. B) Quantitative analysis derived from image processing with ImageJ software.

4. CONCLUSIONS

This work points out that parameters such as surface treatment, texture and chemistry should be taken into consideration concerning the biofilm formation on stainless steel electrodes. Understanding the dynamics of the phenomenon can contribute to the inhibition of the process in the initial stage and the further evolvement into mature biofilm structures which would threaten the effectiveness and sensitivity of the electrical impedance spectroscopy measurements. Moreover, the results can be utilized for the design of a standard cleaning-in-place method.

5. REFERENCES

- Avgoulas, D.I., Petala, M., Briandet, R., Dergham, Y., Noirot-Gros, M.F., Konstantinidis, A., Kostoglou, M., Karapantsios, T.D., 2024. Effect of surface treatment and shear flow on biofilm formation over materials employed in space water storage and distribution systems. *Front. Mater.*, 11:1401764
- Kampouraki, Z.C., Petala, M., Zacharias, K., Konstantinidis, A., Zabulis, X., Karamaounas, P., Kostoglou, M., Karapantsios, T. D., 2024. Highly sensitive resistance spectroscopy technique for online monitoring of biofilm growth on metallic surfaces. *Environ. Res.*, 240, 117401
- Karapantsios, T.D., Evgenidis, S.P., Zacharias, K., Mesimeris, T., 2016. Method for the detection and characterization of bubbles in liquids and device therefor, resp. system. European Patent Office, EP 3005942 A1
- Zarei, M., Rahimi, S., Saris, P. E. J., Yousefvand, A., 2022. Pseudomonas fluorescens group bacterial strains interact differently with pathogens during dual-species biofilm formation on stainless steel surfaces in milk. *Front. Microbiol.*, 13.

ACKNOWLEDGEMENTS

This work was supported by the project «Innovative device for measuring milk collection rate and quality features during goat and sheep milking, exploiting an electrical impedance spectroscopy technique» (Project code: KMP6-0269405) under the framework of the Action «Investment Plans of Innovation» of the Operational Program «Central Macedonia 2014-2020», that is co-funded by the European Regional Development Fund and Greece.



REGION OF CENTRAL MACEDONIA
MANAGING AUTHORITY
O.P. Region of Central Macedonia



Co-financed by Greece and the European Union

STUDY OF EMULSION DYNAMICS UNDER VARYING GRAVITY CONDITIONS THROUGH ELECTRICAL AND OPTICAL MEASUREMENTS

Chondrou A. P., Evgenidis S. P., Karapantsios T. D., Kostoglou M.*

Department of Chemical Technology and Industrial Chemistry, Faculty of Chemistry, Aristotle University of Thessaloniki, 54124, Thessaloniki, Greece

[*kostoglu@chem.auth.gr](mailto:kostoglu@chem.auth.gr)

Keywords: emulsion stability, parabolic flights, droplet size distribution, droplets coalescence, electrical impedance

1. INTRODUCTION

Emulsions dominate in our daily life. They are encountered in a great variety of industrial applications, e.g. foods, cosmetics, pharmaceuticals and in petroleum industry. Milk (oil-in-water emulsion) is one of the most stable emulsions produced in nature and is used to produce several dairy products e.g. cream, butter and cheese (*Chappat, 1994*). This work aims to exploit the different gravity conditions evolving during Parabolic Flights for the dynamic behavior and stability study of emulsions. On earth, gravity triggers the rapid separation of the aqueous phase from the creamy phase after the end of the emulsification process. Micro-gravity, on the other hand, provides a simplified environment where the buoyancy related phenomena are eliminated. Consequently, droplets motion and droplet-droplet interactions after emulsification get slower and can be studied thoroughly and individually employing optical and electrical diagnostics.

2. MATERIALS AND METHODS

The emulsification process takes place every time inside a rectangular aluminum experimental cell using a piston with a plate at its tip which moves periodically and repeatedly up and down. As a result it produces, deforms and breaks up oil droplets (*Chondrou et al., 2023*). The Photron Multi FASTCAM high speed camera is used to investigate droplet-droplet interactions (e.g. coalescence events) and the CANON EOS 70D digital camera is utilized to capture high resolution images for the determination of droplet size distribution. An EU patented, electrical impedance spectroscopy technique (*EP 3005942, 2016*) developed by *Evgenidis and Karapantsios (2015)* is used for the registration of oil volumetric fraction exploiting the gravity dependent separation of oil droplets from the aqueous phase during the hyper-gravity period following microgravity conditions in a parabola. Electrical measurements are conducted using non-intrusive, circular (edge of rods) electrodes which are flush-mounted to two parallel plexiglass walls of the experimental cell. The output of data reduction is an electrical impedance time-series which is transformed to oil volumetric fraction time-series employing the appropriate model (e.g. Maxwell or Bruggeman) (*Vlachou et al., 2020*). In total, ninety experiments are conducted during the European Space Agency 79th Parabolic Flight Campaign. The materials used for the preparation of oil-in-water emulsions are millipore water, MCT oil, and Nikkol BL-21 (water soluble, nonionic surfactant, CMC: $2.5 \cdot 10^{-4}$ M) surfactant as emulsifier. The four parameters examined during micro-gravity experiments are: a) oil volumetric fraction ϕ (from 0.05 to 0.20), b) surfactant Nikkol BL-21 concentration C_{surf} (from 0 to $2 \cdot 10^{-4}$ M), c) pulsation stroke frequency f (10 and 15 Hz) and d) number of strokes (from 9 to 90).

3. RESULTS

3.1 High resolution imaging

Image analysis of high resolution images allows the determination of droplet size distribution which is presented in graphs of the % droplet number probability density function (PDF) versus droplet diameter (**Fig. 1a**). The three pictures at $t = 0$ s (immediately after the end of the emulsification process), 5 s and 10 s are taken during micro-gravity conditions while the next two, $t = 15$ s and 20 s are captured during hyper-gravity conditions. During micro-gravity conditions a broad droplet size distribution (~ 30 to $350 \mu\text{m}$) is observed while during hyper-gravity conditions the droplet size distribution becomes narrower (and accordingly sharper) towards smaller sizes (~ 30 - $150 \mu\text{m}$). This proves that under hyper-gravity conditions, buoyancy triggers the rapid separation of creamy phase from the aqueous phase during which oil droplets move faster to the top of the cell than the smaller ones. A comparative figure regarding the evolution of the number-based droplet average diameter is presented in **Fig. 1b** in which the examined parameter is the pulsation stroke frequency. It is observed that in the examined range the number-based average diameter decreases as the pulsation stroke frequency increases.

3.2 High speed imaging

Indicative directly evidenced coalescence events in the aqueous phase are shown in **Fig. 2**. In this case, the two droplets that coalesce are clearly seen to be next to each other. It is noticed that two droplets of either the same or different size is possible to merge to a single droplet. Furthermore, droplet coalescence may happen at different directions (vertically, horizontally and diagonally).

3.3 Electrical measurements

Fig. 3a presents the evolution of electrical resistance during the periodical movement of the piston with a frequency of 15 Hz for 1 s. Thirty intense signal peaks can be clearly noticed in 1 s, corresponding to two passes (downwards/upwards) of the piston plate per stroke in front of the measuring electrodes for the applied pulsation frequency. The electrical resistance evolution during the total duration of a parabolic maneuver is translated into oil volumetric fraction evolution (**Fig. 3b**) via the Bruggeman equation (Vlachou *et al.*, 2020). In the first region of the signal (~ 0 g conditions) fluctuations in the value of the electrical resistance are observed. These fluctuations are due to the residual motion after pulsation of the entire liquid volume in the experimental cell which makes oil droplets move in and out of the measuring region between the rod electrodes. Furthermore, the two distinct major slopes observed in the second region of the signal (~ 1.8 g conditions), indicate that the droplet size distribution can be approximated by a bidispersed distribution rather than by a monodispersed one.

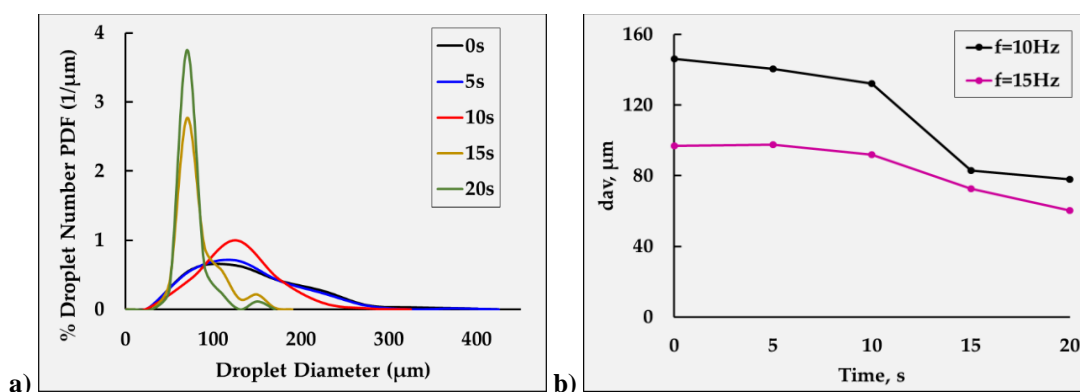


Fig. 1. a) Droplet size distributions evolution as a function of time and gravity ($\phi=0.1$, $C_{\text{surf}}=2 \cdot 10^{-4}$ M, $f=10$ Hz, No of strokes=18) and b) Evolution of number-based droplet average diameter of emulsions for different pulsation stroke frequencies ($\phi=0.1$, $C_{\text{surf}}=2 \cdot 10^{-4}$ M, No of strokes=18).

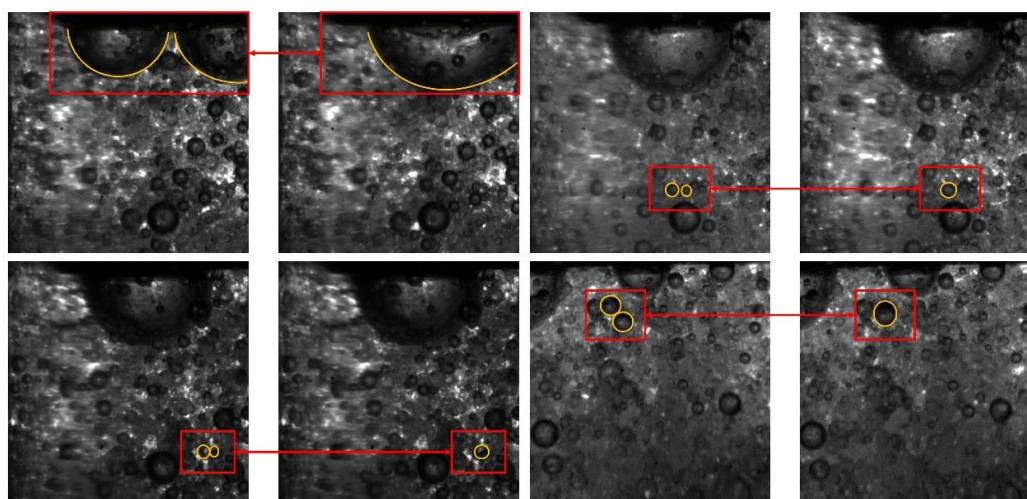


Fig. 2. Indicative directly evidenced coalescence events in the aqueous phase of emulsion ($\phi=0.1$, $C_{\text{surf}}=10^{-5}$ M, $f=15$ Hz, No of strokes=18).

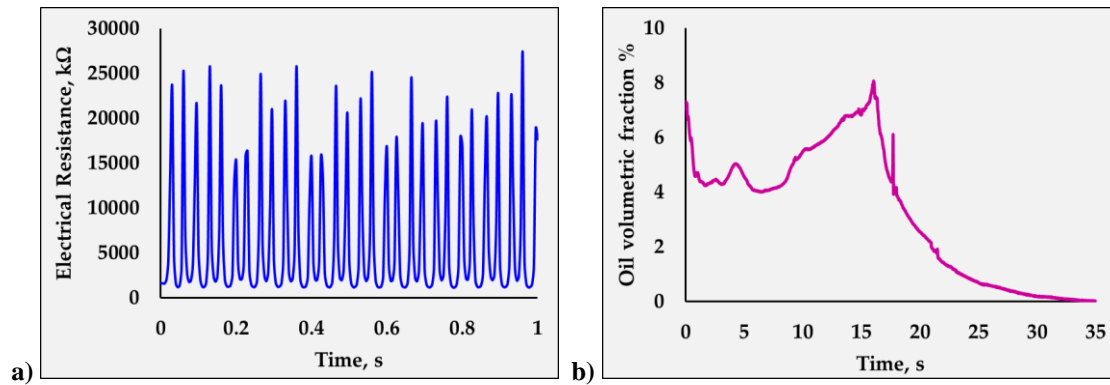


Fig. 3. Evolution of **a)** electrical resistance during the periodical movement of the piston with a pulsation stroke frequency of 15 Hz for 1 s and **b)** oil volumetric fraction as a function of time during phase separation of an emulsion (for $t < \sim 16$ s microgravity phase; for $t > \sim 16$ s hypergravity phase) ($\phi=0.05$, $C_{surf}=10^{-5}$ M, $f=15$ Hz, No of strokes=18).

4. CONCLUSIONS

A novel emulsification cell is used to produce oil-in-water emulsions and provide information on their behavior at varying gravity conditions during parabolic flights. Both optical and electrical measurements proved that during microgravity conditions the buoyancy related phenomena are eliminated and, thus, phase gravitational separation between the two phases does not take place. Optical measurements allowed to determine the droplet size distribution evolution in time and some tendencies are illustrated with regard to the experimental conditions. Moreover, different coalescence events are observed between droplets of either the same or different sizes while they come in close contact from different directions. The employed electrical impedance spectroscopy technique was capable of registering non-intrusively the spatial distribution of volumetric oil fraction in the measuring region inside the experimental cell during ~ 0 g. These electrical signals carry useful information on the destabilization of emulsions. It is found that the oil fraction evolution curves are compatible with a bidisperse oil droplet size distribution.

5. REFERENCES

- Chappat, M., 1994. Some applications of emulsions, *Colloids Surf. A: Physicochem. Eng. Asp.*, 91, 57-77.
- Chondrou, A. P., Evgenidis, S. P., Zacharias, K. A., Kostoglou, M., Karapantsios, T. D., 2023. Development of an Experimental Device for the Assessment of Emulsions Dynamic Behavior and Stability in Micro-gravity, *Microgravity Sci. Technol.*, 35, 28.
- Evgenidis, S.P., Karapantsios, T., 2015. Effect of bubble size on void fraction fluctuations in dispersed bubble flows. *Int. J. Multiph. Flow*, 75, 163–173.
- Vlachou, M. C., Zacharias, K. A., Kostoglou, M., Karapantsios, T. D., 2020. Droplet size distributions derived from evolution of oil fraction during phase separation of oil-in-water emulsions tracked by electrical impedance spectroscopy, *Colloids Surf A: Physicochem. Eng. Asp.*, 586, 124292.

ACKNOWLEDGEMENTS

This work was supported by the project «Innovative device for measuring milk collection rate and quality features during goat and sheep milking, exploiting an electrical impedance spectroscopy technique» (Project code: KMP6-0269405) under the framework of the Action «Investment Plans of Innovation» of the Operational Program «Central Macedonia 2014-2020», that is co-funded by the European Regional Development Fund and Greece.



REGION OF CENTRAL MACEDONIA
MANAGING AUTHORITY
O.P. Region of Central Macedonia



Co-financed by Greece and the European Union

MACH-ZEHNDER INTERFEROMETRY FOR FLUID PHYSICS EXPERIMENTS INVOLVING CONTACT LINES AND PHASE CHANGE

Pierre Colinet^{a,*}, Senthil K. Parimalanathan^a, Alexey Rednikov^a, Adam Chafar^a, and Sam Dehaeck^a

^aUniversité Libre de Bruxelles, TIPs (Transfers, Interfaces and Processes) – Fluid Physics,
Av. F.D. Roosevelt 50, CP 165/67,
B-1050 Bruxelles, Belgium
*pierre.colinet@ulb.be

Keywords: droplet, wetting, spreading, evaporation, apparent contact angle

1. INTRODUCTION

This talk presents an overview of experimental works and related theory/numerics of the authors (and several other post-doc or PhD students¹) during the last decade. These studies have in common the use of Mach-Zehnder (transmission) interferometry, for the measurement of either liquid film thickness profiles (e.g., thin sessile droplets) or refractive index gradients due to thermal or compositional changes (e.g. a cloud of vapor emitted from a droplet, flow in Hele-Shaw cell).

2. MACH-ZEHNDER INTERFEROMETRY: A TYPICAL SET-UP ENABLING CHARACTERISATION OF THIN SESSILE DROPLETS ...

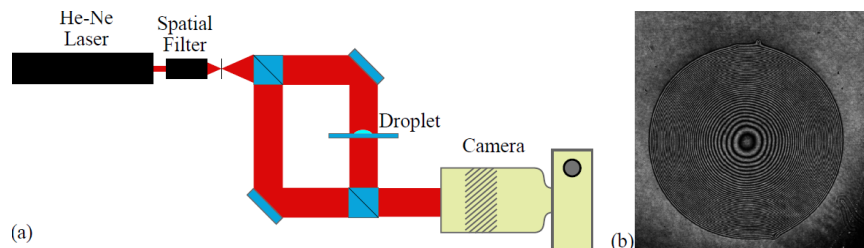


Figure 1. (a) optical set-up, consisting in a coherent laser beam split in two paths, one of them passing through the sample, while the other is used as a reference, both paths interfering on the camera chip ; (b) raw image of a millimetric sessile droplet showing iso-thickness contours, hence enabling extraction of the apparent contact angle of the droplet.

3. ... AND VAPOR CLOUDS OF VOLATILE LIQUID SAMPLES

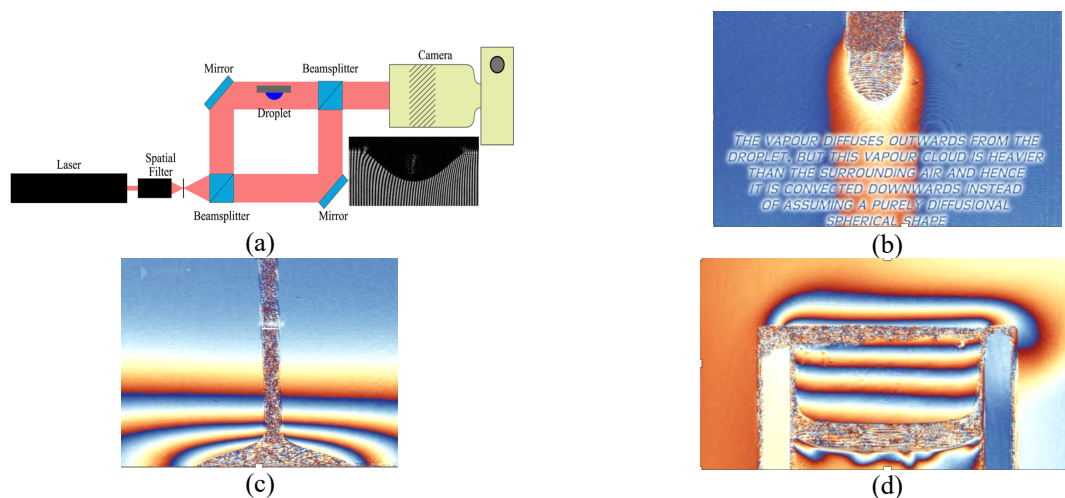


Figure 2. (a) same set-up but droplet facing down (inset=corresponding raw image). Wrapped phase images of the vapor cloud of (b) a pendent sessile droplet; (c) a sessile droplet fed by a syringe; (d) liquid/gas meniscus in a square cuvette.

¹ Other contributors: Dr Loucine Mekhitarian, Dr Hosein Sadafi, Dr Benjamin Sobac, Dr Yannis Tsoumpas

4. THICKNESS PROFILES OF PURE THIN VOLATILE DROPLETS

As seen from the example in Fig. 1, interferometry leads to the full shape of sessile droplets, from which the apparent contact angle can in principle be extracted [Tsoumpas *et al.* (2014, 2015)]. In general, both gravity and thermocapillarity induce some deviation of the profile from the classical parabolic shape of a small droplet. The Marangoni effect can in particular yield “inflated” or “contracted” shapes featuring an inflection point at some small distance of the contact line, as sketched in Fig. 3 (see also next section). In this case, definition of an apparent contact angle is still a matter of debate.

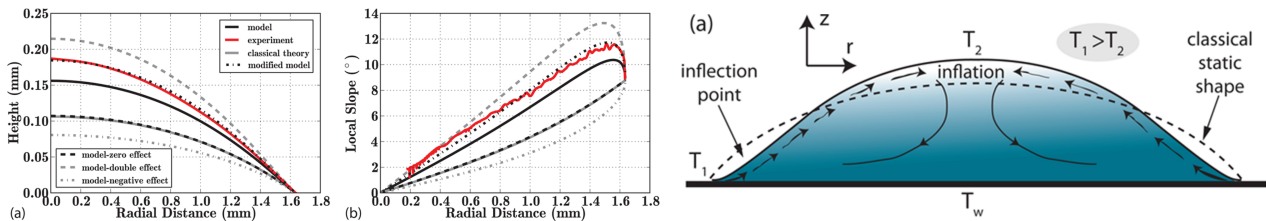


Figure 3. Nearly parabolic profile (left) and local slope (middle) of a droplet with fixed radius and volume. Sketch (right) of a droplet contracted by the thermal Marangoni effect, leading to a surface flow from the contact line to the apex.

5. VOLATILE DROPLETS OF BINARY MIXTURES

Similarly, in the case of a volatile binary mixture, contracted shapes may occur when the higher surface tension liquid happens to be more volatile than the other [such as a water-propylene glycol mixture, as used by Cira *et al.* (2015) to study “dancing droplets”]. In the opposite case of a less-volatile lower surface tension liquid [such as a water-ethyl alcohol mixture, such as used by Keiser *et al.* (2017)], one rather observes rapid Marangoni-enhanced spreading and possibly “bursting” (though this is highly dependent upon the substrate properties).

Parimalanathan *et al.* (2021) tested the limits of this scenario for various configurations such as sessile drops with free or pinned contact lines, without or with microparticles, and tears-of-wine menisci. Contraction regimes are found in situations where spreading is expected, despite the alcohols being more volatile than water. Such surprising observations were rationalized by a simple model highlighting the often overlooked role of the diffusion coefficient ratio of the two vapors in conjunction with the non-ideality of the mixture. The crucial role played by ambient humidity is also highlighted, for the different situations studied.

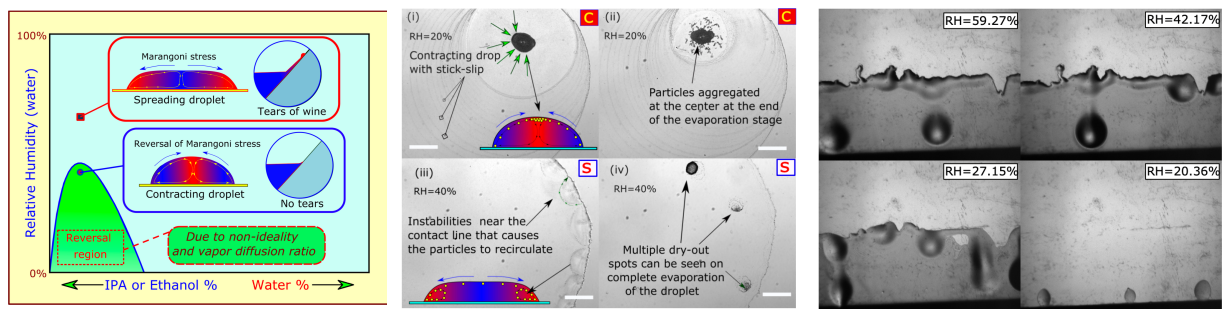


Figure 4. (left) Typical map of regimes predicted for aqueous solutions; (middle) Segregation patterns upon adding particles for 20% initial water mass fraction and relative humidity RH=20% and RH=40% ; (right) Effect of relative humidity RH on ‘tears of wine’ (10% water mass fraction in the liquid).

6. TEXTURED SUBSTRATES

As shown by Mekhitarian *et al.* (2017), interferometry is also applicable to measure thickness profiles of droplets undergoing spreading and evaporation on a textured substrate, provided the latter is made of a transparent material (e.g. SU-8 resins used for soft lithography). In this case, it is shown that two different dynamics are observed (see Fig. 5) : i) an evaporation-dominated regime, where the droplet almost “does not feel” the presence of small pillars; ii) a spreading-dominated regime where part of the liquid rapidly wets the taller pillars (adopting their symmetry properties), while a central droplet remains (similarly to hemi-wicking) and slowly evaporates.

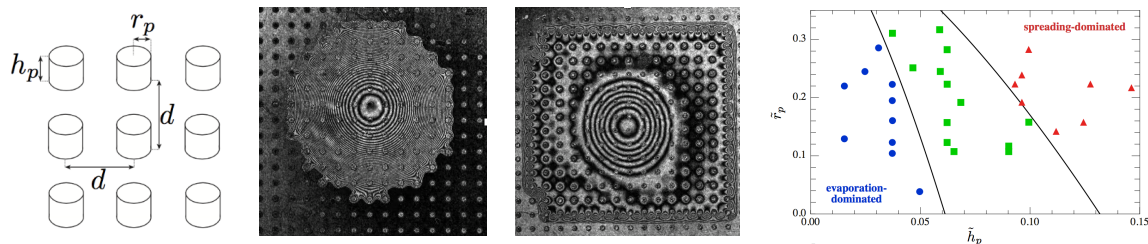


Figure 5. (left) geometry of SU-8 pillars; (middle) interferograms of evaporation-dominated and spreading-dominated regimes; (right) map of regimes as a function of aspect ratios h_p/d and r_p/d for $d=160 \mu\text{m}$ (the liquid used is HFE-7100).

7. HELE-SHAW CELL CONFIGURATIONS

Finally, this talk will also briefly describe some cases of concentration fields measured in Hele-Shaw cells (two glass plates separated by a thin gap filled by the liquid sample), where the interference fringes are induced by refractive index spatio-temporal variations in the mixture.

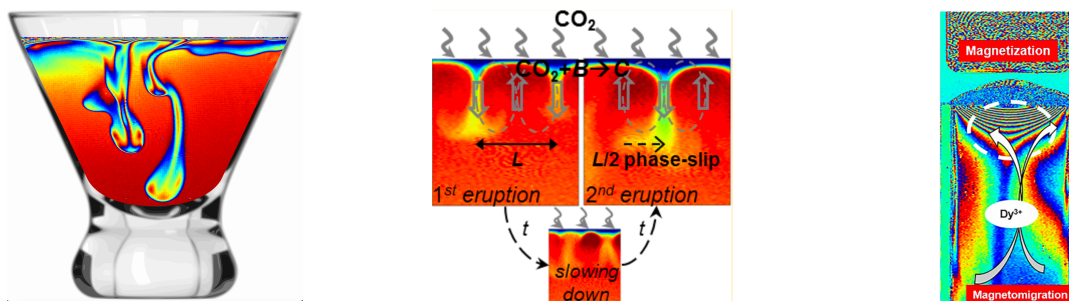


Figure 6. Rayleigh-Taylor-like unstable regimes of (left) a water-ethyl alcohol solution evaporating into ambient [Dehaeck *et al.* (2009)]; (middle) CO_2 chemisorption from the ambient, resulting in a damped oscillatory dynamics [Wylock *et al.* (2014)]; (right) Magnetomigration of rare-earth ions triggered by concentration gradients generated by evaporation [Rodrigues *et al.* (2017)].

8. REFERENCES

- Charlier, J., Rednikov, A., Dehaeck, S., Colinet, P., and Terwagne, D. (2022). “Water–propylene glycol sessile droplet shapes and migration: Marangoni mixing and separation of scales”. *Journal of fluid mechanics*, 933, 33.
- Cira, N., Benusiglio, A., and Prakash, M. (2015). “Vapour-mediated sensing and motility in two-component droplets”. *Nature*, 519 (7544), 446.
- Dehaeck, S., and Colinet, P. (2016). “Improving Speed and Precision of Local Frequency Analysis using Gaussian Ridge Interpolation for Wavelet and Windowed Fourier Ridge Algorithms », *Optics and Lasers in Engineering*, 77, 54.
- Dehaeck, S., Tsoumpas, Y., and Colinet, P. (2015). “Analysing closed-fringe images using 2D Fan wavelets”, *Applied Optics*, 54, 2939–2952.
- Dehaeck, S., Wylock, C., and Colinet, P. (2009). “Evaporating cocktails”, *Phys. Fluids*, 21, 091108 (2009).
- Keiser, L., Bense, H., Colinet, P., Bico, J., and Reyssat, E. (2017). “Marangoni bursting: evaporation-induced emulsification of binary mixtures on a liquid layer”. *Phys. Rev. Lett.*, 118, 074504.
- Mekhitarian, L., Sobac, B., Dehaeck, S., Haut, B., and Colinet, P. (2017). “Evaporation dynamics of completely wetting drops on geometrically textured surfaces”, *Europhysics Letters*, 120, 16001.
- Parimalanathan, S. K., Dehaeck, S., Rednikov, A., and Colinet, P. (2021). “Controlling the wetting and evaporation dynamics of non-ideal volatile binary solutions”. *Journal of colloid and interface science*, 592C, 319-328.
- Rodrigues, I. R., Lukina, L., Dehaeck, S., Colinet, P., Binnemans, K., and Fransaer, J. (2017). « Magnetomigration of Rare-Earth Ions Triggered by Concentration Gradients », *J. Phys. Chem. Lett.*, 8, 21, 5301-5305.
- Sadafi, H., Dehaeck, S., Rednikov, A., and Colinet, P. (2019). “Vapor-mediated versus substrate-mediated interactions between sessile volatile drops”, *Langmuir*, 35, 7060-7065.
- Tsoumpas, Y., Dehaeck, S., Galvagno, M., Rednikov, A., Ottevaere, H., Thiele, U. and Colinet, P. (2014). “Non-equilibrium Gibbs' criterion for completely wetting volatile liquids », *Langmuir*, 30, 11847–11852.
- Tsoumpas, Y., Dehaeck, S., Rednikov, A., and Colinet, P. (2015). “Effect of Marangoni Flows on the Shape of Thin Sessile Droplets Evaporating into Air », *Langmuir*, 31,13334–13340.
- Wylock, C., Rednikov, A., Haut, B. and Colinet, P. (2014). “Non-Monotonic Rayleigh-Taylor Instabilities Driven by Gas-Liquid CO_2 Chemisorption”, *J. Phys. Chem. B.*, 118, 11323–11329.

Growth of pool boiling bubbles of ESA Multiscale Boiling Experiment on ISS

Ourania Oikonomidou^{a,*}, Sotiris Evgenidis^a, Xenophon Zabulis^b, Polykarpos Karamaounas^b, Axel Sielaff^c, Martin Schinnerl^c, Peter Stephan^c, Margaritis Kostoglou^a, Thodoris Karapantsios^a

^a Department of Chemical Technology and Industrial Chemistry, Faculty of Chemistry, Aristotle University of Thessaloniki, 54124, Thessaloniki, Greece

^b Institute of Computer Science, Foundation for Research and Technology, Hellas, N. Plastira 100 Vassilika Vouton, 700 13 Heraklion, Crete, Greece

^c Institute for Technical Thermodynamics, Technische Universität Darmstadt, Alarich-Weiss-Str. 10, 64287 Darmstadt, Germany

*oikonomid@chem.auth.gr

Keywords: boiling, microgravity, image processing, bubble growth, power law exponents

1. INTRODUCTION

The Multiscale Boiling Experiment of ESA was held on-board the International Space Station, at 2019 and 2020. Its perspective is to investigate the growth of vapor bubbles during subcooled boiling in microgravity, under or in the absence of shear flow and electric field forces. The absence of gravity cancels the transfer of heat through natural convection and elucidates the impact of surface tension and pressure forces on bubble growth instead. Moreover, it hinders bubble detachment from the heated surface and thus allows prolonged examination of bubble growth phenomena and in depth understanding of boiling principles. This work presents the custom, highly accurate, image processing algorithm that is specialized on the analysis of the particular boiling optical data and correlation of the resulting bubble growth rates to the corresponding experimental boiling parameters.

2. METHODS

The concept of Multiscale Boiling Experiment is as follows (Sielaff et al. 2022). The boiling experimental cell in Fig. 1 is filled with the test liquid (coolant FC-72) and thermalized at the desired subcooled temperature. The heated substrate (heater) at the bottom of the test cell provides some constant heat flux to the liquid bulk above. As a result, a temperature gradient evolves with time across the liquid bulk as receding from the heater. At the middle of the heated substrate there is a microcavity that acts like the nucleation site for boiling bubbles. Sometime after the heater activation (termed as waiting time), a laser beam hits the cavity and initiates nucleation of a single, isolated, vapor bubble. In case of shear flow application, the bubble slides away from the cavity, a new bubble forms instead and as a result a series of bubbles form, grow and slide away. Similarly, electric field application forces a series of bubble formation, growth and detachment events. The present work is focused on the analysis of pool boiling cases (growth of an isolated boiling bubble, in the absence of gravity and other external forces). The boiling experimental parameters tested in this campaign are i) the heat flux (HF), ii) the subcooling degree of liquid temperature (T_{sub}), iii) the waiting time before laser activation (t_{wait}) and iv) the pressure (P). Combination of the parameters above gives a matrix of 160 different successful pool boiling experiments in total. A black and white camera is used to observe the evolution of boiling bubbles geometry. An IR camera gives the temperature profile across the heater surface.

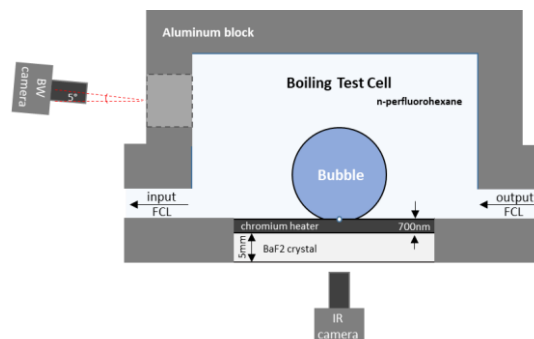


Figure 1. Illustration of the Multiscale Boiling Experiment test cell configuration.

Bubble image analysis allows to study the evolution of boiling for the different experimental conditions. However, image analysis is complicated for the present experiments, as the light reflections at the top and the bottom part of the bubbles make the detection of bubble contour quite tricky. Moreover, the temperature gradient of the liquid bulk close to the heater changes the refractive index and distorts the vertical dimension of bubble boundary. Thus, image analysis using

conventional image processing software is not that efficient. For this, the research teams involved in this project developed image processing algorithms of different complexity and concept, so as to treat the inconsistencies (Oikonomidou et al. 2022). These algorithms are able to detect the bubble edges and use them to calculate basic bubble geometrical features such as contact line diameter, bubble diameter and contact angles. Aristotle University research team developed an algorithm that detects a series of trusted points around the bubble contour and hence excludes light reflections at the entire bubble periphery with subpixel accuracy, as illustrated in Fig. 2 (Zabulis et al. 2023). At a later stage the trusted points are fitted with a circle curve, considering the spherical shape of a bubble in zero gravity. To eliminate the refractive image distortion, the circular fit is applied to the trusted points at the top half part of the bubble that is not exposed to thermal irregularities. The bubble contact points are vertically displaced till they meet the fitted circle. Contact angles are calculated as the tangent of the circle at the corrected contact point's location (Fig. 2).

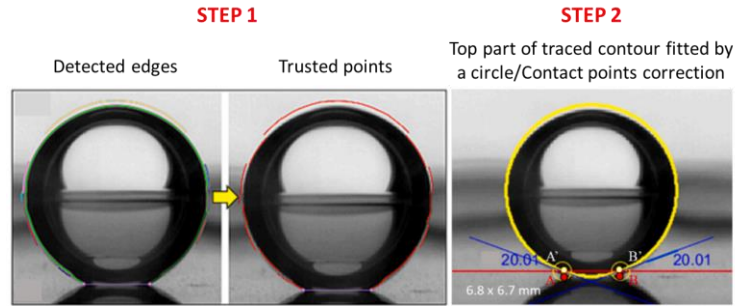


Figure 2. Bubble contour detection and calculation of bubble contact angles.

3. BUBBLE GROWTH ANALYSIS

Finally, the output of image analysis is the time evolution of bubble diameter per case (Oikonomidou et al. 2024). Figure 3 shows indicative bubble growth curves under different experimental conditions. Power law equation corrected by a time shift factor (b) is able to fit adequately all bubble growth curves (Eq. 1).

$$D = a(t + b)^n \quad (1)$$

Where D is the bubble diameter, a is the coefficient, t is the time and n is the power law exponent.

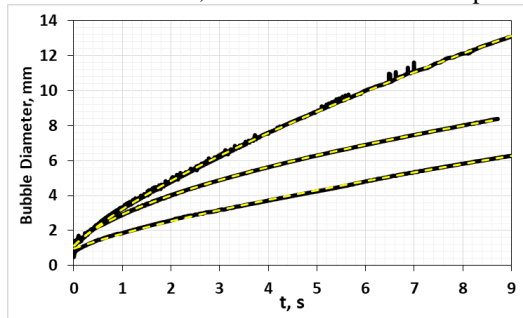


Figure 3. Indicative bubble curves fitted by power law curves depicted as yellow dashed lines.

The factor b is to consider the rapid bubble growth at time zero due to the instantaneous heat provided by the laser and has no further physical meaning. Each pool boiling experiment can be described and reproduced by a couple of numbers; the power law coefficient a and exponent n . Secondary power law equations can correlate the power law numbers to the waiting time parameter (Eq. 2 and 3).

$$a = a_1 * (t_{wait})^{a_2} \quad (2)$$

$$n = n_1 * (t_{wait})^{n_2} \quad (3)$$

Secondary power law numbers are provided in tables (Fig. 4) for the different heat flux and subcooling temperature combinations (4 tables per pressure value) and allow the compression of a large number of pool boiling data in a simple function with a small number of parameters (Eq. 4).

$$D = a_1 * (t_{wait})^{a_2} * (t)^{n_1 * (t_{wait})^{n_2}} \quad (4)$$

n_1	Tsub [K]			
	1	3	5	10
0.50	0.761	1.157		
0.75	0.748	0.998		
1.00	0.705	0.928	1.135	
1.50	0.670	0.867	1.038	

n_2	Tsub [K]			
	1	3	5	10
0.50	-0.175	-0.330		
0.75	-0.190	-0.311		
1.00	-0.187	-0.329	-0.399	
1.50	-0.193	-0.298	-0.367	

a_1	Tsub [K]			
	1	3	5	10
0.50	1.788	0.367		
0.75	2.301	0.789		
1.00	2.934	1.241	0.449	
1.50	3.848	1.968	0.903	

a_2	Tsub [K]			
	1	3	5	10
0.50	0.388	0.845		
0.75	0.399	0.706		
1.00	0.377	0.640	0.771	
1.50	0.379	0.586	0.821	

Figure 4. Secondary power law exponents for different heat fluxes and subcooling temperatures, for P=600mbar.

Aiming to study the temperature evolution at the interface of the liquid bulk and the heater (T_{int}) in the absence of a bubble, an approximating solution has been developed based on the thermal conductivity and specific heat capacity of

the liquid and the heater materials. Next step is to study the ongoing bubble growth mechanism. IR images and slow bubble growth rates imply that the heat transfer area for bubble growth is the contact line region (footprint of the bubble on the heater). Assuming that the bubble grows in a saturated liquid and that the temperature of the heater surface is not affected/decreased by bubble growth, the bubble volume is proportional to the area of heat transfer and the difference between the T_{int} and the saturation temperature (T_{sat}). The analytical solution shows that $T_{int}-T_{sat}$ is increasing with time following approximately a first order equation ($A + Bt$). At time zero this difference equals $T_{nuc}-T_{sat}$ where T_{nuc} is the interfacial temperature at the moment of bubble nucleation. The slope of $T_{int}-T_{sat}$ increase with time is proportional to the local heat flux at the nucleation point q . The above correlations are described in Eq. 5.

$$(T_{int} - T_{sat}) = A + Bt = (T_{nuc} - T_{sat}) + q(a_s/k_s \cdot L)t \quad (5)$$

Where a_s is the thermal diffusivity, k_s is the thermal conductivity and L is the thickness of the heater solid material.

The B/A ratio is proportional to $q/(T_{nuc} - T_{sat})$ ratio, from now on expressed as z . Results show that z number can be well correlated to the power law exponent n for each pool boiling experiment (Fig. 5). The bubble growth exponent n takes values between 0.4 and 1. For the cases that the heater temperature remains constant ($(T_{nuc} - T_{sat}) = A, B = 0$), $z=0$ and $n=0.5$. For the cases that the heater temperature increases linearly with time ($(T_{nuc} - T_{sat}) = Bt, A = 0$), $n=1$ and $z>0$, as at the moment of nucleation the liquid is subcooled thus $T_{nuc} < T_{sat}$. For the cases that n is below 0.5 the liquid bulk remains subcooled during the entire experiment. Figure 5 shows n to z correlations for an indicative pressure.

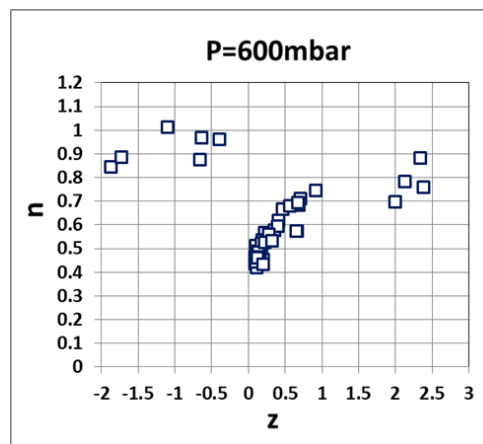


Figure 5. Correlation between z number and power law exponent n for the pool boiling cases at 600mbar pressure.

4. REFERENCES

- Sielaff, A., Mangini, D., Kabov, O., Raza, M.Q., Garivalis, A.I, Zupancic, M., Dehaeck, S., Evgenidis, S., Jakobs, C., Hoof, D.V., Oikonomidou, O., Zabulis, X., Karamaounas, P., Bender, A., Ronshin, F., Schinnerl, M., Sebilleau, J., Colin, C., di Marco, P., Karapantsios, T., Golobic, I., Rednikov, A., Colinet, P., Stephan, P., Tadrist, L., 2022. "The Multiscale Boiling Investigation on-board the International Space Station: An overview", *Applied Thermal Engineering*, Vol. 205, pp. 117932.
- Oikonomidou, O., Evgenidis, S., Argyropoulos, C., Zabulis, X., Karamaounas, P., Raza, M.Q., Sebilleau, J., Ronshin, F., Chinaud, M., Garivalis, A.I., Kostoglou, M., Sielaff, A., Schinnerl, M., Stephan, P., Colin, C., Tadrist, L., Kabov, O., Di Marco, P., Karapantsios, T., 2022. "Bubble growth analysis during subcooled boiling experiments on-board the International Space Station: Benchmark Image Analysis", *Advances in Colloid and Interface Science*, Vol. 308, pp. 102751.
- Zabulis, X., Karamaounas, P., Oikonomidou, O., Evgenidis, S., Kostoglou, M., Schinnerl, M., Sielaff, A., Stephan, P., Karapantsios, T., 2023. "Advances on the detection and measurement of bubble contours during subcooled boiling in microgravity", *Measurement*, Vol. 222, pp. 113644.
- Oikonomidou, O., Kostoglou, M., Evgenidis, S., Zabulis, X., Karamaounas, P., Sielaff, A., Schinnerl, M., Stephan, P., Karapantsios, T., 2024. "Power law exponents for single bubbles growth in nucleate pool boiling at zero gravity", *International Communications in Heat and Mass Transfer*, Vol. 150, pp. 10717.

ACKNOWLEDGEMENTS

The present work has been carried out in the framework of the European Space Agency Research Projects AO-2004-111:BOILING, AO-1999-110: EVAPORATION, AO-2004-096: CONDENSATION.

SIMULATING BUBBLE SIZE EFFECT ON ELECTRICAL SIGNAL FLUCTUATIONS

Ourania Oikonomidou*, Sotiris Evgenidis, Thodoris Karapantsios, Margaritis Kostoglou

Department of Chemical Technology and Industrial Chemistry, Faculty of Chemistry, Aristotle University of Thessaloniki, 54124, Thessaloniki, Greece

*oikonomid@chem.auth.gr

Keywords: bubbly flow, simulation, electrical resistance, stochastic model

1. INTRODUCTION

Bubbly flow is a special type of gas-liquid flow characterized by random dispersion of small, discrete bubbles inside a continuous liquid phase. It is found in several applications in power engineering, chemical, food, pharmaceutical and other industries. All these applications take the advantage of high mixing properties and enhanced heat, mass and momentum transfer during bubbly flow. Specifically, flow of sub-millimeter bubbles at low void fractions can be encountered also in human physiology when gas bubbles get into the blood stream during Decompression Sickness incidents. Decompression Sickness (DCS), which is a major concern for astronauts, aviators, scuba divers and metro workers, is a clinical syndrome caused by bubbles formation in human blood or tissues as a result of prolonged ambient pressure reduction (decompression). Such bubbly flow conditions, combining sub-millimeter bubbles and low void fractions ($<10^{-1}$), are also found in other two-phase flow applications, e.g., flow boiling in macro-channels. The primary aim of this study is to analyze statistically the simulated electrical signals for varying bubbles populations, void fractions and BSD types (mono-disperse and uniform/non-uniform bi-disperse of different bubble sizes), in order to provide physical insight to the correlation of average bubbles size with signal features. The work below starts with an effort to investigate whether the estimated arithmetic average bubbles diameter by the empirical equation of *Evgenidis and Karapantsios (2015)* represents adequately Bubble Size Distribution (BSD) features. In the following, the mathematical model is first described in detail and then simulated bubbly flow electrical signals are presented, analyzed and discussed as well.

2. PROBLEM FORMULATION

The map constructed by the authors and presented elsewhere is employed for the effect on electrode resistance of a bubble. In this view the resistance can be calculated for an arbitrary configuration of the bubbles. However such configuration must be modeled in some way. An algorithmic construction of (two dimensional) bubbles configuration and motion in a two dimensional domain is pursued. In the present work, mono-disperse and bi-disperse bubble size distributions are considered. The one alternative of creating a bubble configuration on a long strip and then moving the strip through the computational domain is not favored due to the requirement of keeping in memory a very large number of bubbles. The other alternative of creating the bubbles at one edge of the domain and following their motion up to the other edge is followed. The basic variables of the model are the discretization time t_d which is the time between consecutive conductance computation and the average time t_a between bubbles appearances in the domain. A formal statistical procedure requires that the latter time follows an exponential distribution with average value t_a (based on the concept of quiescent interval). The relative concentration between the two particle sizes of the bi-disperse distribution is also treated in a semi-stochastic manner to reduce statistical fluctuation. Every N_a bubbles of type "1", a bubble of type "2" is introduced. It was found that the optimum value of t_d (leading to discretization-independent results) is the time needed for a bubble to move over 1% of the domain so this value is used in all simulations. Two lists of bubble positions for the two bubble types are constructed and they are updated by varying the position of existing bubbles and introducing new bubbles. The introduction of a new bubble is followed by checking the position of the previous M bubbles to avoid overlapping events. The optimum number of M is chosen such to be large enough to surely avoid overlapping but small enough to increase significantly the computational effort. At specific time intervals the lists are checked for bubbles having crossed the outlet boundaries. These bubbles are deleted and the lists are resorted. The whole approach is optimized by properly choosing algorithm parameters that give the required configurations with minimum computational effort. All the calculated variables presented here are averages over ten repetitions of the algorithm. This work does not focus on the actual algorithm parameters but on the physical parameters to which they correspond. In this respect, the following are considered as the input variables of the model (the ratio λ is considered fixed and equal to 0.5 as the experimental one in *Evgenidis and Karapantsios (2015)*: i) distance between electrodes (fixed equal to 0.00325 m), ii) fluid velocity (fixed equal to 0.005 m/s), iii) bubbles volume fraction (void fraction), iv) sizes of the two types of bubbles and v) number fractions of the two bubbles types. The variable (iii) can be replaced by the bubbles number in the computational domain. The output of the model refers to 60 s-long normalized conductance reduction (ϕ) time-series for varying bubble sizes and numbers, where ϕ is defined as follows:

$$\varphi = \frac{K_0 - K}{K_0} \quad (1)$$

where K_0 and K represent one-phase (liquid) and two-phase (gas-liquid) flow electrical conductance, respectively. The following quantities are calculated for each time-series: a) average value of normalized conductance reduction (φ_{ave}), b) standard deviation of normalized conductance reduction (φ_{std}) and c) coefficient of variation of normalized conductance reduction ($\varphi_{CV} = \varphi_{std} / \varphi_{ave}$). A typical configuration of the bubbles resulting from Monte Carlo algorithm for a bi-disperse bubble size distribution appears in Fig. 1.

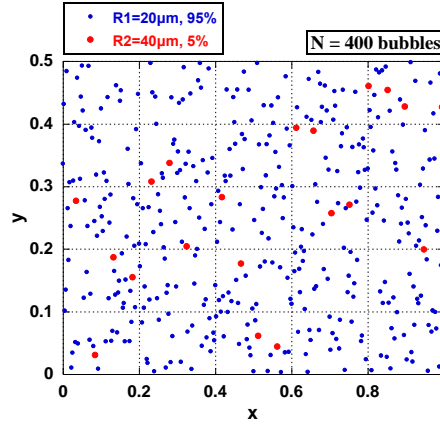


Figure 1. Visualization of the field in the presence of 95% bubbles $R_1=20 \mu\text{m}$ and 5% of bubbles $R_2=40 \mu\text{m}$ ($N = 400$ bubbles).

3. INDICATIVE RESULTS

Simulations are performed for eight distinct numbers of bubbles in the control volume. For each N value, three to six different bubble radius R values are used to derive void fractions from $\varepsilon \sim 0.001$ to $\varepsilon \sim 0.05$, as those found experimentally in *Evgenidis and Karapantsios (2015)*. Fig. 2 shows indicative simulated 30s-long normalized conductance reduction (φ) time-series for varying bubble radius and number of bubbles. In all cases, electrical signals demonstrate clear fluctuations around an average value, whose intensity is strongly associated to the number and size of bubbles. Interestingly, simulated bubbly flow electrical signals do not differ qualitatively from the corresponding experimental ones found in our previous in-vitro and in-vivo studies (e.g. *Evgenidis and Karapantsios, 2015*). Fig. 3 presents the dependence of signal statistics, calculated for all the 31 different simulated cases of this sub-section, on bubble radius and number of bubbles. Specifically, Figs 3a, 3b and 3c demonstrate the effect of N (ranging from 100 to 2000) and R (ranging from $10 \mu\text{m}$ to $60 \mu\text{m}$) on the average value (φ_{ave}), on the standard deviation (φ_{std}) and on the coefficient of variation (φ_{CV}) of the normalized conductance reduction, respectively. Figs 3a and 3b confirm the previous remarks; φ_{ave} and φ_{std} (which quantifies signal fluctuations) get higher values as bubbles increase in number and size. This is in agreement with the experimental findings of *Evgenidis and Karapantsios (2015)*, who noticed that the increase of gas volumetric concentration in a bubbly flow due to more and/or larger bubbles: a) decreases the measured electrical conductance of the two-phase medium resulting in higher void fraction and b) causes more intense electrical signal fluctuations. Contrary to φ_{std} , φ_{CV} decreases with N and R increase, as shown in Fig 3c. Moreover, the distribution of φ values of each simulated signal approximates the normal distribution since calculated skewness and kurtosis are pretty close to zero. This finding is experimentally confirmed by *Evgenidis and Karapantsios (2015)* as well.

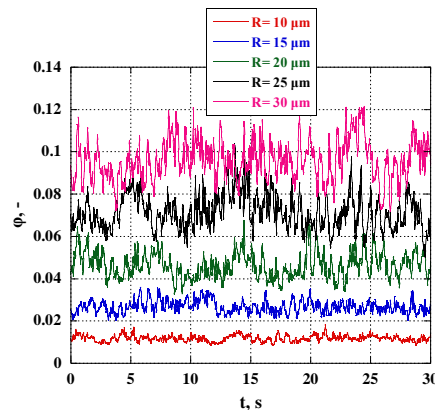


Figure 2. Simulated normalized conductance reduction (φ) time-series for varying bubble radius (R) and $N = 400$ bubbles.

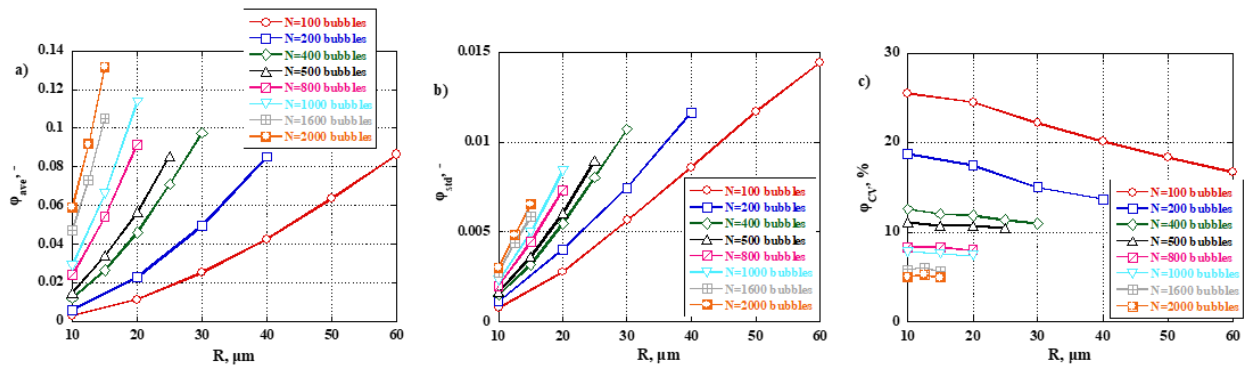


Figure 3. Influence of bubbles population (N) and bubble radius (R) on the: a) average value (ϕ_{ave}), b) standard deviation (ϕ_{std}) and c) coefficient of variation (ϕ_{cv}) of normalized conductance reduction.

4. CONCLUSIONS

This work develops and evaluates a novel mathematical model which simulates electrical conductance signals of bubbly flow of sub-mm bubbles and void fraction values below 0.1. The aim is to shed light and test the physical significance of the empirical correlation between average bubbles size and electrical signal fluctuations that was derived by *Evgenidis and Karapantsios (2015)*. Simulations take place for varying bubbles populations, void fractions and BSD types (mono-disperse and uniform/non-uniform bi-disperse of different bubble sizes) and result in various 60 s-long normalized conductance reduction (ϕ) time-series which are statistically investigated by means of average (ϕ_{ave}), standard deviation (ϕ_{std}) and coefficient of variation (ϕ_{cv}). In agreement with the experimental findings of *Evgenidis and Karapantsios (2015)*, the obtained results clearly demonstrate that both ϕ_{ave} and ϕ_{std} (which quantifies the intensity of signal fluctuations) get higher values as bubbles increase in number and size. Compared to mono-disperse BSD, uniform bi-disperse BSD causes greater signal fluctuations that, interestingly, increase with the width of the distribution. Additionally, signal fluctuations increase with the population (proportion) and size of a minority of large bubbles whose size differs significantly from the dominant smaller size in the case of a non-uniform BSD. As concerns the validity of the formerly suggested empirical equation that estimates the arithmetic average bubble diameter ($D_{1,0}$) from the coefficient of variation of the measured void fraction (ε_{cv}), in-depth investigation of simulated signal statistics shows that: a) BSD width affects significantly the calculated bubble diameter and, consequently, a relevant correction factor should be incorporated in the empirical equation, b) the linear dependence between $D_{1,0}$ and ε_{cv} in 2D simulations is not far from the exponent dependence of 0.827 in 3D experiments (*Evgenidis and Karapantsios, 2015*) and c) an average bubble diameter of higher order than the arithmetic one may be directly proportional to ε_{cv} . The present work will be expanded in the future in several directions as the incorporation of the third spatial dimension, the consideration of more complicated bubbles size distribution and the accounting for velocity profile in the liquid.

5. REFERENCES

Evgenidis, S.P., Karapantsios, T., 2015. "Effect of bubble size on void fraction fluctuations in dispersed bubble flows". *International Journal of Multiphase Flow*, Vo 1.75, pp. 163–173.

ACKNOWLEDGEMENTS

This work was supported by the project «Innovative device for measuring milk collection rate and quality features during goat and sheep milking, exploiting an electrical impedance spectroscopy technique» (Project code: KMP6-0269405) under the framework of the Action «Investment Plans of Innovation» of the Operational Program «Central Macedonia 2014-2020», that is co-funded by the European Regional Development Fund and Greece.



A TECHNIQUE FOR CALCULATING THE ELECTRICAL RESISTANCE OF RING ELECTRODES IN A DOMAIN WITH MANY BUBBLES

Kostoglou M.*, Evgenidis S.P., Karapantsios T.D.

Department of Chemical Technology and Industrial Chemistry, Faculty of Chemistry, Aristotle University of Thessaloniki, 54124, Thessaloniki, Greece

[*kostoglu@chem.auth.gr](mailto:kostoglu@chem.auth.gr)

Keywords: mathematical model, multiscale analysis, electrical resistance, bubble

1. INTRODUCTION

Void fraction and Bubble Size Distribution (BSD) constitute two key parameters in gas-liquid flows. They contribute to the determination of flow regime, heat/mass transfer coefficients, pressure drop, two-phase mixture density and viscosity, actual phase velocities, interfacial area, etc. Furthermore, void fraction and BSD are widely exploited for the setup and validation of CFD models. Established methods for void fraction estimation include the quick closing valve technique, or employ sensing of parameters such as pressure drop, electrical impedance, ultrasound/light attenuation, neutron/ γ -ray/X-ray absorption, etc. Electrical impedance technology is advantageous over other methods due to its high temporal and spatial resolution, effortless implementation, simple use and convenient mobility. As a result, it has attracted the interest of engineers and scientists who have developed different types of electrical impedance sensors depending on the application field, such as plate-type, ring-type, helical-type, grid-type and wire electrodes. Although in cases where local information inside the flow field is required electrical sensors can be intrusive (e.g., grid-type), in applications where cross-section average information is enough non-intrusive sensors, flush mounted to the wall, are employed.

Prof. T.D. Karapantsios' group has developed an EU patented ultra-sensitive electrical impedance spectroscopy method for non-intrusive, real-time bubbles detection in humans under the umbrella of the European Space Agency Project "In-Vivo Embolic Detector, I-VED". I-VED has been calibrated and validated in-vitro using a fully automated flow-loop, equipped with electrical, optical, pressure and acoustical diagnostics, which provided well-controlled bubbly flow with liquid velocities, bubble sizes and void fractions similar to those observed during DCS (*Evgenidis and Karapantsios, 2015, 2018a, 2018b, 2022*). Obtained results have shown that novel hardware and signal analysis algorithms make I-VED sensitive enough to detect even the presence of a few micro-bubbles in a liquid flow and capture void fraction fluctuations down to 10^{-5} , when employing two parallel ring electrodes which are flush mounted to the inner walls of a cylindrical vessel apart from each other by a certain (but variable) distance. For sub-millimeter bubbles at low void fractions, I-VED presents its highest sensitivity at a specific excitation frequency (determined experimentally) where the signal is dominated by the resistance/conductance component. Apart from the conventional experimental determination of the instantaneous average (at a cross-section) void fraction value in the flow, *Evgenidis and Karapantsios (2015)* examined systematically for the first time the relation between the intensity of electrical signal fluctuations with the arithmetic average bubbles size and suggested an empirical correlation between these two parameters which in the range of the examined conditions can estimate the arithmetic average bubbles size with an accuracy of $\pm 20\%$.

This work employs a unique mathematical model to simulate electrical signals for the case of bubbly flow where bubble sizes and void fraction values are alike with those examined experimentally by *Evgenidis and Karapantsios (2015)*. The model is just a two-dimensional simplification allowing at this stage to depict trends and draw mainly qualitative conclusions. At the heart of the model is the solution of the Laplace equation in a multiscale domain arising by the existence of bubbles. A previous attempt to attack the problem was based on a heuristic approach for the solution of the Laplace equation and it was restricted to single size bubbles (*Kostoglou, 2012*). Here a much more reliable technique is developed for the solution of the Laplace equation in a domain with many bubbles of arbitrary sizes.

2. PROBLEM FORMULATION AND SOLUTION

The steady-state mathematical problem for a particular bubbles configuration described by the location of the surfaces of the bubbles S_i (where the index i includes all the bubbles) is presented here. The length variables of the problem are normalized with respect to the half distance between the closest edges of the electrodes (denoted by δ). The lateral electrode width (from upstream to downstream edge) is denoted as λ . The coordinate origin, ($x=0$, $y=0$), is located at the middle point between the electrodes. The electrical potential is normalized by V_0 . The potential field V can be found from the solution of the Laplace equation:

$$\frac{\partial^2 V}{\partial x^2} + \frac{\partial^2 V}{\partial y^2} = 0 \quad (1)$$

The voltage values at the electrodes are selected to be -1 and 1. The resulting anti-symmetry simplifies the problem. The boundary conditions on the wall are:

$$\frac{\partial V}{\partial y} = 0 \text{ for } x < -(1+\lambda), -1 < x < 1, x > 1+\lambda \quad (2)$$

$$V = 1 \text{ for } 1 \leq x \leq 1+\lambda \quad (3)$$

$$V = -1 \text{ for } -(1+\lambda) \leq x \leq -1 \quad (4)$$

The boundary conditions on the bubbles are (where i is the identity index of a bubble taking values from 1 to N where N is the number of bubbles in the domain of observation):

$$\frac{\partial V}{\partial \vec{n}} = 0 \text{ on } S_i, \text{ for } i=1 \text{ to } N \quad (5)$$

where \vec{n} is the vector normal to the surface direction.

The following far field condition completes the problem:

$$V = 0 \text{ far from the electrode (i.e. } x, y \rightarrow \infty). \quad (6)$$

The above condition at infinity has to be replaced by the weaker zero flux condition on the domain boundaries during the truncation procedure. The solution of the above equations leads to the field $V(x,y)$. This field can be employed for the computation of the instantaneous normalized conductance:

$$G = \frac{1}{2} \int_{-(1+\lambda)}^1 \left(\frac{\partial V}{\partial y} \right)_{y=0} dx \quad (7)$$

The practical measured quantity is the dimensional conductance γ which is related to G through $G = \gamma / (\delta \sigma)$, where σ is the specific electrical conductivity of the continuous phase (water).

In the limit of low volume fraction (e.g less than 5%), the potential field V is decomposed to $N+1$ independent

fields according to the relation $V = V^{(0)} + \sum_{i=1}^N (V^{(i)} - V^{(0)})$, i.e. one field $V^{(i)}$ for each bubble and the field $V^{(0)}$ in

the absence of bubbles (undisturbed field). These fields obey the same governing equation and wall boundary conditions with the original field but the boundary condition (5) holds only for a single bubble with surface S_i . For each field, the conductance $G^{(i)}$ can be computed from equation (7) and the total conductance can be found as

$$G = G^{(0)} + \sum_{i=1}^N (G^{(i)} - G^{(0)}), \text{ where } G^{(0)} \text{ is the conductance in the absence of bubbles. The above relation is the}$$

zeroth and the first term of the conductance expansion discussed before. The effect of each bubble on the conductance is a function of its radius R and location x_o, y_o . Let us denote as $g(x_o, y_o, R)$ the quantity $G/G^{(0)} - 1$ for a bubble of radius R having its center at x_o, y_o . In this respect, the value of conductance G for any configuration of N particles can be easily computed as:

$$G = G^{(0)} \left(1 + \sum_{i=1}^N g(x_{oi}, y_{oi}, R_i) \right) \quad (8)$$

The single bubble problem appears to be easy since the geometry is simple but there is a hidden difficulty. On one hand, the discontinuity of the boundary condition (from Dirichlet to Neumann) appearing at the edges of the electrode leads to a singularity of the local current density at these edges. The appeared singularities are integrable so they do not create fundamental problems. On the other hand, they create severe numerical problems. A very fine discretization is needed at the region of the electrodes but even in the limits of a very fine grid, an accuracy much better than one percent cannot be achieved. The effect of a single bubble on the conductance is of the order of the above error (it is the combined effect of all bubbles that leads to measurable variation of conductance). So the numerical solution of the single bubble problem is not possible because the size of the bubble effect is comparable to the (inevitable due to the existence of singularity) discretization error. This problem is overcome by decomposing the single bubble linear problem into two components: The undistributed problem is solved first for the field $V^{(0)}$ in the absence of the bubble. The singularity discretization error is adsorbed in this solution but this is not a problem since this error is small compared to the returned $G^{(0)}$ value. Then the disturbance field v for the single particle problem is introduced as $v = V^{(i)} - V^{(0)}$ (the index i for field v is omitted for clarity of presentation). This field obeys the same equation and boundary

conditions with V except that $\frac{\partial v}{\partial \vec{n}} = \frac{\partial V^{(0)}}{\partial \vec{n}}$ on S_i , and $v = 0$ on the electrodes. The application of equation (7) with v

instead of V allows the direct computation of $G^{(i)}$ as the numerical solution main result (in contrast to its computation as correction term in the original single bubble problem). A schematic of the procedure used to solve the conductance problem appears in Fig. 1.

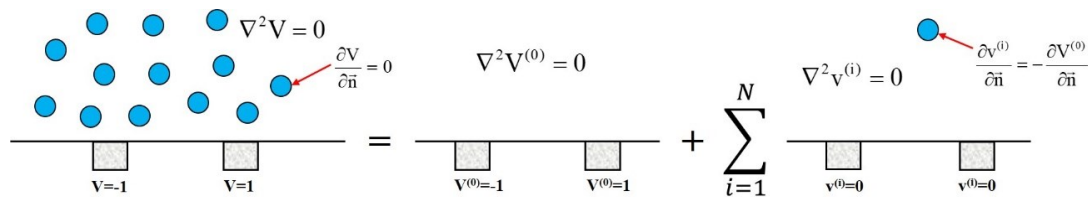


Figure 1. A schematic of the procedure of solution of the conductance problem in the presence of bubbles.

An additional problem that arises is that in order to resemble practical conditions the bubble size may be much smaller than the electrode size so the single bubble effect is vanishingly small and in addition the grid must be very dense around the tiny bubble. Although the case can be handled by the proposed procedure there is an obvious loss of accuracy as the bubble size decreases. In addition, a large number of problem solutions is required in order to construct the function $g(x_o, y_o, R)$ for all possible R values. The above problems are resolved by assuming a functional relation of the form $g(x_o, y_o, R) = g_0(x_o, y_o)R^2 + g_1(x_o, y_o)R^4 + g_2(x_o, y_o)R^6$. The above relation gives the function g for every bubble size. The particular functional dependence on R is chosen based on the fact that in the limit of small R the function g is proportional to bubble area (it is reminded that the two dimensional analogue is treated here). The condition for this behavior is that the electrical field in the scale of a bubble can be considered uniform. As bubble size increases the field cannot be considered uniform and the additional terms in the expansion for g appear. The functions g_i for a specific position x_o, y_o is found by quadratic interpolation of function g for three bubble sizes ($R=0.05, 0.01, 0.015$) located at the particular position.

A Cartesian grid of bubble positions (coordinates x_o and y_o) is constructed. The anti-symmetry of the problem permits the consideration of bubble appearance only to the one half of the computational domain (the effect on conductance is the same for bubbles appearing at symmetric positions). The grid includes about 200 bubble positions and it is adapted to have more points at regions of high variation of g value. Following this procedure, values of g_i 's at specific locations in the computational domain is found. The value of g_i at an arbitrary position x_o, y_o in the computational domain is given by bilinear interpolation to the corresponding values at the grid points.

3. CONCLUSIONS

The need to simulate the electrical resistance of ring electrodes for bubbly flows led to the development of a special technique for solving Laplace equation in a multiple scales domain. The scales are defined by the pipe diameter, the electrode width, the distance between electrodes, the distance between bubbles and finally the size of the bubble. The method is based on the decomposition of the problem to a sum of "unit" problems, one for each bubble in the domain of interest. The singularities at the edges of the electrodes are deal with a further decomposition of the "unit" problem in to one in absence of the bubble and to one for the disturbance created by the bubble. All the problems are solved by means of high resolution finite elements and influence maps are constructed. The results are taken for finite sizes of bubbles. Smaller bubbles (that cannot be directly analyzed) are considered by extrapolation of the results of larger bubbles.

4. REFERENCES

- Evgenidis, S.P., Karapantsios, T., 2015. "Effect of bubble size on void fraction fluctuations in dispersed bubble flows". *International Journal of Multiphase Flow*, Vol.75, pp. 163–173.
- Evgenidis, S.P., Karapantsios, T., 2018a. "Gas–liquid flow of sub-millimeter bubbles at low void fractions: experimental study of bubble size distribution and void fraction". *International Journal of Heat and Fluid Flow*, Vol.71, pp353–365.
- Evgenidis, S.P., Karapantsios, T.D., 2018b. "Gas–liquid flow of sub-millimeter bubbles at low void fractions: Void fraction prediction using drift-flux model". *Experimental Thermal and Fluid Science*, Vol. 98, pp.195–205.
- Evgenidis, S.P., Karapantsios, T.D., 2022. "Pulsatile gas-liquids flow resembling Decompression Sickness: Computational Fluid Dynamics simulation and experimental validation". *International Maritime Health*, Vol.73: pp.189-198.
- Kostoglou, M., 2012. "On the effect of flowing circular entities swarms on strip electrodes conductance", *Industrial and Engineering Chemistry Research*, Vol.51, pp.5615–5625.

ACKNOWLEDGEMENTS

This work was supported by the project «Innovative device for measuring milk collection rate and quality features during goat and sheep milking, exploiting an electrical impedance spectroscopy technique» (Project code: KMP6-0269405) under the framework of the Action «Investment Plans of Innovation» of the Operational Program «Central Macedonia 2014-2020», that is co-funded by the European Regional Development Fund and Greece.



IN-VITRO AND IN-VIVO DETECTION AND CHARACTERIZATION OF SUB-MILLIMETER BUBBLES IN LIQUID FLOWS THROUGH HIGHLY-SENSITIVE ELECTRICAL IMPEDANCE MEASUREMENTS

Evgenidis S.P.*, Kostoglou M., Karapantsios T.D.

Department of Chemical Technology and Industrial Chemistry, Faculty of Chemistry, Aristotle University of Thessaloniki, 54124, Thessaloniki, Greece

*sevgenid@chem.auth.gr

Keywords: void fraction; bubble size; electrical impedance; signal analysis

1. INTRODUCTION

Bubbles in liquids can be found in a variety of industrial processes, e.g. chemical and petroleum processing, oil and gas extraction and transportation, nuclear power generation, etc. They are also encountered in the human bloodstream during either open heart surgery with extracorporeal circulation due to hardware malfunction or during Decompression Sickness incidents, e.g. in scuba divers, metro workers and astronauts. Void fraction (volumetric gas fraction) and Bubble Size Distribution (BSD) are fundamental two-phase flow parameters. They enable the computation of interfacial area, which is the main parameter for the evaluation of heat and mass transfer at the interface. Additionally, void fraction and BSD information are necessary to properly set-up a Computational Fluid Dynamics (CFD) model. Consequently, the concept of void fraction and BSD has been attractive for researchers resulting in several intrusive and non-intrusive measuring techniques (Evgenidis and Karapantsios, 2015, 2018).

This work employs an EU patented electrical impedance spectroscopy technique of exceptional temporal and spatial resolution, called I-VED (EP 3005942 A1, 2016), to estimate void fraction and BSD features (average bubble size and respective standard deviation) in both in-vitro and in-vivo bubbly flow applications of low void fraction values (<0.1) and sub-millimeter bubbles. Electrical measurements are compared and validated against ultrasound/optical/pressure measurements as well as against mathematical modelling and 2D/3D CFD analysis to allow a comprehensive study of two-phase flow dynamics. Furthermore, this study contributes to the technical/functional validation and sensitivity analysis of an I-VED based device for measuring milk collection rate during goat/sheep milking.

2. MATERIALS AND METHODS

2.1 In-vitro study

Experiments were conducted in a vertical, co-current, upward, gas–liquid flow, in order to investigate the effect of liquid properties (Newtonian/non-Newtonian behavior, viscosity, salinity, surface tension), gas/liquid velocities and flow type (steady vs pulsatile) on void fraction and Bubble Size Distribution (BSD) features. Void fraction and BSD were experimentally investigated along and across the vertical pipe in a fully automated flow-loop by means of electrical (I-VED impedance spectroscopy -EP 3005942 A1, 2016- and resistance tomography), optical and pressure (absolute and differential) diagnostics. Moreover, different drift-flux model based correlations for the prediction of void fraction in such unusual conditions combining sub-millimeter bubbles and low void fractions (<0.1) were examined and optimized, while 2D and 3D CFD simulations were performed in parallel to study the evolution of void fraction and velocity profiles along the vertical pipe (e.g. Gkotsis et al., 2020; Evgenidis and Karapantsios, 2024).

2.2 In-vivo study

I-VED performance was tested on detecting: a) infused bubbles of a few tenths μm —representing Decompression Sickness conditions—in the bloodstream of swines that have similar cardio-vascular system with humans and b) post-dive decompression-induced bubbles in the body of scuba divers who performed standardized pool dives (20 minutes to a depth of 33 m) in NEMO33 pool (Brussels, Belgium). In both cases, I-VED measurements were validated against ultrasound measurements (Evgenidis et al., 2023; 2024).

3. INDICATIVE RESULTS

3.1 In-vitro study

Obtained results showed that I-VED is capable of sensing even the presence of a few micro-bubbles in a liquid flow when conducting measurements with electrodes in direct contact with the bubbly flow inside the flow-loop. Innovative hardware and signal analysis/processing have improved the sensitivity about two orders of magnitude compared to conventional techniques allowing capturing of void fraction fluctuations down to 10^{-5} . Statistical analysis of void fraction and BSD measurements revealed that the intensity of void fraction fluctuations is positively correlated with the intensity of bubble size fluctuations. Elaborating more on the obtained statistical quantities, an empirical expression was derived capable of describing ($\pm 20\%$) the average bubble size ($d_{1,0}$) with respect to two experimental ratios, **Fig. 1**. One is the ratio of the standard deviation over the average of void fraction and the other is the ratio of the gas over the liquid superficial velocity (Evgenidis and Karapantsios, 2015).

3.2 In-vivo study

In-vivo trials on swines showed that I-VED demonstrates pretty high sensitivity to detect bubbles of a few tenths μm without direct contact of electrodes and bubbly medium, over partially conductive vessel walls of an isolated animal vein (**Fig. 2**). To the best of our knowledge, this is the first time that an electrical technique accomplishes such a task (Evgenidis et al., 2023). In-vivo trials on humans showed that I-VED is capable of sensing decompression bubbles performing electrical measurements over the skin: BPF frequency component standard deviation of I-VED signal (Band-Pass Frequency-BPF: 0.5-10 Hz) is statistically significantly decreased post-dive compared to pre-dive ($p=0.008$), **Fig. 3** (Evgenidis et al., 2024).

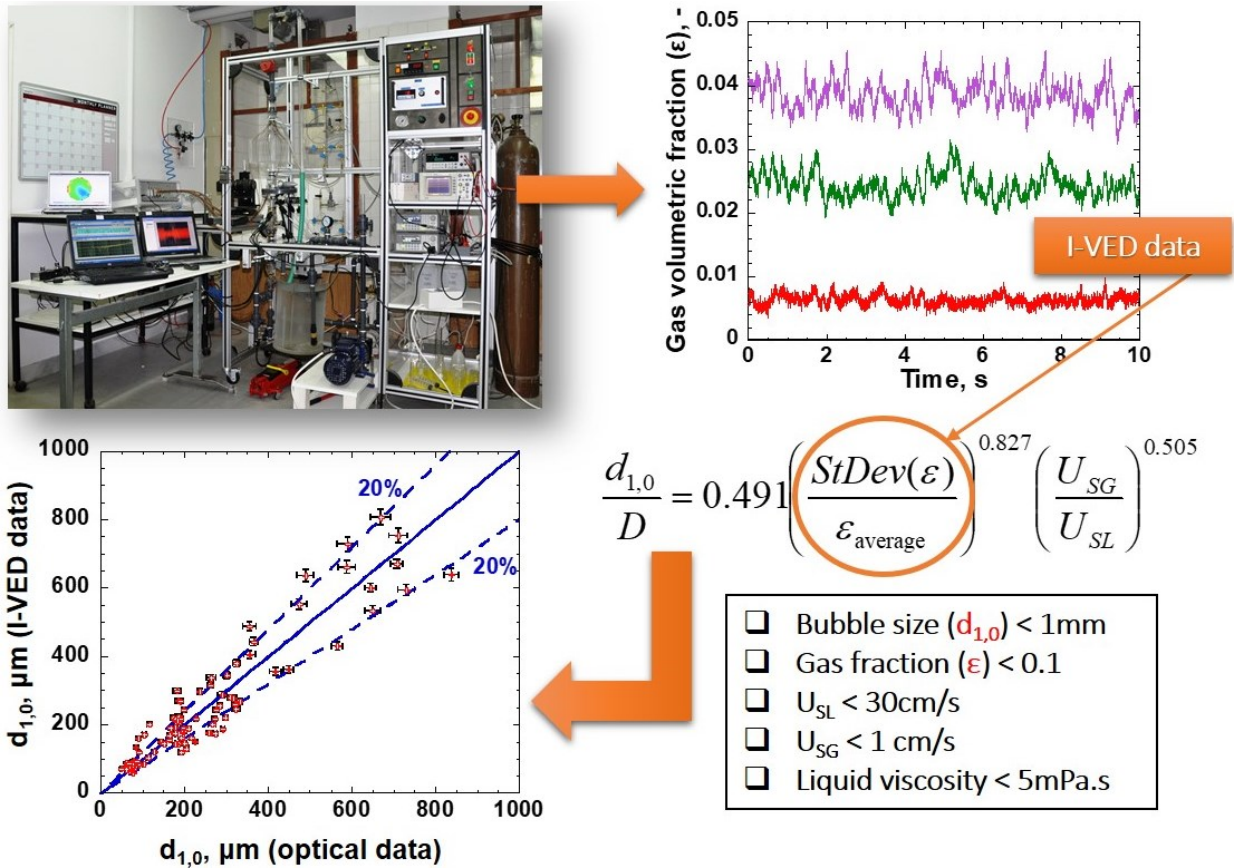


Figure 1. Empirical expression for the estimation of average bubble size ($d_{1,0}$) from void fraction (I-VED) signal features in a gas-liquid flow (D : pipe diameter, $\epsilon_{average}$: average of void fraction signal, $StDev(\epsilon)$: standard deviation of void fraction signal, U_{SG} : gas superficial velocity, U_{SL} : liquid superficial velocity) (Evgenidis and Karapantsios, 2015).

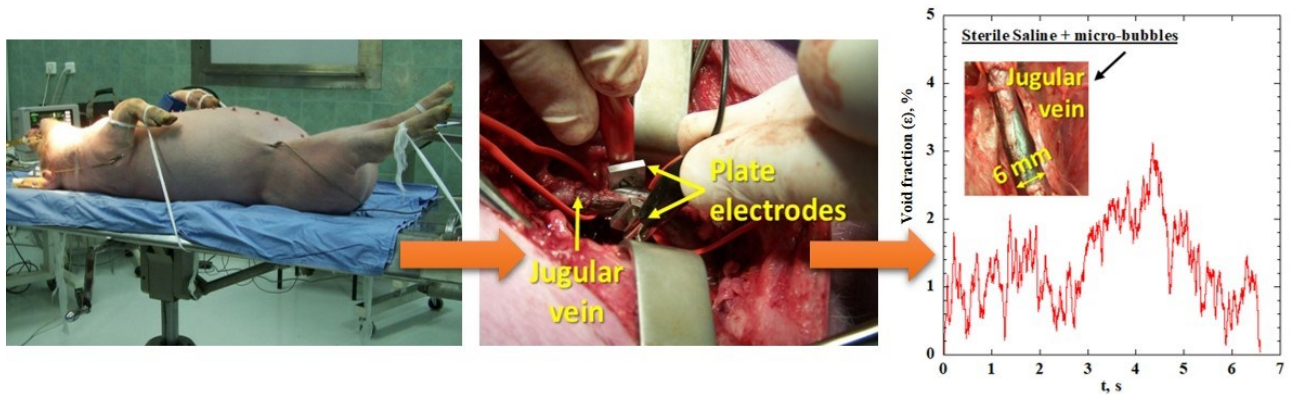


Figure 2. Detection of infused bubbles of a few tenths μm without direct contact of I-VED electrodes and bubbly medium, over partially conductive vessel walls of an isolated swine vein (Evgenidis et al., 2023).

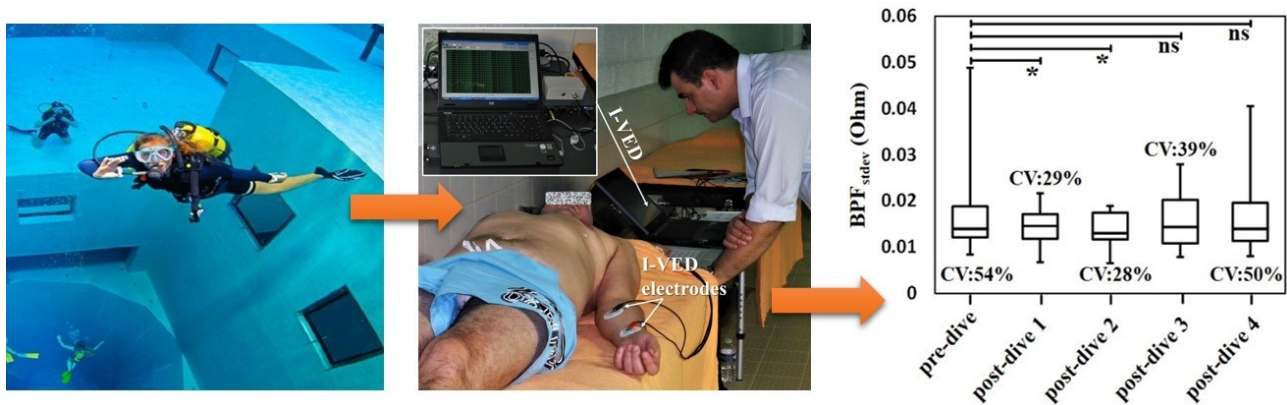


Figure 3. Post-dive detection of decompression-induced bubbles in scuba divers performing electrical measurements over the skin: BPF frequency component standard deviation of I-VED signal (Band-Pass Frequency-BPF: 0.5-10 Hz) is statistically significantly decreased post-dive compared to pre-dive ($p=0.008$) (Evgenidis et al., 2024).

4. CONCLUSIONS

I-VED is an electrical impedance spectroscopy technique for the detection and characterization of bubbles in liquids. In-vitro experiments showed not only that I-VED is sensitive enough to detect the presence of a few micro-bubbles in a liquid, but also that its high temporal and spatial resolution enables the determination of the average bubble size from electrical signal fluctuations. Also, I-VED was used for the first time in humans and operated to provide qualitative in-vivo electrical impedance measurements that may contribute to the detection of bubbles and, therefore, the early diagnosis of Decompression Sickness. Compared to ultrasound imaging, the proposed method is less expensive, not operator-dependent and compatible with continuous monitoring and application of multiple probes. Abovementioned experiments and respective data analysis provided valuable information for the adjustment and fine tuning of the I-VED based device for measuring milk collection rate during goat/sheep milking, that contributed substantially to its debugging and operation optimization.

5. REFERENCES

- Evgenidis, S.P., Chondrou, A., Karapantsios, T.D., 2023. A new phantom that simulates electrically a human blood vessel surrounded by tissues: Development and validation against in-vivo measurements. *Ann. Biomed. Eng.*, 51(6), 1284-1295.
- Evgenidis, S.P., Karapantsios, T., 2015. Effect of bubble size on void fraction fluctuations in dispersed bubble flows. *Int. J. Multiph. Flow*, 75, 163-173.
- Evgenidis, S.P., Karapantsios, T.D., 2018. Gas-liquid flow of sub-millimeter bubbles at low void fractions: experimental study of bubble size distribution and void fraction. *Int. J. Heat Fluid Fl.*, 71, 353-365.
- Evgenidis, S.P., Karapantsios, T., 2024. Increase of gas-liquid interfacial area in bubbly flows by pulsating flow conditions. *J. Chem. Eng.*, 486, 150107.
- Evgenidis, S.P., Zacharias, K., Papadopoulou, V., Theunissen, S., Balestra, C., Karapantsios, T., 2024. In-field use of I-VED electrical impedance sensor for assessing post-dive decompression stress in humans. *Undersea Hyperb. Med.*, 51, 1.
- Gkotsis, P., Evgenidis, S.P., Karapantsios, T., 2020. Associating void fraction signals with bubble clusters features in co-current, upward gas-liquid flow of a non-Newtonian liquid. *Int. J. Multiph. Flow*, 131, 103297.

ACKNOWLEDGEMENTS

This work was supported by the project «Innovative device for measuring milk collection rate and quality features during goat and sheep milking, exploiting an electrical impedance spectroscopy technique» (Project code: KMP6-0269405) under the framework of the Action «Investment Plans of Innovation» of the Operational Program «Central Macedonia 2014-2020», that is co-funded by the European Regional Development Fund and Greece.



REGION OF CENTRAL MACEDONIA
MANAGING AUTHORITY
O.P. Region of Central Macedonia



Co-financed by Greece and the European Union

STUDY OF BUBBLE CLUSTERS MORPHOLOGICAL FEATURES THROUGH ELECTRICAL IMPEDANCE AND OPTICAL MEASUREMENTS

Evgenidis S.P.*, Gkotsis P., Chatzipapa N., Karapantsios T.D.

Department of Chemical Technology and Industrial Chemistry, Faculty of Chemistry, Aristotle University of Thessaloniki, 54124, Thessaloniki, Greece

[*sevgenid@chem.auth.gr](mailto:sevgenid@chem.auth.gr)

Keywords: bubble clusters, electrical impedance, signal analysis, void fraction, bubbly flow, non-Newtonian liquid

1. INTRODUCTION

This work studies the behavior of bubble clusters rising amongst single bubbles in a non-Newtonian liquid. At total solids concentrations above 30%, milk concentrates exhibit pseudoplastic (shear thinning) behavior. During goat/sheep milking there are moments where the concentration of solids and bubbles reaches high values in the milk flow. This work contributes to the sensitivity analysis of a novel electrical impedance spectroscopy device for measuring milk collection rate during goat/sheep milking. Further, it provides useful insight on the effect of bubble clustering on milk flow. Similar phenomena are encountered in ultra-sound medical applications (e.g. dissolution of blood clots during thrombosis).

2. MATERIALS AND METHODS

Experiments are conducted in a vertical, co-current, upward bubbly flow provided by a fully controllable flow loop (Evgenidis and Karapantsios, 2015). An EU patented, electrical impedance spectroscopy technique (EP 3005942, 2016) is used for the measurement of volumetric void fraction inside the vertical pipe. It employs innovative hardware and signal processing tools to capture void fraction fluctuations down to 10^{-5} . Electrical measurements are conducted by a pair of metallic ring electrodes which are flush-mounted to the inner walls of the test tube, while the final output of data processing is a set of 60 s long electrical impedance time-series which are transformed to void fraction time-series. Electrical measurements are performed simultaneously with optical ones, employing a method described in details by Evgenidis and Karapantsios (2018), for the macroscopic characterization of bubble clusters (size and shape). The employed test liquid is a shear-thinning aqueous solution which consists of glycerol (35% v/v), NaCl (0.9% w/v) and Xanthan gum (1000 ppm). Liquid superficial velocity, U_{sl} , remains constant during the experiments (2.89 cm/s), since bubble clustering is hindered at higher U_{sl} due to stronger flow inertia. Gas superficial velocity (U_{sg}) effect on the behavior of bubble clusters is investigated employing three values (0.048, 0.217 and 0.385 cm/s). Furthermore, the influence of surface tension is examined by adding 0.01% w/w (100 ppm) of the non-ionic surfactant Triton X-100.

3. RESULTS

3.1 Bubble cluster formation

The formation of stable bubble clusters consisting of sub-mm bubbles in the gas-liquid flow of the present shear-thinning test liquid can be explained by a modified Drafting-Kissing-Tumbling (DKT) process. The DKT process has been originally proposed to describe bubble clustering for bubbles ranging from 1.5 mm to 4.5 mm (Vélez-Cordero *et al.*, 2011). Yet its basic principle is still valid if somebody aims to explain clustering of sub-mm bubbles. During the first stage of the DKT process, a trailing bubble can easily approach a leading one due to viscosity gradients that appear in the wake of bubbles rising in a shear-thinning liquid and which reduce the repulsive force from bubble vortices (drafting stage). As a result a trailing bubble eventually touches the leading one (kissing stage). The third stage (tumbling) is not favorable in sub-mm bubbles. Such small bubbles behave like rigid spheres and cannot elongate or tumble across each other. Once two bubbles form a pair, they create a wake with lower viscosity which attracts more bubbles, leading to the formation of bubble clusters; however, the increase of cluster size decreases the viscosity gradient (attaining a Newtonian-like behavior) and the growth of clusters then stops. It is worthy to note that the formation of bubble clusters consisting of sub-mm bubbles is noticed when $Mo \geq 4 \times 10^{-4}$, a threshold value suggested in literature for larger bubbles (1.5 mm - 4.5 mm) (Vélez-Cordero *et al.*, 2011).

3.2 Bubbly flow images

Fig. 1 displays representative bubbly flow images demonstrating the effect of gas superficial velocity (U_{sg}) and Triton X-100 addition on the size and shape of bubble clusters. These two features are significantly influenced by gas superficial velocity: clusters are small and quite spherical at $U_{sg} = 0.048$ cm/s, larger and 'bullet-shaped' at $U_{sg} = 0.217$ cm/s and even larger and elongated/spiral at $U_{sg} = 0.385$ cm/s. On the contrary, a decrease of liquid surface tension (by adding Triton X-100) increases slightly the size of clusters and has little effect on their shape (Gkotsis *et al.*, 2020).

3.3 Analysis of void fraction (electrical) signal peaks

Fig. 2 displays a part of a typical void fraction (electrical) time-series, where the parameters of signal peaks caused by the presence of bubble clusters are properly identified. Two specific features of void fraction peaks (ϵ_{peak} : void fraction value at the maximum point of each peak, Δt : $t_2 - t_1$) can be associated with cluster size and shape. The distribution of ϵ_{peak} shifts to higher values with increasing U_{sg} and decreasing liquid surface tension that make clusters larger, **Fig. 3**. On the other hand, Δt remains almost constant with increasing U_{sg} and decreasing surface tension. This has been attributed to the higher cluster buoyant velocity as cluster size increases. The ratio $\Sigma(\Delta t)/t_{\text{total}}$ (%) and the frequency of bubble clusters (f , s^{-1}) are two key statistical quantities calculated for each electrical impedance signal. Results demonstrate that both of them increase with U_{sg} and decrease with Triton X-100 addition (*Gkotsis et al., 2020*).

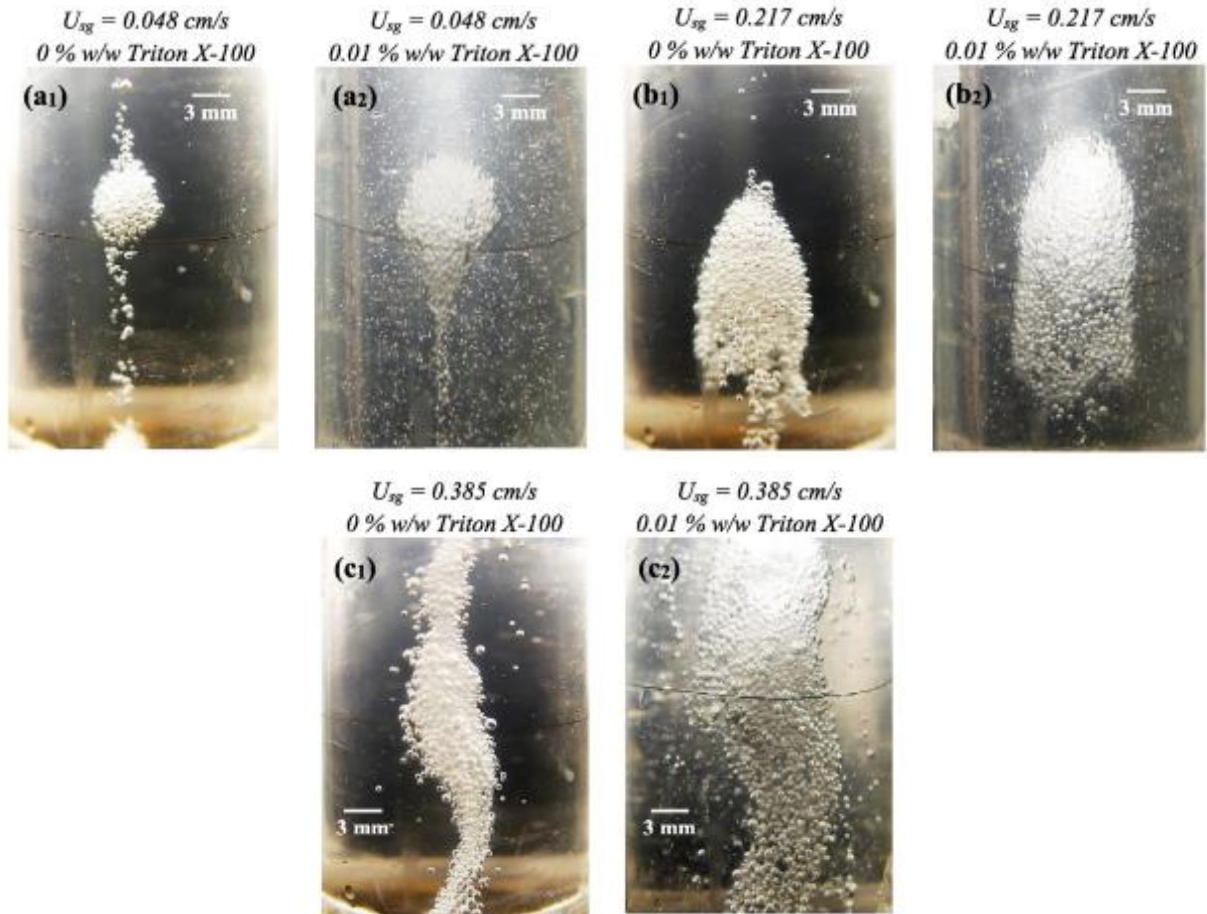


Figure 1. Effect of gas superficial velocity (U_{sg}) on bubble clusters in the absence of Triton X-100 (a₁, b₁ and c₁) and in the presence of 0.01% w/w Triton X-100 (a₂, b₂ and c₂).

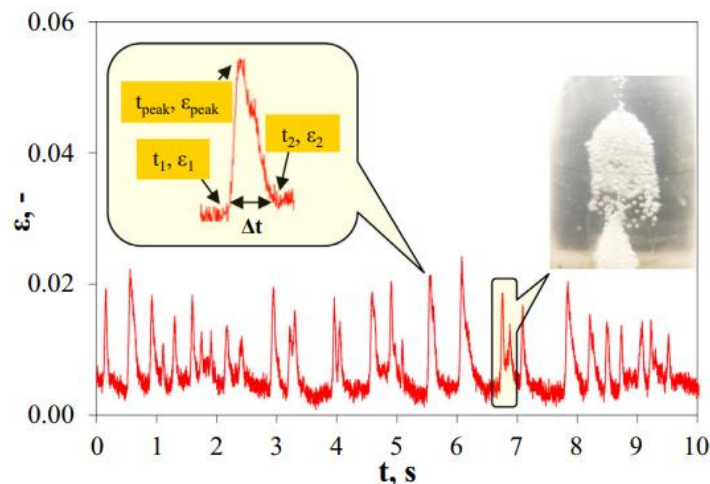


Figure 2. Definition of parameters of void fraction signal peaks caused by the presence of bubble clusters.

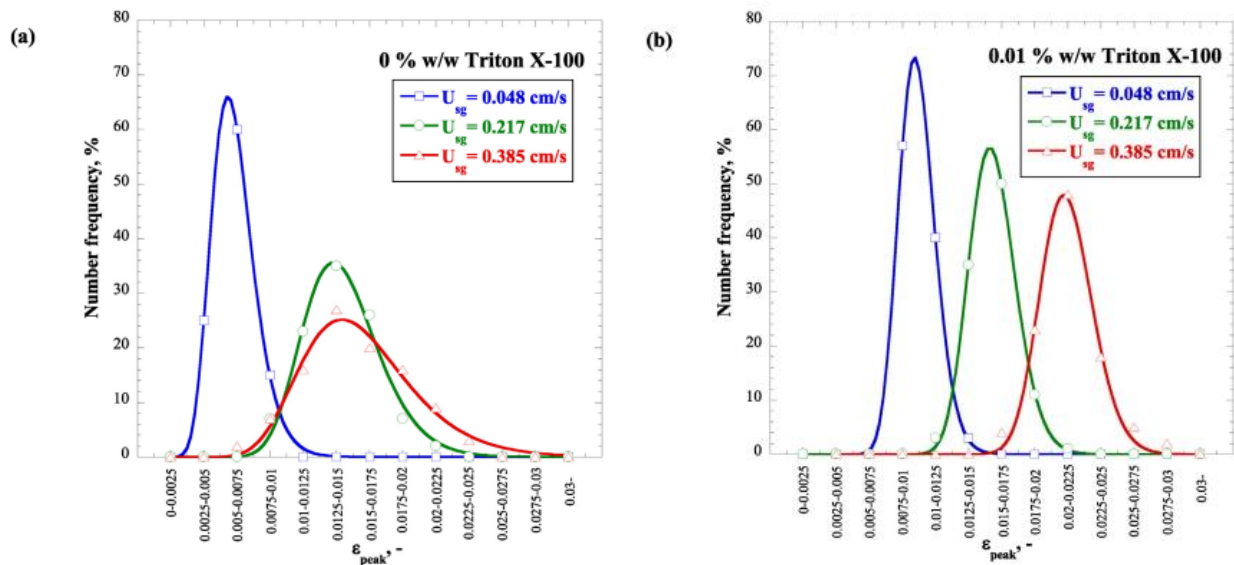


Figure 3. Effect of gas superficial velocity (U_{sg}) on ϵ_{peak} distribution: (a) in the absence of Triton X-100 and (b) in the presence of Triton X-100 (0.01% w/w).

4. CONCLUSIONS

This work examines the behavior of bubble clusters rising along with single bubbles in a shear-thinning liquid which consists of glycerol, NaCl and Xanthan gum. Clustering is strongly favored by Xanthan gum presence that renders test liquid non-Newtonian and increases liquid viscosity. The size and shape of clusters are significantly influenced by gas superficial velocity. The addition of Triton X-100, that decreases liquid surface tension, increases slightly the size of clusters and has little effect on their shape. Bubble clusters cause intense peaks on acquired void fraction (electrical) signals for all U_{sg} values and Triton X-100 concentrations and their features can be associated with cluster size and shape.

5. REFERENCES

- Evgenidis, S.P., Karapantsios, T., 2015. Effect of bubble size on void fraction fluctuations in dispersed bubble flows. *Int. J. Multiph. Flow*, 75, 163–173.
- Evgenidis, S.P., Karapantsios, T.D., 2018. Gas-liquid flow of sub-millimeter bubbles at low void fractions: experimental study of bubble size distribution and void fraction. *Int. J. Heat Fluid Fl.*, 71, 353–365.
- Gkotsis, P., Evgenidis, S.P., Karapantsios, T., 2020. Associating void fraction signals with bubble clusters features in co-current, upward gas-liquid flow of a non-Newtonian liquid. *Int. J. Multiph. Flow*, 131, 103297.
- Vélez-Cordero, J.R., Sámano, D., Yue, P., Feng, J.J., Zenit, R., 2011. Hydrodynamic interaction between a pair of bubbles ascending in shear-thinning inelastic fluids. *J. Non-Newton. Fluid Mech.*, 166, 118–132.

ACKNOWLEDGEMENTS

This work was supported by the project «Innovative device for measuring milk collection rate and quality features during goat and sheep milking, exploiting an electrical impedance spectroscopy technique» (Project code: KMP6-0269405) under the framework of the Action «Investment Plans of Innovation» of the Operational Program «Central Macedonia 2014-2020», that is co-funded by the European Regional Development Fund and Greece.



REGION OF CENTRAL MACEDONIA
MANAGING AUTHORITY
O.P. Region of Central Macedonia



Co-financed by Greece and the European Union

RECENT DEVELOPMENTS IN MEASURING THE SMALLEST VELOCITY SCALES

Philippe M Bardet^{a,*}, Charles Fort^a, Mark Yamakaitis^a, and Steven Williams^a

^aMechanical and Aerospace Engineering, The George Washington University, Washington, DC, USA

*bardet@gwu.edu

Keywords: Molecular Tagging Velocimetry, Particle Tracking Velocimetry, Integral microscopy, plenoptic 3.0

1. INTRODUCTION

The velocity length-scales at interfaces are often the smallest encountered in many flows. They drive important phenomena, such as skin friction, heat and mass transfers, etc. For example, in high-Reynolds number wall-bounded flows the viscous wall unit can be on the order of the micrometer along the hull of ships or in the core of nuclear reactors; in some boiling conditions, micro-layers can be only a few micrometers thick. Historically, it has been challenging to directly probe flows in such conditions, which has led to much empiricism in numerical models.

This manuscript presents recent developments in optical diagnostics to measure wall shear and flow dynamics in the direct vicinity of walls. The developments include the extension of molecular tagging velocimetry (MTV) to measure instantaneous wall shear stress in high-Reynolds number flows, the adaptation of Fourier integral microscopy (FIMic) to MTV and particle tracking velocimetry, and the generalization of FIMic to plenoptic 3.0.

2. MOLECULAR TAGGING VELOCIMETRY

MTV is a non-intrusive laser spectroscopy technique that provides continuous velocity profiles; this makes it well-suited to measure velocity gradients. In water, MTV has long suffered from intrinsic limitations, namely limited spatio-temporal resolutions; over the last several years, our group has significantly improved on these limitations and we are now able to measure directly the instantaneous wall shear stress in various wall-bounded flows including at high Reynolds numbers.

We rely on a two-laser (write/read) photobleaching-based MTV approach, which can be characterized as MTV based on reverse photoproduct fluorescence (Fort & Bardet, 2022). The technique involves the irreversible photodegradation of a fluorescent dye induced by intense UV illumination. The fluorescent dye molecules that are photobleached are permanently destroyed. During the read pulse, the pattern of tracers appears dark against a bright background from laser-induced fluorescence (LIF). The photobleaching is a prompt process at the fluid mechanic scale (sub-ns) and the pattern can be probed in a time-of-flight manner, limited only by the cameras and lasers.

We have demonstrated the technique with patterns on the order of 10 μm in diameter and acquisition rate of 10 kHz. By judiciously selecting the camera and lens combination, we have been able to discretize the pattern in the wall normal direction with a resolution superior to 2 μm . Figure 1 shows one MTV frame on the leading edge of a 1.6 mm plate. The spacing between beamlets is 100 μm . The camera is a streaming IDT Phoenix UHD with 5.2 μm pixel and able to stream to computer harddrive at more than 4 kHz and 11 Mpixel. Beyond the camera streaming ability that enables long recording time, its low noise and by small pixels facilitate obtaining a resolution of 2 $\mu\text{m}/\text{pixel}$ with reasonable optics (Canon 100 mm macrolens with a 2x teleconverter).

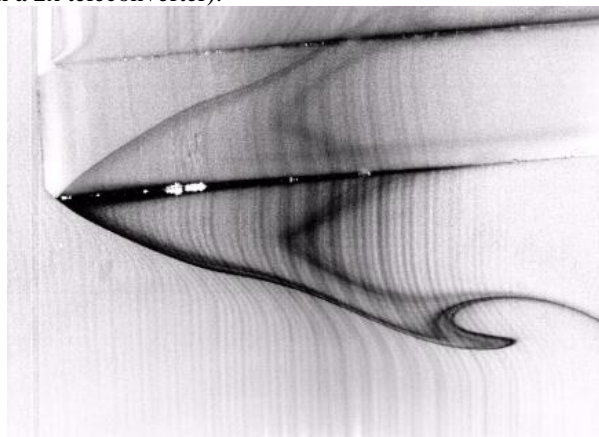


Figure 1. MTV frame. The dark lines are the deformed pattern on the leading edge of a 1.6 mm plate; flow is left to right.

3. FOURIER INTEGRAL MICROSCOPY

Plenoptic imaging is a technique that samples the angular and lateral components of the lightfield; thus, it enables to reconstruct a 3D scene with a single imager. Fourier integral microscopy (FIMic) is the latest evolution of plenoptic imaging applied to microscopy, otherwise referred to as integral microscopy. It offers the highest spatial resolution of all the integral microscopic techniques. This approach places the microlens array (MLA) at the Fourier plane (or aperture stop) of a microscope objective and the sensor one microlens focal length away (Llavador et al., 2016; Scrofani et al., 2018; Liu et al., 2020). This effectively divides the sensor into a grid of micro-images, or elemental images, of the entire imaged volume, each from a distinct perspective angle. In practice, the Fourier plane of the objective is not always mechanically accessible and a relay system is used to conjugate the objective Fourier plane with the MLA. Figure 2 shows the two configurations we have implemented to date. The first configuration uses a set of tube and relay lenses to optically position the MLA within the aperture plane of the objective, while in the second configuration, the MLA is directly inserted in the objective. That last configuration makes the system very compact. We are reporting on one implementation of each imager that are applied to MTV and PTV.

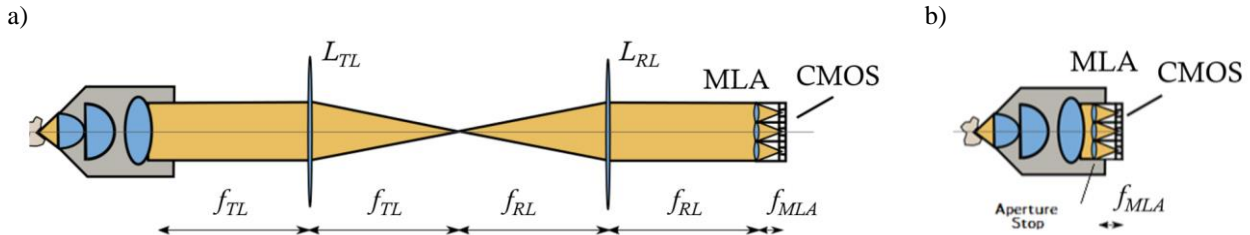


Figure 2. FIMic configurations. a) relayed system; b) compact system with MLA within the microscope objective

A high-spatio-temporal resolution system was built based on configuration of Figure 2.a). The microscope objective has a numerical aperture of 1.0, the tube and relay lenses have focal lengths of 165 mm and 200 mm, respectively. The MLA has a 2 mm pitch and 17 mm focal length; the imager is an IDT Phoenix Gold 6K high-speed camera ($6,400 \times 5,120$ 3.55- μm pixel, streaming at 1,000 fps). The combination of high numerical aperture, relay lens systems, and small pixels provide a diffraction-limited integral microscope with a 1.7 μm lateral resolution and 2.5 μm axial (or depth) resolution. The overall magnification is 5.2, resulting in 0.68 $\mu\text{m}/\text{pixel}$. Field of view is 350 μm and depth of field is 50 μm .

A 500 μm width square channel is seeded with 1.7-2.2 μm fluorescent particles. Figure 3 shows particle tracks reconstructed with LaVision Davis Shake-The-Box (STB). STB reconstruct estimates a particle centroid with a sub-pixel accuracy, which it estimates here on the order of 100 nm, which is below the wavelength of the light source (535 nm).

Configuration of Figure 2.b) was implemented to reconstruct velocity profiles along a surface with MTV. The microscope objective has a 0.4 numerical aperture. By characterizing its lens elements and performing ray tracing simulations, we were able to identify its aperture plane. Thus, the MLA is inserted directly within the objective making a very compact integral imager. The MLA has a 3.2 mm pitch and 47 mm focal length. The imager is an IDT Phoenix Gold 6K.

Rhodamine 6G dye is uniformly dissolved in water. The photobleached beamlets are generated at the focal plane of a square pattern MLA with a pitch 300 μm with frequency-tripled Nd:YLF laser (351 nm). The fluorescence signal is excited with a frequency-doubled Nd:YLF laser. Data in Figure 4 are reconstructed with Richardson-Lucy deconvolution (RLD). The overall field of view is 1 mm in diameter and the first 160 μm above the wall resolved. The RLD algorithm gives spurious reconstruction in the upper part of the depth of field.

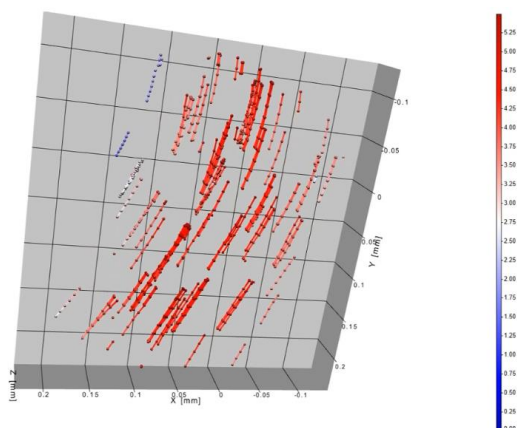


Figure 3. Sample PTV frame in micro-channel.

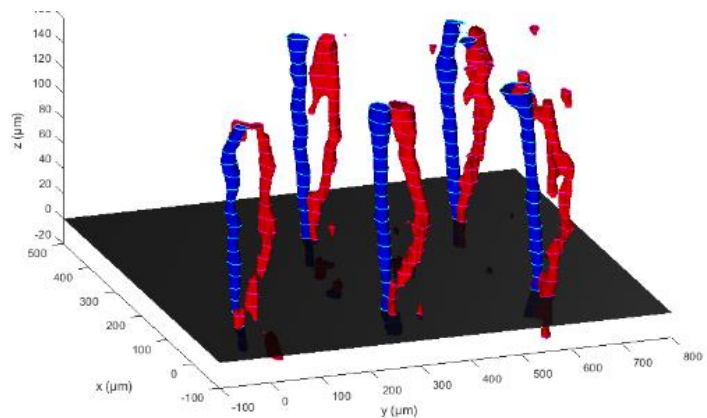


Figure 4. Sample MTV frame in a wall-bounded flow. Undeformed beams are in blue, deformed in red.

4. PLENOPTIC 3.0

We have extended the FIMic design to macroscopy. Here 4 independent views are acquired with a single imager (IDT Phoenix HD, 2.8 Mpixel, streaming at 9,800 fps). Four views are sufficient for tomographic PIV or PTV algorithms like STB. Overall, the field of view is 1 cm in diameter with 3.5 mm depth of field. The 24° angle between each view is optimized to achieve adequate depth resolution for our field of view. The overall system magnification is 0.67, which leads to resolution of $15.5 \mu\text{m}/\text{pixel}$; the diffraction limited resolution was measured at about $60 \mu\text{m}$. Note that for PTV algorithms, the particle centroid is found with a sub-pixel accuracy, which was estimated by LaVision Davis STB to be on the order of $2 \mu\text{m}$.

Sample boundary layer profiles along an oscillatory plunging rod are shown in Figure 5. This flow is Stokes second problem in an axisymmetric geometry; the oscillation frequency controls the boundary layer thickness, which is here on the order of $500 \mu\text{m}$.

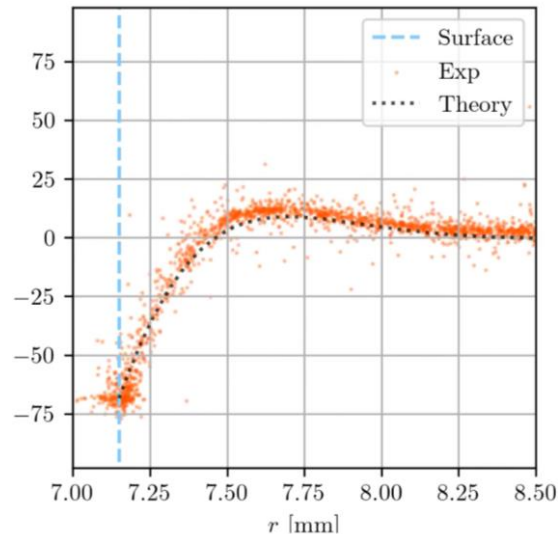


Figure 5. Sample instantaneous boundary layer profile along the plunging rod. The rod surface is the blue dashed line, the analytical solution the dotted black line, dots are experimental data point ensemble averaged over one frame.

4. CONCLUSIONS

Two configurations of Fourier integral microscopy are presented and applied to near-wall flows as well as a micro-channel flow. Fourier integral microscopy was also extended to macroscopy. Together, these configurations represent a new configuration of plenoptic imagers that we call plenoptic 3.0 to distinguish it from traditional plenoptic 1.0 and 2.0. Plenoptic 3.0 forms distinct perspective views that can be treated as mini-cameras, and thus the views can be separated and the data treated with commercially available software, such as Shake-The-Box.

The imagers were deployed with particle tracking velocimetry and molecular tagging velocimetry. In its highest resolution, the approach resolves location of particles in three-dimensions to a resolution superior to the light wavelength. New generation of high-speed streaming cameras, with small pixels, enable the data to also be time-resolved.

5. REFERENCES

- Fort, C., and Bardet, P. M. (2022). "Wall shear stress measurements in water by molecular tagging velocimetry at high spatio-temporal resolution". *20th International Symposium on Applications of Laser and Imaging Techniques to Fluid Mechanics*, Lisbon.
- Liu, F. L., Kuo, G., Antipa, N., Yanny, K., & Waller, L. (2020). "Fourier DiffuserScope: single-shot 3D Fourier light field microscopy with a diffuser". *Optics Express*, vol. 28(20), pp. 28969–28986. doi:10.1364/OE.400876.
- Llavador, A., Sola-Pikabea, J., Saavedra, G., Javidi, B., & Martínez-Corral, M. (2016). "Resolution improvements in integral microscopy with fourier plane recording." *Optics Express*, vol. 24(18), pp. 20792-20798. doi: 10.1364/oe.23.03012.
- Scrofani, G., Sola-Pikabea, J., Llavador, A., Sanchez-Ortiga, E., Barreiro, J. C., Saavedra, G., Martínez-Corral, M. (2018). FIMic: design for ultimate 3D-integral microscopy of in-vivo biological samples." *Biomed. Optics Express*, Vol. 9(1), pp. 335–346. doi: 10.1364/BOE.9.000335.

DEGRADATION OF PLASTICS IN MODEL MARINE ENVIRONMENT: OPTICAL VISUALIZATION THROUGH ADVANCED MICROSCOPY TECHNIQUES

Alessandro Marino^a, Sergio Caserta^{b,a,*}, Stefano Guido^{b,a}

^aDepartment of Chemical, Materials and Production Engineering, University of Naples Federico II, P.le V. Tecchio 80, 80125 Naples, Italy

^bCEINGE Advanced Biotechnologies Franco Salvatore, Via G. Salvatore 436, 80131 Naples, Italy

*sergio.caserta@unina.it

Keywords: Microplastics, Degradation, Polarized light microscopy, Confocal microscopy

1. BACKGROUND

The pervasive pollution of marine environments by plastics poses significant ecological threats, with degradation processes playing a crucial role in the environmental fate of these materials. Degradation of plastics also facilitates their dispersal and ingestion by marine organisms. Upon ingestion, persistent organic pollutants (POPs) and heavy metals, which can adsorb onto their surfaces, can leach into the tissues of marine organisms, leading to bioaccumulation and biomagnification through the food web, ultimately reaching human consumers, leading to potential health risks including endocrine disruption and carcinogenic effects. Microplastics, defined as plastic particles smaller than 5 mm, primarily derived from larger plastic debris, undergo complex degradation pathways influenced by exposure to ultraviolet (UV) radiation, oxygen, and environmental factors such as temperature and salinity. UV radiation initiates photo-oxidative degradation by breaking chemical bonds within plastic polymers, generating reactive oxygen species and free radicals. These radicals propagate chain reactions that lead to the formation of oxidized functional groups, such as carbonyls and hydroxyls. The degradation is significantly accelerated by mechanical abrasion, a physical process that leads to fragmentation, structural weakening, and surface erosion. The impact of waves, currents, and sediment interactions induces repeated frictions, leading to the physical fragmentation of plastic materials. This increases the surface area exposed to UV radiation and oxygen, thereby accelerating photo-oxidative processes. Abrasion also creates microfractures, further propagating the breakdown of polymer chains. Additionally, the roughened surfaces and microcracks provide enhanced habitats for microbial colonization. The presence of biofouling organisms, which further modify the surface properties of MPs, enhance the degradation rates. Recently, Sun J. et al. (2023) combined UV radiation and mechanical abrasion as degradation mechanisms, resulting in the formation of plastic particles also in the micron range. Consequently, the identification and quantification of microplastics in large volumes of marine samples pose significant analytical challenges. As highlighted by Xu J. L. et al. (2019), although Fourier-transform infrared spectroscopy (FTIR) and Raman spectroscopy offer high specificity, there is a lack of research on spectral changes during sample preparation, biofouling and degradation such as UV radiation, thermal oxidation and humidity that could alter the chemical structure of MPs through oxidative reactions. FTIR and Raman also require extensive sample preparation and are limited by their capacity to handle large quantities of environmental samples. Additionally, both techniques are constrained by their resolution limits; they may not effectively detect particles smaller than a few micrometers, thus missing a significant portion of microplastics. Polarized Light Microscopy (PLM) leverages birefringence properties to distinguish microplastics from organic and inorganic particulates, providing rapid and non-destructive analysis with relatively simple sample preparation. However, PLM is limited in its ability to provide detailed chemical information and may struggle with complex matrices where optical properties overlap. Maes T. et al. (2017) showed that Confocal Laser Scanning Microscopy (CLSM) offers high-resolution, three-dimensional imaging and the ability to perform optical sectioning, allowing for precise localization and morphological analysis of microplastics within a sample. This technique excels in providing detailed structural information, but often requires fluorescent labeling or staining, which can introduce additional preparation steps and potential artifacts.

2. OBJECTIVES

This study aims to replicate marine environmental conditions to investigate the degradation process of plastics. By simulating factors such as UV radiation, temperature, and mechanical abrasion, we can better understand the mechanisms and timescales involved in plastic degradation. After the degradation process, we employ a combination of analytical techniques to characterize the structural and morphological changes in the resulting microplastics. Polarized Light Microscopy (PLM) is used to assess variations in crystallinity and birefringence of the as received samples and the degraded ones. PLM is a valuable tool for detecting changes in the optical properties of polymers, providing insights

into how their crystalline structure evolves during degradation. CLSM is then utilized to examine the as receive samples and degraded ones at specific wavelengths, allowing us to visualize and analyze structural changes with high resolution. To quantify and evaluate the dimensional changes in the MPS, we use Image Pro Plus software. This software enables precise measurement and statistical analysis of particle size and distribution, offering a comprehensive understanding of the degradation process. By integrating these techniques, we aim to provide a detailed analysis of plastic degradation in simulated marine conditions, contributing to the broader understanding of plastic pollution and its environmental implications. This study not only highlights the degradation pathways of plastics but also demonstrates the application of advanced microscopy techniques in environmental research.

3. METHODS

In this research, a polypropylene bag was initially cut into small, uniform pieces measuring 2 x 3 cm. The samples were then exposed to UV-A radiation from a transilluminator (VilberLourmat 312nm) for a total of 45 hours, with intermittent cooling periods to prevent the temperatures from exceeding those typical of the marine environment, thereby avoiding the creation of artifacts. The sand used for mechanical abrasion was sieved to achieve a particle size range of 1 to 5 mm.

A glass flask was filled with 150 grams of the sieved sand, 100 grams of a saltwater solution composed by deionized water from Microtech Ltd. and sodium chloride sourced from Sigma Aldrich at the same concentration as Mediterranean seawater, and the UV-A degraded plastic pieces. This flask was placed in an incubator (MinitronInfors HT) set at 37°C and 190 rpm to simulate the typical summer temperature and the friction with sand typically occurring on shore. The mechanical abrasion process was carried out for a total duration of 72 hours.

The subsequent step following degradation involved sampling in glass Petri dishes, covered with a coverslip to prevent contamination. The samples were examined using an optical inverted microscope (Zeiss Axiovert 200 M) equipped with polarized light at different magnifications: 10x and 20x yielded better resolution compared to 40x. Consequently, we selected 20x magnification to achieve a more accurate image analysis in terms of size range. For confocal microscopy, the previous microscope was equipped with lasers having wavelengths of 488 nm and 543 nm (LSM 510 META) to evaluate the change in structure of the degraded microplastics in solution. Finally, image analysis conducted using Image Pro Plus allowed for the assessment of the size distribution of the MPs.

4. RESULTS

Figure 1 presents the effect of UV radiation on the PP sample showing how the degradation affects crystallinity, birefringence and structure of plastics. Once this result is reached, the sample is ready to be ulteriorly degraded due to mechanical abrasion in the glass flask.

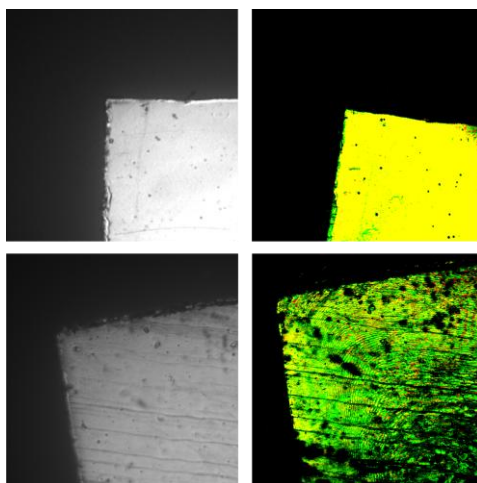


Figure 1. PLM images (left) and CLSM images (right) depicting the difference between the as received PP and the degraded one only with UV radiation.

Figure 2 shows how mechanical abrasion plays a fundamental role in the fragmentation of plastics, changing shape and dimensions

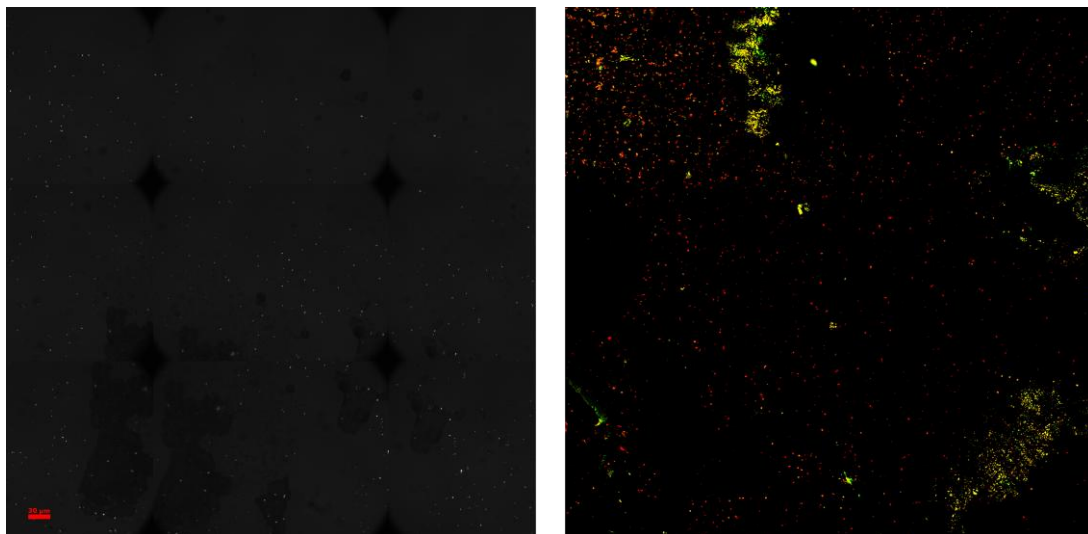


Figure 2. PLM images (left) and CLSM images (right) depicting the size of MPs at the end of the degradation process.

Figure 3 shows the results of the size distribution of MPs as obtained by image analysis.

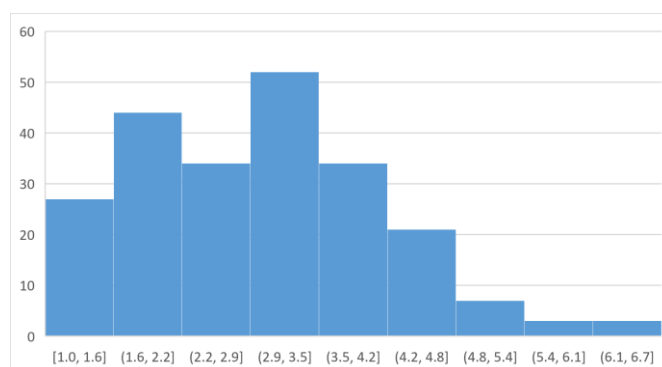


Figure 3. Size distribution of MPs diameter.

4. CONCLUSIONS

In this work we found that the time required to fragment plastics at micron range can be estimated as three whole days of exposure to sunlight and friction. The mean dimension exceeds the resolution limits of FTIR and Raman while combining PLM and CLSM gives us clearer results without a heavy sample preparation and without the use of fluorescent markers such as Nile Red. Using these techniques coupled with image analysis underscore the potential use of microscopy as a more sensitive method to detect MPs in environmental samples. This study provides a basis for analyzing the biodegradation of microplastics and how the bacteria could increase the degradation rate.

5. REFERENCES

- Maes, T., Jessop, R., Wellner, N., Haupt, K., & Mayes, A. G. (2017). A rapid-screening approach to detect and quantify microplastics based on fluorescent tagging with Nile Red. *Scientific reports*.
- Sun, J., Wang, X., Zheng, H., Xiang, H., Jiang, X., & Fan, J. (2024). Characterization of the degradation products of biodegradable and traditional plastics on UV irradiation and mechanical abrasion. *Science of The Total Environment*.
- Xu, J. L., Thomas, K. V., Luo, Z., & Gowen, A. A. (2019). FTIR and Raman imaging for microplastics analysis: State of the art, challenges and prospects. *TrAC Trends in Analytical Chemistry*.

Financial support was provided by Italian PRIN 2022 PNNRR "BREAKUP - Numerical and Experimental Investigation of Small Plastics Breakup in Complex Flows".

POSTER PRESENTATIONS	
#	Title & Authors
1	PIV experimental analysis of the gasper jet in an aircraft cabin (<i>João Gouveia and Jurandir Yanagihara</i>)
2	Effect of ZnO nanowires coating hydrophobicity on vapor film formation and friction reduction (<i>Lina Vorotinskienė, Raminta Skvorčinskienė, Vladas Šatas, Aine Povilaikaitė, Simas Račkauskas and Rita Kriūkienė</i>)
3	Experimental and numerical investigation of the multiphase flow characteristics of the in-line type separator (<i>Han Sang Mok, Jo Hae Jin, Woo Nam Sub, Lee Wang Do and Kim Young Ju</i>)
4	Contact behavior between soft wall and bubble formed near rigid wall sandwiched by soft walls (<i>Jun Matsui and Yasuhiro Sugimoto</i>)
5	Research on friction heat generation of high speed and heavy-duty rotors in turbo-expander (<i>Xiaohua Zhang, Hongbo Xu, Kongrong Li, Ning Shi, Shun Qiu, Changlei Ke, Ly Xiong, Nan Peng, Liqiang Liu, Linghui Gong and Bin Dong</i>)
6	Experimental Study on the Rotor Dynamic Characteristics of High-Speed Heavy-Load Cryogenic Turbo-Expanders during the Speed-up Process (<i>Changlei Ke, Hongbo Xu, Kongrong Li, Xiaohua Zhang, Bin Dong, Lianyou Xiong, Nan Peng, Shun Qiu, Ningyu Shi,</i>
7	Mathematical description of the temperature-effective heat capacity relationship obtained by differential scanning calorimetry for phase change modelling (<i>Martin Zálešák, Pavel Charvát, Lubomír Klimeš and Jakub Kúdela</i>)
8	Experimental investigation on thermal performances of the cold plates in a pump driven two-phase cooling system (<i>Xu Hongbo, Liu Ming and Kongrong Li</i>)
9	Modeling of effective heat insulation methods for vertical farming in a greenhouse (<i>Vitaly Haslavsky and Helena Vitoshkin</i>)
10	Modeling and investigation of the turbulent wake recovery in the wind farm area (<i>Vladislav Kovalnogov, Andrei Chukalin, Maria Kornilova and Ruslan Fedorov</i>)
11	Development of stator sector mock-up of a hairpin electric motor for detailed thermal testing of direct cooled end-windings (<i>Steven Vanhee, Jasper Nonneman, Frederik Desmet and Michel De Paepe</i>)
12	Velocity Measurements of Thin Falling Films Using Nuclear Magnetic Resonance (<i>Georges Saliba, Jan Korvink and Jürgen Brandner</i>)
13	Visualization Measurement of Mixing Process of Viscous Liquid Contained in a Rotating Cylindrical Vessel (<i>Tomoya Taguchi, Tetsuro Yanaseko, Masaki Hiratsuka and Koji Hasegawa</i>)
14	Effects of the rheological properties of a viscoplastic fluid on the slug flow pattern (<i>Daiane Miekó Iceri, Gláucio Kenji Matoba, Roney Leon Thompson, Annie Fidel-Dufour and Marcelo Souza Castro</i>)
15	Experimental Measurement Technique for the Determination of Flow and Heat Transfer Characteristics of Impinging Jets in Industrial Thermoprocessing Plants (<i>Jan Erik Menzler, Eileen Trampe, Nico Rademacher, Dominik Büschgens and Herbert Pfeifer</i>)
16	Evaporation-induced emulsification and phase separation dynamics of ternary droplets in acoustic levitation (<i>Misaki Mitsuno and Koji Hasegawa</i>)
17	Application of the optical flow method in PIV images: non-newtonian fluid flow in a horizontal pipe (<i>Helder Lima Moura, Gláucio Kenji Matoba, Daiane Miekó Iceri, Eshail Miguel Vallejos Melendres, Roney Leon Thompson, Annie Fidel-Dufour and Marcelo Souza Castro</i>)
18	Heat transfer characteristics of water-oil plug flow in a horizontal circular tube (<i>Takashi Morimoto, Toshikazu Esaki, Takato Kimura and Hiroyuki Kumano</i>)
19	Exploring phase separation dynamics in block copolymer solutions: innovative experimental techniques with thermodynamic analysis (<i>Irene Perna, Gaia Paradiso, Rosalia Ferraro, Marta Gamberoni, Salvatore Coppola and Sergio Caserta</i>)
20	Experimental investigation of the influence of ethanol/water mixture on nucleate pool boiling for structured surfaces (<i>Panagiota Xanthopoulou, Axel Sielaff and Peter Stephan</i>)

21	Impact and boiling of single and multiple droplets on a heated solid surface (Tianhan Chen and Koji Hasegawa)
22	Intermittency of flow meandering in a gap of a model of a peripheral subchannel of a fuel rod assembly (Maxim Shestakov and Mikhail Tokarev)
23	Machine learning of scattering signals in optical fiber to identify coolant leakage location of fusion reactor (Shun Nukaga , Daiki Mori , Tsuyoshi Kodera , Masahiro Furuya and Takuya Katagiri)
24	Preliminary experimental and computational investigation of a laboratory gas turbine combustor (Gonçalo de Sousa Pina Pacheco , Afonso Santoalha , Bruno Pinto , Miguel Mendes and Pedro Coelho)
25	Experimental study on freezing of supercooled water droplet impacting on curved cold surfaces (Shinan Chang , Zhaoyang Sun and Shuyi Zhang)
26	Study of droplet motion and freezing under shear of cold air streams (Shinan Chang , Xibo Qiao and Shuoshuo Wang)
27	Study of castor oil/diesel emulsified fuels: Behavior of a single droplet in high temperature environments using image analysis methods and combustion characteristics of emulsions in diesel engines (Shuhn-Shyung Hou , Chun-Ta Chen , Wei-Cheng Chiu and Ming-Da Lai)
28	Experimental and numerical study to investigate subcooled boiling in minichannels (Beata Maciejewska and Magdalena Piasecka)
29	Boiling heat transfer research during flow in rectangular minichannels (Magdalena Piasecka , Sylwia Hożejowska and Artur Piasecki)
30	Steam explosion retardant for molten Lead-Bismuth to stabilize vapor film (Masahiro Furuya and Takahiro Arai)
31	Effects of refrigerant charge in heat pump on thermohydraulic performance of microchannel evaporator (Georges El Achkar , Jalal Faraj and Mahmoud Khaled)
32	Effect mechanism of 5-Amino-1H-Tetrazole on the pyrolysis and combustion behaviors of Nano-Al@Fe ₂ O ₃ thermite reaction (Jiu Chen)
33	Investigation of the effect of nonmetallic oxides on the properties of 5-Amino-1H-Tetrazole: microscopic morphology, kinetics, and thermal safety parameters (Si-yuan Zhou , Xuan Li , Dan Zhang , Bin Li , Li-Feng Xie)
34	Vitrification of biological material by immersion in liquid nitrogen and slush:an experimental study (Jacqueline B. Copetti , Alisson S. Silva , Matheus Chanan , Jeferson D. Oliveira , Elaine M. Cardoso , Mario H Macagnan , Andre C Monteiro , Henrique Vidaletti and Karolyn Ogliari)
35	Flow boiling heat transfer of propane (HC-R290) in multiport minichannels (Jeferson D. Oliveira , Jacqueline B. Copetti , Priscila F. Silva , Mario H. Macagnan and Elaine M. Cardoso)
36	Effect of stainless-steel surfaces on biofilm formation: implications during electrical impedance spectroscopy measurements (Dimitrios Avgoulas , Maria Petala , Margaritis Kostoglou and Thodoris Karapantsios)
37	Simulating bubble size effect on electrical signal fluctuations (Ourania Oikonomidou , Sotiris Evgenidis , Thodoris Karapantsios and Margaritis Kostoglou)
38	A technique for calculating the electrical resistance of ring electrodes in a domain with many bubbles (Margaritis Kostoglou , Sotiris Evgenidis and Thodoris Karapantsios)
39	Study of bubble clusters morphological features through electrical impedance and optical measurements (Sotiris Evgenidis , Petros Gkotsis , Nikoleta Chatzipapa and Thodoris Karapantsios)
40	Exploring fluid dynamics in cardiovascular system with electrical impedance measurements (Nikoleta Chatzipapa , Sotiris Evgenidis , Kostas Zacharias , Georgios Karagiannis , Michail Doumas , Thodoris Karapantsios)
41	Degradation of plastics in model marine environment: optical visualization through advanced microscopy techniques (Alessandro Marino , Sergio Caserta and Stefano Guido)



ExHFT-10

10th World Conference on Experimental Heat
Transfer, Fluid Mechanics and Thermodynamics



RESEARCH COMMITTEE
ARISTOTLE UNIVERSITY OF THESSALONIKI



ExHFT-10

10th World Conference on Experimental Heat Transfer, Fluid Mechanics and Thermodynamics

